

# nature

## POLAR OPPOSITE

Evidence for a temperate  
rainforest near the South  
Pole 90 million years ago

**High stakes at sea**  
Will treaty to protect  
ocean resources  
hamper research?

**Chemical switch**  
Light turns neutral  
radical into powerful  
reducing agent

**Behind your back**  
Visualization of the  
clock that governs  
spine formation

© 2020 Nature  
nature.com



## Researchers: show world leaders how to behave in a crisis

**Scientists are dropping everything to team up and fight COVID-19. Presidents and prime ministers should, too.**

**A**lthough the coronavirus pandemic has become a threat to every country on Earth, world leaders are all at sea – showing few signs that they wish to cooperate genuinely to combat it. By contrast, tens of thousands of researchers from different disciplines and countries have joined research and public-health efforts to fight COVID-19 (see page 13). They are working across continents, lending their time, ideas, expertise, equipment and money to the emergency public-health effort. They are providing virus testing facilities; donating personal protective equipment; designing and manufacturing ventilators and other breathing apparatus. And when it comes to the research effort itself, thousands of volunteers from all over the world are enthusiastically signing up to say they are available to do what they can.

University-based laboratories such as those at the Broad Institute of MIT and Harvard in Cambridge, Massachusetts, and at the National University of Colombia in Bogotá, are carrying out COVID-19 tests. That said, more universities with medical schools need to provide access to virus testing facilities.

The emergency response to the pandemic is also creating new types of collaboration. For example, researchers and clinicians in the United Kingdom, China and Italy have been working at speed with engineers from Formula 1 motor racing. In the space of a week, they have managed to reverse-engineer a device that helps people with serious lung infections to breathe more easily.

The breathing aid uses a method known as continuous positive airway pressure. It works by supplying people experiencing breathing difficulties with relatively small but continuous amounts of air, and it has the potential to reduce the numbers of people needing ventilators in hospitals. We urge the project's partners to publish and share their designs so that the device can be tested globally, and so that it can eventually be made available to health authorities in low- and middle-income countries.

The COVID-19 research effort also got a welcome boost. Researchers from around the world have set up an online platform for those who want to volunteer for research-related tasks. The platform, Crowdfight COVID-19, matches volunteers to researchers who have specific tasks or needs – anything from transcribing data from notebooks and searching the literature, to providing specific expertise. As this editorial went to press, Crowdfight



Clinicians and automotive engineers are jointly developing breathing aids.

**It is only a matter of time before world leaders will have to step up.”**

COVID-19 had attracted more than 35,000 volunteers.

These efforts are important because world leaders need to see that international coordination on COVID-19 is thriving. Presidents and prime ministers are moving too slowly, in stark contrast to their response to the financial crisis of 2008, when heads of government, ministries of finance, central banks and other multilateral lending agencies got together and agreed what needed to be done.

Although different funding agencies are collaborating on coronavirus research, there is less consensus at the highest levels of government, and most countries seem to be making independent decisions about how to protect their citizens.

As infections and deaths continue to rise, it is only a matter of time before world leaders will have to step up. They have no choice, because there's little point in extinguishing the virus in one country when it's exploding elsewhere. A genuinely global response is needed – and world leaders must follow the fine example being set by researchers.



## Women's History Month: celebrate more researchers

**This year's event was derailed because of COVID-19. Next year, let's hear about more female scientists, clinicians and engineers.**

Last week, academic and performance artist Colleen Webster was looking forward to doing her one-woman show on the life of the biologist, science writer and environmental pioneer Rachel Carson. "She was shy. She was humble. Devoted to family. Committed to research and to protecting nature. That, and she changed the world," Webster told *Nature* from her home in Maryland.

With coronavirus raging across the United States, Webster's performance at Harford Community College in Bel Air, Maryland, had to be postponed. Instead, she recorded a short video, with a promise to be back performing live as soon as conditions allow.

Had it gone ahead, the play would have been one of hundreds of events during Women's History Month, commemorating and celebrating women's contributions to society. Women often have to fight at great cost to make themselves heard, and in some cases their achievements are overlooked, underplayed, denied or undermined by male colleagues – and by some historians, too.

Today's environmental regulators – including ministries and environmental-protection agencies – can trace some of their lineage to the movement inspired by warnings in Carson's 1962 book *Silent Spring*. But Carson endured persistent personal and sexist attacks from the chemical industry and from elected politicians who supported the industry. The attacks also questioned the careful research that had led to her landmark conclusion that the pesticide DDT was killing not only insects, but also the birds that feed on those insects.

The severity of the attacks prompted a book review in *Nature* to call for an end to "impugning her scientific quality" (C. W. Hume *Nature* 18, 117; 1963). The review added: "She rests her case not on vague generalizations but on concrete instances, and authenticates it with forty-eight pages of references to scientific literature."

Prejudice was a constant in the life of double Nobel laureate Marie Curie, too, as the British actor Rosamund Pike powerfully demonstrates in the biopic *Radioactive*. The film premiered in London on 8 March – International Women's Day – but, sadly, it is likely that few people will be able to see it on the big screen, because cinemas worldwide are closing their doors.

But it isn't only well-known scientists whose recognition is lacking during this event. More also needs to be done



**Silent Spring** author Rachel Carson helped inspire the global green movement.

**Let's ensure that the achievements of all women are recognized."**

to highlight the contributions of women from low- and middle-income regions, and those from under-represented or minority groups in their countries. The lack of such recognition is surprising, considering the hard work being done to update Wikipedia pages with profiles of female researchers, as well as the increasing trend to call out sexism and discrimination in science, past and present.

In the United States, the main coalition of organizations behind Women's History Month – including the Smithsonian Institution, the US National Archives and Records Administration and the US National Endowment for the Humanities – have research in their DNA. It shouldn't be beyond them to more actively and strategically highlight a wider range of contributions and achievements from women in research, to feature alongside the other professions.

At a minimum, they need to make it easier for readers to find researchers or scientists on the official Women's History Month website ([go.nature.com/2xysrj4](https://go.nature.com/2xysrj4)). At present, the website hosts links to exhibitions and collections highlighting researchers, but a reader searching for female researchers would have to scroll through pages of individual entries from many different professions. And often, these links are to existing content – rather than bespoke material.

The cancellation or postponement of many events celebrating Women's History Month because of the coronavirus is undoubtedly a setback. As planning begins for next year's events, institutions should do more to identify and celebrate women who made important contributions to discovery, invention and innovation. And *Nature* is keen to help.

Women are making history right now as they work intensely – increasingly as equal partners – in the global effort to research and understand the devastating coronavirus pandemic. Let's ensure that the achievements of all women are recognized, recorded and hopefully one day celebrated, so that the history being made today is recorded more accurately than how it was in the past.



# World view

## We practised for a pandemic, but didn't brace



By Ian Boyd

**Unheeded lessons from simulations of health and other disasters could still assist recovery.**

**P**lanners have known that something like COVID-19 would come, even if they could never be sure when or from where. It is hard for politicians to garner the social licence to prepare for catastrophes that people see as unlikely and far from their daily lives.

From 2012 to 2019, I was a chief scientific adviser – a technocratic expert – in the UK government. When an emergency did happen, such as the release of a nerve agent in the city of Salisbury in 2018, I knew that real people might die if I made mistakes.

I took part in simulated exercises to prepare my country for the practical, economic and social shock waves from rare but devastating events – volcanic eruptions that affect whole hemispheres, meteor strikes, zoonotic epidemics and other calamities. I recall a practice run for an influenza pandemic in which about 200,000 people died. It left me shattered.

We learnt what would help, but did not necessarily implement those lessons. The assessment, in many sectors of government, was that the resulting medicine was so strong that it would be spat out. Nobody likes living under a fortress mentality.

Two messages were clear. First, that we were poorly prepared. Second, that governments would quickly be called on to cover the damage. They are the insurers of last resort, even if they rarely quantify and plan for those risks. Our experience of COVID-19 is showing just how true this is, and suggests what we should do once recovery begins.

My experiences also highlighted two priorities. One is that the teams fighting COVID-19 need resilience. Health-care specialists are the most vulnerable, but people throughout government are under strain. Politicians, specialists and others must cope with mental exhaustion, something most people never experience or witness. They are just flesh and blood, with family to worry about, and they get sick. Indeed, we have already seen politicians and government experts across the world fall ill. We need contingency plans to keep government functional at all levels.

The other priority is getting people to respond well to interventions, especially changes to routine. This is one of the biggest unknowns in these scenarios, and yet compliance can be the most crucial factor in determining whether an intervention works. Balancing lockdown against the social licence to act as one sees fit is essential. Ideally, policy implementers would land the perfect response at the first try, but this almost never happens. It's messy and full of uncertainty. This can make the government seem indecisive, as we've seen as some governments shift their



**A successful response uses social forces such as peer pressure and altruism to help people adapt."**

position on the role of herd immunity or whether alcohol outlets counted as 'essential services' that can remain open when other shops closed. But being flexible is actually a strategic imperative.

After the first few days (if that) of emergencies such as COVID-19, there is no manual to follow. It is important to learn from previous epidemics, as well as to respond to the evidence emerging in real time. But every country will require its own approach, even if the same epidemiological principles for reducing transmission apply everywhere. Plans provide only a template – command and control, reserve personnel and resources, computer models and communications tools and so on. How these are deployed and coordinated needs to be highly fluid.

The priority in all instances is to get ahead of this fast-moving disease. This means looking beyond purely technical measures such as tests, therapies and vaccines. A successful response uses social forces such as peer pressure and altruism to help people adapt to changing circumstances. It delivers messages and support that promote self-reliance rather than encourage people to fall back on stressed state support. Cultures and communities used to providing some of their own services (for example, neighbourhood-watch programmes) often fare better than those accustomed to relying on state support.

Recovery, when it eventually happens, is going to bring fresh challenges. In New Orleans, Louisiana, flooding led to long-term mental-health problems; in Salisbury, it took more than a year of diligent cleaning to return parts of the city to public use.

While I was chief scientific adviser at the UK Department for Environment, Food and Rural Affairs, much of the talk while planning for Brexit was about keeping food, drugs, fuel and so on available. It showed how little we knew about those vulnerabilities. If they fail, many of our life-support systems, such as the water supply, fail, too. Ironically, Brexit planning might help the United Kingdom to tackle the greater challenge of COVID-19. We need to start planning now for how we will rebuild.

Despite financial safety nets spread out by some governments, we should not expect our systems of resources and service provision to bounce back to the way they were. COVID-19 is bringing systemic change on a global scale.

Having been faced with our weaknesses, I hope we see a shift in values so that we are less likely to continue with our unsustainable rates of resource consumption, assumptions that there will always be a benevolent government to fall back on and disregard for vulnerabilities attributable to climate change.

COVID-19 might be just a wake-up call: let's use it to rebuild our systems into something more resilient.

**Ian Boyd** is a biologist at the University of St Andrews, UK. [ilb@st-andrews.ac.uk](mailto:ilb@st-andrews.ac.uk)



# News in brief



## TENS OF THOUSANDS OF SCIENTISTS JOIN THE FIGHT AGAINST CORONAVIRUS

As they shutter their labs indefinitely, tens of thousands of researchers are volunteering to help fight the pandemic in any way they can. Working around the clock, scientists at the Broad Institute of MIT and Harvard in Cambridge, Massachusetts, can run about 2,000 COVID-19 tests per day (pictured). In places where testing is still scarce – which is to say, in much of the world – their actions can provide crucial relief to public-health systems stretched to their limits.

Universities are organizing, researchers are banding together, and efforts to get volunteers and equipment where they are most needed are in progress around the globe. “All of the people who are now suddenly not working have skills that can be applied,” says Michael Monaghan, a molecular ecologist at the Leibniz Institute of Freshwater Ecology and Inland Fisheries in Berlin.

The Association of American Universities, a consortium of 65 leading US research institutions based in Washington DC, has used Twitter to urge its community members to donate spare personal protective equipment to hospitals and medical facilities. Many have heeded the call.

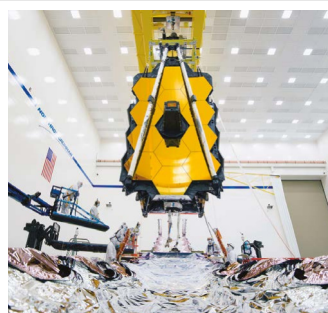
## BUSH-FIRE SMOKE LINKED TO HUNDREDS OF AUSTRALIA DEATHS

Researchers estimate that smoke pollution probably killed more than 400 people from November to February during the unprecedented bush fires across southeast Australia. Thirty-three people were killed in incidents directly related to the fires.

Air-pollution researcher Fay Johnston at the University of Tasmania in Hobart led a team that collected data on the average number of emergency-department admissions, hospitalizations and deaths on any given day. The researchers mapped detailed data on air-pollution levels from 1 October to 10 February and modelled how these would have increased the emergency admissions.

Their model suggests that there could have been around 417 additional deaths and 1,305 emergency-department admissions for asthma attacks over the period of the fires. An extra 3,151 people could also have been admitted to hospital for heart and respiratory problems.

The results are reported in *The Medical Journal of Australia*, and are the first published estimate of the scale of the medical impact of the bush-fire smoke (N. Borchers Arriagada *et al.* *Med. J. Aust.* <http://doi.org/dqrg>; 2020). Johnston calculates that the haze affected around 80% of Australia’s 25 million people, some for many weeks at a time.



## OUTBREAK COULD DELAY SPACE TELESCOPE LAUNCH

The world’s most expensive telescope is the latest project to fall foul of the coronavirus pandemic. The James Webb Space Telescope (pictured) was supposed to launch in March 2021, but faces possible delays because NASA halted most work on the US\$8.8-billion telescope on 20 March. The telescope had been going through final assembly and tests in Southern California – a region now locked down to stop people spreading the coronavirus.

“Delaying launch is absolutely the right thing to do, if it will keep the people working on the mission safe,” says Zachory Berta-Thompson, an exoplanet researcher at the University of Colorado Boulder. “We astronomers can continue to be patient.”

The hold-up adds to a long list of woes for the Webb telescope, which has experienced years of delays and cost overruns.

NASA is pushing ahead with work on its Mars rover, slated to blast off between 17 July and 5 August. If it misses the launch window, the mission must wait two years to try again. They are doing “heroes’ work” in keeping the mission on track for a July launch, said Thomas Zurbuchen, NASA’s head of science.

The European Space Agency has already delayed a Mars rover it planned to launch in July, in part because of the outbreak.

## UNIVERSITY PAYS MILLIONS IN SEXUAL-HARASSMENT SETTLEMENT

The University of Rochester in New York has agreed to pay a US\$9.4-million settlement to researchers who sued the institution over how it handled allegations of sexual harassment against a cognitive scientist. The settlement, announced on 27 March, brings to a close one of the most prominent harassment cases at a US university.

The nine researchers sued the institution in December 2017 over its response to allegations that Florian Jaeger, a professor in the department of brain and cognitive sciences, had sexually harassed students.

The researchers – who include former faculty members and a former student who collectively filed complaints against Jaeger on behalf of other students – argued that the university retaliated against them for reporting Jaeger, harming their careers.

In 2018, the university commissioned an investigation into the allegations against Jaeger, which cleared him of the most serious complaints. Jaeger, who continues to deny the substance of the allegations made against him, was not a party in the suit and is still employed at the university.

University spokesperson Sara Miller confirmed the amount of the settlement. “No party to the settlement admitted liability or fault,” she said. “The university is committed to providing a safe and inclusive environment for its students, faculty, and staff.”

All nine plaintiffs have left the University of Rochester.



# News in focus



ALBERTO PIZZOLI/AFP/GETTY

Clinical research has been disrupted as hospitals devote more resources to caring for people critically ill with COVID-19.

## CORONAVIRUS SHUTS DOWN TRIALS OF DRUGS FOR MULTIPLE OTHER DISEASES

Studies grind to a halt as fears of health-care shortages and risk of exposure put the brakes on clinical research.

By Heidi Ledford

**W**hen 2020 began, Neena Nizar and her family were poised to harvest the fruits of a decade of hard work and sacrifice: a clinical trial of an experimental treatment for her two sons' rare genetic disorder that was slated to start before the year's end.

"I can't even put into words what we've been able to do to get to this point," she says. "My kids have given bone biopsies; I gave up my job and moved to a new country. We've just been going, going, going."

Then came COVID-19. Now, Nizar wipes

away tears in her Nebraska home as she reads a message from researchers at the US National Institutes of Health. Work to assess the toxicity of the experimental therapy in animals has stalled because laboratories have been forced to close. The same might be true, she has heard, of the firm hired to manufacture the drug for clinical testing.

Nizar's sons have a painful degenerative disorder called Jansen's disease, which has hampered their bodies' ability to regulate calcium and phosphate, causing kidney damage and bone deformations. Her older son, who is 11, has had at least one operation every year for the past five years. The longer he has to wait to

receive the experimental treatment, the less likely it is to work.

"My son asks me all the time, 'So when are we doing this trial? When can I? I don't want to feel this pain anymore,'" Nizar says. "I feel like we were chugging along on a train and then somebody dropped a huge boulder on it."

Scientists are rushing to launch clinical trials of experimental vaccines against the coronavirus, and treatments for COVID-19. But as hospitals brace for an onslaught of critically ill patients and laboratories worldwide are disrupted, researchers have had to shelve clinical trials of therapies for other illnesses.

"We're going to see a nearly complete



## News in focus

close-down in clinical research,” says Tim Dyer, chief executive of Addex Therapeutics, a biotechnology company based in Geneva, Switzerland. “The health-care systems will simply be overloaded.” On 18 March, Addex announced that it would delay the start of a clinical trial to treat involuntary movements in people with Parkinson’s disease.

At Yale University in New Haven, Connecticut, lung-cancer researcher Roy Herbst says clinical trials for cancer have been cut to “almost zero” and are allowed only when a participant is deemed to have exceptional need.

“The whole process has really ground to a halt,” he says, “and I feel bad because there are patients who might have benefited from those trials.”

But the measures are necessary, he adds. Many people with advanced cancer are vulnerable to infection, and trips to the clinic for treatment and assessments could be deadly if patients are exposed to the coronavirus.

Herbst has had to ask three-quarters of his colleagues in the oncology department at Yale to stay away from the hospital to minimize their risk of infection. Instead, they are being held in reserve to treat people with COVID-19 if the first round of clinicians become infected. Even routine procedures such as biopsies, sometimes required for enrolment in a clinical trial, are now difficult to schedule as hospitals struggle with personnel and equipment shortages.

### Agencies adapt

Government agencies have released guidance for investigators who need to suspend or modify trials. The US Food and Drug Administration, for example, has issued guidance for trials that might have to pause, change their study plans or make do with incomplete data because of the COVID-19 pandemic. Ethics committees are working overtime as researchers file requests to alter their clinical-trial plans in ways that minimize how often participants need to venture into the clinic, says Barbara Bierer, who directs the Multi-Regional Clinical Trials Center of Brigham and Women’s Hospital and Harvard in Boston, Massachusetts.

Agencies and funders have shown remarkable flexibility, says Charles Blanke, an oncologist at Oregon Health & Science University in Portland and leader of the publicly funded SWOG Cancer Research Network. The US National Cancer Institute announced on 23 March that it would allow the investigators it funds to assess trial participants’ health remotely where possible. Some doctors’ assessments may be carried out over video calls, and some audits of clinical-trial procedures will be conducted virtually, with inspectors examining the paperwork online rather than visiting the clinic to assess standards.

The rapid release of these guidelines is a particular relief because many clinical-trial

sites did not plan for a pandemic such as that of COVID-19, says Blanke, despite warnings from experts that one was inevitable. After this outbreak, he says, clinical researchers will be better prepared, and the increased capacity for virtual visits will be a lasting boon to both researchers and patients.

For now, it’s unclear what long-term effects the outbreak will have on drug regulation. “There will be a disruption, obviously,” says Bierer. “And whether that delay manifests in delaying final approvals is unknowable today.”

It’s that uncertainty that haunts Nizar. She worries that her concerns might sound selfish

in the face of the global suffering caused by the pandemic. But she also knows that the delay to her clinical trial could last well beyond the months of social isolation and lockdowns.

Her best hope now, she says, is that regulators will learn from the speed and urgency with which a candidate vaccine for the COVID-19 virus has been rushed into clinical trials, foregoing some of the usual pre-trial animal tests. Nizar wants to see therapies for rare diseases treated with the same urgency.

“Our lives have always been in panic mode,” she says. “Now the world has a glimpse into what our reality is.”

## HOW BLOOD FROM COVID-19 SURVIVORS MIGHT SAVE LIVES

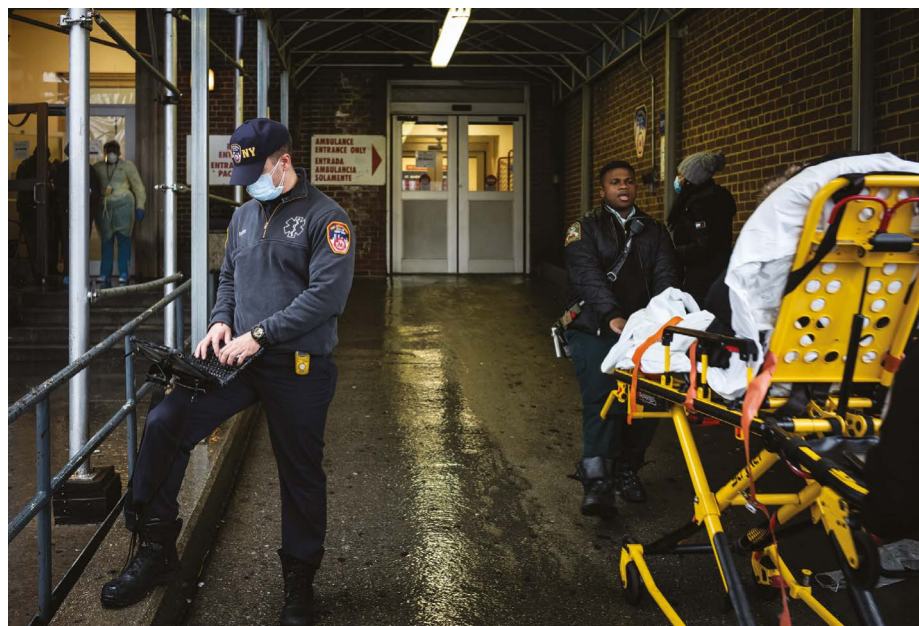
New York City researchers hope antibody-rich plasma can keep people out of intensive care.

By Amy Maxmen

**H**ospitals in New York City are gearing up to use the blood of people who have recovered from COVID-19 as a possible antidote for the disease. Researchers hope that the century-old approach of infusing patients with the antibody-laden blood of those who have survived an infection will help the city – now the US epicentre of the outbreak – to avoid the

fate of Italy, where intensive-care units (ICUs) are so crowded that doctors have turned away people who need ventilators to breathe.

The efforts follow studies in China that infused patients with plasma – the fraction of blood that contains antibodies, but not red blood cells – taken from people who had recovered from COVID-19. But these studies have reported only preliminary results so far. The ‘convalescent plasma’ approach has also seen modest success during outbreaks



Hospitals in New York City are becoming overwhelmed with coronavirus cases.

of severe acute respiratory syndrome (SARS) and Ebola – but US researchers are hoping to increase the value of the treatment by selecting donor blood that is packed with antibodies and giving it to people most likely to benefit.

A key advantage of convalescent plasma is that it's available immediately, whereas drugs and vaccines take months or years to develop. Infusing blood in this way seems to be relatively safe, as long as it is screened for viruses and other infectious agents. Scientists who have led the charge to use plasma want to deploy it now as a stopgap measure, to keep serious infections at bay and hospitals afloat as a tsunami of cases comes crashing their way. "Every patient that we can keep out of the ICU is a huge logistical victory because there are traffic jams in hospitals," says Michael Joyner, an anaesthesiologist and physiologist at Mayo Clinic in Rochester, Minnesota.

Thanks to the researchers' efforts, the US Food and Drug Administration announced last week that it will permit the emergency use of plasma for patients in need. As early as this week, at least two hospitals in New York City – Mount Sinai and Albert Einstein College of Medicine – hope to start using survivor plasma to treat people with the disease, Joyner says.

After this first roll-out, researchers hope the use will be extended to people at a high risk of developing COVID-19, such as nurses and physicians. For them, it could prevent illness so that they can remain in the hospital workforce, which can't afford to be depleted.

## Hard evidence

At the same time, US academic hospitals are planning to launch placebo-controlled clinical trials to collect hard evidence on how well the treatment works.

Liise-anne Pirofski, an infectious-disease specialist at Albert Einstein College of Medicine, says that, in one proposed trial, researchers plan to infuse patients at an early stage of the disease and see how often they advance to critical care. Another trial would enrol people with severe infections. A third would explore plasma's use as a preventive measure for people in close contact with those confirmed to have COVID-19, and would evaluate how often such people fall ill after an infusion, compared with others who were similarly exposed but not treated. These outcomes can be measured within a month, she says. "Efficacy data could be obtained very, very quickly."

Even if it works well enough, convalescent serum might be replaced by modern therapies later this year. Research groups and biotechnology companies are identifying antibodies against the coronavirus, with plans to develop these into precise formulas. "The biotech cavalry will come on board with isolating antibodies, testing them, and developing drugs and vaccines, but that takes time," says Joyner.

## Q&A



## Should we infect healthy people with coronavirus?

**With no end to the coronavirus pandemic in sight, researchers are discussing a dramatic approach that could help to end it: infecting a handful of healthy volunteers with the virus to speed up vaccine testing.**

Many scientists see a vaccine as the only solution to the pandemic. At least one candidate is in safety trials, but a major hurdle is showing that a vaccine works. This typically requires large studies in which thousands of people receive a vaccine or a placebo, and researchers track who becomes infected naturally.

It would be quicker to do a 'human challenge' study, argue scientists in a March preprint (N. Eyal *et al.* Preprint at DASH <http://go.nature.com/33y1hey>; 2020). This would involve exposing healthy people to the virus and seeing whether those who are vaccinated escape infection.

Nir Eyal, the director of the Center for Population-Level Bioethics at Rutgers University in New Brunswick, New Jersey, and co-author of the preprint, tells *Nature* how the study could be done.

**Why should we consider human-challenge studies of coronavirus vaccines?**

They could greatly accelerate the time to approval and potential use. Testing vaccines

**"There are some historical precedents for exposure to very deadly viruses."**

in phase III trials takes a long time. That's done on many people, some of whom get the vaccine and some of whom get placebos or competing vaccine candidates. Researchers then look for differences between these groups in infection rates.

But many people will try to be careful in this outbreak – by self-isolating, say – and it will take a very long time until interpretable results emerge. If, instead, one exposes all study participants to the pathogen, one can not only rely on far fewer volunteers but, more importantly, take a much shorter period to get results.

**Are there any precedents for infecting healthy people with a pathogen?**

We do human-challenge studies for less deadly diseases quite frequently – for example, for influenza, typhoid, cholera and malaria. There are some historical precedents for exposure to very deadly viruses. The thing that demarcates the design that we propose from some of these historical instances is that we feel there is a way to make these trials surprisingly safe.

**How could you conduct such a study?**

You would start only after some preliminary testing to ensure that a vaccine candidate is safe and that it raises an immune response in humans. You then gather a group of people at low risk from any exposure – young and healthy individuals – and ensure that they are not already infected. You give them either the vaccine candidate or a placebo and wait for an immune response. Then you expose them to the virus.

You follow all the participants closely to catch any signs of infection as early as possible. You are trying to check whether the vaccine group is doing better than the placebo group. That might be in terms of viral levels, the time until symptoms emerge or whether they're infected or not.

**Is this ethical?**

It might seem that anybody volunteering to participate in such a study lacks capacity for rational decision-making. But humans do many important things out of altruism. And although the study introduces risks, it also removes them. And the net risks, although unclear, are not clearly extremely high. So, it is potentially rational – even from a selfish point of view – to participate in such a study.

We also let humans volunteer to do risky things all the time; for example, to be in the emergency medical services during this period. That elevates their risk of getting infected but it's very important. In this case, vaccines could be our societies' only way out of the bind between economic stagnation and widespread mortality.

**Interview by Ewen Callaway**

This interview has been edited for length and clarity.



# WHAT THE CRUISE-SHIP OUTBREAKS REVEAL ABOUT COVID-19

Closed environments are an ideal place to study how the new coronavirus behaves.

By Smriti Mallapaty

**W**hen COVID-19 was detected among passengers on the cruise ship *Diamond Princess*, the vessel offered a rare opportunity to understand features of the new coronavirus that are otherwise hard to investigate. Some of the first studies from the ship have provided estimates of the disease's severity and allowed researchers to investigate the share of infections with no symptoms.

Information gleaned from such outbreaks is crucial for people making decisions on how to manage the epidemic, say researchers.

"Cruise ships are like an ideal experiment of a closed population. You know exactly who is there and at risk and you can measure everyone," says John Ioannidis, an epidemiologist at Stanford University in California. This is different from studying the spread in a wider population, where only some people, typically with severe symptoms, are tested and monitored.

On 1 February, a passenger who had disembarked from the *Diamond Princess* days earlier in Hong Kong tested positive for the COVID-19 coronavirus. The ship was quarantined immediately after it arrived in Japanese waters on 3 February, with 3,711 passengers and crew members on board. Over the next month, more than 700 people were infected.

Outbreaks seed easily on cruise ships because of the close confines and high proportions of older people, who tend to be more vulnerable to the disease. Since the *Diamond Princess*, at least 25 other such vessels have confirmed COVID-19 cases – including 78 cases on the *Grand Princess*, which was quarantined off the coast of California.

Japanese officials ran more than 3,000 tests aboard the *Diamond Princess*. Testing almost all of the passengers and crew helped researchers to understand a key blind spot in many infectious-disease outbreaks – how many people are actually infected, including those who have mild symptoms or none at all. These cases often go undetected in the population.

One team reports in *Eurosurveillance* that by 20 February, 18% of all infected people on the ship had no symptoms (K. Mizumoto *et al.* *Euro Surveill.* **25**, 2000180; 2020). "That is a substantial number," says co-author Gerardo

Chowell, an epidemiologist at Georgia State University in Atlanta.

Another team used data from the ship to estimate that in China, the proportion of deaths among people confirmed to have the disease – the case fatality rate (CFR) – was 1.1% (T. W. Russell *et al.* Preprint at medRxiv <http://doi.org/dqqrk>; 2020), lower than the 3.8% estimated by the World Health Organization.

The agency divided China's total number of deaths by the number of confirmed infections,

says Timothy Russell, an epidemiologist at the London School of Hygiene and Tropical Medicine. This does not take into account that only a fraction of infected people are tested, and makes the disease seem more deadly than it is, he says.

Russell and his colleagues used data from the ship – where almost everyone was tested, and all 7 deaths recorded – and compared it with more than 72,000 confirmed cases in China, making their CFR estimate more robust.

The group also estimates that the infection fatality rate (IFR) in China – the proportion of all infections, including asymptomatic ones, that result in death – is even lower, at roughly 0.5%. The IFR is especially tricky to calculate in the population, because some deaths go undetected if the person didn't show symptoms.

The IFR helps public-health officials to understand disease severity and how to intervene, says Marc Lipsitch, an infectious-disease epidemiologist at the Harvard T.H. Chan School of Public Health in Boston, Massachusetts.

## RARE OZONE HOLE OPENS OVER THE ARCTIC — AND IT'S BIG

Cold temperatures created the hole, which is about three times the size of Greenland.

By Alexandra Witze

**A**vast ozone hole – probably the biggest on record in the north – has opened in the skies above the Arctic. It rivals the better-known Antarctic ozone hole that forms in the Southern Hemisphere each year.

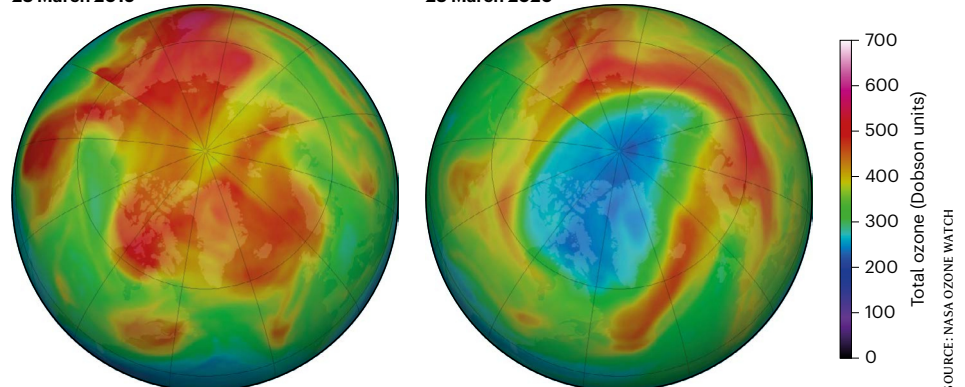
Record-low ozone levels currently stretch across much of the central Arctic, covering an area about three times the size of Greenland (see 'Arctic opening'). The hole doesn't threaten people's health, and will probably disappear in the coming weeks. But it is an extraordinary atmospheric phenomenon that will go down in the record books.

### ARCTIC OPENING

A rare and record ozone hole has formed over the Arctic. An opening in the ozone layer appears each spring over the Antarctic, but the last time this phenomenon was seen in the north was in 2011.

23 March 2019

23 March 2020



“From my point of view, this is the first time you can speak about a real ozone hole in the Arctic,” says Martin Dameris, an atmospheric scientist at the German Aerospace Center in Oberpfaffenhofen.

Ozone normally forms a protective blanket in the stratosphere, about 10 to 50 kilometres above the ground, where it shields life from solar ultraviolet radiation. But each year in the Antarctic winter, frigid temperatures allow high-altitude clouds to coalesce above the South Pole. Chemicals, including chlorine and bromine, which come from refrigerants and other industrial sources, trigger reactions on the surfaces of those clouds that chew away at the ozone layer. These cold conditions are much rarer in the Arctic, which has more-variable temperatures and isn’t usually primed for ozone depletion, says Jens-Uwe Grooß, an atmospheric scientist at the Jülich Research Centre in Germany.

But this year, powerful westerly winds flowed around the North Pole and trapped cold air in a ‘polar vortex’. There was more cold air above the Arctic than in any winter recorded since 1979, says Markus Rex, an atmospheric scientist at the Alfred Wegener Institute in Potsdam, Germany. In the chilly temperatures, the high-altitude clouds formed, and the ozone-destroying reactions began.

### Balloon measurements

Researchers measure ozone levels by releasing weather balloons from observing stations around the Arctic. By late March, these balloons had measured a 90% drop in ozone at an altitude of 18 kilometres, which is right in the heart of the ozone layer. Where the balloons would normally measure around 3.5 parts per million of ozone, they recorded only around 0.3 parts per million, says Rex. “That beats any ozone loss we have seen in the past,” he notes.

The Arctic experienced ozone depletion in 1997 and in 2011 (G. L. Manney *et al.* *Nature* 478, 469–475; 2011), but this year’s loss looks on track to surpass those. “We have at least as much loss as in 2011, and there are some indications that it might be more than 2011,” says Gloria Manney, an atmospheric scientist at NorthWest Research Associates in Socorro, New Mexico. She works with a NASA satellite instrument that measures chlorine in the atmosphere, and says there is still quite a bit of chlorine available to deplete ozone in the coming days.

The Arctic ozone hole isn’t a health threat because the Sun is only just starting to rise above the horizon in high latitudes, says Rex. However, in the coming weeks, there is a small possibility that the hole will drift to lower latitudes over more populated areas – in which case, people might need to apply sunscreen to avoid sunburn. “It wouldn’t be difficult to deal with,” Rex says.

# TOUGH CHOICES LOOM FOR RESEARCHERS WORKING WITH ANIMALS

Cull, release or relocate: scientists are struggling to protect their research and their lab animals.

By Anna Nowogrodzki

**T**he eggs were close to hatching, but Vivian Páez wasn’t sure they would survive. She and her husband Brian Bock, both herpetologists, were incubating nearly 100 temperature-sensitive turtle and tortoise eggs in their laboratory at the University of Antioquia in Medellín, Colombia. By 17 March, they realized that a lockdown due to COVID-19 was imminent.

The next day, as the university shut down all of its research and teaching activities, Bock and Páez carefully moved all of the eggs into their garage at home. They placed them in plastic containers on Bock’s workbench, covered them with a tarpaulin and held their breath.

Researchers everywhere are facing difficult decisions over what to do with research organisms amid lockdowns, university closures and shelter-in-place orders. Some scientists are able to care for animals in their usual facilities, with animal-care workers taking extra precautions for social distancing. Others, like Bock and Páez, have taken animals home or re-released wild-caught specimens. And many creatures have been, or will be, killed, particularly small animals such as mice.

### Life-and-death decisions

The choices are particularly hard for scientists whose work directly affects human patients. Maria Eugênia Duarte, research chief at the National Institute of Traumatology and Orthopedics in Rio de Janeiro, Brazil, oversees studies on rare and malignant sarcomas, mostly in children. Her team cares for roughly 100 immunocompromised mice, which have been implanted with patient tumours to study how these grow and how best to treat them.

With Rio on lockdown, only one researcher can go into the animal facility per day. Duarte herself can’t, because she’s over 60. Her lab members take turns spending 12 hours in the lab feeding the mice, cleaning and sterilizing cages, and checking on the animals’ health. But if equipment breaks, such as the machine used to sterilize the cages, no one will be able to fix it. “We don’t know how long this is going to be possible,” Duarte says. “Maybe we will need to prioritize and sacrifice [some of] the animals.”

Many labs have already taken this difficult decision. One researcher at Oregon Health &



A tortoise hatches, shortly after relocation.

Science University has had to euthanize more than two-thirds of her mice. Elsewhere in the United States, a researcher at Carnegie Mellon University reports culling 600 mice; two scientists at Harvard say they have had to kill half of their research mice; and a team at the Memorial Sloan Kettering Cancer Center has been asked to designate no more than 60% of its animals as essential.

The Jackson Laboratory, a non-profit biomedical research institute based in Bar Harbor, Maine, that sells millions of research mice per year, has noticed a several-fold increase in requests to freeze mouse sperm or embryos so that specific lines can be re-established later, says Rob Taft, a senior programme manager at Jackson. The institute has sent trucks to various cities to collect mice for cryopreservation; more pickups are planned.

But for some labs, particularly those that use wild-caught research organisms, there are few options when it comes to maintaining or preserving a research programme. Solomon David, a fish biologist at Nicholls State University in Thibodaux, Louisiana, decided last week to re-release 48 wild spotted gar (*Lepisosteus oculatus*) that his team had recently collected.

As for Páez and Bock’s turtles, about 15 eggs have hatched so far, and the animals are living with the family until travel restrictions are lifted and they can be returned to their wild habitats. “At least we don’t work with jaguars or crocodiles,” Páez says.



# HELP FOR THE HIGH SEAS

As a treaty to protect life in the open ocean nears completion, scientists applaud the new pact and worry about provisions that could hamper research. **By Olive Heffernan**

**I**n 1945, a young chemist called Werner Bergmann was diving off the Florida coast, scouring its waters for undiscovered marine life. One of the species he came across was a rather plain brown sponge. A colleague named the new-found creature *Cryptotethia crypta*, and Bergmann isolated from it two unknown compounds – spongothymidine and spongouridine.

He suspected they could have medical uses, but their true value didn't become apparent for more than 40 years. In 1987, the US Food and Drug Administration approved the first therapy for HIV; that drug, called azidothymidine (AZT), was modelled on the sponge compounds that Bergmann had identified. By 1989, AZT had become the most expensive drug known, at US\$8,000 per patient per year, generating more than \$100 million a year in profits for the drug company.

Eight other natural marine products have led to clinically approved drugs and another 28 are in clinical trials. Projections suggest that the global marine biotechnology market – which includes products for the pharmaceutical, bio-fuels and chemical industries – could reach \$6.4 billion by 2025. There's even a chance that a marine organism could help to combat viruses, such as the one responsible for the current pandemic; a compound isolated from red algae has shown promise in tests on different types of coronavirus (see A. Zumla *et al.* *Nature Rev. Drug Discov.* **15**, 327–347; 2016). Commercial interest in the genetic resources of the high seas has never been greater.

It has also never been more divisive. In the next few months, barring delays caused by

the COVID-19 pandemic, nations are expected to strike a historic deal to protect marine life in the high seas – the ocean beyond national governance. This region accounts for 90% of Earth's available living space, and is thought to be home to millions of undiscovered species.

For the deal to go ahead, nations must agree to a system for creating large marine sanctuaries on the high seas and must lay out rules for how industry operates in these waters. But by far the most contentious issue they will tackle is how to regulate the use of the genetic resources of the high seas – both the marine creatures themselves and their gene sequences. The goal is to prevent 'biopiracy' – attempts by wealthy nations or companies to commercialize biological resources without sharing the benefits with their rightful owners. In the case of the high seas, those owners are all nations.

Researchers are overjoyed by the prospects of a high-seas treaty, but they are worried that efforts to prevent biopiracy will curtail their ability to do basic research in the open ocean.

It's not an idle concern. Although almost all details of the treaty have yet to be agreed, the draft text includes several ideas that would change how high-seas research happens. Most notable are proposals that scientists would need to notify the United Nations before conducting research cruises in the high seas, or that they would need to obtain permits for such work, which would require them to share data or other benefits from their research.

Most scientists are keen to share benefits with developing nations and Indigenous groups, but they do not favour constraints on research. Some fear that the proposed

anti-biopiracy regulations will mirror those of the Convention on Biological Diversity, most notably the Nagoya Protocol, an international agreement adopted in 2010 that restricts scientists' access to the territories of other nations, including their coastal waters. Nations drafted the Nagoya Protocol to prevent companies from patenting Indigenous medicines without sharing the profits, and now some researchers say it has made it difficult to get permits to work in some developing nations.

"I'm delighted that the UN is undertaking this effort as a way of trying to ensure conservation and appropriate oversight of the high seas," says Peter Girguis, an ocean scientist and evolutionary biologist at Harvard University in Cambridge, Massachusetts. But Girguis says he is "hugely concerned that we'll find



DAVID SHOLE/NPL



A new treaty will govern uses of organisms from the open ocean, such as this hydromedusa.

by the UN Convention on the Law of the Sea, but there is no law to protect marine life in this vast region.

Up to now, some 34,000 marine natural products have been identified that could potentially be used in medicine, food and cosmetics. Of the eight existing marine drugs, five are cancer treatments. With the global marine biotechnology market growing rapidly, concern has mounted about ownership of these resources. At present, it's possible for anyone to develop and profit from a product derived from biological samples taken in the high seas, and some developing nations are concerned that wealthy nations or companies will reap most of the profits to be made from this global commons.

Already, 12,998 genetic sequences from marine species have been patented. The multinational chemical giant BASF, based in Ludwigshafen in Germany, has registered 47% of those gene sequences in patents – a figure that Robert Blasiak, an ocean-governance researcher at the Stockholm Resilience Centre in Sweden, and his colleagues say represents a worrying trend of corporate control over marine genetic resources. A sequence from an alga, for example, has been used to fortify canola oil, from the rapeseed plant, with omega-3 fatty acids.

When nations meet to thrash out the treaty, they will have to decide whether the new law to prevent biopiracy covers physical samples only, such as an alga and its DNA – or whether it extends to digital sequence information, such as a gene sequence from an alga stored in a data repository.

They will also have to consider two other issues related to biopiracy: how to ensure equal access to marine genetic resources and how to share benefits from them. These provisions would parallel the protections adopted through the Nagoya Protocol. Developing nations pushed for the protocol out of concern that companies were patenting Indigenous medicines without sharing the profits.

One example involves the Madagascar periwinkle, *Catharanthus roseus*, which has been used for centuries as a medicine in Africa and China. Compounds from the plant and their derivatives are now ingredients of numerous medications patented and sold by large pharmaceutical companies. So far, the provisions included in the Nagoya Protocol have led to one profit-sharing arrangement, for South African rooibos tea.

Nations hope to strike a high-seas deal this year, but there are still deep philosophical divides. Countries such as Russia, the United States and Japan, which have the technological and financial clout to scour the deep sea in search of new drugs, cosmetics and food products, are advocating a 'free seas' mentality that favours unrestricted access, patent protection and sharing of non-financial benefits such as data. Developing nations, typified by the

ourselves hindering access for everybody to do academic research”.

### Final stretch

Conservationists and scientists have pushed for a high-seas treaty for more than a decade, and they are now entering the home stretch. Negotiators were scheduled to start the fourth and final round of talks on 23 March in New York, but that meeting has been postponed until further notice because of the COVID-19 pandemic.

The treaty would close a giant gap in the existing network of international and national laws. Countries have exclusive rights to fish and mine in waters up to a distance of 200 nautical miles from their shores. Beyond that are the high seas. Right now, certain activities on the high seas, such as mining and cable laying, are regulated



**THE GLOBAL MARINE BIOTECHNOLOGY MARKET COULD REACH \$6.4 BILLION BY 2025.”**



## Feature

Group of African States (the African Group), argue that marine genetic resources are 'common heritage' and need some oversight so that their use can be monitored and any profits, as well as other benefits, shared. "If there's almost no form of regulation, there wouldn't be any opportunities for us to track and trace when there is commercialization," says Michael Kanu, deputy permanent representative to the UN for Sierra Leone, and coordinator of the African Group at the treaty talks.

Christian Tiambo, a livestock scientist at the International Livestock Research Institute in Nairobi, agrees. He says that developing nations and Indigenous people should be worried about biopiracy, and that it's very important to regulate access to the high seas to prevent biopiracy from happening there.

### Global permit scheme

Just what those regulations would look like is up for discussion, but the draft text includes several ideas. One is to create a global body that would authorize, and possibly even grant permits to, scientists to undertake research on life in the high seas – a first for researchers. An alternative idea is for scientists to submit their post-cruise data, research findings and sporadic progress reports to a committee or a platform created by the UN. There is also a proposal to assign unique identifiers to all marine genetic resources on collection, allowing their use to be tracked.

Siva Thambisetty, who studies patents and biotechnology at the London School of Economics, says that these options essentially follow two different paths. A light-touch approach would require researchers and companies to give notification of their research plans and voluntarily share any benefits, such as data. A more tightly regulated scheme would grant permits to scientists for access to the high seas in exchange for their sharing benefits, such as data or any profits made from new products.

Thambisetty says she favours conditional permits, rather than a system that assumes scientists will be given approval and encouraged to share benefits voluntarily. She says that granting scientists exclusive rights to data for a short period, perhaps one or two years, might be a fair exchange for a permit.

Although researchers accept the idea of some controls, they worry that certain ones could be too onerous.

Muriel Rabone, for example, a curator and ecologist at the Natural History Museum in London, recognizes problems with the current system but has concerns about changes. "It's not good for the science community to have this big north-south divide in terms of research capacity," she says, adding that "we need things that are going to streamline processes rather than hamper them".

"The idea that approval would be given by an overseeing body before a cruise is allowed



**WE NEED THINGS THAT ARE GOING TO STREAMLINE PROCESSES RATHER THAN HAMPER THEM."**



Cancer drugs are derived from this tunicate.

throws up a lot of questions: who's approving this, how and why? What sort of bottleneck is that going to create?" she says.

Scientists are wary because similar anti-biopiracy laws – and the Nagoya Protocol in particular – have hampered foreign researchers from gaining access to certain countries, such as Colombia and Sri Lanka. "A lot of the biodiversity research community has been a little bit bruised by Nagoya," says Rabone. Shirley Pomponi, a marine biodiversity researcher at Florida Atlantic University Harbor Branch in Fort Pierce, Florida, says that before access and benefit-sharing laws came into place, her team collected samples from around the world. But she has now had to stop working in some countries, such as Brazil and Colombia.

"It just got to be harder and harder," she says. "We would be days away from an expedition that was going to cost us hundreds of thousands of dollars and still not have permits from the countries to be able to bring our ship into their waters. And it's just not worth the hassle. So we thought, 'let's just focus on the US'."

Although some scientists say that the Nagoya Protocol has restricted their work, Tiambo says he already sees many benefits coming out of the agreement. Scientists are now being trained to better understand the value of genetic information, he says, and "this information is trickling down to local communities, who can now really take advantage of the genetic resources that they have been keeping for generations". Researchers working on dairy-cattle genomics, for example, have shared data and expertise with African scientists and communities, which has allowed them to improve their national breeding programmes.

Rachel Wynberg, a bio-economics expert at the University of Cape Town, South Africa, agrees that anti-biopiracy laws, including the Nagoya Protocol, have had benefits. "There has definitely been a shift in perception and in the ethics of working with biodiversity. There has also been a significant shift in company practices," she says. But she questions whether the Nagoya Protocol has had any meaningful impact on economic development, conservation and Indigenous people.

### Balancing act

Despite the concerns, many see a way to craft an agreement that both restricts biopiracy and fosters research. If, for example, a unique identifier is assigned to each sample, then if a product is developed, a share of profits will go into a pot that could be shared between nations for use in biodiversity conservation. "This would allow for full traceability of materials all the way from the ocean floor to commercialization," says Marcel Jaspars, a biodiversity researcher at the University of Aberdeen, UK, who is advising the UN on how to design the treaty.

Another possibility that's been floated is that the treaty could support, rather than restrict, access to the high seas, treating access as a benefit. Scientists from developing countries could join research cruises with other nations, finding available berths on ships through a global registry of research cruises. "This could promote access to the high seas by all scientists who are interested, ensuring that those scientists are there when discoveries are made," says Girguis. Scientists from the developing world would then also have a share of patents arising from that research.

Rather than resisting change, marine scientists need to step up to the mark, and accept the need for new research protocols, says Thambisetty.

Now is the time to engage, say researchers who have followed the negotiations. "If we get it right, this treaty could be transformational," says Jaspars. "We could actually end up with more knowledge about the deep oceans than we had before."

**Olive Heffernan** is a science journalist in Dublin.

MICHAEL LAWRENCE/LONELY PLANET IMAGES/GETTY

# Books & arts



A 3D magnetic resonance imaging scan of the brain.

## Neuroscience needs some new ideas

A history of the metaphors behind brain research faces a dark past and disquieting future. **By Stephen Casper**

**T**he poet Emily Dickinson rendered the brain wider than the sky, deeper than the sea, and about the weight of God. Scientists facing the daunting task of describing this organ conventionally conjure up different kinds of metaphor – of governance; of maps, infrastructure networks and telecommunications; of machines, robots, computers and the Internet. The comparisons have been practical and abundant. Yet, perhaps because of their ubiquity, the metaphors we use to understand the brain often go unnoticed. We forget that they are descriptors, and see them instead as natural properties.

Such hidden dangers are central to biologist and historian Matthew Cobb's *The Idea of the Brain*. This ambitious intellectual history follows the changing understanding of the brain from antiquity to the present, mainly in Western thought. Cobb outlines a growing challenge to the usefulness of metaphor in directing and explaining neuroscience

research. With refreshing humility, he contends that science is nowhere near working out what brains do and how – or even if anything is like them at all.

Cobb shows how ideas about the brain have always been forged from the moral, philosophical and technological frameworks to hand for those crafting the dominant narratives of the time. In the seventeenth century, the French philosopher René Descartes imagined an animal brain acting through hydraulic mechanisms, while maintaining a view of the divine

nature of a mind separate from matter. Later authorities, such as the eighteenth-century physician and philosopher Julien Offray de Le Mettrie, secularized the image and compared the human to a machine. The Italian physicist Alessandro Volta rejected the idea of 'animal electricity', proposed by his rival Luigi Galvani as a vital force that animates organic matter. Volta was driven at least partly by his aversion to the mechanistic view.

New metaphors came from nineteenth-century phrenology, evolutionary theory and the doctrine of inhibition in physiology – the idea that the nervous system could repress actions and behaviours. Then came the age of communication, and with it fresh language for the brain.

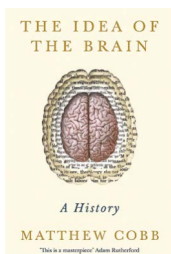
### Image clash

The late-nineteenth-century discovery of neurons led to a clash of rival images. Reformers imagined separate components, comparable to the wires and signals of the nascent telecommunications infrastructure. Conservatives cast the nervous system as a continuous network (or reticulum) akin to the blood circulation, feeling that this explained how volition and mind might work; to them, discrete signalling implied heterodox notions of mind, perhaps even of the soul.

The post-1940 proliferation of references to enchanted looms, ghosts in machines, logical circuits, reptile brains, parallel processors and uploaded minds grew from those foundations. Cobb notes, but only in passing, that we need new images to make sense of research developments ranging from artificial intelligence to mini-brains grown in the laboratory to brain implants. He doesn't try to invent examples.

The narrative Cobb offers is familiar. The epistemic power of metaphors in science has long been recognized by historians and philosophers of science. Yet for the popular audience he targets, Cobb's account is an important contribution: few have offered such accessible insights, with choice examples and clear explanations of the societal factors that lie beneath. Cobb also eloquently shows how figurative language does much more than simply distil or give shape to complex, intangible subjects. Metaphors change how science is done, by licensing new interpretations or inspiring new experiments.

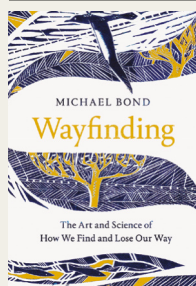
Cobb also reminds us that metaphors conceal as much as they reveal. The ideas that they so persuasively represent often ignore key elements. Comparing the brain to a computer is beguiling, but neglects that brains are also organs, and aware ones at that. Our existing images and language are desperately limiting when it comes to imagining a situation in



**The Idea of the Brain: A History**  
Matthew Cobb  
Profile (2020)



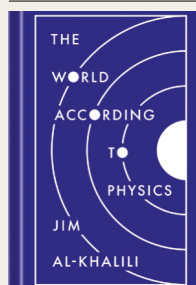
## Books in brief



### Wayfinding

Michael Bond Picador (2020)

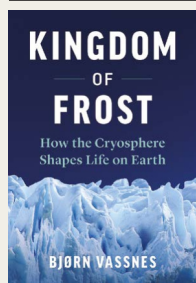
This rewarding meditation on “how we find and lose our way” might have been called “Am I here?” — the tragic refrain of science writer Michael Bond’s grandmother after she developed dementia. The book astonishes as it ranges from the neuroscience of meandering rats to the deleterious effects of satellite navigation. A desert ant, we learn, can forage at least 100 metres from its nest, then scurry back in a straight line — equivalent to a human wandering for a day and a night, then heading straight home without help from GPS.



### The World According to Physics

Jim Al-Khalili Princeton Univ. Press (2020)

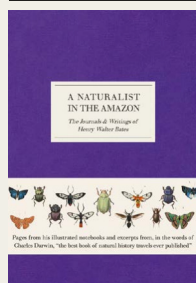
Quantum physicist, historian and science broadcaster, Jim Al-Khalili is well placed to summarize the past, present and future of physics for a lay audience, without using mathematics. After a tantalizing chapter on scale, he analyses space, time, energy, matter, quanta, thermodynamics and various attempts to unify the general theory of relativity with quantum field theory — although he never defines a black hole. On the debate between Niels Bohr and Albert Einstein, Al-Khalili sides with Einstein, who believed in an objective reality.



### Kingdom of Frost

Bjørn Vassnes (transl. Lucy Moffatt) Greystone (2020)

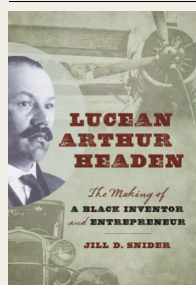
Science journalist Bjørn Vassnes’s brief book demonstrates how “life’s different revolutions have been intertwined with the history of the cryosphere”. He includes memories of digging tunnels to his house in the Norwegian Arctic during snowy 1970s winters, and experience of Bangladesh, which never sees snow yet survives on river water from threatened Himalayan glaciers. Vassnes discusses how reindeer grazing eradicates vegetation that reduces the Arctic’s heat-deflecting albedo effect; perhaps it could aid the fight against global warming?



### A Naturalist in the Amazon

Henry Walter Bates Natural History Museum (2020)

“The best book of Natural History Travels ever published in England,” said Charles Darwin of entomologist Henry Walter Bates’s 1863 *The Naturalist on the River Amazons*, an 11-year journal inspired partly by Darwin’s diary of his 1831–36 journey on the HMS *Beagle*. This enchanting part-facsimile justifies his words. Bates writes grippingly on anacondas, bird-killing spiders and blowpipes. Although little-known now, his name endures in ‘Batesian mimicry’: a survival strategy based on apeing harmful species, which he observed in butterflies.



### Lucean Arthur Headen

Jill D. Snider Univ. North Carolina Press (2020)

There are no references to Lucean Arthur Headen on Wikipedia; nor did he leave behind significant personal papers. Yet this black inventor and entrepreneur, born in racially segregated North Carolina in 1879 among formerly enslaved artisans, deserves study. Local historian Jill Snyder’s biography reconstructs him. By his death in 1957, 26 years after moving to Britain, Headen had spent almost 4 decades running US and UK companies making cars and products based on his patents — some of which are still cited. **Andrew Robinson**

which the mental, physical and embodied are so tightly enmeshed.

Thus, despite their power, our metaphors have done little to bridge the divisions that emerge as scientists seek to understand what brains are. After centuries of research, including recent advances in exploring consciousness through imaging techniques such as functional magnetic resonance imaging, there’s still no answer to Shakespeare’s question in *The Merchant of Venice* — “Tell me where is fancy bred, Or in the heart or in the head?”

We can’t stop using metaphors. Scientists depend on figurative language to organize and communicate thoughts and ideas. But whether the neurosciences can get closer to a compelling idea of the brain in the decades ahead might depend on a full reckoning of the role of metaphors. Top of the list: researchers should acknowledge that although certain word choices seem innocent, many carry malign overtones. Ideas of the brain have often embedded inequities and prejudices about race, class, gender, sexuality and agency.

On these matters, Cobb should have said more. The word ‘racist’ appears only a few times in his book, and then only in footnotes. But a little thought makes clear that seemingly innocent metaphors like ‘higher’ and ‘lower’ functions, or descriptions of specific anatomical structures as ‘primitive’, carry racialized baggage. When originally characterized, they spoke to the ghastly view that the nervous systems of white, upper-class men made them evolutionarily superior to those they subordinated at home and abroad. Similarly, it is discomfiting to realize that Broca’s area, linked to language processing, is named for the French physician Paul Broca, who believed in a hierarchy of peoples. That, in 2020, there are scientists who still talk about ‘female brains’, an idea Cobb rightly derides, is evidence that gender (a word that appears only in the bibliography) remains central to too many people’s ideas of how the brain is constructed. And he makes no mention of what neurodiversity advocacy might mean for figurative language. Whatever new metaphors are to come, ones that embrace differences inclusively will be more insightful and more profound.

*The Idea of the Brain* puts our current predicament in context and synthesizes much that needs attention. It is a very good book. It could have done more in a time when science is coming to terms with the limitations of the straight, white, wealthy, Western, non-disabled, male perspective. But I hope it provokes contemplation about why certain metaphors linger, where they come from, how they persist, and in what ways they burden us with the invisible assumptions of past cultures.

**Stephen Casper** is professor of history at Clarkson University, Potsdam, New York, USA.  
e-mail: scasper@clarkson.edu

# Comment



The elongated bristlemouth (*Sigmops elongatus*) is abundant in the oceans' twilight zone.

## Study the twilight zone before it is too late

Adrian Martin, Philip Boyd, Ken Buesseler, Ivona Cetinic, Hervé Claustre, Sari Giering, Stephanie Henson, Xabier Irigoien, Iris Kriest, Laurent Memery, Carol Robinson, Grace Saba, Richard Sanders, David Siegel, María Villa Alfageme & Lionel Guidi

**Exploitation and degradation of the mysterious layer between the sunlit ocean surface and the abyss jeopardize fish stocks and the climate.**

**T**he twilight zone contains the largest and least exploited fish stocks of the world's oceans. Spanning from just below 200 metres to 1,000 metres deep, it is an interface between the well-studied marine life in the sunlit zone above and the ecosystems of the abyss below. It has a major role in removing carbon dioxide from the atmosphere and storing it for centuries or longer. The twilight zone is also privy to the largest migration on Earth. Huge numbers of fishes and zooplankton move hundreds of metres towards the surface each night to feed, before retreating back down at dawn.

Yet the zone is poorly understood – physically, biogeochemically and ecologically.

Even the number of organisms that live there remains a mystery, let alone their diversity and function.

It is alarming, then, that this vast ocean domain is at risk in three ways – even before any of the potential consequences are understood<sup>1</sup>. First, the world's growing population has an increasing need for food. Second, sea-floor mining for minerals and metals could release waste into the region<sup>2</sup>. And third, climate change is altering temperature, acidification and oxygen levels in ways that are likely to affect life there<sup>3</sup>.

The twilight zone is hard to study. Its organisms are difficult to sample and analyse, being sparsely distributed, elusive and often fragile. They also live at pressures of up to 100 atmospheres, which poses problems for laboratory-based investigations.

Critics might argue that waters near coasts and above shelves are more deserving of study, given the huge environmental pressures there, as well as their importance to societies. And, of course, they need attention. Sadly, however, it is too late to avoid widespread environmental damage to these inshore regions. Instead, research efforts and local policies must aim at mitigating the worst effects.

By contrast, the twilight zone is almost pristine. Moreover, the majority of it lies beyond national jurisdiction. This makes it of common interest and responsibility, and means that global agreement is necessary to manage it.

Here, we outline the steps needed to ensure that enough is known about this complex global ecosystem to inform decisions about the impacts of climate change and potential future exploitation. We call on the international marine research community to focus its attention on the twilight zone during the upcoming United Nations Decade of the Ocean, which runs from 2021 to 2030. In the spirit of the UN's Sustainable Development Goals, we should seize the opportunity to establish a global policy that will protect this vast ecosystem for present and future generations.

### Carbon pump

At present, we know just enough about the twilight zone to recognize its importance in maintaining a healthy ocean.

Phytoplankton growing in the sunlit layer fuel multiple food-supply routes into the zone that sustain organisms from bacteria to giant squid. In the process of consuming this food, and each other, the twilight-zone animals produce CO<sub>2</sub>, consume oxygen and release nutrients back into the water (see 'Twilight zone').

WOODS HOLE OCEANOGRAPHIC INSTITUTION/PAUL CAIGER



In the winter, cold, windy weather mixes water containing the recycled nutrients with water from the surface layer<sup>4</sup>. In this way, the twilight zone has an important role in supporting phytoplankton growth the next spring.

Although winter mixing can release carbon back into the atmosphere, a fraction of it ends up in deeper waters, where it can be locked away, typically for centuries. This downward transport of organic matter, mediated by life in the twilight zone, is called the biological carbon pump, and the twilight zone is central to its strength<sup>5</sup>. This deeper flux of material becomes food for the animals there. The small amount that eventually reaches the sea floor sustains everything from bacteria to sea cucumbers.

### Glaring gaps

Unfortunately, little is known about how the twilight zone performs these roles. This makes it difficult to predict future ocean oxygen levels or how organic carbon will be stored in the long term. Moreover, the effects of climate change on ocean temperatures and oxygen levels will alter how the biological pump operates.

Knowledge gaps range from fundamental information, such as what species dwell there and what their metabolic rates are, to

how they behave and adapt to their environment. Bacteria colonize 'marine snow' (sinking aggregates of organic material); krill form dense, localized swarms; and some fishes have evolved vision that is tuned to dawn and dusk. But how do such adaptations affect the functioning of the twilight zone?

## "The twilight zone is privy to the largest migration on Earth."

The patchiness of the information makes it hard to predict how the twilight zone might respond to human pressures. For example, the fishing industry is likely to target species that are very abundant, such as elongated bristlemouth (*Sigmops elongatus*), but will also remove many other animals in the process. This could reduce the ecosystem's resilience and change global nutrient and carbon cycles<sup>6</sup>.

### Research priorities

The following three questions should be prioritized to plug these knowledge gaps.

**How many organisms live in the twilight zone, and how diverse are they?** Estimates

for the volume of fishes there range between 1 billion and 20 billion tonnes<sup>7</sup>. Surface waters are estimated to hold 1 billion tonnes. (The world's human population has a total weight of 0.5 billion tonnes.) But it is not clear what fraction of the organisms are siphonophores (relatives of jellyfish) or cephalopods (such as squid).

**Which ecological processes transform and consume organic material?** Marine snow is common in the twilight zone. Zooplankton could be breaking it up so that it forms a slow-sinking substrate for bacteria – a nutritious food for the zooplankton<sup>8</sup>. But this theory, known as microbial gardening, is yet to be tested.

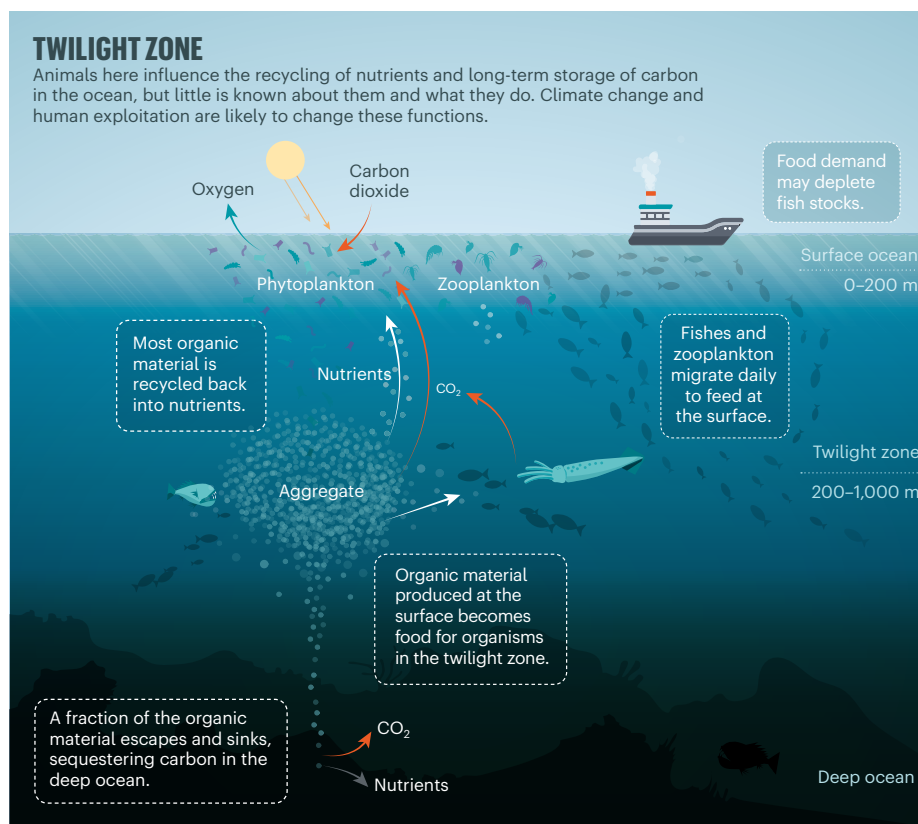
**How is organic material transported into and out of the twilight zone?** Researchers need to determine the relative importance of a range of mechanisms that vary with location, time and depth<sup>9</sup>. These span from physical processes to animal behaviour. Ocean currents transport tiny particulate and dissolved organic matter to greater depths. Larger organic aggregates and faecal pellets sink. And daily and seasonal animal migrations release waste products at depth.

Addressing these three questions will help to clarify what sets the balance between how much organic material is consumed in the twilight zone, restoring nutrients and sustaining the fish stock, and how much passes on to greater depths, sequestering carbon away from the atmosphere<sup>10</sup>. Only with this knowledge can the wider consequences of exploiting the region be predicted.

### Three steps

The following three steps will help in addressing these research priorities. They make use of a range of innovative tools and techniques.

**Conduct a census.** Organisms ranging from bacteria to large cetaceans need to be counted. Devices such as the Underwater Vision Profiler (UVP) can be deployed in the twilight zone to capture images of plankton that can be identified and counted using a web-based application known as EcoTaxa, which is linked to a taxonomic database containing roughly 100 million images of planktonic organisms and particles. A smaller version of the UVP can be attached to autonomous vehicles to extend sampling beyond the times and places that research vessels can visit. Larger organisms can be identified with short-range



## Comment

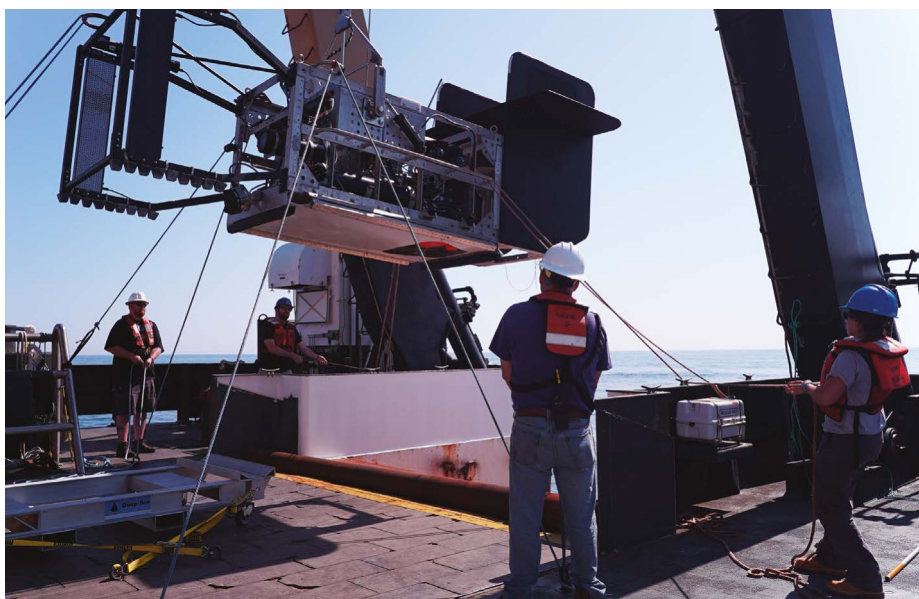
high-frequency acoustic sensors. When deployed at depth, these sensors can help sort fishes from siphonophores. DNA harvested from the environment can also be used to infer the identity and diversity of elusive or fragile animals, including large fishes, marine mammals such as beaked whales and gelatinous organisms. Any new approaches should be calibrated against conventional physical sampling methods and follow internationally recognized, standardized procedures.

**Determine what is processing and consuming organic material.** To do this, changes in the size, source and sinking speed of organic aggregates need to be observed *in situ* as the particles descend through the water column. This should be done mainly using optical sensors. The information gleaned could then be combined with simultaneous estimates of the abundance of zooplankton and fishes and the intensity of ocean mixing, to determine what is breaking up the aggregates and retaining them in the twilight zone<sup>11</sup>. A range of 'omics' approaches should be used to provide insight into how the associated organic material is being eaten by microorganisms<sup>12</sup>, including metagenomics, metatranscriptomics and metabarcodes.

**Track organic material.** Argo floats already roam the ocean and collect information on properties such as temperature, phytoplankton abundance and nutrient levels as they shuttle between the surface and a depth of 2,000 metres every 10 days. Imaging systems capable of measuring the size and abundance of organic particles are being added to these floats. The current network needs to be increased from 200 to 1,000 operating floats, with imaging sensors added to all. Optical sensors on other autonomous underwater vehicles such as gliders can be used to yield information on the size and shape of organic particles.

These data could be combined with information from the Plankton, Aerosol, Cloud, ocean Ecosystem (PACE) mission, which NASA plans to launch in December 2022. The satellite will use a spectrometer to measure the colour of the ocean. Those data will be useful in determining the types of phytoplankton in the surface layer of the ocean, fuelling the twilight zone. The discovery that laser-mapping technology such as LIDAR (Light Detection and Ranging) can observe the daily migrations of zooplankton from space should be combined with sparse local data<sup>13</sup>.

To obtain the most complete picture possible of the global twilight zone, we call on national and international ocean projects to coordinate efforts, rather than duplicate them. We encourage researchers and institutions to link up with JETZON (Joint Exploration of the Twilight Zone



The Deep-See sensor platform heads for its first dive into the twilight zone.

Ocean Network), an initiative launched earlier this year to improve communication and coordination. Currently, 15 projects involving 12 countries are involved, each studying just a few locations. This is a good start. But given the vast size and complexity of the twilight zone, everyone, from independent researchers to international projects, needs to join forces to succeed.

There is no time to waste. We cannot let climate warming and human exploitation fundamentally alter the twilight zone before we even begin to understand the potential consequences for the health of the planet.

### The authors

**Adrian Martin** is a research scientist at the National Oceanography Centre, Southampton, UK. **Philip Boyd** is a professor at the Institute of Marine and Antarctic Studies, Hobart, University of Tasmania, Australia. **Ken Buesseler** is a senior scientist at Woods Hole Oceanographic Institution, Woods Hole, Massachusetts, USA. **Ivona Cetinic** is an oceanographer in the Ocean Ecology Laboratory at NASA/Goddard Space Flight Center, Greenbelt, Maryland, USA. **Hervé Claustre** is director of research in biogeochemical oceanography at Sorbonne University, CNRS, Villefranche Laboratory of Oceanography, Villefranche-sur-mer, France. **Sari Giering** is a research scientist at the National Oceanography Centre, Southampton, UK. **Stephanie Henson** is a principal scientist at the National Oceanography Centre, Southampton, UK. **Xabier Irigoien** is Ikerbasque Research Professor and scientific director in marine ecology at AZTI-Basque Research and Technology Alliance, Pasaia Gipuzkoa, Spain.

**Iris Kriest** is a research scientist at GEOMAR, Kiel, Germany. **Laurent Memery** is director of research in environmental marine sciences at LEMAR Laboratory, European Maritime University Institute, Brest, France. **Carol Robinson** is a professor at the Centre for Ocean and Atmospheric Sciences, School of Environmental Sciences, University of East Anglia, Norwich, UK. **Grace Saba** is an assistant professor in the Department of Marine and Coastal Sciences, Rutgers University, New Brunswick, USA. **Richard Sanders** is director of the ICOS Ocean Thematic Centre at NORCE, the Norwegian Research Centre and the Bjerknes Centre, Bergen, Norway. **David Siegel** is a professor at the Earth Research Institute, University of California, Santa Barbara, USA. **Maria Villa Alfageme** is a professor at the Department of Applied Physics, University of Seville, Spain. **Lionel Guidi** is a research scientist at Sorbonne University, CNRS, Villefranche Laboratory of Oceanography, Villefranche-sur-mer, France. e-mails: lguidi@obs-vlfr.fr; adrian.martin@noc.ac.uk

1. Hidalgo, M. & Browman, H. J. *ICES J. Mar. Sci.* **76**, 609–615 (2019).
2. Drazen, J. C. *Res. Ideas Outcomes* **5**, e33527 (2019).
3. Seibel, B. A. & Wishner, K. F. in *Ocean Deoxygenation: Everyone's Problem* (eds Laffoley, D. & Baxter, J. M.) Ch. 8.1, 265–276 (IUCN, 2019).
4. DeVries, T., Primeau, F. & Deutsch, C. *Geophys. Res. Lett.* **39**, L13601 (2012).
5. Giering, S. L. et al. *Nature* **507**, 480–483 (2014).
6. Davison, P. C., Checkley, D. M., Koslow, J. A. & Barlow, J. *Progr. Oceanogr.* **116**, 14–30 (2013).
7. Irigoien, X. et al. *Nature Commun.* **5**, 3271 (2014).
8. Mayor, D. M., Sanders, R., Giering, S. L. C. & Anderson, T. R. *Bioessays* **36**, 1132113 (2014).
9. Boyd, P. W., Claustre, H., Levy, M., Siegel, D. & Weber, T. *Nature* **568**, 327–335 (2019).
10. Kwon, E. Y., Primeau, F. & Sarmiento, J. L. *Nature Geosci.* **2**, 630–635 (2009).
11. Briggs, N., Dall'Omo, G. & Claustre, H. *Science* **367**, 791–793 (2020).
12. Guidi, L. et al. *Nature* **532**, 465–470 (2016).
13. Behrenfeld, M. J. et al. *Nature* **576**, 257–261 (2019).



# Correspondence

## Share mobile data to curb COVID-19

Open sharing of clinical, epidemiological and virological data between governments and researchers during the current COVID-19 pandemic is shaping international public-health strategies. However, digital data from billions of mobile phones and footprints from web searches and social media remain largely inaccessible to researchers and governments. These data could support community surveillance, contact tracing, social mobilization, health promotion, communication with the public and evaluation of public-health interventions.

We urge technology companies to work with researchers and governments to find ways to share their data rapidly in a legal, proportionate, ethical and privacy-preserving manner. The public's consent to sharing personal data for the common good can be obtained dynamically through existing mobile applications, putting the public at the heart of the public-health response to COVID-19. We ask governments and funders to create new centres of digital public health to deploy and evaluate proven innovations.

The technology sector has benefited from massive public investment in the Internet, the GPS and mobile technologies. Now is the time for tech to invest in society.

**Rachel A. McKendry\*** University College London, UK.

r.a.mckendry@ucl.ac.uk

\*On behalf of 8 correspondents; see [go.nature.com/2ub8qjq](https://go.nature.com/2ub8qjq)

## Predatory journals: dodging the radar

Agnes Grudniewicz and colleagues highlight the need to define what constitutes a predatory journal (*Nature* 576, 210–212; 2019). History shows, however, that such journals and their publishers rapidly adapt to filters that might discredit them.

In their early days, such journals were ephemeral, with false claims of indexing, vague titles (such as *International Journal of Applied Sciences and Engineering*), fraudulent publication fees and dubious-looking websites. By contrast, modern predatory journals use more specific titles and release well-designed issues. They have real indexing and well-developed websites. They are owned by supposedly legitimate organizations, publish for free (because they have other interests), run counterfeit archives and safeguard themselves with plagiarism checks (see F. H. Kakamad *et al.* *Int. J. Surg. Open* 17, 5–7; 2019).

However, the skipping or faking of scientific review remain cornerstones for predatory journals and publishers. In our opinion, it is dangerous to exclude the criterion of inadequate peer review from any definition of predatory journals, as Grudniewicz and colleagues propose, because that definition would then fail to catch its criminal targets.

**Fahmi H. Kakamad, Abdulwahid M. Salih** University of Sulaimani, Sulaimani, Kurdistan, Iraq.

**Shvan H. Mohammed** Kscien Organization for Scientific Research, Sulaimani, Kurdistan, Iraq.

fahmi.hussein@univsul.edu.iq

## Predatory journals: tell-tale lax review

Agnes Grudniewicz and colleagues argue for a definition of a predatory journal that will protect scholarship (*Nature* 576, 210–212; 2019). Their proposed definition excludes an important feature of predatory journals – poor-quality peer review – on the grounds that such reviews are not accessible for analysis. It is a sad irony that this lack of transparency – a tell-tale trait of predatory journals – should be used to justify omitting an assessment of peer-review quality.

If misuse of the peer-review label is not included in the definition of predatory journals, it could strengthen rather than weaken them. Formal listings of those journals might shrink under such a definition: many journals would be removed because their questionable peer-review procedures have escaped scrutiny and they seem otherwise respectable. They could then become attractive outlets to potential authors.

As Grudniewicz and colleagues point out, legitimate journals that keep their peer-review processes under wraps encourage predatory practices. If publication of signed referees' comments were standard, journals publishing unrefereed papers would quickly be exposed. In our view, therefore, open peer review should be compulsory and the definition of predatory journals should include the quality of peer review.

**Leonhard Dobusch\*** University of Innsbruck, Austria.

leonhard.dobusch@uibk.ac.at

\*On behalf of 4 correspondents; see [go.nature.com/2qltuv2](https://go.nature.com/2qltuv2)

## Röntgen, Becquerel and radiation

Last month marked the 175th anniversary of the birth of German physicist Wilhelm Conrad Röntgen (1845–1923), who won the 1901 Nobel prize for his discovery of X-rays. His work is still a linchpin of modern science and medicine.

Röntgen's academic career had a less-than-propitious start. Wrongly accused of being the author of a caricature of his class teacher, he was expelled from high school in the Netherlands without graduating. His application to Utrecht University in the Netherlands was rejected as a result, but he went on to study mechanical engineering at the Federal Polytechnical School (now the Swiss Federal Institute of Technology) in Zurich. He was then rejected by Julius Maximilian University of Würzburg in Germany for a postdoctoral qualification, which he eventually secured at the University of Strasbourg, France.

Despite this rejection, Röntgen later donated his Nobel Prize money to the University of Würzburg. In another example of his philanthropy, he declined to patent his X-ray discovery, thereby making it available to the world. He also turned down the honour of a noble title.

In 1903, French engineer Henri Becquerel was awarded the Nobel Prize in Physics, along with Marie and Pierre Curie (see also *Nature* 579, 490–491; 2020), for their pioneering work on radioactivity. Becquerel was inspired by Röntgen's X-rays, which gave him insight into other forms of radiation, such as phosphorescence (see *Nature* 78, 414–416; 1908).

**Andreas Otte** Offenburg University, Germany.  
andreas.otte@hs-offenburg.de

# News & views

## Organic chemistry

# Strong chemical reducing agents produced by light

Radek Cibulka

An electrically neutral radical has been found to be a potent chemical reducing agent when excited by light. Remarkably, it is produced from a positively charged precursor that has long been used as a strong excited-state oxidizing agent. **See p.76**

When molecules absorb light, they enter an excited state and become more reactive than when in their ground state. Light energy can therefore be used to generate reactive molecules that undergo chemical transformations that would otherwise be difficult to achieve. Several powerful oxidizing agents have been generated using light excitation, but strong reductants have been more difficult to produce. On page 76, MacKenzie *et al.*<sup>1</sup> report the discovery of a light-generated molecular species that exhibits reducing properties comparable to those of alkali metals – and which is therefore one of the strongest known chemical reductants.

Chemical reactions mediated by visible light are important tools in organic synthesis. These reactions occur analogously to light-driven biological processes such as photosynthesis – with the help of a light-absorbing catalyst. In photoredox catalysis<sup>2</sup>, an excited catalyst molecule exchanges a single electron with a reaction partner (the substrate). During this process, which is known as photoinduced electron transfer (PET), the substrate is transformed into a reactive free radical; this undergoes a subsequent reaction to give one or more final products. Such processes usually occur at ambient temperature because their energy barrier is overcome using light energy.

Photoredox catalysis has undergone unprecedented development in the past decade, but some challenges remain. One is that no photoredox catalyst provides a reductant comparable in strength to that of alkali metals such as lithium and sodium. Alkali metals are still used in various reactions as potent reductants, despite their associated hazards and their tendency to produce undesired side products (that is, they have relatively low selectivity).

One example of a photoredox reductive process is the generation of molecular species called aryl radicals, which, when organic compounds are being synthesized, can be used as a source of aryl groups (groups derived from a benzene ring or a benzene analogue by the removal of a hydrogen atom). Aryl halide compounds, in which an aryl group is attached to a halogen atom (chlorine, bromine or iodine), are preferred starting materials for generating

aryl radicals because they are widely available and easy to handle. Aryl chlorides are the most preferred, but they are the most difficult aryl halides to reduce – as reflected by their highly negative reduction potentials. Reduction potentials quantify the tendency of a compound to acquire electrons from other compounds; for example, the reduction potential of chlorobenzene, a simple aryl chloride, is  $-2.78$  volts relative to the potential of a saturated calomel electrode (SCE), a standard reference used in reduction-potential measurements<sup>3</sup>.

It has not been possible to reduce aryl chlorides using a single PET process with visible light, because visible-light photons don't have enough energy for the task. To reduce another compound, an excited photoredox catalyst must have an oxidation potential (a measure of its ability to lose electrons to other compounds) lower than the reduction potential of the compound to be reduced. 10-Phenylphenothiazine, for example, is one of the most strongly reducing photoredox catalysts when excited by light, but the oxidation potential of excited phenothiazine is only  $-2.1$  V relative to SCE<sup>4</sup> (versus SCE) – insufficient to convert

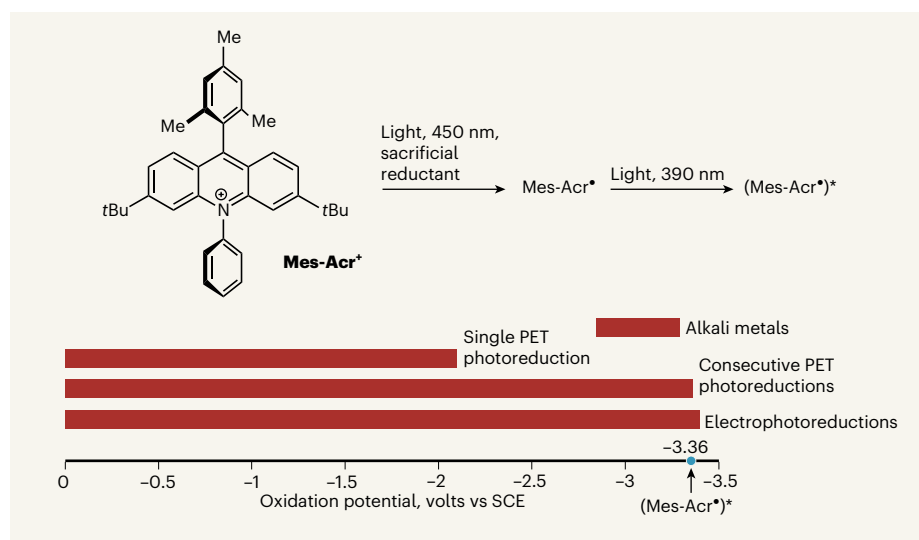


**Figure 1 | An excited neutral radical acts as a potent reductant.** The strength of chemical reductants is quantified by their oxidation potential, which is measured in volts relative to the potential of a reference electrode (such as a saturated calomel electrode; SCE). Two of the strongest reductants are the alkali metals sodium and lithium. Relatively strong reductants can also be produced from organic molecules in light-driven processes called photoinduced electron transfers (PETs), but the oxidation potentials are insufficiently negative for many reductions<sup>3</sup>. More-negative values can be achieved using two consecutive PET steps (see ref. 5, for example), or in electrophotoreduction processes that combine an electrochemical step with a PET step<sup>8,9</sup>. The mesitylacridinium ion (Mes-Acr<sup>+</sup>) can be converted into a radical (Mes-Acr<sup>•</sup>) when irradiated by light of wavelength 450 nanometres in the presence of a sacrificial reductant. MacKenzie *et al.*<sup>1</sup> report that when this radical is irradiated by light of wavelength 390 nm, it produces an excited radical, (Mes-Acr<sup>•</sup>)<sup>\*</sup>, that is a potent reductant. Me, methyl group; tBu, tertiary butyl group.



chlorobenzene into aryl radicals, for instance.

To overcome this problem, various systems have been reported that involve the use of two consecutive PET steps (see ref. 5, for example). In these approaches, a 'sacrificial' reducing agent reduces the excited catalyst molecule produced in the first step, forming a radical anion that is then excited by another photon. The resulting excited radical anion is a strong reducing agent. For instance, the excited radical anion formed from the catalyst Rhodamine 6G has an oxidation potential of  $-2.4$  V versus SCE, which is sufficiently negative to reduce aryl bromides and aryl chlorides that have a reduction-facilitating group<sup>6</sup>.

MacKenzie *et al.* now report an approach based on a salt that contains a mesitylacridinium ion (Mes-Acr<sup>+</sup>; Fig. 1). Mesitylacridinium salts have been used for almost two decades in photo-oxidation reactions<sup>7</sup> – when irradiated by visible light, the resulting excited species is a potent oxidant that takes an electron from a substrate and is thereby converted into an acridine radical (Mes-Acr<sup>•</sup>). The electrically neutral radical is converted back to Mes-Acr<sup>+</sup> by an oxidant for subsequent catalytic cycles.

The authors recognized that Mes-Acr<sup>•</sup> is a relatively stable species that absorbs light mainly from two ranges of wavelengths: 350–400 nanometres and 450–550 nm. They report that, when Mes-Acr<sup>•</sup> is irradiated with light of wavelength 390 nm, it forms an excited neutral radical that acts as an extremely strong reducing agent, with a maximum oxidation potential of  $-3.36$  V versus SCE. They propose that this large negative value is the result of charge transfer within the excited radical.

The use of an excited neutral organic radical is rare in photoredox catalysis. MacKenzie and colleagues formulated a reductive photocatalytic cycle based on Mes-Acr<sup>•</sup> using 390-nm light and a sacrificial reducing agent. This system can carry out several reduction reactions, such as the removal of tosyl groups from tosylated amine compounds (a type of reaction commonly used in organic synthesis; see Fig. 3 of the paper<sup>1</sup>). The researchers demonstrated that the new system is robust enough to work on scales that are useful for preparing compounds in the laboratory, by performing a detosylation reaction with 1.28 grams of a starting material.

The same approach can also be used to replace bromine or chlorine atoms with hydrogen atoms in aryl bromides and chlorides, respectively – such reactions are known as dehalogenations (see Fig. 2 of the paper<sup>1</sup>). This procedure is possible when various groups are present in the substrates, and it even works with 4-chloroanisole, an aryl chloride that has a reduction potential of  $-2.9$  V versus SCE.

Another approach for the catalytic production of strongly reducing species was reported simultaneously earlier this year in two papers from different groups<sup>8,9</sup>. In both

cases, a neutral organic molecule acts as the catalyst; this is reduced electrochemically on a cathode to produce a radical anion, which is then excited by visible light to form a strong reductant with an oxidation potential more negative than  $-3.0$  V versus SCE. These electrophotocatalytic systems were used to dehalogenate electron-rich aryl chlorides, and also in a series of arylation reactions (transformations in which an aryl group is attached to another molecule).

The use of electrochemical reduction, instead of photochemical methods, to generate radicals allows catalysts to be used that do not absorb visible light. For example, naphthalene monoimide, a catalyst used in one<sup>9</sup> of the two papers, falls into this category and cannot undergo the initial conversion to a radical anion using visible light. By contrast, once it is transformed electrochemically into a visible-light-absorbing radical, it can enter a photocatalytic cycle.

MacKenzie and colleagues' observation of the strong reductant character of excited neutral Me-Acr<sup>•</sup> will inspire investigations into whether other molecules show similar behaviour. One can also expect increased interest in other photocatalytic approaches for the production of reductive systems<sup>10–13</sup>. Taking into account the highly negative oxidation potentials observed for various light-generated agents in the current work

and by other research groups, we can look forward to new arylation reactions, and even to ambitious applications such as the Birch reduction<sup>14</sup> – a classic synthetic reaction typically performed using alkali metals.

**Radek Cibulka** is in the Department of Organic Chemistry, University of Chemistry and Technology, Prague, Prague 16628, Czech Republic.  
e-mail: cibulka@vscht.cz

1. MacKenzie, I. A. *et al.* *Nature* **580**, 76–80 (2020).
2. Shaw, M. H., Twilton, J. & MacMillan, D. W. C. *J. Org. Chem.* **81**, 6898–6926 (2016).
3. Enemærke, R. J., Christensen, T. B., Jensen, H. & Daasbjerg, K. *J. Chem. Soc. Perkin Trans. 2*, 1620–1630 (2001).
4. Discekici, E. H. *et al.* *Chem. Commun.* **51**, 11705–11708 (2015).
5. Ghosh, I., Ghosh, T., Bardagi, J. I. & König, B. *Science* **346**, 725–728 (2014).
6. Ghosh, I. & König, B. *Angew. Chem. Int. Edn* **55**, 7676–7679 (2016).
7. Romero, N. A. & Nicewicz, D. A. *Chem. Rev.* **116**, 10075–10166 (2016).
8. Kim, H., Kim, H., Lambert, T. H. & Lin, S. *J. Am. Chem. Soc.* **142**, 2087–2092 (2020).
9. Cowper, N. G. W., Chernowsky, C. P., Williams, O. P. & Wickens, Z. K. *J. Am. Chem. Soc.* **142**, 2093–2099 (2020).
10. Kerzig, C., Guo, X. & Wenger, O. S. *J. Am. Chem. Soc.* **141**, 2122–2127 (2019).
11. Ghosh, I., Shaikh, R. S. & König, B. *Angew. Chem. Int. Edn* **56**, 8544–8549 (2017).
12. Ravetz, B. D. *et al.* *Nature* **565**, 343–346 (2019).
13. Majek, M., Faltermeier, U., Dick, B., Pérez Ruiz, R. & von Wangelin, A. *J. Chem. Eur. J.* **21**, 15496–15501 (2015).
14. Chatterjee, A. & König, B. *Angew. Chem. Int. Edn* **58**, 14289–14294 (2019).

## Developmental biology

# A clock that controls human spine development

**Adelaida Palla & Helen Blau**

Visualization of the rhythmic oscillations of the mouse and human segmentation clocks, which are crucial to spine development, is now possible thanks to the development of sophisticated cell-culture systems. **See p.113, p.119 & p.124**

What do the flashes of a firefly and the chirpings of a cricket have in common? Both occur in a regular rhythm, which is controlled by an oscillating biological clock<sup>1</sup>. Another oscillating genetic clock controls the development of embryonic structures called somites, which give rise to the vertebrae that protect the spinal cord. Our knowledge of this segmentation clock stems almost entirely from research on animals<sup>2,3</sup>, because technical and ethical considerations limit the study of human embryos in culture. Diaz-Cuadros *et al.*<sup>4</sup> (page 113) and Matsuda *et al.*<sup>5</sup> (page 124) now report a breakthrough that enables studies

of the human segmentation clock *in vitro*. In addition, Yoshioka-Kobayashi *et al.*<sup>6</sup> (page 119) use sophisticated techniques in mice to provide insights into the mechanisms that control the mammalian segmentation clock.

Somites arise from a tissue called the presomitic mesoderm (PSM). During somite formation, temporally and spatially controlled oscillations in transcription yield gene-expression waves that propagate through the PSM along the embryo's head-to-tail axis. The result is a striped pattern of somites that forms the blueprint for the spine. Although the molecular components of the segmentation

clock are highly evolutionarily conserved across vertebrates, new somites form with different rhythms in each species. For instance, gene oscillations have a period of 30 minutes in zebrafish and 2 hours in mice. Oscillations have been estimated to occur every 4 to 5 hours in humans<sup>2</sup> – although until now they have never been directly observed.

Diaz-Cuadros *et al.* and Matsuda *et al.* set out to model the human clock using induced pluripotent stem cells (iPSCs) – cells that are generated *in vitro* from differentiated human cells and, similarly to embryonic stem cells, can give rise to every cell type in the body. The groups used established protocols<sup>7–9</sup> to convert iPSCs into PSM *in vitro*.

To visualize and monitor the dynamic oscillations of clock genes in the cultured PSM in real time, each group used a different ‘reporter’ protein. Matsuda and colleagues used a reporter in which a key segmentation-clock gene<sup>10</sup>, *Hes7*, drives production of the bioluminescent enzyme luciferase. As *Hes7* expression oscillates, levels of the reporter increase and decrease. Diaz-Cuadros *et al.* used an engineered version of *Hes7* fused to a gene that encodes Achilles, which is a more rapidly generated variant of yellow fluorescent protein developed by Yoshioka-Kobayashi and colleagues. The use of Achilles enabled Diaz-Cuadros and co-workers to track fluorescent waves of *Hes7* expression at the single-cell level<sup>4</sup> – a resolution not possible with the luciferase reporter. Analyses using both reporters provide the first definitive evidence that the human segmentation clock has a period of approximately 5 hours (Fig. 1a).

Three key signalling pathways – the Notch, Wnt and FGF pathways – act in sequential negative feedback loops to regulate oscillating gene expression during somite formation<sup>2,3,11,12</sup>. Diaz-Cuadros and colleagues used their culture system to investigate these pathways in detail. They confirmed the roles of these pathways in PSM cells taken from mouse embryos, and then showed that similar pathways govern segmentation in human PSM differentiated from iPSCs, with oscillations dependent on Notch signalling and another pathway, mediated by a protein called YAP. They found that FGF signalling not only determines the positions along the body axis at which oscillations stop, as previously reported<sup>2</sup>, but also regulates the complex dynamics of the oscillations – their period, phase and amplitude.

Matsuda and colleagues used their culture protocol to study a human genetic disease, congenital spondylocostal dysostosis, in which defects in segmentation of the vertebrae lead to skeletal anomalies<sup>13,14</sup>. The authors generated PSM from iPSCs derived from two people with the disease, who each had mutations in a different gene of the Notch signalling pathway. Surprisingly, despite these mutations and differences in overall gene

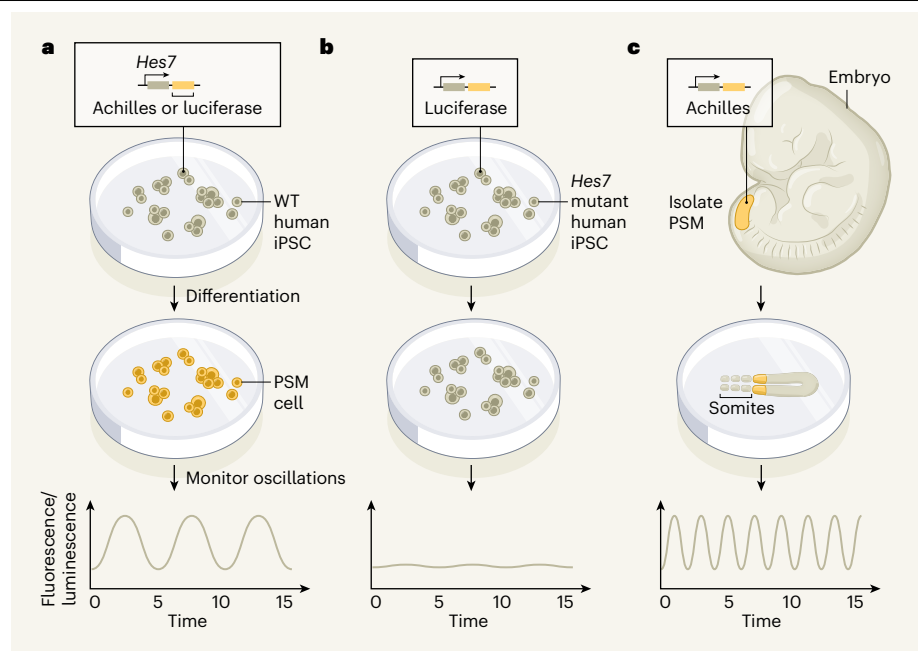


**Figure 1 | Modelling embryonic segmentation *in vitro*.** A tissue called the presomitic mesoderm (PSM) gives rise to somites – embryonic precursors of vertebrae. This process involves a ‘segmentation clock’ that drives rhythmic oscillations of gene expression, including that of the gene *Hes7*. Three groups have developed systems to analyse the clock in culture using live-cell imaging. **a**, Diaz-Cuadros *et al.*<sup>4</sup> and Matsuda *et al.*<sup>5</sup> directed wild-type (WT) human induced pluripotent stem cells (iPSCs) to become PSM cells. The iPSCs had been engineered to express a version of *Hes7* that drives expression (arrow) of genes encoding the fluorescent molecule Achilles<sup>4</sup> or the luminescent molecule luciferase<sup>5</sup>. Monitoring the oscillations of these genes in PSM cells revealed that the human segmentation clock has a period of about 5 hours. **b**, Matsuda *et al.* performed the same experiment using iPSCs in which *Hes7* is mutated, as in the skeletal disorder spondylocostal dysostosis, and found a lack of oscillations. **c**, Yoshioka-Kobayashi *et al.*<sup>6</sup> isolated the PSM from mouse embryos carrying a *Hes7*–Achilles reporter, and monitored oscillations, which have a 2-hour period.

expression, the authors observed normal oscillations in the PSM. By contrast, when the authors produced PSM from cells genetically engineered to carry a *Hes7* mutation that had previously been identified as a cause of spondylocostal dysostosis<sup>15</sup>, they observed a dramatic loss of oscillations (Fig. 1b). This work highlights the potential of using iPSC-derived PSM to determine the relative roles of various clock components in development.

It is known that, although individual PSM cells show autonomous oscillations, Notch signalling between cell neighbours synchronizes these oscillations<sup>1,16</sup> to produce gene-expression waves at the population level. Yoshioka-Kobayashi *et al.* set out to examine this role for Notch signalling in detail. The authors engineered mice to carry a *Hes7*–Achilles reporter, and to lack a protein called Lunatic fringe that modulates Notch signalling. They then isolated the entire PSM from embryos that lacked Lunatic fringe and from controls that did not, and made use of optogenetics, a light-triggered gene-expression system, to visualize somite development in culture by tracking *Hes7* oscillations over time (Fig. 1c). Although the autonomous oscillations of single PSM cells were unaffected by loss of Lunatic fringe, the researchers observed oscillation defects at the population level.

Notch signalling involves the release of the protein DLL1 from one cell and its binding by Notch receptors on another. This interaction triggers a downstream signalling cascade in the receiving cell that causes increases in the expression of various genes, including *Hes1* (ref. 17). This sender–receiver system can be modulated using a genetically engineered optogenetic variant of the *Dll1* gene that is expressed in response to stimulation by light<sup>18</sup>. The authors stimulated *Dll1*, and compared how long it took for neighbouring cells to exhibit *Hes1* upregulation in mice lacking Lunatic fringe with the time it took in controls. The study revealed that Lunatic fringe controls population-level oscillations by regulating the timing and amplitude of the signal-sending and signal-receiving process in adjacent cells. This work underscores the intricate role of Notch components in the cell–cell interactions that control clock oscillations.

Together, the current studies provide a remarkable demonstration that simple iPSC culture systems can be used for in-depth analysis of the oscillatory gene expression associated with somite segmentation at single-cell resolution. However, they also have limitations. For instance, Diaz-Cuadros *et al.* and Matsuda *et al.* did not observe final stages of somite development and vertebra



formation in their human culture systems. Nonetheless, their protocols will undoubtedly help to advance our understanding of the molecular basis of normal segmentation and to reveal the genes that, when mutated, lead to the development of disorders of the spine.

More broadly, gene-regulatory networks are highly conserved between mammals, regardless of the animals' size or whether they are bipedal or quadrupedal. This is in stark contrast to the species-specific timing of gene oscillations, which is fundamental to body-plan development. What causes these crucial differences in timing remains an enigma – but one that can now begin to be unravelled.

**Adelaida Palla** and **Helen Blau** are in the Baxter Laboratory for Stem Cell Biology, Department of Microbiology and Immunology, Institute for Stem Cell Biology and Regenerative Medicine, Stanford School of Medicine, Stanford,

California 94305-5175, USA.  
e-mail: hblau@stanford.edu

1. Herrgen, L. et al. *Curr. Biol.* **20**, 1244–1253 (2010).
2. Hubaud, A. & Pourquié, O. *Nature Rev. Mol. Cell Biol.* **15**, 709–721 (2014).
3. Oates, A. C., Morelli, L. G. & Ares, S. *Development* **139**, 625–639 (2012).
4. Diaz-Cuadros, M. et al. *Nature* **580**, 113–118 (2020).
5. Matsuda, M. et al. *Nature* **580**, 124–129 (2020).
6. Yoshioka-Kobayashi, K. et al. *Nature* **580**, 119–123 (2020).
7. Chal, J. et al. *Nature Biotechnol.* **33**, 962–969 (2015).
8. Loh, K. M. et al. *Cell* **166**, 451–467 (2016).
9. Xi, H. et al. *Cell Rep.* **18**, 1573–1585 (2017).
10. Bessho, Y. et al. *Genes Dev.* **15**, 2642–2647 (2001).
11. Hofmann, M. et al. *Genes Dev.* **18**, 2712–2717 (2004).
12. Wahl, M. B., Deng, C., Lewandoski, M. & Pourquié, O. *Development* **134**, 4033–4041 (2007).
13. Sparrow, D. B. et al. *Am. J. Hum. Genet.* **78**, 28–37 (2006).
14. Whittick, N. V. et al. *Am. J. Hum. Genet.* **74**, 1249–1254 (2004).
15. Sparrow, D. B., Guillén-Navarro, E., Fatkin, D. & Dunwoodie, S. L. *Hum. Mol. Genet.* **17**, 3761–3766 (2008).
16. Jiang, Y.-J. et al. *Nature* **408**, 475–479 (2000).
17. Jouve, C. et al. *Development* **127**, 1421–1429 (2000).
18. Isomura, A., Ogushi, F., Kori, H. & Kageyama, R. *Genes Dev.* **31**, 524–535 (2017).

knowledge of the whereabouts of ecologically significant marine areas<sup>10</sup>. However, accurately defining these areas in a highly dynamic, changing environment is challenging.

Monitoring predators at the top of a marine food web can help with this task. Such predators migrate within and between ecosystems, and can be used as indicator species<sup>11</sup> – those able to provide information on the status of an ecosystem or habitat if alterations occur in their movement patterns, behaviour or reproductive success. In particular, tracking top predators can assist with identifying the areas that they use most, which can be considered as regions of great ecosystem importance, not only for the predators but also for a wide range of other species<sup>11</sup>. Indeed, tracking data are increasingly being used to inform conservation policy around the world<sup>12</sup>, and have been used to quantify the extent of spatial overlaps between species and fishing activities globally<sup>3</sup>.

Hindell et al. report analyses of tracking data from 4,060 individuals of 17 species of marine predators (seabirds and mammals), and suggest a way to use such data to predict key ecological regions in the Southern Ocean. Tracking data were collected between 1991 and 2016 using electronic tags attached to the animals. These tags provided location estimates (obtained using satellite information or other methods) as the animals migrated. The authors used some of these data (for 2,823 individuals) to develop predictive models to identify crucial habitats in the Antarctic region for all of the predator species combined. These integrated results provide a spatially defined assessment of areas of high biodiversity that includes species across multiple levels of the food chain (termed trophic levels) in the Southern Ocean.

Defining a single, integrated result from such varied data sets and from so many species is a complex undertaking. Predators in the Southern Ocean include a large range of species from across different taxonomic groups. These include species living in the Antarctic region and species residing immediately north of it (in the sub-Antarctic), all with different diets and patterns of movement. The authors used a series of data-processing steps to generate a value they termed 'habitat importance', which they predicted using data across all of these species together (assemblage-level maps). To do this, Hindell and colleagues first mapped habitat importance for the species living in the Antarctic separately from those living in the sub-Antarctic, and then selected the maximum habitat-suitability values in those two maps to generate an overall assemblage-level map for all of the predator species combined.

Finally, the authors defined the regions in the top 10% of their calculated habitat importance value as the areas of the most ecological significance in the Southern Ocean. This final

## Marine conservation

# Predators on track for ocean protection

**Ana M. M. Sequeira**

Satellite tracking of marine predators in the Southern Ocean has revealed key ecological areas under disproportionate pressure from human activities. These results show the value of tracking data for informing conservation efforts. **See p.87**

Even the most remote marine ecosystems on Earth – such as those at high latitudes, including in the Southern Ocean around Antarctica – can no longer be considered pristine<sup>1</sup>. The effects of humans on marine ecosystems now have a global footprint<sup>2–4</sup>, and mitigation of associated threats requires knowledge of the areas of particular ecological and biological significance. Such areas sustain the healthy functioning of marine ecosystems and should therefore be protected. On page 87, Hindell et al.<sup>5</sup> report analyses of tracking data for marine species that reveal these key areas in the Southern Ocean.

The waters of the Southern Ocean encircle the Earth through the Drake Passage, the ocean region between the tip of South America and Antarctica. Because of this passage, the Southern Ocean has a key role in global climate and ocean circulation<sup>6</sup>. This ocean is also home to a unique range of marine fauna, including many charismatic predators, such as penguins (Fig. 1) and seals, as well as the precious Antarctic krill (*Euphausia superba*). These krill are at the base of the marine food web, and,

alongside species of toothfish (*Dissostichus eleginoides* and *Dissostichus mawsoni*), are the target of the largest fishing industries in the Southern Ocean<sup>7,8</sup>. The fisheries compete with animals for food resources, and fishing activities along with the pressures from

**“Tracking data are increasingly being used to inform conservation policy around the world.”**

climate change are raising concerns about the possibility of ecosystem collapses there<sup>8,9</sup>.

The Commission for the Conservation of Antarctic Marine Living Resources is the main management body for the Southern Ocean, and is tasked with ensuring the preservation of this ecosystem. To succeed, the commission needs to take precautionary steps, including the establishment of more and better-designed marine reserves as has been suggested<sup>8</sup>, and sites for these should be chosen on the basis of





**Figure 1 | Emperor penguins (*Aptenodytes forsteri*) in Antarctica.** Hindell *et al.*<sup>5</sup> report analyses of tracking data for marine predators, including this penguin species. The authors' results pinpoint regions of the Southern Ocean around Antarctica that should be protected.

step was a central part of their study. It enabled comparisons to be made between the areas of ecological significance and the areas affected by human activities, as well as between the levels of existing protection inside and outside these areas.

Hindell and co-workers report that the predicted areas of ecological significance they identified match the ocean regions of known elevated productivity for Antarctic krill<sup>13</sup> and for other organisms at the base of the food web, including myctophids (lanternfish)<sup>14</sup>. This result is consistent with the idea that marine predators can be used as indicators to identify areas of ecological significance. The authors report the particularly striking finding that a disproportionately higher level of human pressures (fishing and the effects of climate change) occurred inside rather than outside the areas identified as being of ecological significance. On the basis of this, the authors recommend that the current network of protected marine areas in the Southern Ocean be extended. They confirm that these extensions should include the areas for which protection is already being planned.

It would have been interesting if the authors

had suggested how an approach similar to theirs could best be used to tackle comparable problems on a global scale. For example, the authors' views on the best strategy for contributing scientific knowledge to inform efforts to protect biodiversity on the high seas (the waters outside national jurisdictions) would have been a valuable addition. This topical issue is currently being discussed by the United Nations General Assembly, and negotiations are under way to develop an international legally binding solution to address the problem<sup>15</sup>.

Scientists have tracked marine predators for decades<sup>3,4,12</sup>. It is time to pool all these existing data sets to address pressing conservation challenges on a global scale. To succeed, a worldwide movement is needed within the community of animal-tracking researchers, to drive the sharing of these data and to combine them with information about human activities at sea. Combining such information will deliver much-needed evidence of the extent of existing threats, to inform managers and policymakers in a timely manner. As Hindell and colleagues state, the Southern Ocean has the potential to provide an example of how "science, policy and management can interact

to meet the challenges of a changing planet", and their work highlights a pathway for how best to direct policy efforts.

**Ana M. M. Sequeira** is at the Oceans Institute and School of Biological Sciences, University of Western Australia, Perth, Western Australia 6009, Australia.

e-mail: ana.sequeira@uwa.edu.au

1. Blight, L. K. & Ainley, D. G. *Science* **321**, 1443 (2008).
2. Halpern, B. S. *et al.* *Science* **319**, 948–952 (2008).
3. Queiroz, N. *et al.* *Nature* **572**, 461–466 (2019).
4. Sequeira, A. M. M. *et al.* *Front. Mar. Sci.* **6**, 639 (2019).
5. Hindell, M. A. *et al.* *Nature* **580**, 87–92 (2020).
6. Rintoul, S. R. *Nature* **558**, 209–218 (2018).
7. Nicol, S., Foster, J. & Kawaguchi, S. *Fish Fish.* **13**, 30–40 (2012).
8. Brooks, C. M. *et al.* *Nature* **558**, 177–180 (2018).
9. Atkinson, A. *et al.* *Nature Clim. Change* **9**, 142–147 (2019).
10. Dunstan, P. K. *et al.* *Ocean Coastal Mgmt* **121**, 116–127 (2016).
11. Sergio, F. *et al.* *Annu. Rev. Ecol. Evol. Systemat.* **39**, 1–19 (2008).
12. Hays, G. C. *et al.* *Trends Ecol. Evol.* **34**, 459–473 (2019).
13. Atkinson, A. *et al.* *Mar. Ecol. Prog. Ser.* **362**, 1–23 (2008).
14. Freer, J. J., Tarling, G. A., Collins, M. A., Partridge, J. C. & Genner, M. J. *Diversity Distrib.* **25**, 1259–1272 (2019).
15. Wright, G. *et al.* *Mar. Policy* <https://doi.org/10.1016/j.marpol.2018.12.003> (2019).

This article was published online on 18 March 2020.



## Cell biology

# Ghostly metabolic messages from dying cells

Douglas R. Green

Cell death by a process called apoptosis inhibits inflammation in surrounding tissue. The finding that dying apoptotic cells release a tailored cocktail of metabolite molecules reveals a way in which they influence their living neighbours. **See p.130**

"Marley was dead, to begin with. There is no doubt whatever about that." The iconic opening lines of Charles Dickens's novel *A Christmas Carol* convey the idea of the finality of death, a concept that pervades our thinking even when considering the demise of cells. A dead cell is, to echo Dickens's description of Marley, "as dead as a doornail". But just as Marley had an influence from beyond the grave to change the character of Ebenezer Scrooge in the story, cells that die can have a vital effect on the living cells around them. Medina *et al.*<sup>1</sup> bring this process to life on page 130 by uncovering metabolic processes in dying cells that have important consequences for the organism.

Every second, millions of cells die in our bodies owing to processes that are a normal part of life, such as tissue turnover and responses to environmental stresses<sup>2</sup>. The vast majority of these deaths occur by a process called apoptosis. This is a form of cellular suicide that is orchestrated by the actions of enzymes called caspases, which cleave hundreds of different intracellular proteins<sup>3</sup>. This regulated cleavage of various caspase targets effectively 'packages' the dying cell through an orderly dismantling process. DNA in the nucleus is cut into small pieces, the cytoplasmic 'skeleton' of filamentous actin protein is remodelled to break the cell into smaller fragments, and the exposure of a particular lipid on the cell surface signals to immune cells, such as macrophages, to take up (engulf) and digest the dying cell<sup>2</sup>.

Ever since the original description of apoptosis<sup>4</sup>, it has been known that this form of cell death does not trigger an inflammatory response, as occurs in other types of cell death, such as necrosis. Subsequent research<sup>5</sup> confirmed that apoptotic cell death is anti-inflammatory, leading to proposals that the injection of apoptotic cells might be used to control inflammatory disease. The inflammation caused by necrotic cell death has been attributed to the release of molecules called damage-associated molecular patterns (DAMPs), of which several have been identified<sup>6</sup>. By

contrast, little is known about the mechanism underlying the anti-inflammatory properties of apoptotic cells. The engulfment of apoptotic cells by macrophages promotes tissue repair<sup>7</sup>, and the apoptosis-associated molecules responsible for this effect are unknown.

Medina and colleagues discovered that, during the apoptosis of mammalian cells (including human cells) grown *in vitro*, small molecules released from the dying cells can induce macrophages to express genes involved in tissue repair and the inhibition

of inflammation. The authors speculated that metabolites – molecules arising from metabolic processes – were responsible for this effect. By profiling different cell types undergoing apoptosis in response to different triggers, Medina *et al.* identified metabolites that were consistently released from all dying cells, whereas other metabolites in the cells were not released. This specificity was due, at least in part, to the selectivity of a particular protein channel on the cell surface, pannexin 1 (PANX1), which opens when it is cleaved by caspases<sup>8</sup>. Apoptotic cells engineered to lack PANX1 did not release the apoptosis-associated metabolites.

The authors examined six metabolites released from all apoptotic cells and found that none, individually, had a significant effect on the gene-expression profile of macrophages. However, administration of all six had a robust effect on the gene-expression pattern, and a similar expression profile could be induced, at least partially, by exposing macrophages to a mixture of just three of the metabolites: spermidine, guanosine monophosphate and inosine monophosphate. The authors report that administering a mixture of these three metabolites had remarkable anti-inflammatory effects *in vivo* – inhibiting disease in a mouse model of arthritis and limiting the rejection of lung transplants in mice.

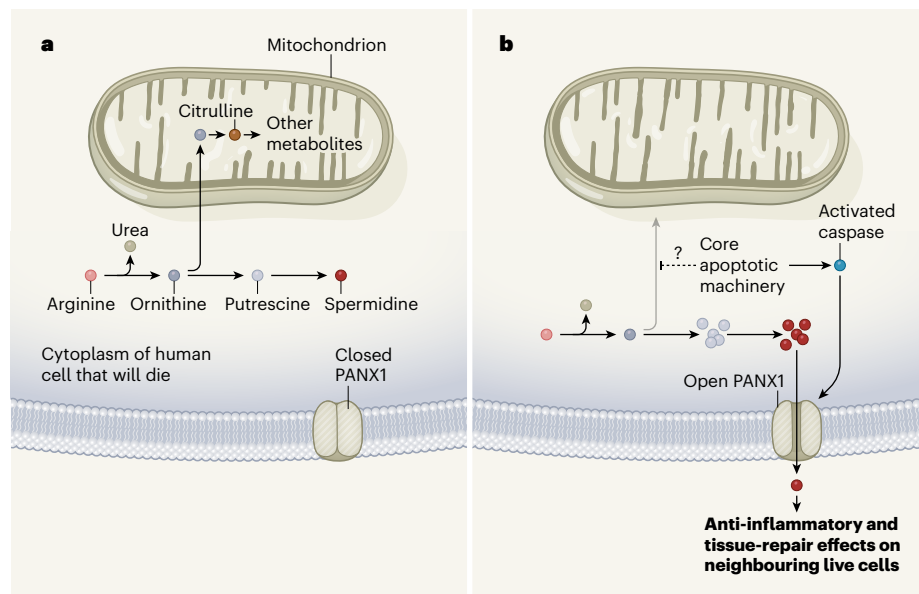


**Figure 1 | Cells that die by a process called apoptosis signal to neighbouring cells.** Medina *et al.*<sup>1</sup> report that dying human apoptotic cells release molecules produced by metabolic processes, and that these metabolites have anti-inflammatory and tissue-repair effects. **a**, In healthy human cells, the amino-acid arginine is often converted to the molecule ornithine, which is either used in a pathway that generates the molecule spermidine or transported into a mitochondrion (a type of organelle), where it is converted to citrulline and other metabolites. Until the cell starts to die, a channel protein on the cell surface called pannexin 1 (PANX1) remains closed. **b**, As the cell undergoes apoptosis, the core apoptotic machinery activates enzymes termed caspases, which cleave PANX1, and the channel then opens. Production of the molecules spermidine and putrescine becomes higher than normal. One possible way to explain this is if the core apoptotic machinery prevents ornithine from entering the mitochondrion and instead diverts it towards spermidine production. Spermidine and other specific metabolites (not shown) are selectively released through PANX1 and influence adjacent cells.

Spermidine is a type of molecule called a polyamine. It is mainly produced from a metabolic pathway that converts the amino acid arginine to polyamines through intermediates that include the molecule ornithine (Fig. 1). Medina and colleagues traced the conversion of arginine to spermidine by this pathway, and found that cells induced to undergo apoptosis increased their synthesis of spermidine and its precursor, the molecule putrescine, before dying. The apoptotic cells released spermidine, but not putrescine. Spermidine release occurred in a PAX1-dependent manner.

Although this phenomenon was monitored using just one apoptosis-inducing condition (namely, ultraviolet radiation), the finding raises the possibility that activation of apoptosis drives this pathway, which synthesizes spermidine. The hint that suggests this is the authors' observation of the effects of administering a type of drug called a BH3 mimetic. This drug directly triggers a core step in apoptosis, the permeabilization of mitochondrial organelles in an event called mitochondrial outer membrane permeabilization (MOMP) – and its use led to spermidine release at levels comparable to those observed in apoptosis mediated by ultraviolet radiation. Perhaps MOMP prevents the transport of ornithine into mitochondria (where ornithine is converted to the molecule citrulline), and leads instead to ornithine being mobilized in cytoplasmic pathways leading to spermidine production. This model could be tested in cells engineered to lack components required for MOMP and exposed to BH3 mimetics.

The molecule urea is formed as a by-product of the conversion of arginine to ornithine. Urea is an inflammatory DAMP that is released from necrotic cells<sup>6</sup>, but the authors did not determine whether urea is released through PAX1 during apoptosis. However, because Medina and colleagues observed a rise in arginine metabolism during apoptosis, if urea is not released through PAX1, this might provide a further reason why apoptosis is not inflammatory.

How do spermidine, guanosine monophosphate and inosine monophosphate induce responses in macrophages, and why do the three metabolites work only when given together? Guanosine monophosphate and inosine monophosphate are known to signal to G-protein-coupled adenosine receptors<sup>9</sup>, and spermidine can participate in a broad range of activities. The molecule inosine (which can be derived from inosine monophosphate) has anti-inflammatory effects<sup>9</sup> and can prevent lethal inflammation in response to a bacterial toxin in mice<sup>10</sup>. It is possible that spermidine acts to increase such anti-inflammatory signalling from the adenosine receptors. Human cells are ten times less sensitive than mouse cells to the anti-inflammatory effects of inosine, probably owing to differences in

adenosine-receptor expression and function between the species<sup>8</sup>, and therefore efforts to use these metabolites to treat human disease might prove challenging.

Medina and colleagues' work opens rich possibilities for future investigations into how apoptosis triggers metabolic changes, and how the regulated release of metabolites influences tissues. In contrast to apoptosis, other forms of cell death, such as regulated forms of necrosis, have profoundly different effects on surrounding cells, and whether and how changes in metabolism triggered by those cell-death pathways influence their surroundings is unknown. Cells that die by a form of regulated necrosis termed necroptosis continue to synthesize and secrete molecules called cytokines that affect inflammation<sup>11</sup>. In these dead 'zombie' cells, this synthesis occurs in an organelle called the endoplasmic reticulum<sup>11</sup>, raising the possibility that metabolites produced in the functioning endoplasmic reticulum of these zombie cells also signal to living cells in the surrounding tissue. Marley's ghost appears in chains that he said were

forged in life; what other chains are forged in cell death?

**Douglas R. Green** is in the Department of Immunology, St. Jude Children's Research Hospital, Memphis, Tennessee 38105, USA. e-mail: douglas.green@stjude.org

1. Medina, C. B. *et al.* *Nature* **580**, 130–135 (2020).
2. Green, D. R. *Cell Death: Apoptosis and Other Means to an End* 2nd edn (Cold Spring Harb. Lab. Press, 2018).
3. Lüthi, A. U. & Martin, S. J. *Cell Death Differ.* **14**, 641–650 (2007).
4. Kerr, J. F. R., Wyllie, A. H. & Currie, A. R. *Br. J. Cancer* **26**, 239–257 (1972).
5. Henson, P. M. *Annu. Rev. Cell Dev. Biol.* **33**, 127–144 (2017).
6. Garg, A. D. & Agostinis, P. *Immunol. Rev.* **280**, 126–148 (2017).
7. Bosurgi, L., Hughes, L. D., Rothlin, C. V. & Ghosh, S. *Immunol. Rev.* **280**, 8–25 (2017).
8. Cheken, F. B. *et al.* *Nature* **467**, 863–867 (2010).
9. Haskó, G., Sitkovsky, M. V. & Szabó, C. *Trends Pharmacol. Sci.* **25**, 152–157 (2004).
10. Haskó, G. *et al.* *J. Immunol.* **164**, 1013–1019 (2000).
11. Orozco, S. L. *et al.* *Cell Rep.* **28**, 2275–2287 (2019).

The author declares competing financial interests: see [go.nature.com/zpmkml](https://go.nature.com/zpmkml) for details.

This article was published online on 18 March 2020.

## Nuclear physics

# A broken nuclear mirror

**Bertram Blank**

The principle of mirror symmetry, which states that nuclear structure remains the same when protons are swapped for neutrons and vice versa, has been found to be broken in the lowest-energy forms of a mirror pair of nuclei. **See p.52**

Nature likes symmetry. Examples range across size scales from macroscopic objects, such as spiderwebs or honeycombs, to the microscopic world with its arrangement of atoms in molecules, or of electrons around an atomic nucleus. Symmetry also exists at the level of nuclei, but on page 52, Hoff *et al.*<sup>1</sup> report one way of breaking it.

Atomic nuclei are composed of two different types of particle – protons and neutrons – which, if we ignore the charge on the proton, resemble each other so much that they are often treated as a single particle, the nucleon. Mirror pairs of nuclei, in which the numbers of neutrons and protons have been exchanged, therefore have similar properties.

In particular, the sequence of energies of a mirror pair's nuclear states should be the same, from the ground state in which the nucleons are in the lowest possible energy level, to excited states of increasing energy<sup>2</sup>. A change in this sequence has, however, previously been observed for excited states of mirror partners<sup>3</sup>. Hoff and co-workers now

report the breaking of mirror symmetry at the level of bound nuclear ground states (Fig. 1). They report that the ground states of the mirror partners bromine-73 and strontium-73 are not simply 'mirror images' in which protons and neutrons have been swapped, but have a different configuration of protons and neutrons.

How does this difference arise? The most basic building blocks of matter known today are quarks, of which there are six types. Protons and neutrons are both constructed from three quarks, and the most important difference between them is that their different quark combinations give the proton an electric charge of +1, whereas the neutron ends up neutral.

The strong nuclear interaction that binds nucleons together in an atomic nucleus is essentially the same between protons and neutrons. For protons, however, the electric repulsion between identically charged particles adds together. When building two mirror-symmetric atomic nuclei, one with



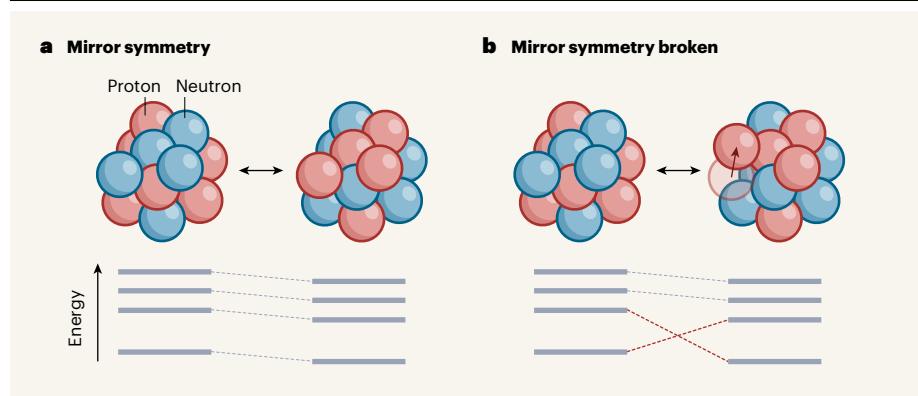


**Figure 1 | Breaking nuclear mirror symmetry.** **a**, In a pair of mirror nuclei, the number of protons in one nucleus equals the number of neutrons in the other, and vice versa. For perfect mirror symmetry, the nuclear structure and energy levels of the ground and excited states (shown schematically; dashed lines connect equivalent states) are essentially the same on swapping protons for neutrons, apart from a small overall shift caused by proton repulsion in the proton-rich nucleus. **b**, Hoff *et al.*<sup>1</sup> report that the lowest-energy states of a mirror pair can have a different configuration of protons and neutrons; red dashed lines indicate that the lowest energy levels in one nucleus have swapped places compared with **a**. The cartoon illustrates a simple example of mirror symmetry and how it might be broken.

$Z$  protons and  $N$  neutrons and the other with  $N$  protons and  $Z$  neutrons, this repulsion adds an extra global energy (mass) to the nucleus that has the more protons, but does not modify the arrangement of protons and neutrons. This symmetry explains why several of the properties of mirror partners are nearly identical: in their shape; their behaviour when excited (that is, when energy is added); and the properties of the decay processes through which unstable nuclei lose energy by emitting particles or radiation.

To determine nuclear properties such as energy levels, energy is pumped into a nucleus (for instance, by colliding it with another nucleus), and the decay process in which  $\gamma$ -rays are emitted from the resulting excited nucleus is observed. The previously observed difference<sup>3</sup> in the sequence of energy levels for the excited states of mirror partners occurred particularly at higher excitation energies, in which the density of states increases (that is, the neighbouring states come closer to each other). This difference of energy levels is a sign that mirror symmetry is only approximate and can be broken in particular circumstances.

A different structure in nuclear ground states has been observed<sup>4</sup> previously for only one pair of mirror nuclei, nitrogen-16 and fluorine-16. In that case, however, one of the two partners (fluorine-16) is unbound – that is, the repulsion between protons outweighs the attraction from the strong nuclear force. It therefore decays rapidly by ejecting a proton in around  $10^{-20}$  seconds (ref. 5), comparable to the time it takes a nucleon to travel across the nucleus. However, nitrogen-16 is much more stable, with a half-life of about 7 seconds (ref. 6). So the mirror difference there can be explained by the unbound nature of one partner.

Hoff *et al.* reveal that the situation is

different for bromine-73 and strontium-73, because both are long-lived and quasi-stable. To break mirror symmetry, nature had to play a trick: the ground states of these two nuclei are very close in energy to their respective first excited states. Mirror symmetry, being only an approximate symmetry, can therefore be violated by exchanging the ground and the first excited states in one of the two nuclei.

The properties of bromine-73 have been well characterized for 50 years<sup>7</sup>, whereas information about strontium-73 is limited: we have a rough value for its half-life<sup>8</sup>, and know its strongest mode of decay<sup>9</sup>. The originality of Hoff and co-workers' study is that the authors did not study the properties of strontium-73 directly, but through its two consecutive radioactive decays: the first decay occurs through the emission of  $\beta$ -particles and produces a particular state in the daughter nucleus, rubidium-73, which immediately decays by proton emission to produce krypton-72. The observed properties of the proton emission allowed the authors to deduce the structure of the proton-emitting state in rubidium-73, and, from this, the structure of the ground state of strontium-73.

The results allowed a nuclear property known as spin to be characterized, and revealed something unexpected. The ground state of strontium-73 turns out not to have a spin of  $1/2$ , as the ground state of bromine-73 does, but instead has a spin of  $5/2$ , which corresponds to the first excited state of its mirror partner. Thus, mirror symmetry has now been shown to be broken in bound nuclear ground states.

Is this breaking of mirror symmetry a disaster for our understanding of the structure of the atomic nucleus? Not at all. Deviations from expectations challenge our knowledge of nuclear structure, and allow nuclear scientists

to fine-tune their models to describe atomic nuclei. As Hoff *et al.* show, the observed mirror-symmetry breaking might be triggered by the existence of two competing nuclear shapes, a prolate (rugby-ball) shape and an oblate (disk) shape. Both structures give the nuclei approximately the same energy and mass. These two shapes can mix, and the symmetry breaking in bromine-73 and strontium-73 might arise because there is a different degree of mixing in the two nuclei.

It will be interesting to see whether other cases of ground-state mirror-symmetry breaking can be found. No other candidates seem to exist for nuclei that have similar numbers of nucleons to bromine-73 and strontium-73, because no nucleus is known for which the first excited state lies very close to the ground state. However, heavier nuclei are promising candidates. With more nucleons, more nuclear energy levels can be built, and the energy levels come closer together. By contrast, no mirror partners exist for nuclei whose mass number (the sum of the proton number and the neutron number) is greater than about 100 (ref. 10), because the nuclear interaction can no longer overcome the electrical repulsion associated with interactions between the protons in the 'proton-rich' mirror partner. The race is on to find more cases of broken mirror symmetry in nuclear ground states.

**Bertram Blank** is at the Centre d'Etudes Nucléaires de Bordeaux-Gradignan, 33175 Gradignan Cedex, France.  
e-mail: blank@cenbg.in2p3.fr

- Hoff, D. E. M. *et al.* *Nature* **580**, 52–55 (2020).
- Boso, A. *et al.* *Acta Phys. Pol. B* **48**, 313–318 (2017).
- Bentley, M. A. *et al.* *Phys. Rev. C* **73**, 024304 (2006).
- Wu, Z. D. *et al.* *Phys. Rev. C* **89**, 054315 (2014).
- Charity, R. J. *et al.* *Phys. Rev. C* **97**, 054318 (2018).
- Dryák, P., Novotný, T., Kovář, P. & Králík, M. *Nucl. Instrum. Meth. Phys. Res. A* **369**, 441–444 (1996).
- Murray, G., White, W. J. K., Willmott, J. C. & Entwistle, R. F. *Nucl. Phys. A* **142**, 21–34 (1970).
- Sinclair, L. *et al.* *Phys. Rev. C* **100**, 044311 (2019).
- Batchelder, J. C. *et al.* *Phys. Rev. C* **48**, 2593–2597 (1993).
- Möller, P., Myers, W. D., Sagawa, H. & Yoshida, S. *Phys. Rev. Lett.* **108**, 052501 (2012).

# Rebuilding marine life

<https://doi.org/10.1038/s41586-020-2146-7>

Received: 24 May 2019

Accepted: 18 February 2020

Published online: 1 April 2020



Carlos M. Duarte<sup>1,2,3</sup>✉, Susana Agusti<sup>1</sup>, Edward Barbier<sup>4</sup>, Gregory L. Britten<sup>5</sup>, Juan Carlos Castilla<sup>6</sup>, Jean-Pierre Gattuso<sup>7,8,9</sup>, Robinson W. Fulweiler<sup>10,11</sup>, Terry P. Hughes<sup>12</sup>, Nancy Knowlton<sup>13</sup>, Catherine E. Lovelock<sup>14</sup>, Heike K. Lotze<sup>15</sup>, Milica Predragovic<sup>1</sup>, Elvira Poloczanska<sup>16</sup>, Callum Roberts<sup>17</sup> & Boris Worm<sup>15</sup>

Sustainable Development Goal 14 of the United Nations aims to “conserve and sustainably use the oceans, seas and marine resources for sustainable development”. Achieving this goal will require rebuilding the marine life-support systems that deliver the many benefits that society receives from a healthy ocean. Here we document the recovery of marine populations, habitats and ecosystems following past conservation interventions. Recovery rates across studies suggest that substantial recovery of the abundance, structure and function of marine life could be achieved by 2050, if major pressures—including climate change—are mitigated. Rebuilding marine life represents a doable Grand Challenge for humanity, an ethical obligation and a smart economic objective to achieve a sustainable future.

The ability of the ocean to support human wellbeing is at a crossroads. The ocean currently contributes 2.5% of global gross domestic product (GDP) and provides employment to 1.5% of the global workforce<sup>1</sup>, with an estimated output of US\$1.5 trillion in 2010, which is expected to double by 2030<sup>1</sup>. Furthermore, there is increased attention on the ocean as a source of food and water<sup>2</sup>, clean energy<sup>1</sup> and as a means to mitigate climate change<sup>3,4</sup>. However, many marine species, habitats and ecosystems have suffered catastrophic declines<sup>5–8</sup>, and climate change is further undermining ocean productivity and biodiversity<sup>9–14</sup> (Fig. 1).

The conflict between the growing dependence of humans on ocean resources and the decline in marine life under human pressures (Fig. 1) is focusing the attention on the connection between ocean conservation and human wellbeing<sup>15</sup>. The United Nations Sustainable Development Goal 14 (UN SDG 14 or ‘life below water’) aims to “conserve and sustainably use the oceans, seas and marine resources for sustainable development” (<https://sustainabledevelopment.un.org/sdg14>). Achieving this goal will require rebuilding marine life, defined in the context of SDG 14 as the life-support systems (populations, habitats and ecosystems) that deliver the many benefits that society receives from a healthy ocean<sup>16,17</sup>. Here we show that, in addition to being a necessary goal, substantially rebuilding marine life within a human generation is largely achievable, if the required actions—including, notably, the mitigation of climate change—are deployed at scale.

## Reversing the decline of marine life

By the time the general public admired life below water through the television series ‘The Undersea World of Jacques Cousteau’ (1968–1976), the abundance of large marine animals was already greatly reduced<sup>5–7,18</sup>. Since the first frameworks to conserve and sustain marine life were

introduced in the 1980s, the abundance of marine animals and habitats that provide essential ecosystems services has shrunk even further<sup>5,6,19,20</sup> (Fig. 1). Currently, at least one-third of fish stocks are overfished<sup>21</sup>, one-third to half of vulnerable marine habitats have been lost<sup>8</sup>, a substantial fraction of the coastal ocean suffers from pollution, eutrophication, oxygen depletion and is stressed by ocean warming<sup>22,23</sup>, and many marine species are threatened with extinction<sup>7,24,25</sup>. Nevertheless, biodiversity losses in the ocean are less pronounced than on land<sup>7</sup> and many marine species are capable of recovery once pressures are reduced or removed (Figs. 2, 3). Substantial areas of wilderness remain in remote regions<sup>26</sup> and large populations of marine animals are still found, for example, in mesopelagic (200–1,000 m depth) ocean waters<sup>27</sup>.

Regional examples of impressive resilience include the rebound of fish stocks during World War I and World War II following a marked reduction in fishing pressure<sup>28</sup>, the recovery since 1958 of coral reefs in the Marshall Islands from 76 megatons of nuclear tests<sup>29</sup> and the improved health of the Black Sea<sup>30</sup> and Adriatic Sea<sup>31</sup> following a sudden reduction in the application of fertilizers after the collapse of the Soviet Union. Although these rapid recoveries were unrelated to conservation actions, they helped to inform subsequent interventions that have been deployed in response to widespread ocean degradation<sup>7,32,33</sup>. These interventions include a suite of initiatives to save threatened species, protect and restore vulnerable habitats, constrain fishing, reduce pollution and mitigate climate change (Fig. 1 and Table 1).

## Impactful interventions

**The regulation of hunting.** The protection of species through the Convention on International Trade of Endangered Species (CITES, 1975, <https://cites.org/>) and the global Moratorium on Commercial Whaling (1982, <https://iwc.int/home>) are prominent examples of inter-

<sup>1</sup>Red Sea Research Center (RSRC), King Abdullah University of Science and Technology, Thuwal, Saudi Arabia. <sup>2</sup>Arctic Research Centre, Department of Biology, Aarhus University, Aarhus, Denmark. <sup>3</sup>Computational Bioscience Research Center (CBRC), King Abdullah University of Science and Technology, Thuwal, Saudi Arabia. <sup>4</sup>Department of Economics, Colorado State University, Fort Collins, CO, USA. <sup>5</sup>Department of Earth, Atmospheric, and Planetary Sciences, Massachusetts Institute of Technology, Cambridge, MA, USA. <sup>6</sup>Departamento de Ecología, Facultad de Ciencias Biológicas and Centro Interdisciplinario de Cambio Global, Pontificia Universidad Católica de Chile, Santiago, Chile. <sup>7</sup>Laboratoire d’Océanographie de Villefranche, Sorbonne Université, CNRS, Villefranche-sur-Mer, France. <sup>8</sup>Institute for Sustainable Development and International Relations, Sciences Po, Paris, France. <sup>9</sup>Monegasque Association on Ocean Acidification, Prince Albert II of Monaco Foundation, Monaco, Monaco. <sup>10</sup>Department of Earth & Environment, Boston University, Boston, MA, USA. <sup>11</sup>Department of Biology, Boston University, Boston, MA, USA. <sup>12</sup>Australian Research Council Centre of Excellence for Coral Reef Studies, James Cook University, Townsville, Queensland, Australia. <sup>13</sup>National Museum of Natural History, Smithsonian Institution, Washington, DC, USA. <sup>14</sup>School of Biological Sciences, The University of Queensland, St Lucia, Queensland, Australia. <sup>15</sup>Department of Biology, Dalhousie University, Halifax, Nova Scotia, Canada. <sup>16</sup>Alfred Wegener Institute, Integrative Ecophysiology, Bremerhaven, Germany. <sup>17</sup>Department of Environment and Geography, University of York, York, UK.

✉e-mail: carlos.duarte@kaust.edu.sa



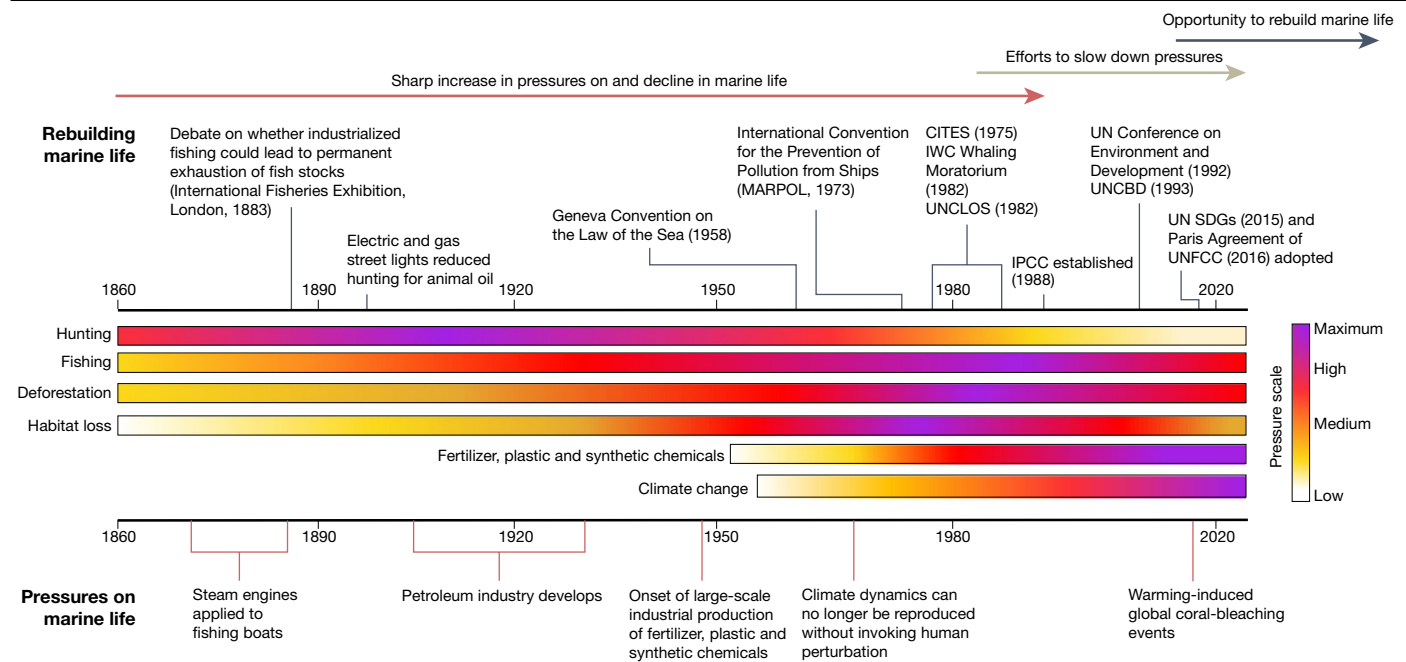


**Fig. 1 | Global pressures on marine life.** Many human pressures commenced well before the industrial revolution; a number of those pressures peaked in the 1980s and are slowing down at present (with great regional variation), with the notable exceptions of pollution and climate change. Initially, hunting and fishing were followed by deforestation, leading to excess sediment export and the direct destruction of coastal habitats. Pollution (synthetic fertilizers, plastic and industrial chemicals) and climate change represent more-recent threats. Hunting of megafauna has been heavily regulated or banned and

fishing is now progressing towards more-sustainable harvests in many regions, and regulatory frameworks are reducing some forms of pollution. Climate change—caused by greenhouse gas emissions that have accumulated since the onset of the industrial revolution—became considerable compared with background variability in the 1960s, and is escalating as greenhouse gases continue to accumulate. As a net result of these cumulative human pressures, marine biodiversity experienced a major decline by the end of the twentieth century.

national actions to protect marine life<sup>34</sup> (Fig. 1). These actions have been supplemented by national initiatives to reduce hunting pressure on endangered species and protect their breeding habitat<sup>34,35</sup>.

**Management of fisheries.** Successful rebuilding of depleted fish populations has been achieved at local and regional scales through well-proven management actions, including catch and effort restrictions, closed areas, regulation of fishing capacity and gear, catch shares and co-management arrangements<sup>35–39</sup> (Supplementary Information 1). These interventions require detailed consideration of socio-economic circumstances, with solutions being tailored to the local context<sup>37</sup>. Persistent challenges include harmful subsidies, poverty and lack of alternative employment, illegal, unregulated and unreported fishing, and the disruptive ecological impacts of many fisheries<sup>36–39</sup>.

**Water-quality improvement.** Policies to lower inputs of nutrients and sewage to reduce coastal eutrophication and hypoxia were initiated four decades ago in the United States and European Union (EU), leading to major improvements today<sup>40–42</sup>. Many hazardous pollutants have been regulated or phased out through the Stockholm Convention (<http://www.pops.int/>) and, specifically in the ocean, by the MARPOL Convention (<http://www.imo.org/>), often reinforced by national and regional policies. Recent attention has focused on reducing and preventing plastic pollution from entering the ocean, which remains a growing problem; inputs of plastic are currently estimated at between 4.8 to 12.7 million metric tons per year<sup>43</sup>.

**Habitat protection and restoration.** The need to better protect sensitive habitats, including non-target species, has inspired the use of Marine Protected Areas (MPAs) as a comprehensive management tool<sup>3,15,19,44</sup>. In 2000, only 3.2 million km<sup>2</sup> (0.9%) of the ocean was protected, but MPAs now cover 26.9 million km<sup>2</sup> (7.4% of ocean area, or

5.3% if only considering fully implemented MPAs (<http://mpatlas.org/>, accessed 6 March 2020). MPA coverage continues to grow at about 8% per year<sup>19</sup> (Fig. 2 and Supplementary Video 1).

The twenty-first century has also seen a global surge of active habitat protection and restoration initiatives (Fig. 2, Supplementary Information 1 and Supplementary Videos 1, 2), even in challenging environments adjoining coastal megacities (Supplementary Information 1). These efforts have delivered benefits, such as improved water quality following oyster reef restoration. Additionally, Blue Carbon strategies, submitted within the nationally determined contributions (NDCs) of more than 50 nations—at the heart of the Paris Agreement—are being used to mitigate climate change and improve coastal protection by restoring seagrass, saltmarsh and mangrove habitats<sup>45–47</sup> (Supplementary Information 1).

## Recovery to date

**Reductions to the risk of extinction.** The proportion of marine species assessed by the IUCN (International Union for Conservation of Nature) Red List as threatened with global extinction (Supplementary Information 2) has decreased from 18.0% in 2000 to 11.4% in 2019 (s.d. = 1.7%,  $n = 1,743$ ), with trends being relatively uniform across ocean basins and guilds (Supplementary Fig. 2.1). In part, this reflects the growing number of species that have been assessed. However, many assessed species have improved their threat status over the past decade<sup>48–51</sup>. For marine mammals, 47% of 124 well-assessed populations<sup>34</sup> showed a significant increase over the past decades, with 40% unchanged and only 13% decreasing (Fig. 3b and Supplementary Table 2). Some large marine species have exhibited particularly notable rebounds, even from the brink of extinction (Fig. 3c). Humpback whales migrating from Antarctica to eastern Australia have been increasing at 10% to 13% per year, from a few hundred animals in 1968 to more than 40,000 currently<sup>49</sup>. Northern elephant seals recovered from about 20 breeding individuals

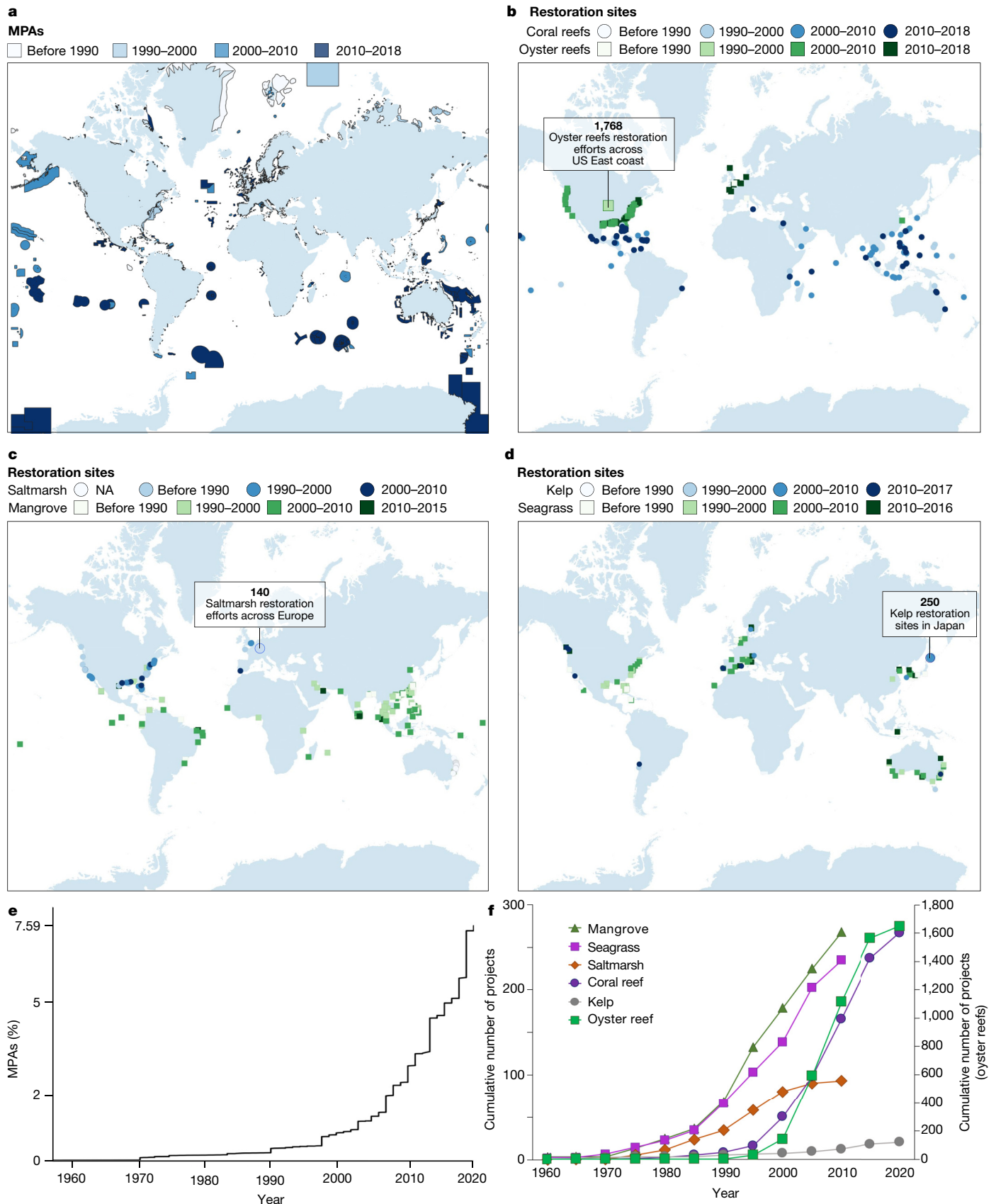


**Fig. 2 | Global growth of restoration interventions.** Distribution and growth of MPAs (a) and ecosystem restoration projects for coral and oyster reefs (b), saltmarshes and mangroves (c), and kelps and seagrasses (d); and the growth of MPAs as per cent of the total ocean area (e) and reported restoration projects (f) over time. NA, date not available. Numbers within symbols represent

aggregated restoration projects for which the location was not provided (see Supplementary Information 1 for detailed examples, Supplementary Information 2 for data sources and Supplementary Videos 1, 2 for the animation of growth over time).



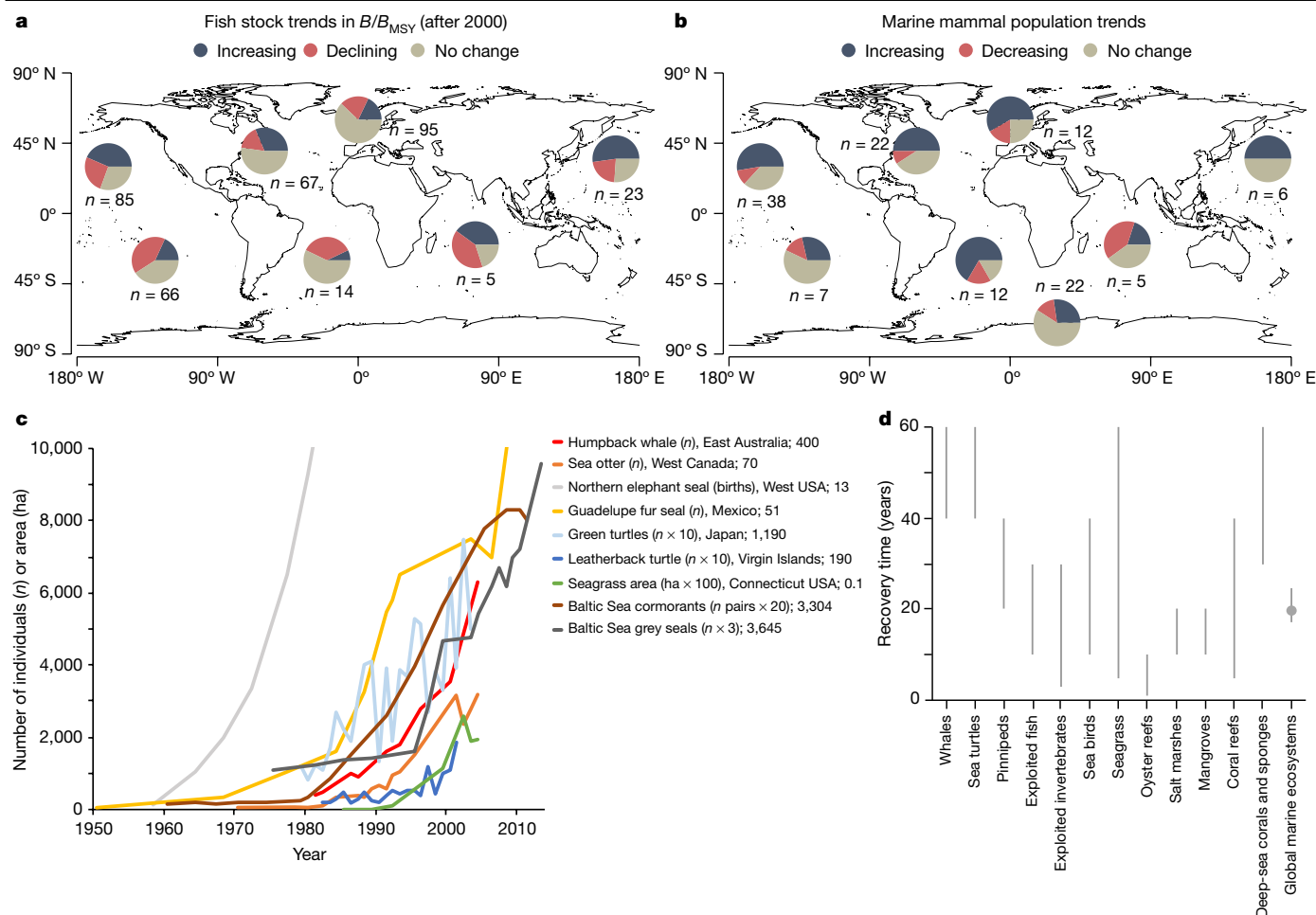


**Fig. 3 | Recovery trends of marine populations.** **a**, Current population trends in scientifically assessed fish stocks based on the ratio of the annual biomass  $B$  relative to the biomass that produces the maximum sustainable yield ( $B_{MSY}$ ). **b**, Percentage of assessed marine mammal populations that showed increasing or decreasing population trends or showed no change. **c**, Sample trajectories of recovering species and habitats from different parts of the world. Units were adjusted to a common scale by multiplying or dividing as indicated in the

legend ( $n \times$ ), numbers at the end of the legends indicate the initial count at the beginning of time series. **d**, Range of recovery times for marine populations and habitats, and mean  $\pm$  95% confidence limits recovery times for marine ecosystems. Lines indicate the reported range; where extending to 60 years, the maximum recovery time is 60 years or longer. See Supplementary Information 2 for details on data sources and methods, and Supplementary Table 3 for data sources for data shown in **d**.

in 1880 to more than 200,000 today<sup>50</sup>, and grey seal populations have increased by 1,410% in eastern Canada<sup>51</sup> and 823% in the Baltic Sea<sup>41</sup> since 1977. Southern sea otters have grown from about 50 individuals in 1911 to several thousand at present<sup>35</sup>. While still endangered, most sea turtle populations for which trends are available are increasing in size<sup>52</sup>, with increases in green turtle nesting populations ranging from 4 to 14% per year<sup>52</sup>.

**Recovery of fish stocks.** Using a comprehensive stock-assessment database<sup>53</sup>, we find that fish stocks with available scientific assessments are increasingly managed for sustainability. The proportion of stocks with fishing mortality estimates ( $F$ ) below the level that would produce a maximum sustainable yield ( $F < F_{MSY}$ ) has increased from 60% in 2000 to 68% in 2012. Many fish stocks that are subject to such management interventions display positive trends (Fig. 3a), and globally aggregated stock assessments suggest a slowing down of the depletion of fish stocks<sup>21,36,39</sup>, although this trend cannot be verified for the majority of stocks, which lack scientific assessments<sup>36</sup>. The most recent report of the Food and Agriculture Organization on global fisheries<sup>21</sup> also suggests that two thirds of large-scale commercial fish stocks are exploited at sustainable rates—although, again, this figure does also not account for smaller stocks or non-target bycatch species, which are often not

assessed and in poor condition<sup>36,54</sup>. Available data suggests that scientifically assessed stocks generally have a better likelihood of recovery owing to improved management and regulatory status compared with unassessed stocks<sup>36</sup>, which still represent the majority of exploited fish stocks, especially in developing countries.

**Reduction in pollution.** Time-series analyses show that legacy persistent organic pollutants have declined even in marine environments that tend to accumulate them (for example, the Arctic<sup>55</sup>). The transition towards unleaded gasoline since the 1980s has reduced lead concentrations to concentrations comparable to baseline levels across the global ocean by 2010–2011<sup>56</sup>. Similarly, the total ban in 2008 of the anti-fouling chemical tributyltin (TBT) has led to rapid declines of imposex (females that develop male sexual organs)—a TBT-specific symptom—in an indicator gastropod<sup>57</sup>. Improved safety regulations have also led to a 14-fold reduction in large oil spills from oil tankers from 24.7 events per year in the 1970s to 1.7 events per year in 2010–2019<sup>58</sup>. Whereas evidence of improved coastal water quality following nutrient reductions was equivocal a decade ago<sup>59</sup>, multiple success stories have now been confirmed<sup>41,60</sup>, with positive ecosystem effects such as the net recovery of seagrass meadows in the United States<sup>61</sup> (Fig. 1), Europe<sup>62</sup>, the Baltic Sea<sup>41</sup> and Japan<sup>63</sup>.

**Habitat restoration.** Evidence that mangrove restoration can be achieved at scale first came from the Mekong Delta mangrove forest, possibly the largest (1,500 km<sup>2</sup>) habitat restoration undertaken to date<sup>64,65</sup>. Global loss of mangrove forests has since slowed to 0.11% per year<sup>66,67</sup>, with stable mangrove populations along the Pacific coast of Colombia, Costa Rica and Panama<sup>68</sup>, and increasing populations in the Red Sea<sup>69</sup>, Arabian Gulf<sup>70</sup> and China<sup>71</sup>. Large-scale restoration of saltmarshes and oyster reefs has occurred in Europe and the United States (Fig. 2 and Supplementary Information 1). Restoration attempts of seagrass, seaweed and coral reef ecosystems are also increasing globally, although they are often small in scale (Fig. 2, Supplementary Video 2 and Supplementary Information 1). Notably, a global inventory of total restored area is missing.

## Potential for rebuilding

Efforts to rebuild marine life cannot aim to return the ocean to any particular past reference point. Our records of marine life are too fragmented to compose a robust baseline, and the ocean has changed considerably and—in some cases—irreversibly, including the extinction of at least 20 marine species<sup>25</sup>. We argue instead that the focus should be on increasing the abundance of key habitats and keystone species, and restoring the three-dimensional complexity of benthic ecosystems. The yardstick of success should be the restoration of marine ecological structure, functions, resilience and ecosystem services, increasing the capacity of marine biota to supply the growing needs of an additional 2 to 3 billion people by 2050. To meet this goal, rebuilding of depleted populations and ecosystems must replace the goal of conserving and sustaining the status quo, and swift action should be taken to avoid potential tipping points beyond which collapse may be irreversible<sup>11,18,33</sup>.

Here we examine the rates of recovery of marine species and habitats to date, and propose a tentative timeframe in which substantial recovery of marine life may be possible, should major pressures, including climate change, be mitigated. We broadly define recovery as the rebound in populations of marine species and habitats following losses, which can be partial (that is, 10–50% increase), substantial (50–90% increase) or complete (>90% increase)<sup>47</sup> (Table 1).

## Marine megafauna

A number of megafauna species, including humpback whales and northern elephant seals, have recovered to historical baselines following protection (Fig. 3c); however, rates of recovery depend on the life history of the species: some large whales may require more than 100 years to recover, whereas smaller pinnipeds may only need several decades<sup>35</sup> (Fig. 3c, d). Sea turtles have recovery timescales of up to 100 years, although some populations have partially recovered much faster (for example, green turtles in Hawaii increased sixfold between 1973 and 2016)<sup>72</sup>. Seabird populations typically require a few decades to recover<sup>35,41</sup> (Fig. 3c, d).

## Fish stocks

Recovery can also refer to achieving resilient populations that support the full extent of ecosystem functions and services that characterize them. For instance, fish stock recovery is often defined in terms of biomass increases to the level that enables the maximum sustainable yield ( $B_{MSY}$ ), which fisheries harvest theory predicts to be between 37% and 50% of the virgin biomass ( $B_0$ ), depending on the particular model used (Supplementary Information 2 and Supplementary Fig. 2.2). This range is consistent with an empirical estimate of  $B_0$  for 147 exploited fish stocks, which found that contemporary  $B_{MSY}$  values were 40% of  $B_0$ , on average, with a range of 26% to 46% across taxa<sup>73</sup>. Reported recovery times to  $B_{MSY}$  for overexploited finfish and invertebrate stocks range between 3 and 30 years<sup>35</sup> (Figs. 3, 4), which is consistent with palaeo-ecological reconstructions of prehistoric collapse and recovery of

anchovy, sardine and hake stocks<sup>74</sup>, data from fisheries closures<sup>54,75</sup> and fish stock assessments<sup>76</sup>. However,  $B_{MSY}$  should be considered to represent a minimum recovery target<sup>39</sup>, as it does not account for ecosystem interactions, and might provide only limited resilience in the face of environmental uncertainty and change.

Minimum recovery times of populations are set by the maximum intrinsic rate of population increase ( $r_{max}$ ), which is typically higher than observed rates, resulting in longer recovery times<sup>77,78</sup>. Recovery rates also depend on the fishing pressure imposed on the stock; for example, rebuilding depleted populations to  $B_{MSY}$  may take less than a decade, if fishing mortality is rapidly reduced below  $F_{MSY}$ . Longer recovery times are expected if fishing pressure is reduced more slowly<sup>36,79</sup> (Fig. 4). Recovery for longer-lived, slow-growing species such as most elasmobranchs (sharks, rays and skates), depleted coral reef fish and deep-sea species may take much longer<sup>35,78</sup>.

## Coastal habitats

The recovery of coastal habitats after the removal of stressors or following active restoration of the habitat typically occurs on a similar timescale as fish stock recovery, less than a decade for oyster reefs<sup>80</sup> and other invertebrate populations (Supplementary Information 3), and kelp-dominated habitats<sup>81,82</sup>, between one to two decades for saltmarsh<sup>83</sup> and mangrove<sup>84</sup> habitats, and one to several decades for seagrass meadows<sup>85</sup> (Fig. 3d). Deep-sea corals and sponges grow more slowly and recovery times from trawling disturbance or oil spills may range from 30 years to more than a century<sup>86,87</sup>. Recovery timescales of coral reefs that are affected by local stressors range from a few years to more than a decade (Fig. 3d). However, recovery from severe coral bleaching has taken well over a decade and will slow in the future as ocean warming shortens the interval between bleaching events<sup>12</sup>, with an associated steep reduction in coral-reef recruitment<sup>88</sup>.

In summary, available data suggest that many marine species and habitats require one to three decades to approach undisturbed or reference abundance ranges and fish stock biomass that supports maximum sustainable fish catches after removal of the causes of decline<sup>35,88–92</sup>, with longer recovery times required for some slow-growing groups<sup>35</sup> (Fig. 3).

## Recovery times

The time that is required to rebuild components of marine life depends on the extent of previous declines, which are often substantial. The reduction in species abundance and biomass relative to predisturbance baselines averages about 44 and 56%, respectively, across affected marine ecosystems<sup>89</sup>. Similarly, the Living Blue Planet Report estimated a 49% decline in the abundance of marine animal populations between 1970 and 2012<sup>93</sup>, although many species and habitats have declined further since<sup>90,94</sup>. Moreover, although the maximum rates of recovery of marine populations typically range from 2 to 10% per year<sup>20</sup> (Fig. 3c), rates slow down as carrying capacity is approached<sup>20</sup>. Assuming a reported average annual recovery rate of 2.95% (95% confidence interval, 2.42–3.41%) across marine ecosystems<sup>20</sup> and a characteristic rebuilding deficit of about 50% of predisturbance baselines<sup>89</sup>, we provisionally estimate that the average time to reach 90% of undisturbed baselines (that is, achieve substantial recovery) would be about 21 years (95% confidence interval, 18–25 years) (Fig. 3d). However, the expectation of an average recovery time of about two decades is compromised by the fact that many species and habitats continue to decline and some pressures, such as climate change and plastic pollution, are still increasing (Fig. 1). Thus, substantial (50–90%), rather than complete (>90%), recovery may be a more realistic target for rebuilding marine life in the short term.

Based on the case studies examined, we provisionally propose three decades from today (2050) as a target timeline for substantial (that is, 50–90%) recovery of many components of marine life (Table 1),



# Review

**Table 1 | Scenarios conducive to achieving the best aspirational outcomes towards rebuilding marine life**

Rebuilding wedges	Saltmarshes	Mangroves	Seagrass	Coral reefs	Kelp	Oyster reefs	Fisheries	Megafauna	Deep-sea habitats
<b>Protect species</b>	Low	Low	Low	Low	Low	High	Critical	Critical	Critical
<b>Harvest wisely</b>	Low	Critical	Low	High	High	Critical	Critical	Critical	Critical
<b>Protect spaces</b>	Critical	Critical	Medium	High	Medium	Critical	High	High	Critical
<b>Restore habitats</b>	Critical	Critical	High	Medium	Medium	Critical	Medium	Medium	Medium
<b>Reduce pollution</b>	Medium	Medium	Critical	Critical	Critical	High	Medium	Medium	High
<b>Mitigate climate change</b>	High	High	High	Critical	High	High	High	High	High
<b>Recovery targets by 2050</b>	Substantial to complete	Substantial to complete	Substantial to complete	Partial to substantial	Substantial to complete	Substantial to complete	Substantial to complete	Substantial	Partial to substantial
<b>Key Actors</b>	Government, civil society and NGOs.	Government, civil society and NGOs.	Government, civil society and NGOs.	Government, tourism operators, fishers organizations, civil society and NGOs.	Government, fishers organizations and civil society.	Government, fishers organizations, NGOs and civil society.	Government, fishers organizations and civil society.	Government, fishers organizations, NGOs and civil society.	International seabed authority, state and federal governments, mining/ exploration companies, civil society and fishing industry.
<b>Key Actions</b>	Protection of remaining saltmarshes, providing sources of sediment, potentially planting native species, providing space for landward migration and restoring hydrological connections.	Protection, provide alternative livelihoods for dependent communities, provide space for landward migration, restore hydrological connections, maintain sediment supply and restore damaged forests.	Reduce nutrient inputs, protect, avoid physical impacts, and conduct restoration projects.	Ambitious reduction in greenhouse gas emissions. Reduce excess sediment and nutrient inputs, improve water quality, protect reefs, rebuild food webs and restore damaged reefs.	Restoration requires removal of excess herbivores, by rebuilding their predators, and a reduction in sediment loads on rocky substrates and kelps.	Protect remaining reefs, prohibition of natural reef harvests, improve water quality and restore reefs.	Reduce overfishing, bycatch and incidental mortality, ban destructive fishing practices, protect spawning/ breeding areas and nursery grounds, and remove perverse incentives.	Protect, reduce bycatch, reduce incidental mortality (ship strikes, entanglement, ghost gear), reduce pollution (noise, debris, chemical), protect breeding/ haul-out sites, safeguard migration routes and reduce competition with fisheries.	Regulate industries that operate in the deep sea. Ban deep-sea fishing and impose a moratorium on deep-sea mining until technologies free of impact are available. Improve environmental safety of oil and gas operations. Develop facilities to test technologies before real-ocean deployment.
<b>Key Opportunities</b>	Blue Carbon and coastal defence strategies against storms and sea-level rise, links to management for enhancing water quality, food provision and biodiversity strategies.	Blue Carbon and coastal defence strategies against storms and sea-level rise, links to management for enhancing water quality, food provision and biodiversity strategies.	Blue Carbon and coastal defence strategies against storms and sea-level rise, links to management for enhancing water quality, food provision and biodiversity strategies.	Link to coastal defence, food provision and biodiversity strategies.	Emerging role in Blue Carbon, water quality and biodiversity strategies.	Link to water quality improvement, biodiversity and coastal protection strategies.	Sustainable seafood, MSC-certified fisheries, develop sustainable aquaculture to reduce pressure on wild stocks.	Marine wildlife tourism, cultural benefits and ethics.	High percentage of unique, unexplored habitats and new species, potential for novel products important in fighting/ preventing disease. Huge carbon-sink potential.

Continued

Rebuilding wedges	Saltmarshes	Mangroves	Seagrass	Coral reefs	Kelp	Oyster reefs	Fisheries	Megafauna	Deep-sea habitats
<b>Key Benefits</b>	Improved fisheries, protection from sea-level rise and storm surges, recreational and cultural benefits, hunting.	Improved fisheries, biodiversity and coastal defence, recreation and cultural benefits.	Protect shoreline from erosion and rebuilding biodiversity and fisheries.	Provision of fish, protection from sea-level rise and storm surges, recreational and cultural benefits.	Enhanced fisheries.	Improved water quality, increased habitat, recreational and cultural benefits, food sources.	Improved quality and quantity of seafood supply.	Increased connectivity among ocean basins, enhanced nutrient cycling and ocean productivity.	Huge potential for discoveries and new resources. Avoidance of irreversible damage.
<b>Roadblocks</b>	Many saltmarshes are filled, landward migration impeded because of infrastructure, not enough sediment supply, sea-level rise, increased decomposition rates with rising temperatures and/or excess nutrient loading, reverting land use.	Alternative land uses and infrastructure, lack of alternative livelihoods and incentives for communities, uncertainties around climate change impacts.	Infrastructure (for example, areas occupied by harbours), severe and frequent heat waves with climate change.	Dependence on climate change trajectories, mortality with ocean warming, ocean acidification and increased cyclone activity.	Climate change at the edge of the equatorial range of kelp species, high herbivore pressure and sediment accumulation on rocky substrates.	Poor management of fisheries on remaining reefs, degraded habitats, restoration costs, increased prevalence of disease with rising water temperatures.	Cumulative impacts from fishing, pollution, habitat alterations, changing distribution ranges, habitats and food due to climate change.	Losses due to extinction, continued impacts from ship strikes, pollution, habitat alterations, changing habitats and food due to climate change.	Slow and uncertain recovery and success of, hugely costly restoration, which will be extremely difficult and expensive. Development multi-governmental cooperation, buy-in, and action towards this goal.
<b>Remedial Actions</b>	Restore hydrological flows and sediment delivery, restore native plants, restore transitional upland boundaries where possible, increase incentives to relocate users.	Increase incentives to improve management and develop alternative livelihoods, restoration, landscape planning for landward migration.	Compensatory restoration, improve water quality and reduce local stressors.	Ambitious efforts to mitigate climate change and manage to improve resilience.	Restore with thermal-resistant genotypes and reduce sediment delivery to rocky habitats.	Protect remaining reefs, large-scale restoration efforts, defining success with not just increased harvest in mind but the many other benefits oyster reefs provide.	Create MPAs as refuge sites, restore coastal breeding/nursery sites to aid recovery, develop breeding programmes for critically endangered species	Create MPAs as refuge sites, safeguard migration routes, restore coastal breeding/nursery sites to aid recovery and develop breeding programmes for critically endangered species.	Protect what has not been damaged or destroyed and prevent further destruction in places that have already been affected. Widespread education on the fragility of the deep sea and benefits of deep-sea ecosystems, strengthen regulation, decrease pollution and recycle products that require rare earth metals.

Actions include rebuilding wedges, assessment of the maximum recovery targets by 2050 if these wedges are fully activated, as well as key actors, opportunities, benefits, roadblocks and remedial actions to rebuild different components of marine life (priority increases from low to critical). See Supplementary Information 3 for details.

recognizing that many slow-growing, severely depleted species and threatened habitats may take longer to recover (Fig. 3), and that natural variability may delay recovery further (Fig. 4).

Importantly, achieving substantial recovery by 2050 requires that major pressures are mitigated soon, including climate change under the Paris Agreement. Climate change affects the demography, phenology and biogeography of many marine species and compromises the productivity of marine ecosystems<sup>9–13,91,92,95</sup> (Fig. 4). Current impacts of realized climate change on many coral reefs<sup>12</sup> raise concerns about the future prospects of these ecosystems (Table 1). If we succeed in mitigating climate change and other pressures, we may witness a trend change from a previous steep decline to stabilization and, in many cases, substantial global recovery of marine life in the twenty-first century (Figs. 1–4).

## A roadmap to recovery

Steps taken to rebuild marine life to date have involved a process of trial and error that delayed positive outcomes (for example, reduction of excessive nutrient inputs in the EU and United States<sup>41,42</sup>), but that generated know-how to cost-effectively propel subsequent efforts at scale. Improved ocean stewardship, as required by UN SDG 14, is a goal shared across many nations, cultures, faiths and political systems, occupying a more-prominent place in the agendas of governments, corporations, philanthropists and individuals than ever before<sup>17,96</sup>. This provides a window of opportunity to mitigate existing pressures over the next decade while supporting global initiatives to achieve substantial recovery of marine life by 2050 (Table 1 and Supplementary Information 3). We are at a point at which we can choose between



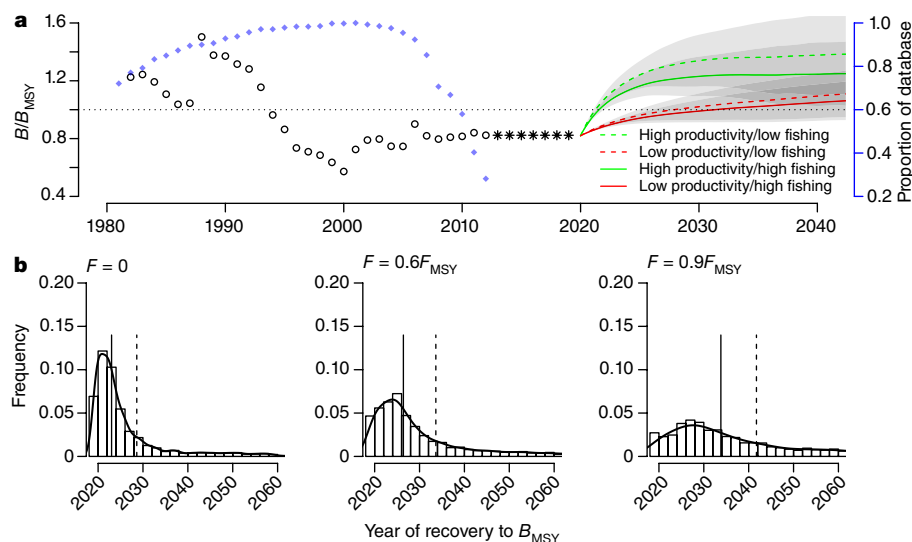


**Fig. 4 | Recovery projections for assessed fish stocks.** **a**, Trajectories of exploited fish stock biomass ( $B$ ) relative to the biomass supporting the maximum sustainable yield ( $B_{MSY}$ ; the ratio of which is denoted  $B/B_{MSY}$ ) over time based on the scientific assessment of 371 globally distributed fish stocks in the RAM Legacy Stock Assessment Database (version 4.44). Open circles indicate the biomass-weighted global average of stock  $B/B_{MSY}$ , asterisks represent years without sufficient data, red and green lines represent four idealized future scenarios ( $B_{MSY}$  values were taken from stock assessments where available and estimated as 50% of the maximum historical biomass otherwise; see Supplementary Information 2). Grey shading represents the one s.d. range of the simulations. Purple diamonds give the proportion of the database used in the calculation of  $B/B_{MSY}$  for each year. **b**, Frequency

distributions for estimated recovery times to  $B_{MSY}$  for 172 stocks that are currently depleted to below  $B_{MSY}$ . Projections refer to three scenarios, corresponding to no fishing, fishing at 60% or 90% of fishing pressure associated with the maximum sustainable yield ( $F_{MSY}$ ). Projections show that under various scenarios of reduced fishing pressure ( $F < F_{MSY}$ ) and different productivity regimes, the majority of fish stocks could recover to  $B_{MSY}$  with high probability before 2040. Recovery to virgin biomass ( $B_0$ ) would take much longer. Solid lines indicate the median and hashed lines the mean estimate of years to recovery. Productivity for each stock in **b** was fixed to the mean stock-specific historical productivity. See Supplementary Information 2 for details of data sources and methods.

a legacy of a resilient and vibrant ocean or an irreversibly disrupted ocean, for the generations to follow.

Some of the interventions required to rebuild marine life have already been initiated, but decadal time lags suggest that the full benefits are yet to be realized<sup>35,36,39,47,48,59</sup>. Because most policies to reduce local pressures and prompt recovery of marine life were introduced after the 1970s (Figs. 1, 2), it is only now that comprehensive benefits (Fig. 3) are becoming evident at a larger scale. Similarly, as most current MPAs are less than 10 years old (Fig. 2), their full benefits, which increase with the age of the reserve, are yet to be realized<sup>97</sup>, particularly for MPAs that are properly managed and enforced<sup>97</sup>.

### Recovery wedges

There is no single solution for achieving substantial recovery of marine life by 2050. Rather, recovery requires the strategic stacking of a number of complementary actions, here termed recovery wedges, each of which will help to increase the recovery rate to reach or exceed the target of 2.4% increase per year across different ecosystem components (Table 1 and Supplementary Information 1, 3, 4). These wedges include protecting vulnerable habitats and species, adopting cautionary harvesting strategies, restoring habitats, reducing pollution and mitigating climate change (Table 1 and Supplementary Information 1, 3, 4). The strength of the contribution of each of these wedges to the recovery target can be expected to vary across species and ecosystems. For instance, mitigating climate change is the critical wedge to set coral reefs on a recovery trajectory, whereas improved habitat protection and fisheries management are the critical wedges for the recovery of marine vertebrates and deep-sea habitats (Table 1 and Supplementary Information 3).

Ongoing efforts to remove pressures on marine life from anthropogenic climate change, hunting, fishing, habitat destruction, pollution and eutrophication (Fig. 1) must be expanded and made more effective

(Table 1). A new framework to predict risks of new synthetic chemicals is required to avoid circumstances in which industry introduces new chemicals faster than their risks can be assessed. Challenges remain for persistent legacy pollutants (for example,  $CO_2$ , organochlorines and plastics) that are already added to the atmosphere and oceans, the removal of which requires novel removal technologies and protection of long-term sinks, such as marine sediments, to avoid their remobilization.

MPAs represent a necessary and powerful recovery wedge across multiple components of the ocean ecosystem, spanning from coastal habitats to fish and megafauna populations (Table 1). The current growth of MPAs (Fig. 2, Supplementary Video 1) is currently on track to meet ambitious targets<sup>98</sup>, 10% of ocean area protected by 2020, 30% by 2037 and 50% by 2044. Many fish stocks could recover to  $B_{MSY}$  by 2030, assuming global management reforms couple the use of closed and protected areas to measures that reduce overall fishing pressure and collateral ecosystem damage that are adapted to the local context (Fig. 4 and Table 1). However, projected climate impacts on ocean productivity and an increase in extreme events<sup>95</sup> can delay recovery and, depending on emission pathways, may prevent recovery of some components altogether (Fig. 4). The current focus on quantitative targets of the percentage of the ocean area that is protected has prompted concerns over the quality and effectiveness of MPAs<sup>99</sup>. Although 71% of assessed MPAs have been successful in enhancing fish populations, the level of protection is often weak (94% allow fishing<sup>100</sup>), and many areas are undermined by insufficient human and financial capacity<sup>101</sup>. Improving the effectiveness of MPAs requires enhanced resourcing, governance, level of protection<sup>100–102</sup> and siting to better match the geography of threats<sup>103</sup> and to ensure desired outcomes.

The current surge in restoration efforts (Fig. 2 and Supplementary Video 2) can, if sustained, be an instrumental recovery wedge to meet rebuilding targets for marine habitats by 2050 (Table 1). For instance,

assuming a mean project size of 4,197 ha (ref. <sup>104</sup>), restoring mangroves to their original extent of 225,000 km<sup>2</sup> by 2050 would require the initiation of 70 projects per year. This is not unrealistic, as realization of the benefits, such as reducing storm damage in low-lying areas<sup>40,105,106</sup>, encourages further growth in restoration efforts (Fig. 2 and Supplementary Video 2). Past coastal restoration projects have reported average success rates ranging from 38% (seagrass) to 64% (saltmarshes and corals)<sup>104</sup>; however, reasons for failure are well understood<sup>80,107–109</sup>, which should improve future outcomes. Much can be learned from increased reporting of failed attempts, because the published literature may be biased towards successful restoration projects<sup>104</sup>. Emerging technologies are now being developed to restore coral species in the presence of climate change<sup>110,111</sup>, although long-term testing is required before their effectiveness and lack of negative consequences are demonstrated. Kelp restoration at a national scale in Japan provides a successful model, rooted in cultural practices, for linking restoration to sustainable fishing (Supplementary Information 1). More broadly, these practices recognize that sustainable harvest of marine resources ought to be balanced by broader restoration actions embedded in a socio-ecological context, including reducing greenhouse gas emissions, restoring habitats, removing marine litter or managing hydrological flows to avoid hypoxia (Supplementary Information 1). These restoration experiences (Supplementary Information 1) also show that involvement of local communities is essential, because of their economic dependence, commitment to place and ownership<sup>112</sup>.

Removing pollution is a critical recovery wedge for seagrass meadows, coral reefs and kelp forests (Table 1). Three decades of efforts to abate coastal eutrophication have provided valuable knowledge on how actionable science can guide restoration successes<sup>41,42,113</sup>. Additional interventions (for example, restoring hydrological flows or rebuilding oyster reefs) can catalyse the additional removal of nutrients while improving biodiversity<sup>113</sup>. Seaweed aquaculture can help to alleviate eutrophication and reduce hypoxia<sup>113,114</sup>. Nutrient reduction has the additional benefit of locally reducing coastal acidification<sup>115</sup> and hypoxia<sup>23</sup> directly and indirectly through the recovery of seagrass meadows. Reducing sulfur dioxide precipitation, hypoxia, eutrophication, emissions and runoff from acidic fertilizers also helps to reduce acidification of coastal waters<sup>22,115</sup>. Large-scale experiments in anoxic basins of the Baltic Sea, for example, have shown that treatment of sediments with phosphorus-binding agents helps to break biogeochemical feedback loops that keep ecosystems in an alternative anoxic stable state<sup>116</sup>.

Oil spills from oil tankers should decline further with the incoming International Maritime Organisation (IMO) requirement (13F of Annex 1 of MARPOL) for double hulls in new large oil tankers, although deep-water drilling, illustrated by the catastrophic Deepwater Horizon spill in 2010<sup>117</sup>, and increasing risks of oil spills from future oil drilling and oil tanker routes in the Arctic<sup>118</sup> present new challenges. Noise pollution from shipping and other industrial activities, such as drilling, pile driving and seismic surveys, should be reduced<sup>119</sup>. Similarly, worldwide efforts to reduce or ban single-use plastic (initiated in developing nations), taxes on plastic bags, deposits and refunds on bottles, and other market-based instruments are being deployed to reduce marine litter, while providing incentives to build a circular economy for existing plastics while developing safer materials.

## Roadblocks

A number of roadblocks may delay or prevent recovery of some of the critical components of marine life (Table 1). These include natural variability and intensification of environmental extremes caused by anthropogenic climate change (Fig. 4), unexpected natural or social events, and a failure to meet commitments to reduce existing pressures and mitigate climate change. In addition, the growing human population, which will probably exceed 9 billion individuals by 2050, will create additional demands for seafood, coastal space and other ocean resources. Accordingly, if all necessary recovery wedges are

stacked, a 2050 target of substantial to complete recovery (that is, 50–100% increase relative to the present) for most rebuilding components appears realistic and achievable (Table 1). Partial to substantial (10 to >50%) recovery can be targeted for deep-sea habitats, where slow recovery rates lead to a modest rebuilding scope by 2050, and for coral reefs, where existing and projected climate change severely limits the rebuilding prospects<sup>13,95</sup> (Table 1).

A major roadblock to recovery for intertidal habitats, such as mangroves and saltmarshes, is their conversion to urban areas, aquaculture ponds or infrastructure (Table 1). However, even in large cities, such as New York and Shenzhen, some restoration of degraded habitats has been achieved (Supplementary Information 1). Incentives to develop alternative sources of livelihood, relocate landholders, mediate land-tenure conflicts<sup>112</sup> and improve land-use planning can release more habitat for coastal restoration (Table 1). Tools are emerging to prioritize sites for restoration based on past experience and a broad suite of biophysical and socio-economic predictors of success<sup>120</sup>. Reduced sediment supply due to dam construction in watersheds<sup>121</sup> is also an important challenge for the recovery of salt marshes and mangroves, and these challenges are exacerbated by sea-level rise and climate change (Table 1). However, these habitats may be less vulnerable than previously thought<sup>122</sup>, with a recent assessment concluding that global gains of 60% of coastal wetland area are possible under sea-level rise<sup>122</sup>. By contrast, enhanced sediment load from land clearing is often responsible for losses of nearshore coral reefs and hinders their capacity to recover from coral bleaching<sup>123</sup>.

## Overcoming the climate change roadblock

Climate change is the critical backdrop against which all future rebuilding efforts will play out. Current trajectories of greenhouse gas emissions lead to warming by 2100 of 2.6 to 4.5 °C above preindustrial levels, far exceeding the long-term goal of the Paris Agreement (holding the increase in global average temperature to well below 2 °C above preindustrial levels)<sup>124</sup>. Much stronger efforts to reduce emissions<sup>124,125</sup> are needed to reduce the gap between target emissions and projected emissions under the present voluntary NDCs<sup>126</sup> a challenging but not impossible task<sup>125</sup>. Efforts to rebuild marine life need to consider unavoidable impacts brought about by ocean warming, acidification and sea-level rise already committed by past emissions, even if the climate mitigation wedge, represented by the Paris Agreement, is fully implemented. These changes include projected shifts in habitats and communities at subtropical–tropical (coral to algal turf and seaweed), subtropical–temperate (kelp to coral and urchin barrens, saltmarsh to mangrove) temperate–Arctic (bare to kelp, ice fauna to pelagic) and intertidal (coastal squeeze) boundaries<sup>10–13,95</sup>, propelled by species displacements and mass mortalities from future heat waves<sup>11–13,95</sup>. Mapping the areas where the likelihood of these transitions is high can help to prioritize where and how restoration interventions should be deployed<sup>120</sup>. For instance, conserving and restoring vegetated coastal habitats will help to defend shorelines against increased risks from sea-level rise while helping to mitigate climate change<sup>4,40,105</sup>. Well-managed MPAs may help to build resilience to climate change<sup>3</sup>. However, many of them are already affected by ocean warming and further climate change may potentially compromise their performance in the future<sup>127</sup>.

Rebuilding coral reefs carries the highest risk of failure (Table 1), as cumulative pressures (for example, overfishing and pollution) that drove their historical decline are now increasingly compounded by warming-induced bleaching<sup>11,12</sup>. The IPCC (Intergovernmental Panel on Climate Change) projects that global warming to 1.5 °C above preindustrial levels will result in very high risks and losses of coral reefs<sup>13</sup> unless adaptation occurs faster than currently anticipated. A recent study<sup>13</sup> shows that while coral bleaching has increased in frequency and intensity in the last decade, the onset of coral bleaching is now occurring at significantly warmer temperatures (around 0.5 °C) than previously, suggesting that the remaining coral populations now have a higher



thermal threshold for bleaching, due to a decline in thermally vulnerable species and genotypes and/or acclimatization<sup>128</sup>. However, the capacity to restore coral reefs lags behind that of all other marine habitats, because coral-reef restoration efforts typically have a very small footprint, and are expensive and slow<sup>104</sup>. Coral restoration often fails because the original causes of mortality remain unchecked, and despite decades of effort (Fig. 2), only tens of hectares have been regrown so far. Our growing knowledge of ecological processes in coral reefs provides opportunities to catalyse recovery by reducing multiple pressures while repairing key processes, including herbivory and larval recruitment<sup>111,111</sup>. Mitigating the drivers of coral loss, particularly climate change, and developing innovative approaches to restoration within this decade are imperative to revert coral losses at scale<sup>110,111</sup>. Efforts are underway to find corals that are resistant to the temperatures and acidity levels expected by the end of the twenty-first century, to understand the mechanisms of their resistance and to use 'assisted evolution' to engineer these characteristics into other corals<sup>110,111</sup>. However, these efforts are in their infancy and their benefits currently unproven.

Overall, the societal benefits that would accrue from substantially rebuilding marine life by 2050 will depend on the mitigation of greenhouse gas emissions and on the development of efficient CO<sub>2</sub> capture and removal technologies to meet or, preferably, exceed the targets of the Paris Agreement.

## Necessary investments and expected returns

Substantial rebuilding of marine life by 2050 requires sustained effort and financial support (Supplementary Information 4), with an estimated cost of at least US\$10–20 billion per year to extend protection actions to reach 50% of the ocean space<sup>129</sup> and substantial additional funds for restoration. This is comparable to establishing a global MPA network that conserves 20–30% of the ocean (US\$5–19 billion annually<sup>129,130</sup>). Yet the economic return from this commitment will be considerable, around US\$10 per US\$1 invested and in excess of one million new jobs<sup>129,130</sup>. Ecotourism in protected areas provides 4–12 times greater economic returns than fishing without reserves<sup>36</sup> (for example, AUS\$5.5 billion annually and 53,800 full time jobs in the Great Barrier Reef<sup>31</sup>). Rebuilt fisheries alone could increase the annual profits of the global seafood industry by US\$53 billion<sup>128</sup>. Conserving coastal wetlands could save the insurance industry US\$2 billion annually by reducing storm flooding<sup>129</sup>, while providing additional benefits of carbon sequestration, income and subsistence from harvesting, and from fisheries supported by coastal wetlands<sup>40,129</sup>.

A global rebuilding effort of exploited fish stocks could increase fishing yields by around 15% and profits by about 80%<sup>36,79</sup> while reducing bycatch mortality, thereby also helping to promote recovery in non-target species<sup>132</sup>. Rebuilding fish stocks can be supported by market-based instruments, such as rationalizing global fishing subsidies<sup>79</sup>, taxes and catch shares<sup>38</sup>, to end perverse incentives<sup>133</sup> and by the growth of truly sustainable aquaculture to reduce pressure on wild stocks<sup>2</sup>. Whereas most regulatory measures focus on commercial fisheries, subsistence<sup>134</sup> and recreational<sup>135</sup> fishing are also globally relevant and need to be aligned with rebuilding efforts to achieve sustainability.

## Call to action

Rebuilding marine life requires a global partnership of diverse interests, including governments, businesses, resource users and civil society<sup>129,136</sup>, aligned around an evidence-based action plan supported by a sound policy framework, a science and educational plan, quantitative targets, metrics for success and a business plan. It also requires leadership to assemble the scientific and socio-economic knowledge and the technologies required to rebuild marine life and the capacity to deploy them. A concerted global effort to restore and protect marine life and ecosystems could create millions of new—and in many cases—well-paying jobs<sup>129,137</sup>. Thus, commitments of governments, which are required to meet the UN SDGs by 2030, need to be supported and

reinforced by commitments from society, non-government organizations (NGOs) and other agents, such as philanthropic groups, corporations and industry (Supplementary Information 4). The sectors that operate in the ocean spaces, which bear considerable responsibility for the losses thus far experienced and, in many cases, are likely to be the main beneficiaries of efforts to rebuild marine life, must change their ethos to commit to a net positive conservation impact as part of their social license to operate in the ocean space. The use of the ocean by humans should be designed for net positive conservation impact, creating additional benefits<sup>138</sup> that increase prosperity and catalyse political will to deploy further efforts in a positive feedback spiral of ocean bounty.

The long-term commitment to rebuilding marine life requires a powerful narrative, supported by scientific evidence that conveys its feasibility in the face of climate change and a growing human population, its alignment with societal values, and its widespread societal benefits. Growing numbers of success stories could shift the balance from a wave of pessimism that dominated past scientific narratives of the future ocean<sup>5,7,11,32,33</sup> to evidence-based 'ocean optimism'<sup>139</sup> (for example, #oceanoptimism in social media), conveying solutions and opportunities for actions that help to drive positive change<sup>140</sup>. This optimism must be balanced with transparent and robust communication of the risks posed by relevant pressures that are yet to be mitigated.

Rebuilding marine life will benefit from nations declaring, analogous to the Paris Agreement on climate change, NDCs towards rebuilding marine life<sup>129</sup>. NDCs aimed at rebuilding marine life will be essential for accountability, auditing milestones and forecasting success in reaching goals. NDCs can include both commitments for action within national Economic Exclusive Zones, as well as a catalogue of actionable opportunities available to investors, corporations and philanthropists<sup>129</sup>.

The global policy framework required to rebuild marine life is largely in place through existing UN mechanisms (targets to be adopted in 2020 under the Global Biodiversity Framework of the CBD, SDGs and Paris Agreement of the UNFCCC), if their most ambitious goals are implemented, along with additional international conventions such as the Bonn Convention on the Conservation of Migratory Species of Wild Animals, the Moratorium on Commercial Whaling of the International Whaling Commission (1982), Ramsar Convention on Wetlands of International Importance and CITES, among others. High-level coordination among all UN instruments and international policies addressing the oceans, including the high seas, is needed.

The UN initiated, in 2018, an Intergovernmental Conference to reach a new legally binding treaty to protect marine life in the high seas by 2020. This proposed treaty could enhance cooperation, governance and funds for conservation and restoration of high-seas and deep-sea ecosystems damaged or at risk from commercial interests<sup>141</sup>. This mandate would require funding of around US\$30 million annually, which could be financed through long-term bonds in international capital markets or taxes on resource extraction<sup>141</sup>. Internationally agreed contributions will also be required, because populations of many species are shared across Exclusive Economic Zones of multiple nations. This approach could follow the model of the Regional Fisheries Management Organizations, bringing together nations to manage shared fish stocks that straddle national waters and the high seas<sup>141</sup>. For example, in September 2010 the Convention for the Protection of the Marine Environment of the North-East Atlantic (OSPAR) established the world's first MPA network on the high seas covering 286,200 km<sup>2</sup> (ref. <sup>142</sup>).

Rebuilding marine life will also require active oversight, participation and cooperation by local, regional and national stakeholders. A readiness and the capacity to implement recovery wedges differs across nations, and cooperation to rebuild marine life should remain flexible to adapt to variable cultural settings; locally designed approaches may be most effective<sup>143</sup> (Supplementary Information 1). Past failures in some nations can inform new governance arrangements to avoid repeating

the same mistakes elsewhere. Rebuilding marine life should draw on successful marine policy formulation, management actions and technologies to nurture a learning curve that will propel future outcomes while reducing cost<sup>105,107–109</sup>. For instance, many developed nations have already implemented nutrient reduction plans; however, fertilizer use is rising globally, supported mainly by demands from developing nations that also continue to develop their shorelines. Adopting the measures now in place in developed nations to increase nitrogen-use efficiency in South and East Asia could lower global synthetic fertilizer use by 2050, even under the increased crop production required to feed a growing population<sup>144</sup>.

Calls for international assistance to support recovery, whether it is for coastal wetlands to reduce risks of damages from natural disasters<sup>105</sup> or marine life generally<sup>129</sup>, should include assistance to improve governance and build institutional capacities. However, the capacity of both developed and developing nations to deploy effective recovery actions is already substantial. Mangrove restoration projects are considerably larger and cheaper but similarly successful (about 50% survival reported) in developing nations compared with developed countries<sup>104</sup>, and small-island states are showing growing leadership in response to plastic pollution and the marine impacts of climate change (<https://www.aosis.org/>). However, many developing countries need particularly high levels of investment to conserve and restore habitats that protect populations at risk in low-lying coastal areas, which could be financed through international climate change adaptation funds<sup>105</sup>. Currently, the UN's Green Climate Fund has mobilized US\$10.3 billion annually to assist developing countries to adapt to climate change, with a goal of US\$100 billion per year in 2020 (<https://www.greenclimate.fund/how-we-work/resource-mobilization>). Allocating a sizeable fraction of these funds to developing countries for the conservation and restoration of 'blue infrastructure' (for example, saltmarshes, oyster and coral reefs, mangroves and seagrass beds) could increase the resilience of coastal communities to climate change and to extreme events while improving their livelihoods<sup>105</sup>.

## Conclusion

Based on the data reviewed here, we conclude that substantial rebuilding across many components of marine life by 2050 is an achievable Grand Challenge for science and society. Meeting this challenge requires immediate action to reduce relevant pressures, including climate change, safeguarding places of remaining abundance, and recovering depleted populations, habitats and ecosystems elsewhere. This will require sustained perseverance and substantial commitment of financial resources, but we suggest that the ecological, economic and social gains will be far-reaching. Success requires the establishment of a committed and resilient global partnership of governments and societies aligned with this goal, supported by coordinated policies, adequate financial and market mechanisms, and evolving scientific and technological advances that nurture a fast learning curve of rebuilding interventions. Meeting the challenge of substantially rebuilding marine life would be a historic milestone in humanity's quest to achieve a globally sustainable future.

1. OECD. *The Ocean Economy in 2030* (OECD Publishing, 2016).
  2. Duarte, C. M. et al. Will the oceans help feed humanity? *Bioscience* **59**, 967–976 (2009).
  3. Roberts, C. M. et al. Marine reserves can mitigate and promote adaptation to climate change. *Proc. Natl Acad. Sci. USA* **114**, 6167–6175 (2017).
  4. Gattuso, J.-P. et al. Ocean solutions to address climate change and its effects on marine ecosystems. *Front. Mar. Sci.* **5**, 337 (2018).
  5. Jackson, J. B. et al. Historical overfishing and the recent collapse of coastal ecosystems. *Science* **293**, 629–637 (2001).
  6. Lotze, H. K. & Worm, B. Historical baselines for large marine animals. *Trends Ecol. Evol.* **24**, 254–262 (2009).
  7. McCauley, D. J. et al. Marine defaunation: animal loss in the global ocean. *Science* **347**, 1255641 (2015).
- This paper reviews the historical hunting and associated loss of animals in the ocean and examines current threats that may result in future losses.**

8. IPBES. IPBES Global Assessment Summary for Policymakers. <https://www.ipbes.net/news/ipbes-global-assessment-summary-policymakers-pdf> (2019).
  9. Wassmann, P. et al. Footprints of climate change in the Arctic marine ecosystem. *Glob. Change Biol.* **17**, 1235–1249 (2011).
  10. Gattuso, J.-P. et al. Contrasting futures for ocean and society from different anthropogenic CO<sub>2</sub> emissions scenarios. *Science* **349**, aac4722 (2015).
  11. Hughes, T. P. et al. Coral reefs in the Anthropocene. *Nature* **546**, 82–90 (2017).
  12. Hughes, T. P. et al. Spatial and temporal patterns of mass bleaching of corals in the Anthropocene. *Science* **359**, 80–83 (2018).
- This study provides a global assessment of the extent of coral bleaching, with emphasis on the 2015–2016 global coral-reef bleaching events.**
13. Hoegh-Guldberg, O. et al. in *Special Report on Global Warming of 1.5°C* (eds Masson-Delmotte, V. et al.) 175–311 (WMO, 2018).
- This IPCC report suggests that, in light of recent coral losses, the research community may have underestimated the risks of climate change for coral reefs, and concludes that even achieving the ambitious goal of 1.5°C of global warming under the Paris Agreement could result in the loss of 70–90% of reef-building corals compared to that at the time the assessment was made.**
14. Lotze, H. K. et al. Global ensemble projections reveal trophic amplification of ocean biomass declines with climate change. *Proc. Natl Acad. Sci. USA* **116**, 12907–12912 (2019).
  15. Lubchenco, J. & Grorud-Colvert, K. Making waves: the science and politics of ocean protection. *Science* **350**, 382–383 (2015).
  16. Costanza, R. et al. The value of the world's ecosystem services and natural capital. *Nature* **387**, 253–260 (1997).
  17. Silver, J. J. et al. Blue economy and competing discourses in international oceans governance. *J. Environ. Dev.* **24**, 135–160 (2015).
  18. Roberts, C. M. *The Unnatural History of the Sea* (Island Press, 2007).
- This book reviews how human pressures drove changes in marine ecosystems and to marine life, providing evidence that the observed impacts on marine ecosystems are not a recent phenomenon.**
19. Worm, B. Marine conservation: how to heal an ocean. *Nature* **543**, 630–631 (2017).
  20. Jones, H. P. et al. Restoration and repair of Earth's damaged ecosystems. *Proc. R. Soc. Lond. B* **285**, 20172577 (2018).
  21. FAO. *The State of World Fisheries and Aquaculture: Meeting the Sustainable Development Goals* (Food and Agriculture Organization of the United Nations, 2018).
  22. Doney, S. C. The growing human footprint on coastal and open-ocean biogeochemistry. *Science* **328**, 1512–1516 (2010).
  23. Breitburg, D. et al. Declining oxygen in the global ocean and coastal waters. *Science* **359**, eaam7240 (2018).
  24. IUCN. The IUCN Red List of Threatened Species. <https://www.iucnredlist.org/> (accessed 1 April 2019).
  25. Dulvy, N. K., Pinnegar, J. K. & Reynolds, J. D. in *Holocene Extinctions* (ed. Turvey, S. T.) 129–150 (Oxford Univ. Press, 2009).
  26. Jones, K. R. et al. The location and protection status of Earth's diminishing marine wilderness. *Curr. Biol.* **28**, 2506–2512 (2018).
  27. Irigoien, X. et al. Large mesopelagic fishes biomass and trophic efficiency in the open ocean. *Nat. Commun.* **5**, 3271 (2014).
- This study reports an estimate of mesopelagic fish abundance, which exceeds the biomass of all other fish stocks by about 30 times and remains unexploited by fisheries.**
28. Beare, D., Hölker, F., Engelhard, G. H., McKenzie, E. & Reid, D. G. An unintended experiment in fisheries science: a marine area protected by war results in Mexican waves in fish numbers-at-age. *Naturwissenschaften* **97**, 797–808 (2010).
  29. Richards, Z. T., Beger, M., Pinca, S. & Wallace, C. C. Bikini Atoll coral biodiversity resilience five decades after nuclear testing. *Mar. Pollut. Bull.* **56**, 503–515 (2008).
  30. Oguz, T. & Velikova, V. Abrupt transition of the northwestern Black Sea shelf ecosystem from a eutrophic to an alternative pristine state. *Mar. Ecol. Prog. Ser.* **405**, 231–242 (2010).
  31. Mozetič, P. et al. Recent trends towards oligotrophication of the northern Adriatic: evidence from chlorophyll a time series. *Estuaries Coast.* **33**, 362–375 (2010).
  32. Jackson, J. B. C. Colloquium paper: ecological extinction and evolution in the brave new ocean. *Proc. Natl Acad. Sci. USA* **105**, 11458–11465 (2008).
  33. Duarte, C. M. Global change and the future ocean: a grand challenge for marine sciences. *Front. Mar. Sci.* **1**, 63 (2014).
  34. Magera, A. M., Mills Flemming, J. E., Kaschner, K., Christensen, L. B. & Lotze, H. K. Recovery trends in marine mammal populations. *PLoS ONE* **8**, e77908 (2013).
  35. Lotze, H. K., Coll, M., Magera, A. M., Ward-Paige, C. & Airoldi, L. Recovery of marine animal populations and ecosystems. *Trends Ecol. Evol.* **26**, 595–605 (2011).
- This paper provides a discussion of the recovery potential and timescales for marine animal populations and ecosystems.**
36. Costello, C. et al. Global fishery prospects under contrasting management regimes. *Proc. Natl Acad. Sci. USA* **113**, 5125–5129 (2016).
  37. Castilla, J. C. & Defeo, O. Latin American benthic shell fisheries: emphasis on co-management and experimental practices. *Rev. Fish Biol. Fish.* **11**, 1–30 (2001).
  38. Birkenbach, A. M., Kaczan, D. J. & Smith, M. D. Catch shares slow the race to fish. *Nature* **544**, 223–226 (2017).
  39. Worm, B. et al. Rebuilding global fisheries. *Science* **325**, 578–585 (2009).
  40. Duarte, C. M. et al. The role of coastal plant communities for climate change mitigation and adaptation. *Nat. Clim. Change* **3**, 961–968 (2013).
- This review summarizes how Blue Carbon strategies, based on the conservation and restoration of vegetated coastal habitats, can help to mitigate climate change and can provide coastal protection, thereby helping coastal communities to adapt to climate change.**
41. Reusch, T. B. et al. The Baltic Sea as a time machine for the future coastal ocean. *Sci. Adv.* **4**, eaar8195 (2018).
- This review provides a narrative of the difficulties and successes in achieving environmental improvements and recovery of the Baltic Sea, with an emphasis on lessons learned to guide future efforts elsewhere.**



42. Boesch, D. F. Barriers and bridges in abating coastal eutrophication. *Front. Mar. Sci.* **6**, 123 (2019).
43. Jambeck, J. R. et al. Plastic waste inputs from land into the ocean. *Science* **347**, 768–771 (2015).
44. Roberts, C. M., Hawkins, J. P. & Gell, F. R. The role of marine reserves in achieving sustainable fisheries. *Phil. Trans. R. Soc. B* **360**, 123–132 (2005).
45. Das, S. & Vincent, J. R. Mangroves protected villages and reduced death toll during Indian super cyclone. *Proc. Natl Acad. Sci. USA* **106**, 7357–7360 (2009).
46. Taillardat, P., Friess, D. A. & Lupascu, M. Mangrove blue carbon strategies for climate change mitigation are most effective at the national scale. *Biol. Lett.* **14**, 20180251 (2018).
47. Lotze, H. K. et al. Depletion, degradation, and recovery potential of estuaries and coastal seas. *Science* **312**, 1806–1809 (2006).
48. Roman, J., Dunphy-Daly, M. M., Johnston, D. W. & Read, A. J. Lifting baselines to address the consequences of conservation success. *Trends Ecol. Evol.* **30**, 299–302 (2015).
49. Beijer, M. et al. Embracing conservation success of recovering humpback whale populations: evaluating the case for downlisting their conservation status in Australia. *Mar. Policy* **66**, 137–141 (2016).
50. Lowry, M. S. et al. Abundance, distribution, and population growth of the northern elephant seal (*Mirovunga angustirostris*) in the United States from 1991 to 2010. *Aquat. Mamm.* **40**, 20–31 (2014).
- This paper provides a compelling overview of how hunting regulation and protection allowed the remarkable comeback of the northern elephant seal in the Pacific coast of the United States.**
51. Fisheries and Oceans Canada. Stock Assessment of Canadian Grey Seals (*Halichoerus grypus*). *Canadian Science Advisory Secretariat Research Document 2014/010* (Fisheries and Oceans Canada, 2014).
52. Mazaris, A. D., Schofield, G., Gkazinou, C., Alpanidou, V. & Hays, G. C. Global sea turtle conservation successes. *Sci. Adv.* **3**, e1600730 (2017).
53. Ricard, D. et al. Examining the knowledge base and status of commercially exploited marine species with the RAM Legacy Stock Assessment Database. *Fish. Fish.* **13**, 380–398 (2012).
54. Hutchings, J. A. & Reynolds, J. D. Marine fish population collapses: consequences for recovery and extinction risk. *Bioscience* **54**, 297–309 (2004).
55. Rigét, F. et al. Temporal trends of persistent organic pollutants in Arctic marine and freshwater biota. *Sci. Total Environ.* **649**, 99–110 (2019).
56. Pinedo-González, A. J. et al. Concentration and isotopic composition of dissolved Pb in surface waters of the modern global ocean. *Geochim. Cosmochim. Acta* **235**, 41–54 (2018).
57. Schøyen, M. et al. Levels and trends of tributyltin (TBT) and imposex in dogwhelk (*Nuccella lapillus*) along the Norwegian coastline from 1991 to 2017. *Mar. Environ. Res.* **144**, 1–8 (2019).
58. IOTOPF. Oil Tanker Spill Statistics 2016 <http://www.itopf.org/> (2016).
59. Duarte, C. M. et al. Return to Neverland: shifting baselines affect eutrophication restoration targets. *Estuaries Coast.* **32**, 29–36 (2009).
60. Lefcheck, J. S. et al. Long-term nutrient reductions lead to the unprecedented recovery of a temperate coastal region. *Proc. Natl Acad. Sci. USA* **115**, 3658–3662 (2018).
61. Tomasko, D. et al. Widespread recovery of seagrass coverage in Southwest Florida (USA): temporal and spatial trends and management actions responsible for success. *Mar. Pollut. Bull.* **135**, 1128–1137 (2018).
62. de los Santos, C.B. et al. Recent trend reversal for declining European seagrass meadows. *Nat. Commun.* **10**, 3356 (2019).
- This study reports how decades of efforts to reduce nutrient inputs, improve coastal water quality and conserve and restore seagrass meadows has led to a remarkable trend reversal from sustained losses of seagrass across Europe throughout the twentieth century to a substantial increase between 2000 and 2010.**
63. Yoshida, G. et al. in *Blue Carbon in Shallow Coastal Ecosystems* (eds Kuwae, T. & Hori, M.) (Springer Nature, 2019).
64. Arnaud-Haond, S. et al. Genetic recolonization of mangrove: genetic diversity still increasing in the Mekong Delta 30 years after Agent Orange. *Mar. Ecol. Prog. Ser.* **390**, 129–135 (2009).
65. Nam, V. N., Sasmito, S. D., Murdiyarto, D., Purbopuspito, J. & MacKenzie, R. A. Carbon stocks in artificially and naturally regenerated mangrove ecosystems in the Mekong Delta. *Wetl. Ecol. Manag.* **24**, 231–244 (2016).
66. Bunting, P. et al. The global mangrove watch—a new 2010 global baseline of mangrove extent. *Remote Sens.* **10**, 1669 (2018).
67. Hamilton, S. E. & Casey, D. Creation of a high spatio-temporal resolution global database of continuous mangrove forest cover for the 21st century (CGMFC-21). *Glob. Ecol. Biogeogr.* **25**, 729–738 (2016).
68. López-Angarita, J. et al. Land use patterns and influences of protected areas on mangroves of the eastern tropical Pacific. *Biol. Conserv.* **227**, 82–91 (2018).
69. Almahasheer, H. et al. Decadal stability of Red Sea mangroves. *Estuar. Coast. Shelf Sci.* **169**, 164–172 (2016).
70. Almahasheer, H. Spatial coverage of mangrove communities in the Arabian Gulf. *Environ. Monit. Assess.* **190**, 85 (2018).
71. Chen, L. Z. et al. Recent progresses in mangrove conservation, restoration and research in China. *J. Plant Ecol.* **2**, 45–54 (2009).
72. Piacenza, S. E. et al. Trends and variability in demographic indicators of a recovering population of green sea turtles *Chelonia mydas*. *Endanger. Species Res.* **31**, 103–117 (2016).
73. Thorson, J. T., Cope, J. M., Branch, T. A. & Jensen, O. P. Spawning biomass reference points for exploited marine fishes, incorporating taxonomic and body size information. *Can. J. Fish. Aquat. Sci.* **69**, 1556–1568 (2012).
74. McClatchie, S. et al. Collapse and recovery of forage fish populations prior to commercial exploitation. *Geophys. Res. Lett.* **44**, 1877–1885 (2017).
75. Rosenberg, A. A., Swasey, J. H. & Bowman, M. Rebuilding US fisheries: progress and problems. *Front. Ecol. Environ.* **4**, 303–308 (2006).
76. Neubauer, P., Jensen, O. P., Hutchings, J. A. & Baum, J. K. Resilience and recovery of overexploited marine populations. *Science* **340**, 347–349 (2013).
77. Safina, C., Rosenberg, A. A., Myers, R. A., Quinn, T. J. II & Collie, J. S. U.S. ocean fish recovery: staying the course. *Science* **309**, 707–708 (2005).
78. MacNeil, M. A. et al. Recovery potential of the world's coral reef fishes. *Nature* **520**, 341–344 (2015).
79. Sumaila, U. R. et al. Benefits of rebuilding global marine fisheries outweigh costs. *PLoS ONE* **7**, e40542 (2012).
80. Bersosa Hernández, A. et al. Restoring the eastern oyster: how much progress has been made in 53 years? *Front. Ecol. Environ.* **16**, 463–471 (2018).
81. Graham, M. H. et al. Population dynamics of giant kelp *Macrocystis pyrifera* along a wave exposure gradient. *Mar. Ecol. Prog. Ser.* **148**, 269–279 (1997).
82. Dayton, P. K., Tegner, M. J., Parnell, P. E. & Edwards, P. B. Temporal and spatial patterns of disturbance and recovery in a kelp forest community. *Ecol. Monogr.* **62**, 421–445 (1992).
83. Williams, P. B. & Orr, M. K. Physical evolution of restored breached levee salt marshes in the San Francisco Bay estuary. *Restor. Ecol.* **10**, 527–542 (2002).
84. Alongi, D. M. Mangrove forests: resilience, protection from tsunamis, and responses to global climate change. *Estuar. Coast. Shelf Sci.* **76**, 1–13 (2008).
85. Duarte, C. M. Submerged aquatic vegetation in relation to different nutrient regimes. *Ophelia* **41**, 87–112 (1995).
86. Rooper, C. N. et al. Modeling the impacts of bottom trawling and the subsequent recovery rates of sponges and corals in the Aleutian Islands, Alaska. *Cont. Shelf Res.* **31**, 1827–1834 (2011).
87. Girard, F., Shea, K. & Fisher, C. R. Projecting the recovery of a long-lived deep-sea coral species after the Deepwater Horizon oil spill using state-structured models. *J. Appl. Ecol.* **55**, 1812–1822 (2018).
88. Hughes, T. P. et al. Global warming impairs stock-recruitment dynamics of corals. *Nature* **568**, 387–390 (2019).
89. Moreno-Mateos, D. et al. Anthropogenic ecosystem disturbance and the recovery debt. *Nat. Commun.* **8**, 14163 (2017).
90. Thurstan, R. H. & Roberts, C. M. Ecological meltdown in the Firth of Clyde, Scotland: two centuries of change in a coastal marine ecosystem. *PLoS ONE* **5**, e11767 (2010).
91. Britten, G. L. et al. Extended fisheries recovery timelines in a changing environment. *Nat. Commun.* **8**, 15325 (2017).
92. Moore, J. K. et al. Sustained climate warming drives declining marine biological productivity. *Science* **359**, 1139–1143 (2018).
93. WWF. *Living Blue Planet Report* (WWF, 2015).
94. Thurstan, R. H., Brockington, S. & Roberts, C. M. The effects of 118 years of industrial fishing on UK bottom trawl fisheries. *Nat. Commun.* **1**, 15 (2010).
95. IPCC. *IPCC Special Report on the Ocean and Cryosphere in a Changing Climate*. (eds. Pörtner, H.-O. et al.) (IPCC, 2019).
- This IPCC Special Report contains an updated assessment of the impacts—both realized and projected—of climate change on the oceans as well as projections on sea-level rise and its associated impacts.**
96. Jepson, P. Recoverable Earth: a twenty-first century environmental narrative. *Ambio* **48**, 123–130 (2019).
97. Molloy, P. P., McLean, I. B. & Côté, I. M. Effects of marine reserve age on fish populations: a global meta-analysis. *J. Appl. Ecol.* **46**, 743–751 (2009).
98. Dinerstein, E. et al. A global deal for nature: guiding principles, milestones, and targets. *Sci. Adv.* **5**, eaaw2869 (2019).
99. Sala, E. et al. Assessing real progress towards effective ocean protection. *Mar. Policy* **91**, 11–13 (2018).
100. Costello, M. J. & Ballantine, B. Biodiversity conservation should focus on no-take marine reserves: 94% of marine protected areas allow fishing. *Trends Ecol. Evol.* **30**, 507–509 (2015).
101. Gill, D. A. et al. Capacity shortfalls hinder the performance of marine protected areas globally. *Nature* **543**, 665–669 (2017).
102. O'Leary, B. C. et al. Addressing criticisms of large-scale marine protected areas. *Bioscience* **68**, 359–370 (2018).
103. O'Hara, C. C., Villaseñor-Derbez, J. C., Ralph, G. M. & Halpern, B. S. Mapping status and conservation of global at-risk marine biodiversity. *Conserv. Lett.* **12**, e12651 (2019).
104. Bayraktarov, E. et al. The cost and feasibility of marine coastal restoration. *Ecol. Appl.* **26**, 1055–1074 (2016).
105. Barbier, E. B. Policy: Hurricane Katrina's lessons for the world. *Nature* **524**, 285–287 (2015).
106. Temmerman, S. et al. Ecosystem-based coastal defence in the face of global change. *Nature* **504**, 79–83 (2013).
107. van Katwijk, M. M. et al. Global review of seagrass restoration: the importance of large-scale planting. *J. Appl. Ecol.* **53**, 567–578 (2016).
108. Suggett, D. J. et al. Optimizing return-on-effort for coral nursery and outplanting practices to aid restoration of the Great Barrier Reef. *Restor. Ecol.* **27**, 683–693 (2019).
109. Lewis, R. R. III. Ecological engineering for successful management and restoration of mangrove forests. *Ecol. Eng.* **24**, 403–418 (2005).
110. van Oppen, M. J., Oliver, J. K., Putnam, H. M. & Gates, R. D. Building coral reef resilience through assisted evolution. *Proc. Natl Acad. Sci. USA* **112**, 2307–2313 (2015).
111. National Academies of Sciences, Engineering, and Medicine. *A Research Review of Interventions to Increase the Persistence and Resilience of Coral Reefs* <https://doi.org/10.17226/25279> (National Academies Press, 2019).
112. Lovelock, C. E. & Brown, B. M. Land tenure considerations are key to successful mangrove restoration. *Nat. Ecol. Evol.* **3**, 1135 (2019).
113. Duarte, C. M. & Krause-Jensen, D. Intervention options to accelerate ecosystem recovery from coastal eutrophication. *Front. Mar. Sci.* **5**, 470 (2018).
114. Xiao, X. et al. Nutrient removal from Chinese coastal waters by large-scale seaweed aquaculture. *Sci. Rep.* **7**, 46613 (2017).
115. Carstensen, J. & Duarte, C. M. Drivers of pH variability in coastal ecosystems. *Sci. Technol.* **53**, 4020–4029 (2019).
116. Rydin, E., Kumbblad, L., Wulff, F. & Larsson, P. Remediation of a eutrophic bay in the Baltic Sea. *Environ. Sci. Technol.* **51**, 4559–4566 (2017).

117. Boesch, D. Deep-water drilling remains a risky business. *Nature* **484**, 289 (2012).
  118. Johannsdottir, L. & Cook, D. Systemic risk of maritime-related oil spills viewed from an Arctic and insurance perspective. *Ocean Coast. Manage.* **179**, 104853 (2019).
  119. Kunc, H. P., McLaughlin, K. E. & Schmidt, R. Aquatic noise pollution: implications for individuals, populations, and ecosystems. *Proc. R. Soc. Lond. B* **283**, 20160839 (2016).
  120. Worthington, T. & Spalding, M. *Mangrove Restoration Potential: A global map highlighting a critical opportunity*. <https://doi.org/10.17863/CAM.39153> (2018).
  121. Kondolf, G. M., Rubin, Z. K. & Minear, J. T. Dams on the Mekong: cumulative sediment starvation. *Water Resour. Res.* **50**, 5158–5169 (2014).
  122. Schuerch, M. et al. Future response of global coastal wetlands to sea-level rise. *Nature* **561**, 231–234 (2018).
  123. Fabricius, K. E. Effects of terrestrial runoff on the ecology of corals and coral reefs: review and synthesis. *Mar. Pollut. Bull.* **50**, 125–146 (2005).
  124. Rogelj, J. et al. Paris Agreement climate proposals need a boost to keep warming well below 2°C. *Nature* **534**, 631–639 (2016).
  125. Tokarska, K. B. & Gillett, N. P. Cumulative carbon emissions budgets consistent with 1.5°C global warming. *Nat. Clim. Change* **8**, 296–299 (2018).
  126. UNEP. *Emissions Gap Report 2019*. <https://www.unenvironment.org/resources/emissions-gap-report-2019> (UNEP, 2019).
  127. Bruno, J. F. et al. Climate change threatens the world's marine protected areas. *Nat. Clim. Change* **8**, 499–503 (2018).
  128. Sully, S., Burkepile, D. E., Donovan, M. K., Hodgson, G. & van Woesik, R. A global analysis of coral bleaching over the past two decades. *Nat. Commun.* **10**, 1264 (2019).
  129. Barbier, E. B., Burgess, J. C. & Dean, T. J. How to pay for saving biodiversity. *Science* **360**, 486–488 (2018).
- This study provides estimates and funding mechanisms to pay for biodiversity conservation globally, including estimates of investment and benefits for conserving marine biodiversity.**
130. Balmford, A., Gravestock, P., Hockley, N., McClean, C. J. & Roberts, C. M. The worldwide costs of marine protected areas. *Proc. Natl Acad. Sci. USA* **101**, 9694–9697 (2004).
  131. McCook, L. J. et al. Adaptive management of the Great Barrier Reef: a globally significant demonstration of the benefits of networks of marine reserves. *Proc. Natl Acad. Sci. USA* **107**, 18278–18285 (2010).
  132. Burgess, M. G. et al. Protecting marine mammals, turtles, and birds by rebuilding global fisheries. *Science* **359**, 1255–1258 (2018).
  133. Lubchenco, J. et al. The right incentives enable ocean sustainability successes and provide hope for the future. *Proc. Natl Acad. Sci. USA* **113**, 14507–14514 (2016).
  134. Cisneros-Montemayor, A. M., Pauly, D., Weatherdon, L. V. & Ota, Y. A global estimate of seafood consumption by coastal indigenous peoples. *PLoS ONE* **11**, e0166681 (2016).
  135. Arlinghaus, R. et al. Opinion: governing the recreational dimension of global fisheries. *Proc. Natl Acad. Sci. USA* **116**, 5209–5213 (2019).
  136. Bäckstrand, K. et al. Non-state actors in global climate governance: from Copenhagen to Paris and beyond. *Env. Polit.* **26**, 561–579 (2017).
  137. Hudson, A. Restoring and protecting the world's large marine ecosystems: an engine for job creation and sustainable economic development. *Environ. Dev.* **22**, 150–155 (2017).
  138. Gelcich, S., Godoy, N., Prado, L. & Castilla, J. C. Add-on conservation benefits of marine territorial user rights fishery policies in central Chile. *Ecol. Appl.* **18**, 273–281 (2008).
  139. Johns, L. N. & Jacquet, J. Doom and gloom versus optimism: an assessment of ocean-related US science journalism (2001–2015). *Glob. Environ. Change* **50**, 142–148 (2018).
  140. Balmford, A. & Knowlton, N. Why Earth optimism? *Science* **356**, 225 (2017).
  141. Barbier, E. B. et al. Protect the deep sea. *Nature* **505**, 475–477 (2014).
  142. O'Leary, B. C. et al. The first network of marine protected areas (MPAs) in the high seas: the process, the challenges and where next. *Mar. Policy* **36**, 598–605 (2012).
  143. Rodríguez, J. P. et al. Environment: globalization of conservation: a view from the south. *Science* **317**, 755–756 (2007).
  144. Mogollón, J. M. et al. Assessing future reactive nitrogen inputs into global croplands based on the shared socioeconomic pathways. *Environ. Res. Lett.* **13**, 044008 (2018).
- Acknowledgements** This work was supported by King Abdullah University of Science and Technology through baseline funding to C.M.D. and S.A. G.L.B. was supported by the Simons Collaboration on Computational Biogeochemical Modeling of Marine Ecosystems/CBIOMES (grant number 549931); J.-P.G. was supported by the Prince Albert II of Monaco Foundation, the Ocean Acidification International Coordination Centre of the International Atomic Energy Agency, the Veolia Foundation and the French Facility for Global Environment; H.K.L. and B.W. were supported by the Natural Sciences and Engineering Research Council of Canada (NSERC) and the Ocean Frontier Institute (Module G); J.C.C. was supported by the Catedra Arauco in Environmental Ethic-UC and Centro Interdisciplinario de Cambio Global-UC. We thank T. Kuwae, R. J. Orth, the Mars Sustainable Solutions (part of Mars Inc), and C. Haight and B. DeAngelis for supplying details on restoration projects; L. Valuzzi, R. Devassy, A. Parry and F. Baalkhuyur for help with the inventory of restoration projects, E. McLeod for help locating materials, and A. Buxton and S. Gasparian for help with displays.
- Author contributions** C.M.D. developed the concept and all authors contributed to the design, data compilation, analysis and writing of the Review.
- Competing interests** The authors declare no competing interests.
- Additional information**
- Supplementary information** is available for this paper at <https://doi.org/10.1038/s41586-020-2146-7>.
- Correspondence and requests for materials** should be addressed to C.M.D.
- Peer review information** *Nature* thanks Jonathan S. Lefcheck, Brian MacKenzie and the other, anonymous, reviewer(s) for their contribution to the peer review of this work.
- Reprints and permissions information** is available at <http://www.nature.com/reprints>.
- Publisher's note** Springer Nature remains neutral with regard to jurisdictional claims in published maps and institutional affiliations.
- © The Author(s), under exclusive licence to Springer Nature Limited 2020

# Mirror-symmetry violation in bound nuclear ground states

<https://doi.org/10.1038/s41586-020-2123-1>

Received: 23 August 2019

Accepted: 22 January 2020

Published online: 1 April 2020



D. E. M. Hoff<sup>1</sup>✉, A. M. Rogers<sup>1</sup>✉, S. M. Wang<sup>2</sup>, P. C. Bender<sup>1</sup>, K. Brandenburg<sup>3</sup>, K. Childers<sup>2,4</sup>, J. A. Clark<sup>5</sup>, A. C. Dombos<sup>2,6,7</sup>, E. R. Doucet<sup>1</sup>, S. Jin<sup>2,7</sup>, R. Lewis<sup>2,4</sup>, S. N. Liddick<sup>2,4</sup>, C. J. Lister<sup>1</sup>, Z. Meisel<sup>3</sup>, C. Morse<sup>1,9</sup>, W. Nazarewicz<sup>6,8</sup>, H. Schatz<sup>2,6,7</sup>, K. Schmidt<sup>2,7,10</sup>, D. Soltesz<sup>3</sup>, S. K. Subedi<sup>3</sup> & S. Waniganeththi<sup>1</sup>

Conservation laws are deeply related to any symmetry present in a physical system<sup>1,2</sup>. Analogously to electrons in atoms exhibiting spin symmetries<sup>3</sup>, it is possible to consider neutrons and protons in the atomic nucleus as projections of a single fermion with an isobaric spin (isospin) of  $t = 1/2$  (ref. <sup>4</sup>). Every nuclear state is thus characterized by a total isobaric spin  $T$  and a projection  $T_z$ —two quantities that are largely conserved in nuclear reactions and decays<sup>5,6</sup>. A mirror symmetry emerges from this isobaric-spin formalism: nuclei with exchanged numbers of neutrons and protons, known as mirror nuclei, should have an identical set of states<sup>7</sup>, including their ground state, labelled by their total angular momentum  $J$  and parity  $\pi$ . Here we report evidence of mirror-symmetry violation in bound nuclear ground states within the mirror partners strontium-73 and bromine-73. We find that a  $aJ^\pi = 5/2^-$  spin assignment is needed to explain the proton-emission pattern observed from the  $T = 3/2$  isobaric-analogue state in rubidium-73, which is identical to the ground state of strontium-73. Therefore the ground state of strontium-73 must differ from its  $J^\pi = 1/2^-$  mirror bromine-73. This observation offers insights into charge-symmetry-breaking forces acting in atomic nuclei.

Determining the properties and structure of <sup>73</sup>Rb was primarily motivated by the role this nucleus plays in the rapid proton capture process<sup>8</sup> that is thought to drive thermonuclear type-I X-ray bursts<sup>9,10</sup>. Previous attempts to detect <sup>73</sup>Rb directly have not been successful, owing to its very short half-life, which arises as a result of its proton-unbound ground state<sup>11</sup>. In order to characterize the structure of states in <sup>73</sup>Rb, the nucleus was populated via the  $\beta$  decay of the longer-lived <sup>73</sup>Sr, a technique that has proved effective for several other proton-unbound nuclei<sup>12,13</sup>.

The experiment was performed at the National Superconducting Cyclotron Laboratory (NSCL), which provided a mixed beam of radioactive nuclei containing <sup>73</sup>Sr, derived from fragmentation of <sup>92</sup>Mo (see Methods). Each ion was identified (shown in Fig. 1) before passing through a stack of silicon detectors where they were stopped in a double-sided segmented silicon implantation detector to study their subsequent decays. The segments on the front and back of the detector are perpendicular to each other, enabling spatial localization of the implantation event, which considerably reduces the background when searching for decay events. Over the course of the run, 427 <sup>73</sup>Sr implantation events were unambiguously identified. In a given <sup>73</sup>Sr decay event, a positron ( $\beta^+$ ) is emitted first, quickly followed by the emission of a proton. The  $\beta^+$  particles have a continuous energy distribution, and usually leave only a small fraction of their energy in the silicon

detector. However, the emitted proton is stopped and deposits all of its energy into the silicon implantation detector. The summed energy deposited by the  $\beta^+$  particles and protons results in an energy broadening and shift in the charged-particle spectra (referred to as  $\beta$  summing). The implantation detector was surrounded by germanium detectors to measure  $\gamma$ -rays in coincidence with these decay events to connect the de-excitation of the daughter nucleus to proton-emitting states.

The time between the implantation of <sup>73</sup>Sr ions into the silicon detector and the subsequent charged-particle events is presented in Fig. 2a, and the data show good agreement with an exponential decay of one species and a constant random background. The half-life of <sup>73</sup>Sr was determined to be  $t_{1/2} = 23.1 \pm 1.4$  ms (all errors herein are  $1\sigma$ ) from the logarithmic-bin method<sup>14</sup>, providing, to our knowledge, the best direct half-life measurement of <sup>73</sup>Sr so far (see Extended Data Fig. 1 and Methods).

The energy spectrum of <sup>73</sup>Sr  $\beta$ -delayed proton-emission events is shown in Fig. 2b, with the measured background denoted by the shaded blue overlay (see Methods). Two strong peaks are observed. The largest peak—found at  $3.93 \pm 0.012$  MeV—is attributed to protons emitted from the  $T = 3/2$  isobaric-analogue state (IAS) in <sup>73</sup>Rb—referred to as <sup>73</sup>Rb\*(IAS)—which leaves behind <sup>72</sup>Kr in its ground state. Correcting for  $\beta$  summing (see Methods) gives a proton energy of  $3.80 \pm 0.02$  MeV, which is in agreement with the previous direct measurement<sup>15</sup> of

<sup>1</sup>Department of Physics and Applied Physics, University of Massachusetts Lowell, Lowell, MA, USA. <sup>2</sup>National Superconducting Cyclotron Laboratory, Michigan State University, East Lansing, MI, USA. <sup>3</sup>Department of Physics and Astronomy, Ohio University, Athens, OH, USA. <sup>4</sup>Department of Chemistry, Michigan State University, East Lansing, MI, USA. <sup>5</sup>Physics Division, Argonne National Laboratory, Argonne, IL, USA. <sup>6</sup>Department of Physics and Astronomy, Michigan State University, East Lansing, MI, USA. <sup>7</sup>JINA-CEE, Michigan State University, East Lansing, MI, USA. <sup>8</sup>FRIB Laboratory, Michigan State University, East Lansing, MI, USA. <sup>9</sup>Present address: Nuclear Science Division, Lawrence Berkeley National Laboratory, Berkeley, CA, USA. <sup>10</sup>Present address: Institute of Nuclear and Particle Physics, TU Dresden, Dresden, Germany. ✉e-mail: dan@demhoff.com; Andrew\_Rogers@umt.edu



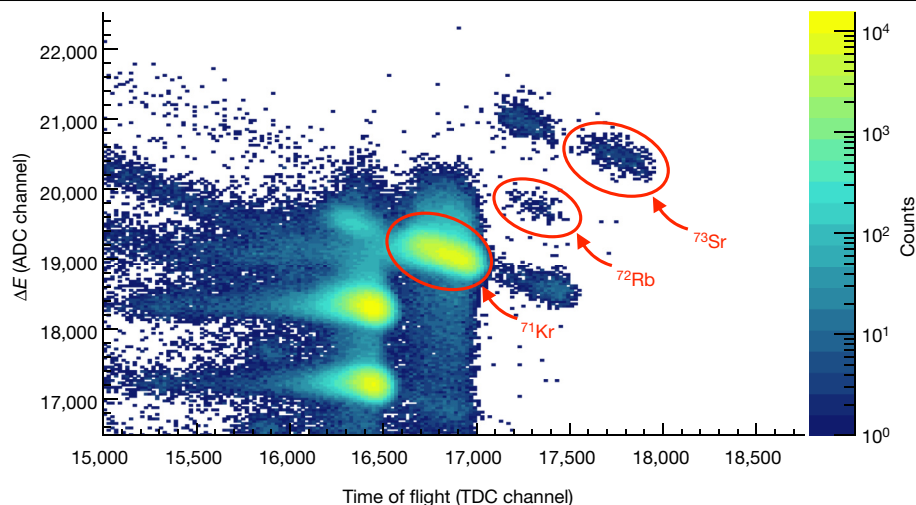


**Fig. 1 | Particle identification plot.** Particle identification was deduced from the energy loss of the incoming heavy ions passing through the first silicon detector in the stack ( $\Delta E$ ) versus the time of flight of the ion after exiting the A1900 fragment separator. The raw uncalibrated signals from the detectors are presented, with the analogue-to-digital converter (ADC) channel for the

relative energy loss on the vertical axis and the recorded time-to-digital converter (TDC) channel on the horizontal axis. The colours represent the total number of counts found. The ion of interest,  $^{73}\text{Sr}$ , is unambiguously isolated from neighbouring ions.

$3.75 \pm 0.04$  MeV. The second strong peak is attributed to the branching of  $^{73}\text{Rb}^*(\text{IAS})$  decays to the  $^{72}\text{Kr}^*(2^+)$  excited state. This is confirmed by the observation of 709-keV  $\gamma$ -rays that are promptly correlated with events in this second proton peak, shown by the inset to Fig. 2b. A peak in the  $\gamma$ -ray spectrum at 511 keV is expected, because two 511-keV  $\gamma$ -rays are emitted in the annihilation of the  $\beta^+$  with electrons. The observation of 10 coincident 709-keV  $\gamma$ -ray events is consistent with almost all protons in this lower-energy peak proceeding to the  $J^\pi = 2^+$  state, and  $<10\%$  to the nearby 671-keV excited  $^{72}\text{Kr}^*(0^+)$  state at the 90% confidence limit.

After accounting for the branching of the proton emission, the  $\beta$ -decay feeding to  $^{73}\text{Rb}^*(\text{IAS})$  was determined to be 63(3)%, as indicated in Fig. 3. This branching ratio, when combined with the predicted  $^{73}\text{Sr}$  mass from the most recent atomic mass evaluations<sup>16</sup>, yields a value of  $\log(ft)$ —a measure of the structural overlap between the initial and final states—of 3.45(6). This value of  $\log(ft)$  is consistent with the conservation of isobaric spin (that is, a  $\Delta T = 0$  superallowed decay) between pure IASs<sup>17</sup>. It should be noted that some isobaric-spin mixing is expected in the  $A = 73$  atomic mass region (enabling  $\Delta T = 1$  transitions) which would reduce the  $\beta$  branching to the IAS<sup>18–20</sup>, but our measurements cannot assess the degree of such mixing.

The branching of  $^{73}\text{Rb}^*(\text{IAS})$  is unusual as compared to similar systems just below the  $A = 73$  mass region. In particular,  $\beta$ -delayed protons from the nuclei  $^{65}\text{Se}$  and  $^{69}\text{Kr}$  predominately populate either the ground state or the excited states of the daughter nucleus<sup>12</sup>, rather than fractionating to the degree observed for  $^{73}\text{Rb}^*(\text{IAS})$ . In the case of  $^{65}\text{Se}$ , which has a  $J^\pi = 3/2^-$  ground state, the resulting decay of  $^{65}\text{As}^*(\text{IAS})$  almost completely proceeds to the  $0^+$  ground state of  $^{64}\text{Ge}$ . The opposite is true for  $^{69}\text{Kr}$ , for which the ground state and the corresponding  $^{69}\text{Br}^*(\text{IAS})$  have  $J^\pi = 5/2^-$ , and thus  $^{69}\text{Br}^*(\text{IAS})$  decays almost exclusively to the first excited  $2^+$  state in  $^{68}\text{Se}$  by emitting a proton that carries away one unit of orbital angular momentum ( $\ell = 1$ ).

For the nuclei involved in the  $\beta$ -delayed proton emission of  $^{73}\text{Sr}$ , the structural situation is more intricate, and thus the standard shell model approach to the wavefunctions is not appropriate<sup>21</sup>. The  $T = 3/2$  mirror-partner nucleus to  $^{73}\text{Sr}$  is  $^{73}\text{Br}$ , which has a highly collective and complex structure; its ground-state spin assignment had been under debate for almost two decades. The rotational band structure of  $^{73}\text{Br}$  suggests that it has a substantial deformation, and a ground state with  $J^\pi = 1/2^-$  that is possibly triaxially shaped<sup>22–26</sup>. Isobaric-spin symmetry would lead us

to expect that  $^{73}\text{Sr}$  should have a similarly highly collective structure, and therefore  $^{73}\text{Rb}^*(\text{IAS})$  as well. The key issue in this discussion is the degree to which strontium and bromine differ.  $^{73}\text{Br}$  has two differently shaped, low-lying collective configurations, separated by only 27 keV, where the ground state has  $J^\pi = 1/2^-$  and the excited configuration has  $J^\pi = 5/2^-$ . It requires only a small degree of charge-symmetry breaking to invert the sequence of these two structures and cause a breakdown of ground-state mirror symmetry. To this extent, the  $A = 73$  isobar is a special case.

To understand the continuum and deformation effects on the open quantum system  $^{73}\text{Rb}^*(\text{IAS})$ , we adopted the Gamow coupled-channel (GCC) approach to model its decay<sup>27,28</sup>. In the framework of GCC, we used the Berggren basis, which is a complete ensemble that includes bound, Gamow and scattering states<sup>21,27,29</sup>. Hence, it provides the correct outgoing asymptotic behaviour to describe the decay of particle-unbound resonances, and in essence enables the treatment of nuclear structure and reactions on the same footing. For this study,  $^{73}\text{Rb}^*(\text{IAS})$  was divided into a deformed core ( $^{72}\text{Kr}$ ) plus a valence proton. The interaction between the deformed  $^{72}\text{Kr}$  core and the valence proton is represented by a Woods–Saxon potential with a quadrupole deformation  $\beta_2$ .

The states in the  $T = 3/2$  quartet along the  $A = 73$  isobar are dominated by prolate deformation, and the daughter nucleus  $^{72}\text{Kr}$  is believed to show strong shape-mixing effects with a predominately oblate-shaped ground state<sup>30–32</sup>. Therefore, the decay of  $^{73}\text{Rb}^*(\text{IAS})$  to the ground-state rotational band of  $^{72}\text{Kr}$  might undergo a transition from a prolate to oblate shape, which would suppress the decay process by reducing the decay width,  $\Gamma_p$ . As no shape-mixing effect can be incorporated into the GCC model, calculations were performed for different deformations and spin assignments of  $^{73}\text{Rb}^*(\text{IAS})$ . The spin assignments were chosen based on the ground-state and first-excited-state spins of  $^{73}\text{Br}$ . The values  $\beta_2 = -0.34$  and  $+0.4$  were chosen for the oblate and prolate shapes, respectively, taken from experimental values for the ground states of  $^{73}\text{Br}$  and  $^{72}\text{Kr}$ <sup>23,25,31</sup>.

On the basis of the predicted branching ratios for  $^{73}\text{Rb}^*(\text{IAS})$  obtained from the GCC calculations, shown in Extended Data Table 1, the only spin assignment consistent with the data is  $J^\pi = 5/2^-$ , when the  $^{72}\text{Kr}$  core is described with oblate-shaped deformation. In this case,  $^{73}\text{Rb}^*(\text{IAS})$  decays to the ground state of  $^{72}\text{Kr}$  through the  $\ell = 3$  channel, and to the first excited  $J^\pi = 2^+$  state through the  $\ell = 3$  and  $\ell = 1$

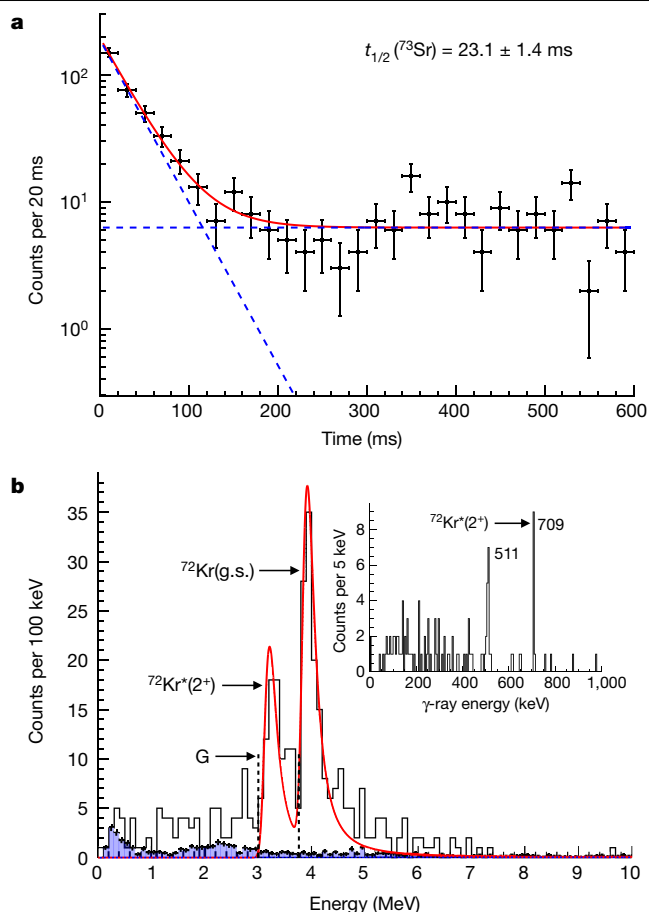


**Fig. 2 | Decay spectra of  $^{73}\text{Sr}$   $\beta$ -delayed proton emission.** **a**, A plot of the correlation time between implantation of  $^{73}\text{Sr}$  ions and their subsequent decay. The solid red curve shows the resulting fit for an exponential with a constant background. The individual components of the fit are shown by the blue dashed lines. The horizontal error bars correspond to the bin size, and the vertical error bars correspond to one standard deviation from counting. **b**, The time-gated ( $t < 200$  ms) energy spectrum of  $\beta + p$  decay events observed after the implantation of  $^{73}\text{Sr}$  ions. The solid red curve is the best fit of the  $^{73}\text{Rb}^*$ (IAS) decay peaks in the spectrum ( $\chi^2_{\text{red}} = 1.5$ ). The inset shows the  $\gamma$ -ray spectrum gated on the lower energy peak by the gate G, highlighting the de-excitation of  $^{72}\text{Kr}^*(2^+)$ . The shaded blue overlay shows the measured background; the horizontal error bars correspond to the bin size and the vertical error bars correspond to one standard deviation from counting. g.s., ground state.

channels. The lower centrifugal barrier of the  $p$ -wave ( $\ell = 1$ ) component compensates for the smaller decay energy of the first excited  $J^\pi = 2^+$  state. Therefore, the decay widths for the ground state and the first excited state are roughly equivalent, even though the configurations of the calculation might be slightly different when considering the effect of shape mixing or changing calculation parameters. The shape-mixing effect is expected to have a similar impact on both transitions; it should roughly cancel out in the branching ratio. Nevertheless, the conclusion that the small admixture of low-angular-momentum components into the wavefunction has a major impact on the decay process is robust and indicates the important role of deformation on the fine structure of decays via proton emission. This feature has been observed before—though not to the same degree—in the proton emitters  $^{131}\text{Eu}$  and  $^{141}\text{Ho}$ <sup>33–36</sup>.

Isobaric spin is clearly not a perfect symmetry considering protons and neutrons have different electric charges<sup>37</sup>, their masses are slightly different (0.14%)<sup>38</sup> and their magnetic moments differ substantially in both magnitude and sign<sup>39</sup>. Moreover, the nuclear force is stronger between neutron–proton ( $np$ ) pairs than between like-nucleon pairs

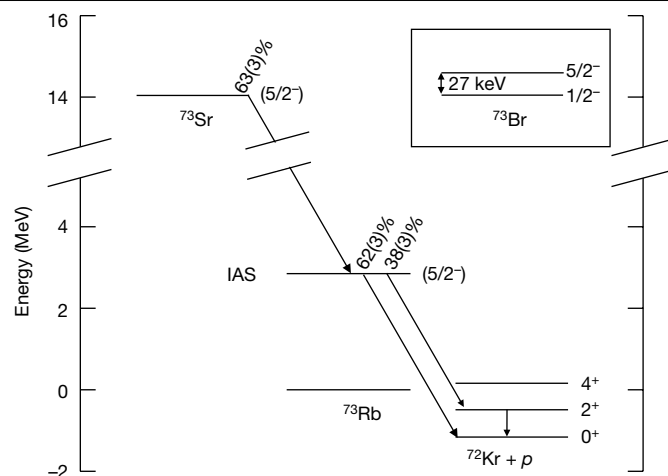


**Fig. 3 | Proposed level scheme.** The level scheme details the  $\beta$ -delayed proton emission of  $^{73}\text{Sr}$  through the IAS in  $^{73}\text{Rb}$ , providing the measured  $\beta$  branching to the IAS and the subsequent proton branching. The ground state and first excited state of  $^{73}\text{Br}$  are given in the inset, contrasted with the ground-state spin assignment of  $^{73}\text{Sr}$ .

( $nn$  and  $pp$ )<sup>40</sup>. With that in mind, it is not at all surprising that nuclear charge-symmetry breaking emerges from the small differences between nucleons and their interactions. Indeed, it is the robust nature of isobaric-spin symmetry that is noteworthy, but those occasions when it breaks down offer a chance to learn more about the forces acting inside the atomic nucleus.

The only other known case of isobaric-spin-symmetry breaking that results in different ground states between mirror nuclei (see Extended Data Fig. 2) is in the  $T = 1$  mirror pair  $^{16}\text{F}/^{16}\text{N}$ , in which  $^{16}\text{F}$  is particle unbound and  $^{16}\text{N}$  is particle bound. This case of isobaric-spin-symmetry breaking is well explained as a consequence of the Coulomb force, in an effect known as the Thomas–Ehrman shift<sup>41–43</sup>. The Thomas–Ehrman shift comes into play for an unbound or loosely bound proton state (the valence proton of  $^{16}\text{F}$ ), because the wavefunction of the proton extends well beyond the surface of the nucleus, resulting in a different asymptotic behaviour than for the bound mirrored neutron (the valence neutron of  $^{16}\text{N}$ ). Such a mechanism is not immediately apparent in the case of  $^{73}\text{Sr}/^{73}\text{Br}$ , and it may be that charge-symmetry-breaking forces need to be incorporated into the nuclear Hamiltonian to fully describe the presented results.

In this Article we report the breakdown of mirror symmetry between the ground states of the particle-bound nuclei  $^{73}\text{Sr}$  and  $^{73}\text{Br}$ , which appear to have  $J^\pi = 5/2^-$  and  $J^\pi = 1/2^-$ , respectively. This difference probably comes about from an inversion of states, which in  $^{73}\text{Br}$  are only 27 keV apart. However, the consequences are appreciable because the  $\beta$  decay is strongly modified. This inversion could be due to small changes in the two competing shapes, particularly their degree of triaxiality, and the coupling to the proton continuum in the IAS of  $^{73}\text{Rb}$ . In fact, in the exotic region of the chart of nuclides near  $^{73}\text{Sr}$ , where the limits of existence for proton-rich nuclei intersect with the  $N = Z$  line, there may be many more instances of mirror-symmetry breaking.

To confirm the findings presented here, the ground-state spin of  $^{73}\text{Sr}$  should be directly measured through  $\beta$ -NMR or similar methods. A direct measurement of the mass of  $^{73}\text{Sr}$  would also be informative in determining the degree to which isobaric-spin symmetry is broken. With existing facilities it will be difficult to make such direct determinations, because the yield of  $^{73}\text{Sr}$  atoms is low; however, as new facilities come on line, studying such exotic nuclei should become possible, enabling continued investigations and a deeper understanding of the cracked isobaric-spin mirror.

## Online content

Any methods, additional references, Nature Research reporting summaries, source data, extended data, supplementary information, acknowledgements, peer review information; details of author contributions and competing interests; and statements of data and code availability are available at <https://doi.org/10.1038/s41586-020-2123-1>.

- Noether, E. Invariantenprobleme. *Nachr. Ges. Wiss. Göttingen Math.-Phys. Kl.* **1918**, 235–257 (1918).
- Elliott, J. & Dawber, P. *Symmetry in Physics: Principles and Simple Applications* (Oxford Univ. Press, 1984).
- Dirac, P. A. M. The quantum theory of the electron. *Proc. R. Soc. Lond. A* **117**, 610–624 (1928).
- Heisenberg, W. On the structure of atomic nuclei. *Z. Phys.* **77**, 1–11 (1932).
- Wigner, E. On the consequences of the symmetry of the nuclear Hamiltonian on the spectroscopy of nuclei. *Phys. Rev.* **51**, 106–119 (1937).
- Wilkinson, D. H. *Isospin in Nuclear Physics* (North Holland Pub. Co., 1970).
- Warner, D., Bentley, M. & Van Isacker, P. The role of isospin symmetry in collective nuclear structure. *Nat. Phys.* **2**, 311–318 (2006).
- Schatz, H. et al. rp-process nucleosynthesis at extreme temperature and density conditions. *Phys. Rep.* **294**, 167–263 (1998).
- Grindlay, J. et al. Discovery of intense X-ray bursts from the globular cluster NGC 6624. *Astrophys. J.* **205**, L127–L130 (1976).
- Woosley, S. E. & Taam, R. E.  $\gamma$ -ray bursts from thermonuclear explosions on neutron stars. *Nature* **263**, 101–103 (1976).
- Suzuki, H. et al. Discovery of  $^{72}\text{Rb}$ : a nuclear sandbank beyond the proton drip line. *Phys. Rev. Lett.* **119**, 192503 (2017).
- Rogers, A. M. et al.  $^{69}\text{Kr}$   $\beta$ -delayed proton emission: a Trojan horse for studying states in proton-unbound  $^{69}\text{Br}$ . *Phys. Rev. C* **84**, 051306 (2011).
- Del Santo, M. et al.  $\beta$ -delayed proton emission of  $^{68}\text{Kr}$  and the  $^{68}\text{Se}$  rp-process waiting point. *Phys. Lett. B* **738**, 453–456 (2014).
- Schmidt, K. H. A new test for random events of an exponential distribution. *Eur. Phys. J. A* **8**, 141–145 (2000).
- Batchelder, J. C. et al. Beta-delayed proton decay of  $^{73}\text{Sr}$ . *Phys. Rev. C* **48**, 2593–2597 (1993).
- Wang, M. et al. The AME2016 atomic mass evaluation: (II). Tables, graphs and references. *Chinese Phys. C* **41**, 030003 (2017).
- Singh, B., Rodriguez, J., Wong, S. & Tuli, J. Review of  $\log ft$  values in  $\beta$  decay. *Nucl. Data Sheets* **84**, 487–563 (1998).
- Hagberg, E. et al. Tests of isospin mixing corrections in superallowed  $0^+ \rightarrow 0^+$   $\beta$  decays. *Phys. Rev. Lett.* **73**, 396–399 (1994).
- Konieczka, M., Baczyk, P. & Satula, W.  $\beta$ -decay study within multireference density functional theory and beyond. *Phys. Rev. C* **93**, 042501 (2016).
- Baczyk, P. et al. Isospin-symmetry breaking in masses of  $N \simeq Z$  nuclei. *Phys. Lett. B* **778**, 178–183 (2018).
- Michel, N., Nazarewicz, W., Płoszajczak, M. & Vertse, T. Shell model in the complex energy plane. *J. Phys. G* **36**, 013101 (2009).
- Murray, G., White, W., Willmott, J. & Entwistle, R. The decay of  $^{73}\text{Br}$ . *Nucl. Phys. A* **142**, 21–34 (1970).
- Wörmann, B. et al. Rotational bands in  $^{73}\text{Br}$ : the disappearance of shape coexistence in  $^{73}\text{Se}$ . *Z. Phys. A* **322**, 171–172 (1985).
- Heese, J. et al. Spectroscopy of high spin states in  $^{73}\text{Br}$ . *Phys. Rev. C* **36**, 2409–2421 (1987).
- Heese, J. et al. Conversion electron and yrast state measurements in  $^{73}\text{Br}$ . *Phys. Rev. C* **41**, 1553–1561 (1990).
- Griffiths, A. G. et al. Magnetic moments and shape coexistence in the light Br isotopes. *Phys. Rev. C* **46**, 2228–2240 (1992).
- Wang, S. M., Michel, N., Nazarewicz, W. & Xu, F. R. Structure and decays of nuclear three-body systems: the Gamow coupled-channel method in Jacobi coordinates. *Phys. Rev. C* **96**, 044307 (2017).
- Wang, S. M. & Nazarewicz, W. Puzzling two-proton decay of  $^{67}\text{Kr}$ . *Phys. Rev. Lett.* **120**, 212502 (2018).
- Berggren, T. On the use of resonant states in eigenfunction expansions of scattering and reaction amplitudes. *Nucl. Phys. A* **109**, 265–287 (1968).
- Bouchez, E. et al. New shape isomer in the self-conjugate nucleus  $^{72}\text{Kr}$ . *Phys. Rev. Lett.* **90**, 082502 (2003).
- Gade, A. et al. Quadrupole deformation of the self-conjugate nucleus  $^{72}\text{Kr}$ . *Phys. Rev. Lett.* **95**, 022502 (2005).
- Iwasaki, H. et al. Evolution of collectivity in  $^{72}\text{Kr}$ : evidence for rapid shape transition. *Phys. Rev. Lett.* **112**, 142502 (2014).
- Rykaczewski, K. et al. Proton emitters  $^{140}\text{Ho}$  and  $^{141}\text{Ho}$ : probing the structure of unbound Nilsson orbitals. *Phys. Rev. C* **60**, 011301 (1999).
- Sonzogni, A. A. et al. Fine structure in the decay of the highly deformed proton emitter  $^{131}\text{Eu}$ . *Phys. Rev. Lett.* **83**, 1116–1118 (1999).
- Kruppa, A. T., Barmore, B., Nazarewicz, W. & Vertse, T. Fine structure in the decay of deformed proton emitters: nonadiabatic approach. *Phys. Rev. Lett.* **84**, 4549–4552 (2000).
- Karny, M. et al. Shell structure beyond the proton drip line studied via proton emission from deformed  $^{141}\text{Ho}$ . *Phys. Lett. B* **664**, 52–56 (2008).
- Miller, G. A., Opper, A. K. & Stephenson, E. J. Charge symmetry breaking and QCD. *Annu. Rev. Nucl. Part. Sci.* **56**, 253–292 (2006).
- Borsanyi, S. et al. Ab initio calculation of the neutron–proton mass difference. *Science* **347**, 1452–1455 (2015).
- Alvarez, L. W. & Bloch, F. A quantitative determination of the neutron moment in absolute nuclear magnetons. *Phys. Rev.* **57**, 111–122 (1940).
- Wiringa, R. B., Stoks, V. G. J. & Schiavilla, R. Accurate nucleon–nucleon potential with charge-independence breaking. *Phys. Rev. C* **51**, 38–51 (1995).
- Thomas, R. G. On the determination of reduced widths from the one-level dispersion formula. *Phys. Rev.* **81**, 148–149 (1951).
- Ehrman, J. B. On the displacement of corresponding energy levels of  $^{13}\text{C}$  and  $^{13}\text{N}$ . *Phys. Rev.* **81**, 412–416 (1951).
- Thomas, R. G. An analysis of the energy levels of the mirror nuclei,  $^{13}\text{C}$  and  $^{13}\text{N}$ . *Phys. Rev.* **88**, 1109–1125 (1952).

**Publisher's note** Springer Nature remains neutral with regard to jurisdictional claims in published maps and institutional affiliations.

© The Author(s), under exclusive licence to Springer Nature Limited 2020



### Experimental method

The experiment used a primary  $^{92}\text{Mo}$  beam at an energy of 140 MeV per nucleon, undergoing projectile fragmentation on a  $152.2\text{ mg cm}^{-2}$  beryllium target. Fragmentation products were then passed through the A1900 fragment separator, selecting for  $^{73}\text{Sr}$  (ref. <sup>44</sup>). The secondary  $^{73}\text{Sr}$  beam was further purified by a factor of 4,500 after passing through the Radio Frequency Fragment Separator (RFFS)<sup>45</sup>. The remaining transmitted ions were then sent through a telescope stack<sup>46</sup> consisting of a  $1,041\text{-}\mu\text{m}$  silicon p-i-n detector, a variable-thickness aluminium degrader, a  $989\text{-}\mu\text{m}$  silicon p-i-n detector, a  $520\text{-}\mu\text{m}$  double-sided silicon strip detector (DSSSD) used for implantation, and another  $996\text{-}\mu\text{m}$  single-sided silicon strip detector followed by a plastic scintillator that was used for vetoing ions that were not implanted. The DSSSD was segmented with 40 front and 40 back strips, and the SSSD had 16 strips. The stack was surrounded by a high-purity germanium array—the Segmented Germanium Array (SeGA)—that was used to measure  $\gamma$ -rays<sup>47</sup>.

Nuclei of interest were implanted into the DSSSD detector, allowing for spatial and temporal correlations of implantation and decay events. These heavy ions were identified event-by-event using the measured energy loss in the  $1,041\text{-}\mu\text{m}$  silicon detector at the front of the stack, and the time of flight between the second silicon detector in the stack and a scintillator located at the exit of the focal plane of the A1900. The resulting particle identification spectrum for the region of interest is shown in Fig. 1. Ion identification was confirmed by the observation of known  $\gamma$ -rays in the region of interest.

All of the detector signals were collected using a digital data-acquisition system<sup>48</sup> that used XIA Pixie-16 digitizers, which provided waveforms of the signals as well as timing and pulse-height data. The digitizers had 250-MHz ADCs and 100-MHz clocks that gave 10-ns timestamps. For the presented offline analysis, a  $5\text{-}\mu\text{s}$  gate was used to determine prompt coincidences. The beam rate was about  $6.5(1.3)$  particles per second.

Because the energies associated with the implantation and decay event are several orders of magnitude different (GeV and MeV, respectively), the DSSSD detector was connected to dual-gain preamplifiers. The low-gain setting was used for implantation events and the high-gain setting for decay events. The DSSSD high-gain channels were energy calibrated with  $^{228}\text{Th}$  and  $^{148}\text{Gd}$  sources. SeGA was energy calibrated with a mixed source of well known activity (primarily containing  $^{154}\text{Eu}$ ), that was also used for determining an absolute efficiency curve.

### Experimental analysis

After an ion was tagged by energy-loss and time-of-flight measurements, the ion-implantation event was localized within a pixel defined by the perpendicular front and back strips of the DSSSD with the largest charge deposition. Decay events were searched for within a 5-s correlation window, and only events that were within two neighbouring pixels (for a total of 24 surrounding pixels) of the implantation event were considered. All decay events were rejected if another implantation event occurred within 10 half-lives of the ion of interest,  $^{73}\text{Sr}$ .

### Logarithmic-bin method

The half-life was determined using the logarithmic-bin method, in which the ratio of the bin size to the correlation time ( $\Delta t/t$ ) is constant, which is better suited for low-statistics analysis<sup>14</sup>. The resulting plot is shown in Extended Data Fig. 1, and the maximum logarithmic likelihood fit is given by the solid red curve. Because of the nature of this method, instead of correlating all events within a given time window after the implantation—as was done for analysing the decay energy—only the first event after implantation was considered. Furthermore, the peak position of the probability distribution is directly related to the half-life of the species. Therefore, if other species are present then they will be well separated. Thus in the fit to the peak shown in Extended Data Fig. 1 the events

above  $3 \times 10^8$  ns were not considered. The resulting fit of this distribution ( $\chi^2_{\text{red}} = 1.3$ ) provided a better limit on the half-life of  $^{73}\text{Sr}$ , and so this is the half-life reported and used for the exponential in Fig. 2a. The half-life obtained from directly fitting the data in Fig. 2a is  $t_{1/2} = 23.5 \pm 1.8$  ms.

It should also be noted that the observation of only one species, deduced from Extended Data Fig. 1, suggests that we are only considering ground-state decays of  $^{73}\text{Sr}$ . In the fragmentation process we do expect the population of excited states in the nucleus, and thus a potential low-lying  $J^\pi = 1/2^-$  state may be populated. Such states will predominantly decay by internal conversion (ejecting an orbital electron) and thus be enhanced. Since the ions are fully stripped while in flight, decays via internal conversion will be completely suppressed. However, once the ion is implanted it will recombine with electrons from the detector medium, opening up this decay path. The half-lives for such low-lying excited states—in particular E2 transitions separated by  $\sim 10$  keV—will be  $\sim 1\text{--}100\text{ }\mu\text{s}$ , considering the conversion coefficients for strontium<sup>49</sup> and the Weisskopf estimates of the  $\gamma$ -decay half-lives<sup>50</sup>. These estimates are also consistent with systematic trends in the region<sup>51</sup>. With a deadtime after implantation of  $\sim 5\text{ }\mu\text{s}$  for our measurements, the population of such states will mostly decay to the ground state of  $^{73}\text{Sr}$  before the implantation detector will become sensitive. In any case, if a separate species were present with a half-life greater than our deadtime then it would be observed in Extended Data Fig. 1.

### $\beta$ -summing correction

GEANT4 simulations of the detector configuration, coupled with LISE++ simulations of the implantation depth distribution, suggest that a  $\beta$ -summing correction of  $110 \pm 15$  keV needs to be applied to extract the proton energies<sup>52</sup>. This gives a value of  $Q_{p,\text{measured}} = 3.82$  MeV, where  $Q_{p,\text{measured}}$  is the total measured energy released in the decay, which is split between the proton and the remaining nucleus. However, we also need to include the effect of pulse-height defects in measuring the energy of the recoil nucleus<sup>53</sup>, using  $Q_p = Q_{p,\text{measured}} + (1 - K)Q_p/M$ , where  $K$  is the detection efficiency of the recoil ( $\sim 30\%$  for our case) and  $M$  is the total mass of the decaying system ( $M = 73$  AMU in our case). Applying this correction gives the true value,  $Q_p = 3.85$  MeV. To obtain the value of the emitted protons in the laboratory frame, we also need to account for the recoil energy of the resulting  $^{72}\text{Kr}$ . Thus, the reported energy of the proton is  $E_p = [(M - 1)/M]Q_p$ .

### Fitting the decay-energy spectrum

The background of the decay-energy spectrum—the shaded blue overlay in Fig. 2b—was determined by analysing decay events in the 5-s correlation window that occurred 1 s after implantation. After background subtraction, a  $\chi^2$  minimization of the fit to the decay-energy spectrum was constrained by fitting the largest peak with a Landau distribution (generated by the  $\beta^+$  particle) convoluted with a Gaussian distribution (generated by the proton) of the measured intrinsic detector resolution ( $\sigma = 45$  keV). These shape parameters for the distribution were then fixed, and a second peak with the same shape parameters was added. The energy of the second peak was fixed to be 709 keV lower than original peak. The two peak heights, as well as the energy of the original peak, were then allowed to vary.

From the spectrum shown in Fig. 2b, we do not see a notable number of events above background that are below 1 MeV. Owing to the thickness of our detector and the large value of  $Q_{\beta^+}$  (the total energy released in the  $\beta^+$  decay), we do not expect many, if any,  $\beta^+$  particles to deposit more than 1 MeV into a single (or several) strip(s) of our detector especially when considering the results of our simulation. As such, our data indicate that virtually all  $\beta$ -decay events of  $^{73}\text{Sr}$  are followed by the emission of a proton from  $^{73}\text{Rb}$ .

### Gamow coupled-channel analysis

For this work, the rotational band of the core ( $^{72}\text{Kr}$ ) with  $J \leq J_{\text{core}}^{\text{max}} = 8^+$  is included, of which the core rotational energies were taken from

experiment<sup>54</sup>. The effective core–valence potential has been taken to be a deformed Woods–Saxon form including the spherical spin–orbit term with the ‘universal’ parameter set, which has been successfully applied to nuclei from the  $A \approx 80$  region<sup>55,56</sup>. The Coulomb core–proton potential is calculated assuming that the core charge  $Z_{\text{core}}e$  ( $e$ , unit of electron charge) is uniformly distributed inside the deformed nuclear surface. Since the decay width is very sensitive to the separation energy, in order to have a better description of the decay width, the Woods–Saxon depth  $V_0$  is readjusted to fit the experimental decay energy  $Q_p = 3.85$  MeV. The predicted spectra of  $^{73}\text{Sr}$  and  $^{73}\text{Br}$  using this decay energy and the ‘universal’ parameter set is shown in Extended Data Table 2.

The calculations were carried out in the model space defined by  $\max(\ell) \leq 20$ , where  $\ell$  is the orbital angular momentum between the proton and core. The Berggren basis was used for all channels, and the complex-momentum contour of the Berggren basis is defined by the path  $k = 0 \rightarrow 0.4 \rightarrow 0.2i \rightarrow 0.6 \rightarrow 2 \rightarrow 4 \rightarrow 8 \text{ fm}^{-1}$ , with each segment discretized by 30 points (scattering states).

### Pauli blocking

The supersymmetric transformation method<sup>28,57,58</sup> is a projection technique that can prevent the valence proton from being emitted through already filled orbitals by adding a repulsive core near the origin. For simplicity, spherical orbitals that correspond to the deformed levels occupied in the daughter nucleus are projected out. Hence, to estimate the uncertainty, another calculation was done with the removal of Pauli blocking, which causes the GCC calculations to reduce to solving the coupled-channel Schrödinger equation using nonadiabatic coupling<sup>35</sup>.

To estimate the uncertainty of this projection technique, additional calculations were performed with the removal of Pauli blocking. As a result, the branching to  $^{72}\text{Kr}^*(2^+)$  for the oblate  $J^\pi = 5/2^-$  solution was decreased to 15%, because the  $p_{1/2}$  configuration was considerably reduced (down to 0.02%). However, the presence of a very small  $\ell = 1$  component still allows for a large degree of branching. Therefore, both cases indicate that  $^{73}\text{Rb}^*(\text{IAS})$  has spin and parity  $J^\pi = 5/2^-$ , and thus that  $^{73}\text{Sr}$  has a  $J^\pi = 5/2^-$  ground state, suggesting that the ground and first excited states of  $^{73}\text{Br}$  are inverted relative to its mirror  $^{73}\text{Sr}$ .

### Data availability

Raw data were generated at the National Superconducting Cyclotron Laboratory large-scale facility. All of the relevant data that support the findings of this study are available from the corresponding authors upon reasonable request.

44. Morrissey, D., Sherrill, B., Steiner, M., Stolz, A. & Wiedenhoever, I. Commissioning the A1900 projectile fragment separator. *Nucl. Instrum. Methods Phys. Res. B* **204**, 90–96 (2003).

45. Bazin, D. et al. Radio Frequency Fragment Separator at NSCL. *Nucl. Instrum. Methods Phys. Res. A* **606**, 314–319 (2009).
46. Prisciandaro, J., Morton, A. & Mantica, P. Beta counting system for fast fragmentation beams. *Nucl. Instrum. Methods Phys. Res. A* **505**, 140–143 (2003).
47. Mueller, W. et al. Thirty-two-fold segmented germanium detectors to identify  $\gamma$ -rays from intermediate-energy exotic beams. *Nucl. Instrum. Methods Phys. Res. A* **466**, 492–498 (2001).
48. Prokop, C. et al. Digital data acquisition system implementation at the National Superconducting Cyclotron Laboratory. *Nucl. Instrum. Methods Phys. Res. A* **741**, 163–168 (2014).
49. Kibédi, T., Burrows, T. W., Trzhaskovskaya, M. B., Davidson, P. M. & Nestor, C. W. Jr. Evaluation of theoretical conversion coefficients using Brcc. *Nucl. Instrum. Methods Phys. Res. A* **589**, 202–229 (2008).
50. Condon, E. U. & Odishaw, H. *Handbook of Physics* (McGraw-Hill, 1958).
51. Hagberg, E. et al. The decay of a new nuclide:  $^{73}\text{B}$ . *Nucl. Phys. A* **383**, 109–118 (1982).
52. Meisel, Z. et al.  $\beta$ -particle energy-summing correction for  $\beta$ -delayed proton emission measurements. *Nucl. Instrum. Methods Phys. Res. A* **844**, 45–52 (2017).
53. Huang, W. J. & Audi, G. Corrections of alpha- and proton-decay energies in implantation experiments. *EPJ Web Conf.* **146**, 10007 (2017).
54. International Network of Nuclear Structure and Decay Data Evaluators. Evaluated nuclear structure data file (ENSDF) *National Nuclear Data Center* (Brookhaven National Laboratory, 2020); <https://www.nndc.bnl.gov/ensdf/>.
55. Cwiok, S., Nazarewicz, W., Dudek, J., Skalski, J. & Werner, T. Single-particle energies, wave functions, quadrupole moments and g-factors in an axially deformed Woods–Saxon potential with applications to the two-centre-type nuclear problems. *Comput. Phys. Commun.* **46**, 379–399 (1987).
56. Nazarewicz, W., Dudek, J., Bengtsson, R., Bengtsson, T. & Ragnarsson, I. Microscopic study of the high-spin behaviour in selected  $A \approx 80$  nuclei. *Nucl. Phys. A* **435**, 397–447 (1985).
57. Thompson, I. J. et al. Pauli blocking in three-body models of halo nuclei. *Phys. Rev. C* **61**, 024318 (2000).
58. Thompson, I. J., Nunes, F. M. & Danilin, B. V. FaCE: a tool for three body Faddeev calculations with core excitation. *Comput. Phys. Commun.* **161**, 87–107 (2004); erratum **170**, 296–297 (2005).

**Acknowledgements** We would like to thank T. Ginter for his effort in providing the  $^{73}\text{Sr}$  beam used in the experiment. We acknowledge support from the US DOE, Office of Science, Office of Nuclear Physics under award numbers DE-FG02-94ER40848 (UML), DE-AC02-06CH11357 (ANL), DE-SC0013365 and DE-SC0018083 (FRIB), as well as DE-FG02-88ER40387 and DE-SC0019042 (OU); the NNSA through award numbers DE-NA0003180 (NSSC), DE-NA0000979 (NSSC), DE-NA0003221, DE-NA0003909 and/or DE-NA0002132; and the NSF under contract numbers PHY-1-102511 and PHY 14-30152.

**Author contributions** D.E.M.H. performed the offline analysis and prepared the figures as well as the writing for the manuscript. A.M.R. was the principle investigator of the  $^{73}\text{Sr}$  experiment, was responsible for preparing and executing the measurement with C.M., and aided in writing and preparing the manuscript. S.M.W. performed the GCC calculations, prepared tables and prepared the text for these aspects of the manuscript. C.J.L. and W.N. aided in writing and preparing the manuscript. C.M. led the experimental preparations and oversaw conducting the measurement. S.N.L. assisted in the design, setup, and execution of the experiment. P.C.B., K.B., K.C., J.A.C., A.C.D., E.R.D., S.J., R.L., Z.M., H.S., K.S., D.S. and S.K.S. assisted in setting up the experiment and/or checked the data accumulation online and maintained operation of the experiment. S.W. aided in the offline analysis.

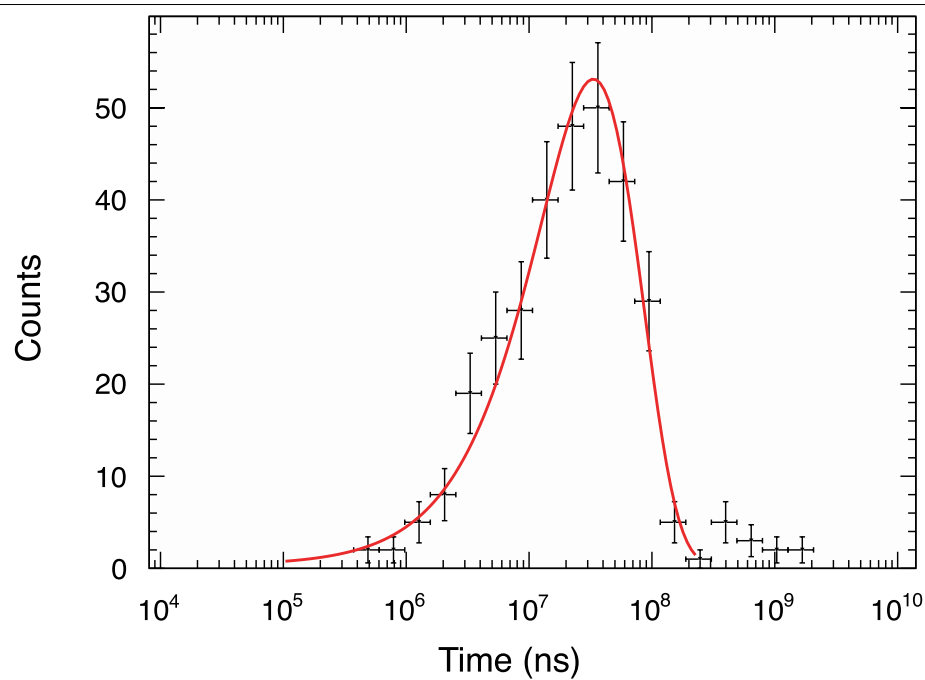
**Competing interests** The authors declare no competing interests.

### Additional information

**Correspondence and requests for materials** should be addressed to D.E.M.H. or A.M.R.

**Peer review information** *Nature* thanks Bertram Blank and the other, anonymous, reviewer(s) for their contribution to the peer review of this work.

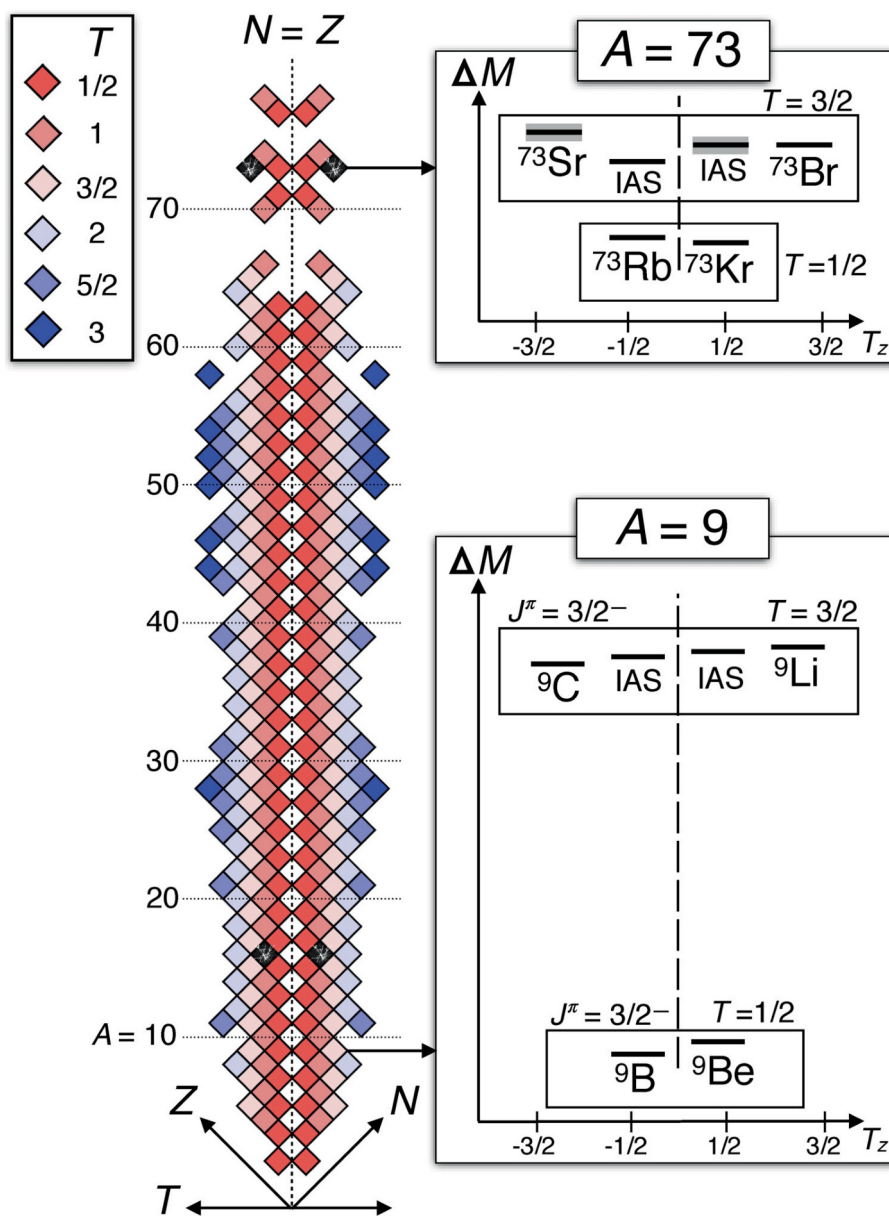
**Reprints and permissions information** is available at <http://www.nature.com/reprints>.



**Extended Data Fig. 1 | Time between implantation of  $^{73}\text{Sr}$  and first decay event with logarithmic bins.** The first decay events found after implantation are plotted with logarithmic bins. The resulting maximum logarithmic

likelihood fit to the data is shown as the solid red curve. The horizontal error bars correspond to the bin size, and the vertical error bars correspond to one standard deviation from counting.





**Extended Data Fig. 2 | The mirror chart of nuclides.** Mirror nuclei are plotted according to the isobaric spin ( $T$ ) of their ground-state configurations. For almost the entire mirror chart, the spin and parity,  $J^\pi$ , of the ground states are identically reflected across the  $N=Z$  line<sup>54</sup>. The black squares with cracks show the only two places on the mirror chart where this ground-state mirror symmetry is known or believed to be broken. Once adjusting for the energy

shift of levels due to charge-breaking forces, the relative masses ( $\Delta M$ ) of mirror pairs (with the same magnitude  $T_z$ ) become comparable, and the connection to IASs in neighbouring nuclei becomes clearer. This is illustrated by the isobar diagrams comparing the relative masses for two  $T=3/2$  multiplets, one in the  $A=9$  system and the other in the  $A=73$  system of interest.

Extended Data Table 1 | GCC analysis

Transitions	$\Gamma_p$ (keV)*	Branching	Configurations†
$5/2^- \rightarrow$ g.s. band (oblate)	1.8	49.6% $0^+$ 49.5% $2^+$ 1.1% $4^+$	51.4% ( $f_{5/2}, 0^+$ ) 35.0% ( $f_{5/2}, 2^+$ ) 6.2% ( $p_{1/2}, 2^+$ ) 6.3% ( $f_{5/2}, 4^+$ )
$1/2^- \rightarrow$ g.s. band (oblate)	39.8	99.6% $0^+$ 0.4% $2^+$ 0.1% $4^+$	78.8% ( $p_{1/2}, 0^+$ ) 19.8% ( $f_{5/2}, 2^+$ ) 1.0% ( $p_{3/2}, 2^+$ ) 0.4% ( $h_{9/2}, 4^+$ )
$5/2^- \rightarrow$ g.s. band (prolate)	7.3	8.2% $0^+$ 90.5% $2^+$ 1.2% $4^+$	23.1% ( $f_{5/2}, 0^+$ ) 40.7% ( $p_{1/2}, 2^+$ ) 20.2% ( $f_{5/2}, 2^+$ ) 10.8% ( $f_{5/2}, 4^+$ )
$1/2^- \rightarrow$ g.s. band (prolate)	30.5	98.5% $0^+$ 0.8% $2^+$ 0.6% $4^+$	52.3% ( $p_{1/2}, 0^+$ ) 42.8% ( $f_{5/2}, 2^+$ ) 2.6% ( $p_{3/2}, 2^+$ ) 1.9% ( $h_{9/2}, 4^+$ )

The possibilities for the decay of  $^{73}\text{Rb}^*(\text{IAS})$  via proton emission using two different deformations for the  $^{72}\text{Kr}$  core ( $\beta_2 = -0.34$  and  $\beta_2 = 0.4$  for oblate and prolate, respectively) and spin assignments ( $J^\pi = 1/2^-$  or  $5/2^-$ ).

g.s., ground state;  $\Gamma_p$ , decay width.

\*The decay width is inversely related to the half-life of the transition by the Heisenberg uncertainty principle.

†The configurations adopt the spectroscopic notation for angular momentum.

Extended Data Table 2 | Predicted spectra of <sup>73</sup>Sr and <sup>73</sup>Br

Nuclei	oblate ( $\beta_2 = -0.34$ )			prolate ( $\beta_2 = 0.4$ )		
	1/2 <sup>-</sup>	5/2 <sup>-</sup>	$E_x$ (MeV)	1/2 <sup>-</sup>	5/2 <sup>-</sup>	$E_x$ (MeV)
<sup>73</sup> Sr ( $Q_n$ )	-14.945	-15.430	-0.485	-15.219	-15.019	0.200
<sup>73</sup> Br ( $Q_p$ )	-2.927	-3.402	-0.475	-3.139	-2.946	0.193

The core–nucleon interaction is the Woods–Saxon potential with the ‘universal’ parameter. The depth of the Woods–Saxon potential is fitted to the experimental decay energy  $Q_n$  ( $Q_p$ ) for <sup>73</sup>Sr (<sup>73</sup>Br).  
 $E_x$  is the excitation energy of the  $J^\pi = 5/2^-$  state, that is, the energy difference between the two presented states.



# Spin-cooling of the motion of a trapped diamond

<https://doi.org/10.1038/s41586-020-2133-z>

T. Delord<sup>1,2</sup>, P. Huillery<sup>1,2</sup>, L. Nicolas<sup>1</sup> & G. Hétet<sup>1</sup>✉

Received: 27 March 2019

Accepted: 17 January 2020

Published online: 23 March 2020

 Check for updates

Observing and controlling macroscopic quantum systems has long been a driving force in quantum physics research. In particular, strong coupling between individual quantum systems and mechanical oscillators is being actively studied<sup>1–3</sup>. Whereas both read-out of mechanical motion using coherent control of spin systems<sup>4–9</sup> and single-spin read-out using pristine oscillators have been demonstrated<sup>10,11</sup>, temperature control of the motion of a macroscopic object using long-lived electronic spins has not been reported. Here we observe a spin-dependent torque and spin-cooling of the motion of a trapped microdiamond. Using a combination of microwave and laser excitation enables the spins of nitrogen–vacancy centres to act on the diamond orientation and to cool the diamond libration via a dynamical back-action. Furthermore, by driving the system in the nonlinear regime, we demonstrate bistability and self-sustained coherent oscillations stimulated by spin–mechanical coupling, which offers the prospect of spin-driven generation of non-classical states of motion. Such a levitating diamond—held in position by electric field gradients under vacuum—can operate as a ‘compass’ with controlled dissipation and has potential use in high-precision torque sensing<sup>12–14</sup>, emulation of the spin-boson problem<sup>15</sup> and probing of quantum phase transitions<sup>16</sup>. In the single-spin limit<sup>17</sup> and using ultrapure nanoscale diamonds, it could allow quantum non-demolition read-out of the spin of nitrogen–vacancy centres at ambient conditions, deterministic entanglement between distant individual spins<sup>18</sup> and matter-wave interferometry<sup>16,19,20</sup>.

Since the experiment by Einstein and de Haas in 1915<sup>21</sup>, much work has been carried out on the detection of atomic spins through mechanical motion<sup>22</sup>, culminating in the observation of a magnetic force from single spins<sup>10,11</sup> and magnetometry at the nanoscale<sup>13</sup>. Conversely, single spins and qubits have also been used to sense the motion of objects. Single-qubit thermometry of mechanical oscillators was realized using a superconducting qubit coupled to membranes<sup>4,8</sup> and nitrogen–vacancy (NV) centres coupled to cantilevers<sup>5–7</sup>. A crucial next step is to reach strong coupling between long-lived spins and mechanical oscillators, which will enable ground-state cooling, as in tethered quantum opto-mechanical platforms<sup>23–25</sup>, and the observation of quantum superpositions of macroscopic systems<sup>2</sup>. One further prospect is the entanglement between multiple spins<sup>18</sup>, with far-reaching implications for quantum information science and metrology<sup>26</sup>. Obtaining coupling rates that surpass the decoherence of both the spin and the mechanical system is however still a challenge for most state-of-the-art platforms. Recently, there has been renewed focus on levitating objects<sup>27,28</sup> motivated by the low mass and high *Q*-factors that they offer, together with the possibility of cooling their motion using embedded spins. There is a strong analogy between this platform—where spins move a levitating crystal—and laser-cooled atoms, where electrons move atomic nuclei. It may thus be forecast that a levitating particle

containing a few long-lived spins will ultimately reach a level of control similar to that of trapped ions<sup>3</sup>, with bright prospects for the above-mentioned applications.

In this work, we report a controllable torque induced by the spins of atoms embedded in a microscale object. Specifically, we couple the spin of many NV centres to the orientation of a trapped diamond particle. This coupling then enables us to show mechanical read-out of the spin resonance of the NV centres together with cooling and lasing of the diamond motion.

The crystallographic structure of the NV centres is depicted in Fig. 1A. The spin–spin interaction between the two electrons in the NV-centre ground state lifts the degeneracy of the spin-triplet eigenstates by  $D = 2.87$  GHz at room temperature. Such an interaction implies that the NV centre has a preferential quantization axis that is along one of the four crystal axes  $\langle 111 \rangle$ . In the presence of a magnetic field  $\mathbf{B}$  at an angle  $\phi$  with respect to the NV axis, the energy difference between the two energy eigenstates  $|m'_s = \pm 1\rangle$  is about  $\gamma_e B \phi$ , where  $\gamma_e$  is the gyro-magnetic ratio of the electron. Spin control can then be performed using optical and microwave excitation, and the angular dependence of the NV spin energy eigenstates is expected to allow rotation and cooling of the diamond angular motion. Once in a magnetic state via a resonant microwave excitation, the NV centre will tend to align the

<sup>1</sup>Laboratoire de Physique de l'Ecole Normale Supérieure, ENS, Université PSL, CNRS, Sorbonne Université, Université de Paris, Paris, France. <sup>2</sup>These authors contributed equally: T. Delord, P. Huillery. ✉e-mail: gabriel.hetet@ens.fr

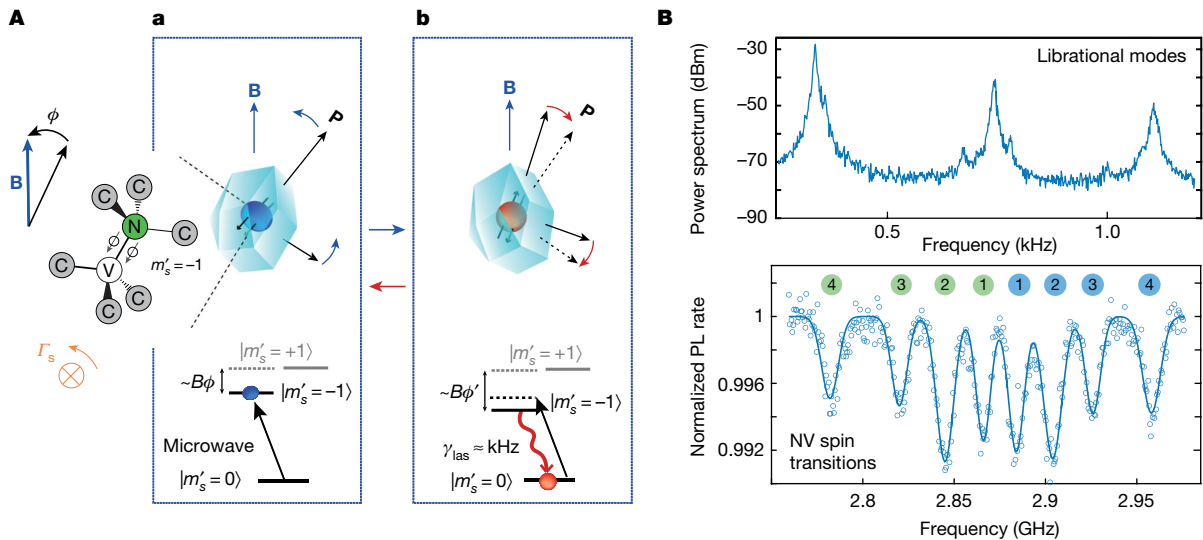


**Fig. 1 | Spin and mechanical systems.** **A**, Sketch of the diamond crystallographic structure hosting NV defects and the effects of rotation. **a**, Equilibrium position of the diamond in the Paul trap before the microwave excitation. The principal diamond axis **P** points towards the main trap axis. The ground state spin levels and microwave drive are depicted below. The magnetic field **B** lifts the degeneracy between the excited spin states by about  $\gamma_e B \phi$ , where  $\phi$  is the angle between the magnetic field and the NV axis. The microwave signal prepares the NV in a magnetic state, which induces a torque on the diamond. Inset: left, definition of  $\phi$ ; right, representation of the NV (N, nitrogen; V, vacancy; C, carbon). **b**, Once at the new angular position, the spin projection onto the magnetic field is changed to  $\gamma_e B \phi'$ . The microwave

frequency is then no longer resonant: the spin relaxes to the ground state and the diamond returns to its initial position. The red wavy arrow represents the polarization at a rate  $\gamma_{\text{las}}$  from the excited state to the ground state induced by the green laser. **B**, Measurements of the three librational modes undergoing Brownian motion at 1 mbar of vacuum pressure (top) and of the typical electron spin resonances from the NV ensemble within a microdiamond outside the trap using standard optically detected magnetic resonance (ODMR) at 30 G (bottom; PL, photoluminescence). The filled circles label the four orientations of the NV spins. Green (blue) circles correspond to the  $m_s = 0$  to  $m_s = -1$  ( $m_s = +1$ ) transitions. Solid lines are a fit to the data.

corresponding diamond crystalline axis to the magnetic field, as illustrated in Fig. 1A, a. Further, laser-triggered relaxation from the excited state can then extract the work exchanged between the spin magnetic energy and the librational motion (see Fig. 1A, b).

In our experiment, harmonic librational (sometimes called torsional, pendular or rotational) confinement is provided both by the Paul trap (Methods) and the particle asymmetry. We measure the libration of the diamond by using the reflection of the laser from the diamond surface. The micrometre-size roughness of our 15- $\mu\text{m}$  particles enables a specular pattern to be detected at the particle image plane, which after mode-matching one of the many bright spots to an optical fibre yields an angular sensitivity of about  $0.3 \text{ mrad Hz}^{-1/2}$  and a resolution of about  $10 \text{ mrad Mcounts s}^{-1}$  (see Methods and Extended Data Fig. 4). Under vacuum conditions ( $\sim 1 \text{ mbar}$ ), the signal power spectrum plotted in Fig. 1B shows harmonic motion of the three librational modes with frequencies  $\omega_\phi/2\pi$  ranging from 200 Hz to 1.2 kHz and with a damping rate of about 15 Hz. Figure 1B also shows an ODMR spectrum for a diamond outside the trap, in the presence of a magnetic field  $B \approx 30 \text{ G}$ . Eight transitions, corresponding to the projections of the **B** field onto the four NV orientations, are observed, with typical spin decoherence rates  $1/T_2^* \approx 7 \text{ MHz}$ .

We now measure the diamond rotation induced by the  $N \approx 10^9$  NV electronic spins inside the diamond, with the same optical read-out as for the librational mode detection, as depicted in Fig. 2A, a. The expected magnitude of the spin torque is  $\Gamma_s = \hbar N \gamma_e B S_z \approx 10^{-19} \text{ N m}$ . Here  $S_z$  is the population in one of the magnetic states, determined by the competition between the microwave and laser polarization (both at rates in the 100 kHz range, see Methods and Extended Data Fig. 5). This torque gives a displacement of the particle angle in the trap,  $\delta\phi = \Gamma_s / I \omega_\phi^2 \approx 10 \text{ mrad}$ , where  $I \approx 10^{-22} \text{ kg m}^2$  is the particle moment of inertia. As can be seen in Fig. 2A, b, sweeping a microwave frequency around the spin resonances indeed enables conspicuous features to appear. Once in the magnetic state  $|m'_s = -1\rangle$  or  $|m'_s = +1\rangle$ , the NV centres tend to align or anti-align the diamond orientation to the magnetic field, which is manifest in the anti-correlation between the detected

intensity levels for all pairs of transitions. A standard ODMR also measured under the same magnetic field amplitude and measurement time (see Fig. 2A, c) demonstrates perfect correlation of the frequencies of the peaks in the two measurements.

This spin-mechanical effect is in fact much richer than a static spin-dependent torque. As shown in Fig. 1A, the NV centres are magnetized through a microwave tone whose detuning from the NV resonances changes as the diamond rotates. To first order, such a torque will increase (decrease) the confinement of the Paul trap if the microwave frequency is blue (red) detuned from the spin resonance at the equilibrium angular position. Further, since the spin lifetime is of the order of the libration period a delay between the NV magnetization and the angular oscillation, observed in ref. <sup>29</sup>, can indeed induce a torque that depends on the velocity, in close analogy with opto-mechanical schemes<sup>23–25</sup> and with Sisyphus cooling of cold atoms. The net result is a pronounced cooling (heating) of the diamond motion when the microwave is red (blue) detuned from the spin resonance as sketched in Fig. 2B. In order to observe such spin-spring and spin-cooling effects, we monitor the librational power spectrum as a function of the microwave detuning from the electronic spin resonance. Figure 2B also shows the result of measurements taken for three different microwave frequencies. A strongly modified spring and damping of the mechanical mode are observed. Assuming that the initial temperature is 300 K (see Methods), the resulting temperature after spin-cooling is here 80 K. Figure 2C shows measurements of the damping rate and spring effects as a function of microwave frequency in good agreement with a theoretical model (see Methods and Extended Data Fig. 1). Cooling is ultimately limited by heating from the microwave excitation of the motion on the blue side. This could be eliminated by increasing the trapping frequency  $\omega_\phi/2\pi$  above the NV spin-transition linewidth.

We now make a step into a regime where the spin-mechanical interaction induces nonlinear effects on the librational mode. With a stronger spin torque (see Methods), Fig. 3A, a displays the expected bistable behaviour for the angular degree of freedom when the microwave

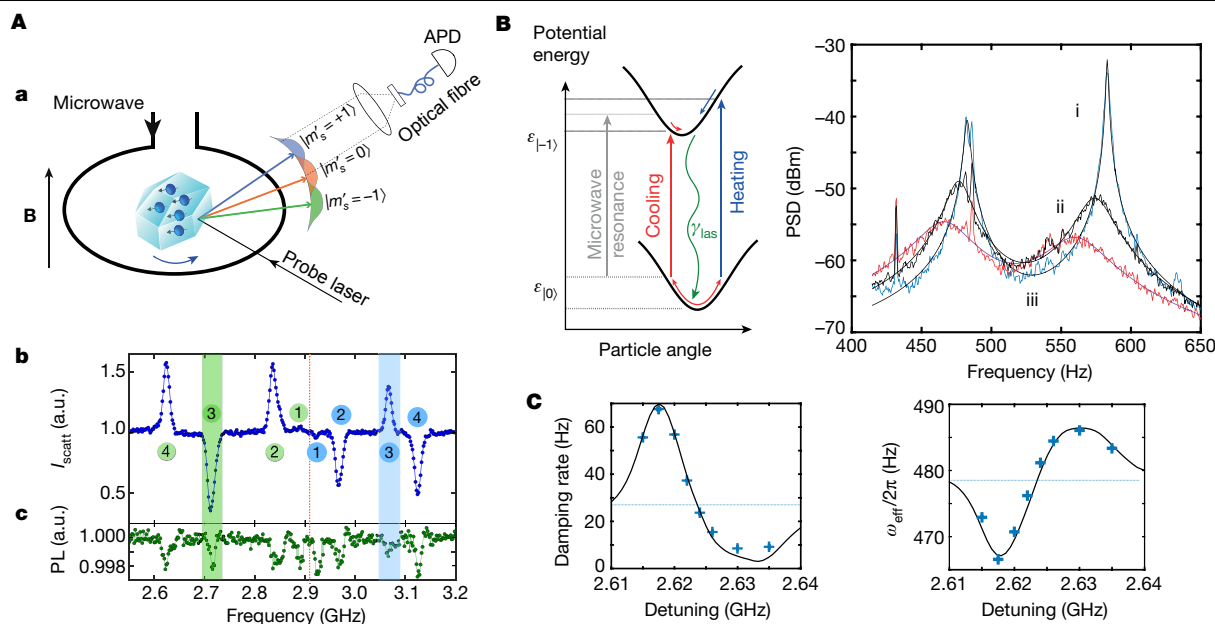


**Fig. 2 | Spin-dependent torque and cooling of a levitating diamond.**

**A**, Rotation of a diamond particle when NV centres are in a magnetic state. **a**, Sketch of the laser beam deflection induced by the NV spin torque. **APD**, avalanche photodiode. **b**, Detected APD count-rate  $I_{\text{scatt}}$  as a function of the microwave frequency. The green (blue) filled circles correspond to the  $m_s = 0$  to  $m_s = -1$  ( $m_s = +1$ ) transitions, while the green (blue) bars highlight the NV orientations that rotate the diamond as per sketch **a**. **c**, Corresponding ODMR. a.u., arbitrary units. **B**, Left, cooling/heating cycle of the librational motion induced by the spin-mechanical coupling. Right, power spectrum of the

detected light intensity reflected from the diamond surface when the microwave frequency is tuned to the blue (trace i), to the centre (trace ii), and to the red (trace iii) of the spin resonance. The alignment of the reflected light from the diamond surface in the fibre was optimized to only let these two librational modes appear in the power spectrum. Note that the particle is here different from the one used in Fig. 1B. PSD, power spectral density. **C**, Effective damping rates (left) and librational mode frequencies  $\omega_{\text{eff}}/2\pi$  (right) as a function of the microwave detuning. Lines show a fit to the experimental data using numerical simulations.

frequency is scanned across the spin resonance. The angle can be found at two metastable positions A or B depending on the history of the angular trajectory (see Supplementary Information). The hysteresis behaviour is indeed observed in the experiment, and shown in Fig. 3A, b.

The evolution of the particle orientation over time at a fixed microwave tone is also plotted in Fig. 3A, c. We note that the particle orientation jumps from site A to B in a seemingly unpredictable manner owing to random kicks given to the particle. The average population at the

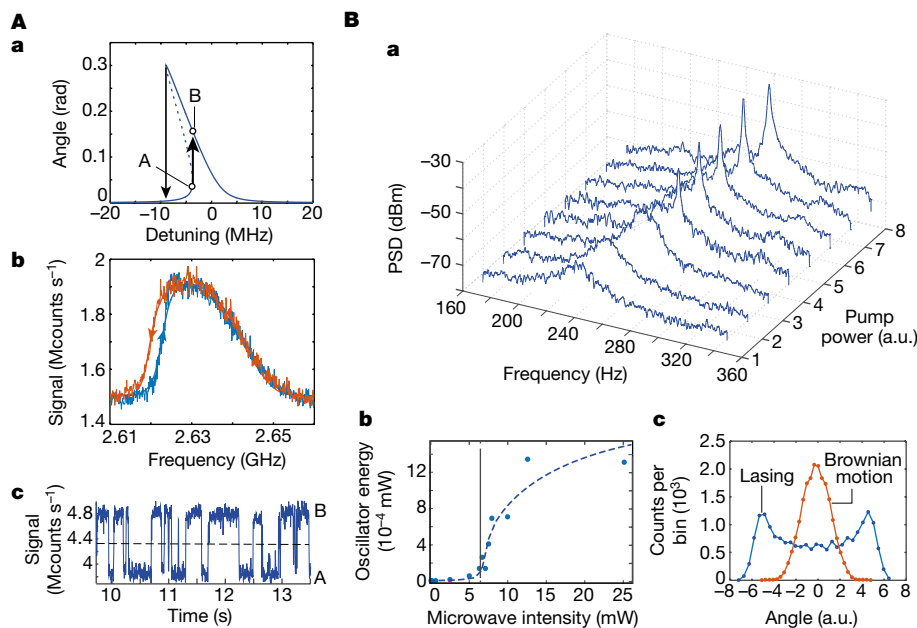


**Fig. 3 | Nonlinear spin-motion dynamics.** **A**, Bistability. **a**, Evolution of the particle angle as a function of the microwave detuning (see below for points A and B). **b**, Hysteresis behaviour of the particle orientation when the microwave signal is scanned from the red to the blue (blue curve) or from the blue to the red (red curve), as indicated by the arrows. **c**, Particle orientation as a function of time for a fixed microwave frequency tuned to the hysteretic frequencies

(2.625 GHz), showing angular jumps between two stable sites A and B. **B**, Phonon lasing. **a**, Evolution towards lasing of the power spectrum of the librational motion as a function of the microwave power. **b**, Oscillator energy as a function of microwave intensity using microwave powers ranging from -44 dBm to -16 dBm in steps of 4 dBm. The dashed line is a fit to the data. **c**, Histogram of the Brownian and lasing angular motions.



angular position B can also be studied as a function of microwave detuning, and was shown to increase as the microwave frequency is tuned towards the blue side of the spin resonance (see Extended Data Fig. 6 and Supplementary Information).

We now set the microwave frequency to the blue side of the spin resonance in this strong spin-torque regime. Figure 3B, a shows the power spectral density as a function of the microwave pump power, where a transition from Brownian motion to a self-sustained oscillation is observed (see also Extended Data Fig. 3). Such a lasing-like action of a mechanical oscillator was observed in the first radiation pressure cooling experiments<sup>6</sup> with proposed applications in metrology. The spin-mechanical gain that enables such lasing action here is provided by blue-detuned microwave excitation, which amplifies the angular motion up to a point where losses are compensated by the magnetic gain (see Extended Data Fig. 2 for numerical results). The oscillator energy as a function of the microwave power is shown in Fig. 3B, b. A lasing threshold is observed at 6 mW of microwave excitation. Another signature of mechanical lasing is shown in Fig. 3B, c, which displays the probability distribution of the angular degree of freedom with and without microwaves. Under blue detuned microwave excitation, the probability distribution departs from the Gaussian process (red curve) for Brownian motion, and turns into the characteristic probability distribution of a coherent oscillation (blue curve). This effect shows that the librational mode can operate stably, deep in the nonlinear regime, and highlights further the analogy between the present spin-mechanical platform and opto-mechanical systems.

Coupling individual spins to the motion of a macroscopic oscillator will have far-reaching applications in fundamental science, quantum information and metrology. The present spin-dependent torque itself may be used for detecting atomic defects with electron spins that cannot be efficiently detected through ODMR. Further, the approach may also be applied to other torsional nano-mechanical platforms<sup>30</sup>, which can exploit the long NV spin–lattice relaxation at low temperatures for longer interrogation times and efficient cooling. Last, operation in the resolved sideband regime where  $\omega_p/2\pi \gg 1/T_2^*$  could be realized after modest improvements to the present set-up. We estimate that using a 1- $\mu\text{m}$ -diameter pure diamond grown by chemical vapour deposition (CVD) attached to a 1- $\mu\text{m}$ -diameter ferromagnet would enable the resolved sideband regime to be entered for this hybrid structure. Librational frequencies  $\omega_p/2\pi$  above 200 kHz have indeed been observed recently<sup>29</sup> and NV centres with  $1/T_2^* = 50$  kHz electron-spin decoherence rates can readily be obtained in CVD-grown microdiamonds enriched in  $^{12}\text{C}$ . Entering this regime would offer the immediate prospects of ground-state cooling the diamond libration and multipartite spin entanglement, and would provide strong impetus to bridge the gap between trapped particles and trapped atoms.

## Online content

Any methods, additional references, Nature Research reporting summaries, source data, extended data, supplementary information, acknowledgements, peer review information; details of author contributions and competing interests; and statements of data and code availability are available at <https://doi.org/10.1038/s41586-020-2133-z>.

1. Treutlein, P., Genes, C., Hammerer, K., Poggio, M. & Rabl, P. In *Cavity Optomechanics: Nano- and Micromechanical Resonators Interacting with Light* (eds Aspelmeyer, M., Kippenberg, T. J. & Marquardt, F.) 327–351 (Springer, 2014).
2. Rabl, P. et al. Strong magnetic coupling between an electronic spin qubit and a mechanical resonator. *Phys. Rev. B* **79**, 041302 (2009).
3. Leibfried, D., Blatt, R., Monroe, C. & Wineland, D. Quantum dynamics of single trapped ions. *Rev. Mod. Phys.* **75**, 281–324 (2003).
4. LaHaye, M. D., Suh, J., Echterbach, P. M., Schwab, K. C. & Roukes, M. L. Nanomechanical measurements of a superconducting qubit. *Nature* **459**, 960–964 (2009).
5. Kolkowitz, S. et al. Coherent sensing of a mechanical resonator with a single-spin qubit. *Science* **335**, 1603–1606 (2012).
6. Arcizet, O. et al. A single nitrogen-vacancy defect coupled to a nanomechanical oscillator. *Nat. Phys.* **7**, 879–883 (2011).
7. Lee, D., Lee, K. W., Cady, J. V., Ovarthaiyapong, P. & Jayich, A. C. B. Topical review: spins and mechanics in diamond. *J. Opt.* **19**, 033001 (2017).
8. O'Connell, A. D. et al. Quantum ground state and single-phonon control of a mechanical resonator. *Nature* **464**, 697–703 (2010).
9. Treutlein, P., Hunger, D., Camerer, S., Hānsch, T. W. & Reichel, J. Bose-Einstein condensate coupled to a nanomechanical resonator on an atom chip. *Phys. Rev. Lett.* **99**, 140403 (2007).
10. Mamin, H. J., Poggio, M., Degen, C. L. & Rugar, D. Nuclear magnetic resonance imaging with 90-nm resolution. *Nat. Nanotechnol.* **2**, 301–306 (2007).
11. Rugar, D., Budakian, R., Mamin, H. J. & Chui, B. W. Single spin detection by magnetic resonance force microscopy. *Nature* **430**, 329–332 (2004).
12. Kim, P. H., Hauer, B. D., Doolin, C., Souris, F. & Davis, J. P. Approaching the standard quantum limit of mechanical torque sensing. *Nat. Commun.* **7**, 13165 (2016).
13. Burgess, J. A. J. et al. Quantitative magneto-mechanical detection and control of the Barkhausen effect. *Science* **339**, 1051–1054 (2013).
14. Hoang, T. M. et al. Torsional optomechanics of a levitated nonspherical nanoparticle. *Phys. Rev. Lett.* **117**, 123604 (2016).
15. Leggett, A. J. et al. Dynamics of the dissipative two-state system. *Rev. Mod. Phys.* **59**, 1–85 (1987).
16. Yin, Z. Q., Zhao, N. & Li, T. C. Hybrid opto-mechanical systems with nitrogen-vacancy centers. *Sci. China Phys. Mech. Astron.* **58**, 1–12 (2015).
17. Conangla, P. G., Schell, A. W., Rica, R. A. & Quidant, R. Motion control and optical interrogation of a levitating single nitrogen vacancy in vacuum. *Nano Lett.* **18**, 3956–3961 (2018).
18. Rabl, P. et al. A quantum spin transducer based on nanoelectromechanical resonator arrays. *Nat. Phys.* **6**, 602–608 (2010).
19. Yin, Z., Li, T., Zhang, X. & Duan, L. M. Large quantum superpositions of a levitated nanodiamond through spin-optomechanical coupling. *Phys. Rev. A* **88**, 033614 (2013).
20. Scala, M., Kim, M. S., Morley, G. W., Barker, P. F. & Bose, S. Matter-wave interferometry of a levitated thermal nano-oscillator induced and probed by a spin. *Phys. Rev. Lett.* **111**, 180403 (2013).
21. Einstein, A. & Johannes de Haas, W. Experimenteller Nachweis der Ampèreschen Molekularströme. *Verh. Deutsch. Physik. Gesellschaft* **17**, 152–170 (1915).
22. Alzetta, G., Arimondo, E. & Ascoli, C. Paramagnetic resonance experiments at low fields with angular-momentum detection. *Nuovo Cim. B* **52**, 392–402 (1967).
23. Arcizet, O., Cohadon, P. F., Briant, T., Pinard, M. & Heidmann, A. Radiation-pressure cooling and optomechanical instability of a micromirror. *Nature* **444**, 71–74 (2006).
24. Gigan, S. et al. Self-cooling of a micromirror by radiation pressure. *Nature* **444**, 67–70 (2006).
25. Schliesser, A., Rivière, R., Anetsberger, G., Arcizet, O. & Kippenberg, T. J. Resolved-sideband cooling of a micromechanical oscillator. *Nat. Phys.* **4**, 415–419 (2008).
26. Barson, M. S. J. et al. Nanomechanical sensing using spins in diamond. *Nano Lett.* **17**, 1496–1503 (2017).
27. Chang, D. E. et al. Cavity opto-mechanics using an optically levitated nanosphere. *Proc. Natl Acad. Sci. USA* **107**, 1005–1010 (2010).
28. Romero-Isart, O., Juan, M. L., Quidant, R. & Cirac, J. I. Toward quantum superposition of living organisms. *New J. Phys.* **12**, 033015 (2010).
29. Huillery, P. et al. Spin-mechanics with levitating ferromagnetic particles. Preprint at <http://arxiv.org/abs/1903.09699> (2019).
30. Wu, M. et al. Nanocavity optomechanical torque magnetometry and radiofrequency susceptometry. *Nat. Nanotechnol.* **12**, 127–131 (2017).

**Publisher's note** Springer Nature remains neutral with regard to jurisdictional claims in published maps and institutional affiliations.

© The Author(s), under exclusive licence to Springer Nature Limited 2020

### Microdiamond properties

The diamonds that we use are in the form of a powder, with particles that have a diameter of 15  $\mu\text{m}$ . They are supplied by the company Adamas, which produces diamonds with a concentration of NV centres in the range 3–4 p.p.m., corresponding to  $(1.5\text{--}2) \times 10^9$  NV centres per microdiamond. Using the same collection optics as was used in ref. <sup>31</sup>, we estimated the number of optically addressed NV centres to lie in that same range. This is 4 to 5 orders of magnitude larger than the concentration used in the experiments reported in refs. <sup>31–33</sup>, where no spin torque was observed. Under continuous laser excitation at around 10  $\mu\text{W}$ , our diamonds started to heat up at 0.1 mbar, which is similar to pressures used in<sup>32</sup>; this points to the role played by impurities other than NV centres in the heating observed in ref. <sup>32</sup>.

### The Paul trap

We operate with a Paul trap that is similar to the one used in ref. <sup>31</sup> except that the particles are stably trapped at the bottleneck region of the trap, where both the electric field gradient and the anisotropy are stronger, yielding higher librational confinement. The pressure we operate at is 1 bar for the spin-torque measurements shown in Fig. 2, and in the millibar range for the cooling and phonon lasing experiments. Below 1 mbar, the diamond starts to rotate owing to a locking mechanism induced by the Paul trap drive, making it impossible to observe the spin-dependent torque, which relies on very stable libration.

### NV spin polarization and read-out

Owing to an intersystem crossing in the excited state of the NV centres, the electronic ground state  $|0\rangle$  is brighter than the  $|\pm 1\rangle$  states under green laser illumination. This provides a means to read out the Zeeman splitting by scanning a microwave tone around the resonance, carrying out ODMR. Here, the microwave is applied directly to the trapping electrode, which provides an efficient means to excite the spins. The photoluminescence is detected using standard confocal microscopy. We use about 100  $\mu\text{W}$  of laser light at 532 nm to polarize the NV centres. The laser is focused via a lens inside the vacuum chamber which has a numerical aperture of 0.5 and a working distance of 8 mm. The focal point of the laser is kept a few tens of micrometres away from the microdiamond to mitigate the effect of radiation pressure and to enable laser excitation of the whole diamond<sup>31,33</sup>. To measure the polarization rates to the ground and to the excited magnetic states, we carry out the sequence depicted in Extended Data Fig. 5a. The photoluminescence rate is measured as a function of the time  $\tau$  for both sequences and is plotted in Extended Data Fig. 5b. The laser induced polarization rate to the  $m'_s = 0$  state is 3.3 kHz. The microwave polarization rate  $\Gamma_M = \Omega^2 T_2^*$  (see Supplementary Information) to the magnetic state  $m'_s = -1$  is found to be 8 kHz when using  $-5$  dBm of microwave power measured before a 25 dB amplifying stage. An estimate based on both the ODMR width and a Ramsey sequence yields  $T_2^* = 70$  ns, implying  $\Omega/2\pi = 60$  kHz.

The degree of spin polarization cannot be estimated precisely without using a full numerical model and the 8 rate equations including mixing by the magnetic field transverse component. The magnetic field transverse component reduces the polarization time owing to mixing of electron spin states both in the ground and excited levels. This enhances the probability of non-radiative crossing to the metastable level and reduces the ODMR contrast by<sup>34</sup> 30%. Overall, this reduces the degree of optical polarization to the  $m'_s = 0$  spin state to about 60%.

### Detection and analysis of the libration

The diamond motion is detected by collecting the back-reflected green light from the diamond surface, separated from the excitation light using a polarizing beamsplitter. The best sensitivity is achieved by taking advantage of the speckle pattern produced by the rough surface of

the microdiamond under coherent illumination. At the particle image plane, which is located a few tens of centimetres away from the particle, an image is formed with an additional speckle feature. To detect the diamond motion, we focus a small area of this image onto a single-mode optical fibre and detect the photons transmitted through the fibre with a single-photon avalanche photodiode. The detected signal is then highly sensitive to the particle position and orientation.

### Angular displacement sensitivity

For a given levitating particle, we can optimize, in real time, the change in the optical signal coming from the angular displacement of the particle by selecting the most favourable region of the particle image. To do this, we look at our optical signal while switching a microwave field tuned to one ODMR transition at a frequency of 1 Hz. Alignment is done by maximizing the change in the coupled light intensity as the diamond jumps between two angular positions. The linearity of the coupled light with the rotating angles can finally be assessed by looking at a higher order of the harmonic motion once the libration frequencies are identified.

While being a sensitive measurement of the angular displacement, our technique does not give an absolute measurement of the angle change. The spin-torque vector  $\Gamma_s$  is orthogonal to the plane defined by the magnetic field and the NV axis (it tends to align the NV axis to the **B** field). However, because the angular confinement is not isotropic, the particle rotation axis is not necessarily collinear with the spin torque. Determining the exact three-dimensional rotational dynamics of the particle would necessitate knowledge of the orientation of the NV axes with respect to the principal axes of the angular motion.

Using NV magnetometry, the mechanically detected spin resonance can nonetheless be used to relate the optical signal change to the angular displacement of the particle. A set of three mechanically detected spin resonances corresponding to three different microwave powers are shown in Extended Data Fig. 4a, under a magnetic field of 144 G. The minimum of each curve falls on the dashed line. The lower panel of Extended Data Fig. 4a is a theoretical curve where the angle between the NV axis and the magnetic field direction is plotted as a function of the frequency of the NV spin transition. This curve is obtained by diagonalizing the NV spin Hamiltonian in the presence of a magnetic field of 144 G. Since the maximum magnetization of the NV spins is obtained when the microwave field is resonant with the spin transition, one can relate the maximal change in the optical signal ( $\Delta S$ ) to the variation of the angle between the NV axis and the magnetic field direction ( $\Delta\theta_{\text{NV}}$ ). Doing so, we obtain here a resolution of 43 mrad Mcounts<sup>-1</sup>s<sup>-1</sup>. Extended Data Fig. 4b shows a time trace of the optical signal upon Brownian motion of the particle. From the standard deviation of this signal and the above calibration, we obtain an angular displacement sensitivity of 0.3 mrad Hz<sup>-1/2</sup>.

These numbers are however only upper bounds for our resolution and sensitivity. To explain why this is the case, Extended Data Fig. 4c shows a sketch of the angular motion of the diamond after magnetizing one class of NV spins. For simplicity, we consider rotation about two axes here. In a reference frame with axes given by the principal librational mode directions, we can parametrize the orientation of the NV axis in a subspace defined by the two angular coordinates  $\theta_x$  and  $\theta_y$ . The orientation without magnetization ( $M_z = 0$ ) is given by the trap and particle geometry and labelled O. The point B in this space is the direction of the magnetic field. Upon magnetization, a torque is applied to the particle such that the orientation follows the OB trajectory over time. However, owing to different confinement of the librational modes  $\omega_x$  and  $\omega_y$  along the *x* and *y* axes, the angular motion takes place along a different trajectory.

In our experiments, the orientation of the magnetic field and NV axes relative to the principal axis of the libration is unknown. This prevents us from fully calibrating our detected angular motion. Nevertheless, provided that the detection is optimized to the librational mode having

the highest confinement, we can ensure that the detected angular displacement  $\theta_d$  is smaller than the angular displacement  $\theta_{NV}$  sensed by the NV spins. This can be seen in Extended Data Fig. 4c, where we note “NV”, the equilibrium position when  $\omega_x > \omega_y$ . Our calibration method thus gives an upper bound to the obtained resolution and sensitivity. Optimization of the detection is performed by monitoring the power spectrum and tuning the speckle angle at the entrance of the fibre to maximize the power spectrum of the mode with the largest frequency. Extended Data Fig. 4d shows the power spectrum of the Brownian motion for two detection alignments. In the red trace, all three librational modes, indicated with black arrows, are clearly visible. In the blue trace, the detection is tuned to be mainly sensitive to the mode with the highest confinement frequency. The latter detection tuning is used for the data shown in Extended Data Fig 4a and b.

The sensitivity could be improved by collecting all the speckle pattern using a camera rather than just a fraction of it as we do now. Using a shorter laser wavelength would also straightforwardly improve the sensitivity. Another technical limitation comes from the trapped diamond motion in other modes than the libration mode of interest which adds noise to the angular displacement signal. In this regard, active stabilization of the centre of mass will greatly increase the sensitivity.

### Power spectral density

Using the above described detection method, motional frequencies can be observed by sending the detected signal to a spectrum analyser. Under vacuum (1 mbar), the power spectrum exhibits narrow peaks at the trapping frequencies of the motional modes which are driven by Brownian motion (see Fig. 1B in the main text). For each librational mode, the power spectrum is fitted by the formula obtained in Supplementary Information:

$$S_\phi(\omega) = \frac{2\gamma kT}{I((\omega_\phi^2 - \omega^2)^2 + \gamma^2 \omega^2)} \quad (1)$$

The librational modes can in fact be unambiguously identified (and separated from the centre of mass modes) using the torque induced by the NV centres. By switching on and off a microwave field tuned to one spin resonance at the same period as that of one diamond libration, one performs parametric excitation of that librational mode. In our experiments, a sequence of five microwave pulses is enough to displace the angle above the Brownian thermal noise. Following a parametric excitation sequence, the diamond orientation ‘ring-down’, or decay, is observed. A typical decay curve is shown in Extended Data Fig. 1a. We typically find librational frequencies in the range 100 Hz to 1 kHz.

### Parameters used for the spin-dependent torque measurements

The ODMR and spin-mechanical measurement scans shown in Fig. 2A of the main text are taken under atmospheric pressure. The green laser power was 330  $\mu$ W and the microwave power was set to 0 dBm. The magnetic field is around 95 G. For the mechanically detected spin resonance (Fig. 2A, b), the microwave detuning is scanned in 2 MHz steps with a duration of 10 ms per point. During those 10 ms, the diamond orientation has enough time to reach its equilibrium position and the spin-torque effect can be observed. The average count rate is  $2.3 \times 10^6 \text{ s}^{-1}$  for a total averaging time of 10 min. For the ODMR trace (Fig. 2A, c), the microwave detuning is scanned in steps of 2 MHz with a duration of 1 ms per point. For each point, the microwave field is switched off for the first 0.5 ms and switched on for the last 0.5 ms during which the signal is acquired. This prevents mechanical effects from altering the detected photoluminescence signal from the NV centres. The photoluminescence count rate is  $5 \times 10^6 \text{ s}^{-1}$  and the total averaging time for this measurement was 3 h.

### Estimation of the temperature

The temperature associated with the librational modes can only be estimated. Obtaining a precise temperature value would require

knowledge about the moment of inertia of the particle, which is prone to strong systematic errors. The standard method is to vary the pressure<sup>35</sup> while observing the power spectrum: over the pressure range where its area is constant (to satisfy Liouville’s theorem under adiabatic transformation), the librational mode temperature is known to be 300 K as it is thermalized with the gas temperature. In our case, pressure variations slightly change the orientation and position of the trapped particle and, incidentally, the sensitivity to angular motion. This prevents such a method from being used. However two observations support the fact that the external degrees of freedom of the particle are thermalized at 300 K when operating in the millibar pressure range. We measured the particle internal temperature with our typical laser powers via NV thermometry<sup>32</sup>, and found it to be close to 300 K. This ensures that no heating of the libration modes comes from the heating of the gas surrounding the particle<sup>36</sup>. We observed that heating of the particle by the laser starts below 0.1 mbar, similar to what was measured using diamonds that were doped with a three orders of magnitude smaller NV concentration. Several sources of noise could also heat up the particle, such as the laser-induced torque<sup>33</sup> or charge fluctuations. Heating by the former can be excluded as no noticeable changes of the power spectrum shape occur when laser power is increased up to 1 mW.

### Parameters and calibration

The power spectrum of the detected librational modes depends strongly on the particle angle. For the same motional amplitude, a change in the particle angle potentially implies a different speckle pattern, which in turn changes the power spectrum sensitivity. Since the particle angle changes with the microwave detuning and power, different power spectra cannot be directly compared when the parameters are changed. Traces i, ii and iii in the right panel of Fig. 2B in the main text have thus been obtained at the same particle angle to enable quantitative comparison between their areas. Operating at the same particle angle was ensured by performing a resonant spin-mechanical detection at different microwave amplitudes and choosing pairs of microwave frequencies and powers that correspond to the same count rates. As shown in the data in Extended Data Fig. 1b, we chose microwave detunings corresponding to the points 1, 2, 3 for the two traces i and ii taken at microwave powers of –20 dBm and –10 dBm, respectively. The frequencies, which are 2.617 GHz, 2.623 GHz and 2.634 GHz, respectively on the blue, resonant and red side of the spin resonance all correspond to the same angle under these power conditions. A fit to the experimental curves in Fig. 2B was obtained using the formula

$$S_\phi(\omega) = \frac{2\gamma_{\text{eff}} kT}{I((\omega_{\text{eff}}^2 - \omega^2)^2 + \gamma_{\text{eff}}^2 \omega^2)} \quad (2)$$

The dependence of the damping  $\gamma_{\text{eff}}$  and frequency shift  $\omega_{\text{eff}}$  on the microwave detuning shown in Fig. 2C was obtained using parametric excitation of the librational mode at 480 Hz. The microwave power is –10 dBm and for this measurement, the above-mentioned calibration issue (change in the sensitivity when the microwave detuning is varied) is not relevant. In order to extract the damping and shifts, the resulting ring-down was fitted by the formula:

$$S(t) = A_1 \sin(\omega_{\text{eff}} t + \phi) \exp(-\gamma_{\text{eff}} t/2) + A_2 \sin(\omega_2 t + \phi_2) \exp(-\gamma_2 t/2) + A_0 \quad (3)$$

where the second exponentially damped sine term takes into account the slightly excited librational mode at 590 Hz. Three of these ring-down traces are shown in Extended Data Fig. 1c. For each curve, the averaging time is around 100 s. An estimation of the temperature relies on comparing the damping with and without spin-cooling, using the relation<sup>23</sup>  $T_{\text{eff}} = T - \frac{\gamma}{\gamma_{\text{eff}}}$ , valid for small spin-spring frequency shifts.



## Modelling of the experiment

For most of this paper, we modelled the experiment numerically using Monte Carlo simulations that include the full three-level structure of the NV spin-1 system in the ground state (see Supplementary Information). For the spin-cooling and spin-spring effects shown in Fig. 2C, the number of NV centres, polarization rate, Rabi frequencies, and angle between the NV centres and the main axis of the diamond are left as free parameters.

## Bistability and phonon-lasing

The curve in Fig. 3A, a, shows the angular evolution of the particle as a function of the microwave detuning obtained using similar parameters to those in the linear regime, but using microwave and laser powers that best fitted the data in Fig. 3A, b, and a lower trapping frequency ( $\omega_{\phi}/2\pi = 240$  Hz). Figure 3A, c, shows the evolution of the librational mode angle as a function of time in this regime. Several such curves were obtained for different microwave detunings, and are shown in Extended Data Fig. 6. A Monte Carlo simulation was also performed using our experimental parameters, with a microwave tuned to the red side, and shows similar jumps between the two stable points A and B. The data shown in Fig. 3B, a, of the main text show the evolution of power spectra for different microwave signal powers, when the microwave frequency is tuned to the blue of the ODMR transition. The onset of instability is seen at approximately 0 dBm. For a quantitative estimate of the threshold, we compute the area below the librational peak as a function of microwave detuning. This is shown in Fig. 3B, b. Note that here the sensitivity of the power spectra to the angle may induce some systematic errors. For these measurements, we fitted the data by the numerical model, and found good agreement with the numerical analysis, but a quantitative comparison with the experiment is difficult owing to the above mentioned angle-dependent sensitivity.

## Data availability

The data that support the findings of this study are available from the corresponding author upon reasonable request.

31. Delord, T. et al. Ramsey interferences and spin echoes from electron spins inside a levitating macroscopic particle. *Phys. Rev. Lett.* **121**, 053602 (2018).
32. Delord, T., Nicolas, L., Bodini, M. & Hétet, G. Diamonds levitating in a Paul trap under vacuum: measurements of laser-induced heating via NV center thermometry. *Appl. Phys. Lett.* **111**, 013101 (2017).
33. Delord, T., Nicolas, L., Schwab, L. & Hétet, G. Electron spin resonance from NV centers in diamonds levitating in an ion trap. *New J. Phys.* **19**, 033031 (2017).
34. Tettienne, J.-P. et al. Magnetic-field-dependent photodynamics of single NV defects in diamond: an application to qualitative all-optical magnetic imaging. *New J. Phys.* **14**, 103033 (2012).
35. Hebestreit, E., René, R., Frimmer, M. & Novotny, L. Measuring the internal temperature of a levitated nanoparticle in high vacuum. *Phys. Rev. A* **97**, 043803 (2018).
36. Millen, J., Deesuwan, T., Barker, P. & Anders, J. Nanoscale temperature measurements using non-equilibrium Brownian dynamics of a levitated nanosphere. *Nat. Nanotechnol.* **9**, 425 (2014).

**Acknowledgements** We thank R. Blatt, C. Voisin, Y. Chassagneux, E. Baudin and S. Deléglise for discussions.

**Author contributions** T.D. and P.H. contributed equally to this work. T.D., P.H., L.N. and G.H. performed the spin-torque experiments; T.D., P.H. and G.H. analysed the data and performed the modelling with assistance from L.N., and G.H., T.D. and P.H. wrote the manuscript. All authors contributed to the interpretation of the data and commented on the manuscript.

**Competing interests** The authors declare no competing interests.

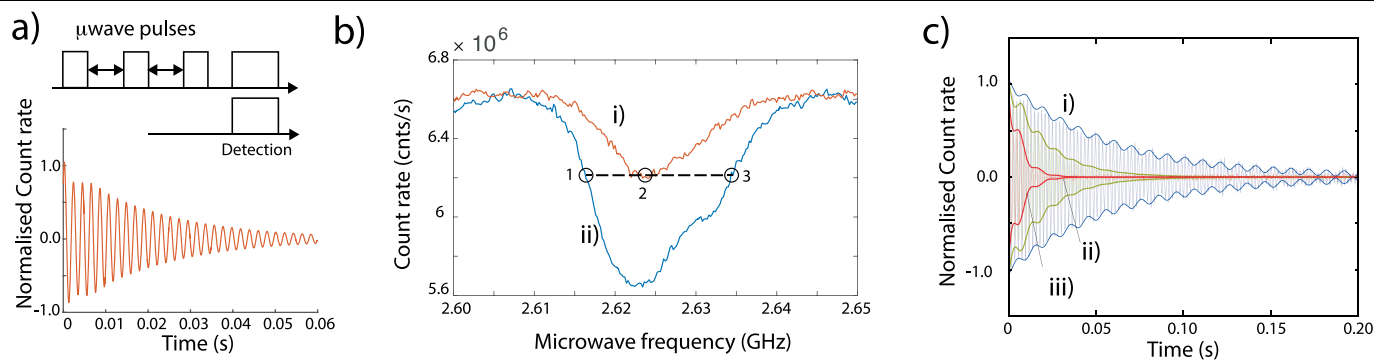
## Additional information

**Supplementary information** is available for this paper at <https://doi.org/10.1038/s41586-020-2133-z>.

**Correspondence and requests for materials** should be addressed to G.H.

**Peer review information** Nature thanks Ashok Ajay and the other, anonymous, reviewer(s) for their contribution to the peer review of this work.

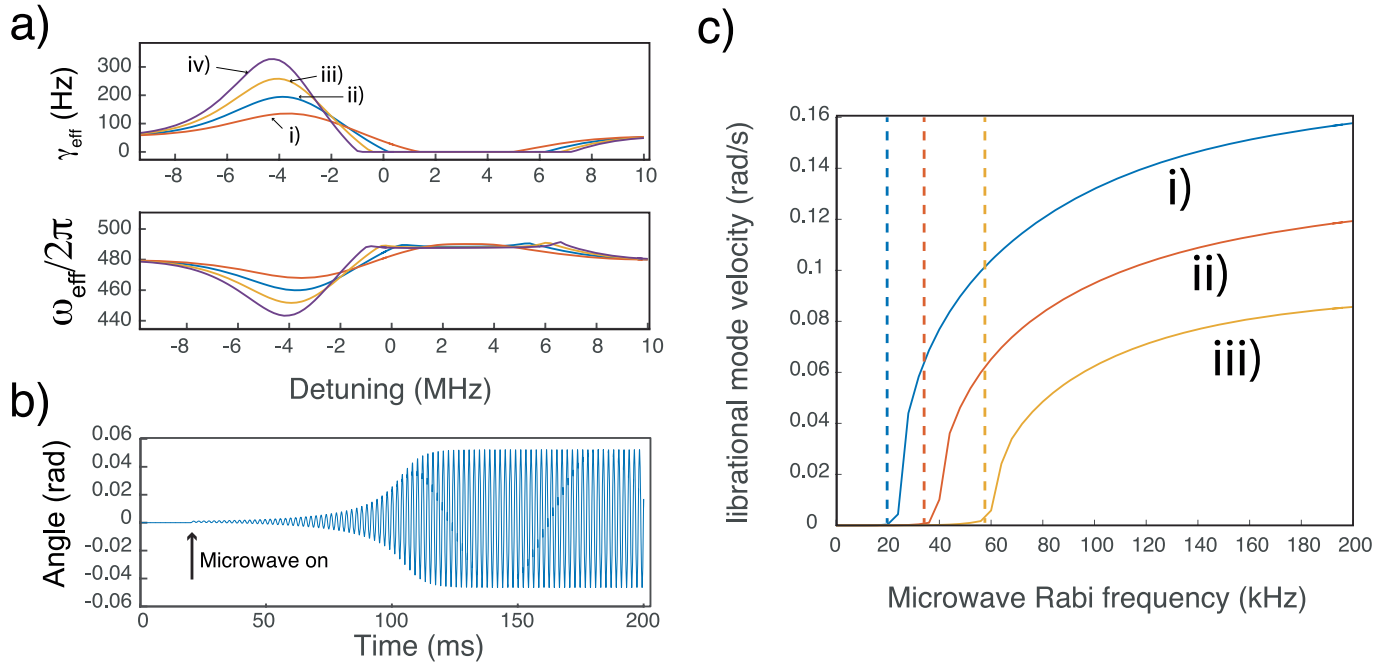
**Reprints and permissions information** is available at <http://www.nature.com/reprints>.



**Extended Data Fig. 1 | Parametric spin-excitation of the librational mode.**

**a,** Detection principle of the librational modes using microwave parametric excitation (top). Reflected light field amplitude as a function of time for one low-frequency librational mode (170 Hz) at 1 mbar (bottom). **b,** Spin-mechanical resonance for two different microwave powers: trace i, 20 dBm; trace ii, -10 dBm. **c,** Reflected light field amplitude as a function of time, for the

three microwave frequencies 2.617 GHz (red thin curve), 2.623 GHz (green) and 2.634 GHz (blue) corresponding to the points 1, 2 and 3 in **b**, respectively. Plain thicker lines show the slow envelope of the fit to the data (see Methods) using two sines at the frequency of the parametrically excited librational mode (480 Hz) and of the closest librational mode (590 Hz) with an amplitude that is 30 times smaller.

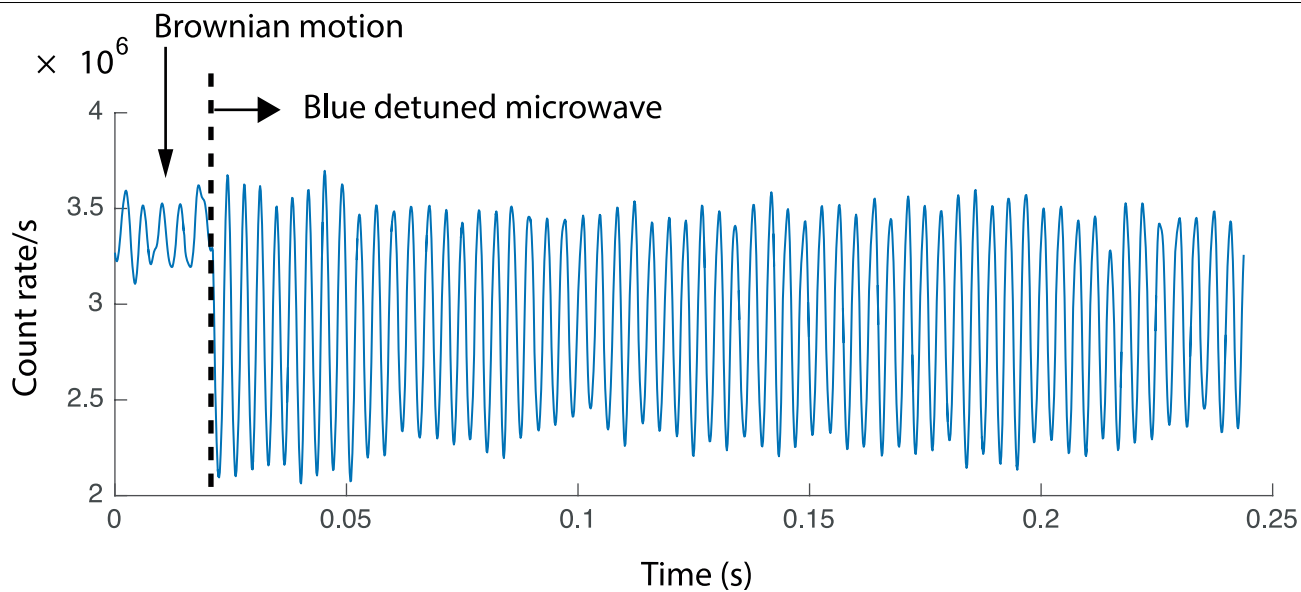


**Extended Data Fig. 2 | Numerical simulations in the nonlinear regime.**

**a**, Effective damping and spring constants as a function of microwave detuning deduced by a numerical fit to the ring-down curves (see Methods). Traces i, ii, iii and iv correspond to increasing microwave Rabi frequencies  $\Omega/2\pi = 50, 150, 200$  and  $250$  kHz, respectively. **b**, Evolution of the angle as a function of time

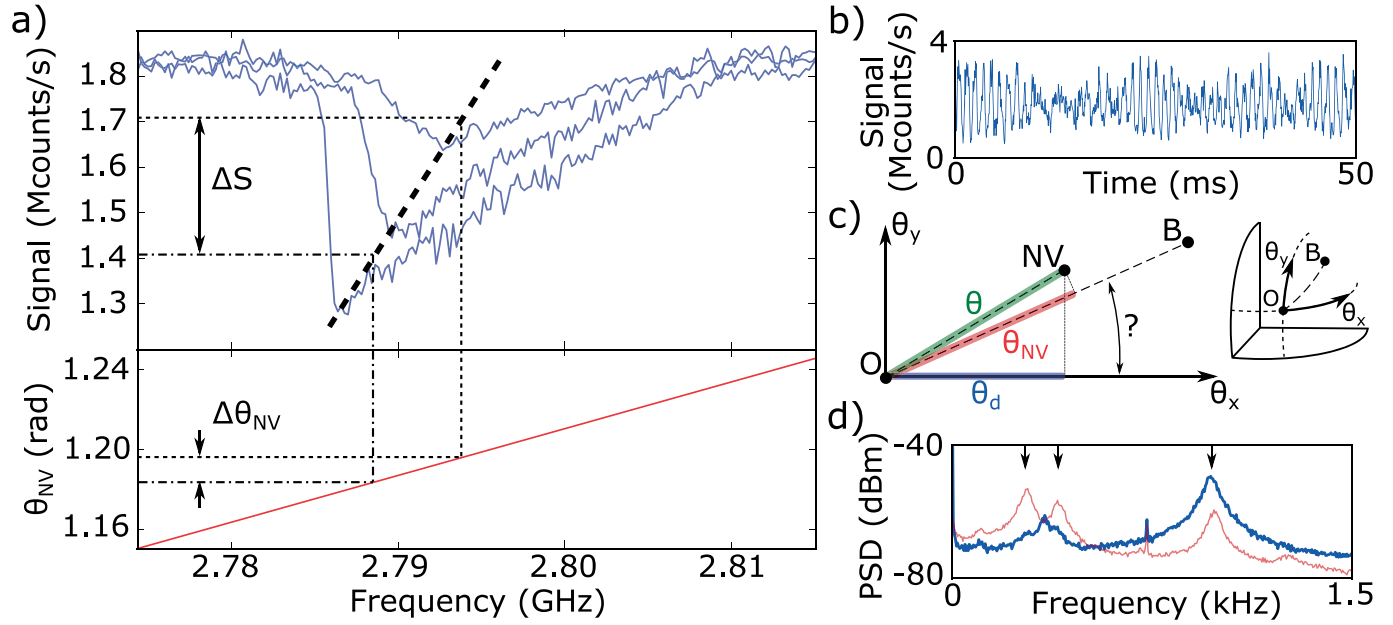
after turning on a microwave frequency to the blue of the spin resonance at a time  $t = 20$  ms, showing amplification and finally lasing at  $t = 120$  ms. **c**, Librational mode velocity as a function of microwave Rabi frequency, for three different values of the spin-lattice relaxation rate  $1/T_1 = 1, 2$  and  $3$  kHz for traces i, ii and iii, respectively.





**Extended Data Fig. 3 | Phonon-lasing as a function of time.** Shown is the reflected light field amplitude as a function of time on sudden switch-on of a microwave signal at a time  $t = 0.02$  s to the blue side of the spin transition.

The microwave power is above threshold so lasing can be observed after the Brownian motion signal (seen before  $t = 0.02$  s). This curve was used to plot the histogram of Fig. 3C in the main text.

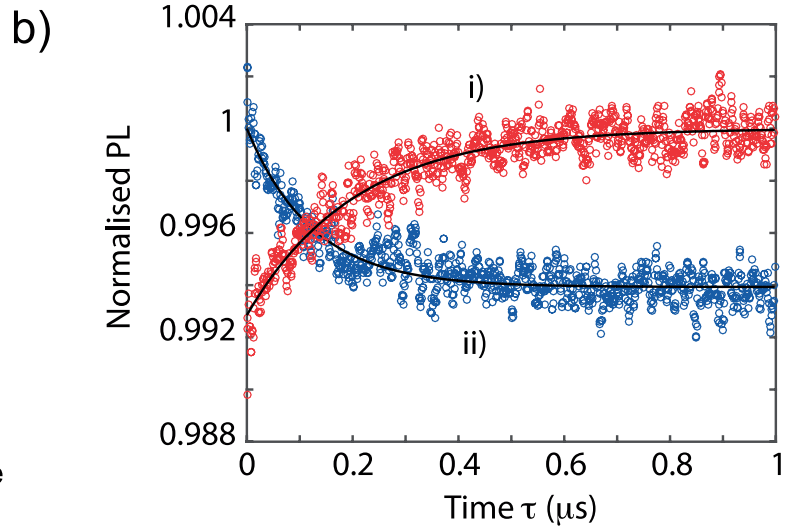
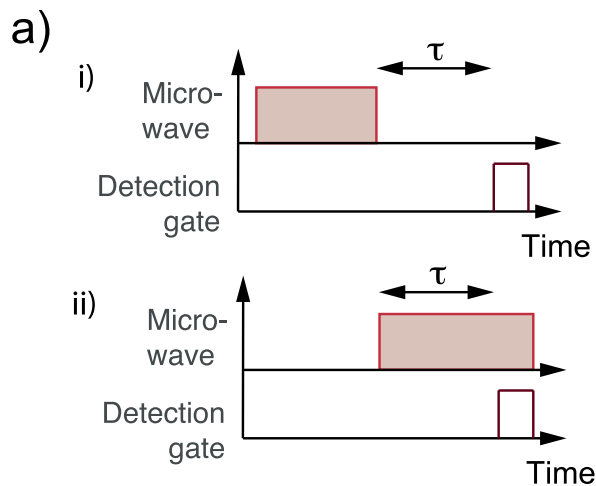


**Extended Data Fig. 4 | Calibration of sensitivity using NV magnetometry.**

**a.** Upper panel, mechanically detected spin resonance for three different microwave powers. The dashed line is the locus of the signal minima. Lower panel, angle between the NV axis and magnetic field direction versus NV spin transition frequency.  $\Delta S$  is the maximal change of the optical signal.  $\Delta\theta_{NV}$  is the maximum angle between the NV axis and the magnetic field direction.

**b.** Optical signal as a function of time. **c.** Left panel, sketch depicting the angular motion of the diamond on magnetization of one class of NV spins using only two angles  $\theta_x$  and  $\theta_y$  for simplicity. B is the orientation of the magnetic

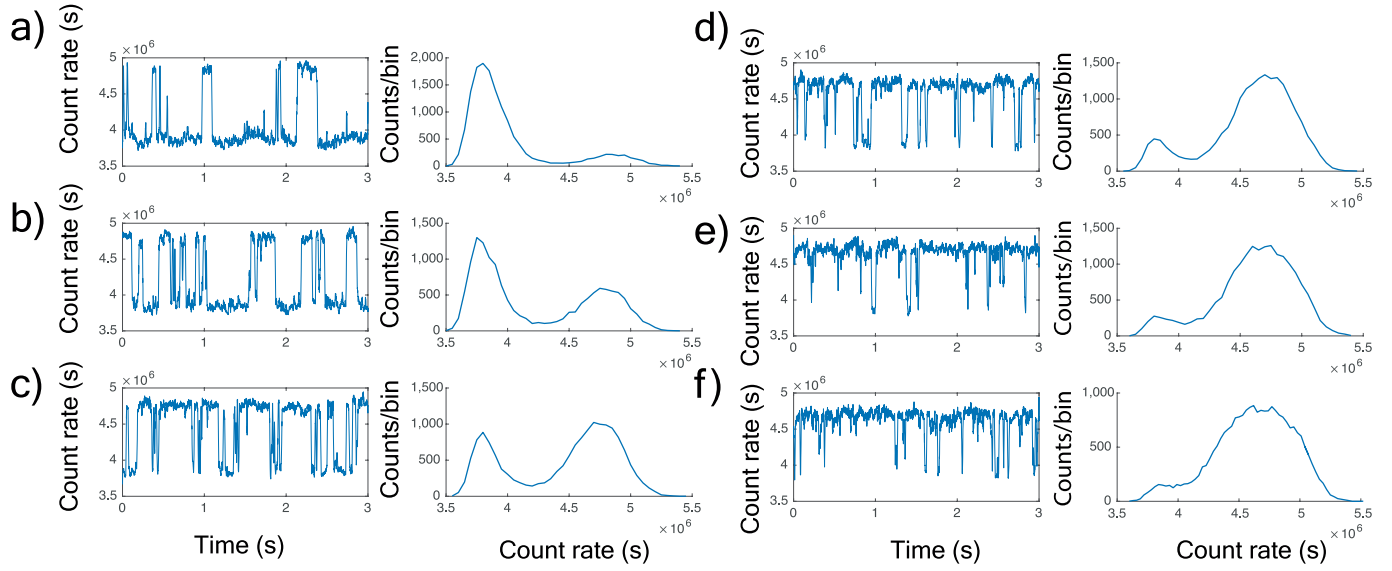
field. Right panel, angular trajectory represented in  $(\theta_x, \theta_y)$  space. We note O is the particle orientation without NV magnetization ( $M_z = 0$ ). The red (green) line is the trajectory in the isotropic (anisotropic) case (see Methods).  $\theta_d$  is the detected angle. **d.** Power spectra of the librational Brownian motion for two different speckle alignments taken with a resolution bandwidth of 1 Hz. The red curve shows all three librational modes. For the blue curve, the detection is tuned to be mainly sensitive to the mode with the highest confinement frequency. The latter detection setting is used for the data shown in **a** and **b**.



**Extended Data Fig. 5 | Measurement of spin polarization rates.** a, Sequences employed to measure the laser induced polarization rate to the ground state (i) and to measure the microwave induced polarization rate to the magnetic state  $m'_s = -1$  (ii). The laser is kept on at all times for both sequences. b, Trace i shows the photoluminescence (PL) rate at a time  $\tau$  after having turned off the

microwave signal. An exponential fit to the data gives a laser polarization time of  $300 \mu\text{s}$ . Trace ii shows the photoluminescence rate at a time  $\tau$  after having turned on the microwave signal. The polarization time to the magnetic state is here  $124 \mu\text{s}$ .





**Extended Data Fig. 6 | Particle angle dynamics for different microwave detunings in the bistable regime. a–f,** Left panel, experimental observation of the reflected signal amplitude as a function of time for microwave frequencies

(in GHz) of 2.8000 (a), 2.8010 (b), 2.8020 (c), 2.8030 (d), 2.8035 (e), 2.8040 (f), tuned to the red of the spin transition. Right panel, histogram showing the number of counts within each bin.

# Experimental demonstration of memory-enhanced quantum communication

<https://doi.org/10.1038/s41586-020-2103-5>

Received: 19 August 2019

Accepted: 16 January 2020

Published online: 23 March 2020

 Check for updates

M. K. Bhaskar<sup>1</sup>, R. Riedinger<sup>1</sup>, B. Machielse<sup>1</sup>, D. S. Levonian<sup>1</sup>, C. T. Nguyen<sup>1</sup>, E. N. Knall<sup>2</sup>, H. Park<sup>1,3</sup>, D. Englund<sup>4</sup>, M. Lončar<sup>2</sup>, D. D. Sukachev<sup>1</sup> & M. D. Lukin<sup>1✉</sup>

The ability to communicate quantum information over long distances is of central importance in quantum science and engineering<sup>1</sup>. Although some applications of quantum communication such as secure quantum key distribution<sup>2,3</sup> are already being successfully deployed<sup>4–7</sup>, their range is currently limited by photon losses and cannot be extended using straightforward measure-and-repeat strategies without compromising unconditional security<sup>8</sup>. Alternatively, quantum repeaters<sup>9</sup>, which utilize intermediate quantum memory nodes and error correction techniques, can extend the range of quantum channels. However, their implementation remains an outstanding challenge<sup>10–16</sup>, requiring a combination of efficient and high-fidelity quantum memories, gate operations, and measurements. Here we use a single solid-state spin memory integrated in a nanophotonic diamond resonator<sup>17–19</sup> to implement asynchronous photonic Bell-state measurements, which are a key component of quantum repeaters. In a proof-of-principle experiment, we demonstrate high-fidelity operation that effectively enables quantum communication at a rate that surpasses the ideal loss-equivalent direct-transmission method while operating at megahertz clock speeds. These results represent a crucial step towards practical quantum repeaters and large-scale quantum networks<sup>20,21</sup>.

Efficient, long-lived quantum memory nodes are expected to play an essential part in extending the range of quantum communication<sup>9</sup>, as they enable asynchronous quantum logic operations, such as Bell-state measurements (BSMs), between optical photons. Such an asynchronous BSM is central to many quantum communication protocols, including the realization of scalable quantum repeaters<sup>9</sup> with multiple intermediate nodes. Its elementary operation can be understood by considering a specific implementation of quantum cryptography<sup>22,23</sup> illustrated in Fig. 1a. Here two remote communicating parties, Alice and Bob, try to agree on a key that is secure against potential eavesdroppers. They each send a randomly chosen photonic qubit  $\{|\pm x\rangle, |\pm y\rangle\}$  encoded in one of two conjugate bases ( $X$  or  $Y$ ) across a lossy channel to an untrusted central node (Charlie), who performs a BSM and reports the result over an authenticated public channel. After a number of iterations, Alice and Bob publicly reveal their choice of bases to obtain a correlated bit string (a sifted key) from the cases when they used a compatible basis. A potentially secure key can subsequently be distilled provided the BSM error rate is low enough.

Although a photonic BSM can be implemented with linear optics and single-photon detectors, the BSM is only successful in this ‘direct-transmission’ approach when photons from Alice and Bob arrive simultaneously. Thus, when Alice and Bob are separated by a lossy fibre with a total transmission probability  $p_{A \rightarrow B} \ll 1$ , Charlie measures photon coincidences with probability also limited by  $p_{A \rightarrow B}$ , leading to a fundamental bound<sup>8</sup> on the maximum possible distilled key rate of  $R_{\max} = p_{A \rightarrow B}/2$  bits per channel use for an unbiased basis choice<sup>4</sup>. Although

linear optical techniques to circumvent this bound are now being actively explored<sup>24</sup>, they offer only limited improvement and cannot be scaled beyond a single intermediate node.

Alternatively, this bound can be surpassed using a quantum memory node at Charlie’s location. In this approach, illustrated in Fig. 1b, the state of Alice’s photon is stored in the heralded memory while awaiting receipt of Bob’s photon over the lossy channel. Once the second photon arrives, a BSM between Alice’s and Bob’s qubits yields a distilled key rate that for an ideal memory scales as<sup>25</sup>  $R_s \propto \sqrt{p_{A \rightarrow B}}$ , potentially leading to substantial improvement over direct transmission.

## Efficient nanophotonic quantum node

In this work we realize and use a quantum node that enables BSM rates exceeding those of an ideal system based on linear optics. We focus on the demonstration and characterization of the BSM node, leaving the implementation of source-specific technical components of full-scale quantum key distribution systems, such as decoy states<sup>26</sup>, basis biasing<sup>27</sup>, a finite key error analysis<sup>28</sup> and a physical separation of Alice and Bob for future work. Our realization is based on a single silicon–vacancy (SiV) colour centre integrated inside a diamond nanophotonic cavity<sup>17–19</sup> (Fig. 2a). Its key figure-of-merit, the cooperativity<sup>13</sup>  $C$ , describes the ratio of the interaction rate with individual cavity photons compared to all dissipation rates. A low mode volume  $(0.5(\lambda/n)^3)$ , with wavelength  $\lambda$  and refractive index  $n$ , high quality factor ( $2 \times 10^4$ ), and nanoscale positioning of SiV centres enable an exceptional  $C = 105 \pm 11$ . Cavity photons at 737 nm wavelength are critically coupled to a waveguide

<sup>1</sup>Department of Physics, Harvard University, Cambridge, MA, USA. <sup>2</sup>John A. Paulson School of Engineering and Applied Sciences, Harvard University, Cambridge, MA, USA. <sup>3</sup>Department of Chemistry and Chemical Biology, Harvard University, Cambridge, MA, USA. <sup>4</sup>Research Laboratory of Electronics, MIT, Cambridge, MA, USA. ✉e-mail: lukin@physics.harvard.edu

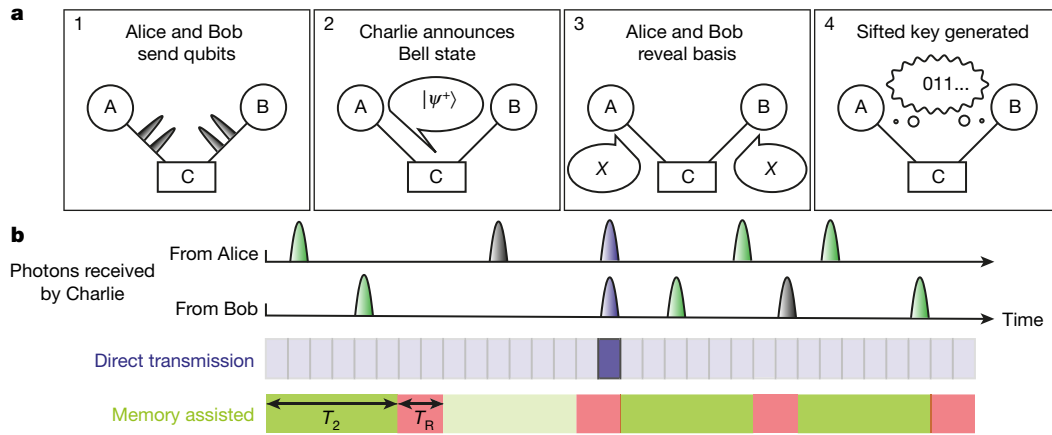


**Fig. 1 | Concept of memory-enhanced quantum communication.**

**a**, Quantum communication protocol. Alice and Bob (A and B, respectively) send qubits encoded in photons to a measurement device (Charlie; C) in between them. Charlie performs a BSM and announces the result. After verifying in which rounds Alice and Bob sent qubits in compatible bases, a sifted key is generated. **b**, Illustration of memory-enhanced protocol. Photons arrive at Charlie from A and B at random times over a lossy channel, and are

unlikely to arrive simultaneously (rare success indicated in purple), leading to a low BSM success rate for direct transmission. Despite overhead time  $T_R$  associated with operating a quantum memory (red), a BSM can be performed between photons that arrive at Charlie within memory coherence time  $T_2$ , leading to higher success rates (green). BSM successes and failures are denoted by dark and light shaded windows respectively for both approaches.

and adiabatically transferred into a single-mode optical fibre<sup>18</sup> that is routed to superconducting nanowire single-photon detectors, yielding a full system detection efficiency of about 85% (Methods). The device is placed inside a dilution refrigerator, resulting in an electronic spin quantum memory<sup>19</sup> time  $T_2 > 0.2$  ms at temperatures below 300 mK.

The operating principle of the SiV–cavity-based spin–photon interface is illustrated in Fig. 2. Spin-dependent modulation of the cavity reflection at incident probe frequency  $f_0$  (Fig. 2b) results in the direct observation of electron spin quantum jumps (Fig. 2c, inset), enabling non-destructive single-shot readout of the spin state (Fig. 2c) in 30  $\mu$ s with fidelity  $F = 0.9998^{+0.0002}_{-0.0003}$ . Coherent control of the SiV spin qubit ( $f_0 \approx 12$  GHz) is accomplished using microwave fields delivered via an on-chip gold coplanar waveguide<sup>19</sup>. We utilize both optical readout and microwave control to perform projective feedback-based initialization of the SiV spin into the  $|\downarrow\rangle$  state with a fidelity of  $F = 0.998 \pm 0.001$ . Spin-dependent cavity reflection also enables quantum logic operations between an incoming photonic time-bin qubit, defined by a phase-coherent pair of attenuated laser pulses, and the spin memory<sup>19,29</sup>. We characterize this by using the protocol illustrated in Fig. 2d to generate the spin–photon entangled state  $(|\uparrow\rangle + |\downarrow\rangle)/\sqrt{2}$  conditioned on successful reflection of an incoming single photon with overall heralding efficiency  $\eta = 0.423 \pm 0.004$  (Methods). Here,  $|\uparrow\rangle$  and  $|\downarrow\rangle$  denote respectively the presence of a photon in an early or a late time-bin, separated by  $\delta t = 142$  ns. We characterize the entangled state by performing measurements in the joint spin–photon ZZ and XX bases (Fig. 2e), implementing local operations on the reflected photonic qubit with a time-delay interferometer (TDI; Fig. 2a, dashed box). By lowering the average number of photons  $\langle n \rangle_m$  incident on the device during the SiV memory time, we reduce the possibility that an additional photon reaches the cavity without being subsequently detected, enabling high spin–photon gate fidelities for small  $\langle n \rangle_m$  (Fig. 2f). For  $\langle n \rangle_m = 0.002$  we measure a lower bound on the fidelity<sup>19</sup> of the spin–photon entangled state of  $F \geq 0.944 \pm 0.008$ , primarily limited by residual reflections from the  $|\downarrow\rangle$  state.

### Asynchronous BSMs

This spin–photon logic gate can be directly used to herald the storage of an incoming photonic qubit by interferometrically measuring the reflected photon in the X basis<sup>19</sup>. To implement a memory-assisted BSM, we extend this protocol to accommodate a total of  $N$  photonic qubit time-bins within a single initialization of the memory (Fig. 3a). Each

individual time-bin qubit is encoded in the relative amplitudes and phases of a pair of neighbouring pulses separated by  $\delta t$ . Detection of a reflected photon heralds the arrival of the photonic qubit formed by the two interfering pulses without revealing its state<sup>19</sup>. Two such heralding events, combined with subsequent spin-state readout in the X basis, constitute a successful BSM on the incident photons. This can be understood without loss of generality by restricting input photonic states to be encoded in the relative phase  $\phi$  between neighbouring pulses with equal amplitude:  $(|e\rangle + e^{i\phi}|l\rangle)/\sqrt{2}$  (Fig. 3b). Detection of the first reflected photon in the X basis teleports its quantum state onto the spin, resulting in the state  $(|\uparrow\rangle + m_1 e^{i\phi}|\downarrow\rangle)/\sqrt{2}$ , where  $m_1 = \pm 1$  depending on which detector registers the photon<sup>19</sup>. Detection of a second photon at a later time within the electron spin  $T_2$  results in the spin state  $(|\uparrow\rangle + m_1 m_2 e^{i(\phi_1 + \phi_2)}|\downarrow\rangle)/\sqrt{2}$ . The phase of this spin state depends only on the sum of the incoming phases and the product of their detection outcomes, but not the individual phases themselves. As a result, if the photons were sent with phases that meet the condition  $\phi_1 + \phi_2 \in \{0, \pi\}$ , a final measurement of the spin in the X basis ( $m_3 = \pm 1$ ) completes an asynchronous BSM, distinguishing two of the four Bell states based on the total parity  $m_1 m_2 m_3 = \pm 1$  (Supplementary Information, Extended Data Table 3).

This approach can be directly applied to generate a correlated bit-string within the protocol illustrated in Fig. 1a. We analyse the system performance by characterizing the overall quantum-bit error rate (QBER)<sup>4,22</sup> for  $N = 124$  photonic qubits per memory initialization. We use several random bit strings of incoming photons from  $\{|\pm x\rangle, |\pm y\rangle\}$  and observe strong correlations between the resulting BSM outcome and the initial combination of input qubits for both bases (Fig. 3c). Using this method, we estimate the average QBER to be  $E = 0.116 \pm 0.002$  for all combinations of random bit strings measured, significantly ( $P < 10^{-20}$ ) below the limit of  $E_{\text{ia}} = 0.146$ , which could provide security against individual attacks<sup>4</sup> (note that the measured error rate is also well below the minimum average QBER<sup>22</sup> of  $E_{\text{lo}} = 0.125$  achievable using a linear optics BSM with weak coherent pulse inputs, see Supplementary Information). In our experiment, the QBER is affected by technical imperfections in the preparation of random strings of photonic qubits. We find specific periodic patterns of photonic qubits to be less prone to these effects, resulting in a QBER as low as  $E = 0.097 \pm 0.006$ , which falls within the threshold corresponding to unconditional security<sup>3</sup> of  $E_u = 0.110$  with a confidence level of 0.986 (Supplementary Information). We further verify security by testing the Bell-CHSH inequality<sup>14</sup>

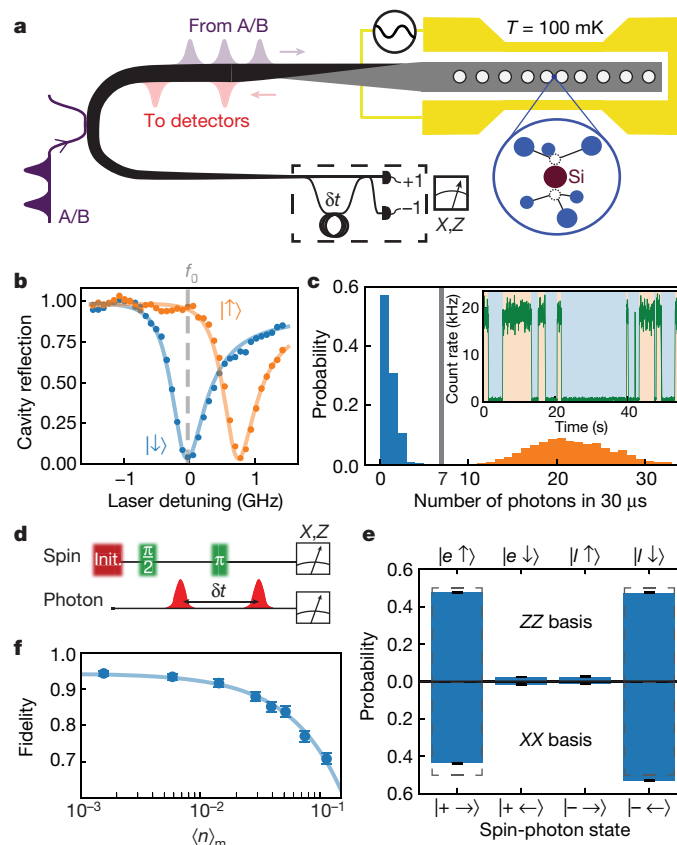


**Fig. 2 | Realization of heralded spin-photon gate.** **a**, Schematic of memory-assisted implementation of Charlie's measurement device, consisting of a diamond nanophotonic resonator (grey) containing SiV quantum memory (blue circle) with an integrated microwave stripline (yellow). Weak pulses derived from a single laser simulate incoming photons from Alice and Bob (purple). Reflected photons (red) are detected in a heralding set-up (dashed box). **b**, Reflection spectrum of the memory node, showing spin-dependent device reflectivity. **c**, Histogram of detected photon numbers during a 30-μs laser pulse, enabling single-shot readout based on a threshold of 7 photons.

Inset, electron spin quantum jumps under weak illumination. **d**, Schematic of spin-photon quantum logic operation used to generate and verify spin-photon entangled state. **e**, Characterization of resulting spin-photon correlations in the ZZ and XX bases. Dashed bars show ideal values. **f**, Measured spin-photon entanglement fidelity as a function of  $\langle n \rangle_m$ , the average incident photon number during each initialization of the memory. Error bars, 68% confidence interval (c.i.). See main text and Methods for details of nomenclature used in this figure.

using input states from four different bases, each separated by an angle of  $45^\circ$  (Supplementary Information). We find that the correlations between input photons (Fig. 3d) violate the Bell-CHSH inequality  $S_{\pm} \leq 2$ , observing  $S_+ = 2.21 \pm 0.04$  and  $S_- = 2.19 \pm 0.04$  for positive and negative BSM parity results, respectively. This result demonstrates that this device can be used for quantum communication that is secured by Bell's theorem.

### Benchmarking quantum memory advantage

To benchmark the performance of memory-assisted quantum communication, we model an effective channel loss by reducing the mean photon number  $\langle n \rangle_p$  incident on the device per photonic qubit. Assuming that Alice and Bob emit roughly one photon per qubit, this yields an effective channel transmission probability  $p_{A \rightarrow B} = \langle n \rangle_p^2$ , resulting in the maximal distilled key rate  $R_{\max}$  per channel use for the direct-transmission approach<sup>22</sup>, given by the red line in Fig. 4. We emphasize that this is a theoretical upper bound for a linear-optics-based BSM, assuming ideal single-photon sources and detectors and balanced basis choices. The measured sifted key rates of the memory-based device are plotted as open circles in Fig. 4. Owing to the high overall heralding efficiency and the large number of photonic qubits per memory time (up to  $N = 504$ ), the memory-assisted sifted key rate exceeds the capability of a linear-optics-based BSM device by a factor of  $78.4 \pm 0.7$  at an effective channel loss of about 88 dB.

In practice, errors introduced by the quantum memory node could leak information to the environment, reducing the quality and potential security of the sifted key<sup>3</sup>. A shorter secure key can be recovered from a sifted key with finite QBER using classical error correction and privacy amplification techniques. The fraction of distilled bits  $r_s$  that can be secure against individual attacks rapidly diminishes<sup>4</sup> as the QBER approaches  $E_{\text{ia}} = 0.147$ . For each value of the effective channel loss, we estimate the QBER and use it to compute  $r_s$ , enabling extraction of distilled key rates  $R_s$ , plotted in black in Fig. 4. Even after error correction, we find that the memory-assisted distilled key rate outperforms the ideal limit for the corresponding direct-transmission implementation by a factor of up to  $R_s/R_{\max} = 4.1 \pm 0.5$  ( $\pm 0.1$  systematic uncertainty, for  $N = 124$ ). We further find that this rate also exceeds the fundamental bound on repeaterless communication<sup>8</sup>  $R_s \leq 1.44 p_{A \rightarrow B}$  with a statistical confidence level of 99.2% (with  $+0.2\%$ / $-0.3\%$  systematic uncertainty, see Methods). Despite experimental overhead time associated with operating the device ( $T_R$  in Fig. 1b), the performance of the memory-assisted BSM node (for  $N = 248$ ) is competitive with an ideal unassisted system running at a 4 MHz average clock rate (Methods).

### Outlook

These experiments demonstrate a form of quantum advantage allowed by memory-based communication nodes and represent a crucial step towards realizing functional quantum repeaters. Several important



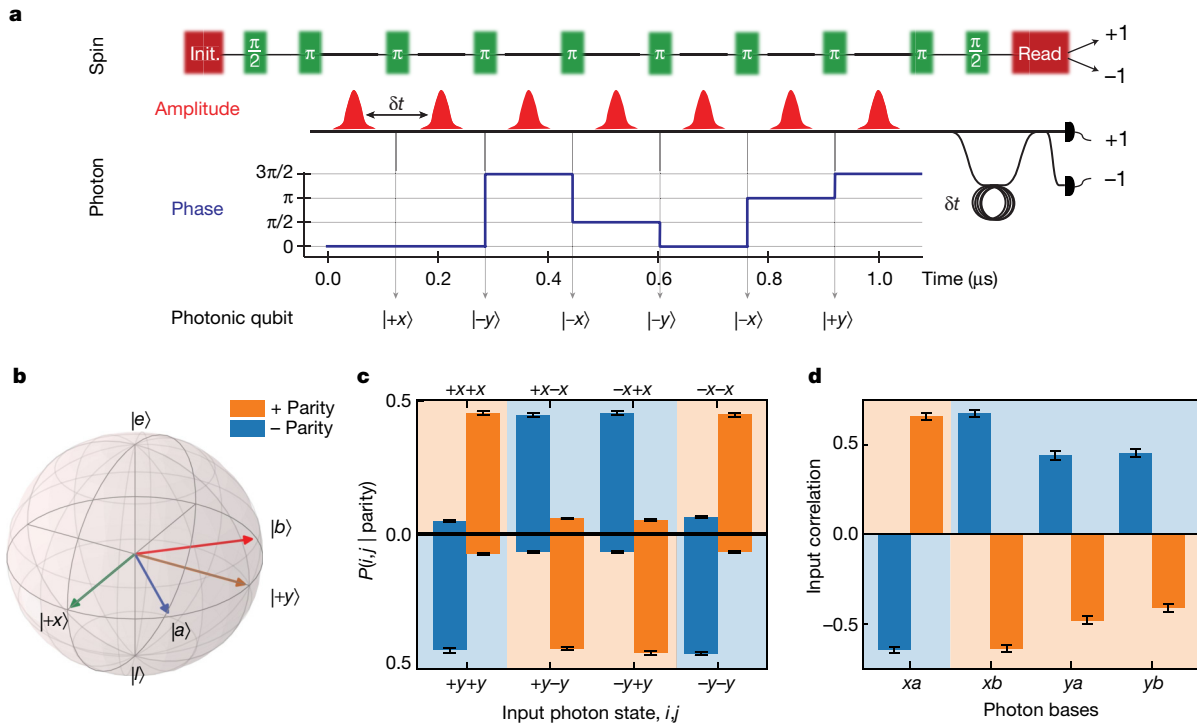


**Fig. 3 | Asynchronous BSMs using quantum memory.** **a**, Example sequence with  $N = 6$  photonic qubits sent in a single memory time. Microwave  $\pi$  pulses (green) are interleaved with incoming optical pulses. Photons have fixed amplitude (red) and qubits are defined by the relative phases between subsequent pulses (blue). **b**, Bloch sphere representation of input photonic time-bin qubits used for characterization. **c**, Characterization of asynchronous

BSM. Shown are conditional probabilities for Alice and Bob to have sent input states ( $i, j$ ) given a particular parity outcome for input states in the  $X$  (top) and  $Y$  (bottom) bases. **d**, Bell test using the CHSH inequality. Conditioned on the BSM outcome, the average correlation between input photons is plotted for each pair of bases used (Supplementary Information). Shaded backgrounds denote the expected parity. Error bars, 68% c.i. See main text for details.

technical improvements will be necessary to apply this advance to practical long-distance quantum communication. First, this protocol must be implemented using truly independent, distant communicating parties. Second, frequency conversion from telecommunications wavelengths to 737 nm, as well as low-loss optical elements used for routing photons to and from the memory node, will need to be incorporated. Last, rapid generation of provably secure keys will require implementation of decoy-state protocols<sup>26</sup>, biased bases<sup>27</sup> and finite-key error analyses<sup>28</sup>, all compatible with the present approach. With these improvements, our approach is well-suited for deployment in real-world settings. It does not require phase stabilization of long-distance links and operates efficiently in the relevant regime of  $p_{A \rightarrow B} \approx 70$  dB, corresponding to about 350 km of telecommunications fibre. Additionally, a single device can be used at the centre of a star network topology<sup>30</sup>, enabling quantum communication between several parties beyond the metropolitan scale.

Furthermore, the present approach could be extended along several directions. The use of long-lived  $^{13}\text{C}$  nuclear spin qubits could eliminate the need to operate at low total  $\langle n \rangle_m$  and would provide longer storage times, potentially enabling 100-fold enhancement of BSM success rates<sup>15,19</sup>. Recently implemented strain-tuning capabilities<sup>31</sup> should allow for operation of many quantum nodes at a common network frequency. Also, unlike linear-optics-based alternatives<sup>24</sup>, the approach presented here could be extended to implement the full repeater protocol, enabling a polynomial scaling of the communication rate with distance<sup>9</sup>. Last, the demonstrated multi-photon gate operations could also be adapted to engineer large cluster-states of entangled photons<sup>32</sup>, which can be used for rapid quantum communication<sup>33</sup>. Implementation of these techniques could enable the realization and application of scalable quantum networks' beyond quantum key distribution, ranging

from non-local quantum metrology<sup>20</sup> to modular quantum computing architectures<sup>21</sup>.

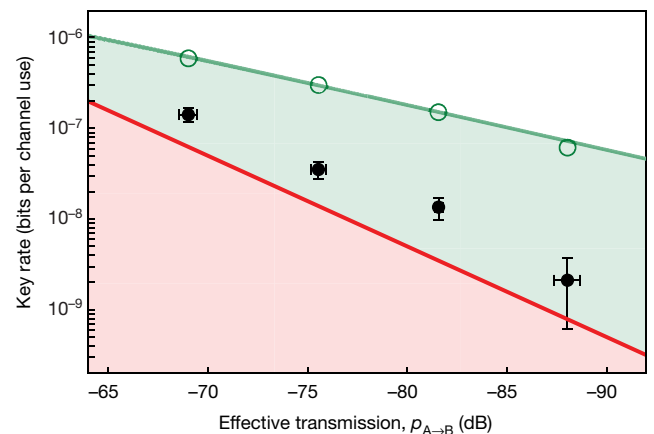


**Fig. 4 | Performance of memory-assisted quantum communication.** Shown is a log-log plot of key rate in bits per channel use versus effective channel transmission ( $p_{A \rightarrow B} = \langle n \rangle_p^2$ , where  $\langle n \rangle_p$  is the average number of photons incident on the measurement device per photonic qubit). Red line, theoretical maximum for loss-equivalent direct-transmission experiment. Green open circles, experimentally measured sifted key rate (green line is the expected rate). To ensure optimal operation of the memory,  $\langle n \rangle_m = \langle n \rangle_p N \approx 0.02$  is kept constant (Methods). From left to right, points correspond to  $N = \{60, 124, 248, 504\}$ . Black filled circles, distilled key rates  $R_s$  using memory device. Vertical error bars, 68% c.i.; horizontal error bars, s.d. of the systematic power fluctuations.

## Online content

Any methods, additional references, Nature Research reporting summaries, source data, extended data, supplementary information, acknowledgements, peer review information; details of author contributions and competing interests; and statements of data and code availability are available at <https://doi.org/10.1038/s41586-020-2103-5>.

1. Kimble, H. J. The quantum internet. *Nature* **453**, 1023–1030 (2008).
2. Bennett, C. H. & Brassard, G. Quantum cryptography: public key distribution and coin tossing. In *Proc. Int. Conf. on Computers, Systems and Signal Processing* Vol. 1, 175–179 (IEEE Computer Society, IEEE Circuits and Systems Society, Indian Institute of Science, 1984).
3. Shor, P. W. & Preskill, J. Simple proof of security of the BB84 quantum key distribution protocol. *Phys. Rev. Lett.* **85**, 441–444 (2000).
4. Gisin, N., Ribordy, G., Tittel, W. & Zbinden, H. Quantum cryptography. *Rev. Mod. Phys.* **74**, 145–195 (2002).
5. Boaron, A. et al. Secure quantum key distribution over 421 km of optical fiber. *Phys. Rev. Lett.* **121**, 190502 (2018).
6. Zhang, Q., Xu, F., Chen, Y.-A., Peng, C.-Z. & Pan, J.-W. Large scale quantum key distribution: challenges and solutions. *Opt. Express* **26**, 24260–24273 (2018).
7. Pirandola, S. et al. Advances in quantum cryptography. Preprint at <http://arxiv.org/abs/1906.01645> (2019).
8. Pirandola, S., Laurenza, R., Ottaviani, C. & Banchi, L. Fundamental limits of repeaterless quantum communications. *Nat. Commun.* **8**, 15043 (2017).
9. Briegel, H.-J., Dür, W., Cirac, J. I. & Zoller, P. Quantum repeaters: the role of imperfect local operations in quantum communication. *Phys. Rev. Lett.* **81**, 5932–5935 (1998).
10. Chou, C.-W. et al. Functional quantum nodes for entanglement distribution over scalable quantum networks. *Science* **316**, 1316–1320 (2007).
11. Yuan, Z.-S. et al. Experimental demonstration of a BDCZ quantum repeater node. *Nature* **454**, 1098–1101 (2008).
12. Gao, W. B., Fallahi, P., Togan, E., Miguel-Sanchez, J. & Imamoglu, A. Observation of entanglement between a quantum dot spin and a single photon. *Nature* **491**, 426–430 (2012).
13. Reiserer, A. & Rempe, G. Cavity-based quantum networks with single atoms and optical photons. *Rev. Mod. Phys.* **87**, 1379–1418 (2015).
14. Hensen, B. et al. Loophole-free Bell inequality violation using electron spins separated by 1.3 kilometres. *Nature* **526**, 682–686 (2015).
15. Kalb, N. et al. Entanglement distillation between solid-state quantum network nodes. *Science* **356**, 928–932 (2017).
16. Kaneda, F., Xu, F., Chapman, J. & Kwiat, P. G. Quantum-memory-assisted multi-photon generation for efficient quantum information processing. *Optica* **4**, 1034–1037 (2017).
17. Evans, R. E. et al. Photon-mediated interactions between quantum emitters in a diamond nanocavity. *Science* **362**, 662–665 (2018).
18. Burek, M. J. et al. Fiber-coupled diamond quantum nanophotonic interface. *Phys. Rev. Appl.* **8**, 024026 (2017).
19. Nguyen, C. T. et al. Quantum network nodes based on diamond qubits with an efficient nanophotonic interface. *Phys. Rev. Lett.* **123**, 183602 (2019).
20. Khabiboulline, E. T., Borregaard, J., De Greve, K. & Lukin, M. D. Optical interferometry with quantum networks. *Phys. Rev. Lett.* **123**, 070504 (2019).
21. Monroe, C. et al. Large-scale modular quantum-computer architecture with atomic memory and photonic interconnects. *Phys. Rev. A* **89**, 022317 (2014).
22. Lo, H.-K., Curty, M. & Qi, B. Measurement-device-independent quantum key distribution. *Phys. Rev. Lett.* **108**, 130503 (2012).
23. Braunstein, S. L. & Pirandola, S. Side-channel-free quantum key distribution. *Phys. Rev. Lett.* **108**, 130502 (2012).
24. Minder, M. et al. Experimental quantum key distribution beyond the repeaterless secret key capacity. *Nat. Photon.* **13**, 334–338 (2019).
25. Panayi, C., Razavi, M., Ma, X. & Lütkenhaus, N. Memory-assisted measurement-device-independent quantum key distribution. *New J. Phys.* **16**, 043005 (2014).
26. Lo, H.-K., Ma, X. & Chen, K. Decoy state quantum key distribution. *Phys. Rev. Lett.* **94**, 230504 (2005).
27. Lo, H.-K., Chau, H. F. & Ardehali, M. Efficient quantum key distribution scheme and a proof of its unconditional security. *J. Cryptol.* **18**, 133–165 (2005).
28. Curty, M. et al. Finite-key analysis for measurement-device-independent quantum key distribution. *Nat. Commun.* **5**, 3732 (2014).
29. Duan, L.-M. & Kimble, H. J. Scalable photonic quantum computation through cavity-assisted interactions. *Phys. Rev. Lett.* **92**, 127902 (2004).
30. Biham, E., Huttner, B. & Mor, T. Quantum cryptographic network based on quantum memories. *Phys. Rev. A* **54**, 2651–2658 (1996).
31. Machielse, B. et al. Quantum interference of electromechanically stabilized emitters in nanophotonic devices. *Phys. Rev. X* **9**, 031022 (2019).
32. Raussendorf, R. & Briegel, H. J. A one-way quantum computer. *Phys. Rev. Lett.* **86**, 5188–5191 (2001).
33. Borregaard, J. et al. One-way quantum repeater based on near-deterministic photon-emitter interfaces. Preprint at <http://arxiv.org/abs/1907.05101> (2019).

**Publisher's note** Springer Nature remains neutral with regard to jurisdictional claims in published maps and institutional affiliations.

© The Author(s), under exclusive licence to Springer Nature Limited 2020

## Methods

### Experimental set-up

We perform all measurements in a dilution refrigerator (BlueFors BF-LD250) with a base temperature of 20 mK. The dilution refrigerator is equipped with a superconducting vector magnet (American Magnets Inc. 6-1-1 T), a home-built free-space wide-field microscope with a cryogenic objective (Attocube LT-APO-VISIR), piezo positioners (Attocube ANPx101 and ANPx311 series), and fibre and microwave feedthroughs. Tuning of the nanocavity resonance is performed using a gas condensation technique<sup>17</sup>. The SiV–cavity system is optically interrogated through the fibre network without any free-space optics<sup>19</sup>. The operating temperature of the memory node during the BSM measurements was 100–300 mK. We note that similar performance at higher temperatures should be feasible in future experiments by using recent developments with heavier group-IV colour centres<sup>34</sup> or highly strained SiV centres<sup>35</sup>. Additional details about the experimental set-up and device fabrication<sup>18,31,36,37</sup> for millikelvin nanophotonic cavity quantum electrodynamic experiments with SiV centres are thoroughly described elsewhere<sup>38</sup>.

### Nanophotonic quantum memory

A spectrum of the SiV–cavity system at large detuning (248 GHz) allows us to measure the cavity linewidth  $\kappa = 21.6 \pm 1.3$  GHz (Extended Data Fig. 2a, blue curve) and natural SiV linewidth  $\gamma = 0.123 \pm 0.010$  GHz (Extended Data Fig. 2a, red curve). We find spectral diffusion of the SiV optical frequency to be much smaller than  $\gamma$  on minute timescales with an excitation photon flux of less than 1 MHz. Next, we estimate the single-photon Rabi frequency,  $g$ , using the cavity reflection spectrum for zero atom–cavity detuning, shown in red in Extended Data Fig. 2a. For a resonant atom–cavity system probed in reflection from a single port with cavity–waveguide coupling  $\kappa_{wg}$ , the cavity reflection coefficient<sup>13</sup> as a function of probe detuning  $\Delta_c$  is given by

$$r(\Delta_c) = \frac{i\Delta_c + \frac{g^2}{i\Delta_c + \frac{\gamma}{2}} - \kappa_{wg} + \frac{\kappa}{2}}{i\Delta_c + \frac{g^2}{i\Delta_c + \frac{\gamma}{2}} + \frac{\kappa}{2}} \quad (1)$$

By fitting  $|r(\Delta_c)|^2$  using known values of  $\kappa$  and  $\gamma$ , we obtain the solid red curve in Extended Data Fig. 2a, which corresponds to a single-photon Rabi frequency  $g = 8.38 \pm 0.05$  GHz, yielding the estimated cooperativity  $C = \frac{4g^2}{\kappa\gamma} = 105 \pm 11$ .

### Microwave control

We use resonant microwave pulses delivered via an on-chip coplanar waveguide to coherently control the quantum memory<sup>19,38</sup>. We measure the spectrum of the spin-qubit transition by applying a weak, 10- $\mu$ s-long microwave pulse of variable frequency, observing the optically detected magnetic resonance spectrum presented in Extended Data Fig. 3a. We note that the spin-qubit transition is split by the presence of a nearby <sup>13</sup>C. While coherent control techniques can be employed to use the <sup>13</sup>C as an additional qubit<sup>19,38</sup>, we do not control or initialize it in this experiment. Instead, we drive the electron spin with strong microwave pulses at a frequency  $f_Q$  such that both <sup>13</sup>C-state-specific transitions are addressed equally. This also mitigates slow spectral diffusion of the microwave transition<sup>38</sup> of ~100 kHz.

After fixing the microwave frequency at  $f_Q$ , we vary the length of this drive pulse ( $\tau_R$  in Extended Data Fig. 3b) and observe full-contrast Rabi oscillations. We choose a  $\pi$  time of 32 ns in the experiments in the main text, which is a compromise between two factors: (1) it is sufficiently fast such that we can temporally multiplex between 2 and 4 time-bin qubits around each microwave  $\pi$  pulse and (2) it is sufficiently weak to minimize heating-related effects from high microwave currents in resistive gold coplanar waveguide.

With known  $\pi$  time, we measure the coherence time of the SiV spin qubit under an XY8-1 dynamical decoupling sequence to exceed 200  $\mu$ s (Extended Data Fig. 3c). In the main experiment we use decoupling sequences with more  $\pi$  pulses. As an example, Extended Data Fig. 3d shows the population in the  $|\uparrow\rangle$  state after the XY8-8 decoupling sequence (total  $N_\pi = 64$   $\pi$  pulses) as a function of  $\tau$ , half of the inter-pulse spacing. For BSM experiments, this inter-pulse spacing,  $2\tau$ , is fixed and is matched to the time-bin interval  $\delta t$ . While at some times (for example,  $\tau = 64.5$  ns) there is a loss of coherence due to entanglement with the nearby <sup>13</sup>C, at  $2\tau = 142$  ns we are decoupled from this <sup>13</sup>C and can maintain a high degree of spin coherence. Thus we chose the time-bin spacing to be 142 ns. The spin coherence at  $2\tau = 142$  ns is plotted as a function of  $N_\pi$  in Extended Data Fig. 3e, and decreases for large  $N_\pi$ , primarily owing to heating-related effects<sup>19</sup>.

### Fibre network

The schematic of the fibre network used to deliver optical pulses to and collect reflected photons from the nanophotonic memory device is shown in Extended Data Fig. 1b. Photons are routed through the lossy (1%) port of a 99:1 fibre beamsplitter to the nanophotonic device. We note that for practical implementation of memory-assisted quantum communication, an efficient optical switch or circulator should be used instead. In this experiment, since we focus on benchmarking the performance of the memory device itself, the loss introduced by this beamsplitter is incorporated into the estimated channel loss. Reflected photons are collected and routed back through the efficient (99%) port of the fibre beamsplitter and are sent to the TDI in the heralding set-up. The outputs of the TDI are sent back into the dilution refrigerator and directly coupled to superconducting nanowire single photon detectors (SNSPDs, PhotonSpot), which are mounted at the 1 kelvin plate of the dilution refrigerator and are coated with dielectrics to optimize detection efficiency exactly at 737 nm.

The total heralding efficiency  $\eta$  of the memory node is an important parameter since it directly affects the performance of the BSM for quantum communication experiments. One of the contributing factors is the detection quantum efficiency (QE) of the fibre-coupled SNSPDs. To estimate it, we compare the performance of the SNSPDs to the specifications of calibrated conventional avalanche photodiode single-photon counters (Laser Components COUNT-10C-FC). The estimated QEs of the SNSPDs with this method are as close to unity as we can verify. Additionally, we measure <1% reflection from the fibre–SNSPD interface, which typically is the dominant contribution to the reduction of QE in these devices. Thus we assume the lower bound of the QE of the SNSPDs to be  $\eta_{QE} = 0.99$  for the rest of this section. Of course, this estimation is subject to additional systematic errors. However, the actual QE of these detectors would be a common factor (and thus drop out) in a comparison between any two physical quantum communication systems.

Here we use two different approaches to estimate  $\eta$ . We first measure the most dominant loss, which arises from the average reflectivity of the critically coupled nanophotonic cavity (Fig. 2b). While the  $|\uparrow\rangle$  state is highly reflecting (94.4%), the  $|\downarrow\rangle$  state reflects only 4.1% of incident photons, leading to an average device reflectivity of  $\eta_{sp} = 0.493$ .

In method (1), we compare the input power photodiode M1 with that of photodiode MC (Extended Data Fig. 1b). This estimates a lower bound on the tapered-fibre diamond waveguide coupling efficiency of  $\eta_c = 0.930 \pm 0.017$ . This error bar arises from uncertainty due to photodiode noise and does not include systematic photodiode calibration uncertainty. However, we note that if the tapered fibre is replaced by a silver-coated fibre-based retroreflector, this calibration technique extracts a coupling efficiency of  $\eta_c^{cal} \approx 0.98$ , which is consistent with the expected reflectivity from such a retroreflector. We independently calibrate the efficiency through the 99:1 fibre beamsplitter and the TDI to be  $\eta_t = 0.934$ . This gives us our first estimate on the overall heralding efficiency  $\eta = \eta_{sp}\eta_c\eta_t\eta_{QE} = 0.425 \pm 0.008$ .

In method (2), during the experiment we compare the reflected counts from the highly reflecting ( $|\uparrow\rangle$ ) spin-state measured on the SNSPDs with the counts on an avalanche photodiode single photon counting module (M2 in Extended Data Fig. 1b) which has a calibrated efficiency of  $\sim 0.7$  relative to the SNSPDs. From this measurement, we estimate an overall efficiency of fibre–diamond coupling, as well as transmission through all relevant splices and beamsplitters, of  $\eta_c\eta_r = 0.864 \pm 0.010$ . This error bar arises from shot noise on the single photon detectors. Overall, this gives us a consistent estimate of  $\eta = \eta_{sp}\eta_c\eta_r\eta_{QE} = 0.422 \pm 0.005$ . Methods (1) and (2), which each have independent systematic uncertainties associated with imperfect photodetector calibrations, are consistent to within a small residual systematic uncertainty, which is noted in the text where appropriate.

## Quantum communication experiment

An asynchronous BSM (Fig. 3a) relies on (1) precise timing of the arrival of optical pulses (corresponding to photonic qubits<sup>39,40</sup> from Alice and Bob) with microwave control pulses on the quantum memory, and (2) interferometrically stable rotations on reflected time-bin qubits for successful heralding, described in Extended Data Fig. 4.

In order to accomplish (1), all equipment used for generation of microwave and optical fields is synchronized by a single device (National Instruments HSDIO, Extended Data Fig. 1a) with programming described in Extended Data Tables 1, 2.

In order to accomplish (2), we use a single, narrow linewidth ( $<50$  kHz) Ti:sapphire laser (M Squared SolisTiS-2000-PSX-XF, Extended Data Fig. 1b) both for generating photonic qubits and locking the TDI used to herald their arrival. In the experiment, photonic qubits are reflected from the device, sent into the TDI, and detected on the SNSPDs. All detected photons are processed digitally on a field-programmable gate array (FPGA, Extended Data Fig. 1a), and the arrival times of these heralding signals are recorded on a time-tagger (TT, Extended Data Fig. 1a), and constitute one bit of information of the BSM ( $m_1$  or  $m_2$ ). At the end of the experiment, a 30- $\mu$ s pulse from the readout path is reflected off the device, and photons are counted in order to determine the spin state ( $m_3$ ) depending on the threshold shown in Fig. 2c.

To minimize thermal drift of the TDI, it is mounted on a thermally weighted aluminium breadboard, placed in a polyurethane-foam-lined and sand-filled briefcase, and secured with glue to ensure passive stability on the minute timescale. We halt the experiment and actively lock the interferometer to the sensitive  $Y$ -quadrature every  $\sim 200$  ms by changing the length of the roughly 28-m-long (142 ns) delay line with a cylindrical piezo. In order to use the TDI for  $X$ -measurements of the reflected qubits, we apply a frequency shift of 1.8 MHz using the qubit AOM, which is 1/4 of the free-spectral range of the TDI. Since the nanophotonic cavity, the TDI and the SNSPDs are all polarization sensitive, we use various fibre-based polarization controllers (Extended Data Fig. 1b). All fibres in the network are covered with aluminium foil to prevent thermal polarization drifts. This results in an interference visibility of the TDI of  $>99\%$  that is stable for several days without any intervention with laboratory temperature and humidity variations of  $\pm 1^\circ\text{C}$  and  $\pm 5\%$ , respectively.

In order to achieve high-fidelity operations, we have to ensure that the laser frequency (which is not locked) is resonant with the SiV frequency  $f_0$  (which is subject to the spectral diffusion<sup>38</sup>). To do that, we implement a so-called preselection procedure, described in Extended Data Tables 1, 2 and Extended Data Fig. 1a. First, the SiV spin state is initialized by performing a projective measurement and applying microwave feedback. During each projective readout, the reflected counts are compared with two thresholds: a ‘readout’ threshold of 7 photons (used only to record  $m_3$ ), and a ‘status’ threshold of 3 photons. The status trigger is used to prevent the experiment from running in cases when the laser is no longer on resonance with  $f_0$ , or if the SiV has ionized to an optically inactive charge state. The duty cycle of the status trigger is externally monitored, and is used to temporarily abort

the experiment and run an automated re-lock procedure that locates and sets the laser to the new frequency  $f_0$ , reinitializing the SiV charge state with a 520 nm laser pulse if necessary. This protocol enables fully automated operation at high fidelities (low QBER) for several days without human intervention.

## Optimal parameters for asynchronous BSMs

We minimize the experimentally extracted QBER for the asynchronous BSM to optimize the performance of the memory node. One major factor contributing to QBER is the scattering of a third photon that is not detected, owing to the finite heralding efficiency  $\eta = 0.423 \pm 0.04$ . This is shown in Fig. 2f, where the fidelity of the spin–photon entangled state diminishes for  $\langle n \rangle_m \gtrsim 0.02$ . At the same time, we would like to work at the maximum possible  $\langle n \rangle_m$  in order to maximize the data rate to get enough statistics to extract QBER (and in the quantum communication setting, efficiently generate a key).

To increase the key generation rate per channel use, one can also fit many photonic qubits within each initialization of the memory. In practice, there are two physical constraints: (1) the bandwidth of the SiV–photon interface; and (2) the coherence time of the memory. We find that one can satisfy (1) at a bandwidth of roughly 50 MHz with no measurable infidelity. For shorter optical pulses ( $<10$  ns), the spin–photon gate fidelity is reduced. In principle, the SiV–photon bandwidth can be increased by reducing the atom–cavity detuning (here  $\sim 60$  GHz) at the expense of having to operate at higher magnetic fields where microwave qubit manipulation is not as convenient<sup>38</sup>.

Even with just an XY8-1 decoupling sequence (number of  $\pi$  pulses  $N_\pi = 8$ ), the coherence time of the SiV is longer than 200  $\mu$ s (Extended Data Fig. 3c) and can be prolonged to the millisecond range with longer pulse sequences<sup>19</sup>. Unfortunately, to satisfy the bandwidth criterion (1) above, and to drive both hyperfine transitions (Extended Data Fig. 3a), we must use short (32-ns-long)  $\pi$  pulses, which already cause additional decoherence from ohmic heating<sup>38</sup> at  $N_\pi = 64$  (Extended Data Fig. 3e). Because of this, we limit the pulse sequences to a maximum  $N_\pi = 128$ , and only use up to  $\sim 20$   $\mu$ s of the memory time. One solution would be to switch to superconducting microwave delivery. Alternatively, we could use a larger value of  $\tau$  to allow the device to cool down between pulses<sup>38</sup> at the expense of having to stabilize a TDI of larger  $\delta t$ . Working at larger  $\delta t$  would also enable temporal multiplexing by fitting multiple time-bin qubits per free-precession interval. In fact, with  $2\tau = 142$  ns, even given constraint (1) and the finite  $\pi$  time, we can fit up to 4 optical pulses per free-precession window, enabling a total number of photonic qubits of up to  $N = 504$  for an  $N_\pi$  of only 128.

In benchmarking the asynchronous BSM for quantum communication, we optimize the parameters  $\langle n \rangle_m$  and  $N$  to maximize our enhancement over the direct-transmission approach. The enhancement is a combination of both increasing  $N$  and reducing the QBER, since a large QBER results in a small distilled key fraction  $r_s$ . As described in the main text, the effective loss can be associated with  $\langle n \rangle_p$ , which is the average number of photons per photonic qubit arriving at the device, and is given straightforwardly by  $\langle n \rangle_p = \langle n \rangle_m / N$ . The most straightforward way to sweep the loss is to keep the experimental sequence the same (fixed  $N$ ) and vary the overall power, which changes  $\langle n \rangle_m$ . The results of such a sweep are shown in Extended Data Fig. 5a, b. For larger  $\langle n \rangle_m$  (corresponding to lower effective channel losses), the errors associated with scattering an additional photon reduce the performance of the memory device.

Owing to these considerations, we work at roughly  $\langle n \rangle_m \lesssim 0.02$  for experiments reported in the main text and shown in Figs. 3 and 4, below which the performance does not improve substantially. At this value, we obtain BSM successes at a rate of roughly 0.1 Hz. By fixing  $\langle n \rangle_m$  and increasing  $N$ , we maintain a tolerable BSM success rate while increasing the effective channel loss. Eventually, as demonstrated in Extended Data Fig. 5c and in the high-loss data point in Fig. 4, effects associated with microwave heating result in errors that again diminish the



performance of the memory node for large  $N$ . As such, we conclude that the optimal performance of our node occurs for  $\langle n \rangle_m \approx 0.02$  and  $N \approx 124$ , corresponding to an effective channel loss of 69 dB between Alice and Bob, which is equivalent to roughly 350 km of telecommunications fibre.

We also find that the QBER and thus the performance of the communication link is limited by imperfect preparation of photonic qubits. Photonic qubits are defined by sending arbitrary phase patterns generated by the optical arbitrary waveform generator to a phase modulator. For an example of such a pattern, see the blue curve in Fig. 3a. We use an imperfect pulse amplifier with finite bandwidth (0.025–700 MHz), and find that the DC component of these waveforms can result in error in photonic qubit preparation at the few per cent level. By using a tailored waveform of phases with smaller (or vanishing) DC component, we can reduce these errors. We run such an experiment during the test of the Bell-CHSH inequality. We find that by evaluating BSM correlations from  $|\pm a\rangle$  and  $|\pm b\rangle$  inputs during this measurement, we estimate a QBER of  $0.097 \pm 0.006$ .

We obtain the effective clock-rate of the communication link by measuring the total number of photonic qubits sent over the course of an entire experiment. In practice, we record the number of channel uses, determined by the number of sync triggers recorded (see Extended Data Fig. 1a) as well as the number of qubits per sync trigger ( $N$ ). We then divide this number by the total experimental time from start to finish (about 1–2 days for most experimental runs), including all experimental downtime used to stabilize the interferometer, read out and initialize the SiV, and compensate for spectral diffusion and ionization. For  $N = 248$ , we extract a clock rate of 1.2 MHz. As the distilled key rate in this configuration exceeds the conventional limit of  $p/2$  by a factor of  $3.8 \pm 1.1$ , it is competitive with a standard linear-optics-based system operating at a  $4.5^{+1.3}_{-1.2}$  MHz clock rate.

### Benchmarking memory-assisted operation

A single optical link can provide many channels—for example, by making use of different frequency, polarization or temporal modes. To account for this, when comparing different systems, data rates can be defined on a per-channel-use basis. In a quantum communication setting, full usage of the communication channel between Alice and Bob means that both links from Alice and Bob to Charlie are in use simultaneously. For an asynchronous sequential measurement, typically only half of the channel is used at a time, for example from Alice to Charlie or Bob to Charlie. The other half can in principle be used for a different task when not in use. For example, the unused part of the channel could be routed to a secondary asynchronous BSM device. In our experiment, we can additionally define as a second normalization the rate per channel ‘occupancy’, which accounts for the fact that only half the channel is used at any given time. The rate per channel occupancy is therefore half the rate per full channel use. For comparison, we typically operate at 1.2% channel use and 2.4% channel occupancy.

To characterize the optimal performance of the asynchronous Bell state measurement device, we operate it in the optimal regime determined above ( $N = 124$ ,  $\langle n \rangle_m \lesssim 0.02$ ). We note that the enhancement in the sifted key rate over direct transmission is given by

$$\frac{R}{R_{\max}} = \eta^2 \frac{(N_{\pi} - 1)(N_{\pi} - 2)N_{\text{sub}}}{2N_{\pi}} \quad (2)$$

and is independent of  $\langle n \rangle_m$  for a fixed number of microwave pulses ( $N_{\pi}$ ) and optical pulses per microwave pulse ( $N_{\text{sub}}$ ) and thus fixed  $N = N_{\pi}N_{\text{sub}}$ .

For low  $\langle n \rangle_m$ , three photon events become negligible and therefore QBER saturates, such that the enhancement in the distilled key rate saturates as well (Extended Data Fig. 5a). We can therefore combine all data sets with fixed  $N = 124$  below  $\langle n \rangle_m \lesssim 0.02$  to characterize the average QBER of  $0.116 \pm 0.002$  (Fig. 3c). The key rates cited in the main text relate to a data set in this series ( $\langle n \rangle_m \approx 0.02$ ), with a QBER of  $0.110 \pm 0.004$ . A summary of key rates calculated on a per-channel use and per-channel occupancy basis, as well as comparisons of performance to an ideal linear-optics BSM and the repeaterless bound<sup>8</sup> are given in Extended Data Table 4.

Furthermore, we extrapolate the performance of our memory node to include biased input bases from Alice and Bob. This technique enables a reduction of channel uses where Alice and Bob send photons in different bases, but is still compatible with secure key distribution<sup>27</sup>, allowing for distilled key rates enhanced by at most a factor of 2. The extrapolated performance of our node for a bias of 99:1 is also displayed in Extended Data Table 4, as well as comparisons to the relevant bounds. We note that basis biasing does not affect the performance when comparing to the equivalent direct-transmission experiment, which is limited by  $p_{A \rightarrow B}/2$  in the unbiased case and  $p_{A \rightarrow B}$  in the biased case. However, using biased input bases does make the performance of the memory-assisted approach more competitive with the fixed repeaterless bound<sup>8</sup> of  $1.44p_{A \rightarrow B}$ .

### Data availability

All data related to the current study are available from the corresponding author on reasonable request.

34. Trusheim, M. E. et al. Lead-related quantum emitters in diamond. *Phys. Rev. B* **99**, 075430 (2019).
35. Meesala, S. et al. Strain engineering of the silicon-vacancy center in diamond. *Phys. Rev. B* **97**, 205444 (2018).
36. Burek, M. J. et al. High quality-factor optical nanocavities in bulk single-crystal diamond. *Nat. Commun.* **5**, 5718 (2014).
37. Atikian, H. A. et al. Freestanding nanostructures via reactive ion beam angled etching. *APL Photon.* **2**, 051301 (2017).
38. Nguyen, C. T. et al. An integrated nanophotonic quantum register based on silicon-vacancy spins in diamond. *Phys. Rev. B* **100**, 165428 (2019).
39. de Riedmatten, H. et al. Tailoring photonic entanglement in high-dimensional Hilbert spaces. *Phys. Rev. A* **69**, 050304 (2004).
40. Sasaki, T., Yamamoto, Y. & Koashi, M. Practical quantum key distribution protocol without monitoring signal disturbance. *Nature* **509**, 475 (2014).

**Acknowledgements** We thank P. Stroganov, K. de Greve, J. Borregaard, E. Bersin, B. Dixon, R. Murphy and N. Sinclair for discussions and experimental help, V. Anant from PhotonSpot for providing SNSPDs, and J. MacArthur for assistance with electronics. This work was supported by the NSF, CUA, DoD/ARO DURIP, AFOSR MURI, ONR MURI, ARL, DOE and a Vannevar Bush Faculty Fellowship. Devices were fabricated at Harvard CNS, NSF award no. 1541959. M.K.B. and D.S.L. acknowledge support from an NDSEG Fellowship. R.R. acknowledges support from the Alexander von Humboldt Foundation. B.M. and E.N.K. acknowledge support from an NSF GRFP.

**Author contributions** M.K.B., R.R., B.M., D.S.L., C.T.N., D.D.S. and M.D.L. planned the experiment, B.M. and E.N.K. fabricated the devices, M.K.B., R.R., B.M., D.S.L., C.T.N. and D.D.S. built the set-up, performed the experiment and analysed the data. All work was supervised by H.P., D.E., M.L. and M.D.L. All authors discussed the results and contributed to the manuscript. M.K.B., R.R., B.M., D.S.L. and C.T.N. contributed equally to this work.

**Competing interests** The authors declare no competing interests.

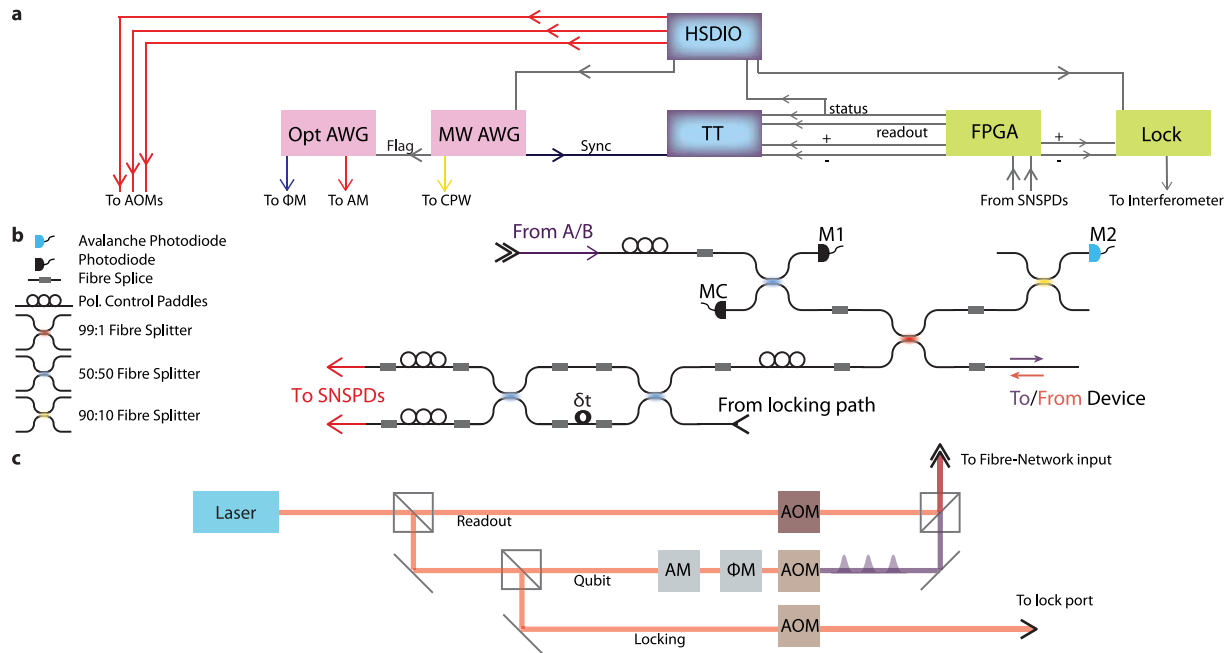
### Additional information

**Supplementary information** is available for this paper at <https://doi.org/10.1038/s41586-020-2103-5>.

**Correspondence and requests for materials** should be addressed to M.D.L.

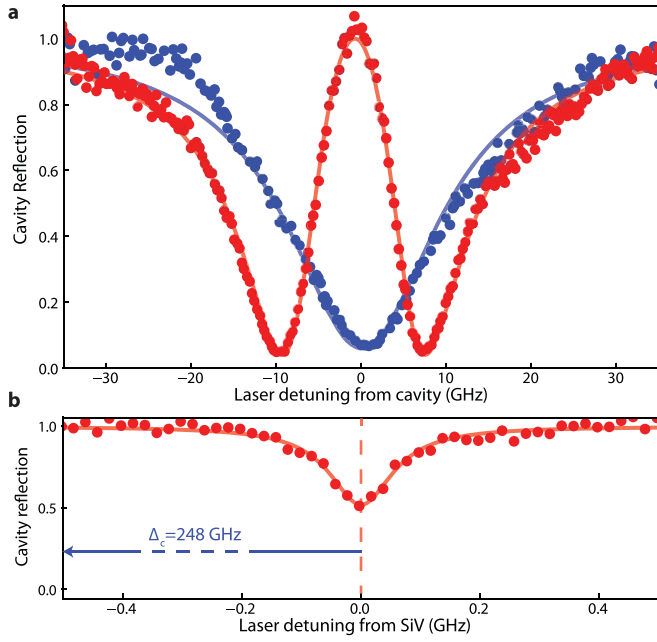
**Peer review information** *Nature* thanks Josh Nunn and Wolfgang Tittel for their contribution to the peer review of this work.

**Reprints and permissions information** is available at <http://www.nature.com/reprints>.

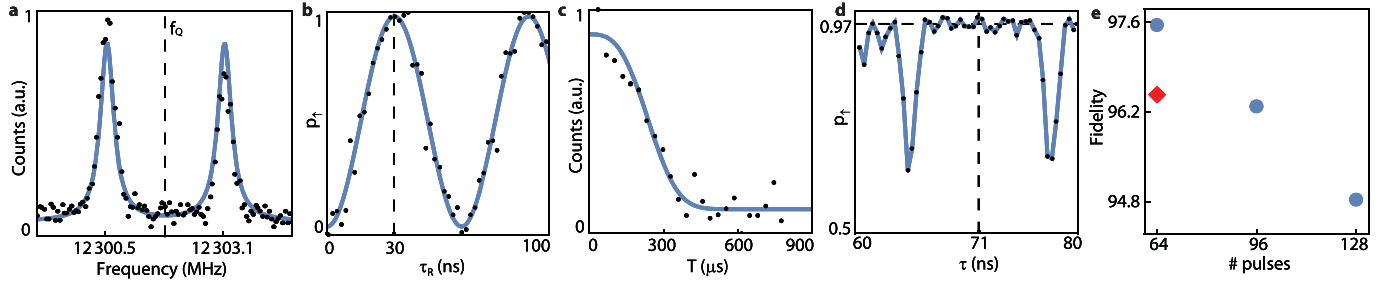


**Extended Data Fig. 1 | Experimental schematic.** **a**, Control flow of experiment. HSDIO (National Instruments) is a digital signal generator that synchronizes the experiment. Opt (MW) AWG is a Tektronix AWG7122B 5 GS/s (Tektronix AWG70001a 50 GS/s) arbitrary waveform generator used to generate photonic qubits (microwave control signals). All signals are recorded on a time-tagger (TT, PicoQuant HydraHarp 400). **b**, Fibre network used to deliver photons to and collect photons from the memory device, including elements for

polarization control and diagnostic measurements of coupling efficiencies using photodiodes M1, M2 and MC. **c**, Preparation of optical fields. The desired phase relation between lock and qubit paths is ensured by modulating AOMs using phase-locked RF sources with a precise 1.8 MHz frequency shift between them. The AM (amplitude modulator) and  $\Phi$ M (phase modulator) are used to define the photonic qubits.



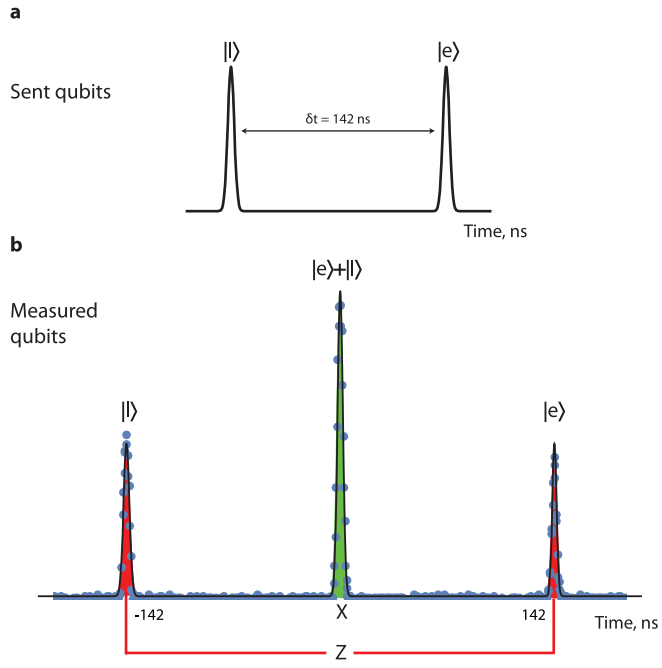
**Extended Data Fig. 2 | Characterization of device cooperativity.** **a**, Cavity reflection spectrum far-detuned (blue) and on resonance (red) with SiV centre. Blue solid line is a fit to a Lorentzian, enabling extraction of linewidth  $\kappa = 21.8$  GHz. Red solid line is a fit to a model used to determine the single-photon Rabi frequency  $g = 8.38 \pm 0.05$  GHz and shows the onset of a normal mode splitting. **b**, Measurement of SiV linewidth far detuned ( $\Delta_c = 248$  GHz) from cavity resonance. Red solid line is a fit to a Lorentzian, enabling extraction of natural linewidth  $\gamma = 0.123$  GHz.



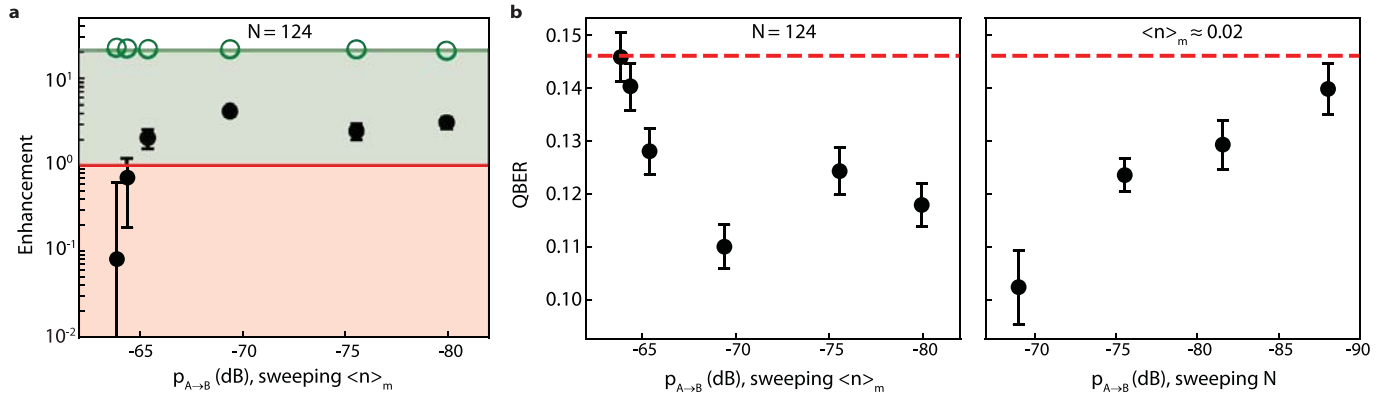
**Extended Data Fig. 3 | Microwave characterization of spin-coherence properties.** **a**, Optically detected magnetic resonance spectrum of the qubit transition at ~12 GHz split by coupling to a nearby  $^{13}\text{C}$ . **b**, Rabi oscillations, read out via the population in the  $|\uparrow\rangle$  state ( $p_{\uparrow}$ ) showing  $\pi$  time of  $\tau_R = 30$  ns. A  $\pi$  time of 32 ns is used for experiments reported in the main text. **c**, XY8-1 dynamical decoupling signal (unnormalized) as a function of total time  $T$ , showing

coherence lasting on the timescale of several hundred microseconds. **d**, XY8-8 dynamical decoupling signal (normalized) revealing a region of high fidelity at the relevant value of  $2\tau = 142$  ns. **e**, Fidelity of spin state after a dynamical decoupling sequence with varying numbers of  $\pi$  pulses ( $N_{\pi}$ ; blue points). Red point (diamond) is under illumination with  $\langle n \rangle_m = 0.02$ .





**Extended Data Fig. 4 | Measurements on a single time-bin qubit in Z and X bases.** **a**, Example of optical pulses sent in the experiment described in Fig. 2d. **b**, Time trace of detected photons on the + detector (see Fig. 2a) when the pulses shown in **a** are sent directly into the TDI. The first and last peaks correspond to late and early photons taking the long and short paths of the TDI, which enable measurements in the Z basis,  $\{|e\rangle, |l\rangle\}$ . The central bin corresponds to the late and early components overlapping and interfering constructively to come out of the + port, equivalent to a measurement of the time-bin qubit in the  $|+x\rangle$  state. A detection event in this same timing window on the other detector (not shown) would constitute a  $| -x\rangle$  measurement. In this measurement, the TDI was left unlocked, so we observe no interference in the central window.



**Extended Data Fig. 5 | Performance of memory device versus channel loss. a.** Enhancement of memory-based approach compared to direct-transmission approach, keeping  $N=124$  fixed and varying  $\langle n \rangle_m$  in order to vary the effective channel transmission probability,  $p_{A \rightarrow B}$ . At high  $p_{A \rightarrow B}$  (larger  $\langle n \rangle_m$ ),  $r_s$  approaches 0 owing to increased QBER arising from undetected scattering of a third

photon. **b.** Left, plot of QBER for same sweep of  $\langle n \rangle_m$  shown in **a**. Right, plot of QBER while sweeping  $N$  in order to vary loss. These points correspond to the same data shown in Fig. 4. At lower  $p_{A \rightarrow B}$  (larger  $N$ ), microwave-induced heating-related dephasing leads to increased QBER. Vertical error bars, 68% confidence interval; horizontal error bars, s.d. of the systematic power fluctuations.

**Extended Data Table 1 | High-level experimental sequence**

Step	Process	Duration	Proceed to
1	Lock time-delay interferometer	200 ms	2
2	Readout SiV	30 $\mu$ s	If status LOW: 4, else: 3
3	Apply microwave $\pi$ pulse	32 ns	
4	Run main experiment script	$\sim$ 200 ms	1

This sequence (described by the ‘Step’ number, description of the ‘Process’, approximate ‘Duration’ and conditional step it ‘Proceeds’ to) is programmed into the HSDIO and uses feedback from the status trigger sent from the FPGA (see Extended Data Fig. 1a). The main experimental sequence is described in Extended Data Table 2. External software with a response time of 100 ms is also used to monitor the status trigger. If it is HIGH for  $\geq 2$ s, the software activates an automatic re-lock procedure which compensates for spectral diffusion and ionization of the SiV centre (Methods). Additionally, we keep track of the timing when the time-delay interferometer (TDI) piezo voltage reaches a limiting value. This guarantees that the SiV is always resonant with the photonic qubits and that the TDI performs high-fidelity measurements in the X basis.

Extended Data Table 2 | Main experimental sequence

Step	Process	Duration	Proceed to
1	Run sequence in Fig. 3a for a given $N$	$10 - 20 \text{ }\mu\text{s}$	2
2	Readout SiV + report readout to TT	$30 \text{ }\mu\text{s}$	If status LOW: 1, else: 3
3	Apply microwave $\pi$ pulse	$32 \text{ ns}$	4
4	Readout SiV	$30 \text{ }\mu\text{s}$	If status LOW: 3, else: 1

This script is followed until step 1 is run a total of 4,000 times, and then terminates and returns to step 1 of Extended Data Table 1. The longest step is the readout step, which is limited by the fact that we operate at a photon detection rate of ~1 MHz to avoid saturation of the SNSPDs.



**Extended Data Table 3 | Truth table of asynchronous BSM protocol**

Alice	Bob	Parity	Bell state
$ +x\rangle$	$ +x\rangle$	+1	$ \Phi_+\rangle$
$ +x\rangle$	$ -x\rangle$	-1	$ \Phi_-\rangle$
$ -x\rangle$	$ +x\rangle$	-1	$ \Phi_-\rangle$
$ -x\rangle$	$ -x\rangle$	+1	$ \Phi_+\rangle$
$ +y\rangle$	$ +y\rangle$	-1	$ \Phi_-\rangle$
$ +y\rangle$	$ -y\rangle$	+1	$ \Phi_+\rangle$
$ -y\rangle$	$ +y\rangle$	+1	$ \Phi_+\rangle$
$ -y\rangle$	$ -y\rangle$	-1	$ \Phi_-\rangle$

Shown is the parity (and BSM outcome) for each set of valid input states from Alice and Bob. In the case of Y-basis inputs, Alice and Bob adjust the sign of their input state depending on whether it was commensurate with an even- or odd-numbered free-precession interval, based on timing information provided by Charlie (Supplementary Information).

Extended Data Table 4 | Quantum-memory-based advantage

	per channel occupancy	per channel occupancy	per channel use	per channel use
X:Y basis bias	50 : 50	99 : 1	50 : 50	99 : 1
Distilled key rate $R$ [ $10^{-7}$ ]	$1.19^{+0.14}_{-0.14}$	$2.33^{+0.28}_{-0.28}$	$2.37^{+0.29}_{-0.28}$	$4.66^{+0.56}_{-0.55}$
$R/R_{\max}(\text{X:Y})$	$2.06^{+0.25}_{-0.25}$	$2.06^{+0.25}_{-0.25}$	$4.13^{+0.50}_{-0.49}$	$4.13^{+0.50}_{-0.49}$
$R/(1.44p_{A\rightarrow B})$	$0.71^{+0.09}_{-0.08}$	$1.40^{+0.17}_{-0.17}$	$1.43^{+0.17}_{-0.17}$	$2.80^{+0.34}_{-0.33}$
1–confidence level		$1.1^{+0.4}_{-0.3} \times 10^{-2}$	$8^{+3}_{-2} \times 10^{-3}$	$1.3^{+0.5}_{-0.3} \times 10^{-7}$

Overview of distilled key rates  $R$  using the asynchronous BSM device and comparison to ideal direct-communication implementations, based on the performance of our network node for  $N = 124$  and  $\langle n \rangle_m \approx 0.02$ . Distillable key rates for  $E = 0.110 \pm 0.004$  are expressed in a per-channel-occupancy and per-channel-use normalization for unbiased and biased basis choice (X:Y basis bias) (Methods). Enhancement (fraction of key rates  $R/R_{\max}$  and  $R/(1.44p_{A\rightarrow B})$ ) is calculated versus the linear optics BSM limit ( $R_{\max}(50:50) = p_{A\rightarrow B}/2$  for unbiased bases,  $R_{\max}(99:1) = 0.98p_{A\rightarrow B}$  with biased bases) and versus the fundamental repeaterless channel capacity<sup>8</sup> ( $1.44p_{A\rightarrow B}$ ). Confidence levels for surpassing the latter bound<sup>8</sup> are given in the final row.

# Imaging the energy gap modulations of the cuprate pair-density-wave state

<https://doi.org/10.1038/s41586-020-2143-x>

Received: 15 August 2019

Accepted: 20 January 2020

Published online: 1 April 2020



Zengyi Du<sup>1,7</sup>, Hui Li<sup>1,2,7</sup>, Sang Hyun Joo<sup>3</sup>, Elizabeth P. Donoway<sup>1,4</sup>, Jinho Lee<sup>3</sup>, J. C. Séamus Davis<sup>5,6</sup>, Genda Gu<sup>1</sup>, Peter D. Johnson<sup>1</sup> & Kazuhiro Fujita<sup>1,2,3</sup>

The defining characteristic<sup>1,2</sup> of Cooper pairs with finite centre-of-mass momentum is a spatially modulating superconducting energy gap  $\Delta(\mathbf{r})$ , where  $\mathbf{r}$  is a position. Recently, this concept has been generalized to the pair-density-wave (PDW) state predicted to exist in copper oxides (cuprates)<sup>3,4</sup>. Although the signature of a cuprate PDW has been detected in Cooper-pair tunnelling<sup>5</sup>, the distinctive signature in single-electron tunnelling of a periodic  $\Delta(\mathbf{r})$  modulation has not been observed. Here, using a spectroscopic technique based on scanning tunnelling microscopy, we find strong  $\Delta(\mathbf{r})$  modulations in the canonical cuprate  $\text{Bi}_2\text{Sr}_2\text{CaCu}_2\text{O}_{8+\delta}$  that have eight-unit-cell periodicity or wavevectors  $\mathbf{Q} \approx (2\pi/a_0)(1/8, 0)$  and  $\mathbf{Q} \approx (2\pi/a_0)(0, 1/8)$  (where  $a_0$  is the distance between neighbouring Cu atoms). Simultaneous imaging of the local density of states  $N(\mathbf{r}, E)$  (where  $E$  is the energy) reveals electronic modulations with wavevectors  $\mathbf{Q}$  and  $2\mathbf{Q}$ , as anticipated when the PDW coexists with superconductivity. Finally, by visualizing the topological defects in these  $N(\mathbf{r}, E)$  density waves at  $2\mathbf{Q}$ , we find them to be concentrated in areas where the PDW spatial phase changes by  $\pi$ , as predicted by the theory of half-vortices in a PDW state<sup>6,7</sup>. Overall, this is a compelling demonstration, from multiple single-electron signatures, of a PDW state coexisting with superconductivity in  $\text{Bi}_2\text{Sr}_2\text{CaCu}_2\text{O}_{8+\delta}$ .

The exact nature of the cuprate pseudogap state<sup>8</sup> has been the focus of extensive research as a route to understanding high-temperature superconductivity. Attention has recently focused on a pair-density-wave (PDW) state<sup>3,4</sup> as a leading candidate to be the fundamental order parameter that characterizes the pseudogap. This was originally motivated by transport studies<sup>9</sup>, which led to the hypothesis of ‘stripe superconductivity’, in which the superconducting order parameter is spatially modulated and thus a PDW<sup>10,11</sup>. Equally, the highly unusual band structure reconstruction near the pseudogap opening temperature  $T^*$  as observed by angle-resolved photoemission spectroscopy<sup>12</sup> can be explained relatively simply by the formation of a PDW state<sup>13,14</sup>. Indeed, a wide variety of microscopic theories based on strong, local electron–electron interactions now envisage a copper oxide (cuprate) PDW state<sup>15–22</sup>, while experimental evidence for its existence is rapidly emerging from multiple techniques<sup>4,5,23,24</sup>.

## Characteristic signatures in single-electron tunnelling of the PDW state

Here we focus on the challenge of detecting the cuprate PDW state using single-electron tunnelling. First, we consider a PDW, whose spatially dependent energy gap is  $\Delta(\mathbf{r}) = F_p \Delta_Q^p [e^{i\mathbf{Q}\cdot\mathbf{r}} + e^{-i\mathbf{Q}\cdot\mathbf{r}}]$ , where  $\Delta_Q^p$  is the amplitude of gap modulations at wavevector  $\mathbf{Q}$ ,  $\mathbf{r}$  is a position and  $F_p$  is the form factor with either  $s$ - or  $d$ -symmetry. The most obvious and immediate prediction is that the single-electron tunnelling should

detect a gap in the density-of-states spectrum  $N(E)$  (where  $E$  is energy), which modulates at  $\mathbf{Q}$ . It is striking, therefore, that no such modulating  $\Delta(\mathbf{r})$  has ever been observed in the cuprates. Second, if such a PDW coexists with  $d$ -wave superconductivity (SC), whose homogeneous gap is  $\Delta^s(\mathbf{r}) = F_{sc}\Delta^s$ , where  $F_{sc}$  exhibits  $d$ -symmetry, then Ginzburg–Landau theory predicts the form of  $N(\mathbf{r}, E)$  modulations generated by the interactions between the PDW  $\Delta(\mathbf{r})$  and the superconducting  $\Delta^s(\mathbf{r})$ . These modulations are identifiable from products of these two order parameters that transform as density-like quantities. Thus, considering the product of the PDW and SC order parameters,  $\Delta_Q^p \Delta^s$  predicts  $N(\mathbf{r}) \propto \cos(\mathbf{Q} \cdot \mathbf{r})$  modulations at the PDW wavevector  $\mathbf{Q}$ , while the product of a PDW with itself  $\Delta_Q^p \Delta_Q^p$  predicts  $N(\mathbf{r}) \propto \cos(2\mathbf{Q} \cdot \mathbf{r})$  at twice the PDW wavevector. Therefore, a second unique signature of a PDW with wavevector  $\mathbf{Q}$  in the superconducting cuprates would be the coexistence of two sets of  $N(\mathbf{r}, E)$  modulations at  $\mathbf{Q}$  and  $2\mathbf{Q}$ . Finally, a topological defect with  $2\pi$  phase winding<sup>25</sup> in the induced density wave  $N(\mathbf{r}) \propto \cos(2\mathbf{Q} \cdot \mathbf{r})$  is predicted to generate a local phase winding of  $\pi$  in the PDW order, at a half-vortex<sup>6</sup> (Fig. 1a). This is the topological signature of a PDW coexisting with homogeneous SC. Experimental detection of these phenomena in single-electron tunnelling would constitute compelling evidence for the PDW state.

To explore these predictions, we use spectroscopic imaging scanning tunnelling microscopy<sup>26</sup> (SI-STM) with a  $\text{Bi}_2\text{Sr}_2\text{CaCu}_2\text{O}_{8+\delta}$  nano-flake tip<sup>5</sup> to visualize the single-electron tunnelling. Utilization of the superconducting tip enhances the energy resolution due to the

<sup>1</sup>CMPMS Department, Brookhaven National Laboratory, Upton, NY, USA. <sup>2</sup>Department of Physics and Astronomy, Stony Brook University, Stony Brook, NY, USA. <sup>3</sup>Department of Physics and Astronomy, Seoul National University, Seoul, Republic of Korea. <sup>4</sup>Department of Physics, University of California, Berkeley, Berkeley, CA, USA. <sup>5</sup>Department of Physics, University College Cork, Cork, Ireland. <sup>6</sup>Clarendon Laboratory, University of Oxford, Oxford, UK. <sup>7</sup>These authors contributed equally: Zengyi Du, Hui Li. <sup>✉</sup>e-mail: kfujita@bnl.gov

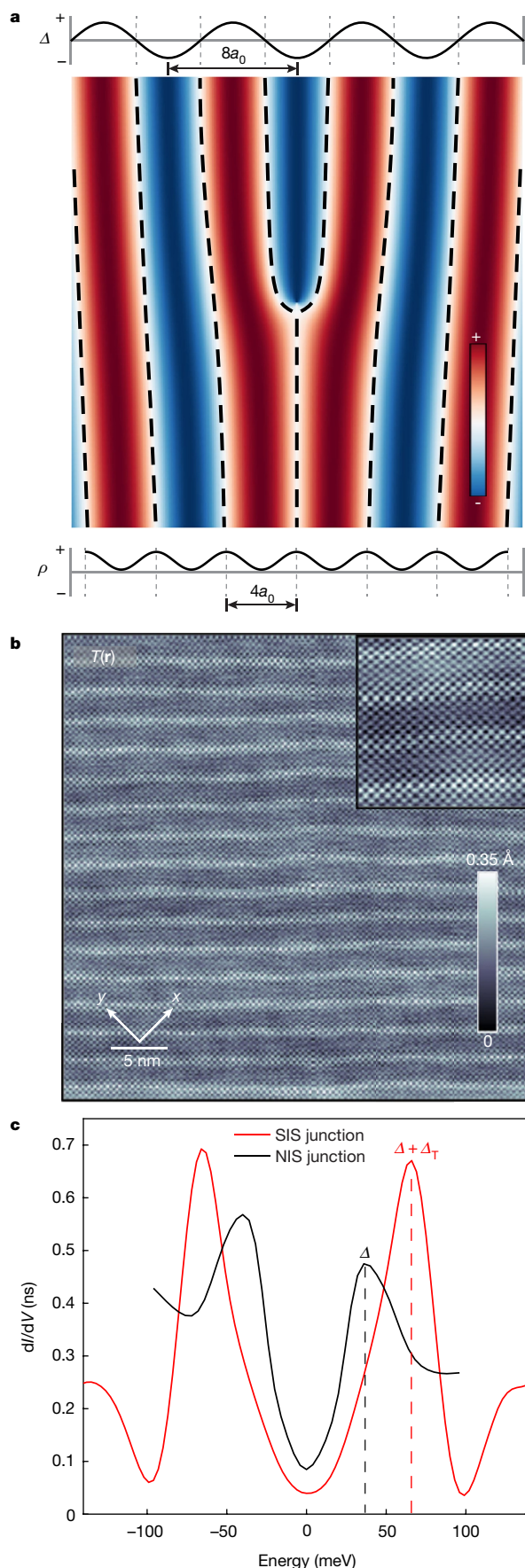


**Fig. 1 | Schematic of unidirectional  $8a_0$  PDW order intertwined with a density wave.** **a**, Unidirectional PDW order parameter is modulated along the horizontal axis at eight-unit-cell periodicity. The sign of  $\Delta(\mathbf{r})$  is coloured in red for positive and in blue for negative. The periodicity in the unidirectional density-of-electronic-states  $N(\mathbf{r})$  detectable by NIS tunnelling, which is intertwined with unidirectional PDW, is depicted by a black broken line. The  $N(\mathbf{r})$  wavelength is half that of the unidirectional PDW. When a dislocation occurs in unidirectional  $N(\mathbf{r})$ , where the  $2\pi$  phase winding is realized in its phase, a possible fluctuation in unidirectional PDW order amplitude and/or half-vortices is predicted. The relative phase of the spatial variations in the PDW order and the induced density-wave modulations in  $N(\mathbf{r})$  are also plotted at the top and bottom, respectively. **b**, Typical SIS topography of  $\text{Bi}_2\text{Sr}_2\text{CaCu}_2\text{O}_{8+\delta}$  within  $40\text{ nm} \times 40\text{ nm}$  FOV at  $5\text{ G}\Omega$  junction resistance ( $I = 30\text{ pA}$  at  $V_{\text{bias}} = 150\text{ meV}$ ). Cu–O–Cu bond directions are parallel to the  $x$  and  $y$  axes. Individual Bi atoms are clearly observed as shown in the inset with intra-unit-cell resolution. **c**, Spatially averaged SIS  $g(\mathbf{r})$  spectrum (red) together with that taken with NIS junction (black). The spatially averaged SIS  $g(\mathbf{r}, E)$  spectrum shows particle–hole symmetric peaks with energies at  $E = \pm 66\text{ meV}$ . As the spatially averaged NIS  $g(\mathbf{r})$  peaks at  $\pm 37\text{ meV}$ , we estimate the average gap value on the  $\text{Bi}_2\text{Sr}_2\text{CaCu}_2\text{O}_{8+\delta}$  nanoflake tip,  $\Delta_T$ , to be about  $29\text{ meV}$ .

convolution of spectra that sharply peak at the superconducting gap edge, in the density of states  $N_T(E)$  of the tip and  $N(\mathbf{r}, E)$  of the sample. Thus, energy sensitivity to modulations in  $\Delta(\mathbf{r})$  should be enhanced with this superconductor–insulator–superconductor (SIS) tunnelling technique. To enable detection of the gap modulation, a bulk single-crystal sample of  $\text{Bi}_2\text{Sr}_2\text{CaCu}_2\text{O}_{8+\delta}$  at the hole density  $p \approx 0.17 \pm 0.01$  (the error approximately corresponds to a transition width) and superconducting transition temperature  $T_c = 91\text{ K}$  is cleaved at room temperature under ultrahigh vacuum conditions ( $3 \times 10^{-10}$  torr) and then inserted into the cryogenic STM head. The superconducting tip is created by picking up a nanometre-scale  $\text{Bi}_2\text{Sr}_2\text{CaCu}_2\text{O}_{8+\delta}$  flake from the sample<sup>5</sup> to form the SIS junction. The SI-STM measurements throughout this study are then all performed using such SIS junctions at  $T = 9\text{ K}$ . A typical SIS topography is shown in Fig. 1b for a  $40\text{ nm} \times 40\text{ nm}$  field of view (FOV). The individual Bi atoms in the BiO plane with subatomic resolution are resolved as shown in the inset. The  $\text{CuO}_2$  plane exists about  $6\text{ \AA}$  below the BiO plane.

## Direct visualization of the periodic energy gap modulations

Differential SIS conductance spectra  $g(\mathbf{r}, E) \equiv dI/dV(\mathbf{r}, E = eV)$ , where  $I$  is the tunnelling current,  $V$  is the bias voltage and  $e$  is the elementary charge are then measured as a function of position in this FOV for the energy range from  $-150\text{ meV}$  to  $+150\text{ meV}$ . A typical such spatially averaged  $g(\mathbf{r}, E)$  spectrum is shown in red in Fig. 1c, together with a normal–insulator–superconductor metal (NIS) spectrum performed earlier on the same sample but in a different FOV. The SIS  $g(\mathbf{r}, E)$  spectrum, being a convolution of the tip  $N_T(E)$  and sample  $N(E)$  demonstrates enhanced energy resolution as expected (red in Fig. 1c). Here, as the spatially averaged NIS  $g(\mathbf{r}, E)$  spectrum peaks at  $\pm 37\text{ meV}$ , while the equivalent SIS spectrum peaks at  $\pm 66\text{ meV}$ , we estimate the average energy gap of the tip  $\Delta_T$  to be  $29\text{ meV}$ .

Next, by measuring half the magnitude of the energy that separates the SIS spectrum peaks at every location, and then subtracting  $\Delta_T$ , we determine the local gap energy map  $\Delta(\mathbf{r})$  in the sample. A typical example is shown in Fig. 2a. Figure 2b shows the magnitude of the power-spectral-density Fourier transform  $\Delta(\mathbf{q})$  of  $\Delta(\mathbf{r})$  from Fig. 2a, where  $\mathbf{q}$  is a wavevector. Equivalent results have been achieved using SIS tunnelling with three different  $\text{Bi}_2\text{Sr}_2\text{CaCu}_2\text{O}_{8+\delta}$  nanoflake tips, on three different samples and with two different STMs (Methods section ‘Motivation of searches for a PDW signature in  $\Delta(\mathbf{r})$ ’). In Fig. 2b,  $\mathbf{q}_{\text{SM}}$  corresponds to a wavevector of the crystal-structure supermodulation. This supermodulation does indeed produce a type of PDW detectable



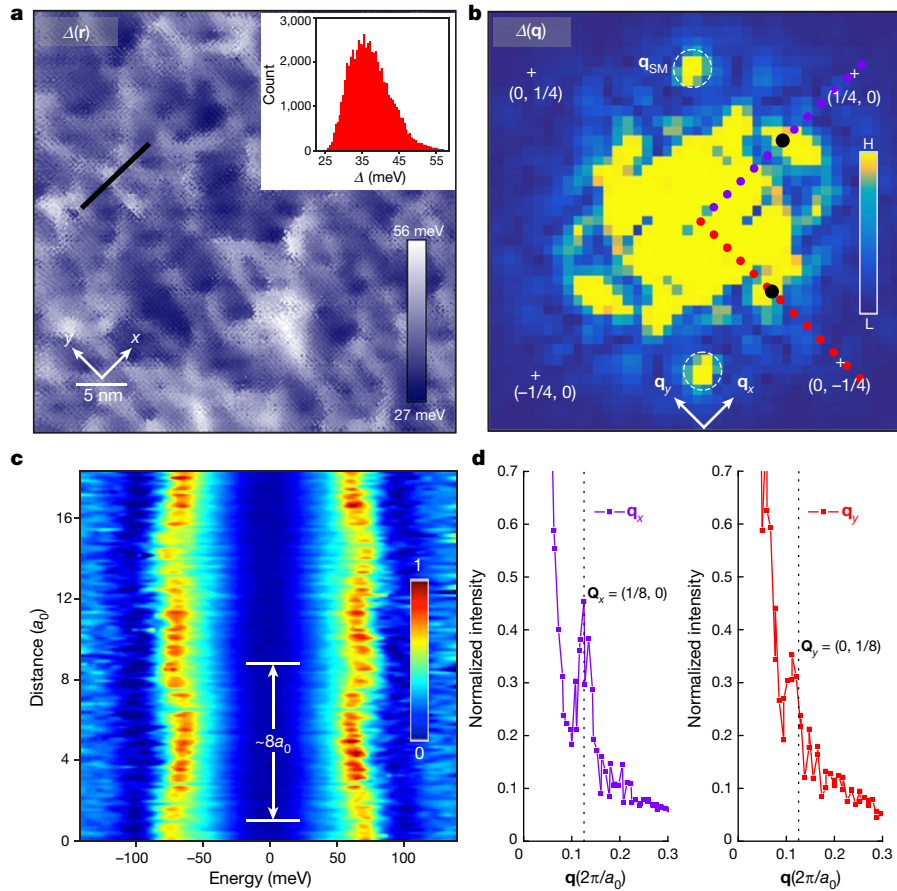


**Fig. 2 | Superconducting gap energy modulations.** **a**, Measured  $\Delta(\mathbf{r})$  within  $40 \text{ nm} \times 40 \text{ nm}$  FOV. The energy-gap data presented here and throughout the manuscript are all the measured values of the magnitude of  $\Delta(\mathbf{r})$ , which is half the energy separation between the coherence peaks minus the gap value of the  $\text{Bi}_2\text{Sr}_2\text{CaCu}_2\text{O}_{8+\delta}$  nanoflake tip. The inset shows a distribution of measured  $\Delta(\mathbf{r})$  in the same FOV, ranging from 27 to 56 meV. The eight-unit-cell modulation is clearly resolved in  $\Delta(\mathbf{r})$ , primarily running along the  $x$  direction of Cu–O–Cu bond exhibiting the unidirectional signature of the PDW. **b**, The magnitude Fourier transform of **a**. Well defined Fourier peaks at  $\mathbf{Q} \approx (2\pi/a_0)(\pm 1/8, 0)$  and

$\mathbf{Q} \approx (2\pi/a_0)(0, \pm 1/8)$ , corresponding to the eight-unit-cell modulations for both the  $x$  and  $y$  directions, are observed. H and L denote high and low, respectively. **c**, The series of SIS  $g(\mathbf{r}, E)$  spectra intensity along the line in **a**. The eight unit-cell modulation of the energies of the coherence peaks is clearly resolved. The modulation amplitude is about 6 meV. **d**, The line cut of  $|\Delta(\mathbf{q})|$  along both  $x$  and  $y$  directions from **b**. As seen in **b**,  $\mathbf{Q} \approx (2\pi/a_0)(\pm 1/8, 0)$  and  $\mathbf{Q} \approx (2\pi/a_0)(0, \pm 1/8)$  peaks are present for both directions, but a peak height is about twice larger for  $x$  than that for  $y$  direction indicating that the PDW is rather unidirectional.

by its energy gap modulations; but this PDW is trivial, occurring due to modulation of the crystal unit-cell dimensions (Methods section ‘Effect of structural supermodulation on measured  $\Delta(\mathbf{r})$ ’). Second, there is a very broad peak in  $\Delta(\mathbf{q})$  surrounding  $\mathbf{q} = 0$  due to the well known random energy-gap disorder of  $\text{Bi}_2\text{Sr}_2\text{CaCu}_2\text{O}_{8+\delta}$ , and this is equivalent to the broad range of gap values in the histogram inset to Fig. 2a. Finally, there are four distinct local maxima in  $\Delta(\mathbf{q})$  at the points indicated by black solid dots surrounding  $\mathbf{q} \approx (0, \pm 0.125)$  and  $\mathbf{q} \approx (\pm 0.125, 0)(2\pi/a_0)$ , where  $a_0$  is the periodicity.

These features indicate that there is a strong, if disordered, modulation in  $\Delta(\mathbf{r})$ , running parallel to the Cu–O–Cu bonds of the  $\text{CuO}_2$  plane. This modulation exists on top of a non-periodic energy gap of about 37 meV. It exhibits well defined peaks at  $\mathbf{Q}_x \approx (2\pi/a_0)(1/8, 0)$  and  $\mathbf{Q}_y \approx (2\pi/a_0)(0, 1/8)$  meaning that  $\Delta(\mathbf{r})$  is modulating with about  $8a_0$  periodicity along both axes. Such a variation in  $\Delta(\mathbf{r})$  can be seen directly in a series of SIS  $g(\mathbf{r}, E)$  spectra, extracted along the line in Fig. 2a and shown in Fig. 2c. Here we see a local demonstration of the energy of maximum  $N(\mathbf{r})$  (that is, of the coherence peak) modulating at about  $8a_0$  periodicity in a particle–hole symmetric fashion with an amplitude of approximately 6 meV. More fundamentally, line profiles from  $\Delta(\mathbf{q})$  in Fig. 2b are plotted in Fig. 2d for both directions. The two well defined peaks in Fig. 2d characterize a PDW with wavevectors  $\mathbf{Q}_x \approx (0.129 \pm 0.003, 0)$  and  $\mathbf{Q}_y \approx (2\pi/a_0)(0, 0.118 \pm 0.003)$ . This is an

observation of coherent modulation in the superconducting energy gap  $\Delta(\mathbf{r})$ , and is precisely what is expected for a PDW state. Moreover, it reveals directly that the cuprate PDW occurs at wavevectors  $\mathbf{Q} \approx (2\pi/a_0)(1/8, 0)$  and  $\mathbf{Q} \approx (2\pi/a_0)(0, 1/8)$ .

### Relationship to PDW visualization using scanned Josephson tunnelling microscopy

Using the same  $\text{Bi}_2\text{Sr}_2\text{CaCu}_2\text{O}_{8+\delta}$  nanoflake tip technology, on samples at the same doping as herein but operating at millikelvin temperatures, the magnitude of the Josephson current  $|I_J(\mathbf{r})|$  is found to modulate with a wavelength of about  $4a_0$ . Thus, modulations of  $|I_J(\mathbf{r})|$  and of  $\Delta(\mathbf{r})$  are both detectable when using nanoflake tips that are extracted from the same crystal that is being studied, and are likely in the same coexisting SC and PDW state. Because the nanoflake tip is extended, an approximation to planar tunnelling must be considered. Here  $I_J$  from an extended tip to the crystal is composed of two contributions:  $I_J^S$  due to pair tunnelling from  $c_k^\dagger c_{-k}^\dagger$  to  $c_k^\dagger c_{-k}^\dagger$  states, and  $I_J^P$  due to pair tunnelling from  $c_k^\dagger c_{k+Q}^\dagger$  to  $c_k^\dagger c_{k+Q}^\dagger$  states, where  $c_k^\dagger$  is an electron creation operator at a momentum  $k$ , which are independent of each other when pair momentum is conserved (Methods section ‘Independent pair tunnelling process’). In scanned Josephson tunnelling microscopy, the circuitry measures the magnitude of Josephson critical current

magnitude:  $|J| = |J_s| + |J_p|$ , for which  $|J_s|$  is a roughly constant spatially but  $|J_p| \propto |\sin(Q_p \delta)|$  where  $\delta$  is the spatial displacement between the PDW in the extended tip and the PDW in the sample (Methods section ‘Independent pair tunnelling process’). Under these circumstances, if the PDW has periodicity  $8a_0$ , its gap modulates with periodicity  $8a_0$ , but the magnitude of the total Josephson current  $|J|$  will have periodicity  $4a_0$ . This is the specific phenomenology detectable using the  $\text{Bi}_2\text{Sr}_2\text{CaC}_2\text{O}_{8+\delta}$  nanoflake tips for SIS spectroscopy and to measure the magnitude of Josephson critical currents<sup>5</sup>, respectively. Furthermore, enhanced sensitivity to the basic energy modulations when using SIS spectroscopy is consistent with a ‘lock-in’ effect from a PDW state in the nanoflake tip (Methods section ‘Effect of  $\Delta(\mathbf{r})$  on nanoflake’).

### Detection of two unidirectional PDWs within distinct nanoscale domains

Next, to explore the unidirectionality of  $\Delta(\mathbf{r})$ , we employ a two-dimensional lock-in technique to determine the amplitude and phase of the modulations<sup>27</sup>. Thus

$$A_{\mathbf{Q}}(\mathbf{r}) = \int d\mathbf{R} A(\mathbf{R}) e^{i\mathbf{Q}\cdot\mathbf{R}} e^{-\frac{(\mathbf{r}-\mathbf{R})^2}{2\sigma^2}} \quad (1)$$

$$|A_{\mathbf{Q}}(\mathbf{r})| = \sqrt{\text{Re}A_{\mathbf{Q}}(\mathbf{r})^2 + \text{Im}A_{\mathbf{Q}}(\mathbf{r})^2} \quad (2)$$

$$\phi_{\mathbf{Q}}^A(\mathbf{r}) = \tan^{-1} \frac{\text{Im}A_{\mathbf{Q}}(\mathbf{r})}{\text{Re}A_{\mathbf{Q}}(\mathbf{r})} \quad (3)$$

where  $A(\mathbf{r})$  represents any arbitrary real space image,  $\mathbf{Q}$  the wavevector of interest and  $\sigma$  the averaging length-scale in  $r$ -space (or equivalently the cut-off length in  $q$ -space). The key ingredients of such an analysis are the amplitude  $|A_{\mathbf{Q}}(\mathbf{r})|$  and the spatial phase  $\phi_{\mathbf{Q}}^A(\mathbf{r})$  of modulations at  $\mathbf{Q}$ . Using this technique on our  $\Delta(\mathbf{r})$  data, Fig. 3a, b shows the amplitudes of the PDW for the  $x$  and  $y$  directions,  $|\Delta_{\mathbf{Q}_x}(\mathbf{r})|$ ,  $|\Delta_{\mathbf{Q}_y}(\mathbf{r})|$ , respectively. The local ‘magnitude’ of PDW unidirectionality is then defined as

$$F(\mathbf{r}) = \frac{|\Delta_{\mathbf{Q}_x}(\mathbf{r})| - |\Delta_{\mathbf{Q}_y}(\mathbf{r})|}{|\Delta_{\mathbf{Q}_x}(\mathbf{r})| + |\Delta_{\mathbf{Q}_y}(\mathbf{r})|} \quad (4)$$

When  $F(\mathbf{r}) > 0$ , represented in orange, the PDW along the  $x$  direction is dominant, and similarly when  $F(\mathbf{r}) < 0$ , represented in blue, the PDW order along the  $y$  direction is dominant. As shown in Fig. 3c,  $F(\mathbf{r})$  is spatially heterogeneous forming a domain structure indicating that the cuprate PDW  $\Delta(\mathbf{r})$  is microscopically unidirectional, with one direction predominant in any particular domain. In addition, it appears that the domain size in orange is much bigger than that of blue within the  $40 \text{ nm} \times 40 \text{ nm}$  FOV, which may indicate a vestigial nematic<sup>28</sup> PDW state, although one cannot be certain without independent knowledge of the shape anisotropy of the nanoflake tip. Overall, these data indicate that the cuprate PDW state is locally strongly unidirectional, and possibly in a vestigial nematic state due to quenched disorder<sup>28</sup>.

### How a coexisting PDW and superconductor induce the CDW modulations

Although the SI-STM technique cannot be used to image a charge density  $\rho(\mathbf{r})$  or any of its modulations, a mapping of  $g(\mathbf{r}, E)$  and its ratio  $Z(\mathbf{r}, E) = g(\mathbf{r}, +E)/g(\mathbf{r}, -E)$  enables one to study how the related  $N(\mathbf{r}, E)$  modulates. It has been found that the form-factor symmetry for the induced CDW in cuprates exhibits primarily  $d$ -symmetry<sup>27</sup>. In that case, the CDW modulation does not appear primarily at  $\mathbf{Q}$  and  $2\mathbf{Q}$  in the Fourier transform of  $g(\mathbf{r}, E)$  or  $Z(\mathbf{r}, E)$ . Instead, to detect the  $d$ -symmetry form factor CDW signal at  $\mathbf{Q}$  and  $2\mathbf{Q}$ , one must first use the  $d$ -symmetry

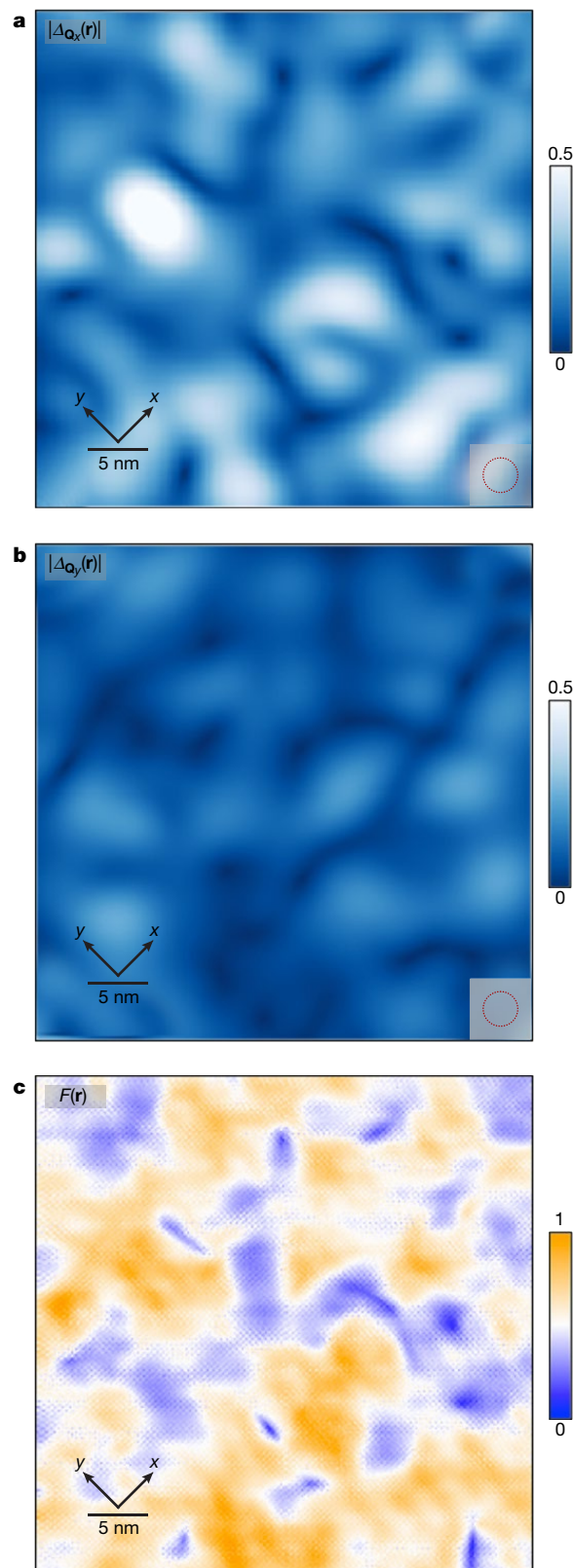


**Fig. 3 | The PDW order parameter amplitude and phase. a**, The spatial variation of the PDW amplitude  $|\Delta_{\mathbf{Q}_x}(\mathbf{r})|$  along the  $x$  direction obtained by the two-dimensional lock-in technique. **b**, The spatial variation of the PDW amplitude  $|\Delta_{\mathbf{Q}_y}(\mathbf{r})|$  along the  $y$  direction obtained by the two-dimensional lock-in technique. The cut-off length is denoted by the broken circle. **c**, The local directionality map defined by equation (4). An orange domain is the region where the PDW amplitude along the  $x$  axis is predominant, while a blue domain is the region where the PDW amplitude along the  $y$  axis is predominant.



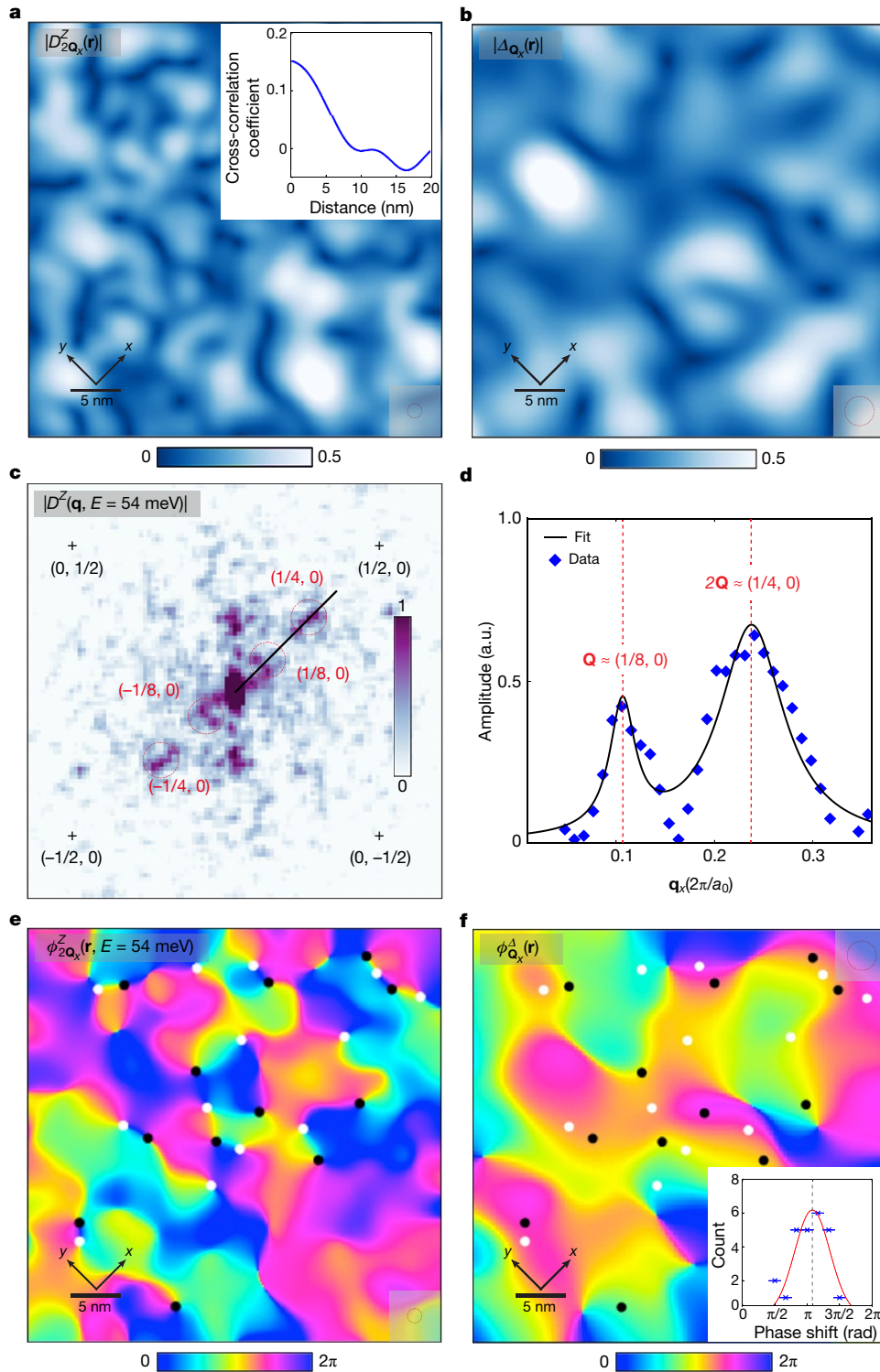


**Fig. 4 | The interplay of  $N(r)$  and PDW, and the possible half-vortices.** **a**, The spatial variation of the  $N(r)$  amplitude  $D_{2Q_x}^Z(r)$  obtained by equations (1) and (2). The inset shows an azimuthal angular averaged cross-correlation coefficient as a function of distance. **b**, The spatial variation of the  $\Delta_{Q_x}(r)$  amplitude obtained by equations (1) and (2). **c**, The magnitude of the phase-resolved Fourier transform,  $|D^Z(q)|$  exhibiting both  $Q = (2\pi/a_0)(\pm 1/8, 0)$  and  $2Q = (2\pi/a_0)(\pm 1/4, 0)$  and peaks encircled by red broken lines, respectively. Coordinates are in units of  $2\pi/a_0$ . **d**, The line cut of  $|D^Z(q)|$ , in which the Lorentzian background is subtracted, in **c** from  $(2\pi/a_0)(0, 0)$  to  $(2\pi/a_0)(\pm 1/4, 0)$ , exhibiting well defined peaks at  $Q$  and  $2Q$ . Data points are fitted by Lorentzians and the obtained peak

positions are  $(2\pi/a_0)(0.113 \pm 0.002)$  and  $(2\pi/a_0)(0.241 \pm 0.003)$  for  $Q$  and  $2Q$ , respectively, with the peak widths  $(2\pi/a_0)(0.016 \pm 0.004)$  and  $(2\pi/a_0)(0.068 \pm 0.006)$  for  $Q$  and  $2Q$ , respectively. **e**, The spatial phase of the  $2Q N(r)$  order  $\phi_{2Q_x}^Z(r)$  obtained by equation (3).  $2\pi$  topological defects are marked by solid dots. White (black) dots indicate  $2\pi$  phase winding along clockwise (anticlockwise). **f**, The spatial phase of the PDW  $\phi_{Q_x}^A(r)$ . The  $2\pi$  topological defects in  $\phi_{2Q_x}^Z(r)$  from **e** are plotted on top of  $\phi_{Q_x}^A(r)$ . The inset shows the distribution of  $\phi_{Q_x}^A(r)$  values at all the locations where the  $2\pi$  topological defects in  $\phi_{2Q_x}^Z(r)$  are found. The blue crosses are the count and the horizontal bars represent the bin size.

sublattice-phase-resolved Fourier analysis (Methods section ‘Sublattice phase-resolved analysis’). For this reason, we apply a phase-resolved visualization of the  $d$ -symmetry modulations to our measured  $Z(\mathbf{r}, E)$  (ref. <sup>27</sup>), extracting the value of  $Z(\mathbf{r}, E)$  at the oxygen sites within each  $\text{CuO}_2$  unit cell:  $O_x^Z(\mathbf{r}) \equiv Z(\mathbf{r})\delta(\mathbf{r} - \mathbf{r}_{O_x})$  at  $O_x$  and similarly for  $O_y^Z(\mathbf{r})$  at  $O_y$ . We then subtract these values throughout the image to yield

$$D^Z(\mathbf{r}) = O_x^Z(\mathbf{r}) - O_y^Z(\mathbf{r}) \quad (5)$$

In Fig. 4a, b, we show the amplitudes of  $|\Delta_{\mathbf{Q}_x}(\mathbf{r})|$  and  $|D_{2\mathbf{Q}_x}^Z(\mathbf{r}, E=54 \text{ meV})|$ ; systematics of the  $q$ -space cut-off length used are discussed in Methods section ‘Cut-off dependence’. If we then consider the magnitude of the Fourier transform of  $D^Z(\mathbf{r}, E)$  for  $E=54 \text{ meV}$  where SIS tunnelling has the maximum energy sensitivity (Fig. 1c), a key fact emerges. In the Fourier transform  $|D^Z(\mathbf{q}, 54 \text{ meV})|$ , we find two strong peaks at  $\mathbf{Q}$  and  $2\mathbf{Q}$  (Fig. 4c), which are the clearest in these data when presented along the line  $(0, 0) - (2\pi/a_0)(0.4, 0)$  in Fig. 4d (from which a Lorentzian background has been subtracted). This complex density wave structure is the expected signature in  $N(\mathbf{r}, E)$  modulations<sup>29–31</sup> of the PDW with wavevector  $\mathbf{Q}$  coexisting with the homogeneous SC.

Finally, utilizing the two-dimensional lock-in technique to generate phase-resolved images, the spatial phase  $\phi_{2\mathbf{Q}_x}^Z(\mathbf{r})$  of  $D_{2\mathbf{Q}_x}^Z(\mathbf{r}, 54 \text{ meV})$  is extracted using equation (3), and is shown in Fig. 4e. The topological defects with  $2\pi$  phase winding in the  $N(\mathbf{r}, 54 \text{ meV})$  density wave are marked by the black and white dots, for which the winding direction is clockwise and anticlockwise, respectively. The presence of these  $2\pi$  topological defects in the  $N(\mathbf{r}, 54 \text{ meV})$  density wave at  $2\mathbf{Q}$  is due microscopically to a dislocation as schematically shown in Fig. 1a (black line). To visualize the interplay of the  $2\mathbf{Q}$  density wave and the PDW, the spatial phase  $\phi_{\mathbf{Q}_x}^A$  of the PDW order is extracted in the same way, but now at  $(2\pi/a_0)(\pm 1/8, 0)$ . In Fig. 4f, the locations of the  $\phi_{2\mathbf{Q}_x}^Z(\mathbf{r})$  topological defects from Fig. 4e are also plotted on top of the PDW spatial phase  $\phi_{\mathbf{Q}_x}^A(\mathbf{r})$ . Intriguingly, the  $\phi_{2\mathbf{Q}_x}^Z(\mathbf{r})$  topological defects are always found in the vicinity of the yellow strings in  $\phi_{\mathbf{Q}_x}^A(\mathbf{r})$ , where the PDW phase is  $\pi$  (see Extended Data Fig. 8 for an evolution of the PDW spatial phase). The inset in Fig. 4f shows that the probability distribution of the PDW phase  $\phi_{\mathbf{Q}_x}^A$ , at which all the topological defects in  $\phi_{2\mathbf{Q}_x}^Z(\mathbf{r})$  are found, is clearly centred around  $\pi$  (see Extended Data Fig. 7 for an independent analysis yielding the same conclusion). Thus, the local phase in the PDW surrounding the topological defects in  $\phi_{2\mathbf{Q}_x}^Z(\mathbf{r})$  always changes by approximately  $\pi$  (see Extended Data Fig. 8) precisely as expected when a topological defect in the induced density wave at  $2\mathbf{Q}$  interacts with the PDW order<sup>6</sup>.

## Multiple single-electron signatures of a PDW coexisting with SC

To summarize, use of  $\text{Bi}_2\text{Sr}_2\text{CaCu}_2\text{O}_{8+\delta}$  nanoflake scanned tips allows the detection of the spatially modulating energy gap  $\Delta(\mathbf{r})$  with eight-unit-cell periodicity, or with axial wavevectors  $\mathbf{Q} \approx (2\pi/a_0)(1/8, 0)$  and  $\mathbf{Q} \approx (2\pi/a_0)(0, 1/8)$ , in superconducting  $\text{Bi}_2\text{Sr}_2\text{CaCu}_2\text{O}_{8+\delta}$  (Fig. 2). The spatial analysis of the  $\Delta(\mathbf{r})$  modulations shows that they are rather unidirectional within nanoscale domains (Fig. 3). Simultaneous density-of-states imaging reveals two pairs of coexisting  $N(\mathbf{r}, E)$  modulations, at wavevectors  $\mathbf{Q} \approx (2\pi/a_0)(1/8, 0)$  and  $\mathbf{Q} \approx (2\pi/a_0)(0, 1/8)$ , and  $2\mathbf{Q} \approx (2\pi/a_0)(1/4, 0)$  and  $2\mathbf{Q} \approx (2\pi/a_0)(0, 1/4)$  (Fig. 4c, d). Finally, the topological defects in the  $N(\mathbf{r}, E)$  density wave at  $2\mathbf{Q}$  are concentrated along the lines where the PDW spatial phase changes by  $\pi$  (Fig. 4f). All of these phenomena are canonical signatures<sup>4,6,28,30,31</sup> of a PDW coexisting with homogeneous SC. Thus,  $\Delta(\mathbf{r})$  modulation imaging provides direct spectroscopic evidence of the existence of a PDW, at zero magnetic field in cuprates.

## Online content

Any methods, additional references, Nature Research reporting summaries, source data, extended data, supplementary information, acknowledgements, peer review information; details of author contributions and competing interests; and statements of data and code availability are available at <https://doi.org/10.1038/s41586-020-2143-x>.

- Fulde, P. & Ferrel, R. A. Superconductivity in a strong spin-exchange field. *Phys. Rev.* **135**, A550 (1964).
- Larkin, A. I. & Ovchinnikov, Yu. N. Inhomogeneous state of superconductors. *Sov. Phys. JETP* **20**, 762–769 (1965).
- Fradkin, E., Kivelson, S. A. & Tranquada, J. M. Colloquium: theory of intertwined orders in high temperature superconductors. *Rev. Mod. Phys.* **87**, 457–482 (2015).
- Agterberg, D. F. et al. The physics of pair density waves: cuprate superconductors and beyond. Preprint at <https://arxiv.org/abs/1904.09687> (2019).
- Hamidian, M. H. et al. Detection of a Cooper-pair density wave in  $\text{Bi}_2\text{Sr}_2\text{CaCu}_2\text{O}_{8+\delta}$ . *Nature* **532**, 343–347 (2016).
- Agterberg, D. F. & Tsunetsugu, H. Dislocations and vortices in pair-density-wave superconductors. *Nat. Phys.* **4**, 639–642 (2008).
- Berg, E., Fradkin, E. & Kivelson, S. A. Charge-4e superconductivity from pair-density-wave order in certain high-temperature superconductors. *Nat. Phys.* **5**, 830–833 (2009).
- Norman, M. R., Pines, D. & Kallin, C. The pseudogap: friend or foe of high  $T_c$ ? *Adv. Phys.* **54**, 715–733 (2005).
- Li, Q., Hücker, M., Gu, G. D., Tsvetlik, A. M. & Tranquada, J. M. Two-dimensional superconducting fluctuation in stripe-ordered  $\text{La}_{1.875}\text{Ba}_{0.125}\text{CuO}_4$ . *Phys. Rev. Lett.* **99**, 067001 (2007).
- Berg, E., Fradkin, E., Kivelson, S. A. & Tranquada, J. M. Striped superconductors: how spin, charge, and superconducting orders intertwine in the cuprates. *New J. Phys.* **11**, 115004 (2009).
- Berg, E. et al. Dynamical layer decoupling in a stripe-ordered high- $T_c$  superconductor. *Phys. Rev. Lett.* **99**, 127003 (2007).
- He, R.-H. et al. From a single-band metal to a high-temperature superconductor via two thermal phase transitions. *Science* **331**, 1579–1583 (2011).
- Lee, P. A. Amperean pairing and the pseudogap phase of cuprate superconductors. *Phys. Rev. X* **4**, 031017 (2014).
- Norman, M. R. & Davis, J. C. Quantum oscillations in biaxial pair density wave state. *Proc. Natl Acad. Sci. USA* **115**, 5389–5391 (2018).
- Himeda, A., Kato, T. & Ogata, M. Stripe states with spatially oscillating  $d$ -wave superconductivity in the two-dimensional  $t$ - $t'$ - $J$  model. *Phys. Rev. Lett.* **88**, 117001 (2002).
- Raczowski, M., Capello, M., Poilblanc, D., Frésard, R. & Oleś, A. M. Unidirectional  $d$ -wave superconducting domains in the two-dimensional  $t$ - $J$  model. *Phys. Rev. B* **76**, 140505 (2007).
- Yang, K.-Y., Chen, W. Q., Rice, T. M., Sigrist, M. & Zhang, F.-C. Nature of stripes in the generalized  $t$ - $J$  model applied to the cuprate superconductors. *New J. Phys.* **11**, 055053 (2009).
- Loder, F., Graser, S., Kampf, A. P. & Kopp, T. Mean-field pairing theory for the charge-stripe phase of high-temperature cuprate superconductors. *Phys. Rev. Lett.* **107**, 187001 (2011).
- Corboz, P., Rice, T. M. & Troyer, M. Competing states in the  $t$ - $J$  model: uniform  $d$ -wave state versus stripe state. *Phys. Rev. Lett.* **113**, 046402 (2014).
- Tu, W.-L. & Lee, T.-K. Genesis of charge orders in high temperature superconductors. *Sci. Rep.* **6**, 18675 (2016).
- Choubey, P., Tu, W.-L., Lee, T. K. & Hirschfeld, P. J. Incommensurate charge ordered states in the  $t$ - $t'$ - $J$  model. *New J. Phys.* **19**, 013028 (2017).
- Verret, S., Charlebois, M., Sénéchal, D. & Tremblay, A.-M. S. Subgap structures and pseudogap in cuprate superconductors: role of density waves. *Phys. Rev. B* **95**, 054518 (2017).
- Edkins, S. D. et al. Magnetic field-induced pair density wave state in the cuprate vortex halo. *Science* **364**, 976–980 (2019).
- Rajasekaran, S. et al. Probing optically silent superfluid stripes in cuprates. *Science* **359**, 575–579 (2018).
- Mesaros, A. et al. Topological defects coupling smectic modulations to intra-unit-cell nematicity in cuprates. *Science* **333**, 426–430 (2011).
- Fujita, K. et al. In Strongly Correlated Systems: *Experimental Techniques* (eds Avella, A. & Mancini, F.) Ch. 3 (Springer, 2015).
- Fujita, K. et al. Direct phase-sensitive identification of a  $d$ -form factor density wave in underdoped cuprates. *Proc. Natl Acad. Sci. USA* **111**, E3026–E3032 (2014).
- Nie, L., Tarjus, G. & Kivelson, S. A. Quenched disorder and vestigial nematicity in the pseudogap regime of the cuprates. *Proc. Natl Acad. Sci. USA* **111**, 7980–7985 (2014).
- Agterberg, D. F. & Garaud, J. Checkerboard order in vortex cores from pair-density-wave superconductivity. *Phys. Rev. B* **91**, 104512 (2015).
- Dai, Z., Zhang, Y.-H., Senthil, T. & Lee, P. A. Pair-density waves, charge-density waves, and vortices in high- $T_c$  cuprates. *Phys. Rev. B* **97**, 174511 (2018).
- Wang, Y. et al. Pair density waves in superconducting vortex halos. *Phys. Rev. B* **97**, 174510 (2018).

© The Author(s), under exclusive licence to Springer Nature Limited 2020



## Methods

### Sample preparation and measurement

High-quality  $\text{Bi}_2\text{Sr}_2\text{CaCu}_2\text{O}_{8+\delta}$  single crystals were grown by the travelling-solvent floating zone method. Here we measured a sample with hole doping level of  $p \approx 0.17$ . The sample, covered by the Kapton tape, was loaded into the load-lock chamber with pressure better than  $3 \times 10^{-10}$  torr and quickly inserted into the STM head at  $T \approx 9$  K, after cleavage by removing the Kapton tape.

### Tip preparation and characterization

The tip isotropy is checked by comparing the height of the Bragg peaks for  $x$  and  $y$  directions in the Fourier transform  $T(\mathbf{q})$  of topographic images using the nanoflake tip  $T(\mathbf{r})$ . A  $40 \text{ nm} \times 40 \text{ nm}$  FOV  $T(\mathbf{r})$  and its real-part Fourier transform  $\text{Re}T(\mathbf{q})$  are shown in Extended Data Fig. 1a, b, respectively. Extended Data Fig. 1c shows line profiles of  $\text{Re}T(\mathbf{q})$  along the lines in Extended Data Fig. 1b across the Bragg peaks at (1, 0) and (0, 1). Bragg peak heights at (1, 0) and (0, 1) are found to be comparable within 7%.

### Motivation and model for $\Delta(\mathbf{r})$ modulation detection

**Motivation of searches for a PDW signature in  $\Delta(\mathbf{r})$ .** Here we discuss preliminary  $\Delta(\mathbf{r})$  data, as shown in Extended Data Fig. 4a, c, that motivated and provide reinforcement for the data presented in this study, which is completely independent of them. These data in Extended Data Fig. 4 were acquired with two different  $\text{Bi}_2\text{Sr}_2\text{CaCu}_2\text{O}_{8+\delta}$  nanoflake tips, on two different samples, using two different SI-STM instruments. Although experimental conditions were not optimized for detection of  $\Delta(\mathbf{r})$  modulations in a PDW, the peaks in  $\Delta(\mathbf{q})$  at  $\mathbf{Q} = (0, \pm 0.125)$  and  $\mathbf{Q} = (0, \pm 0.125)(2\pi/a_0)$  are weakly visible as marked by dashed white circles in Extended Data Fig. 4b, d. Such data, along with those reported in the main text from an experiment designed and optimized for the purpose, provide the type of experimental evidence available on the existence of  $8a_0$  modulations in  $\Delta(\mathbf{r})$ .

**Independent pair tunnelling process.** Here we discuss how the  $4a_0$  modulation observed in the magnitude of the Josephson critical current and the  $8a_0$  modulation observed in  $\Delta(\mathbf{r})$  in the present study may be linked. We consider a simple model for pair tunnelling from a nanoflake  $\text{Bi}_2\text{Sr}_2\text{CaCu}_2\text{O}_{8+\delta}$  tip that is in the coexisting SC and PDW state, to the parallel surface of a bulk  $\text{Bi}_2\text{Sr}_2\text{CaCu}_2\text{O}_{8+\delta}$  crystal in the same state (Extended Data Fig. 3). Because the tip is extended and parallel to the surface, the effects of planar tunnelling must be considered. In perfect planar tunnelling, the  $c_k^\dagger c_{-k}^\dagger$  Cooper pairs of the homogenous SC cannot tunnel into the  $c_k^\dagger c_{-k+Q}^\dagger$  Cooper pairs of the PDW, because that violates conservation of momentum. In that limit, the Josephson current  $I_J$  from a  $\text{Bi}_2\text{Sr}_2\text{CaCu}_2\text{O}_{8+\delta}$  extended tip to the  $\text{Bi}_2\text{Sr}_2\text{CaCu}_2\text{O}_{8+\delta}$  crystal is composed of two independent contributions:  $I_J^S$  due to pair tunnelling from  $c_k^\dagger c_{-k}^\dagger$  to  $c_k^\dagger c_{-k}^\dagger$  states, and  $I_J^P$  due to pair tunnelling from  $c_k^\dagger c_{-k+Q}^\dagger$  to  $c_k^\dagger c_{-k+Q}^\dagger$  states.

Consider two PDW, one in the nanoflake tip  $\psi_T$  and one in the sample  $\psi_S$ , with order parameters

$$\psi_T = \Delta_1 e^{i\theta_1} (e^{i(Q(x+\delta))}) \text{ and } \psi_S = \Delta_2 e^{i\theta_2} (e^{iQx})$$

where  $x$  is the position and  $\theta$  is the phase of the order parameter. The Josephson coupling will be of the form  $K(\psi_T \psi_S^* + \psi_T^* \psi_S) \propto \cos(\theta_1 - \theta_2) \cos(Q\delta)$  where  $K$  is a constant and  $\delta$  is the variable spatial displacement of the tip PDW relative to the sample PDW. In this case, the inter-PDW Josephson current takes the form

$$I_J^P \propto \sin(\theta_1 - \theta_2) \sin(Q\delta)$$

It is the magnitude  $|I_J^P|$  that is measured as a function of transverse displacement  $\delta$  between nanoflake tip and sample where  $Q = 2\pi/\lambda$  and  $\lambda$  a

wavelength, and this obviously modulates as  $|I_J^P| \propto |\sin(Q\delta)|$  or with a periodicity of  $\lambda/2$ .

Our previous studies using scanned Josephson tunnelling<sup>32</sup> actually measured the magnitude of the Josephson current  $|I_J|$ . Thus, if  $I_J^S$  and  $I_J^P$  are independent, then  $|I_J| = |I_J^S| + |I_J^P|$ . Assuming that  $|I_J^S|$  is roughly constant spatially, then  $|I_J^P| \propto |\sin(Q\delta)|$ , where  $\delta$  is the transverse displacement between the PDW in the extended tip and the PDW in the sample. Therefore, in this model for our experiment, if the PDW has true periodicity  $8a_0$  then its gap modulation  $\Delta(\mathbf{r})$  will necessarily have periodicity  $8a_0$  but, critically, the modulations in magnitude of the total Josephson current  $|I_J|$  will have periodicity  $4a_0$ .

Note that if there are two strictly independent unidirectional PDWs with wavevectors  $\mathbf{Q}_x$  and  $\mathbf{Q}_y$ , and Cooper pair momentum of each is conserved, then the  $\mathbf{Q}_x$  PDW cannot tunnel to the  $\mathbf{Q}_y$  PDW and vice versa. This would pose a challenge to the above analysis. However, if the PDW state in the tip is somewhat biaxial (for example, ref.<sup>33</sup>), then this analysis would retain validity.

**Effect of structural supermodulation on measured  $\Delta(\mathbf{r})$ .** One might ask whether there is an effect of the crystal supermodulation with  $\mathbf{Q}_{\text{SM}} \parallel (1, 1)(2\pi/a_0)$  that produces an energy gap modulation at its wavevector, on our measured  $\Delta(\mathbf{r})$ . As we reported in ref.<sup>5</sup>, we observed the modulations both in  $\Delta(\mathbf{r})$  and the Josephson critical current at  $\mathbf{Q}_{\text{SM}}$ . However, this is a trivial effect and its wavevector is at 45° degrees off the Cu–O–Cu direction. Most importantly, a spatial convolution between the tip and sample of their modulating  $\Delta(\mathbf{r})$  at  $\mathbf{Q}_{\text{SM}}$  cannot produce any additional modulations at different wavevectors. Thus, the effect of structural supermodulation does not produce any other gap modulation signals, especially at  $\mathbf{Q} = (0, \pm 0.125)$  and  $\mathbf{Q} = (0, \pm 0.125)(2\pi/a_0)$ .

**Effect of  $\Delta(\mathbf{r})$  on nanoflake.** Here we discuss how  $\Delta(\mathbf{r})$  modulation detection is enhanced in  $\text{Bi}_2\text{Sr}_2\text{CaCu}_2\text{O}_{8+\delta}$  nanoflake SIS tunnelling. Here the measured  $\Delta(\mathbf{r})$  can be regarded as a consequence of a spatial convolution between the sample and nanoflake PDW order parameters. The nanoflake is most likely in the same PDW state as it is picked up from the same sample. Thus, the order parameter on the nanoflake is approximated in a form of  $\Delta_{\text{nanoflake}} \exp(i\mathbf{Q}_P \cdot \mathbf{r}) \exp\left(-\frac{r^2}{2\sigma^2}\right)$ , where the exponential term is approximated to represent a nanoflake structure factor with size of nanoflake (about 3 nm, see Extended Data Fig. 2). This acts as a low-pass filter in the convolution between gap modulations at the same wavevector  $\mathbf{Q}_P$  in the tip and in the sample. Such a convolution effect naturally works as a ‘lock-in’, mitigating the signals unrelated to the gap modulation wavevector  $\mathbf{Q}_P$ . This process makes the signal of  $\Delta(\mathbf{r})$  modulation detectable.

### Data analysis

**Sublattice phase-resolved analysis.** To reveal any possible local-density-of-states  $N(\mathbf{r}, E)$  modulations, we analyse differential conductance  $g(\mathbf{r}, E)$  to yield  $Z(\mathbf{r}, E) = g(\mathbf{r}, +E)/g(\mathbf{r}, -E)$  (Extended Data Fig. 5 and ref.<sup>26</sup>). Intensities at oxygen sites  $\mathbf{r}_{O_x}$  and  $\mathbf{r}_{O_y}$  are extracted separately from  $Z(\mathbf{r}, E = 54 \text{ meV})$  and used to form two new maps,  $O_x^Z(\mathbf{r}, E = 54 \text{ meV})$  and  $O_y^Z(\mathbf{r}, E = 54 \text{ meV})$ , respectively. We then calculate each sublattice-phase-resolved  $Z(\mathbf{r}, E)$  image and separate it into three: the first,  $\text{Cu}(\mathbf{r})$ , contains only the measured values of  $Z(\mathbf{r})$  at Cu sites while the other two,  $O_x(\mathbf{r})$  and  $O_y(\mathbf{r})$ , contain only the measurements at the  $x$ -/ $y$ -axis oxygen sites.

Phase-resolved Fourier transforms of the  $O_x(\mathbf{r})$  and  $O_y(\mathbf{r})$  sublattice images  $\tilde{O}_x(\mathbf{q}) = \text{Re}\tilde{O}_x(\mathbf{q}) + i\text{Im}\tilde{O}_x(\mathbf{q})$ ;  $\tilde{O}_y(\mathbf{q}) = \text{Re}\tilde{O}_y(\mathbf{q}) + i\text{Im}\tilde{O}_y(\mathbf{q})$ , are used to determine the form factor symmetry for modulations at any  $\mathbf{q}$

$$\tilde{D}^Z(\mathbf{q}) = (\tilde{O}_x(\mathbf{q}) - \tilde{O}_y(\mathbf{q}))/2$$

$$\tilde{S}^Z(\mathbf{q}) = (\tilde{O}_x(\mathbf{q}) + \tilde{O}_y(\mathbf{q}))/2$$

$$\tilde{S}^Z(\mathbf{q}) = \widetilde{Cu}(\mathbf{q})$$

Specifically, for a density wave occurring at  $\mathbf{Q}$ , one can then evaluate the magnitude of its  $d$ -symmetry form factor  $\tilde{D}(\mathbf{Q})$  and its  $s'$ - and  $s$ -symmetry form factors  $\tilde{S}'(\mathbf{Q})$  and  $\tilde{S}(\mathbf{Q})$ , respectively. In terms of the segregated sublattices, a  $d$ -form factor density wave is one for which the density wave on the  $O_x$  sites is in antiphase with that on the  $O_y$  sites. Studies of electronic structure in underdoped  $\text{Bi}_2\text{Sr}_2\text{CaCu}_2\text{O}_{8+x}$  and  $\text{Ca}_{2-x}\text{Na}_x\text{CuO}_2\text{Cl}_2$  consistently exhibit a relative phase of  $\pi$  and therefore a  $d$ -symmetry form factor.

Hence the peaks at  $\pm\mathbf{Q}_x$  and  $\pm\mathbf{Q}_y$  present in both  $\tilde{O}_x(\mathbf{q})$  and  $\tilde{O}_y(\mathbf{q})$  must cancel exactly in  $\tilde{O}_x(\mathbf{q}) + \tilde{O}_y(\mathbf{q})$ . Therefore, if a density wave at  $\mathbf{Q}$  and  $2\mathbf{Q}$  has predominantly  $d$ -symmetry form factor, there is no detectable signal in  $g(\mathbf{r}, E)$  or  $Z(\mathbf{r}, E)$  at  $\mathbf{Q}$  and  $2\mathbf{Q}$ , and why the  $d$ -symmetry Fourier transform  $D^g(\mathbf{q}, E)$  or  $D^Z(\mathbf{q}, E)$  are used in these studies. Specifically, by calculating  $D^Z(\mathbf{q}) = \text{FFT}(D^Z(\mathbf{r}))$  one correctly extracts the  $d$ -symmetry density wave modulations that are occurring at  $\mathbf{Q}$  and  $2\mathbf{Q}$ .

**Cut-off dependence.** Here we show how the images shown in Fig. 4 evolve as a function of cut-off length used in the two-dimensional lock-in technique. In Extended Data Fig. 6, both  $D_{2\mathbf{Q}_x}^Z(\mathbf{r}, 54 \text{ meV})$  and  $\Delta_{\mathbf{Q}_x}(\mathbf{r})$  are shown at different real-space cut-off lengths: 8, 16, 24, 32 and 40 Å. In the left column, we can see a big change between 8 and 16 Å in the spatial structure of  $|D_{2\mathbf{Q}_x}^Z(\mathbf{r})|$  as oscillatory components are vanished, while  $|D_{2\mathbf{Q}_x}^Z(\mathbf{r})|$  at 16, 24, 32 and 40 Å are virtually identical. For  $\Delta_{\mathbf{Q}_x}(\mathbf{r})$  in the right column in Extended Data Fig. 6, the oscillatory components are gone between 16 and 24 Å. Thus, the cut-off lengths used in Fig. 3, 16 and 40 Å, do not introduce erroneous oscillations by picking up irrelevant contributions from other wavevectors and are reasonable choices.

**Interplay of the eight-unit-cell periodic PDW and the four-unit-cell induced  $N(\mathbf{r}, E)$  modulation.** To support the Fig. 4f inset, in which  $2\pi$  topological defects in the induced  $N(\mathbf{r})$  modulation at  $2\mathbf{Q}$  tends to be found in the vicinity of the locus of  $\pi$  phase in  $\Phi_{\mathbf{Q}_x}^A(\mathbf{r})$  (yellow strings), we performed an independent analysis: the distances of the white and black dots to the nearest position on the yellow strings are calculated and compared with randomly distributed results. Extended Data Fig. 7a shows the distance distribution of the total 25 topological defects in Fig. 4e. Then we generate randomly distributed 25 'topological defects' inside the same FOV and calculate distances to the same yellow strings, and this process has been repeated 100 times. The average result of the 100 different configurations is shown in Extended Data Fig. 7b.

It is clear that the distribution from the measured  $N(\mathbf{r})$  topological defects at  $2\mathbf{Q}$  is in a smaller range with higher magnitude compared with random results. This supports that the topological defects in the measured  $N(\mathbf{r})$  modulation at  $2\mathbf{Q}$  actually show a statistically strong tendency to be found near the locus of  $\pi$  phase in  $\Phi_{\mathbf{Q}_x}^A(\mathbf{r})$ .

**$\pi$  phase winding and possible half-vortex in PDW.** In search for half-vortices in PDW, we analysed PDW phase  $\Phi_{\mathbf{Q}_x}^A(\mathbf{r})$  in the vicinity of the  $2\pi$  topological defects from the induced  $N(\mathbf{r})$  modulation at  $2\mathbf{Q}$ . We extracted the values along each contour surrounding the  $2\pi$  topological defects from the induced  $N(\mathbf{r})$  modulation at  $2\mathbf{Q}$  (Extended Data Fig. 8a) and plotted an evolution of the PDW phase for each contour in Extended Data Fig. 8b. Although no singularities that have a  $\pi$  phase winding in  $\Phi_{\mathbf{Q}_x}^A(\mathbf{r})$  are found, indeed PDW phases are changing by  $\pi$  along each contour, indicating the presence of possible half-vortices.

## Data availability

The data that support the findings of this study are available from the corresponding author upon reasonable request.

32. Cho, D. et al. A strongly inhomogeneous superfluid in an iron-based superconductor. *Nature* **571**, 541–545 (2016).
33. Norman, M. R. & Davis, J. C. Quantum oscillations in a biaxial pair density wave state. *Proc. Natl Acad. Sci. USA* **115**, 5389–5391 (2018).

**Acknowledgements** We thank S. D. Edkins, E. Fradkin, M. H. Hamidian, S. A. Kivelson, P. A. Lee and J. M. Tranquada, for discussions and advice. Z.D., H.L., K.F. G.G. and P.D.J. acknowledge support from the US Department of Energy, Office of Basic Energy Sciences, under contract number DEAC02-98CH10886. S.H.J. and J.L. acknowledge support from the Institute for Basic Science in Korea (grant number IBS-R009-G2), the Institute of Applied Physics of Seoul National University and a National Research Foundation of Korea (NRF) grant funded by the Korea government (MSIP) (number 2017R1A2B3009576). E.P.D. was supported by the Brookhaven National Laboratory Supplemental Undergraduate Research Program (SURP). J.C.S.D. acknowledges support from the Science Foundation of Ireland under award SFI 17/RP/5445 and from the European Research Council (ERC) under award DLV-788932.

**Author contributions** K.F. designed and led the project. Z.D., H.L., S.H.J., E.P.D. and K.F. carried out experiments at the MIRAGE STM of the OASIS complex at Brookhaven National Laboratory; G.G. synthesized and characterized the samples; Z.D., H.L. and K.F. developed and carried out analysis. K.F. wrote the paper with key contributions from J.C.S.D., Z.D., H.L., J.L. and P.D.J. The manuscript reflects the contributions and ideas of all authors.

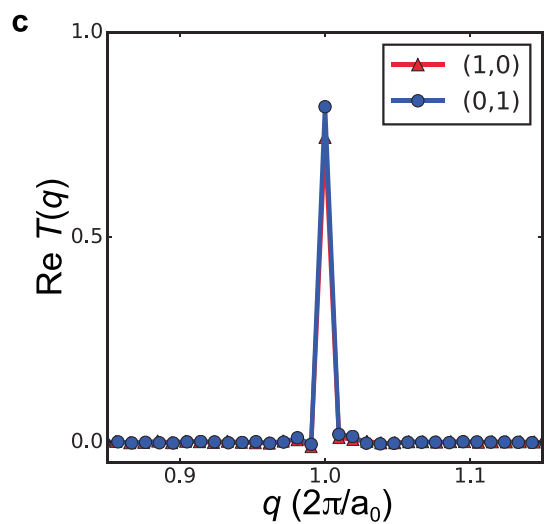
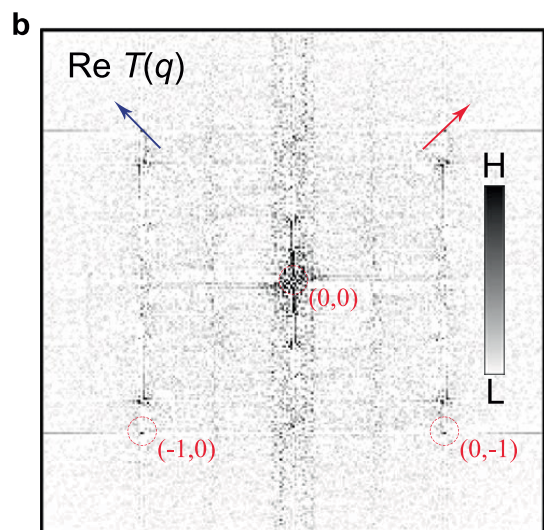
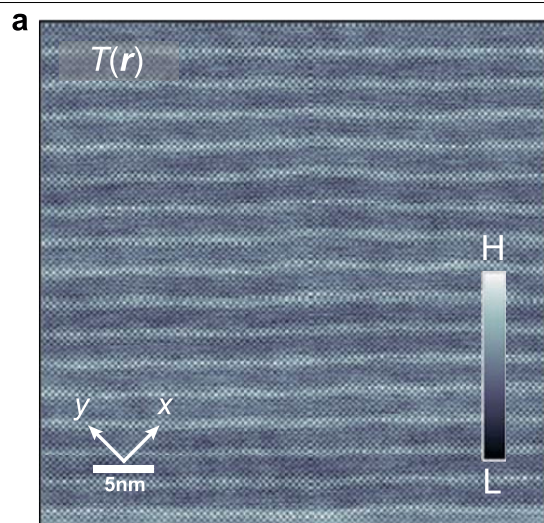
**Competing interests** The authors declare no competing interests.

## Additional information

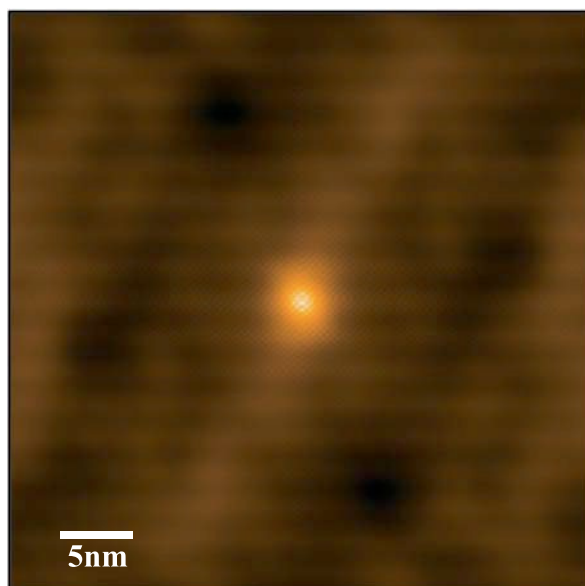
**Correspondence and requests for materials** should be addressed to K.F.

**Peer review information** *Nature* thanks Ting-Kuo Lee, Yi Yin and the other, anonymous, reviewer(s) for their contribution to the peer review of this work.

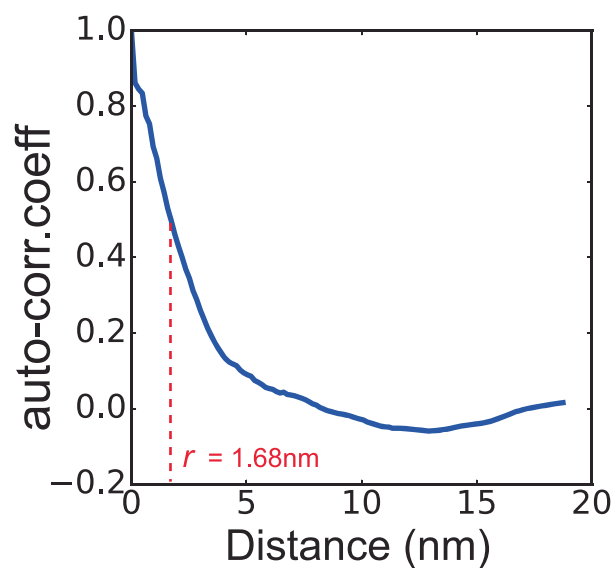
**Reprints and permissions information** is available at <http://www.nature.com/reprints>.



**Extended Data Fig. 1 | Analysis of the tip isotropy.** **a**, Topography  $T(r)$  within  $40 \text{ nm} \times 40 \text{ nm}$  FOV. **b**, Real part of Fourier transform of  $T(r)$ . **c**, Line profile  $\text{Re } T(q)$  along the line in the middle panel, representing nearly equal Bragg peak height (difference is less than 7%).

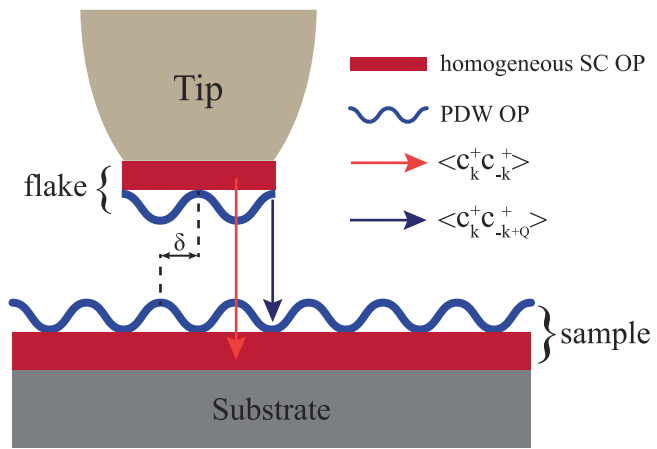
**a**

-0.3  1.0

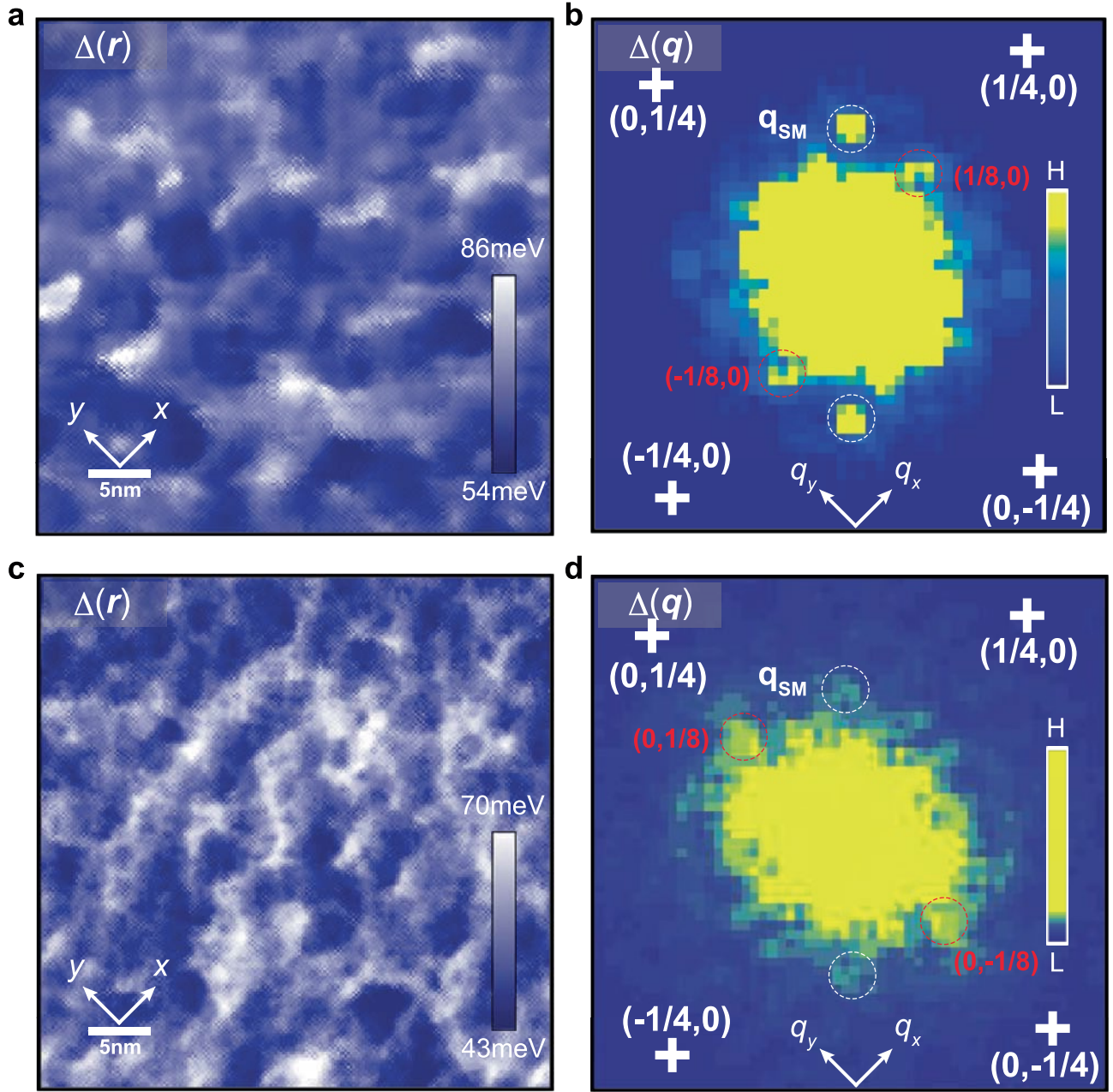
**b****Extended Data Fig. 2 | Estimation of the nanoflake tip geometry.**

**a**, Autocorrelation of  $\Delta(\mathbf{r})$ . **b**, Line profile measured from centre in **a** is azimuthal-angle averaged. The size of the nanoflake on the tip is estimated from the full-width at half-maximum and is around 3.3 nm.



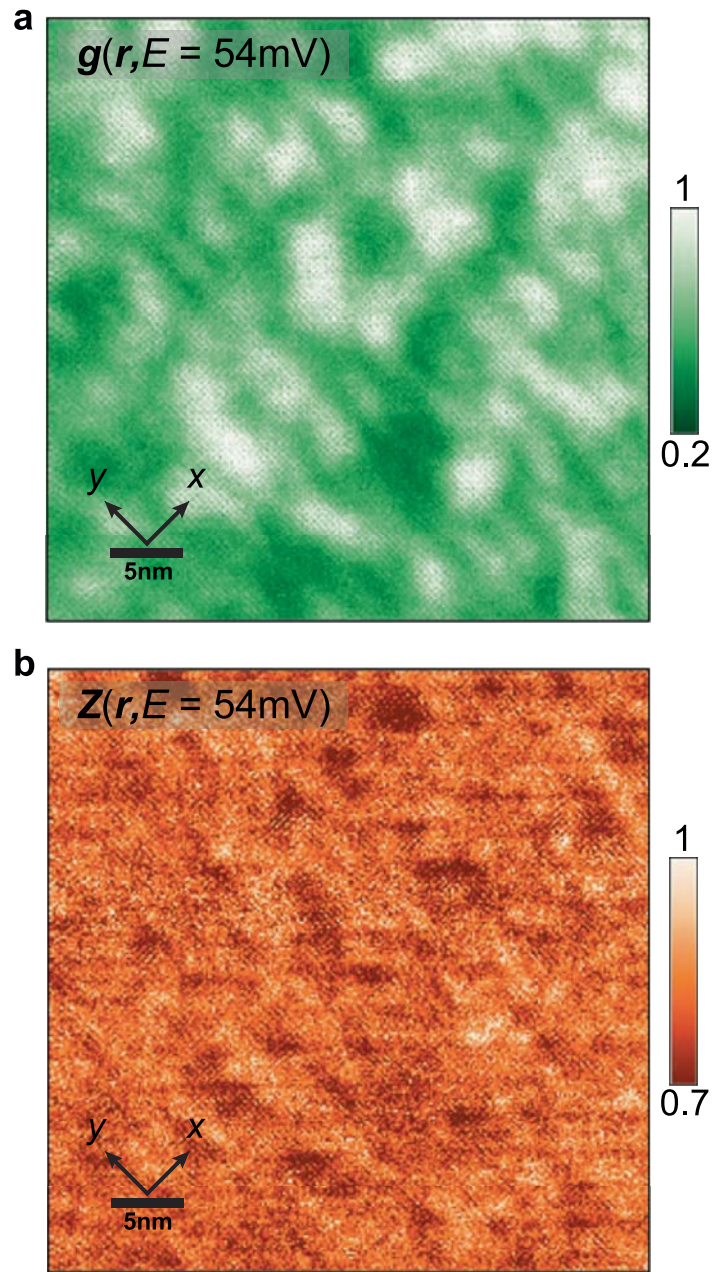


**Extended Data Fig. 3 | Possible process of the Josephson tunnelling.**  
Schematic representation of planar Josephson tunnelling in the presence of two order parameters (OPs): homogeneous SC and PDW.

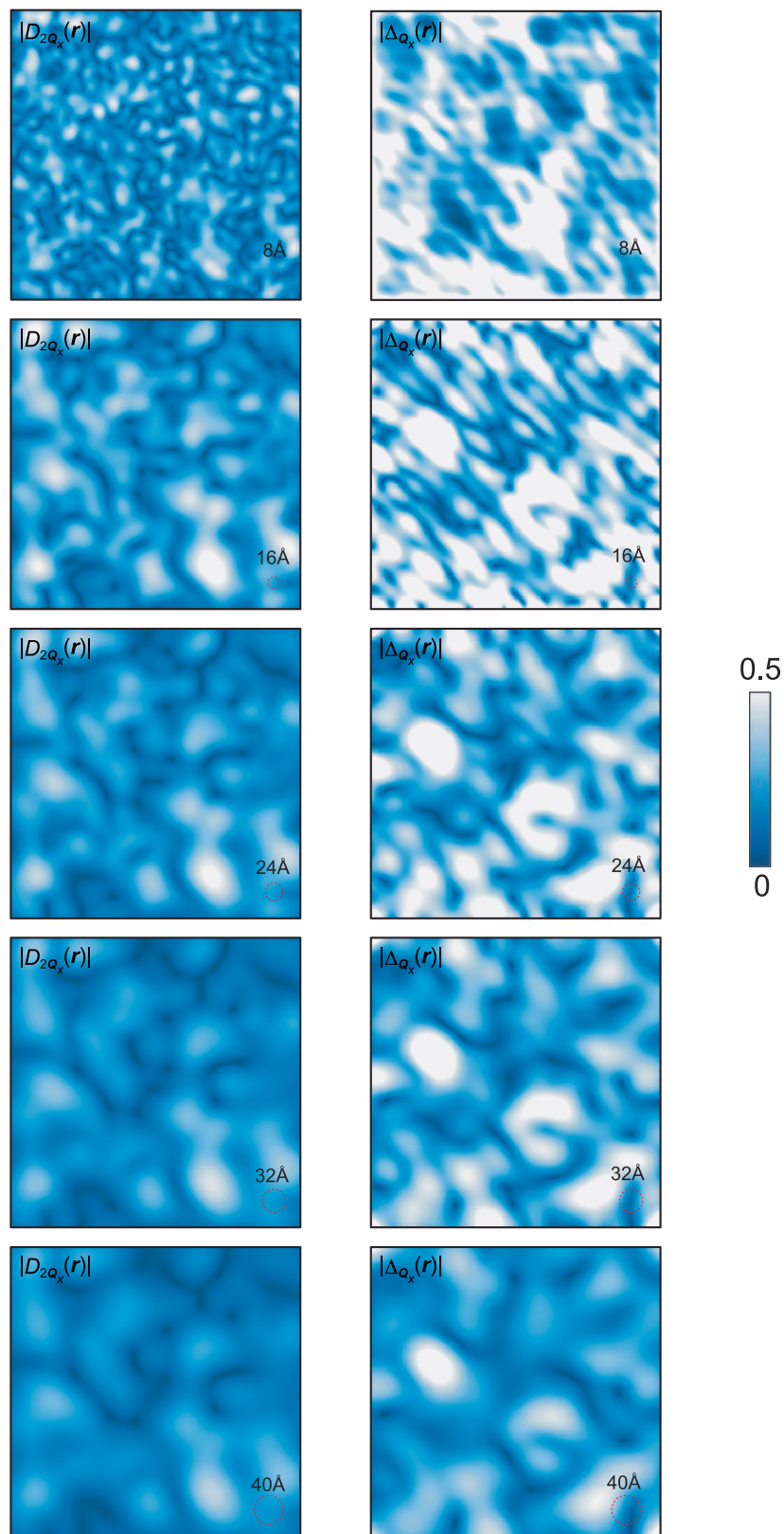


**Extended Data Fig. 4 | Preliminary experimental data analysis.**  
**a, c**, Preliminary  $\Delta(r)$  independently measured at 4.2 K on different pieces of nearly optimally doped  $\text{Bi}_2\text{Sr}_2\text{CaCu}_2\text{O}_{8+\delta}$ . **b, d**, The magnitude of Fourier

transform of  $\Delta(r)$  in **a** and **c**, respectively, representing early observations of  $1/8$  peaks marked by the red circles.

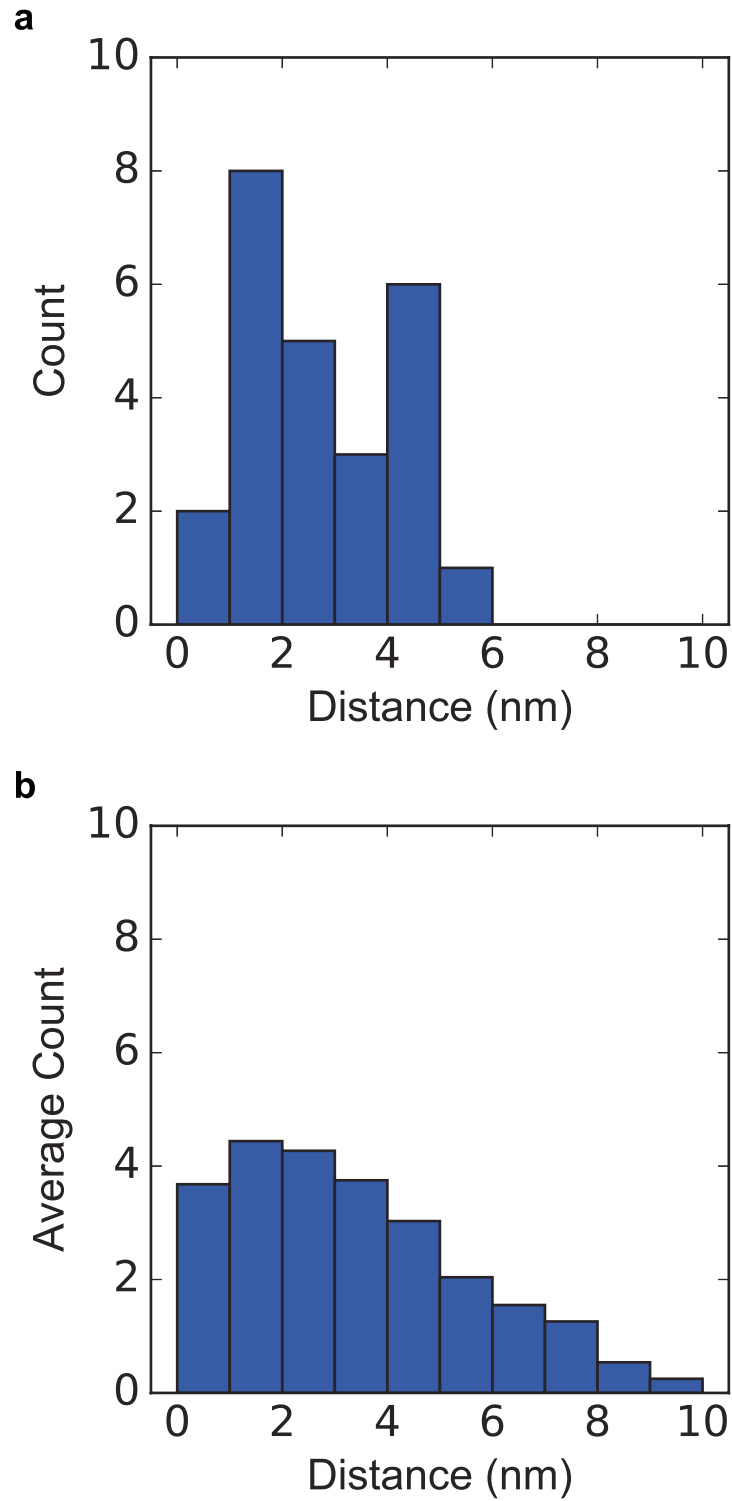


**Extended Data Fig. 5 | Differential conductance map and its ratio. a,**  $g(\mathbf{r}, E = 54\text{ meV})$  map. The eight-unit-cell CDW modulation, that is, the PDW induced  $N(\mathbf{r})$  modulation at  $\mathbf{Q}$ , can be seen. **b,**  $Z(\mathbf{r}, E = 54\text{ meV})$  calculated by  $Z(\mathbf{r}, E) = g(\mathbf{r}, E)/g(\mathbf{r}, -E)$ .



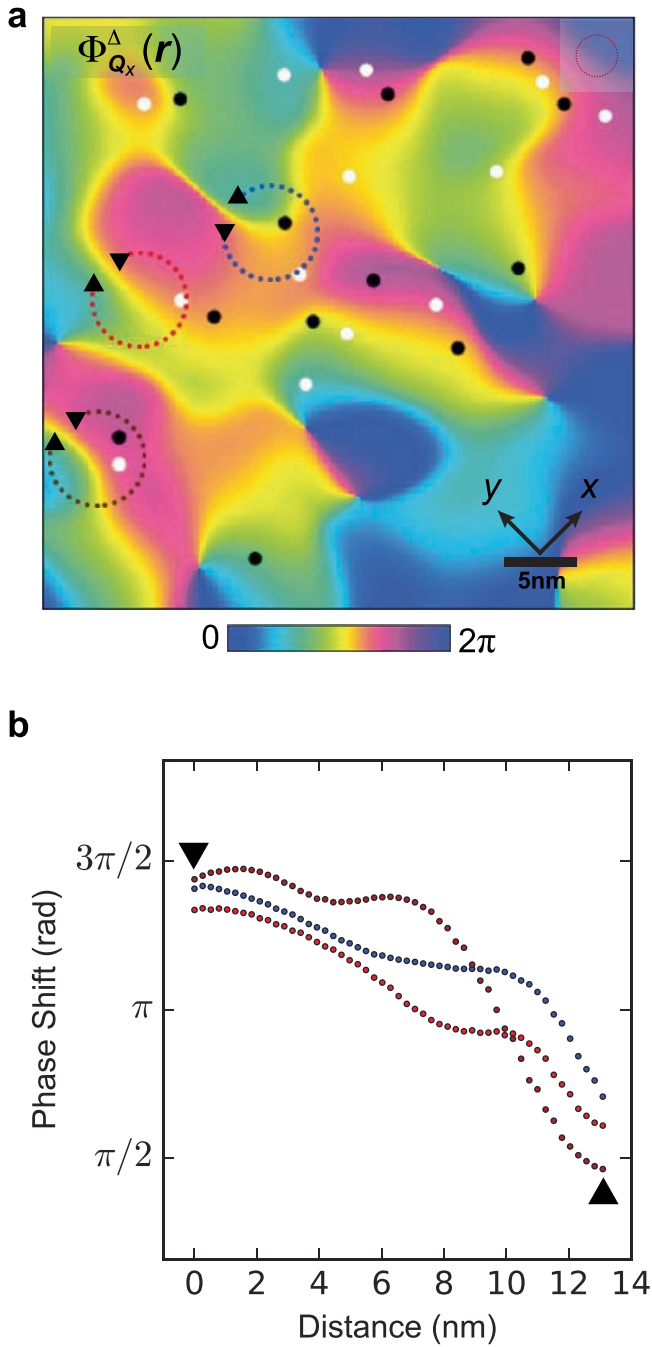
**Extended Data Fig. 6** | Cut-off length dependence of  $|D_{2Q_x}^Z(r)|$  and  $|\Delta_{Q_x}(r)|$ . The left column shows  $|D_{2Q_x}^Z(r)|$  at different cut-off lengths, similarly for the right column for  $|\Delta_{Q_x}(r)|$ .





**Extended Data Fig. 7 | Distance analysis. a.** A count distribution sorted by distances between the topological defects in the induced  $N(\mathbf{r})$  modulation at  $2Q$  from Fig. 4b and the nearest point on the yellow strings in the PDW phase

map from Fig. 4c. **b.** Average distribution of 100 configurations, within each configuration 25 points are randomly generated in the same FOV and distances to the same yellow strings are calculated and sorted.



**Extended Data Fig. 8 | Spatial evolution of the PDW phase. a,** A phase map  $\Phi_{Q_x}^{\Delta}(r)$  of the PDW order. Three representative contours surrounding the  $2\pi$  topological defects from  $\Phi_{2Q_x}^Z(r)$  across the yellow strings. **b,** An evolution of the phase along each contour in **a**. The upside-down black triangle marks the starting point of winding and the upright black triangle marks the ending point, in correspondence with the winding directions in **a**.  $\pi$  phase windings are clearly seen in the PDW phase surrounding the  $2\pi$  topological defects from  $\Phi_{2Q_x}^Z(r)$ .

# A map of the amine–carboxylic acid coupling system

<https://doi.org/10.1038/s41586-020-2142-y>

Babak Mahjour<sup>1</sup>, Yuning Shen<sup>1</sup>, Wenbo Liu<sup>1</sup> & Tim Cernak<sup>1</sup>✉

Received: 16 August 2019

Accepted: 17 January 2020

Published online: 1 April 2020

 Check for updates

Chemical transformations determine the structure of a product, and therefore its properties, which in turn affect complex macroscopic functions such as the metabolic stability of pharmaceuticals or the volatility of perfumes. Therefore, reaction selection can influence the success or failure of a candidate molecule to meet a functional objective. The coupling of an amine with a carboxylic acid to form an amide bond is the most popular chemical reaction used for drug discovery<sup>1</sup>. However, there are many other ways to connect these two common functional groups together. Here we show computationally that amines and acids can couple via hundreds of hypothetical yet plausible transformations, and we demonstrate experimentally the application of a dozen such reactions. To investigate the contribution of chemical transformations to properties, we developed a string-based notation and used an enumerative combinatorics approach to produce a map of conceivable amine–acid coupling transformations, which can be charted using chemoinformatic techniques. We find that critical physicochemical parameters of the products, such as partition coefficient and polar surface area, vary considerably depending on the transformation chosen. Data mining the amine–acid coupling system produced here should enable reaction discovery, which we demonstrate by developing an esterification reaction found within the mapped space. Complex molecules with distinct property profiles can also be discovered within the amine–acid coupling system, as we show here via the late-stage diversification of drugs and natural products.

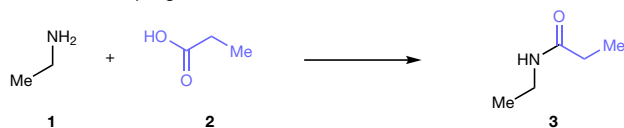
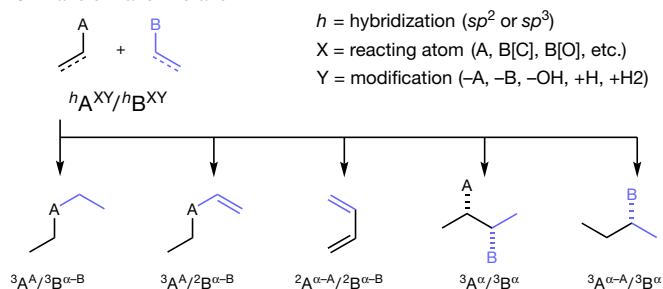
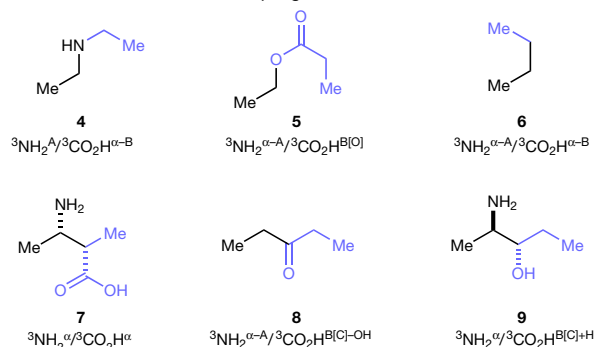
The amide coupling is a robust and popular reaction used frequently in chemical synthesis. The transformation couples an amine (**1**) and a carboxylic acid (**2**) to form an amide (**3**) (Fig. 1a). Viewed in the context of physicochemical properties, the transformation unites a hydrophilic basic moiety (**1**) bearing two hydrogen bond donors, with a hydrophilic acidic moiety (**2**) bearing one hydrogen bond donor and two hydrogen bond acceptors, to generate a neutral product, **3**. The amide product is more lipophilic than the starting reagents, and has one hydrogen bond donor and one hydrogen bond acceptor. Chemoinformatic studies have linked physicochemical properties to functions as complex as toxicity<sup>2</sup> and even successful market launch<sup>3</sup>, and so the ability to modulate the numbers of hydrogen bond donors, hydrogen bond acceptors, the partition coefficient  $\log P$ , the molecular weight, and other properties of a molecule via chemical synthesis is of high importance. Control over physicochemical properties using chemical synthesis is typically achieved by varying starting materials iteratively or in a combinatorial manner<sup>4</sup>, or by varying build–couple–pair reaction sequences to introduce skeletal diversity<sup>5</sup>. We hypothesized that physicochemical properties could be varied simply by switching the chemical transformation while holding the building blocks constant. In our view, transformations describes the mapping of atoms and bonds from starting materials to products<sup>6</sup>, and can be described as reactions only when accompanied by experimental reaction conditions. We reasoned that

a map of conceivable transformations would provide opportunities in reaction discovery, especially given contemporary developments in robotic<sup>7–11</sup> and algorithmic<sup>12–16</sup> techniques for predicting reaction conditions, in addition to presenting a strategy for chemical-space exploration.

The amide coupling is used in one quarter of the reactions reported in small-molecule pharmaceutical patents<sup>1</sup>. As a result, there is an abundance of available amine and acid building blocks. We questioned how many other transformations exist for the amine–acid coupling pair. Considering amine–acid couplings at the transformation level reveals opportunities for reaction discovery. For example, instead of coupling **1** and **2** to form **3** (Fig. 1a), a decarboxylation could occur to give **4**, or a deamination could occur to give **5**; likewise, a tandem decarboxylation–deamination could occur to forge a carbon–carbon bond as in **6** (Fig. 1b). Compounds **7–9** are also possible, and the set of compounds **3–9** collectively reveals that **1** and **2** could couple to form acidic products, basic products, neutral products and zwitterionic products. We used enumerative combinatorics (Extended Data Fig. 1) to create simplified molecular-input line-entry system (SMILES) strings for all products arising from the coupling of two generic functional groups, A and B.

A notation was developed (Fig. 1c) to describe how functional groups A or B can couple at the atoms of the functional group (A, B[C], or B[O], when B is CO<sub>2</sub>H), or at the  $\alpha$  or  $\beta$  carbon atoms. The notation also

<sup>1</sup>Department of Medicinal Chemistry, College of Pharmacy, University of Michigan, Ann Arbor, MI, USA. ✉e-mail: tcernak@med.umich.edu

**a** The amide coupling**c** Transformation notation**b** Conceivable amine-acid coupling transformations

**Fig. 1 | Transformation enumeration strategy and notation.** **a**, Ethylamine (1) and propanoic acid (2) can couple to form amide 3, but can also couple to form 79 other products, including 4–9. **b**, Enumerating all combinations of  $sp^2$  or  $sp^3$

hybridization for the 80 coupling patterns yields 320 product substructures. **c**, A notation system for classifying transformations; see also Extended Data Fig. 1.

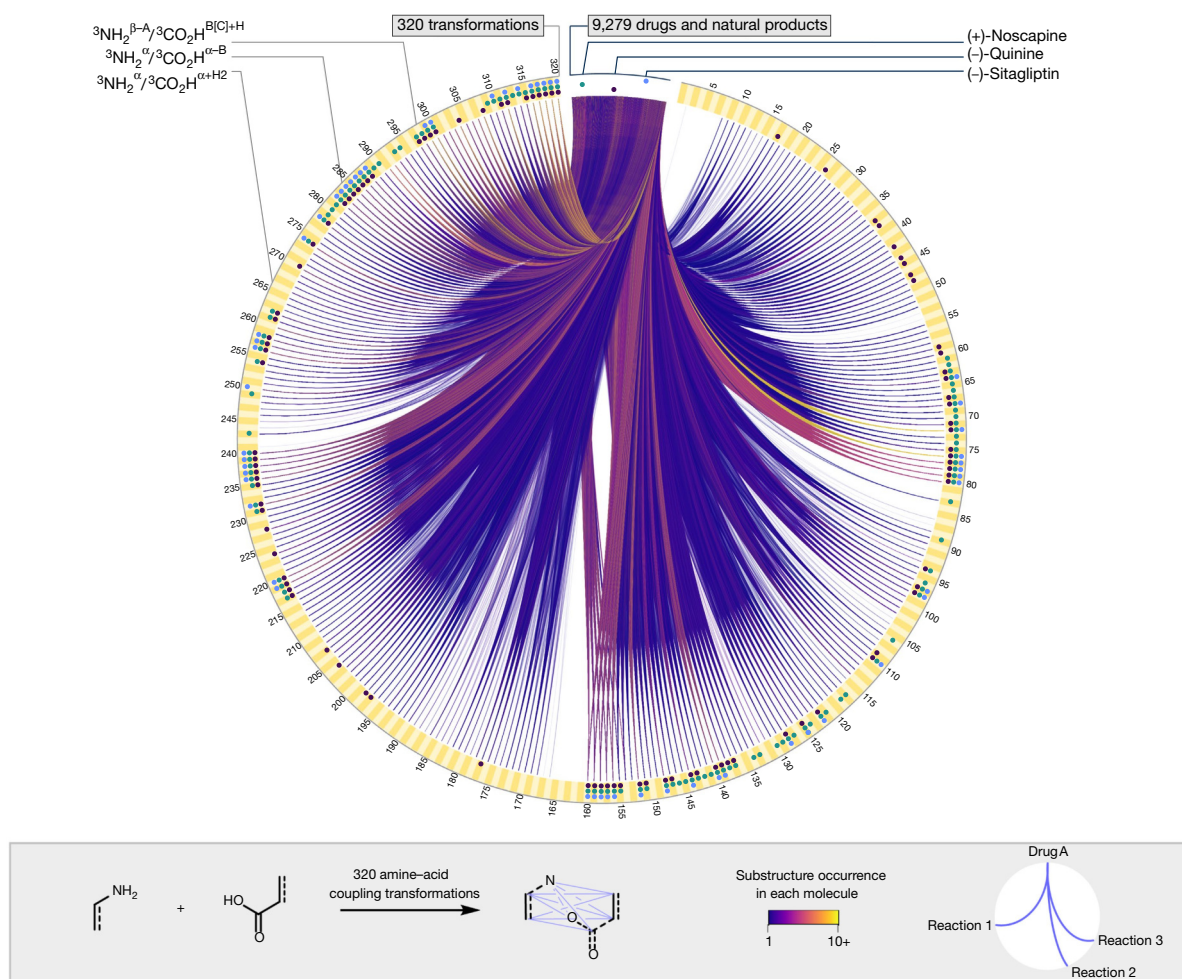


**Fig. 2 | Substructure search of 320 amine-acid coupling transformations within 9,279 complex molecules from DrugBank.** Each line represents the appearance of a product substructure of a transformation in a complex molecule, and the colour of the line represents the frequency of occurrence of that substructure in that molecule. The dots around the periphery denote

which specific transformations appear in complex molecules (+)-noscapine (green dots), (-)-quinine (purple dots) and (-)-sitagliptin (blue dots), which connect to 112, 96 and 55 transformations, respectively. The numbers around the periphery can be matched to a full list of transformation notation labels found in Extended Data Table 1.



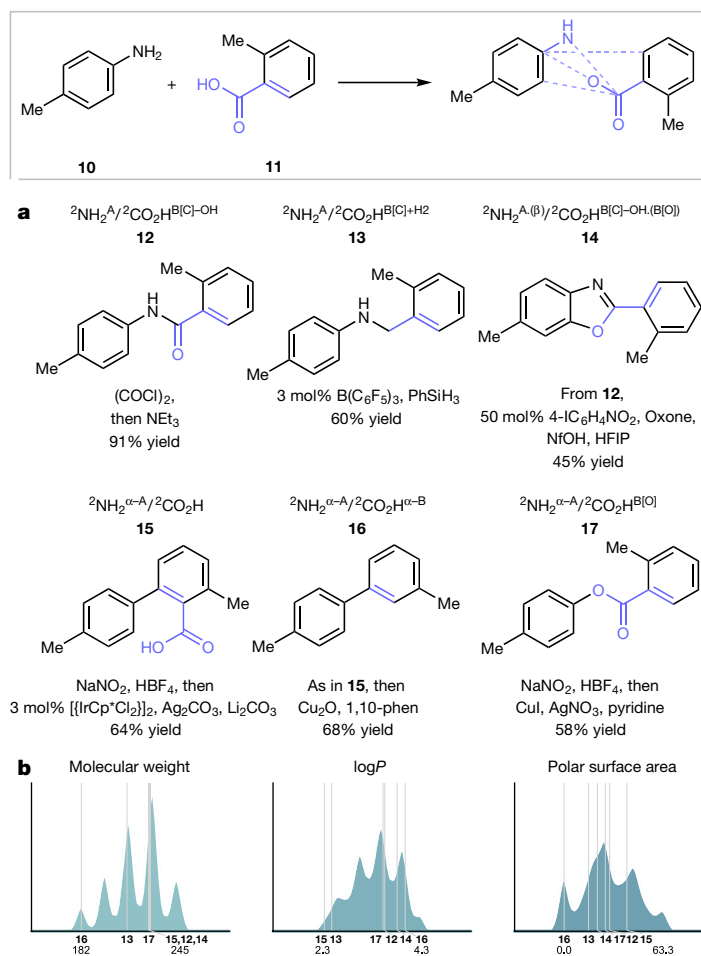


**Fig. 3 | Experimental exploration of the  $sp^2$ - $sp^2$  amine-acid coupling transformation space. a**, Products with different property profiles (for example, basic, acidic, neutral, lipophilic) can be produced from the same two starting materials, **10** and **11** (top), by varying the transformation and reaction conditions. NfOH, nonafluorobutanesulfonic acid; HFIP, hexafluoroisopropanol; Cp\*, pentamethylcyclopentadiene; 1,10-phen,

1,10-phenanthroline. **b**, Kernel density estimation plots show the range of accessible molecular weight, partition coefficient ( $\log P$ ) and polar surface area by coupling **10** to **11** via various amine-acid coupling transformations. Grey lines denote the molecular weight,  $\log P$  and polar surface area of **12-17**. The calculations use **13** and **15** in their charged protonation state.

describes how functional groups A, B or both may appear in or be absent from the product. The transformation notation is written in the form  $h\text{A}^{XY}/h\text{B}^{XY}$ , where  $h$  is the hybridization ( $2 = sp^2$ ,  $3 = sp^3$ ), X is the reacting atom and Y is any additional modification including loss of A or B ( $-A$ ,  $-B$ ), dehydration ( $-\text{OH}$ ), or reduction ( $+\text{H}$ ,  $+\text{H}_2$ ). All combinations of  $sp^2$ - $sp^2$ ,  $sp^2$ - $sp^3$ ,  $sp^3$ - $sp^2$  and  $sp^3$ - $sp^3$  transformations from **1**, **2** and their  $sp^2$  variants ethenamine and acrylic acid (Fig. 2) were included, leading to 320 product substructures. Four of the transformations produced the amides resulting from coupling  $sp^2$ - $sp^2$ ,  $sp^2$ - $sp^3$ ,  $sp^3$ - $sp^2$  or  $sp^3$ - $sp^3$  amines and acids, respectively, but the vast majority of the enumerated transformations are currently unknown as reactions. By charting the amine-acid cross-coupling space, we aim to understand how chemical transformations affect physicochemical properties.

The enumerated SMILES strings were used as inputs to a series of chemoinformatic calculations. First, SMILES strings of the products were computationally ionized at pH 7.4 (Supplementary Information), and then used to calculate a range of physicochemical properties (Extended Data Fig. 2). The full set of 320 products spans a range of molecular weights from 54.1 to 120.2 g mol<sup>-1</sup>,  $\log P = -2.29$  to 2.19 units, hydrogen bond acceptors from 0 to 3, hydrogen bond donors from 0 to 2, polar surface area = 0 to 67.8 Å<sup>2</sup>, fraction  $sp^3 = 0$  to 1, number of rotatable bonds from 1 to 4, and a formal charge between -1 and 1. A composite function of drug-like properties, the quantitative estimate of

drug-likeness<sup>17</sup>, ranged from 0.27 to 0.54. These findings demonstrate that the choice of transformation can have a sizeable effect on properties. In the context of drug discovery, it may be necessary to decrease the number of hydrogen bond donors when optimizing a molecule for the ability to cross the blood-brain barrier<sup>18</sup>, whereas it may be necessary to increase the number of hydrogen bond donors to improve aqueous solubility<sup>19</sup>. In this way, transformation mapping can enable studies in property optimization.

The 320 product molecules from the combinatorial enumeration were next used as substructures to search 9,279 pharmaceuticals and natural products from the DrugBank database<sup>20</sup>. As can be seen in Fig. 2, there is a high degree of connectivity between the products of nearly every amine-acid coupling transformation with diverse pharmaceuticals and natural products. Each connecting line represents the successful identification of an enumerated product substructure within a drug, and the colour of the line depicts the frequency that a substructure occurs in that molecule. The density of connections in this system suggests that nearly every one of the 320 transformations depicted on the periphery of Fig. 2 could find use in the synthesis of complex molecules. As expected, the simple alkyl chain **6**, formed by coupling **1** to **2** ( $3\text{NH}_2^{\alpha-A}/3\text{CO}_2\text{H}^{\alpha-B}$ ), occurs frequently as a product substructure: 59,432 times among the DrugBank molecules (Extended Data Fig. 3). Likewise, decarboxylative transformations to produce an

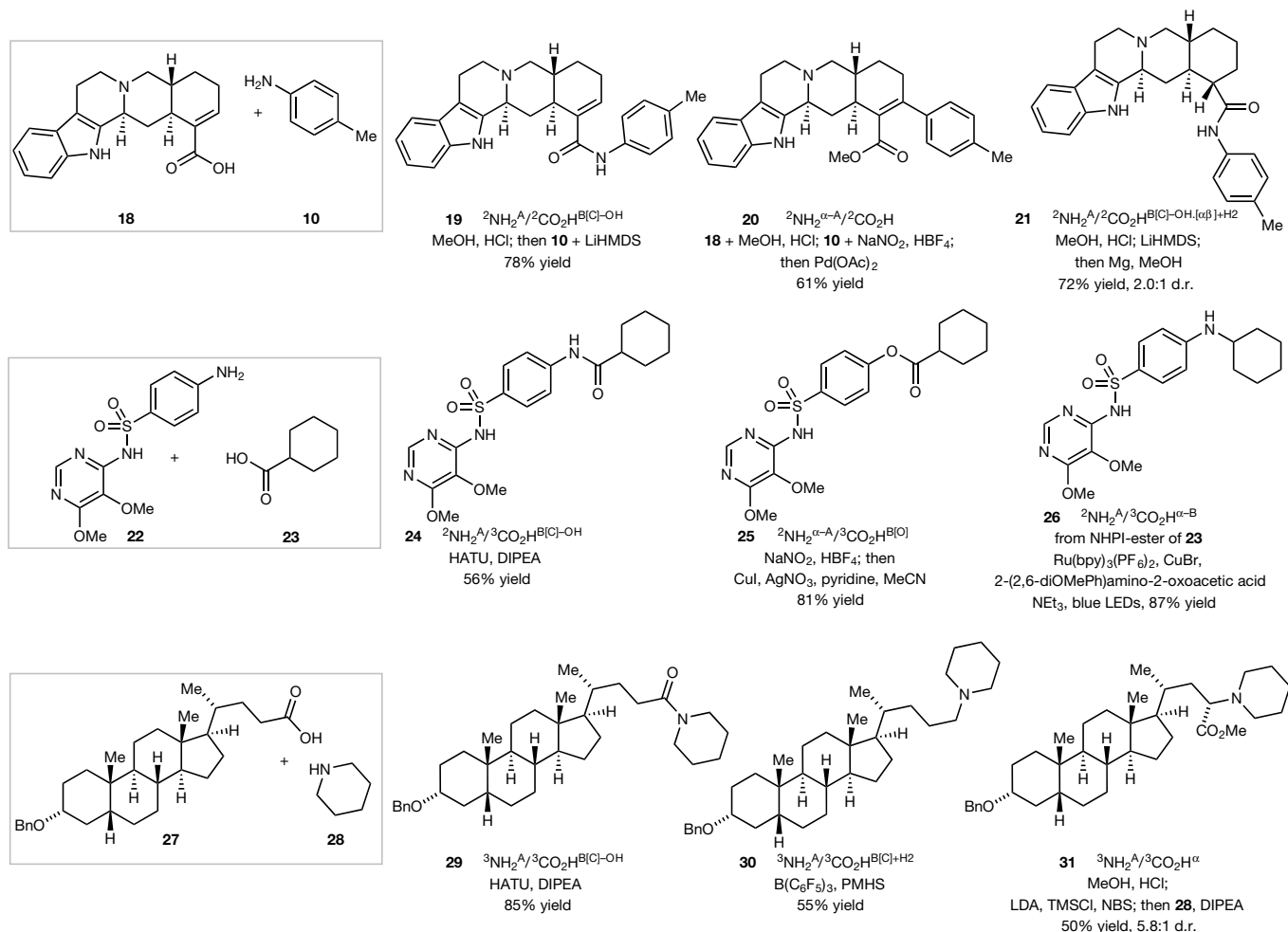


**Fig. 4 | Late-stage diversification.** Various transformations enable the diversification of the complex molecules **18**, **22** and **27**. We performed a virtual enumeration of other complex molecules—shown in Extended Data Fig. 9—wherein the full transformation set was enumerated for four complex molecule pairings to demonstrate that a wide range of properties can be accessed, depending on which transformation is selected. LiHMDS, lithium

bis(trimethylsilyl)amide; HATU, 1-[bis(dimethylamino)methylene]-1*H*-1,2,3-triazolo[4,5-*b*]pyridinium 3-oxide hexafluorophosphate; DIPEA, *N,N*-diisopropylethylamine; NHPI, *N*-hydroxyphthalimide; PMHS, polymethylhydrosiloxane; LDA, lithium diisopropylamide; TMSCl, trimethylsilyl chloride; NBS, *N*-bromosuccinimide.

amine bound to an  $sp^3$ - or  $sp^2$ -carbon chain (such as  $^2\text{NH}_2^A/{}^3\text{CO}_2\text{H}^{A-B}$  to produce amines) appear in high frequency (Extended Data Fig. 4). Some transformations, such as  $^2\text{NH}_2^A/{}^3\text{CO}_2\text{H}^{B[O]}$ , do not appear as substructures in pharmaceuticals or natural products at all. This finding can be rationalized because, in this case, the transformation produces a hydroxyl amine ester, which is probably too reactive a functionality to persist in any of the complex molecules found in DrugBank. Analysing the system in the other direction, novel retrosynthetic strategies emerge by using amine–acid coupling transformations. For instance, (+)-noscaphine connects to 112 transformations, (–)-quinine connects to 96 transformations and (–)-sitagliptin connects to 55 transformations (Extended Data Fig. 5), providing strategies for total synthesis. Our analysis until this point focused solely on achiral bond connectivities. In three-dimensional space, there are many more possible transformations, because some transformations produce *syn*-diastereomers whereas others produce *anti*-diastereomers (Extended Data Fig. 6). These chiral coupling transformations sample a substantial assortment of three-dimensional shapes (Extended Data Fig. 7).

To demonstrate our ability to control properties with atom-level precision, several transformations were selected and realized experimentally (Fig. 3a). We selected the amide coupling as well as four known reactions, which maximized the diversity of properties

attainable from the coupling of *p*-toluidine (**10**) to *o*-toluic acid (**11**). Using the free amine and acid directly, we executed the amide coupling ( $^2\text{NH}_2^A/{}^2\text{CO}_2\text{H}^{B[C]-\text{OH}}$ ) under Schotten–Baumann conditions to give **12** in 91% yield. A  $\text{B}(\text{C}_6\text{F}_5)_3$ -catalysed reductive *N*-alkylation<sup>21</sup> was used to realize the  $^2\text{NH}_2^A/{}^2\text{CO}_2\text{H}^{B[C]+\text{H}_2}$  transformation, giving amine **13** in 60% yield. A cyclized benzoxazole (**14**) was also generated from **12** under oxidative conditions<sup>22</sup>. Through activation of the amine as the diazonium salt, an *ortho*-arylation  $^2\text{NH}_2^A/{}^2\text{CO}_2\text{H}^B$  and a corresponding decarboxylative variation  $^2\text{NH}_2^A/{}^2\text{CO}_2\text{H}^{B-B}$  were achieved via Gooßen's conditions<sup>23</sup> giving **15** or **16** in 64% and 68% isolated yield, respectively.

The mapping of amine–acid coupling space provides opportunities to devise reaction methods, and we discovered one reaction within this system. We reasoned that fruitful combinations of reagents, catalysts, ligands, activating groups and directing groups could be identified to realize hypothetical reactions. Towards this objective, we applied high-throughput experimentation techniques to interrogate the coupling of amine–acid derivatives using transition metal complexes, ligands and additives (Extended Data Fig. 8). We discovered a reaction based on the  $^2\text{NH}_2^A/{}^2\text{CO}_2\text{H}^{B[O]}$  transformation, which generated ester **17** from acid **11** and the diazonium salt of **10** under influence of copper(I) iodide, silver nitrate and pyridine. This reaction transforms a C–N bond into the C–O bond of the ester. The product, **17**, is a matched molecular pair to

the corresponding amide **12**, but bears one less hydrogen bond donor. Thus, starting from **10** and **11** and simply by varying reaction conditions, we could produce the traditional amide (**12**), as well as closely related analogues that are basic (**13**), acidic (**15**), neutral and lipophilic (**14**, **16** and **17**), or neutral and hydrophilic (**12**). The products we obtained experimentally span a substantial portion of the full range of molecular weight, log*P* and polar surface area values achievable from all coupling transformations of **10** and **11** (Fig. 3b), showcasing the utility of our approach for fine-tuning molecular properties.

Many complex molecules contain an amine or an acid functional group, so we anticipated that the application of diverse amine–acid coupling transformations to late-stage diversification would enable access to congeners with diverse property profiles. We used chemoinformatics to evaluate late-stage diversification in the amine–acid coupling system on a series of complex substrates (Extended Data Fig. 9). Examination of the properties of the products reveals that the choice of transformation can determine whether an analogue will pass or fail the Lipinski rule of five<sup>24</sup>, leading to a range in desirability score (quantitative estimate of drug-likeness)<sup>17</sup> of 0.31 to 0.70 for the couplings of the acid-containing antibiotic levofloxacin with 3,5-dichloroaniline, and 0.29 to 0.61 for the pairing of yohimbine and α-methylbenzylamine (Extended Data Fig. 9). To experimentally demonstrate the value of the late-stage diversification concept (Fig. 4), enones derived from yohimbine (**18**), sulfadoxin (**22**) and lithocholic acid benzyl ether (**27**) were used as substrates. In the first instance, **18** was esterified and then converted to amide **19** in 78% yield by heating with **10** in the presence of lithium hexamethyldisilazide. Concurrently, **18** was esterified and then β-arylated to produce **20** upon palladium-catalysed Heck–Matsuda arylation using the diazonium salt of *p*-toluidine (**10**). We determined that **18** could be converted to **19**, then treated with magnesium in a one-pot operation to introduce an additional stereocentre, as in **21**. Likewise, **22** and cyclohexane carboxylic acid (**23**) coupled to form amide **24**, ester **25** by our copper(I)-promoted C–N to C–O<sup>2</sup>NH<sub>2</sub><sup>α-A</sup>/CO<sub>2</sub>H<sup>B(O)</sup> reaction, or amine **26** under decarboxylative conditions<sup>25</sup>. Finally, **27** served as a framework to produce amide **29**, amine **30** or aminoester **31** via a one-pot <sup>3</sup>NH<sub>2</sub><sup>A</sup>/CO<sub>2</sub>H<sup>α</sup> α-amination sequence using piperidine (**28**). In this work we focused on amines and acids, but transformations of any pair of functional groups can be enumerated to serve as inspiration for the development of novel reaction methods and as a strategy for chemical-space exploration. All of the transformations mapped in the amine–acid coupling system could exist, but most are not yet linked to viable reaction conditions, making this transformation space a fertile proving ground for manual or automated reaction discovery.

## Online content

Any methods, additional references, Nature Research reporting summaries, source data, extended data, supplementary information,

acknowledgements, peer review information; details of author contributions and competing interests; and statements of data and code availability are available at <https://doi.org/10.1038/s41586-020-2142-y>.

- Boström, J. et al. Expanding the medicinal chemistry synthetic toolbox. *Nat. Rev. Drug Discov.* **17**, 709–727 (2018); correction **17**, 922 (2018).
- Liu, J. et al. Predicting organ toxicity using in vitro bioactivity data and chemical structure. *Chem. Res. Toxicol.* **30**, 2046–2059 (2017).
- Waring, M. J. et al. An analysis of the attrition of drug candidates from four major pharmaceutical companies. *Nat. Rev. Drug Discov.* **14**, 475–486 (2015).
- Liu, R., Li, X. & Lam, K. S. Combinatorial chemistry in drug discovery. *Curr. Opin. Chem. Biol.* **38**, 117–126 (2017).
- Burke, M. D. & Schreiber, S. L. A planning strategy for diversity-oriented synthesis. *Angew. Chem. Int. Ed.* **43**, 46–58 (2003).
- Ugi, I. et al. New elements in the representation of the logical structure of chemistry by qualitative mathematical models and corresponding data structures. In *Computer Chemistry* (ed. Ugi, I.) 199–233 (Springer, 1993).
- Gesmundo, N. J. et al. Nanoscale synthesis and affinity ranking. *Nature* **557**, 228–232 (2018).
- Buitrago Santanilla, A. et al. Nanomole-scale high-throughput chemistry for the synthesis of complex molecules. *Science* **347**, 49–53 (2015).
- Granda, J. M. et al. Controlling an organic synthesis robot with machine learning to search for new reactivity. *Nature* **559**, 377–381 (2018); correction **570**, E67–E69 (2019).
- Perera, D. et al. A platform for automated nanomole-scale reaction screening and micromole-scale synthesis in flow. *Science* **359**, 429–434 (2018).
- Coley, C.W. et al., A robotic platform for flow synthesis of organic compounds informed by AI planning. *Science* **365**, eaax1566 (2019).
- Zahrt, A. F. et al. Prediction of higher-selectivity catalysts by computer-driven workflow and machine learning. *Science* **363**, eaau5631 (2019).
- Ahneman, D. T. et al. Predicting reaction performance in C–N cross-coupling using machine learning. *Science* **360**, 186–190 (2018).
- Reid, J. P. & Sigman, M. S. Holistic prediction of enantioselectivity in asymmetric catalysis. *Nature* **571**, 343–348 (2019).
- McNally, A., Prier, C. K. & MacMillan, D. W. Discovery of an α-amino C–H arylation reaction using the strategy of accelerated serendipity. *Science* **334**, 1114–1117 (2011).
- Troshin, K. & Hartwig, J. F. Snap deconvolution: an informatics approach to high-throughput discovery of catalytic reactions. *Science* **357**, 175–181 (2017).
- Bickerton, G. R. et al. Quantifying the chemical beauty of drugs. *Nat. Chem.* **4**, 90–98 (2012).
- Wager, T. T. et al. Moving beyond rules: the development of a central nervous system multiparameter optimization (CNS MPO) approach to enable alignment of druglike properties. *ACS Chem. Neurosci.* **1**, 435–449 (2010).
- Hill, A. P. & Young, R. J. Getting physical in drug discovery: a contemporary perspective on solubility and hydrophobicity. *Drug Discov. Today* **15**, 648–655 (2010).
- Wishart, D. S. et al. DrugBank 5.0: a major update to the DrugBank database for 2018. *Nucleic Acids Res.* **46**, D1074–D1082 (2018).
- Fu, M. C. et al. Boron-catalyzed *N*-alkylation of amines using carboxylic acids. *Angew. Chem. Int. Ed.* **54**, 9042–9046 (2015).
- Alla, S. K., Sadhu, P. & Punniyamurthy, T. Organocatalytic syntheses of benzoxazoles and benzothiazoles using aryl iodide and oxone via C–H functionalization and C–O/S bond formation. *J. Org. Chem.* **79**, 7502–7511 (2014).
- Huang, L., Hackenberger, D. & Gooßen, L. J. Iridium-catalyzed ortho-arylation of benzoic acids with arenediazonium salts. *Angew. Chem. Int. Ed.* **54**, 12607–12611 (2015).
- Lipinski, C. A. Drug-like properties and the causes of poor solubility and poor permeability. *J. Pharmacol. Toxicol. Methods* **44**, 235–249 (2000).
- Mao, R., Frey, A., Balon, J. & Hu, X. Decarboxylative C(sp<sup>3</sup>)–N cross-coupling via synergetic photoredox and copper catalysis. *Nat. Catal.* **1**, 120–126 (2018).

**Publisher's note** Springer Nature remains neutral with regard to jurisdictional claims in published maps and institutional affiliations.

© The Author(s), under exclusive licence to Springer Nature Limited 2020

# Article

## Data availability

All data, including experimental details, spectral data and raw .fid files generated or analysed during this study are included in Supplementary Information. Chemoinformatic data are available at <https://github.com/cernaklab/acid-amine-enumeration>.

## Code availability

All code produced during this study can be found at <https://github.com/cernaklab/acid-amine-enumeration>.

**Acknowledgements** We thank the University of Michigan College of Pharmacy for start-up funds. S. McCarty is thanked for preliminary experiments and R. Zhang is thanked for discussions.

**Author contributions** B.M. performed chemoinformatic studies. Y.S., W.L., B.M. and T.C. performed chemistry experiments. All authors analysed the data. B.M. and T.C. wrote the manuscript. T.C. designed and supervised the study.

**Competing interests** The University of Michigan has filed a patent on the technique described herein that lists T.C., B.M. and Y.S. as inventors.

## Additional information

**Supplementary information** is available for this paper at <https://doi.org/10.1038/s41586-020-2142-y>.

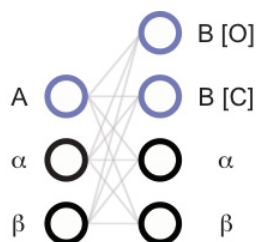
**Correspondence and requests for materials** should be addressed to T.C.

**Peer review information** *Nature* thanks Connor W. Coley and the other, anonymous, reviewer(s) for their contribution to the peer review of this work.

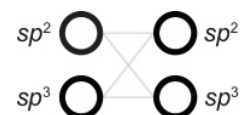
**Reprints and permissions information** is available at <http://www.nature.com/reprints>.



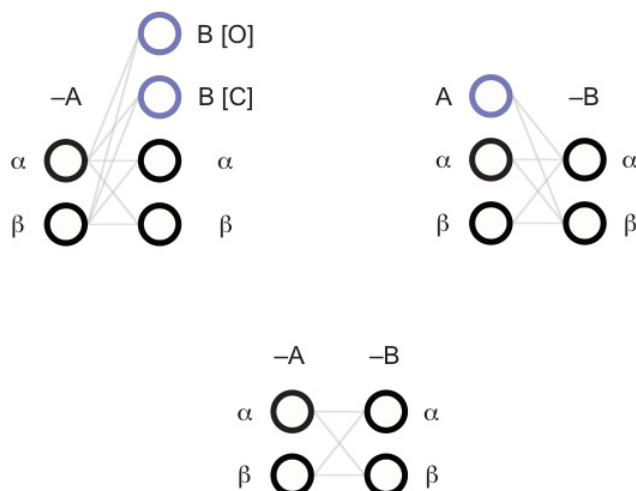
## 1. Enumerate bond arrangements



## 2. Enumerate hybridization

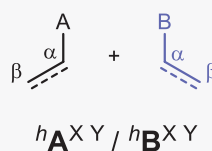


## 3. Enumerate reduction of carboxylates to ketones, alcohols, alkanes.



## 4. Enumerate all *syn*- and *anti*-stereochemical outcomes

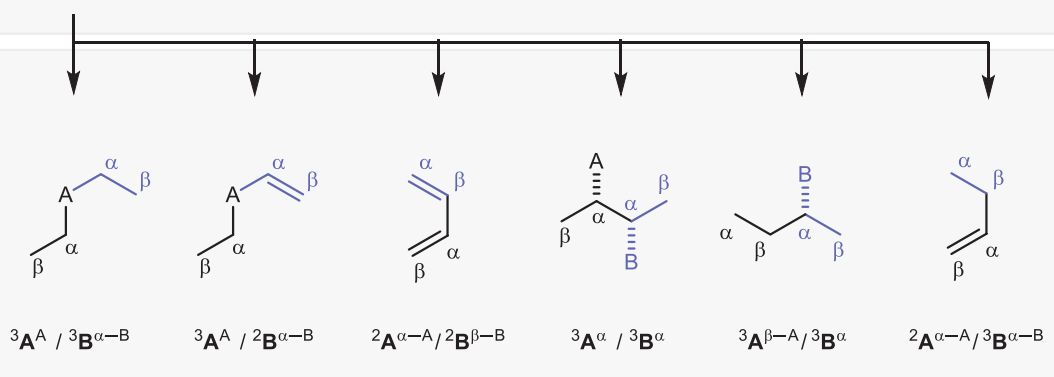
### transformation notation



$h$  = hybridization ( $sp^2$  or  $sp^3$ )

$X$  = reacting atom (A, B[C], B[O],  $\alpha$ ,  $\beta$ )

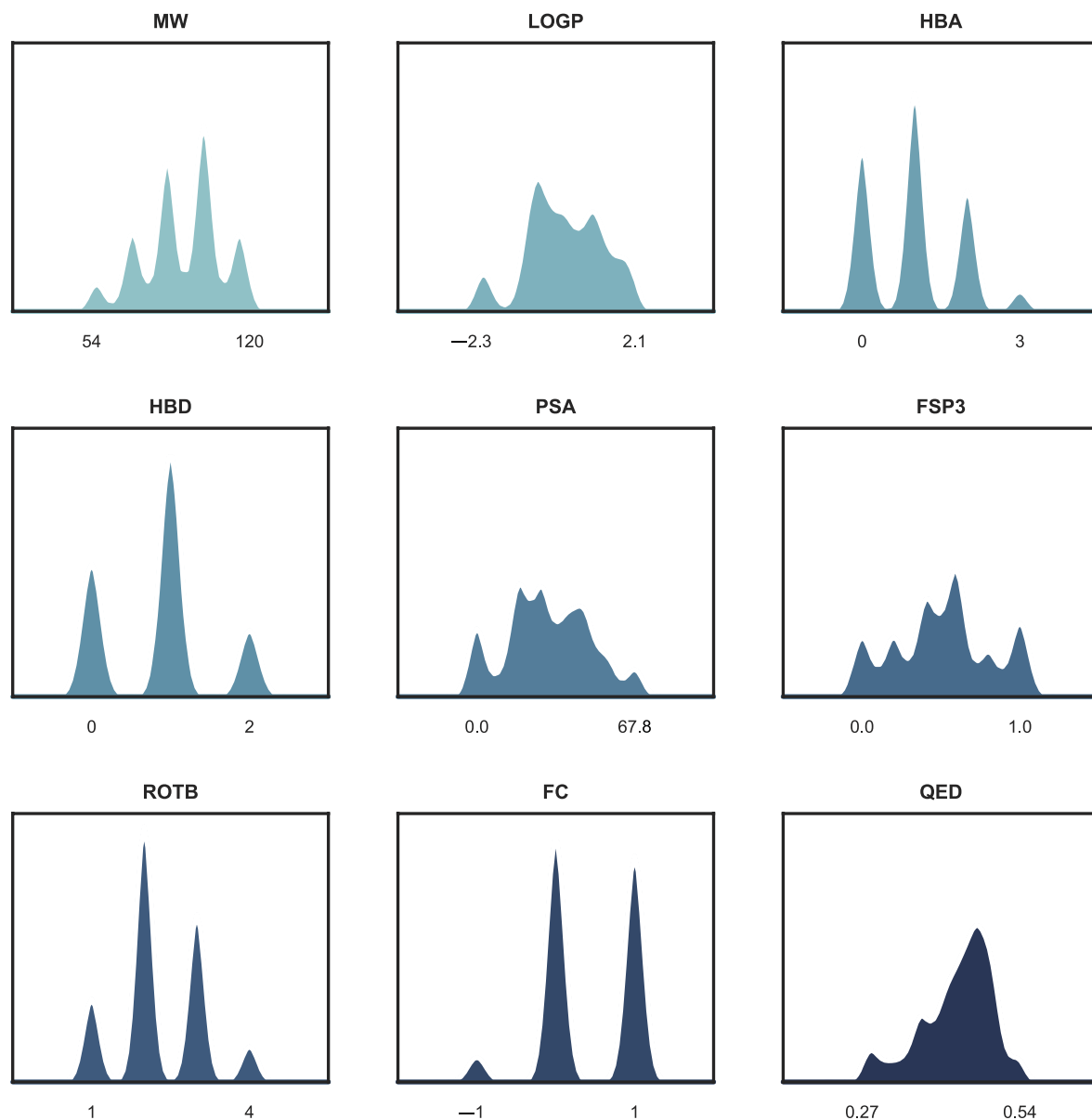
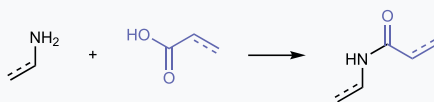
$Y$  = modification ( $-A$ ,  $-B$ ,  $-OH$ ,  $+H$ ,  $+H_2$ )



**Extended Data Fig. 1 | Workflow for enumeration of amine–acid transformations.** For a pair of coupling partners, we consider a reaction at the functional group A (amine) and B (carboxylic acid oxygen, B[O] or carbon, B[C]). Deamination reactions are noted as  $-A$  and decarboxylation reactions

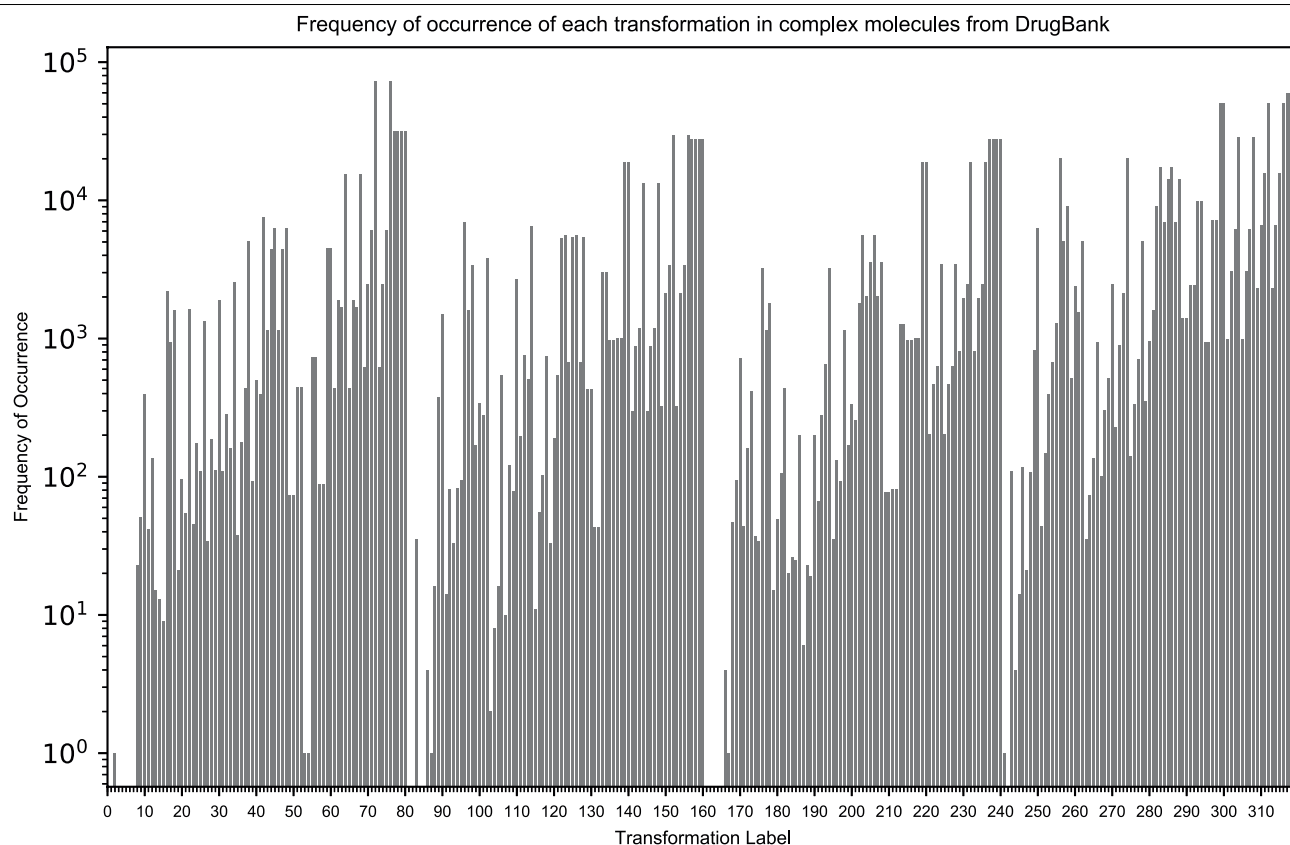
are noted as  $-B$ . Enumeration following steps 1–3 produces 320 transformations. For the enumeration of all *syn*- and *anti*-diastereomers (step 4), consult also Extended Data Fig. 6.

## 320 amine-acid coupling transformations



**Extended Data Fig. 2 | Kernel density estimate plots for 320 conceivable amine-acid coupling transformations.** Distribution of common physical properties from the achiral amine-acid coupling of ethylamine, ethenamine, propanoic acid and acrylic acid. MW, molecular weight; HBA, hydrogen bond

acceptor; HBD, hydrogen bond donor; PSA, polar surface area; FSP3, fraction  $sp^3$ ; ROTB, rotatable bonds; FC, formal charge; QED, quantitative estimate of drug-likeness.



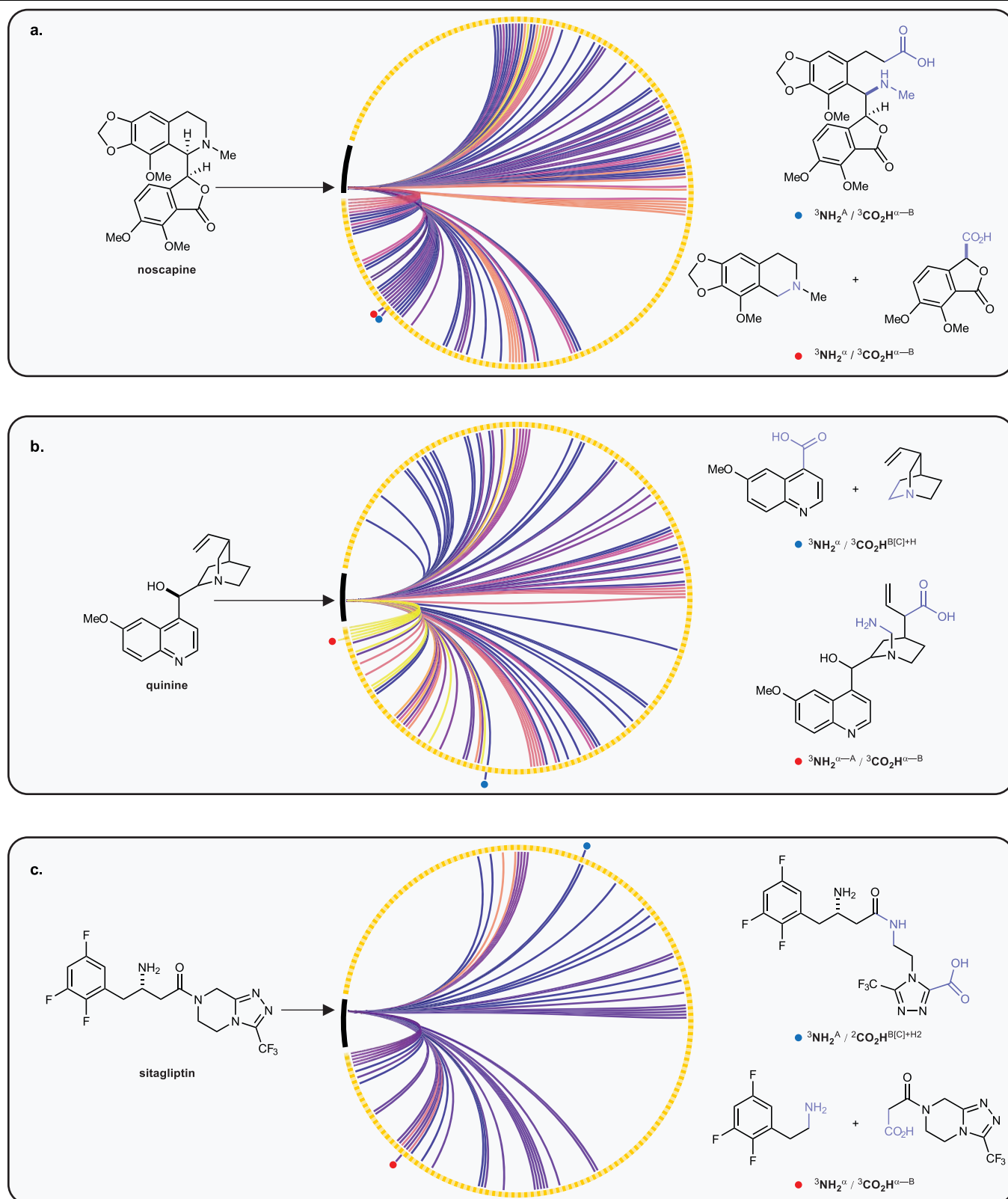
**Extended Data Fig. 3 | Number of DrugBank hits per transformation.** This bar chart shows how many times a transformation is found in the DrugBank database. Each number on the abscissa maps to a transformation listed in Extended Data Table 1.



**Extended Data Fig. 4 | Decarboxylative transformations from the enumeration scheme.** Decarboxylative reactions that produce an amine bound to an  $sp^3$  or  $sp^2$  carbon chain appear in high frequency. These reactions

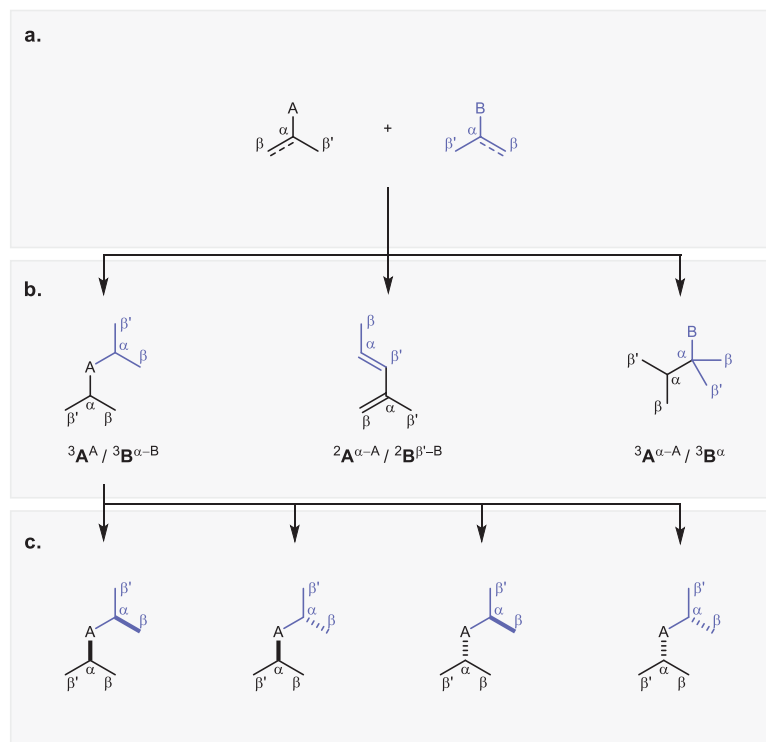
can be used to synthesize a large number of drugs contained in DrugBank. Each transformation can be found by its corresponding number in Extended Data Table 1. The colour scale is the same as in Fig. 2. rxn, reaction.





**Extended Data Fig. 5 | Transformations from the enumeration scheme found in specific drugs.** The chord diagrams show connectivity of transformation substructures as retrosynthetic disconnections in target molecules, with red and blue dots highlighting the transformations shown at left in each panel. **a.**

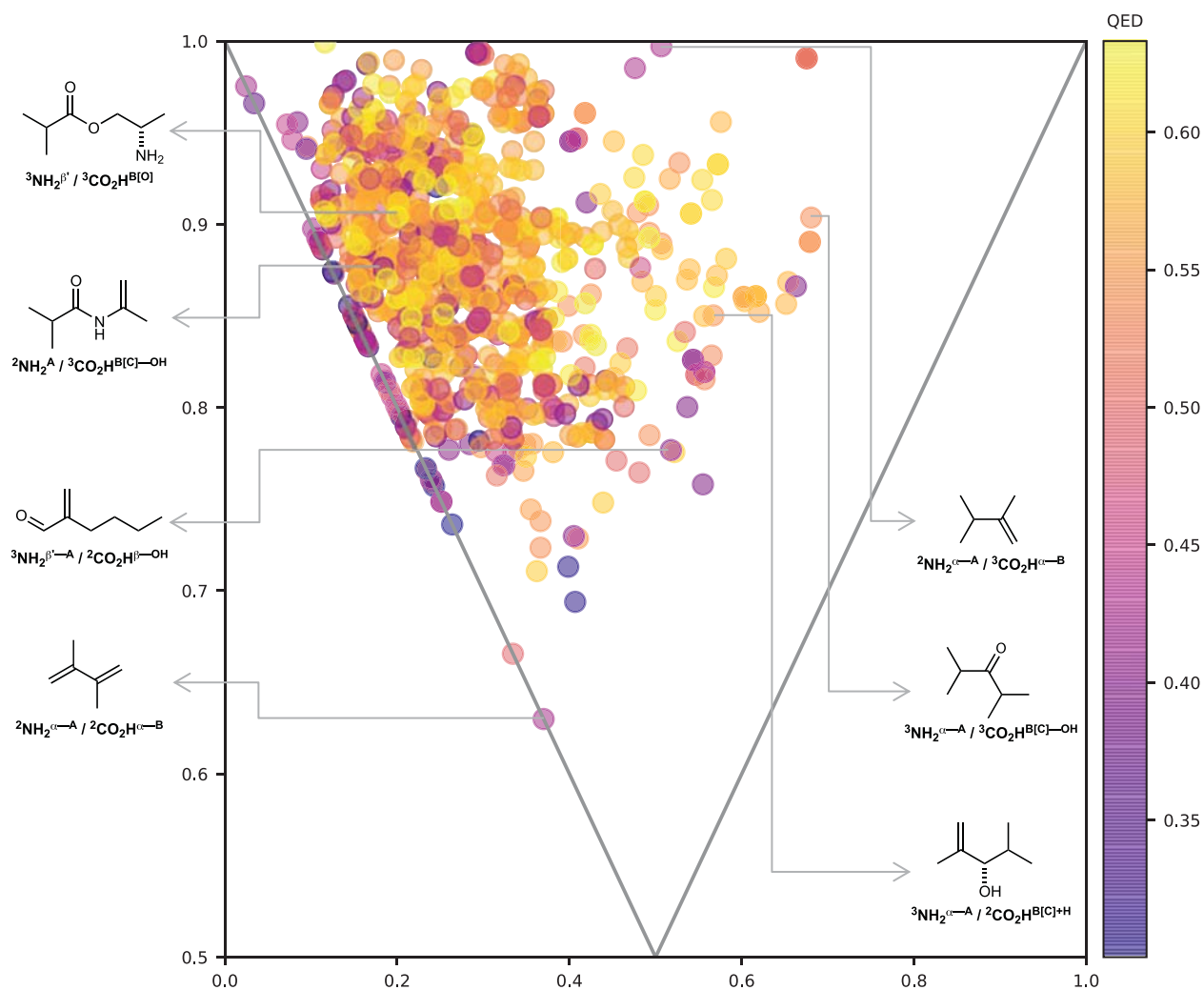
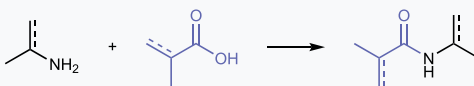
Noscapine connects to 112 of the transformations. **b.** Quinine connects to 96 transformations. **c.** Sitagliptin connects to 55 transformations. The colour scale is the same as in Fig. 2.



**Extended Data Fig. 6 | Enumeration of regioisomers and diastereomers.**  
**a,** The transformation substructures enumerated in Fig. 3 are from the 320 achiral bond arrangements available from coupling **1**, **2** and their  $sp^2$  variants ethenamine and acrylic acid. **b,** To sample three-dimensional and regiochemical space, a  $\beta'$  substituent was added as a differentiating substituent. The  $\beta'$  substituent may be any substituent, but is enumerated as

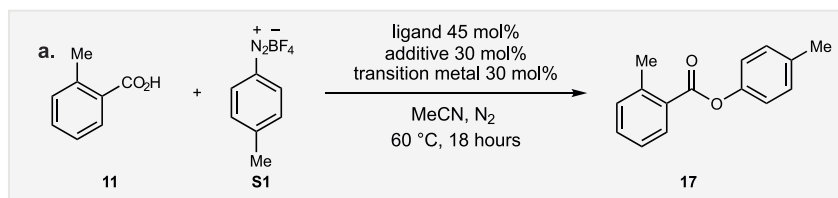
being distinct from the  $\beta$  substituent. Considering this regiochemical enumeration increases the 320 achiral coupling transformations to 588. **c,** Subsequent enumeration of all possible diastereomers leads to 1,005 chiral coupling transformations. These 1,005 three-dimensional substructures were used as inputs in the principle moment of inertia plot in Extended Data Fig. 7.

### 1,005 amine-acid coupling transformations



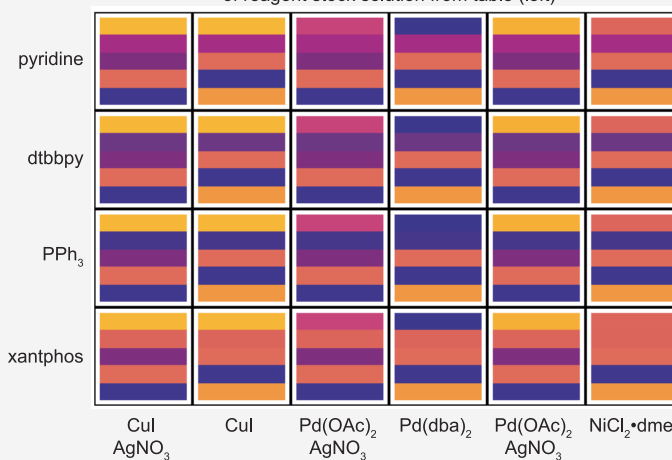
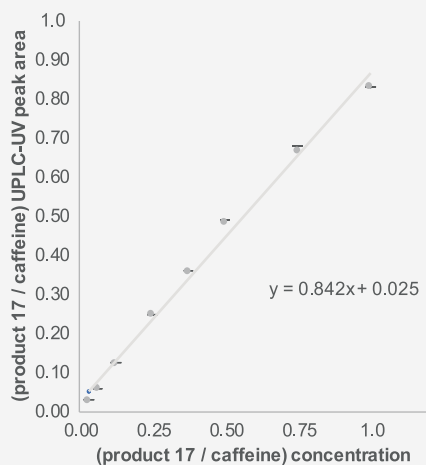
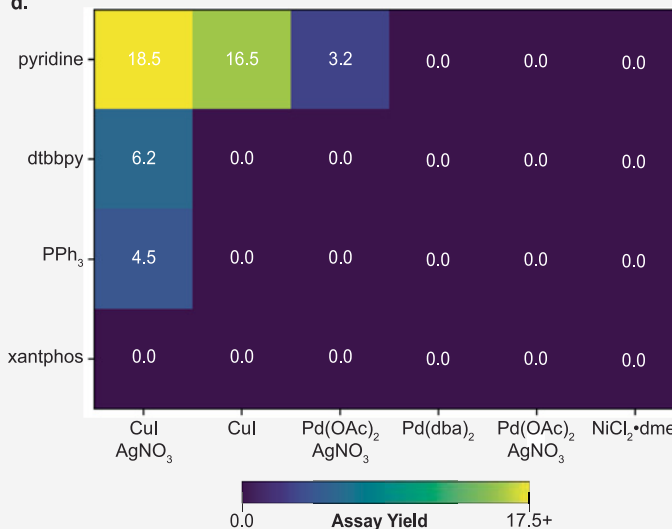
**Extended Data Fig. 7 | Principal moment of inertia plot of 1,005 amine-acid coupling transformations incorporating stereochemistry and regiochemistry.** In this expanded three-dimensional space, regiochemistry and stereochemistry of the transformations were considered. A total of 1,005

ways to connect an amine to an acid were found. The products presented a diversity of properties and three-dimensional shapes. Each molecule is coloured by its quantitative estimate of drug-likeness.

**b.**

reaction conc.	reagent	color
0.045 M	pyridine	
0.045 M	dtbbpy	
0.045 M	PPh <sub>3</sub>	
0.045 M	xantphos	
0.030 M	CuI	
0.030 M	AgNO <sub>3</sub>	
0.030 M	Pd(OAc) <sub>2</sub>	
0.030 M	Pd(dba) <sub>2</sub>	
0.030 M	NiCl <sub>2</sub> ·dme	
0.030 M	NiI <sub>2</sub>	
0.100 M	11	
0.150 M	S1	
N/A	acetonitrile	

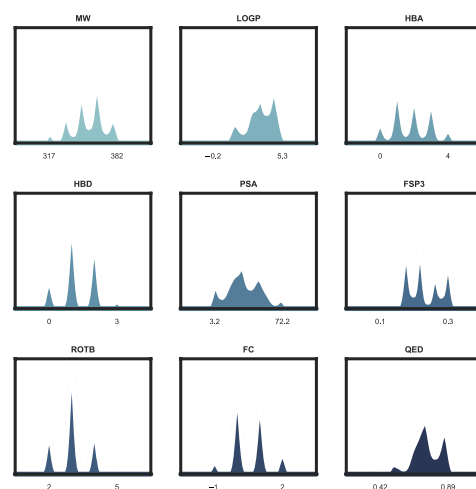
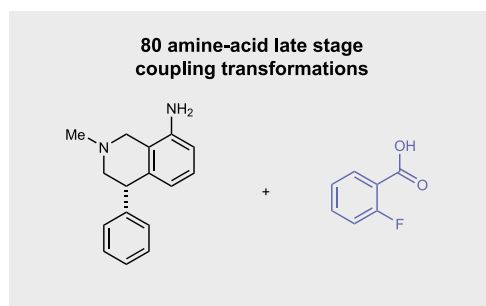
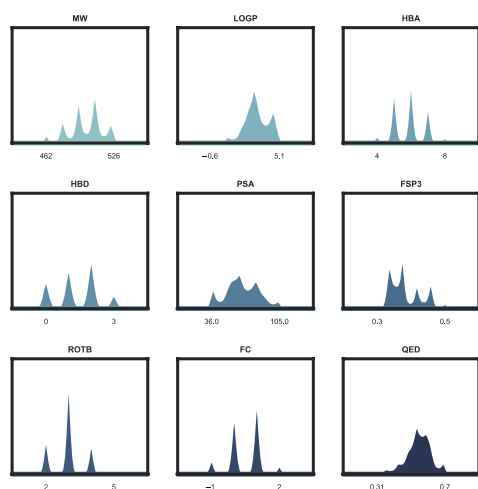
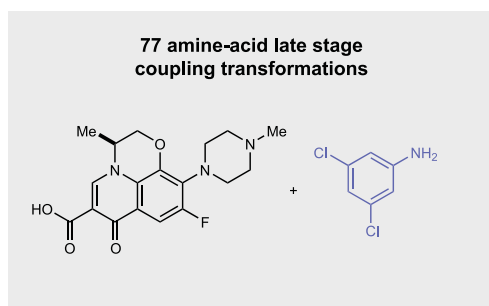
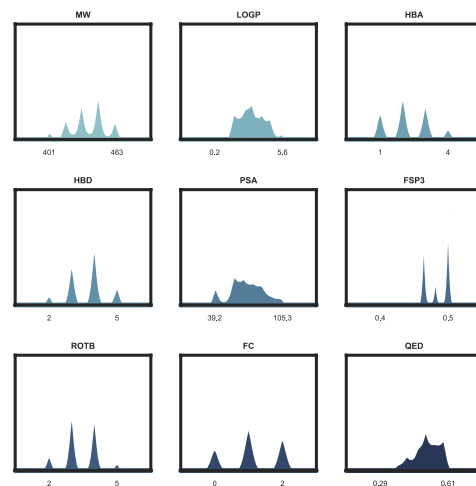
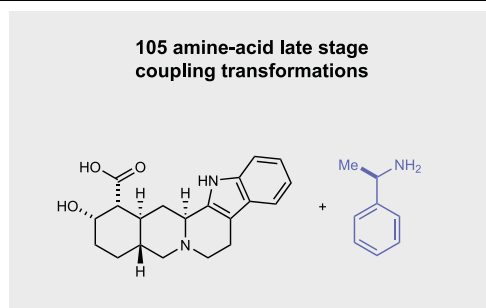
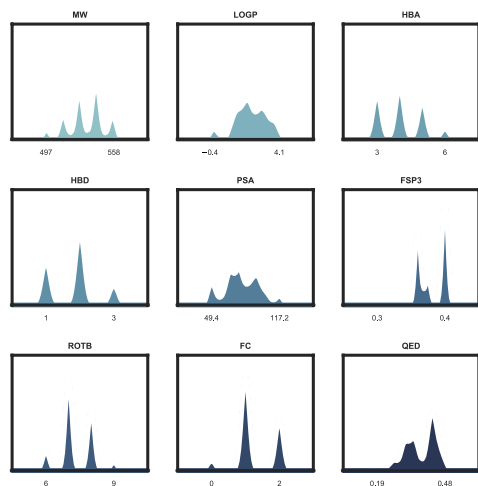
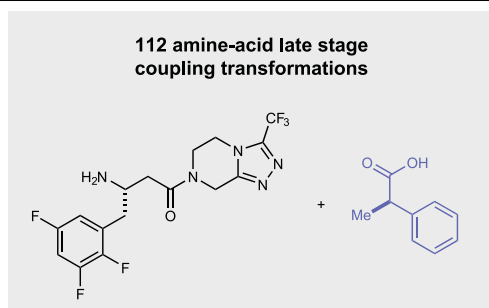
Each colored bar represents a 20  $\mu\text{L}$  dose of reagent stock solution from table (left)

**c.****d.**

**Extended Data Fig. 8 | High-throughput experimentation for the discovery of a copper-promoted esterification reaction. a,** An esterification reaction discovered through reaction screening of transition metals with ligands and additives. **b,** Recipe and well mapping. **c,** Calibration curve, for product **17** versus caffeine internal standard, used to convert the ultraperformance liquid

chromatography with ultraviolet-visible spectrometry peak area to concentration, and thus to assay yield. Error bars show deviation among triplicate injections. **d,** Heat map depicting assay yield screening results. CuI with AgNO<sub>3</sub> and pyridine showed the most promising results, achieving 18.5% assay yield using 30 mol% CuI with AgNO<sub>3</sub>.





**Extended Data Fig. 9 | Kernel density estimate plots of a series of complex molecules as substrates in the amine-acid coupling system.** The amine-acid pair depicted was used as an input to combinatorial enumeration, and the

number of valid products identified is noted for each pairing. Distributions of common physical properties are shown for each coupling set. Abbreviations are as in Extended Data Fig. 2.

### Extended Data Table 1 | Transformation labels

This table maps each transformation number from the periphery of the chord diagram in Fig. 2 to a transformation label.

# Discovery and characterization of an acridine radical photoreductant

<https://doi.org/10.1038/s41586-020-2131-1>

Received: 13 December 2019

Accepted: 18 February 2020

Published online: 1 April 2020

 Check for updates

Ian A. MacKenzie<sup>1,4</sup>, Leifeng Wang<sup>1,4</sup>, Nicholas P. R. Onuska<sup>1,4</sup>, Olivia F. Williams<sup>1</sup>, Khadiza Begam<sup>2</sup>, Andrew M. Moran<sup>1</sup>, Barry D. Dunietz<sup>3</sup> & David A. Nicewicz<sup>1✉</sup>

Photoinduced electron transfer (PET) is a phenomenon whereby the absorption of light by a chemical species provides an energetic driving force for an electron-transfer reaction<sup>1–4</sup>. This mechanism is relevant in many areas of chemistry, including the study of natural and artificial photosynthesis, photovoltaics and photosensitive materials. In recent years, research in the area of photoredox catalysis has enabled the use of PET for the catalytic generation of both neutral and charged organic free-radical species. These technologies have enabled previously inaccessible chemical transformations and have been widely used in both academic and industrial settings. Such reactions are often catalysed by visible-light-absorbing organic molecules or transition-metal complexes of ruthenium, iridium, chromium or copper<sup>5,6</sup>. Although various closed-shell organic molecules have been shown to behave as competent electron-transfer catalysts in photoredox reactions, there are only limited reports of PET reactions involving neutral organic radicals as excited-state donors or acceptors. This is unsurprising because the lifetimes of doublet excited states of neutral organic radicals are typically several orders of magnitude shorter than the singlet lifetimes of known transition-metal photoredox catalysts<sup>7–11</sup>. Here we document the discovery, characterization and reactivity of a neutral acridine radical with a maximum excited-state oxidation potential of –3.36 volts versus a saturated calomel electrode, which is similarly reducing to elemental lithium, making this radical one of the most potent chemical reductants reported<sup>12</sup>. Spectroscopic, computational and chemical studies indicate that the formation of a twisted intramolecular charge-transfer species enables the population of higher-energy doublet excited states, leading to the observed potent photoreducing behaviour. We demonstrate that this catalytically generated PET catalyst facilitates several chemical reactions that typically require alkali metal reductants and can be used in other organic transformations that require dissolving metal reductants.

Our laboratory, as well as others, has published numerous examples highlighting the diverse reactivity of acridinium salts, such as Mes-Acr<sup>+</sup>BF<sub>4</sub><sup>–</sup> (Mes, mesityl; Acr, acridinium), as photooxidation catalysts in the excited state (\*Mes-Acr<sup>+</sup>; Fig. 1a)<sup>13</sup>. Upon absorption of visible light, the corresponding excited state of the acridinium salt is populated and may be quenched via electron transfer from an electrochemically matched substrate, resulting in the formation of an acridine radical (Mes-Acr<sup>•</sup>; Fig. 1a). In past work using acridinium photoredox catalysts, this radical was typically oxidized to regenerate the parent acridinium and close a catalytic cycle. During previous mechanistic studies conducted by our laboratory, it was noted that solutions of Mes-Acr<sup>•</sup> generated via reduction of Mes-Acr<sup>+</sup>BF<sub>4</sub><sup>–</sup> with cobaltocene were indefinitely stable under oxygen-free conditions and possessed two major absorption features (at 350–400 nm and 450–550 nm; Fig. 1b)<sup>14</sup>. These observations led us to explore the photophysical behaviour of this

radical, with a focus on identifying potential PET behaviour. Previous studies have detailed the in situ generation and excitation of stable cation and anion radical species and their use in catalytic reactions<sup>15–19</sup>, indicating the potential feasibility of this strategy and prompting our studies of the photophysical behaviour of Mes-Acr<sup>•</sup>.

Upon investigation of the excited-state dynamics of Mes-Acr<sup>•</sup>, we found that there are two main excited states, tentatively assigned as a lower-energy doublet (D<sub>1</sub>) and a higher-energy twisted intramolecular charge-transfer (TICT) state. The excited-state energy for the doublet excited state of Mes-Acr<sup>•</sup> is estimated by averaging the energies of the lowest-energy absorption maximum and the highest-energy emission observed upon excitation at 484 nm. The energy of the proposed higher-order excited state is estimated by averaging the energies of the emission maximum near 490 nm and the maximum of the corresponding excitation spectrum monitored at this wavelength

<sup>1</sup>Department of Chemistry, University of North Carolina at Chapel Hill, Chapel Hill, NC, USA. <sup>2</sup>Department of Physics, Kent State University, Kent, OH, USA. <sup>3</sup>Department of Chemistry and Biochemistry, Kent State University, Kent, OH, USA. <sup>4</sup>These authors contributed equally: Ian A. MacKenzie, Leifeng Wang, Nicholas P. R. Onuska. ✉e-mail: nicewicz@unc.edu

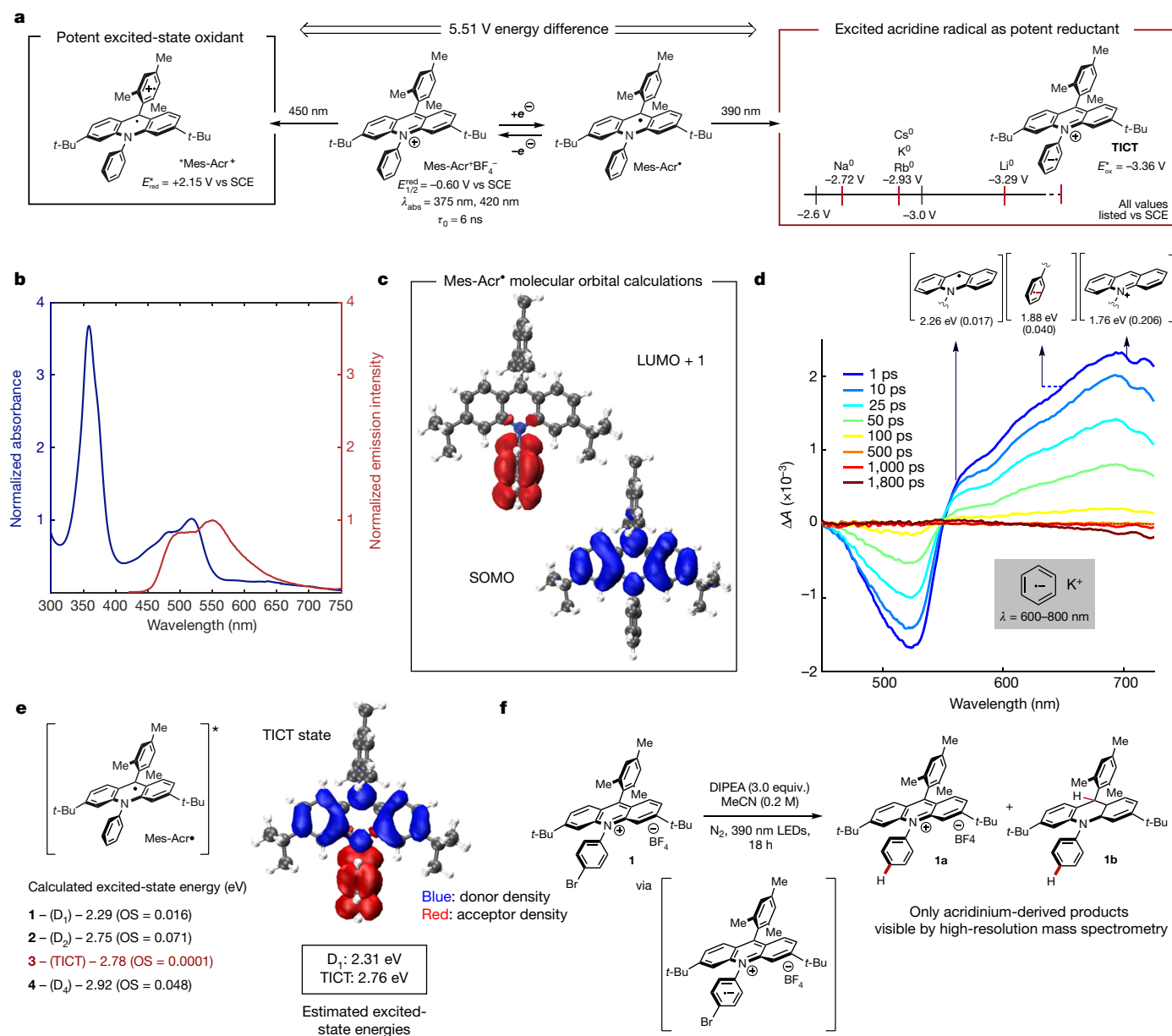


**Fig. 1 | Mechanistic studies of Mes-Acr radical.** **a**, Reduction potential of various elemental alkali metals compared to the peak reducing potential of Mes-Acr<sup>+</sup>.  $E_{\text{ox}}^*$ , excited-state oxidation potential;  $E_{\text{red}}^*$ , excited-state reduction potential;  $E_{1/2}^{\text{red}}$ , half-wave reduction potential. **b**, Absorbance and emission (excitation, 400 nm) profiles for Mes-Acr<sup>+</sup> in MeCN (5 mM, 1 mm path length). **c**, SOMO and LUMO + 1 visualizations for Mes-Acr<sup>+</sup>. **d**, Transient absorption spectra of Mes-Acr<sup>+</sup> (2.5 mM, THF, 1 mm path length) collected with a 250-fs

pump pulse centred at 400 nm. **e**, Excited-state energies calculated using the SRS-PCM/TD-DFT method for Mes-Acr<sup>+</sup> (left) and frontier orbital plot showing the donor and acceptor density for the TICT excited state (right). **f**, Debromination reaction of brominated acridinium derivative giving circumstantial evidence for the TICT state. Mes, mesityl; DIPEA, *N,N*-diisopropylethylamine; *t*-Bu, *tert*-butyl.

(see Supplementary Information for details of the excited-state energy calculations). Estimation of excited-state energies in this fashion gives values of 2.31 eV for the energy of the proposed D<sub>1</sub> excited state and 2.76 eV for the corresponding higher-energy excited state (Fig. 1e). Using the known electrochemical potential of Mes-Acr<sup>+</sup> (ref. <sup>20</sup>), the excited-state oxidation potentials of these states were estimated to be -2.91 V and -3.36 V, respectively, with respect to a saturated calomel electrode (vs SCE). To our knowledge, these values represent some of the most negative excited-state oxidation potentials reported for an organic molecule.

Before we proceed to discuss the calculated excited-state energies, we consider the key orbitals involved in the low-lying excited states. We find that the singly occupied molecular orbital (SOMO) density is

localized on the acridine core, and LUMO + 1 (where LUMO is the lowest unoccupied molecular orbital) is localized on the *N*-phenyl ring of Mes-Acr<sup>+</sup> (Fig. 1c). On the basis of this observation of small spatial overlap between these two orbitals, we expect to find a relatively low-lying excitation of an intramolecular charge-transfer state. To further probe the excited-state behaviour of Mes-Acr<sup>+</sup>, we performed transient absorption experiments (Fig. 1d). At early pump-probe delay times in tetrahydrofuran (THF), the ground state of Mes-Acr<sup>+</sup> is bleached (change in absorption,  $\Delta A < 0$ ) and excited-state absorbance resonances ( $\Delta A > 0$ ) with maxima at 550 nm and ~650 nm are observed. Aromatic radical anions are known to exhibit broad absorbance peaks in the 600–800 nm range as do aqueous solvated electrons<sup>21–25</sup>. The observed excited-state absorbance signal at ~550 nm also matches the



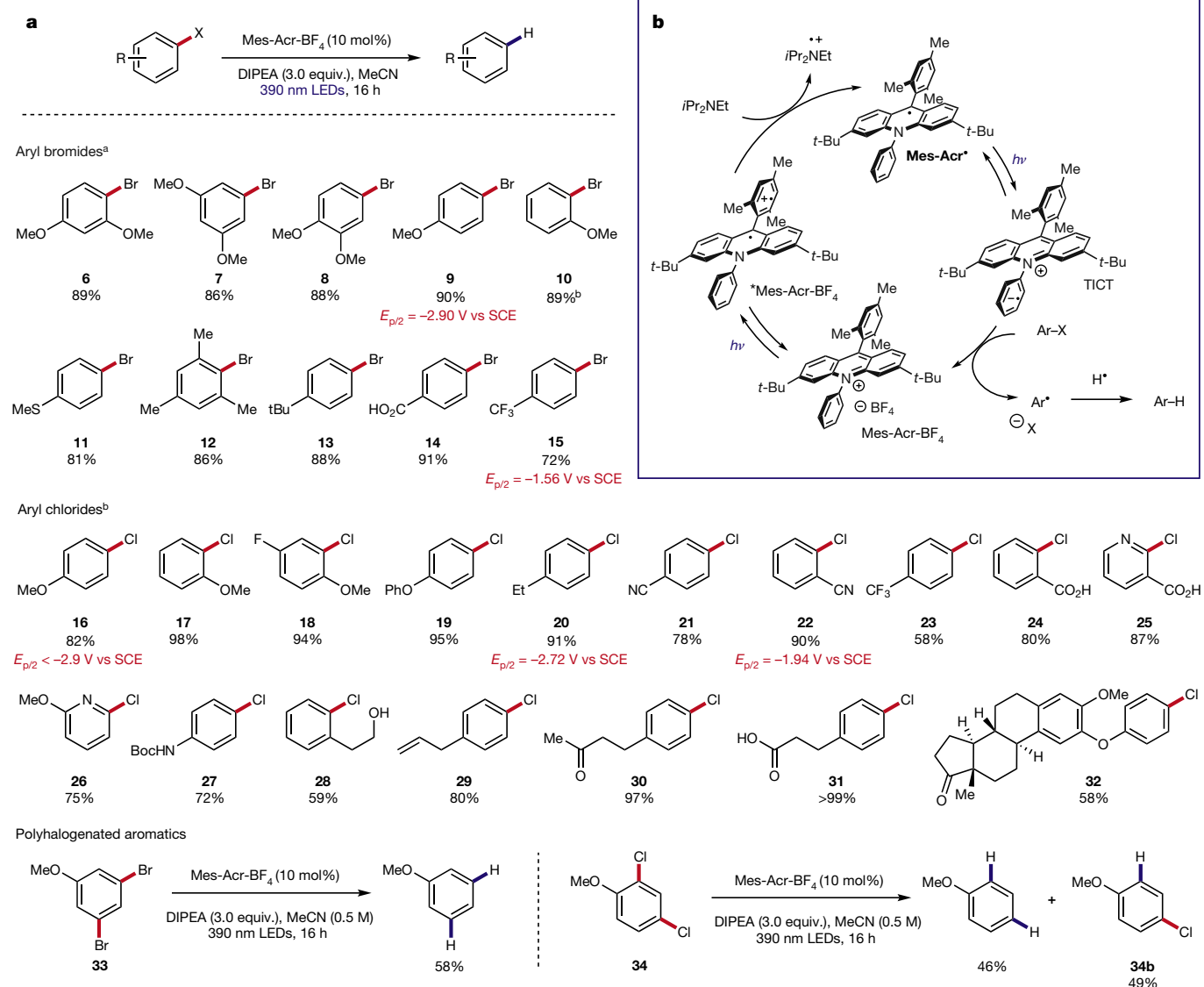


**Fig. 2 | Reductive dehalogenation of aryl halides enabled by acridine radical photoredox catalysis. a**, Reaction scope. **b**, Proposed mechanism. <sup>a</sup>0.3 M reaction concentration. <sup>b</sup>0.5 M reaction concentration.  $E_{p/2}$ , half-peak potential; LEDs, light-emitting diodes; H<sup>+</sup>, hydrogen atom source;  $h\nu$ , photon.

absorbance profile expected for a general acridine excitonic structure. Simple first-order decay to the ground state occurs after ~100 ps, matching well with previously reported values for excited-state lifetimes of organic radicals. Time-dependent density functional theory (TD-DFT) calculations indicate that other red-shifted absorptions present are well matched with energies calculated for a general acridinium structure. These spectral features support the formation of a charge-transfer state possessing both aromatic radical anion and acridinium features, as expected for the proposed TICT state.

To better understand the effect of rotation of the *N*-phenyl ring on the excited-state energetics of the acridine radical, we employ the recently reported polarization-consistent TD-DFT-based framework for obtaining excited-state energies of solvated molecular systems. The approach addresses dielectric polarization consistently by invoking the same dielectric constant in the screened range-separated hybrid (SRSH) functional parameters and in the polarizable continuum mode (PCM). SRSH-PCM was benchmarked well in the calculation of charge-transfer state energies of solvated donor-acceptor complexes and in the analysis of the spectral trends of several pigments with increased accuracy, where conventional TD-DFT calculations fail to reproduce the observed trends (see Supplementary Information for full computational details)<sup>26–29</sup>.

The calculated doublet excited-state energies for Mes-Acr<sup>•</sup> agree very well (within 0.1 eV) with values determined through spectroscopic measurements for both the absorption and emission spectra (Fig. 1e). The calculated lowest-energy D<sub>1</sub> state, with an excited-state energy of 2.29 eV, agrees with the experimentally determined D<sub>1</sub> value of 2.31 eV. Additionally, two excited states with substantial charge-transfer character were identified and the corresponding energies were calculated to be 2.75 eV and 2.78 eV, matching closely the estimated spectroscopic values for the proposed TICT state energy of 2.76 eV. As such, the identified D<sub>1</sub> (2.29 eV) state is assigned as an untwisted excitonic state, whereas the calculated 2.78 eV state is assigned as a TICT state. These excited-state energies also correspond well with previously reported excited-state energies for neutral radical species<sup>9</sup>. Additionally, visualizations of the geometries of the corresponding TICT state indicate sizeable rotation of the *N*-phenyl ring (36°) relative to the more planarized geometry of the D<sub>1</sub> state, providing further evidence of the profound effects of *N*-phenyl rotation on excited-state energy.

With the electronic and excited-state behaviour of Mes-Acr<sup>•</sup> elucidated, we sought to use this species as a catalytic reductant in a photoredox manifold. Previous work in reductive photoredox catalysis has established the reduction of aryl halides as a common benchmark

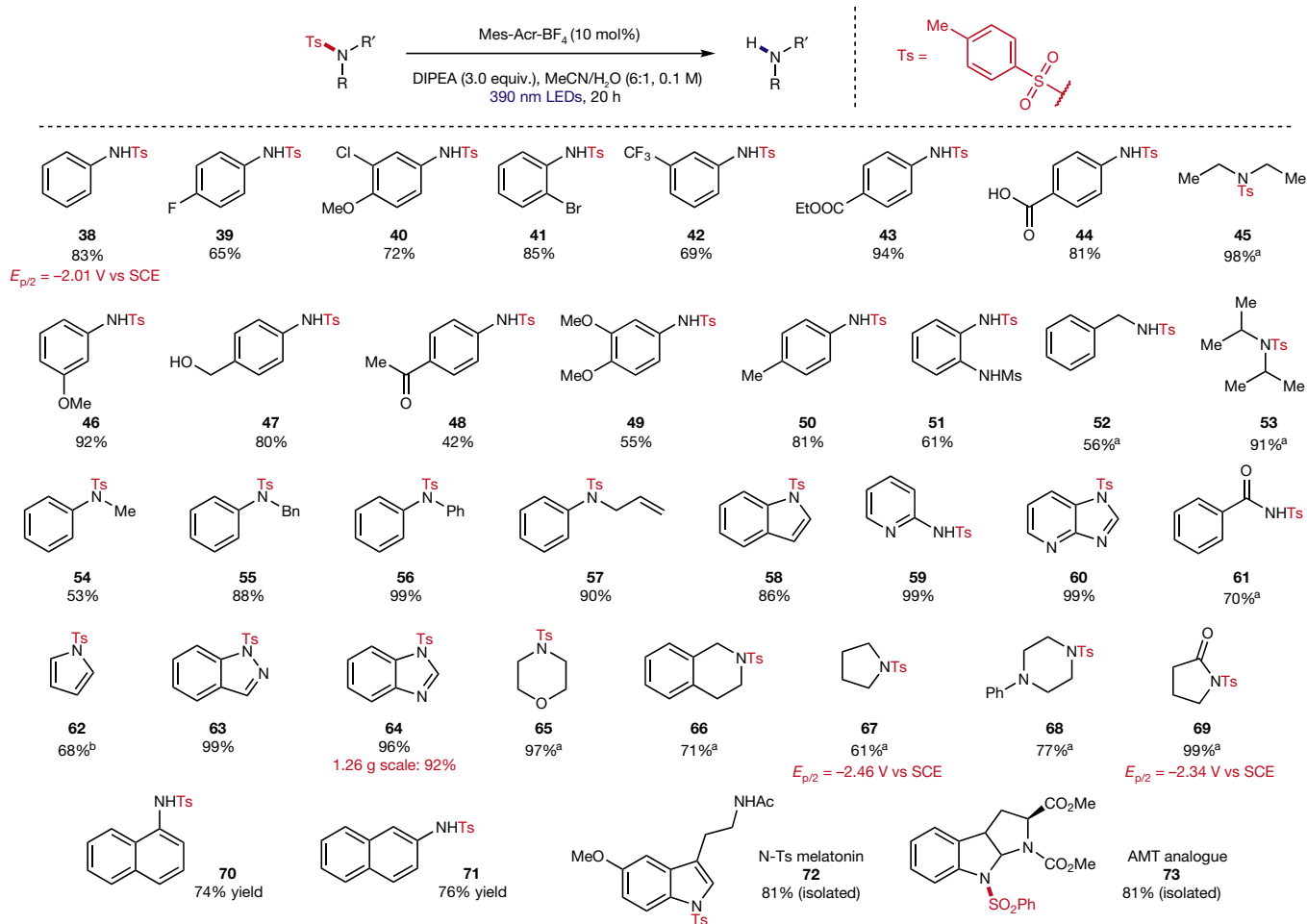


**Fig. 3 | Scope of reductive detosylation catalysed by Mes-Acr<sup>•</sup>.** <sup>1</sup>H NMR yields obtained using DMSO or pyrazine as the internal standard. <sup>a</sup>48 h reaction time. <sup>b</sup>0.5 M reaction concentration. Ts, *p*-toluenesulfonyl.

reaction<sup>15,25,29,30</sup>. Furthermore, the extremely potent reducing behaviour of the acridine radical should enable the reduction of a wide range of electronically diverse substrates. Diisopropylamine (DIPEA) was identified as a suitable single-electron reductant for the generation of Mes-Acr<sup>•</sup> from Mes-Acr<sup>+</sup>BF<sub>4</sub><sup>−</sup> in situ. Following excitation, Mes-Acr<sup>+</sup>BF<sub>4</sub><sup>−</sup> undergoes single-electron reduction via electron transfer from DIPEA, generating the desired radical Mes-Acr<sup>•</sup>. To chemically probe the possibility of charge transfer to the *N*-phenyl ring, brominated acridinium (**1**) was prepared. In the presence of 3 equiv. DIPEA, **1** was completely converted to a mixture of debrominated acridinium (**1a**) and hydroacridine (**1b**) following irradiation at 390 nm for 18 h (Fig. 1f). As aryl halide radical anions are known to quickly fragment to yield the corresponding aryl radicals, this experiment is indicative of the formation of radical anion character localized on the *N*-phenyl ring during excitation.

To evaluate the competency of this radical species as a catalytic reductant, conditions for the reductive dehalogenation of aryl halides were developed (Fig. 2a). A variety of both electron-rich (**6–13**) and electron-poor (**14, 15**) aryl bromides afforded the desired hydrodebrominated products in good to excellent yields (nuclear magnetic resonance, NMR, yields of products were taken using hexamethyldisiloxane as an internal standard). It is of note that reductively recalcitrant aryl chlorides also participated efficiently in this reaction, in contrast to previously reported methods that are only effective for electron-poor (under visible-light irradiation) or moderately electron-rich aryl chlorides (under UVA irradiation)<sup>31–35</sup>. A variety of both electron-donating (**16–20**) and electron-withdrawing (**21–24**) substituents were tolerated, with only slightly reduced yields in the case of electron-poor substrates.

Substrates bearing ketone (**30**), carboxylic acid (**31**) and alcohol (**28**) functionalities all afforded the desired hydrodechlorinated products in good to excellent yield. Medically relevant pyridine (**25, 26**) and aryl carbamate (**27**) derivatives were also efficient substrates for this transformation. When substrate (**23**), which bears a trifluoromethyl substituent, was subjected to the reaction conditions, partial hydrodefluorination (5%) that yielded the corresponding difluoromethyl derivative was observed in addition to hydrodechlorination. In all other examples, no Birch-type products resulting from overreduction were detected. The bis-reduction of polyhalogenated compounds (**9a**) and (**9b**) gave the corresponding bis-hydrodebromination (**9**) and bis-hydrodechlorination products in 58% and 46% yield, respectively. For compound (**9b**), 49% yield of the product resulting from mono-hydrodechlorination (**9c**) was observed in addition to the fully dechlorinated product.

On the basis of prior work in reductive dehalogenation, the following mechanism is proposed (Fig. 2b). Following excitation, Mes-Acr<sup>+</sup>BF<sub>4</sub><sup>−</sup> engages in single electron transfer with the tertiary amine reductant DIPEA, generating Mes-Acr<sup>•</sup> and the corresponding amine cation radical. Mes-Acr<sup>•</sup> is then excited by 390-nm light, populating a combination of highly reducing D<sub>π</sub>/TICT excited states, and undergoes electron transfer with an electronically matched aryl halide, generating an arene radical anion and reforming Mes-Acr<sup>+</sup>BF<sub>4</sub><sup>−</sup>. The arene radical anion then fragments, yielding an aryl radical. The resulting aryl radical abstracts a hydrogen atom from the amine cation radical, yielding the desired product as well as the corresponding iminium salt. Deuterium-labelling studies confirmed the amine cation radical as the

primary source of hydrogen atoms in this system (see Supplementary Information section 8).

The reductive detosylation of amines was identified as another possible transformation, which may be facilitated by Mes-Acr<sup>+</sup> (Fig. 3). Typically, strong-acid, dissolving-metal (Li/Mg) or low-valent transition-metal reductions are employed in detosylation reactions<sup>36–38</sup>. A variety of electronically diverse tosylated aniline derivatives were smoothly converted to the desired free anilines in moderate-to-excellent yield. Interestingly, substrates containing aryl halides were tolerated under the reaction conditions. As this reaction is conducted at a much lower concentration of substrate compared to the reductive dehalogenation method (0.1 M versus 0.5 M), the observed lack of aryl halide reduction may be a function of concentration. Esters (**43**, **73**), free carboxylic acids (**44**), ketones (**48**) and free alcohols (**58**) were tolerated under the reaction conditions, showing the high functional-group tolerance of this method relative to methods relying on harsh dissolving-metal conditions. Benzylic (**52**) and secondary alkyl amines (**45**, **53**, **65–68**) were efficient substrates for this transformation as well. Medicinally relevant heterocycles—including pyridines (**59**), indoles (**58**), pyrroles (**62**), pyrrolidines (**67**), indazoles (**63**), benzimidazoles (**64**) and morpholines (**65**)—were deprotected in good-to-excellent yields, with no reduction of the aromatic system observed in all cases. Of note is the ability of this method to chemoselectively and efficiently deprotect tosyl amines over mesyl-protected amines, as shown by the reaction of substrate **51**, yielding the desired detosylation product in 61% yield with no observed cleavage of the mesyl amine. Additionally, the reaction performed well with 1.28 g of starting tosylamine, with substrate **64** giving 92% yield when the desired detosylation was conducted in a standard round-bottom flask irradiated with light-emitting diode lamps (see Supplementary Information for experimental details).

In conclusion, an acridine radical generated in situ from single-electron reduction of an acridinium derivative may act as a potent single-electron reductant upon excitation with 390-nm light. Spectroscopic and computational investigations indicate the formation of at least two distinct excited states, one of which may be characterized as a TICT state. The development of chemoselective dehalogenation and desulfonylation reactions using Mes-Acr<sup>+</sup> complement the well known oxidative chemistry associated with acridinium salts and highlight the potential for the development of other types of reaction based on excitation of organic radicals.

## Online content

Any methods, additional references, Nature Research reporting summaries, source data, extended data, supplementary information, acknowledgements, peer review information; details of author contributions and competing interests; and statements of data and code availability are available at <https://doi.org/10.1038/s41586-020-2131-1>.

- Mattay, J. Photoinduced electron transfer in organic synthesis. *Synthesis* **1989**, 233–252 (1989).
- Bauer, A., Westkämper, F., Grimme, S. & Bach, T. Catalytic enantioselective reactions driven by photoinduced electron transfer. *Nature* **436**, 1139–1140 (2005).
- Fox, M. A. Photoinduced electron transfer. *Photochem. Photobiol.* **52**, 617–627 (1990).
- Fukuzumi, S. New development of photoinduced electron-transfer catalytic systems. *Pure Appl. Chem.* **79**, 981–991 (2007).
- Romero, N. A. & Nicewicz, D. A. Organic photoredox catalysis. *Chem. Rev.* **116**, 10075–10166 (2016).
- Prier, C. K., Rankic, D. A. & MacMillan, D. W. C. Visible light photoredox catalysis with transition metal complexes: applications in organic synthesis. *Chem. Rev.* **113**, 5322–5363 (2013).
- Johnston, L. J. Photochemistry of radicals and biradicals. *Chem. Rev.* **93**, 251–266 (1993).
- Arnold, B. R., Scaiano, J. C. & McGimpsey, W. G. Electron-transfer quenching of excited diphenylmethyl radicals. *J. Am. Chem. Soc.* **114**, 9978–9982 (1992).

- Scaiano, J. C., Tanner, M. & Weir, D. Exploratory study of the intermolecular reactivity of excited diphenylmethyl radicals. *J. Am. Chem. Soc.* **107**, 4396–4403 (1985).
- Samanta, A. et al. Quenching of excited doublet states of organic radicals by stable radicals. *J. Phys. Chem.* **93**, 3651–3656 (1989).
- Weir, D. & Scaiano, J. C. Substituent effects on the lifetime and fluorescence of excited diphenylmethyl radicals in solution. *Chem. Phys. Lett.* **128**, 156–159 (1986).
- Scordilis-Kelley, C. Alkali metal reduction potentials measured in chloroaluminate ambient-temperature molten salts. *J. Electrochem. Soc.* **139**, 694–699 (1992).
- Margrey, K. A. & Nicewicz, D. A. A general approach to catalytic alkene anti-Markovnikov hydrofunctionalization reactions via acridinium photoredox catalysis. *Acc. Chem. Res.* **49**, 1997–2006 (2016).
- Romero, N. A. & Nicewicz, D. A. Mechanistic insight into the photoredox catalysis of Anti-Markovnikov alkene hydrofunctionalization reactions. *J. Am. Chem. Soc.* **136**, 17024–17035 (2014).
- Ghosh, I., Ghosh, T., Bardagi, J. I. & König, B. Reduction of aryl halides by consecutive visible light-induced electron transfer processes. *Science* **346**, 725–728 (2014).
- Connell, T. U. et al. The tandem photoredox catalysis mechanism of [Ir(ppy)<sub>3</sub>](dtb-bpy)]<sup>+</sup> enabling access to energy demanding organic substrates. *J. Am. Chem. Soc.* **141**, 17646–17658 (2019).
- Lu, C., Fujitsuka, M., Sugimoto, A. & Majima, T. Dual character of excited radical anions in aromatic diimide bis(radical anion)s: donor or acceptor? *J. Phys. Chem. C* **121**, 4558–4563 (2017).
- Christensen, J. A. et al. Phenothiazine radical cation excited states as super-oxidants for energy-demanding reactions. *J. Am. Chem. Soc.* **140**, 5290–5299 (2018).
- Gumy, J.-C. & Vauthey, E. Investigation of the excited-state dynamics of radical ions in the condensed phase using the picosecond transient grating technique. *J. Phys. Chem. A* **101**, 8575–8580 (1997).
- Romero, N. A., Margrey, K. A., Tay, N. E. & Nicewicz, D. A. Site-selective arene C-H amination via photoredox catalysis. *Science* **349**, 1326–1330 (2015).
- Brancato, G. et al. Dual fluorescence through Kasha's rule breaking: an unconventional photomechanism for intracellular probe design. *J. Phys. Chem. B* **119**, 6144–6154 (2015).
- Demchenko, A. P., Tomin, V. I. & Chou, P.-T. Breaking the Kasha rule for more efficient photochemistry. *Chem. Rev.* **117**, 13353–13381 (2017).
- Peng, Z. et al. Expression of anti-Kasha's emission from amino benzothiadiazole and its utilization for fluorescent chemosensors and organic light emitting materials. *J. Mater. Chem. C* **6**, 7864–7873 (2018).
- Scuppa, S., Orian, L., Donoli, A., Santi, S. & Meneghetti, M. Anti-Kasha's rule fluorescence emission in (2-ferrocenyl)indene generated by a twisted intramolecular charge-transfer (TICT) process. *J. Phys. Chem. A* **115**, 8344–8349 (2011).
- Shida, T. *Electronic Absorption Spectra of Radical Ions* (Elsevier, 1988).
- Bhandari, S. & Dunietz, B. D. Quantitative accuracy in calculating charge transfer state energies in solvated molecular complexes using a screened range separated hybrid functional within a polarized continuum model. *J. Chem. Theory Comput.* **15**, 4305–4311 (2019).
- Song, Y. et al. Vibronic structure of photosynthetic pigments probed by polarized two-dimensional electronic spectroscopy and ab initio calculations. *Chem. Sci.* **10**, 8143–8153 (2019).
- Bhandari, S., Cheung, M. S., Geva, E., Kronik, L. & Dunietz, B. D. Fundamental gaps of condensed-phase organic semiconductors from single-molecule calculations using polarization-consistent optimally tuned screened range-separated hybrid functionals. *J. Chem. Theory Comput.* **14**, 6287–6294 (2018).
- Maiti, B. et al. Enhancing charge mobilities in organic semiconductors by selective fluorination: a design approach based on a quantum mechanical perspective. *Chem. Sci.* **8**, 6947–6953 (2017).
- Kerzig, C. & Goez, M. Generating hydrated electrons through photoredox catalysis with 9-anthrolate. *Phys. Chem. Chem. Phys.* **17**, 13829–13836 (2015).
- Kerzig, C., Guo, X. & Wenger, O. S. Unexpected hydrated electron source for preparative visible-light driven photoredox catalysis. *J. Am. Chem. Soc.* **141**, 2122–2127 (2019).
- Poelma, S. O. et al. Chemoselective radical dehalogenation and C–C bond formation on aryl halide substrates using organic photoredox catalysts. *J. Org. Chem.* **81**, 7155–7160 (2016).
- Discekici, E. H. et al. A highly reducing metal-free photoredox catalyst: design and application in radical dehalogenations. *Chem. Commun.* **51**, 11705–11708 (2015).
- Narayanam, J. M. R., Tucker, J. W. & Stephenson, C. R. J. Electron-transfer photoredox catalysis: development of a tin-free reductive dehalogenation reaction. *J. Am. Chem. Soc.* **131**, 8756–8757 (2009).
- Yin, H. et al. The hexachloroacetate(III) anion: a potent, benchtop stable, and readily available ultraviolet A photosensitizer for aryl chlorides. *J. Am. Chem. Soc.* **138**, 16266–16273 (2016).
- Javorskis, T. & Orentas, E. Chemoselective deprotection of sulfonamides under acidic conditions: scope, sulfonyl group migration, and synthetic applications. *J. Org. Chem.* **82**, 13423–13439 (2017).
- Shohji, N., Kawaji, T. & Okamoto, S. Ti(O-*i*-Pr)<sub>4</sub>/Me<sub>3</sub>SiCl/Mg-mediated reductive cleavage of sulfonamides and sulfonates to amines and alcohols. *Org. Lett.* **13**, 2626–2629 (2011).
- Alonso, E., Ramón, D. J. & Yus, M. Reductive deprotection of allyl, benzyl and sulfonyl substituted alcohols, amines and amides using a naphthalene-catalysed lithiation. *Tetrahedron* **53**, 14355–14368 (1997).

**Publisher's note** Springer Nature remains neutral with regard to jurisdictional claims in published maps and institutional affiliations.

© The Author(s), under exclusive licence to Springer Nature Limited 2020

## Data availability

The data supporting the findings of this study are available within the paper and its Supplementary Information.

**Acknowledgements** This work was supported in part by the National Institutes of Health (NIGMS) Award number R01 GM120186 (D.A.N.). L.W. was supported by the National Natural Science Foundation of China (21801011) and the International Postdoctoral Exchange Fellowship Program (20180033). O.F.W. and A.M. were supported by the National Science Foundation under grant CHE-1763207. Photophysical measurements were performed in the AMPED EFRC Instrumentation Facility established by the Alliance for Molecular PhotoElectrode Design for Solar Fuels (AMPED), an Energy Frontier Research Center (EFRC) funded by the US Department of Energy, Office of Science, Office of Basic Energy Sciences under Award DE-SC0001011. B.D.D. acknowledges support for this project by the Department

of Energy, Office of Basic Energy Sciences through the Chemical Sciences Geosciences and Biosciences Division, under grant number DE- SC0016501.

**Author contributions** I.A.M. and D.A.N. were responsible for the initial conception of the project. I.A.M., L.W. and N.P.R.O. devised and executed all experimental work. N.P.R.O., D.A.N., K.B., B.D.D., O.F.W. and I.A.M. assisted in the preparation and editing of the final manuscript. O.F.W. assisted in the collection and O.F.W. and A.M.M. performed analysis of transient absorption data. B.D.D. designed the computational approach, K.B. executed the calculations and K.B., B.D.D., N.P.R.O. and D.A.N. were responsible for the analysis of computations.

**Competing interests** The authors declare no competing interests.

### Additional information

**Supplementary information** is available for this paper at <https://doi.org/10.1038/s41586-020-2131-1>.

**Correspondence and requests for materials** should be addressed to D.A.N.

**Reprints and permissions information** is available at <http://www.nature.com/reprints>.



# Temperate rainforests near the South Pole during peak Cretaceous warmth

<https://doi.org/10.1038/s41586-020-2148-5>

Received: 1 October 2019

Accepted: 23 January 2020

Published online: 1 April 2020

 Check for updates

Johann P. Klages<sup>1✉</sup>, Ulrich Salzmann<sup>2</sup>, Torsten Bickert<sup>3</sup>, Claus-Dieter Hillenbrand<sup>4</sup>, Karsten Gohl<sup>1</sup>, Gerhard Kuhn<sup>1</sup>, Steven M. Bohaty<sup>5</sup>, Jürgen Titschack<sup>3,6</sup>, Juliane Müller<sup>1,3,7</sup>, Thomas Frederichs<sup>3,7</sup>, Thorsten Bauersachs<sup>8</sup>, Werner Ehrmann<sup>9</sup>, Tina van de Flierdt<sup>10</sup>, Patric Simões Pereira<sup>10,14</sup>, Robert D. Larter<sup>4</sup>, Gerrit Lohmann<sup>1,3,11</sup>, Igor Niezgodzki<sup>1,12</sup>, Gabriele Uenzelmann-Neben<sup>1</sup>, Maximilian Zundel<sup>7</sup>, Cornelia Spiegel<sup>7</sup>, Chris Mark<sup>13,15</sup>, David Chew<sup>13</sup>, Jane E. Francis<sup>4</sup>, Gernot Nehrke<sup>1</sup>, Florian Schwarz<sup>2</sup>, James A. Smith<sup>4</sup>, Tim Freudenthal<sup>3</sup>, Oliver Esper<sup>1</sup>, Heiko Pälike<sup>3,7</sup>, Thomas A. Ronge<sup>1</sup>, Ricarda Dziadek<sup>1</sup> & the Science Team of Expedition PS104\*

The mid-Cretaceous period was one of the warmest intervals of the past 140 million years<sup>1–5</sup>, driven by atmospheric carbon dioxide levels of around 1,000 parts per million by volume<sup>6</sup>. In the near absence of proximal geological records from south of the Antarctic Circle, it is disputed whether polar ice could exist under such environmental conditions. Here we use a sedimentary sequence recovered from the West Antarctic shelf—the southernmost Cretaceous record reported so far—and show that a temperate lowland rainforest environment existed at a palaeolatitude of about 82° S during the Turonian–Santonian age (92 to 83 million years ago). This record contains an intact 3-metre-long network of in situ fossil roots embedded in a mudstone matrix containing diverse pollen and spores. A climate model simulation shows that the reconstructed temperate climate at this high latitude requires a combination of both atmospheric carbon dioxide concentrations of 1,120–1,680 parts per million by volume and a vegetated land surface without major Antarctic glaciation, highlighting the important cooling effect exerted by ice albedo under high levels of atmospheric carbon dioxide.

The Cretaceous Period (144–66 million years ago (Ma)) hosted some of the warmest intervals in Earth's history<sup>1–3</sup>, particularly during the Turonian to Santonian stages (93.9–83.6 Ma)<sup>4,5</sup>. At that time, atmospheric carbon dioxide (CO<sub>2</sub>) concentrations were reconstructed to be around 1,000 parts per million by volume (ppmv; ref. <sup>6</sup>), and average annual low-latitude sea surface temperatures probably reached ~35 °C (ref. <sup>4</sup>), with only a minor bihemispheric temperature gradient extending polewards from palaeolatitudes between 50 and 60° N (refs. <sup>7–9</sup>). Only small to medium-sized ice sheets may have existed<sup>10,11</sup> and global sea level was up to 170 m higher than at present<sup>11,12</sup>.

Records documenting the Antarctic terrestrial environment during this mid-Cretaceous warmth are sparse<sup>5,13–17</sup> and particularly rare south of the palaeo-Antarctic Circle<sup>13,14</sup>. Such records, however, are critical to constrain state-of-the-art Late Cretaceous climate models<sup>5</sup> for predicting the magnitude of atmospheric CO<sub>2</sub> concentrations<sup>18</sup> and their effectiveness in inhibiting the build-up of major ice sheets<sup>19</sup>.

Here we reconstruct mid-Cretaceous terrestrial environmental conditions in West Antarctica by combining micro- and

macropalaeontological, sedimentological, inorganic and organic geochemical, mineralogical and palaeomagnetic data, as well as X-ray computed tomography (CT) imagery, obtained from drill cores recovered from a site within the Pine Island cross-shelf trough in the Amundsen Sea Embayment (ASE), West Antarctica (Fig. 1a). Site PS104\_20-2 (73.57° S, 107.09° W; 946 m water depth) was drilled during RV *Polarstern* expedition PS104 in 2017 (ref. <sup>20</sup>). The Pine Island Trough extends from the modern fronts of the Pine Island and Thwaites glaciers, and was eroded into the ASE shelf during repeated advances of a West Antarctic Ice Sheet palaeo-ice stream throughout the Miocene to Pleistocene epochs<sup>21–23</sup>. On the inner to middle continental shelf, glacial erosion combined with tectonic uplift<sup>22</sup> exposed seaward-dipping sedimentary strata of postulated Cretaceous to Miocene age near the seafloor<sup>24</sup> (Fig. 1b). Widespread till cover on the shelf previously prevented sampling of these strata using conventional coring techniques<sup>24</sup>. Deployment of the remotely operated seafloor drill rig MARUM-MeBo70 (ref. <sup>25</sup>) enabled drilling to 30.7 m below seafloor (mbsf) into the seabed to recover the dipping strata<sup>20</sup> (Figs. 1 and 2).

<sup>1</sup>Alfred-Wegener-Institut Helmholtz-Zentrum für Polar- und Meeresforschung, Bremerhaven, Germany. <sup>2</sup>Department of Geography and Environmental Sciences, Northumbria University, Newcastle upon Tyne, UK. <sup>3</sup>MARUM—Center for Marine Environmental Sciences, University of Bremen, Bremen, Germany. <sup>4</sup>British Antarctic Survey, Cambridge, UK. <sup>5</sup>School of Ocean and Earth Science, University of Southampton, Southampton, UK. <sup>6</sup>Marine Research Department, Senckenberg am Meer, Wilhelmshaven, Germany. <sup>7</sup>Faculty of Geosciences, University of Bremen, Bremen, Germany. <sup>8</sup>Institute of Geosciences, Christian-Albrechts-University, Kiel, Germany. <sup>9</sup>Institute for Geophysics and Geology, University of Leipzig, Leipzig, Germany. <sup>10</sup>Department of Earth Science and Engineering, Imperial College London, London, UK. <sup>11</sup>Environmental Physics, University of Bremen, Bremen, Germany. <sup>12</sup>ING PAN—Institute of Geological Sciences, Polish Academy of Sciences, Biogeosystem Modelling Laboratory, Kraków, Poland. <sup>13</sup>Department of Geology, Trinity College Dublin, Dublin, Ireland. <sup>14</sup>Present address: Department of Marine Sciences, University of Gothenburg, Gothenburg, Sweden. <sup>15</sup>Present address: School of Earth Sciences, University College Dublin, Dublin, Ireland. \*A list of authors and their affiliations appears at the end of the paper. ✉e-mail: [Johann.Klages@awi.de](mailto:Johann.Klages@awi.de)

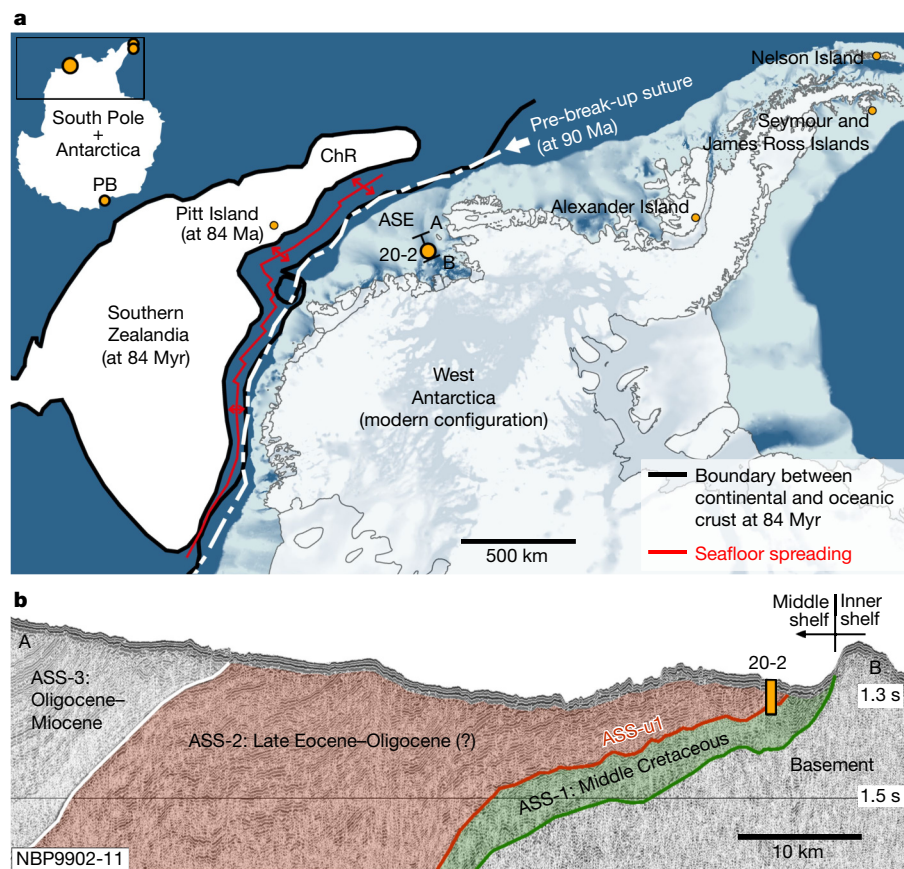


**Fig. 1 | Setting of MARUM-MeBo70 drill site PS104\_20-2 on the ASE shelf.**

**a**, The present-day location of West Antarctica is shown in relation to the reconstructed boundary between continental and oceanic crust at 84 Ma (refs. <sup>31,32</sup>) (thick black lines). The pre-break up suture (dashed white line) indicates the position of the reconstructed Zealandian and West Antarctic continental and oceanic crust before initial break-up starting at -90 Ma (ref. <sup>31</sup>). Orange circles mark the locations of other outcrops of mid-Cretaceous sedimentary strata<sup>13–17</sup>. **b**, Seismic reflection profile NBP9902-11<sup>21</sup> (A–B)

crossing drill site PS104\_20-2. The orange bar indicates the drilled core length. The profile position is indicated in **a**. The drill hole penetrated Amundsen Sea shelf unconformity ASS-u1, which separates seismic units ASS-1 and ASS-2 (ref. <sup>26</sup>). The interpretation of seismostratigraphic units and unconformities is based on both previous work<sup>24</sup> and this study. Pitt Island belongs to the Chatham Island group of New Zealand. PB, Prydz Bay; ChR, Chatham Rise. Shelf bathymetry and sub-ice topography data derive from refs. <sup>54,55</sup>.

## Lithology and stratigraphy

Beneath a few metres of glacial marine and reworked glacial sediments, MARUM-MeBo70 penetrated an occasionally stratified but microfossil-barren -17–24-m-thick quartzitic gravelly sandstone with uranium–lead (U–Pb) dates on apatite and zircon grains (see Methods) constraining its maximum depositional age to -40 Myr in the late Eocene (Extended Data Fig. 1). Cores 9R and 10R recovered strata from 26.3 mbsf to the base of the hole. At -26.8 mbsf, a prominent thin (5 cm) layer of indurated lignite fragments separates the overlying sandstone unit from a ≥3-m-thick, palynomorph-rich, laminated to stratified carbonaceous mudstone below. This mudstone contains an intact and continuous network of fossil plant roots that reaches down to at least 30 mbsf (Fig. 2; Supplementary Video 1).

Based on New Zealand's biostratigraphic ranges<sup>26</sup>, the presence of the pollen taxon *Phyllocladites mausonii* (nearest living relative (NLR): *Lagarostrobos*, Huon Pine) and the absence of both *Nothofagidites* (NLR: *Nothofagus*, Southern Beech) and *Forcipites sabulosus* within the carbonaceous mudstone indicate its deposition during the mid-Cretaceous (Turonian–Santonian; -92–83 Ma, PM1a-subzone) (Extended Data Fig. 2; Extended Data Tables 1 and 2). Abundant pollen of conifer trees (for example, *Podocarpidites*, *Trichotomosulcites*) and tree ferns (*Cyatheidites*) and the presence of accessory taxa such as *Ruffordiaspora ludbrookiae* and *Tricolpites* spp. in our assemblage resemble the uppermost strata of the Turonian–Santonian Tupuangi

Formation on Pitt Island, New Zealand, dated to 92–89 Ma (refs. <sup>27,28</sup>) (Extended Data Table 3). However, the regular occurrence of pollen of the family Proteaceae, including *Beauprea*-type pollen (for example, *Peninsulapollis gillii*, *Beaupreaidites*), which are absent from the Tupuangi Formation, suggest that the ASE core is slightly younger than 89 Myr old. Recent molecular phylogenetic reconstructions indicate an early Antarctic–Southeastern Australian origin of *Beauprea* (~88 Ma), whereas the oldest palynological record of these angiosperm fossils on Antarctica and Australia date back to 81.4 Ma and 83.8 Ma, respectively<sup>29</sup>.

These biostratigraphic age estimates are consistent with palaeomagnetic data obtained from discrete sediment samples showing normal polarity, expected for deposition during the 'Cretaceous Normal Polarity Superchron' (C34n; 121–83 Ma; ref. <sup>30</sup>) (see Methods). The layer of indurated lignite and the underlying carbonaceous mudstone show very similar pollen assemblages, which indicate a similar age and palaeoenvironment for both units (Fig. 2; Extended Data Fig. 2).

## Turonian–Santonian position of the record

To assess the palaeoclimatic importance of this record, we determined the palaeogeographical position of site PS104\_20-2 at 90 Ma. Today, the site is located near the Pacific continental margin of West Antarctica, about 250 km away from the modern boundary between continental and oceanic crust (Fig. 1). At the time of sediment deposition,

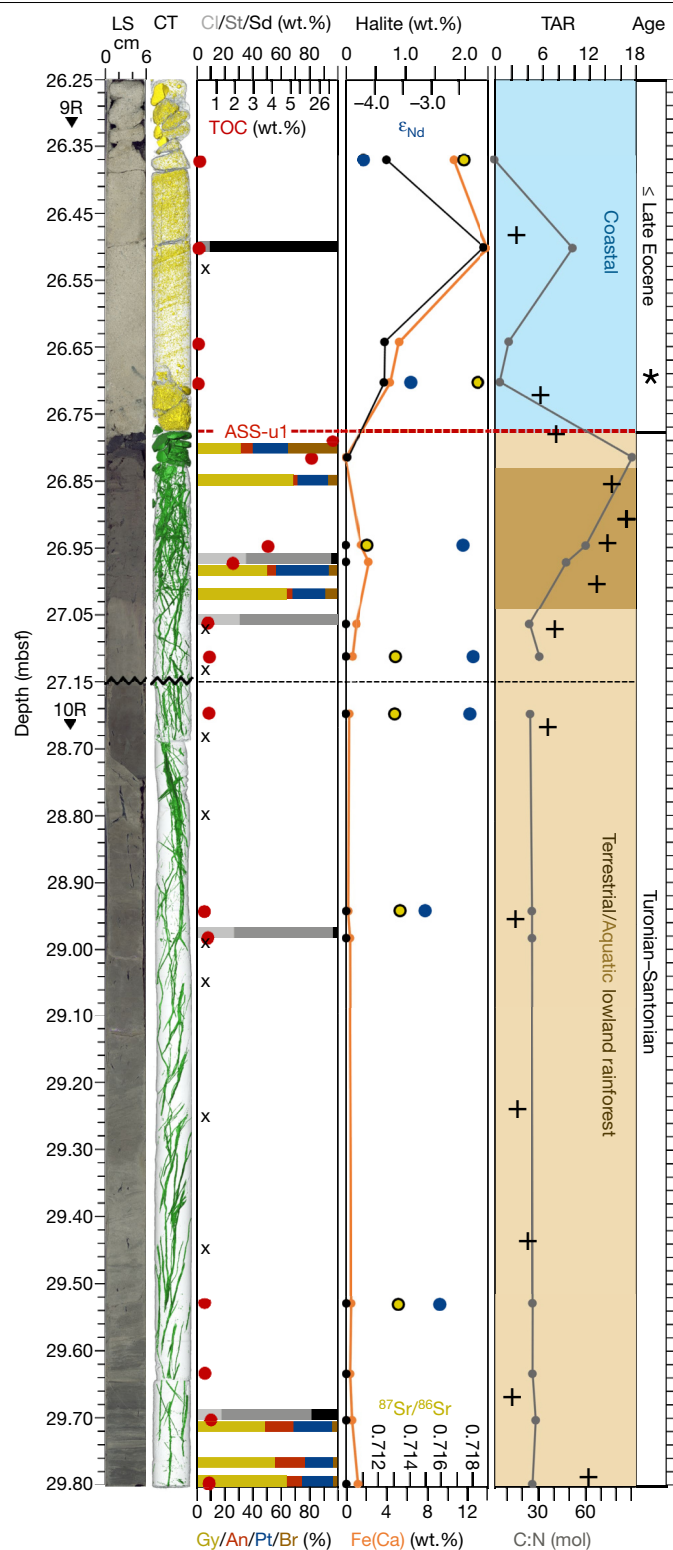


**Fig. 2 | Multi-proxy parameter reconstruction of cores 9R and 10R at site PS104\_20-2.** The MARUM-MeBo70 seafloor drill rig drilled 30.7 m into the seafloor and recovered 5.91 m of core length. The lower ~3 m consists of a fossil root-bearing mudstone with an ~5-cm-thick layer of brecciated lignite on top (from ~26.77 mbsf downwards), both of Turonian–Santonian age. A Late Eocene or younger quartzitic gravelly sandstone overlies the lignite. The upper lignite boundary defines the impedance contrast between the underlying mudstone and overlying gravelly sandstone and probably coincides with the prominent regional unconformity ASS-u1<sup>24</sup> (see the thick red line in Fig. 1b). Note the core break between 9R and 10R at 27.15 mbsf. LS, linescan; CT, X-ray computed tomography; Cl/St/Sd, clay/silt/sand ( $n = 6$ ); TOC, total organic carbon ( $n = 16$ ); Gy/An/Pt/Br, gymnosperms/angiosperms/pteridophytes/bryophytes ( $n = 7$ ); X, barren palynomorph samples ( $n = 9$ ); Halite ( $n = 16$ ); Bulk sediment neodymium ( $\epsilon_{Nd}$ ) values ( $\pm 2$  s.d. = 0.27) and strontium ( $^{87}\text{Sr}/^{86}\text{Sr}$ ) ratios ( $\pm 2$  s.e.; see Source Data) ( $n = 7$ ) (median centre values) (see Methods); Fe(Ca), iron carbonate ( $n = 16$ ); TAR, ratio of terrestrial and aquatic-sourced  $n$ -alkanes ( $n = 14$ ); C:N (mol), molar ratio of TOC/TN ( $n = 16$ ). \* Zircon U–Pb age (45.5 million years (Myr)) ( $n = 1$ ). Inferred ages are based on palynomorph biostratigraphy for the mudstone and U–Pb ages of apatite and zircon grains for the sandstone (see the main text).

wide rift zone between Zealandia and West Antarctica, just before the initiation of continental break-up<sup>24,31</sup>. In a previous study<sup>34</sup>, a mean palaeomagnetic pole position at 100 Ma of 75.7° S and 135.9° W with a 95% confidence radius of 3.8° for Marie Byrd Land was determined from 19 rock sample sites. By accounting for the great-circle distance of 7.84° to our drill site and rotating points on the East Antarctic polar wander path<sup>34</sup> into the Marie Byrd Land reference frame, we derive a core site palaeolatitude of 81.9° S at 90 Ma. The uncertainty in this position is estimated to be not larger than the maximum 95% confidence radius of 5.9° of the respective part of the polar wander path<sup>34</sup>.

### Palaeoenvironment

The indurated lignite layer as well as the laminated to stratified carbonaceous mudstone comprising the fossil plant roots in cores 10R and lower 9R at site PS104\_20-2 contain a highly diverse and entirely terrestrial palynomorph assemblage of more than 62 pollen and spore taxa (Fig. 2; Extended Data Figs. 2, 3; Extended Data Table 3). The absence of palynomorphs with different stratigraphic ranges or varying thermal maturity suggests that this purely terrestrial microfossil assemblage has not been reworked. The assemblage is dominated by pollen of the conifer tree families Podocarpaceae and Araucariaceae with abundant ferns, including the tree ferns *Cyathea*, documenting the initial stages of an austral temperate rainforest (Fig. 2; Extended Data Fig. 2; Extended Data Table 2). The presence of the heterocyst glycolipids HG<sub>30</sub> triol and keto-diol (Extended Data Fig. 4; see Methods) also indicates that benthic cyanobacterial mats colonized fresh water bodies within this temperate rainforest, providing additional evidence for the development of a highly complex ecosystem in the ASE during the Turonian–Santonian. In combination with published palaeo-topographic and palaeo-tectonic information<sup>22,24,31,32</sup>, the different taxa and their bioclimatic importance (see Methods) were combined and visualized to create Fig. 3. Members of the Proteaceae family presumably formed a flowering shrub understorey in the tall Late Cretaceous conifer rainforest of the ASE depicted in Fig. 3. The lignite layer is rich in spores of *Stereisporites antiquasporites* (NLR: Bryophyte, *Sphagnum*), which further suggest the temporary existence of a peat swamp in the diverse temperate lowland rainforest. This coincides with increasing *Peninsulapollis* pollen, indicating increasing humidity<sup>35</sup> towards the record's top. Thin sections were carefully prepared from resin-impregnated core samples selected from cores 9R and 10R (see Methods) to characterize the fossil roots. Although cell structures were not sufficiently preserved for identification of the plant that grew the roots, the presence of parenchyma cells within the long and continuous roots makes it likely that the network comprises

between 93 and 83 Ma, the continent of Zealandia started to rift and separate from West Antarctica<sup>31,32</sup>. We applied a relative plate reconstruction between Zealandia and West Antarctica for the middle Cretaceous using the GPlates (version 2.2) plate reconstruction tool<sup>33</sup> with up-to-date rotation parameters of the South Pacific realm<sup>31</sup>. This resulted in a 736 km great-circle distance (265 km north–south distance) between the drill site and the hitherto southernmost mid-Cretaceous terrestrial palaeoenvironmental record on Pitt Island on Chatham Rise, New Zealand<sup>14</sup>. The close-fit reconstruction at 90 Ma indicates a





**Fig. 3 | Reconstruction of the West Antarctic Turonian–Santonian temperate rainforest.** The painting is based on palaeofloral and environmental information inferred from palynological, geochemical, sedimentological and organic biomarker data obtained from cores 9R and 10R

at site PS104\_20-2. The creation of the painting was further complemented by published palaeotopographic and palaeotectonic information<sup>22,24,31,32</sup>. Original size of painting: 83.8 cm × 41.5 cm. Alfred-Wegener-Institut/J. McKay; this image is available under Creative Commons licence CC-BY 4.0.

vascular plant remains and thus confirms active plant growth at our site (Extended Data Fig. 5b–e). Furthermore, the alignment of organic and clastic material within the laminated to stratified mudstone matrix (Extended Data Fig. 5a) suggests synchronous deposition of clastic particles and organic fragments.

Our environmental reconstruction is further supported by geochemical and biomarker data. In the mudstone between 29.80 and 27.03 mbsf and the indurated lignite interval (26.83–26.77 mbsf), zero to very low halite and carbonate contents in the bulk sediment fraction combined with low total organic carbon/total nitrogen (TOC/TN) ratios and low ratios of land-plant-derived long-chain *n*-alkanes versus aquatic-sourced short-chain *n*-alkanes (TAR), point to swampy aquatic freshwater conditions (Fig. 2). This interpretation is supported by the identification of cells that closely resemble aerenchyma (Extended Data Fig. 5d), which is usually responsible for intercellular gas exchange under (semi-) permanent subaquatic growing conditions<sup>36</sup>. In mudstone samples taken from the core segment that contains a particularly dense root network (27.03–26.83 mbsf), pollen and biomarkers indicate the establishment of terrestrial forest-type vegetation, while elevated pristane/*n*-C<sub>17</sub> and pristane/phytane ratios point to a high abundance of terrigenous plant material (Extended Data Fig. 6; see also refs.<sup>37,38</sup>), which is in line with the pollen-based interpretation of a terrestrial rainforest environment. TOC/TN ratios >20 (Fig. 2) are consistent with this interpretation and indicate a primarily land-plant source of organic matter<sup>39</sup> within this mudstone sequence.

The clay mineral assemblage in cores 9R and 10R is dominated by kaolinite (67–72%) and smectite (26–29%), both indicating chemical weathering activity under humid and (sub-) tropical climate conditions<sup>40</sup>. However, as this is not corroborated by our reconstructed climatic setting, we attribute kaolinite formation in the mudstone to the repeated establishment of swampy conditions, in which organic acids altered silicate minerals to kaolinite ('Moorverwitterung')<sup>41</sup>.

The lithological successions in cores 9R and 10R resemble the uppermost strata of the Turonian–Santonian Tupuangi Formation on Pitt Island, New Zealand<sup>27</sup>. The Pitt Island strata are characterized

by interbedded carbonaceous siltstone, quartzofeldspathic sandstone, lignite and/or peat layers. Similar to the sediment sequence described for the ASE, the Tupuangi Formation records a terrestrial, densely vegetated and partly swampy fluviodeltaic environment<sup>14</sup>. At around 90 Ma, the Tupuangi Formation was located in one of the rift basins developing before Zealandia separated from West Antarctica<sup>24,31</sup>, ~736 km from Site PS104\_20-2 (Fig. 1). A diverse conifer forest surrounded by extensive river systems<sup>42,43</sup> seems to have covered both the Zealandian<sup>14</sup> and the West Antarctic conjugate continental margin during this early break-up phase.

The sharp lithological change from the root-bearing fossiliferous mudstone with the thin layer of indurated lignite on top into the sandstone at 26.77 mbsf is marked by increased iron carbonate and halite contents and decreased TOC/TN and TAR ratios within the sandstone (Fig. 2), suggesting an estuarine and coastal environment. The maximum U–Pb dates of ~40 Ma obtained from the sandstone (see Extended Data Fig. 1), which is coarse-grained at its base, indicate a considerable hiatus between the mudstone (including the lignite) and the sandstone. Such a hiatus is consistent with neodymium (Nd) and strontium (Sr) isotope data, which reflect both a change in sediment provenance and a decrease in weathering intensity between the two lithologies (Fig. 2; see Methods). The time window of the hiatus coincides with slow erosion rates of a tectonically quiescent passive margin<sup>22,44</sup>, whereas Eocene–Oligocene tectonic activity of the West Antarctic Rift System might have triggered renewed sedimentation of dominantly clastic material<sup>44,45</sup>.

### Palaeoclimate

Multi-proxy evidence from our mid-Cretaceous sedimentary record reveals an environment at a palaeolatitude of ~82° S on the Antarctic continental margin that was characterized by a regional temperate climate warm enough to maintain a diverse temperate rainforest (Fig. 3) only ~900 km from the palaeo-South Pole. Our palynomorph-based climate reconstruction following the approach outlined in ref.<sup>46</sup> returns a mean annual temperature of 13 °C with precipitation of

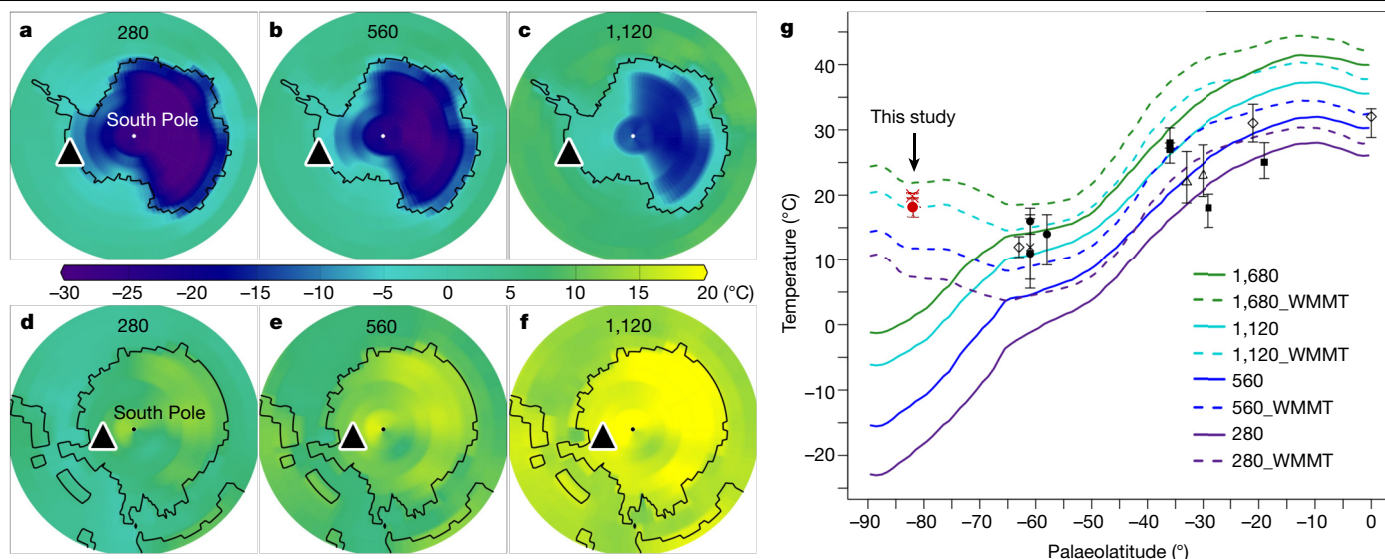


**Fig. 4 | Modern and mid-Cretaceous CO<sub>2</sub> sensitivity runs.** **a–f**, Distribution of warmest mean month temperatures (WMMT, colour scale) for present-day (**a–c**) and mid-Cretaceous at 90 Ma (**d–f**) configurations under atmospheric CO<sub>2</sub> levels of 280, 560 and 1,120 ppmv (representing 1×, 2× and 4× PI CO<sub>2</sub>). The black triangle indicates the approximate position of site PS104\_20-2. **g**, Modelled mid-Cretaceous WMMT (dashed lines) and zonal mean temperatures (solid lines) for different atmospheric CO<sub>2</sub> concentrations. The

temperature estimates (data points), including their respective calibration error ( $2\sigma$ ), were derived from the following proxies referred to in ref. <sup>5</sup>: terrestrial  $\delta^{18}\text{O}$  of vertebrate tooth enamel and/or pedogenic carbonate (filled squares), palaeobotanical data (filled circles), fish enamel  $\delta^{18}\text{O}$  (open triangles), marine calcareous fossil  $\delta^{18}\text{O}$  (open diamonds) and biomarkers (cross). Temperature estimates from this study are indicated by a red filled circle (palaeobotany) and red cross (HG palaeothermometry).

around 1,120 mm yr<sup>-1</sup>. The average temperature of the warmest summer month was 18.5 °C. Previous quantitative climate analyses from Antarctic records ~2,500 km further north resulted in Coniacian–Santonian (–89–84 Ma) mean annual air temperatures of 15–21 °C (refs. <sup>47,48</sup>), suggesting a shallow temperature gradient towards our site. Estimates of the Late Cretaceous climate based on NLRs generally agree well with other temperature proxies<sup>47</sup>. However, the approach assumes similarity of climate requirements for fossil taxa and their NLRs. With increasing age, the phylogenetic relationships of a fossil taxon become more disparate and the assumption thus becomes less robust. We therefore applied an independent geochemical palaeothermometer (HTI<sub>30</sub>) based on the distribution of the heterocyst glycolipids (ref. <sup>49</sup>), which corroborated our bioclimatic reconstructions by indicating austral summer lake or river-surface water temperatures of –20 °C for the swampy rainforest (Extended Data Fig. 4; see Methods). Our record contains, to our knowledge, the hitherto southernmost evidence of Cretaceous terrestrial environmental conditions and reveals a mid-Cretaceous ‘greenhouse climate’ that was capable of maintaining temperate conditions much farther south than previously documented<sup>14</sup>.

### Palaeoclimate modelling

In light of extremely limited mid-Cretaceous CO<sub>2</sub> proxy data<sup>6</sup> and widely scattered existing data estimates<sup>5</sup>, and to identify some of the pivotal driving mechanism of high-latitude mid-Cretaceous environmental conditions reconstructed for our new record, we ran the global climate model COSMOS<sup>5</sup> in a coupled atmosphere–ocean configuration with fixed vegetation. We did so under present-day (Fig. 4a–c) and mid-Cretaceous configurations at 90 Ma (Fig. 4d–g) for 1×, 2×, 4× and 6× pre-industrial (PI) CO<sub>2</sub> levels of 280 ppmv (280, 560, 1,120 and 1,680 ppmv, respectively; see Methods). Although the model predicts a mid-Cretaceous climate in West Antarctica that is already warmer under PI CO<sub>2</sub> levels (Fig. 4d), summer surface air and water temperatures of –20 °C at –82° S can only be reproduced by forcing the climate with very high atmospheric CO<sub>2</sub> levels between 1,120 and 1,680 ppmv (Fig. 4f, g). Our reconstructed mean annual air temperature of 13 °C, however, still remains strongly underestimated by the model (Fig. 4g).

We conclude that a temperate climate at such a high latitude with more than four months of complete polar night darkness requires a combination of both strongly elevated atmospheric CO<sub>2</sub> concentrations and dense surface vegetation that generates a low planetary albedo with an associated high radiant energy absorption and pronounced seasonality. This largely precludes the existence<sup>10</sup> of any substantial ice-sheet and sea-ice cover in and around Antarctica during the Turonian to Santonian stages of the Late Cretaceous epoch, an interpretation supported by palaeogeographic reconstructions of that period<sup>50</sup>. Conversely, the present Antarctic Ice Sheet and its associated climate feedbacks, such as ice albedo, would provide a stabilizing cooling effect in a future high-CO<sub>2</sub> world (Fig. 4a–c).

To further elaborate on the importance of additional forcing mechanisms, to discover the interdependency of surface vegetation and temperature sensitivity in more detail and to explore the drivers of the paradox in the late Cretaceous latitudinal temperature gradient visible in Fig. 4, future work should aim to run the model with various types of vegetation cover coupled with other drivers such as palaeogeography<sup>50</sup> or changes in cloudiness<sup>51</sup>.

Our findings highlight the importance of including land–ice changes in long-term climate simulations to accurately estimate climate sensitivity on these extended timescales<sup>52</sup>. We provide key data for constraining the response of polar terrestrial ecosystems to very high atmospheric CO<sub>2</sub> concentrations and for assessing the impact of Antarctic ice sheet presence under high-CO<sub>2</sub> scenarios—both of which are essential for modelling past and future climate change<sup>53</sup>.

### Online content

Any methods, additional references, Nature Research reporting summaries, source data, extended data, supplementary information, acknowledgements, peer review information; details of author contributions and competing interests; and statements of data and code availability are available at <https://doi.org/10.1038/s41586-020-2148-5>.



1. Forster, A., Schouten, S., Baas, M. & Sinninghe Damsté, J. S. Mid-Cretaceous (Albian–Santonian) sea surface temperature record of the tropical Atlantic Ocean. *Geology* **35**, 919–922 (2007).
2. Forster, A. et al. Tropical warming and intermittent cooling during the Cenomanian/Turonian Oceanic Anoxic Event (OAE 2): sea surface temperature records from the equatorial Atlantic. *Paleoceanography* **22**, PA1219 (2007).
3. Tarduno, J. A. et al. Evidence for extreme climatic warmth from late Cretaceous Arctic vertebrates. *Science* **282**, 2241–2243 (1998).
4. O'Brien, C. L. et al. Cretaceous sea-surface temperature evolution: constraints from TEX<sub>86</sub> and planktonic foraminiferal oxygen isotopes. *Earth Sci. Rev.* **172**, 224–247 (2017).
5. Niezgodzki, I. et al. Late Cretaceous climate simulations with different CO<sub>2</sub> levels and subarctic gateway configurations: a model-data comparison. *Paleoceanography* **32**, 980–998 (2017).
6. Foster, G. L., Royer, D. L. & Lunt, D. J. Future climate forcing potentially without precedent in the last 420 million years. *Nat. Commun.* **8**, 14845 (2017).
7. O'Connor, L. K. et al. Late Cretaceous temperature evolution of the southern high latitudes: a TEX<sub>86</sub> perspective. *Paleoceanogr. Paleoclimatol.* **34**, 436–454 (2019).
8. Jenkyns, H. C., Forster, A., Schouten, S. & Sinninghe Damsté, S. High temperatures in the Late Cretaceous Arctic Ocean. *Nature* **432**, 888–892 (2004).
9. Ditchfield, P. W., Marshall, J. D. & Pirrie, D. High latitude palaeotemperature variation: new data from the Tithonian to Eocene of James Ross Island, Antarctica. *Paleoceanogr. Paleoclimatol. Palaeoecol.* **107**, 79–101 (1994).
10. Bornemann, A. et al. Isotopic evidence for glaciation during the Cretaceous supergreenhouse. *Science* **319**, 189–192 (2008).
11. Müller, R. D. et al. Long-term sea-level fluctuations driven by ocean basin dynamics. *Science* **319**, 1357–1362 (2008).
12. Miller, K. G. et al. The Phanerozoic record of global sea-level change. *Science* **310**, 1293–1298 (2005).
13. McPhail, M. K. & Truswell, E. M. Palynology of Site 1166, Prydz Bay, East Antarctica. In *Proc. ODP Sci. Res. Vol. 188* (eds Cooper, A. K., O'Brien, P. E. & Richter, C.) 1–43 (Ocean Drilling Program, 2004).
14. Mays, C., Steinhilber, M. & Stilwell, J. D. Climatic implications of *Ginkgoites waarensis* Douglas emend. from the south polar Tupuangi flora, Late Cretaceous (Cenomanian), Chatham Islands. *Paleoceanogr. Paleoclimatol. Palaeoecol.* **438**, 308–326 (2015).
15. Pujana, R. R., Raffi, M. E. & Olivero, E. B. Conifer fossil woods from the Santa Marta Formation (Upper Cretaceous), Brandy Bay, James Ross Island, Antarctica. *Cretac. Res.* **77**, 28–38 (2017).
16. Manfroi, J. et al. The first report of a Campanian palaeo-wildfire in the West Antarctic Peninsula. *Paleoceanogr. Paleoclimatol. Palaeoecol.* **418**, 12–18 (2015).
17. Falcon-Lang, H. J., Cantrill, D. J. & Nichols, G. J. Biodiversity and terrestrial ecology of a mid-Cretaceous, high-latitude floodplain, Alexander Island, Antarctica. *J. Geol. Soc. Lond.* **158**, 709–724 (2001).
18. Wang, Y. et al. Paleo-CO<sub>2</sub> variation trends and the Cretaceous greenhouse climate. *Earth Sci. Rev.* **129**, 136–147 (2014).
19. Huber, B. T., MacLeod, K. G., Watkins, D. K. & Coffin, M. F. The rise and fall of the Cretaceous Hot Greenhouse climate. *Glob. Planet. Change* **167**, 1–23 (2018).
20. Gohl, K. et al. MeBo70 seabed drilling on a polar continental shelf: operational report and lessons from drilling in the Amundsen Sea Embayment of West Antarctica. *Geochim. Geophys. Res.* **18**, 4235–4250 (2017).
21. Lowe, A. L. & Anderson, J. B. Reconstruction of the West Antarctic ice sheet in Pine Island Bay during the Last Glacial Maximum and its subsequent retreat history. *Quat. Sci. Rev.* **21**, 1879–1897 (2002).
22. Spiegel, C. et al. Tectonomorphic evolution of Marie Byrd Land—implications for Cenozoic rifting activity and onset of West Antarctic glaciation. *Glob. Planet. Change* **145**, 98–115 (2016).
23. Larter, R. D. et al. Reconstruction of changes in the Amundsen Sea and Bellingshausen Sea sector of the West Antarctic Ice Sheet since the Last Glacial Maximum. *Quat. Sci. Rev.* **100**, 55–86 (2014).
24. Gohl, K. et al. Seismic stratigraphic record of the Amundsen Sea Embayment shelf from pre-glacial to recent times: Evidence for a dynamic West Antarctic ice sheet. *Mar. Geol.* **344**, 115–131 (2013).
25. Freudenthal, T. & Wefer, G. Drilling cores on the sea floor with the remote-controlled sea floor drilling rig MeBo. *Geosci. Instrum. Methods Data Syst.* **2**, 329–337 (2013).
26. Crampton, J. S. et al. in *The New Zealand Geological Timescale Monograph 22* (ed. Cooper, R. A.) 103–122 (Institute of Geological and Nuclear Sciences, 2004).
27. Mays, C. & Stilwell, J. D. Pollen and spore biostratigraphy of the mid-Cretaceous Tupuangi Formation, Chatham Islands, New Zealand. *Rev. Palaeobot. Palynol.* **192**, 79–102 (2013).
28. Mildenhall, D. C. *Palynological Reconnaissance of Early Cretaceous to Holocene Sediments, Chatham Islands, New Zealand Monograph 7* (Institute of Geological & Nuclear Sciences, 1994).
29. He, T., Lamont, B. B. & Fogliani, B. Pre-Gondwanan-breakup origin of *Beauprea* (Proteaceae) explains its historical presence in New Caledonia and New Zealand. *Sci. Adv.* **2**, e1501648 (2016).
30. Gee, J. & Kent, D. in *Treatise on Geophysics* Vol. 5 (ed. Kono, M.) Ch. 5.12 (Elsevier, 2007).
31. Wobbe, F., Gohl, K., Chambord, A. & Sutherland, R. Structure and breakup history of the rifted margin of West Antarctica in relation to Cretaceous separation from Zealandia and Bellingshausen plate motion. *Geochim. Geophys. Res.* **13**, Q04W12 (2012).
32. Jordan, T. A., Riley, T. R. & Siddoway, C. S. The geological history and evolution of West Antarctica. *Nat. Rev. Earth Environ.* **1**, 117–133 (2020).
33. Müller, R. D. et al. GPlates: building a virtual Earth through deep time. *Geochim. Geophys. Res.* **19**, 2243–2261 (2018).
34. DiVenere, V. J., Kent, D. V. & Dalziel, I. W. D. Mid-Cretaceous paleomagnetic results from Marie Byrd Land, West Antarctica: a test of post-100 Ma relative motion between East and West Antarctica. *J. Geophys. Res.* **99** (B8), 15115–15139 (1994).
35. Pocknall, D. T. & Crosbie, Y. M. Pollen morphology of *Beauprea* (Proteaceae): modern and fossil. *Rev. Palaeobot. Palynol.* **53**, 305–327 (1988).
36. Jackson, M. B. & Armstrong, W. Formation of aerenchyma and the processes of plant ventilation in relation to soil flooding and submergence. *Plant Biol.* **1**, 274–287 (1999).
37. Lijmbach, G. W. M. On the origin of petroleum. In *Proc. 9th World Petroleum Congress Vol. 2*, 357–369 (World Petroleum Congress, 1975).
38. Peters, K. E., Walters, C. C. & Moldowan, J. M. *The Biomarker Guide* (Cambridge Univ. Press, 2004).
39. Meyers, P. A. Applications of organic geochemistry to paleolimnological reconstructions: a summary of examples from the Laurentian Great Lakes. *Org. Geochem.* **34**, 261–289 (2003).
40. Robert, C. & Kennett, J. P. Antarctic subtropical humid episode at the Paleocene–Eocene boundary: clay-mineral evidence. *Geology* **22**, 211–214 (1994).
41. Huang, W. H. & Keller, W. D. Dissolution of rock-forming silicate minerals in organic acids: simulated first-stage weathering of fresh mineral surfaces. *Am. Mineral.* **55**, 2076–2094 (1970).
42. Sugden, D. E. & Jamieson, S. S. R. The pre-glacial landscape of Antarctica. *Scott. Geogr. J.* **134**, 203–223 (2018).
43. Uenzelmann-Neben, G. & Gohl, K. Early glaciation already during the Early Miocene in the Amundsen Sea, Southern Pacific: indications from the distribution of sedimentary sequences. *Glob. Planet. Change* **120**, 92–104 (2014).
44. Zundel, M. et al. Thurston Island (West Antarctica) between Gondwana subduction and continental separation: A multistage evolution revealed by apatite thermochronology. *Tectonics* **38**, 878–897 (2019).
45. Müller, R. D., Gohl, K., Cande, S. C., Goncharov, A. & Golynsky, A. V. Eocene to Miocene geomorphology of the West Antarctic rift system. *Aust. J. Earth Sci.* **54**, 1033–1045 (2007).
46. Harbert, R. S. & Nixon, K. C. Climate reconstruction analysis using coexistence likelihood estimation (CRACLE): a method for the estimation of climate using vegetation. *Am. J. Bot.* **102**, 1277–1289 (2015).
47. Poole, I., Cantrill, D. J. & Utescher, T. Reconstructing Antarctic palaeoclimate from wood floras: a comparison using multivariate anatomical analysis and the coexistence approach. *Paleoceanogr. Paleoclimatol. Palaeoecol.* **222**, 95–121 (2005).
48. Francis, J. E. et al. 100 million years of Antarctic climate evolution: evidence from fossil plants. In *Proc. 10th Int. Symp. on Antarctic Earth Sciences* (eds Cooper, A. K. et al.) 19–27 (National Academies, 2007).
49. Bauersachs, T., Rochelmeier, J. & Schwark, L. Seasonal lake surface water temperature trends reflected by heterocyst glycolipid-based molecular thermometers. *Biogeosciences* **12**, 3741–3751 (2015).
50. Ladant, J. L. & Donnadiet, Y. Paleogeographic regulation of glacial events during the Cretaceous supergreenhouse. *Nat. Commun.* **7**, 12771 (2016).
51. Upchurch, G. R., Jr, Kiehl, J., Shields, C., Scherer, J. & Scotese, C. Latitudinal temperature gradients and high-latitude temperatures during the latest Cretaceous: congruence of geologic data and climate models. *Geology* **43**, 683–686 (2015).
52. Farnsworth, A. et al. Climate sensitivity on geological timescales controlled by non-linear feedbacks and ocean circulation. *Geophys. Res. Lett.* **46**, 9880–9889 (2019).
53. *IPCC Special Report on the Ocean and Cryosphere in a Changing Climate* (eds Pörtner, H. O. et al.) (IPCC, 2019); [https://www.ipcc.ch/site/assets/uploads/sites/3/2019/12/SROCC\\_FullReport\\_FINAL.pdf](https://www.ipcc.ch/site/assets/uploads/sites/3/2019/12/SROCC_FullReport_FINAL.pdf)
54. Arndt, J. E. et al. A new bathymetric compilation covering circum-Antarctic waters. *Geophys. Res. Lett.* **40**, 3111–3117 (2013).
55. Fretwell, P. et al. Bedmap2: improved ice bed, surface and thickness datasets for Antarctica. *Cryosphere* **7**, 375–393 (2013).

**Publisher's note** Springer Nature remains neutral with regard to jurisdictional claims in published maps and institutional affiliations.

© The Author(s), under exclusive licence to Springer Nature Limited 2020

## Science Team of Expedition PS104

V. Afanasyeva<sup>16</sup>, J. E. Arndt<sup>1</sup>, B. Ebermann<sup>17</sup>, C. Gebhardt<sup>1</sup>, K. Hochmuth<sup>119</sup>, K. Küssner<sup>1</sup>, Y. Najman<sup>18</sup>, F. Riefstahl<sup>1</sup> & M. Scheinert<sup>17</sup>

<sup>16</sup>VNIOkeangeologie, St Petersburg, Russia. <sup>17</sup>Technische Universität Dresden, Dresden, Germany. <sup>18</sup>Lancaster Environment Centre, Lancaster University, Lancaster, UK. <sup>19</sup>Present address: School of Geology, Geography & the Environment, University of Leicester, Leicester, UK.

## Methods

### Seafloor drill rig MARUM-MeBo70

MARUM-MeBo70 is a robotic drill rig that was deployed on the seabed and remotely controlled from RV *Polarstern* during expedition PS104<sup>20</sup>. Detailed information about the drill rig and its operation is published in ref. <sup>25</sup>.

### X-ray CT

Whole rounds of MeBo core PS104\_20-2 were scanned by a Toshiba Aquilion 64 computer tomograph at the hospital Klinikum Bremen-Mitte, with an X-ray source voltage of 120 kV and a current of 600 mA. The CT scans have a resolution of 0.351 mm in x and y directions and 0.5 mm resolution in the z direction (resolution of scaled reconstruction:  $0.195 \times 0.195 \times 0.3 \text{ mm}^3$ ). Images were reconstructed using Toshiba's patented helical cone beam reconstruction technique. The obtained CT data were processed using the ZIB edition of the Amira software (version 2017.39)<sup>56</sup>. Within Amira, the CT scans of the core sections were merged when necessary and core liners, including about 2 mm of the core rims, were removed from the dataset until all marginal artefacts from the coring process were removed. Subsequently, all clasts larger than -1 mm, root-traces (where present) and matrix sediment were segmented with the (marker-based) watershed tool of the Segmentation Editor. Markers were predominantly set with the threshold tool. For only rarely occurring clasts with an X-ray attenuation close to the matrix sediment, the magix wand tool was used to manually set additional markers. Holes within clasts after the watershed segmentation were added to the clasts with the selection fill tool.

### Palynology

Between 2 and 6 g of dry-weight sediment per sample were processed at Northumbria University following standard palynological techniques, including sieving (10 µm) and acid treatment with 10% HCl (hydrochloric acid) and cold 38% HF (hydrofluoric acid). The processed residue was transferred to microscope slides using glycerine jelly as a mounting medium, and 2–3 slides were analysed per sample at 400× magnification. Of the 17 samples analysed for pollen and spores, 7 were productive, and total counts range from 340 to 360 pollen grains and spores per sample (Extended Data Figs. 2, 3; Extended Data Table 1). Pollen concentrations increase from an average of ~6,500 grains per gram of sediment in the lower three samples to 61,000–121,500 g<sup>-1</sup> at the top. We could not identify any reworking of palynomorphs. Percentages were calculated on the basis of the sum total of pollen and spores; 65 pollen and spore taxa were identified from the literature<sup>57–59</sup> (Extended Data Table 3). All samples contained a high morphological diversity of *Podocarpus* pollen, which we classified as *Podocarpidites* undiff. as many of these grains were either folded or damaged and were therefore unidentifiable beyond family level. Marine dinoflagellate cysts were absent in all samples.

### Palynomorph-based climate reconstructions (bioclimatic analysis)

We reconstructed terrestrial mean annual temperature (MAT), precipitation (MAP) and WMMT using the NLR approach. The NLR approach uses the climatic requirements of the NLR of fossil taxa to reconstruct the past climatic range and assumes that the climatic requirements of the fossil taxa are similar to those of their NLR (Extended Data Table 2). NLR approaches use the presence or absence of individual taxa in a fossil assemblage rather than relative abundance, which reduces the likelihood of taphonomic biases. This facilitates, to some extent, the reconstruction of past, non-modern analogue climates and environments<sup>60</sup>. NLR-based temperature estimates are generally in good agreement with estimates from geochemical and other palaeobotanical methods, including the Climate Leaf Analysis Multivariate

Program (CLAMP) and leaf margin analysis<sup>61–67</sup>, providing confidence in the utility of the method for the reconstruction of pre-Quaternary climates.

However, quantitative climate estimates from the fossil plant record of deep-time geological intervals are always accompanied by large uncertainties. Incorrect use of outliers and fossil taxa with ambiguous affinity can result in erroneous climate estimates<sup>68</sup>. One of the greatest weaknesses that affects all NLR approaches is the assumption of uniformitarianism—namely, that the climate tolerances of modern species can be extended into the past. This assumption inevitably introduces uncertainty that increases with the age of the geological formation<sup>69</sup>. To statistically constrain the most likely climatic co-occurrence envelope, we combined the NLR approach with the probability density function (PDF) method<sup>46,70,71</sup>. In contrast to other NLR methods, such as the coexistence approach, the PDF method has the advantage that it statistically constrains the most likely climatic co-occurrence envelope, thereby offering a solution that mathematically reduces the potential impact of wrongly defined climate tolerance on upper and lower limits of palaeoclimatic estimates. To further reduce uncertainties caused by potentially wrong identification of NLR, we removed fossil taxa with potentially ambiguous affinity or very rare occurrence in the fossil record (Extended Data Table 2). This includes *Microcachrydites antarcticus*, a taxon abundant and widespread in the Antarctic fossil record, with the NLR *Microcachrys tetragona* (the sole species of the genus *Microcachrys* that is now endemic to Tasmania). Another example is *Peninsulapollis gillii* with close links to the modern genus *Beauprea*, and endemic to New Caledonia. In both cases we used the family, Podocarpaceae and Proteaceae, respectively, rather than the genus or species as the NLR.

To generate the paleoclimate estimate, we followed the procedure described in refs. <sup>59,63</sup>. We first identified the bioclimatic envelope for each NLR by cross-plotting their modern distribution from the Global Biodiversity Information Facility (GBIF)<sup>72</sup> with the gridded WorldCLIM climate surface<sup>73</sup> using the dismo package<sup>74</sup> in R. We then filtered the dataset and removed redundant data, 'exotic' occurrences (such as garden plants) as well as multiple entries per climate grid cell to avoid the climatic probability function becoming highly slanted towards that location<sup>75</sup>. Before establishing the PDFs, bootstrapping was applied to test the robustness of the dataset, which is of particular interest for taxa with only few modern occurrences. Following the bootstrapping, we calculated the likelihood ( $f$ ) of a taxon ( $t$ ) occurring at value ( $x$ ) for a certain climatic variable by using the mean ( $\mu$ ) and standard deviation ( $\sigma$ ) of the modern distribution range of each taxa<sup>65,70</sup>.

$$f(x)_t = \frac{1}{\sqrt{2\pi\sigma_x^2}} e^{-\frac{(x-\mu_x)^2}{2\sigma_x^2}}$$

Because the separate reconstruction of climate ranges for each variable can lead to bioclimatic envelopes that include intervals, where no modern-day occurrence of  $t$  is observed<sup>65</sup>, we calculated joint likelihood PDFs for each combination of the climate variables MAT, MAP and WMMT using the correlation coefficient  $p(x, y)$ :

$$f(x, y)_t = \frac{1}{2\pi\sigma_x\sigma_y\sqrt{1-p^2}} e^{-\frac{1}{2(1-p^2)}\left(\frac{(x-\mu_x)^2}{\sigma_x^2} + \frac{(y-\mu_y)^2}{\sigma_y^2} - 2p\frac{(x-\mu_x)(y-\mu_y)}{\sigma_x\sigma_y}\right)}$$

After assessing whether all bioclimatic envelopes share a coexistence interval, the climate estimates of the NLR assemblage were reconstructed by multiplying the individual joint likelihoods of taxa  $f(x, y)_{t1} \dots f(x, y)_{tn}$  with each other:

$$f(x, y)_{\text{Combined}} = f(x, y)_{t1} \times f(x, y)_{t2} \times \dots \times f(x, y)_{tn}$$

To constrain the core distribution of a group, we determined the range of one ( $f(x, y)_{\text{relative}} = 0.157$ ) and two standard deviations ( $f(x, y)_{\text{relative}} = 0.023$ ) from the occurrence within a group with  $f(x, y)_{\text{max}}$  representing the most likely climate conditions<sup>75</sup>.

$$f(x, y)_{\text{relative}} = \frac{f(x, y)}{f(x, y)_{\text{max}}}$$

For our bioclimatic analysis, we used all pollen and spore taxa that could be related to an NLR (following ref.<sup>59</sup>, Extended Data Table 2). Climatic ranges are indicated with their  $\pm 2\sigma$  range. We calculated an MAT of  $12.8 \pm 2.2$  °C, WMMT of  $18.4 \pm 1.9$  °C and MAP of  $1,120 \pm 330$  mm yr<sup>-1</sup>. It should be noted that the ranges of these values show the mathematical error and not the real range, which might result from the uncertainties in using an NLR approach. To avoid misunderstandings, we therefore indicated in the main text the pollen-based climate estimates without  $2\sigma$  ranges.

### Organic geochemistry

Freeze-dried and homogenized sediment samples were extracted by means of ultrasonication using a dichloromethane:methanol mixture (2:1, v-v). After centrifugation, the total lipid extract was dried by rotary evaporation. The extraction was repeated twice. The combined total lipid extract was fractionated using silica open-column chromatography and hexane as eluent to obtain apolar lipids. Hydrocarbons were analysed using an HP gas chromatograph 6890 (30 m DB-5MS column, 0.25 mm diameter, 0.25 µm film thickness). The identification of *n*-alkanes, pristane and phytane was based on comparison of their retention times with those of reference compounds that were run on the same instrument. The TAR<sup>76</sup> was calculated using peak areas of long-chain (*n*-C<sub>27</sub>, *n*-C<sub>29</sub>, *n*-C<sub>31</sub>) against short-chain (*n*-C<sub>15</sub>, *n*-C<sub>17</sub>, *n*-C<sub>19</sub>) alkanes. The carbon preference index (CPI) was calculated as follows<sup>38</sup>:

$$\text{CPI} = \frac{2 \times (n\text{-C}_{23} + n\text{-C}_{25} + n\text{-C}_{27} + n\text{-C}_{29})}{n\text{-C}_{22} + 2 \times (n\text{-C}_{24} + n\text{-C}_{26} + n\text{-C}_{28}) + n\text{-C}_{30}} \quad (1)$$

### Heterocyst glycolipid palaeothermometry

Sediment samples from the coastal sandstone (9R, 50–52 cm; 26.76 mbsf) and the carbonaceous mudstone (9R, 76.5–78 cm; 27.02 mbsf; 10R, 60–62 cm; 29.21 mbsf) were lyophilized and ground to a fine sediment powder using a solvent-cleaned agate pestle and mortar. Between 20.1 and 29.7 g of sediment were extracted using a modified Bligh and Dyer procedure<sup>77</sup>. Briefly, sediment samples were extracted ultrasonically (for 10 min.) three times in a solvent mixture of MeOH, DCM and phosphate buffer (2:1:0.8; v-v:v). After each sonication step, the solvent mixture was centrifuged at 1,500g for 3 min and the supernatant transferred to a centrifuge tube. The combined supernatants were phase separated by adding DCM and phosphate buffer to a final solvent ratio of 1:1:0.9 (v-v:v). The organic bottom layer was collected in a round bottom flask and reduced under vacuum using a rotary evaporator. Each Bligh and Dyer extract (BDE) was transferred to a preweighed vial using DCM:MeOH (1:1, v-v) and dried under a gentle stream of N<sub>2</sub>. Before analysis, all BDEs were redissolved in a solvent mixture of *n*-hexane:2-propanol:H<sub>2</sub>O (72:27:1; v-v:v) to a concentration of 8 mg ml<sup>-1</sup>. A procedural blank was added to the sample batch and treated as a regular sample to test for possible cross-contamination during sample preparation.

High-performance liquid chromatograph coupled to electrospray ionisation tandem mass spectrometry (HPLC/ESI-MS<sup>2</sup>) was performed on the BDEs following the analytical procedure given by ref.<sup>78</sup> to establish heterocyst glycolipid (HG) distribution patterns and determine relative abundances. Separation of HGs was achieved using a Waters Alliance 2690 HPLC system fitted with a Phenomenex Luna NH<sub>2</sub> column (150 × 2 mm<sup>2</sup>; 3 µm particle size) and a guard column of the same

material. Both were maintained at a constant temperature of 30 °C. The applied gradient profile was as follows: 95% A:5% B to 85% A:15% B in 10 min. (isocratic for 7 min) at 0.5 ml min<sup>-1</sup>, followed by back flushing with 30% A:70% B at 0.2 ml min<sup>-1</sup> for 25 min and re-equilibrating the column with 95% A:5% B for 15 min. Solvent A was *n*-hexane:2-propanol:HCO<sub>2</sub>H:14.8 M NH<sub>3</sub> aq. (79:20:0.12:0.04; v-v:v:v) and Solvent B was 2-propanol:water:HCO<sub>2</sub>H:14.8 M NH<sub>3</sub> aq. (88:10:0.12:0.04; v-v:v:v).

HGs were detected using a Micromass Quattro LC triple quadrupole mass spectrometer equipped with an electrospray ionization interface and operated in positive ion mode. Source conditions were as given in ref.<sup>79</sup>. All BDEs were analysed in multiple reaction monitoring mode to achieve maximum specificity. HGs were identified on the basis of a comparison of retention times with those of HGs in cultured cyanobacteria, as well as published mass spectra<sup>80–84</sup>. HGs were monitored using the following transitions: *m/z* 547 → 415 (pentose HG<sub>26</sub> diol), *m/z* 603 → 471 (pentose HG<sub>30</sub> diol), *m/z* 619 → 487 (pentose HG<sub>30</sub> triol), *m/z* 647 → 515 (pentose HG<sub>32</sub> triol), *m/z* 561 → 415 (deoxyhexose HG<sub>26</sub> diol), *m/z* 575 → 413 (HG<sub>26</sub> keto-ol), *m/z* 577 → 415 (HG<sub>26</sub> diol), *m/z* 603 → 441 (HG<sub>28</sub> keto-ol), *m/z* 605 → 443 (HG<sub>28</sub> diol), *m/z* 619 → 457 (HG<sub>28</sub> keto-diol), *m/z* 621 → 459 (HG<sub>28</sub> triol), *m/z* 635 → 459 (methylated hexose HG<sub>28</sub> triol), *m/z* 647 → 485 (HG<sub>30</sub> keto-diol), *m/z* 649 → 487 (HG<sub>30</sub> triol), *m/z* 675 → 513 (HG<sub>32</sub> keto-diol), *m/z* 677 → 515 (HG<sub>32</sub> triol) and quantified by integrating peak areas using the QuanLynx application software (version 4.1 SCN856).

Surface water temperatures (SWTs) during the deposition of the coastal Eocene sandstone were reconstructed using the HDI<sub>26</sub> (heterocyst diol index of 26 carbon atoms) and HDI<sub>28</sub> (HDI of 28 carbon atoms) lipid palaeothermometers as described in ref.<sup>49</sup>. As the HG content of the swampy palaeoenvironment exclusively consisted of HG<sub>30</sub> triols and HG<sub>30</sub> keto-diol (Extended Data Fig. 4), which are specific to cyanobacteria that form benthic microbial mats<sup>82</sup>, we here applied the HTI<sub>30</sub> (heterocyst triol index of 30 carbon atoms) to the mudstone sequence. This index is defined as follows:

$$\text{HTI}_{30} = \text{HG}_{30} \text{ triol} / (\text{HG}_{30} \text{ triol} + \text{HG}_{30} \text{ keto-diol})$$

The HTI<sub>30</sub> was transferred to absolute temperatures using a surface sediment calibration obtained from a large set of East African lakes (*n* = 47) located on an altitudinal transect from 615 to 4,504 m above sea level with SWTs ranging from 5.7 to 27.9 °C. In this setting, the HTI<sub>30</sub> showed a strong linear correlation with SWT, which is expressed in the equation below (T.B., unpublished data):

$$\text{SWT} = (\text{HTI}_{30} / 0.0249) - (0.2609 / 0.0249)$$

Independent confirmation for the robustness of the HG-based temperature reconstruction is obtained by comparing HG distribution patterns and HTI<sub>30</sub> values in the mudstone sequence with those reported for an axenic culture of the heterocystous cyanobacterium *Scytonema* sp. PCC (Pasteur Culture collection of Cyanobacteria) 10023 (ref.<sup>84</sup>). This cyanobacterium exclusively contains HG<sub>30</sub> triols and HG<sub>30</sub> keto-diols. The above transfer function yields an HTI<sub>30</sub> value of ~0.88 for the culture grown at an ambient temperature of 25 °C. This value is identical to the HTI<sub>30</sub> (0.88) calculated using the relative abundances of the major HG<sub>30</sub> triol and HG<sub>30</sub> keto-diol isomers reported in ref.<sup>84</sup>.

### Grain-size analyses

A set of discrete samples was wet sieved at 2 mm and 63 µm to separate the gravel, sand and mud grain-size classes. The <63 µm (mud) suspension was separated into silt (2–63 µm) and clay (<2 µm) using settling velocity (Stokes' Law) in Atterberg tubes.

### Clay mineral analyses

An aliquot of the clay fraction was used to determine the relative contents of the clay minerals smectite, illite, chlorite and kaolinite using an automated powder diffractometer system Rigaku MiniFlex with Co

K $\alpha$  radiation (30 kV, 15 mA) at the Institute for Geophysics and Geology (University of Leipzig). The clay mineral identification and quantification followed standard X-ray diffraction methods<sup>85</sup>.

### Bulk sediment composition

Total carbon (TC) and total nitrogen (TN) contents were analysed with an Elementar Vario EL III. The TOC contents were determined after removal of the total inorganic carbon (carbonates) with HCl using an ELTRA CS-2000. Carbonate content was calculated by subtracting the TOC from the TC and multiplying the difference (total inorganic carbon) by 8.33; that is, the ratio between the molecular weights of CaCO<sub>3</sub> and C. The TOC:TN (C:N) ratio was calculated on a molar basis.

The mineralogical composition of the milled bulk sediment was analysed semiquantitatively with X-ray diffraction using peak intensities and area ratios analysed with the MacDiff program (version 4.2.6).<sup>86</sup> For the Fe(Ca) carbonates the peak intensities for ankerite (at 2.906 Å) and siderite (at 2.795 Å) were used and summed up as percentages for Fe(Ca) carbonates (ankerite and siderite) in relation to the absolute percentage of other carbonates (calcite, Mg calcite and dolomite).

### Thin sections

After drying the untreated soft sediment in the fridge for 2–3 days, the sediment was dried at room temperature (20–22 °C) for another 2–3 days. During that time the sediment was checked daily for crack formation. Under low pressure, the sediment was impregnated stepwise in a vacuum exicator with epoxy araldite 2020 resin until full coverage of the sample was achieved. After complete hardening, the bottom of the sample was ground by a Tegrapol with silicon carbide (SiC) paper sizes from 80 to 800—depending on sediment characteristics—and a maximum of 150 rotations per minute until the sediment surface was reached. The glass slides for the thin sections, which were 3 mm thick and 35 × 120 mm in area, were ground with a 9- $\mu$ m-fraction SiC paper to achieve both grip and an even surface (alternative machine system: Logitech LP50 auto). Then the sample was attached to the slide with the same resin used for impregnation by a pressure block. Afterwards, the surface of the glass was cleaned and labelled with a diamond pen. Most samples were then cut by a WOCO 50 diamond saw to achieve 250- $\mu$ m-thick sediment strips on the glass, before grinding with SiC paper or the Logitech LP50 to reach a thickness of 30  $\mu$ m. Only some sections were covered with 150- $\mu$ m-thick glasses, for which an ultraviolet resin (cyanacrylate) was used. Most sections remained uncovered for Raman and SEM-EDX spectroscopy. Finally, all thin sections were cleaned with ethanol. The set of thin sections was prepared by MKfactory.

### Palaeomagnetic measurements

Five discrete samples were taken at variable spacings from cores 9R and 10R of core PS104\_20-2 for palaeomagnetic investigations using plastic boxes with inner dimensions of 2 × 2 × 2 cm<sup>3</sup>. The directions and intensities of natural remanent magnetization were measured on a cryogenic magnetometer (model 2G Enterprises 755 HR). Subsequent alternating field (AF) demagnetization of natural remanent magnetization involved 15 steps to a maximum AF intensity of 100 mT. A detailed vector analysis<sup>87</sup> was applied to the results to determine the characteristic remanent magnetization of each sample and to unravel its magnetic polarity. Samples showing no systematic demagnetization pattern were excluded from further interpretation.

### Palaeoclimate modelling

We use the COSMOS model (see Code availability) in a coupled atmosphere–ocean configuration with fixed vegetation. The atmosphere component ECHAM5 is run in a T31/L19 resolution<sup>88</sup>. It consists of 19 vertical layers and has a horizontal resolution of ~3.75°. The ocean component MPI-OM runs in a GR30/L40 configuration<sup>89</sup>. It has a formal horizontal resolution of 3.0° × 1.8° and consists of 40 unequal vertical

layers. The high-resolution hydrological discharge model is a part of ECHAM5<sup>90</sup>, while MPI-OM includes a dynamic–thermodynamic sea-ice model using a viscous–plastic rheology<sup>91</sup>. Climate simulations were run for present-day and mid-Cretaceous configurations under different CO<sub>2</sub> levels in the atmosphere. Other greenhouse gases (such as CH<sub>4</sub> and N<sub>2</sub>O) were set to PI levels. In the mid-Cretaceous simulations, we employed published paleogeography<sup>92</sup> and vegetation<sup>93</sup> as well as no ice sheets in both hemispheres. The orbital configurations in all Cretaceous experiments were fixed at 800 common era (CE) and hence represent values from the beginning of externally forced simulation from 800 to 1800 CE (a so-called millennial run). The solar constant was reduced by 1% for the mid-Cretaceous experiments relative to the present-day value. The simulations with 1× and 2× PI CO<sub>2</sub> levels were run for 9,200 and 9,000 years, respectively, and 10,600 years for 4× PI CO<sub>2</sub> (ref. <sup>94</sup>). All simulations reached equilibrium at the surface. The experiment with a 6× PI CO<sub>2</sub> level had a slightly different atmospheric land–sea mask than the other three simulations. It was run for ~500 years and was not in a full equilibrium at the surface<sup>5</sup>. The PI control simulation was run for ~7,500 years. The simulations with 2× and 4× PI CO<sub>2</sub> levels were branched off from the 1× PI simulation from model year 6,800 and were further run for 700 years. The simulations reach either full or quasi-equilibrium at the surface. For the analyses the mean was taken over the last 100 years of each simulation. The model has been successfully applied previously for scientific questions focusing on the Quaternary<sup>95,96</sup>, Neogene<sup>97–99</sup>, Palaeogene<sup>100,101</sup> and Late Cretaceous<sup>5</sup>, as well as estimates of future climate<sup>99,102</sup>.

### Sr and Nd isotopic measurements

A total of seven samples were selected for processing from cores 9R and 10R at site PS104\_20-2. A detailed method description that was applied for determining their Sr and Nd isotopic compositions is given in ref. <sup>103</sup>.

### Zircon and apatite U–Pb geochronology

The youngest detrital zircon and apatite U–Pb ages obtained from the cores 2R (sample AWI-35 at 9.9 mbsf) and 9R (sample AWI-25 at 26.7 mbsf) were used for constraining maximum deposition ages of the sandstone. The samples yielded Eocene apatite ( $n = 2$ ) and zircon ( $n = 1$ ) ages. The single Eocene zircon grain yields a Concordia age of  $45.5 \pm 2.0$  Myr (Extended Data Fig. 1a). The apatite grains all yield analyses discordant in U–Pb isotopic space due to the presence of common Pb (Pb<sub>c</sub>; that is, Pb incorporated during crystallization as opposed to radiogenic Pb\* generated in situ by radionuclide decay). For single-grain ages, a terrestrial Pb isotope evolution model<sup>104</sup> was used for an initial estimate of  $^{207}\text{Pb}/^{206}\text{Pb}_c$ , followed by an iterative approach to the  $^{207}\text{Pb}$ -based corrected age calculation<sup>105</sup>.

As only two Eocene single-grain apatite ages are reported, the calculation of an array age would not normally be appropriate. However, comparison of the trace element chemistry (REE–Sr–Y) to an apatite compositional reference library<sup>106</sup> indicates that both Eocene grains are chemically, as well as chronologically, indistinguishable (Extended Data Fig. 1b), increasing the likelihood of a common source. Therefore, the two youngest apatite grains from AWI-35 were jointly regressed with the range of  $^{207}\text{Pb}/^{206}\text{Pb}_c$  values ( $0.834 \pm 0.018$ ) for West Antarctic crystalline basement<sup>107</sup> (Extended Data Fig. 1a) to obtain a lower-intercept age of  $39.3 \pm 3.8$  Myr (mean standard weighted deviation, MSWD = 0.99), similar to the independently obtained single-grain Concordia age of  $45.5 \pm 2.0$  Myr determined from the youngest zircon from AWI-25. A Lutetian maximum deposition age (approximately 43 Myr) for AWI-35 and AWI-25 is therefore indicated.

Pure apatite and zircon separates were hand-picked from the non-magnetic heavy mineral 63–315  $\mu$ m size fraction, mounted in epoxy resin, ground to reveal internal surfaces and polished. Almost no sample bias was introduced by grain selection because in most cases all of the observed mineral grains were picked as the amount of sample material was very small. All U–Pb analyses were carried out using a Photon



# Article

Machines Analyte Excite 193 nm ArF excimer laser-ablation system with a HelEx 2-volume ablation cell coupled to an Agilent 7900 ICPMS at the Department of Geology, Trinity College Dublin. Laser fluence was  $2.5 \text{ J cm}^{-2}$  with a repetition rate of 15 Hz and an analysis time of 20 s, followed by an 8 s pause to allow for signal wash-out and a subsequent baseline measurement. Spot sizes of  $47 \mu\text{m}$  and  $24 \mu\text{m}$  were employed for apatite and zircon respectively, in separate analytical sessions.

Data reduction employed the VizualAge and VizualAge\_UComPbine data reduction schemes (DRS) for Iolite for zircon and apatite, respectively<sup>108–110</sup>. Each DRS corrects for intrasession analytical drift, mass bias and downhole fractionation using a user-specified fractionation model based on measurements of the primary standard; VizualAge\_UComPbine also permits the presence of a variable  $\text{Pb}_c$  content in a primary age standard that must be corrected using a known initial  $^{207}\text{Pb}/^{206}\text{Pb}_c$  value. Final U–Pb age calculations were made using the Isoplot add-in for Excel<sup>111</sup>.

Single-grain zircon U–Pb Concordia ages were calculated, and analyses with a probability of concordance  $<0.001$  were rejected<sup>111</sup>. The primary standard was Plešovice zircon; the GZ7 and 91,500 zircons were used as secondary standards and treated as unknowns during data reduction and age calculation<sup>112</sup>, yielding Concordia ages of  $530.1 \pm 3.7 \text{ Myr}$  and  $1,060.4 \pm 6.8 \text{ Myr}$ , respectively.

For apatite analyses, Madagascar apatite was employed as the primary standard and McClure Mountain and Durango apatites were employed as secondary standards<sup>113,114</sup>. The  $\text{Pb}_c$  value in the secondary standards was corrected using fixed initial ratios, yielding weighted mean ages of  $532.2 \pm 6.0 \text{ Myr}$  and  $32.3 \pm 0.7 \text{ Myr}$ , respectively. Variable  $\text{Pb}_c$  contents in the detrital apatite unknowns were corrected by using a terrestrial Pb evolution model<sup>103</sup> for the calculation of single-grain ages followed by an iterative calculation to obtain single-analysis  $^{207}\text{Pb}$ -corrected ages<sup>104</sup>. Alternatively, the range of the  $^{207}\text{Pb}/^{206}\text{Pb}_c$  values for West Antarctic basement<sup>105</sup> can be used for the single-grain age calculation: the resulting single-grain ages are within 1 Myr of the single-grain ages obtained using the iterative calculation. Apatite U–Pb age filtering<sup>115</sup> results in  $2\sigma$  errors of  $\leq 50\%$  for grains with ages of 10–100 Myr and  $2\sigma$  errors of  $\leq 25\%$  for grains with ages  $>100 \text{ Myr}$ . For apatite trace-element analysis, the Iolite Trace Elements DRS was used. NIST612 glass and Madagascar apatite<sup>116</sup> were employed as the primary and secondary reference materials respectively, with  $^{43}\text{Ca}$  as an internal elemental standard<sup>117</sup>.

## Data availability

All data are available online via PANGAEA at <https://doi.org/10.1594/PANGAEA.906092>.

## Code availability

The standard model code of the ‘Community Earth System Models’ (COSMOS) version COSMOS-landveg r2413 (2009) is available upon request from the Max Planck Institute for Meteorology (Reinhard. Budich@mpimet.mpg.de). Analytical scripts are available via PANGAEA at <https://doi.org/10.1594/PANGAEA.910179>.

56. Stalling, D., Westerhoff, M. & Hege, H.-C. in *The Visualization Handbook* (eds Hansen, C. D. & Johnson, C. R.) 749–767 (Elsevier, 2005).
57. Raine, J. I., Mildenhall, D. C. & Kennedy, E. M. *New Zealand Fossil Spores and Pollen: An Illustrated Catalogue* 4th edn Science Miscellaneous Series Vol. 4 (GNS, 2011); <http://data.gns.cri.nz/sporepollen/index.htm>
58. Mays, C. A late Cretaceous (Cenomanian-Turonian) south polar palynoflora from the Chatham Islands, New Zealand. *Mem. Assoc. Aust. Palaeontol.* **47**, 92 (2015).
59. Bowman, V. C., Francis, J. E., Askin, R. A., Riding, J. B. & Swindles, G. T. Latest Cretaceous-earliest Paleogene vegetation and climate change at the high southern latitudes: palynological evidence from Seymour Island, Antarctic Peninsula. *Palaeogeogr. Palaeoclimatol. Palaeoecol.* **408**, 26–47 (2014).
60. Utescher, T. et al. The coexistence approach—theoretical background and practical considerations of using plant fossils for climate quantification. *Palaeogeogr. Palaeoclimatol. Palaeoecol.* **410**, 58–73 (2014).

61. Ballantyne, A. P. et al. Significantly warmer Arctic surface temperatures during the Pliocene indicated by multiple independent proxies. *Geology* **38**, 603–606 (2010).
62. Uhl, D., Mosbrugger, V., Bruch, A. & Utescher, T. Reconstructing palaeotemperatures using leaf floras—case studies for a comparison of leaf margin analysis and the coexistence approach. *Rev. Palaeobot. Palynol.* **126**, 49–64 (2003).
63. Pound, M. J. & Salzmann, U. Heterogeneity in global vegetation and terrestrial climate change during the late Eocene to early Oligocene transition. *Sci. Rep.* **7**, 43386 (2017).
64. Pross, J. et al. Persistent near-tropical warmth on the Antarctic continent during the early Eocene epoch. *Nature* **488**, 73–77 (2012).
65. Willard, D. A. et al. Arctic vegetation, temperature, and hydrology during Early Eocene transient global warming events. *Glob. Planet. Change* **178**, 139–152 (2019).
66. Kennedy, E. M. Late Cretaceous and Paleocene terrestrial climates of New Zealand: leaf fossil evidence from South Island assemblages. *N. Z. J. Geol. Geophys.* **46**, 295–306 (2003).
67. Kennedy, E. M. et al. Deriving temperature estimates from southern hemisphere leaves. *Palaeogeogr. Palaeoclimatol. Palaeoecol.* **412**, 80–90 (2014).
68. Grimm, G. W., Bouchal, J. M., Denk, T. & Potts, A. Fables and foibles: a critical analysis of the Palaeoflora database and the coexistence approach for palaeoclimate reconstruction. *Rev. Palaeobot. Palynol.* **233**, 216–235 (2016).
69. Hollis, C. J. et al. The DeepMIP contribution to PMIP4: methodologies for selection, compilation and analysis of latest Paleocene and early Eocene climate proxy data, incorporating version 0.1 of the DeepMIP database. *Geosci. Model Dev.* **12**, 3149–3206 (2019).
70. Köhl, N., Gebhardt, C., Litt, T. & Hense, A. Probability density functions as botanical-climatological transfer functions for climate reconstruction. *Quat. Res.* **58**, 381–392 (2002).
71. Greenwood, D. R., Keefe, R. L., Reichgelt, T. & Webb, J. A. Eocene paleobotanical altimetry of Victoria's Eastern Uplands. *Aust. J. Earth Sci.* **64**, 625–637 (2017).
72. What is GBIF? (GBIF, 2019); <https://www.gbif.org/what-is-gbif>
73. Fick, S. E. & Hijmans, R. J. WorldClim 2: new 1-km spatial resolution climate surfaces for global land areas. *Int. J. Climatol.* **37**, 4302–4315 (2017).
74. Hijmans, R. J., Phillips, S., Leathwick, J. & Elith, J. *dismo: Species Distribution Modeling R package version 1.1-4* (2017); <http://cran.r-project.org/web/packages/dismo/index.html>
75. Reichgelt, T., West, C. K. & Greenwood, D. R. The relation between global palm distribution and climate. *Sci. Rep.* **8**, 4721 (2018).
76. Bourbonniere, R. A. & Meyers, P. A. Sedimentary geolipid records of historical changes in the watersheds and productivities of Lakes Ontario and Erie. *Limnol. Oceanogr.* **41**, 352–359 (1996).
77. Rütters, H., Sass, H., Cypionka, H. & Rullkötter, J. Phospholipid analysis as a tool to study complex microbial communities in marine sediments. *J. Microbiol. Methods* **48**, 149–160 (2002).
78. Bauersachs, T., Talbot, H. M., Sidgwick, F., Sivonen, K. & Schwark, L. Lipid biomarker signatures as tracers for harmful cyanobacterial blooms in the Baltic Sea. *PLoS ONE* **12**, (2017).
79. Bauersachs, T. et al. Rapid analysis of long-chain glycolipids in heterocystous cyanobacteria using high-performance liquid chromatography coupled to electrospray ionization tandem mass spectrometry. *Rapid Commun. Mass Spectrom.* **23**, 1387–1394 (2009).
80. Bauersachs, T. et al. Distribution of long chain heterocyst glycolipids in cultures of the thermophilic cyanobacterium *Mastigocladus laminosus* and a hot spring microbial mat. *Org. Geochem.* **56**, 19–24 (2013).
81. Wörmer, L. et al. Cyanobacterial heterocyst glycolipids in cultures and environmental samples: diversity and biomarker potential. *Limnol. Oceanogr.* **57**, 1775–1788 (2012).
82. Schouten, S. et al. Endosymbiotic heterocystous cyanobacteria synthesize different heterocyst glycolipids than free-living heterocyst cyanobacteria. *Phytochemistry* **85**, 115–121 (2013).
83. Bale, N. J. et al. A novel heterocyst glycolipid detected in a pelagic  $\text{N}_2$ -fixing cyanobacterium of the genus *Calothrix*. *Org. Geochem.* **123**, 44–47 (2018).
84. Bauersachs, T. et al. Heterocyst glycolipids indicate polyphyly of stigonematalean cyanobacteria. *Phytochemistry* **166**, (2019).
85. Ehrmann, W. et al. Provenance changes between recent and glacial-time sediments in the Amundsen Sea Embayment, West Antarctica: clay mineral assemblage evidence. *Antarct. Sci.* **23**, 471–486 (2011).
86. Petschick, R., Kuhn, G. & Ginge, F. Clay mineral distribution in surface sediments of the South Atlantic: sources, transport, and relation to oceanography. *Mar. Geol.* **130**, 203–229 (1996).
87. Kirschvink, J. L. The least-squares line and plane and the analysis of paleomagnetic data. *Geophys. J. Int.* **62**, 699–718 (1980).
88. Roeckner, E. et al. (eds) *PART I: Model Description* Report No. 349 (Max-Planck-Institut für Meteorologie, 2003); [http://www.mpimet.mpg.de/fileadmin/models/echam/mpi\\_report\\_349.pdf](http://www.mpimet.mpg.de/fileadmin/models/echam/mpi_report_349.pdf)
89. Marsland, S. J., Haak, H., Jungclaus, J. H., Latif, M. & Roske, F. The Max-Planck-Institute global ocean/sea ice model with orthogonal curvilinear coordinates. *Ocean Model.* **5**, 91–127 (2003).
90. Hagemann, S. & Dumenil, L. A parametrization of the lateral waterflow for the global scale. *Clim. Dynam.* **14**, 17–31 (1997).
91. Hibler, W. D., III. A dynamic thermodynamic sea ice model. *J. Phys. Oceanogr.* **9**, 815–846 (1979).
92. Markwick, P. J. & Valdes, P. J. Palaeo-digital elevation models for use as boundary conditions in coupled ocean–atmosphere GCM experiments: a Maastrichtian (late Cretaceous) example. *Palaeogeogr. Palaeoclimatol. Palaeoecol.* **213**, 37–63 (2004).
93. Sewall, J. O. et al. Climate model boundary conditions for four Cretaceous time slices. *Clim. Past* **3**, 647–657 (2007).
94. Niezgodzki, I., Tyska, J., Knorr, G. & Lohmann, G. Was the Arctic Ocean ice free during the latest Cretaceous? The role of  $\text{CO}_2$  and gateway configurations. *Glob. Planet. Change* **177**, 201–212 (2019).

95. Wei, W. & Lohmann, G. Simulated Atlantic Multidecadal Oscillation during the Holocene. *J. Clim.* **25**, 6989–7002 (2012).
96. Zhang, X., Lohmann, G., Knorr, G. & Purcell, C. Abrupt glacial climate shifts controlled by ice sheet changes. *Nature* **512**, 290–294 (2014).
97. Stepanek, C. & Lohmann, G. Modelling mid-Pliocene climate with COSMOS. *Geosci. Model Dev.* **5**, 1221–1243 (2012).
98. Knorr, G. & Lohmann, G. Climate warming during Antarctic ice sheet expansion at the Middle Miocene transition. *Nat. Geosci.* **7**, 376–381 (2014).
99. Stein, R. et al. Evidence for ice-free summers in the late Miocene central Arctic Ocean. *Nat. Commun.* **7**, 11148 (2016).
100. Walliser, E. O., Lohmann, G., Niezgodzki, I., Tütken, T. & Schöne, B. R. Response of Central European SST to atmospheric  $p\text{CO}_2$  forcing during the Oligocene—a combined proxy data and numerical climate model approach. *Palaeogeogr. Palaeoclimatol. Palaeoecol.* **459**, 552–569 (2016).
101. Vahlenkamp, M. et al. Astronomically paced changes in deep-water circulation in the Western North Atlantic during the Middle Eocene. *Earth Planet. Sci. Lett.* **484**, 329–340 (2018).
102. Gierz, P., Lohmann, G. & Wei, W. Response of Atlantic Overturning to future warming in a coupled atmosphere–ocean–ice sheet model. *Geophys. Res. Lett.* **42**, 6811–6818 (2015).
103. Simões Pereira, P. et al. Geochemical fingerprints of glacially eroded bedrock from West Antarctica: detrital thermochronology, radiogenic isotope systematics and trace element geochemistry in Late Holocene glacial-marine sediments. *Earth Sci. Rev.* **182**, 204–232 (2018).
104. Stacey, J. S. & Kramers, J. D. Approximation of terrestrial lead isotope evolution by a two-stage model. *Earth Planet. Sci. Lett.* **26**, 207–221 (1975).
105. Chew, D. M., Sylvester, P. J. & Tubrett, M. N. U–Pb and Th–Pb dating of apatite by LA-ICPMS. *Chem. Geol.* **280**, 200–216 (2011).
106. O’Sullivan, G. J., Chew, D. M., Morton, A. C., Mark, C. & Henrichs, I. A. An integrated apatite geochronology and geochemistry tool for sedimentary provenance analysis. *Geochem. Geophys. Geosyst.* **19**, 1309–1326 (2018).
107. Flowerdew, M. J. et al. Distinguishing East and West Antarctic sediment sources using the Pb isotope composition of detrital K-feldspar. *Chem. Geol.* **292–293**, 88–102 (2012).
108. Petrus, J. A. & Kamber, B. S. VizualAge: a novel approach to laser ablation ICP-MS U–Pb geochronology data reduction. *Geostand. Geoanal. Res.* **36**, 247–270 (2012).
109. Chew, D. M., Petrus, J. A. & Kamber, B. S. U–Pb LA-ICPMS dating using accessory mineral standards with variable common Pb. *Chem. Geol.* **363**, 185–199 (2014).
110. Paton, C., Hellstrom, J., Paul, B., Woodhead, J. & Hergt, J. Iolite: freeware for the visualisation and processing of mass spectrometric data. *J. Anal. Atom. Spectrom.* **26**, 2508–2518 (2011).
111. Ludwig, K. R. *User’s Manual for Isoplot 3.75: A Geochronological Toolkit for Microsoft Excel* Special Publication No. 4 (Berkeley Geochronology Center, 2012).
112. Nasdala, L. et al. GZ7 and GZ8—two zircon reference materials for SIMS U–Pb geochronology. *Geostand. Geoanal. Res.* **42**, 431–457 (2018).
113. McDowell, F. W., McIntosh, W. C. & Farley, K. A. A precise  $^{40}\text{Ar}$ – $^{39}\text{Ar}$  reference age for the Durango apatite (U–Th)/He and fission-track dating standard. *Chem. Geol.* **214**, 249–263 (2005).
114. Schoene, B. & Bowring, S. A. U–Pb systematics of the McClure Mountain syenite: thermochronological constraints on the age of the  $^{40}\text{Ar}$ – $^{39}\text{Ar}$  standard MMhb. *Contrib. Mineral. Petrol.* **151**, 615 (2006).
115. Mark, C., Cogné, N. & Chew, D. Tracking exhumation and drainage divide migration of the western Alps: a test of the apatite U–Pb thermochronometer as a detrital provenance tool. *Geol. Soc. Am. Bull.* **128**, 1439–1460 (2016).
116. Mao, M., Rukhlov, A. S., Rowins, S. M., Spence, J. & Coogan, L. A. Apatite trace element compositions: a robust new tool for mineral exploration. *Econ. Geol.* **111**, 1187–1222 (2016).
117. Woodhead, J. D., Hellstrom, J., Hergt, J. M., Greig, A. & Maas, R. Isotopic and elemental imaging of geological materials by laser ablation inductively coupled plasma-mass spectrometry. *Geostand. Geoanal. Res.* **31**, 331–343 (2007).

**Acknowledgements** We thank the captain and crew of RV *Polarstern* Expedition PS104, as well as the MARUM-MeBo70 team for their support; S. Wiebe, R. Fröhlking-Teichert, V. Schumacher, N. Lensch, M. Arevalo, M. Seebeck and H. Grobe for their help on board and in the lab, respectively; the Klinikum Bremen-Mitte (A.-J. Lemke and C. Tiemann, Gesundheit Nord Bremen) for providing facilities for computed core tomographies and M. Köhler (MKfactory, Stahnsdorf, Germany) for preparing the thin sections; and J. McKay (University of Leeds, UK) for creating and painting the Late Cretaceous West Antarctic palaeoenvironment based on reconstructions presented here. The operation of MARUM-MeBo70 was funded by the Alfred Wegener Institute (AWI) through its Research Program PACES II Topic 3 and grant no. AWI\_PS104\_001, the MARUM Center for Marine Environmental Sciences, the British Antarctic Survey through its Polar Science for Planet Earth programme and the Natural Environmental Research Council-funded UK IODP programme. J.P.K., G.K., K.G., J.M. G.U.-N., O.E., C.G., T.R. and R.D. were funded by the AWI PACES II programme. J.P.K. and J.M. were also funded through the Helmholtz Association (PD-201 and VH-NG-1101). UK IODP funded the participation of T.v.d.F., P.S.P. and S.M.B. in expedition PS104. J.T. was funded through the Cluster of Excellence “The Ocean Floor – Earth’s Uncharted Interface” at the University of Bremen. Y.N. was funded by Lancaster University, UK.

**Author contributions** J.P.K. led the study and together with U.S., T. Bickert, C.-D.H., K.G. and G.K., conceived the idea for the study and wrote the manuscript. J.P.K., T. Bickert, C.-D.H., S.M.B., J.A.S., K.G., T. Freudenthal, T.v.d.F., P.S.P., W.E., O.E., H.P. and T.R. collected the cores. J.P.K., C.-D.H., T. Bickert and G.K. undertook the sedimentological and U.S. and S.M.B. the palynological analyses. T. Bickert and G.K. conducted the XRF scanning and processing of the cores. G.K. carried out the grain-size and bulk mineralogical analyses. J.T. led the CT scanning, processing and visualization. J.M. performed the biomarker analyses (apolar hydrocarbons) together with T. Bauersachs (HG palaeothermometry). T. Frederichs conducted the palaeomagnetic measurements. J.E.F., G.N., G.K. and J.P.K. investigated the thin sections. W.E. analysed the clay mineral assemblages and T.v.d.F. and P.S.P. measured bulk sediment Nd and Sr isotope compositions. K.G., R.D.L. and T. Frederichs helped determine the palaeolatitude of the drill site. G.L. and I.N. undertook the modelling with COSMOS. M.Z., C.S., C.M. and D.C. provided the U–Pb age constraints. U.S. and F.S. performed the bioclimatic analyses. J.P.K., T.B., C.-D.H., S.M.B., T. Frederichs, W.E., J.A.S., O.E., H.P., T.R. and R.D. helped with sampling and scanning the cores. K.G., G.U.-N. and R.D.L. undertook the seismic pre-site survey. All members of the Expedition PS104 Science Team helped with pre-site survey investigations, core recovery, onboard analyses and/or shore-based measurements. K.G., G.K., C.-D.H., G.U.-N., T. Bickert and R.D.L. acquired funding and proposed and planned RV *Polarstern* expedition PS104. All co-authors commented on the manuscript and provided input to its final version.

**Competing interests** The authors declare no competing interests.

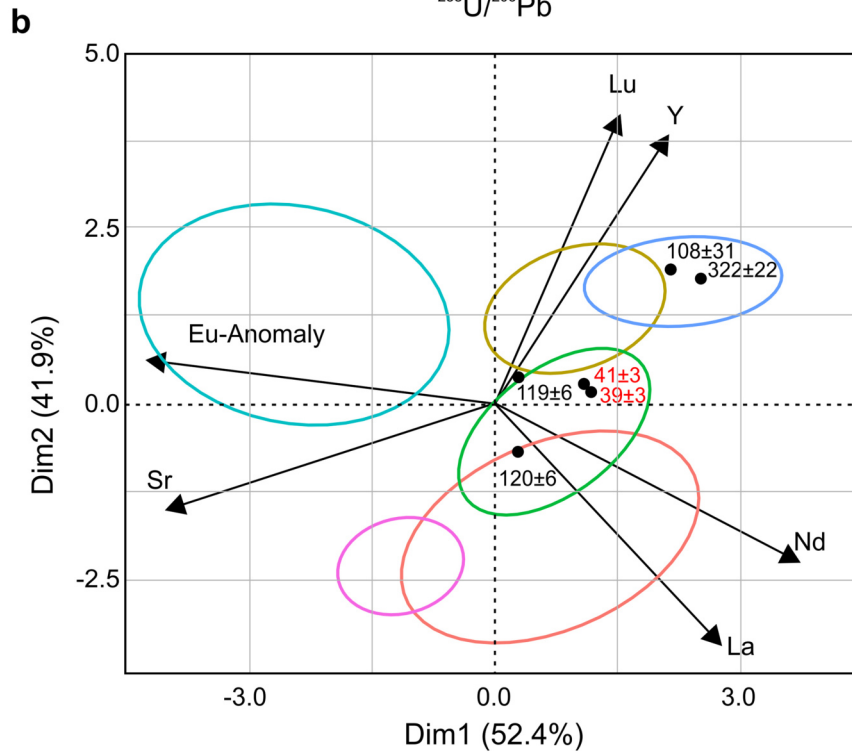
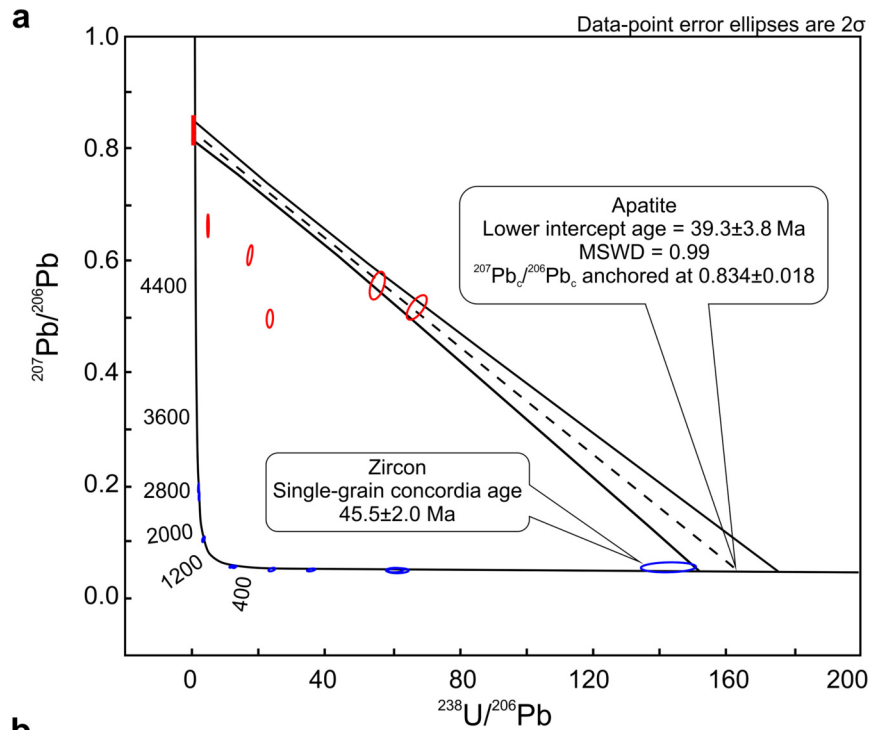
#### Additional information

**Supplementary information** is available for this paper at <https://doi.org/10.1038/s41586-020-2148-5>.

**Correspondence and requests for materials** should be addressed to J.P.K.

**Peer review information** *Nature* thanks Dietmar Muller, Anne-Marie Tosolini and the other, anonymous, reviewer(s) for their contribution to the peer review of this work.

**Reprints and permissions information** is available at <http://www.nature.com/reprints>.



## Reference Data

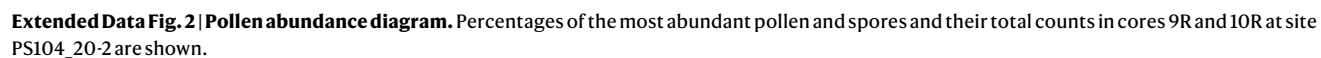
Low- to mid-grade metamorphic  
High-grade metamorphic  
Intermediate-mafic igneous

Alkaline igneous  
S-type igneous  
Ultra-mafic igneous

● Detrital apatite  
data with U-Pb  
age in Ma

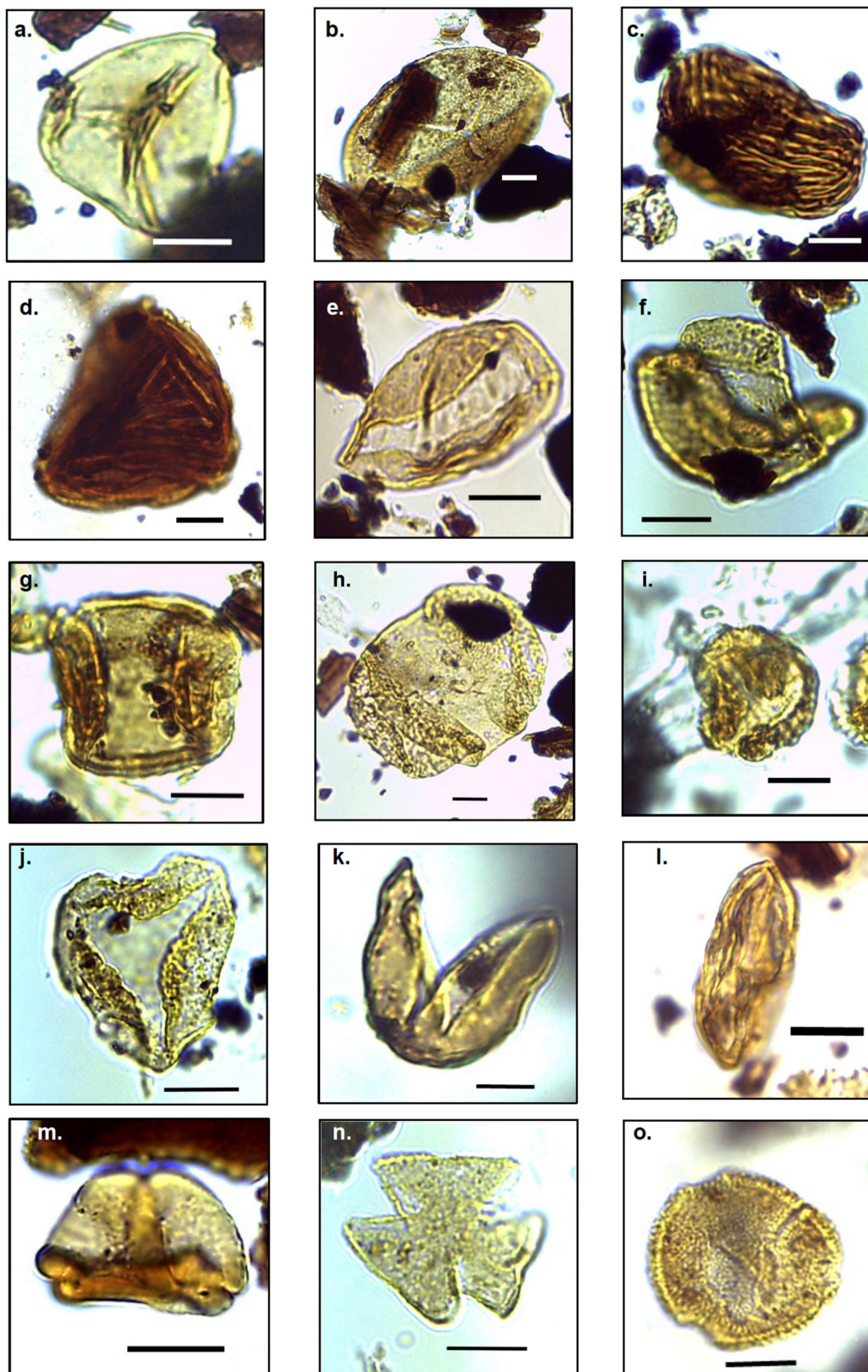
**Extended Data Fig. 1 | Tera-Wasserburg and PCA plots for U-Pb ages (in  $\pm$ Ma).** **a**, Tera-Wasserburg diagram showing apatite (red; 9.9 mbsf) and zircon (blue; 26.7 mbsf) U-Pb data. The red bar at the upper array intercept for Eocene apatite is the range of crystalline basement  $^{207}\text{Pb}/^{206}\text{Pb}_c$  values reported by (ref. <sup>104</sup>) for West Antarctica, which anchor the apatite age

calculation. **b**, PCA plot showing trace-element data and single-grain ages (in Myr) for AWI-35 (9.9 mbsf) apatite, and lithological fields derived from a bedrock apatite reference library<sup>104</sup>. Eocene grains (labelled in red) are chemically and chronologically distinct from other detrital apatite in the same sample. Data point error ellipses are  $2\sigma$ .



PS104\_20-2 are shown.

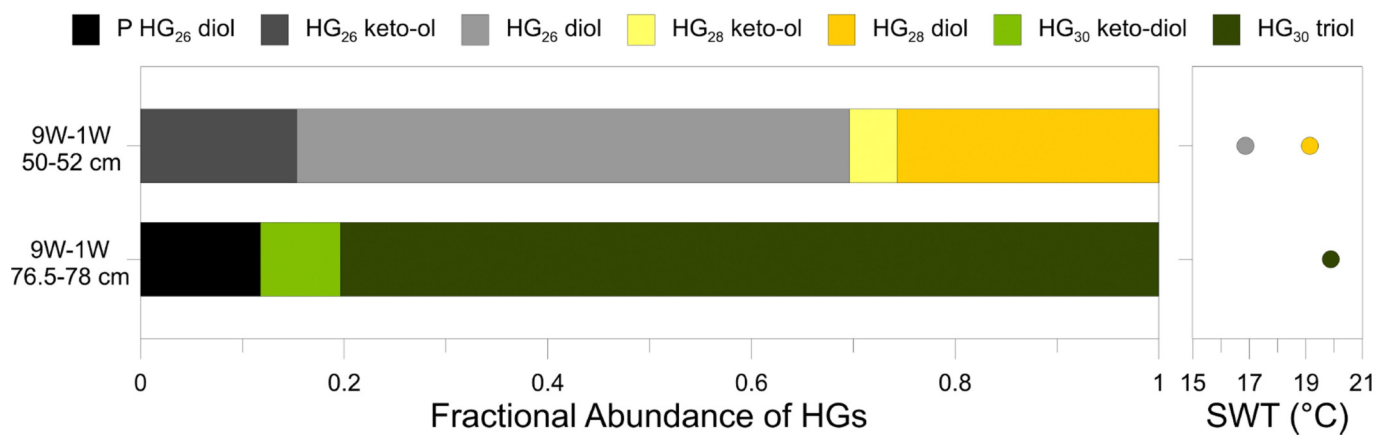
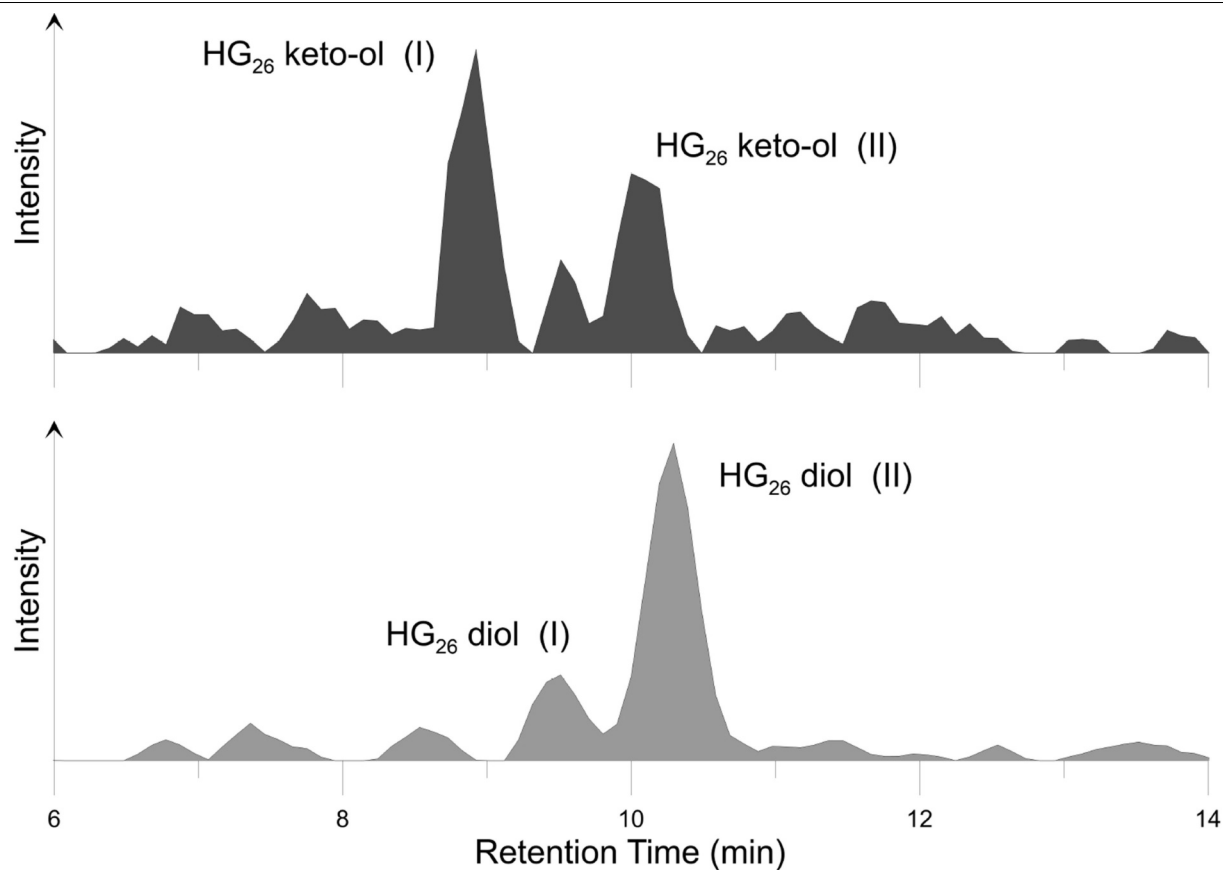




**Extended Data Fig. 3 | Photomicrographs of selected pollen and spores.**

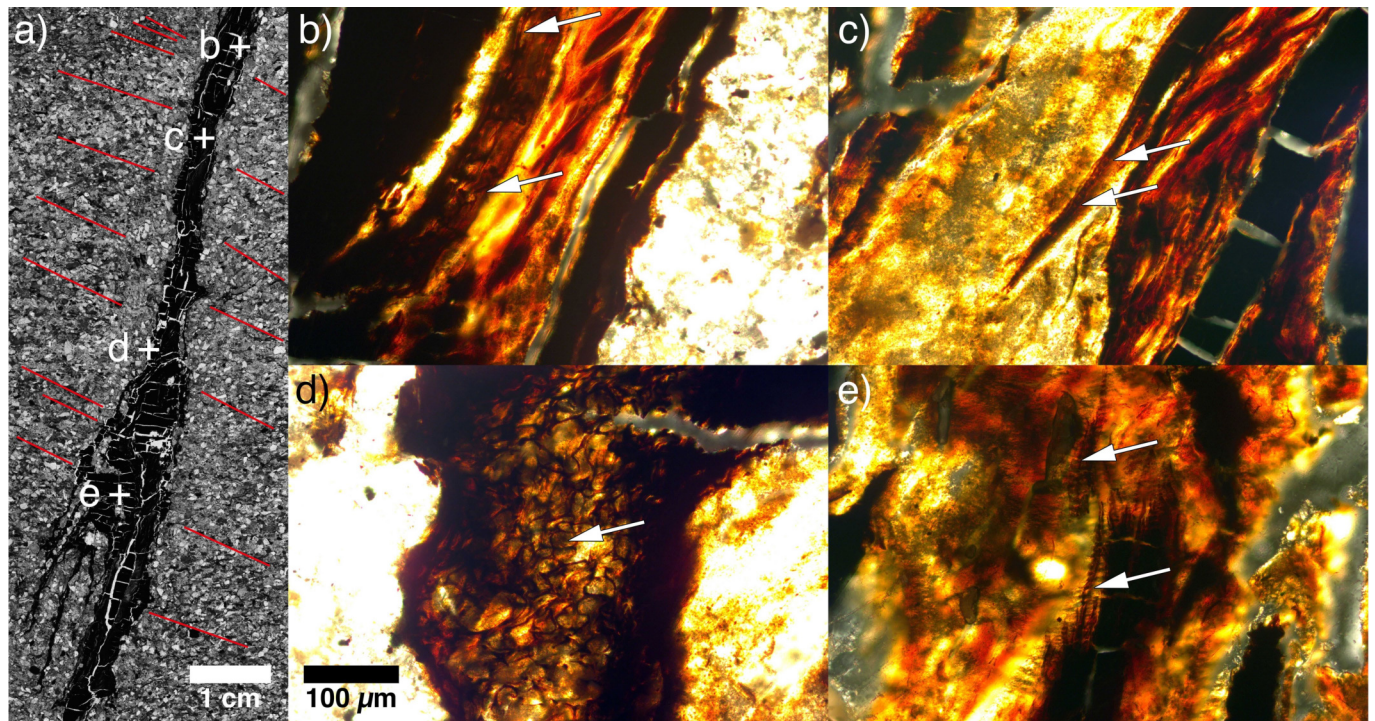
**a**, *Cyathidites australis*. **b**, *Osmundacidites wellmanii*. **c**, *Ruffordiaspora australiensis*. **d**, *Ruffordiaspora ludbrookiae*. **e**, *Cycadopites follicularis*. **f**, *Microcachrydites antarcticus*. **g**, *Phyllocladidites mawsonii*. **h**, *Podocarpidites*

*major*. **i**, *Trichotomosulcites hemisphaerius*. **j**, *Trichotomosulcites subgranulatus*. **k**, *Taxodiaceapollenites hiatus*. **l**, *Equisetosporites* sp. **m**, *Nyssapollenites chathamicus*. **n**, *Peninsulapollis gillii*. **o**, *Proteacidites subpalisadus*. Scale bars, 10  $\mu$ m.



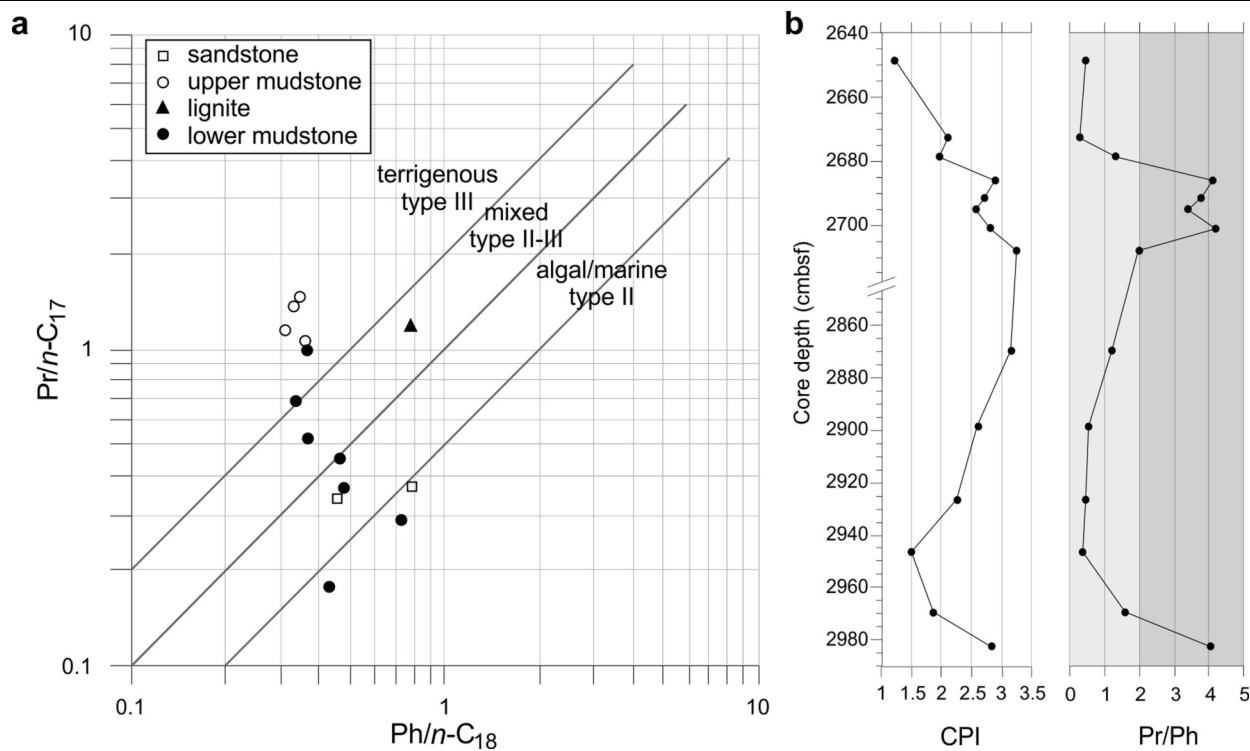
**Extended Data Fig. 4 | HG palaeothermometry.** Presence of HGs at 27.03–27.04 mbsf at site PS104\_20-2 (core 9R) and river or lake surface water temperature (SWT) estimates from the HG-based molecular palaeothermometer (HTI<sub>30</sub>).





**Extended Data Fig. 5 | Example microscopic images from thin sections.** The sections are taken from a fossil root fragment between 29.34 and 29.43 mbsf in core 10R at site PS104\_20-2. **a**, Overview scan of root fragment with indicated

locations of detailed microscopic images **b–e**. White arrows indicate the locations of preserved parenchyma storage cells, including potential aerenchyma gas exchange cells (**d**). The scale bar in **d** applies to **b–e**.



**Extended Data Fig. 6 | Biomarker presence. a,** Pristane/ $n-C_{17}$  versus phytane/ $n-C_{18}$  to infer organic matter type during sediment deposition (after refs. <sup>37,38</sup>). **b,** CPI (left) and pristane/phytane (Pr/Ph; right) ratios. The CPI points

to a low maturity and land plant origin of the organic matter (CPI > 1) deposited in an aquatic environment (Pr/Ph < 2) and a peat swamp environment (Pr/Ph > 2), respectively.



# Article

**Extended Data Table 1 | Percentages of the most abundant pollen and spore taxa**

Depth (cmbfsf)	2680	2685	2698	2702	2971	2977	2984
Core	020--2	020--2	020--2	020--2	020--2	020--2	020--2
Section	9R-1W	9R-1W	9R-1W	9R-1W	10R-1W	10R-1W	10R-1W
Core depth (cm)	55	60	73	77	111	117	172
<b>Gymnosperms</b>	31.4	69.1	49.6	63.1	49.1	54.4	63.2
<b>Angiosperms</b>	8.7	4.3	7.4	4.3	20.6	22.5	10.3
<b>Pteridophytes</b>	23.8	21.7	37.9	23	27.9	20.2	23.7
<b>Bryophytes</b>	36.1	4.9	5.1	9.7	2.4	2.9	2.8
<i>Araucariacites/Dilwynites</i>	1.1	4.9	4.2	2.8	7.3	8.2	4.7
<i>Cycadopites follicularis</i>	0.3	2.9	1.7	2.6	6.4	11.4	6.4
<i>Microcachrydites antarcticus</i>	0.8	2.3	1.1	0.9	0	0.6	4.2
<i>Phyllocladidites mawsonii</i>	1.1	0	0.6	0.9	0.6	0	0.6
<i>Podocarpidites spp.</i>	13.7	34.1	28.1	19.3	20.3	17.8	36.5
<i>Taxodiaceapollenites hiatus</i>	0.8	0.6	2.2	0.6	1.2	1.8	0
<i>Trichitomosulcites spp.</i>	13.4	21.5	9.8	35.2	12.8	14.6	10.9
<i>Nyssapollenites chathamicus</i>	1.7	1.1	0.3	0	11	12	3.3
<i>Peninsulapollis spp.</i>	4.5	1.1	2.5	0.6	2	1.8	1.9
<i>Proteacidites spp.</i>	2.5	0.9	1.4	1.1	5.2	5	2.8
<i>Baculatisporites comaumensis</i>	1.1	0	2	4	2	2.9	3.9
<i>Ceratosporites equalis</i>	0	0.3	2	2	3.2	2.9	0.3
<i>Cyathidites spp.</i>	8.4	8.3	9.8	9.9	8.7	8.8	7
<i>Gleicheniidites senonicus</i>	0.8	0.3	1.7	0.6	0.9	0	0
<i>Laevigatosporites ovatus</i>	10.6	7.4	12.9	2.8	4.4	2.6	7.2
<i>Lycopodiumsporites spp.</i>	0	0.9	1.7	0.3	1.2	0.3	1.4
<i>Osmundacidites wellmanii</i>	0.3	0.6	0.8	2.3	2.6	2	2.5
<i>Stereisporites antiquasporites</i>	36.1	4.9	4.5	9.4	0.6	2.9	2.2
<b>Total Pollen Sum</b>	357	349	356	352	344	342	359
Pollen concentration (grains/g)	69320	55144	61895	121476	4250	6900	7869

**Extended Data Table 2 | Key pollen taxa and the NLRs used to derive quantitative climate estimates**

Selected Pollen Taxa	Botanical Affinity (after Raine et al. 2011)	Selected NLRs for Bioclimatic Analysis
<b>Gymnosperms</b>		
<i>Araucariacites/Dilwynites</i>	Araucariaceae ( <i>Araucaria</i> , <i>Agathis</i> )	<i>Araucaria</i>
<i>Cycadopites follicularis</i>	Gymnospermopsida	<i>Cycadales</i>
<i>Equisetosporites</i>	Ephedraceae ( <i>Ephedra</i> , cf. <i>E. chinleana</i> )	<i>Ephedra</i>
<i>Microcachrydites antarcticus</i>	Podocarpaceae ( <i>Microstrobos</i> , <i>Microcachrys tetragona</i> )	<i>Podocarpus</i>
<i>Phyllocladites mawsonii</i>	Podocarpaceae (aff. <i>Lagarostrobos franklinii</i> )	<i>Lagarostrobos</i>
<i>Podocarpidites ellipticus</i> ; <i>P. major</i>	Podocarpaceae ( <i>Podocarpus</i> ?)	<i>Podocarpus</i>
<i>Podocarpidites otagoensis</i>	Podocarpaceae ( <i>Podocarpus</i> ?, or <i>Lagarostrobos</i> )	<i>Podocarpus</i>
<i>Taxodiaceapollenites hiatus</i>	Cupressaceae, Taxodiaceae	Cupressaceae
<i>Trichotomosulcites subgranulatus</i>	Podocarpaceae. Extinct <i>Microcachrys</i>	Podocarpaceae
<b>Angiosperms</b>		
<i>Liliacidites cf. variegatus</i>	Liliaceae; Monimiaceae (cf. <i>Laurelia novaezealandiae</i> )	Liliaceae
<i>Peninsulapollis gillii</i> ; <i>P. truswellia</i>	Proteaceae	Proteaceae
<i>Proteacidites parvus</i>	Proteaceae ( <i>Bellendena montana</i> type)	Proteaceae
<i>Proteacidites minimus</i>	Proteaceae ( <i>Knightia excelsa</i> )	Proteaceae
<b>Pteridophytes</b>		
<i>Baculatisporites comaumensis</i>	Osmundaceae ( <i>Osmunda</i> , <i>Leptopteris</i> ); Hymenophyllaceae ( <i>Hymenophyllum flexuosum</i> , <i>H. cruentum</i> )	Hymenophyllaceae
<i>Ceratospores equalis</i>	Lycopodiaceae, Selaginellaceae ( <i>Selaginella</i> , e.g. <i>S. tenuispinulosa</i> )	Selaginellaceae
<i>Cibotiidites tuberculiformis</i>	Dicksoniaceae (cf. <i>Dicksonia squarrosa</i> , <i>D. dissecta</i> ); Schizaeaceae	Dicksoniaceae
<i>Cyathidites australis</i> ; <i>C. minor</i>	Cyatheaaceae ( <i>Cyathea</i> ), Dicksoniaceae, Schizaeaceae ( <i>Lygodium</i> )	Cyatheaaceae
<i>Gleicheniidites senonicus</i>	Gleicheniaceae ( <i>Gleichenia circinata</i> group, <i>Dicranopteris</i> )	Gleicheniaceae
<i>Laevigatosporites ovatus</i>	Aspleniaceae, Blechnaceae, Polypodiaceae, Schizaeaceae	Polypodiaceae
<i>Lycopodiumsporites sp.</i>	Lycopodiaceae ( <i>Lycopodium</i> )	Lycopodiaceae
<i>Osmundacidites wellmanii</i>	Osmundaceae ( <i>Todea barbara</i> )	Osmundaceae
<i>Perotrilites majus</i>	Selaginellaceae?	Selaginellaceae
<i>Polypodiisporites cf. minimus</i>	Davalliaceae ( <i>Nephrolepis</i> )	Davalliaceae
<i>Ruffordiaspora australiensis</i>	Schizaeaceae	Schizaeaceae
<b>Bryophytes</b>		
<i>Stereisporites antiquasporites</i>	Bryophyta; <i>Sphagnum</i>	<i>Sphagnum</i>

Extended Data Table 3 | Full list of identified pollen and spore taxa

<b>Bryophytes</b> * <i>Aequitriradites spinulosus</i> (Cookson & Dettmann) * <i>Annulispora folliculosa</i> (Rogalska) * <i>Coptospora striata</i> (Dettmann) * <i>Foraminisporis cf. F. wonthaggiensis</i> (Cookson & Dettmann) * <i>Stereisporites antiquasporites</i> (Dettmann)	<b>Pteridophytes</b> * <i>Baculatisporites comaumensis</i> (Cookson) * <i>Biretisporites</i> sp. * <i>Ceratosporites equalis</i> (Cookson & Dettmann) * <i>Cibotidites tuberculiformis</i> (Cookson) * <i>Crybelosporites striatus</i> (Cookson & Dettmann) * <i>Cyathidites cf. C. asper</i> (Bolkhovitina) * <i>Cyathidites minor</i> (Couper) * <i>Cyathidites cf. C. punctatus</i> (Delcourt & Sprumont) * <i>Cyathidites</i> undiff. * <i>Gleicheniidites senonicus</i> (Ross) <i>Herkosporites</i> sp. * <i>Laevigatosporites ovatus</i> (Wilson & Webster) <i>Lycopodiacidites cf. L. dettmannae</i> (Burger) * <i>Lycopodiumsporites</i> sp. * <i>Osmundacidites wellmanii</i> (Couper) <i>Polypodiisporites</i> sp. * <i>Perotriletes cf. P. majus</i> (Cookson & Dettmann) * <i>Reticulatisporites cf. R. pudens</i> (Balme) * <i>Retriletes austroclavatidites</i> (Cookson) <i>Retriletes cf. R. rosewoodensi</i> (de Jersey) <i>Retriletes</i> undiff. * <i>Ruffordiaspora australiensis</i> (Cookson) * <i>Ruffordiaspora ludbrookiae</i> (Dettmann)	<b>Gymnosperms</b> * <i>Araucariacites/Dilwynites</i> * <i>Callialasporites dampieri</i> (Balme) * <i>Classopollis cf. chateaunovi</i> (Reyre) * <i>Cycadopites follicularis</i> (Wilson & Webster) * <i>Dacrydiumites praecupressinoides</i> (Couper) * <i>Equisetosporites</i> sp. * <i>Microcachryidites antarcticus</i> (Cookson) * <i>Phyllocladidites mawsonii</i> (Cookson) * <i>Podocarpidites cf. P. ellipticus</i> (Cookson) * <i>Podocarpidites cf. P. major</i> (Couper) * <i>Podocarpidites cf. P. otagoensis</i> (Couper) * <i>Podocarpidites</i> undiff. * <i>Podosporites</i> sp. * <i>Taxodiaceapollenites hiatus</i> (Potonie) * <i>Trichotomosulcites hemisphaerius</i> (Mays) * <i>Trichotomosulcites subgranulatus</i> (Couper) * <i>Triletes</i> undiff.	<b>Angiosperms</b> * <i>Beaupreaidites verrucosus</i> (Cookson) * <i>Cupuliferoidaepollenites cf. C. parvulus</i> (Groot & Penny) * <i>Liliacidites cf. L. intermedius</i> (Couper) * <i>Monosulcites</i> undiff. * <i>Nyssapollenites chathamicus</i> (Mildenhall) <i>Peninsulapollis gillii</i> (Cookson) <i>Peninsulapollis truswellia</i> (Dettmann & Jarzen) *? <i>Phimopollenites augathallaensis</i> *? <i>Polycopropollenites esobalteus</i> <i>Proteacidites parvus</i> (Cookson) <i>Proteacidites cf. P. subpalisadus</i> (Couper) <i>Proteacidites cf. P. subscabratus</i> (Couper) <i>Proteacidites minimus</i> (Couper) <i>Proteacidites</i> sp. * <i>Rousea georgensis</i> (Brenner) * <i>Tetracolpites</i> sp. * <i>Tricolpites cf. T. pachyexinus</i> (Couper) * <i>Tricolpites minutus</i> (Brenner) * <i>Tricolpites</i> sp. <i>Trilorites</i> sp.
--	---	---	--

All taxa identified during the current study are included. Question marks show uncertain taxon identifications that require further study. \*Taxa described from the Tupuangi Formation on the Chatham Islands<sup>28,58</sup>.

# Tracking of marine predators to protect Southern Ocean ecosystems

<https://doi.org/10.1038/s41586-020-2126-y>

Received: 21 December 2018

Accepted: 20 February 2020

Published online: 18 March 2020

 Check for updates

Mark A. Hindell<sup>1,2,45</sup>✉, Ryan R. Reisinger<sup>3,4,5,45</sup>, Yan Ropert-Coudert<sup>3,45</sup>, Luis A. Hückstädt<sup>6</sup>, Philip N. Trathan<sup>7</sup>, Horst Bornemann<sup>8</sup>, Jean-Benoît Charrassin<sup>5</sup>, Steven L. Chown<sup>9</sup>, Daniel P. Costa<sup>6</sup>, Bruno Danis<sup>10</sup>, Mary-Anne Lea<sup>1,2</sup>, David Thompson<sup>11</sup>, Leigh G. Torres<sup>12</sup>, Anton P. Van de Putte<sup>13,14</sup>, Rachael Alderman<sup>15</sup>, Virginia Andrews-Goff<sup>1,16</sup>, Ben Arthur<sup>1</sup>, Grant Ballard<sup>17</sup>, John Bengtson<sup>18</sup>, Marthán N. Bester<sup>19</sup>, Arnoldus Schytte Blix<sup>20</sup>, Lars Boehme<sup>21</sup>, Charles-André Bost<sup>3</sup>, Peter Boveng<sup>18</sup>, Jaimie Cleeland<sup>1</sup>, Rochelle Constantine<sup>22</sup>, Stuart Corney<sup>1</sup>, Robert J. M. Crawford<sup>23</sup>, Luciano Dalla Rosa<sup>24</sup>, P. J. Nico de Bruyn<sup>19</sup>, Karine Delord<sup>3</sup>, Sébastien Descamps<sup>25</sup>, Mike Double<sup>16</sup>, Louise Emmerson<sup>16</sup>, Mike Fedak<sup>21</sup>, Ari Friedlaender<sup>6,26</sup>, Nick Gales<sup>16</sup>, Michael E. Goebel<sup>26</sup>, Kimberly T. Goetz<sup>11</sup>, Christophe Guinet<sup>3</sup>, Simon D. Goldsworthy<sup>27</sup>, Rob Harcourt<sup>28</sup>, Jefferson T. Hinke<sup>29</sup>, Kerstin Jerosch<sup>8</sup>, Akiko Kato<sup>3</sup>, Knowles R. Kerry<sup>16</sup>, Roger Kirkwood<sup>16</sup>, Gerald L. Kooyman<sup>30</sup>, Kit M. Kovacs<sup>25</sup>, Kieran Lawton<sup>16</sup>, Andrew D. Lowther<sup>25</sup>, Christian Lydersen<sup>25</sup>, Phil O'B. Lyver<sup>31</sup>, Azwianewi B. Makhado<sup>23</sup>, Maria E. I. Márquez<sup>32</sup>, Birgitte I. McDonald<sup>33</sup>, Clive R. McMahon<sup>1,28,34</sup>, Monica Muelbert<sup>1,24</sup>, Dominik Nachtsheim<sup>8,35</sup>, Keith W. Nicholls<sup>7</sup>, Erling S. Nordøy<sup>20</sup>, Silvia Olmastroni<sup>36,37</sup>, Richard A. Phillips<sup>7</sup>, Pierre Pistorius<sup>38</sup>, Joachim Plötz<sup>8,46</sup>, Klemens Pütz<sup>39</sup>, Norman Ratcliffe<sup>7</sup>, Peter G. Ryan<sup>40</sup>, Mercedes Santos<sup>32</sup>, Colin Southwell<sup>16</sup>, Iain Staniland<sup>7</sup>, Akinori Takahashi<sup>41</sup>, Arnaud Tarroux<sup>25,42</sup>, Wayne Trivelpiece<sup>29</sup>, Ewan Wakefield<sup>43</sup>, Henri Weimerskirch<sup>3</sup>, Barbara Wienecke<sup>16</sup>, José C. Xavier<sup>7,44</sup>, Simon Wotherspoon<sup>1,16,47</sup>, Ian D. Jonsen<sup>28,47</sup> & Ben Raymond<sup>1,2,16,47</sup>

Southern Ocean ecosystems are under pressure from resource exploitation and climate change<sup>1,2</sup>. Mitigation requires the identification and protection of Areas of Ecological Significance (AESs), which have so far not been determined at the ocean-basin scale. Here, using assemblage-level tracking of marine predators, we identify AESs for this globally important region and assess current threats and protection levels. Integration of more than 4,000 tracks from 17 bird and mammal species reveals AESs around sub-Antarctic islands in the Atlantic and Indian Oceans and over the Antarctic continental shelf. Fishing pressure is disproportionately concentrated inside AESs, and climate change over the next century is predicted to impose pressure on these areas, particularly around the Antarctic continent. At present, 7.1% of the ocean south of 40°S is under formal protection, including 29% of the total AESs. The establishment and regular revision of networks of protection that encompass AESs are needed to provide long-term mitigation of growing pressures on Southern Ocean ecosystems.

The Southern Ocean—defined here as the circumpolar waters south of 40°S—is home to a unique fauna and has an important role in biogeochemical cycles and the global climate system<sup>1</sup>. Past industrial sealing, whaling and demersal fishing caused marked perturbations from which some Southern Ocean ecosystems are only now starting to recover<sup>3</sup>. The harvesting of squid and toothfish continues<sup>4,5</sup> and interest is growing in the expansion of Antarctic krill (*Euphausia superba*) fisheries<sup>6</sup>. These target species are crucial prey for upper trophic organisms—krill is a key component of the Southern Ocean food web—and their potential depletion raises substantial concerns about the effects on Southern Ocean ecosystems<sup>2</sup>. Anthropogenic greenhouse gas emissions are simultaneously causing large changes to the Southern Ocean<sup>7</sup>. Strong interest has therefore developed in the long-term conservation of the Southern Ocean, but authorities face the considerable challenge of implementing conservation goals within existing management frameworks<sup>2</sup>.

A first step in meeting this challenge is to identify regions that should be considered for protection, for reasons such as their high biodiversity, biological productivity or particular importance for certain life-history stages of species<sup>8,9</sup>. The distribution and demography of marine predators provides a viable basis for this<sup>10</sup>—particularly in the vast and remote Southern Ocean, where integrated ecosystem measures are difficult to obtain at management-relevant, ocean-basin scales<sup>11</sup>. Indeed, on-shore measures of Southern Ocean marine predators have been used as regional indicators of ecosystem status for several decades<sup>12</sup>. Spatial aggregations of predators at sea identify not only areas that are important to the predator species themselves—which depend on lower trophic levels<sup>13</sup>—but also areas of broader ecosystem importance, such as regions of elevated productivity and biomass at lower trophic levels<sup>14</sup>. Combining information across predator species with diverse diets and life histories is essential for an ecosystem-wide approach that is less susceptible to



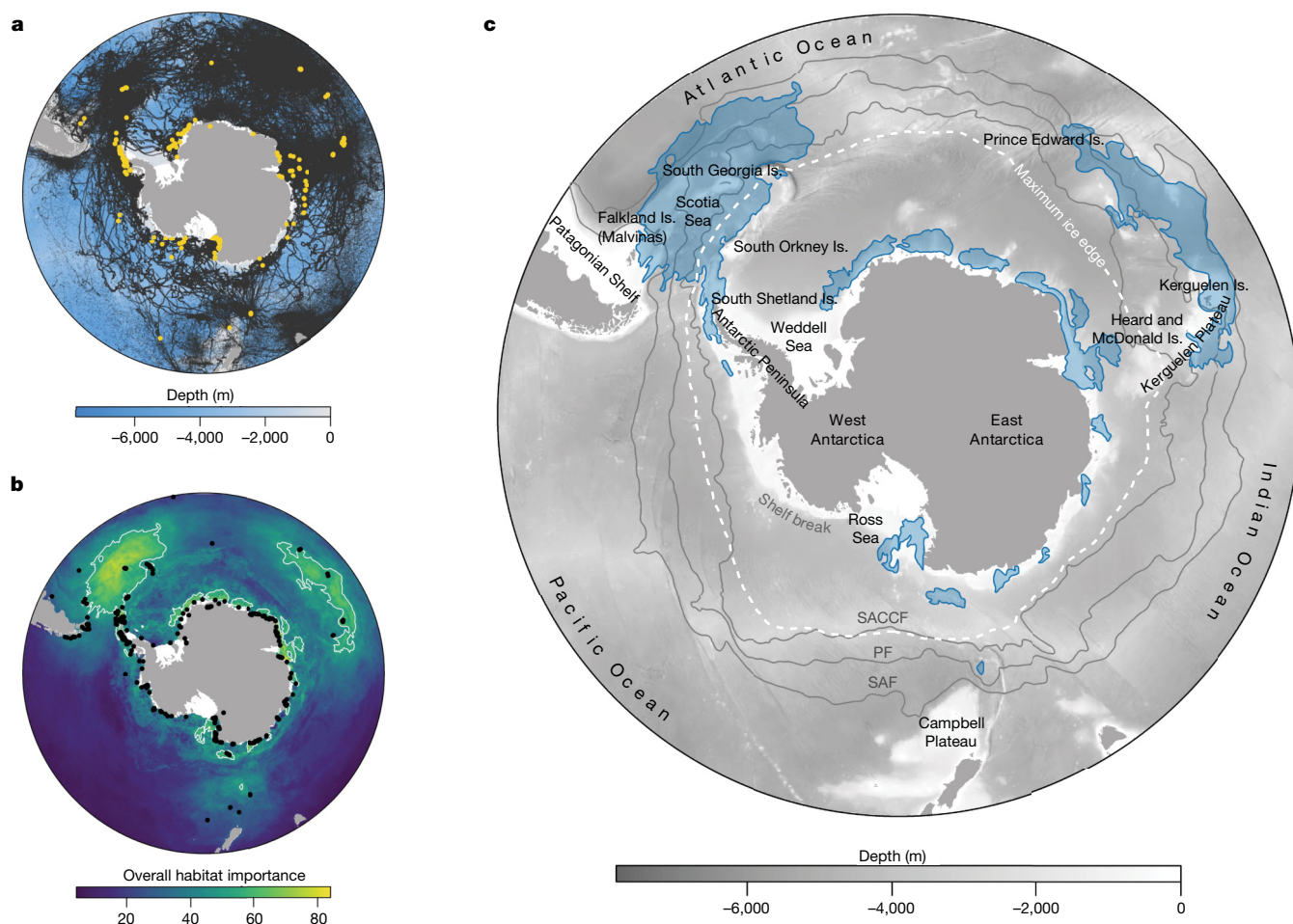


**Fig. 1 | AEs in the Southern Ocean.** **a**, Tracking data from 17 predator species were used to model the habitat importance for each species. Black points indicate tracking data and yellow points indicate tagging locations<sup>16</sup>. **b**, Combining these model outputs gives the overall habitat importance, and the upper decile of overall habitat importance delimits AEs (white contours). Black

points indicate colony locations for the 14 colony-breeding species.

**c**, AEs (blue) shown in context. Major oceanographic fronts are shown with grey lines: SAF, Sub-Antarctic Front; PF, Polar Front; SACC, Southern Antarctic Circumpolar Current Front.

factors that affect individual species<sup>12</sup>. There is a growing recognition of the value of tracking data for making decisions about conservation<sup>15</sup>.

### Using predator tracking data to identify AEs

In the Southern Ocean, many predator species with differing diets and movement patterns have been tracked<sup>16</sup>. We synthesized tracking data from 4,060 individuals of 17 species (Fig. 1a) to provide a circumpolar assessment of regions of ecological importance in the Southern Ocean. We identified regions that were preferred by multiple predator species as indicators of high levels of lower trophic biomass and biodiversity, and refer to these regions as AEs<sup>17</sup>. Our definition of AEs is not the same as Ecologically and Biologically Significant Marine Areas or Key Biodiversity Areas. However, it is consistent with several of the criteria that are used for defining Ecologically and Biologically Significant Marine Areas or Key Biodiversity Areas—particularly biological productivity and diversity<sup>8</sup>—and so provides a similar qualitative, integrated assessment of biodiversity patterns.

We assembled tracking data from 12 species of seabird and 5 species of marine mammal. The data were collected between 1991 and 2016<sup>16</sup>. We used habitat-selection models (Methods, Supplementary Information, Extended Data Figs. 1–3) of individual predator species and then combined their spatial predictions to identify regions that were important

to our full suite of species (Fig. 1b). This enabled us to account for incomplete tracking coverage (that is, colonies from which no animals were tracked) and predict habitat importance for each species across the entire Southern Ocean. Combined, these predictions provided an integrated and spatially explicit assessment of areas of high biodiversity and biomass at multiple trophic levels. Sea surface temperature (SST) and wind strength were most often the best predictors of habitat selectivity in these species-specific models (Extended Data Fig. 4). SST has been linked to global patterns of marine biodiversity<sup>18</sup>, and in the Southern Ocean it acts as an indicator of water masses with different ecological properties<sup>19</sup>. Wind exerts several influences—including driving ocean currents and mixing; transporting iron; affecting the dynamics of sea ice; and ultimately determining primary production<sup>20</sup>—and has been linked, for example, to the global distribution of albatrosses and petrels<sup>21</sup>. The importance of other predictor variables differed among species (Extended Data Fig. 4). The relationship between habitat selectivity and environmental predictors differed across species, showing how species used their environments in different ways (Extended Data Fig. 5).

### Distribution of AEs

Regions with the highest scores for overall habitat importance were identified as AEs (calculated as the upper decile of those scores).

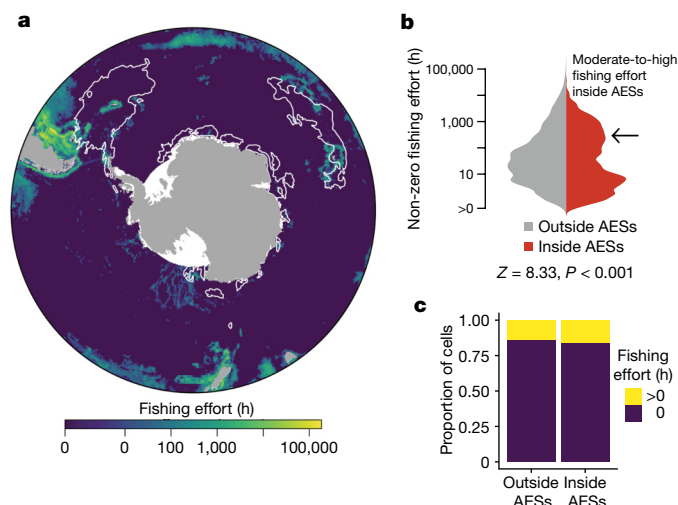


**Fig. 2 | Fishing effort in the Southern Ocean.** **a**, Map showing fishing effort (total fishing hours between 2012 and 2016<sup>29</sup>). Contour lines (white) indicate AESs. **b**, Kernel density plot showing the distribution of values of fishing effort (zero values not shown) inside (red) and outside (grey) AESs. Two-tailed permutation tests ( $n = 1,098,226$  grid cells) indicate a significant difference ( $P < 0.001$ ). **c**, Proportion of cells inside and outside AESs that had some (more than 0 h; yellow) or no (0 h; purple) fishing effort.

These were located over the Antarctic continental shelf (89% of AES pixels south of 60°S were over or within 200 km of the shelf) and in two northerly aggregations: one encompassing much of the Scotia Sea and surrounding waters, and the second covering the chain of sub-Antarctic islands from the Prince Edward Islands through to parts of the Kerguelen Plateau (Fig. 1c). Regions of lower importance were identified in the southern Pacific and Indian Oceans. The distribution of AESs is associated with the availability of suitable habitats for breeding and resting, as well as regional oceanography and sea-ice dynamics that affect biological production (Fig. 1c). The AESs were based on a combination of island-breeding and wholly pelagic species, and therefore reflect broad-scale patterns of importance. These patterns are supported by: (i) broad-scale patterns of primary production (Southern Ocean land masses provide iron fertilization that stimulates downstream production in this otherwise iron-limited ecosystem<sup>22</sup>); (ii) historical whaling catches north of 60°S, which show that relatively few whales were taken in the southern Indian or Pacific Oceans, and that the region identified as an AES in the south Atlantic corresponds with high whaling catches<sup>23</sup>; and (iii) previous estimates of Antarctic krill distribution, which suggest that concentrations are high in the south Atlantic and lower in the south Pacific and southern Indian Ocean<sup>24</sup>. The AES in the south Atlantic corresponds to the area of increased krill biomass, whereas the AES in the Indian Ocean partially corresponds to a region dominated by myctophid fish and other euphausiids<sup>25</sup>.

### Exposure of AESs to potential stressors

The Southern Ocean is subject to several stressors that influence its ecosystems, including an expansion of resource extraction and rapid climate change<sup>26</sup>. We note that both temperature and wind—which were key parameters in many of our species-specific habitat models—are changing, and are projected to continue to do so<sup>27</sup>.

Fishing has both direct effects on Southern Ocean biota through incidental bycatch and indirect effects through resource competition<sup>28</sup>. Many demersal finfish were exploited during the latter part of the 20th century, which led to the decimation of some stocks in the Antarctic and sub-Antarctic<sup>5</sup>. Finfish fishing in the Antarctic is now regulated, and is focused on toothfish species caught with longlines. Fisheries for Antarctic krill

began in the 1960s and are now concentrated in the south Atlantic sector, most notably at the Antarctic Peninsula and South Shetland Islands, the South Orkney Islands and South Georgia<sup>6</sup>. Krill is managed with a low, precautionary catch limit that takes account of the key role of krill in the Antarctic food web. By global standards, fishing pressure in the Southern Ocean is low<sup>29</sup>, but indications are that pressure on its marine resources will grow<sup>2,5,6</sup>. Fishing effort (Fig. 2a) was significantly different inside and outside of AESs (Fig. 2b), with a disproportionate amount of moderate-to-high effort (100 or more total hours of fishing) occurring inside AESs. Of cells with a moderate-to-high fishing effort, 37.9% were inside AESs, despite AESs only representing 10% of the study area. Areas of conspicuous fishing effort around southern South America, New Zealand and Australia should be treated with caution, as our study does not include temperate predator species that are likely to figure prominently in these ecosystems (Fig. 2a). Nonetheless, relatively high-intensity areas of fishing that are directly relevant to the Southern Ocean occurred around the Falkland Islands (Islas Malvinas), where squid and some finfish are targeted; around South Georgia (ice fish, krill and toothfish); at the West Antarctic Peninsula (krill); and over the Kerguelen (toothfish and ice fish) and Campbell (squid and finfish) plateaux<sup>4–6</sup>. Relatively important fisheries for toothfish also occur within the Ross Sea<sup>30</sup>.

The physical attributes of the Southern Ocean are changing. Sea ice is a critical component of high-latitude ecosystems and has central roles in oceanographic, biogeochemical and ecological processes. The biological consequences of sea-ice changes in the Southern Ocean include changes in breeding-site availability or access and prey availability, and changes to the structure and function of ecosystems<sup>31</sup>. The pattern of sea-ice change in the Antarctic displays considerable regional and temporal variation. In the West Antarctic Peninsula, the extent of sea ice has declined markedly in recent decades, but has increased in other areas<sup>32</sup>. Most climate projections indicate that overall sea ice will decline over the next century<sup>27</sup>. Given the broad influence of both SST and wind on ecosystems, these components can also influence aspects of the biology of animals, including their breeding phenology, foraging success, survival and reproductive performance<sup>26</sup>. However, when we contrasted the rates of change of sea-ice duration, SST and wind patterns inside and outside of AESs there were only slight differences, and considerable regional variation (Extended Data Fig. 6). The subtle nature of the differences in environmental change inside versus outside AESs does not negate the fact that the study area overall is undergoing marked changes in physical environmental processes, and that ecologically important areas are not being spared from these changes.

### Assessment of spatial management

Management of marine systems is complex, especially in areas that lie beyond national jurisdiction<sup>33</sup> and where international effort is therefore required, particularly for species that move between national and international waters<sup>34</sup>. Relevant management includes traditional process-oriented tools such as individual species protection, stock assessments, decision rules and catch limits, as well as spatial tools such as marine protected areas (MPAs)<sup>35</sup>, but also altered fishing practices for mitigating bycatch<sup>36</sup>. In the high-latitude Southern Ocean, the Commission for the Conservation of Antarctic Marine Living Resources (CCAMLR) uses an ecosystem-based management framework that is intended to ensure that there are no long-term effects from fisheries on marine ecosystems<sup>37</sup>. This includes setting precautionary, spatially explicit catch quotas and a call for the establishment of a network of MPAs—the design considerations of which can include the potential to provide climate change refugia and the inclusion of reference areas to help separate the effects of fishing from climate-related environmental change. Both approaches will benefit from better understanding of the locations of AESs. Outside the CCAMLR framework, MPAs have also been established by sovereign management authorities around some sub-Antarctic islands (Fig. 3a). Several other MPAs are currently under

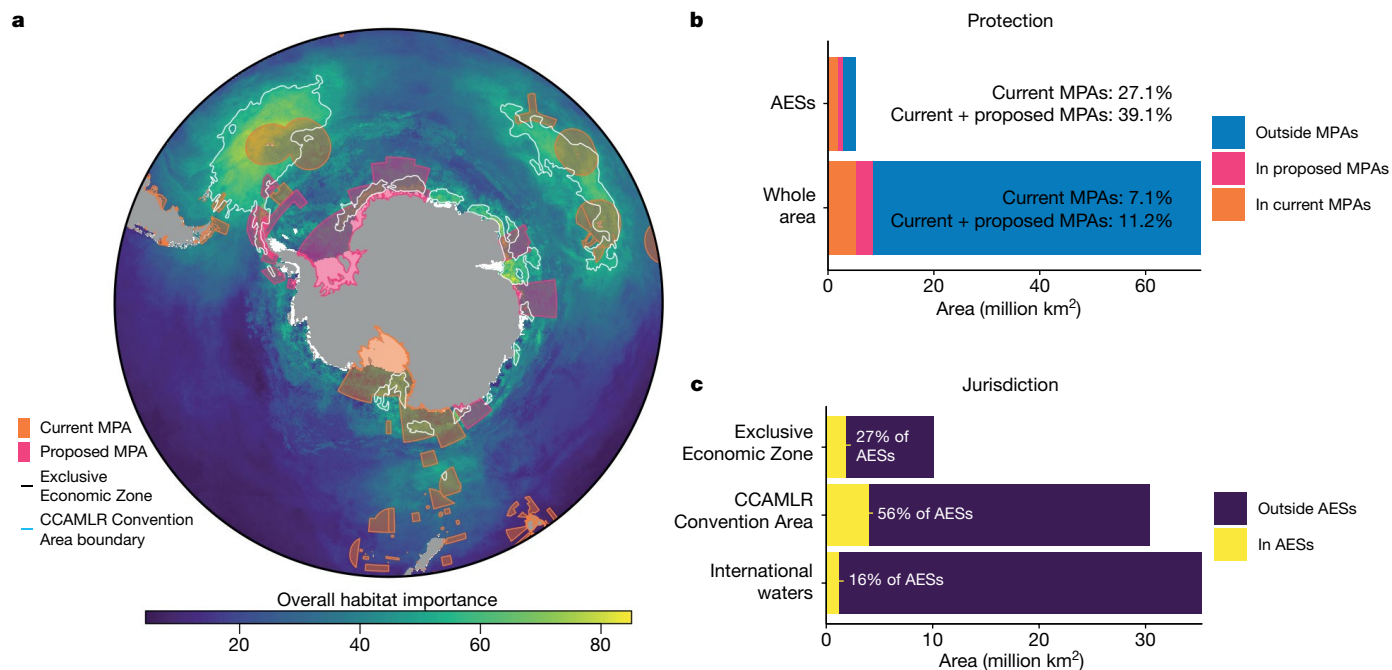


**Fig. 3 | Spatial protection of Southern Ocean AESs. a**, Current (orange) and proposed (magenta) MPAs superimposed on overall habitat importance. White contours denote AESs, black lines show national Exclusive Economic Zones and the blue line shows the CCAMLR Convention Area. **b**, Area in current (orange)

development, including within CCAMLR and by national authorities (Fig. 3a). However, the level of protection afforded by any individual MPA depends on its governance structure and the type and level of permitted activities (for example, fishing)<sup>9,38</sup>.

An appropriately designed network of protected areas can help to buffer the effects of climate change and reduce the effect of stressors such as bycatch or competition from fisheries<sup>39</sup>. We therefore quantified the coverage and placement of individual MPAs with reference to identified AESs. Overall, 7.1% of the ocean south of 40°S is currently protected by MPAs, and this would increase to 11.2% if all currently proposed MPAs were implemented (Fig. 3b). This already meets, in a regional setting, the global Aichi Biodiversity Target 11 of 10% by 2020. The level of protection of the Southern Ocean is high by global standards—only 3.6% of the world's oceans has MPA status at present, increasing to 7.3% with the addition of planned and announced MPAs<sup>38</sup>. However, protection needs to be targeted at areas of high conservation value, including those that are important for the persistence of biodiversity<sup>9</sup>. Existing MPAs cover 27% of the AESs identified (Fig. 3b). Southern Ocean MPAs are predominantly in sub-Antarctic regions, and here they show high levels of congruence with AESs (Fig. 3a). Of note is the Davis Bank region, south of the Falkland Islands (Islas Malvinas), where there are high levels of fishing inside AESs (Figs. 1, 2a, b). This area is now part of an MPA that was recently implemented by Argentina (Fig. 3a). Adoption of proposed MPAs for the Antarctic continental margins would raise the MPA coverage of AESs to 39% (Fig. 3b), including areas in East Antarctica, the Weddell Sea and the Antarctic Peninsula. The largest total AESs (4.0 million km<sup>2</sup>; 56% of AESs) are under CCAMLR jurisdiction (Fig. 3a, c), followed by 1.9 million km<sup>2</sup> (27% of AESs) in national waters (Exclusive Economic Zones), and only 1.2 million km<sup>2</sup> (16% of AESs) are outside the CCAMLR Convention Area and national waters (Fig. 3c). Implementation of MPA proposals would benefit Southern Ocean ecosystems, especially those in the Antarctic Peninsula, East Antarctic and Weddell Sea.

### Likely effects of future climate change

We estimated the likely effects of future climate change on the distribution of AESs under two representative concentration pathway (RCP)

and proposed (magenta) MPAs, and outside MPAs (blue). **c**, Area inside and outside AESs in national Exclusive Economic Zones, the CCAMLR Convention Area and the international waters outside these two areas.

simulations: a medium-forcing scenario (RCP4.5) and a more extreme, high-forcing scenario (RCP8.5)<sup>40</sup>. For each scenario, eight global climate models—considered to be most suitable for Southern Ocean studies owing to their reliable reproduction of extant sea-ice conditions—were used to predict the locations of AES-like habitats in 2100. Here we discuss only the RCP8.5 results, as current emissions of carbon dioxide are in line with this scenario<sup>41</sup>. Results for the moderate RCP4.5 scenario are presented in Extended Data Fig. 7. There was an overall reduction in the AES-like area (−3.3%), partitioned into an increase in sub-Antarctic AES-like cells (+5.7%) and a decrease in Antarctic AES-like cells (−10.2%) that outweighed this increase.

In the sub-Antarctic, AES-like areas generally moved south (Fig. 4a), resulting in an overall growth in the area of sub-Antarctic AESs (Fig. 4b). This general southward migration of important habitat is consistent with projections for individual predator species (for example, king penguins (*Aptenodytes patagonicus*))<sup>42</sup>, as well as for other species including krill and salps<sup>43,44</sup>. The advantages that predators gain from the overall increase in the area of sub-Antarctic AESs may be offset by the increased cost of travel to more-distant foraging grounds—at least for central-place foragers that dive (penguins and fur seals)—whereas volant species (albatrosses and petrels) or those that are unconstrained by terrestrial breeding sites (whales) may benefit from increased sub-Antarctic foraging opportunities<sup>45</sup>. Changes in the future distribution of AES-like areas along the Antarctic margin are more spatially heterogeneous, with areas where AESs are lost interspersed with areas where they are gained or retained (Fig. 4a). However, there will be a net loss (−10.2%) of AES-like cells in the CCAMLR Convention Area (Fig. 4b). The heterogeneity of this pattern is in part a result of the dynamic nature of the high-latitude Antarctic marine environment and the uncertainty across a number of climate-model variables in this region. This uncertainty is due to the variability in the skill of models in reproducing current climate, and the large range of projected responses from those models. Our projections are based on unchanged future availability (that is, colony locations and sizes) and species–environment relationships. However, as species adapt to future pressures and changes to their available breeding habitat, populations are likely to change both their



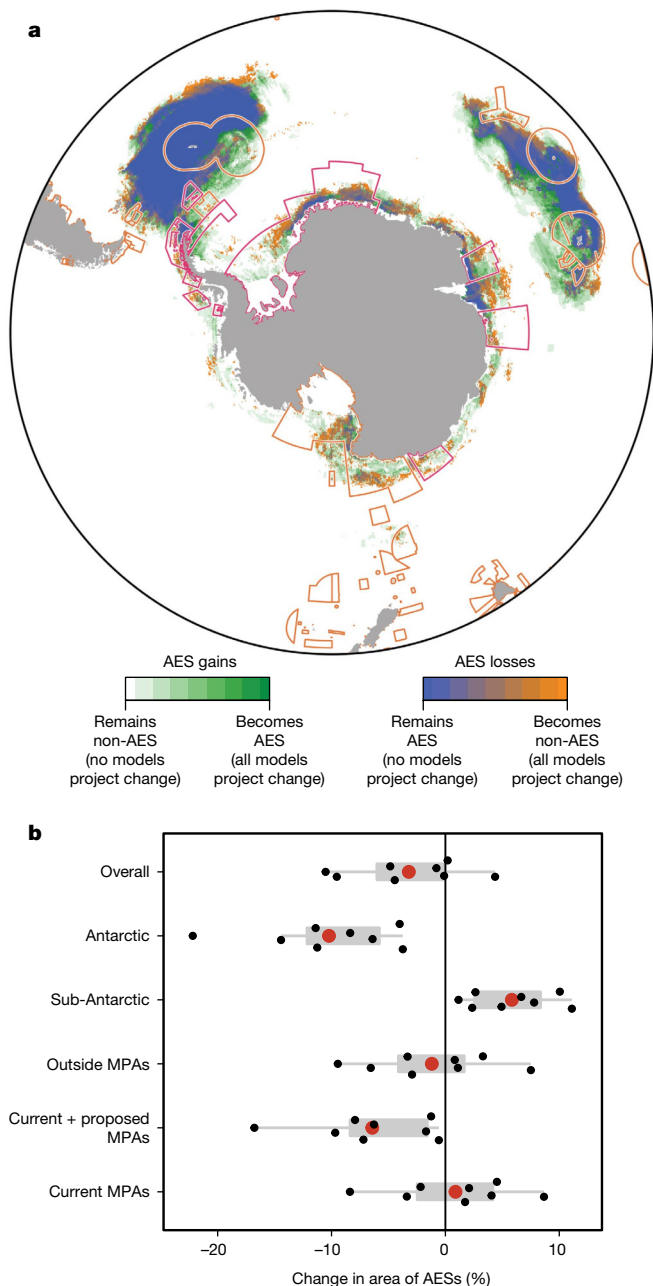


**Fig. 4 | Projected change in the distribution of AESs under RCP8.5. a**, Cells that were AESs in the original results are shown in blue (remain as AES) or orange (become non-AES in the future). The gradation from orange to blue shows the proportion of climate models that indicate loss (orange) or retention (blue) of AESs. Similarly, the gradation from white to green shows the proportion of models that indicate that non-AES cells will remain as non-AES (white) or become AES (green). Orange and magenta outlines show current and proposed MPAs, respectively. **b**, Percentage change in the area of AESs according to the eight different climate models (black points), and the mean of these (red points). In the box plots, the box indicates the 25th–75th percentiles, and the whiskers extend to the smallest value or largest value that is not further than 1.5 times the interquartile range from the 25th or 75th percentile, respectively.

preferred colony locations and habitat usage. Sub-Antarctic-breeding species have limited availability of alternative breeding sites, but colony sizes might change. Ice-breeding species might be able to relocate, and land-breeding species that require ice-free terrain might be able to occupy previously vacant areas, or some might move to regions that become ice-free owing to changing local conditions<sup>46</sup>. The loss

of AES-like habitat on the Antarctic margin that our models project suggests that these populations will be under pressure as the climate continues to change, and therefore continued monitoring of these species and ongoing assessment of the effectiveness of management actions (for example, MPAs) will be important. Monitoring of colonies will need to detect local colonizations, particularly when populations are small<sup>47</sup>. As part of the designation of MPAs within CCAMLR, research and monitoring plans are necessary and required; these plans should—among other factors—consider changes to species–environment relationships and other dynamic processes within and adjacent to the protected area, given the pressures of ongoing climate change.

There was a mixed response across the eight climate models, with changes in the number of AES-like cells that are included in current MPAs ranging from –8.7% to +8.4% (Fig. 4b). When the proposed MPAs were included (current + proposed MPAs in Fig. 4b), all climate models indicated a decrease (between –16.9% and –0.9%) in the number of AES-like cells within MPAs. This suggests that proposed MPAs are in areas that are projected to become less similar to existing AESs by 2100. Any protection afforded by MPAs in such areas could provide better medium-term opportunities for populations to adapt, as they will not have to cope with both climate change and other stressors during that period.

## Conclusion

Our work provides strong evidence in support of the ecological importance of existing and proposed Southern Ocean MPAs. By integrating tracking data from a suite of predators, we identified regions that are likely to have high biodiversity and biomass of the prey (and concomitant ecosystems) of the animals that were tracked. Our AESs are clearly candidates for protection, and the implementation of the proposed MPAs within the CCAMLR region would greatly increase the protection of important habitats in the Southern Ocean. Several MPA proposals have failed to reach consensus within the CCAMLR process, and even when adopted result in MPAs with varying degrees of protection. Many sources of input are needed to establish MPAs, but the AESs that we have described here will help to make the scientific case in this multifaceted process<sup>2,48</sup> by providing an ecosystem-level analysis of the areas that most warrant protection. The design of MPAs should also consider future conditions. Pressures on AESs owing to climate change will affect all parts of the Southern Ocean, but their effects are likely to be strongest along the Antarctic margin. The responses of species to these pressures are currently difficult to predict, highlighting the need for continued monitoring as part of ongoing management actions. Because only 16% of all Southern Ocean AESs are outside the CCAMLR Convention Area or national waters, the responsibilities for these future actions lie mostly with CCAMLR members and those nations with sovereign territory in the sub-Antarctic. Adaptive management approaches to conservation measures (including MPAs) will be necessary to deal with these future changes in a timely way. The Southern Ocean can be an exemplar of how science, policy and management can interact to meet the challenges of a changing planet. In the Southern Ocean, these challenges will be considerable, and will include increased fishing pressure as the global demand for marine resources grows<sup>49</sup>. Our results highlight where future science-informed policy efforts might best be directed, including both adaptive spatial protection and improved robust management of fisheries. Similar synthetic approaches should capitalize on the increasing amount of tracking data that are being collected through large-scale initiatives<sup>50</sup> to indicate regions in need of protection globally.

## Online content

Any methods, additional references, Nature Research reporting summaries, source data, extended data, supplementary information,



acknowledgements, peer review information; details of author contributions and competing interests; and statements of data and code availability are available at <https://doi.org/10.1038/s41586-020-2126-y>.

1. Stark, J. S., Raymond, T., Deppeler, S. L. & Morrison, A. K. *Antarctic Seas. World Seas: an Environmental Evaluation* (Elsevier, 2019).
2. Chown, S. L. & Brooks, C. M. The state and future of Antarctic environments in a global context. *Annu. Rev. Environ. Resour.* **44**, 1–30 (2019).
3. Ainley, D. G. & Blight, L. K. Ecological repercussions of historical fish extraction from the Southern Ocean. *Fish. Fish.* **10**, 13–38 (2009).
4. Agnew, D. J., Hill, S. L., Beddington, J. R., Purchase, L. V. & Wakeford, R. C. Sustainability and management of southwest Atlantic squid fisheries. *Bull. Mar. Sci.* **76**, 579–594 (2005).
5. Kock, K. H., Reid, K., Croxall, J. & Nicol, S. Fisheries in the Southern Ocean: an ecosystem approach. *Phil. Trans. R. Soc. B* **362**, 2333–2349 (2007).
6. Nicol, S., Foster, J. & Kawaguchi, S. The fishery for Antarctic krill—recent developments. *Fish. Fish.* **13**, 30–40 (2012).
7. Swart, N. C., Gille, S. T., Fyfe, J. C. & Gillett, N. P. Recent Southern Ocean warming and freshening driven by greenhouse gas emissions and ozone depletion. *Nat. Geosci.* **11**, 836–841 (2018).
8. Convention on Biological Diversity. *Decisions Adopted by the Conference of the Parties to the Convention on Biological Diversity at its Ninth Meeting*. Report No. UNEP/CBD/COP/9/29 (CBD, 2008).
9. Visconti, P. et al. Protected area targets post-2020. *Science* **364**, 239–241 (2019).
10. Hazen, E. L. et al. Marine top predators as climate and ecosystem sentinels. *Front. Ecol. Environ.* **17**, 565–574 (2019).
11. Constable, A. J. et al. Developing priority variables (“ecosystem Essential Ocean Variables”—eEOVs) for observing dynamics and change in Southern Ocean ecosystems. *J. Mar. Syst.* **161**, 26–41 (2016).
12. Reid, K., Croxall, J. P., Briggs, D. R. & Murphy, E. J. Antarctic ecosystem monitoring: quantifying the response of ecosystem indicators to variability in Antarctic krill. *ICES J. Mar. Sci.* **62**, 366–373 (2005).
13. Cury, P. M. et al. Global seabird response to forage fish depletion—one-third for the birds. *Science* **334**, 1703–1706 (2011).
14. Nicol, S. et al. Ocean circulation off east Antarctica affects ecosystem structure and sea-ice extent. *Nature* **406**, 504–507 (2000).
15. Hays, G. C. et al. Translating marine animal tracking data into conservation policy and management. *Trends Ecol. Evol.* **34**, 459–473 (2019).
16. Ropert-Coudert, Y. et al. The Retrospective Analysis of Antarctic Tracking Data project. *Sci. Data* <https://doi.org/10.1038/s41597-020-0406-x> (2020).
17. Hindell, M. A. et al. in *The Kerguelen Plateau: Marine Ecosystem and Fisheries* (eds Duhamel, G. & Welsford, D.) 203–215 (Société Française d’Ichtyologie, 2011).
18. Tittensor, D. P. et al. Global patterns and predictors of marine biodiversity across taxa. *Nature* **466**, 1098–1101 (2010).
19. Hindell, M. A. et al. Decadal changes in habitat characteristics influence population trajectories of southern elephant seals. *Glob. Chang. Biol.* **23**, 5136–5150 (2017).
20. Sallée, J.-B., Speer, K. G. & Rintoul, S. R. Zonally asymmetric response of the Southern Ocean mixed-layer depth to the Southern Annular Mode. *Nat. Geosci.* **3**, 273–279 (2010).
21. Davies, R. G., Irlach, U. M., Chown, S. L. & Gaston, K. J. Ambient, productive and wind energy, and ocean extent predict global species richness of procellariiform seabirds. *Glob. Ecol. Biogeogr.* **19**, 98–110 (2010).
22. Ardyna, M. et al. Delineating environmental control of phytoplankton biomass and phenology in the Southern Ocean. *Geophys. Res. Lett.* **44**, 5016–5024 (2017).
23. Ropert-Coudert, Y. et al. in *Biogeographic Atlas of the Southern Ocean* (eds De Broyer, C. et al.) 364–387 (Scientific Committee on Antarctic Research, 2014).
24. Atkinson, A. et al. Oceanic circumpolar habitats of Antarctic krill. *Mar. Ecol. Prog. Ser.* **362**, 1–23 (2008).
25. Nicol, S. & Raymond, D. B. in *Antarctic Ecosystems: an Extreme Environment in a Changing World* (eds Rogers, A. D. et al.) 243–254 (Wiley, 2012).
26. Constable, A. J. et al. Climate change and Southern Ocean ecosystems I: how changes in physical habitats directly affect marine biota. *Glob. Chang. Biol.* **20**, 3004–3025 (2014).
27. Meijers, A. J. S. The Southern Ocean in the Coupled Model Intercomparison Project phase 5. *Phil. Trans. R. Soc. A* **372**, 20130296 (2014).
28. Dayton, P. K., Thrush, S. F., Agardy, M. T. & Hofman, R. J. Environmental effects of marine fishing. *Aquat. Conserv.* **5**, 205–232 (1995).
29. Kroodsma, D. A. et al. Tracking the global footprint of fisheries. *Science* **359**, 904–908 (2018).
30. Mormede, S., Dunn, A., Parker, S. & Hanchet, S. Using spatial population models to investigate the potential effects of the Ross Sea region Marine Protected Area on the Antarctic toothfish population. *Fish. Res.* **190**, 164–174 (2017).
31. Massom, R. A. & Stammerjohn, S. E. Antarctic sea ice change and variability—physical and ecological implications. *Polar Sci.* **4**, 149–186 (2010).
32. Vaughan, D. et al. in *Climate Change 2013: the Physical Science Basis. Contribution of Working Group I to the Fifth Assessment Report of the Intergovernmental Panel on Climate Change* (eds Stocker, T. F. et al.) 317–382 (Cambridge University Press, 2013).
33. Game, E. T. et al. Pelagic protected areas: the missing dimension in ocean conservation. *Trends Ecol. Evol.* **24**, 360–369 (2009).
34. Harrison, A.-L. et al. The political biogeography of migratory marine predators. *Nat. Ecol. Evol.* **2**, 1571–1578 (2018).
35. Hilborn, R. Policy: marine biodiversity needs more than protection. *Nature* **535**, 224–226 (2016).
36. Phillips, R. A. et al. The conservation status and priorities for albatrosses and large petrels. *Biol. Conserv.* **201**, 169–183 (2016).
37. Constable, A. J., De LaMare, W. K., Agnew, D. J., Everson, I. & Miller, D. Managing fisheries to conserve the Antarctic marine ecosystem: practical implementation of the Convention on the Conservation of Antarctic Marine Living Resources (CCAMLR). *ICES J. Mar. Sci.* **57**, 778–791 (2000).
38. Sala, E. et al. Assessing real progress towards effective ocean protection. *Mar. Policy* **91**, 11–13 (2018).
39. Roberts, C. M. et al. Marine reserves can mitigate and promote adaptation to climate change. *Proc. Natl Acad. Sci. USA* **114**, 6167–6175 (2017).
40. Moss, R. H. et al. The next generation of scenarios for climate change research and assessment. *Nature* **463**, 747–756 (2010).
41. Peters, G. P. et al. The challenge to keep global warming below 2°C. *Nat. Clim. Chang.* **3**, 4–6 (2013).
42. Péron, C., Weimerskirch, H. & Bost, C.-A. Projected poleward shift of king penguins’ (*Aptenodytes patagonicus*) foraging range at the Crozet Islands, southern Indian Ocean. *Proc. R. Soc. Lond. B* **279**, 2515–2523 (2012).
43. Atkinson, A. et al. Krill (*Euphausia superba*) distribution contracts southward during rapid regional warming. *Nat. Clim. Chang.* **9**, 142–147 (2019).
44. Atkinson, A., Siegel, V., Pakhomov, E. & Rothery, P. Long-term decline in krill stock and increase in salps within the Southern Ocean. *Nature* **432**, 100–103 (2004).
45. Weimerskirch, H., Louzao, M., de Grissac, S. & Delord, K. Changes in wind pattern alter albatross distribution and life-history traits. *Science* **335**, 211–214 (2012).
46. Cristofari, R. et al. Climate-driven range shifts of the king penguin in a fragmented ecosystem. *Nat. Clim. Chang.* **8**, 245–251 (2018).
47. Southwell, C. et al. Recent studies overestimate colonization and extinction events for Adelle penguin breeding colonies. *Auk* **134**, 39–50 (2017).
48. Jacquet, J., Blood-Patterson, E., Brooks, C. & Ainley, D. ‘Rational use’ in Antarctic waters. *Mar. Policy* **63**, 28–34 (2016).
49. Grémillet, D. et al. Persisting worldwide seabird-fishery competition despite seabird community decline. *Curr. Biol.* **28**, 4009–4013 (2018).
50. Block, B. A. et al. Tracking apex marine predator movements in a dynamic ocean. *Nature* **475**, 86–90 (2011).

**Publisher’s note** Springer Nature remains neutral with regard to jurisdictional claims in published maps and institutional affiliations.

© The Author(s), under exclusive licence to Springer Nature Limited 2020

<sup>1</sup>Institute for Marine and Antarctic Studies, University of Tasmania, Hobart, Tasmania, Australia. <sup>2</sup>Antarctic Climate and Ecosystems Cooperative Research Centre, University of Tasmania, Hobart, Tasmania, Australia. <sup>3</sup>Centre d’Etudes Biologiques de Chizé, Station d’Écologie de Chizé-La Rochelle Université, CNRS UMR7372, Villiers-en-Bois, France. <sup>4</sup>CESAB-FRB, Institut Bouisson Bertrand, Montpellier, France. <sup>5</sup>LOCEAN/IPSL, Sorbonne Université-CNRS-IRD-MNHN, UMR7159, Paris, France. <sup>6</sup>Department of Ecology and Evolutionary Biology, University of California Santa Cruz, Santa Cruz, CA, USA. <sup>7</sup>British Antarctic Survey, Natural Environment Research Council, Cambridge, UK. <sup>8</sup>Alfred-Wegener-Institut Helmholtz-Zentrum für Polar- und Meeresforschung, Bremerhaven, Germany. <sup>9</sup>School of Biological Sciences, Monash University, Melbourne, Victoria, Australia. <sup>10</sup>Marine Biology Laboratory, Université Libre de Bruxelles, Brussels, Belgium. <sup>11</sup>National Institute of Water and Atmospheric Research, Wellington, New Zealand. <sup>12</sup>Marine Mammal Institute, Oregon State University, Newport, OR, USA. <sup>13</sup>BEDIC, OD Nature, Royal Belgian Institute for Natural Sciences, Brussels, Belgium. <sup>14</sup>Laboratory of Biodiversity and Evolutionary Genomics, Department of Biology, University of Leuven, Leuven, Belgium. <sup>15</sup>Department of Primary Industries, Parks, Water and Environment, Hobart, Tasmania, Australia. <sup>16</sup>Australian Antarctic Division, Department of Agriculture, Water and the Environment, Kingston, Tasmania, Australia. <sup>17</sup>Point Blue Conservation Science, Petaluma, CA, USA. <sup>18</sup>Marine Mammal Laboratory, Alaska Fisheries Science Center, NOAA Fisheries, Seattle, WA, USA. <sup>19</sup>Mammal Research Institute, Department of Zoology and Entomology, University of Pretoria, Hatfield, South Africa. <sup>20</sup>UiT-The Arctic University of Norway, Tromsø, Norway. <sup>21</sup>Scottish Oceans Institute, St Andrews, UK. <sup>22</sup>School of Biological Sciences, University of Auckland, Auckland, New Zealand. <sup>23</sup>Oceans and Coasts, Department of Environment, Agriculture and Fisheries, Cape Town, South Africa. <sup>24</sup>Instituto de Oceanografia, Universidade Federal do Rio Grande, Rio Grande, Brazil. <sup>25</sup>Norwegian Polar Institute, Fram Centre, Tromsø, Norway. <sup>26</sup>Institute of Marine Sciences, University of California Santa Cruz, Santa Cruz, CA, USA. <sup>27</sup>South Australian Research and Development Institute, West Beach, South Australia, Australia. <sup>28</sup>Department of Biological Sciences, Macquarie University, Sydney, New South Wales, Australia. <sup>29</sup>Antarctic Ecosystems Research Division, Southwest Fisheries Science Center, NOAA Fisheries, La Jolla, CA, USA. <sup>30</sup>Center for Marine Biotechnology and Biomedicine, Scripps Institution of Oceanography, University of California San Diego, La Jolla, CA, USA. <sup>31</sup>Landcare Research, Lincoln, New Zealand. <sup>32</sup>Instituto Antártico Argentino, Buenos Aires, Argentina. <sup>33</sup>Moss Landing Marine Laboratories, San José State University, Moss Landing, CA, USA. <sup>34</sup>Sydney Institute of Marine Science, Mosman, New South Wales, Australia. <sup>35</sup>Institute for Terrestrial and Aquatic Wildlife Research, University of Veterinary Medicine Hannover, Büsum, Germany. <sup>36</sup>Dipartimento di Scienze Fisiche, della Terra e dell’Ambiente, Università di Siena, Siena, Italy. <sup>37</sup>Museo Nazionale dell’Antartide, Siena, Italy. <sup>38</sup>DST-NRF Centre of Excellence at the FitzPatrick Institute of African Ornithology, Nelson Mandela University, Port Elizabeth, South Africa. <sup>39</sup>Antarctic Research Trust, Bremerhöhe, Germany. <sup>40</sup>DST-NRF Centre of Excellence at the FitzPatrick Institute of African Ornithology, University of Cape Town, Rondebosch, South Africa. <sup>41</sup>National Institute of Polar Research, Tachikawa, Japan. <sup>42</sup>Norwegian Institute for Nature Research, Fram Centre, Tromsø, Norway. <sup>43</sup>Institute of Biodiversity, Animal Health and Comparative Medicine, University of Glasgow, Glasgow, UK. <sup>44</sup>Marine and Environmental Sciences Centre, Department of Life Sciences, University of Coimbra, Coimbra, Portugal. <sup>45</sup>These authors contributed equally: Mark A. Hindell, Ryan R. Reisinger, Yan Ropert-Coudert. <sup>46</sup>Deceased. <sup>47</sup>These authors jointly supervised this work: Simon Wotherspoon, Ian D. Jonsen, Ben Raymond. <sup>✉</sup>e-mail: mark.hindell@utas.edu.au

## Methods

### Data reporting

No statistical methods were used to predetermine sample size. The experiments were not randomized and the investigators were not blinded to allocation during experiments and outcome assessment.

### Analytical overview

We assembled tracking data from 17 species of seabirds and marine mammals, collected between 1991 and 2016, from across the Antarctic predator research community<sup>16</sup>. Birds and mammals comprise the majority of top predator species in the Southern Ocean, which has few other large, highly mobile marine predator taxa (bony and cartilaginous fishes). These include toothfish, southern bluefin tuna (*Thunnus maccoyii*), which occur in the northernmost part of our study area) and a small number of shark species. Very few of these fish and shark species have been tracked, with very few tracking data available south of 40°S<sup>51</sup>. Although some bias might result from our use of species, this does not detract from the underlying logic of our approach: that by using the at-sea distributions of an ecologically diverse suite of predators we can identify areas of ecological importance. Our dataset represents 4,060 individual tracks and more than 2.9 million location estimates (Fig. 1a). After filtering and quality control, we retained 2,823 tracks comprising 2.3 million locations<sup>16</sup>. The approximately 30% of tracks that were excluded were those with poor-quality location fixes that could not be properly filtered, tracks from individuals that did not actually depart the colony, or tracks with other problems detected during the rigorous quality control process that we implemented. The full process is described in our companion data paper<sup>16</sup>, which makes available all of the data for use by the broader community, without providing further analytical investigation to consider the matters raised here. The environmental covariate values along each of these tracks (the 'used' habitat) were compared statistically with the habitat available to each animal, thereby allowing the habitat selection of each species to be determined<sup>52,53</sup> (Extended Data Figs. 1, 2). We fitted habitat-selection models for different life-history stages within a species. Despite the considerable size of the dataset, it is not an exhaustive representation of animals from all known colonies (for central-place foragers) or geographic regions (for non-central-place foragers). To account for incomplete tracking coverage, we used the fitted habitat-selection models to map habitat importance for each life-history stage of each species across the entire Southern Ocean, including areas around colonies without tracking deployments (Extended Data Fig. 3). For each species, we calculated the average habitat importance across life-history stages. For colony-breeding species, colony sizes were used to weight the habitat-importance values, upweighting areas that were of importance to large colonies (Extended Data Fig. 8). Southern Ocean predator species can be clustered into Antarctic and sub-Antarctic species (Extended Data Fig. 9). We mapped assemblage-level habitat importance (Extended Data Fig. 10) for each of these two groups (hereafter 'overall habitat importance' maps) by averaging across species-level maps. To calculate the overall map, we took the maximum of the two assemblage-level importance values in each cell. Areas with high values of overall habitat importance (in the top decile of values) indicate areas that are attractive to many species; these represent AESs<sup>17</sup>. We then compared the overall habitat-importance values inside and outside AESs in the context of fishing effort and changes in physical environmental conditions (duration of sea-ice cover, SST and wind speed). We finally quantified the spatial protection afforded to AESs under current and proposed spatial management plans.

We describe the methods in more detail in the Supplementary Information. We conducted all the analyses in R<sup>54</sup>.

### Tracking data

The data represent the output from a variety of types of tracking tags, providing location estimates at different spatio-temporal resolution and accuracy. We applied a state-space model<sup>55</sup> to estimate the most-probable locations at regular temporal intervals, while accounting for potential errors in the location estimates with automatic and manual quality control before and after filtering<sup>16</sup>. Although this procedure does not make the track from a light-based tag as accurate as one from a GPS device, it does provide a consistent characterization of the positional accuracy across different tag types, allowing the uncertainty in position to propagate into the uncertainty in the parameters of the fitted movement model and in the track simulation step (see below). We note that the GLS errors are larger than the resolution of the grids used, especially near the poles, which may be problematic for the analyses. However, the light-based tag deployments were made almost exclusively on sub-Antarctic animals (albatrosses and fur seals). The spatial scale of our results (AESs) in the sub-Antarctic zone (around 5 million km<sup>2</sup>) is considerably larger than the probable scale of positional error of light-based tags (around 100 km) and so we do not believe that using a mixture of tag types has adversely affected our results.

### Life-history stages

Most of the species in the study are central-place foragers (that is, they return periodically to land or sea ice to breed, moult or rest). The constraints faced by these predators at different stages in their life-history cycle mean that their movements differ markedly across these stages. We therefore fitted models separately for up to five predefined life-history stages in the breeding cycle of each species. We automatically assigned tracks to these stages on the basis of calendar date, with manual reassignment where necessary following examination of individual movement patterns. This resulted in 40 data subsets (17 species with 1–4 life-history stages) with sufficient data for habitat-selection modelling (Supplementary Table 1).

### Simulating tracks to estimate available space

The observed locations only provide information about where animals occur, not about where they could have gone. To estimate the geographic space potentially available to animals, we simulated sets of tracks for each observed track. For each observed track, we simulated 50 tracks using the movement model described above<sup>55</sup>. This yielded simulated tracks with movement characteristics (distributions of step length and turning angle) that are the same as the observed track, but they are random and independent of environmental effects. Thus, the simulated tracks provide an estimate of the geographic space that each animal could have occupied (given its movement characteristics and track length) if it had no habitat preferences. The environmental differences between the available geographic space and the used geographic space allow the habitat selection of the organisms to be estimated, as detailed below. Locations at the animal's home colony, and locations at known terrestrial resting sites, were fixed at the corresponding time and date in the simulated tracks to accurately simulate central-place foraging behaviour (Supplementary Information).

### Environmental data

To characterize the biophysical environment at observed and simulated locations, we compiled a suite of 19 environmental covariates (Extended Data Fig. 2, Supplementary Table 2) and extracted the value of these at each location. The covariates were remotely sensed, measured in situ or model-estimated and represent biophysical features that influence the movement, distribution and density of marine predators<sup>52,53</sup>. It was not computationally feasible to temporally match environmental data to each location estimate. Rather, we created a climatology that spanned each tracking data subset (species by the combination of life-history stages), using the predefined stage dates. We took the mean

# Article

(or standard deviation) of the environmental data that fell on these days of the year (stage dates) over the whole study period (November 1991 to June 2016). Some covariates (for example, salinity difference) were only available as monthly climatologies, and we used the months corresponding with the stage dates to calculate the mean (or standard deviation). All covariates were resampled to a  $0.1^\circ \times 0.1^\circ$  grid; hereafter we refer to the pixels of this grid as 'cells'. We checked the covariates for each data subset for missing values and if more than 10% of values were missing we excluded the covariate from that model. This influenced mainly the chlorophyll *a* concentration variable, which was excluded from 17 of the 40 habitat models (Supplementary Table 1). This affected life-history stages with a large proportion of winter days, as chlorophyll *a* has poor winter satellite coverage owing to being obscured by extensive cloud cover. However, chlorophyll *a* was rarely an important predictor in the models in which it was included; thus, excluding it from models probably had only a negligible effect.

## Habitat-selection models

We used a habitat-selection modelling framework<sup>56</sup> to model and predict the space use of marine birds and mammals of the Southern Ocean. These models use the observed locations of each individual animal and an estimate of the geographic space available to each individual, along with covariates that characterize their environment. The environmental differences between the habitat that was used and the habitat that was available allow the habitat selection of the organisms to be estimated. To fit the models, we used boosted regression trees, a machine-learning algorithm that produces an ensemble of regression trees that have been iteratively fitted in a boosting process to improve accuracy<sup>57</sup>. We tested several other algorithms but boosted regression trees showed the best predictive performance in another study<sup>53</sup> and in our tests. For a given location, the response variable was whether the location was an observed or simulated (available) location, and the explanatory covariates were the associated environmental covariates. Boosted regression trees have four parameters that must be set: the number of trees (boosting iterations), the maximum tree depth, the learning rate (shrinkage) and the minimum number of observations in a node. We chose these values as the combination that minimized the area under the receiver operating characteristic curve (a measure of model predictive performance) during tenfold cross-validation. We also used this metric to evaluate the final fitted models. We used the fitted model to generate spatial predictions for the entire study region and we estimated the uncertainty associated with these predictions using a bootstrap approach (Supplementary Information)

## Accessibility model

The modelling procedure described above does not account for the accessibility of a given location to an individual animal (in effect, it estimates the habitat selection of a given location in terms of its environmental characteristics, but without considering whether or not the animal could actually reach that location). For central-place foragers in particular, this is an important consideration. We therefore used a second set of models to account for this<sup>53</sup>. We modelled accessibility in terms of the number of observed plus simulated locations in a given cell as a function of the distance of the cell to the deployment colony. We fitted binomial models with a smooth, monotonic decreasing constraint<sup>58</sup>, under the assumption that the accessibility of cells should decrease with geographic distance. To estimate uncertainty, we sampled curves from the posterior distribution of each fitted accessibility model to use in a bootstrap approach (Supplementary Information).

We used these models to predict the accessibility of each cell over the study region to each species during each life-history stage (that is, given the distance of a cell from a colony, the fitted accessibility model provides an estimate of the probability that animals from that colony would be able to visit that cell). For colony-breeding species (those other than humpback whales, crabeater and Weddell seals), colony

sizes were used to weight this accessibility estimate: for a given cell, the accessibility from all known colonies of that species was calculated. A weighted mean of these accessibilities was then taken, using colony sizes as weights. Thus, this weighted accessibility represents the probability that a randomly selected individual from the global population would be able to visit that cell, effectively upweighting cells in the vicinity of large colonies.

For the non-colony breeding, ice-associated seals (crabeater and Weddell seals), we modelled accessibility as a function of distance beyond the ice edge (15% ice concentration contour), rather than distance to the colony. For humpback whales, we assumed that the whole study area was equally accessible.

## Transforming output and combining models to predict habitat importance

The habitat-selection models predict the value of the habitat at a location given that the animals could access that location. The predictions of the habitat-selection models were therefore multiplied by the predictions of the accessibility models to yield an index that reflects both the habitat selection of each cell and its accessibility to the animals. This is not an estimate of the probability of a species using a given cell, because that probability also depends on the prevalence of the species<sup>59</sup>. As prevalence varies between species, our habitat-selection estimates cannot be compared directly between species. We therefore partitioned the cells into decreasing percentiles based on area<sup>52</sup> to obtain a map of habitat importance expressed in terms of area (for example, cells with values of 90 or higher represent the top 10% most-important habitat by area for that species). We refer to this as habitat importance, and these maps can be compared among species. To create a single habitat-importance layer for each species, we averaged the stage-specific habitat-importance layers.

## Species-specific habitat importance

We calculated community-level habitat importance by averaging the species-specific maps of habitat importance. Sub-Antarctic regions are naturally more species-diverse than those of the Antarctic, and so a simple average of all species together tended to strongly favour sub-Antarctic areas simply because of their greater species diversity. To account for the differences in species richness between the Antarctic and sub-Antarctic, we first defined two species groups using an unweighted pair group method with arithmetic mean (UPGMA) hierarchical clustering with Manhattan distance, applied to habitat-importance scores (Extended Data Fig. 9). This produced two clear groups: an Antarctic species group (emperor penguin, crabeater seal, Antarctic petrel, Adélie penguin and Weddell seal) and a sub-Antarctic species group (Antarctic fur seal, black-browed albatross, wandering albatross, sooty albatross, grey-headed albatross, king penguin, macaroni and royal penguin, light-mantled albatross and white-chinned petrel). The wide-ranging humpback whales and southern elephant seals did not clearly fall into either cluster, and so were treated as belonging to both groups. The mean habitat importance was calculated for each of these groups separately and then combined (Extended Data Fig. 10) by taking the maximum of the two values (Antarctic and sub-Antarctic) in each pixel. We refer to this final layer as the overall habitat importance.

## AESs

To identify the most-important areas, we calculated the 90th percentile (top decile) of the overall habitat-importance values. Cells with overall habitat-importance values above this threshold together comprised AESs.

## Environmental pressures

To assess past environmental stressors on the Southern Ocean ecosystem, we calculated change in SST, wind speed and sea-ice duration. We selected SST and wind because they were frequently the

most-important predictor variables in the habitat models (Extended Data Fig. 4), and sea-ice concentration as this was an important predictor for Antarctic species. Moreover, these variables are considered to be important drivers of ocean and ecosystem dynamics<sup>18,60</sup>, and key axes on which environmental change in the Southern Ocean has been detected<sup>26</sup>. For each cell, we calculated the change in SST ( $^{\circ}\text{C}$ ) or wind speed ( $\text{m s}^{-1}$ ) as the difference between mean SST or wind speed in 1987–1999 and 2007–2017. For sea-ice duration, we calculated the difference in the mean number of days per year that each pixel had a sea-ice concentration of higher than 15%, for the same periods. These periods represent the decades at the beginning and end of a 30-year period that covers our study period. Thirty years is also the recommended period for climate assessments<sup>61</sup>. We also obtained data on fishing effort—which is considered to be a major environmental stressor in many regions of the Southern Ocean<sup>29,62</sup>—from the Global Fishing Watch dataset, covering the period from 2012 to 2016<sup>29</sup>. We compared the values of these four stressors in the AESs and outside cells using random permutation tests with 10,000 permutations. The null hypothesis is that stressor values inside and outside AESs are from the same distribution.

### Future projections of AESs

Our predicted AESs (under current environmental conditions) are determined by both the oceanographic and climatic conditions of an area, as well as the accessibility of that area to each of our species of interest. In principle it would be possible to use future projections of environmental data and accessibility along with our fitted models to obtain future projections of AESs. However, some predictor variables are not available from the climate models used for the future projections, and although other variables might appear to be available, they have different properties owing to factors such as different temporal and spatial resolution in the output, or the ability of the climate model to resolve the relevant processes. For example, sea surface height from satellite altimetry gives information about frontal and mesoscale features. Yet, although sea surface height is available as an output from many CMIP5 models, those models do not explicitly resolve mesoscale features<sup>63</sup> and so the model-output data for sea surface height will not be acting as a proxy for the same oceanographic properties as the data from satellite-derived altimetry.

To assess future distributions of AES-like habitat, we therefore used a *k*-nearest neighbour classifier approach that is conceptually similar to climate analogues<sup>64</sup>. For each grid cell we compiled current (end of 20th century) environmental conditions, as well as projected conditions at the end of the 21st century from climate models (see below). In terms of accessibility, most of our study species breed in colonies, and ‘accessibility’ for these species is determined both by the geographic distribution of their colonies and by the colony sizes. Future projections of colony location and size do not exist for our study species at present, although initial work has begun for some species, such as king penguins<sup>46</sup>. Colony locations and sizes were therefore assumed to remain constant, and so the accessibility of each grid cell to each species was assumed to remain unchanged. For each grid cell, we compared its projected future environmental and accessibility conditions to every cell in the current (20th century) grid and selected the five cells that were most similar. If the majority of those cells were from current AESs, the projected cell was labelled as ‘AES-like’; otherwise, it was labelled as ‘not AES-like’. These projections therefore provide an indication of the future distribution of AES-like environmental conditions, under the assumptions that colonies do not move or change in size, and that the animals do not change their habitat preferences. These assumptions are unlikely to hold in reality; however, examining the changes in AES-like habitat under these assumptions allows us to isolate the effects of environmental change from colony or habitat-usage changes. As environmental change occurs, species are likely to adapt by changing their colony distributions and habitat usage. The AES projections offer

insights into the likely distribution of environmental pressures, and thus where adaptation by species might be important.

Climate data were compiled from eight global climate models (ACCESS1.0, BCC-CSM1.1, CanESM2, CMCC-CM, EC-EARTH, GISS-E2-H-CC, MIROC-ESM and NorESM-M), which were considered to be most suitable for Southern Ocean studies by virtue of reliably reproducing extant sea-ice conditions<sup>65</sup>. These models were from phase five of the Coupled Model Intercomparison Project (CMIP5) of the World Climate Research Programme. For each model, we extracted data for a 30-year period concomitant with our tracking data (1976–2005), and for a 30-year period at the end of the 21st century (2071–2100). We extracted future (2071–2100) climate data from projections under two RCP simulations: a medium-forcing scenario (RCP4.5, which assumes that society implements changes to limit future  $\text{CO}_2$  emissions in the near future, with peak emissions occurring in 2040) and a more-extreme, high-forcing scenario (RCP8.5, which assumes little curbing of emissions and retains a strong reliance on fossil fuels into the foreseeable future)<sup>40</sup>. Reference data (1976–2005) were extracted from hindcast model runs that attempt to simulate historical conditions, and consequently use observed  $\text{CO}_2$  concentrations over the past 160 years to guide the models.

A maximum of eight variables were extracted for each model, depending on the available data (not all models provide all variables), at monthly time resolution. The variables used were sea-ice concentration, SST, sea surface salinity, sea surface height, the spatial gradient of sea surface height, near-surface current speed, near-surface wind speed and surface downward heat flux. The 30-year mean and standard deviation of each variable was calculated over summer (December to February) and winter (July to September) months. All variables were normalized to the range 0–1 before further analysis.

The resulting set of up to 48 predictors (mean and standard deviation of up to 8 environmental variables, each for summer and winter, plus accessibility layers for 16 species) naturally showed high correlation between many of the variables. We used a principal component analysis to reduce the dimensionality of this dataset, choosing the lowest number of principal components required to explain at least 95% of the variance in the original data; this number ranged from 14 to 17 components, depending on the model and scenario. For each projected-climate cell, the nearest neighbours in the historical-climate grid were calculated using Euclidean distance on these normalized and dimension-reduced data.

### Animal ethics statement

All work was conducted under the appropriate national or institutional ethics approvals. These were: Argentina (Dirección Nacional del Antártico); Australia (Australian Antarctic program; the University of Tasmania); Belgium (Belgian Science Policy Office); Brazil (Brazilian Antarctic Programme; National Council for Scientific and Technological Development (CNPq); Ministry of Science, Technology, Innovation and Communications (MCTIC); Ministry of the Environment; CAPES); France (Terres Australes et Antarctiques Françaises); Germany (Germany Umweltbundesamt (German Environment Agency) and Bundesamt für Naturschutz (Federal Agency for Nature Conservation)); Italy (Programma Nazionale di Ricerche in Antartide (PNRA)); Japan (Japanese Antarctic Research Expedition; National Institute of Polar Research); Monaco (Fondation Prince Albert II de Monaco); New Zealand (Ministry for Primary Industries BRAG); Norway (Norwegian Antarctic Research Expeditions; Norwegian Research Council; Norwegian Animal Research Authority); Portugal (Foundation for Science and Technology); South Africa (Department of Environmental Affairs; National Research Foundation; South African National Antarctic Programme); UK (British Antarctic Survey; Natural Environment Research Council); and USA (NOAA Fisheries Office of Protected Resources; National Science Foundation Office of Polar Programs).



## Reporting summary

Further information on research design is available in the Nature Research Reporting Summary linked to this paper.

## Data availability

The tracking data are available through our companion paper<sup>16</sup>.

## Code availability

Computer code is available at <https://github.com/SCAR/RAATD>.

51. Queiroz, N. et al. Global spatial risk assessment of sharks under the footprint of fisheries. *Nature* **572**, 461–466 (2019).
52. Raymond, B. et al. Important marine habitat off east Antarctica revealed by two decades of multi-species predator tracking. *Ecography* **38**, 121–129 (2015).
53. Reisinger, R. R. et al. Habitat modelling of tracking data from multiple marine predators identifies important areas in the Southern Indian Ocean. *Divers. Distrib.* **24**, 535–550 (2018).
54. R Core Team. R: a language and environment for statistical computing. (R Foundation for Statistical Computing, 2018).
55. Jonsen, I. D. et al. Movement responses to environment: fast inference of variation among southern elephant seals with a mixed effects model. *Ecology* **100**, e02566 (2019).
56. Aarts, G., MacKenzie, M., McConnell, B., Fedak, M. & Matthiopoulos, J. Estimating space-use and habitat preference from wildlife telemetry data. *Ecography* **31**, 140–160 (2008).
57. Elith, J., Leathwick, J. R. & Hastie, T. A working guide to boosted regression trees. *J. Anim. Ecol.* **77**, 802–813 (2008).
58. Pya, N. & Wood, S. N. Shape constrained additive models. *Stat. Comput.* **25**, 543–559 (2015).
59. Phillips, S. J. et al. Sample selection bias and presence-only distribution models: implications for background and pseudo-absence data. *Ecol. Appl.* **19**, 181–197 (2009).
60. Rintoul, S. R. The global influence of localized dynamics in the Southern Ocean. *Nature* **558**, 209–218 (2018).
61. World Meteorological Organization. *Guide to Climatological Practices* (WMO No. 100) (World Meteorological Organization, 2011).
62. Halpern, B. S., Selkoe, K. A., Micheli, F. & Kappel, C. V. Evaluating and ranking the vulnerability of global marine ecosystems to anthropogenic threats. *Conserv. Biol.* **21**, 1301–1315 (2007).
63. He, J. et al. Impact of ocean eddy resolution on the sensitivity of precipitation to CO<sub>2</sub> increase. *Geophys. Res. Lett.* **45**, 7194–7203 (2018).
64. Williams, J. W., Jackson, S. T. & Kutzbach, J. E. Projected distributions of novel and disappearing climates by 2100 AD. *Proc. Natl Acad. Sci. USA* **104**, 5738–5742 (2007).
65. Cavanagh, R. D. et al. A synergistic approach for evaluating climate model output for ecological applications. *Front. Mar. Sci.* **4**, 308 (2017).

**Acknowledgements** This contribution is part of the Retrospective Analysis of Antarctic Tracking Data (RAATD), a project of the Expert Group on Birds and Marine Mammals of the Scientific Committee on Antarctic Research (SCAR; [www.scar.org](http://www.scar.org)). The RAATD project would not have been possible without the many scientists, students and field assistants who helped collect data in the field or process them, including S. Adlard, A. Agüera, M. Biuw, M.-A. Blanchet, J. Clarke, P. Cock, H. Cox, M. Connan, A. R. Carlini, S. Corsolini, M. Cottin, J. D. Le Croquant, G. A. Danieri, D. Davies, B. Dilley, R. Downie, M. Dunn, B. M. Dyer, S. Focardi, H. O. Gillett, S. Haaland, L. Jonsen-Humble, H. Kane, B. A. Krafft, C. Kroeger, C. A. E.

Lemon, G. Mabile, M. Marczak, T. McIntyre, S. McKooy, J. A. Mennucci, T. Nordstad, C. Oosthuizen, R. Orben, T. Photopoulou, B. Picard, O. Prud'homme, T. Raclot, S. Ramdohr, D. H. Raymond, L. Riekkola, G. Richard, G. Robertson, T. Rogers, K. Roper-Kato, S. Schoombie, T. N. Snakes, E. Soininen, A. Specht, K. Stevens, J. N. Swærd, C. Tosh, S. G. Trivelpiece, O. S. G. Trolli, T. Truly, L. Upfold, M. Le Vaillant, Y. Watanabe, M. Wege, C. Wheeler, T. O. Whitehead, M. Widmann, A. G. Wood, N. Youdjou and I. Zimmer. We also thank the large number of fieldworkers without whom these data would not have been collected. D. G. Ainley and A. Constable commented on an earlier version of the manuscript. Support and funding were provided by supranational committees and organizations including SCAR, BirdLife International and the European Commission (IUCN BEST program), as well as various national institutions (see also author affiliations) and foundations, including but not limited to: Argentina (Dirección Nacional del Antártico); Australia (Australian Antarctic program; Australian Research Council; Sea World Research and Rescue Foundation; Australian Integrated Marine Observing System (IMOS) (IMOS is a national collaborative research infrastructure, supported by the Australian Government and operated by a consortium of institutions as an unincorporated joint venture, with the University of Tasmania as Lead Agent)); Belgium (Belgian Science Policy Office/Lifewatch), Brazil (Brazilian Antarctic Programme; National Council for Scientific and Technological Development (CNPq); Ministry of Science, Technology, Innovation and Communications (MCTIC); Ministry of the Environment; CAPES); France (Agence Nationale de la Recherche; Centre National d'Etudes Spatiales; Centre National de la Recherche Scientifique; the French Foundation for Research on Biodiversity (FRB; [www.fondationbiodiversite.fr](http://www.fondationbiodiversite.fr)) in the context of the CESAB project 'RAATD'; Fondation Total; Institut Paul-Emile Victor; Programme Zone Atelier de Recherches sur l'Environnement Antarctique et Subantarctique; Terres Australes et Antarctiques Françaises); Germany (Alfred-Wegener-Institut Helmholtz-Zentrum für Polar- und Meeresforschung, Deutsche Forschungsgemeinschaft, Hanse-Wissenschaftskolleg (Institute for Advanced Study)); Italy (Programma Nazionale di Ricerche in Antartide (PNRA)); Japan (Japanese Antarctic Research Expedition; JSPS Kakenhi grant 20310016; NIPR visiting professor fellowship for M.A.H.); Monaco (Fondation Prince Albert II de Monaco); New Zealand (Ministry for Primary Industries BRAG; Pew Charitable Trusts); Norway (Norwegian Antarctic Research Expeditions; Norwegian Research Council); Portugal (Foundation for Science and Technology); South Africa (Department of Environmental Affairs; National Research Foundation; South African National Antarctic Programme); UK (Darwin Plus; Ecosystems Programme at the British Antarctic Survey; Natural Environment Research Council; WWF); and USA (US AMLR Program of NOAA Fisheries; National Science Foundation Office of Polar Programs).

**Author contributions** M.A.H. conceived and led the project. R.A., B.A., G.B., J.B., M.N.B., L.B., H.B., C.-A.B., P.B., J.-B.C., R.C., D.P.C., R.J.M.C., L.D.R., P.J.N.d.B., K.D., S.D., M.D., L.E., M.F., A.F., N.G., M.G., K.T.G., C.G., S.D.G., R.H., J.T.H., M.A.H., L.A.H., A.K., K.R.K., R.K., G.L.K., K.M.K., K.L., A.D.L., C.L., M.-A.L., P.O.B.L., A.B.M., M.E.I.M., B.I.M., C.R.M., M.M., K.W.N., E.S.N., S.O., R.A.P., P.P., J.P., K.P., N.R., Y.R.-C., P.G.R., M.S., A.S.B., C.S., I.S., A. Takahashi, A. Tarroux, L.G.T., P.N.T., W.T., E.W., H.W., B.W. and J.C.X. collected and contributed data. V.A.-G., H.B., J.-B.C., S.L.C., B.D., M.A.H., L.A.H., K.J., A.K., I.D.J., M.-A.L., D.N., B.R., R.R.R., Y.R.-C., D.T., L.G.T., P.N.T., A.P.V. and S.W. processed and analysed the data. M.A.H., H.B., J.-B.C., D.P.C., S.L.C., B.D., L.A.H., I.D.J., M.-A.L., B.R., R.R.R., Y.R.-C., L.G.T., P.N.T., A.P.V., S.W. and S.L.C. drafted the paper. All authors edited and proofread the paper.

**Competing interests** H.B., J.-B.C., D.P.C., B.D., M.A.H., L.A.H., I.D.J., M.-A.L., M.M., B.R., R.R.R., Y.R.-C., P.G.R., A. Takahashi, D.T., L.G.T., P.N.T., A.P.V. S.W. and J.C.X. are members of the SCAR Expert Group on Birds and Marine Mammals. S.L.C. is President of SCAR.

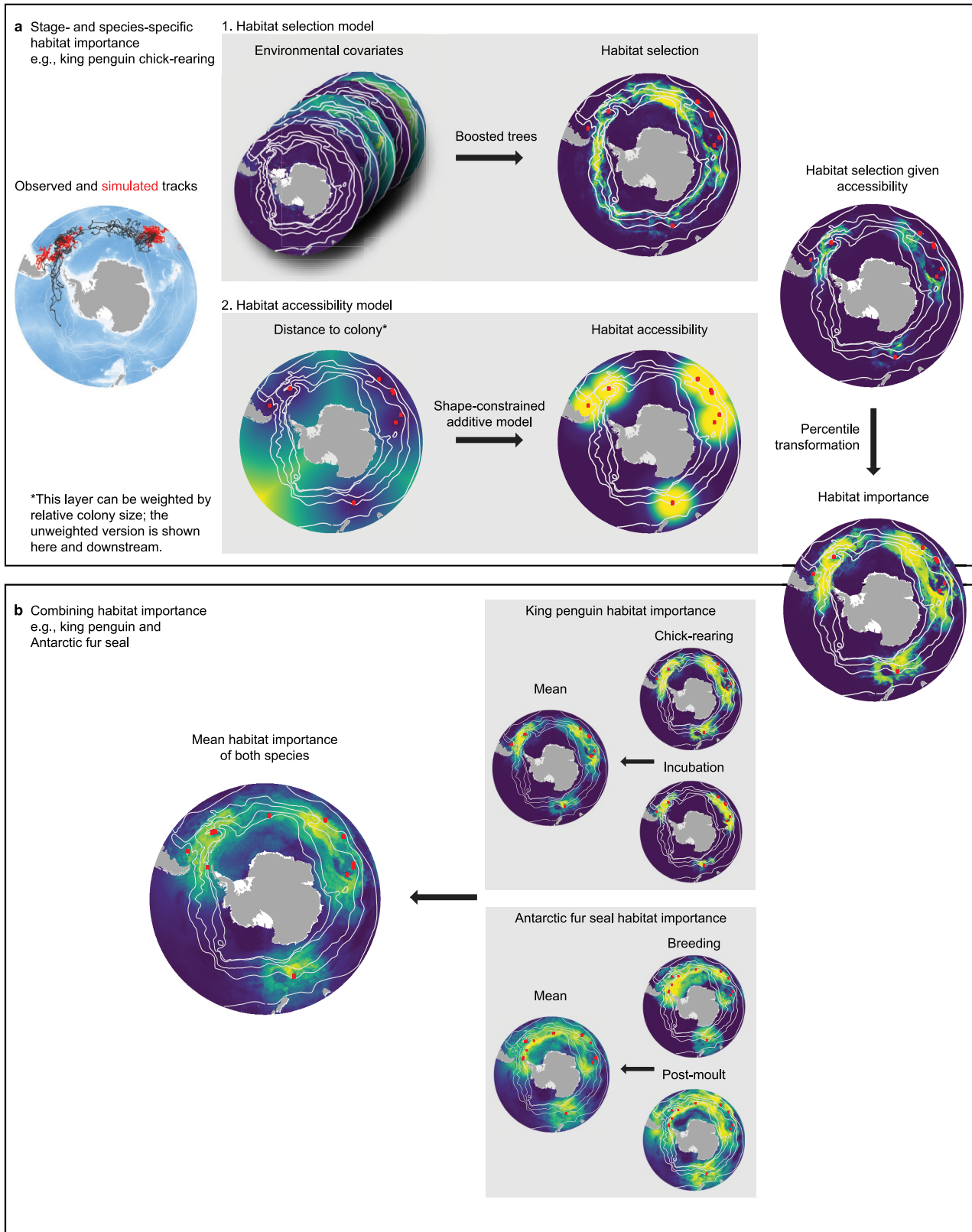
## Additional information

**Supplementary information** is available for this paper at <https://doi.org/10.1038/s41586-020-2126-y>.

**Correspondence and requests for materials** should be addressed to M.A.H.

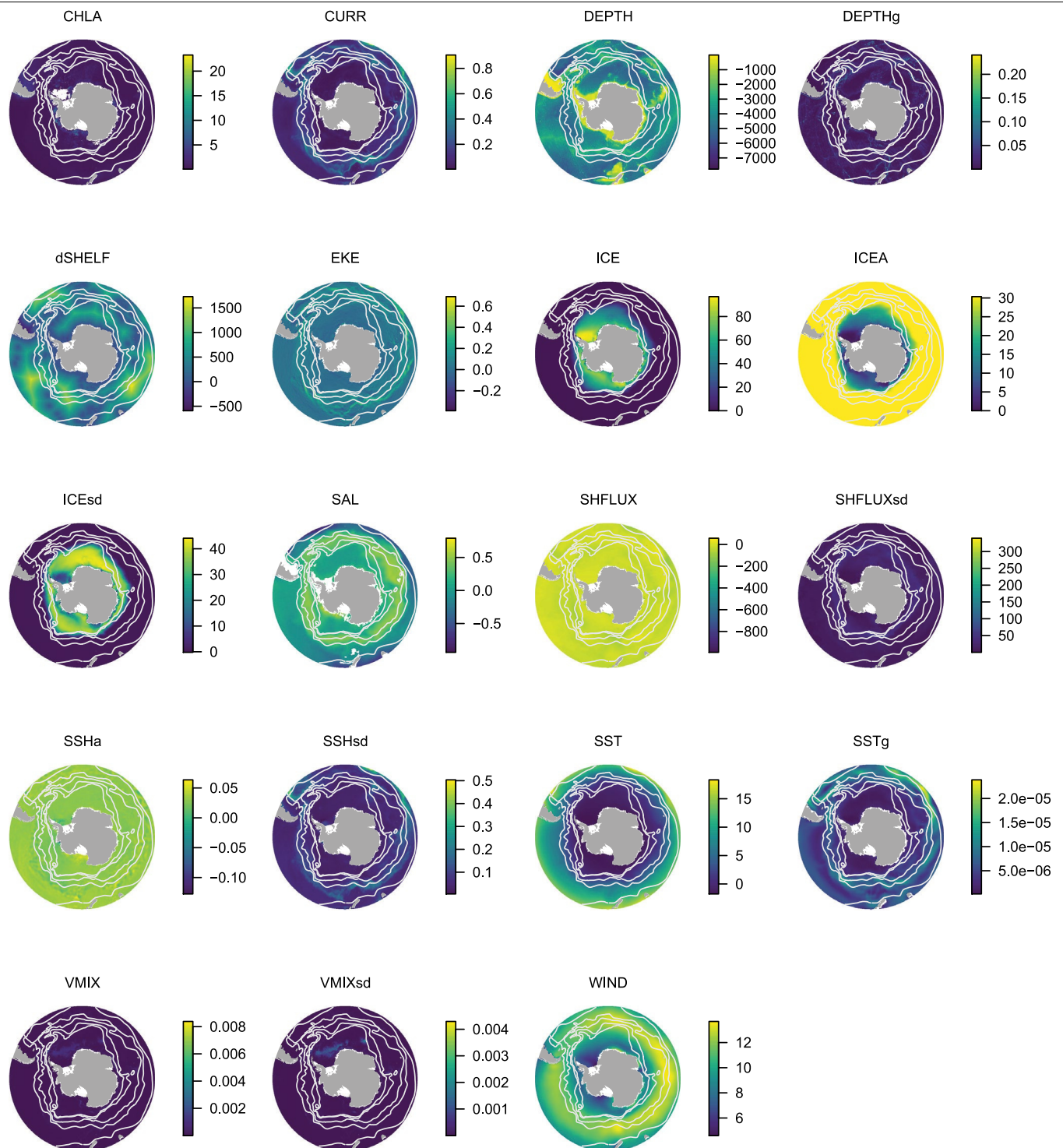
**Peer review information** Nature thanks Tiago Marques and the other, anonymous, reviewer(s) for their contribution to the peer review of this work.

**Reprints and permissions information** is available at <http://www.nature.com/reprints>.



**Extended Data Fig. 1 | Overview of the modelling process. a,** Habitat importance for a given life-history stage (for example, chick-rearing) of a given species (for example, king penguin (*A. patagonicus*)) is calculated using two models (grey boxes): the habitat-selection model (box 1) and the habitat accessibility model (box 2). **b,** These stage-specific, species-specific

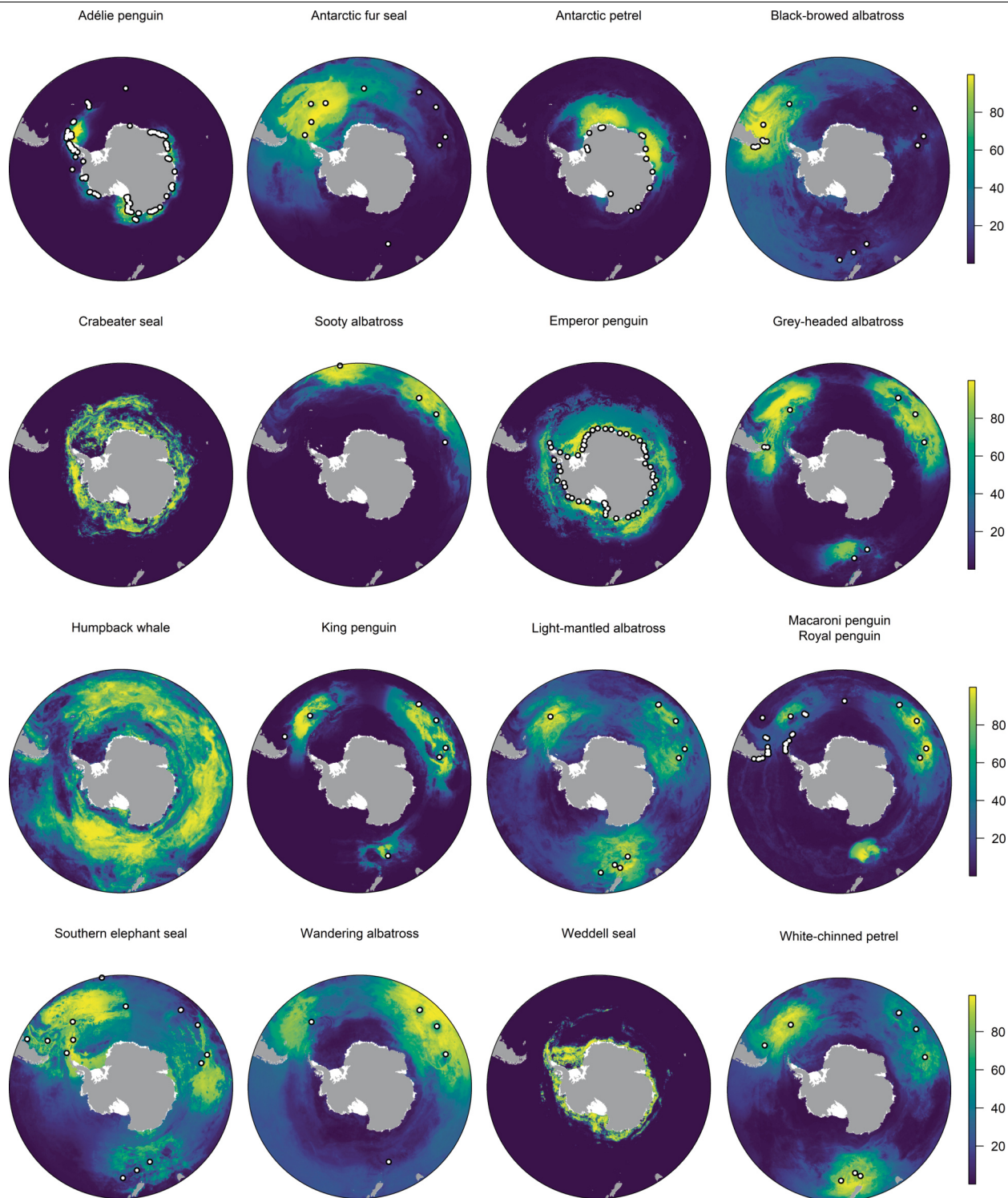
predictions of habitat importance are combined to calculate the mean habitat importance for multiple species (for example, king penguin and Antarctic fur seal (*Arctocephalus gazella*)). In the habitat accessibility model (box 2 in **a**) the distance to colony can be weighted by relative colony size or not. The unweighted version is shown here.



**Extended Data Fig. 2 | Maps showing the 19 environmental covariates that were used to model the habitat selection of marine predators in the Southern Ocean.** Grey lines indicate major oceanographic fronts. CHLA, chlorophyll *a* concentration; CURR, geostrophic current velocity; DEPTH, depth; DEPTHg, depth gradient; dSHELF, distance to shelf; EKE, eddy kinetic energy; ICE, sea-ice concentration; ICEA, accessibility through sea ice; ICEsd, standard deviation of sea-ice concentration; SAL, salinity difference; SHFLUX,

surface heat flux; SHFLUXsd, standard deviation of surface heat flux; SSHa, sea surface height anomaly; SSHsd, sea surface height standard deviation; SST, sea surface temperature; SSTg, sea surface temperature gradient; VMIX, vertical velocity; VMIXsd, standard deviation of vertical velocity; WIND, surface wind speed. Sources and units of measurement are defined in Supplementary Table 2.

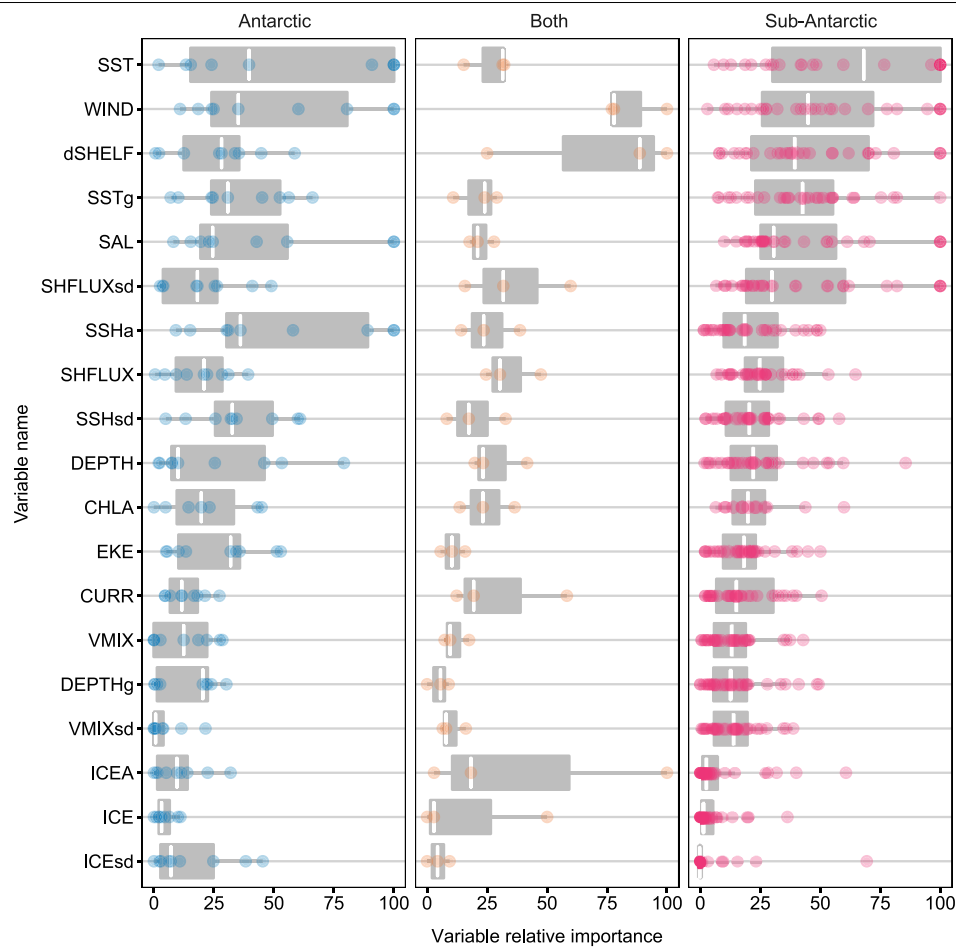




**Extended Data Fig. 3 | Habitat-importance scores for 16 marine predator species in the Southern Ocean.** The maps show predicted habitat importance for each species. Predictions for macaroni penguins (*Eudyptes chrysocome*)

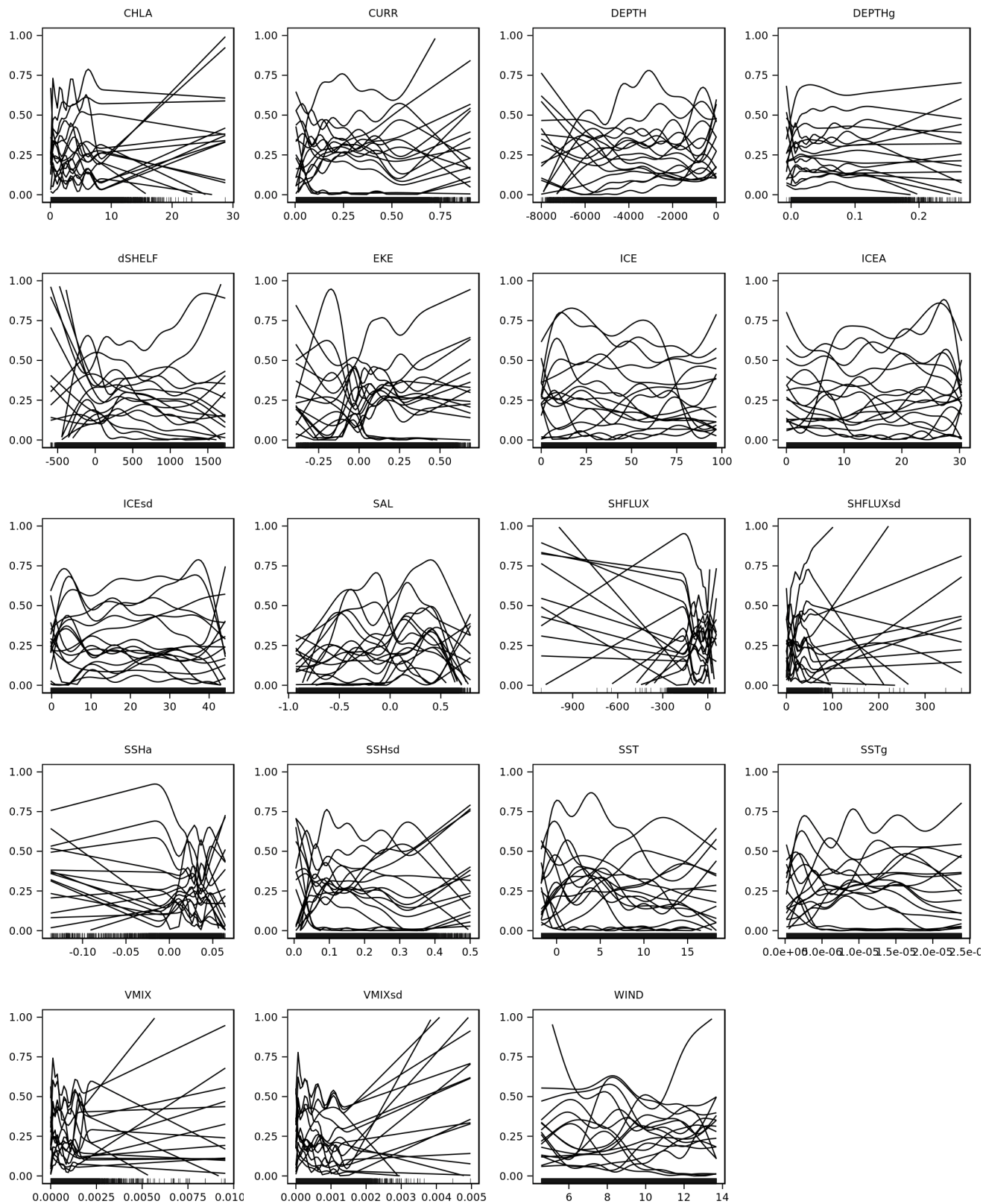
and royal penguins (*Eudyptes schlegeli*) are combined. Black circles show all known colony locations for the 14 colony-breeding species, which we used to predict the models across the whole Southern Ocean.





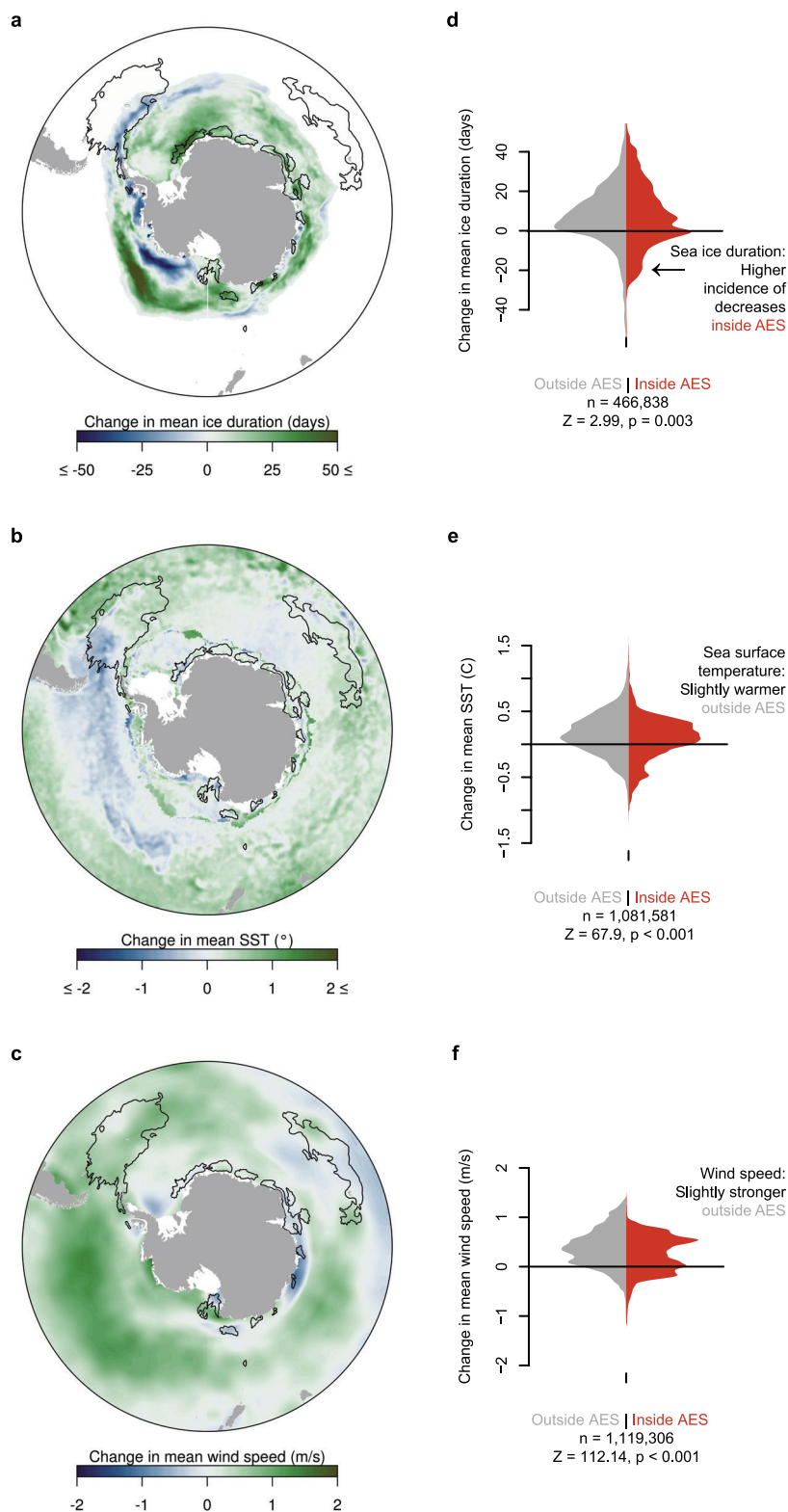
**Extended Data Fig. 4 | Covariate importance.** Relative importance of 19 environmental variables that were used as predictors in 40 boosted regression tree models of the habitat selection of Southern Ocean marine predators. Higher values of variable relative importance indicate that the variable has higher predictive power. Points show the values for each model and box plots (in grey, behind) show the distribution of values. Variables are

ordered (top to bottom) by decreasing median importance. The three panels show the results for three different groups of species that were identified by hierarchical cluster analysis (see ‘Species grouping’ in Methods, and Extended Data Fig. 7). Full covariate names are provided in Supplementary Table 2. Box plots as in Fig. 4.



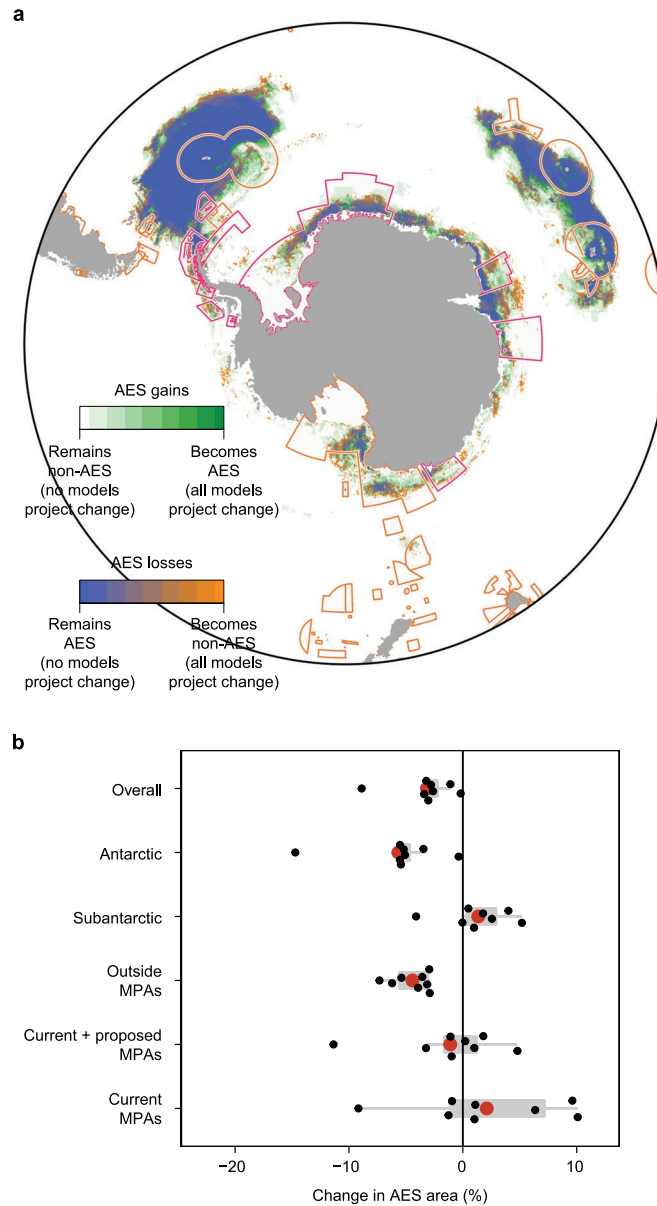
**Extended Data Fig. 5 | Varied relationships between covariates and habitat selection across species.** Scatter plot smoothed curves (black lines) of the relationship between predictions of the species habitat-selection models (boosted regression trees) (vertical axis) and the values of covariates used as predictors in our boosted regression tree models (horizontal axis). The smoothed curves were drawn by fitting generalized additive models for large datasets with a thin plate regression spline basis, as LOESS (locally estimated

scatter plot) smoothing was not computationally feasible. Full covariate names and units are provided in Supplementary Table 2. Higher habitat-selection values indicate higher probabilities of use, irrespective of availability in this case. A smooth curve is shown for each species. Because each species had one to five predictions, for different life-history stages, we took the mean habitat-selection estimate per cell for each species. Rug marks on the horizontal axis indicate the distributions of the data points.



**Extended Data Fig. 6 | Potential environmental stressors in the Southern Ocean.** **a–c**, Maps showing the change (mean in 1987–1998 compared to mean in 2007–2017) in sea-ice duration (days) (**a**), SST ( $^{\circ}\text{C}$ ) (**b**) and wind speed ( $\text{m s}^{-1}$ ) (**c**). Contour lines (black) indicate AESs. **d–f**, Kernel density plots show the

distribution of values of each of **a–c** inside (red) and outside (grey) AESs. Horizontal lines represent zero change. Two-tailed permutation tests indicate significant differences in each case, and the number of grid cells included in the test is given in each case ( $n$ ).

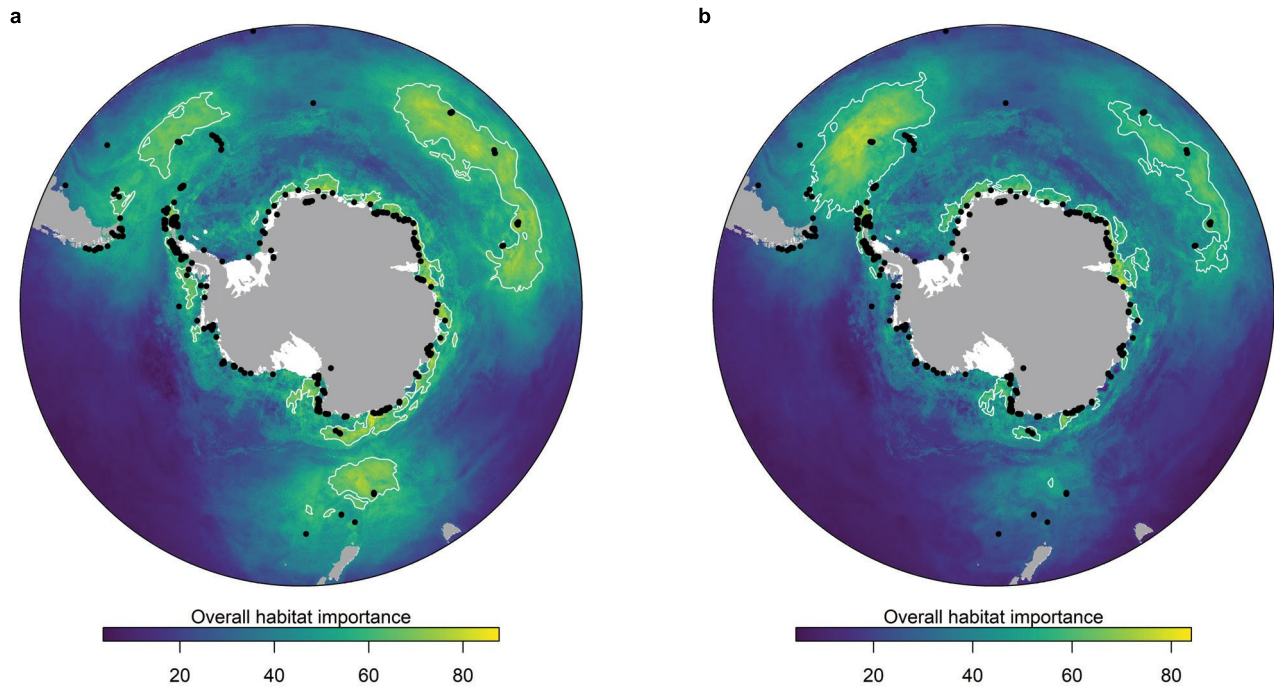


**Extended Data Fig. 7 | Change in the distribution of AESs under RCP4.5.**

**a**, Cells that were AES in the original results are shown in blue (remain as AES) or orange (become non-AES in the future). The gradation from orange to blue shows the proportion of climate models that indicate loss (orange) or retention (blue) of AESs. Similarly, the gradation from white to green shows the

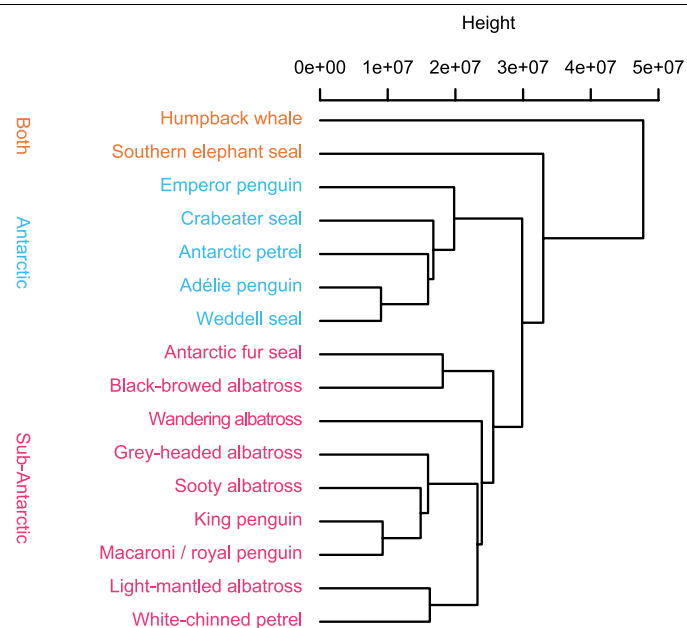
proportion of models that indicate that non-AES cells will remain as non-AES (white) or become AES (green). Orange and magenta outlines show current and proposed MPAs, respectively. **b**, Percentage change in the area of AESs according to the eight different climate models (black points), and the mean of these (red points). Box plots as in Fig. 4.



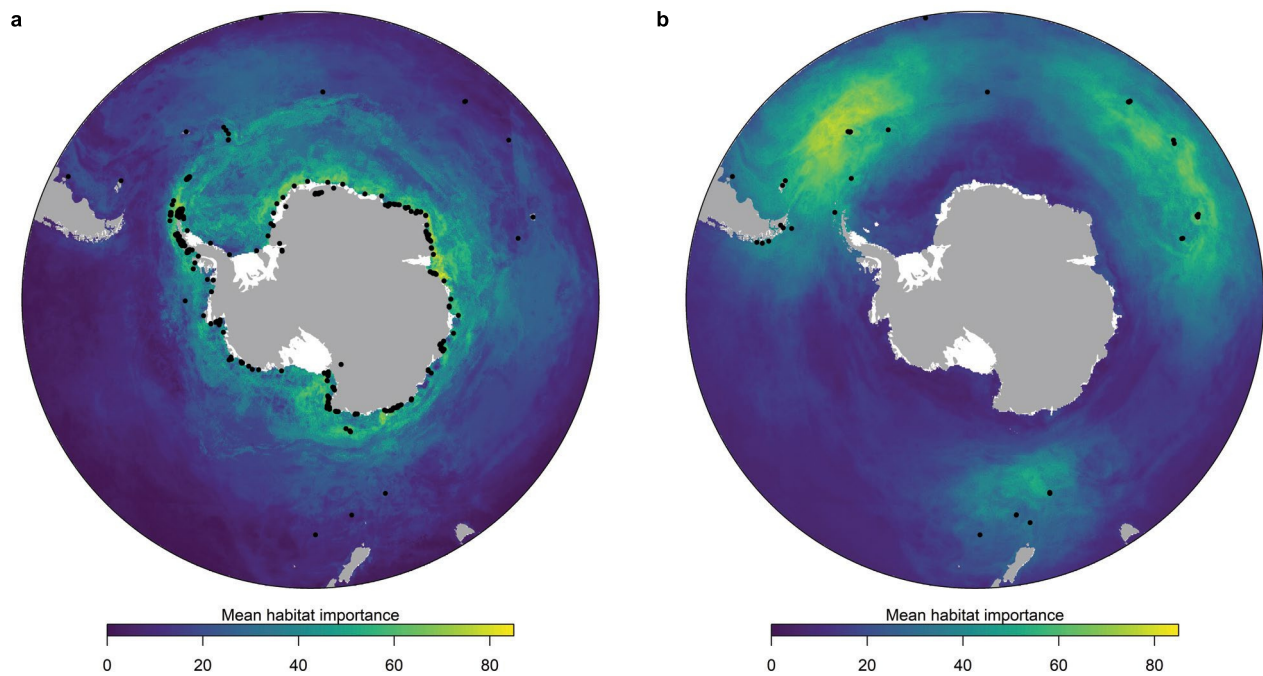


**Extended Data Fig. 8 | Comparison of unweighted and weighted overall habitat importance.** **a**, Overall habitat importance, calculated without accounting for colony sizes. **b**, Overall habitat importance if colony sizes are

taken into account. Black points indicate colony locations for the 14 colony-breeding species; white contours indicate AESs. See Methods and Supplementary Information for details.



**Extended Data Fig. 9 | Dendrogram of hierarchical cluster analysis showing species groups in the dataset.** We performed UPGMA hierarchical cluster analysis on the Manhattan distance among species, calculated from the habitat-importance scores. The results show two clear species groups: Antarctic (blue) and sub-Antarctic (magenta). Humpback whales and southern elephant seals (orange) did not fall into either group and we assigned them to both groups for subsequent analyses. The cophenetic correlation coefficient between the distance matrix and the dendrogram was 0.86, which means that the dendrogram is a good representation of the Manhattan distance values among the species. Values can range from 0 (no correlation) to 1 (perfect correlation).



**Extended Data Fig. 10 | Mean habitat importance of Antarctic and sub-Antarctic species. a, b,** To account for regional differences in species richness we defined two species groups (Methods and Extended Data Fig. 5) and calculated the mean habitat importance for these two groups separately. These

two mean habitat-importance layers (**a** and **b**) were then combined into a single overall habitat-importance layer by choosing the maximum value in each cell. Black points indicate the colony locations of colony-breeding species in each species group.

## Reporting Summary

Nature Research wishes to improve the reproducibility of the work that we publish. This form provides structure for consistency and transparency in reporting. For further information on Nature Research policies, see [Authors & Referees](#) and the [Editorial Policy Checklist](#).

### Statistics

For all statistical analyses, confirm that the following items are present in the figure legend, table legend, main text, or Methods section.

n/a Confirmed

- ☐ ☒ The exact sample size ( $n$ ) for each experimental group/condition, given as a discrete number and unit of measurement
- ☐ ☒ A statement on whether measurements were taken from distinct samples or whether the same sample was measured repeatedly
- ☐ ☒ The statistical test(s) used AND whether they are one- or two-sided  
*Only common tests should be described solely by name; describe more complex techniques in the Methods section.*
- ☐ ☒ A description of all covariates tested
- ☐ ☒ A description of any assumptions or corrections, such as tests of normality and adjustment for multiple comparisons
- ☐ ☒ A full description of the statistical parameters including central tendency (e.g. means) or other basic estimates (e.g. regression coefficient) AND variation (e.g. standard deviation) or associated estimates of uncertainty (e.g. confidence intervals)
- ☐ ☒ For null hypothesis testing, the test statistic (e.g.  $F$ ,  $t$ ,  $r$ ) with confidence intervals, effect sizes, degrees of freedom and  $P$  value noted  
*Give  $P$  values as exact values whenever suitable.*
- ☐ ☒ For Bayesian analysis, information on the choice of priors and Markov chain Monte Carlo settings
- ☐ ☒ For hierarchical and complex designs, identification of the appropriate level for tests and full reporting of outcomes
- ☐ ☒ Estimates of effect sizes (e.g. Cohen's  $d$ , Pearson's  $r$ ), indicating how they were calculated

*Our web collection on [statistics for biologists](#) contains articles on many of the points above.*

### Software and code

Policy information about [availability of computer code](#)

Data collection No computer code was used to obtain the data

Data analysis All analyses were done using R.v3.6 The code are available at <https://github.com/SCAR/RAATD>

For manuscripts utilizing custom algorithms or software that are central to the research but not yet described in published literature, software must be made available to editors/reviewers. We strongly encourage code deposition in a community repository (e.g. GitHub). See the Nature Research [guidelines for submitting code & software](#) for further information.

### Data

Policy information about [availability of data](#)

All manuscripts must include a [data availability statement](#). This statement should provide the following information, where applicable:

- Accession codes, unique identifiers, or web links for publicly available datasets
- A list of figures that have associated raw data
- A description of any restrictions on data availability

The data and metadata are available to the public through the Australian Antarctic Data Centre (standardized data, doi:10.4225/15/5afcb927e8162; state-space model-processed (filtered) data, doi:10.4225/15/5afcadad6c130).

## Field-specific reporting

Please select the one below that is the best fit for your research. If you are not sure, read the appropriate sections before making your selection.

- ☒ Life sciences ☐ Behavioural & social sciences ☐ Ecological, evolutionary & environmental sciences



# Life sciences study design

All studies must disclose on these points even when the disclosure is negative.

Sample size	Our sample size was determined by the availability of tracking data provided for each species. It is nonetheless the largest data set of this type ever compiled. The number of individuals per species ranged from 35 to 820 which were sufficient to develop a species distribution model for each species
Data exclusions	We excluded some individual tracks that were either too short (i.e. less than 20 locations or were less than 1 days) or for which movement models failed to converge. This reduced our sample size from 4060 to 2823 individual tracks. There exclusion criteria were pre-established in our companion Scientific Data paper
Replication	Experimental replication was not attempted
Randomization	Individuals in the study were randomly selected for wild populations
Blinding	Blinding was not required for this study as it involved random selections of wild animals

# Reporting for specific materials, systems and methods

We require information from authors about some types of materials, experimental systems and methods used in many studies. Here, indicate whether each material, system or method listed is relevant to your study. If you are not sure if a list item applies to your research, read the appropriate section before selecting a response.

Materials & experimental systems	Methods
n/a	Involved in the study
<input checked="" type="checkbox"/> <input type="checkbox"/> Antibodies	<input checked="" type="checkbox"/> <input type="checkbox"/> ChIP-seq
<input checked="" type="checkbox"/> <input type="checkbox"/> Eukaryotic cell lines	<input checked="" type="checkbox"/> <input type="checkbox"/> Flow cytometry
<input checked="" type="checkbox"/> <input type="checkbox"/> Palaeontology	<input checked="" type="checkbox"/> <input type="checkbox"/> MRI-based neuroimaging
<input type="checkbox"/> <input checked="" type="checkbox"/> Animals and other organisms	
<input checked="" type="checkbox"/> <input type="checkbox"/> Human research participants	
<input checked="" type="checkbox"/> <input type="checkbox"/> Clinical data	

# Animals and other organisms

Policy information about [studies involving animals](#); [ARRIVE guidelines](#) recommended for reporting animal research

Laboratory animals	The study did not involve laboratory animals
Wild animals	This study was a synthesis of existing animal tracking data. it involved 17 species (each with its own particular method of capture) and over 4000 individual animals. In all cases, the animals were released back into the wild at the point of capture after 10-30 minutes of handling. A full breakdown of the data set is provided in our Scientific Data paper: Robert-Coudert, Y. et al. (In Press) The Retrospective Analysis of Antarctic Tracking Data Project. Sci. Data
Field-collected samples	The study did not involve samples collected in the field
Ethics oversight	All work was conducted under the appropriate National or Institutional Ethics approvals. There were: Argentina (Dirección Nacional del Antártico), Australia (Australian Antarctic program; the University of Tasmania a, Belgium (Belgian Science Policy Office), Brazil (Brazilian Antarctic Programme; National Council for Scientific and Technological Development - CNPq; Ministry of Science, Technology, Innovation and Communications – MCTIC; Ministry of the Environment; CAPES), France (Agence Nationale de la Recherche; Centre National d’Etudes Spatiales; Centre National de la Recherche Scientifique; Fondation Total; Institut Paul-Emile Victor; Programme Zone Atelier de Recherches sur l’Environnement Antarctique et Subantarctique; Terres Australes et Antarctiques Françaises), Germany (Deutsche Forschungsgemeinschaft, Hanse-Wissenschaftskolleg - Institute for Advanced Study), Italy (Programma Nazionale di Ricerche in Antartide, PNRA), Japan (Japanese Antarctic Research Expedition; JSPS Kakenhi grant), Monaco (Fondation Prince Albert II de Monaco), New Zealand (Ministry for Primary Industries - BRAG; Pew Charitable Trusts), Norway (Norwegian Antarctic Research Expeditions; Norwegian Research Council), Portugal (Foundation for Science and Technology), South Africa (Department of Environmental Affairs; National Research Foundation; South African National Antarctic Programme), UK British Antarctic Survey; Natural Environment Research Council, and USA U.S. AMLR Program of NOAA Fisheries; US Office of Polar Programs.

Note that full information on the approval of the study protocol must also be provided in the manuscript.

# A genomic and epigenomic atlas of prostate cancer in Asian populations

<https://doi.org/10.1038/s41586-020-2135-x>

Received: 21 November 2018

Accepted: 17 January 2020

Published online: 25 March 2020

 Check for updates

Jing Li<sup>1,2,3,28</sup>, Chuanliang Xu<sup>1,3,28</sup>, Hyung Joo Lee<sup>4,5,28</sup>, Shancheng Ren<sup>1,3</sup>, Xiaoyuan Zi<sup>1</sup>, Zhiming Zhang<sup>6</sup>, Haifeng Wang<sup>1</sup>, Yongwei Yu<sup>7</sup>, Chenghua Yang<sup>1,8</sup>, Xiaofeng Gao<sup>1</sup>, Jianguo Hou<sup>1</sup>, Linhui Wang<sup>9</sup>, Bo Yang<sup>1</sup>, Qing Yang<sup>1</sup>, Huamao Ye<sup>1</sup>, Tie Zhou<sup>1</sup>, Xin Lu<sup>1</sup>, Yan Wang<sup>1</sup>, Min Qu<sup>1</sup>, Qingsong Yang<sup>10</sup>, Wenhui Zhang<sup>1</sup>, Nakul M. Shah<sup>4,5</sup>, Erica C. Pehrsson<sup>4,5</sup>, Shuo Wang<sup>11</sup>, Zengjun Wang<sup>12</sup>, Jun Jiang<sup>13</sup>, Yan Zhu<sup>7</sup>, Rui Chen<sup>1</sup>, Huan Chen<sup>1</sup>, Feng Zhu<sup>1</sup>, Bijun Lian<sup>1</sup>, Xiaoyun Li<sup>6</sup>, Yun Zhang<sup>1</sup>, Chao Wang<sup>1</sup>, Yue Wang<sup>3,14</sup>, Guangan Xiao<sup>1</sup>, Junfeng Jiang<sup>3,14</sup>, Yue Yang<sup>1</sup>, Chaozhao Liang<sup>15</sup>, Jianquan Hou<sup>16</sup>, Conghui Han<sup>17</sup>, Ming Chen<sup>18</sup>, Ning Jiang<sup>19</sup>, Dahong Zhang<sup>20</sup>, Song Wu<sup>21</sup>, Jinjian Yang<sup>22</sup>, Tao Wang<sup>22</sup>, Yongliang Chen<sup>23</sup>, Jiantong Cai<sup>24</sup>, Wenzeng Yang<sup>25</sup>, Jun Xu<sup>26</sup>, Shaogang Wang<sup>27</sup>, Xu Gao<sup>1,3,29</sup>, Ting Wang<sup>4,5,29</sup> & Yinghao Sun<sup>1,3,29</sup>✉

Prostate cancer is the second most common cancer in men worldwide<sup>1</sup>. Over the past decade, large-scale integrative genomics efforts have enhanced our understanding of this disease by characterizing its genetic and epigenetic landscape in thousands of patients<sup>2,3</sup>. However, most tumours profiled in these studies were obtained from patients from Western populations. Here we produced and analysed whole-genome, whole-transcriptome and DNA methylation data for 208 pairs of tumour tissue samples and matched healthy control tissue from Chinese patients with primary prostate cancer. Systematic comparison with published data from 2,554 prostate tumours revealed that the genomic alteration signatures in Chinese patients were markedly distinct from those of Western cohorts: specifically, 41% of tumours contained mutations in *FOXA1* and 18% each had deletions in *ZNF292* and *CHD1*. Alterations of the genome and epigenome were correlated and were predictive of disease phenotype and progression. Coding and noncoding mutations, as well as epimutations, converged on pathways that are important for prostate cancer, providing insights into this devastating disease. These discoveries underscore the importance of including population context in constructing comprehensive genomic maps for disease.

Prostate cancer remains the second most common cancer in men worldwide, with more than 1,275,000 new diagnoses and 350,000 deaths annually<sup>1</sup>. It is characterized by a long and variable natural history, extensive intra- and inter-tumour heterogeneity, and diverse clinical behaviour<sup>4</sup>. Our understanding of the genomic definition and molecular complexity of prostate cancer has markedly improved over the past decade, owing to the advent of next-generation sequencing-based technologies and integrative genomics. Large consortia, including The Cancer Genome Atlas (TCGA), have profiled the molecular signatures of both primary and metastatic castration-resistant prostate cancer, providing insights into the disease and an invaluable community resource<sup>2,5</sup>.

However, until now, most prostate cancer genomics data have been derived from Western populations<sup>2,3,6–17</sup> (Supplementary Data 1), although ethnic and racial background can profoundly influence the disease<sup>18</sup>. The incidence and mortality rates of prostate cancer for Asians and Pacific Islanders are lower than those of the general US population<sup>5</sup>. In addition, Asian patients with prostate cancer often present with higher tumour grades at diagnosis, but have similar or better prognosis with androgen deprivation therapy<sup>5</sup>. In a recent pilot

study, we found that Chinese patients with prostate cancer featured genomic abnormalities that were distinct from those of Western patients<sup>19</sup>. Therefore, we sought to define the genomic underpinnings of prostate cancer in Western and Chinese men.

Here, we deliver the first, to our knowledge, Chinese Prostate Cancer Genome and Epigenome Atlas (CPGEA). Along with a new cohort of more than 200 Chinese men, we integrated existing datasets from 2,554 patients with prostate cancer representing 13 Western cohorts, as well as our pilot Chinese cohort<sup>2,3,6–15,19</sup>. Our study revealed markedly different distributions of genetic lesions from those established by the TCGA<sup>2</sup> and defined genomic signatures both unique to Chinese populations and common to Chinese and Western disease. We also defined epimutation patterns for Chinese prostate cancer and illustrated the interaction between genetic mutations and epimutations. Finally, we highlighted that coding and noncoding mutations and epimutations converge on common pathways that underscore the biology of prostate cancer. Our study illustrates a paradigm for comprehensive cancer genome atlases in which population-specific contexts are taken into consideration.

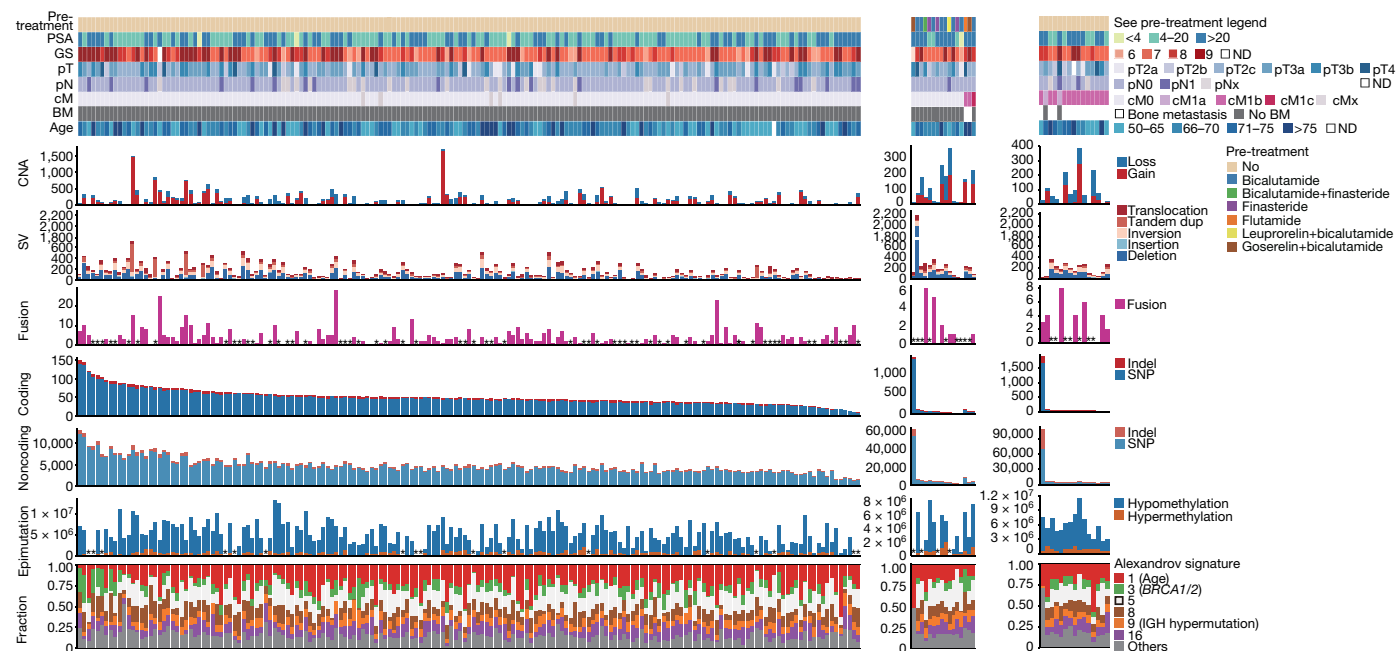


**Fig. 1 | Molecular landscape of the CPGEA cohort.** Each column represents an individual tumour ( $n = 208$ ). Patients were separated into three groups: those without treatment (left), with pre-treatment (centre,  $n = 16$ ) and with metastatic cancer (right,  $n = 18$ ). The top panel shows clinical features, including PSA level, Gleason score (GS), T-category, and age, as per the colour

key. Each subsequent panel displays a specific molecular profile: CNA segments per patient; number of structural variations (SV); number of gene-to-gene fusions; coding and noncoding mutations; number of hyper- and hypomethylated CpGs; and the fraction of each Alexandrov signature in the genome. ND, not determined. Asterisks indicate no data available.

## Clinical samples and data generation

We analysed primary tumour tissue and matched healthy tissue from 208 patients who underwent radical prostatectomy for clinically localized prostate cancer. Confirmation procedures, age, levels of prostate-specific antigen (PSA), Gleason scores, and other clinical and pathological characterizations are described in Extended Data Fig. 1a, Supplementary Data 2 and Supplementary Discussion. We characterized all samples with whole-genome sequencing (WGS), whole-genome bisulfite sequencing (WGBS), RNA sequencing (RNA-seq) and microRNA sequencing (miRNA-seq) for a total of 1,268 datasets (Extended Data Fig. 1b). Treatment-naïve tumours (177 out of 208) were used in the integrative and comparative analysis (Fig. 1), with the exclusion of two outliers (Supplementary Discussion). The study populations and results are summarized in a supporting website (<http://www.cpgea.com>).

## Somatic mutation landscape

To compare the CPGEA cohort with previously profiled populations, we defined tumour mutation burden, mutation signature, and copy number variation, as well as identifying significantly mutated genes and recurrently mutated noncoding regions, using custom bioinformatics pipelines based on the TCGA<sup>2</sup> and Pan-Cancer Analysis of Whole Genomes (PCAWG)<sup>9</sup> pipelines (Methods). To ensure meaningful comparison between Chinese and Western prostate cancer cohorts, we reprocessed the raw TCGA data using our pipelines. The results were strongly concordant with published TCGA results and recapitulated all major genomic signatures of Western primary prostate cancer (Extended Data Fig. 1c–f, Supplementary Discussion, Supplementary Data 3). Therefore, most comparisons between CPGEA and TCGA were based on uniformly processed data using the CPGEA pipelines, and all other comparisons were kept at a high level.

Across the CPGEA cohort, the median substitution rate was 1.4 per megabase (Mb) and the mutation burden was 1.0 per Mb, confirming the low mutation burden observed in prostate cancer in Western cohorts<sup>20</sup>

(Figs. 1, 2a). Alexandrov signatures<sup>21</sup> 1, 3, 5, 8, 9 and 16 were predominant in most samples and comprised 78% of mutations (Fig. 1, Extended Data Fig. 1g, h). Signatures 8 and 16 strongly correlated with Gleason score.

Prostate cancer is characterized by genomic instability, manifesting as recurrent copy number alterations (CNAs)<sup>22</sup> and DNA rearrangements<sup>23</sup>. We detected 20,375 copy number gains and 11,187 losses across the CPGEA cohort (Fig. 1), including 14 recurrent gains and 17 losses involving 921 amplified and 1,373 deleted genes (Fig. 2b, Supplementary Data 4). Consistent with previous studies<sup>2,12</sup>, the tumours clustered into three groups based on CNA frequency (Extended Data Fig. 2a), and CNA burden was a prognostic biomarker for biochemical recurrence (BCR) (Extended Data Fig. 2b). However, Chinese and Western prostate cancer exhibited some differences in CNA frequency (Fig. 2b, c). For example, *PABPC1* and *YWHAZ* were more often amplified in CPGEA (5.8% versus 0.88% in TCGA,  $P = 0.04$ , Pearson's  $\chi^2$  test), whereas *CHD1* was more often deleted (17.8% versus 4.4%,  $P = 3 \times 10^{-4}$ ) (Fig. 2d, Extended Data Fig. 2c, Supplementary Data 3). Known lesions in DNA repair pathways did not explain these patterns of structural variations<sup>24</sup>, but the *CHD1* deletion was associated with intra-chromosomal changes, reflecting its role in genome stability<sup>6</sup> (Extended Data Fig. 2d). These CNAs broadly influenced 12 oncogenic pathways (<http://www.cpgea.com>).

In addition, we detected 34,598 somatic structural variations, 5,144 of which were inter-chromosomal (Fig. 1, Extended Data Fig. 3a, b). The recently reported high-frequency structural variation involving an androgen receptor (AR) enhancer<sup>24,25</sup> was undetectable in our cohort, although whether it is present in more advanced, metastatic prostate cancer remains to be determined. We identified the mutational processes chromothripsis in 49% of our cohort (101 out of 208) and chromoplexy in 42% (87 out of 208), which was comparable to the rate identified in Western primary cancer (45%, PCAWG)<sup>6,26</sup> (Extended Data Fig. 3a, Supplementary Data 5). Finally, we identified potential driver events stemming from structural rearrangements (Extended Data Fig. 3c–e, Supplementary Data 5).

From the RNA-seq data, we detected 382 gene-to-gene fusions, 4 of which were previously reported in prostate cancer, 73 in other cancers,

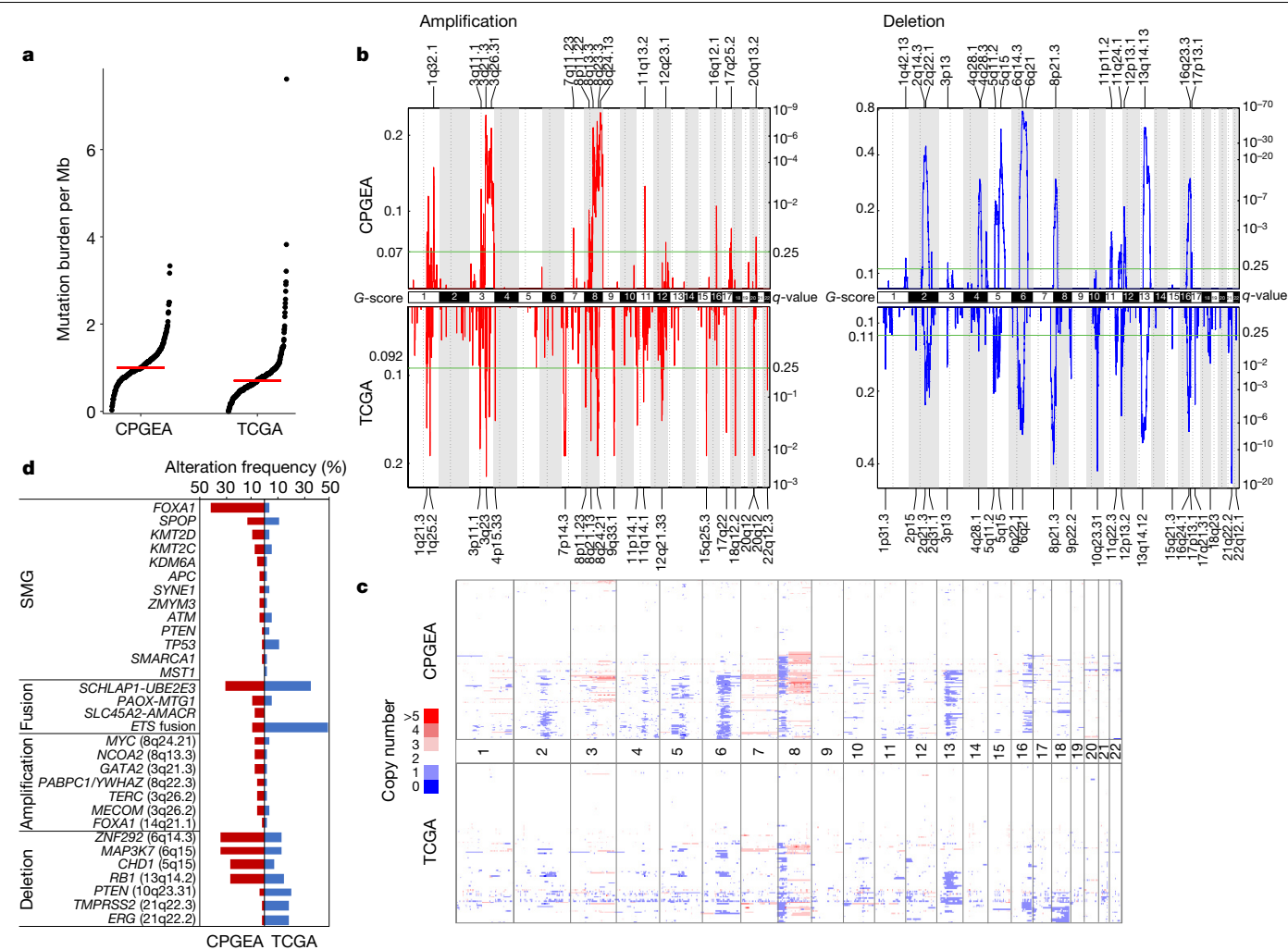


**Fig. 2 | The genomic alteration landscape in CPGEA and TCGA.**

**a**, Distribution of mutation burdens in each cohort. Each dot corresponds to a mutation burden calculated from a tumour–normal pair. The red horizontal bar indicates the median mutation burden for the CPGEA (1.00 per Mb) and TCGA (0.70 per Mb) cohorts. **b**, Genomic regions with significantly recurrent

somatic CNAs. **c**, Heat map showing genome-wide CNAs with estimated actual copy numbers. **d**, Gene-level alteration frequencies in CPGEA and TCGA. The same pipeline used for the CPGEA cohort was used to predict genomic alterations for the TCGA cohort from raw sequencing data.

and 305 of which were novel (Extended Data Fig. 4a). There were 71 inter-chromosomal fusions. We found support for 132 (34.6%) of the fusion candidates in matched WGS data, and validated 79 out of 88 selected candidates (90%) using Sanger sequencing (Extended Data Fig. 4b, Supplementary Data 6, <http://www.cpgea.com>). In stark contrast to Western prostate cancer, the hallmark ETS fusion (53%)<sup>2</sup> was much less frequent (9% of CPGEA tumours) (Fig. 2d, Extended Data Figs. 3a, 4c). Instead, the top gene fusions in Chinese prostate cancer were *SCHLAP1-UBE2E3* (29%) and *PAOX-MTG1* (10%) (Extended Data Fig. 4d). *SLC45A2-AMACR* was identified in 7% of CPGEA tumours, versus 15% in progressive prostate cancer<sup>27</sup> (Extended Data Fig. 4e). We also identified and validated a rare *SND1-BRAF* fusion<sup>28</sup> (Extended Data Fig. 4f).

We defined 83 significantly mutated genes in the CPGEA cohort, including *SPOP*, *FOXA1*, *KDM6A* and *ZMYM3*, as well as new prostate cancer driver genes (Extended Data Fig. 4g–i). There were 625 genes significantly differentially mutated between Chinese and Western primary prostate cancer (Extended Data Fig. 4j, Supplementary Data 3).

Finally, we defined the spectrum of noncoding mutations, obtaining 41,109 potentially functional noncoding single nucleotide variants (SNVs) (Extended Data Fig. 5a). Recurrent noncoding mutations occurred at a frequency comparable to that of driver coding mutations, and more than half were within regulatory elements, including 7.8% in

promoters and 54% in enhancers<sup>29</sup> (Extended Data Fig. 5b). Recurrent mutations targeted the enhancers of 184 genes, including *TBLIXR1*, *FOXA1* and *FLII* (Extended Data Fig. 5c–h, Supplementary Data 7). Noncoding mutations resulted in the gain or loss of binding sites for 20 or 97 transcription factors, respectively (Extended Data Fig. 5e, Supplementary Data 7). For example, the mutation associated with *TBLIXR1* disrupted a predicted NRF1-binding site, which correlated with lower expression of *TBLIXR1* in affected tumours (Extended Data Fig. 5f). However, although genome-wide association studies routinely suggest that most important variants are in noncoding regions, only mutations in the *TERT* promoter have been proven to drive cancer<sup>30</sup>. Despite state-of-the-art pipelines (Methods), we were also unable to confirm that any of the somatic noncoding mutations was a cancer driver. In agreement with PCAWG<sup>31,32</sup>, we conclude that a larger sample size and more sophisticated analytical paradigms are needed to comprehensively catalogue noncoding driver mutations, which are likely to have both a small and complex effect.

### **FOXA1 mutation in Chinese prostate cancer**

*FOXA1* is a pioneer factor that targets AR and has a demonstrated role in the oncogenesis of prostate cancer<sup>33</sup>. High levels of *FOXA1* are



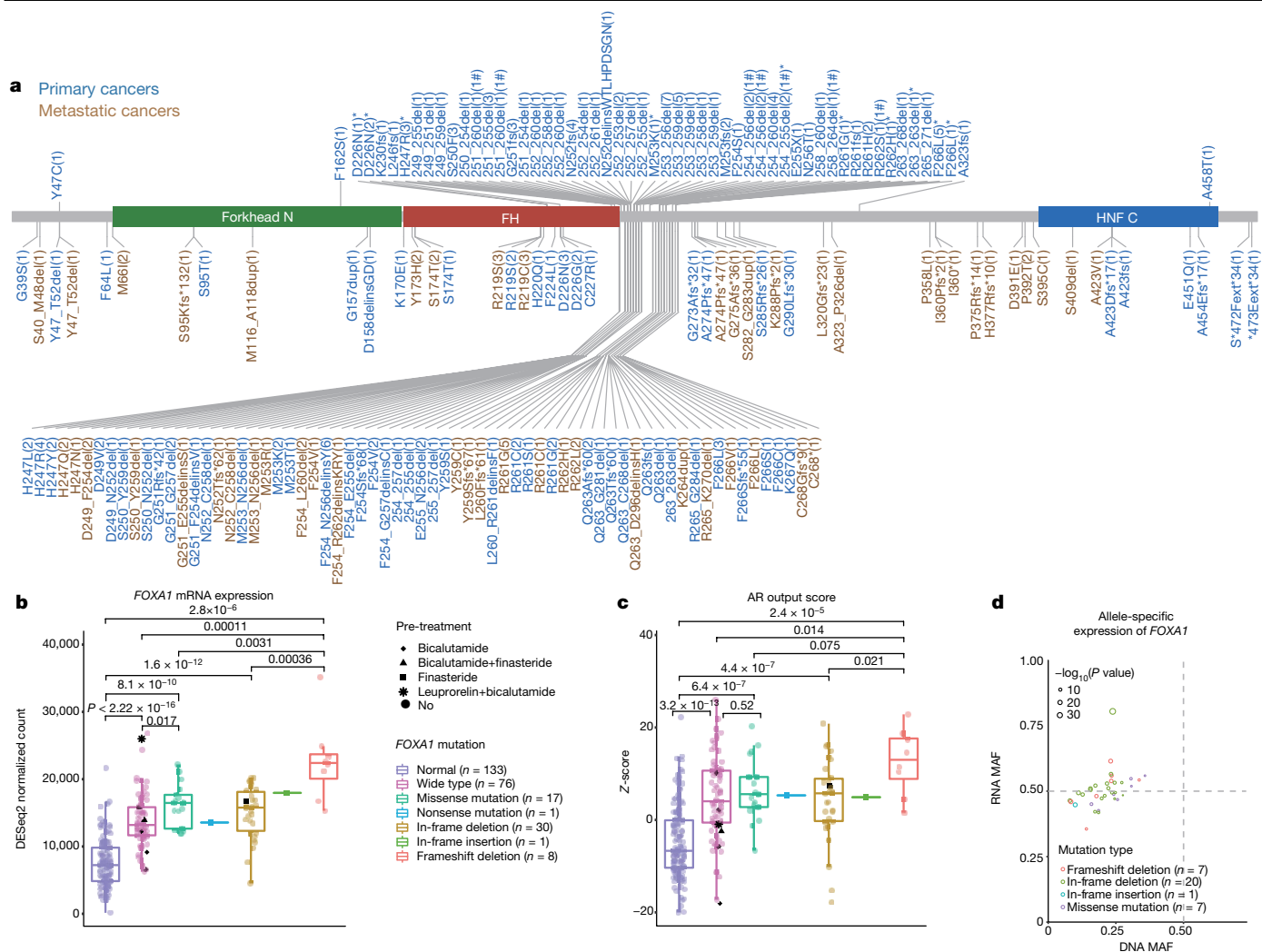


**Fig. 3 | FOXA1 mutations in CPGA. a**, Mirror distribution plot of FOXA1 somatic SNVs in CPGA primary (blue, top), Western primary (blue, bottom), and Western metastatic (orange, bottom) cancers. Asterisks indicate mutations found in both CPGA and Western cohorts. The hash symbol (#) indicates mutations also identified in a pre-treated CPGA patient. FH, forkhead. **b**, FOXA1 expression level as a function of FOXA1 mutation type.

associated with poor prognosis, whereas low FOXA1 levels, even in the presence of high AR expression, predict good prognosis<sup>34</sup>. Notably, FOXA1 was the most highly mutated gene in our Chinese cohort (41%) (Figs. 2d, 3a). By contrast, FOXA1 was mutated in only 4% of TCGA prostate cancer and in 8–9% of primary prostate cancer and 12–13% of metastatic prostate cancer<sup>2,6–15,35</sup> in other cohorts (Fig. 2d, Supplementary Data 3). In total, 26 of the CPGA FOXA1 mutations were missense and 63 were insertions or deletions (indels), 13 of which resulted in a frameshift (Fig. 3a, Supplementary Data 8). All were validated by Sanger sequencing and RNA-seq analysis (Extended Data Fig. 6a, Supplementary Discussion). Proteomic profiling of one tumour with a FOXA1 in-frame deletion detected a peptide confirming the deletion (Extended Data Fig. 6b).

The mutational spectrum of FOXA1 in tissue samples from Chinese and Western patients exhibited notable differences (Fig. 3a). In tissue samples from the Western cohort, mutations covered the entire coding sequence, although there was a hot spot immediately after the forkhead domain, which mediates DNA binding (Extended Data Fig. 6c). By contrast, almost all mutations in samples from the Chinese cohort occurred within the hot spot. This region may mediate the FOXA1–AR

interaction<sup>36</sup>, which suggests that FOXA1 mutations in Chinese patients may drive oncogenesis by modulating AR signalling.

Two recent studies characterized the molecular mechanism of many of the FOXA1 mutations found here, providing direct support for their oncogenic capacity<sup>37,38</sup>. Most missense and in-frame indel mutations were activating mutations that targeted the wing-2 region and enabled enhanced chromatin mobility and binding frequency. The frameshift mutations truncated the C-terminal domain and increased FOXA1 binding affinity, expanded the target site repertoire, and abolished the TLE3-mediated WNT pathway. All of the mutations promoted growth and enhanced FOXA1 binding to AR binding regions, while reducing AR binding. Accordingly, we observed higher FOXA1 expression in tumours with FOXA1 mutations than those with the wild-type gene (Fig. 3b). Tumours with FOXA1 frameshift deletions had the highest expression, which translated to the highest AR score<sup>2</sup> (Fig. 3c). In addition, FOXA1 mutant alleles were almost always more highly expressed than the wild-type allele in patients with both (Fig. 3d).

Consistent with its role as a pioneer factor, known FOXA1-binding regions remained hypomethylated in both normal tissue and tumours (Extended Data Fig. 6d). However, we also observed a statistically

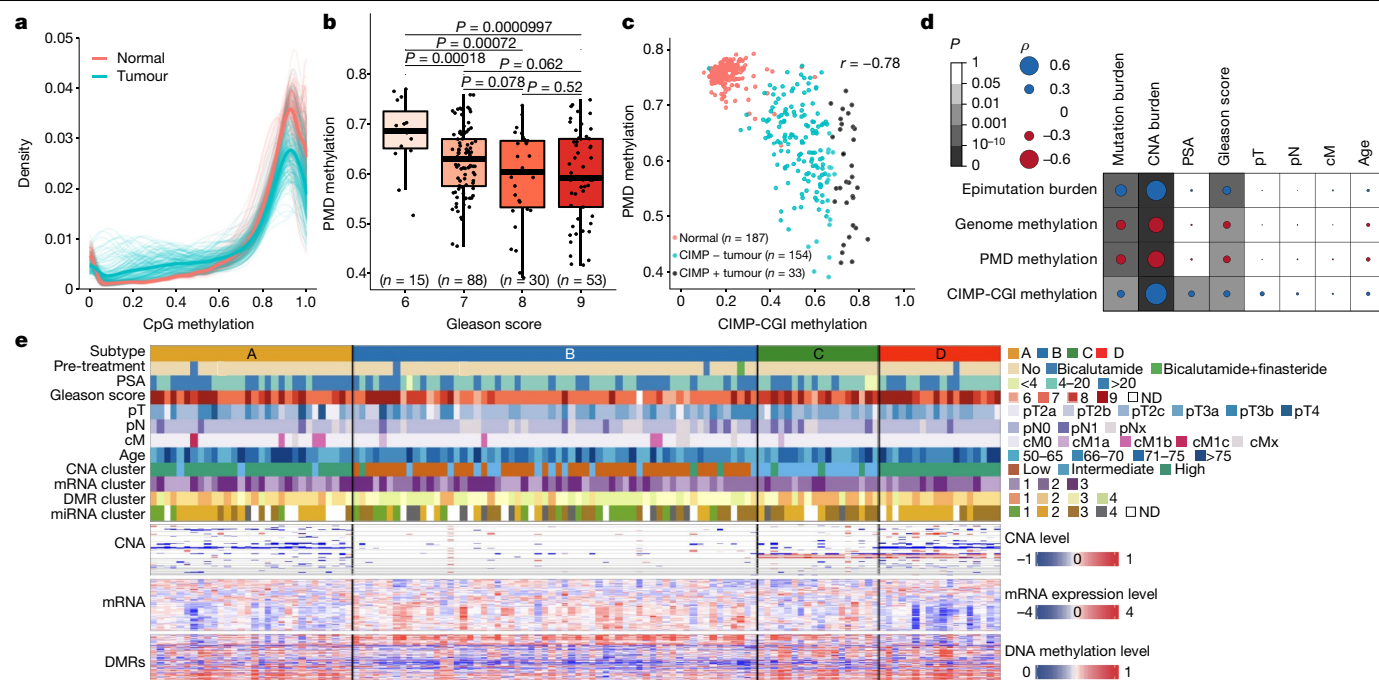


**Fig. 4 | DNA methylation abnormalities and subtypes of the CPGA prostate cancer cohort.** **a**, Distribution of CpG methylation levels in tumours and matched normal samples. Thin lines represent 187 pairs of normal and tumour samples; thick lines represent the average across each group. **b**, Average CpG methylation levels in PMDs as a function of Gleason score for each patient.  $P$  values determined by one-sided Mann-Whitney  $U$ -test. Box plots show median levels and the first and third quartiles, and whiskers show  $1.5 \times$  the interquartile range. Each dot indicates a tumour. **c**, Correlation of CIMP-CGI methylation with PMD methylation (Pearson's correlation

coefficient  $r = -0.78$ ,  $P = 8.8 \times 10^{-79}$ ). Each dot represents a sample. **d**, Correlations between epigenetic alterations and genetic alterations or clinicopathological features of tumours ( $n = 187$ ). Dot size and colour indicate the magnitude and direction of Spearman's rank order correlation coefficient  $\rho$ , respectively.  $P$  value indicated by background colour. **e**, CPGA prostate cancer subtyping. iClusterPlus integration of three techniques defined four molecular subtypes for Chinese prostate cancer. Clinical features (top) and molecular data for 126 tumours (rows) are displayed as heat maps.

significant reduction in DNA methylation in tumours with frameshift *FOXA1* deletions over *FOXA1* binding motifs that were normally hypermethylated and cryptic binding sites specific to mutated *FOXA1*<sup>38</sup>. These results suggest that specific *FOXA1* mutations could result in a gain-of-function oncogenic protein that potentially activates ectopic binding sites.

Most *FOXA1* mutations in Chinese prostate cancer were clonal based on the cancer cell fraction score<sup>39</sup> (Extended Data Fig. 6e–h), underscoring the likelihood that these mutations were driver events. We also examined the pairwise co-occurrence or mutual exclusivity of major genetic alterations using SELECT<sup>40</sup> (Supplementary Data 8). Notably, *FOXA1* was mutually exclusive with ETS fusions. We also found that *FOXA1* mutation significantly co-occurred with *CHD1* deletion and a *CECR7-IL17RA* gene fusion.

To dissect the downstream effects of *FOXA1* mutations, we examined differential gene activities based on *FOXA1* mutation patterns. For instance, the nicotinate and nicotinamide metabolism pathway was differentially expressed between the in-frame indel and missense groups (Extended Data Fig. 6i). Some differentially affected genes are directly implicated in metabolizing chemicals involved in androgen deprivation therapy<sup>41</sup>, such as *HSD17B6*, which catalyses the conversion of androstenediol to dihydrotestosterone. Expression of *HSD17B6* was much higher in tumours with missense *FOXA1* mutations than those with frameshift deletions. Thus, *FOXA1* mutation patterns might be an important indicator of the efficacy of androgen deprivation therapy.

## DNA methylation abnormalities

To complement our analysis of genetic alterations in prostate cancer, we profiled DNA methylation in the CPGA cohort using WGBS (Extended Data Fig. 7a). DNA methylation was profiled using probe arrays in TCGA,

such that our study represents the first, to our knowledge, joint analysis of genome-wide genetic mutation and epimutation rates in prostate cancer. As expected<sup>42,43</sup>, prostate cancer genomes were hypomethylated relative to normal prostate tissue (Fig. 4a, Extended Data Fig. 7b, Supplementary Discussion), and 5' untranslated regions (UTRs) and CpG islands (CGIs) were relatively hypermethylated, whereas exons, introns and repetitive elements were hypomethylated (Extended Data Fig. 7c, d). By contrast, non-CG methylation was negligible and exhibited no significant difference between normal tissue and tumours (Extended Data Fig. 7e).

Megabase-scale partially methylated domains (PMDs)<sup>42–44</sup> were widespread and accounted for the observed global hypomethylation, affecting up to half of the cancer genome (Extended Data Fig. 7f, g). One-third of these were recurrent in most tumours (Extended Data Fig. 7h). PMDs exhibited a significantly higher somatic mutation frequency and lower gene expression compared with non-PMD regions (Extended Data Fig. 7i, j). Notably, tumours with a Gleason score greater than six exhibited much lower levels of PMD methylation than those with a score of six (Fig. 4b), which suggests that tumour progression correlates with the degree of genome-wide hypomethylation.

We further defined local differentially methylation regions (DMRs), including 96,037 hypomethylated DMRs (hypoDMRs), 1.2% of which were recurrent (shared by at least 10 tumours), and 17,131 hypermethylated DMRs (hyperDMRs), 25% of which were recurrent (Extended Data Fig. 8a, b, Supplementary Discussion). Both sets were significantly enriched in promoters and enhancers (Extended Data Fig. 8c), with 19% and 44% of recurrent hypo- and hyperDMRs overlapping promoters, respectively (Extended Data Fig. 8d). Recurrent hyperDMRs were associated with genes involved in the regulation of development and cell fate, whereas hypoDMRs were associated with genes that were upregulated in prostate cancer, in human prostate adenocarcinoma

LNCAp cells, and in cells exposed to androgen (Extended Data Fig. 8e, f). Hypermethylated promoters silenced the expression of well-known tumour-suppressor genes, including miRNAs (Extended Data Fig. 8g). In total, 289 CGIs displayed significant hypermethylation consistent with the CpG island methylator phenotype (CIMP) (Extended Data Fig. 8h–j). Notably, the DNA methylation level of CIMP CGIs negatively correlated with the PMD methylation level (Fig. 4c). CIMP<sup>+</sup> tumours had a shorter BCR (Extended Data Fig. 8k).

Finally, we calculated the epimutation burden as the fraction of CpGs that were significantly differentially methylated between each tumour and its paired normal sample (0.013 to 0.45). The epimutation burden was positively correlated with mutation burden and CNA burden (Fig. 4d, Extended Data Fig. 8l, m). A concordance of genetic and epigenetic alterations was also observed during tumour evolution in individual patients<sup>45</sup>, and we now confirm this phenomenon across tumours in a large population.

### Molecular subtypes of Chinese prostate cancer

Next, we defined molecular subtypes for the CPGEA prostate cancer cohort. The seven molecular classes defined by TCGA using oncogenic drivers<sup>2</sup> were all present in the Chinese population, although at very different proportions (Extended Data Fig. 9a). Integrative analysis with iCluster on CNA, gene expression and DNA methylation data defined four subtypes within the CPGEA patients (Fig. 4e), three of which (subtypes B–D) correspond to subtypes identified by TCGA in Western populations (Extended Data Fig. 9b–e). Subtype A was unique to CPGEA and was characterized by numerous CNAs affecting genes, including *RB1*, *HDAC2* and *ZNF292*, which was previously associated with an ERG fusion-negative pattern<sup>46</sup>. Subtype A also exhibited high expression of AR and related pathways and was the only subtype with *ZNF365* mutations. Although *FOXA1* mutation did not segregate cleanly with any subtype, more than half of the patients in subtypes A (60%) and D (56%) had a *FOXA1* mutation, compared to 35% in subtype B and 44% in subtype C.

Clustering using individual data types mostly recapitulated the subtypes, including miRNA expression, which was not included in the integrative analysis (Fig. 4e, Extended Data Figs. 2a, 9f–h, Supplementary Discussion).

### Convergence on common oncogenic pathways

Genomic alterations are known to target common cancer pathways, even though component genes are not altered at equal frequency. We next compared the mutational landscape between Chinese and Western prostate cancer in a pathway-centric manner, focusing on 12 important pathways (Extended Data Fig. 10a–c, Supplementary Data 9, Supplementary Discussion, <http://www.cpgea.com>). The overall pathway-level mutation burden was similar between Chinese and Western primary tumours, whereas metastatic tumours exhibited a much higher burden (Extended Data Fig. 10d). Notably, although AR itself was unaltered in the CPGEA primary prostate cancer cohort, other genes in the AR pathway were altered in 61% of Chinese patients, versus 84% in Western metastatic prostate cancer, in which direct alterations of the AR gene dominate (Extended Data Fig. 10d). In addition, we observed repeated noncoding and epimutations in these pathways, supporting the paradigm that noncoding alterations can contribute to pathway-level differential expression (Extended Data Fig. 10e, <http://www.cpgea.com>). Despite different patient cohorts, experimental and sequencing technologies, and molecular alterations, the same key pathways emerged as crucial for prostate cancer in the Western and Chinese cohorts.

Although pathway disturbance could potentially explain 85.4% of the Chinese prostate cancer cases (Extended Data Fig. 10d), we identified few druggable pathways. Querying the OncoKB knowledge base<sup>47</sup>,

we found no level 1 or 2A potentially actionable alterations in either the Chinese or the Western cohorts. Only 5.3% of patients contained a lower level potentially actionable mutation (Extended Data Fig. 10f), highlighting the considerable challenge in treating this deadly disease.

### Conclusions

In this study, we present a comprehensive atlas of prostate cancer in Chinese men (CPGEA), which deepens our understanding of the disease by incorporating ethnic background. Comparative analysis of samples from CPGEA and Western cohorts revealed marked disparities in the mutational landscape of the same disease. Although ETS fusions have long been regarded as the flagship mutation for prostate cancer, our study indisputably positions *FOXA1* mutations as the most prominent signature in Chinese populations. The frequency and unique pattern of *FOXA1* mutations in Chinese prostate cancer underscores the need to investigate the oncogenic mechanism of individual mutations<sup>37,38,48,49</sup>, as well as factors that predispose Chinese individuals to them. In addition, a lack of targetable genetic mutations in either population suggests that future investigations should focus on understanding the tumorigenic potential of noncoding mutations, structural variations and epimutations and on translating this knowledge into therapeutic interventions. Answers to these questions could improve targeted therapy and prevention in the era of precision medicine while increasing global health equity.

### Online content

Any methods, additional references, Nature Research reporting summaries, source data, extended data, supplementary information, acknowledgements, peer review information; details of author contributions and competing interests; and statements of data and code availability are available at <https://doi.org/10.1038/s41586-020-2135-x>.

- Bray, F. et al. Global cancer statistics 2018: GLOBOCAN estimates of incidence and mortality worldwide for 36 cancers in 185 countries. *CA Cancer J. Clin.* **68**, 394–424 (2018).
- Cancer Genome Atlas Research Network. The molecular taxonomy of primary prostate cancer. *Cell* **163**, 1011–1025 (2015).
- Armenia, J. et al. The long tail of oncogenic drivers in prostate cancer. *Nat. Genet.* **50**, 645–651 (2018).
- Shoag, J. & Barbieri, C. E. Clinical variability and molecular heterogeneity in prostate cancer. *Asian J. Androl.* **18**, 543–548 (2016).
- Kimura, T. East meets West: ethnic differences in prostate cancer epidemiology between East Asians and Caucasians. *Chin. J. Cancer* **31**, 421–429 (2012).
- Baca, S. C. et al. Punctuated evolution of prostate cancer genomes. *Cell* **153**, 666–677 (2013).
- Barbieri, C. E. et al. Exome sequencing identifies recurrent *SPOP*, *FOXA1* and *MED12* mutations in prostate cancer. *Nat. Genet.* **44**, 685–689 (2012).
- Beltran, H. et al. Divergent clonal evolution of castration-resistant neuroendocrine prostate cancer. *Nat. Med.* **22**, 298–305 (2016).
- Fraser, M. et al. Genomic hallmarks of localized, non-indolent prostate cancer. *Nature* **541**, 359–364 (2017).
- Gao, D. et al. Organoid cultures derived from patients with advanced prostate cancer. *Cell* **159**, 176–187 (2014).
- Grasso, C. S. et al. The mutational landscape of lethal castration-resistant prostate cancer. *Nature* **487**, 239–243 (2012).
- Hieronymus, H. et al. Copy number alteration burden predicts prostate cancer relapse. *Proc. Natl Acad. Sci. USA* **111**, 11139–11144 (2014).
- Kumar, A. et al. Substantial interindividual and limited intraindividual genomic diversity among tumors from men with metastatic prostate cancer. *Nat. Med.* **22**, 369–378 (2016).
- Robinson, D. et al. Integrative clinical genomics of advanced prostate cancer. *Cell* **161**, 1215–1228 (2015).
- Taylor, B. S. et al. Integrative genomic profiling of human prostate cancer. *Cancer Cell* **18**, 11–22 (2010).
- Yuan, J. et al. Integrated analysis of genetic ancestry and genomic alterations across cancers. *Cancer Cell* **34**, 549–560.e9 (2018).
- Abida, W. et al. Prospective genomic profiling of prostate cancer across disease states reveals germline and somatic alterations that may affect clinical decision making. *JCO Precis. Oncol.* <https://doi.org/10.1200/PO.17.00029> (2017).
- Dall'Era, M. A., deVere-White, R., Rodriguez, D. & Cress, R. Changing incidence of metastatic prostate cancer by race and age, 1988–2015. *Eur. Urol. Focus* **5**, 1014–1021 (2019).
- Ren, S. et al. Whole-genome and transcriptome sequencing of prostate cancer identify new genetic alterations driving disease progression. *Eur. Urol.* **73**, 322–339 (2017).

20. Vogelstein, B. et al. Cancer genome landscapes. *Science* **339**, 1546–1558 (2013).
21. Alexandrov, L. B. et al. Signatures of mutational processes in human cancer. *Nature* **500**, 415–421 (2013).
22. Shen, M. M. & Abate-Shen, C. Molecular genetics of prostate cancer: new prospects for old challenges. *Genes Dev.* **24**, 1967–2000 (2010).
23. Tomlins, S. A. et al. Recurrent fusion of *TMPRSS2* and *ETS* transcription factor genes in prostate cancer. *Science* **310**, 644–648 (2005).
24. Quigley, D. A. et al. Genomic hallmarks and structural variation in metastatic prostate cancer. *Cell* **174**, 758–769.e9 (2018).
25. Viswanathan, S. R. et al. Structural alterations driving castration-resistant prostate cancer revealed by linked-read genome sequencing. *Cell* **174**, 433–447.e19 (2018).
26. Cortés-Ciriano, I. et al. Comprehensive analysis of chromothripsis in 2,658 human cancers using whole-genome sequencing. *Nat. Genet.* **52**, 331–341 (2020).
27. Yu, Y. P. et al. Novel fusion transcripts associate with progressive prostate cancer. *Am. J. Pathol.* **184**, 2840–2849 (2014).
28. Jang, J. S. et al. Common oncogene mutations and novel *SND1-BRAF* transcript fusion in lung adenocarcinoma from never smokers. *Sci. Rep.* **5**, 9755 (2015).
29. Fishilevich, S. et al. GeneHancer: genome-wide integration of enhancers and target genes in GeneCards. *Database (Oxford)* **2017**, bax028 (2017).
30. Huang, F. W. et al. Highly recurrent *TERT* promoter mutations in human melanoma. *Science* **339**, 957–959 (2013).
31. Rheinbay, E. et al. Analyses of non-coding somatic drivers in 2,658 cancer whole genomes. *Nature* **578**, 102–111 (2020).
32. Zhu, H. et al. Candidate cancer driver mutations in distal regulatory elements and long-range chromatin interaction networks. *Mol. Cell.* <https://doi.org/10.1016/j.molcel.2019.12.027> (2020).
33. Jozwik, K. M. & Carroll, J. S. Pioneer factors in hormone-dependent cancers. *Nat. Rev. Cancer* **12**, 381–385 (2012).
34. Sahu, B. et al. Dual role of FoxA1 in androgen receptor binding to chromatin, androgen signalling and prostate cancer. *EMBO J.* **30**, 3962–3976 (2011).
35. Espiritu, S. M. G. et al. The evolutionary landscape of localized prostate cancers drives clinical aggression. *Cell* **173**, 1003–1013.e15 (2018).
36. Gao, N. et al. The role of hepatocyte nuclear factor-3 alpha (Forkhead Box A1) and androgen receptor in transcriptional regulation of prostatic genes. *Mol. Endocrinol.* **17**, 1484–1507 (2003).
37. Adams, E. J. et al. *FOXA1* mutations alter pioneering activity, differentiation and prostate cancer phenotypes. *Nature* **571**, 408–412 (2019).
38. Parolia, A. et al. Distinct structural classes of activating *FOXA1* alterations in advanced prostate cancer. *Nature* **571**, 413–418 (2019).
39. McGranahan, N. et al. Clonal status of actionable driver events and the timing of mutational processes in cancer evolution. *Sci. Transl. Med.* **7**, 283ra54 (2015).
40. Mina, M. et al. Conditional selection of genomic alterations dictates cancer evolution and oncogenic dependencies. *Cancer Cell* **32**, 155–168.e6 (2017).
41. Ishizaki, F. et al. Androgen deprivation promotes intratumoral synthesis of dihydrotestosterone from androgen metabolites in prostate cancer. *Sci. Rep.* **3**, 1528 (2013).
42. Berman, B. P. et al. Regions of focal DNA hypermethylation and long-range hypomethylation in colorectal cancer coincide with nuclear lamina-associated domains. *Nat. Genet.* **44**, 40–46 (2011).
43. Hansen, K. D. et al. Increased methylation variation in epigenetic domains across cancer types. *Nat. Genet.* **43**, 768–775 (2011).
44. Hon, G. C. et al. Global DNA hypomethylation coupled to repressive chromatin domain formation and gene silencing in breast cancer. *Genome Res.* **22**, 246–258 (2012).
45. Mazar, T. et al. DNA methylation and somatic mutations converge on the cell cycle and define similar evolutionary histories in brain tumors. *Cancer Cell* **28**, 307–317 (2015).
46. Xiao, Q. et al. Systematic analysis reveals molecular characteristics of ERG-negative prostate cancer. *Sci. Rep.* **8**, 12868 (2018).
47. Chakravarty, D. et al. OncoKB: a precision oncology knowledge base. *JCO Precis. Oncol.* <https://doi.org/10.1200/PO.17.00011> (2017).
48. Xu, B. et al. Altered chromatin recruitment by *FOXA1* mutations promotes androgen independence and prostate cancer progression. *Cell Res.* **29**, 773–775 (2019).
49. Gao, S. et al. Forkhead domain mutations in *FOXA1* drive prostate cancer progression. *Cell Res.* **29**, 770–772 (2019).

**Publisher's note** Springer Nature remains neutral with regard to jurisdictional claims in published maps and institutional affiliations.

© The Author(s), under exclusive licence to Springer Nature Limited 2020

<sup>1</sup>Department of Urology, Changhai Hospital, Second Military Medical University, Shanghai, China. <sup>2</sup>Center for Translational Medicine, Second Military Medical University, Shanghai, China. <sup>3</sup>Shanghai Key Laboratory of Cell Engineering, Shanghai, China. <sup>4</sup>Department of Genetics, Washington University School of Medicine, St Louis, MO, USA. <sup>5</sup>The Edison Family Center for Genome Sciences and Systems Biology, Washington University School of Medicine, St Louis, MO, USA. <sup>6</sup>Novogene Co, Ltd, Beijing, China. <sup>7</sup>Department of Pathology, Changhai Hospital, Second Military Medical University, Shanghai, China. <sup>8</sup>CAS Key Laboratory of Tissue Microenvironment and Tumor, Shanghai Institute of Nutrition and Health, Shanghai Institutes for Biological Sciences, University of Chinese Academy of Sciences, Chinese Academy of Sciences, Shanghai, China. <sup>9</sup>Department of Urology, Changzheng Hospital, Second Military Medical University, Shanghai, China. <sup>10</sup>Department of Radiology, Changhai Hospital, Second Military Medical University, Shanghai, China. <sup>11</sup>Department of Urology, First Affiliated Hospital, College of Medicine, Zhejiang University, Hangzhou, China. <sup>12</sup>State Key Laboratory of Reproductive Medicine and Department of Urology, the First Affiliated Hospital of Nanjing Medical University, Nanjing, China. <sup>13</sup>Department of Urology, Institute of Surgery Research, Daping Hospital, Third Military Medical University, Chongqing, China. <sup>14</sup>Department of Histology and Embryology, Second Military Medical University, Shanghai, China. <sup>15</sup>Department of Urology, First Affiliated Hospital of Anhui Medical University, Hefei, China. <sup>16</sup>Department of Urology, First Affiliated Hospital of Soochow University, Suzhou, China. <sup>17</sup>Department of Urology, Xuzhou Central Hospital, The Affiliated Xuzhou Hospital of Medical College of Southeast University, Xuzhou, China. <sup>18</sup>Department of Urology, Zhongda Hospital, Southeast University, Nanjing, China. <sup>19</sup>Department of Urology, Gongli Hospital, Second Military Medical University, Shanghai, China. <sup>20</sup>Department of Urology, Zhejiang Provincial People's Hospital, Hangzhou Medical College, Hangzhou, China. <sup>21</sup>Department of Urology Institute of Shenzhen University, Shenzhen Luohu People's Hospital, Shenzhen, China. <sup>22</sup>Department of Urology, First Affiliated Hospital of Zhengzhou University, Zhengzhou, China. <sup>23</sup>Department of Urology, Shaoxing Central Hospital, Shaoxing, China. <sup>24</sup>Department of Urology, Shishi Hospital, Shishi, China. <sup>25</sup>Department of Urology, The Affiliated Hospital of Hebei University, Baoding, China. <sup>26</sup>Department of Urology, Huadong Hospital, Fudan University, Shanghai, China. <sup>27</sup>Department of Urology, Tongji Hospital, Tongji Medical College Huazhong University of Science and Technology, Wuhan, China. <sup>28</sup>These authors contributed equally: Jing Li, Chuanliang Xu, Hyung Joo Lee. <sup>29</sup>These authors jointly supervised this work: Xu Gao, Ting Wang, Yinghao Sun. <sup>✉</sup>e-mail: gaoxu.changhai@foxmail.com; twang@wustl.edu; sunyhsmmu@126.com



# Article

## Methods

### Data reporting

No statistical methods were used to predetermine sample size. The experiments were not randomized, and investigators were not blinded to allocation during experiments and outcome assessment.

### Pathological evaluation of specimens

The CPGEA project was initiated in 2010. Ethical committee approval was obtained from Changhai Hospital (TMEC2014-001). Written informed consent was obtained in accordance with Chinese legislation. In total, 210 prostate tumour samples and non-cancerous matched healthy prostate tissue were collected from patients surgically treated in the Urology Department of Changhai Hospital. All samples were immediately frozen in liquid nitrogen and stored at  $-80^{\circ}\text{C}$ . Thin slices of snap-frozen, OCT-embedded tissue blocks were sent for haematoxylin and eosin (H&E) staining. After independent review by two professional uropathologists (Y. Yu and Y. Zhu), DNA and RNA were extracted from the same tissue blocks. Gleason score, tumour purity, extraprostatic extension, surgical margin and seminal vesicles were all evaluated according to EAU guidelines ([https://uroweb.org/wp-content/uploads/09-Prostate-Cancer\\_2017\\_web.pdf](https://uroweb.org/wp-content/uploads/09-Prostate-Cancer_2017_web.pdf)).

All patient clinical information was deposited in our follow-up database PC-Follow<sup>50</sup>. The concentrations of PSA ( $\text{ng ml}^{-1}$ ) in serum for each patient were measured at the time of diagnosis. We used the pathological T and N categories and the clinical M category to assign final stage information to each patient using standard National Comprehensive Cancer Network (NCCN) criteria ([http://www.nccn.org/professionals/physician\\_gls/pdf/prostate.pdf](http://www.nccn.org/professionals/physician_gls/pdf/prostate.pdf)). BCR was defined as a rise in the blood level of PSA to two consecutive measurements of  $0.2 \text{ ng ml}^{-1}$  or greater after treatment with surgery or radiation. Bone metastases were defined using emission computed tomography (ECT). Detailed clinicopathological data are available in Supplementary Data 2. All tumours with metastases were hormone-sensitive.

### DNA and RNA isolation, quantification and qualification

Genomic DNA was isolated using the Qiagen MinElute Kit. Quality was verified by the following two methods: (1) DNA degradation and contamination were monitored on 1% agarose gels; (2) DNA concentration was measured using the Qubit DNA Assay Kit and a Qubit 2.0 Fluorometer (Life Technologies).

RNA was isolated in TRIzol reagent. Quality was verified by the following four methods: (1) RNA degradation and contamination was monitored on 1% agarose gels; (2) RNA purity was checked using the NanoPhotometer spectrophotometer (IMPLEN); (3) RNA concentration was measured using the Qubit RNA Assay Kit and a Qubit 2.0 Fluorometer (Life Technologies); (4) RNA integrity was assessed using the RNA Nano 6000 Assay Kit and the Bioanalyzer 2100 system (Agilent Technologies).

### WGS library generation

A total of  $0.5 \mu\text{g}$  of genomic DNA per sample was used as input material for library preparation. Sequencing libraries were generated using the TruSeq Nano DNA HT Sample Prep Kit (Illumina) following manufacturer's recommendations, and index codes were added to each sample. In brief, genomic DNA was fragmented by sonication to a median size of 350 bp. Then, DNA fragments were end-repaired, A-tailed, and ligated with the full-length Illumina sequencing adapters, followed by further PCR amplification. PCR products were purified (AMPure XP system), and libraries were analysed for size distribution using an Agilent Bioanalyzer 2100 and quantified via real-time PCR.

### WGBS library generation

A total of  $5.2 \mu\text{g}$  of genomic DNA per sample plus 26 ng of spiked-in lambda DNA were fragmented via sonication to 200–300 bp with a

Covaris S220, followed by end repair and A-tailing. Cytosine-methylated barcodes were ligated to sonicated DNA as per manufacturer's instructions. DNA fragments were then treated twice with bisulphite using the EZ DNA Methylation-Gold Kit (Zymo Research), and the resulting single-stranded DNA fragments were PCR amplified using KAPA HiFi HotStart Uracil + ReadyMix ( $2\times$ ). Library concentration was quantified using a Qubit 2.0 Fluorometer (Life Technologies) and quantitative PCR, and the insert size was assayed on an Agilent Bioanalyzer 2100 system.

### RNA-seq library generation

A total of  $2 \mu\text{g}$  of RNA per sample was used as input material. Ribosomal RNA was removed using an Epicentre Ribo-zero rRNA Removal Kit (Epicentre), and rRNA-free residue was cleaned up via ethanol precipitation. Subsequently, sequencing libraries were generated using the rRNA-depleted RNA using a NEBNext Ultra Directional RNA Library Prep Kit for Illumina (NEB) following manufacturer's recommendations. In brief, fragmentation was carried out using divalent cations under elevated temperature in the NEBNext First Strand Synthesis Reaction Buffer ( $5\times$ ). First strand cDNA was synthesized using random hexamer primers and M-MuLV Reverse Transcriptase (RNase H minus). Second-strand cDNA synthesis was subsequently performed using DNA polymerase I and RNase H. In the reaction buffer, dNTPs with dTTP were replaced by dUTP. Remaining overhangs were converted into blunt ends via exonuclease/polymerase treatment. After 3' adenylation, NEBNext Adaptors with a hairpin loop structure were ligated to the DNA fragments to prepare for hybridization. To preferentially select cDNA fragments of 150–200 bp, the library fragments were purified using an AMPure XP system (Beckman Coulter). Size-selected, adaptor-ligated cDNA was treated with  $3 \mu\text{l}$  of USER Enzyme (NEB) at  $37^{\circ}\text{C}$  for 15 min followed by 5 min at  $95^{\circ}\text{C}$  before PCR. PCR was performed with Phusion High-Fidelity DNA polymerase, Universal PCR primers, and Index (X) Primer. At last, products were purified (AMPure XP system), and library quality was assessed on the Agilent Bioanalyzer 2100 system.

### miRNA-seq library generation

A total of  $3 \mu\text{g}$  of total RNA per sample was used as input material for a small RNA library. Sequencing libraries were generated using the NEBNext Multiplex Small RNA Library Prep Set for Illumina (NEB) following manufacturer's recommendations, and index codes were added to associate sequences with each sample. In brief, 3' SR Adaptor (NEB) was ligated to the 3' end of small RNA. The SR RT Primer (NEB) was hybridized to excess 3' SR adaptor, and the 5' end adaptor was then ligated. First-strand cDNA was synthesized using M-MuLV Reverse Transcriptase (RNase H minus). PCR amplification was performed using LongAmp Taq  $2\times$  Master Mix, SR Primer for Illumina, and Index (X) primer. PCR products were purified on an 8% polyacrylamide gel (100 V, 80 min). DNA fragments corresponding to 140–160 bp (the length of a small noncoding RNA plus the 3' and 5' adaptors) were recovered and dissolved in  $8 \mu\text{l}$  of elution buffer. Finally, library quality was assessed on the Agilent Bioanalyzer 2100 system using DNA High Sensitivity Chips.

### Generation of sequencing data and quality control

Clustering of the indexed samples was performed on a cBot Cluster Generation System using a HiSeq X PE Cluster Kit V2.5 (Illumina) according to the manufacturer's instructions. WGS (208 tumour/normal sample pairs), WGBS (187 pairs), and RNA-seq (134 pairs) libraries were sequenced on the Illumina HiSeq X TEN platform ( $2\times 150$ -bp paired-end reads). 50-bp single-end reads for miRNA-seq (105 tumour and normal sample pairs) were also generated on the Illumina HiSeq X TEN platform.

Read pairs were discarded if (1) either read contained adaptor sequences ( $>10$  nucleotides aligned to the adaptor, allowing  $\leq 10\%$  mismatches); (2) either read contained more than 10% uncertain bases; or (3) either read contained more than 50% low quality bases (Phred quality  $< 5$ ). The following statistics were calculated (and are

available at <http://www.cpgea.com>): total number of reads; sequencing error rate; percentage of reads with average quality score > 20; percentage of reads with average quality score > 30; and GC content distribution.

### WGS processing

Sequencing reads were aligned to the Human Genome Reference Consortium build 38 (GRCh38) using BWA v.0.7.8 (BWA-mem). Unaligned reads that passed Illumina's quality filter (PF reads) were retained. We used the 'Picard' pipeline (<http://broadinstitute.github.io/picard>) to combine data from multiple libraries and flow cell runs into a single BAM file per sample. Only uniquely aligned, de-duplicated reads were used in subsequent analyses. Quality scores were recalibrated using the Genome Analysis Toolkit (GATK) Table Recalibration tool. All sites potentially containing small insertions or deletions in either the tumour or the matched normal were realigned using GATK. The sample cross-individual contamination levels were estimated using the Conpair program<sup>51</sup>. A total of 208 tumour–normal pairs from samples with contamination less than 5% (maximum 4.7%, minimum 0.4%) were included in downstream analysis.

### WGBS processing

FastQC v.0.11.5 was used to estimate the quality of the raw reads. Reads were pre-processed with Trimmomatic v.0.36 using the parameters (SLIDINGWINDOW:4:15 LEADING:3 TRAILING:3 ILLUMINACLIP:adaptor.fa:2:30:10 MINLEN:36). Reads that passed all filtering steps were considered clean reads, and all subsequent analyses were performed on those reads. FastQC was used to perform basic statistics on the quality of the clean reads.

Bismark<sup>52</sup> v.0.16.3 was used to align bisulphite-treated reads to a human bisulfite-converted reference genome (-X 700 --dovetail). The human reference genome was first transformed into a bisulfite-converted version (C-to-T and G-to-A converted) and then indexed using bowtie2<sup>53</sup>. Sequence reads were also transformed into fully bisulfite-converted versions before they were aligned to the genome in a directional manner. Reads that produced a unique best alignment from the two alignment processes (original top and bottom strand) were then compared to the normal genomic sequence, and the methylation state of each cytosine position in the read was inferred. Reads aligned to the same genomic region were considered duplicates, and sequencing depth and coverage were summarized using de-duplicated reads.

Methylation extractor results (bismark\_methylation\_extractor --no\_overlap) were converted to bigWig format for visualization using the IGV browser. The bisulfite conversion rate was calculated as the percentage of thymine sequenced at cytosine reference positions in the lambda genome.

### RNA-seq processing

RNA-seq reads were aligned to the Ensembl reference genome and gene model annotation files (release 84, [http://ftp.ensembl.org/pub/release-84/fasta/homo\\_sapiens/dna/](http://ftp.ensembl.org/pub/release-84/fasta/homo_sapiens/dna/) and [http://ftp.ensembl.org/pub/release-84/gtf/homo\\_sapiens/](http://ftp.ensembl.org/pub/release-84/gtf/homo_sapiens/)). A reference genome index was built using Bowtie v.2.0.6<sup>53</sup>, and paired-end clean reads were aligned to the reference genome using TopHat v.2.0.9<sup>54</sup>.

Raw count data per gene was calculated using HTSeq<sup>55</sup>. The raw count matrix was then used by DESeq2<sup>56</sup> to quantify gene expression level as normalized counts. Cuffdiff<sup>57</sup> was used to detect differentially expressed genes between tumours and normal samples<sup>58</sup>. Transcripts with an adjusted  $P < 0.05$  were considered differentially expressed.

### miRNA-seq processing

High-quality, 18–35-bp miRNA-seq reads were aligned to the reference genome using bowtie v.1.0.1. Aligned small RNA tags were matched to the known reference miRNA database, miRBase20.0, using mirdeep2 v.1.1<sup>59</sup> with the following modified parameters: -i -r -M -m -k -p 10 -g

50000. srna-tools-cli was then used to obtain the potential miRNA and to draw the secondary structures. Small RNA tags originating from protein-coding genes, repeat sequences, rRNA, tRNA, small nuclear RNA and small nucleolar RNA were removed by mapping tags to RepeatMasker v.4.0.3 (-species -nolow -no\_is -norna -pa 8), Rfam database. Known miRNA expression levels were estimated as TPM using the formula: normalized expression = (mapped read counts)/(total reads) × 1,000,000.

### Mutation calling

The GATK HaplotypeCaller<sup>60</sup> was used to perform germline mutation calling. Somatic SNVs were detected using MuTect<sup>61</sup> v.1.1.4. A minimum of five variant-containing reads and a variant allele frequency (VAF) ≥ 0.04 in the tumour were required for mutation calling. In addition, we used the 208 matched normal samples from this study to build the panel of normals (PoNs) and removed any mutation with a corresponding alternate allele appearing in >1 PoN samples. Further filtering was performed using the fpfilter.pl script (<https://github.com/ckandoth/variant-filter>) with default parameters and a VAF threshold of 4%.

Because MuTect cannot call somatic indels, somatic indels were detected using Strelka<sup>62</sup> and Mutect2<sup>61</sup>. Only indels agreed on by both tools were retained. A minimum of five variant-containing reads and VAF ≥ 0.04 in the tumour were required for mutation calling. Any indel appearing in more than 1 PoN samples was removed. In total, 1,167,497 somatic mutations were included in our final set.

ANNOVAR<sup>63</sup> was used to annotate VCF (variant call format) files. To ensure that no candidate driver mutations were mistakenly removed by the post-processing filtering, candidate mutations in previously implicated cancer genes were manually reviewed using the IGV browser<sup>64</sup>.

### Mutation burden and substitution rate

Mutation burden was defined as the total number of non-synonymous somatic coding mutations within exonic regions (36 Mb for CPGEA and 32.7 Mb for TCGA). Non-synonymous mutations were defined as missense, nonsense and nonstop mutations; splice site mutations; frameshift deletions and insertions; and in-frame deletions and insertions. The substitution rate was calculated as the number of somatic variants across the entire genome (3,257,319,537 bp), including coding and noncoding regions. Outliers (T13 and T502) were not included in substitution rate and mutation burden calculations.

### Somatic CNA detection

Control-FREEC<sup>65</sup> v.6.7 was used to detect genomic segments with somatic CNAs from matched normal and tumour WGS mapped data. Genomic segments with frequent germline CNVs or intersecting black-list regions<sup>66</sup> were filtered out. The GISTIC2<sup>67</sup> algorithm was used to detect recurrently amplified or deleted genomic regions with the following modified parameters: -ta 0.2 -td 0.2 -js 100 -broad 1 -brlen 0.7 -conf 0.95 -genegistic 1 -savegene 1. In chromosome arm level analysis, chromosomal arms were considered altered if at least 60% of the arm was lost or gained with a relative log<sub>2</sub>-transformed copy number change > 0.1. The CNV level for all genes was extracted from the GISTIC output files (all\_threshold\_by\_genes) using a cutoff of ± 2.

### CNA clustering, CNA burden and BCR

Tumours were clustered based on chromosome arm-level alterations identified by GISTIC. Hierarchical clustering was performed in R based on Euclidean distance using Ward's method. To calculate CNA burden, the total genomic length of CNA segments was summed and divided by the total genomic length of the autosomal chromosomes per tumour. The mean CNA burden of 11.28% was used to stratify the patients as described<sup>12</sup>. Biochemical recurrence-free survival was calculated from the date of surgery to the date of diagnosis of biochemical

recurrence. Differences in the BCR of patients in the two CNA burden groups were assessed using Kaplan–Meier analysis followed by a log-rank test.

## Somatic structural variation detection and validation

To accurately detect somatic breakpoints, we used the MeerKat software with default parameters<sup>68</sup>. The set of structural variant calls from each tumour was filtered by the calls from its matched normal to remove germ-line variants, as described<sup>68</sup>.

Recurrent structural variation events affecting important genes were chosen for validation. The primers were designed using MeerKat's primers.pl function. Sanger sequencing was performed on PCR products, and the reads were mapped to the SV breakpoints using UCSC's BLAT tool. The validation process is described in detail in the supporting website (<http://www.cpgea.com>).

## Evaluation of chromothripsis and chromoplexy

Chromothripsis was evaluated by Shatterseek (<https://github.com/parklab/ShatterSeek>). Chromoplexy was evaluated by ChainFinder v.1.0.1<sup>6</sup> using a deletion threshold of 0.278 and a significance threshold of 0.05. The presence of chromoplexy was defined by the presence of a chromoplexy chain connecting at least three chromosomes.

## Fusion detection

Fusion gene refers to the event in which partial or complete sequences of two individual genes are fused together and result in a chimeric gene, usually caused by chromosomal translocation. We used SOAPfuse<sup>69</sup> v.1.27 software to detect and analyse fusion genes. SOAPfuse filtering was applied with default parameters: junction reads = 1 and split reads = 1. In addition, the junction location and whether it was an in-frame or out-of-frame fusion were considered. To remove fusion genes present in normal samples, all fusion genes detected by SOAPfuse in normal samples were merged together into a PoN. If a fusion breakpoint from a tumour sample was detected in the PoN, the corresponding fusion was removed. We compared fusion candidates to public fusion databases including FusionHub<sup>70</sup> and Oncofuse<sup>71</sup>, and annotated them in Supplementary Data 6.

The MeerKat fusions.pl module was used to call fusions using WGS structural variation data, and the results were used to estimate the proportion of fusion candidates that resulted from genomic structural variation events.

## Fusion RT–PCR validation

cDNA was synthesized from 300 ng of RNA using SuperScript II reverse transcriptase (Life Technologies) according to the manufacturer's instructions. Primer sequences for fusion validations are listed in the supporting website (<http://www.cpgea.com>). Reverse transcription PCR (RT–PCR) was performed using standard protocols, after which products were visualized on a 1.2% agarose gel and purified using BigDye Terminator v.3.1 Cycle Sequencing Kits (Life Technologies).

## Genes associated with structural variation, and intersection of breakpoints with topologically associating domains

The nearest-gene method was used to identify candidate genes affected by two different breakpoints. New structural variation events were identified in our cohort using the following method. First, events were categorized based on the location of the two breakpoints (Extended Data Fig. 3d): (1) tier 1, the two breakpoints hit the same gene (defined as 5' UTR, promoter, coding exon, intron, or 3' UTR); (2) tier 2, the two breakpoints hit two different genes; (3) tier 3, the first breakpoint hit a gene, and the second hit the intergenic region. If the gene was the closest gene to the second breakpoint within a 100-kb region, then the structural variation was categorized as tier 3.1. If the closest gene was another gene, the variation was categorized as tier 3.2. If the nearest was an enhancer, the variation was categorized as tier 3.3; (4) tier 4, the

two breakpoints both hit the intergenic region. If one of the nearest genes was located within 100 kb, it was categorized as tier 4.1. If both were within 100 kb, it was categorized as tier 4.2. If the nearest genomic features for both breakpoints were enhancers, it was categorized as tier 4.3. If one was close to an enhancer and the other was close to a gene, it was categorized as tier 4.4. If one was located in an enhancer and the other was at least 100 kb away from any gene, then it was categorized as tier 4.5; and (5) tier 5, the two breakpoints were at least 100 kb from any gene. These annotations were used to look for functional events related to structural variation, such as enhancer hijacking and disruption of topologically associating domains (TADs).

The TAD definitions for the LNCaP cell line were downloaded from <http://promoter.bx.psu.edu/hi-c/publications.html>. We intersected our structural variation breakpoints with TAD assignments. Structural variation events with breakpoints located in different TADs were considered potential candidates for destroying the TAD boundary. The expression level of genes within the TADs was compared between tumours with and without the structural variation event (Extended Data Fig. 3c).

## Detection of significantly mutated genes

To identify driver mutations and genes, we adopted previously described methods<sup>72,73</sup>. For mutation calling, we used the classic GATK toolbox and annotated mutations using ANNOVAR, as described in 'Mutation calling'. After filtering for artefacts and defining a final set of mutations, the MAF was analysed to determine significantly mutated genes (SMGs). This was accomplished using the MutSigCV<sup>61</sup> and MuSiC<sup>74</sup> algorithms based on 206 samples<sup>72,73</sup>. Two outliers were not included in this analysis. For the MuSiC SMG test, genes with an FDR < 0.2 in two out of three tests were retained. For MutSigCV,  $q < 0.01$  was used as a cut-off value. We carefully curated the SMGs in our study as follows. We compiled a blacklist according to the MutSigCV paper<sup>75</sup>. Furthermore, genes were removed if they had an average reads per kilobase per million reads (RPKM) value less than 1.5. In our study, we not only compared our SMGs to those previously reported in 12 large Western cohorts, but also to two expert-curated databases (1,086 consensus cancer genes from Cancer Gene Census (CGC)<sup>76</sup> and OncoKB<sup>47</sup>).

## Comparison of mutation landscapes across cohorts of prostate cancer

From 14 previous prostate cancer studies (13 Western cohorts and 1 Chinese cohort), we compiled a total of 2,641 non-redundant tumours, including 1,656 primary tumours and 880 metastatic tumours. In addition, 54 samples were prostate neuroendocrine carcinoma. We excluded 8 cell lines, 8 xenografts, and 35 samples with unclear definition. Metadata for the Western cohorts is presented in Supplementary Data 1, and all codes are provided at <http://www.cpgea.com>. For CPGEA, 206 samples were used, excluding 2 outliers.

For mutations in protein-coding genes, non-synonymous coding mutations were counted per tumour and then divided into primary, metastatic or neuroendocrine subsets based on sample metadata. A Pearson's  $\chi^2$  test was used to evaluate the difference in mutation frequencies. The Benjamini–Hochberg method was used to correct P values.

For gene-level CNA comparisons, we converted gene IDs into the consistent gene symbol by removing duplicated and nonsense symbols. Eleven Western cohorts were used in this analysis (CPCG-2017 does not have CNA data). In addition, 208 CPGEA tumours and 114 TCGA WGS datasets were processed using the CPGEA pipeline and included in the comparison. For the cases used in several studies, we kept only one result. In total, 1,326 primary, 868 metastatic, and 54 neuroendocrine prostate tumours were included in the comparison of gene-level amplification and deletion frequencies. GISTIC2 was also used to identify recurrent CNA genomic lesions. The CNA status of all genes was extracted from the GISTIC output files (all\_threshold\_by\_genes) using a cutoff of  $\pm 2$ . We annotated CNAs found both in CPGEA and in

any Western cohort as 'recurrent 1', and CNAs found more than twice in the Western cohorts but not in CPGEA as 'recurrent 2'. We annotated CNAs found only in CPGEA as 'novel'. These annotations can be found in the column 'class' in Supplementary Data 3. A Pearson's  $\chi^2$  test was used to evaluate differences in CNA frequency. The Benjamini–Hochberg method was used to correct *P* values. We also annotated the genes with the CGC; OncoKB, which called oncogenes and tumour-suppressor genes; and pathways curated from the literature. SMGs detected in this study were also annotated. The CNA circos plot includes 225 genes that were significantly altered between CPGEA and Western primary tumours ( $P < 0.01$ ) and that were either SMGs or annotated by the CGC or OncoKB databases.

### Noncoding mutation detection

We used FunSeq2<sup>77</sup> to detect recurrent noncoding mutations. FunSeq2 prioritizes noncoding mutations based on their relative location within regulatory elements, nucleotide-level affect, conservation, potential target gene, and recurrence across cancer samples. After choosing noncoding SNVs with a FunSeq2 score  $\geq 1.5$ , we applied hotspot analysis, regional recurrence analysis, and transcription factor motif analysis<sup>78</sup> to the 41,109 potentially functional somatic noncoding SNVs, following previously described methods<sup>79</sup> (Extended Data Fig. 5).

### AR output score of FOXA1-mutant tumours

The AR output score was calculated as previously described<sup>2</sup>. In brief, z-scores for 20 androgen-induced genes were computed by subtracting the pooled mean from the RNA-seq expression values and dividing by the pooled standard deviation. The sum of the z-scores for the AR signalling gene signature represents the AR output score for each sample.

### Allele-specific expression of FOXA1

For SNP mutations, WGS and RNA-seq read counts were extracted directly from the corresponding BAM files. For indel mutations, we constructed the de novo mutation in silico and extracted the corresponding read counts. The minimum coverage for both DNA and RNA was 20. Variants with  $|RNA\_MAF - DNA\_MAF| > 0.2$  and an FDR  $< 0.01$  (calculated using R package *q*-value on the *P* value from the two-sided Fisher's exact test) were considered to show allele-specific expression.

### Clonal analysis of FOXA1 mutations

The clonal status of FOXA1 mutations was determined using the cancer cell fraction (CCF) following the previously described method<sup>39</sup>. CCF was estimated as the proportion of cancer cells with an alteration, and the recommended threshold was used to separate clonal events and subclonal events. The algorithm takes into consideration VAF, tumour purity (*p*), and local copy number calls ( $CN_{normal}$  and  $CN_{tumour}$ ) to calculate CCF using the following formula:

$$CCF = VAF \times (CN_{normal} \times (1 - p) + CN_{tumour} \times p) / p$$

Then, a binomial distribution was used to estimate the probability of being clonal or subclonal, and the 95% confidence interval was calculated. For each variant, the alternative reads *t* and total depth *R* met the following binomial distribution:  $P(CCF) = \text{binom}(t | R, VAF(CCF))$ . As previously described<sup>39</sup>, if the 95% confidence interval of CCF overlapped 1, the variant was determined to be clonal; otherwise, the variant was determined to be subclonal. In total, 2 of the 90 FOXA1 mutations from tumours T211 and T521 were excluded owing to the absence of local copy numbers for those samples, and the clonal status of 88 FOXA1 mutations was determined using the R package Hmisc and the binconf function.

### Crystal structure of mutant FOXA1

The primary amino acid sequence of human FOXA1 was obtained from the SWISS-PROT protein sequence database (ID: P55317). The sequence template homologous to FOXA1 was obtained from the Protein Data

Bank (PDB; <http://www.rcsb.org/pdb>) using a PSI-BLAST search (PDB code 1VTN<sup>80</sup>). The VMD<sup>81</sup> program was used to embed the complexes of wild-type FOXA1 and mutant FOXA1 interacting with DNA.

### DNA methylation level of mutant FOXA1-binding sites

As a surrogate for new FOXA1-binding sites in tumours with mutant FOXA1, we identified FOXA1 binding motifs outside of FOXA1 ChIP-seq peaks from ENCODE (aggregate peaks from all cell lines)<sup>82</sup> (Extended Data Fig. 6d, top). Motifs within the union set of hypoDMRs in tumours were chosen for DNA methylation analysis, using the strongest binding motif per peak or per hypoDMR. DNA methylation levels per FOXA1 motif ( $\pm 50$  bp) were calculated, and an average methylation level was calculated per sample. FOXA1 frameshift or truncated mutations include frameshift indel, in-frame indel and nonsense mutations.

We also used two sets of FOXA1-binding sites experimentally validated in a prostate tumour cell line in a recent publication<sup>38</sup>: binding sites for wild-type FOXA1 and class-2 mutant FOXA1 (Extended Data Fig. 6d, bottom). Wild-type FOXA1-binding sites were obtained by merging two sets of ChIP-seq peaks (GSM3508092 and GSM3508095) and intersecting ENCODE FOXA1 peaks. Class-2 mutant FOXA1-binding sites were obtained by merging three ChIP-seq peaks (GSM3508089, GSM3508098 and GSM3508101) and excluding wild-type binding sites. Peak summits were used as FOXA1-binding sites, and DNA methylation levels were calculated using smoothed CpG methylation levels from DSS<sup>83</sup>.

### PMD detection and analysis

PMDs were identified in each sample using a hidden Markov model-based tool, MethPipe v.3.4.3<sup>84</sup>. Raw CpG methylation data with methylated and unmethylated read counts were used as input. The default non-overlapping bin size of 1,000 bp was used, and the bin-level was modelled with a two-state hidden Markov model. MethPipe further processed candidate PMDs by trimming ends and merging adjacent candidate PMDs. PMDs with a score lower than 100 or whose genomic length was less than 100 kb were filtered out. PMDs from individual tumours were merged to make a union set of 2,218 PMDs. The average PMD methylation level was calculated using smoothed CpG methylation levels from DSS<sup>83</sup> over the union set of PMDs. Mutation frequencies inside and outside PMDs were calculated based on individual tumour-specific PMDs (Extended Data Fig. 7i). Comparison of gene expression levels inside and outside PMDs were based on the union set of PMDs, so that gene sets were identical across samples (Extended Data Fig. 7j). The mean expression level across tumours or normal samples was calculated per gene.

### DMR detection and analysis

DMRs were identified using DSS v.2.14.0<sup>83</sup> with the raw CpG methylation data with methylated and unmethylated read counts as input. Differential methylation of CpGs between each tumour and matched normal sample was first statistically tested without replicates using the following command and parameters: `DMLtest(smoothing = TRUE, smoothing.span = 500)`. The number of epimutations per tumour was calculated by counting CpGs with an absolute methylation difference  $> 0.2$  (Fig. 1). Then, a stringent set of DMRs per tumour were identified using the following command and parameters: `callDMR(delta = 0.2, p.threshold =  $10^{-16}$ , minlen = 200, minCG = 5, dis.merge = 50, pct.sig = 0.5)`. DMRs were divided into hypo- and hyperDMRs based on the direction of methylation change. To exclude the large-scale hypo-methylation effect of PMDs, hypoDMRs within the PMDs were excluded. DMRs from individual tumours were merged to make a union set of 96,037 hypoDMRs and 17,131 hyperDMRs. Recurrent DMRs were defined as DMRs shared by at least 10 tumours (Extended Data Fig. 8a, b). Average methylation levels of DMRs were calculated using smoothed CpG methylation levels in the union set of hypoDMRs and hyperDMRs. The genomic location of recurrent DMRs was annotated using BED



# Article

Tools v.2.27.1<sup>85</sup> with gene annotations downloaded from GENCODE release 27<sup>86</sup>. Promoters were defined as 2 kb upstream and 200 bp downstream of the transcription start sites. The enhancer database was downloaded from GeneHancer v.4.7<sup>29</sup>. The genomic location of DMRs was assigned in the following order: coding exon, promoter, enhancer, 5' UTR, 3' UTR, intron and intergenic regions. Gene Ontology analysis was performed using the tool GREAT v.3.0.0<sup>87</sup>. Genomic coordinates of DMRs were lifted over to hg19 from hg38 for GREAT input.

## CIMP detection and analysis

The CpG island methylator phenotype was identified based on recurrently methylated promoter CGIs. The mean methylation level for 18,584 CGIs located in gene promoters was calculated for each sample using smoothed CpG methylation levels. The CGIs defining the CIMP (CIMP-CGIs) were selected based on the following criteria: (1) average methylation level across normal samples  $< 0.4$ ; (2) difference in methylation level between tumour and matched normal samples  $> 0.3$  in more than half ( $> 93$ ) of sample pairs. A total of 289 CIMP-CGIs were identified. Hierarchical clustering was performed across all tumours using the methylation levels of these CGIs. CIMP<sup>+</sup> tumours were defined as a cluster with most hypermethylated CIMP-CGIs, similar to the method previously described<sup>88,89</sup>. A Fisher's exact test was performed to identify associations of CIMP<sup>+</sup> tumours with genetic alterations. Differences in the BCR of subjects with CIMP<sup>+</sup> and CIMP<sup>-</sup> tumours were assessed using Kaplan–Meier analysis followed by a log-rank test.

## Epimutation burden and analyses

The epimutation burden of a tumour was calculated as the number of CpGs with a methylation difference  $\geq 0.2$  between the tumour and its matched normal sample divided by the total number of CpGs in the genome. Correlation between the epimutation burden and other mutational or clinicopathological features were tested using Spearman's rank order correlation.

## miRNA clustering

We selected the 98 most variant miRNA (17%) from 105 tumours for clustering. Only miRNA expressed in more than 10% of samples were used. We transformed each row of the matrix by  $\log_{10}(\text{TPM} + 1)$  and median-centred the matrix, then used the pheatmap package to scale the rows. We used ward.D2 and Euclidean distance measures for clustering of the columns and rows, respectively.

## iCluster

Integrative clustering of three genomic data types for all available samples (127 patients) was performed using the R package iClusterplus<sup>90</sup>, with the following inputs: (1) somatic CNAs defined as the merged copy-number segments identified by Control-FREEC; (2) the 1,600 most variable genes detected by RNA-seq; and (3) the 4,890 most variable DMRs defined using WGBS.

We ran iClusterPlus.tune with different numbers of possible clusters ( $n = 3-5$ ), choosing the number of clusters at which the percentage of explained variation levelled off ( $n = 4$ ) and the clustering with the lowest Bayesian information criterion. The number of clusters ( $k$ ) was estimated. We computed a deviance ratio metric, in which  $k$  was chosen to maximize the deviance ratio. We chose  $k = 3$ , which is the elbow point to construct the model. We also performed unsupervised clustering on each of the three data types individually. Gene expression data were clustered by hierarchical clustering with the Ward.D2 method and Pearson correlation as the distance metric. Somatic CNA data were clustered by hierarchical clustering with the Ward.D2 method and Manhattan distance. Methylation data were clustered by hierarchical clustering with the Ward.D2 method and Manhattan distance.

Association analysis of clinical features and molecular changes with different iCluster subtypes was performed using Kruskal–Wallis,

Wilcoxon rank-sum, or Fisher's exact tests. Differences in somatic CNAs, fusions, somatic mutations and DNA methylation across different iCluster subtypes was tested using ANOVA. Gene set enrichment analysis<sup>91</sup> was used to detect the gene sets more highly expressed in one subtype than the other three subtypes. Difference in the BCR of the subjects across the iCluster subtypes was assessed using Kaplan–Meier analysis followed by a log-rank test.

## Pathway comparison and visualization

Genetic lesions in 12 selected oncogenic pathways were compared between the CPGEA, TCGA and SU2C cohorts, which represent Chinese primary, Western primary, and Western metastatic prostate cancer, respectively. Genetic alterations included coding mutations and CNAs. We used information about oncogenic and clinically actionable mutations from the OncoKB database and CGC to determine whether the predicted effect would manifest in the tumour based on the observed genomic alteration. Somatic alterations that were labelled oncogenic, TSG, or oncogene/TSG either in OncoKB or CGC were used. For CNAs, we determined whether the annotated genes were functionally amplified or deleted in each sample, and only amplifications and deletions were used for oncogenes and tumour-suppressor genes, respectively. Genes with discordant annotations in the two databases were used only if their expression levels were significantly different in tumours ( $P < 0.05$ ). If the gene expression was upregulated, we annotated the gene as an oncogene, and if downregulated, as a TSG (Extended Data Fig. 10b, c, <http://www.cpgea.com>).

For noncoding mutations, the mutations selected from the hotspot analysis (Extended Data Fig. 5c) were assigned to oncogenic pathway genes. For epigenetic alterations, we assigned local recurrent DMRs to their nearest gene. For structural variation deletions and amplifications, we assigned all genes within the alteration to the event. For inversions, inter-chromosomal structural variations, and tandem duplications, we calculated the genes hit by breakpoints (Extended Data Fig. 10e).

## Supporting website

The supporting website (<http://www.cpgea.com>) contains the following: (1) an analysis workflow page that contains all bioinformatics pipelines for data processing and genetic and epigenetic mutation detection with detailed parameters; (2) a sequencing information page with WGS, WGBS, RNA-seq and miRNA-seq data by sample; (3) a validation page with all validation results, including *FOXA1* mutations, fusion events, and structural variation events; and (4) a pathway page that contains the alteration frequencies of important oncogenic pathway genes by cohort (CPGEA, TCGA and SU2C) and by alteration type (fusion, structural variation, noncoding and DNA methylation), including alterations in individual patients. Detailed information such as percentage by alteration type, the location of coding mutations as a lollipop diagram, and a link to the epigenome browser can be found by clicking gene names or frequencies.

## Reporting summary

Further information on research design is available in the Nature Research Reporting Summary linked to this paper.

## Data availability

All data, including raw data, mutation calls, and clinical information, have been deposited to the Genome Sequence Archive for Human (<http://bigd.big.ac.cn/gsa-human/>) at the BIG Data Center, Beijing Institute of Genomics, Chinese Academy of Sciences, under the accession number PRJCA001124. The raw sequencing data and somatic and germ-line mutation calls contain information unique to an individual and require controlled access. The deposited and publicly available data are compliant with the regulations of the Ministry of Science and

Technology of the People's Republic of China. Source Data for Figs. 2, 4 and Extended Data Figs. 6–8 are provided with the paper.

## Code availability

All computational code used in this study is available at the supporting website (<http://www.cpgea.com>).

50. Gao, X., Wang, H., Wang, Y., Xu, C. & Sun, Y. Construction and clinical application of prostate cancer database (PC-Follow) based on browser/server schema. *Chin. J. Urol.* **36**, 694–698 (2015).
51. Bergmann, E. A., Chen, B. J., Arora, K., Vacic, V. & Zody, M. C. Conpair: concordance and contamination estimator for matched tumor-normal pairs. *Bioinformatics* **32**, 3196–3198 (2016).
52. Krueger, F. & Andrews, S. R. Bismark: a flexible aligner and methylation caller for Bisulfite-Seq applications. *Bioinformatics* **27**, 1571–1572 (2011).
53. Langmead, B. & Salzberg, S. L. Fast gapped-read alignment with Bowtie 2. *Nat. Methods* **9**, 357–359 (2012).
54. Kim, D. et al. TopHat2: accurate alignment of transcriptomes in the presence of insertions, deletions and gene fusions. *Genome Biol.* **14**, R36 (2013).
55. Anders, S., Pyl, P. T. & Huber, W. HTSeq—a Python framework to work with high-throughput sequencing data. *Bioinformatics* **31**, 166–169 (2015).
56. Love, M. I., Huber, W. & Anders, S. Moderated estimation of fold change and dispersion for RNA-seq data with DESeq2. *Genome Biol.* **15**, 550 (2014).
57. Trapnell, C. et al. Differential analysis of gene regulation at transcript resolution with RNA-seq. *Biotechnol.* **31**, 46–53 (2013).
58. Trapnell, C. et al. Differential gene and transcript expression analysis of RNA-seq experiments with TopHat and Cufflinks. *Nat. Protocols* **7**, 562–578 (2012).
59. Friedländer, M. R., Mackowiak, S. D., Li, N., Chen, W. & Rajewsky, N. miRDeep2 accurately identifies known and hundreds of novel microRNA genes in seven animal clades. *Nucleic Acids Res.* **40**, 37–52 (2012).
60. McKenna, A. et al. The Genome Analysis Toolkit: a MapReduce framework for analyzing next-generation DNA sequencing data. *Genome Res.* **20**, 1297–1303 (2010).
61. Cibulskis, K. et al. Sensitive detection of somatic point mutations in impure and heterogeneous cancer samples. *Nat. Biotechnol.* **31**, 213–219 (2013).
62. Saunders, C. T. et al. Strelka: accurate somatic small-variant calling from sequenced tumor-normal sample pairs. *Bioinformatics* **28**, 1811–1817 (2012).
63. Wang, K., Li, M. & Hakonarson, H. ANNOVAR: functional annotation of genetic variants from high-throughput sequencing data. *Nucleic Acids Res.* **38**, e164 (2010).
64. Thorvaldsdóttir, H., Robinson, J. T. & Mesirov, J. P. Integrative Genomics Viewer (IGV): high-performance genomics data visualization and exploration. *Brief. Bioinform.* **14**, 178–192 (2013).
65. Boeva, V. et al. Control-FREEC: a tool for assessing copy number and allelic content using next-generation sequencing data. *Bioinformatics* **28**, 423–425 (2012).
66. Amemiya, H. M., Kundaje, A. & Boyle, A. P. The ENCODE blacklist: identification of problematic regions of the genome. *Sci. Rep.* **9**, 9354 (2019).
67. Mermel, C. H. et al. GISTIC2.0 facilitates sensitive and confident localization of the targets of focal somatic copy-number alteration in human cancers. *Genome Biol.* **12**, R41 (2011).
68. Yang, L. et al. Diverse mechanisms of somatic structural variations in human cancer genomes. *Cell* **153**, 919–929 (2013).
69. Jia, W. et al. SOAPfuse: an algorithm for identifying fusion transcripts from paired-end RNA-Seq data. *Genome Biol.* **14**, R12 (2013).
70. Panigrahi, P., Jere, A. & Anamika, K. FusionHub: A unified web platform for annotation and visualization of gene fusion events in human cancer. *PLoS One* **13**, e0196588 (2018).
71. Shugay, M., Ortiz de Mendivil, I., Vizmanos, J. L. & Novo, F. J. Oncofuse: a computational framework for the prediction of the oncogenic potential of gene fusions. *Bioinformatics* **29**, 2539–2546 (2013).
72. Gonzalez-Perez, A. et al. Computational approaches to identify functional genetic variants in cancer genomes. *Nat. Methods* **10**, 723–729 (2013).
73. Porta-Pardo, E. et al. Comparison of algorithms for the detection of cancer drivers at subgene resolution. *Nat. Methods* **14**, 782–788 (2017).
74. Dees, N. D. et al. MuSiC: identifying mutational significance in cancer genomes. *Genome Res.* **22**, 1589–1598 (2012).
75. Lawrence, M. S. et al. Mutational heterogeneity in cancer and the search for new cancer-associated genes. *Nature* **499**, 214–218 (2013).
76. Sondka, Z. et al. The COSMIC Cancer Gene Census: describing genetic dysfunction across all human cancers. *Nat. Rev. Cancer* **18**, 696–705 (2018).
77. Fu, Y. et al. FunSeq2: a framework for prioritizing noncoding regulatory variants in cancer. *Genome Biol.* **15**, 480 (2014).
78. Melton, C., Reuter, J. A., Spacek, D. V. & Snyder, M. Recurrent somatic mutations in regulatory regions of human cancer genomes. *Nat. Genet.* **47**, 710–716 (2015).
79. Weinhold, N., Jacobsen, A., Schultz, N., Sander, C. & Lee, W. Genome-wide analysis of noncoding regulatory mutations in cancer. *Nat. Genet.* **46**, 1160–1165 (2014).
80. Clark, K. L., Halay, E. D., Lai, E. & Burley, S. K. Co-crystal structure of the HNF-3/fork head DNA-recognition motif resembles histone H5. *Nature* **364**, 412–420 (1993).
81. Humphrey, W., Dalke, A. & Schulten, K. VMD: visual molecular dynamics. *J. Mol. Graph.* **14**, 33–38 (1996).
82. The ENCODE Project Consortium. An integrated encyclopedia of DNA elements in the human genome. *Nature* **489**, 57–74 (2012).
83. Wu, H. et al. Detection of differentially methylated regions from whole-genome bisulfite sequencing data without replicates. *Nucleic Acids Res.* **43**, e141 (2015).
84. Kishore, K. et al. methylPipe and compEpiTools: a suite of R packages for the integrative analysis of epigenomics data. *BMC Bioinformatics* **16**, 313 (2015).
85. Quinlan, A. R. & Hall, I. M. BEDTools: a flexible suite of utilities for comparing genomic features. *Bioinformatics* **26**, 841–842 (2010).
86. Harrow, J. et al. GENCODE: the reference human genome annotation for The ENCODE Project. *Genome Res.* **22**, 1760–1774 (2012).
87. McLean, C. Y. et al. GREAT improves functional interpretation of cis-regulatory regions. *Nat. Biotechnol.* **28**, 495–501 (2010).
88. Weisenberger, D. J. et al. CpG island methylator phenotype underlies sporadic microsatellite instability and is tightly associated with BRAF mutation in colorectal cancer. *Nat. Genet.* **38**, 787–793 (2006).
89. Noshmeh, H. et al. Identification of a CpG island methylator phenotype that defines a distinct subgroup of glioma. *Cancer Cell* **17**, 510–522 (2010).
90. Mo, Q. et al. Pattern discovery and cancer gene identification in integrated cancer genomic data. *Proc. Natl Acad. Sci. USA* **110**, 4245–4250 (2013).
91. Subramanian, A. et al. Gene set enrichment analysis: a knowledge-based approach for interpreting genome-wide expression profiles. *Proc. Natl Acad. Sci. USA* **102**, 15545–15550 (2005).
92. Cerami, E. et al. The cBio cancer genomics portal: an open platform for exploring multidimensional cancer genomics data. *Cancer Discov.* **2**, 401–404 (2012).

**Acknowledgements** We thank the patients and their families. This study was supported by the 'Key Research and Development Project on Precision Medicine' fund (2016YFC090220) granted by the Chinese Ministry of Science and Technology, the Shanghai Key Laboratory of Cell Engineering (14DZ2272300), the Shanghai 'Top Priority' Medical Center Project (2017ZZ01005), the 'National Major New Drug Discovery Initiative' Fund (2017ZX093040300002) granted by the '13th Five-Year Plan' (Subproject), National Natural Science Foundation of China (81602467, J.L.), and the 'Zhangjiang National Innovation Demonstration Zone' Initiative Development Fund. H.J.L., N.M.S., E.C.P. and Ting Wang were supported by American Cancer Society grant RSG-14-049-01-DMC, and E.C.P. was supported by a Postdoctoral Fellowship, PF-17-201-01, from the American Cancer Society. We thank K.-L. Huang for technical assistance on iCluster, and X. Zhang for managing and organizing this project.

**Author contributions** J.L., Ting Wang and Y.S. conceived and implemented the study. Xu Gao performed surgeries and set up the follow-up database. J.L. and H.J.L. performed data analyses. Z.Z. performed basic WGS analysis. X. Li performed basic RNA-seq analysis. C.X., S.R., H.W., Xiaofeng Gao, J.H., L.W., B.Y., Qing Yang, H.Y., T.Z., Shuo Wang, Z.W., Jun Jiang, C.L., Jianquan Hou, C.H., M.C., N.J., D.Z., S. Wu, Jinjiang Yang, Y.C., J.C. and W.Y. contributed to sample collection as surgeons. X. Lu, Yan Wang, M.Q., R.C., H.C., F.Z. and B.L. took care of patients as attending doctors. Qingsong Yang performed radiology review of all patients. Y. Yu and Y. Zhu performed pathology review of all samples. Y. Zhang, J.X. and Shaogang Wang followed up the patients. W.Z., N.M.S., E.C.P. and Tao Wang contributed to computational analysis. X.Z. stored samples in liquid nitrogen. C.Y. and C.W. generated sequencing libraries. Y.W. and G.X. performed Sanger sequencing validation. Junfeng Jiang and Y. Yang performed fusion validation experiment. J.L., H.J.L. and Ting Wang prepared the manuscript with input from all authors.

**Competing interests** The authors declare no competing interests.

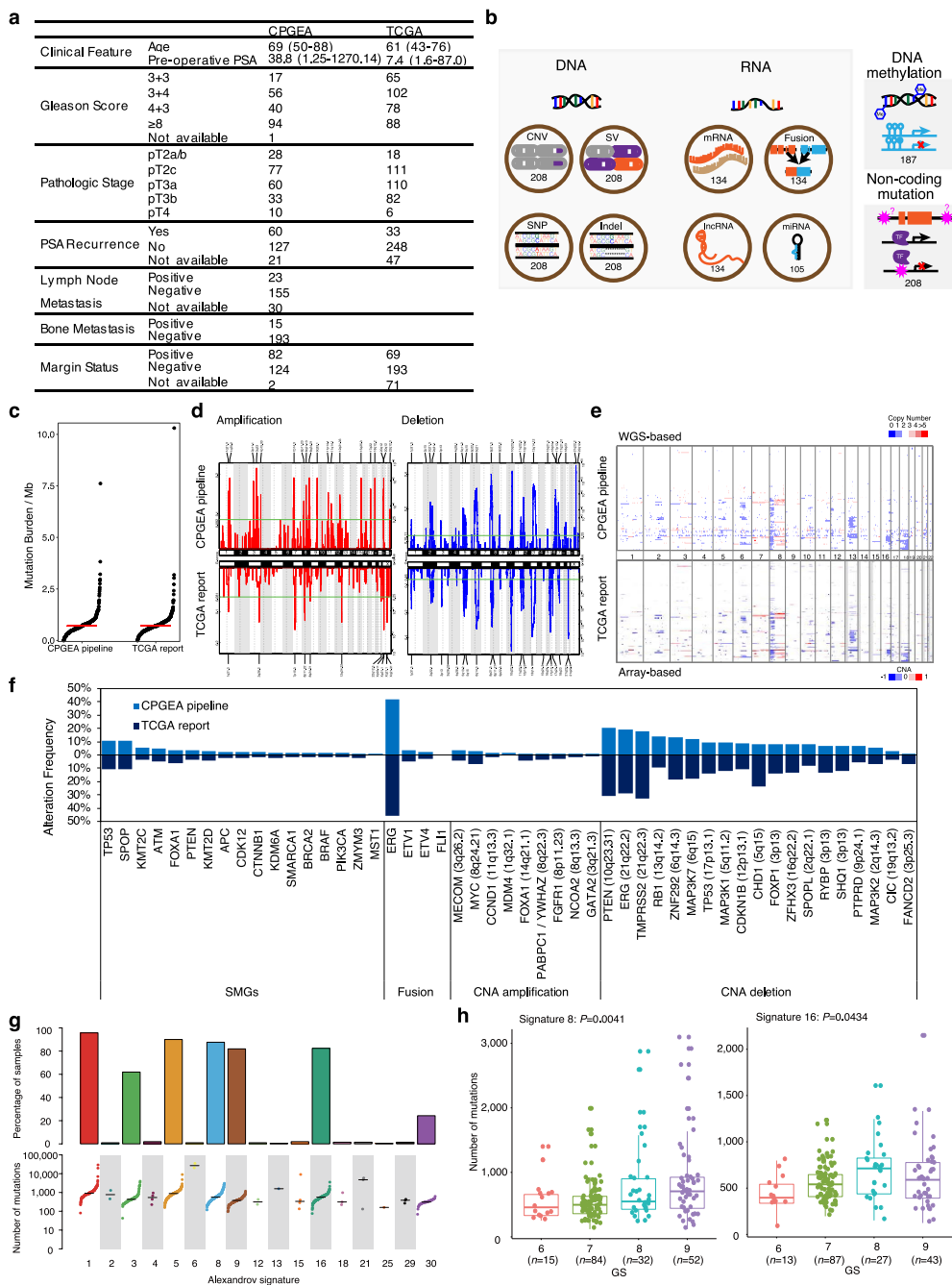
## Additional information

**Supplementary information** is available for this paper at <https://doi.org/10.1038/s41586-020-2135-x>.

**Correspondence and requests for materials** should be addressed to X.G., Ting Wang or Y.S.

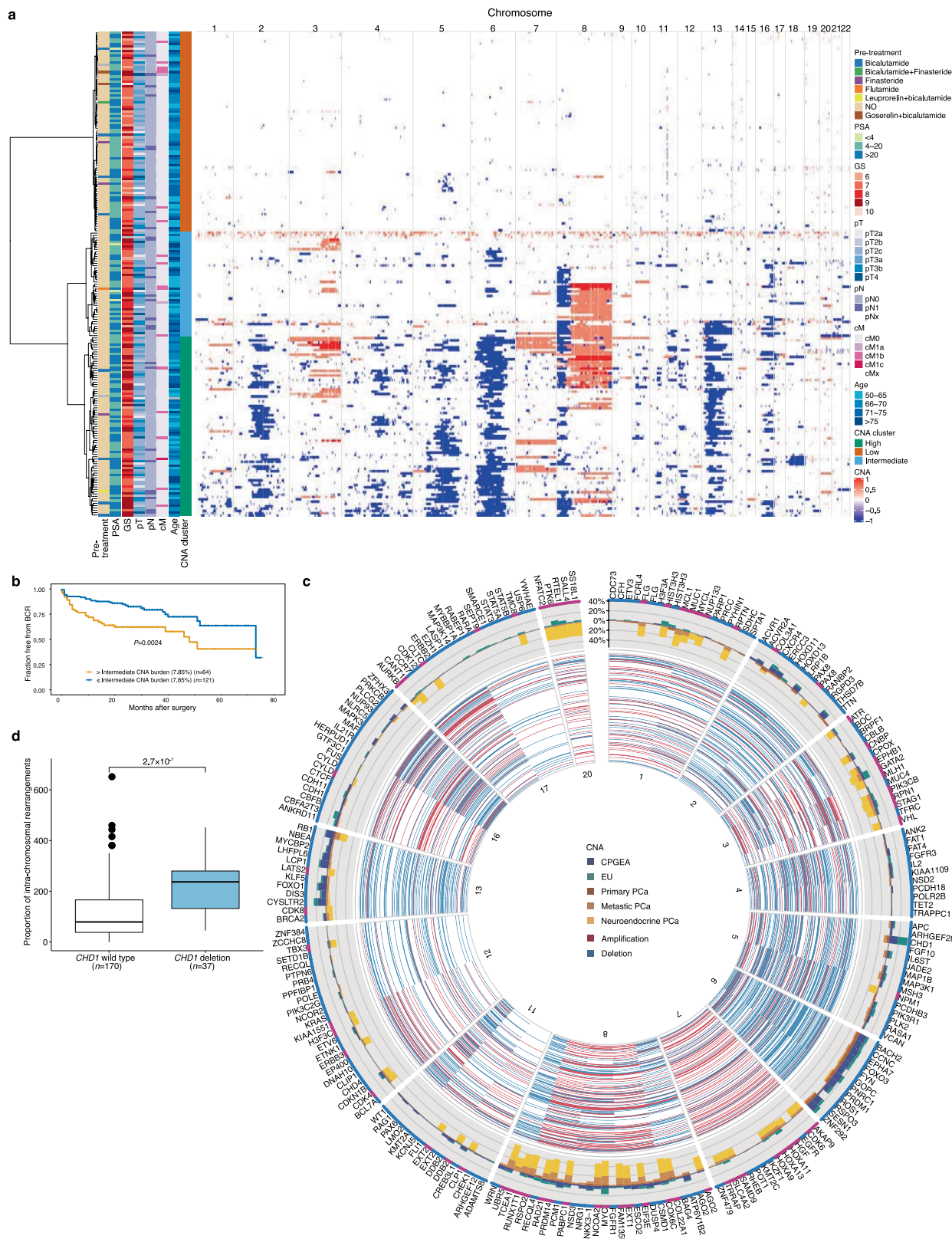
**Peer review information** Nature thanks Arul Chinnaiyan, Colin Collins, Colin Cooper and Charlie Massie for their contribution to the peer review of this work.

**Reprints and permissions information** is available at <http://www.nature.com/reprints>.



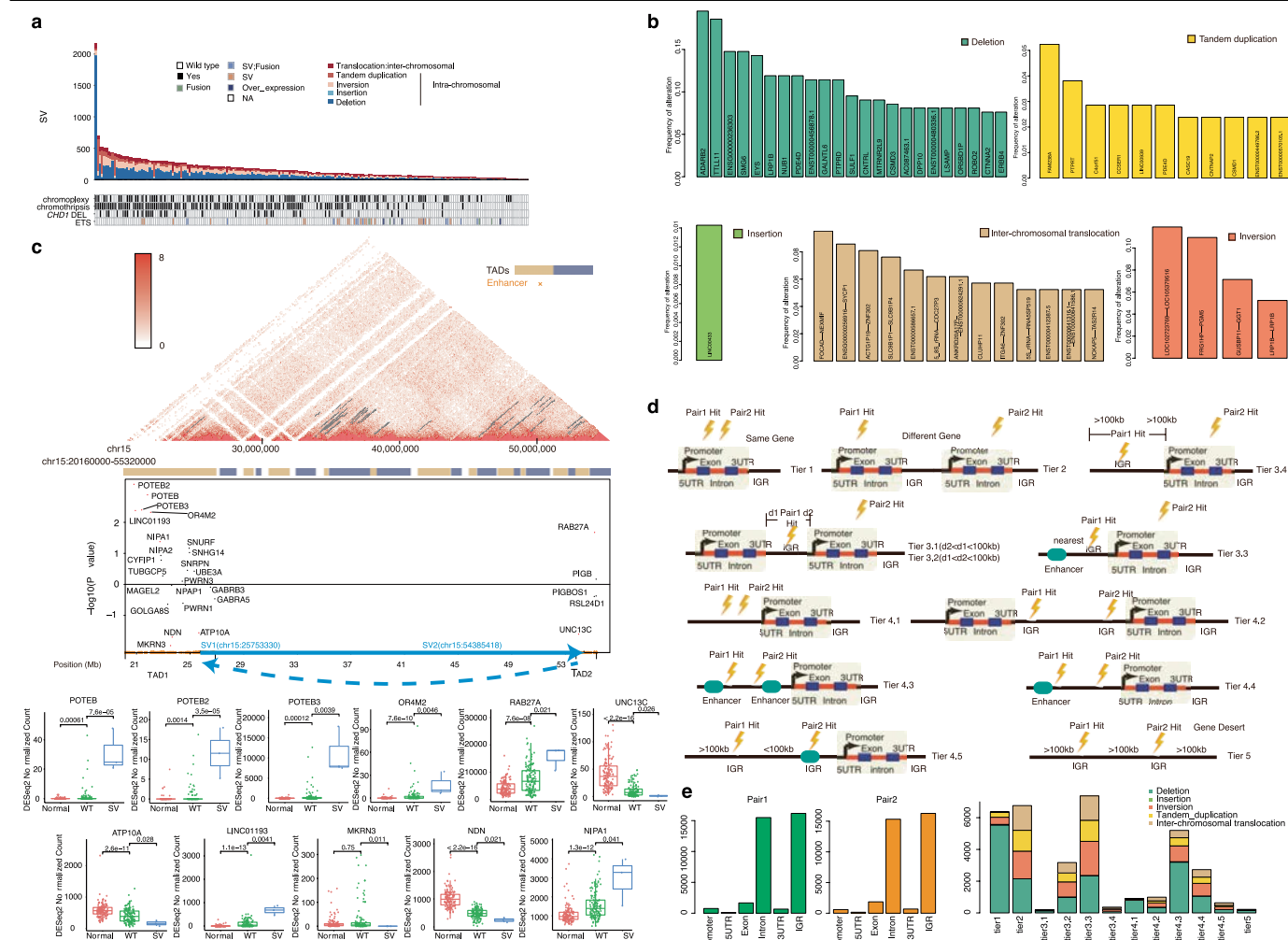
**Extended Data Fig. 1 | Clinical samples, data generation and somatic mutation landscape of CPGEA.** **a**, Clinical and pathological patient characterization. **b**, Study design, indicating the number of tumours with each data type. The cohort consisted of 208 patients who underwent radical prostatectomy. All tumours were analysed by WGS, as was a matched normal para-tumour specimen from each patient. In addition, RNA-seq ( $n=134$  tumours), miRNA-seq ( $n=105$ ), and whole-genome DNA methylation ( $n=187$ ) data were generated for a subset of patients. **c–f**, Comparison between somatic alteration calls from two pipelines for the TCGA PRAD (primary prostate tumour) cohort. ‘CPGEA pipeline’ indicates the pipeline used in this study. ‘TCGA report’ indicates publicly available somatic alteration calls. **c**, Distribution of mutation burdens in each cohort. Each dot corresponds to a

mutation burden calculated from a tumour–normal pair. Red horizontal bars indicate the median mutation burden from the CPGEA pipeline and TCGA (both 0.70 per Mb). **d**, Genomic regions with significantly recurrent somatic CNAs called by GISTIC2.0. **e**, Heat map showing genome-wide CNAs. Top, 114 tumours clustered using the WGS-based CPGEA pipeline. Bottom, array-based TCGA results for the same tumours, arranged in the same order. **f**, Gene-level alteration frequencies from the two pipelines for the TCGA cohort. **g**, Alexandrov signatures in CPGEA and their association with clinical features. Top, percentage of samples per signature. Bottom, mutation counts for each signature, ordered from low to high by individual patient. **h**, Box plot showing the correlation of signatures 8 and 16 with Gleason score (Kruskal–Wallis test). Box plots as in Fig. 4b. Each dot corresponds to a tumour sample.



**Extended Data Fig. 2 | Landscape of CNA in CPGEA. a**, Heat map representation of CNA segments grouped by CNA burden subgroup (high, intermediate and low). **b**, Kaplan–Meier plot of biochemical relapse-free survival in different CNA burden subgroups, using the intermediate CNA burden (7.85%) as a cut-off value.  $P=0.0024$ , two-sided log-rank test. **c**, Cancer genes with a significant CNA in CPGEA and Western cohorts. The inner circle

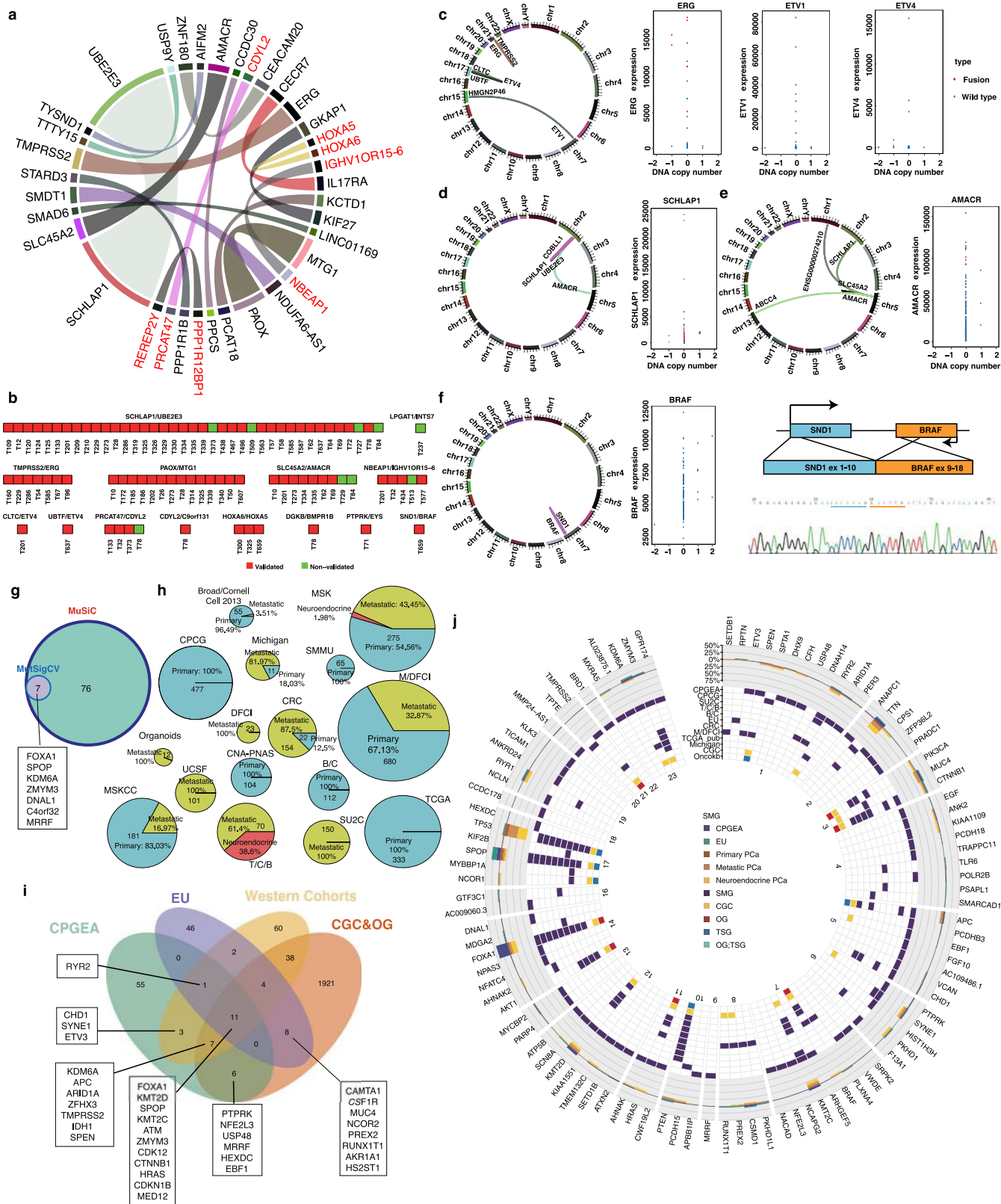
displays a CNA heat map of individual patients sorted by chromosome, with CNA frequencies and significantly altered genes on the outer rim. **d**, Number of intra-chromosomal rearrangements as a function of the deletion status of *CHD1*.  $P$  values were determined by two-sided Mann–Whitney  $U$ -test. Box plots as in Fig. 4b.



**Extended Data Fig. 3 | Landscape of structural variations in CPGA.** **a**, Types of structural variation and numbers for individual tumours (columns). Chromoplexy and chromothripsis status, *CHD1* deletion status, and ERG fusion status are displayed as a heat map. **b**, Frequency of recurrent structural variations and their affected genes for five types of structural variation. **c**, A recurrent inversion potentially disrupts a TAD boundary and results in enhancer hijacking. Hi-C map for the LNCaP cell line over the inversion. The inversion and TAD boundaries are marked. Expression levels of potentially

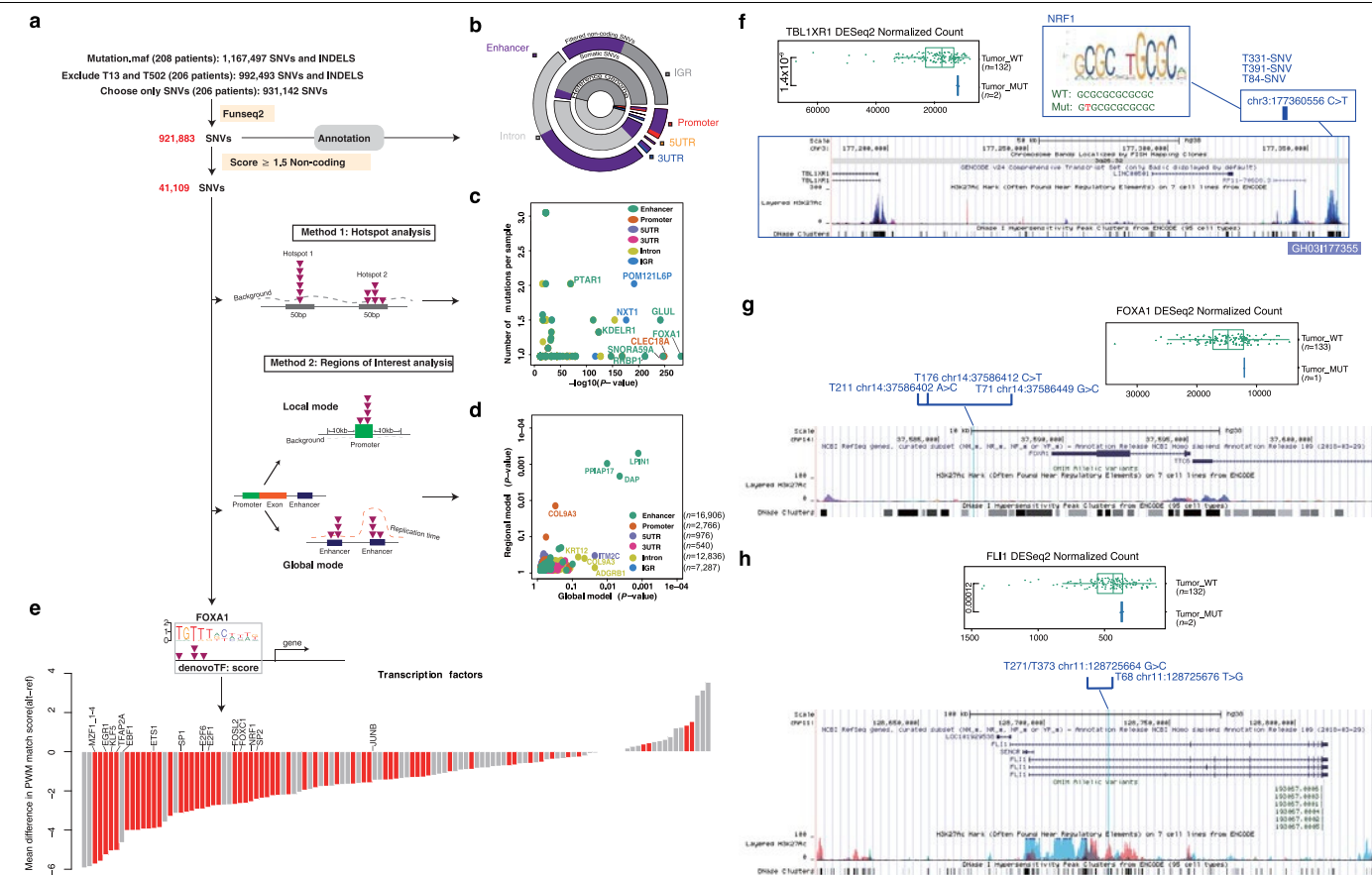
affected genes are displayed as box plots. *P* values were determined by two-sided Mann-Whitney *U*-test. Box plots are as in Fig. 4b. Each dot corresponds to a normal sample ( $n = 134$ ), a tumour with no structural variation (wild-type (WT),  $n = 131$ ), or a tumour with structural variation ( $n = 3$ ). **d**, Definition of five tiers of structural variation patterns based genomic annotation of the 5' and 3' breakpoints. **e**, Genomic location distribution of 5' (left) and 3' (middle) breakpoints, and distribution of different types of structural variation across the five defined tiers (right).





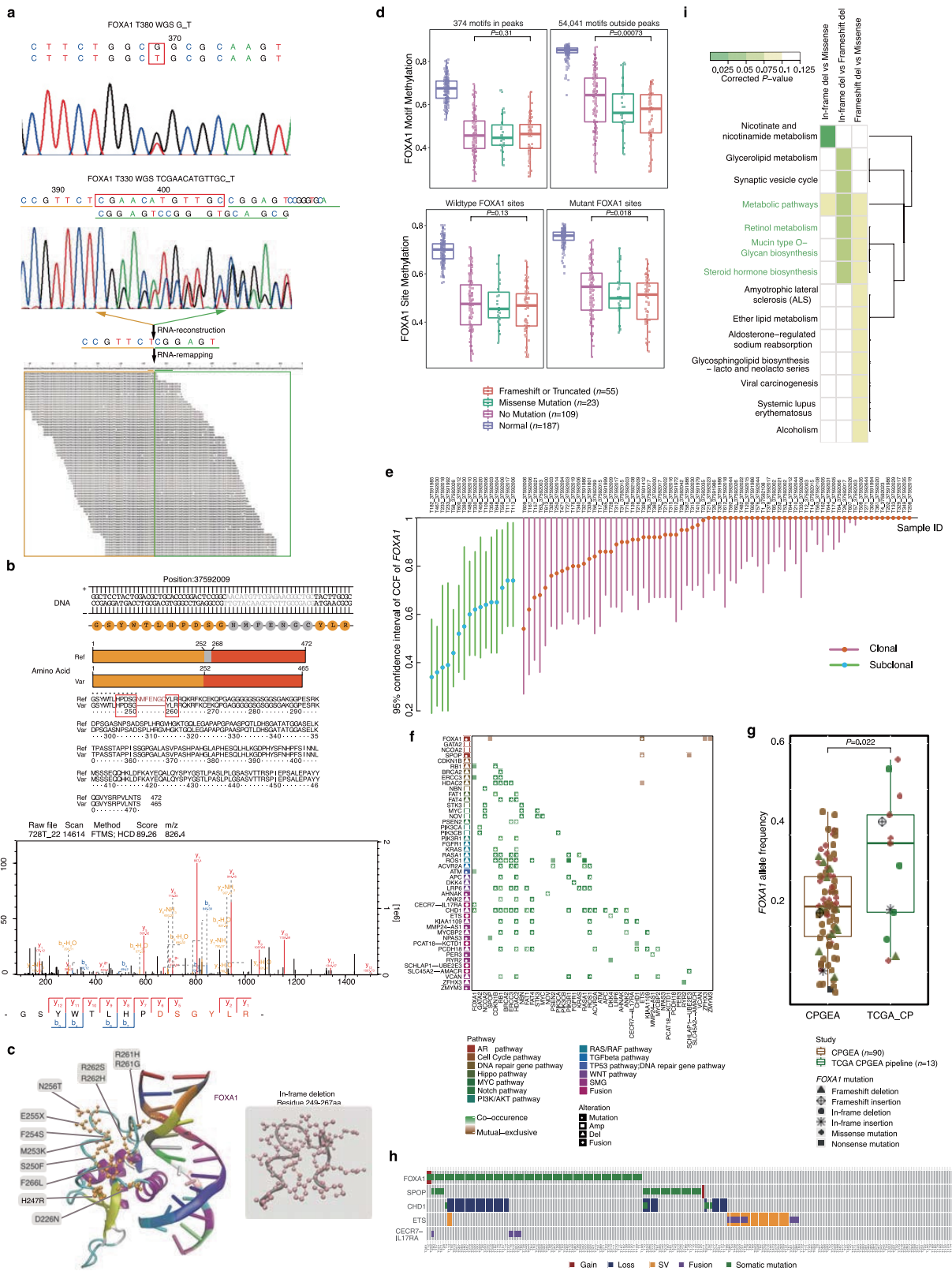
Extended Data Fig. 4 | See next page for caption.

**Extended Data Fig. 4 | Landscape of gene fusions and SMGs in CPGEA.** **a**, The circle represents gene fusions in Chinese and Western cohorts. Recurrent fusions (more than two samples) are displayed as connected gene pairs, in which the width of the connecting arc represents the number of samples that contained the fusion. Red indicates novel gene fusions not present in public databases (FusionHub). **b**, Fusion was validated by Sanger sequencing and RNA-seq data. Red cells indicate validated fusion events, and green cells indicate PCR failure. **c**, Circos plot displaying ETS family fusions. Expression levels are shown as a function of copy number. **d**, The *SCHLAPI-UBE2E3* gene fusion. **e**, AMACR fusions. **f**, A heterozygous *SND1-BRAF* fusion found in CPGEA. **g**, In total, 83 SMGs were detected by MuSiC, including 7 genes called by both MuSiC and MutSigCV. **h**, Fraction of primary, metastatic, and other cancer types investigated by each study. **i**, Venn diagrams of SMGs defined in different studies. **j**, Genes significantly mutated in CPGEA, Western primary, and Western metastatic cohorts. Purple cells indicate that the gene was defined as an SMG in the study. **h–j**, The Western cohorts are from CPCG<sup>9</sup>, SU2C<sup>11</sup>, T/C/B (Trento/Cornell/Broad, neuroendocrine prostate cancer)<sup>8</sup>, B/C (Broad/Cornell)<sup>7</sup>, CRC<sup>13</sup>, M/DFCI<sup>3</sup>, TCGA<sup>2</sup>, Michigan<sup>11</sup>, MSKCC<sup>15</sup>, Organoid<sup>10</sup>, CNA-PNAS<sup>12</sup> and MSK<sup>17</sup>.



**Extended Data Fig. 5 | Noncoding mutations in CPGEA.** **a**, Schematic workflow of noncoding mutation analysis in CPGEA. **b**, Distribution of noncoding mutations across different genomic features. **c**, Significance of mutation hotspots in noncoding regulatory regions. Each hotspot is colour-coded for its regulatory region annotation, and the statistical significance (false discovery rate (FDR)) and number of hits per sample are displayed. **d**, Significance of recurrent mutations in regulatory regions of interest. Regulatory regions for individual genes are displayed based on local and global measures of statistical significance (FDR). Colours indicate regulatory region annotations, and key genes are labelled. **e**, Enrichment of noncoding mutations resulting in gain or loss of transcription factor-binding sites. For each

transcription factor, the match score to the position weight matrix (PWM) was determined for mutations that could potentially destroy or create a binding site for that transcription factor. Plotted for each transcription factor is the mean difference in the match scores for the mutated and reference alleles. Red indicates FDR < 0.05. P-values for differences in mean match score were computed by two-sided paired Wilcoxon rank-sum test. **f-h**, Examples of noncoding mutations in selected genes. *TBL1XR1* (**f**), *FOXA1* (**g**) and *FLI1* (**h**) are shown. Genome browser views show the location of the noncoding mutation. The genomic coordinates and types of noncoding mutation are labelled above the genome browser. Gene expression of genes with noncoding mutations is depicted.

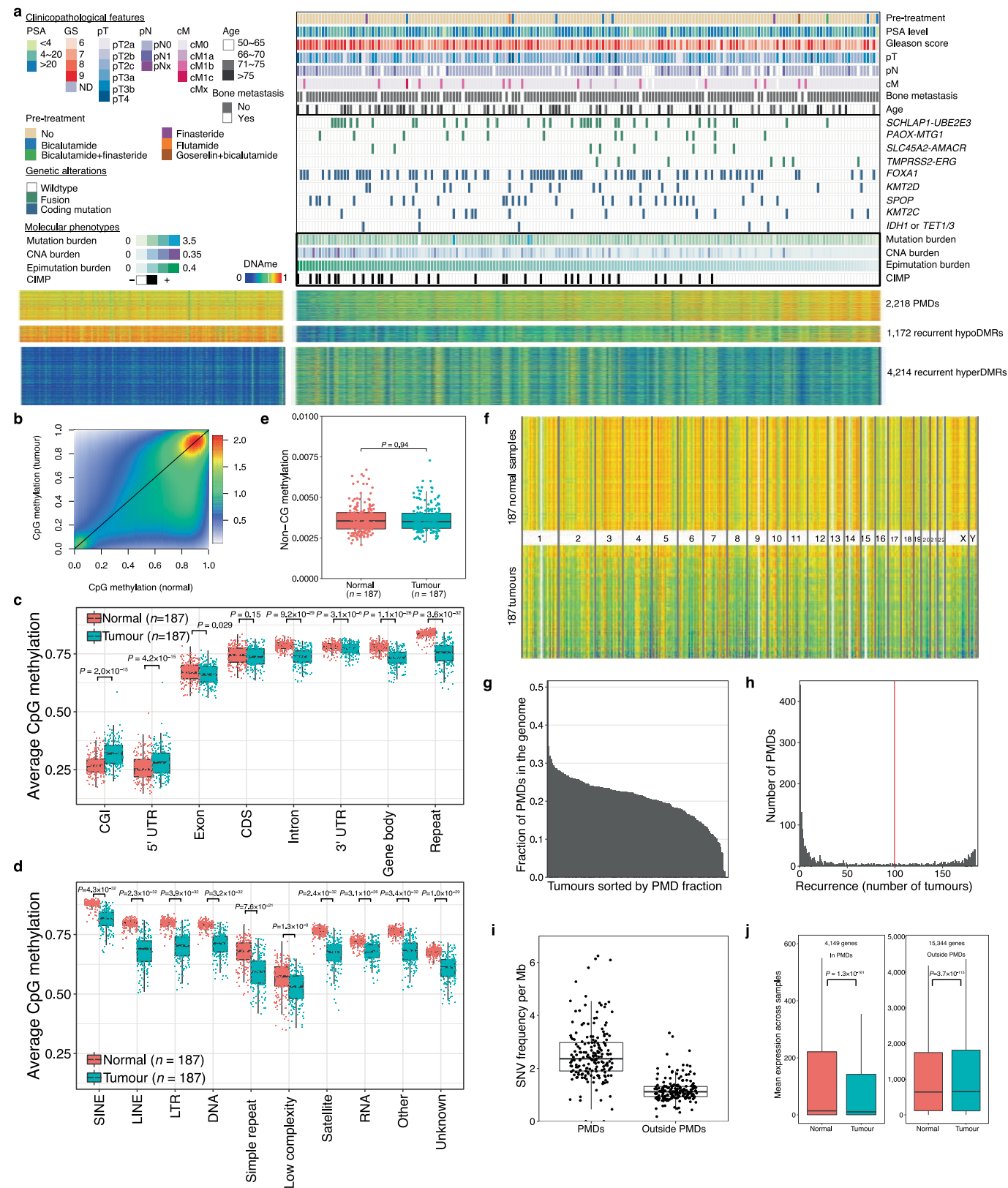


Extended Data Fig. 6 | See next page for caption.

**Extended Data Fig. 6 | FOXA1 mutations in CPGEA.** **a**, FOXA1 mutation validation. Two representative validations by Sanger sequencing and reconstructed RNA-seq analysis. **b**, Validation of a FOXA1 in-frame deletion-derived peptide by mass spectrometry. **c**, Mapping of FOXA1 mutations onto the three-dimensional structure of FOXA1 and bound DNA (based on PDB registry 1VTN<sup>78</sup>). **d**, DNA methylation over FOXA1-binding sites in tumours with FOXA1 truncation/in-frame deletion. Top, FOXA1-binding motifs in the ENCODE chromatin immunoprecipitation with high-throughput sequencing (ChIP-seq) dataset (left) versus FOXA1-binding motifs outside of FOXA1 ChIP-seq peaks (right). Bottom, wild-type FOXA1-binding sites (left) and mutant FOXA1-binding sites (right) from recently published ChIP-seq data<sup>38</sup>. *P* values were determined by one-sided Mann-Whitney *U*-tests. Box plots are as in

Fig. 4b. Each dot corresponds to a normal or tumour sample. **e**, Clonal analysis of FOXA1 in CPGEA. **f**, Mutual exclusivity or co-occurrence of gene alterations between genes belonging to 12 important curated pathways. Only alterations with at least one significant interaction ( $P < 0.05$ ) are included. Asterisks indicate significant relationships. **g**, Allele frequency distribution of FOXA1 mutations in CPGEA and TCGA processed with the CPGEA pipeline. **h**, Significant mutual exclusions and co-occurrences between FOXA1 mutations and other genetic lesions in CPGEA, identified by OncoPrint from cBioPortal<sup>92</sup>. **i**, FOXA1 mutations and downstream pathways. Pairwise comparison of expression levels of important pathways. The z-score of specific genes and clinical features are displayed in a heat map grouped by different mutation subtypes.

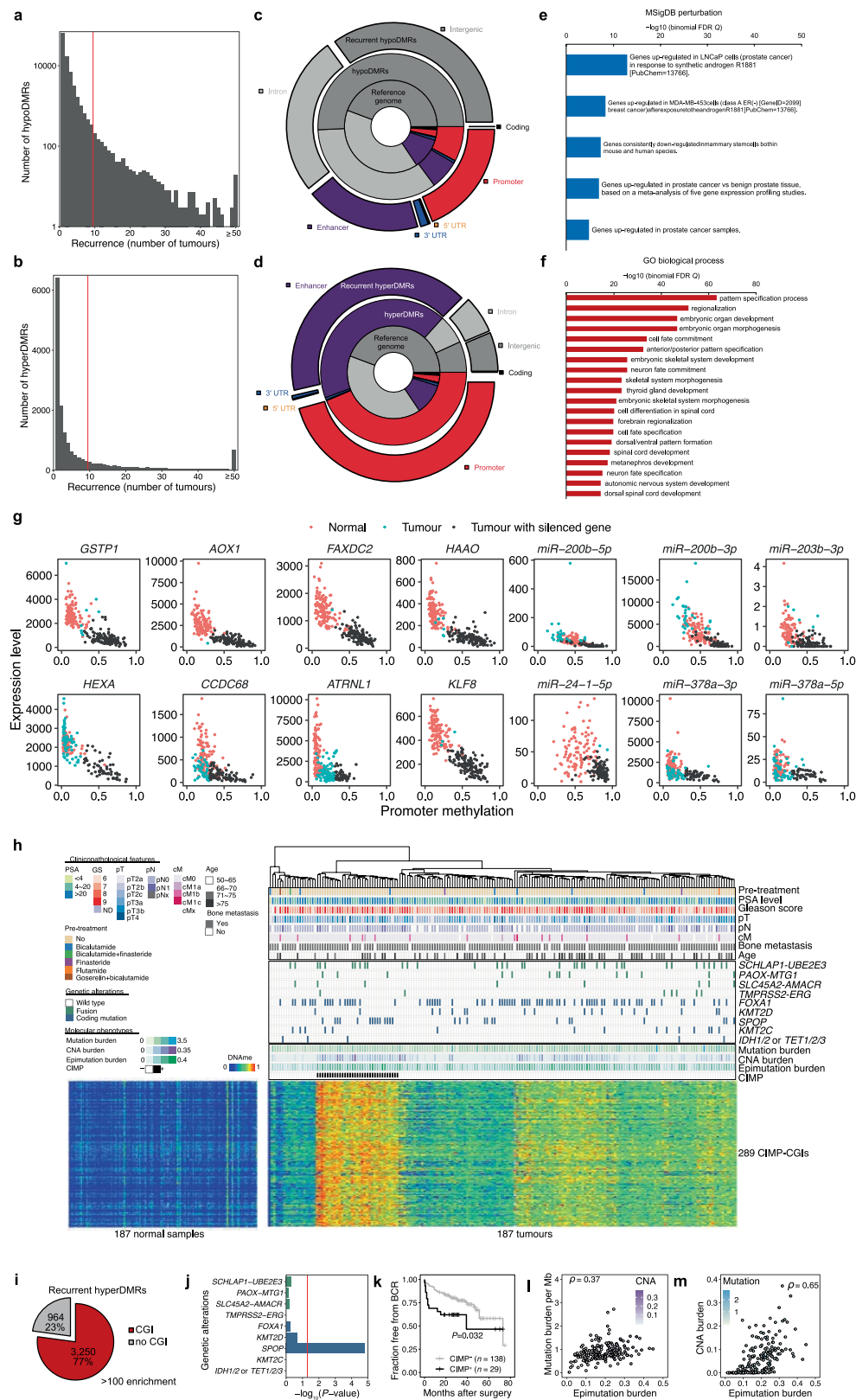




Extended Data Fig. 7 | See next page for caption.

**Extended Data Fig. 7 | DNA methylation abnormalities in CPGEA.** **a**, Heat map of DNA methylation levels in the CPGEA cohort. Rows represent defined genomic regions including PMDs, hypoDMRs and hyperDMRs, and columns represent samples. Tumours (right) and matched normal samples (left) are sorted by epimutation rate. In each category, genomic regions are sorted by chromosomal coordinates. The top panel shows clinicopathological features of patients (as in Fig. 1), genetic alterations including fusions and coding mutations, and other molecular phenotypes. **b**, Two-dimensional density plot of the average CpG methylation level in normal versus tumour samples from the same patient. **c**, Average methylation level of CpGs overlapping different genomic features. *P* values determined by two-sided Wilcoxon signed-rank test. CDS, coding sequence. Each dot corresponds to a normal prostate or tumour sample. **d**, Average methylation level of CpGs overlapping different repeat element classes. *P* values were determined by two-sided Wilcoxon signed-rank test. Each dot corresponds to a normal prostate or tumour sample. **e**, Average non-CG methylation level in tumours and matched normal samples. Each dot represents a sample. Mean 0.37% for each group. *P* values were

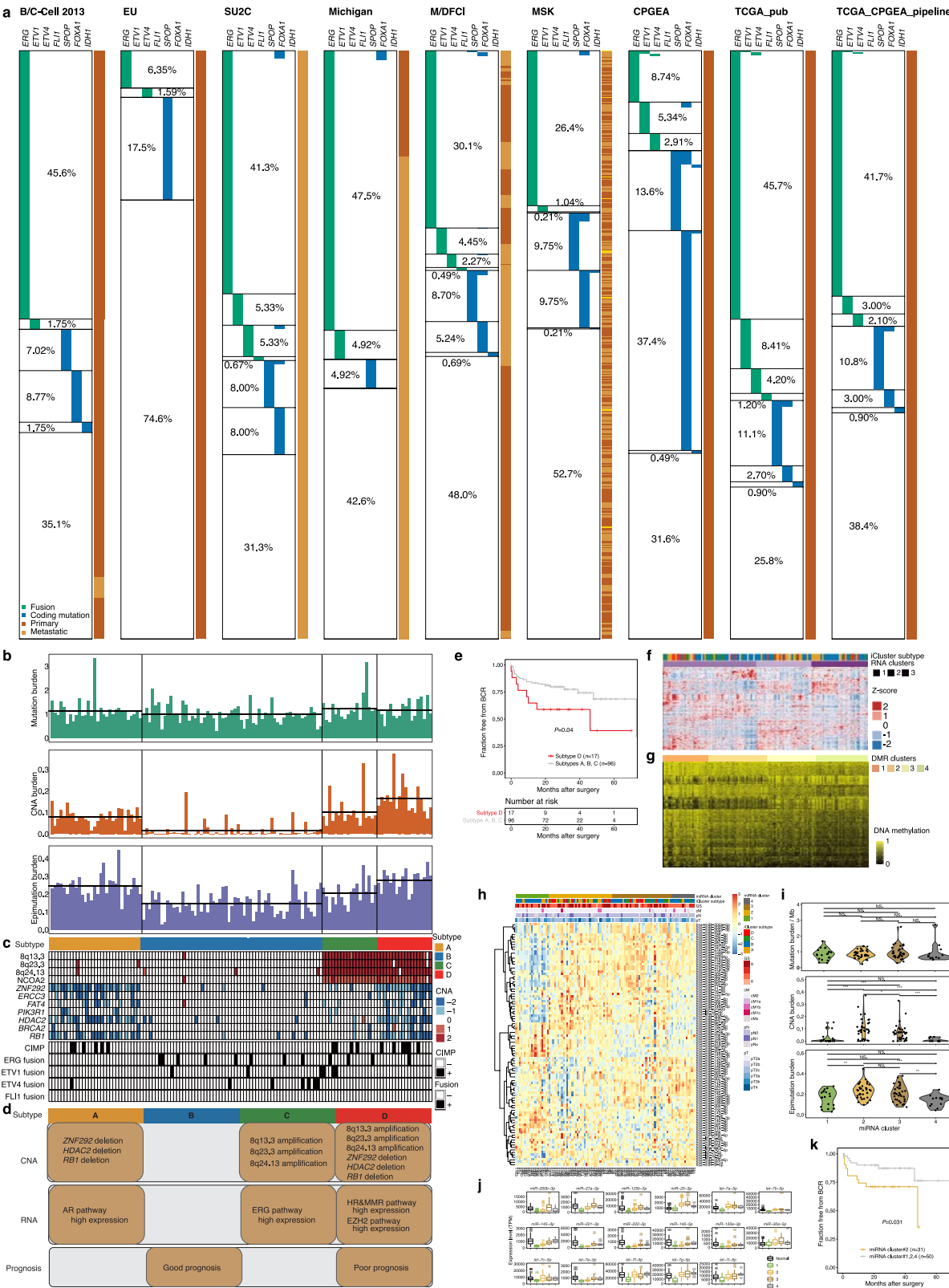
determined by two-sided Wilcoxon signed-rank test. Each dot corresponds to a normal prostate or tumour sample. **f**, Genome-wide methylation levels in 100-kb bins, clustered across tumour samples. Rows represent samples, and columns represent 100-kb genomic bins, with the DNA methylation level of each bin represented by the heat map. **g**, The genome fraction of total PMD length in each tumour, in decreasing order. The leftmost bar represents the genome fraction of the union set of PMDs across all tumours. **h**, PMD recurrence. The red line represents PMDs shared by at least 100 tumours (711 out of 2,218). **i**, Mutation frequency inside versus outside PMDs.  $P = 7.5 \times 10^{-32}$ , two-sided Wilcoxon signed-rank test. Mutation frequency was measured as the average number of SNVs per Mb. Each dot corresponds to a tumour sample ( $n = 187$ ). **j**, Expression level of genes located in PMDs ( $n = 4,043$ ) or outside PMDs ( $n = 15,344$ ) in tumours versus matched normal samples. *P* values determined by one-sided Wilcoxon signed-rank test. Genes in PMDs had significantly lower expression than genes outside PMDs in both tumours and normal samples ( $P = 0$ , two-sided Mann-Whitney *U*-test). Outlier genes with very high expression were omitted from the plot. All box plots are as in Fig. 4b.



Extended Data Fig. 8 | See next page for caption.

**Extended Data Fig. 8 | DMRs and CIMP in CPGEA.** **a**, Recurrence of hypoDMRs. There were 1,172 hypoDMRs were shared by at least 10 tumours (red line). **b**, Recurrence of hyperDMRs. There were 4,214 hyperDMRs were shared by at least 10 tumours (red line). **c**, Genomic location of the union set of hypoDMRs and recurrent hypoDMRs. The innermost circle represents the reference genome background. **d**, Genomic location of the union set of hyperDMRs and recurrent hyperDMRs. The innermost circle represents the reference genome background. **e**, MSigDB perturbation enrichment analysis of recurrent hypoDMRs ( $n = 1,172$ ) using GREAT<sup>87</sup>. **f**, Gene Ontology (GO) enrichment analysis of recurrent hyperDMRs ( $n = 4,214$ ) using GREAT. The top 20 GO biological process terms are shown. **g**, Scatter plots of example epigenetically silenced genes. Each dot represents a normal sample (red), a tumour without a silenced gene (blue), or a tumour with a silenced gene (black). TPM, transcripts per million. **h**, Heat map of CIMP-CGI methylation levels. Rows represent CIMP-

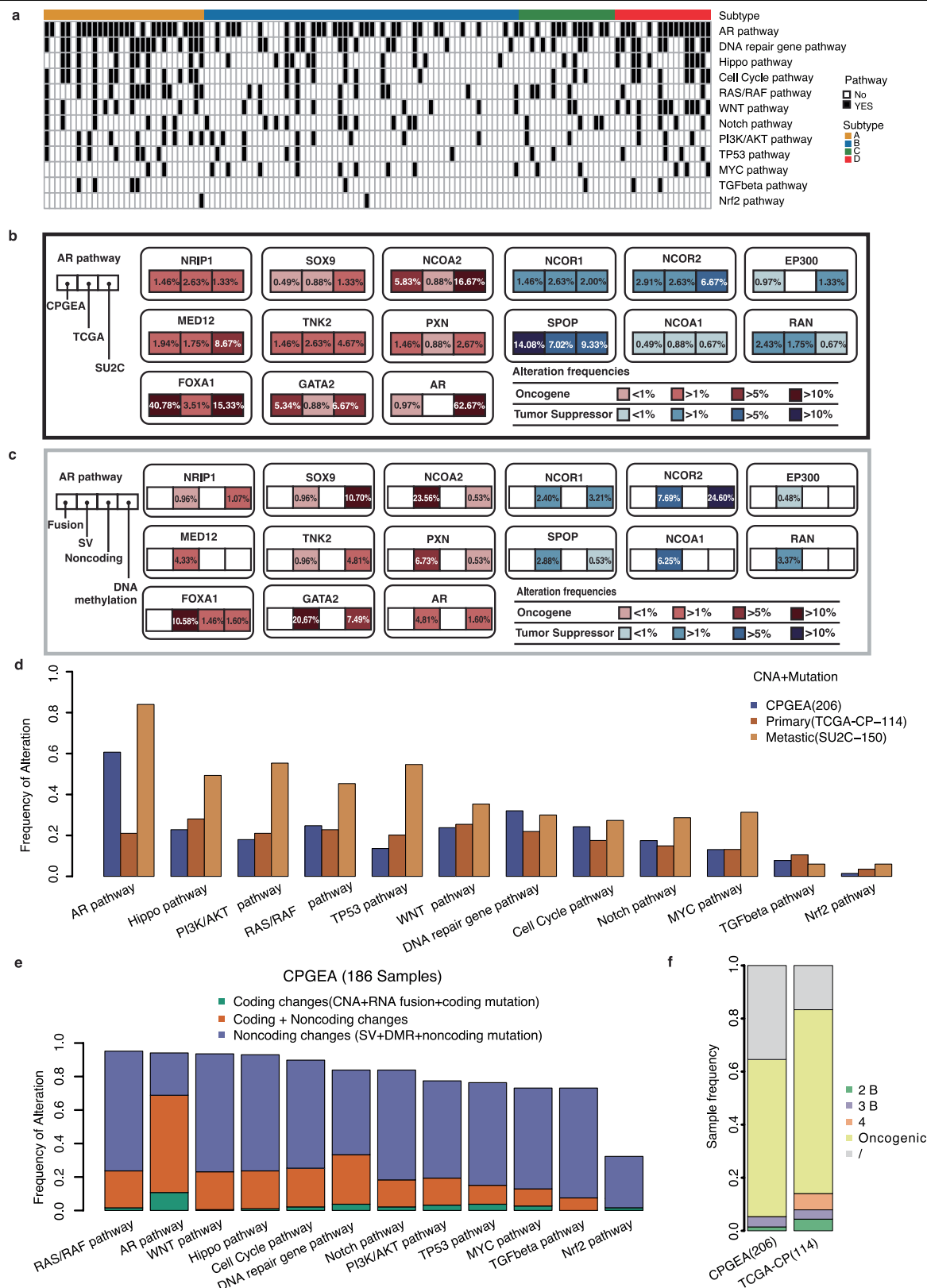
CGIs, and columns represent samples. Tumours (right) were clustered by CIMP-CGI methylation levels, and matched normal samples (left) were sorted in the same order. CIMP-CGIs were sorted by chromosome and genomic coordinates. The top panel shows clinicopathological features of patients (as in Fig. 1), genetic alterations, including fusions and coding mutations, and other molecular phenotypes. **i**, Proportion of recurrent hyperDMRs overlapping CGIs. **j**, Association of CIMP<sup>+</sup> tumours ( $n = 33$ ) with gene mutation status. Red vertical line represents  $P = 0.05$  (two-sided Fisher's exact test). **k**, Kaplan-Meier plot of biochemical recurrence-free survival in patients with CIMP<sup>+</sup> and CIMP<sup>-</sup> tumours.  $P$  values were determined by two-sided log-rank test. **l**, **m**, Correlation between epimutation burden and mutation (**l**) or CNA (**m**) burden. Spearman's correlation coefficient  $\rho = 0.37$ ,  $P = 2.5 \times 10^{-7}$  for mutation burden, and  $\rho = 0.65$ ,  $P = 1.2 \times 10^{-23}$  for CNA burden. Each dot represents a tumour ( $n = 187$ ).





**Extended Data Fig. 9 | Molecular subtypes of prostate cancer.** **a**, Molecular taxonomy across eight cohorts based on seven important oncogenic drivers identified by TCGA. **b**, Mutation burden, CNA burden and epimutation burden across the four molecular subtypes in CPGEA. **c**, Key CNA events, CIMP and fusion events across the four subtypes. ERG fusion-positive genes were combined results from Meerkat, SOAPfuse and high expression samples. **d**, Annotation of each molecular subtype. **e**, Kaplan–Meier plot of biochemical relapse-free survival for iCluster subtype D compared to the other three iCluster subtypes. *P* values were determined by two-sided log-rank test. **f–h**, Clustering of tumours using single datasets, using RNA-seq analysis (**f**), DNA methylation (**g**), and miRNA data (**h**). **h**, Rows represent miRNAs and columns represent tumours. The top panel shows clinical features of patients (as in Fig. 1) along with four miRNA clusters and four iCluster subtypes. **i**, Violin

plots of mutation, CNA and epimutation burdens for four miRNA clusters. Mutation burden, *P* = 0.85, 0.43, 0.61, 0.58, 0.24 and 0.16, for the comparison between miRNA clusters of 1–2, 1–3, 1–4, 2–3, 2–4 and 3–4, respectively. CNA burden, *P* =  $5.9 \times 10^{-6}$ , 0.00025, 0.29, 0.045,  $1.3 \times 10^{-26}$ , and  $4.1 \times 10^{-5}$ , in the same order. Epimutation burden, *P* = 0.0052, 0.090, 0.24, 0.20,  $6.1 \times 10^{-5}$  and 0.0080, in the same order. *P* values determined by two-sided Mann–Whitney *U*-test. Each dot corresponds to a tumour sample belong to miRNA cluster 1 (*n* = 21), 2 (*n* = 37), 3 (*n* = 34), or 4 (*n* = 13). **j**, Box plots of miRNA expression levels in normal samples and four miRNA-based tumour clusters (cluster 1 (*n* = 21), 2 (*n* = 37), 3 (*n* = 34), or 4 (*n* = 13)). Box plots are as in Fig. 4b. **k**, Kaplan–Meier plot of biochemical recurrence-free survival in patients with tumours belonging to miRNA cluster 2 or other clusters. *P* values were determined by two-sided log-rank test. Primary tumours without any treatment were included.



**Extended Data Fig. 10 | Oncogenic pathways in prostate cancer. a**, Summary of genetic and epigenetic lesions in 12 curated pathways across the Chinese prostate cancer subtypes. **b**, Comparison of the frequency of disturbances in the AR pathway between CPGA (primary), TCGA (primary) and SU2C (metastasis) cohorts. The frequency of coding mutations in each AR pathway gene is shown. **c**, The frequency of fusions, structural variations, noncoding mutations and epimutations in each AR pathway gene in the CPGA cohort. Information on additional pathways is provided at <http://www.cpgea.com>.

**d**, Comparison of pathway-level alterations across the CPGA (206 samples, excluding 2 microsatellite instability (MSI) samples), TCGA (114 samples processed with the CPGA pipeline), and SU2C cohorts (150 samples downloaded from cBioPortal). To compare across cohorts, only coding mutations and CNAs were considered. **e**, Frequency of coding alterations (CNAs, fusion genes and nonsynonymous coding mutations) noncoding alterations, and both for each pathway in the CPGA cohort. **f**, Different levels of actionable mutations predicted by OncoKB in CPGA and TCGA.

## Reporting Summary

Nature Research wishes to improve the reproducibility of the work that we publish. This form provides structure for consistency and transparency in reporting. For further information on Nature Research policies, see [Authors & Referees](#) and the [Editorial Policy Checklist](#).

### Statistics

For all statistical analyses, confirm that the following items are present in the figure legend, table legend, main text, or Methods section.

- |                                     |  |
|-------------------------------------|--|
| n/a                                 | Confirmed  |
| <input type="checkbox"/>            | <input checked="" type="checkbox"/> The exact sample size ( $n$ ) for each experimental group/condition, given as a discrete number and unit of measurement  |
| <input type="checkbox"/>            | <input checked="" type="checkbox"/> A statement on whether measurements were taken from distinct samples or whether the same sample was measured repeatedly  |
| <input type="checkbox"/>            | <input checked="" type="checkbox"/> The statistical test(s) used AND whether they are one- or two-sided<br><i>Only common tests should be described solely by name; describe more complex techniques in the Methods section.</i>   |
| <input checked="" type="checkbox"/> | <input type="checkbox"/> A description of all covariates tested  |
| <input type="checkbox"/>            | <input checked="" type="checkbox"/> A description of any assumptions or corrections, such as tests of normality and adjustment for multiple comparisons  |
| <input type="checkbox"/>            | <input checked="" type="checkbox"/> A full description of the statistical parameters including central tendency (e.g. means) or other basic estimates (e.g. regression coefficient) AND variation (e.g. standard deviation) or associated estimates of uncertainty (e.g. confidence intervals) |
| <input type="checkbox"/>            | <input checked="" type="checkbox"/> For null hypothesis testing, the test statistic (e.g. $F$ , $t$ , $r$ ) with confidence intervals, effect sizes, degrees of freedom and $P$ value noted<br><i>Give <math>P</math> values as exact values whenever suitable.</i>                            |
| <input checked="" type="checkbox"/> | <input type="checkbox"/> For Bayesian analysis, information on the choice of priors and Markov chain Monte Carlo settings  |
| <input checked="" type="checkbox"/> | <input type="checkbox"/> For hierarchical and complex designs, identification of the appropriate level for tests and full reporting of outcomes  |
| <input type="checkbox"/>            | <input checked="" type="checkbox"/> Estimates of effect sizes (e.g. Cohen's $d$ , Pearson's $r$ ), indicating how they were calculated   |

Our web collection on [statistics for biologists](#) contains articles on many of the points above.

### Software and code

Policy information about [availability of computer code](#)

#### Data collection

The tumor and matched normal samples from 208 Chinese prostate cancer patients were collected by ourselves. Our cohort was consisted of 416 WGS, 268 RNA-seq, 374 WGBS, and 210 miRNA-seq datasets. Sequencing was performed using an Illumina HiSeq X TEN instrument running HiSeq Control software v3.5.0.

We also collected existing public datasets from 2,554 PCa representing 13 Western cohorts as well as our pilot Chinese cohort published in European Urology. All the access codes for the public datasets have been shown in Supplementary Data 1.

To obtain new FOXA1 binding sites experimentally validated in prostate tumor cell line, we collected the following ChIP-seq data from GSE123618: GSM3508089, GSM3508092, GSM3508095, GSM3508098, and GSM3508101.

No special software was used to download the public datasets.

#### Data analysis

Here we listed the versions of all the software we used and all the details can be found in the Methods section. All the code we used has been deposited in our supporting website (<http://www.cpgea.com>).

Sequencing reads were aligned to the Human Genome Reference Consortium build 38 (GRCh38) using BWA v0.7.8.

BWA v0.7.8 (BWA-mem);

TopHat v2.0.9;

Bowtie2 v2.0.6;

Bismark v0.16.3;

miRBase20.0;

mirdeep2 v1.1.1;

RepeatMasker v4.0.3;

Picard v1.111;

Genome Analysis Toolkit (GATK) v3.1;

GATK's HaplotypeCaller;

MuTect v1.1.4;

Strelka v1.0.13;

SOAPfuse v1.27;

ANNOVAR (Sun, 22 Mar 2015);  
 SomaticSignatures package v2.9.4;  
 Control-FREEC v6.7;  
 GISTIC 2.0 v6.2 GenePattern module;  
 Meerkat v0.189;  
 Shatterseek v0.4;  
 ChainFinder v1.0.1;  
 MutSigCV v1.4;  
 MuSiC v0.04;  
 funseq2 v2-1.6;  
 denovoTF;  
 Cuffdiff v1.3.0;  
 VMD v1.9.3;  
 FastQC v0.11.5;  
 Trimmomatic v0.36;  
 MethPipe v3.4.3;  
 DSS v2.14.0;  
 BEDTools v2.27.1;  
 GENCODE Release 27;  
 GeneHancer v4.7;  
 GREAT v3.0.0; and  
 iClusterplus v1.16.0

For manuscripts utilizing custom algorithms or software that are central to the research but not yet described in published literature, software must be made available to editors/reviewers. We strongly encourage code deposition in a community repository (e.g. GitHub). See the Nature Research [guidelines for submitting code & software](#) for further information.

## Data

Policy information about [availability of data](#)

All manuscripts must include a [data availability statement](#). This statement should provide the following information, where applicable:

- Accession codes, unique identifiers, or web links for publicly available datasets
- A list of figures that have associated raw data
- A description of any restrictions on data availability

All data, including raw data, mutation calls, and clinical information, were deposited to Genome Sequence Archive for Human (<http://bigd.big.ac.cn/gsa-human/>) at BIG Data Center, Beijing Institute of Genomics, Chinese Academy of Sciences, under project number PRJCA001124, GSA number HRA000099. The data deposited and made public is compliant with the regulations of Ministry of Science and Technology of the People's Republic of China.

## Field-specific reporting

Please select the one below that is the best fit for your research. If you are not sure, read the appropriate sections before making your selection.

☒ Life sciences ☐ Behavioural & social sciences ☐ Ecological, evolutionary & environmental sciences

For a reference copy of the document with all sections, see [nature.com/documents/nr-reporting-summary-flat.pdf](https://www.nature.com/documents/nr-reporting-summary-flat.pdf)

## Life sciences study design

All studies must disclose on these points even when the disclosure is negative.

Sample size	Sample sizes were determined in order to obtain more than 200 normal-tumor pairs. All primary tumor and matched normal tissue from 208 patients were used to generate sequencing data in this study. In all, 1,268 datasets including 416 WGS, 268 RNA-seq, 210 miRNA-seq, and 374 WGBS were used in this study.
Data exclusions	Two tumor cases exhibited extreme hypermutation phenotypes and were determined to contain mutations in DNA repair genes. Patient 13 who also had pre-surgery treatment history (Zoladex+bicalutamide) had a germline mutation in MSH6 (3991C>T, Arg1331Ter). Patient 502, who also had bone metastasis, had a somatic indel in MLH1 (Fig. 1). These outliers were excluded from the integrative analysis.
Replication	This is not applicable to our study.
Randomization	This is not relevant since we did not use different experimental groups or conditions in our study.
Blinding	This is not relevant since we did not use different experimental groups or conditions in our study.

## Reporting for specific materials, systems and methods

We require information from authors about some types of materials, experimental systems and methods used in many studies. Here, indicate whether each material, system or method listed is relevant to your study. If you are not sure if a list item applies to your research, read the appropriate section before selecting a response.

## Materials &amp; experimental systems

## Methods

n/a	Involvement in the study
<input checked="" type="checkbox"/>	<input type="checkbox"/> Antibodies
<input checked="" type="checkbox"/>	<input type="checkbox"/> Eukaryotic cell lines
<input checked="" type="checkbox"/>	<input type="checkbox"/> Palaeontology
<input checked="" type="checkbox"/>	<input type="checkbox"/> Animals and other organisms
<input type="checkbox"/>	<input checked="" type="checkbox"/> Human research participants
<input checked="" type="checkbox"/>	<input type="checkbox"/> Clinical data

n/a	Involvement in the study
<input checked="" type="checkbox"/>	<input type="checkbox"/> ChIP-seq
<input checked="" type="checkbox"/>	<input type="checkbox"/> Flow cytometry
<input checked="" type="checkbox"/>	<input type="checkbox"/> MRI-based neuroimaging

## Human research participants

Policy information about [studies involving human research participants](#)

## Population characteristics

Our cohort was consisted of only Chinese patients with prostate cancer. Patient ages ranged from 50 to 88 years (median 69 years). Preoperative PSA levels ranged from 1.25 to 1270.14 ng/ml (median 38.8 ng/ml). The Gleason scores were distributed as follows: Gleason score 6:17 (8%); 7: 96 (46%); 8–10: 94 (45%). Organ-confined carcinoma (pT2) was found in 105 patients; 93 showed extra-prostatic tumor extension (pT3); 10 patients had advanced disease which invaded bladder, rectum or pelvic muscles (pT4). 15 patients (7%) had bone metastasis at the discretion of the referring urologist, prior to surgery. 11 percent of patients who underwent the lymph nodes dissection had positive lymph nodes invasion. Our cohort also contained 18 patients who exhibited some level of metastasis at diagnosis, and they were hormone sensitive. 16 patients were treated with ADT before surgery, mostly to reduce the size of their primary tumor. The clinical and pathological characterization of the final cohort were summarized in Supplementary Data 2.

## Recruitment

After obtained the consent of patients, a series of 210 prostate tumor samples and their non-tumor counterparts were collected from patients surgically treated in the Urology Department. We focused on the primary tumors in our study.

## Ethics oversight

Ethical committee approval for this study was obtained from Changhai Hospital (TMEC2014-001), the first hospital affiliated to Second Military Medical University. Written informed consent was obtained in accordance with Chinese legislation.

Note that full information on the approval of the study protocol must also be provided in the manuscript.



# Fundamental bounds on the fidelity of sensory cortical coding

<https://doi.org/10.1038/s41586-020-2130-2>

Received: 1 August 2017

Accepted: 21 January 2020

Published online: 18 March 2020

 Check for updates

Oleg I. Rumyantsev<sup>1,2,3</sup>✉, Jérôme A. Lecoq<sup>1,2,4,5</sup>, Oscar Hernandez<sup>1,2</sup>, Yanping Zhang<sup>1,2,6</sup>, Joan Savall<sup>1,2,6</sup>, Radostaw Chrapkiewicz<sup>1,2</sup>, Jane Li<sup>1,4</sup>, Hongkui Zeng<sup>5</sup>, Surya Ganguli<sup>1,3</sup>✉ & Mark J. Schnitzer<sup>1,2,3,4,6</sup>✉

How the brain processes information accurately despite stochastic neural activity is a longstanding question<sup>1</sup>. For instance, perception is fundamentally limited by the information that the brain can extract from the noisy dynamics of sensory neurons. Seminal experiments<sup>2,3</sup> suggest that correlated noise in sensory cortical neural ensembles is what limits their coding accuracy<sup>4–6</sup>, although how correlated noise affects neural codes remains debated<sup>7–11</sup>. Recent theoretical work proposes that how a neural ensemble's sensory tuning properties relate statistically to its correlated noise patterns is a greater determinant of coding accuracy than is absolute noise strength<sup>12–14</sup>. However, without simultaneous recordings from thousands of cortical neurons with shared sensory inputs, it is unknown whether correlated noise limits coding fidelity. Here we present a 16-beam, two-photon microscope to monitor activity across the mouse primary visual cortex, along with analyses to quantify the information conveyed by large neural ensembles. We found that, in the visual cortex, correlated noise constrained signalling for ensembles with 800–1,300 neurons. Several noise components of the ensemble dynamics grew proportionally to the ensemble size and the encoded visual signals, revealing the predicted information-limiting correlations<sup>12–14</sup>. Notably, visual signals were perpendicular to the largest noise mode, which therefore did not limit coding fidelity. The information-limiting noise modes were approximately ten times smaller and concordant with mouse visual acuity<sup>15</sup>. Therefore, cortical design principles appear to enhance coding accuracy by restricting around 90% of noise fluctuations to modes that do not limit signalling fidelity, whereas much weaker correlated noise modes inherently bound sensory discrimination.

The sensitivity and noise fluctuations of primary sensory neurons, such as photoreceptors or mechanoreceptors, limit the perception of weak stimuli<sup>16–18</sup>, although disagreement persists about which downstream noise sources limit perceptual discriminations when sensory inputs exceed detection thresholds<sup>4–14</sup>. A groundbreaking experiment spurred this debate by identifying individual visual cortical neurons that signal visual attributes nearly as reliably as an animal's perceptual reports<sup>2,3</sup>. One proposed explanation is that similarly tuned cortical neurons might share positively correlated noise fluctuations that limit the perceptual improvements attainable by averaging signals from multiple cells with similar response properties<sup>2,4</sup> (Extended Data Fig. 1a–c).

Theoretical studies show that positively correlated noise limits the information that cells with similar sensory-evoked responses can encode<sup>4,5,7</sup>, but this is not necessarily the case for ensembles of cells with diverse tuning properties<sup>8–10</sup> (Extended Data Fig. 1d–f). A recent framework based on a feedforward neural network asserts that, in the space of all possible neural ensemble dynamics, it is only noise in the

dimensions of sensory representations that constrains coding fidelity<sup>13,14</sup> (Extended Data Fig. 1g–m). Previous experiments have examined noise in cell pairs, but this approach incurs substantial measurement errors<sup>13,19,20</sup> and the results were conflicting<sup>4,6,21–23</sup>. To our knowledge, no previous study has recorded neural ensemble noise patterns, related these to sensory signals, and tested the idea that only specific noise patterns confine the information encoded by large neural populations<sup>13,14</sup>.

## A multi-beam two-photon microscope

To make such measurements, we built a laser-scanning two-photon microscope with a 4-mm<sup>2</sup> field of view for imaging across the span of the mouse primary visual cortex (V1). The microscope has 16 photodetectors and 16 corresponding beams, which originate from one laser and are focused 500 µm apart in the specimen in a 4 × 4 array (Fig. 1). Four beams are active at any instant, and switching to a different four beams takes about 50 ns; this enables scanning of a larger area per unit time

<sup>1</sup>James H. Clark Center for Biomedical Engineering & Sciences, Stanford University, Stanford, CA, USA. <sup>2</sup>CNC Program, Stanford University, Stanford, CA, USA. <sup>3</sup>Department of Applied Physics, Stanford University, Stanford, CA, USA. <sup>4</sup>Department of Biology, Stanford University, Stanford, CA, USA. <sup>5</sup>Allen Institute for Brain Science, Seattle, WA, USA. <sup>6</sup>Howard Hughes Medical Institute, Stanford University, Stanford, CA, USA. ✉e-mail: [rumyantsev.oleg@gmail.com](mailto:rumyantsev.oleg@gmail.com); [sganguli@stanford.edu](mailto:sganguli@stanford.edu); [mschnitz@stanford.edu](mailto:mschnitz@stanford.edu)

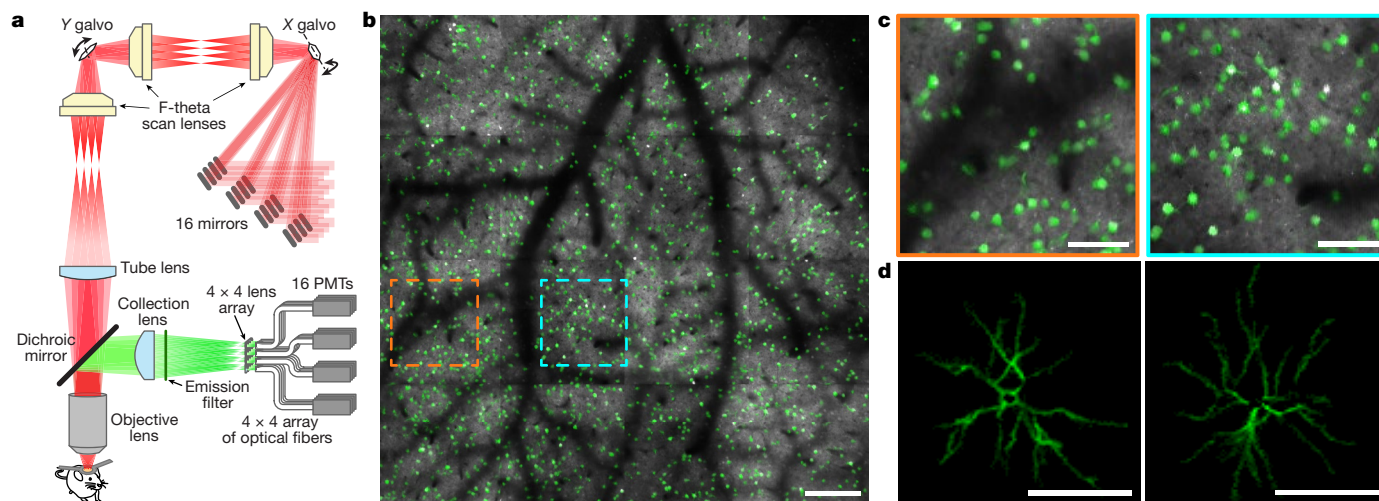


**Fig. 1 | Two-photon  $\text{Ca}^{2+}$  imaging over a 4-mm<sup>2</sup> field of view.** **a**, Schematic of the microscope. Sixteen laser beams converge on a pair of galvanometer mirrors (X- and Y-galvos). Sixteen photomultiplier tubes (PMTs) detect fluorescence. **b**, Two-photon image (greyscale, mean of 1,000 frames taken at 7.23 Hz) of GCaMP6f-expressing layer 2/3 pyramidal neurons in the visual

cortex of an awake mouse. Overlaid are >2,000 neuronal somata (green) identified in the  $\text{Ca}^{2+}$  video. Boxed areas are magnified in **c**. **c**, Magnifications of the boxed areas in **b**. **d**, Example  $\text{Ca}^{2+}$ -activity sources (computationally identified), revealing dendrites. Images in **b–d** are representative of results from 10 mice. Scale bars: **b**, 250  $\mu\text{m}$ ; **c**, **d**, 100  $\mu\text{m}$ .

than would be feasible with one beam and the same optics (Extended Data Figs. 2–4). Compared to 16 active beams, our approach yields fourfold greater fluorescence for any given time-averaged illumination power and delivers fourfold less heat to the brain for an equivalent rate of fluorescence emission (Supplementary Note). The active laser foci are  $\geq 1\text{ mm}$  apart, so fluorescence scattering between the four active image tiles is  $<2\%$ ; scattering into inactive tiles can be corrected computationally using the 16 photocurrents (Extended Data Fig. 4). Our system images neocortical activity down to layer 5 with full-frame acquisition rates of 7.23–17.5 Hz (Supplementary Videos 1–3), whereas other two-photon microscopes with large fields of view attain similar imaging rates over smaller sub-fields<sup>24–27</sup> (Extended Data Fig. 2j, k).

## Imaging studies across cortical area V1

We studied layer 2/3 pyramidal neurons, which project extensive connections from V1 to higher visual areas. In awake mice expressing the  $\text{Ca}^{2+}$ -indicator GCaMP6f in these neurons, we imaged around 1,000–2,000 cells concurrently as mice viewed, with one eye, a random sequence of moving gratings. Each grating was oriented at either  $+30^\circ$  or  $-30^\circ$  from vertical, lasted 2 s and spanned the central  $\sim 50^\circ$  deg of the eye's visual field (Fig. 2a–c). There were 350 trials with each stimulus, but because locomotion modulates vision<sup>28</sup> we analysed only trials with locomotor speeds of less than  $0.2\text{ mm s}^{-1}$  (217–332 trials per stimulus). From these recordings we extracted 8,029 neurons, mainly in V1 (1,031–2,191 cells in each of 5 mice; Extended Data Figs. 5, 6).

A total of 5,008 cells responded at least weakly to the stimuli, with activity rates and stimulus preferences consistent with those found in previous studies<sup>28,29</sup> (Extended Data Fig. 6a–d). These neurons likely had substantially overlapping inputs, because mouse V1 neurons respond to large portions of the visual field that are comparable in size to our stimuli<sup>29</sup>. Noise correlation coefficients in pairs of concurrently recorded cells were widely distributed, with positive mean values ( $r = 0.06 \pm 0.01$ ; mean  $\pm$  s.d.; 5 mice) as in most previous reports<sup>6</sup> (Fig. 2d–g, Extended Data Fig. 6e–i). Active cell pairs that on average responded similarly to the two stimuli had, on average, noise correlation coefficients about twice as large as those that responded dissimilarly (Fig. 2f, g).

To evaluate the significance of these correlations, we created trial-shuffled datasets in which the responses of each cell were permuted across different trials, thereby mimicking cells with statistically

identical individual responses as in the real data but with uncorrelated noise fluctuations. Non-zero noise correlations in trial-shuffled datasets merely reflect the finite number of trials. Indeed, noise correlation coefficients were more narrowly distributed than in real data, although many deviated substantially from zero (Fig. 2d, g). This confirms the difficulty of measuring noise correlations given limited trials<sup>13,19</sup> and likely explains why previous studies of cell pairs yielded divergent results<sup>4,6,21–23</sup>.

## Evaluations of cortical coding fidelity

To study visual coding, we represented the dynamics using a population vector (one cell per dimension) and used the discriminability index,  $d'$ , to assess the statistical confidence in distinguishing the stimuli on the basis of their evoked neural responses<sup>30</sup>.  $(d')^2$  relates to the Fisher information that the cell ensembles convey about stimulus identity<sup>8,13,30</sup>, which even for binary classifications ( $\leq 1$  bit of Shannon entropy) can be infinite—that is, 100% confidence<sup>31</sup>. Theories of noise correlations and neural coding have largely examined pairwise discriminations, as error rates discriminating more than two stimuli are well approximated using  $d'$  values from all the pairwise comparisons<sup>31</sup>.

To enable us to determine  $d'$  accurately despite having about 5- to 10-fold fewer trials than cells recorded per mouse, we created analyses to extract the primary, ensemble noise modes without measuring noise in cell pairs (Appendix). First, we performed a dimensional reduction by using partial least squares (PLS) analysis to identify and retain only five population vector dimensions in which the stimuli were highly distinguishable; retaining more than five dimensions only added noise and decreased the ability to distinguish the stimuli (Fig. 3a, b, Extended Data Figs. 5b, 7a–c). In this five-dimensional representation, the neural dynamics evoked by the two stimuli became distinguishable over the first  $\sim 0.5$  s of stimulus presentation (Fig. 3b–d). Using an optimal linear decoder of the ensemble activity,  $d'$  values rose to a plateau within  $\sim 0.5$  s of the stimulus onset; the optimal decoder then remained stable until stimulus offset (Extended Data Fig. 7d). In shuffled datasets the stimuli were even more distinguishable, as  $d'$  values attained greater values than in real datasets, indicating that correlated noise degrades stimulus representations in the real data.

We also evaluated decoders that ignore noise correlations. ‘Diagonal decoders’, which neglect off-diagonal elements of the noise covariance

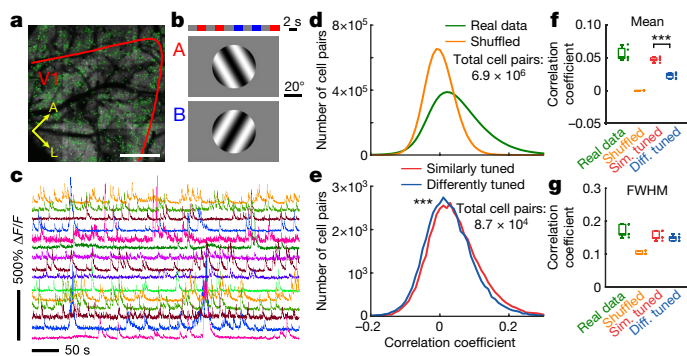


**Fig. 2 | Noise correlations of cell pairs are difficult to estimate from hundreds of stimulus trials.** **a**, Image of visual cortex, processed as in Fig. 1b. The coordinate system indicates anterior (A) and lateral (L) directions. The red line marks the area V1 boundary, found by retinotopic mapping. Scale bar, 500  $\mu$ m. **b**, Top, in each trial, one of two randomly chosen stimuli (A or B) appeared for 2 s, followed by a uniform background for 2 s. Bottom, each stimulus was a drifting grating, oriented at either  $+30^\circ$  or  $-30^\circ$  from vertical. The analyses in **d–g** used 217–332 trials per stimulus in each of 5 mice. **c**, Example  $\text{Ca}^{2+}$  activity traces. **f**, fluorescence intensity. **d**, Histograms of noise correlation coefficients (Pearson's  $r$ ) for concurrently imaged cell pairs (6,946,280 cell pairs; 5 mice), computed using the estimated spike count of each cell within [0.5 s, 2 s] of stimulus onset.  $r$  values are averages across both stimuli for real and trial-shuffled datasets. The latter histogram was Gaussian ( $R^2 = 0.9982 \pm 0.0005$  (95% confidence interval)) with a variance around 50% of that of the real data, showing the difficulty of accurately determining pairwise noise correlations with hundreds of trials. Error bars estimated as counting errors are too small to see. **e**, Histograms of noise correlation coefficients differed significantly for cell pairs with similarly or differently tuned mean responses to the two stimuli, computed for the top 10% most active cells and by grouping cell pairs into those with positively or negatively correlated mean responses to the two stimuli. ( $***P < 1.3 \times 10^{-6}$  for all 5 mice; two-tailed Kolmogorov–Smirnov test; 901 cells, 43,887 positively and 43,768 negatively correlated pairs). For exact  $P$  values for this and all subsequent figures, see Supplementary Information. **f, g**, Box plots of mean (**f**) and full width at half maximum (FWHM) (**g**) values of the colour-corresponding distributions in **d, e**. Circles indicate data points for 5 individual mice. Noise correlations in **f** were greater for cell pairs with similarly tuned responses (one-tailed Wilcoxon rank sum test,  $***P < 0.001$  for all 5 mice). Extended Data Fig. 6g–i shows results for all cell pairs. Boxes cover the middle 50% of values, horizontal lines denote medians, and whiskers span the full range of the data.

matrix<sup>30</sup>, performed nearly as well as optimal linear decoders, although the decrement was statistically significant (Fig. 3d–h). Thus, although correlated neural noise degraded stimulus encoding, using the noise structure to improve decoding brought only modest benefit.

The stability of the optimal decoder across most of the stimulus duration suggested that, by integrating neural activity across the stimulus presentation, the brain might in principle average out noise in its sensory representations to improve discrimination. To test this, we examined the optimal linear decoder of the time-integrated neural responses over each trial, which indeed yielded greater  $d'$  values (Extended Data Fig. 7e). For comparison, we examined decoders of the cumulative set of neural responses that had occurred up to each moment in the stimulation trial (Fig. 3e–h). Cumulative decoders surpassed those using individual time-bins of neural activity, but not the simple decoder of time-integrated activity (Extended Data Fig. 7e). This suggests that there was little temporal structure in the sustained neural responses that might improve decoding beyond that attained using time-integrated activity, at least as reported by  $\text{Ca}^{2+}$  imaging.

We next examined how decoding varied with  $n$ , the number of cells analysed. In the absence of correlated noise, each additional cell used should linearly increase the Fisher information that is conveyed about the identity of the stimulus<sup>5,12</sup>. Trial-shuffled datasets confirmed this, as  $(d')^2$

increased linearly with  $n$  (Fig. 3f, g). In real data,  $(d')^2$  reached a plateau when  $n$  exceeded  $\sim 1,000$  cells, for both instantaneous and cumulative decoders (Fig. 3f–i). This constitutes direct evidence of information saturation in large neural populations, without extrapolations from cell pairs.

Several control analyses bolstered these conclusions. First, we validated linear decoding as a way of assessing Fisher information. The noise covariance matrix was stimulus-independent, with similar matrix elements for both stimuli ( $r = 0.81 \pm 0.16$ ; mean  $\pm$  s.d.; 20 off-diagonal matrix elements for each of 5 mice). Thus, nonlinear decoders should have similar accuracy as the optimal linear decoder, which we confirmed by quantifying the additional information that an optimal quadratic decoder could extract from the data (Extended Data Fig. 7f–h). Second, we verified that there were a sufficient number of trials to estimate  $d'$  accurately. In every mouse the empirically determined values of  $d'$  approached a stable estimate with increasing numbers of trials and were stationary across the imaging session (Extended Data Fig. 7g, i, j). Third, we confirmed that alternative decoding methods using regularized regression yielded similar  $d'$  values and identical conclusions to those from PLS analysis (Extended Data Fig. 8a, b). Further, we used regularized regression to analyse publicly available neural activity datasets<sup>32</sup>, which also showed that  $d'$  reached a plateau (Appendix). Fourth, we used simulations to verify that our decoders were robust to potential large sources of neural variability, such as common mode noise and gain modulation of visual responses (Extended Data Fig. 8c–h). Fifth, we mathematically derived the accuracy of  $d'$  determinations made via PLS analysis (Appendix). Altogether, numerous analyses and derivations upheld the information saturation that we found in ensembles of  $\sim 1,000$  neurons or more.

The data also enabled us to test a framework for understanding cortical noise fluctuations based on a feedforward network<sup>12,13</sup>. In this framework, the encoded information,  $I$ , as a function of the ensemble size,  $n$ , obeys  $I(n) = (I_0 n) / [1 + \varepsilon n]$ , where the constant  $I_0$  is the mean encoded information per cell in the shuffled data and the parameter  $\varepsilon$  characterizes the strength of information-limiting correlations<sup>13</sup>. Our data matched this prediction (Fig. 3f, g), verifying the existence of information-limiting correlations and establishing the effect size. The minimum set of cells needed to detect information saturation is approximately  $2\varepsilon^{-1}$ , which is around 800–1500 cells for the instantaneous decoders (Fig. 3h, i). This shows the importance of large recordings to adjudicate whether correlated noise limits coding accuracy, and likely explains why previous recordings of less than 350 cells did not observe information saturation<sup>19,21</sup>.

## Comparing neural coding to visual acuity

An additional benefit of recordings across V1 is to enable estimates of the attainable perceptual acuity given only the information encoded in the early visual cortex, which is important for fine discriminations of grating stimuli<sup>33</sup>. To approximate conditions more representative of the perceptual threshold, we examined another 5 mice that viewed the same grating stimuli as before but with  $\pm 6^\circ$  orientations—closer to the discriminability limits.

As expected, these stimuli were harder to distinguish from their evoked neural activity stimuli (Extended Data Fig. 9). The asymptotic  $d'$  value ( $\sim 2.5$ ) for large  $n$  suggests that gratings presented at  $\pm 2.4^\circ$  under otherwise identical viewing conditions would have the minimal, perceptibly distinct orientations ( $d' \approx 1$ ). Behavioural studies of mouse visual spatial acuity under photopic illumination<sup>15</sup> yield similar predictions of  $\pm 2.3^\circ$  (Methods). Direct measurements of mouse visual orientation sensitivity have been slender and used different stimuli from ours, but yielded similar values<sup>34</sup>. The fine agreement in these numbers is probably fortuitous, but the similar values estimated from cortical responses and behavioural studies<sup>15,34</sup> suggest that the information signalling limits of visual cortical coding likely have an important role in setting perceptual bounds.



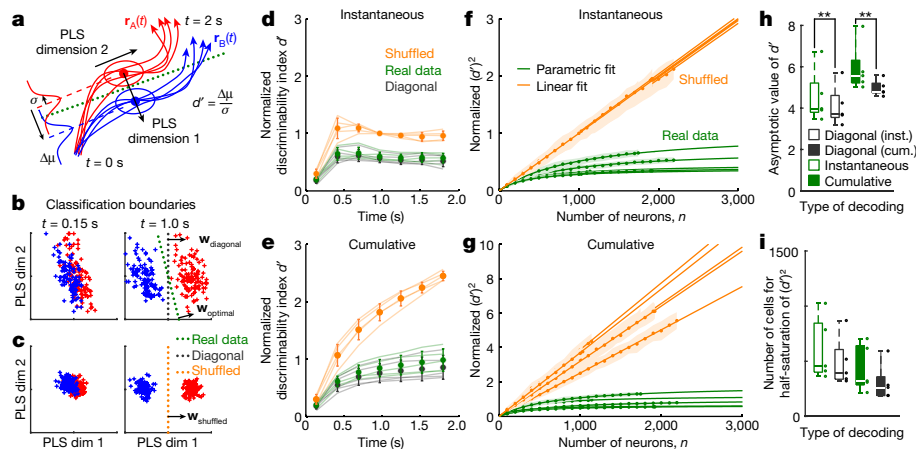


**Fig. 3 | Correlated noise limits the information conveyed by cortical neural ensembles.** **a**, Schematic of neural ensemble dynamics in a population vector representation of reduced dimensionality. Trajectories,  $\mathbf{r}_A(t)$  and  $\mathbf{r}_B(t)$ , depict single-trial responses to different (red, blue) stimuli. At a fixed time after stimulus onset, the sets of responses to the two stimuli form two distributions of points (ellipses). At the bottom left are projections of these distributions onto a subspace, found by PLS analysis, in which responses to the two stimuli are most distinct. The green line indicates the optimal linear boundary for classifying stimuli in this subspace. The stimulus discriminability,  $d'$ , equals the separation,  $\Delta\mu$ , of the two distributions along the dimension orthogonal to this boundary, divided by the s.d.,  $\sigma$ , of each distribution along this dimension. **b, c**, Neural ensemble responses, 0.15 s (left) and 1 s (right) after stimulus onset, in the two-dimensional space in which the sets of responses to the two stimuli are most distinct, for real (b) or trial-shuffled (c) datasets. The blue and red crosses denote individual trials (220 trials per stimulus); the green and orange lines mark the classification boundaries for real and trial-shuffled data, respectively; and the vertical black line in **b** is the classification boundary for diagonal discrimination, which ignores correlations in the responses of the cells.  $\mathbf{w}_{\text{optimal}}$ ,  $\mathbf{w}_{\text{shuffled}}$  and  $\mathbf{w}_{\text{diagonal}}$  represent directions normal to the classification boundaries.  $\mathbf{w}_{\text{shuffled}} = \mathbf{w}_{\text{diagonal}}$ , as the corresponding classification boundaries are identical. **d**, Mean values of  $d'$  (coloured data points;  $N = 5$  mice) plotted as a function of time after stimulus onset, for the classifiers in **b, c**. Error bars represent the standard deviation. Coloured lines show the  $d'$  values for individual mice, computed using the protocol of Extended Data Fig. 5b and

averaged over 100 different randomly chosen subsets of 1,000 cells and randomly chosen assignments of trials to decoder training sets and test sets in each mouse.  $d'$  values are normalized by those obtained for trial-shuffled data (averaged across 0.83–1.11 s). **e**, Same as **d** but using cumulative decoding, which considers the full time-course of the activity of each cell up to time  $t$ . For each mouse,  $d'$  values in **e–h** have the same normalizations as in **d, f**,  $(d')^2$  values during the interval 0.83–1.11 s from stimulation onset, plotted against the number of cells,  $n$ , used for analysis. Data points in **f–i** are averages over 100 different subsets of cells, and the shading in **f, g** indicates the standard deviation. For real data,  $(d')^2$  values were well fit by the expression  $(d')^2 = (d')^2_{\text{shuffled}} / (1 + \varepsilon \times n)$ , (green curves;  $R^2 = 0.88 \pm 0.03$  (s.d);  $\varepsilon = 0.0019 \pm 0.0007$ ; 5 mice), where  $\varepsilon$  is the fit parameter and  $(d')^2_{\text{shuffled}}$  is the  $(d')^2$  value for  $n$  cells in a linear regression to the shuffled data (orange lines). **g**, Same as **f**, but for  $(d')^2$  values computed using cumulative decoding for the interval 0–1.11 s. **h, i**, Asymptotic  $d'$  values in the limit of many cells (**h**) and the number of cells at which  $(d')^2$  attains half its asymptotic value (**i**) determined from curve fits as in **f, g** for instantaneous (open boxes) and cumulative (filled boxes) decoding. Optimal linear decoders (green) slightly but significantly outperformed diagonal decoders (black) ( $**P < 10^{-11}$ ; one-tailed Wilcoxon rank sum test;  $N = 100$  different assignments to decoder testing and training sets using all cells recorded in each mouse; dots are mean values from individual mice). Boxes cover the middle 50% of values, horizontal lines denote medians, and whiskers span the full range of the data. Analyses in **d–i** are based on 217–332 trials per stimulus in each of 5 mice and time bins of 0.275 s.

## Origins of information-limiting noise

To identify why the information saturates, we analysed the neural noise structure by finding the principal eigenvectors of the neural noise covariance matrix and the mean amplitudes of visual signals encoded along each of these eigenvectors. This allowed us to decompose  $(d')^2$  into a sum of signal-to-noise ratios, one for each eigenvector<sup>13</sup> (Methods). Although visual signal amplitudes increase linearly with ensemble size,  $n$  (Fig. 4a, b), certain noise eigenvalues might also increase with  $n$ , which could offset the greater signalling capacity of a larger ensemble and cause the information saturation.

We developed methods to determine the principal eigenvectors of the noise covariance matrix without needing accurate estimates of its matrix elements—a key distinction from previous analyses<sup>13,19,20</sup>. Contravening prevailing thinking, with our approach recordings of more cells enable accurate estimates of these eigenvectors and of  $d'$  using fewer trials (Extended Data Fig. 10). As  $n$  increased, mean ensemble responses to the two stimuli became increasingly distinct while staying aligned to the dimensions important for optimal decoding (Fig. 4b, c). In real but not in shuffled datasets the noise covariance matrix had 2–3 eigenvalues that also increased linearly with  $n$  (Fig. 4d, e). We examined how these particular noise eigenmodes related to the dimensions in which the neural ensembles represented visual signals.

In every mouse the visual signalling dimensions were nearly orthogonal to the largest noise mode, which therefore had almost no effect on coding fidelity even though it was around tenfold greater than any other noise mode (Fig. 4e–h; Extended Data Fig. 10). Instead, it was the third-largest noise mode that primarily aligned with the visual coding dimensions and thereby limited coding accuracy (Fig. 4f–h). These properties were sometimes seen, to a lesser extent, in the second-largest mode. The existence of noise eigenvectors that closely align to the dimensions used for visual representations and have eigenvalues that grow with  $n$  explains the information saturation for large  $n$  and why there was little performance decrement for decoders that did not account for correlated noise. Although these inferences rely on  $\text{Ca}^{2+}$  signals, not electrical recordings, this is unlikely to affect the conclusions, as variability in how spikes produce  $\text{Ca}^{2+}$  signals arises mainly from fluctuations in  $\text{Ca}^{2+}$  levels, photon emission and detection, which are statistically independent across cells and are not information-limiting.

A key question is how does information-limiting noise arise. Recent work examines this issue in a two-layer, feedforward network model with sensory inputs and intrinsic noise in both its input and its output layers<sup>12</sup>. As more cells are added to the output layer, the encoded information approaches a plateau, the value of which depends on the noise levels and synaptic weights<sup>12</sup> (Extended Data Fig. 1j–m). Our re-analysis of this model<sup>12</sup> revealed that the dimensionality of the space of receptive fields in the output layer equals the number of noise covariance matrix

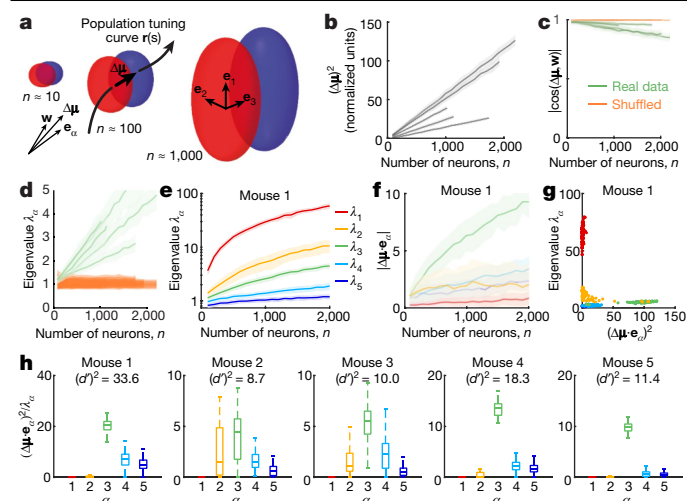


**Fig. 4 | The largest noise mode is orthogonal to the dimensions encoding sensory information.** **a**, Schematics of trial-to-trial variability in ensemble neural responses with increasing numbers of cells,  $n$ . Ellipsoids represent 1 s.d. fluctuations around mean ensemble responses,  $\mathbf{r}(s)$ , to two similar stimuli parameterized by a variable  $s$  (here the stimulus orientation). For large  $n$ , response variability along the tuning curve,  $\mathbf{r}(s)$ , increases proportionally to the separation,  $\Delta\boldsymbol{\mu}$ , between the two mean responses, leading to a saturation of  $d'$ .  $\mathbf{w}$  is the normal to the optimal linear classification boundary between the two response sets.  $\mathbf{e}_{1,2,3}$  are three eigenvectors,  $\mathbf{e}_\alpha$ , of the noise covariance matrix, averaged across both stimuli. The eigenvalues,  $\lambda_\alpha$ , are the noise variances along each eigenvector. **b**, Mean values of  $(\Delta\boldsymbol{\mu})^2$  plotted against  $n$  for 5 mice in units of the variance in the shuffled datasets, which have isotropic noise covariance matrices. Analyses in **b–h** used instantaneous decoding in the five-dimensional space found by PLS analysis and 100 different randomly chosen subsets of cells and assignments of trials to decoder training sets and test sets. Given these 100 sets of results, lines and shading in **b–f** denote mean  $\pm$  s.d., **g** shows 100 individual results, and **h** has box plots. **c**, Cosine of the angle between  $\Delta\boldsymbol{\mu}$  and  $\mathbf{w}$  plotted against  $n$  for 5 individual mice in real and trial-shuffled datasets. Because  $\Delta\boldsymbol{\mu}$  is nearly collinear with  $\mathbf{w}$ , optimal linear decoding—which accounts for noise correlations—only modestly outperforms diagonal decoding, which does not (Fig. 3h). **d**, Eigenvalues,  $\lambda_\alpha$ , for the eigenvectors best-aligned with  $\Delta\boldsymbol{\mu}$  in 5 individual mice (green lines) increase linearly with  $n$ , revealing the origin of information-limiting correlations. For trial-shuffled data (25 orange lines, 5 eigenvalues for each of 5 mice), the noise variance along  $\Delta\boldsymbol{\mu}$  is independent of  $n$  and is uniform for all eigenvectors of the noise covariance matrix. **e, f**, The geometric relationships between visual signals and noise indicate that the largest noise mode is not the one that is information-limiting. Each colour denotes a different eigenvector,  $\mathbf{e}_\alpha$ , of the noise covariance matrix in the reduced five-dimensional space,  $\alpha \in \{1, 2, 3, 4, 5\}$ . In each individual mouse (**e**) there were multiple eigenvalues,  $\lambda_\alpha$ , of the noise covariance matrix that increased with  $n$ . Extended Data Fig. 10 shows results for all mice. Visual signals (**f**) also increased with  $n$ , as shown by decomposing  $\Delta\boldsymbol{\mu}$  into components along the five eigenvectors,  $\mathbf{e}_\alpha$ . In each mouse the eigenvector with the largest eigenvalue,  $\mathbf{e}_1$ , was the least well aligned with the visual encoding direction,  $\Delta\boldsymbol{\mu}$  (compare the red curves in **e, f**). **g**, A plot of noise values computed as in **e** against signal values computed as in **f**, using all recorded cells from mouse 1. The largest noise mode (red points) is an order of magnitude greater than the noise modes that limit neural ensemble signalling (green and yellow points), yet it is the least aligned with the signal direction. **h**, Signal-to-noise ratios for all five eigenvectors, computed using the values in **g**.  $(d')^2$  equals the sum of these five signal-to-noise ratios. Boxes cover the middle 50% of values for the same 100 data subsets used in **e–g**, horizontal lines denote medians, and whiskers span 1.5 times the interquartile range. Analyses in **b–h** are based on 217–332 trials per stimulus in each of 5 mice.

eigenvectors for which the eigenvalues increase linearly with the number of output cells (Appendix). This shows that information-limiting correlations arise even in rudimentary networks, and reflect the co-propagation of signals and noise through the same synaptic connections.

## Discussion

Our findings address longstanding questions about how the brain computes accurately despite neural noise<sup>1</sup>, and help to resolve a 30-year-old puzzle by providing direct evidence that correlated noise limits cortical coding accuracy<sup>2–4</sup>. These results adjudicate against models in which noise correlations do not limit—or even improve—cortical ensemble coding<sup>7,8</sup>. Encoded visual signals in our recordings were orthogonal to the largest noise eigenmode, enhancing coding accuracy by restricting ~90% of noise fluctuations to dimensions that did not impede signalling. This strategy allows cortical codes to evade a majority of noise, although coding fidelity is ultimately bounded by the weaker correlated noise patterns that cannot be disambiguated from signal. (This strategy might not apply to sensory variables, such as full-field luminance, that animals rarely use for fine discriminations.) In support of these conclusions, mouse visual acuity measured using stimuli similar to ours<sup>15,34</sup> is around tenfold better than would be predicted from the total noise amplitude in the visual cortex, but fits with the amplitudes of the information-limiting noise modes.

Nevertheless, rigorous comparisons between the accuracies of sensory cortical coding and psychophysical discriminations will require concurrent evaluations in individual animals, using identical stimuli. Visual stimuli of greater size can increase  $d'$  values<sup>32</sup> by decreasing the mean level of shared inputs among responsive cells and thereby reducing  $\varepsilon$ , whereas stimuli of greater saliency should increase  $d'$  by increasing  $I_0$ . The recent history of sensory stimuli will also influence  $d'$  owing to sensory adaptation. Although specific values of  $d'$  will vary across stimulus types, information-limiting noise correlations and the saturation of information for large  $n$  arise generically from the propagation of signals and noise through common circuitry and place fundamental constraints on coding accuracy. Therefore, our experimental results likely reflect basic attributes of hierarchical networks and should generalize to diverse stimuli and sensory modalities.

The brain probably cannot learn its own correlated noise structure to decode sensory features optimally, as any particular sensory scene almost never repeats precisely. Nonetheless, decoders that ignore noise correlations can still be near optimal (Fig. 3d, e, h, Extended Data Fig. 9c), as predicted for large networks with information-limiting noise correlations<sup>14</sup>. Therefore, information-limiting cortical noise might help downstream circuits to readout diverse sensory features nearly optimally.

Future work should extend our experiments to different stimuli, sensory modalities and behavioural conditions. Together with our analyses tailored for large-scale recordings, microscopes that image multiple brain regions concurrently<sup>24–26,35</sup> will enable studies of noise correlations and information flow across successive cortical areas. Such measurements will help to address longstanding questions about the decoding strategies that the brain uses for perception, and the effect of attention on perceptual sensitivity and neural ensemble noise.

## Online content

Any methods, additional references, Nature Research reporting summaries, source data, extended data, supplementary information, acknowledgements, peer review information; details of author contributions and competing interests; and statements of data and code availability are available at <https://doi.org/10.1038/s41586-020-2130-2>.

1. von Neumann, J. *The Computer and the Brain* 2nd edn (Yale Univ. Press, 1958).
2. Britten, K. H., Shadlen, M. N., Newsome, W. T. & Movshon, J. A. The analysis of visual motion: a comparison of neuronal and psychophysical performance. *J. Neurosci.* **12**, 4745–4765 (1992).
3. Newsome, W. T., Britten, K. H. & Movshon, J. A. Neuronal correlates of a perceptual decision. *Nature* **341**, 52–54 (1989).
4. Zohary, E., Shadlen, M. N. & Newsome, W. T. Correlated neuronal discharge rate and its implications for psychophysical performance. *Nature* **370**, 140–143 (1994).



5. Averbek, B. B., Latham, P. E. & Pouget, A. Neural correlations, population coding and computation. *Nat. Rev. Neurosci.* **7**, 358–366 (2006).
6. Cohen, M. R. & Kohn, A. Measuring and interpreting neuronal correlations. *Nat. Neurosci.* **14**, 811–819 (2011).
7. Sompolinsky, H., Yoon, H., Kang, K. & Shamir, M. Population coding in neuronal systems with correlated noise. *Phys. Rev. E* **64**, 051904 (2001).
8. Abbott, L. F. & Dayan, P. The effect of correlated variability on the accuracy of a population code. *Neural Comput.* **11**, 91–101 (1999).
9. Shamir, M. & Sompolinsky, H. Implications of neuronal diversity on population coding. *Neural Comput.* **18**, 1951–1986 (2006).
10. Ecker, A. S., Berens, P., Tolias, A. S. & Bethge, M. The effect of noise correlations in populations of diversely tuned neurons. *J. Neurosci.* **31**, 14272–14283 (2011).
11. Oram, M. W., Földiák, P., Perrett, D. I. & Sengpiel, F. The ‘Ideal Homunculus’: decoding neural population signals. *Trends Neurosci.* **21**, 259–265 (1998).
12. Kanitscheider, I., Coen-Cagli, R. & Pouget, A. Origin of information-limiting noise correlations. *Proc. Natl Acad. Sci. USA* **112**, E6973–E6982 (2015).
13. Moreno-Bote, R. et al. Information-limiting correlations. *Nat. Neurosci.* **17**, 1410–1417 (2014).
14. Pitkow, X., Liu, S., Angelaki, D. E., DeAngelis, G. C. & Pouget, A. How can single sensory neurons predict behavior? *Neuron* **87**, 411–423 (2015).
15. Prusky, G. T., West, P. W. & Douglas, R. M. Behavioral assessment of visual acuity in mice and rats. *Vision Res.* **40**, 2201–2209 (2000).
16. Baylor, D. A., Lamb, T. D. & Yau, K. W. Responses of retinal rods to single photons. *J. Physiol. (Lond.)* **288**, 613–634 (1979).
17. Barlow, H. B. Retinal noise and absolute threshold. *J. Opt. Soc. Am.* **46**, 634–639 (1956).
18. Siebert, W. M. Some implications of the stochastic behavior of primary auditory neurons. *Kybernetik* **2**, 206–215 (1965).
19. Yatsenko, D. et al. Improved estimation and interpretation of correlations in neural circuits. *PLoS Comput. Biol.* **11**, e1004083 (2015).
20. Kanitscheider, I., Coen-Cagli, R., Kohn, A. & Pouget, A. Measuring Fisher information accurately in correlated neural populations. *PLoS Comput. Biol.* **11**, e1004218 (2015).
21. Ecker, A. S. et al. Decorrelated neuronal firing in cortical microcircuits. *Science* **327**, 584–587 (2010).
22. Reich, D. S., Mechler, F. & Victor, J. D. Independent and redundant information in nearby cortical neurons. *Science* **294**, 2566–2568 (2001).
23. Renart, A. et al. The asynchronous state in cortical circuits. *Science* **327**, 587–590 (2010).
24. Stirman, J. N., Smith, I. T., Kudenov, M. W. & Smith, S. L. Wide field-of-view, multi-region, two-photon imaging of neuronal activity in the mammalian brain. *Nat. Biotechnol.* **34**, 857–862 (2016).
25. Chen, J. L., Voigt, F. F., Javadzadeh, M., Krueppel, R. & Helmchen, F. Long-range population dynamics of anatomically defined neocortical networks. *eLife* **5**, e14679 (2016).
26. Sofroniew, N. J., Flickinger, D., King, J. & Svoboda, K. A large field of view two-photon mesoscope with subcellular resolution for in vivo imaging. *eLife* **5**, e14472 (2016).
27. Tsai, P. S. et al. Ultra-large field-of-view two-photon microscopy. *Opt. Express* **23**, 13833–13847 (2015).
28. Niell, C. M. & Stryker, M. P. Modulation of visual responses by behavioral state in mouse visual cortex. *Neuron* **65**, 472–479 (2010).
29. Bonin, V., Histed, M. H., Yurgenson, S. & Reid, R. C. Local diversity and fine-scale organization of receptive fields in mouse visual cortex. *J. Neurosci.* **31**, 18506–18521 (2011).
30. Averbek, B. B. & Lee, D. Effects of noise correlations on information encoding and decoding. *J. Neurophysiol.* **95**, 3633–3644 (2006).
31. Cover, T. M. & Thomas, J. A. *Elements of Information Theory* 2nd edn, (John Wiley & Sons, 2006).
32. Stringer, C., Michaelos, M. & Pachitariu, M. High precision coding mouse visual cortex. Preprint at <https://www.biorxiv.org/content/10.1101/679324v1> (2019).
33. Prusky, G. T. & Douglas, R. M. Characterization of mouse cortical spatial vision. *Vision Res.* **44**, 3411–3418 (2004).
34. Glickfeld, L. L., Histed, M. H. & Maunsell, J. H. Mouse primary visual cortex is used to detect both orientation and contrast changes. *J. Neurosci.* **33**, 19416–19422 (2013).
35. Lecoq, J. et al. Visualizing mammalian brain area interactions by dual-axis two-photon calcium imaging. *Nat. Neurosci.* **17**, 1825–1829 (2014).

**Publisher’s note** Springer Nature remains neutral with regard to jurisdictional claims in published maps and institutional affiliations.

© The Author(s), under exclusive licence to Springer Nature Limited 2020

### Microscope design

We used a systems-engineering approach to design the two-photon microscope. To simulate its optical performance and assess component suitability, we used optical design software (ZEMAX) to simulate both ray and wave propagation through the optical pathway. To validate the multiplexing strategy (Extended Data Fig. 2b–d) and the computational un-mixing of crosstalk between image tiles (Extended Data Figs. 3c–e, 4a–c), we simulated fluorescence scattering in brain tissue using the non-sequential mode of ZEMAX. We created an optomechanical design of the microscope using CREO Parametric 3.0 CAD mechanical design software.

### Laser source and control of illumination

We used an ultrashort-pulsed Ti:sapphire laser (MaiTai eHP DeepSee; Spectra Physics) with an 80 MHz repetition rate. We tuned the emission wavelength to 910 nm and used the laser's built-in pre-chirping module to attain pulses of  $130 \pm 20$  fs duration (FWHM) at the sample plane. For general purpose routing of the laser light to and within the microscope we used broadband dielectric mirrors (BB1-E03, Thorlabs). A computer-driven rotating half-wave ( $\lambda/2$ ) plate (WP, AHWP05M-980; Thorlabs) controlled the laser beam polarization and hence the power transmitted through a polarizing beam splitter (PBS) (PBS102, Thorlabs) and into the microscope's illumination pathway (Extended Data Fig. 2d). To block all laser illumination to the microscope during the turnaround portion of the fast galvanometer mirror's scanning cycle, we used a custom laser chopper wheel (90:10 duty ratio), positioned after the PBS and synchronized in frequency and phase with the fast-axis galvanometer cycle.

### Multiplexing of the 16 illumination pathways

Owing to the powerful ultrafast lasers that are now commercially available, past users of two-photon microscopy have often had more than enough illumination power at their disposal but remained limited with regards to the imaging speeds and the fields of view that were attainable with a single beam and existing scanning hardware. We therefore developed a multi-beam, two-photon microscope that puts the (previously) excess laser power to good use, by using multiple beam paths that enable the coverage of larger fields of view at faster image-frame acquisition rates. The Supplementary Note, Extended Data Fig. 2j, k and Supplementary Fig. 1 quantitatively compare our imaging system to other recent approaches to large-scale two-photon microscopy.

To steer laser illumination into four different sets of four beam paths, we used three pairs of electro-optic modulators (EOM) (LM0202 3 × 3 mm 5W, LIV20 pulse amplifier; QIOptic) and PBS cubes (PBS102, Thorlabs) (Extended Data Fig. 2d). We drove each EOM with a high-voltage (310 V amplitude) square wave oscillation, with the period matched to that of the microscope's pixel clock. When imaging using the 4 × 4 set of beams, the square waves driving the second and third EOMs were both phase-shifted by  $\frac{1}{4}$  period relative to the square wave driving the first EOM (Extended Data Fig. 2c). By toggling the beam exiting each EOM between the two linear orthogonal polarization states (the transition time between polarizations was around 50 ns), these three square-wave signals steered the beam from the laser successively into each of the four sets of four beam paths (that is, 16 total), with each set of four illuminated for  $\frac{1}{4}$  of each pixel clock cycle (Extended Data Fig. 2b–d). Within each set, three beamsplitters (10RQ00UB.2 and 10RQ00UB.4, respectively, for S and P polarizations; Newport) divided the beam power equally between four different paths corresponding to four non-neighbouring image tiles in the 4 × 4 array (Extended Data Fig. 2b). Because the efficiency of two-photon fluorescence excitation increases as the square of the peak illumination intensity, this temporal multiplexing scheme enabled fourfold greater fluorescence excitation compared with an otherwise identical, 4 × 4 set of beams that were not multiplexed in time.

### Illumination pathways

Each of the 16 beam pathways contained a pair of kinematically mounted mirrors, a 1:2 telescope implemented using a pair of lenses (AC254-500-B-ML, LA1464-B; Thorlabs), and a gimbal-mounted mirror (GMB1/M; Thorlabs). The 16 beam paths converged on a 6-mm-diameter, Ag-coated mirror mounted on a galvanometer scanner (621SHSM40B scanner, 671215HHJ-1HP driver; Cambridge Technologies). This galvanometer served as our slow-axis scanner.

To image the 16 beams striking the first scanning mirror onto an identical galvanometer scanning mirror serving as the fast-axis scanner, we used a pair of telecentric f-theta lenses designed to induce minimal group velocity dispersion with ultrashort-pulsed illumination (S4LFT0089/094; Sill Optics) in a 1:1 telescope configuration (Fig. 1a). A third, identical f-theta lens and a tube lens ( $f = 300$  mm, G322-372-525, Linos) imaged all 16 beams striking the second scanning mirror onto the back aperture of the microscope objective. The objective focused the 16 beams to a square array of 4 × 4 foci, which together scanned a 2 mm × 2 mm specimen area at image frame acquisition rates up to around 8 Hz.

Alternatively, to enable image frame acquisition rates up to 20 Hz over a 2 mm × 2 mm specimen area, we used a resonant galvanometer scanner (6SC08KA040-02Y, Cambridge Technology, 8 kHz, 7 mm clear aperture) as the fast-axis scanner. The 8 kHz rate of resonant line-scanning allowed us to use a data acquisition scheme based on line multiplexing instead of pixel multiplexing. In this mode we used EOM3 to direct the laser illumination into one of its two optical output paths (Extended Data Fig. 1d, phase I and phase IV). During the resonant scanner turnaround times, we used EOM1 to redirect the laser illumination towards EOM2, the output pathway of which was blocked. During both the forward and backward motion of the resonant scanner a set of 4 laser beams scanned across a total of 8 image tiles—that is, 2 tiles per beam. By using a different set of 4 beams during the forward and backward scanning motions, we sampled one image line in all 16 image tiles during each cycle of the resonant scanner while using only 8 of the 16 beam paths. As with the pixel-multiplexing approach, only 4 beams were active at any instant in time.

For the microscope objective lens, we used either an air objective lens (Leica, 5.0 × Planapo 0.5 NA; 19 mm working distance; anti-reflection (AR) coated for 400–1,000 nm light; transmission >90% at 520 nm, >75% at 910 nm) or a water-immersion lens optimized for large-scale two-photon imaging<sup>26</sup> (1.0 numerical aperture (NA) fluorescence collection, objective (Jenoptik; 2.5 mm working distance). The illumination beams underfilled the back aperture of the microscope objective lens, leading to an optical resolution of approximately 1.2  $\mu$ m and 8  $\mu$ m in the lateral and axial dimensions, respectively, as determined from the FWHM values of the microscope's optical point-spread function.

### Fluorescence collection pathway

Fluorescence emanating from the sample returned through the objective lens, reflected from a dichroic mirror (FF735-Di02-58x82, Semrock) and passed through a collection lens (AC508-180-A, Thorlabs) and a fluorescence emission filter (FF02-525/40-25, Semrock).

The objective and the collection lens project a magnified image of the fluorescence foci in the sample. To optimize the efficiency of fluorescence detection, we designed a custom 4 × 4 lens array (4.5 mm pitch, plano-convex lenslets, custom injection-moulded in poly(methyl methacrylate) (AR-coated: reflectivity <0.5%, 450–650 nm) that efficiently coupled fluorescence emissions into a 4 × 4 array of 3-mm diameter (0.5 NA) plastic optical fibres (FF-CK-120, AR-coated, FibreFin) (Fig. 1a).

To capture the maximum amount of fluorescence near the edges of the large field of view, the outer lenslets in the array were slightly larger than the others, extending outward from the perimeter of the array. Because even the outer lenslets had a maximum numerical aperture (0.19 NA) much lower than that of the plastic fibres (0.5 NA), this lenslet design yielded a theoretical efficiency of >97% for coupling

fluorescence into the array of 16 optical fibres. The fibre array delivered the fluorescence to a set of 16 GaAsP photomultiplier tubes (PMT) (H10770PA-40, Hamamatsu). Each 400-mm-long fibre had a specified transmission efficiency of >98%, yielding an overall design efficiency of >95% for conveying fluorescence into the photomultiplier tubes.

### Optomechanics

We custom-fabricated the majority of the structural components of the microscope at our laboratory's machine shop using high-strength 7075-aluminium alloy and computer numeric control machining. We used three-dimensional (3D) printing to create a cover for the microscope objective lens and a mount for the dichroic mirror. The optomechanical components were generally catalogue parts from standard vendors, mainly Thorlabs, Newport and Linos.

### Data acquisition electronics

Owing to the unique multiplexing scheme of our microscope, data acquisition differs from that in a conventional two-photon microscope (Extended Data Fig. 3a). A major concern was to ensure that the signals from each of the four phases per pixel clock cycle were correctly assigned. This necessitated sampling the 16 PMTs sufficiently rapidly to ensure that the signals corresponding to different pixels and phases were not conflated. Hence, we chose a sampling rate of 50 MHz for each PMT. Because the duration of each of the four multiplexing phases was 400 ns, this sampling rate yielded 20 samples per pixel per multiplexing phase (Extended Data Fig. 3b).

To implement data sampling at this rate, we first converted the photocurrents from the 16 PMTs into voltage signals using a set of four transimpedance amplifiers, each with four input channels (SR445A, Stanford Research Systems). We then sampled the resulting voltage signals using a 16-channel, 50 MS/s analogue-to-digital converter (ADC; 14-bit-samples encoded in 2 bytes) module (NI 5751, National Instruments). The ADC connected to the NIFlexRIO field programmable gate array (FPGA) Module for PXI Express, which was controlled by a host computer (Win 64-bit, 2 Intel E5-2630 processors, 32 GB RAM, Lenovo) through a PCIe-PXLe link (NIPXLe-7962R, NIPXLe-1082 chassis, PXIe-PCIe8381 link, National Instruments) (Extended Data Fig. 3a). For each multiplexing phase, the FPGA module summed the digitally sampled values of the photocurrents into pixel intensities. All subsequent data manipulations involved only the pixel intensities, yielding a total data throughput rate of 60 MB s<sup>-1</sup> or 105 MB s<sup>-1</sup>, for image frame acquisition at 7.23 Hz or 17.5 Hz, respectively, as opposed to the 1.6 GB s<sup>-1</sup> raw data stream. To eliminate any residual crosstalk between pixels resulting from the approximately 50-ns switching time of the EOMs, the software interface gave the user the flexibility to discard the first few samples of each pixel.

### Instrument control

When imaging in pixel-multiplexing mode, we used ScanImage<sup>36</sup> software (version 3.8) to generate the analogue signals driving the galvanometer scanners and the digital line-clock and frame-clock signals (Extended Data Fig. 3a). Using the clock signals from ScanImage, the FPGA module generated signals to drive the EOMs. We created custom LabVIEW (National Instruments, version 2012 SP1, 32 bit) code to initiate the imaging sessions and control the data acquisition parameters. When imaging in line-multiplexing mode, we controlled the instrumentation fully using custom software written in LabVIEW. We synchronized laser line-scanning and data acquisition by using the clock of the resonant scanner as a master clock.

In both imaging modes, the FPGA module continually transmitted to the host computer the imaging data in packets of pixels, combined into image lines, via a high-speed direct memory access first-in first-out (DMA FIFO) data link. The host computer constructed image tiles from the image line data, accounting for the number of photodetection channels and temporal multiplexing phases. The computer then streamed the image data onto its hard drive (Extended Data Fig. 3a).

### Mice

The Stanford Administrative Panel on Laboratory Animal Care (APLAC) approved all procedures involving animals, and we complied with all of the panel's ethical regulations. We analysed data acquired from 6 male and 4 female Ai93 triple transgenic *GCaMP6f-tTA-dCre* mice from the Allen Institute (*Rasgrf2-2A-dCre/CaMK2a-tTA/Ai93*), which expressed the Ca<sup>2+</sup>-indicator GCaMP6f in layer 2/3 pyramidal cells<sup>37</sup>. Mice resided on a 12-h reverse light cycle in standard plastic disposable cages. Experiments occurred during the dark cycle. All animals in the experiment belonged to the same group, so blinding and random assignments were neither needed nor feasible.

For illustrative purposes only, we imaged a single *tetO-GCaMP6s/CaMK2a-tTA* mouse<sup>38</sup>, which expressed the Ca<sup>2+</sup>-indicator GCaMP6s in a subset of neocortical pyramidal neurons (Supplementary Video 3).

### Surgical procedures

At the start of surgery we gave adult mice (12–17 weeks old) buprenorphine (0.1 mg kg<sup>-1</sup>) and carprofen (5 mg kg<sup>-1</sup>) and anaesthetized them with 1–2% isoflurane in O<sub>2</sub>. We implanted a glass window within a 5-mm-diameter craniotomy positioned over the right visual cortical area V1 and surrounding cortical tissue. The window was a round #1 cover glass (5 mm diameter, 0.15 ± 0.02 mm thickness, Warner Instruments) that we attached to a circular steel annulus (1 mm thick, 4.9 mm outer diameter, 4.4 mm inner diameter) using adhesive cured with ultraviolet light (NOA81, Norland Products). To fill the gap between skull and glass window we applied 1.5% agarose. We secured the window on the cranium with dental acrylic. We also implanted an aluminium metal bar atop the cranium, allowing the mice to be head-restrained during in vivo brain imaging. For two days after surgery, we gave the mice buprenorphine (0.1 mg kg<sup>-1</sup>) and carprofen (5 mg kg<sup>-1</sup>) to reduce post-surgical discomfort. Mice recovered for at least one month before any imaging experiments began.

### Visual stimulation

Mice viewed visual stimuli on a gamma-corrected computer monitor (Lenovo LT2323p; 58.4 cm diagonal extent) that was 10 cm away from the left eye and spanned around 142° of this eye's accessible, angular field of view. We generated visual stimuli using the psychophysics toolbox libraries of the MATLAB (Mathworks; version 2017b) programming environment. Stimuli were sinusoidal drifting gratings (spatial frequency, 0.04 cycles per degree; stimulus angular diameter, 50 deg; drifting rate, 50 deg s<sup>-1</sup>, centred on the left eye's visual field; stimulation duration, 2 s; amplitude modulation depth, 100%; screen background intensity, 50%; Fig. 2b). During each experiment, we presented the gratings at two different angles, ±30° or ±6° to the vertical, in a random sequence. Between successive stimuli, the monitor was uniformly illuminated at the background intensity for a 2-s inter-trial interval. To prevent light from the visual stimuli from entering the fluorescence collection pathway of the microscope, the stimuli used only the blue component of the RGB colour model, which was blocked by the fluorescence emission filter. We also placed a colour filter (Rosco, 382 Congo Blue) on the monitor screen. The mean luminance from the stimulus at the mouse eye was approximately 5 × 10<sup>10</sup> photons mm<sup>-2</sup> s<sup>-1</sup>, which is more than two orders of magnitude higher than the transition threshold to photopic vision in mice<sup>15</sup>.

### Imaging sessions

To reduce the stress of head restraint, we head-fixed mice on a 100-mm-diameter Styrofoam ball that could rotate in two angular dimensions. We tracked the movement of the ball with an optical computer mouse. Because running or walking is known to alter visual processing in rodents<sup>28</sup>, we ensured that all visual stimulation trials used for analysis were those when the mice were passively viewing the video monitor, without locomotion, by excluding all trials during which the mice had

an ambulatory speed of greater than  $0.2 \text{ mm s}^{-1}$ . We imaged the  $\text{Ca}^{2+}$  activity of neocortical layer 2/3 pyramidal neurons, 150–250  $\mu\text{m}$  below the cortical surface. The pixel clock cycle duration was 1.6  $\mu\text{s}$ , hence the pixel dwell time in each of the four multiplexing phases was 400 ns. Owing to the ~50-ns switching time of the EOMs, we discarded four samples at the start of each phase, removing any crosstalk between phases. Across the full duration of each imaging session, fluorescence intensities decreased by ~9% owing to photobleaching. The total laser illumination power was 280–320 mW, divided evenly amongst the 4 beams that were active at any instant in time. Hence, each of the 16 image tiles (each  $500 \mu\text{m} \times 500 \mu\text{m}$  in size) received a time-averaged power of 17.5–20 mW, for a time-averaged illumination intensity of 70–80  $\text{mW mm}^{-2}$ . Previous  $\text{Ca}^{2+}$  imaging studies of layer 2/3 neocortical neurons with conventional two-photon microscopy<sup>39–42</sup> have used mean illumination intensities of 89–1,800  $\text{mW mm}^{-2}$ .

For studies in which the visual stimulation comprised moving gratings oriented at  $\pm 30^\circ$ , we used the air objective lens and the pixel-multiplexing approach to image acquisition. We acquired images with  $1,024 \times 1,024$  pixels at a 7.23 Hz frame rate across the  $2 \text{ mm} \times 2 \text{ mm}$  field of view using the air objective lens. The total imaging duration per session was 2,800 s (about 20,000 two-photon image frames), resulting in 700 visual stimulation trials, 350 for each of the two visual stimuli.

For studies in which the moving grating stimuli were oriented at  $\pm 6^\circ$  to vertical, we used the water-immersion objective lens and line-multiplexing to acquire images with  $1,728 \times 1,728$  pixels at 17.5 Hz across the  $2 \text{ mm} \times 2 \text{ mm}$  field of view, which we averaged and downsampled on the FPGA module to  $864 \times 864$  pixels (Extended Data Fig. 9a–c, e, Supplementary Videos 2, 3). The total imaging duration per session was around 1,500 s.

## Image reconstruction

We wrote custom MATLAB (Mathworks; version 2017b) scripts to manipulate the experimental datasets directly from the computer hard drive, without loading all the data into the computer's random-access memory.

The first step of image reconstruction accounted for the differences in the gain values of the 16 PMTs. We determined the gain values by imaging a static fluorescence sample and then analysing the statistics of the photon shot-noise limited fluorescence detection. Specifically, we performed a linear regression between the mean signal from each PMT and its variance. In the shot-noise limited regime, the slope of this relationship equals the combined gain of the PMT, pre-amplifier and ADC. Knowledge of the pre-amplifier and ADC gain values enabled us to determine the PMT gain. Given these empirically determined PMT gain values, the first step of image reconstruction was normalization of the fluorescence signals from each PMT channel by its gain.

The second step in image reconstruction was un-mixing of the crosstalk between the different PMT channels (Extended Data Fig. 3). In principle, when using laser-scanning microscopes with multiple illumination beams, one can apply to the set of PMT signal traces an un-mixing matrix that represents the inverse of a pre-calibrated, empirically determined matrix of crosstalk coefficients between the different photodetection channels<sup>43</sup>. However, this approach assumes that the biological sample is uniform and hence that a single un-mixing matrix will apply equally well across the entire specimen. In practice, brain tissue is not optically uniform, and it is challenging to precisely determine the crosstalk matrix in image sub-regions with low fluorescence levels, such as in blood vessels. Furthermore, two-photon neural  $\text{Ca}^{2+}$  imaging routinely involves modest signal-to-noise ratios and consequently the application of the inverse crosstalk matrix introduces additional error, analogous to the errors introduced by deconvolution methods when applied to weak signals.

For these reasons, we used a more straightforward, conservative and computationally efficient method of image reconstruction. Because crosstalk was only present in our microscope near the boundaries

between image tiles, for each of the four sub-frames per image we computationally reassigned the signals from the boundary regions between tiles to the nearest neighbour source tile from which the cross-talk signals originated according to Extended Data Fig. 3c. We empirically determined that boundary regions 50 pixels wide contained ~75% of the scattered fluorescence photons from each laser focus. Hence, computational re-assignment of the photons from these boundary regions enabled conservative estimates of cells' fluorescence signals, near continuous stitching of the images (Extended Data Fig. 3d, e), and high-fidelity extraction of neural activity (Extended Data Fig. 4).

Beyond each 50-pixel-wide boundary region, there were generally residual scattered fluorescence photons. Thus, for purposes of visual display only (Fig. 1b, c; Supplementary Video 1), we removed boundary artefacts left over after computational re-assignment (Extended Data Fig. 3c) by parameterizing the boundary with a smoothly decaying function:

$$\text{sigmoid}(x) = \frac{1}{1 + e^{\left(\frac{x-d}{a}\right)}}$$

where  $x$  is the distance from the tile edge,  $d = 70$  pixels is the width of the boundary region, and  $a = 25$  pixels characterizes the smoothness of the boundary decay.

## Image pre-processing

After image reconstruction, each dataset comprised 16 videos, each  $256 \text{ pixels} \times 256 \text{ pixels} \times 21,000$  frames for a typical experiment, corresponding to the 16 tiles of each image frame. To correct for lateral displacements of the brain during image acquisition, we applied a rigid image registration algorithm (Turboreg<sup>44</sup>; <http://bigwww.epfl.ch/thevenaz/turboreg/>) to each of the individual video tiles. We chose this approach because the application of a single, rigid image registration algorithm over the entire  $2 \text{ mm} \times 2 \text{ mm}$  field of view did not account for variations in tissue motion between the different image tiles. After image registration, for display purposes only we merged the 16 motion-corrected video tiles into images or videos of the entire field of view (Supplementary Videos 1–3). We performed all further analysis on individual tiles.

For display purposes only (Supplementary Video 2, 3), to minimize stitching artefacts during video playback we applied to each image frame a linear-blending stitching algorithm<sup>45,46</sup>. We then computationally corrected the movie for lateral displacements of the brain by using a piecewise rigid image registration algorithm<sup>47</sup>. To highlight the details for viewers using a typical computer monitor, we saved the processed video using a contrast ( $\gamma$ ) value of 0.75.

## Computational extraction of neural activity traces

To identify individual neurons in the  $\text{Ca}^{2+}$  imaging data, we separately analysed the 16 individual video tiles in each movie and applied an established algorithm for cell sorting based on the successive application of principal component and independent component analyses<sup>35,48</sup> (Mosaic software, version 0.99.17; Inscopix). We visually screened the resulting set of putative cells and removed any that were clearly not neurons (about 50% of candidate cells were removed). For the resulting set of cells, we created a corresponding set of truncated spatial filters that were localized to the cell bodies by setting to zero all pixels in the filter with values <5% of the peak amplitude of the filter. After thresholding, we removed any connected components containing less than 30 pixels. To obtain traces of neural  $\text{Ca}^{2+}$  activity, we applied the truncated spatial filters to the  $(F(t) - F_0)/F_0$  movies (Extended Data Fig. 5), where  $F(t)$  denotes the time-dependent fluorescence intensity of each pixel and  $F_0$  is its mean intensity value, time-averaged over the entire movie.

For each cell, we used fast non-negative deconvolution to estimate the number of spikes fired in each time bin<sup>49</sup>. We then temporally down-sampled twofold the resulting traces by summing the estimated numbers

of spikes in pairs of adjacent time bins, yielding time bins of 0.276 ms. We performed all subsequent analysis on the down-sampled traces.

Moreover, previous work has shown that the activity of mouse visual cortical neurons differs substantially between behavioural states of passive viewing and viewing during active locomotion<sup>28,35</sup>. To ensure that all visual stimulation trials used for analysis were those when the mice were passively viewing the video monitor, we excluded from analysis all trials during which the mice were running or walking (at speeds greater than 0.2 mm s<sup>-1</sup>). The resulting set of trials retained for data analysis in each mouse was 217–332 for each stimulus condition, except for the analysis of Extended Data Fig. 9a–c, e, which involved 122–167 trials per stimulus condition.

### Trial-shuffled datasets

To create trial-shuffled datasets, we randomly permuted the activity traces of each cell across the full set of trials in which the same stimulus was presented, using a different random permutation for each individual cell. Thus, the trial-shuffled datasets preserved the statistical distributions of each cell's responses to the two stimuli, but any temporally correlated fluctuations in different cells' stimulus-evoked responses were scrambled. For analyses of trial-shuffled data, we averaged results over 100 different randomly chosen subsets of cells and/or stimulation trials, each of which was trial-shuffled with its own distinct permutations; exceptions to this statement are the analyses of Extended Data Figs. 8c–h, 10a, b, for which we averaged results over 30 such calculations instead of 100.

### Noise correlations in the visual stimulus-evoked responses of pairs of cells

To compute correlation coefficients for the noise in the visual responses of a pair of neurons, we first integrated the estimated spike count of each cell between [0.5 s, 2 s] from the start of visual stimulation. After separating the trials for each of the two visual stimuli, we subtracted from each trace the mean stimulus-evoked response of the cell and then calculated the Pearson correlation coefficient,  $r$ , for the resulting set of responses from the two cells. We then averaged these noise correlation coefficients over the two stimulus conditions. Figure 2d, e and Extended Data Fig. 6e, g show statistical distributions of the resulting mean correlation coefficients across many cell pairs.

We compared the statistical distributions of mean correlation coefficients for two different sets of cell pairs, those with positive and those with negative covariance of their mean stimulus responses (that is, cell pairs with similar or dissimilar visual tuning) (Extended Data Fig. 6e, g). To visually highlight the differences between the two distributions (Fig. 2e), we also analysed only the most responsive cells, defined as those cells with the top 10% values of  $\sqrt{\langle r_A \rangle^2 + \langle r_B \rangle^2}$ , where  $r_A$  and  $r_B$  are the mean responses to the two stimuli.

### Dimensionality reduction and computation of $d'$ for neural responses to visual stimuli

To estimate how much information the neural activity conveyed about the stimulus identity, we used the metric  $d'$ , which characterizes how readily the distributions of the neural responses to the two different sensory stimuli can be distinguished<sup>30</sup>. The quantity  $(d')^2$  is the discrete analogue of Fisher information<sup>30</sup>. We evaluated three different approaches to computing  $d'$  values for the discrimination of the two different visual stimuli (Fig. 3).

In the first approach, which we termed 'instantaneous decoding' (Fig. 3d, f, Extended Data Figs. 7a, 9a), we chose for analysis a specific time bin relative to the onset of visual stimulation. To examine the time-dependence of  $d'$ , we used the instantaneous decoding approach and varied the selected time bin from  $t = 0$  s to  $t = 2$  s relative to the start of the trial. The number of dimensions of the neural ensemble activity evoked in response to the visual stimulus was  $N_o$ , the number

of recorded neurons ( $N_o \approx 1,500$ ). Said differently, the set of estimated spike traces provided an  $N_o$ -dimensional population vector response to each stimulus presentation.

In the second approach, termed 'cumulative decoding' (Fig. 3e, g, Extended Data Figs. 7b, 9b), we concatenated the responses of each neuron over time, from the start of the trial up to a chosen time,  $t$ . In this case, the dimensionality of the population activity vector was  $N_o \times N_t$ , where  $N_t$  is the number of time bins spanning the interval [0 s,  $t$ ].

In the third approach, termed 'integrated decoding' (Extended Data Fig. 7c), we examined the neural ensemble responses integrated over the interval from [0 s, 2 s] relative to stimulation onset. In the plots of  $d'$  against time as computed by instantaneous decoding, the interval [0.5 s, 2 s] is when the  $d'$  values have already reached an approximate plateau (Extended Data Fig. 7e). With integrated decoding, the dimensionality of the population vector response was  $N_o$ , the number of recorded neurons, as in the instantaneous decoding approach.

In each of the three decoding approaches, we arranged the traces of estimated spike counts into three-dimensional data structures (number of neurons  $\times$  number of time bins  $\times$  number of trials), for each of the two visual stimuli (Extended Data Fig. 5b).

A challenge was that calculation of  $d'$  in an  $N_o$ -dimensional population vector space would have involved estimation of a  $N_o \times N_o$  noise covariance matrix with over a million matrix elements. Direct estimation of the covariance matrix would have been unreliable, because the typical number of cells per dataset,  $N_o \approx 1,500$ , was much larger than the typical number of trials  $P \approx 600$ . This issue was even more severe in the case of cumulative decoding, for which the population activity vector had  $N_o \times N_t$  dimensions. However, we found mathematically that by reducing the dimensionality of the space used to represent the ensemble neural responses, one can reliably estimate eigenvalues for the largest eigenvectors of the noise covariance matrix, which govern how well the two visual stimuli can be discriminated based on the neural responses (Appendix).

Our approach to dimensional reduction relied on a PLS discriminant analysis<sup>31</sup>. The PLS analysis enabled us to find the dimensions of the population vector space that were most informative about which visual stimulus was shown. To determine how many dimensions were important for discriminating the two stimuli, we constructed an orthonormal projection operator, which projected the  $N_o$ -dimensional (or  $N_o \times N_t$  dimensional) ensemble neural responses onto a truncated set of the  $N_R$  dimensions identified by the PLS analysis as being the most informative about the identity of the visual stimulus.

In the reduced space with  $N_R$  dimensions, we calculated the  $(d')^2$  value of the optimal linear discrimination strategy as:

$$(d'_{\text{opt}})^2 = \Delta \mu^T \Sigma^{-1} \Delta \mu = \Delta \mu^T \mathbf{w}_{\text{opt}}$$

where  $\Sigma = \frac{1}{2}(\Sigma_A + \Sigma_B)$  the noise covariance matrix averaged across two stimulation conditions,  $\Delta \mu = \mu_A - \mu_B$  is the vector difference between the mean ensemble neural responses to the two stimuli and  $\mathbf{w}_{\text{opt}} = \Sigma^{-1} \Delta \mu$ , which is normal to the optimal linear discrimination hyperplane in the response space<sup>30</sup>.

To determine the optimal value of  $N_R$  for these computations of  $d'$ , we split the data into three sets, each comprising a third of all trials. We used the first set to identify the PLS dimensions, the second 'training' set to find the optimal discrimination boundary defined by  $\mathbf{w}_{\text{opt}}$ , and the third 'test' set to estimate the discrimination performance  $d'$ . We then varied  $N_R$  and plotted the resulting  $d'$  values for both the training and test datasets (Extended Data Fig. 7a–c).

For all three decoding strategies, we chose  $N_R = 5$  for all subsequent determinations of  $d'$ , because the addition of further dimensions led to overfitting, as shown by the increase in discrimination performance using the training set and the decline in performance (that is, poorer generalization to previously unseen data) using the test set (Extended Data Fig. 7a–c).



After picking  $N_R = 5$ , for all further computations of  $d'$  we first chose a subset of neurons and divided the set of stimulation trials into two groups of equal size. We used the first group of trials to conduct the PLS analysis and the second group to determine  $d'$  and the eigenvalue spectrum of the noise covariance matrix (Extended Data Fig. 5b). To make plots of  $d'$  (Fig. 3d–g), we averaged  $d'$  values across 100 different randomly chosen subsets of cells, which we analysed independently for every time bin. For each subset of cells and every time bin, we randomly split the set of visual stimulation trials into two halves, one half for determination of the five-dimensional sub-space and decoder training, and the other half for decoder testing. In Fig. 3d, e, we kept constant the number of cells per subset. In Fig. 3f, g, we varied the number of cells per subset. For instantaneous and cumulative decoders in the experiment with visual gratings oriented at  $\pm 30^\circ$ , we used [0.83 s, 1.11 s] and [0 s, 1.11 s] time intervals, respectively (Fig. 3f–i). For the experiment with gratings oriented at  $\pm 6^\circ$ , the time intervals used for instantaneous and cumulative decoding were respectively [0.70 s, 0.94 s] and [0 s, 0.94 s] (Extended Data Fig. 9a–c).

To determine the asymptotic value of  $d'$  in the limit of many neurons, and the number of cells,  $n_{1/2}$ , at which  $(d')^2$  attains half of its asymptotic value (Fig. 3h, i), we performed a two-parameter fit to the growth of  $d'$  with increasing numbers of neurons,  $n$ :  $(d')^2 = (sn) / (1 + \varepsilon n)$ . We determined the asymptotic value of  $d'$  as  $(s/\varepsilon)^{1/2}$  and  $n_{1/2}$  as  $\varepsilon^{-1}$ .

To verify that linear decoding is a near optimal decoding strategy, we confirmed that the noise covariance matrix  $\Sigma$  was stimulus-independent in the reduced, five-dimensional space used to calculate  $d'$  (Extended Data Fig. 7f). We found that the matrix elements of the noise covariance matrix were highly correlated across the two stimulus conditions ( $r$ :  $0.81 \pm 0.16$ , mean  $\pm$  s.d.,  $N = 5$  mice). This indicates that other more complex, nonlinear decoding strategies are unlikely to substantially surpass the accuracy of the linear strategy, which we further confirmed via an analysis of quadratic decoding (Extended Data Fig. 7h).

We also verified that we had sufficient numbers of visual stimulation trials to estimate  $d'$  accurately (Extended Data Fig. 7g). For every mouse,  $d'$  approached an asymptote as the number of stimulation trials used for analysis was increased; this indicates that beyond a certain point the computed value of  $d'$  is insensitive to the number of trials. Moreover, we developed an analytic theory describing how the accuracy of our estimates of  $d'$  depends jointly on the numbers of neurons and experimental trials (Extended Data Fig. 10f–k, Appendix).

In addition to our analyses of real data, we also calculated  $(d'_{\text{shuffled}})^2$  (Fig. 3b–g), the optimal linear discrimination performance using trial-shuffled datasets, which we created by shuffling the responses of each cell across stimulation trials of the same type. Owing to this shuffling procedure, the off-diagonal elements of  $\Sigma_A$  and  $\Sigma_B$  become near zero.

We further calculated the performance of a 'diagonal' discrimination strategy (Fig. 3b, d, e) that was blind to the noise correlations between neurons, using the actual (unshuffled) datasets<sup>30</sup>. For this sub-optimal strategy,  $(d'_{\text{diagonal}})^2$  determines the separation of two response distributions obtained when the vector of decoding weights  $\mathbf{w}$  is collinear with  $\Delta\boldsymbol{\mu}$  (Fig. 3), which we calculated according to:

$$(d'_{\text{diagonal}})^2 = \frac{(\Delta\boldsymbol{\mu}^T \Sigma^{-1} \Delta\boldsymbol{\mu})^2}{\Delta\boldsymbol{\mu}^T \Sigma_d^{-1} \Sigma_d^{-1} \Delta\boldsymbol{\mu}}$$

where  $\Sigma_d$  is the diagonal covariance matrix.

## Eigenvalues of the noise covariance matrix

To examine how the statistical structure of neural noise affects the ability to discriminate neural responses to the two different visual stimuli (Fig. 4, Extended Data Fig. 10a–e), we expressed  $(d')^2$  in terms of the eigenvalues  $\lambda_\alpha$  and eigenvectors  $\mathbf{e}_\alpha$  of the noise covariance matrix  $\Sigma$ :

$$(d')^2 = \Delta\boldsymbol{\mu}^T \Sigma^{-1} \Delta\boldsymbol{\mu} = \sum_\alpha \left( \frac{|\Delta\boldsymbol{\mu} \cdot \mathbf{e}_\alpha|^2}{\lambda_\alpha} \right)$$

which can be viewed as a sum of signal-to-noise ratios, one for each eigenvector. Clearly, the eigenvectors well aligned with  $\Delta\boldsymbol{\mu}$  are the most important for discriminating between the two distributions of neural responses. Noting that  $\lambda_\alpha$  equals the noise variance along  $\mathbf{e}_\alpha$ , our data revealed noise modes that were well aligned with  $\Delta\boldsymbol{\mu}$  and for which the variance increased linearly with the number of cells. The combination of these two attributes is what leads to the saturation of  $d'$  as the number of cells in the ensemble becomes large (Fig. 4). Notably, our analysis also uncovered noise modes with much larger variance that are not information-limiting, as they do not align well with  $\Delta\boldsymbol{\mu}$ .

## Calculation of decoding weights

We calculated the vector of optimal linear decoding weights,  $\mathbf{w}_{\text{opt}}$ , in the reduced space identified by PLS analysis:

$$\mathbf{w}_{\text{opt}} = \Sigma^{-1} \Delta\boldsymbol{\mu}$$

For moving grating visual stimuli oriented at  $\pm 30^\circ$ ,  $\mathbf{w}_{\text{opt}}$  was generally well aligned to  $\Delta\boldsymbol{\mu}$ , indicating that correlation-blind decoding performed near optimally (Figs. 3b, h, 4a, c). This was somewhat less the case with moving gratings oriented at  $\pm 6^\circ$  (Extended Data Fig. 9c). To assess the contributions of individual cells to the optimal decoder, we estimated the vector of decoding weights in the space of all neurons as:

$$\mathbf{w}_{\text{decoding}} = \frac{T^T \mathbf{w}_{\text{opt}}}{\|\mathbf{w}_{\text{opt}}\|}$$

where  $T$  is a transformation matrix from the high-dimensional population vector space, in which the responses of each cell occupy an individual dimension, into the five-dimensional space identified by PLS analysis. Starting around 0.4 s after the onset of visual stimulation,  $\mathbf{w}_{\text{decoding}}$  was largely time-invariant (Extended Data Fig. 7d).

## L2-regularized regression

Because our method for computing  $d'$  via PLS analysis involved a dimensional reduction, we compared the  $d'$  values found with PLS analysis to those determined via a different method, L2-regularized regression<sup>52</sup>, which does not depend on dimensional reduction (Extended Data Fig. 8a, b). This form of regression uses a regression vector,  $\mathbf{b}$ , that lies within the high-dimensional space of all ensemble neural activity patterns, but its length is limited by the use of an adjustable regularization parameter,  $k$ . For each subset of neurons considered, we randomly chose 90% of the visual stimulation trials for the determination of  $\mathbf{b}$ . We projected the neural responses from the remaining 10% of trials onto the dimension determined by  $\mathbf{b}$ . We then computed  $d'$  with the same formula as used with PLS analysis, except with  $\mathbf{b}$  replacing  $\mathbf{w}_{\text{opt}}$ , the optimal linear discrimination hyperplane. Using this approach, we found the maximum value of  $d'$  across all values of  $k$  within the range [1,  $10^5$ ]. We averaged these maximal  $d'$  values across 100 different subsets of neurons and visual stimulation trials (Extended Data Fig. 8a).

## Kullback–Leibler divergence

To assess the extent to which quadratic decoding might surpass the optimal linear decoder, we computed the Kullback–Leibler (KL) divergence<sup>31</sup> between the two distributions of ensemble neural responses to the two different visual stimuli (Extended Data Fig. 7h). The KL divergence is a generalization of  $d'$  to arbitrary distributions and, like  $d'$ , provides an assessment of the statistical differences between two distributions. When the two distributions are Gaussians with equal covariance matrices, the KL divergence reduces to  $(d')^2$ , and linear decoding methods suffice to optimally discriminate between the two distributions<sup>52</sup>. By comparison, for two Gaussian distributions with different means and covariance matrices,  $(d')^2$  is not equivalent to the KL divergence, and quadratic decoding methods are required to optimally discriminate between the two distributions<sup>52</sup>.

To assess the potential benefits of quadratic decoding, we fit multivariate Gaussians to the two stimulus response distributions without assuming they had equal covariance matrices. We computed the KL divergence of the response distribution to stimulus A relative to the response distribution to stimulus B according to:

$$\text{KL}_{A||B} = \frac{1}{2} \left( \text{tr}(\Sigma_A^{-1}\Sigma_B) + \Delta\boldsymbol{\mu}^T \Sigma_A^{-1} \Delta\boldsymbol{\mu} - N + \ln \left( \frac{\det(\Sigma_A)}{\det(\Sigma_B)} \right) \right)$$

where  $\Sigma_A, \Sigma_B$  are the noise covariance matrices for the two stimulation conditions,  $\Delta\boldsymbol{\mu} = \boldsymbol{\mu}_A - \boldsymbol{\mu}_B$  is the vector difference between the mean ensemble neural responses to the two stimuli, and  $N$  is the dimensionality of the response distribution (that is, the number of cells in the ensemble). The KL divergence saturated as  $N$  increased and was generally not much greater than  $(d')^2$  (Extended Data Fig. 7h). This result was consistent with the finding that the noise covariance matrix was similar for the two different visual stimuli (Extended Data Fig. 7f) and supported the conclusion that quadratic decoding would achieve little performance gain beyond that of the optimal linear decoder.

### Computational studies of the robustness of empirically determined $d'$ values

To verify that our decoding methods were robust to the potential presence of effects such as common mode fluctuations and multiplicative gain modulation that could increase the trial-to-trial variability of neural responses, we compared the  $d'$  values obtained from PLS analysis versus L2-regularized regression using computationally simulated datasets of neural population responses (Extended Data Fig. 8c–h).

First, to examine the combined effects of information-limiting correlations and common mode fluctuations (Extended Data Fig. 8c–f), we studied a model of the neural ensemble responses in which the noise covariance matrix exhibited information-limiting noise correlations via a single eigenvector,  $\mathbf{f}$ , the eigenvalue of which grew linearly with the number of cells in the ensemble. In addition to this rank 1 component, we included a noise term that was uncorrelated between different cells, as well as a common mode fluctuation, yielding a noise covariance matrix with the form

$$\Sigma^* = \sigma^2 I + \varepsilon_{\text{common}} J + \varepsilon \mathbf{f} \mathbf{f}^T$$

where  $\sigma^2 = 1$  is the amplitude of uncorrelated noise,  $I$  is the identity matrix,  $J$  is a rank 1 matrix of all ones, and  $\mathbf{f}$  is the information-limiting direction, a vector that we chose randomly in each individual simulation from a multi-dimensional Gaussian distribution with unity variance in each dimension. The amplitude of information-limiting correlations was  $\varepsilon = 0.002$ , approximately matching the level observed in the experimental data. In the model version without common mode fluctuations, we set  $\varepsilon_{\text{common}}$  to zero. In the version with common mode fluctuations, we set  $\varepsilon_{\text{common}} = 0.02$ , ten times the value of  $\varepsilon$ . We chose the difference in the means of the two stimulus response distributions,  $\Delta\boldsymbol{\mu}$ , to be aligned with  $\mathbf{f}$  (Fig. 3a) and to have a magnitude of 0.2, so that the asymptotic value of  $d'$  for large numbers of cells approximately matched that of the data. We compared the decoding results attained with and without the presence of common mode fluctuations in the neural responses.

Second, to study the possible effects of multiplicative gain modulation (Extended Data Fig. 8g, h), we compared two versions of a model in which the responses of the V1 neural population either were or were not subject to a multiplicative stochastic gain modulation but were otherwise statistically equivalent. We modelled the V1 cell population as a set of linear Gabor filters (see Appendix section 5). In the version with gain modulation, on each visual stimulation trial we multiplied the output of the Gabor filter by a randomly chosen factor, uniformly distributed between 50–150%, the value of which was the same for every cell but varied from trial to trial.

### Estimates of perceptual acuity

We used the empirical determinations of  $d'$  based on visual cortical activity and the parameters of the moving grating visual stimuli to estimate the minimum perceptible orientation difference between the two stimuli. We compared the resulting values to those estimated from past behavioural measurements of visual acuity in mice<sup>15,34</sup>, all of which agree well.

One behavioural study assessed how well three individual mice could discriminate the orientations of visual gratings<sup>34</sup>. The best trained of these three mice—that is, the mouse that performed the most sessions and had the smallest error bars in the threshold determination—had a behavioural threshold for orientation discrimination ( $4.6^\circ \pm 0.1^\circ$ ;  $n = 7$  sessions) close to the value estimated from our neural data ( $4.8^\circ$ ). The second mouse had a  $5.7^\circ \pm 0.6^\circ$  threshold ( $n = 4$  sessions), and the third mouse had a threshold of  $6.9^\circ$  ( $n = 1$  session).

Another behavioural study examined visual acuity in 13 mice and determined the highest visual spatial frequencies the mice could discern<sup>15</sup>. To compare our results to this study, we used the fact that our grating stimuli had a low spatial frequency (0.04 cycles per degree) to approximate the perceptual challenge of estimating the grating orientation as being equivalent to that of estimating the orientation of the line of peak illumination intensity over the same viewing diameter. In the behavioural study of acuity<sup>15</sup>, the mice used both eyes to view the stimulus, whereas in our studies mice viewed the stimulus with one eye, and we recorded neural activity from only one cerebral hemisphere. To account for these differences, we posited that neural noise fluctuations should be nearly independent across the visual streams from the two eyes, which would boost  $d'$  values by about a factor of  $\sqrt{2}$  over those achievable with one eye. However, our determinations of  $d'$  from neural activity concern the discrimination of two distinct visual stimuli, which should also increase  $d'$  values by a factor of about  $\sqrt{2}$  over those for a single stimulus viewed with one eye. Given these counterbalancing factors, we used the  $d'$  values to estimate the highest perceptible spatial frequency as  $f \approx d'(\theta)/D \sin \theta$ , where  $D$  is the diameter of the visual stimuli (50 deg; Fig. 2b) presented at orientations of  $\pm\theta$ . For the grating stimuli oriented at  $\pm 30^\circ$  to vertical,  $d' \approx 6$ , yielding  $f \approx 0.3$  cycles per degree. For the grating stimuli oriented at  $\pm 6^\circ$ , which are more representative of the perceptual threshold,  $d' \approx 2.5$  and thus  $f \approx 0.48$  cycles per degree, comparable to the value of  $f \approx 0.5$  cycles per degree attained from the behavioural studies at a unity  $d'$  value for the behavioural performance<sup>15</sup>. We converted values of  $f$  into the minimum perceptible orientation difference,  $2\theta_{\min}$ , between two grating stimuli oriented at  $\pm\theta_{\min}$  by using  $\theta_{\min} = \sin^{-1}(1/Df)$ . This conversion yielded a prediction of  $\theta_{\min} \approx 2.3^\circ$  based on the behavioural studies of mouse visual acuity<sup>15</sup>, as compared to  $\theta_{\min} \approx 2.4^\circ$  based on our neural data.

### Computational simulations of activity in a two-layer neural network

To illustrate that cells whose receptive fields overlap exhibit shared noise correlations, we simulated a simple two-layer feed-forward network of linear neurons, with 14 input neurons and 3 output neurons (Extended Data Fig. 1j–m). The neurons in each layer were equally spaced along a linear axis. We defined the strengths of the connections,  $\mathbf{w}_i$ , between the input and output neurons such that the receptive field profiles of the different output neurons were spatially overlapping Gaussian functions of the linear separation between each output neuron and the input neurons (Extended Data Fig. 1j).

For the three example cells shown in Extended Data Fig. 1j, the unity-normalized overlap between their connection weight vectors was:  $\mathbf{w}_1 \cdot \mathbf{w}_2 = 0.165$ ,  $\mathbf{w}_1 \cdot \mathbf{w}_3 = 0.022$  and  $\mathbf{w}_2 \cdot \mathbf{w}_3 = 0.038$ . The activity of cells in the output layer,  $\mathbf{r}$  was defined as:  $r_i = [\mathbf{w}_i \cdot (\mathbf{x} + \mathbf{n})]$ , where  $\mathbf{x}$  is the mean activity of the input cells in response to a given stimulus,  $\mathbf{n}$  is a noise term in which each element is Poisson-distributed with mean 0.1, and  $[\ ]$  denotes rounding to the nearest integer. We simulated the activity

# Article

of this two-layer network across 10,000 time bins and calculated the noise correlation coefficients between three different pairs of output neurons.

## Measurements of fluorescence scattering

To examine the extent of fluorescence scattering between active image tiles within one temporal phase of our multiplexed imaging scheme (Extended Data Fig. 4d–g), we measured the spatial distribution function,  $P_s(x, y)$ , governing the probability that a two-photon excited fluorescence photon will exit the cortical tissue surface at a point with lateral displacement coordinates  $(x, y)$  relative to the laser focus. To directly observe the distributions  $P_s(x, y)$  of scattered fluorescence, we built a custom optical setup that used the Ti:sapphire laser beam to excite fluorescence in fixed cortical tissue slices from adult *GCaMP6f-tTA-dCre* mice and imaged the resulting distribution of fluorescence signals on a scientific grade CMOS camera (Orca Flash, Hamamatsu). Owing to the use of an imaging detector in this setup, the fluorescence detection pathway had to be optically corrected for field curvature and other image plane distortions, whereas the primary two-photon microscope (Fig. 1) had no such requirement. For this reason, our studies of scattering used an Olympus XLUMPLFN objective lens (0.95 NA, 20×), which provided fluorescence images of ~1.2 mm in width. We positioned the laser focal spot on one side of the field of view, so as to image scattered fluorescence up to about 1.1 mm away from the focal spot (Extended Data Fig. 4e, f). We computed the mean  $P_s(x, y)$  distribution, averaged over 100 different locations of the laser focus in each of 3 different brain slices, at tissue depths up to 600 μm beneath the surface of the slice. To determine the mean cross-sectional distribution of fluorescence as a function of the radial distance from the laser focus,  $r = \sqrt{x^2 + y^2}$ , we also averaged over all accessible polar angles. To compute the probability that a fluorescence photon excited in one active tile would scatter into an adjacent active tile, we integrated the circularly symmetric determinations of  $P_s(x, y)$  over the portion of the image area yielding this form of crosstalk (Extended Data Fig. 4g).

## Measurements of brain temperature during two-photon brain imaging

To perform temperature measurements in the brains of awake mice during two-photon imaging (Extended Data Fig. 2f), we surgically prepared *GCaMP6f-tTA-dCre* mice by performing a 5-mm-diameter craniotomy following the same procedures as described above. However, before placement of the cranial window, we inserted a flexible 200-μm-diameter thermocouple probe<sup>53</sup> (IT24P; Physitemp) into the brain, 100–200 μm beneath the dura, within ~0.75 mm of the centre of the field-of-view of the microscope. The thermocouple resided within a 5-mm-long plastic micropipette and extended ~2.5 mm beyond the tip of the micropipette.

Using ultraviolet-light curable glue (Loctite, 4305) and dental cement, we affixed the micropipette to the cranium at a shallow angle of 5° relative to the surface of the cranium. We then placed the glass cranial window onto the craniotomy and fixed the window in place with dental cement. The thermocouple probe was connected to a two-channel digital thermometer (CL3515R; Omega), which conveyed digitized temperature data (10 Hz sampling rate) to a computer via a USB port. We protected the wires of the thermocouple connecting to the digital thermometer using a 5-cm-long piece of flexible plastic tubing. We then commenced concurrent two-photon imaging (17.5 Hz image frame acquisition rate) and temperature recordings (Extended Data Fig. 2f).

## Histology

To check whether in vivo two-photon imaging with the 16-beam instrument induced any brain tissue damage, we performed immunohistochemical analyses of post-mortem brain tissue sections (Extended Data Fig. 2g–i). We compared positive control tissue sections that we had

deliberately damaged in vivo with high-power (2,680 mW mm<sup>-2</sup>) laser illumination, negative control tissue sections that received no laser illumination, and experimental tissue sections that had undergone in vivo two-photon imaging at the highest intensity levels of laser illumination (80 mW mm<sup>-2</sup>) used in this study for tracking neuronal Ca<sup>2+</sup> dynamics.

We euthanized and intracardially perfused the mice in all three groups with phosphate buffered saline followed by a 4% solution of paraformaldehyde in phosphate buffered saline. To allow adequate time for expression of HSP70 following exposure to laser illumination<sup>54</sup>, mice in the positive control and experimental groups were euthanized 21 h after the end of two-photon imaging. We sliced the fixed brain tissue using a vibratome (Leica VT1000 S) to obtain 100-μm-thick coronal sections. We immunostained the tissue sections with antibodies against glial fibrillary activation protein (1:2,500, rabbit anti-GFAP, Sigma HPA056030, Lot C115616) and heat shock protein 70 (1:400, mouse anti-HSP, Enzo ADI-SPA-810, Clone C92F3A-5, Lot 01031912) and then applied fluorophore-conjugated secondary antibodies (goat anti-rabbit-Alexa 594 (Invitrogen, A-11012, Lot 1933366) and goat anti-mouse-Alexa 488 (Invitrogen, A-11001, Lot 56881A)).

We also stained the sections with DAPI (Invitrogen, D1306), which labels cell nuclei by binding to DNA. After mounting the brain sections on glass slides, we visualized immunofluorescence using an epifluorescence microscope (Leica, MZFL III) equipped with a plan 1.0× objective lens, a solid-state white light engine (Lumencor, Sola SM 5-LCR-VA), filter sets for imaging red and green fluorophores (Leica 10450756 and 10450212, respectively) and a CCD camera (QImaging, 01-QIClick-F-M-12). Brain sections from all three groups were imaged under identical optical conditions and with the same camera settings.

## Statistical tests

For comparison of the distributions of noise correlation coefficients in Fig. 2e and Extended Data Fig. 6g, we used two-tailed, two-sample Kolmogorov–Smirnov tests. In Figs. 2f, 3h and Extended Data Fig. 9c we used one-tailed Wilcoxon rank-sum tests. Supplementary Table 1 contains all *P* values associated with the figures and extended data figures.

## Instrument availability

With support from the United States National Institute of Neurological Disorders and Stroke, we are currently converting the large-scale two-photon microscope (Fig. 1, Extended Data Fig. 2) into a research facility that is available to other laboratories and formally overseen by a steering committee. Researchers interested in this facility should please write to its principal investigator (M.J.S.) for more information.

## Reporting summary

Further information on research design is available in the Nature Research Reporting Summary linked to this paper.

## Data availability

The data that support the findings of this study are available from the corresponding authors upon reasonable request.

## Code availability

We used open source software routines for image registration<sup>44</sup> (<http://bigwww.epfl.ch/thevenaz/turboreg/>) and partial least squares analysis (<https://www.mathworks.com/matlabcentral/fileexchange/18760-partial-least-squares-and-discriminant-analysis>). Software code for extracting individual neurons and their Ca<sup>2+</sup> activity traces from Ca<sup>2+</sup> videos using principal component and then independent component analyses<sup>35,48</sup> is freely available (<https://www.mathworks.com/matlabcentral/fileexchange/25405-emukamel-cellsort>), although for convenience we used a commercial version of these routines (Mosaic software, version 0.99.17; Inscopix). We wrote all other analysis routines

in MATLAB (Mathworks; version 2017b). The primary software code used to support the findings of the study is available at Zenodo.org (<https://zenodo.org/record/3593520#.XgWPu-hKg2w>).

36. Pologruto, T. A., Sabatini, B. L. & Svoboda, K. ScanImage: flexible software for operating laser scanning microscopes. *Biomed. Eng. Online* **2**, 13 (2003).
37. Madisen, L. et al. Transgenic mice for intersectional targeting of neural sensors and effectors with high specificity and performance. *Neuron* **85**, 942–958 (2015).
38. Wekesselblatt, J. B., Flister, E. D., Piscopo, D. M. & Niell, C. M. Large-scale imaging of cortical dynamics during sensory perception and behavior. *J. Neurophysiol.* **115**, 2852–2866 (2016).
39. Chettih, S. N. & Harvey, C. D. Single-neuron perturbations reveal feature-specific competition in V1. *Nature* **567**, 334–340 (2019).
40. Harvey, C. D., Coen, P. & Tank, D. W. Choice-specific sequences in parietal cortex during a virtual-navigation decision task. *Nature* **484**, 62–68 (2012).
41. Chen, T. W. et al. Ultrasensitive fluorescent proteins for imaging neuronal activity. *Nature* **499**, 295–300 (2013).
42. Huber, D. et al. Multiple dynamic representations in the motor cortex during sensorimotor learning. *Nature* **484**, 473–478 (2012).
43. Kim, K. H. et al. Multifocal multiphoton microscopy based on multianode photomultiplier tubes. *Opt. Express* **15**, 11658–11678 (2007).
44. Thévenaz, P., Ruttimann, U. E. & Unser, M. A pyramid approach to subpixel registration based on intensity. *IEEE Trans. Image Process.* **7**, 27–41 (1998).
45. Preibisch, S., Saalfeld, S. & Tomancak, P. Globally optimal stitching of tiled 3D microscopic image acquisitions. *Bioinformatics* **25**, 1463–1465 (2009).
46. Brown, M. & Lowe, D. G. Automatic panoramic image stitching using invariant features. *Int. J. Comput. Vis.* **74**, 59–73 (2007).
47. Pnevmatikakis, E. A. & Giovannucci, A. NoRMCorre: An online algorithm for piecewise rigid motion correction of calcium imaging data. *J. Neurosci. Methods* **291**, 83–94 (2017).
48. Mukamel, E. A., Nimmerjahn, A. & Schnitzer, M. J. Automated analysis of cellular signals from large-scale calcium imaging data. *Neuron* **63**, 747–760 (2009).
49. Vogelstein, J. T. et al. Fast nonnegative deconvolution for spike train inference from population calcium imaging. *J. Neurophysiol.* **104**, 3691–3704 (2010).
50. Bishop, C. M. *Pattern Recognition and Machine Learning* Vol. 1 (Springer, 2007).
51. Geladi, P. & Kowalski, B. R. Partial least-squares regression: a tutorial. *Anal. Chim. Acta* **185**, 1–17 (1986).
52. Hastie, T., Tibshirani, R. & Friedman, J. *The Elements of Statistical Learning* (Springer, 2009).
53. Podgorski, K. & Ranganathan, G. Brain heating induced by near-infrared lasers during multiphoton microscopy. *J. Neurophysiol.* **116**, 1012–1023 (2016).
54. Graner, M. W., Cumming, R. I. & Bigner, D. D. The heat shock response and chaperones/heat shock proteins in brain tumors: surface expression, release, and possible immune consequences. *J. Neurosci.* **27**, 11214–11227 (2007).
55. Kalmbach, A. S. & Waters, J. Brain surface temperature under a craniotomy. *J. Neurophysiol.* **108**, 3138–3146 (2012).
56. Wang, H. et al. Brain temperature and its fundamental properties: a review for clinical neuroscientists. *Front. Neurosci.* **8**, 307 (2014).
57. Talan, M. Body temperature of C57BL/6J mice with age. *Exp. Gerontol.* **19**, 25–29 (1984).
58. Greenberg, D. S., Houweling, A. R. & Kerr, J. N. D. Population imaging of ongoing neuronal activity in the visual cortex of awake rats. *Nat. Neurosci.* **11**, 749–751 (2008).
59. Karimipani, Y., Ma, Z., Miller, J. K., Yuste, R. & Wessel, R. Neocortical activity is stimulus- and scale-invariant. *PLoS ONE* **12**, e0177396 (2017).

**Acknowledgements** We acknowledge a Stanford Graduate Fellowship (O.I.R.), research support from the Howard Hughes Medical Institute (M.J.S.), the Stanford CNC Program (M.J.S.), DARPA (M.J.S.), an NSF CAREER Award (S.G.), and the Burroughs-Wellcome (S.G.), McKnight (S.G.), James S. McDonnell (S.G.) and Simons (S.G.) foundations. NIH grants MH085500 and DA028298 to H.Z. funded development of the *GCaMP6f-tTA-dCre* and *Rasgrf2-2A-dCre* mice. NIH grant R24NS098519 (M.J.S.) supports our effort to make the 16-beam two-photon microscope an open resource available to other laboratories. We thank T. Moore, P. Jercog, J. C. Jung, D. Vucinic, B. F. Grewe, E. T. W. Ho, H. Kim, X. Pitkow and T. Zhang for discussions, D. Flickinger and K. Svoboda for providing design files for the water-immersion objective lens, C. Niell for providing *tetO-GCaMP6 s/CaMK2a-tTA* mice, and C. Irimia for animal husbandry.

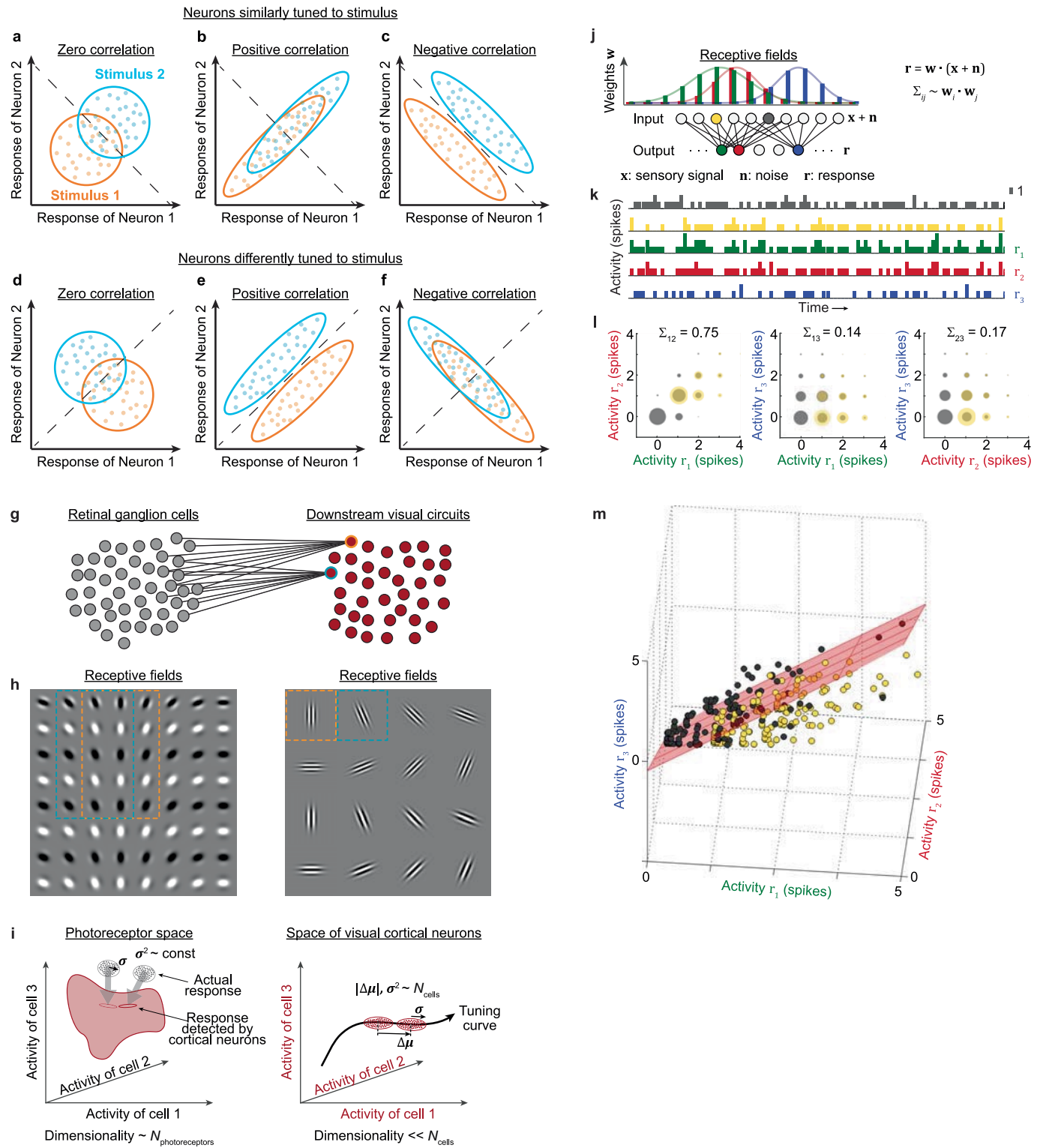
**Author contributions** O.I.R., S.G. and M.J.S. designed experiments and analyses. O.I.R., J.A.L. and J.S. designed and built the microscope. O.I.R., J.A.L., O.H., Y.Z., R.C. and J.L. acquired and analysed data. S.G. developed theory and analysed data. H.Z. provided transgenic mice. O.I.R., S.G. and M.J.S. wrote the paper. All authors edited the paper. S.G. and M.J.S. supervised the research.

**Competing interests** M.J.S. is a scientific co-founder of Inscopix, which produces the Mosaic software used to identify individual neurons in the  $\text{Ca}^{2+}$  videos. J.A.L. is also an Inscopix stockholder.

**Additional information**  
**Supplementary information** is available for this paper at <https://doi.org/10.1038/s41586-020-2130-2>.

**Correspondence and requests for materials** should be addressed to O.I.R., S.G. or M.J.S.  
**Peer review information** *Nature* thanks Stefano Panzeri and the other, anonymous, reviewer(s) for their contribution to the peer review of this work.

**Reprints and permissions information** is available at <http://www.nature.com/reprints>.



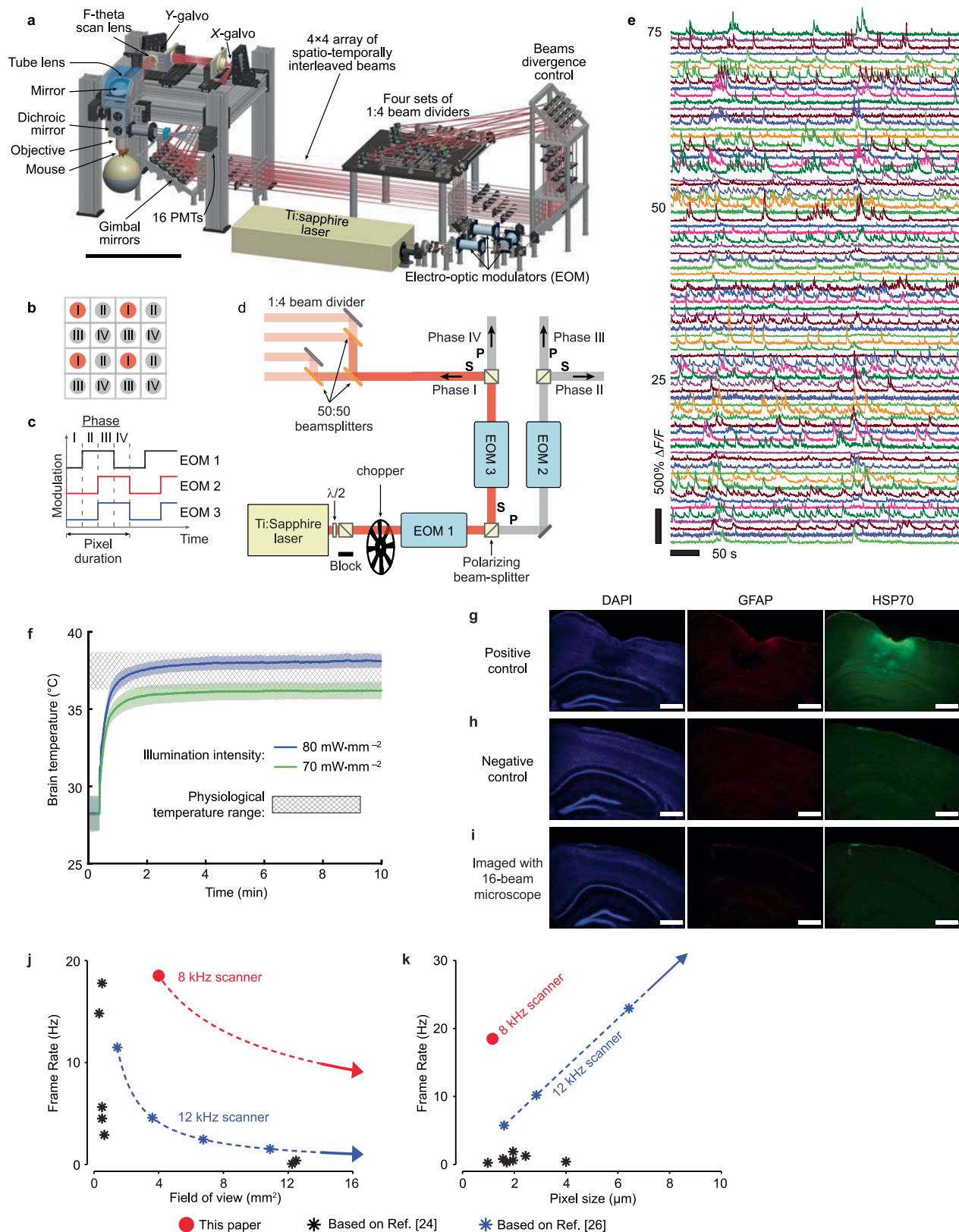
Extended Data Fig. 1 | See next page for caption.



**Extended Data Fig. 1 | The discriminability of two sensory stimuli based on the activity patterns of two or more cells depends on the statistical relationship between the mean responses of the cells and their noise correlations, which in turn depends on visual neural circuitry.**

**a–f**, Schematics of the distributions of responses by two cells to two distinct stimuli in six different cases. Cyan dots indicate joint responses of the cell pair to stimulus 1; orange dots indicate responses to stimulus 2. Ellipses convey the shapes of the statistical distributions of the responses to each stimulus. Three types of noise correlation are depicted. In **a** and **d**, the two cells have statistically independent noise correlations. In **b** and **e**, the cells share positively correlated noise fluctuations. In **c** and **f**, the cells share negatively correlated noise fluctuations. In all six cases, dashed lines indicate optimal linear boundaries for stimulus discrimination. The information in **a–f** is based on similar plots published previously<sup>5,11,30</sup>. **a–c**, When both neurons have similar stimulus-response properties (for example, as schematized, when both cells have a smaller mean response to stimulus 1 than stimulus 2), positively correlated noise fluctuations (**b**) increase the overlap between the two response distributions and thereby impair stimulus discrimination, whereas negatively correlated noise fluctuations (**c**) improve stimulus discrimination as compared to the case with independent noise fluctuations (**a**). **d–f**, When both neurons have opposite stimulus tuning (for example, as schematized, when neuron 1 responds more vigorously to stimulus 1 and neuron 2 responds more vigorously to stimulus 2), positively correlated noise fluctuations (**e**) decrease the overlap between the two response distributions as compared to the case with independent noise fluctuations (**d**) and thereby improve stimulus discrimination, whereas negatively correlated noise fluctuations (**f**) impair stimulus discrimination by increasing the overlap of the two response distributions. **g**, Cells in visual cortical areas, denoted by red circles, integrate signals from earlier stages of the visual pathway, as schematized by the input connections to two example cortical neurons. Thus, as visual information propagates through neural circuitry, noise fluctuations become correlated between cells with similar receptive fields, leading to an upper bound on the amount of information that a neural ensemble can encode. **h**, Example receptive fields for cells in **g**. Cells in early stages of the visual processing pathway have relatively simple receptive fields. Integration of their activity patterns leads to more complex visual receptive fields in downstream visual areas. Dashed boxes enclose receptive fields (right) for the two example cells marked in **g**, as well as the receptive fields of cells providing visual inputs (left). **i**, A network's pattern of synaptic connectivity constrains the dimensionality of the activity in downstream visual circuits<sup>12</sup>. Left, in the early layers of the visual pathway, the dimensionality of ensemble activity is about the same order of magnitude as the number of photoreceptors. In downstream visual areas, due to the extraction of visual features, neural activity is constrained to a manifold

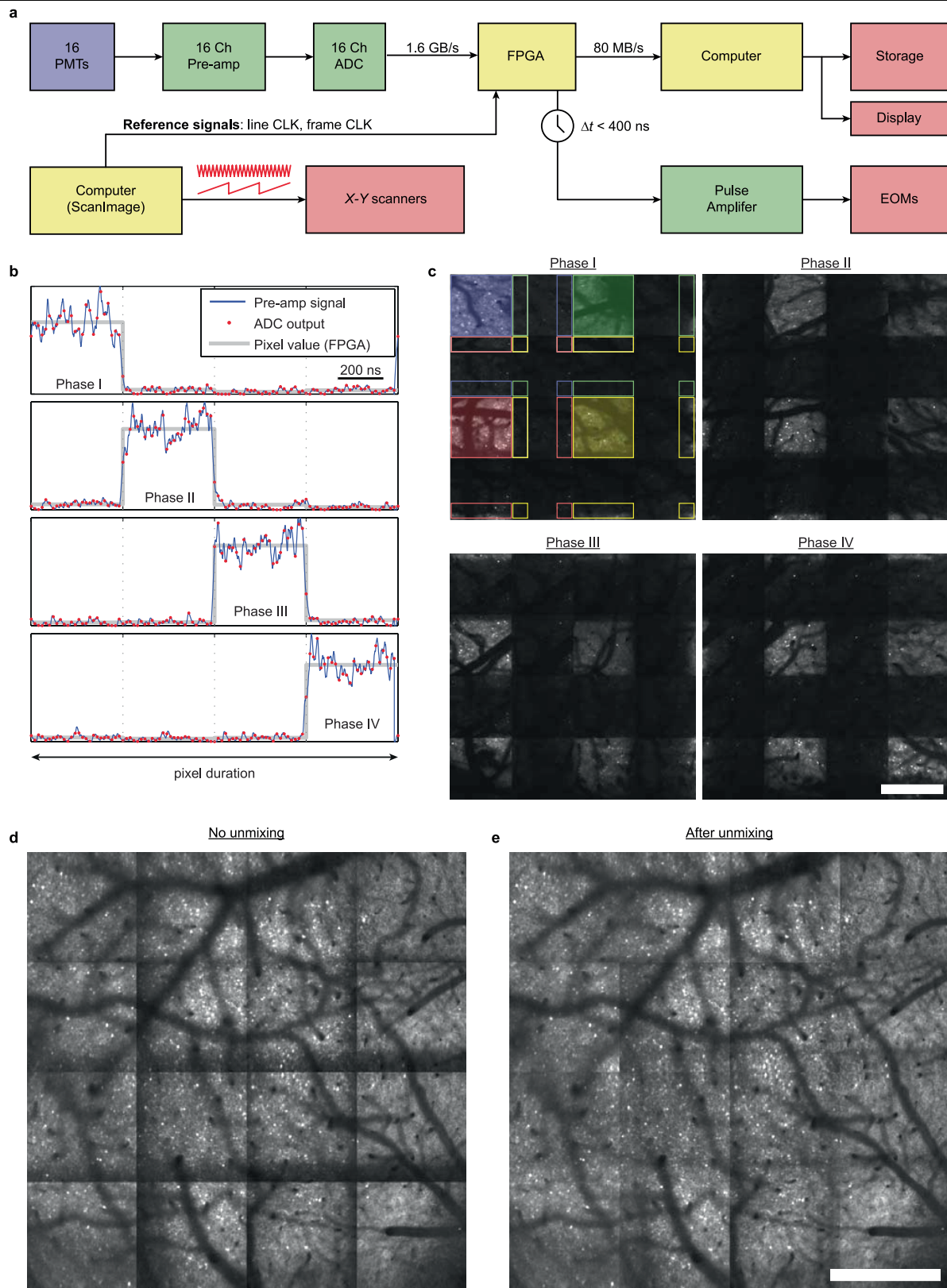
of lower dimensionality (indicated by the red-shaded manifold in the space of all possible photoreceptor inputs). This manifold is determined by the set of receptive fields and hence the visual features that the downstream visual area detects. Grey ellipses (left) depict the distributions of photoreceptor responses to two distinct visual stimuli; after propagating through the visual circuitry these distributions are confined to the lower-dimensional manifold (red ellipses). Right, for a family of visual stimuli parameterized by a single variable, the mean neural ensemble responses lie along a corresponding tuning curve. Noise in the input circuitry propagates to downstream areas and leads to noise fluctuations in downstream neurons that are statistically correlated for cells with similar receptive fields. This, in turn, implies that the magnitude of noise fluctuations along the neural tuning curve becomes proportional to the number of cells in a neural ensemble and indistinguishable from the encoded visual signals, which also increase in proportion to the number of cells. This proportional growth of noise and signal ultimately limits the ability to discriminate two visual stimuli. Thus, for neural ensembles with more than a certain number of cells, the encoded information reaches an upper bound. **j**, We simulated a two-layer, linear feedforward neural network, to illustrate that information-limiting correlations are intrinsic to feed-forward neural networks with overlapping receptive fields<sup>12</sup>. Top, for three example output cells, the plot shows the synaptic weights of the inputs from cells in the first layer of the network. Bottom, diagram of connections between the two layers of the network. Symbols are defined as follows: **x** is the mean activity of cells in the first layer in response to a given stimulus; **n** is the noise in the activity of the input cells; **r** is the activity of the output cells. **k**, Digitized plots of spike counts for simulated activity in the network of **j**, for the two example input cells (yellow and black) and three example output cells (red, green, blue). The noise traces for the input cells came from independent Poisson random processes. External inputs to the network selectively drove either the yellow or the black cell, but owing to the presence of noise the two cells are occasionally active concurrently. **l**, Frequency plots of pairwise activity levels (rounded to the nearest integer) for pairs of output cells in the network of **j**. Yellow and black circles denote which of the two corresponding input cells received external input. The diameter of each circle denotes the number of time bins with a given pair of activity levels in the two cells.  $\Sigma$  values are noise correlation coefficients and are larger for pairs of output cells with greater overlap in their receptive fields. **m**, Plot of the distribution of activity responses in the output cell layer, for the three example cells coloured green, red and blue in **j**. Data points are coloured either yellow or black, to indicate whether the output activity is a response to stimulation of the yellow- or black-coloured cell in the input layer. The red plane denotes the optimal linear classification boundary between the two stimulation conditions.



**Extended Data Fig. 2** | See next page for caption.

**Extended Data Fig. 2 | Spatiotemporal multiplexing of the illumination beams permits imaging of large fields of view at fast frame rates without thermal damage to brain tissue.** **a**, Computer-assisted design of the mechanical layout of the two-photon microscope. Scale bar, 0.5 m. **b**, In the pixel multiplexing mode of imaging, each of the 16 beams are assigned to one of four different temporal phases within each cycle of the pixel clock (Extended Data Fig. 3b). Alternatively, in the line-multiplexing mode of imaging, only 8 of the 16 beam paths are used (Methods). In neither imaging mode are neighbouring beams ever active concurrently (Extended Data Fig. 3c), minimizing fluorescence scattering between active image tiles and allowing scattering into inactive image tiles to be corrected computationally (Extended Data Figs. 3d, e, 4a–g). **c**, To switch between the different sets of active beams, square-wave electronic signals control a set of three electro-optic modulators (EOMs). **d**, A Ti:sapphire laser provides ultrashort-pulsed infrared illumination. A half-wave ( $\lambda/2$ ) plate and a polarizing beam-splitter enable power control. Three pairs of EOMs and polarizing beam-splitters direct the light into one of four main optical paths, with only one path illuminated during each of the four multiplexing phases. In each of these four main paths, three 50:50 beam-splitters create four beams of equal intensity, yielding up to 16 total beams but with only four on at any instant. A chopper blocks all light during the turnaround portion of the galvanometer scanning cycle. **e**, Seventy-five example fluorescence traces of  $\text{Ca}^{2+}$  activity in layer 2/3 pyramidal cells of an awake mouse. **f**, Maintaining brain temperature within physiological ranges during in vivo two-photon imaging requires a proper balance between heat loss through the cranial window and heating induced by the laser illumination<sup>53,55</sup>. To directly verify that our cranial window preparation and imaging conditions properly balanced these two opposing effects, we measured brain temperature during two-photon imaging with the 16-beam microscope. For these studies we used an implanted thermocouple<sup>53</sup> and either the highest (blue trace) or lowest (green trace) time-averaged laser illumination intensity used for  $\text{Ca}^{2+}$  imaging elsewhere in this study (Methods). Consistent with previous work, before laser illumination commenced the brain temperature was about 9 °C below normal mouse body temperature<sup>55</sup>, a state that is considered to be neuroprotective<sup>56</sup>. By about 100 s after the start of imaging, brain temperatures attained steady-state values within the physiological range of C57BL/6 mice<sup>57</sup> (grey shaded region; 36.3 °C–38.7 °C). Each trace is an average of three bouts of imaging for each of three separate mice. Coloured shading denotes the s.d. across the 9 individual measurements acquired at each illumination intensity. **g–i**, Fluorescence immunohistochemical analyses of tissue damage markers. To check whether in vivo imaging of brain tissue with the 16-beam instrument

(4 mm<sup>2</sup> field of view) induced any tissue damage, we immunostained post-mortem brain tissue sections using antibodies to two different damage markers, glial fibrillary activation protein (GFAP) and heat shock protein 70 (HSP70), previously identified as indicators of laser-induced tissue damage<sup>53</sup>. We also stained the sections with DAPI, which labels cell nuclei. We compared positive control tissue sections (**g**) that we had deliberately damaged in vivo with high-power (2,680 mW mm<sup>-2</sup>) laser illumination, negative control sections (**h**) that received no laser illumination, and experimental tissue sections (**i**) that had undergone in vivo two-photon imaging at the highest level of laser illumination (80 mW mm<sup>-2</sup>) used in this study for tracking  $\text{Ca}^{2+}$  dynamics in neocortical layer 2/3 pyramidal neurons. Together, these analyses verified the functionality of the antibodies and revealed no signs of tissue damage from two-photon imaging. To image neurons in cortical layers deeper than layer 2/3, users have several options for doing so without delivering excess heat to the brain (Supplementary Video 3, Supplementary Note). Scale bars, 500  $\mu\text{m}$ . Results shown are representative of those from 8 cerebral hemispheres of 4 different mice. **j**, **k**, Comparisons between recent large-scale two-photon microscopes<sup>24,26</sup>. The performance of a laser-scanning microscope closely relates to four main parameters: the scanner speed, image-frame acquisition rate, field of view, and pixel size (Supplementary Note). For microscopes that use a single laser beam to sweep in two dimensions across the field of view, these parameters obey the relationship  $\text{FOV} = d \times v \times f^{-1}$ , where FOV is the field-of-view area,  $d$  is the spacing between adjacent image lines (or equivalently the pixel width along the slow-axis of laser-scanning),  $v$  is the speed at which the beam is swept across the specimen by the fast-axis scanner, and  $f$  is the image-frame acquisition rate. By comparison, our approach using four active beams leads to an expression for the maximal field of view,  $\text{FOV} = 4 \times d \times v \times f^{-1}$ . These relationships enable performance comparisons with other recently published large-scale two-photon microscopes<sup>24,26</sup>. To illustrate, **j** shows a plot of the image-frame acquisition rate against the field-of-view area, given a line spacing of  $d = 1.15 \mu\text{m}$ . **k** shows how the image-frame acquisition rate depends on  $d$  for a 4 mm<sup>2</sup> field of view. Solid red circles denote the performance of our microscope in its line-multiplexing imaging mode using an 8-kHz resonant galvanometer (Methods). Black data points denote performance options of another large two-photon microscope, which uses pair of laser beams with temporally interleaved pulses<sup>24</sup>, as calculated on the basis of its published capabilities. Blue data points and associated blue dashed lines show performance options for a third large-scale microscope<sup>26</sup>, as calculated on the basis of its published capabilities.

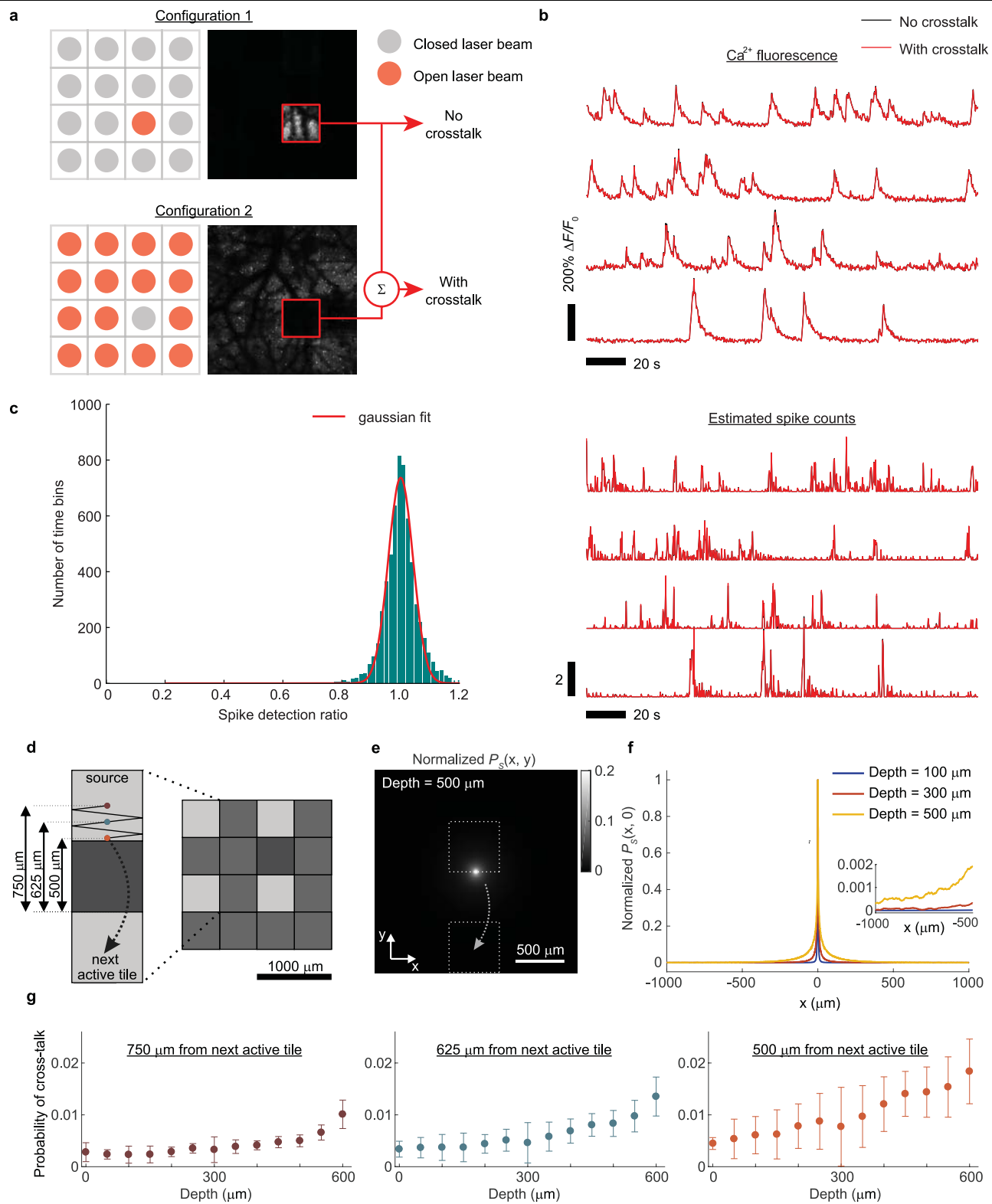


**Extended Data Fig. 3** | See next page for caption.

**Extended Data Fig. 3 | Data acquisition and post-processing for two-photon imaging with 16 time-multiplexed excitation beams.** **a**, Block diagram of the electronics for data acquisition and instrument control. PMT, photomultiplier tube; Pre-amp, pre-amplifier; ADC, analogue-to-digital converter; FPGA, field-programmable gate array; EOM, electro-optic modulator. **b**, Computer simulation of signal sampling in different stages of the pipeline in **a**. The ADC samples the analogue, pre-amplified and low-pass filtered signals (blue) from one of the PMTs at a rate of  $5 \times 10^7$  samples per second. In each of the four temporal phases, the FPGA sums the digitized signals (red) from the ADC to yield the fluorescence intensity values of each image pixel (grey). **c**, Raw fluorescence images for each of the four excitation phases, acquired in an awake mouse expressing GCaMP6f in layer 2/3 cortical pyramidal cells and averaged over 100 frames (7.23 Hz acquisition rate). In each of the four phases, a distinct set of four PMTs detects most of the fluorescence emissions, creating

four active image tiles within the  $4 \times 4$  array. (Each of the four PMTs corresponds to one of the four laser beams that is active in that phase.) To illustrate, the four active tiles within the phase I image are shaded with a different colour (shaded large square regions). However, close to the boundaries of each active tile, some fluorescence photons are detected by the other 12 PMTs. During signal unmixing these photons are reassigned to corresponding pixels in the correct adjacent active image tile. For instance, within the phase I image photons detected in the areas outlined in colour (rectangles and small squares) are reassigned to the colour-corresponding active tiles. **d**, An image compiling the four sets of four active image tiles from the panels in **c**. **e**, During signal unmixing, we re-assign scattered fluorescence photons to their correct pixels of origin, using the method shown in **c**, by reassigning the boundary regions of 128 pixels width. The resulting image is displayed with the mean contrast equalized across tiles. Scale bars: **c**, **e**, 500  $\mu\text{m}$ .



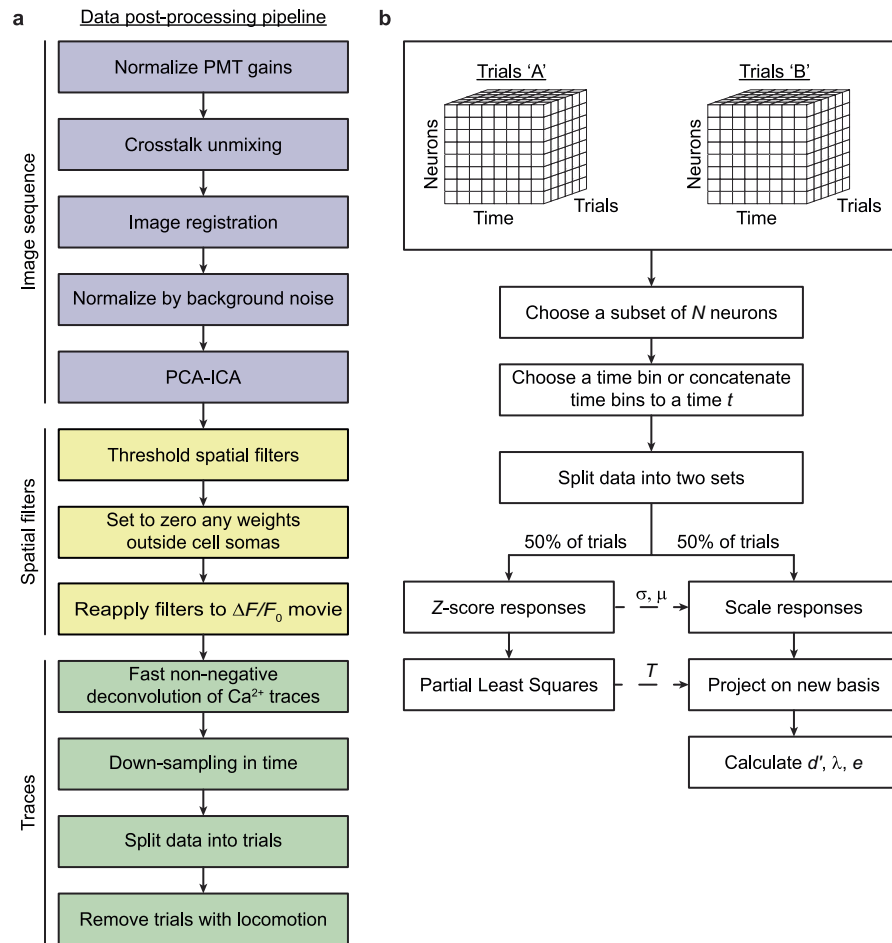


**Extended Data Fig. 4** | See next page for caption.

**Extended Data Fig. 4 | Crosstalk un-mixing procedure for reconstructing the full field-of-view enables accurate estimation of neural activity traces.**

**a**, To quantify the extent of fluorescence scattering across image tiles, we acquired images in two distinct configurations that enabled us to distinguish fluorescence signals from any crosstalk due to fluorescence scattering across image tiles. Using an awake mouse expressing GCaMP6f in layer 2/3 cortical pyramidal cells, we first imaged with only one active laser beam and its corresponding PMT; the other 15 beams were blocked (configuration 1). In this configuration, there is no fluorescence scattering into the active image tile from the other 15 tiles, only the signals from the active tile. In configuration 2, we blocked the beam that had previously been active, unblocked the other 15 beams, operated the microscope with the normal multiplexing approach, and again sampled signals from all 16 PMTs. To estimate the extent of scattering into the tile with the blocked beam, we applied the computational un-mixing procedure to the raw image data. To estimate how much scattered fluorescence affects cell sorting, we first extracted individual cells and their  $\text{Ca}^{2+}$  activity traces from the first dataset, attained in configuration 1 without crosstalk. We then summed the images, frame by frame, from the two datasets, to create a mock dataset comprising unscattered plus scattered fluorescence signals, from which we again computationally extracted cells and their activity traces. This enabled a direct comparison between two datasets containing the exact same patterns of neural activity, with and without fluorescence scattering from other image tiles. **b**, Activity traces for four example cells, enabling comparisons of the  $\text{Ca}^{2+}$  activity traces (top),  $\Delta F(t)/F_0$ , and the resulting traces of the estimated spike counts (bottom), between the datasets with (red traces) and without (black traces) inter-tile scattering. The traces with and without inter-tile scattered fluorescence signals are nearly indistinguishable by eye. **c**, Histogram of the ratio of estimated spikes for the two datasets constructed in **a**, for all time bins (0.14 s per time bin) with an estimated spike count greater than 0.5. The mean ratio is  $1.0 \pm 0.06$  (mean  $\pm$  s.d.;  $N = 31$  cells). Total number of time bins, 5,865. **d–g**, Studies of fluorescence scattering between the active image tiles in one temporal phase

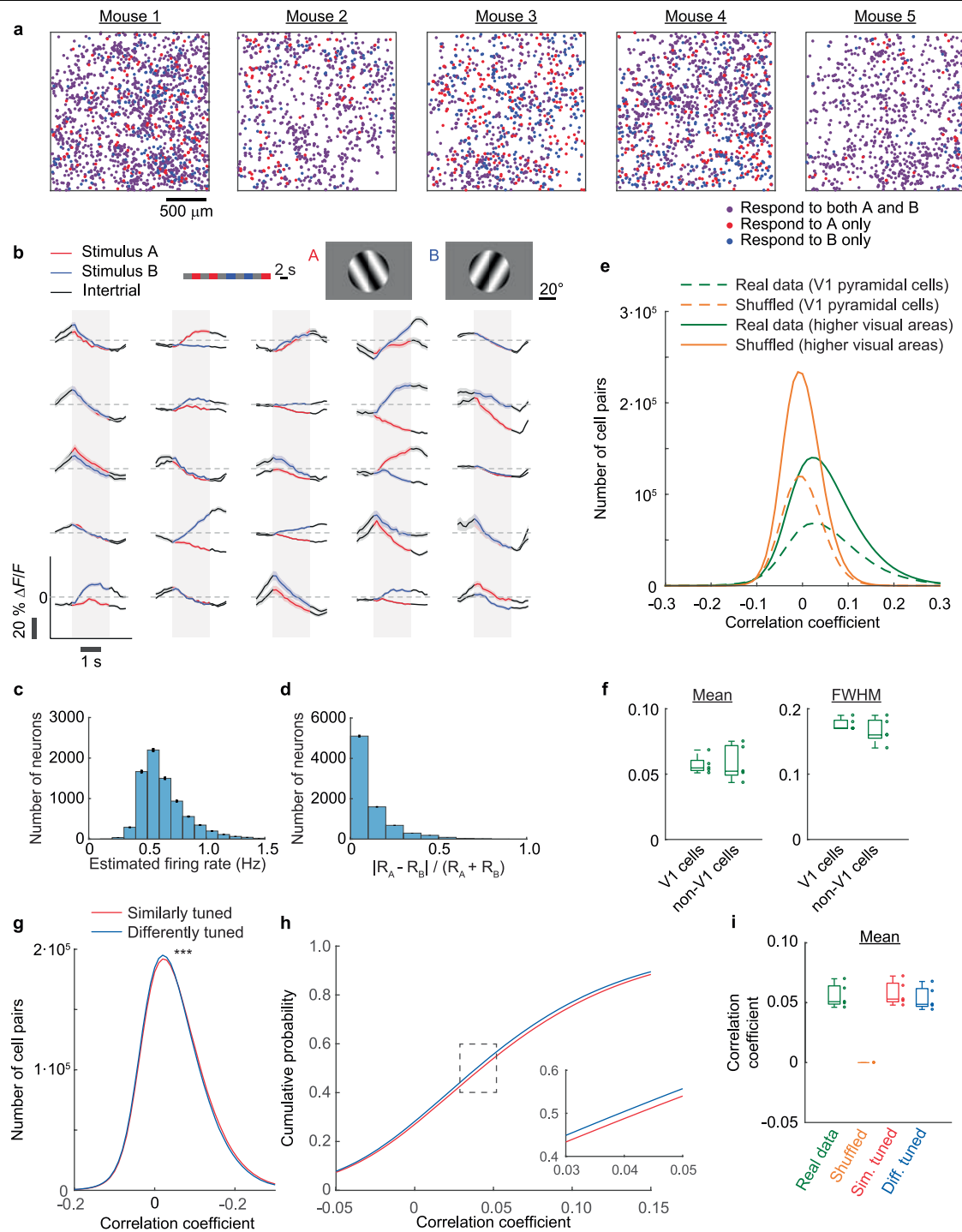
(Extended Data Fig. 2b) of the multiplexing scheme used for two-photon imaging. Throughout the paper, we corrected computationally for fluorescence scattering from active to inactive image tiles within each temporal phase of imaging (Extended Data Fig. 3c, Methods). This approach neglects the small amount of fluorescence scattering from active tiles to other active tiles, which in principle could also be computationally corrected using a more sophisticated method than the one we adopted. Hence, we examined experimentally the validity of our computational approach and the extent to which scattering between active tiles can be justifiably neglected. The amplitude of scattering between active tiles (**d**) varies with the location of each laser beam and its proximity to a tile boundary. We used fixed cortical tissue slices from adult *GCaMP6f-tTA-dCre* mice to measure the amplitude of such scattering effects when imaging at different depths within brain tissue. An image (**e**) of the spatial distribution of two-photon fluorescence excited 500  $\mu\text{m}$  deep within a tissue slice shows that a majority of scattered fluorescence photons exits the brain tissue relatively near to the laser focus. By averaging over 100 different laser foci positions in each of 3 different brain slices, we determined the mean cross-sectional spatial profiles (**f**) of scattered fluorescence excited at different depths in tissue, as a function of the lateral displacement,  $x$ , from the laser focus. Profiles are shown normalized to unity at  $x = 0$ . The inset of **f** shows a magnified view of these cross-sectional profiles for  $x \in [-1,000 \mu\text{m}, -500 \mu\text{m}]$ , that is, up to 1 mm away from the laser focus. We used these empirically determined scattering profiles to compute the probability (mean  $\pm$  s.d.;  $N = 300$  laser focus positions) (**g**) that a fluorescence photon originating in one active image tile would scatter into an adjacent active tile. Even when the laser focus is on the boundary of an image tile, this probability remains less than 0.02 for all tissue depths  $\leq 600 \mu\text{m}$ . For our studies of layer 2/3 cortical pyramidal cells in live mice, the probability of a fluorescence photon scattering between active tiles is less than 0.01. In conclusion, computational corrections for fluorescence scattering that account solely for scattering from active to inactive tiles—and neglect scattering between different active tiles—are empirically well justified.



**Extended Data Fig. 5 | Pipeline of offline data processing and procedures for reducing the dimensionality of the neural ensemble activity data and calculating the decoding accuracy.**

**a**, Pipeline of the offline procedures we applied to the acquired fluorescence signals to attain traces of neural activity. Steps coloured purple involve algorithms that use raw or processed image data. Steps coloured yellow involve algorithms that use cells' spatial filters as their input arguments. Steps coloured green involve algorithms that use cells' activity traces as their inputs. Purple steps, starting from the raw photocurrents from each of the 16 PMTs (sampled at 50 MHz and assigned to individual image pixels corresponding to a 400-ns laser dwell time), we normalized the photocurrent signals by the gain of each individual PMT, to equalize the image intensity scale across the entire image. We then un-mixed scattered fluorescence, as shown in Extended Data Fig. 3, and applied an image registration routine (TurboReg<sup>44</sup>) to the videos from the individual image tiles. To highlight  $\text{Ca}^{2+}$  transients against baseline fluctuations, we used the fact that the two-photon fluorescence increases of GCaMP6 during  $\text{Ca}^{2+}$  transients are many times the s.d. of background noise. Thus, we converted the fluorescence trace of each pixel,  $F(t)$ , into a trace of z-scores,  $\Delta F(t)/\sigma$ . Here  $\Delta F(t) = F(t) - F_0$  denotes the deviation of the pixel from its mean value,  $F_0$ , and  $\sigma$  denotes the background noise of the pixel, which we estimated by taking the minimum of all standard deviation values calculated within a sliding 10-s window<sup>35</sup>. After transforming the movie data into this  $\Delta F(t)/\sigma$  form, we identified neural cell bodies and processes using an established cell-sorting algorithm that sequentially applies principal and independent component analyses (PCA and ICA) to extract the spatial filters and time traces of individual cells<sup>48</sup>. Yellow steps, for all spatial filters corresponding to individual cell bodies, we

thresholded the filters at 5% of each filter's maximum intensity and set to zero any filter components with non-zero weights outside the soma. To attain neural activity traces, we then reapplied the set of resulting filters to the  $\Delta F(t)/F_0$  movies. Green steps, to estimate the most likely number of spikes fired by each cell in each time bin, we applied a fast non-negative deconvolution algorithm to the  $\Delta F/F_0$  trace of the cell<sup>49</sup>. For each neuron, we down-sampled (2×) the activity traces to time bins of 0.275 s by averaging the values within adjacent time bins. To make comparisons across similar behavioural states, we removed all trials during which the mouse was moving. **b**, Neural responses for each visual stimulus (A and B) are represented as matrices of size  $N_{\text{neurons}} \times N_{\text{trials}} \times N_{\text{timebins}}$ . To calculate the accuracy of stimulus discrimination, we first randomly chose a subset of neurons from the dataset. For decoding using the 'instantaneous' strategy (Fig. 3, Extended Data Figs. 7–10), we then chose a specific time bin, whereas for the 'cumulative' decoding strategy we treated all the different time bins up to a specific time,  $t$ , as independent dimensions of the population activity vector. We then split the trials in half, into a training set and a test set, each with equal numbers of trials with the A and B stimuli. We took the neural activity traces in the training set and normalized them by the s.d. of the cell's activity about its mean, to create a set of z-score traces. We then performed PLS analysis to identify a low-dimensional basis that well captured the separation between the neural responses to the two sensory stimuli. Using the activity data in the test set, we applied the same normalization and dimensional reduction procedures and values as for the training set. We used the resulting distributions of responses to calculate  $d'$  values and the eigenvectors of the noise covariance matrix. For each mouse we repeated this entire procedure for 100 different randomly chosen subsets of neurons.

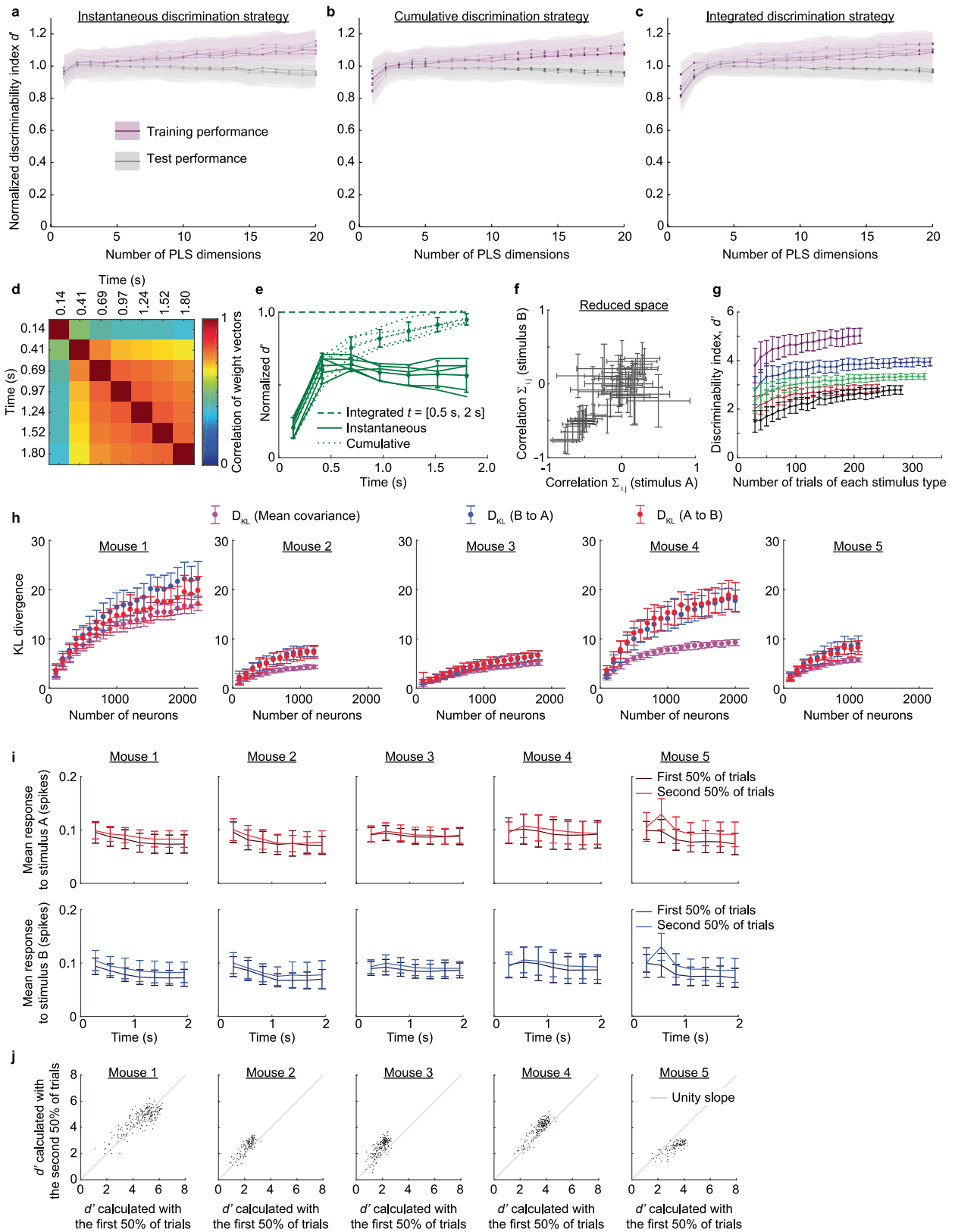


**Extended Data Fig. 6** | See next page for caption.

## Extended Data Fig. 6 | Distributions of pairwise noise correlation coefficients do not differ significantly between pyramidal neurons in area V1 and higher-order visual areas. **a**, Anatomical maps of visual cortical neurons that responded to each of the two stimuli. For these maps (but for no other analyses in the paper), we denoted a cell as responsive to one of the stimuli if, in at least one time bin during the 2-s stimulation period (0.275 s per bin), the difference between the cell's mean response and its mean activity trace during the inter-trial intervals was more than twice the sum of the s.e.m. values for these two traces. Cells that responded to stimulus A only are shown red, those that responded only to stimulus B only are shown blue, those that responded to both stimuli are shown purple. **b**, Mean $\text{Ca}^{2+}$ responses ( $\Delta F/F$ ) of 25 example neurons to the two different moving grating stimuli, oriented at $\pm 30^\circ$ . $\text{Ca}^{2+}$ activity traces are shown coloured during the stimulation period (marked with light grey shading) and black otherwise. Coloured shading about each trace denotes the s.e.m. over 217 trials of each type. The inset shows a schematic of the two stimuli, which appeared for 2 s per trial and were presented in random order. **c**, **d**, Histograms of the estimated mean spiking rates of individual neurons during visual stimulation (**c**) and the absolute values of the differential responses of the individual neurons to the two visual stimuli, $|R_A - R_B| / (R_A + R_B)$ (**d**), where $R_A$ and $R_B$ denote the mean responses of a cell to stimuli A and B, respectively. The distributions of cells' activity rates and preferences for one stimulus over the other were consistent with previous studies of rodent visual cortical neurons<sup>28,29,38,58,59</sup>. Data shown are for $N = 8,029$ individual cells from $N = 5$ mice. Error bars are s.d. as estimated on the basis of counting errors. **e**, Histogram of noise correlation coefficients, $r$ , between pairs of layer 2/3 pyramidal neurons, computed as in Fig. 2d, for V1 cell pairs (dashed lines) and cells pairs in higher-order visual areas (solid lines). The histograms show mean values across the two different visual stimuli for both the real neural activity traces, and for trial-shuffled data in which each cell's

responses to each stimulus presentation were randomly permuted across the set of all presentations of the same stimulus.  $r$  values were computed on the basis of cells' responses integrated over  $t = [0.5 \text{ s}, 2 \text{ s}]$  from the start of each trial. Histogram bin, 0.01. ( $N = 1,331,109$  V1 cell pairs from 5 mice;  $N = 2,428,437$  cell pairs from higher-order visual areas in 5 mice). **f**, Box-and-whisker plots of the mean and FWHM values of the distributions in **e** (real data only). Both statistical metrics are similar for the two classes of visual cortical neurons. Open circles denote individual data points for  $N = 5$  mice. **g**, **h**, Histograms (**g**) and cumulative probability distributions (**h**) of noise correlation coefficients for all cell pairs (based on all recorded V1 and higher-order visual cortical neurons) with similar or differently tuned mean evoked responses to the two visual stimuli. Unlike Fig. 2e, which shows these distributions for only the most active cells (the highest decile), here the distributions include all cell pairs with either positively (red curves) or negatively (blue curves) correlated mean responses to the two stimuli. Within these two groups of cell pairs, we computed the noise correlation coefficient,  $r$ , for each cell pair. Owing to the extremely large number of cell pairs, the two distributions of  $r$  values differed significantly ( $***P < 10^{-13}$  for all 5 individual mice; two-tailed Kolmogorov-Smirnov test; 3,482,186 positively correlated cell pairs in total; 3,464,094 negatively correlated pairs), even though the effect size was tiny and the two distributions were nearly identical. This result shows the difficulty of detecting information-limiting correlations by measuring pairwise noise correlations, because the variance in the individual  $r$  values is much greater than the difference between the mean values of the two distributions. **i**, Box-and-whisker plots of the mean values of the correlation coefficients in **g**, **h**. Open circles mark individual data points for  $N = 5$  mice. **b-i** are based on 217–332 trials per stimulus condition in each of 5 mice. In **f**, **i**, boxes cover the middle 50% of values, horizontal lines denote medians, and whiskers span the full range of the data.

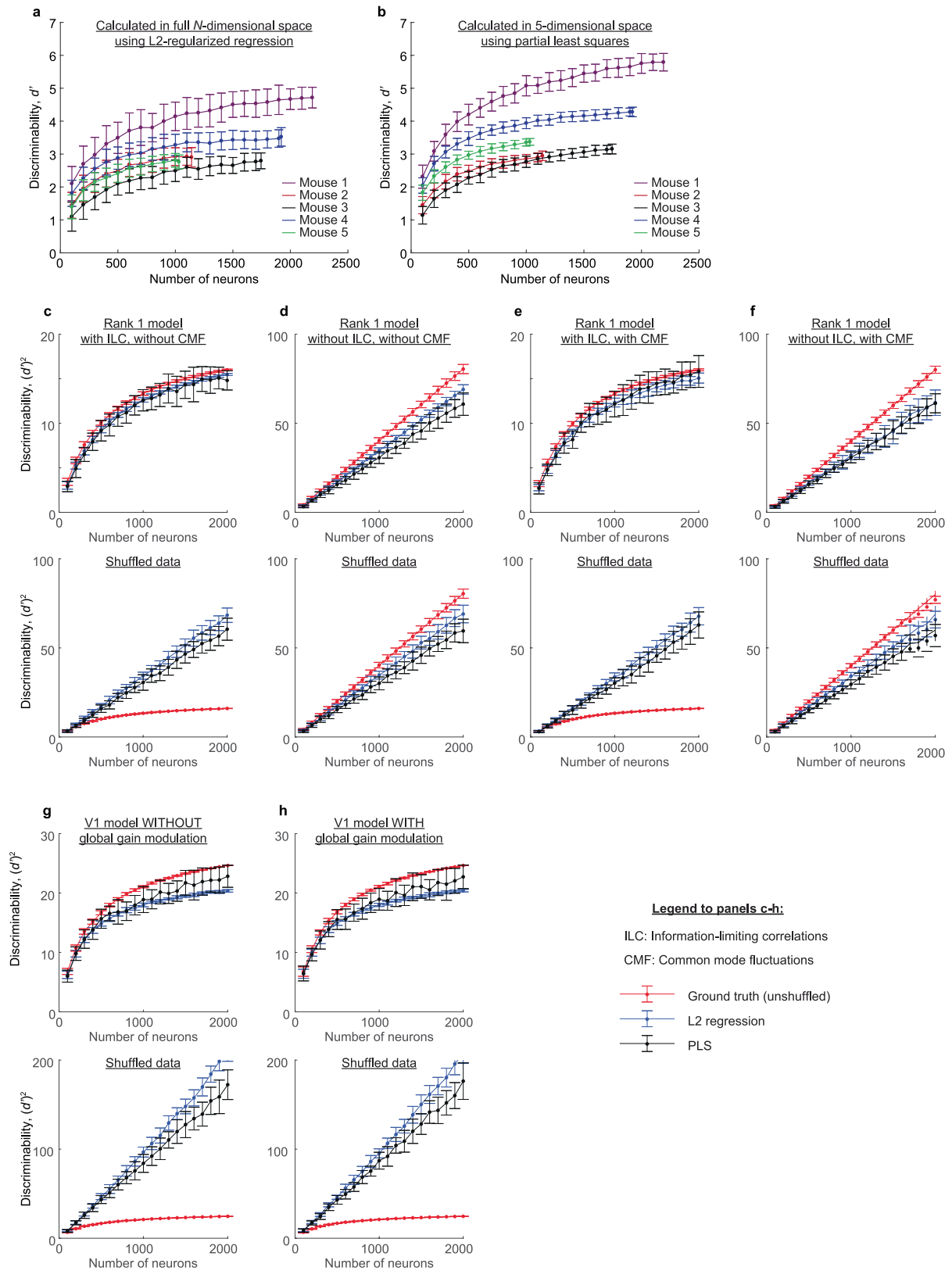




**Extended Data Fig. 7** | See next page for caption.

**Extended Data Fig. 7 | Temporal integration of neural activity improves decoding performance, but quadratic and linear decoding yield identical biological conclusions. a–c.** To identify how many PLS dimensions were needed to determine  $d'$  accurately, we divided data from each of 5 mice into three equally sized portions. We performed PLS analysis using trials in the first third. Onto the PLS dimensions thereby identified, we projected the neural ensemble activity in the second third of the data (training data). We retained only the first  $N_R$  dimensions of this projection and computed  $d'$  in the reduced space (magenta data points) by identifying a hyperplane for optimal stimulus discrimination. Finally, we applied this discrimination strategy to the remaining third of the data (test data) and again calculated  $d'$  (grey points). Plots show mean values of  $d'$  as a function of  $N_R$  for the interval [0.83 s, 1.11 s] from stimulus onset ( $N = 5$  mice; error bars denote s.d. across 100 different subsets of 1,000 neurons per mouse). We normalized  $d'$  values to that found for  $N_R = 5$  on the test dataset. For  $N_R > 5$ , discrimination performance declines owing to overfitting for all discrimination strategies: instantaneous (a), cumulative (b) and integrated (c). Hence, throughout the rest of the study we used  $N_R = 5$  for all calculations of  $d'$ . d, Pearson correlation coefficients between the optimal linear decoding weights attained using instantaneous decoding at different time bins after the onset of grating stimuli ( $\pm 30^\circ$  orientations). These weights were highly correlated for different time bins, especially across the interval [0.5 s, 2 s], during which  $d'$  reaches a plateau. Further, optimal decoders for each time bin yielded nearly equivalent decoding performance when applied to data from other time bins. For instance, the optimal decoder for the fourth time bin ( $t = 0.97$  s), when applied to any other of the last five time bins, yielded a performance within less than 2% of that of the optimal instantaneous decoder in all mice. When applied to the first and second time bins, the decoder from the fourth time bin yielded decoding performances that were, respectively,  $83 \pm 11\%$  and  $90 \pm 3\%$  (mean  $\pm$  s.d.;  $N = 5$  mice; 217–232 trials per stimulus) of that of the optimal decoders. e, Plots of  $d'$  versus time after stimulus onset, for instantaneous and cumulative decoding strategies (Fig. 3). For each mouse that viewed gratings oriented at  $\pm 30^\circ$ , we chose 100 random subsets of 1,000 cells and normalized  $d'$  values by those obtained using a time-integrated decoding strategy, which involved optimal linear discrimination over one interval, [0.28 s, 1.94 s], covering most of the visual stimulation period. Green traces, mean  $d'$  values for individual mice using a time bin of 275 ms. Error bars, s.d. across 5 mice. f, In the five-dimensional space used after truncating ensemble neural responses to the five leading PLS dimensions, the distributions of noise in the responses to the two stimuli were highly similar. Specifically, non-diagonal elements,  $\Sigma_{ij}$ , of the noise covariance matrices for the two stimulus conditions were highly correlated ( $r: 0.81 \pm 0.16$ ; mean  $\pm$  s.d.;

$N = 5$  mice), as computed for the interval [0.83 s, 1.11 s] after stimulus onset. This similarity argues that a linear discrimination strategy to classify the two sets of ensemble neural responses is near optimal, as confirmed in h. Values of  $\Sigma_{ij}$  are plotted as mean  $\pm$  s.d., computed across 100 different randomly chosen subsets of 1,000 neurons per mouse. g, Using optimal linear decoding,  $d'$  values saturated as the number of trials analysed increased. Colours denote individual mice. Data points were calculated for the interval [0.83 s, 1.11 s] after stimulus onset. Error bars, s.d. across 100 different randomly chosen subsets of 1,000 cells per mouse and stimulation trials. h, To check whether our results depended on our use of linear decoding, we tested whether quadratic decoding might yield different conclusions. We examined the KL divergence<sup>31</sup>, a generalization of  $(d')^2$  that makes no assumption about the statistical distributions under consideration. We computed the KL divergence, which equals  $(d')^2$  for linear decoders, by using Gaussian approximations to the distributions of ensemble neural responses to the two different stimuli, and we plotted the results as a function of the number of cells,  $n$ , in the ensemble. First, to recapitulate our determinations of  $(d')^2$  (magenta data points), we computed the KL divergence under the assumption the two different response distributions had distinct means but identical noise covariance matrices, which we estimated as the mean noise covariance matrix averaged over the two different stimulus conditions. This is equivalent to computing  $(d')^2$ . Next, we relaxed the assumption that the two noise covariance matrices were equal and computed the KL divergence between the distributions of neural responses to stimulus B relative to those to stimulus A (blue points), and vice versa (red points) (Methods). For all mice, KL divergence values saturated with increasing  $n$  and, except in one mouse, were not much larger than  $(d')^2$  values. Thus, quadratic decoders (which are optimal for discriminating two Gaussian distributions with different means and covariances) will yield the same basic conclusions as linear decoders (which are optimal for discriminating two Gaussian distributions with the same covariance matrix). Data points and error bars denote mean  $\pm$  s.d. values computed in each mouse across 50 different randomly chosen subsets of cells and assignments of visual stimulation trials to decoder training and testing (Extended Data Fig. 5b). i, Mean neural responses, averaged across all cells, to stimuli A (top) and B (bottom) for the first and second halves of the experimental trials in each mouse. Error bars, s.d. across the set of trials. j,  $d'$  values computed for each mouse using instantaneous decoders trained on the first half of the trials and tested on the second half ( $x$  axis), plotted with  $d'$  values for an instantaneous decoder trained on the second half of the trials and tested on the first half ( $y$  axis). a–j are based on 217–332 trials per stimulus condition in each of 5 mice.

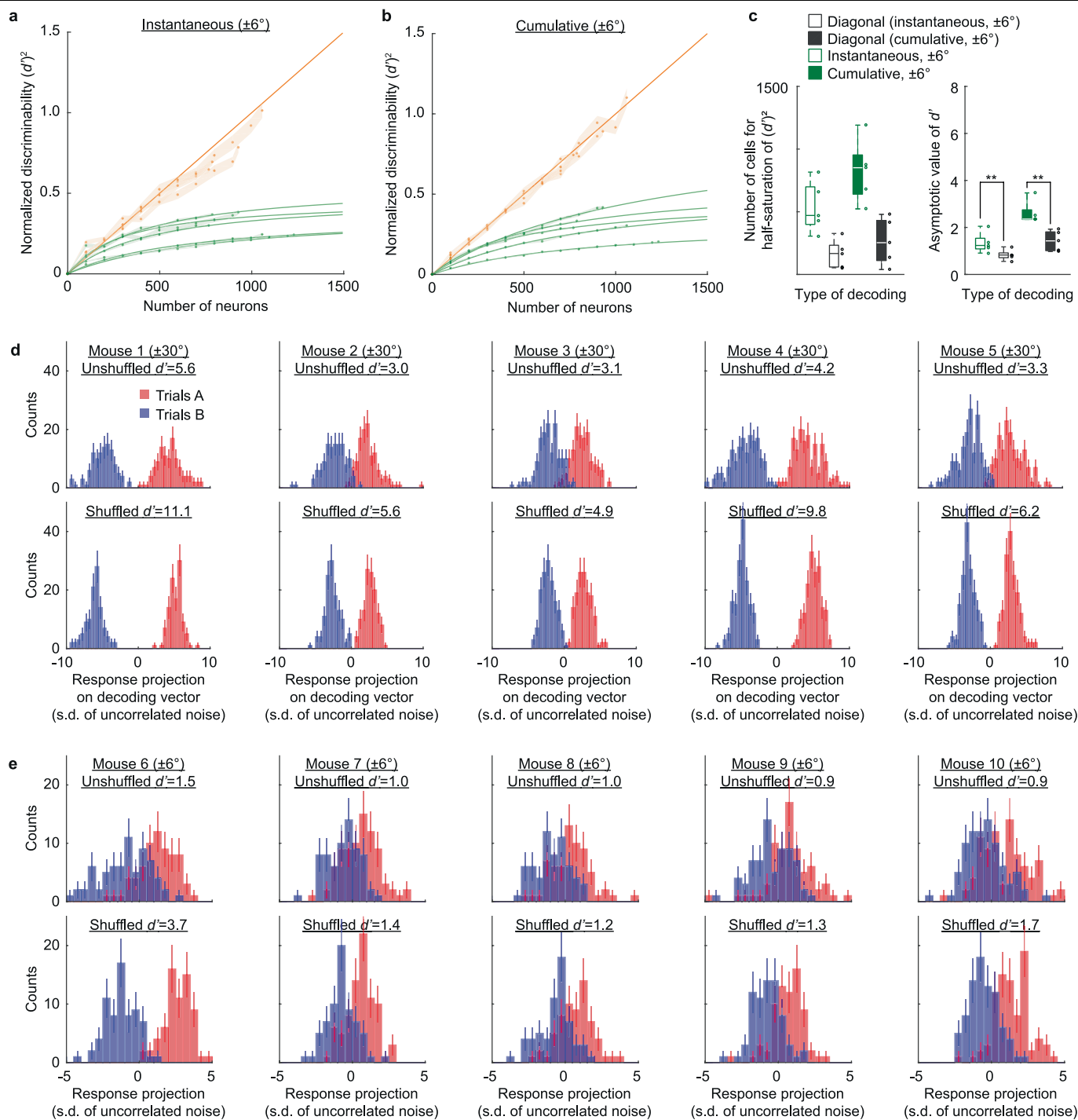


**Extended Data Fig. 8** | See next page for caption.

# Article

**Extended Data Fig. 8 | PLS-based decoding methods are robust to multiplicative gain modulation and common mode fluctuations in the neural ensemble dynamics and yield identical conclusions to regularized regression.** **a, b,** To test whether PLS analysis and dimensionality reduction might lead to underestimates of  $d'$ , we compared  $d'$  values determined using an L2-regularized regression (L2RR) performed in the full space of neural responses (**a**) to those found by PLS analysis (**b**). The two methods yielded similar estimates of  $d'$ , which both saturated with increasing numbers of neurons. Plots show  $d'$  values (mean  $\pm$  s.d.) for neural responses within [0.83 s, 1.11 s] after stimulus onset, computed across 100 different randomly chosen subsets of neurons and visual stimulation trials (Extended Data Fig. 5b). For PLS analyses, we used half of the trials in each subset for decoder training and the other half for testing. For L2RR we used 90% of the trials in each subset to determine the regression vector and the other 10% to determine  $d'$ . We varied the regularization parameter,  $k$ , within  $[1, 10^5]$  and used the maximum  $d'$  value so obtained, as determined independently for each mouse, subset of neurons, and subset of trials (217–332 trials per stimulus condition in each of 5 mice). **c–h,** The conclusions of our study depend on comparisons of decoding performance between real and trial-shuffled datasets. Thus, we checked whether our PLS-based decoding methods would robustly detect information-limiting correlations in models in which such correlations were present but weak; avoid reporting information-limiting correlations in models lacking such correlations; and be robust to the potential presence of other strong sources of neural trial-to-trial variability—such as common mode fluctuations and multiplicative gain modulation—even when they make an order-of-magnitude greater contribution to neural variability than the information-limiting noise fluctuations. We studied these issues using two different computational models (Methods). For both models we plotted empirically determined  $(d')^2$  values as a function of the number of neurons in the ensemble. We compared determinations of  $(d')^2$  using PLS-based decoding and those made using L2RR to the actual ground truth values of  $(d')^2$  in each model. In each panel, the top and bottom plots show results for unshuffled and trial-shuffled datasets, respectively. Data points and error bars denote mean  $\pm$  s.d. values across 30 different simulations. To examine the combined effects of information-limiting noise correlations and common mode fluctuations (**c–f**) we studied a model of neural ensemble responses in which the noise covariance matrix exhibited information-limiting noise correlations via a single eigenvector  $\mathbf{f}$ , the eigenvalue of which grew linearly with the number of cells in the ensemble. In addition to this rank 1 component, we included a noise term that was uncorrelated between different cells, as well as a common mode fluctuation, yielding a noise covariance matrix with the form  $\Sigma^* = \sigma^2 I + \varepsilon_{\text{common}} / + \varepsilon \mathbf{f} \mathbf{f}$ , where  $\sigma^2 = 1$  is the amplitude of uncorrelated noise,  $I$  is the identity matrix,  $J$  is a rank 1 matrix of all ones, reflecting a common mode fluctuation, and  $\mathbf{f}$  is the

information-limiting direction, a vector that we chose randomly in each individual simulation from a multi-dimensional Gaussian distribution with unity variance in each dimension. The amplitude of information-limiting correlations was  $\varepsilon = 0.002$ , approximately matching the level observed in the experimental data. We chose the difference in the means of the two stimulus response distributions,  $\Delta \mu$ , to be aligned with  $\mathbf{f}$  (Fig. 3a) and to have a magnitude of 0.2 so that the asymptotic value of  $d'$  for large numbers of cells approximately matched that of the data. We compared decoding results attained with and without the presence of the common mode fluctuations in the neural responses. In the version of the model without common mode fluctuations, we set  $\varepsilon_{\text{common}}$  to zero. In this case (**c**) both PLS- and L2RR-based decoders correctly detected the saturation of information in the real data but not in trial-shuffled datasets. (See Extended Data Fig. 10h, k for theoretical results showing how the accuracy of  $d'$  estimates from PLS analysis depends on the numbers of neurons and experimental trials in this particular model.) To verify that our methods would not incorrectly report an information saturation when it was in fact absent, we next set  $\varepsilon = 0$  and confirmed that in the absence of information-limiting noise correlations (**d**), neither decoder detected a saturation of information in the real or shuffled data. In the version of the model with common mode fluctuations, we set  $\varepsilon_{\text{common}} = 0.02$ , ten times the value of  $\varepsilon = 0.002$ . In this case (**e**), both PLS- and L2RR-based decoders correctly detected the information saturation in the real but not in the shuffled data. To verify that common mode fluctuations alone cannot induce an illusory saturation of information (**f**), we set  $\varepsilon = 0$  while maintaining  $\varepsilon_{\text{common}} = 0.02$  and confirmed that neither PLS- nor L2RR-based decoders reported an illusory information saturation. Overall, these results indicate that our methods accurately detect the presence of weak information-limiting correlations buried within common mode noise that can be an order of magnitude larger, without falsely detecting information-limiting correlations when they are absent. To study the possible effects of multiplicative gain modulation (**g, h**), we compared two versions of a model in which the responses of the V1 neural population either were or were not subject to a multiplicative stochastic gain modulation but were otherwise statistically equivalent. We modelled the V1 cell population as a set of Gabor filters (see Appendix section 5). In the model version with gain modulation, on each visual stimulation trial we multiplied the output of each Gabor filter by a randomly chosen factor, uniformly distributed between 50%–150%, the value of which was the same for all cells but varied from trial to trial. In the model version without gain modulation (**g**) both PLS- and L2RR-based decoders detected the information saturation in the real but not in the trial-shuffled datasets. When we added global gain modulation to the model (**h**) both decoders correctly found the information saturation in the real but not in the shuffled datasets.



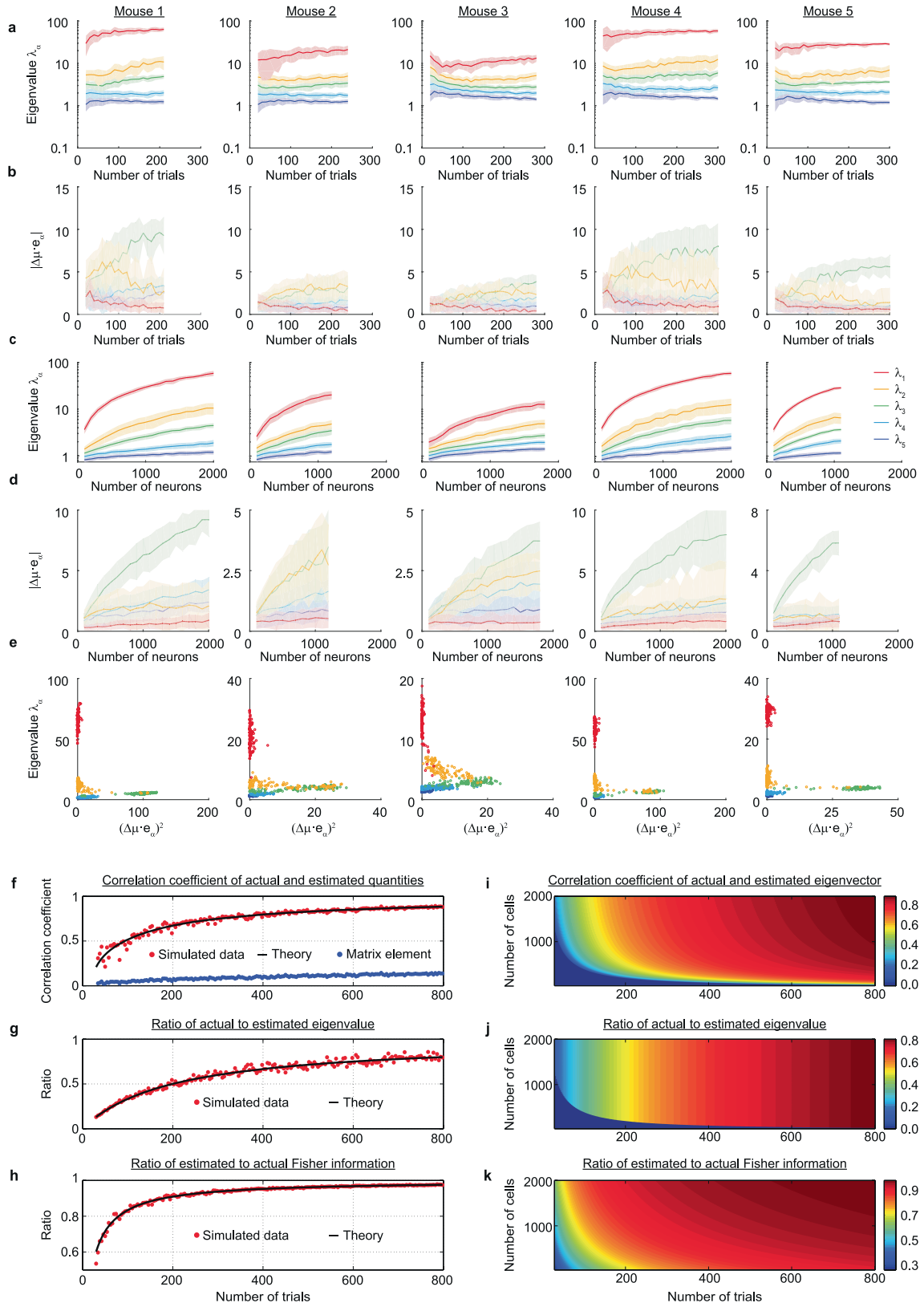
**Extended Data Fig. 9** | See next page for caption.



# Article

**Extended Data Fig. 9 | Moving grating visual stimuli oriented at  $\pm 6^\circ$  are harder to distinguish on the basis of their evoked neural ensemble responses than gratings oriented at  $\pm 30^\circ$ , but also reveal the saturation of information signalling in large neural populations. **a**,  $(d')^2$  values determined using an 'instantaneous' decoder for the interval [0.70 s, 0.94 s] from visual stimulation onset, plotted as a function of the number of cells,  $n$ , in the ensemble in mice presented moving gratings oriented at  $\pm 6^\circ$ . Data points represent mean values determined across 100 different subsets of cells, and the shading represents s.e.m. As in Fig. 3f, g, we fit the  $(d')^2$  values as a function of  $n$  using a one-parameter fit,  $(d')^2 = (d')^2_{\text{shuffled}} / (1 + \varepsilon \times n)$ , where  $(d')^2_{\text{shuffled}}(n)$  is the empirically determined value of  $(d')^2$  for the same number of cells in the shuffled data, and  $\varepsilon$  is the fit parameter. For each mouse, for both real and trial-shuffled data we normalized  $(d')^2$  values by the value of  $(d'_{\text{shuffled}})^2$  for  $n = 1,000$  neurons. Goodness of fit:  $R^2 = 0.41 \pm 0.17$  (s.d.).  $N = 5$  mice.  $\varepsilon = 0.0021 \pm 0.0008$  (s.d.), 122–167 trials per stimulus condition for each mouse. **b**, Same as **a**, but using the 'cumulative' decoding strategy over the [0 s, 0.94 s] time interval. **c**, Box-and-whisker plots of the asymptotic values of  $d'$  in the limit of many neurons (right) and the number of cells at which  $(d')^2$  attains half its asymptotic value (left) as determined from parametric fits to the data of **a** and **b** for the**

instantaneous (open boxes) and cumulative (filled boxes) decoding strategies. Optimal linear decoders (green data) slightly but significantly outperformed diagonal decoders (black data) ( $**P < 0.0001$ ; one-tailed Wilcoxon rank sum test;  $N = 100$  different randomly chosen assignments of trials to decoder training and test sets in each mouse; 122–167 trials per stimulus condition for each mouse; open circles denote mean values from  $N = 5$  individual mice). **d, e**, Histograms for the real (unshuffled) and shuffled datasets of the ensemble neural responses to each of the two visual stimuli, projected onto the direction of the optimal decoding vector determined by PLS analysis, as computed in each mouse viewing moving gratings oriented either at  $\pm 30^\circ$  (**d**) or  $\pm 6^\circ$  (**e**), using all imaged neurons and the instantaneous decoding approach. Error bars denote counting errors. Values on the x axes are plotted for each mouse in units of the s.d. of its neural ensemble responses along the decoding vector for the shuffled data. For each mouse, the histograms have approximately equal shapes for the two visual stimuli, are unimodal and approximately symmetric about their mean values, bolstering the use of linear decoding and  $d'$ . This analysis involved 217–232 trials per stimulus condition per mouse in **d** and 122–167 trials per stimulus condition per mouse in **e**.



**Extended Data Fig. 10** | See next page for caption.

## Extended Data Fig. 10 | Hundreds of experimental trials sufficed to estimate the statistical structure of signals and noise in visual cortical coding.

**a, b**, PLS analysis represents ensemble neural responses in a low-dimensional subspace that helps for understanding visual discrimination (Fig. 4). On the basis of Extended Data Fig. 7a–c, computations here used the five most informative PLS dimensions. Each column shows results from an individual mouse that viewed gratings oriented at  $\pm 30^\circ$  (217–332 trials per stimulus). Each colour denotes a different eigenvector,  $\mathbf{e}_\alpha$ , of the noise covariance matrix in the five-dimensional subspace.  $\alpha$  denotes the dimension index,  $\{1, 2, 3, 4, 5\}$ . As illustrated in Fig. 4e, each mouse had multiple eigenvalues,  $\lambda_\alpha$ , of the noise covariance matrix that increased with the number of cells,  $n$ , used for analysis. As shown in Fig. 4f, visual signals—defined as the mean separation,  $\Delta\boldsymbol{\mu}$ , between the two response distributions—also increased with  $n$ . **a, b** show eigenvalues  $\lambda_\alpha$  (**a**) and signal components  $|\Delta\boldsymbol{\mu} \cdot \mathbf{e}_\alpha|$  (**b**) plotted against the number of trials analysed. Both signal and noise estimates plateau, indicating that there were sufficient trials to accurately estimate signal and noise structure in the reduced five-dimensional space. Throughout **a–d**, lines and shading denote mean  $\pm$  s.d. across 100 different randomly chosen subsets of cells and assignments of trials to decoder training and testing, except in **a, b** we used all cells from each mouse and 30 different assignments of trials. **c, d**, The statistical relationships between visual signals and noise show the largest noise mode is not information-limiting. Each mouse had multiple eigenvalues,  $\lambda_\alpha$ , of the noise covariance matrix (**c**) that increased with  $n$ , the number of cells. Visual signals (**d**) also increased with  $n$ , as shown by decomposing  $\Delta\boldsymbol{\mu}$  into components along the five eigenvectors,  $\mathbf{e}_\alpha$ . In every mouse the eigenvector with the largest eigenvalue,  $\mathbf{e}_1$ , was the least well aligned with the signals,  $\Delta\boldsymbol{\mu}$  (compare red curves in **c, d**). **e**, Plots of noise values, computed as in **c**, versus signal values, computed as in **d**, based on all recorded neurons from each mouse and the same 100 subsets of data used in **c, d**. The largest noise mode (red points) was generally an order of magnitude greater than noise modes that limited neural ensemble signalling (green and yellow points). **f–k**, In **a–e** and throughout much of the paper, we analysed populations of up to 2,191 neurons using 217–332 trials with each stimulus, which sufficed to accurately determine the Fisher information,  $(d')^2$ , and principal eigenvectors of the noise covariance matrix (Fig. 4). By comparison, there were insufficient trials to accurately determine noise covariance matrix elements—that is, noise correlations between cell pairs (Fig. 2d). To explain this, we derived the accuracy with which  $d'$  and principal noise covariance eigenvectors and eigenvalues can be estimated through PLS analysis of recordings of  $n$  neurons across  $P$  trials, using the computational model of Extended Data Fig. 8c (Appendix section 6 has

derivations of results in **f–k**). The central idea, illustrated in **f**, is that one can estimate accurately the principal noise covariance eigenvector, because it has a large eigenvalue,  $\lambda$ , that grows linearly with  $n$  ( $\lambda \cong cn$ , where  $c$  is a constant). The theory predicts that the correlation coefficient,  $C$ , between estimated and actual eigenvectors is given by  $C^2 = \frac{c^2 - 1/(cn)}{c^2 + 1}$ , for  $c^2 Pn > 1$ . Otherwise,  $C = 0$ . **f** shows predictions for  $C$  (black curve) versus the number of trials,  $P$ , for  $n = 2,000$  and  $c = 0.005$ . We chose this  $c$  value to fall within the lower range of growth rates for experimentally determined eigenvalues,  $c$ . The predicted  $C$  values match those describing the accuracy (red points) with which we could estimate the principal noise covariance eigenvector in the computational model. However, correlation coefficients (blue points) between estimated and actual individual elements of the noise covariance matrix were unsatisfactory, even with 800 trials. **i** shows predicted values of  $C$  as a joint function of  $n$  and  $P$ . Iso-contours of  $C$  are hyperbolic, revealing a tradeoff such that recording more cells enables accurate estimation of noise eigenvectors using fewer trials. We also derived how accurately one can estimate eigenvalues of the noise covariance matrix, as quantified using the ratio,  $\mathfrak{R}_\lambda = \lambda / \hat{\lambda}$  where  $\lambda = cn$  is the actual eigenvalue in the model and  $\hat{\lambda}$  is the estimate based on  $P$  trials. The theory predicts  $\mathfrak{R}_\lambda = \frac{c^2 P}{c^2 P + 1}$  when  $c^2 Pn > 1$ ; otherwise we set  $\mathfrak{R}_\lambda = 0$ , because we cannot accurately estimate the corresponding eigenvector when  $c^2 Pn < 1$ . **g** plots predictions of  $\mathfrak{R}_\lambda$  (black curve) versus  $P$  (for  $n = 2,000$  cells and  $c = 0.005$ ), which match the accuracy with which we estimated the model eigenvalues from simulated data (red dots). **j** shows  $\mathfrak{R}_\lambda$  predictions as a joint function of  $n$  and  $P$ . We also studied how well one can estimate the Fisher information,  $(d')^2$ , via PLS analysis of data with fewer trials than recorded neurons. We examined the ratio,  $\mathfrak{R}$ , of the  $d'$  estimate to its actual value using the model and simulated data of Extended Data Fig. 8c and found  $\mathfrak{R}^2 = \frac{1 + n\varepsilon}{1/C_{\text{PLS}}^2 + n\varepsilon}$ , where  $C_{\text{PLS}}^2 = \frac{\Delta s^2 P + 4(\varepsilon + 1/n)}{\Delta s^2 P + 4(\varepsilon + 1)}$  is the predicted correlation coefficient between the PLS regression vector and the optimal one. Here  $\Delta s^2$  and  $\varepsilon$  determine the Fisher information in the model of Extended Data Fig. 8c via  $(d'_{\text{opt}})^2 = \frac{n\Delta s^2}{1 + n\varepsilon}$ . As in Extended Data Fig. 8c, we used  $\varepsilon = 0.002$  to match the growth rate of  $(d')^2$  in experimental data with increasing  $n$ , and  $\Delta s^2 = 0.04$  to approximate the magnitude,  $\frac{\Delta s^2}{\varepsilon}$ , of  $(d')^2$  in the data for large  $n$ .  $C_{\text{PLS}}^2$  increases monotonically with  $P$  and  $n$ , confirming that PLS regression improves as  $n$  and  $P$  increase. As  $C_{\text{PLS}}^2$  nears 1, so does  $\mathfrak{R}^2$ , indicating that PLS analysis can accurately estimate  $(d')^2$ . **h** shows predictions for  $\mathfrak{R}^2$  versus  $P$  for  $n = 2,000$  cells (black curve). The theory matches the accuracy with which we estimated  $(d')^2$  via PLS analyses of the simulated model data (red dots). **k** shows predicted  $\mathfrak{R}^2$  values versus  $n$  and  $P$ . Iso-contours of  $\mathfrak{R}^2$  are hyperbolic, indicating recordings of more neurons permit accurate estimates of  $(d')^2$  based on fewer trials.

# Reporting Summary

Nature Research wishes to improve the reproducibility of the work that we publish. This form provides structure for consistency and transparency in reporting. For further information on Nature Research policies, see [Authors & Referees](#) and the [Editorial Policy Checklist](#).

## Statistics

For all statistical analyses, confirm that the following items are present in the figure legend, table legend, main text, or Methods section.

- |                                     |  |
|-------------------------------------|--|
| n/a                                 | Confirmed  |
| <input type="checkbox"/>            | <input checked="" type="checkbox"/> The exact sample size ( $n$ ) for each experimental group/condition, given as a discrete number and unit of measurement  |
| <input type="checkbox"/>            | <input checked="" type="checkbox"/> A statement on whether measurements were taken from distinct samples or whether the same sample was measured repeatedly  |
| <input type="checkbox"/>            | <input checked="" type="checkbox"/> The statistical test(s) used AND whether they are one- or two-sided<br><i>Only common tests should be described solely by name; describe more complex techniques in the Methods section.</i>   |
| <input checked="" type="checkbox"/> | <input type="checkbox"/> A description of all covariates tested  |
| <input type="checkbox"/>            | <input checked="" type="checkbox"/> A description of any assumptions or corrections, such as tests of normality and adjustment for multiple comparisons  |
| <input type="checkbox"/>            | <input checked="" type="checkbox"/> A full description of the statistical parameters including central tendency (e.g. means) or other basic estimates (e.g. regression coefficient) AND variation (e.g. standard deviation) or associated estimates of uncertainty (e.g. confidence intervals) |
| <input type="checkbox"/>            | <input checked="" type="checkbox"/> For null hypothesis testing, the test statistic (e.g. $F$ , $t$ , $r$ ) with confidence intervals, effect sizes, degrees of freedom and $P$ value noted<br><i>Give <math>P</math> values as exact values whenever suitable.</i>                            |
| <input checked="" type="checkbox"/> | <input type="checkbox"/> For Bayesian analysis, information on the choice of priors and Markov chain Monte Carlo settings  |
| <input checked="" type="checkbox"/> | <input type="checkbox"/> For hierarchical and complex designs, identification of the appropriate level for tests and full reporting of outcomes  |
| <input type="checkbox"/>            | <input checked="" type="checkbox"/> Estimates of effect sizes (e.g. Cohen's $d$ , Pearson's $r$ ), indicating how they were calculated   |

Our web collection on [statistics for biologists](#) contains articles on many of the points above.

## Software and code

Policy information about [availability of computer code](#)

Data collection	For data acquisition, we used custom routines written in LabView software (National Instruments, version 2012 SP1, 32 bit). For instrument control in the pixel-multiplexing acquisition modes, we also used open-source ScanImage software (version 3.8).
Data analysis	We used open source software routines for image registration ( <a href="http://bigwww.epfl.ch/thevenaz/turboreg/">http://bigwww.epfl.ch/thevenaz/turboreg/</a> ), cell sorting, and partial least squares analysis ( <a href="https://www.mathworks.com/matlabcentral/fileexchange/18760-partial-least-squares-and-discriminant-analysis">https://www.mathworks.com/matlabcentral/fileexchange/18760-partial-least-squares-and-discriminant-analysis</a> ). Software code for extracting individual neurons and their calcium activity traces from calcium videos by using principal component and then independent component analyses is freely available ( <a href="https://www.mathworks.com/matlabcentral/fileexchange/25405-emukamel-cellsort">https://www.mathworks.com/matlabcentral/fileexchange/25405-emukamel-cellsort</a> ), although for convenience we used a commercial version of these routines (Mosaic software, version 0.99.17; Inscopix Inc.). We wrote all other analysis software in Matlab (2017b). The primary software code used to support the findings of the study is available at Zenodo.org ( <a href="https://zenodo.org/record/3593520#.XgWPu-hKg2w">https://zenodo.org/record/3593520#.XgWPu-hKg2w</a> ).

For manuscripts utilizing custom algorithms or software that are central to the research but not yet described in published literature, software must be made available to editors/reviewers. We strongly encourage code deposition in a community repository (e.g. GitHub). See the Nature Research [guidelines for submitting code & software](#) for further information.

## Data

Policy information about [availability of data](#)

All manuscripts must include a [data availability statement](#). This statement should provide the following information, where applicable:

- Accession codes, unique identifiers, or web links for publicly available datasets
- A list of figures that have associated raw data
- A description of any restrictions on data availability

The data that support the findings of this study are available from the corresponding authors upon reasonable request.

## Field-specific reporting

Please select the one below that is the best fit for your research. If you are not sure, read the appropriate sections before making your selection.

☒ Life sciences ☐ Behavioural & social sciences ☐ Ecological, evolutionary & environmental sciences

For a reference copy of the document with all sections, see [nature.com/documents/nr-reporting-summary-flat.pdf](https://nature.com/documents/nr-reporting-summary-flat.pdf)

## Life sciences study design

All studies must disclose on these points even when the disclosure is negative.

Sample size	We designed the study such that each of the main results would come from 5 biological replicates, i.e., 5 different mice, for each of 2 different experimental conditions. The experimental results from all 10 mice were similar, affording confidence in the findings.
Data exclusions	To minimize false positives during cell sorting, we adopted a conservative approach during manual classification of candidate cells, such that we accepted for analysis only those candidates whose spatial forms and temporal dynamics were plainly those of neurons. Due to the known modulatory effects of locomotion on mouse visual processing, we used for analysis only those experimental trials during which the mice had no locomotor activity.
Replication	We reproduced the main results of our study across 10 different mice under 2 different experimental conditions (5 mice in each group).
Randomization	We split the datasets randomly into training and test subsets (usually 50% each; see Methods for details). We determined measured quantities by averaging across multiple realizations of such a split. For analysis performed on subsets of neurons, we chose subsets randomly and averaged results across multiple subsets. See Methods and Extended Data Fig. 5b for details.
Blinding	All animals in the experiment belonged to the same experimental group, so blinding was neither needed nor feasible.

## Reporting for specific materials, systems and methods

We require information from authors about some types of materials, experimental systems and methods used in many studies. Here, indicate whether each material, system or method listed is relevant to your study. If you are not sure if a list item applies to your research, read the appropriate section before selecting a response.

### Materials & experimental systems

### Methods

n/a	Involved in the study	n/a	Involved in the study
<input type="checkbox"/>	<input checked="" type="checkbox"/> Antibodies	<input checked="" type="checkbox"/>	<input type="checkbox"/> ChIP-seq
<input checked="" type="checkbox"/>	<input type="checkbox"/> Eukaryotic cell lines	<input checked="" type="checkbox"/>	<input type="checkbox"/> Flow cytometry
<input checked="" type="checkbox"/>	<input type="checkbox"/> Palaeontology	<input checked="" type="checkbox"/>	<input type="checkbox"/> MRI-based neuroimaging
<input type="checkbox"/>	<input checked="" type="checkbox"/> Animals and other organisms		
<input checked="" type="checkbox"/>	<input type="checkbox"/> Human research participants		
<input checked="" type="checkbox"/>	<input type="checkbox"/> Clinical data		

## Antibodies

Antibodies used	We immunostained tissue sections with antibodies against glial fibrillary activation protein (1:2500 dilution, rabbit anti-GFAP, Sigma HPA056030, Lot C115616) and heat shock protein 70 (1:400 dilution, mouse anti-HSP, Enzo ADI-SPA-810, Clone C92F3A-5, Lot 01031912) and then applied fluorophore-conjugated secondary antibodies (goat anti-rabbit-Alexa 594 [Invitrogen, A-11012, Lot 1933366] and goat anti-mouse-Alexa 488 [Invitrogen, A-11001, Lot 56881A]).
Validation	We performed positive control experiments to validate the abilities of these antibodies to detect laser-induced tissue damage (Extended Data Fig. 2g).

## Animals and other organisms

Policy information about [studies involving animals](#); [ARRIVE guidelines](#) recommended for reporting animal research

Laboratory animals	We analyzed data acquired from 6 male and 4 female Ai93 triple transgenic GCaMP6f-tTA-dCre mice from the Allen Institute (Rasgrf2-2A-dCre/CaMK2a-tTA/Ai93), which expressed the calcium indicator GCaMP6f in layer 2/3 pyramidal cells. Mice were 12-17 weeks of age when we implanted the cranial window in preparation for brain imaging. For illustrative purposes only, we imaged a single tetO-GCaMP6s/CaMK2a-tTA mouse42, which expressed the calcium indicator GCaMP6s in a subset of neocortical pyramidal neurons (Supplementary Video 3).
--------------------	---



Wild animals

No wild animals were used.

Field-collected samples

There were no field-collected samples.

Ethics oversight

The Stanford University APLAC approved all procedures involving animals.

Note that full information on the approval of the study protocol must also be provided in the manuscript.

# Centrosome anchoring regulates progenitor properties and cortical formation

<https://doi.org/10.1038/s41586-020-2139-6>

Received: 29 June 2018

Accepted: 28 January 2020

Published online: 25 March 2020

 Check for updates

Wei Shao<sup>1,2,8</sup>, Jiajun Yang<sup>3,8</sup>, Ming He<sup>3,4</sup>, Xiang-Yu Yu<sup>3</sup>, Choong Heon Lee<sup>5</sup>, Zhaohui Yang<sup>1,2</sup>, Alexandra L. Joyner<sup>1,2</sup>, Kathryn V. Anderson<sup>1,2</sup>, Jiangyang Zhang<sup>5</sup>, Meng-Fu Bryan Tsou<sup>2,6</sup>, Hang Shi<sup>7</sup>✉ & Song-Hai Shi<sup>1,2,3</sup>✉

Radial glial progenitor cells (RGPs) are the major neural progenitor cells that generate neurons and glia in the developing mammalian cerebral cortex<sup>1–4</sup>. In RGPs, the centrosome is positioned away from the nucleus at the apical surface of the ventricular zone of the cerebral cortex<sup>5–8</sup>. However, the molecular basis and precise function of this distinctive subcellular organization of the centrosome are largely unknown. Here we show in mice that anchoring of the centrosome to the apical membrane controls the mechanical properties of cortical RGPs, and consequently their mitotic behaviour and the size and formation of the cortex. The mother centriole in RGPs develops distal appendages that anchor it to the apical membrane. Selective removal of centrosomal protein 83 (CEP83) eliminates these distal appendages and disrupts the anchorage of the centrosome to the apical membrane, resulting in the disorganization of microtubules and stretching and stiffening of the apical membrane. The elimination of CEP83 also activates the mechanically sensitive yes-associated protein (YAP) and promotes the excessive proliferation of RGPs, together with a subsequent overproduction of intermediate progenitor cells, which leads to the formation of an enlarged cortex with abnormal folding. Simultaneous elimination of YAP suppresses the cortical enlargement and folding that is induced by the removal of CEP83. Together, these results indicate a previously unknown role of the centrosome in regulating the mechanical features of neural progenitor cells and the size and configuration of the mammalian cerebral cortex.

A notable and unique feature of RGPs is their subcellular organization of the centrosome<sup>7,8</sup>, an organelle that functions as both the microtubule-organizing centre and the basal body for ciliogenesis in vertebrates<sup>9–12</sup>. Unlike typical mammalian cells, in which the centrosome is located next to the nucleus, in RGPs the centrosome is positioned away from the nucleus in the apical endfoot at the surface of the ventricular zone<sup>5–8</sup>. Whereas the nucleus of an RGP exhibits interkinetic movement within the ventricular zone as it proceeds through the cell cycle, the centrosome remains located at the surface of the ventricular zone<sup>5,6,13</sup>. Moreover, individual centrosomes at the surface of the ventricular zone in interphase RGPs support the formation of a primary cilium that projects into the lateral ventricle<sup>14–17</sup>. Although the centrosome has been shown to regulate the division of RGPs and cortical neurogenesis<sup>5,18</sup>, the molecular and cellular basis—and the precise function—of centrosome positioning at the surface of the ventricular zone remain largely unclear.

preferentially located at the surface of the ventricular zone and away from the nuclei (labelled by an antibody against PAX6, a transcription factor that is highly expressed in cortical RGPs)<sup>19,20</sup> (Fig. 1a). To further assess the subcellular organization, we performed serial section transmission electron microscopy (ssTEM) (Fig. 1b). The mother centriole had prominent distal appendages (DAPs) and subdistal appendages (sDAPs), whereas the daughter centriole lacked the appendages. Moreover, the DAPs were in direct contact with a membrane pocket, indicating that the mother centriole is anchored to the apical membrane. In addition, the mother centriole was positioned at the base of a primary cilium arising from the membrane pocket—consistent with the function of the mother centriole as the basal body in primary ciliogenesis. Together, these results show that the centrosomes of interphase cortical RGPs are anchored to the apical membrane by DAPs that are preferentially assembled at the mother centriole.

## Distal appendages anchor the centrosome

As shown previously<sup>5–8</sup>, in RGPs from the mouse embryonic cortex the centrosome (labelled by an antibody against pericentrin; PCNT) was

## Cep83 deletion impairs centrosome anchoring

To investigate the molecular control of centrosome anchorage to the apical membrane, we examined the expression of CEP83 (also known

<sup>1</sup>Developmental Biology Program, Sloan Kettering Institute, Memorial Sloan Kettering Cancer Centre, New York, NY, USA. <sup>2</sup>Biochemistry, Cell and Molecular Biology Allied Graduate Program, Weill Cornell Medical College, New York, NY, USA. <sup>3</sup>IDG/McGovern Institute for Brain Research, Tsinghua-Peking Joint Centre for Life Sciences, Beijing Frontier Research Centre of Biological Structures, School of Life Sciences, Tsinghua University, Beijing, China. <sup>4</sup>School of Life Sciences, Peking University, Beijing, China. <sup>5</sup>Bernard and Irene Schwartz Centre for Biomedical Imaging, Department of Radiology, New York University School of Medicine, New York, NY, USA. <sup>6</sup>Cell Biology Program, Sloan Kettering Institute, Memorial Sloan Kettering Cancer Centre, New York, NY, USA. <sup>7</sup>Beijing Advanced Innovation Centre for Structural Biology, School of Life Sciences, Tsinghua University, Beijing, China. <sup>8</sup>These authors contributed equally: Wei Shao, Jiajun Yang.

✉e-mail: hangshi@mail.tsinghua.edu.cn; shisonghai@mail.tsinghua.edu.cn

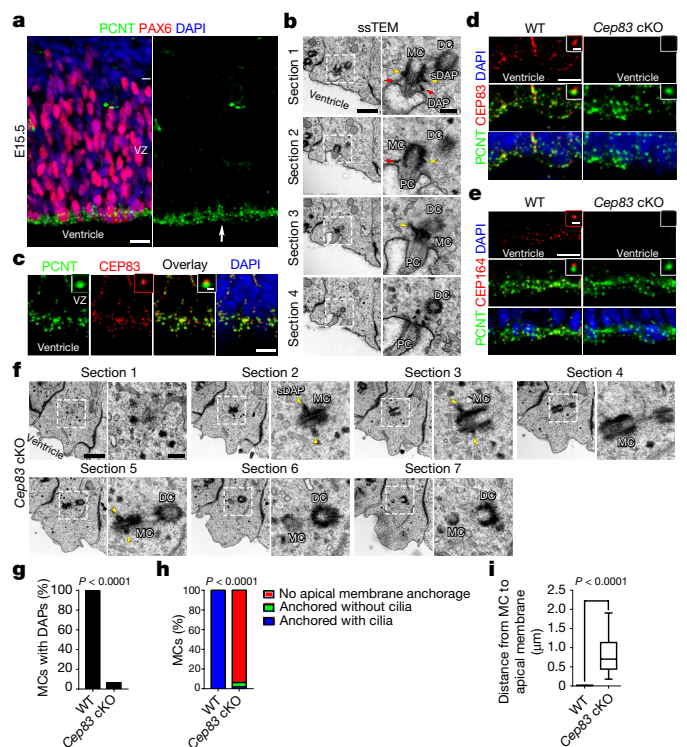


**Fig. 1 | Deletion of *Cep83* disrupts DAPs and the anchorage of the centrosome to the membrane.** **a**, Representative images of E15.5 cortex stained for PCNT (green) and PAX6 (red), and with DAPI (blue) ( $n = 5$ ). The arrow indicates the apical surface of the ventricular zone (VZ), where the centrosomes are located. The white bar indicates the top boundary of the ventricular zone. Scale bar, 25  $\mu\text{m}$ . **b**, Representative ssTEM images of E15.5 cortical ventricular zone surface. Red arrows indicate DAPs; yellow arrows indicate sDAPs. DC, daughter centriole; MC, mother centriole; PC, primary cilium. The white dashed boxes are shown at higher magnification on the right. Scale bars, 800 nm (left); 200 nm (right). **c**, Representative images of E15.5 cortex stained for PCNT (green) and CEP83 (red), and with DAPI (blue) ( $n = 3$ ). **d**, Representative images of E15.5 wild-type (WT) and *Cep83*cKO ventricular zone surface stained for PCNT (green) and CEP83 (red), and with DAPI (blue) ( $n = 3$ ). Scale bars, 10  $\mu\text{m}$  (main image); 1  $\mu\text{m}$  (inset). **e**, Representative ssTEM images of E15.5 *Cep83*cKO ventricular zone surface. Yellow arrows indicate sDAPs. The white dashed boxes are shown at higher magnification on the right. Scale bars, 800 nm (left); 200 nm (right). **g**, **h**, Quantification of the percentage of mother centrioles with DAPs (**g**) and with primary cilia and/or membrane anchorage (**h**). **i**, Quantification of the distance from mother centrioles to the apical membrane. Data are represented as a box plot, with median (centre line), interquartile range (box), and minimum and maximum values (whiskers) shown. Wild type,  $n = 11$  centrosomes; *Cep83*cKO,  $n = 48$  centrosomes (**g**–**i**). A chi-square test (**g**, **h**) or two-sided Mann–Whitney  $U$  test (**i**) was used for statistical analysis.

as CCDC41)—a protein that has been shown to be at the root of the DAP assembly pathway in mammalian cell cultures<sup>21,22</sup>. CEP83 displayed a punctate pattern of expression and was localized to one end of the centrosome at the surface of the ventricular zone (Fig. 1c). These results suggest that CEP83 is expressed and localized at the centrosomes of cortical RGP, and may have a role in the assembly of DAPs and the anchoring of the centrosome to the apical membrane.

To test this, we engineered a conditional *Cep83* mutant mouse allele, *Cep83*<sup>fl/fl</sup>, using a CRISPR–Cas9-mediated double-nicking strategy<sup>23</sup> (Extended Data Fig. 1a, b). We then crossed the *Cep83*<sup>fl/fl</sup> mouse with the *Emx1*<sup>cre</sup> mouse, in which Cre recombinase is selectively expressed in cortical RGP, with strong activity by embryonic day (E) 10.5<sup>24</sup>. Whereas in the E15.5 wild-type cortex CEP83 was abundantly expressed at RGP centrosomes at the surface of the ventricular zone, in the *Emx1*<sup>cre</sup>;*Cep83*<sup>fl/fl</sup>

conditional knockout (hereafter referred to as *Cep83*cKO) cortex CEP83 was depleted (Fig. 1d). The expression of CEP164, a characteristic marker of DAPs<sup>25</sup>, was also lost (Fig. 1e), suggesting a defect in the assembly of DAPs.

We next analysed the *Cep83*cKO cortex using ssTEM (Fig. 1f). Although individual pairs of centrioles were observed with a similar frequency at the surface of the ventricular zone, the mother centrioles had sDAPs but not DAPs (Fig. 1f, g). Moreover, the mother centrioles were not anchored to the apical membrane and no primary cilium was observed (Fig. 1f, h, Extended Data Fig. 1c). Consequently, the mother centriole and centrosome showed a small but significant ( $0.79 \pm 0.44 \mu\text{m}$ ) dislocation away from the apical membrane (Fig. 1f, i). Together, these results demonstrate that removal of CEP83 in RGP disrupts DAP assembly, and impairs the anchoring of the centrosome to the apical membrane as well as primary ciliogenesis.

## *Cep83* deletion causes cortical defects

*Cep83*cKO mice were born at the expected frequency and survived to adulthood. Notably, the brains of *Cep83*cKO mice were significantly larger than those of wild-type littermate control mice at postnatal day (P) 21 (Fig. 2a, b). Magnetic resonance imaging (MRI) analyses showed that the cortex was substantially enlarged, especially in the mediadorsal region (Fig. 2c, d).

The enlarged cortex indicates abnormalities in neuronal production. To examine this, we stained P21 brain sections with antibodies against CTIP2, a marker of layers V and VI neurons, and CUX1, a marker of layers II–IV neurons<sup>26</sup> (Fig. 2e). We observed a significant increase in the overall length, thickness and area of the *Cep83*cKO cortex compared with the wild-type cortex (Fig. 2f–h). In the *Cep83*cKO medial region that showed the largest increase in brain volume, the densities of both CTIP2<sup>+</sup> and CUX1<sup>+</sup> neurons were markedly increased compared with the wild type (Fig. 2i, j). We also observed consistent folding in this region of the *Cep83*cKO cortex, which was never seen in the wild-type cortex (Fig. 2e, i, Extended Data Fig. 1d, e). In the dorsolateral region, the density of CUX1<sup>+</sup> neurons was significantly higher in *Cep83*cKO than wild-type cortex, whereas the density of CTIP2<sup>+</sup> neurons was comparable (Fig. 2k, l). Similar results were obtained with antibodies against FOXP2, a marker of layer-VI neurons, and SATB2, a pan-neuronal marker that is enriched in superficial layers<sup>26</sup> (Extended Data Fig. 2a–d). The densities of glial cells did not show any obvious change (Extended Data Fig. 2e, f).

Even though the densities of deep-layer neurons or glial cells in the dorsolateral region did not significantly change, the increase in the total length, thickness and area of the *Cep83*cKO cortex indicated that the overall production of deep-layer neurons and glial cells was also substantially enhanced. No obvious hydrocephalus was observed (Fig. 2e). Together, these results suggest that the removal of CEP83 in RGP leads to a loss of DAPs; the detaching of the centrosome from the apical membrane; and an enlarged cortex with excessive numbers of superficial-layer neurons, deep-layer neurons and glial cells and abnormal folding in the medial region.

Previous studies suggest that primary cilia are crucial for the early patterning and polarity specification of the cortical primordium, but not essential to subsequent cortical neurogenesis and formation<sup>14,18,27–30</sup>. To further assess the role of primary cilia in cortical RGP, we crossed the conditional intraflagellar transport 88 (*Ift88*) mutant mouse, *Ift88*<sup>fl/fl</sup>, with the *Emx1*<sup>cre</sup> mouse to selectively remove IFT88, a member of the IFT-B complex that is required for proper cilium formation and function<sup>31</sup>. As expected, removal of IFT88 resulted in a loss of primary cilia in RGP by E13.5 (Extended Data Fig. 3a, b). We observed no obvious defect in DAPs, sDAPs or anchoring of the mother centriole to the membrane in RGP that lack IFT88 (Extended Data Fig. 3b–d), nor any defect in cortical size or neuronal density (Extended Data Fig. 3e–k). These results provide further proof that loss of primary cilia in RGP after around E11 does not alter cortical neurogenesis or formation.



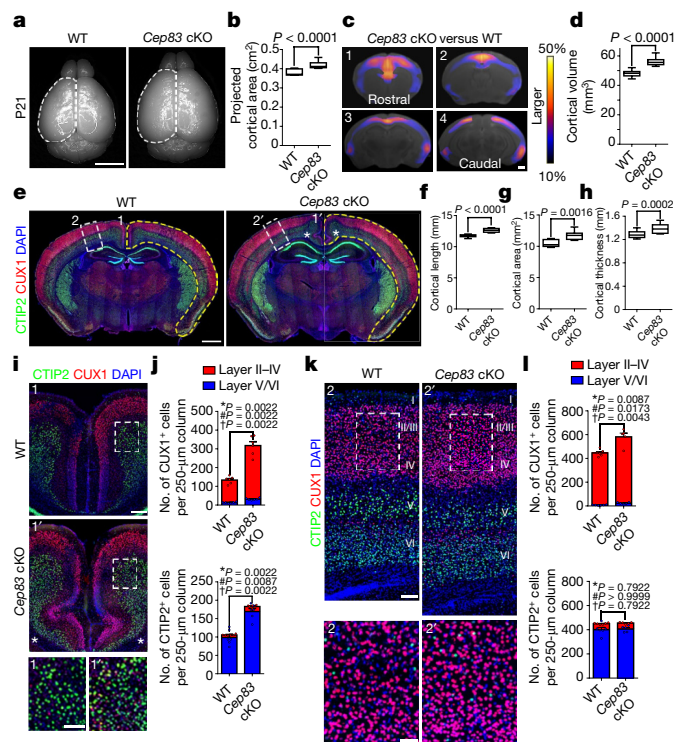


**Fig. 2 | Detachment of the centrosome from the apical membrane leads to an enlarged cortex with abnormal folding.** **a**, Representative whole-mount images of P21 wild-type and *Cep83cKO* brains. Scale bar, 0.5 cm.

**b**, Quantification of the projected cortical area (wild type,  $n = 13$  brains; *Cep83cKO*,  $n = 11$  brains). **c**, MRI images of P21 wild-type and *Cep83cKO* brains along the rostrocaudal axis (numbers 1–4 represent the comparison at 4 different positions along the rostrocaudal axis, in the same brain dataset). Warmer colours indicate a larger difference between wild type and *Cep83cKO*. Scale bar, 1 mm. **d**, Quantification of P21 wild-type and *Cep83cKO* cortical volume ( $n = 7$  brains (14 hemispheres) for each genotype). **e**, Representative images of P21 wild-type and *Cep83cKO* brain sections stained for CTIP2 (green) and CUX1 (red), and with DAPI (blue). Yellow dashed outlines delineate the total cortical area. Asterisks indicate the abnormal cortical folding in the medial region (1 in wild type, 1' in *Cep83cKO*), which is shown at higher magnification in **i**. White dashed rectangles indicate a dorsal region (2 in wild type, 2' in *Cep83cKO*), which is shown at higher magnification in **k**. Scale bar, 1 mm. **f–h**, Quantification of cortical length (**f**), area (**g**) and thickness (**h**) (wild type,  $n = 8$  brains (16 hemispheres); *Cep83cKO*,  $n = 9$  brains (18 hemispheres)). Box plots as in Fig. 1. **i, k**, Representative images of the medial (**i**) or dorsal (**k**) region of P21 wild-type and *Cep83cKO* cortices stained for CTIP2 (green) and CUX1 (red), and with DAPI (blue). Scale bars, 200  $\mu\text{m}$  (top); 100  $\mu\text{m}$  (bottom). **j, l**, Quantification of the number of CUX1<sup>+</sup> (top) and CTIP2<sup>+</sup> (bottom) neurons per 250- $\mu\text{m}$  column in the medial (**j**) or dorsal (**l**) region (wild type,  $n = 6$  brains; *Cep83cKO*,  $n = 5$  brains). The statistical significance of the difference between the wild-type and *Cep83cKO* brains in the total number of neurons ( $^*P$  values), number of superficial-layer neurons ( $^{\#}P$  values) and number of deep-layer neurons ( $^{\dagger}P$  values) is shown. A two-sided Mann–Whitney  $U$  test was used for statistical analysis. Bar charts show mean  $\pm$  s.e.m.

A previous study suggested that increasing Sonic hedgehog (SHH) signalling in the developing cortex by the expression of a constitutively active form of Smoothened, *SmoM2*—an activator of SHH signalling independent of ligand binding—enlarges the cortex and induces folding<sup>32</sup>. To further assess the role of SHH signalling in cortical RGP, we crossed the *SmoM2* transgenic mouse, *R26<sup>SmoM2/+</sup>* (ref. 33), with the *Emx1<sup>cre</sup>* mouse (Extended Data Fig. 4). *Emx1<sup>cre</sup>;R26<sup>SmoM2/+</sup>* mutant (*SmoM2*) mice died at the neonatal stage with severe brain dysplasia. In addition to the loss of the olfactory bulb, the cortex was highly disorganized with no clear laminar organization. Together, these results suggest that increased SHH signalling in RGP does not necessarily lead to an enlarged cortex with folding.

## *Cep83* deletion promotes RGP proliferation

To pinpoint the origins of enhanced neurogenesis and cortical enlargement in the *Cep83cKO* cortex, we examined the behaviour of RGP at the embryonic stage. At E13.5, the *Cep83cKO* cortex was significantly larger than the wild-type cortex (Fig. 3a, b). The total length and area of the PAX6<sup>+</sup> domain in RGP were greatly increased in the *Cep83cKO* cortex (Fig. 3c–e), even though the density of PAX6<sup>+</sup> RGP did not significantly differ from that of the wild-type cortex (Extended Data Fig. 5a, b). These results suggest that the removal of CEP83 in RGP leads to a drastic increase in the total number of RGP, and consequently a lateral expansion of the developing cortex.

RGP divide at the surface of the ventricular zone to produce neurons or intermediate progenitor cells<sup>19,34,35</sup>. We thus stained brain sections with an antibody against TBR2, a T-box transcription factor that is highly expressed in intermediate progenitor cells<sup>19</sup>, and found that the density of TBR2<sup>+</sup> intermediate progenitor cells in the *Cep83cKO* cortex was comparable to that in the wild-type cortex (Extended Data Fig. 5a, c). This indicates that removal of CEP83 in RGP does not lead to an additional increase in the production of intermediate progenitor cells at E13.5, even though the overall generation of intermediate progenitor cells would be enhanced owing to the increase in the number of RGP.

The marked increase in RGP after removal of CEP83 probably arises from enhanced proliferation of RGP. To test this, we performed sequential pulse-chase experiments (Fig. 3f, Extended Data Fig. 5d–f). We administered a single dose of 5-ethynyl-2'-deoxyuridine (EdU; a modified nucleoside) at E12.5, followed by a single dose of 5-bromo-2'-deoxyuridine (BrdU; a thymidine analogue), and collected the brains one hour later for analyses. We found that the percentage of EdU<sup>+</sup> RGP in the ventricular zone that also expressed BrdU (EdU<sup>+</sup>BrdU<sup>+</sup> RGP) was substantially increased in the *Cep83cKO* cortex compared with the wild-type cortex (Fig. 3f, g, Extended Data Fig. 5d, e), suggesting that dividing RGP in the *Cep83cKO* cortex re-enter the cell cycle faster than those in the wild-type cortex. The acceleration of cell-cycle progression was corroborated by an increased density of BrdU<sup>+</sup> RGP (Fig. 3f, h, Extended Data Fig. 5d, f). Collectively, these results suggest that removal of CEP83 in RGP accelerates re-entry into the cell cycle, which leads to an increase in RGP production and a lateral expansion of the developing cortex at the early embryonic stage of cortical development.

## *Cep83* deletion enhances radial neuronal production

To further dissect the cellular basis of the abnormal development of the *Cep83cKO* cortex, we examined the behaviour of cortical progenitor cells at E15.5 (Fig. 3i–o). The *Cep83cKO* cortex remained significantly larger than the wild-type cortex (Fig. 3i, j). The length and area of the PAX6<sup>+</sup> domain in RGP were significantly increased in the *Cep83cKO* cortex (Fig. 3k, l). Although the density of PAX6<sup>+</sup> RGP in the ventricular zone was comparable (Fig. 3m, n), the density of TBR2<sup>+</sup> intermediate progenitor cells in the subventricular zone was significantly increased in the *Cep83cKO* cortex (Fig. 3m, o). These results suggest that removal of CEP83 in RGP leads to a subsequent increase in the production of intermediate progenitor cells at the late embryonic stage of cortical development. Consistently, we observed a substantial increase in mitotic cells labelled by phosphorylated histone H3 (P-HH3) in the subventricular zone, but not at the ventricular zone surface (Extended Data Fig. 6a, e, f). The P-HH3<sup>+</sup> cells in the subventricular zone of the *Cep83cKO* cortex were predominantly intermediate progenitor cells, and not outer subventricular zone RGP (also called basal or intermediate RGP)<sup>36–41</sup> (Extended Data Fig. 6b, c, d, g–l). Notably, the densities of PAX6<sup>+</sup> RGP in the ventricular zone and TBR2<sup>+</sup> intermediate progenitor cells in the subventricular zone were significantly increased in the dorsomedial region (Extended Data Fig. 5g–j), where folding repeatedly occurred—consistent with the more-drastic increase in neuronal densities in this region (Fig. 2i, j).

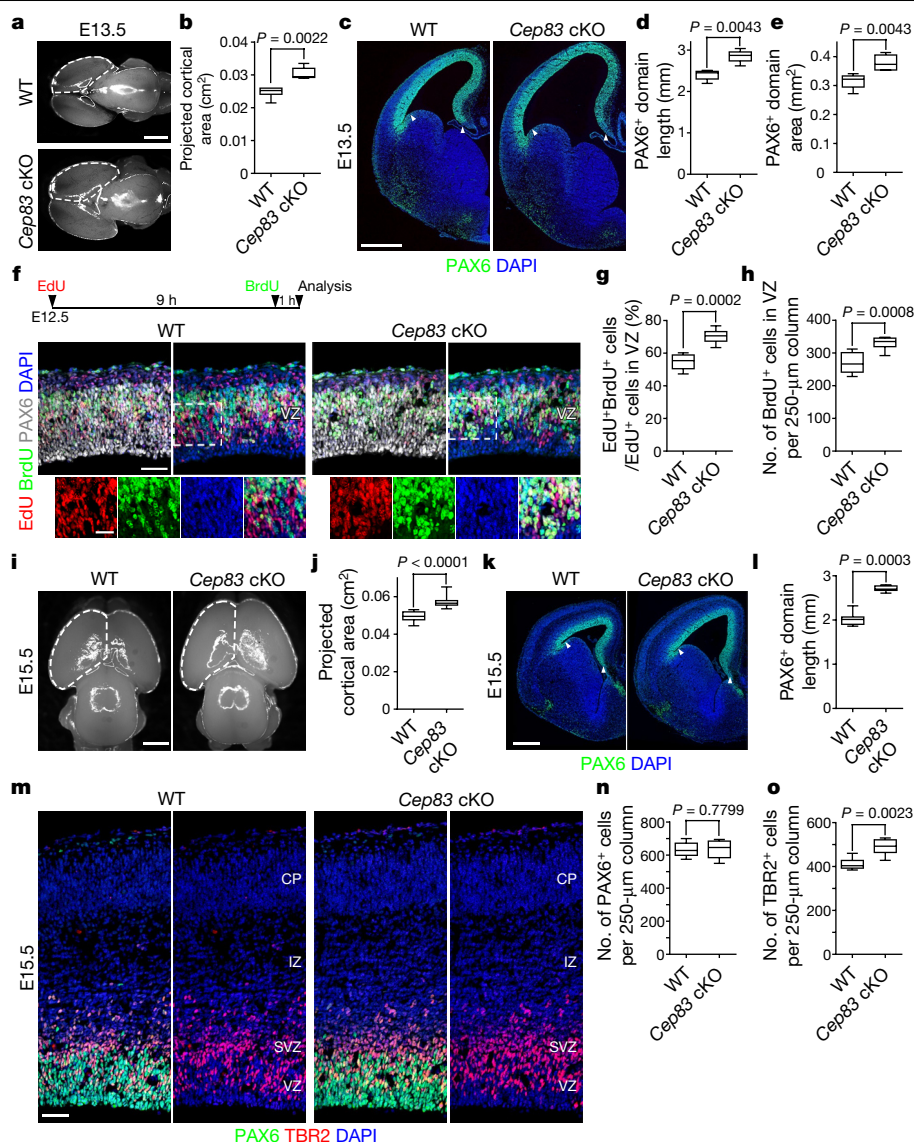


**Fig. 3 | Detachment of the centrosome from the apical membrane leads to excessive proliferation of RGP and an additional increase in the production of intermediate progenitor cells.** **a**, Representative whole-mount images of E13.5 wild-type and *Cep83*cKO brains. Scale bar, 1 mm. **b**, Quantification of the projected cortical area (wild type,  $n = 6$  brains; *Cep83*cKO,  $n = 5$  brains). **c**, Representative images of E13.5 wild-type and *Cep83*cKO cortices stained for PAX6 (green), and with DAPI (blue). The arrowheads indicate the boundaries of the PAX6<sup>+</sup> domain. Scale bar, 0.5 mm. **d, e**, Quantification of the length (**d**) and area (**e**) of the PAX6<sup>+</sup> domain (wild type,  $n = 5$  brains; cKO,  $n = 6$  brains). **f**, Representative images of E12.5 wild-type and *Cep83*cKO cortices (dorsolateral region) that were subjected to EdU (red) and BrdU (green) sequential pulse-chase labelling (top schematic). Cortices were stained for PAX6 (grey), and with DAPI (blue). Scale bars, 50  $\mu$ m (top); 25  $\mu$ m (bottom). **g, h**, Quantification of the percentage of EdU<sup>+</sup>BrdU<sup>+</sup> cells among the total EdU<sup>+</sup> cells in the ventricular zone (**g**), and the number of BrdU<sup>+</sup> cells in the ventricular

zone per 250- $\mu$ m column (**h**) (wild type,  $n = 8$  brains; *Cep83*cKO,  $n = 8$  brains). **i**, Representative whole-mount images of E15.5 wild-type and *Cep83*cKO brains. Scale bar, 1 mm. **j**, Quantification of the projected cortical area (wild type,  $n = 32$  brains; *Cep83*cKO,  $n = 9$  brains). **k**, Representative images of E15.5 wild-type and *Cep83*cKO brain sections stained for PAX6 (green), and with DAPI (blue). Arrowheads indicate the boundaries of the PAX6<sup>+</sup> domain. Scale bar, 0.5 mm. **l**, Quantification of the length of the PAX6<sup>+</sup> domain (wild type,  $n = 8$  brains; *Cep83*cKO,  $n = 7$  brains). **m**, Representative images of E15.5 wild-type and *Cep83*cKO cortices (dorsolateral region). Cortices were stained for PAX6 (green) and TBR2 (red), and with DAPI (blue). CP, cortical plate; IZ, intermediate zone; SVZ, subventricular zone. Scale bar, 50  $\mu$ m. **n, o**, Quantification of the number of PAX6<sup>+</sup> (**n**) and TBR2<sup>+</sup> (**o**) cells per 250- $\mu$ m column (wild type,  $n = 8$  brains; *Cep83*cKO,  $n = 6$  brains). A two-sided Mann–Whitney *U* test was used for statistical analysis. Box plots as in Fig. 1.

To test whether other components of the DAP assembly process regulate the behaviour of RGP and cortical development, we engineered short hairpin RNAs (shRNAs) against *Cep89* and *Sclt1*—two parallel components of DAP assembly downstream of CEP83 (Extended Data Fig. 7a–d). Suppression of the expression of CEP89 and SCLT1 led to a significant increase (relative to controls that were not treated with shRNAs or treated with non-effective shRNAs) in both PAX6<sup>+</sup> RGP and TBR2<sup>+</sup> intermediate progenitor cells (Extended Data Fig. 7e–h), suggesting that removal of other DAP assembly components—similar

to removal of CEP83—leads to the excessive production of RGP and intermediate progenitor cells in the developing cortex.

### Disruption of apical microtubule organization

To further reveal the underlying mechanisms of CEP83 function, we examined the properties of the apical membrane (that is, the surface of the ventricular zone) to which the centrosome is normally anchored. We prepared whole-mount cortical slabs at E15.5, stained these with



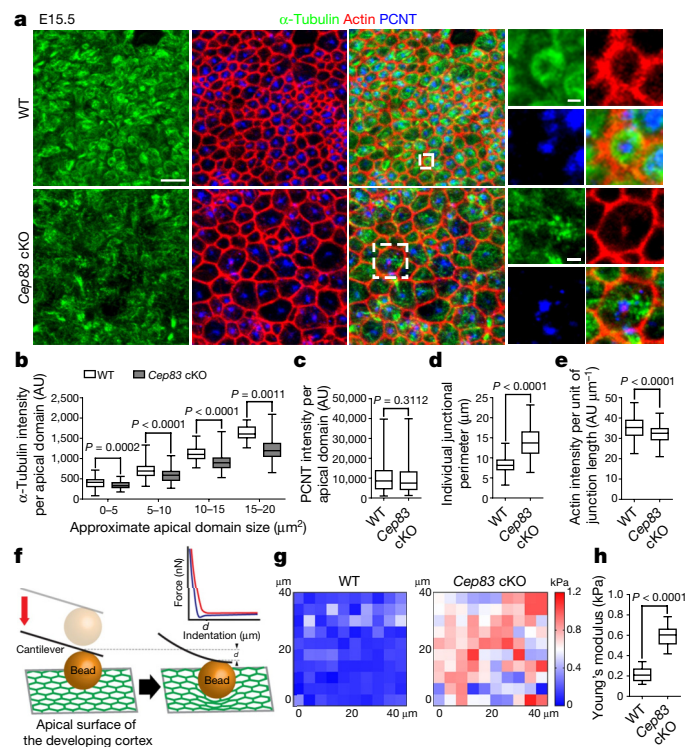


**Fig. 4 | Centrosome detachment disrupts microtubule organization and results in stretching and stiffening of the apical membrane.**

**a**, Representative en face images of E15.5 wild-type and *Cep83*cKO ventricular zone surface stained for  $\alpha$ -tubulin (green), actin (red) and PCNT (blue). Scale bars, 5  $\mu$ m (left), 1  $\mu$ m (right, top) and 2  $\mu$ m (right, bottom). **b–e**, Quantification of the intensity of  $\alpha$ -tubulin (microtubules) (**b**) or PCNT (**c**) per apical domain; the perimeter of individual junctions (**d**); and the intensity of actin per unit of junction length (**e**) (wild type,  $n = 478$  (**b**), 361 (**c**) and 200 (**d**, **e**) apical domains from 4 embryos; *Cep83*cKO,  $n = 443$  (**b**), 258 (**c**) and 200 (**d**, **e**) apical domains from 4 embryos). AU, arbitrary units. **f**, Schematic diagram showing the use of AFM to analyse the stiffness of the apical membrane. The indentation of the cantilever probe generates force–distance curves, including the approach curve (red) and the retraction curve (blue). **d**, indentation depth. **g**, Representative heat maps of Young's modulus, reflecting the stiffness of E15.5 wild-type and *Cep83*cKO ventricular zone surface. **h**, Quantification of the Young's modulus of wild-type and *Cep83*cKO ventricular zone surface (wild type,  $n = 10$  sample areas; *Cep83*cKO,  $n = 9$  sample areas; from 3 brains for each genotype). A two-sided Mann–Whitney  $U$  test was used for statistical analysis. Box plots as in Fig. 1.

antibodies against PCNT,  $\alpha$ -tubulin and actin and acquired en face images of the apical membrane (Fig. 4a). In the wild-type cortex, actin marked cell junctions that were formed between the apical endfeet of neighbouring RGPs, and a prominent centrosome revealed by PCNT staining was commonly found within individual apical endfeet (Fig. 4a, top). Notably, microtubules (labelled by  $\alpha$ -tubulin staining) often formed a ring-like structure in juxtaposition with actin-labelled junctions (Fig. 4a, top insets). Notably, in the *Cep83*cKO cortex, although the junctions and the positioning of the centrosome inside the apical endfeet remained largely intact, the ring-like microtubule structure disappeared (Fig. 4a, bottom insets). Fibrous microtubules were consistently observed. The intensity of microtubules in individual apical domains was significantly reduced (Fig. 4b), whereas the intensity of PCNT was similar (Fig. 4c). The normal expression of PCNT and the existence of fibrous microtubules indicate that microtubule formation is not systematically compromised in the absence of CEP83. Consistent with this, the non-apical membrane microtubules—as well as the microtubules in mitotic RGPs—did not exhibit any obvious difference in the *Cep83*cKO cortex compared to the wild type (Extended Data

Fig. 8a, b). No obvious change was observed in RGP polarity, expression of junction proteins or radial scaffolding in the *Cep83*cKO cortex (Extended Data Fig. 8c–i). Together, these results suggest that centrosome detachment impairs the organization of microtubules specifically at the apical membrane.

### Alteration of apical membrane properties

The junction size that corresponds to the apical membrane of individual RGPs at the surface of the ventricular zone appeared enlarged in the *Cep83*cKO cortex (Fig. 4a). To confirm this, we systematically examined junction size at E13.5 and E15.5 by staining for actin, and found that the junction size of both interphase and mitotic RGPs was significantly larger in the *Cep83*cKO cortex than the wild-type cortex (Fig. 4d, Extended Data Fig. 9a–c), suggesting that the apical membrane of RGPs and the junction between RGPs are stretched and enlarged in the *Cep83*cKO cortex. Coinciding with this, the intensity of actin per unit of junction length was significantly reduced (Fig. 4e).

The stretching and enlargement of the apical membrane and junctions of RGPs suggest that the mechanical properties of the surface of the ventricular zone might be altered. To directly test this, we used atomic force microscopy (AFM), which allows a quantitative examination of the stiffness of live tissue (Fig. 4f). We prepared acute whole-mount wild-type and *Cep83*cKO cortical slabs and performed AFM analysis. The Young's modulus (also known as the elastic modulus) of the apical membrane was significantly higher in the *Cep83*cKO cortex than the wild-type cortex (Fig. 4g, h). These results suggest that the detachment of the centrosome increases the stiffness of the apical membrane, where RGP division selectively occurs.

### Cortical defects depend on YAP

Cell stretching and increased tissue rigidity activates YAP, a crucial transcriptional co-activator in the HIPPO signalling pathway that regulates cell proliferation and organ size<sup>42,43</sup>. In line with this, we found that the expression of YAP in the ventricular zone was significantly higher in the *Cep83*cKO cortex than the wild-type cortex (Fig. 5a, b). Moreover, in the *Cep83*cKO cortex, significantly more PAX6<sup>+</sup> RGPs showed a strong YAP signal in the nucleus (Fig. 5a, c). By contrast, YAP expression in the wild-type RGP nucleus was generally low. Nuclear expression of YAP in TBR2<sup>+</sup> intermediate progenitor cells in the wild-type or *Cep83*cKO cortex was also low (Extended Data Fig. 9d). In addition, we observed no obvious difference in YAP expression between dissociated wild-type and *Cep83*cKO RGPs in culture, with no junction formation (Extended Data Fig. 9e, f). Together, these results suggest that the detachment of the centrosome and the stretching and stiffening of the apical membrane cause YAP overexpression and nuclear localization selectively in RGPs.

We next asked whether the enlargement and folding of the *Cep83*cKO cortex depends on an increase in the expression and activation of YAP. We crossed the conditional *Yap* mutant mouse (*Yap*<sup>fl/fl</sup>) with the *Emx1*<sup>cre</sup> or *Emx1*<sup>cre</sup>; *Cep83*<sup>fl/fl</sup> mouse, to generate mice with individual or simultaneous deletions of *Cep83* and *Yap* (also known as *Yap1*) in cortical RGPs. Compared with wild-type littermate controls, *Emx1*<sup>cre</sup>; *Yap*<sup>fl/fl</sup> (*Yap*cKO) mice did not show any obvious change in the size or neuronal density of the cortex (Fig. 5d–g, Extended Data Fig. 10a, b). This is consistent with a relatively low level of YAP expression in RGP nuclei under normal conditions (Fig. 5a). Although the *Cep83*cKO cortex was significantly enlarged, with abnormal folding and increased neuronal density, the *Emx1*<sup>cre</sup>; *Cep83*<sup>fl/fl</sup>; *Yap*<sup>fl/fl</sup> (*Cep83 Yap* conditional double knockout, cDKO) cortex was comparable to the wild type (Fig. 5d–g, Extended Data Fig. 10a, b), indicating that the simultaneous deletion of *Yap* effectively suppresses the increase in cortical neurogenesis that is triggered by the deletion of *Cep83*. We did not observe any folding in the *Cep83 Yap*cDKO cortex (Fig. 5f). Consistent with the notion that increased YAP expression and activation is downstream of apical

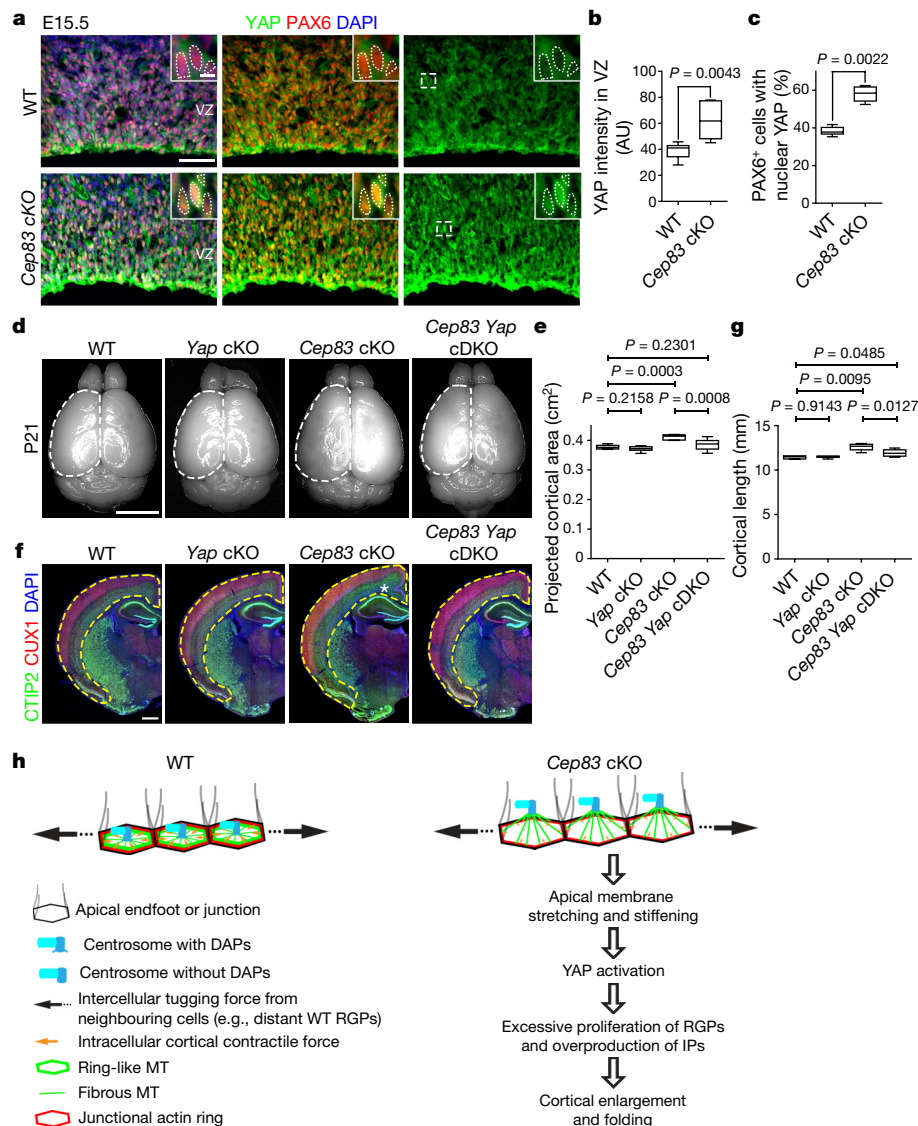


**Fig. 5 | Excessive activation of YAP is essential for the enlargement and abnormal folding of the *Cep83*cKO cortex.** **a**, Representative images of E15.5 wild-type and *Cep83*cKO cortices stained for YAP (green) and PAX6 (red), and with DAPI (blue). Scale bars, 50  $\mu$ m (main image); 5  $\mu$ m (inset). **b**, **c**, Quantification of YAP intensity (**b**) and the percentage of PAX6<sup>+</sup> cells with nuclear YAP (**c**) in the ventricular zone ( $n = 6$  brains for each genotype). **d**, Representative whole-mount images of P21 wild-type, *Yap*cKO, *Cep83*cKO and *Cep83Yap*cDKO brains. Scale bar, 0.5 cm. **e**, Quantification of the projected cortical area (wild type,  $n = 8$  brains; *Yap*cKO,  $n = 6$  brains; *Cep83*cKO,  $n = 7$  brains; *Cep83Yap*cDKO,  $n = 12$  brains). **f**, Representative images of P21 wild-type

and *Cep83*cKO brain sections stained for CTIP2 (green) and CUX1 (red), and with DAPI (blue). Yellow dashed outlines delineate the total cortical area. Asterisk indicates the abnormal cortical folding in the medial region. Scale bar, 1 mm. **g**, Quantification of P21 wild-type, *Yap*cKO, *Cep83*cKO and *Cep83Yap*cDKO cortical length (wild type,  $n = 4$  brains; *Yap*cKO,  $n = 6$  brains; *Cep83*cKO,  $n = 6$  brains; *Cep83Yap*cDKO,  $n = 8$  brains). **h**, Model indicating the positioning and function of the centrosome in cortical RGPs. MT, microtubule; IPs, intermediate progenitor cells. A two-sided Mann–Whitney *U* test was used for statistical analysis. Box plots as in Fig. 1.

membrane stretching and stiffening, the apical domain remained significantly larger in the *Cep83Yap*cDKO cortex than in the wild-type cortex (Extended Data Fig. 10c–f). Together, these results demonstrate that the cortical enlargement and folding caused by the removal of CEP83 in RGPs depend on the overactivation of YAP, which is caused by apical membrane stretching and stiffening.

## Discussion

The centrosome in RGPs is anchored to the apical membrane by the DAPs. Removal of CEP83—a DAP protein—in RGPs disrupts the formation of DAPs and causes the detachment of the centrosome from the apical membrane. This subtle (less than 1  $\mu$ m) dislocation of the centrosome causes substantial changes in the behaviour of RGPs in

the developing cortex. Our side-by-side comparisons of *IFT88*cKO and *SmoM2* brains with *Cep83*cKO brains suggest that the drastic enlargement and abnormal folding (albeit with normal lamination and lateral ventricle size) of the *Cep83*cKO cortex is unlikely to be a result of primary cilium loss or increased SHH signalling. Instead, we have uncovered a previously unrecognized function of the centrosome in RGPs (Fig. 5h). The docking of the centrosome to the apical membrane supports the formation of prominent ring-like microtubule structures that are juxtaposed to the cell junctions, and this is likely to promote intracellular cortical contractile force in conjunction with the actin network. The contractile force of individual RGPs is balanced by the intercellular tugging force exerted between neighbouring RGPs that form junctions with each other, which would determine the overall stiffness or rigidity of the surface of the ventricular zone. Primary

ciliogenesis may further strengthen the tethering of the centrosome and influence the organization of microtubules and the properties of the apical membrane. A similar microtubule ring and intricate organization of the centrosome has been observed in neuroepithelial cells from the spinal cord of chickens<sup>44</sup>, suggesting that this is a common feature of neural progenitor cells.

Although an increase in neuronal density was observed throughout the cortical area in the *Cep83* KO brain, the folding occurred predominantly in the medial region, in which the density of both deep-layer and superficial-layer neurons was markedly increased. These observations are consistent with the notion that a substantial radial expansion in neurogenesis is crucial for the folding of the cortex<sup>45</sup>. The local anatomical organization might also render the medial region more susceptible to folding. Our data suggest that the subcellular organization of the centrosome and the mechanical properties of neural progenitor cells affect their proliferative and neurogenic capacity. Notably, as development proceeds, the stiffness of the surface of the ventricular zone in the mouse cortex gradually decreases<sup>46</sup>. In addition, the surface of the ventricular zone appears to be stiffer in ferrets (which develop a large and gyrated cortex) than in mice<sup>46</sup>. These observations point to a relationship between the mechanical properties of RGP and the size and formation of the cortex. The enlarged cortex with excessive neurogenesis that we observed in the absence of CEP83 reveals a link between centrosomal abnormalities and brain overgrowth (that is, megalencephaly). Biallelic mutations in human *CEP83* have been found to cause infantile nephronophthisis and intellectual disability<sup>47</sup>, underscoring the importance of CEP83 and centrosome positioning in controlling the development and function of the human brain.

## Online content

Any methods, additional references, Nature Research reporting summaries, source data, extended data, supplementary information, acknowledgements, peer review information; details of author contributions and competing interests; and statements of data and code availability are available at <https://doi.org/10.1038/s41586-020-2139-6>.

- Florio, M. & Huttner, W. B. Neural progenitors, neurogenesis and the evolution of the neocortex. *Development* **141**, 2182–2194 (2014).
- Homem, C. C., Repic, M. & Knoblich, J. A. Proliferation control in neural stem and progenitor cells. *Nat. Rev. Neurosci.* **16**, 647–659 (2015).
- Kriegstein, A. & Alvarez-Buylla, A. The glial nature of embryonic and adult neural stem cells. *Annu. Rev. Neurosci.* **32**, 149–184 (2009).
- Rakic, P. Developmental and evolutionary adaptations of cortical radial glia. *Cereb. Cortex* **13**, 541–549 (2003).
- Wang, X. et al. Asymmetric centrosome inheritance maintains neural progenitors in the neocortex. *Nature* **461**, 947–955 (2009).
- Tsai, J. W., Lian, W. N., Kemal, S., Kriegstein, A. R. & Vallee, R. B. Kinesin 3 and cytoplasmic dynein mediate interkinetic nuclear migration in neural stem cells. *Nat. Neurosci.* **13**, 1463–1471 (2010).
- Bultje, R. S. et al. Mammalian Par3 regulates progenitor cell asymmetric division via notch signaling in the developing neocortex. *Neuron* **63**, 189–202 (2009).
- Chenn, A., Zhang, Y. A., Chang, B. T. & McConnell, S. K. Intrinsic polarity of mammalian neuroepithelial cells. *Mol. Cell. Neurosci.* **11**, 183–193 (1998).
- Conduit, P. T., Wainman, A. & Raff, J. W. Centrosome function and assembly in animal cells. *Nat. Rev. Mol. Cell Biol.* **16**, 611–624 (2015).
- Lüders, J. & Stearns, T. Microtubule-organizing centres: a re-evaluation. *Nat. Rev. Mol. Cell Biol.* **8**, 161–167 (2007).
- Bettencourt-Dias, M. & Glover, D. M. Centrosome biogenesis and function: centrosomes brings new understanding. *Nat. Rev. Mol. Cell Biol.* **8**, 451–463 (2007).
- Kobayashi, T. & Dynlacht, B. D. Regulating the transition from centriole to basal body. *J. Cell Biol.* **193**, 435–444 (2011).
- Hu, D. J.-K. et al. Dynein recruitment to nuclear pores activates apical nuclear migration and mitotic entry in brain progenitor cells. *Cell* **154**, 1300–1313 (2013).
- Higginbotham, H. et al. Arl13b-regulated cilia activities are essential for polarized radial glial scaffold formation. *Nat. Neurosci.* **16**, 1000–1007 (2013).
- Paridaen, J. T. M. L., Wilsch-Bräuninger, M. & Huttner, W. B. Asymmetric inheritance of centrosome-associated primary cilium membrane directs ciliogenesis after cell division. *Cell* **155**, 333–344 (2013).
- Higginbotham, H. R. & Gleeson, J. G. The centrosome in neuronal development. *Trends Neurosci.* **30**, 276–283 (2007).
- Louvi, A. & Grove, E. A. Cilia in the CNS: the quiet organelle claims center stage. *Neuron* **69**, 1046–1060 (2011).
- Insolera, R., Bazzi, H., Shao, W., Anderson, K. V. & Shi, S. H. Cortical neurogenesis in the absence of centrioles. *Nat. Neurosci.* **17**, 1528–1535 (2014).
- Englund, C. et al. Pax6, Tbr2, and Tbr1 are expressed sequentially by radial glia, intermediate progenitor cells, and postmitotic neurons in developing neocortex. *J. Neurosci.* **25**, 247–251 (2005).
- Götz, M., Stoykova, A. & Gruss, P. Pax6 controls radial glia differentiation in the cerebral cortex. *Neuron* **21**, 1031–1044 (1998).
- Tanos, B. E. et al. Centriole distal appendages promote membrane docking, leading to cilia initiation. *Genes Dev.* **27**, 163–168 (2013).
- Joo, K. et al. CCDC41 is required for ciliary vesicle docking to the mother centriole. *Proc. Natl Acad. Sci. USA* **110**, 5987–5992 (2013).
- Ran, F. A. et al. Double nicking by RNA-guided CRISPR Cas9 for enhanced genome editing specificity. *Cell* **154**, 1380–1389 (2013).
- Gorski, J. A. et al. Cortical excitatory neurons and glia, but not GABAergic neurons, are produced in the Emx1-expressing lineage. *J. Neurosci.* **22**, 6309–6314 (2002).
- Graser, S. et al. Cep164, a novel centriole appendage protein required for primary cilium formation. *J. Cell Biol.* **179**, 321–330 (2007).
- Greig, L. C., Woodworth, M. B., Galazo, M. J., Padmanabhan, H. & Macklis, J. D. Molecular logic of neocortical projection neuron specification, development and diversity. *Nat. Rev. Neurosci.* **14**, 755–769 (2013).
- Besse, L. et al. Primary cilia control telencephalic patterning and morphogenesis via Gli3 proteolytic processing. *Development* **138**, 2079–2088 (2011).
- Willaredt, M. A. et al. A crucial role for primary cilia in cortical morphogenesis. *J. Neurosci.* **28**, 12887–12900 (2008).
- Han, Y. G. et al. Hedgehog signaling and primary cilia are required for the formation of adult neural stem cells. *Nat. Neurosci.* **11**, 277–284 (2008).
- Snedeker, J. et al. Unique spatiotemporal requirements for intraflagellar transport genes during forebrain development. *PLoS One* **12**, e0173258 (2017).
- Haycraft, C. J. et al. Intraflagellar transport is essential for endochondral bone formation. *Development* **134**, 307–316 (2007).
- Wang, L., Hou, S. & Han, Y.-G. Hedgehog signaling promotes basal progenitor expansion and the growth and folding of the neocortex. *Nat. Neurosci.* **19**, 888–896 (2016).
- Jeong, J., Mao, J., Tenzen, T., Kottmann, A. H. & McMahon, A. P. Hedgehog signaling in the neural crest cells regulates the patterning and growth of facial primordia. *Genes Dev.* **18**, 937–951 (2004).
- Haubensak, W., Attardo, A., Denk, W. & Huttner, W. B. Neurons arise in the basal neuroepithelium of the early mammalian telencephalon: a major site of neurogenesis. *Proc. Natl Acad. Sci. USA* **101**, 3196–3201 (2004).
- Noctor, S. C., Martínez-Cerdeño, V., Ivic, L. & Kriegstein, A. R. Cortical neurons arise in symmetric and asymmetric division zones and migrate through specific phases. *Nat. Neurosci.* **7**, 136–144 (2004).
- Wang, X., Tsai, J.-W., LaMonica, B. & Kriegstein, A. R. A new subtype of progenitor cell in the mouse embryonic neocortex. *Nat. Neurosci.* **14**, 555–561 (2011).
- Hansen, D. V., Lui, J. H., Parker, P. R. L. & Kriegstein, A. R. Neurogenic radial glia in the outer subventricular zone of human neocortex. *Nature* **464**, 554–561 (2010).
- Shitamukai, A., Konno, D. & Matsuzaki, F. Oblique radial glial divisions in the developing mouse neocortex induce self-renewing progenitors outside the germinal zone that resemble primate outer subventricular zone progenitors. *J. Neurosci.* **31**, 3683–3695 (2011).
- Reillo, I., de Juan Romero, C., García-Cabezas, M. A. & Borrell, V. A role for intermediate radial glia in the tangential expansion of the mammalian cerebral cortex. *Cereb. Cortex* **21**, 1674–1694 (2011).
- Fietz, S. A. et al. OSVZ progenitors of human and ferret neocortex are epithelial-like and expand by integrin signaling. *Nat. Neurosci.* **13**, 690–699 (2010).
- Betizeau, M. et al. Precursor diversity and complexity of lineage relationships in the outer subventricular zone of the primate. *Neuron* **80**, 442–457 (2013).
- Aragona, M. et al. A mechanical checkpoint controls multicellular growth through YAP/TAZ regulation by actin-processing factors. *Cell* **154**, 1047–1059 (2013).
- Halder, G., Dupont, S. & Piccolo, S. Transduction of mechanical and cytoskeletal cues by YAP and TAZ. *Nat. Rev. Mol. Cell Biol.* **13**, 591–600 (2012).
- Kasioulis, I., Das, R. M. & Storey, K. G. Inter-dependent apical microtubule and actin dynamics orchestrate centrosome retention and neuronal delamination. *eLife* **6**, e26215 (2017).
- Mota, B. & Herculano-Houzel, S. Cortical folding scales universally with surface area and thickness, not number of neurons. *Science* **349**, 74–77 (2015).
- Nagasaka, A. et al. Differences in the mechanical properties of the developing cerebral cortical proliferative zone between mice and ferrets at both the tissue and single-cell levels. *Front. Cell Dev. Biol.* **4**, 139 (2016).
- Failler, M. et al. Mutations of CEP83 cause infantile nephronophthisis and intellectual disability. *Am. J. Hum. Genet.* **94**, 905–914 (2014).

**Publisher's note** Springer Nature remains neutral with regard to jurisdictional claims in published maps and institutional affiliations.

© The Author(s), under exclusive licence to Springer Nature Limited 2020

## Methods

### Mouse lines

The *Cep83* conditional knockout mice were generated using a CRISPR–Cas9-mediated double-nicking strategy<sup>23</sup>. Guide RNAs (gRNAs) were designed and synthesized according to described methods<sup>23</sup>. A pair of gRNAs, *In3A* (5′-GGTTTCCTGACAACGCAGAT-3′) and *In3B* (5′-TCAGTC-CAGTTCAGTAGCGT-3′), was selected for the high targeting efficiency of these gRNAs based on a Surveyor assay (Integrated DNA Technologies) and cloned into a *pX335* vector. To generate a minivector gene-targeting construct, a DNA fragment of mouse *Cep83* containing the critical exon 3 was amplified from BAC clone RP23-422L20 (Children's Hospital Oakland Research Institute) and cloned into a *pL451* vector using the Golden Gate Assembly method. A mixture of *pX335-In3A*, *pX335-In3B* and *pL451-Cep83* flox-neo plasmids were then electroporated into a W4 mouse embryonic stem (ES) cell line on a 129S6 background for gene targeting (Rockefeller University Gene Targeting Resource Centre). Correctly targeted ES cell clones were screened by Southern blot against the 5′-homology arm, and confirmed by long-range PCR, genotyping and sequencing. ES cell clones were microinjected into C57B6/J blastocysts for chimaera production. Male chimaeras were crossed to multiple C57B6/J females to screen and obtain *Cep83*<sup>fl-neo</sup> mice through genotyping. *Actin-Flp* transgenic mice (005703; The Jackson Laboratory) were used to excise the Neo selection cassette and obtain *Cep83*<sup>fl/-</sup>. Genotyping primers for the *Cep83* floxed allele at the 5′ *loxP* site were: forward, 5′-AGTGGGCTGTGAATGTAGTCTT-3′; reverse, 5′-AGCCAACCAATAATACAGAAACA-3′. Deletion of exon 3 creates a frameshift in subsequent exons and thereby interferes with the expression of the CEP83 protein. *Ift88*<sup>fl/fl</sup> (ref. <sup>31</sup>), *Yap*<sup>fl/fl</sup> (ref. <sup>48</sup>) and *R26-LSL-SmoM2* (ref. <sup>33</sup>) mice were provided by B. Yoder, J. Wrana and A. McMahon, respectively. *Emx1*<sup>Cre</sup> (005628; The Jackson Laboratory) was used to delete genes in the cortex. Genotyping was carried out using standard PCR protocols. Both male and female mice were used in the study. The mice were maintained at the facilities of Memorial Sloan Kettering Cancer Centre and Tsinghua University, and all animal procedures were approved by the Institutional Animal Care and Use Committees. For timed pregnancies, the plug date was designated as E0 and the date of birth was defined as P0. No wild animal or field-collected sample was used in the study.

### shRNA design and in utero electroporation

Three shRNA sequences against *Cep83*, *Cep89* and *Sclt1* were designed as follows: *Cep83* shRNA-a (5′-GCAAGCAAGCCAGGAAAAA-3′), *Cep83* shRNA-b (5′-GCTCCAATGCGAGAACGTT-3′), *Cep83* shRNA-c (5′-GCTA GAACCTTGAGAACAGA-3′); *Cep89* shRNA-a (5′-GGACGTCATTACCA TCCT-3′), *Cep89*-b (5′-GGGCCCCACACCACCTGG-3′), *Cep89*-c (5′-GTCGTGAAGGAAAACGAAGCC-3′); *Sclt1* shRNA-a (5′-GATAAACT AAATGATATT-3′), *Sclt1*-b (5′-AAATGCATCAAAGATGTC-3′), *Sclt1*-c (5′-GGCAAACAGGATGAAAGTGA-3′). All sense and anti-sense oligos were purchased from IDT. Annealed oligos were cloned into the *HpaI* and *XhoI* sites of the lentiviral vector pLL3.7. In utero electroporation was performed as previously described<sup>7</sup>. In brief, a timed pregnant CD-1 mouse at E13.5 was anaesthetized, the uterine horns were exposed and around 1 µl plasmid DNA mixed with Fast Green (Sigma) was microinjected through the uterus into the lateral ventricle manually using a bevelled and calibrated glass micropipette (Drummond Scientific). For electroporation, five 50-ms pulses of around 35 mV with a 950-ms interval were delivered across the uterus with two 5-mm electrode paddles positioned on either side of the head (BTX, ECM830). During the procedure, the embryos were constantly bathed with warm sterile PBS (pH 7.4). After electroporation, the uterus was placed back in the abdominal cavity and the wound was surgically sutured. After surgery, the mouse was placed in a 28 °C recovery incubator with proper analgesic treatments until it recovered and resumed normal activity. All procedures for animal handling and usage were approved by the institutional research animal resource centre.

### Brain sectioning, immunohistochemistry and imaging

Timed pregnant females that carried conditional mutant alleles were anaesthetized and embryos were removed and perfused with ice-cold phosphate buffered saline (PBS, pH 7.4), followed by 4% paraformaldehyde (PFA). Brains were post-fixed with 4% PFA for around 6 h, cryo-protected and sectioned at 12 µm for immunohistochemistry as previously described<sup>18</sup>. Postnatal mice were similarly processed and cryo-sectioned at 40 µm. For en face analysis of the ventricular surface, embryos were perfused with warm PBS and PFA to avoid microtubule depolymerization. The dorsal telencephalon was then dissected out of the embryonic brain to expose the ventricular surface for immunohistochemistry. The following primary antibodies were used: Alexa Fluor 546 phalloidin (A22283; RRID: AB\_2632953; lot 1947552; 1:500, Thermo Fisher Scientific), goat anti-FOXP2 (AB16046; RRID: AB\_2107107; lot GR3237165-1; 1:100, Abcam), goat anti-SOX2 (SC-17320; RRID: AB\_2286684; lot E0715; 1:500, Santa Cruz), chicken anti-GFP (GFP-1020; RRID: AB\_10000240; lot GFP879484; 1:500, Aves), mouse anti-β-catenin (610153; RRID: AB\_397554; lot 7187864; 1:500, BD Bioscience), mouse anti-S100α/β (SC-58839; RRID: AB\_2183338; lot K1215; 1:200, Santa Cruz), mouse anti-phospho-vimentin (AB22651; RRID: AB\_447222; lot GR3233697-1; 1:500, Abcam), mouse anti-N-cadherin (AB98952; RRID: AB\_10696943; lot GR287147-10; 1:500, Abcam), mouse anti-nestin (RAT-401; RRID: AB\_2235915; lot 5/26/2016; 1:500, Developmental Studies Hybridoma Bank), mouse anti-neurofilament (837904; RRID: AB\_2566782; lot B263754; 1:500, BioLegend), mouse anti-PCNT (611814; RRID: AB\_399294; lot 8163868; 1:200, BD Biosciences), mouse anti-α-tubulin (T9026; RRID: AB\_477593; lot 047M4789V; 1:1,000, Sigma-Aldrich), mouse anti-YAP (SC-101199; RRID: AB\_1131430; lot F2916; 1:200, Santa Cruz), mouse anti-ZO-1 (33-9100; RRID: AB\_87181; lot TH275232; 1:200, Thermo Fisher Scientific), rabbit anti-ARL13B<sup>49</sup> (1:500), rabbit anti-BLBP (AB32423; RRID: AB\_880078; lot GR260227-2; 1:500, Abcam), rabbit anti-CEP83 (HPA038161; RRID: AB\_10674547; lot A91789; 1:200, Sigma-Aldrich), rabbit anti-CEP89 (AB204410; validated by western blot and immunostaining; lot GR3247629-1; 1:500, Abcam), rabbit anti-ODF2 (12058-1-AP; RRID: AB\_2156630; lot 00050046; 1:500, Proteintech), rabbit anti-CEP164 (HPA037606; RRID: AB\_10672498; lot A95909; 1:200, Sigma-Aldrich), rabbit anti-CUX1 (SC-13024; RRID: AB\_2261231; lot H2815; 1:200, Santa Cruz), rabbit anti-HOPX (HPA030180; RRID: AB\_10603770; lot C105589; 1:1,000, Sigma-Aldrich), rabbit anti-MAP2 (AB5622; RRID: AB\_11213363; lot 3053795; 1:500, EMD Millipore), rabbit anti-PARD3 (HPA030443; RRID: AB\_10600926; lot C105765; 1:500, Sigma-Aldrich), rabbit anti-PAX6 (901301; RRID: AB\_256003; lot B267205; 1:500, Biolegend), rabbit anti-PAX6 (PD022; RRID: AB\_1520876; lot 005; 1:500, MBL), rabbit anti-PCNT (AB4448; RRID: AB\_304461; lot GR3200989-1; 1:500, Abcam), rabbit anti-OLIG2 (AB9610; RRID: AB\_570666; lot 2950732; 1:500, EMD Millipore), rabbit anti-P-HH3 (AB47297; RRID: AB\_880448; lot GR3190286-11; 1:1,000, Abcam), rabbit anti-PTPRZ1 (HPA015103; RRID: AB\_1855946; lot B105439; 1:500, Sigma-Aldrich), rabbit anti-SATB2 (AB92446; RRID: AB\_10563678; lot GR285095-11; 1:500, Abcam), rabbit anti-TNC (AB108930; RRID: AB\_10865908; lot GR308354-7; 1:500, Abcam), rat anti-BrdU (AB6326; RRID: AB\_305426; lot GR191332-1; 1:500, Abcam), rat anti-CTIP2 (18465; RRID: AB\_2064130; lot GR203038-2; 1:1,000, Abcam), rat anti-TBR2 (12-4875-82; RRID: AB\_1603275; lot 4279686; 1:100, eBioscience), Alexa Fluor 488 donkey anti-rabbit IgG (A-21206; RRID: AB\_141708; lot 1910751; 1:1,000, Thermo Fisher Scientific), donkey anti-mouse IgG (A-21202; RRID: AB\_141607; lot 1890861; 1:1,000, Thermo Fisher Scientific), donkey anti-goat IgG (A-11055; RRID: AB\_2534102; lot 1627966; 1:1,000, Thermo Fisher Scientific), goat anti-rat IgG (A-11006; RRID: AB\_141373; lot 1887148; 1:1,000, Thermo Fisher Scientific), donkey anti-chicken IgY (703-546-155; RRID: AB\_2340376; lot 132803; 1:1,000, Jackson ImmunoResearch), Alexa Fluor 555 donkey anti-rabbit IgG (A-21432; RRID: AB\_141788; lot 1866859; 1:1,000, Thermo Fisher Scientific), donkey anti-mouse IgG (A-31570; RRID:



# Article

AB\_2536180; lot 1850121; 1:1,000, Thermo Fisher Scientific), donkey anti-goat IgG (A-21432; RRID: AB\_141788; lot 2026158; 1:1,000, Thermo Fisher Scientific), Alexa Fluor 594 donkey anti-rat IgG (A-21209; RRID: AB\_2535795; lot 1905801; 1:1,000, Thermo Fisher Scientific), Alexa Fluor 647 donkey anti-rabbit IgG (A-31573; RRID: AB\_2536183; lot 1903516; 1:1,000, Thermo Fisher Scientific), Alexa Fluor 647 donkey anti-mouse IgG (A-31571; RRID: AB\_162542; lot 1839633; 1:1,000, Thermo Fisher Scientific), donkey anti-goat IgG (A-21447; RRID: AB\_141844; lot 1627966; 1:1,000, Thermo Fisher Scientific), goat anti-rat IgG (A-21247; RRID: AB\_141778; lot 1858181; 1:1,000, Thermo Fisher Scientific) conjugated secondary antibodies were used. For EdU and BrdU double pulse-chase analysis, mice were weighted and injected with EdU (10  $\mu$ g per gram body weight) and BrdU (50  $\mu$ g per gram body weight) sequentially. EdU staining was performed using Click-IT EdU Alexa Fluor 647 Imaging Kit (Thermo Fisher Scientific). Before proceeding with BrdU staining, tissue sections were blocked with azidomethylphenylsulfide to minimize the cross-reactivity of anti-BrdU antibody against EdU<sup>50</sup>. BrdU staining was performed as described previously<sup>18</sup>. Coronal sections were imaged with a FV1200 or FV3000 confocal microscope (Olympus) and Nano-Zoomer 2.0 HT slide scanner (Hamamatsu Photonics). Free-floating dorsal telencephalon was submerged in PBS and positioned in an en face view, and imaged with a FV1200 or FV3000 confocal microscope with water-immersion objectives. Cortical length and area were estimated by measuring the overall length and area of the dorsal cortex in individual brain sections at a similar rostrocaudal position. The densities of neurons were quantified by measuring the number of cells positive for specific markers in a 250- $\mu$ m-width rectangular region perpendicular to the pia covering the entire cortex. En face images of the ventricular surface were automatically segmented with the Fiji plug-in Tissue Analyzer<sup>51</sup> and manually corrected. Cell boundaries at the edges of images were manually removed and thereby excluded from analysis. The segmented images were then transformed into labelled images with the Fiji plug-in MorphoLibJ<sup>52</sup>. Subsequently, apical domain sizes were measured through the particle analysis function of Fiji. For visualization of the results, apical domain size was colour-coded with MatLab (v.R2016b, Mathworks). All images were analysed and processed using Fluoview (v.4.2, Olympus), Volocity (v.6.3, Perkin Elmer), ImageJ (Fiji) (1.52p, NIH), NDP viewer (v.2, Hamamatsu Photonics), Imaris (v.9.0.1, Oxford Instruments) and Photoshop (Adobe).

## ssTEM

For TEM analysis, timed pregnant females were prepared and embryos were removed and perfused with 0.1 M sodium cacodylate buffer (pH 7.4) and a fixative containing 2% PFA and 2.5% glutaraldehyde at room temperature, followed by post-fixation overnight with the same fixative at 4 °C. Brains were then sliced into 1-mm thick coronal sections with a mouse brain mould. The selected slices were re-fixed with 2.5% glutaraldehyde and 0.1% tannic acid for one hour and then with 2.5% glutaraldehyde overnight. The slices were post-fixed with 1% osmium tetroxide and 0.4% potassium ferrocyanide for 1 h, followed by en bloc staining with 1% uranyl acetate for 30 min. Sections were subsequently dehydrated with a graded ethanol series, infiltrated and embedded with Eponate12 resin (Electron Microscopy Sciences). Serial sections (70 nm) of brain regions close to the ventricular surface were cut by an ultramicrotome (Ultracut E; Leica). Serial images of centrioles from RGP at the ventricular surface were acquired with a JOEL 100CX transmission electron microscope with a digital imaging system (XR41-C, Advantage Microscopy Technology) at 80 kV at the Rockefeller University Electron Microscopy Resource Centre.

## MRI analysis

Ex vivo MRI of 4% PFA-fixed mouse brain specimens was performed on a horizontal 7 Tesla MR scanner (Bruker Biospin) with a triple-axis gradient system. Images were acquired using a quadrature volume excitation coil (72-mm diameter) and a receive-only 4-channel phased

array cryogenic coil. The specimens were imaged with the skull intact and placed in a syringe filled with Fomblin to prevent tissue dehydration. For MRI-based characterization of macroscopic brain morphology, diffusion MRI data were acquired instead of conventional T<sub>1</sub> or T<sub>2</sub>-weighted MRI, from P21 mouse brains that were not yet fully myelinated<sup>53</sup>. High-resolution diffusion MRI data were acquired using a modified three-dimensional (3D) diffusion-weighted gradient and spin echo (DW-GRASE) sequence<sup>54</sup> with the following parameters: echo time (TE)/repetition time (TR) = 30/500 ms; two signal averages; field of view (FOV) = 12.8 mm  $\times$  10 mm  $\times$  18 mm, resolution = 0.1 mm  $\times$  0.1 mm  $\times$  0.1 mm; two non-diffusion weighted image ( $b_0$ ); 30 diffusion directions; and  $b$  = 2,000 s mm<sup>-2</sup>. The total imaging time was approximately 6 h for each specimen.

From the diffusion MRI data, diffusion tensors were calculated using the log-linear fitting method implemented in DTIStudio (v.2.10.6 (<http://www.mristudio.org>) at each pixel. The mouse brain images were rigidly aligned to an ex vivo mouse brain template in our MRI-based mouse brain atlas<sup>55</sup> using the large deformation diffeomorphic metric mapping (LDDMM) method<sup>56</sup> implemented in the DiffeoMap software (v.2.10.6) (<http://www.mristudio.org>). To further determine the specific cortical regions in the knockout mice that showed significant changes in local tissue volume with respect to the control mice, voxel-based morphometric analysis was also performed as described previously<sup>57</sup> with the false discovery rate (FDR) set at 0.05. Cortical volume was estimated on the basis of the MRI data.

## AFM

To prepare samples for AFM, the dorsal telencephalon was dissected from the embryonic brain in 1 $\times$  DMEM-N2 medium (Thermo Fisher Scientific) to expose the ventricular surface. Tissues were positioned with the ventricular zone surface upward and mounted onto 50-mm glass-bottom Fluorodish cell-culture dishes (World Precision Instruments) coated with Cell Tak tissue adhesive (Corning). Tissues were then covered with 1 $\times$  DMEM-N2 medium and recovered in a 5% CO<sub>2</sub> chamber at 37 °C for 1 h. Stiffness measurement was performed by MFP-3D-BIO AFM (Asylum Research). An Axio Observer Z1 inverted microscope (Zeiss) served as the AFM base (LD Plan-Neofluar 5 $\times$  0.15 NA objective) to locate the sample and position the cantilever tip over the sample. A CP-CONT-BSC-C (sQuBE) probe with a 20- $\mu$ m borosilicate glass bead was used for all measurements. The Asylum Research Get-Real calibration method was used for the determination of the spring constant (around 0.2 N m<sup>-1</sup>). The trigger point was set to 10 nN with an approach and retraction velocity of 5  $\mu$ m s<sup>-1</sup>. To determine the Young's modulus, the force-indentation curves were fit to the Hertz model for spherical tips through the Asylum Research software (v.16), with an assumed Poisson's ratio value of 0.45 for the sample<sup>58</sup>. Three distinct spots (40  $\times$  40  $\mu$ m<sup>2</sup> in size) were measured for each piece of tissue. The average stiffness of each spot was calculated for data analysis.

## Acutely dissociated ventricular zone cell culture

Wild-type or *Cep83*KO embryos were dissected out and sectioned using a vibratome (Leica Microsystems) at E15. The ventricular zone of the cortex was isolated, incubated in a protease solution containing 10 units per ml papain (Fluka) in DMEM (Gibco) and triturated using a fire-polished Pasteur pipette to create a single-cell suspension. Cells were resuspended in a culture medium containing DMEM, glutamine, penicillin/streptomycin, sodium pyruvate (Gibco), 1 mM *N*-acetyl-L-cysteine (Sigma), B27 and N2, and plated onto coverslips coated with poly-L-lysine (Sigma) in 24-well plates. The cultures were maintained in a humidified incubator at 37 °C with a constant supply of 5% CO<sub>2</sub>. About 8–12 h later, the cultures were fixed and analysed for YAP expression.

## Quantification and statistical analysis

For individual experiments, at least three wild-type and mutant mice or brains from multiple litters were examined. For immunohistochemistry



experiments, multiple sections from individual brains were analysed. No statistical methods were used to predetermine sample size. Sample size was determined to be adequate on the basis of the magnitude and consistency of measurable differences between groups. No randomization of samples was performed. Mice subjected to the analyses were littermates, age-matched and included both sexes. Investigators were not blinded to mouse genotypes during experiments. Data are not subjective but are based on quantitative analyses. The number of times each experiment was repeated independently with similar results is provided in the figure legends. Statistical significance was determined using a chi-square or two-sided non-parametric Mann–Whitney *U* test, and exact values from the tests are provided in the figures. Statistical significance was defined as  $P < 0.05$ . Statistical tests were performed with Prism (v.7, GraphPad). Effect sizes were calculated using Pearson's *r* (chi-square) or  $U/(n1 \times n2)$  (Mann–Whitney *U* test). Bar graphs indicate mean + s.e.m. Box plots indicate median (centre line), interquartile range (box) and minimum and maximum values (whiskers).

## Reporting summary

Further information on research design is available in the Nature Research Reporting Summary linked to this paper.

## Data availability

The datasets generated during and/or analysed during the current study are available from the corresponding authors on reasonable request.

48. Reginensi, A. et al. Yap- and Cdc42-dependent nephrogenesis and morphogenesis during mouse kidney development. *PLoS Genet.* **9**, e1003380 (2013).
49. Caspary, T., Larkins, C. E. & Anderson, K. V. The graded response to Sonic Hedgehog depends on cilia architecture. *Dev. Cell* **12**, 767–778 (2007).
50. Liboska, R., Ligasová, A., Strunin, D., Rosenberg, I. & Koberna, K. Most anti-BrdU antibodies react with 2'-deoxy-5-ethynyluridine—the method for the effective suppression of this cross-reactivity. *PLoS One* **7**, e51679 (2012).
51. Aigouy, B., Umetsu, D. & Eaton, S. Segmentation and quantitative analysis of epithelial tissues. *Methods Mol. Biol.* **1478**, 227–239 (2016).
52. Legland, D., Arganda-Carreras, I. & Andrey, P. MorphoLibJ: integrated library and plugins for mathematical morphology with ImageJ. *Bioinformatics* **32**, 3532–3534 (2016).
53. Mori, S. & Zhang, J. Principles of diffusion tensor imaging and its applications to basic neuroscience research. *Neuron* **51**, 527–539 (2006).
54. Wu, D. et al. In vivo high-resolution diffusion tensor imaging of the mouse brain. *Neuroimage* **83**, 18–26 (2013).
55. Chuang, N. et al. An MRI-based atlas and database of the developing mouse brain. *Neuroimage* **54**, 80–89 (2011).
56. Ceritoglu, C. et al. Multi-contrast large deformation diffeomorphic metric mapping for diffusion tensor imaging. *Neuroimage* **47**, 618–627 (2009).
57. Zhang, J. et al. Longitudinal characterization of brain atrophy of a Huntington's disease mouse model by automated morphological analyses of magnetic resonance images. *Neuroimage* **49**, 2340–2351 (2010).
58. Chen, E. J., Novakofski, J., Jenkins, W. K. & Brien, W. D. O. Young's modulus measurements of soft tissues with application to elasticity imaging. *IEEE Trans. Ultrason. Ferroelectr. Freq. Control* **43**, 191–194 (1996).

**Acknowledgements** We thank B. Yoder, J. Wrana and A. McMahon for providing *lft88<sup>fl/fl</sup>*, *Yap<sup>fl/fl</sup>* and *R26-LSL-SmoM2* mice, respectively; M. Brendel and K. Manova-Todorova at the Molecular Cytology Core and Y. Wang and W. Mark at the Mouse Genetics Core Facility of Memorial Sloan Kettering Cancer Centre, K. Uryu at the Electron Microscopy Resource Centre and J. Gao and C. Yang at the Gene Targeting Resource Centre of Rockefeller University for their technical support; and members of the H.S. and S.-H.S. laboratories for their input and comments on the manuscript. This work was supported by grants from the NIH (R01DA024681 and R01NS085004 to S.-H.S., and P30CA008748 to Memorial Sloan Kettering Cancer Centre), the Howard Hughes Medical Institute (to S.-H.S.) and the Beijing Outstanding Young Scientist Program (BJJWZYJH01201910003012 to S.-H.S.).

**Author contributions** W.S. and S.-H.S. conceived and H.S. and S.-H.S. supervised the project; W.S. and J.Y. performed most of the experiments with help from Z.Y., M.H. and X.-Y.Y.; C.H.L. and J.Z. performed the MRI experiment; A.L.J., K.V.A. and M.-F.B.T. advised on the project; W.S., J.Y., H.S. and S.-H.S. wrote the manuscript with input from all authors.

**Competing interests** The authors declare no competing interests.

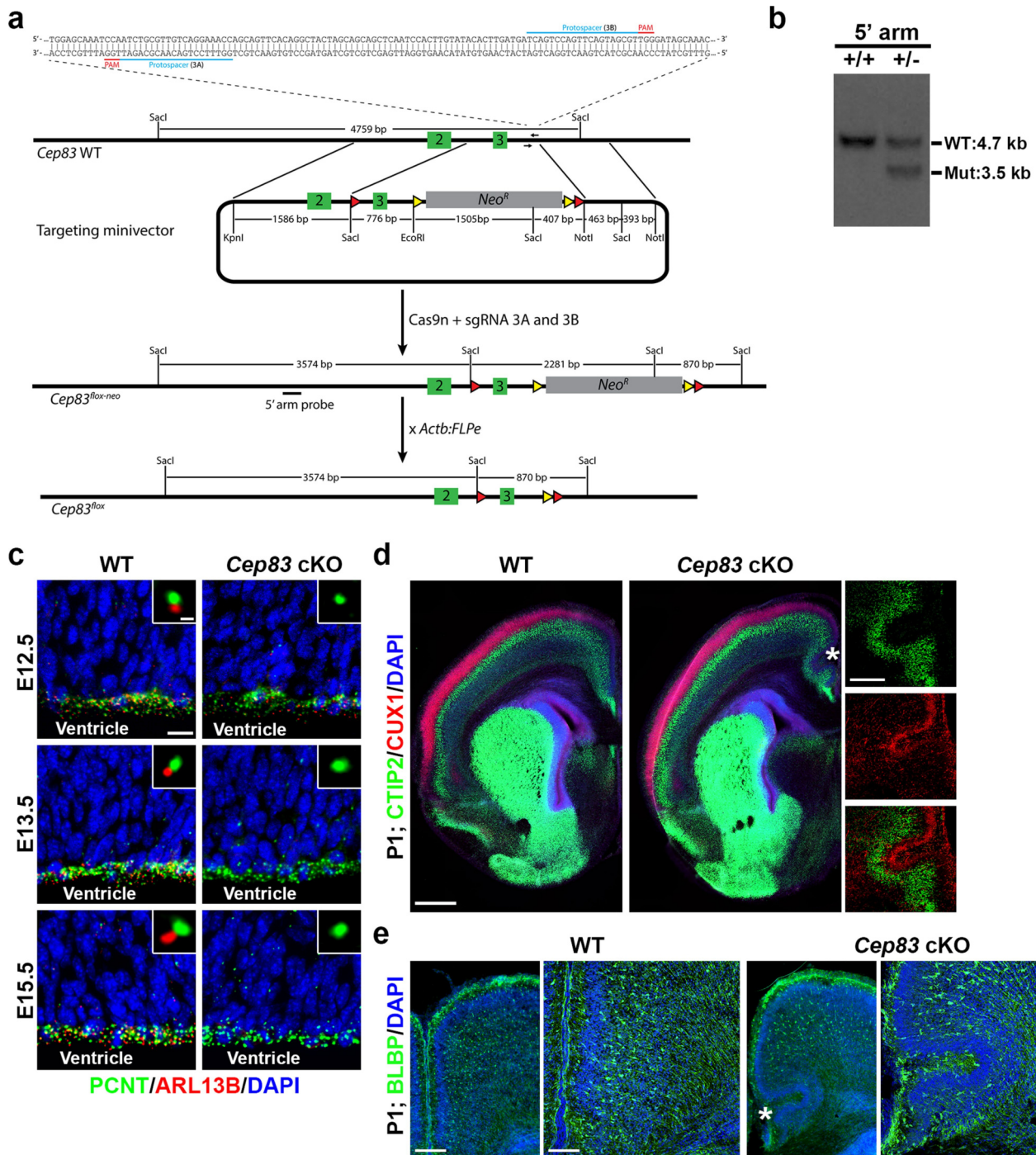
## Additional information

**Supplementary information** is available for this paper at <https://doi.org/10.1038/s41586-020-2139-6>.

**Correspondence and requests for materials** should be addressed to H.S. or S.-H.S.

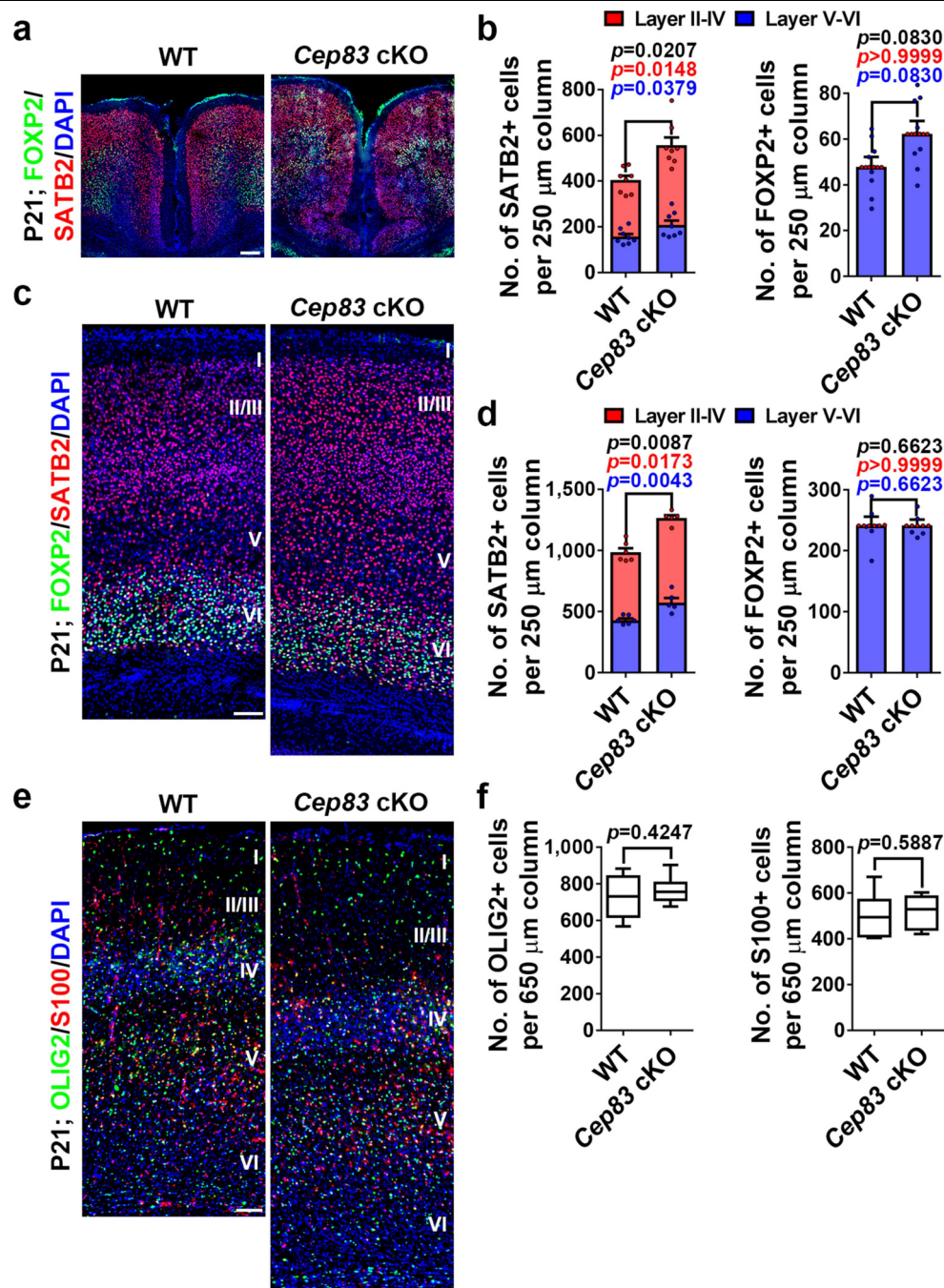
**Peer review information** Nature thanks Gordon Fishell, Anthony Wynshaw-Boris and the other, anonymous, reviewer(s) for their contribution to the peer review of this work.

**Reprints and permissions information** is available at <http://www.nature.com/reprints>.



**Extended Data Fig. 1 | Deletion of *Cep83* in cortical RGPs. a**, Schematic diagram of the generation of the *Cep83*cKO mouse using a CRISPR–Cas9-mediated double-nicking strategy. The DNA sequence at the top depicts the sites targeted by a pair of guide RNAs (outlined in blue) downstream of the critical exon 3 in the *Cep83* gene. Green boxes represent exons, red triangles represent *loxP* sites and yellow triangles represent FRT sites. *Neo<sup>R</sup>*, neomycin-resistance gene cassette. **b**, Representative Southern blot showing the correct gene targeting against the 5'-homology arm of the *Cep83* floxed allele with the presence of the deletion-specific 3.5-kb band ( $n=3$ ). **c**, Representative images of wild-type and *Cep83*cKO cortices at E12.5, E13.5 and E15.5, stained for PCNT (green) and ARL13B (a primary cilium marker; red), and with DAPI (blue) ( $n=3$ ).

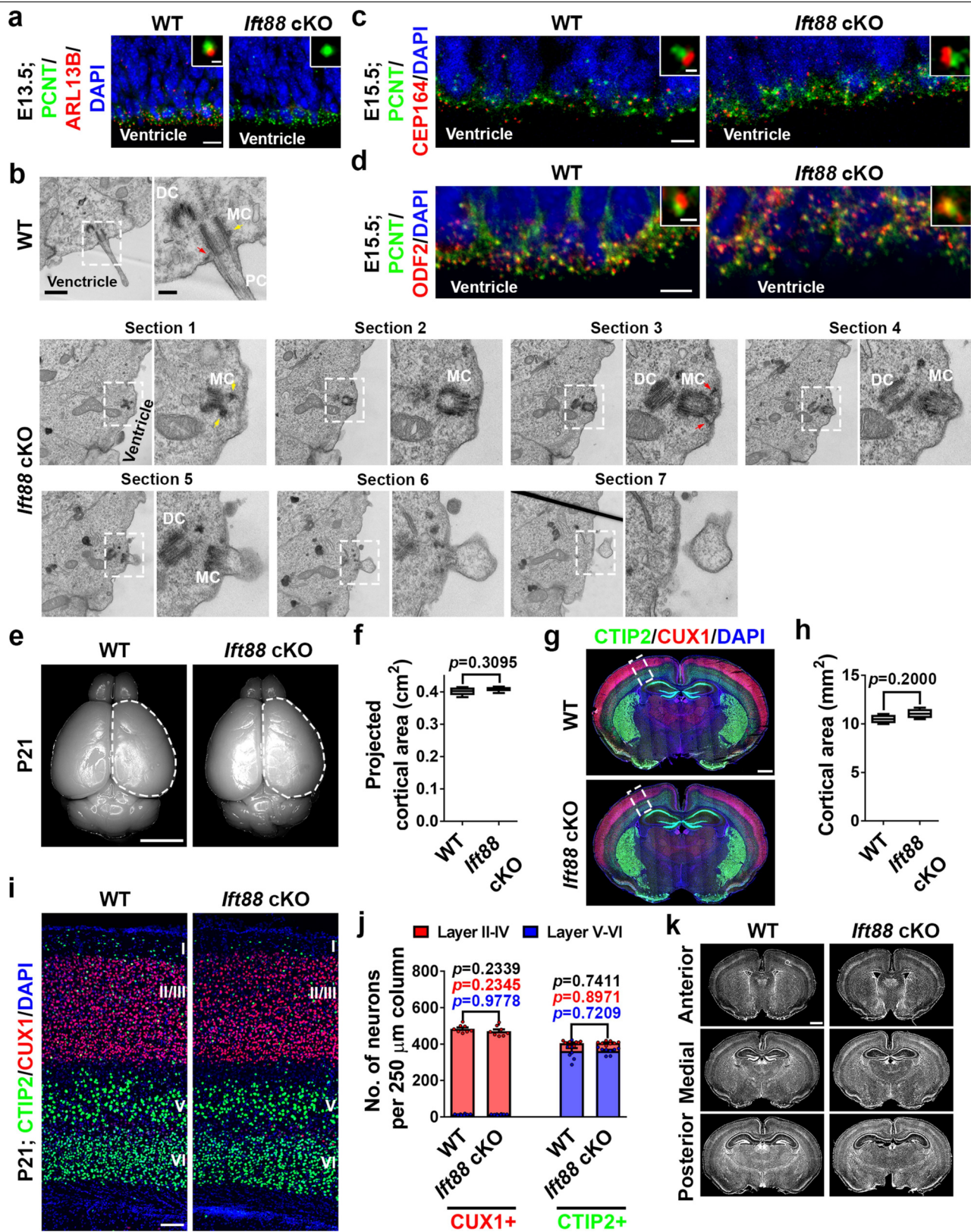
High-magnification images of individual centrosomes are shown in the insets. Note the loss of primary cilia in the *Cep83*cKO cortex by E13.5. Scale bars, 10  $\mu$ m (main image); 1  $\mu$ m (inset). **d**, Representative images of P1 wild-type ( $n=11$ ) and *Cep83*cKO ( $n=12$ ) cortices stained for CTIP2 (green) and CUX1 (red), and with DAPI (blue). The asterisk indicates the folding in the medial region of the *Cep83*cKO cortex. High-magnification images of the folding are shown to the right. Scale bars, 500  $\mu$ m (left); 200  $\mu$ m (right). **e**, Representative images of the medial region of P1 wild-type and *Cep83*cKO cortices stained for brain lipid-binding protein (BLBP; green) and with DAPI (blue). High-magnification images are shown to the right. Scale bars, 500  $\mu$ m (left); 100  $\mu$ m (right).



**Extended Data Fig. 2 | Deletion of *Cep83* in RGP leads to increased neurogenesis and gliogenesis.** **a**, Representative images of the medial regions of P21 wild-type and *Cep83* cKO cortices stained for FOXP2 (green) and SATB2 (red), and with DAPI (blue). Scale bar, 100  $\mu$ m. **b**, Quantification of the number of SATB2<sup>+</sup> (left) and FOXP2<sup>+</sup> (right) neurons per 250- $\mu$ m column (wild type,  $n=8$  brains; *Cep83* cKO,  $n=8$  brains). **c**, Representative images of the dorsal regions of P21 wild-type and *Cep83* cKO cortices stained for FOXP2 (green) and SATB2 (red), and with DAPI (blue). Scale bar, 100  $\mu$ m. **d**, Quantification of the number of SATB2<sup>+</sup> (left) and FOXP2<sup>+</sup> (right) neurons per 250- $\mu$ m column (wild type,  $n=6$

brains; *Cep83* cKO,  $n=5$  brains). **e**, Representative images of P21 wild-type and *Cep83* cKO cortices stained for OLIG2 (an oligodendrocyte marker; green) and S100 (an astrocyte marker; red), and with DAPI (blue). Scale bar, 100  $\mu$ m. **f**, Quantification of the number of OLIG2<sup>+</sup> oligodendrocytes ( $n=10$  regions from 5 brains for each genotype) and S100<sup>+</sup> astrocytes ( $n=6$  regions from 3 brains for each genotype) per 650- $\mu$ m column. A two-sided Mann-Whitney  $U$  test was used for statistical analysis. Bar charts show mean + s.e.m. Box plots as in Fig. 1.



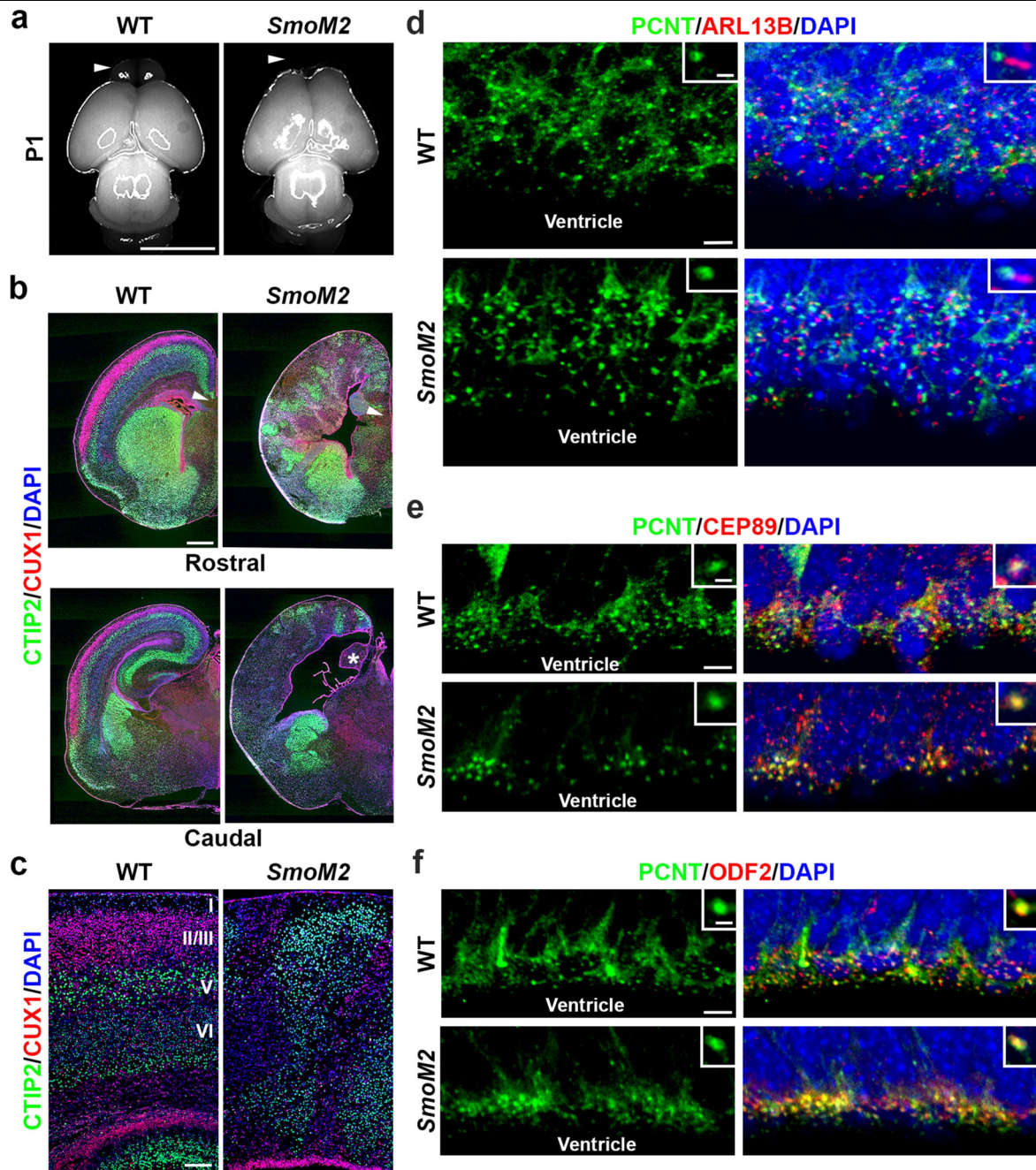


Extended Data Fig. 3 | See next page for caption.

**Extended Data Fig. 3 | Deletion of *lft88* in RGP does not lead to any obvious defect in centrosome appendages, centrosome membrane anchorage or cortical development.** **a**, Representative images of E13.5 wild-type and *lft88*KO ventricular zone surface stained for PCNT (green) and ARL13B (red), and with DAPI (blue) ( $n = 3$ ). High-magnification images of individual centrosomes are shown in the insets. Note the complete loss of primary cilia in the *lft88*KO cortex by E13.5. Scale bars, 10  $\mu\text{m}$  (main image); 1  $\mu\text{m}$  (inset). **b**, Representative ssTEM images of E15.5 wild-type (top) and *lft88*KO (bottom) ventricular zone surface showing individual centrosomes of RGP in the apical endfeet. High-magnification images (white dashed boxes) are shown on the right. Note that the *lft88*KO mother centriole possesses the DAPs that are anchored at the apical membrane (red arrows) and the sDAPs (yellow arrows), but does not support any microtubule-based ciliary axoneme (wild type,  $n = 9$  centrosomes; *lft88*KO,  $n = 20$  centrosomes). All wild-type mother centrioles were anchored to the apical membrane with microtubule-based cilia. All *lft88*KO mother centrioles were anchored to the apical membrane, but none possessed microtubule-based cilia. Scale bars, 800 nm (left); 200 nm (right). **c**, Representative images of E15.5 wild-type and *lft88*KO ventricular zone surface stained for PCNT (green) and CEP164 (red), and with DAPI (blue) ( $n = 3$ ). High-magnification images of individual centrosomes are shown in the insets.

Note the normal presence of CEP164 at the centrosome in the *lft88*KO cortex. Scale bars, 10  $\mu\text{m}$  (main images); 0.5  $\mu\text{m}$  (insets). **d**, Representative images of E15.5 wild-type ( $n = 6$ ) and *lft88*KO ( $n = 6$ ) ventricular zone surface stained for PCNT (green) and ODF2 (an sDAP marker; red), and with DAPI (blue). High-magnification images of individual centrosomes are shown in the insets. Note the normal presence of ODF2 at the centrosome in the *lft88*KO cortex. Scale bars, 5  $\mu\text{m}$  (main image); 1  $\mu\text{m}$  (inset). **e**, Representative whole-mount images of P21 wild-type and *lft88*KO brains. Scale bar, 0.5 cm. **f**, Quantification of the projected cortical area ( $n = 6$  brains for each genotype). **g**, Images of P21 wild-type and *lft88*KO brain sections stained for CTIP2 (green) and CUX1 (red), and with DAPI (blue). Scale bar, 0.5 mm. **h**, Quantification of the cortical area (wild type,  $n = 4$  brains; *lft88*KO,  $n = 4$  brains). **i**, Images of the dorsal regions of P21 wild-type and *lft88*KO cortices stained for CTIP2 (green) and CUX1 (red), and with DAPI (blue). Scale bar, 100  $\mu\text{m}$ . **j**, Quantification of the number of CUX1<sup>+</sup> (left) and CTIP2<sup>+</sup> (right) neurons per 250- $\mu\text{m}$  column ( $n = 8$  brains for each genotype). **k**, Representative images of P21 wild-type and *lft88*KO brain sections along the rostrocaudal axis, stained with DAPI (grey) ( $n = 5$ ). Note that there is no obvious hydrocephalus in the *lft88*KO brain. Scale bar, 1 mm. A two-sided Mann-Whitney  $U$  test was used for statistical analysis. Bar charts show mean + s.e.m. Box plots as in Fig. 1.

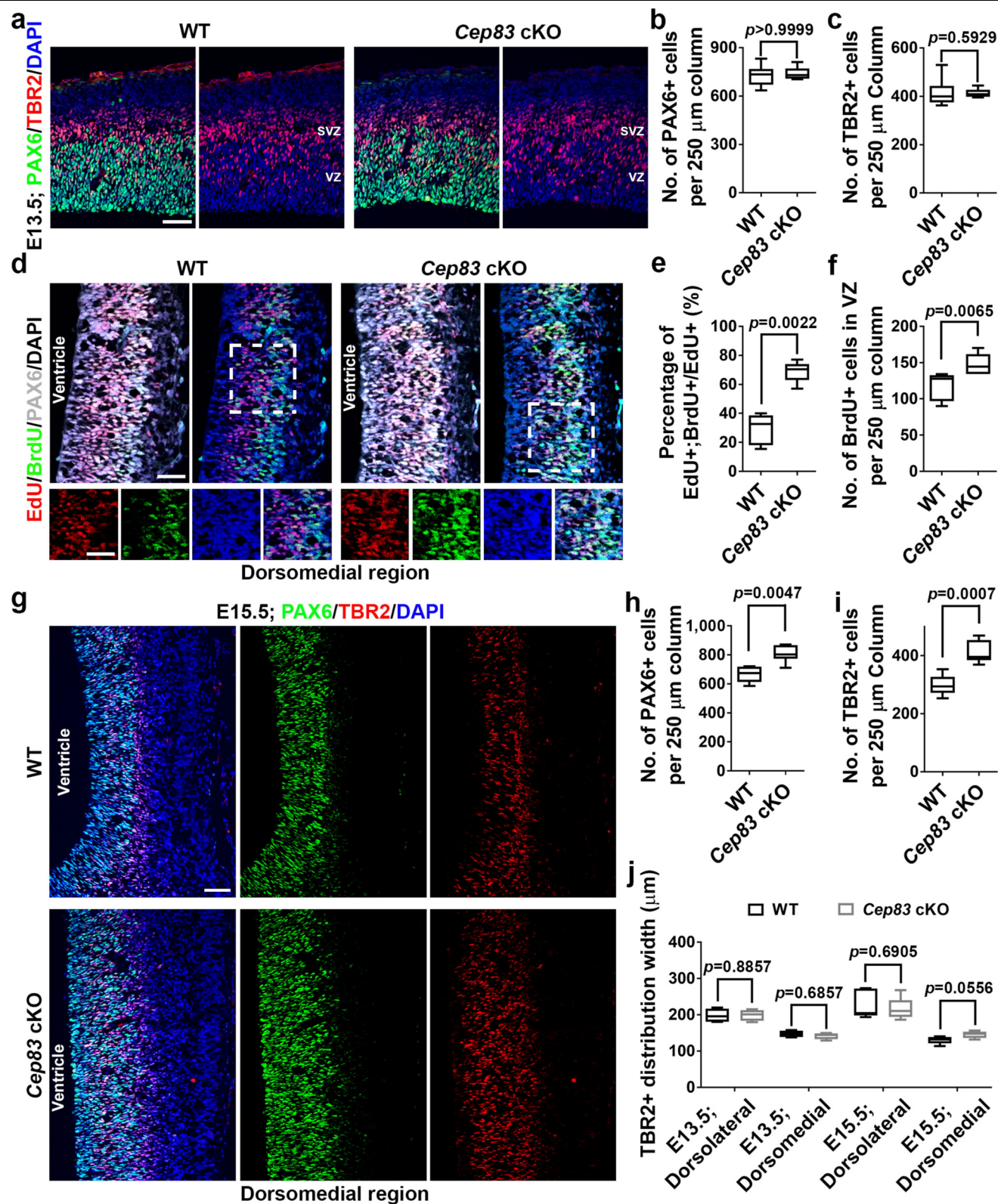




**Extended Data Fig. 4 | Expression of *SmoM2* in RGP leads to cortical dysplasia.** **a**, Representative whole-mount images of P1 wild-type and *SmoM2* brains ( $n = 5$ ). Arrowheads indicate the agenesis of the olfactory bulb in the *SmoM2* brain. Scale bar, 0.5 cm. **b**, Representative images of P1 wild-type and *SmoM2* brain sections stained for CTIP2 (green) and CUX1 (red), and with DAPI (blue) ( $n = 5$ ). Arrowheads indicate the absence of corpus callosum in the *SmoM2* brain. The asterisk indicates the agenesis of the hippocampus in the *SmoM2* brain. Scale bar, 0.5 mm. **c**, Representative images of P1 wild-type and *SmoM2* cortices stained for CTIP2 (green) and CUX1 (red), and with DAPI (blue) ( $n = 4$ ). Note the drastic disorganization of the *SmoM2* cortex. Scale bar, 100  $\mu$ m. **d**, Representative images of E15.5 wild-type and *SmoM2* ventricular zone surface stained for PCNT (green) and ARL13B (red), and with DAPI (blue) ( $n = 3$ ).

High-magnification images of individual centrosomes are shown in the insets. Note the presence of the primary cilium at the *SmoM2* centrosome. Scale bars, 5  $\mu$ m (main image); 1  $\mu$ m (inset). **e**, Representative images of E15.5 wild-type and *SmoM2* ventricular zone surface stained for PCNT (green) and CEP89 (a DAP marker; red), and with DAPI (blue) ( $n = 3$ ). High-magnification images of individual centrosomes are shown in the insets. Note the normal presence of CEP89 at the *SmoM2* centrosome. Scale bars, 5  $\mu$ m (main image); 1  $\mu$ m (inset). **f**, Representative images of E15.5 wild-type and *SmoM2* ventricular zone surface stained for PCNT (green) and ODF2 (red), and with DAPI (blue) ( $n = 3$  brains). High-magnification images of individual centrosomes are shown in the insets. Note the normal presence of ODF2 at the *SmoM2* centrosome. Scale bars, 5  $\mu$ m (main image); 1  $\mu$ m (inset).





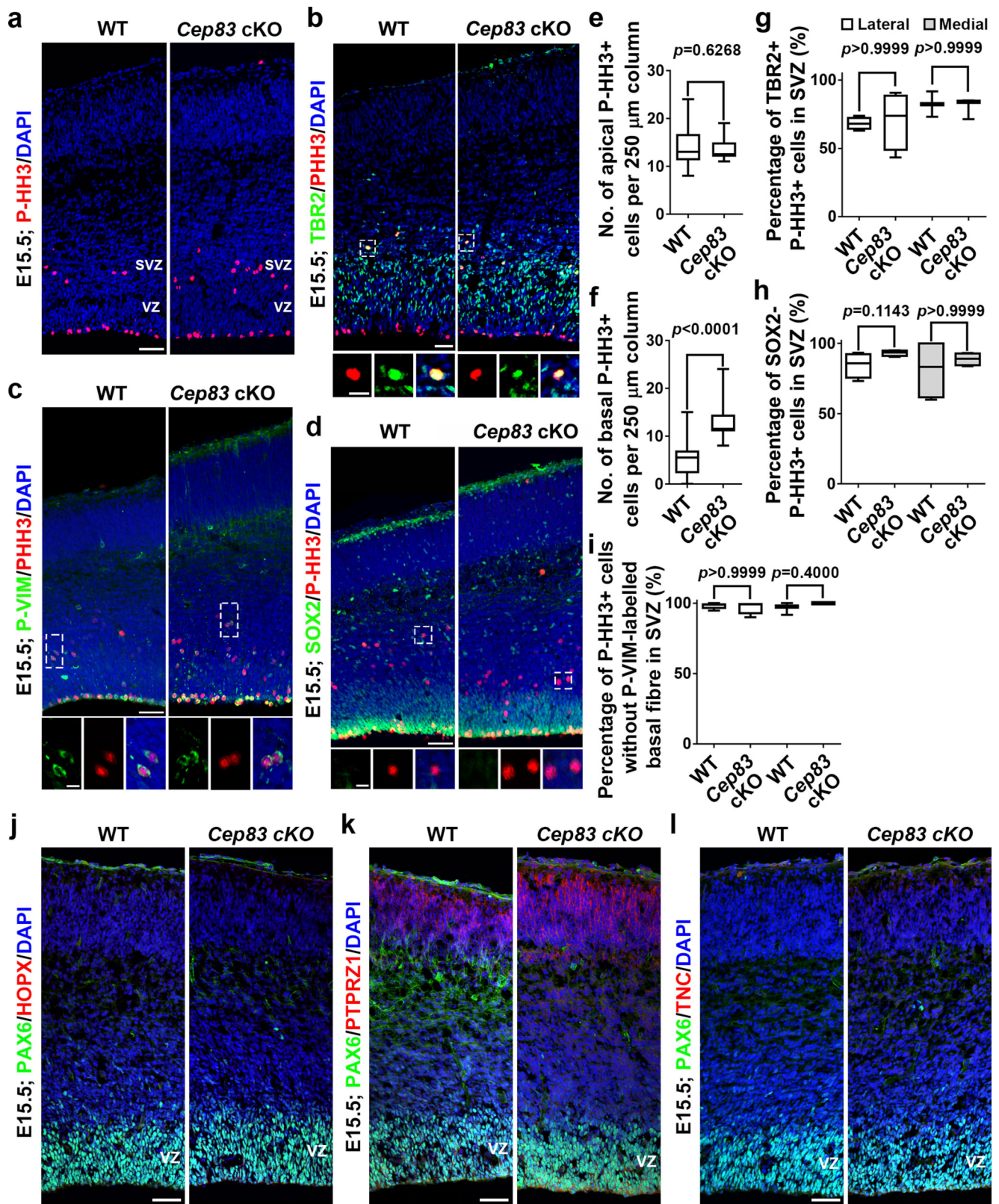
Extended Data Fig. 5 | See next page for caption.

## Extended Data Fig. 5 | Deletion of *Cep83* does not affect the densities of RGPs and intermediate progenitor cells at E13.5, but leads to increased densities of these cells in the dorsomedial cortex at E15.5.

**a**, Representative images of E13.5 wild-type and *Cep83*CKO cortices stained for PAX6 (green) and TBR2 (red), and with DAPI (blue). Scale bar, 50  $\mu$ m. **b, c**, Quantification of the number of PAX6<sup>+</sup> (**b**) and TBR2<sup>+</sup> (**c**) cells per 250- $\mu$ m column in **a**. Wild type,  $n = 8$  brains; *Cep83*CKO,  $n = 8$  brains. **d**, Images of E12.5 wild-type and *Cep83*CKO cortices (dorsomedial region) that were subjected to EdU (red) and BrdU (green) sequential pulse-chase labelling. Cortices were stained for PAX6 (grey), and with DAPI (blue). Example regions (white dashed boxes) are shown at the bottom. Scale bars, 25  $\mu$ m. **e, f**, Quantification of the percentage of EdU<sup>+</sup>BrdU<sup>+</sup>

cells among the total EdU<sup>+</sup> cells in the ventricular zone (**e**), and the number of BrdU<sup>+</sup> cells in the ventricular zone per 250- $\mu$ m column (**f**) (wild type,  $n = 6$  brains; *Cep83*CKO,  $n = 6$  brains). **g**, Images of E15.5 wild-type and *Cep83*CKO cortices (dorsomedial region) stained for PAX6 (green) and TBR2 (red), and with DAPI (blue). Scale bar, 50  $\mu$ m. **h, i**, Quantification of the number of PAX6<sup>+</sup> (**h**) or TBR2<sup>+</sup> (**i**) cells per 250- $\mu$ m column (wild type,  $n = 8$  brains; *Cep83*CKO,  $n = 6$  brains). **j**, Quantification of the distribution width of TBR2<sup>+</sup> cells in wild-type or *Cep83*CKO cortices (E13.5,  $n = 4$  brains for each genotype; E15.5,  $n = 5$  brains for each genotype). A two-sided Mann–Whitney  $U$  test was used for statistical analysis. Box plots as in Fig. 1.





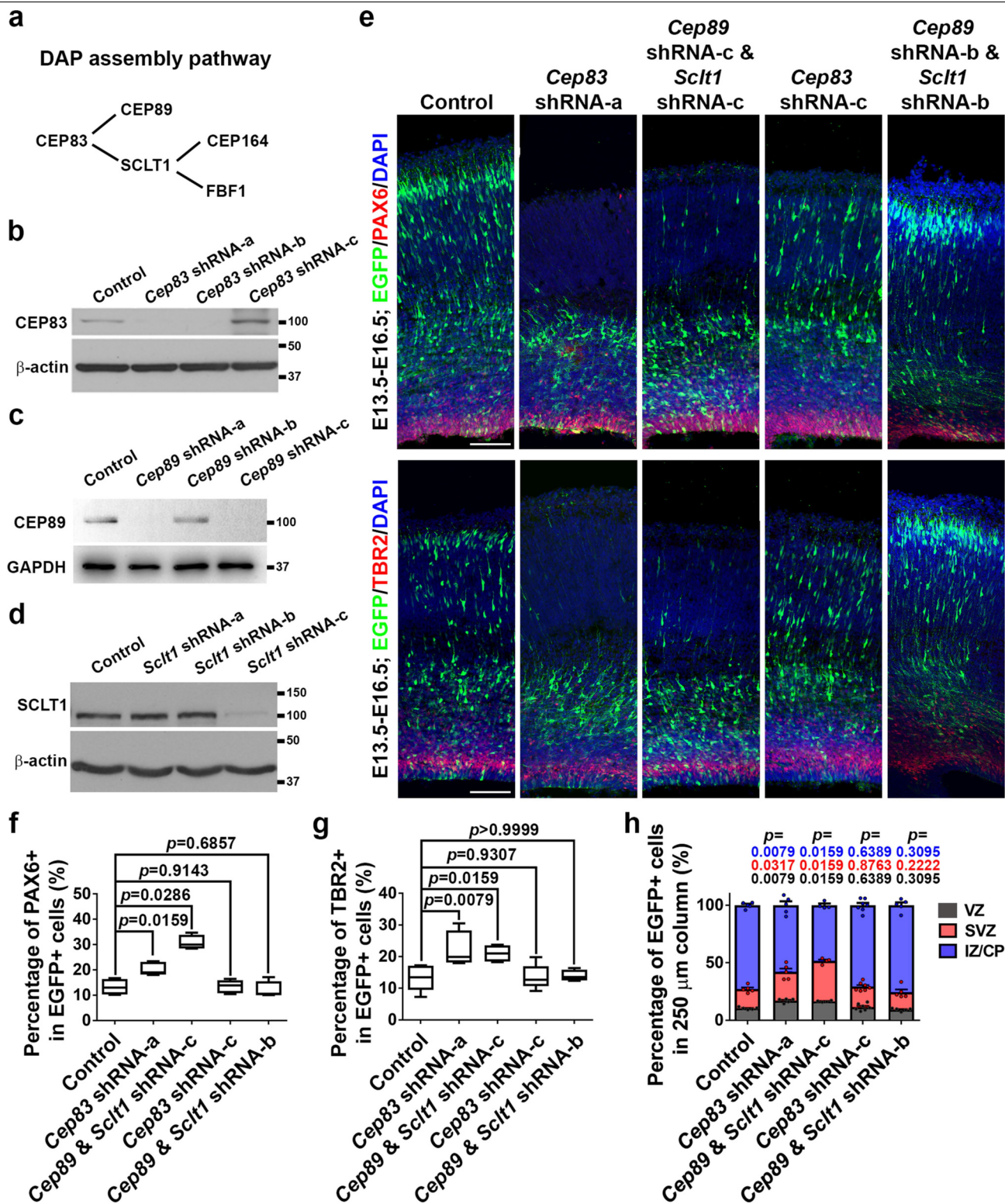
Extended Data Fig. 6 | See next page for caption.

## Extended Data Fig. 6 | Increased mitotic cells in the subventricular zone of the *Cep83cKO* cortex are predominantly intermediate progenitor cells.

**a**, Images of E15.5 wild-type and *Cep83cKO* cortices stained for P-HH3 (a mitotic cell marker; red), and with DAPI (blue). Scale bar, 50  $\mu\text{m}$ . **b, d**, Images of E15.5 wild-type and *Cep83cKO* cortices stained for P-HH3 (red) and TBR2 (green) (**b**) or SOX2 (an RGP marker; green) (**d**), and with DAPI (blue). High-magnification images of individual P-HH3<sup>+</sup> cells are shown at the bottom. Note that P-HH3<sup>+</sup> cells in the subventricular zone of the *Cep83cKO* cortex are predominantly TBR2<sup>+</sup> but SOX2<sup>-</sup>. Scale bars, 25  $\mu\text{m}$  (top); 10  $\mu\text{m}$  (bottom). **c**, Images of E15.5 wild-type and *Cep83cKO* cortices stained for P-HH3 (red) and phosphovimentin (P-VIM; green), and with DAPI (blue). High-magnification images of individual P-HH3<sup>+</sup> cells are shown at the bottom. Scale bars, 25  $\mu\text{m}$  (top); 10  $\mu\text{m}$  (bottom). **e, f**, Quantification of the number of apical (**e**) and basal (**f**) P-HH3<sup>+</sup>

cells per 250- $\mu\text{m}$  column (wild type,  $n = 16$  brains; *Cep83cKO*,  $n = 14$  brains). **g, h**, Quantification of the percentage of P-HH3<sup>+</sup> cells in the subventricular zone that are TBR2<sup>+</sup> (**g**; lateral,  $n = 4$  brains for each genotype; medial,  $n = 3$  brains for each genotype) or SOX2<sup>+</sup> (**h**;  $n = 4$  brains for each genotype). **i**, Quantification of the percentage of P-HH3<sup>+</sup> cells without a P-VIM labelled basal radial glial fibre (lateral,  $n = 4$  brains for each genotype; medial,  $n = 3$  brains for each genotype). **j–l**, Representative images of E15.5 wild-type and *Cep83cKO* cortices stained for PAX6 (green) and three previously suggested markers of outer subventricular zone RGPs (HOPX (**j**), PTPRZ1 (**k**) or TNC (**l**)) (red), and with DAPI (blue) ( $n = 4$ ). Note that there is no obvious increase in the expression of HOPX, PTPRZ1 or TNC in the *Cep83cKO* cortex and low expression in both wild-type and *Cep83cKO* cortices. Scale bars, 50  $\mu\text{m}$ . A two-sided Mann–Whitney  $U$  test was used for statistical analysis. Box plots as in Fig. 1.



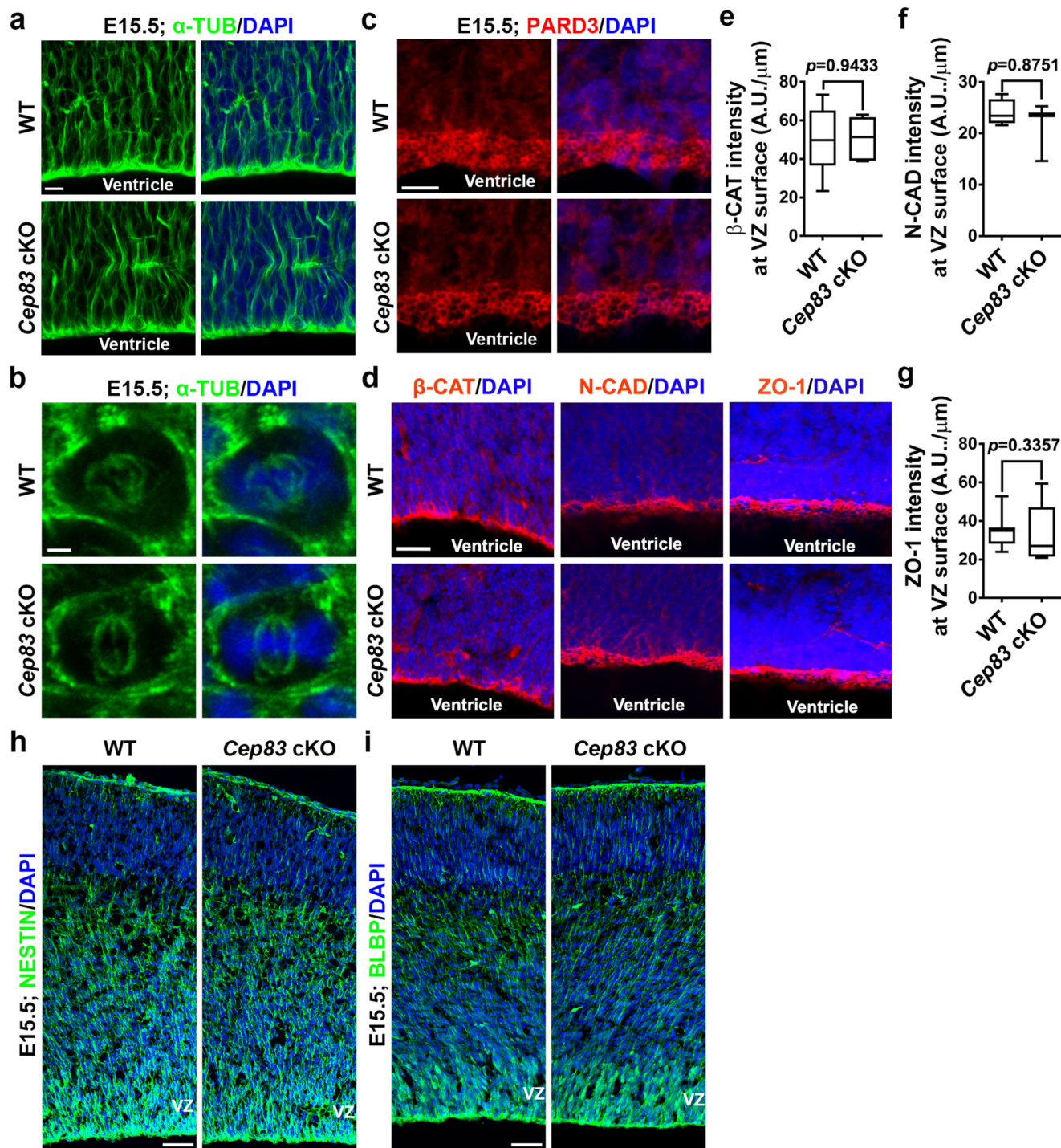


Extended Data Fig. 7 | See next page for caption.

**Extended Data Fig. 7 | Disruption of other components of the DAP assembly pathway leads to the overproduction of RGP and intermediate progenitor cells.** **a**, Diagram of the hierarchical DAP assembly pathway. **b–d**, Western blot assays to show the efficacy of shRNAs against *Cep83* (**b**), *Cep89* (**c**) or *Scrl1* (**d**) in suppressing protein expression ( $n = 3$ ). **e**, Representative images of E16.5 cortices that received in utero electroporation of EGFP (green) together with shRNAs against *Cep83* or against *Cep89* and *Scrl1* at E13.5. Cortices were stained for PAX6 (red, top) and TBR2 (red, bottom), and with DAPI (blue). Note that expression of *Cep83* shRNA-a (which effectively suppresses protein expression), but not that of *Cep83* shRNA-c (which does not suppress protein expression), leads to a significant increase in both PAX6<sup>+</sup> RGP in the ventricular zone and TBR2<sup>+</sup> intermediate progenitor cells in the subventricular zone. Moreover, expression of *Cep89* shRNA-c and *Scrl1* shRNA-c (which effectively suppress protein expression), but not that of *Cep89* shRNA-b and *Scrl1* shRNA-b (neither of which suppresses protein expression), results in a

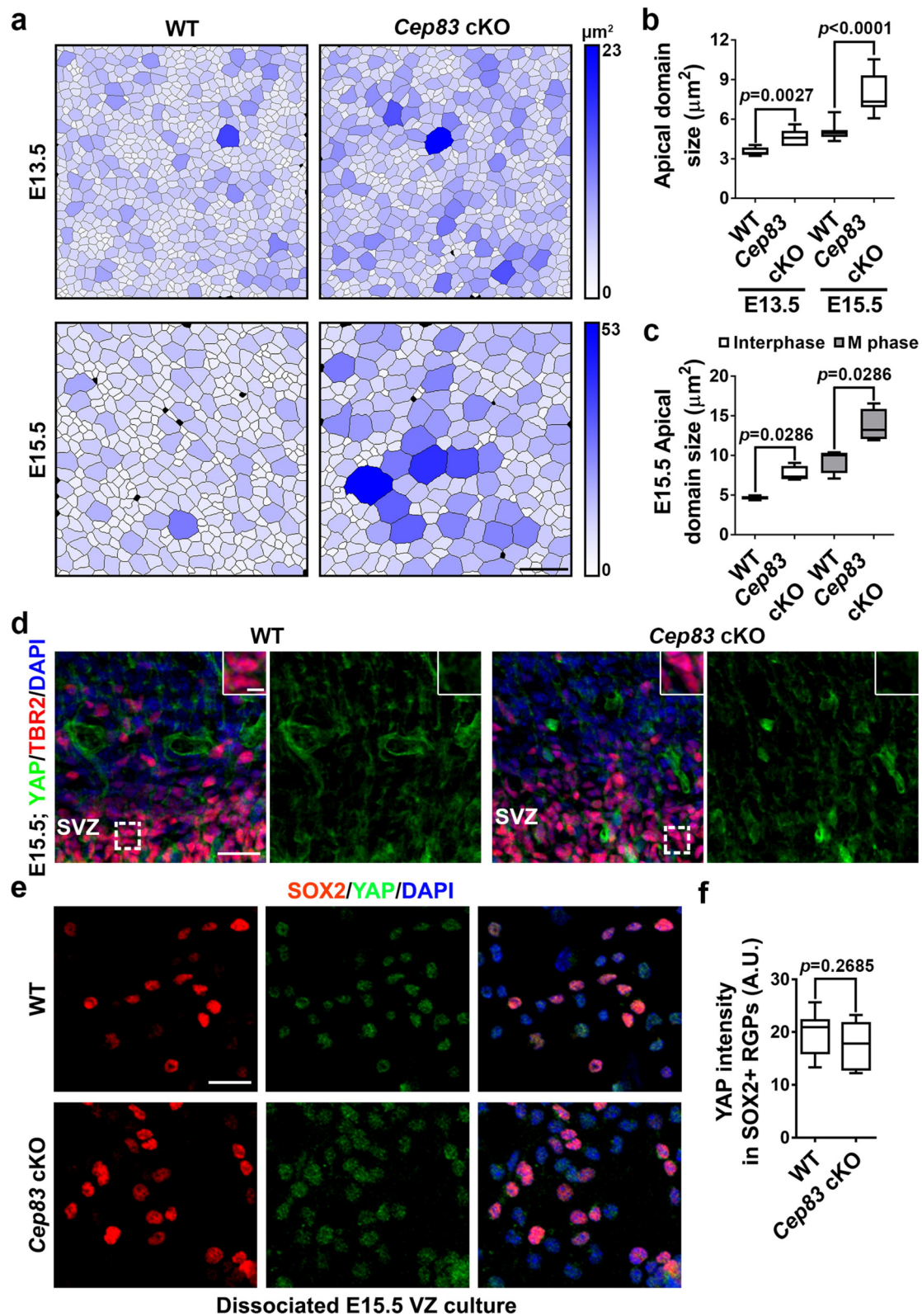
similar increase in both PAX6<sup>+</sup> RGP and TBR2<sup>+</sup> intermediate progenitor cells. Scale bars, 100  $\mu$ m. **f, g**, Quantification of the percentage of EGFP<sup>+</sup> cells that are PAX6<sup>+</sup> (**f**) or TBR2<sup>+</sup> (**g**). Note that similar to the *Cep83* cKO, expression of *Cep83* shRNA-a and *Cep89* and *Scrl1* shRNA-c—but not that of *Cep83* shRNA-c or *Cep89* and *Scrl1* shRNA-b—leads to a significant increase in PAX6<sup>+</sup> RGP and TBR2<sup>+</sup> intermediate progenitor cells, indicating that disruption of other DAP components causes excessive production of RGP and intermediate progenitor cells in a similar manner to the removal of CEP83 (control,  $n = 4$  brains (**f**) and 5 brains (**g**); *Cep83* shRNA-a,  $n = 5$  brains; *Cep89* and *Scrl1* shRNA-c,  $n = 4$  brains; *Cep83* shRNA-c,  $n = 6$  brains; *Cep89* and *Scrl1* shRNA-b,  $n = 4$  brains). **h**, Quantification of the percentage of EGFP<sup>+</sup> cells in different cortical regions (control,  $n = 5$  brains; *Cep83* shRNA-a,  $n = 5$  brains; *Cep89* and *Scrl1* shRNA-c,  $n = 4$  brains; *Cep83* shRNA-c,  $n = 7$  brains; *Cep89* and *Scrl1* shRNA-b,  $n = 5$  brains). A two-sided Mann–Whitney  $U$  test was used for statistical analysis. Bar charts show mean  $\pm$  s.e.m. Box plots as in Fig. 1.





**Extended Data Fig. 8 | Detachment of the centrosome from the apical membrane does not disrupt RGP polarity, junction formation or radial glial fibre scaffolding.** **a**, Representative images of E15.5 wild-type and *Cep83*cKO cortices in coronal sections stained for  $\alpha$ -tubulin ( $\alpha$ -TUB; green), and with DAPI (blue) ( $n=3$ ). Note that there is no obvious difference in non-apical membrane microtubules between the wild-type and *Cep83*cKO cortices. Scale bar, 10  $\mu$ m. **b**, Representative en face images of mitotic RGPs in E15.5 wild-type and *Cep83*cKO cortices stained for  $\alpha$ -tubulin (green), and with DAPI (blue) ( $n=12$ ). Note that there is no obvious difference in microtubule spindles between the wild-type and *Cep83*cKO RGPs. Scale bar, 2  $\mu$ m. **c**, Representative images of E15.5 wild-type and *Cep83*cKO cortices stained for partitioning defective

protein 3 (PARD3; red), an evolutionarily conserved polarity protein, and with DAPI (blue) ( $n=3$ ). Scale bar, 10  $\mu$ m. **d**, Representative images of E15.5 wild-type and *Cep83*cKO cortices stained for three junction markers ( $\beta$ -catenin ( $\beta$ -CAT; left), N-cadherin (N-CAD; middle) or ZO-1 (right)) (red), and with DAPI (blue). Scale bar, 50  $\mu$ m. **e-g**, Quantification of the staining intensity of  $\beta$ -catenin (**e**; wild type,  $n=8$  brains; *Cep83*cKO,  $n=5$  brains), N-cadherin (**f**; wild type,  $n=4$  brains; *Cep83*cKO,  $n=3$  brains) or ZO-1 (**g**; wild type,  $n=8$  brains; *Cep83*cKO,  $n=7$  brains) at the ventricular zone surface. **h, i**, Representative images of E15.5 wild-type and *Cep83*cKO cortices stained for nestin (**h**) or BLBP (**i**) (green), and with DAPI (blue) ( $n=5$ ). Scale bars, 50  $\mu$ m. A two-sided Mann-Whitney *U* test was used for statistical analysis. Box plots as in Fig. 1.



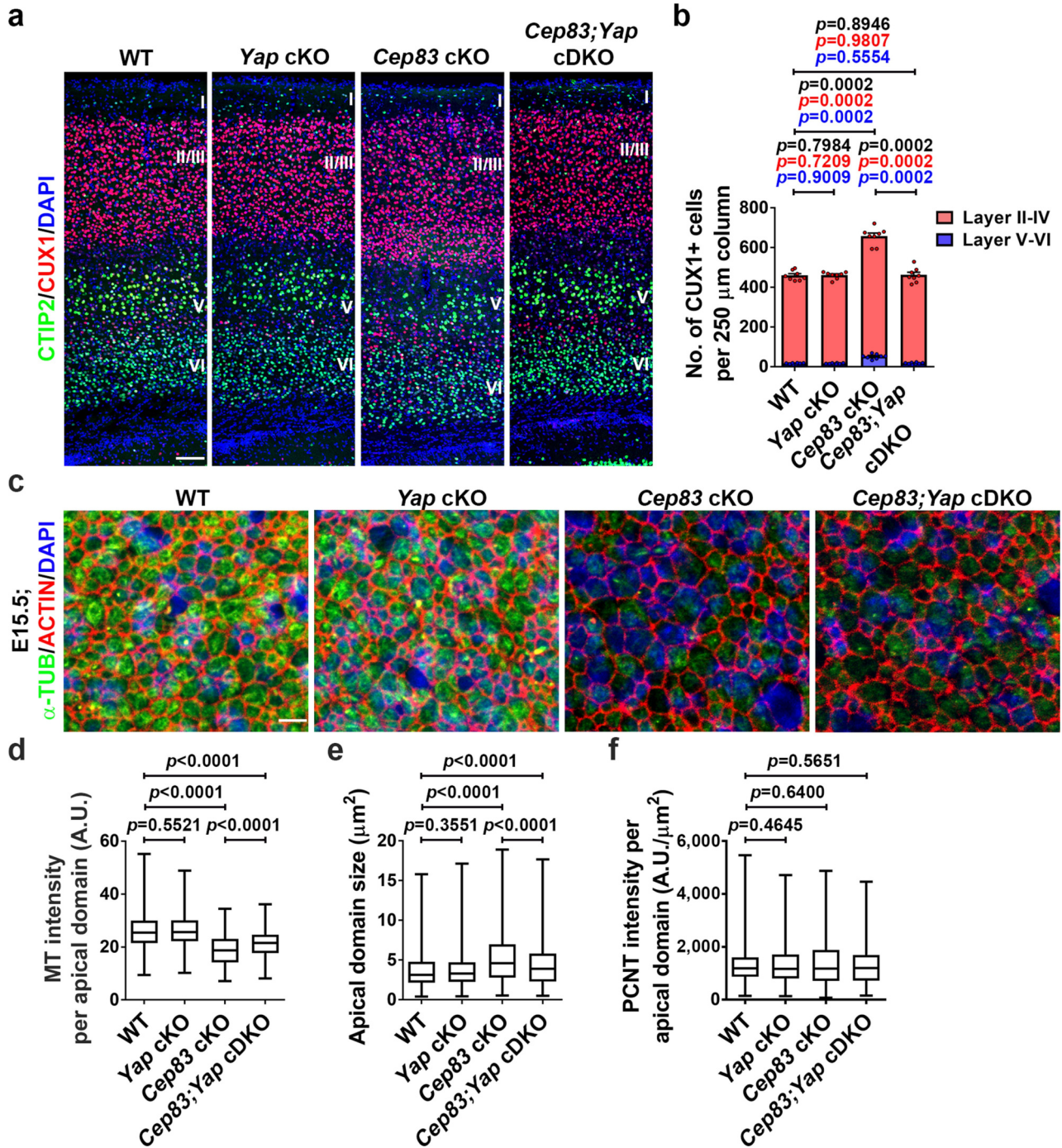
Extended Data Fig. 9 | See next page for caption.

**Extended Data Fig. 9 | Centrosome detachment leads to enlargement of the apical membrane, and nuclear expression of YAP is low in TBR2<sup>+</sup> intermediate progenitor cells and dissociated RGP in culture.**

**a**, Representative en face segmented images of wild-type and *Cep83cKO* ventricular zone surface at E13.5 and E15.5. Each apical domain is colour-coded on the basis of its size: blue colour indicates an apical domain that is relatively larger. Scale bar, 10  $\mu$ m. **b**, Quantification of the size of the apical domain of wild-type and *Cep83cKO* RGP at E13.5 and E15.5 (E13.5: wild type,  $n = 5,038$  apical domains from 8 embryos; *Cep83cKO*,  $n = 2,891$  apical domains from 6 embryos; E15.5: wild type,  $n = 4,780$  apical domains from 12 embryos; *Cep83cKO*,  $n = 1,959$  apical domains from 8 embryos). **c**, Quantification of the size of the apical domain of interphase and mitotic wild-type and *Cep83cKO* RGP at E15.5 (wild type,  $n = 1,703$  interphase apical domains and  $n = 145$  mitotic

apical domains from 4 embryos; *Cep83cKO*,  $n = 988$  interphase apical domains and  $n = 83$  mitotic apical domains from 4 embryos). **d**, Representative images of the subventricular zone of E15.5 wild-type and *Cep83cKO* cortices stained for YAP (green) and TBR2 (red), and with DAPI (blue) ( $n = 5$ ). Individual TBR2<sup>+</sup> intermediate progenitor cells are shown in the insets. Note the low expression of YAP in the nuclei of TBR2<sup>+</sup> intermediate progenitor cells in the subventricular zone of the wild-type and *Cep83cKO* cortices. Scale bars, 50  $\mu$ m (main image); 5  $\mu$ m (inset). **e**, Representative images of acutely dissociated cell cultures of E15.5 wild-type and *Cep83cKO* cortical ventricular zone stained for SOX2 (red) and YAP (green), and with DAPI (blue). Scale bar, 20  $\mu$ m. **f**, Quantification of the YAP staining intensity in SOX2<sup>+</sup> RGP (wild type,  $n = 13$  brains; *Cep83cKO*,  $n = 8$  brains). A two-sided Mann–Whitney  $U$  test was used for statistical analysis. Box plots as in Fig. 1.





**Extended Data Fig. 10 | Excessive neurogenesis in the *Cep83*cKO cortex depends on excessive expression and activation of YAP.** **a**, Representative high-magnification images of P21 wild-type, *Yap*cKO, *Cep83*cKO and *Cep83Yap*cDKO cortices stained for CTIP2 (green) and CUX1 (red), and with DAPI (blue). Scale bar, 100  $\mu\text{m}$ . **b**, Quantification of the number of CUX1<sup>+</sup> neurons per 250- $\mu\text{m}$  column ( $n=8$  brains for each genotype). **c**, Representative en face images of coronal sections of E15.5 wild-type, *Yap*cKO, *Cep83*cKO and *Cep83Yap*cDKO cortices stained for  $\alpha$ -tubulin (green) and actin (red), and with

DAPI (blue). Scale bar, 5  $\mu\text{m}$ . **d-f**, Quantification of the intensity of microtubules per apical domain (**d**), individual apical domain size (**e**) and the intensity of PCNT per apical domain (**f**) (wild type,  $n=1,730$  apical domains from 4 embryos; *Yap*cKO,  $n=1,074$  apical domains from 3 embryos, *Cep83*cKO,  $n=456$  apical domains from 3 embryos; *Cep83Yap*cDKO,  $n=540$  apical domains from 3 embryos). A two-sided Mann-Whitney *U* test was used for statistical analysis. Bar charts show mean  $\pm$  s.e.m. Box plots as in Fig. 1.

## Reporting Summary

Nature Research wishes to improve the reproducibility of the work that we publish. This form provides structure for consistency and transparency in reporting. For further information on Nature Research policies, see [Authors & Referees](#) and the [Editorial Policy Checklist](#).

### Statistics

For all statistical analyses, confirm that the following items are present in the figure legend, table legend, main text, or Methods section.

n/a Confirmed

- ☐ ☒ The exact sample size ( $n$ ) for each experimental group/condition, given as a discrete number and unit of measurement
- ☐ ☒ A statement on whether measurements were taken from distinct samples or whether the same sample was measured repeatedly
- ☐ ☒ The statistical test(s) used AND whether they are one- or two-sided  
*Only common tests should be described solely by name; describe more complex techniques in the Methods section.*
- ☐ ☒ A description of all covariates tested
- ☒ ☐ A description of any assumptions or corrections, such as tests of normality and adjustment for multiple comparisons
- ☐ ☒ A full description of the statistical parameters including central tendency (e.g. means) or other basic estimates (e.g. regression coefficient) AND variation (e.g. standard deviation) or associated estimates of uncertainty (e.g. confidence intervals)
- ☐ ☒ For null hypothesis testing, the test statistic (e.g.  $F$ ,  $t$ ,  $r$ ) with confidence intervals, effect sizes, degrees of freedom and  $P$  value noted  
*Give  $P$  values as exact values whenever suitable.*
- ☒ ☐ For Bayesian analysis, information on the choice of priors and Markov chain Monte Carlo settings
- ☒ ☐ For hierarchical and complex designs, identification of the appropriate level for tests and full reporting of outcomes
- ☐ ☒ Estimates of effect sizes (e.g. Cohen's  $d$ , Pearson's  $r$ ), indicating how they were calculated

*Our web collection on [statistics for biologists](#) contains articles on many of the points above.*

### Software and code

Policy information about [availability of computer code](#)

#### Data collection

FluoView (version 4.2, Olympus) and NDP viewer (version 2, Hamamatsu Photonics) were used for generating fluorescence image data. AMT (version 7.0.0.95) was used for generating electron microscopy data. MRtrix 3.1 and DtiStudio 3.0 (v2 10 6, <http://www.mristudio.org>) were used for generating MRI data. ZEN 2.1 (version 11.0) was used for generating bright-field images. Asylum Research Software (version 16) is used for generating atomic force microscopy data.

#### Data analysis

Volocity (version 6.3, PerkinElmer), ImageJ/Fiji (1.52, NIH) and its plugins (Tissue Analyzer and MorpholibJ, MATLAB (version 2016b, MathWorks) and Imaris (9.0.1, Oxford Instrument) were used for fluorescence image analysis. DTIStudio and DiffeoMap (v2 10 6, <http://www.mristudio.org>) were used for MRI data analysis. Prism (version 7, GraphPad) was used for statistical analysis. MATLAB (version R2016b, MathWorks) was used for generating segmented images of apical domains.

For manuscripts utilizing custom algorithms or software that are central to the research but not yet described in published literature, software must be made available to editors/reviewers. We strongly encourage code deposition in a community repository (e.g. GitHub). See the Nature Research [guidelines for submitting code & software](#) for further information.

### Data

Policy information about [availability of data](#)

All manuscripts must include a [data availability statement](#). This statement should provide the following information, where applicable:

- Accession codes, unique identifiers, or web links for publicly available datasets
- A list of figures that have associated raw data
- A description of any restrictions on data availability

The datasets generated during and/or analysed during the current study are available from the corresponding author on reasonable request.

## Field-specific reporting

Please select the one below that is the best fit for your research. If you are not sure, read the appropriate sections before making your selection.

☒ Life sciences ☐ Behavioural & social sciences ☐ Ecological, evolutionary & environmental sciences

For a reference copy of the document with all sections, see [nature.com/documents/nr-reporting-summary-flat.pdf](https://www.nature.com/documents/nr-reporting-summary-flat.pdf)

## Life sciences study design

All studies must disclose on these points even when the disclosure is negative.

Sample size	No sample-size calculations were performed. Sample size was determined to be adequate based on the magnitude and consistency of measurable differences between groups.
Data exclusions	Data were only excluded for failed experiments.
Replication	The numbers of times each experiment was repeated independently with similar results were provided in the figure legends.
Randomization	No randomization of samples was performed.
Blinding	Investigators were not blinded to mouse genotypes during experiments.

## Reporting for specific materials, systems and methods

We require information from authors about some types of materials, experimental systems and methods used in many studies. Here, indicate whether each material, system or method listed is relevant to your study. If you are not sure if a list item applies to your research, read the appropriate section before selecting a response.

### Materials & experimental systems

n/a	Involved in the study
<input type="checkbox"/>	<input checked="" type="checkbox"/> Antibodies
<input type="checkbox"/>	<input checked="" type="checkbox"/> Eukaryotic cell lines
<input checked="" type="checkbox"/>	<input type="checkbox"/> Palaeontology
<input type="checkbox"/>	<input checked="" type="checkbox"/> Animals and other organisms
<input checked="" type="checkbox"/>	<input type="checkbox"/> Human research participants
<input checked="" type="checkbox"/>	<input type="checkbox"/> Clinical data

### Methods

n/a	Involved in the study
<input checked="" type="checkbox"/>	<input type="checkbox"/> ChIP-seq
<input checked="" type="checkbox"/>	<input type="checkbox"/> Flow cytometry
<input type="checkbox"/>	<input checked="" type="checkbox"/> MRI-based neuroimaging

## Antibodies

Antibodies used	The supplier name, catalog number, lot number, dilution for all the antibodies were provided in the Methods.
Validation	All the primary antibodies used in the study have been used and validated in the previous studies. The antibody registry ID (RRID) for each primary antibody was provided in the Methods.

## Eukaryotic cell lines

Policy information about [cell lines](#)

Cell line source(s)	Rockefeller University Gene Targeting Resource Centre - W4 mouse embryonic stem (ES) cell line of 129S6 background
Authentication	The authors did not authenticate the referred cell line.
Mycoplasma contamination	The authors did not test mycoplasma contamination.
Commonly misidentified lines (See <a href="#">ICLAC</a> register)	Mouse embryonic stem cell

## Animals and other organisms

Policy information about [studies involving animals](#); [ARRIVE guidelines](#) recommended for reporting animal research

Laboratory animals	The following mouse strains including Cep83fl/fl, Actin-Flp (Jax#005703), Emx1-Cre (Jax#005628), Ift88fl/fl, R26-LSL-SmoM2, and Yapfl/fl were used. Both male and female mice were analysed at embryonic or postnatal stages.
Wild animals	No wild animal was used.

Field-collected samples

No field-collected sample was used.

Ethics oversight

All animal procedures were approved by the Institutional Animal Care and Use Committee (IACUC) of the Memorial Sloan Kettering Cancer Center, New York USA and Tsinghua University, Beijing China.

Note that full information on the approval of the study protocol must also be provided in the manuscript.

## Magnetic resonance imaging

### Experimental design

Design type

Post-mortem diffusion MRI/structural MRI

Design specifications

No stimulation block needed

Behavioral performance measures

No behavioral performance

### Acquisition

Imaging type(s)

Diffusion and structural MRI

Field strength

7 Tesla

Sequence &amp; imaging parameters

Gradient and spin echo (GRASE) acquisition, TE = 35 ms, TR = 400 ms, resolution = 0.1 mm x 0.1 mm x 0.1 mm

Area of acquisition

Whole brain

Diffusion MRI



Used



Not used

Parameters 30 diffusion encoding directions, b=2000 s/mm<sup>2</sup>

### Preprocessing

Preprocessing software

MRtrix 3.1, DtiStudio 3.0

Normalization

Images were normalized using the large deformation diffeomorphic metric mapping (LDDMM) implemented in the Diffeomap software ([www.mristudio.org](http://www.mristudio.org))

Normalization template

A template was selected from the control group in this case.

Noise and artifact removal

No noise or artifact removal

Volume censoring

No volume censoring

### Statistical modeling & inference

Model type and settings

No model type and settings

Effect(s) tested

No effect tested

Specify type of analysis:



Whole brain



ROI-based



Both

Statistic type for inference  
(See [Eklund et al. 2016](#))

Voxel-wise comparison

Correction

False discovery rate less than 0.05

### Models & analysis

n/a

Involved in the study



Functional and/or effective connectivity



Graph analysis



Multivariate modeling or predictive analysis

# In vitro characterization of the human segmentation clock

<https://doi.org/10.1038/s41586-019-1885-9>

Received: 13 July 2018

Accepted: 5 November 2019

Published online: 8 January 2020

Margarete Diaz-Cuadros<sup>1,2,9</sup>, Daniel E. Wagner<sup>3,9</sup>, Christoph Budjan<sup>1,2</sup>, Alexis Hubaud<sup>1,2</sup>, Oscar A. Tarazona<sup>1,2</sup>, Sophia Donnelly<sup>1,2</sup>, Arthur Michaut<sup>1,2</sup>, Ziad Al Tanoury<sup>1,2</sup>, Kumiko Yoshioka-Kobayashi<sup>4</sup>, Yusuke Niino<sup>5</sup>, Ryoichiro Kageyama<sup>4</sup>, Atsushi Miyawaki<sup>5</sup>, Jonathan Touboul<sup>6,7</sup> & Olivier Pourquie<sup>1,2,8\*</sup>

The segmental organization of the vertebral column is established early in embryogenesis, when pairs of somites are rhythmically produced by the presomitic mesoderm (PSM). The tempo of somite formation is controlled by a molecular oscillator known as the segmentation clock<sup>1,2</sup>. Although this oscillator has been well-characterized in model organisms<sup>1,2</sup>, whether a similar oscillator exists in humans remains unknown. Genetic analyses of patients with severe spine segmentation defects have implicated several human orthologues of cyclic genes that are associated with the mouse segmentation clock, suggesting that this oscillator might be conserved in humans<sup>3</sup>. Here we show that human PSM cells derived in vitro—as well as those of the mouse<sup>4</sup>—recapitulate the oscillations of the segmentation clock. Human PSM cells oscillate with a period two times longer than that of mouse cells (5 h versus 2.5 h), but are similarly regulated by FGF, WNT, Notch and YAP signalling<sup>5</sup>. Single-cell RNA sequencing reveals that mouse and human PSM cells in vitro follow a developmental trajectory similar to that of mouse PSM in vivo. Furthermore, we demonstrate that FGF signalling controls the phase and period of oscillations, expanding the role of this pathway beyond its classical interpretation in ‘clock and wavefront’ models<sup>1</sup>. Our work identifying the human segmentation clock represents an important milestone in understanding human developmental biology.

In the mouse, the early stages of paraxial mesoderm development can be recapitulated in vitro from mouse embryonic stem (ES) cells by first inducing an epiblast fate with activin A and FGF, followed by culture in medium containing the WNT agonist CHIRON99021 (Chir) and the BMP inhibitor LDN193189 (LDN) (Chir–LDN medium; hereafter, CL medium)<sup>4,6</sup> (Fig. 1a, Extended Data Fig. 1a–c). After 24 h in CL medium, epiblast-like cells acquire a neuromesodermal progenitor<sup>7,8</sup> or anterior primitive streak fate, expressing *T* (also known as *Brachyury*), *Sox2* and *Pou5f1* (also known as *Oct4*) (Fig. 1a, Extended Data Fig. 1b, c). By 48 h, cells activate the PSM markers *Tbx6* and *Msx1* (Fig. 1a, Extended Data Fig. 1b–e). This transition to PSM is paralleled by an epithelium-to-mesenchyme transition, marked by a switch from *Cdh1* to *Cdh2* (Extended Data Fig. 1b).

To further characterize the identity of these mouse PSM cells generated in vitro, we benchmarked their transcriptomes against the embryonic mouse PSM. Using single-cell RNA sequencing (scRNA-seq)<sup>9</sup>, we analysed 5,646 cells dissociated from the posterior region of two mouse embryos at embryonic day (E)9.5. Clustering analysis revealed 21 distinct cell states that correspond to expected derivatives of all three germ layers (Extended Data Fig. 2a–d, Supplementary Table 1). Transcriptomes of paraxial mesoderm and neural tube cells, which share a common developmental origin<sup>7,10</sup>, were represented as

a *k*-nearest neighbour (*k*-NN) graph (Fig. 2a). Genes that were differentially expressed between cell clusters (Extended Data Fig. 3a–d) and along a pseudotemporal trajectory (Fig. 2b, Supplementary Table 2) stratified distinct phases of paraxial mesoderm differentiation as follows. One cluster, which coexpressed *Sox2* and *T*, represented neuromesodermal progenitors and was positioned between the posterior neural tube and paraxial mesoderm clusters, consistent with the known bipotentiality of these cells<sup>7</sup>. Two clusters that expressed *T*, *Rspo3*, *Tbx6*, *Dll3* and *Foxc1* represented mesodermal precursor cells<sup>11</sup> and the more-mature posterior PSM. These two clusters also express the Notch-pathway genes *Hes7*, *Lfng*, *Dll1* and *Dll3* (Extended Data Fig. 3c–e), and probably correspond to the in vivo oscillatory domain. The next cluster corresponds to the anterior PSM, which is marked by expression of *Mesp1* and *Ripply2* (Fig. 2b).

We compared the transcriptomes of these in vivo cell states of the E9.5 mouse to those of 21,478 mouse ES cells differentiated in vitro. Clustering analyses indicated the rapid differentiation of mouse ES cells over the first three days, with each time point largely dominated by a single cluster: naive ES cells (day 0), epiblast (day 2) and neuromesodermal progenitors or anterior primitive streak (day 3), followed by asynchronous transcriptional changes over the final two days (Fig. 2c, Extended Data Fig. 3f, g). A substantial proportion of the differentiating mouse

<sup>1</sup>Department of Genetics, Harvard Medical School, Boston, MA, USA. <sup>2</sup>Department of Pathology, Brigham and Women's Hospital, Boston, MA, USA. <sup>3</sup>Department of Systems Biology, Harvard Medical School, Boston, MA, USA. <sup>4</sup>Institute for Frontier Life and Medical Sciences, Kyoto University, Kyoto, Japan. <sup>5</sup>Laboratory for Cell Function and Dynamics, RIKEN Center for Brain Science, Saitama, Japan. <sup>6</sup>Department of Mathematics, Brandeis University, Waltham, MA, USA. <sup>7</sup>Volen National Center for Complex Systems, Brandeis University, Waltham, MA, USA. <sup>8</sup>Harvard Stem Cell Institute, Harvard University, Cambridge, MA, USA. <sup>9</sup>These authors contributed equally: Margarete Diaz-Cuadros, Daniel E. Wagner. \*e-mail: pourquie@genetics.med.harvard.edu



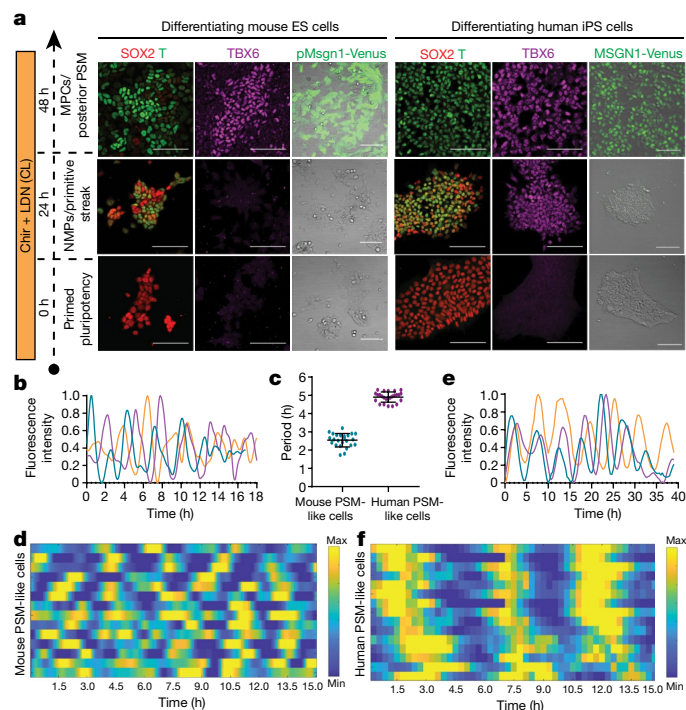


**Fig. 1 | Recapitulation of the mouse and human segmentation clocks in vitro by differentiation of pluripotent stem cells towards PSM fate. a**, Immunofluorescence for stage-specific markers (left) and images of the mouse ES cell *pMsn1-Venus* reporter or human iPS cell *MSGN1-Venus* reporter (right) in differentiating mouse and human pluripotent stem cells. Scale bar, 100  $\mu$ m.  $n = 7$  independent experiments. MPCs, mesodermal precursor cells; NMPs, neuromesodermal progenitors. **b**, Normalized HES7-Achilles intensity profiles for three PSM cells derived from mouse ES cells, imaged in CLFBR medium.  $n = 17$  independent experiments. Normalized fluorescence intensity is expressed in arbitrary units. **c**, Period of HES7-Achilles oscillations in PSM cells derived from mouse ES cells or human iPS cells, cultured in CLFBR medium. Mean  $\pm$  s.d.  $n = 25$  independent experiments. **d**, Heat map of HES7-Achilles intensity over time in PSM cells derived from mouse ES cells, in CLFBR medium. Each row represents one cell.  $n = 15$  cells. **e**, Normalized HES7-Achilles intensity profiles for three PSM cells derived from human iPS cells, imaged in CLFBR medium.  $n = 23$  independent experiments. **f**, Heat map of HES7-Achilles intensity over time in PSM cells derived from human iPS cells, in CLFBR medium. Each row represents one cell.  $n = 15$  cells.

ES cells adopted a fate trajectory similar to that of the cells in vivo, by progressively expressing *Sox2*, *T*, *Rspo3*, *Tbx6*, *Dll3* and *Foxc1* (Fig. 2d, Extended Data Fig. 3h–j). Approximately 46% of differentiating mouse ES cells ultimately adopted a state similar to that of the posterior PSM (Fig. 2c, Extended Data Fig. 3g).

We trained a *k*-NN classifier on the transcriptional signatures of the cell clusters of the E9.5 mouse, and used it to assign identities to individual cells derived from mouse ES cells on days 4 and 5 of differentiation. An identity similar to that of the posterior PSM cells of the E9.5 mouse was the most abundantly classified state within cells of the posterior PSM cluster of mouse ES cells at days 4 and 5 (Fig. 2g). States classified as posterior PSM in the E9.5 mouse were enriched amongst the posterior PSM branch of the *k*-NN graph of mouse ES cells at days 4 and 5 (Fig. 2h), and similar enrichments were observed using three classification algorithms (Extended Data Fig. 4a). We also detected a collinear trend in the expression of Hox genes during the differentiation of mouse ES cells (Extended Data Fig. 4b). Together, these results suggest a broad transcriptional similarity between paraxial mesoderm cells derived from mouse ES cells and their in vivo counterparts.

Oscillations of a *Hes7-luciferase* reporter in PSM cells differentiated from mouse ES cells in 3D cultures have recently been reported<sup>12</sup>.

To visualize oscillations of the segmentation clock in two dimensions, we generated a mouse ES cell reporter line in which a destabilized version of the yellow fluorescent protein variant *Achilles* was knocked in the 3' end of the *Hes7* gene<sup>13</sup> (Extended Data Fig. 1g). When differentiated towards PSM, a subset of cells showed oscillatory expression of the *Hes7-Achilles* gene, with a period of  $2.5 \pm 0.4$  h ( $n = 25$  independent experiments)—similar to the period of the segmentation clock in mouse embryos<sup>14,15</sup> (Fig. 1b–d, Extended Data Fig. 1h–i, Supplementary Video 1). This oscillatory state could be extended by adding FGF4, the retinoic acid inhibitor BMS493 and the Rho kinase inhibitor (ROCKi) Y-27362 to the CL medium (hereafter, CLFBR medium) (CL medium,  $45 \pm 6.6$  h ( $n = 8$  independent experiments) versus CLFBR medium,  $61.2 \pm 5.7$  h ( $n = 12$  independent experiments)) (Extended Data Fig. 1j, k). Therefore, PSM cells differentiated from ES cells in vitro can reliably model the segmentation clock.

We next implemented a similar in vitro strategy to identify the human oscillator. Human induced pluripotent stem (iPS) cells differentiated in CL medium acquire a neuromesodermal progenitor or anterior primitive streak fate, characterized by *T* (also known as *TBX1*) and *SOX2* expression, after 24 h (Fig. 1a), and a PSM fate marked by *MSGN1* and *TBX6* expression after 48 h (Fig. 1a, Extended Data Fig. 1f). A CDH1-to-CDH2 switch is also observed, as in mouse ES cells (Extended Data Fig. 1b). The induction efficiency of human cells carrying a *MSGN1-Venus* knock-in reporter was markedly high compared to that in mouse, reaching  $92.6 \pm 1.5\%$  ( $n = 8$  independent experiments) (Extended Data Fig. 1d, e, Supplementary Video 2).

We compared 14,750 differentiating human iPS cells analysed by scRNA-seq to the in vivo and in vitro mouse-cell states. Early collection time points clustered uniformly and sequentially along the *k*-NN graph, whereas the final two time points displayed continuous and overlapping transcriptional features (Extended Data Fig. 3k, l). Differential gene expression and pseudotemporal ordering analyses revealed shared molecular characteristics between the human clusters and both the in vivo and in vitro mouse PSM lineages (Fig. 2e, f, Extended Data Fig. 3m–o). Cells collected after 1 day exhibited characteristics of neuromesodermal progenitors or anterior primitive streak cells, showing expression of *NODAL*, *T*, *MIXL1* and *SOX2*. By day 2, human cells resembled the mouse mesodermal precursor cell and posterior PSM clusters, showing expression of *T*, *MSGN1*, *TBX6*, *DLL3*, *WNT3A* and *FGF17*, as well as the Notch-associated cyclic genes *LFNG* and *HES7*. At days 3 and 4, cells show the expression of markers of anterior PSM, such as *FOXC1* (Fig. 2f, Extended Data Fig. 3n, o). Machine-learning classifiers trained on the mouse embryonic cell states consistently assigned an identity similar to that of the posterior PSM cluster of E9.5 mouse to clusters of human iPS cells on days 2–4 (Fig. 2g, h, Extended Data Fig. 4c). We detected collinear activation of HOX gene clusters, beginning with *HOXA1* and *HOXA3* on day 1 and culminating with *HOXB9* and *HOXC8* on day 4 (Extended Data Fig. 4d). Thus, the differentiation of human iPS cells to a PSM fate in vitro in CL medium recapitulates a developmental sequence similar to that of the mouse embryo, leading to the production of trunk paraxial mesoderm cells.

To assess whether PSM cells derived from human iPS cells exhibit segmentation clock oscillations, we generated a *HES7-Achilles* iPS cell reporter cell line (Extended Data Fig. 1g). After 48 h in CL medium, most cells started to show reporter oscillations with a mean period of  $4.9 \pm 0.3$  h ( $n = 25$  independent experiments) and constant frequency (Fig. 1c, e, f, Extended Data Fig. 1l–p, Supplementary Videos 3, 4). No oscillations could be detected when LDN was omitted, consistent with the need for BMP4 inhibition to induce the paraxial mesoderm fate<sup>16</sup> (Extended Data Fig. 1q). The total number of oscillations observed could be approximately doubled by culturing in CLFBR medium (CL medium  $4.7 \pm 0.8$  oscillations versus CLFBR medium  $10.2 \pm 1.6$  oscillations ( $n = 15$  independent experiments)) (Extended Data Fig. 1r, s). These experiments support the existence of a human segmentation clock that ticks with an approximately 5-h period.

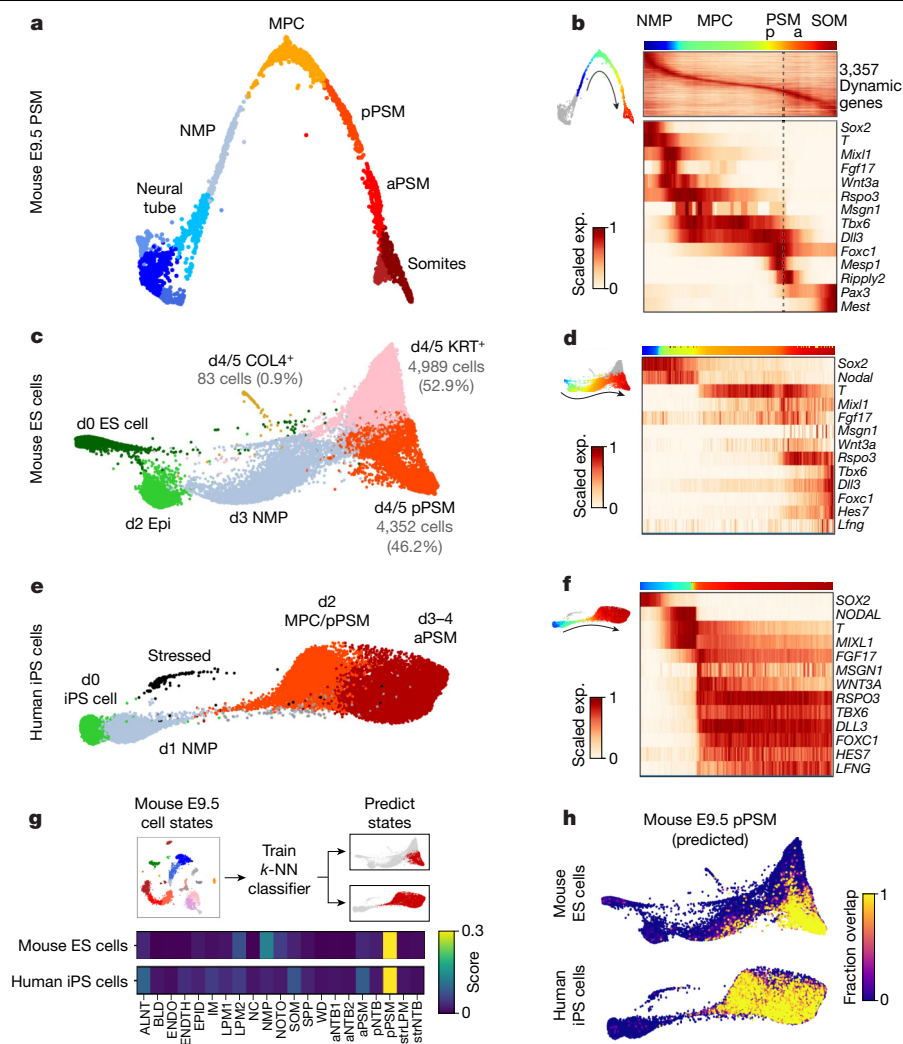


**Fig. 2 | scRNA-seq analysis of differentiating mouse and human PSM. a**, *k*-NN graph of mouse neural tube, PSM and somite clusters at E9.5 (2,340 cells, 20 principal component dimensions), visualized with ForceAtlas2 and coloured using Louvain cluster identities. p, posterior; a, anterior. **b**, Pseudotemporal ordering of non-neural cells at E9.5. Heat maps illustrate genes with significant dynamic expression (exp.) ordered by peak expression (Methods), and selected markers of paraxial mesoderm differentiation. Colour bars indicate pseudotemporal position with approximate locations of Louvain cluster centres indicated. Dotted line marks the determination front (the boundary between the anterior and posterior PSM). SOM, somite. **c**, Batched-balanced *k*-NN graph of single-cell transcriptomes of mouse ES cells (21,478 cells), coloured by Louvain cluster identity and visualized with ForceAtlas2. Cell numbers for the three terminal day-4 and day-5 states are indicated. Epi, epiblast. **d**, Pseudotemporal ordering of mouse ES cells along a path towards

the putative PSM state at days 4 and 5. The heat map shows selected markers of paraxial mesoderm differentiation. **e**, Batched-balanced *k*-NN graph (ForceAtlas2 layout) of single-cell transcriptomes of human iPS cells (14,750 cells), coloured by Louvain cluster identities. **f**, Pseudotemporal ordering of human iPS cells along a path towards the terminal PSM state at days 3 and 4. The heat map shows selected markers of paraxial mesoderm differentiation. **g**, Machine-learning classification of human and mouse in vitro cultured cells. A *k*-NN classifier trained on clusters of the E9.5 mouse was used to predict identities of terminal in vitro states (inset, red cells). The heat maps depict the fraction of E9.5 assignments for mouse ES cells at day 4 and 5 and human iPS cells at days 2–4. **h**, Overlay of *k*-NN classifier scores (fraction of nearest neighbours with the posterior PSM label of the E9.5 mouse) onto the mouse ES cell and human iPS cell *k*-NN graphs.

A characteristic property of the segmentation-clock oscillations in vivo is their high local synchrony<sup>1,2</sup>. Synchronization of oscillations appears to be recapitulated in vitro in human, but not mouse, PSM cells (Fig. 1d, f). To track individual PSM cells derived from human iPS cells, we diluted *HES7*-*Achilles* reporter cells that express a nuclear label (pCAG-H2B-mCherry) in an excess of unlabelled cells (Fig. 3a, Extended Data Fig. 5a, Supplementary Video 5). The average diffusion of cells in vitro ( $2.4 \pm 2.2$  square micrometres per minute) (Extended Data Fig. 5b) was comparable to that of chicken-embryo PSM cells in vivo ( $0.5$ – $8$  square micrometres per minute)<sup>17</sup>. Analysis of the phase of individual oscillators did not reveal any spatial structure, arguing against the existence of travelling waves in these cultures (Extended

Data Fig. 5c, Supplementary Video 6). Tracking large numbers of cells enabled us to assess quantitatively the degree of global synchrony using the Kuramoto order parameter<sup>18</sup>. This analysis confirmed that cells oscillate in synchrony, as the order parameter was significantly higher relative to a model with randomized phases ( $0.43 \pm 0.15$  versus  $0.094 \pm 0.09$ , paired two-sided *t*-test  $P = 5 \times 10^{-107}$  ( $n = 139$  cells)) (Fig. 3b, c, Extended Data Fig. 5d–f).

The Kuramoto order parameter decreased over time, indicating a progressive decay of synchrony (Fig. 3c, Extended Data Fig. 5d, f). This prompted us to explore cell division as a potential source of increasing noise over time. Cell division was not temporally coordinated between cells—roughly 5% of cells were in M phase at any given point



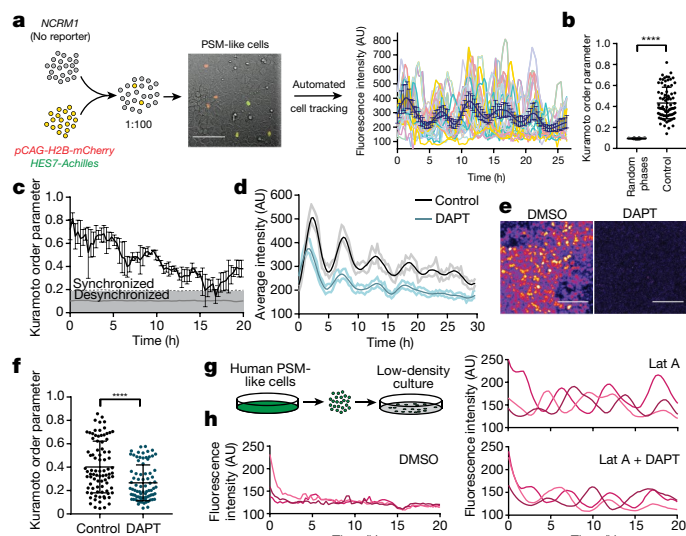


**Fig. 3 | Synchronization of individual oscillators within human PSM cultures.** **a**, Experimental strategy for automated tracking of HES7-Achilles oscillations in individual cells. Scale bar, 100  $\mu$ m. AU, arbitrary units. **b**, Kuramoto order parameter for HES7-Achilles cells versus the same dataset with randomized phases. Mean  $\pm$  s.d. Paired two-sided *t*-test,  $P = 5 \times 10^{-107}$ .  $n = 139$  cells. **c**, Kuramoto order parameter time course of HES7-Achilles human PSM cells. Synchronization threshold shown as mean  $\pm$  s.d. of the Kuramoto order parameter for same dataset, but with randomized phases.  $n = 139$  cells. **d**, Average intensity profiles for individual HES7-Achilles human PSM cells treated with vehicle control (DMSO) or 25  $\mu$ M DAPT. Mean  $\pm$  95% confidence interval.  $n = 152$  cells (control) or 106 cells (DAPT). **e**, HES7-Achilles fluorescence in human PSM cells following treatment with DMSO or DAPT (25  $\mu$ M).  $n = 9$  independent experiments. Scale bar, 100  $\mu$ m. **f**, Kuramoto order parameter for HES7-Achilles cells treated with DMSO or 25  $\mu$ M DAPT. Mean  $\pm$  s.d. Paired two-sided *t*-test,  $P = 2.6 \times 10^{-18}$ .  $n = 131$  cells (control) or 110 cells (DAPT). **g**, Experimental strategy for analysis of oscillations in isolated human PSM cells. **h**, Representative HES7-Achilles intensity profiles for three isolated human PSM cells in medium containing DMSO, 350 nM latrunculin A (lat A), or 350 nM latrunculin A in combination with 25  $\mu$ M DAPT.  $n = 5$  independent experiments.

(Extended Data Fig. 5g, h). The cell-cycle time was  $22 \pm 3.6$  h ( $n = 26$  cells), indicating that division takes place on a time scale different to that of HES7 oscillations (Extended Data Fig. 5i). The ratio between cell-division time and clock period is the same as observed in vivo for chicken PSM<sup>19,20</sup>. The distribution of phases at mitosis was evenly spread, suggesting a lack of correlation between the phase of HES7-Achilles oscillation and cell division (Extended Data Fig. 5j). Inhibiting cell division with aphidicolin (Extended Data Fig. 5h) did not affect oscillations or order-parameter dynamics (control  $0.404 \pm 0.2065$  ( $n = 45$  cells) versus aphidicolin  $0.3465 \pm 0.1526$  ( $n = 48$  cells), paired two-sided *t* test,  $P = 0.348$ ) (Extended Data Fig. 5k–m). Thus, cell division is not an important source of noise for HES7-Achilles oscillations in human PSM cells in vitro.

Notch signalling has previously been implicated in the maintenance and local synchronization of oscillations<sup>5,21–23</sup>. Treating human and mouse HES7-Achilles cells with the Notch inhibitor DAPT (*N*-[*N*-(3,5-difluorophenacetyl)-L-alanyl]-S-phenylglycine *t*-butyl ester) in CLFBR medium led to a dampening of oscillations and eventual loss of HES7-Achilles expression (Fig. 3d, e, Extended Data Fig. 5n–p). Thus, HES7 oscillations require active Notch signalling. The Kuramoto order parameter was lower, and decreased more rapidly, in DAPT-treated cultures relative to control (control  $0.407 \pm 0.22$  ( $n = 131$  cells) versus DAPT-treated  $0.266 \pm 0.153$  ( $n = 110$  cells)  $P < 0.000001$ ) (Fig. 3f, Extended Data Fig. 5q). We conclude that synchronization of HES7-Achilles oscillations in PSM cultures derived from human iPS cells is Notch-dependent.

We further assessed whether YAP signalling regulates oscillations in human cells, as it does in mouse embryos<sup>5</sup>. No oscillations were detected when human PSM cells were cultured as isolated cells (Fig. 3g, h, Supplementary Video 7). However, treatment with latrunculin A—which inhibits YAP signalling<sup>24</sup>—restored oscillations (Fig. 3h, Extended Data Fig. 5r, Supplementary Video 7). Isolated cells treated with latrunculin A continued to oscillate even with DAPT treatment (Fig. 3h, Supplementary Video 7). We could not detect substantial enrichment of NOTCH1 intracellular domain binding at the HES7 or LFNG promoters in isolated cells by chromatin immunoprecipitation followed by quantitative PCR (ChIP–qPCR) (Extended Data Fig. 5s). Isolated cells treated with latrunculin A alone, or in combination with DAPT, showed the characteristic approximately 5-h period observed in confluent cultures, which suggests that the period is controlled autonomously and independently of Notch cleavage (Extended Data Fig. 5u). The Kuramoto order parameter was significantly lower than in confluent controls (control  $0.415 \pm 0.194$  ( $n = 53$  cells) versus latrunculin A treatment  $0.221 \pm 0.137$  ( $n = 18$  cells) versus treatment with latrunculin A and DAPT  $0.1972 \pm 0.095$  ( $n = 18$  cells)), which suggests that cell communication is required for the maintenance of synchrony (Extended Data Fig. 5v, w). Thus, the human segmentation clock—similar to its mouse counterpart<sup>4</sup>—can be viewed as an excitable system in which Notch provides the stimulus and YAP controls the excitability threshold.

In vivo, PSM cells experience posterior-to-anterior gradients of FGF and WNT signalling that control their maturation (Fig. 4a)<sup>1</sup>. In differentiating mouse and human cultures, staining for doubly phosphorylated ERK (dpERK) and  $\beta$ -catenin showed that the FGF and WNT pathways are active at the neuromesodermal progenitor and posterior PSM stages, but are strongly downregulated at later stages in CL medium (Fig. 4a). Treatment with the FGF receptor inhibitor PD173074 (PD17) decreased the dpERK signal (Extended Data Fig. 6a), indicating that ERK activation is FGF-dependent and most probably downstream of FGF8 and FGF17 (which are expressed by the cells) (Extended Data Fig. 6b). Thus, differentiating mouse and human cells are exposed to transient WNT and FGF signalling as in the posterior PSM in vivo (Fig. 4a). The regulation of FGF and WNT signalling in vitro is largely autonomous.

We next assessed the effect of prematurely downregulating FGF and WNT signalling on segmentation-clock oscillations in vitro. FGF signalling was inhibited by treating human PSM cells with PD17 or the MEK1 and MEK2 inhibitor PD0325901 (PD03), whereas WNT signalling was blocked using the tankyrase inhibitors XAV939 (XAV) or IWR-1 (Extended Data Fig. 6a, c–e). Both FGF and WNT inhibition resulted in dampening and eventual arrest of oscillations without affecting their period (Fig. 4b, c, Extended Data Fig. 6f–h). In the case of PD03, higher doses resulted in faster dampening and fewer oscillations before arrest (Fig. 4d, e, Extended Data Fig. 6i–l). Mouse HES7-Achilles cells responded similarly to FGF and WNT inhibitors (Extended Data Fig. 6m). Oscillations in human cells treated with FGF inhibitors—but not cells treated with WNT inhibitors—exhibited a phase shift relative to control cells, regardless of inhibitor dosage (Fig. 4f, Extended Data Fig. 6n, o). We could also detect this phase shift in Notch target gene oscillations upon FGF inhibition, using quantitative PCR with reverse transcription (qRT–PCR) for the HES7 and LFNG genes (Extended Data Fig. 6p, q). These data suggest that FGF functions to modulate oscillator properties in addition to controlling PSM maturation.

To further examine the role of FGF signalling on oscillatory properties, we used an ex vivo system that consists of micropatterned cultures of PSM explants taken from the mouse line LuVeLu (which expresses a *Lfng* transcriptional reporter)<sup>5</sup> (Extended Data Fig. 6r). Treating mouse cultures with increasing doses of FGF inhibitors led to a dose-dependent decrease in number of oscillations (Extended Data Fig. 6s, t). We observed a progressive increase in the period with increasing doses of inhibitor, as observed for *Lfng* oscillations during PSM maturation in vivo<sup>14</sup> (Extended Data Fig. 6u). Our data thus indicate that FGF activity

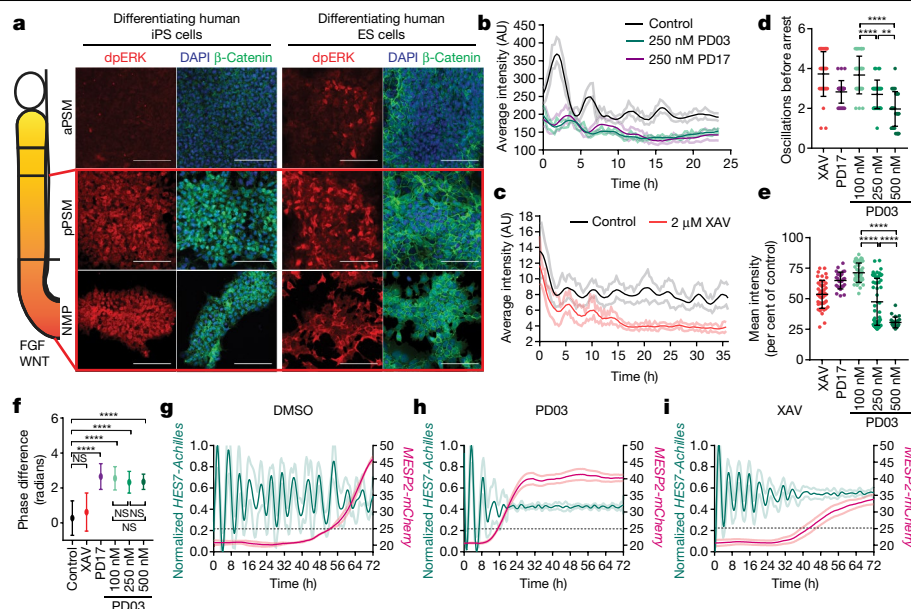


**Fig. 4 | FGF signalling regulates the dynamic properties of the segmentation clock.** **a**, Left, scheme illustrating the posterior-to-anterior gradients of FGF and WNT signalling along the PSM. Right, Immunofluorescence for dpERK,  $\beta$ -catenin and DAPI nuclear stain in differentiating human iPS cells and mouse ES cells.  $n = 8$  independent experiments. Scale bar, 100  $\mu\text{m}$ . **b**, Average intensity profiles for individual *HES7-Achilles* human PSM cells treated with vehicle control (DMSO), 250 nM PD03 or 250 nM PD17. Mean  $\pm$  95% confidence interval.  $n = 89$  cells (control), 30 cells (PD03) or 34 cells (PD17). **c**, Average intensity profiles for individual *HES7-Achilles* human PSM cells treated with vehicle control (DMSO) or 2  $\mu\text{M}$  XAV. Mean  $\pm$  95% confidence interval.  $n = 67$  cells (control) or 29 cells (XAV). **d**, Number of *HES7-Achilles* oscillations before arrest in individual human PSM cells treated with 2  $\mu\text{M}$  XAV, 250 nM PD17, or 100 nM, 250 nM or 500 nM PD03. Mean  $\pm$  s.d. One-way analysis of variance (ANOVA): 100 nM versus 250 nM,  $P = 2.3 \times 10^{-5}$ ; 100 nM versus 500 nM,  $P = 2.2 \times 10^{-10}$ ; 250 nM versus 500 nM,  $P = 1.5 \times 10^{-3}$ .  $n = 34$  cells per condition. **e**, Mean *HES7-Achilles* intensity for individual *HES7-Achilles* human PSM cells treated with 2  $\mu\text{M}$  XAV, 250 nM PD17, or 100 nM, 250 nM or 500 nM PD03.

Mean  $\pm$  s.d. One-way ANOVA: 100 nM versus 250 nM,  $P = 1.2 \times 10^{-13}$ ; 100 nM versus 500 nM,  $P = 3 \times 10^{-13}$ ; 250 nM versus 500 nM,  $P = 6.9 \times 10^{-6}$ .  $n = 46$  cells (XAV),  $n = 28$  cells (PD17),  $n = 47$  cells (100 nM PD03),  $n = 64$  cells (250 nM PD03),  $n = 26$  cells (500 nM PD03). **f**, Summary statistics comparing the instantaneous absolute phase difference relative to control for individual cells treated with vehicle control (DMSO), 2  $\mu\text{M}$  XAV, 250 nM PD17, or 100 nM, 250 nM or 500 nM PD03. Mean  $\pm$  s.d. One-way ANOVA: control versus XAV,  $P = 0.0578$ ; control versus PD17,  $P = 9.2 \times 10^{-8}$ ; control versus 100 nM PD03,  $P = 1.3 \times 10^{-14}$ ; control versus 250 nM PD03,  $P = 1.1 \times 10^{-8}$ ; control versus 500 nM PD03,  $P = 1.1 \times 10^{-5}$ ; 100 nM versus 250 nM PD03,  $P = 0.8338$ ; 100 nM versus 500 nM PD03,  $P = 0.0601$ ; 250 nM versus 500 nM PD03,  $P = 0.061$ . NS, not significant.  $n$  fixed at 11,000 observations. Full histograms are provided in Extended Data Fig. 6n. **g–i**, *HES7-Achilles* and *MESP2-mCherry* intensity profiles in small regions of interest within human PSM cultures. Mean  $\pm$  s.d. Dotted line denotes the threshold for *MESP2-mCherry* activation (25 AU). **g**, Vehicle control (DMSO). **h**, PD03 (250 nM). **i**, XAV (2  $\mu\text{M}$ ).  $n = 15$  replicate experiments.

regulates the dynamics (period, phase and amplitude) of cyclic gene oscillations and does not only control the oscillatory arrest at the wave-front, as proposed in classical models<sup>1,25</sup>.

In vivo in mouse and chicken embryos, cells at the determination front periodically activate *Mesp2* and *Ripply2* in a stripe that defines the boundaries of the future segment<sup>26</sup>. Using quantitative PCR, we observed that the arrest of *HES7-Achilles* oscillations in human cells coincided with *MESP2* and *RIPPLY2* expression, which could be delayed by culturing cells in CLFBR medium (Extended Data Fig. 1f, s). To image the transition from the oscillatory to the segmental fate, we generated a dual human iPS cell reporter line carrying a knock-in *MESP2-H2B-mCherry* reporter in addition to *HES7-Achilles*. When cultured in CLFBR medium, a series of approximately 12 oscillations was followed by the activation of the *MESP2-mCherry* signal in an increasing subpopulation of scattered cells (Fig. 4g, Extended Data Fig. 7a, b, Supplementary Video 8). Treatment with DAPT prevented *MESP2-mCherry* activation—as expected, given that *Mesp2* is a Notch target in mouse embryos (Extended Data Fig. 7c, Supplementary Video 8). Conversely, oscillatory arrest and *MESP2-mCherry* onset was prematurely triggered by either FGF or WNT inhibition (Fig. 4h, i, Extended Data Fig. 7a, b, d, e, Supplementary Video 8). Increasing concentrations of PD03 resulted in faster activation of *MESP2-mCherry* (Extended Data Fig. 7b). Therefore, PSM cells derived from human iPS cells recapitulate segmental determination, which is dynamically controlled by levels of FGF and WNT.

Our work provides evidence for the existence of a human segmentation clock, demonstrating the conservation of this oscillator from fish to human. We identify the human clock period as around 5 h, indicating that it operates roughly 2 $\times$  slower than the mouse counterpart<sup>14</sup>. This is consistent with the known difference in developmental timing between mouse and human embryos<sup>27</sup>. Our culture conditions, in which cells are treated with only two chemical compounds in a defined medium, enable the production of an unlimited supply of human PSM-like cells. This represents an ideal system for investigating the dynamical properties of the oscillator, as well as its dysregulation in pathological segmentation defects such as congenital scoliosis.

## Online content

Any methods, additional references, Nature Research reporting summaries, source data, extended data, supplementary information, acknowledgements, peer review information; details of author contributions and competing interests; and statements of data and code availability are available at <https://doi.org/10.1038/s41586-019-1885-9>.

- Hubaud, A. & Pourquié, O. Signalling dynamics in vertebrate segmentation. *Nat. Rev. Mol. Cell Biol.* **15**, 709–721 (2014).
- Oates, A. C., Morelli, L. G. & Ares, S. Patterning embryos with oscillations: structure, function and dynamics of the vertebrate segmentation clock. *Development* **139**, 625–639 (2012).

3. Sparrow, D. B. et al. Mutation of the LUNATIC FRINGE gene in humans causes spondylocostal dysostosis with a severe vertebral phenotype. *Am. J. Hum. Genet.* **78**, 28–37 (2006).
4. Chal, J. et al. Differentiation of pluripotent stem cells to muscle fiber to model Duchenne muscular dystrophy. *Nat. Biotechnol.* **33**, 962–969 (2015).
5. Hubaud, A., Regev, I., Mahadevan, L. & Pourquie, O. Excitable dynamics and Yap-dependent mechanical cues drive the segmentation clock. *Cell* **171**, 668–682 (2017).
6. Chal, J. et al. Generation of human muscle fibers and satellite-like cells from human pluripotent stem cells *in vitro*. *Nat. Protocols* **11**, 1833–1850 (2016).
7. Henrique, D., Abranches, E., Verrier, L. & Storey, K. G. Neuromesodermal progenitors and the making of the spinal cord. *Development* **142**, 2864–2875 (2015).
8. Gouti, M. et al. A gene regulatory network balances neural and mesoderm specification during vertebrate trunk development. *Dev. Cell* **41**, 243–261 (2017).
9. Klein, A. M. et al. Droplet barcoding for single-cell transcriptomics applied to embryonic stem cells. *Cell* **161**, 1187–1201 (2015).
10. Tzouanacou, E., Wegener, A., Wymeersch, F. J., Wilson, V. & Nicolas, J. F. Redefining the progression of lineage segregations during mammalian embryogenesis by clonal analysis. *Dev. Cell* **17**, 365–376 (2009).
11. Chalamalasetty, R. B. et al. Mesogenin 1 is a master regulator of paraxial presomitic mesoderm differentiation. *Development* **141**, 4285–4297 (2014).
12. Matsumiya, M., Tomita, T., Yoshioka-Kobayashi, K., Isomura, A. & Kageyama, R. ES cell-derived presomitic mesoderm-like tissues for analysis of synchronized oscillations in the segmentation clock. *Development* **145**, dev156836 (2018).
13. Yoshioka-Kobayashi, K. et al. Coupling delay controls synchronized oscillations in the segmentation clock. *Nature* <https://doi.org/10.1038/s41586-019-1882-z> (2019).
14. Aulehla, A. et al. A  $\beta$ -catenin gradient links the clock and wavefront systems in mouse embryo segmentation. *Nat. Cell Biol.* **10**, 186–193 (2008).
15. Masamizu, Y. et al. Real-time imaging of the somite segmentation clock: revelation of unstable oscillators in the individual presomitic mesoderm cells. *Proc. Natl Acad. Sci. USA* **103**, 1313–1318 (2006).
16. Chal, J. et al. Recapitulating early development of mouse musculoskeletal precursors of the paraxial mesoderm *in vitro*. *Development* **145**, dev157339 (2018).
17. Bénazéraf, B. et al. A random cell motility gradient downstream of FGF controls elongation of an amniote embryo. *Nature* **466**, 248–252 (2010).
18. Acebrón, J. A., Bonilla, L. L., Perez Vicente, C. J., Ritort, F. & Spigler, R. The Kuramoto model: a simple paradigm for synchronization phenomena. *Rev. Mod. Phys.* **77**, 137–185 (2005).
19. Palmeirim, I., Henrique, D., Ish-Horowicz, D. & Pourquie, O. Avian hairy gene expression identifies a molecular clock linked to vertebrate segmentation and somitogenesis. *Cell* **91**, 639–648 (1997).
20. Primm, D. R., Norris, W. E., Carlson, G. J., Keynes, R. J. & Stern, C. D. Periodic segmental anomalies induced by heat shock in the chick embryo are associated with the cell cycle. *Development* **105**, 119–130 (1989).
21. Tsiairis, C. D. & Aulehla, A. Self-organization of embryonic genetic oscillators into spatiotemporal wave patterns. *Cell* **164**, 656–667 (2016).
22. Jiang, Y. J. et al. Notch signalling and the synchronization of the somite segmentation clock. *Nature* **408**, 475–479 (2000).
23. Riedel-Kruse, I. H., Muller, C. & Oates, A. C. Synchrony dynamics during initiation, failure, and rescue of the segmentation clock. *Science* **317**, 1911–1915 (2007).
24. Dupont, S. et al. Role of YAP/TAZ in mechanotransduction. *Nature* **474**, 179–183 (2011).
25. Cooke, J. & Zeeman, E. C. A clock and wavefront model for control of the number of repeated structures during animal morphogenesis. *J. Theor. Biol.* **58**, 455–476 (1976).
26. Morimoto, M., Takahashi, Y., Endo, M. & Saga, Y. The Mesp2 transcription factor establishes segmental borders by suppressing Notch activity. *Nature* **435**, 354–359 (2005).
27. Hauschka, S. D. Clonal analysis of vertebrate myogenesis. II. Environmental influences upon human muscle differentiation. *Dev. Biol.* **37**, 329–344 (1974).

**Publisher's note** Springer Nature remains neutral with regard to jurisdictional claims in published maps and institutional affiliations.

© The Author(s), under exclusive licence to Springer Nature Limited 2020



## Methods

No statistical methods were used to predetermine sample size. The experiments were not randomized and investigators were not blinded to allocation during experiments and outcome assessment.

### Generation of reporter lines

The CRISPR–Cas9 system for genome editing<sup>28</sup> was used to generate three reporter lines in human iPS cells (*HES7-Achilles*, *HES7-Achilles;pCAG-H2B-mCherry* and *HES7-Achilles;MESP2-mCherry*) and one mouse ES cell reporter line (*Hes7-Achilles*). To target the *HES7* locus in human NCRM1 iPS cells, a single-guide RNA (Extended Data Table 1) targeting the 3' end of *HES7* was designed using the MIT Crispr Design Tool ([www.crispr.mit.edu](http://www.crispr.mit.edu)) and cloned into the pGuide-it-tdTomato vector (Takara cat. no. 632604). We also generated a repair vector consisting of 1-kb 3' and 5' homology arms flanking a self-cleaving T2A peptide sequence, followed by the fast-folding yellow fluorescent protein (YFP) variant Achilles<sup>16</sup>, two destabilization domains (CL1 and PEST), and a nuclear localization signal (T2A-Achilles-NLS-CL1-PEST) in a pUC19 vector backbone by means of Gibson assembly (NEB). The assembled repair vector was then mutated by site-directed mutagenesis to eliminate the PAM site (specific mutation noted in Extended Data Table 1) in using the In-Fusion cloning kit (Takara). Both the pGuide-it-tdTomato and targeting vectors were delivered to iPS cells by nucleofection using a NEPA 21 electroporator. Twenty-four hours after nucleofection, cells were sorted by TdTomato expression using an S3 cell sorter (Biorad) and seeded at low density in Matrigel-coated plates (Corning, cat. no. 35277) in mTeSR1 (StemCell Technologies cat. no. 05851) + 10  $\mu$ M Y-27362 dihydrochloride (Tocris Bioscience, cat. no. 1254). Single cells were allowed to expand clonally and individual colonies were screened by PCR for targeted homozygous insertion of 2A-Achilles-CL1-PEST-NLS immediately before the stop codon of *HES7*. Positive clones were sequenced to ensure no undesired mutations in the *HES7* locus had been introduced by the genome-editing process. Three homozygous clones were further validated by qRT–PCR and immunofluorescence.

An identical approach was used to target the *Hes7* locus in mouse E14 ES cells, except the pGuide-it-tdTomato and targeting vectors were delivered by lipofection using lipofectamine 3000 (Invitrogen cat. no. L3000001). Following sorting, TdTomato<sup>+</sup> cells were seeded at low density on gelatin-coated dishes (EMD Millipore cat. no. es-006-b) in 2i medium (see below). Individual colonies were then transferred to a 96 well plate for expansion. Once ready to passage, the master plate was split onto 3 different 96-well plates. One plate was used for genotyping and the other two were frozen. Positive clones were then thawed, expanded and had their genotype confirmed by PCR and sequencing. Only one clone carrying the targeted homozygous insertion of 2A-Achilles-CL1-PEST-NLS in the *Hes7* locus was found and further characterized.

To generate the double-reporter line *HES7-Achilles;MESP2-mCherry*, we cotransfected the pGuide-it-tdTomato vector containing a single-guide RNA targeting the 3' end of the *MESP2* coding sequence (Extended Data Table 1), and a targeting vector composed of 1-kb homology arms flanking a *T2A-H2B-mCherry* sequence in the pUC19 backbone, in NCRM1 *HES7-Achilles* cells by nucleofection (Amaxa). We sorted, expanded, genotyped and sequenced individual clones. Three independent instances of successful homozygous insertion were found.

To insert the constitutively expressed *pCAG-H2B-mCherry* reporter in the safe harbour *AAVS1* locus in NCRM1 *HES7-Achilles* cells, we used a previously described approach<sup>29</sup>. In brief, we cloned the *H2B-mCherry* sequence into the pAAVS1-P-CAG-DEST vector (Addgene) by Gibson assembly and co-transfected it along with the pXAT2 vector (Addgene) into *HES7-Achilles* cells. Two days after nucleofection, we selected positive clones by supplementing mTeSR1 with puromycin (0.5  $\mu$ g/ml, Sigma-Aldrich cat. no. P7255) for a total of 10 days. We obtained two

positive clones and confirmed the homozygous insertion of *H2B-mCherry* by PCR.

### Mouse ES cell culture and 2D differentiation

E14 mouse ES cells were maintained under feeder-free conditions in gelatin-coated dishes with 2i medium composed of high-glucose DMEM (Gibco cat. no. 11965-118) supplemented with 1% GlutaMAX (Gibco cat. no. 35050061), 1% non-essential amino acids (Gibco cat. no. 11140-050), 1% sodium pyruvate (Gibco cat. no. 11360-070), 0.01% bovine serum albumin (BSA) (Gibco cat. no. 15260-037), 0.1%  $\beta$ -mercaptoethanol (Gibco cat. no. 21985-023), 15% fetal bovine serum (FBS) (EMD Millipore cat. no. ES009B), 1,000 U/ml LIF (EMD Millipore cat. no. ESG1106), 3  $\mu$ M CHIR99021 (Sigma Aldrich cat. no. SML1046) and 1  $\mu$ M PD0325901 (Stemgent cat. no. 04-006). Mouse ES cells were passaged by TrypLE (Gibco cat. no. 12605010) dissociation every 2 days at a density of  $1 \times 10^4$  cells per square centimetre. ES cells were tested for mycoplasma contamination. We verified cell line identity by staining for pluripotency markers POU5F1 and SOX2. Paraxial mesoderm differentiation was carried out as previously described<sup>20</sup>, with small modifications. Mouse ES cells were seeded at a density of  $1 \times 10^4$  cells per square centimetre in fibronectin-coated dishes (BD Biosciences cat. no. 356008) in N2B27 medium (StemCell Technologies cat. no. 07156 and 05731) supplemented with 25 ng/ml activin A (R&D systems cat. no. 338-AC-050) and 12 ng/ml bFGF (PeproTech cat. no. 450-33). After 48 h in culture, the differentiation medium was changed to high-glucose DMEM (Gibco cat. no. 11965-118) supplemented with 1% GlutaMAX (Gibco cat. no. 35050061), 1% non-essential amino acids (Gibco cat. no. 11140-050), 1% sodium pyruvate (Gibco cat. no. 11360-070), 0.01% BSA (Gibco cat. no. 15260-037), 0.1%  $\beta$ -mercaptoethanol (Gibco cat. no. 21985-023), 15% FBS (EMD Millipore cat. no. ES009B), 3  $\mu$ M CHIR99021 (Sigma Aldrich cat. no. SML1046) and 0.5  $\mu$ M LDN193189 (Stemgent cat. no. 04-0074). Cells were cultured for four additional days, and medium was changed daily. For live-imaging experiments, cells were seeded on 24-well glass-bottomed plates (In vitro Scientific cat. no. P24-1.5H-N) on day 0 and cultured in DMEM without phenol red (Gibco cat. no. 31053028) from day 4 onwards. To extend the time spent in the oscillatory state, we additionally supplemented the differentiation medium with 50 ng/ml mouse FGF4 (R&D Systems cat. no. 5846-F4-025), 1  $\mu$ g/ml heparin (Sigma Aldrich cat. no. H3393-100KU), 2.5  $\mu$ M BMS493 (Sigma Aldrich cat. no. B6688-5MG) and 10  $\mu$ M Y-27362 dihydrochloride (CLFBR medium<sup>3</sup>) from day 4 onwards.

### Human iPS cell culture and 2D differentiation

Human stem cell work was approved by Partners Human Research Committee (Protocol Number 2017P000438/PHS). We complied with all relevant ethical regulations. Written informed consent from the donor of the NCRM1 iPS cells was obtained by Rutgers University at the time of sample collection. NCRM1 iPS cells (RUCDR, Rutgers University) and lines carrying the *MSGN1-Venus*<sup>20</sup>, *HES7-Achilles*, *HES7-Achilles;pCAG-H2B-mCherry* and *HES7-Achilles;MESP2-mCherry* reporters were maintained in Matrigel-coated plates (Corning, cat. no. 35277) in mTeSR1 medium (StemCell Technologies cat. no. 05851) as previously described<sup>9</sup>. All cell lines were tested for mycoplasma contamination. We verified cell line identity by staining for pluripotency markers POU5F1 and SOX2. Paraxial mesoderm differentiation was carried out as previously described<sup>9</sup>. In brief, mature iPS cell cultures were dissociated in Accutase (Corning cat. no. 25058CI) and seeded at a density of  $3 \times 10^4$  cells per square centimetre on Matrigel-coated plates in mTeSR1 and 10  $\mu$ M Y-27362 dihydrochloride (ROCKi; Tocris Bioscience, cat. no. 1254). Cells were cultured for 24–48 h until small, compact colonies were formed. Differentiation was initiated by switching to CL medium consisting of DMEM/F12 GlutaMAX (Gibco cat. no. 10565042) supplemented with 1% insulin-transferrin-selenium (ITS) (Gibco cat. no. 41400045), 3  $\mu$ M Chir 99021 (Tocris cat. no. 4423) and 0.5  $\mu$ M LDN193189 (Stemgent cat. no. 04-0074). On day 3 of differentiation, cells were

# Article

changed to CLF medium consisting of CL medium with 20 ng/ml mouse bFGF (PeproTech cat. no. 450-33). Medium was changed daily.

For live-imaging experiments, differentiation was performed as described, except cells were seeded on 35-mm matrigel-coated glass-bottomed dishes (MatTek cat. no. P35G-1.5-20-C) or 24-well glass-bottomed plates (In vitro Scientific cat. no. P24-1.5H-N). DMEM/F12 without phenol red was used to reduce background fluorescence (Gibco cat. no. 21041025).

To extend the oscillatory window of differentiated PSM cells, we cultured *HES7-Achilles* cells in CLFBR medium consisting of DMEM/F12 GlutaMAX, 1% ITS, 3  $\mu$ M Chir 99021, 0.5  $\mu$ M LDN193189, 50 ng/ml mouse FGF4 (R&D Systems cat. no. 5846-F4-025), 1  $\mu$ g/ml heparin (Sigma Aldrich cat. no. H3393-100KU), 2.5  $\mu$ M BMS493 (Sigma Aldrich cat. no. B6688-5MG) and 10  $\mu$ M Y-27362 dihydrochloride starting on day 2 of differentiation<sup>4</sup>. Medium was refreshed daily.

To automatically track oscillations in individual cells within the culture, we mixed *HES7-Achilles;pCAG-H2B-mCherry* cells with NCRM1 cells in a ratio of 1:100 at the time of seeding for pre-differentiation. Cells were then differentiated normally under CLFBR conditions.

To examine oscillations in isolated cells, we differentiated *HES7-Achilles* cells normally (CL medium) for the first 2 days on 35-mm plastic dishes and dissociated them with accutase (Corning cat. no. 25058CI) on day 2 of the differentiation protocol. Cells were reseeded on fibronectin-coated (BD Biosciences cat. no. 356008) or BSA-coated (Gibco cat. no. 15260-037) 24-well glass-bottomed plates at high (500,000 cells per well) or low density (25,000–50,000 cells per well) in CLFBR medium. Using our regular DMEM/F12 base medium resulted in poor survival of low-density cultures. We found that using RHB basal medium (Takara/Clontech cat. no. Y40000), supplemented with 5% knockout serum replacement (KSR) (Thermo Fisher cat. no. 10828-028) improved survival considerably.

## Explant culture

Explant culture was performed as previously described<sup>4</sup>. LuVeLu CD1 E9.5 mice (both male and female) were killed according to local regulations, consistent with national and international guidelines. We complied with all relevant ethical regulations. The study protocol was approved by Brigham and Women's Hospital IACUC/CCM (protocol number N000478). Sample sizes were not estimated, nor were randomization or blinding performed. Tail buds were dissected with a tungsten needle and ectoderm was removed using accutase (Life Technologies). Explants were then cultured on fibronectin-coated plate (LabTek chamber). The medium consists of DMEM, 4.5g/l Glucose, 2mM L-glutamine, non-essential amino acids 1 $\times$  (Life Technologies), penicillin 100 U/ml, streptomycin 100  $\mu$ g/ml, 15% FBS, Chir-99021 3  $\mu$ M, LDN193189 200 nM, BMS-493 2.5  $\mu$ M, mouse FGF4 50 ng/ml, heparin 1  $\mu$ g/ml, HEPES 10 mM and Y-27632 10  $\mu$ M. Explants were incubated at 37 °C, 7.5% CO<sub>2</sub>. Live imaging was performed on a confocal microscope Zeiss LSM 780, using a 20 $\times$  objective (note that the tiling could create lines between the different images). For micropattern culture, explants were cultured overnight in standard condition, then dissociated using trypsin-EDTA and plated on fibronectin-coated CYTOOchips Arena in a CYTOOchamber 4 wells.

## Small molecule inhibitor treatments

To inhibit Notch signalling, 25  $\mu$ M DAPT (Sigma Aldrich cat. no. D5942-5MG) was added to CLFBR medium on day 2 of differentiation. To inhibit FGF signalling, PD0325901 (Stemgent 04-006) or PD173074 (Cayman Chemical cat. no. 219580-11-7) were added to CL or CLFBR media at the indicated concentrations. WNT signalling was inhibited with the tankyrase inhibitors XAV939 (Sigma Aldrich cat. no. X3004) and IWR-1 (Sigma Aldrich cat. no. I0161) at 2  $\mu$ M and 12  $\mu$ M, respectively, in CLFBR medium. Cell division was blocked by arresting cells at early S phase with 5  $\mu$ M aphidicolin (Sigma Aldrich cat. no. A0781) in CLFBR medium. Cells were pretreated for 24 h with aphidicolin before imaging (during

day 2). The onset of imaging was thus delayed by one day and started only on day 3. Aphidicolin was maintained in the medium throughout imaging. Latrunculin A (Cayman Chemical ca. no. 10010630), which inhibits actin polymerization and YAP signalling, was used at 350 nM in RHB basal medium supplemented with CLFBR and 5% KSR. Mouse explants and micropatterned cultures were treated with PD0325901 (Sigma, at concentration as described in Extended Data Fig. 6) and PD173074 (Sigma, 250 nM).

## Time-lapse microscopy

Time lapse-imaging of PSM cells was performed on a Zeiss LSM 780 point-scanning confocal inverted microscope fitted with a large temperature incubation chamber and a CO<sub>2</sub> module. An Argon laser at 514 nm and 7.5% power was used to excite the Achilles fluorophore through a 20 $\times$  Plan Apo (N.A. 0.8) objective, and a DPSS 561 laser at 561 nm and 2% laser power was used to excite mCherry samples. Images were acquired with an interval of 18 min in the case of human samples and 4.5 min for mouse samples, for a total of 24–48 h. A 3  $\times$  3 tile of 800  $\times$  800 pixels per tile with a single z-slice of 18- $\mu$ m thickness and 12-bit resolution was acquired per position. Multiple positions, with at least two positions per sample, were imaged simultaneously using a motorized stage. Explant imaging was performed on a Zeiss LSM780 microscope using a 20 $\times$ /0.8 objective. For mouse cell imaging, a single section (about 19.6- $\mu$ m wide) with tiling (3  $\times$  3) of a 512  $\times$  512-pixel field was acquired every 7.5 min (in most experiments) at 8-bit resolution.

## Immunostaining

For immunostaining of 2D cultures, cells were grown on Matrigel-coated glass-bottomed plates or 12-mm glass coverslips placed inside plastic dishes or, alternatively, on 24 well glass-bottomed plates (In vitro Scientific cat. no. P24-1.5H-N). Cells were rinsed in Dulbecco's phosphate buffered saline (DPBS) and fixed in a 4% paraformaldehyde solution (Electron Microscopy Sciences cat. no. 15710) for 20 min at room temperature, then washed 3 times with phosphate buffered saline (PBS). Typically, samples were permeabilized by washing 3 times for 3 min each in Tris buffered saline (TBS) with 0.1% Tween (TBST) and blocked for 1 h at room temperature in TBS with 0.1% Triton and 3% FBS. Primary antibodies were diluted in blocking solution and incubated overnight at 4 °C with gentle rocking. Primary antibodies and dilution factors are listed in Extended Data Table 2. Following 3 TBST washes and a short 10-min block, cells were incubated with Alexa-Fluor-conjugated secondary antibodies (1:500) and Hoechst33342 (1:1,000) overnight at 4 °C with gentle rocking. Three final TBST washes and a PBS rinse were performed, and cells were mounted in fluoromount G (Southern Biotech cat. no. 0100-01). Images were acquired using either a Zeiss LSM880 or LSM780 point scanning confocal microscope with a 20 $\times$  objective.

For visualizing dpERK1 and dpERK2 in 2D monolayer differentiated cells, cells were transferred onto ice and quickly rinsed in ice-cold PBS containing 1 mM sodium vanadate (NaVO<sub>4</sub>). Next, cells were fixed in 4% paraformaldehyde for 15 min at room temperature, rinsed 3 times in PBS and dehydrated in cold methanol at –20 °C for 10 min. Following 3 PBS rinses, cells were blocked in PBS containing 0.1% Triton X-100 and 5% goat serum and incubated in dpERK1 and dpERK2 antibody diluted in antibody buffer (0.1% Triton X-100 and 1% BSA in PBS) overnight at 4 °C. Cells were washed in PBS, and incubated in blocking solution for 10 min and with secondary antibody and Hoechst33342 in antibody buffer overnight at 4 °C. Cells were rinsed three times in PBS before mounting and imaging as described in 'Immunostaining'.

## RNA extraction, reverse transcription and qPCR

Cells were collected in Trizol (Life Technologies cat. no. 15596-018), followed by precipitation with chloroform and ethanol and transferred onto Purelink RNA Micro Kit columns (Thermo Fisher cat. no. 12183016) according to manufacturer's protocol, including on-column DNase treatment. A volume of 22  $\mu$ l RNase-free water was used for elution

and RNA concentration and quality were assessed with a Nanodrop. Typically, between 0.2 and 1 µg of RNA was reverse-transcribed using Superscript III First Strand Synthesis kit (Life Technologies cat. no. 18080-051) and oligo-dT primers to generate cDNA libraries.

For real-time quantitative PCR, cDNA was diluted 1:30 in water and qPCR was performed using the iTaQ Universal SYBR Green kit (Bio-Rad cat. no. 1725124). Each gene-specific primer and sample mix was run in triple replicates. Each 10-µl reaction contained 5 µl 2× SYBR Green Master Mix, 0.4 µl of 10 µM primer stock (1:1 mix of forward and reverse primers), and 4.6 µl of diluted cDNA. qPCR plates were run on a Bio-Rad CFX384 thermocycler with the following cycling parameters: initial denaturation step (95 °C for 1 min), 40 cycles of amplification and SYBR green signal detection (denaturation at 95 °C for 5 s, annealing, extension and plate-read at 60 °C for 40 s), followed by final rounds of gradient annealing from 65 °C to 95 °C to generate dissociation curves. Primer sequences are listed in Extended Data Table 3. All unpublished primers were validated by checking for specificity (single peak in melting curve) and linearity of amplification (serially diluted cDNA samples). For relative gene expression analysis, the  $\Delta\Delta C_t$  method was implemented with the CFX Manager software. *PPIA* was used as the housekeeping gene in human iPS cell samples, and *Actb* was used in mouse ES cell samples. Target gene expression is expressed as fold change relative to undifferentiated human iPS or mouse ES cells.

### Flow cytometry analysis

To determine the fraction of PSM cells that express pMsn1–Venus or MSGN1–Venus, cultures were dissociated in Accutase and analysed by flow cytometry using an S3 cell sorter (Biorad). Undifferentiated ES or iPS cells, which do not express the fluorescent protein, were used as a negative control for gating purposes. Samples were analysed in biological triplicates. Results are presented as the percentage of Venus<sup>+</sup> cells in the sorted fraction.

### ChIP–qPCR

Binding of NOTCH1 to the promoters of *ACTB*, *LNFG* and *HES7* was analysed by ChIP. Cells were crosslinked for 30 min using ChIP Cross-link Gold reagent (Diagenode, C01019027), rinsed with PBS and then 1% formaldehyde for 15 min. After quenching with 125 µM glycine and rinsing the crosslinked cells with ice-cold PBS, cells were collected using a cell scraper. Cell lysis and pulldown of chromatin with A/G-protein-coated magnetic beads was performed on approximately 300,000 cells per immunoprecipitation using MAGnify ChIP kit (ThermoFisher cat. no. 492024) following manufacturer's instructions. Chromatin fragmentation was performed using a Covaris M220 sonicator for 5 min (75 W PIP, 5% DF and 200 cycles per burst). NOTCH1 immunoprecipitation was performed using 3.3 µg of anti-NOTCH1 (D1E11, 3608S Cell Signaling) per immunoprecipitation. This antibody binds the transactivation domain of NOTCH1 and has previously been successfully used for ChIP-seq applications<sup>30</sup>. Half a microgram of anti-acetyl-histone H3 (Lys9) (C5B11, 9649S Cell Signaling) was used. Fold enrichment ( $2^{-\Delta C_t}$ ) was calculated relative to isotype IgG controls, immunoprecipitated with 3.3 µg of normal rabbit IgG (2729S Cell Signaling). Enriched loci after ChIP were interrogated by qPCR using primers designed to amplify approximately 100 bp surrounding previously identified RBPJ binding sites in the *HES7* and *LNFG* promoters<sup>31,32</sup>.

### Image analysis

Time-lapse movies of HES7–Achilles were first stitched and separated into subsets by position in the Zen program (Zeiss). Then, background subtraction and Gaussian blur filtering were performed in Fiji<sup>33</sup> to enhance image quality. When single cell tracking was not performed, a small region of interest (ROI) was drawn and the mean fluorescence intensity over time was calculated. Intensity is presented in arbitrary units. When appropriate, the moving average was subtracted with window size of 3 h for human PSM (that is, 10 time points) and

mouse PSM (that is, 40 time points), and then normalized between 0 and 1. For smoothing, we applied the Sgolay filtering function in MATLAB.

Following moving average subtraction, we performed Fourier transformation of *HES7–Achilles* intensity profiles to determine the predominant period of oscillations. The Hilbert transformation was used to calculate the instantaneous frequency and phase of HES7–Achilles oscillations from ROIs. To compare the phase between ROIs in DMSO- and PD17- or PD03-treated cultures, we used the Hilbert transformation to calculate the instantaneous phase of each curve separately, and then subtracted the phase of treated cells from untreated cells at each time point. Phase difference is expressed as the average of instantaneous phase differences before the arrest of oscillations in treated cells.

To manually track oscillations in PSM cells derived from mouse ES cells as well as isolated or sparse human *HES7–Achilles* cells in a NCRM1 background, we tracked cells by drawing a circle around the nucleus of an individual cell at each time point and measuring fluorescence intensity inside the ROI. To remove saturated pixels corresponding to autofluorescent debris in mouse ES cell PSM movies, we set pixels with intensity >700 AU (above the dynamical range of Hes7–Achilles) to the background level (100 AU) in MATLAB. In the case of *MESP2–mCherry*, we established a threshold for activation (25 AU) by taking the mean of several ROIs representing the background noise.

For mouse explants, kymographs were done in Fiji<sup>33</sup> by drawing a rectangle from the starting centre of the travelling waves to the edge of the explant perpendicular to the direction of the wave. The intensity along the long axis was measured and the image was smoothed (this filter replaces each pixel with the average of its 3 × 3 neighbourhood).

Fluorescence intensity profiles were done by selecting a circular region of interest in Fiji<sup>33</sup> and by measuring the total intensity over time for this region; LuVeLu intensity is given in arbitrary units (normalized by the initial value) and a smoothing function (average over three points) was applied. Fluorescence intensity shows the mean fluorescence smoothed by applying a moving average over five points (with equal weight). For the quantification of micropattern experiments, a ROI encompassing the entire surface of one circle was drawn and the LuVeLu intensity was measured using the Time Series Analyzer V3 plugin on Fiji<sup>33</sup>. The period was measured by measuring the time between two peaks or two troughs. The average intensity was measured by averaging the intensity over 3 h to avoid instantaneous variations owing to the oscillations.

### Automatic image segmentation and cell tracking

Cells were automatically segmented and tracked on the microscopy movies using a custom algorithm. To this end, we first identified and listed the cell positions and cell shapes using a detection of the connected components of a thresholded image applied to the *pCAG–H2B–mCherry* channel (using the bwconncomp MATLAB algorithm). For reliability, we used a minimal de-noising based on morphological operations (imopen then imclose functions of MATLAB, both with radius of 1 pixel). The shape of the cell was used to detect the level of expression of *HES7–Achilles* by considering the average HES7–Achilles level within the connected component detected in the *pCAG–H2B–mCherry* channel. This provides us with a list of cell positions together with the associated average HES7–Achilles intensity, for each frame of the microscopy movie.

Tracks were then reconstructed consecutively by finding, given a cell in frame *k*, the closest cell in frame *k* + 1 within a distance of 20 µm, consistent with the typical movement of a cell between two frames, and not too large (to avoid switching tracks). This provided us with cell tracks—the trajectories of the cells in the microscopy field. By matching these tracks with the recorded HES7–Achilles intensity, we thus obtained *HES7–Achilles* activity as a function of time for each single cell tracked by the algorithm.

## Phase analysis

Whereas collective oscillations appear very regular, *HES7-Achilles* expression in single cells shows heterogeneous profiles and fluctuating background fluorescence intensity (Supplementary Video 5), and phase detection requires specific attention<sup>34</sup>. To derive accurately a phase of oscillation for a single cell, we used a custom method based on Hilbert transform (method 1), and two control methods that provided very similar results (methods 2 and 3). We relied on method 1 for the main figures, as this method provided an accurate estimate even during the first periods of the oscillations.

**Hilbert transform (method 1).** The Hilbert transform is a functional transform of time series, the argument of which provides an efficient estimate of the phase of a signal (and its modulus, the envelope amplitude). Hilbert transforms are sensitive to drifts in the signals and changes in the shape of the oscillation. Classically, Hilbert transform follows a detrending preprocessing based on removing a linear drift. To improve the evaluation of the phase using the Hilbert transform in the present case (in which where drifts are nonlinear and amplitudes vary in time), we used a local renormalization algorithm, similar to a previously published algorithm<sup>34</sup>, consisting of (i) centring the signal locally using a moving average computed over a time window of 6 h around the current time point (MATLAB function `movmean`, 6 h providing a duration slightly longer than the period of the average signal), enabling correcting for local changes in the average signal, and (ii) normalizing the amplitude dividing the centred signal by a sliding standard deviation, computed on the same window of 6 h (MATLAB function `movstd`). We then evaluated the phase using the `hilbert` function of MATLAB.

**Cross-correlations (method 2).** We also developed a methodology for evaluating phase shifts between two signals ( $S1(t)$  and  $S2(t)$ ) based on a local cross-correlation estimate. In detail, at a given time  $t$ , the algorithm finds the delay  $dt$  between 0 and 4 h, maximizing the correlation between the chunk of signal  $S1(s)$  and  $S2(s + dt)$  over the time interval  $s \in [t, t + 6 \text{ h}]$ . We developed this algorithm using a custom MATLAB code and used this algorithm to compute phase differences between pairs of cells.

**Method 3.** A third method used for control was developed on the basis of detecting peaks of the signals. In detail, we detected the times at which the signal peaks using the `findpeaks` function of MATLAB. When peaks are detected at times  $t_0, t_1, \dots, t_n$ , the phase of the signal at a given time  $t \in [t_i, t_{i+1}]$  was defined as the relative fraction of time between the two consecutive peaks,

$$\phi = \frac{t - t_i}{t_{i+1} - t_i}$$

The `findpeaks` function was also used to count the number of oscillations before arrest at the single-cell level.

## Synchronization

To quantify the level of synchrony between the *HES7-Achilles* expression in multiple cells, we first selected tracks that were followed for multiple periods of oscillations. We used minimal duration of 15 h and Fourier transform larger than a lower threshold; the selection using Fourier transform did not significantly modify the statistics. Next, we computed the Kuramoto order parameter (also known as vector strength<sup>21,35</sup>) of a given set of signals phases. Considering  $n$  signals with phases  $\theta_1, \dots, \theta_n$ , the Kuramoto order parameter  $Z$  is defined by

$$Z = \frac{1}{n} \sum_{j=1}^n e^{i\theta_j}$$

in which  $i$  is the complex variable. This provides a complex number, the angle of which corresponds to the average phase and the modulus (norm) of which quantifies the level of synchrony. The modulus of  $Z$  is indeed equal to 1 when all oscillators have the same phase (in which case  $Z = e^{i\theta}$ , in which  $\theta$  is the common phase of all oscillators), and it is equal to 0 when the phases are uniformly spread between 0 and  $2\pi$ . For uniformly distributed phases with standard deviation equal to  $\sigma$ , the amplitude of the Kuramoto order parameter is equal to  $\sin(\sigma)/\sigma$ , a function smoothly decaying from 1 to 0 as  $\sigma$  goes from 0 to  $\pi$ .

Using the phases we derived for each track, we evaluated as a function of time the order parameter and its modulus. Because of natural experimental fluctuations and the finite number of cells considered, asynchronous cells are characterized by a low—but non-zero—Kuramoto order parameter. To assess whether the observed Kuramoto order parameter was statistically consistent with synchrony, we evaluated what the level of Kuramoto order parameter norm would be for asynchronous sets of cells. To this end, we used our evaluated phases  $\theta_1(t), \dots, \theta_n(t)$  and constructed multiple surrogate datasets by shuffling the phase relationships between those trajectories, but preserving their intrinsic frequency of oscillations. To this end, we drew time-shifts uniformly in  $[0, T]$ , in which  $T$  is the total time considered for the phases, for each cell. This yields  $n$  times  $\tau_1, \dots, \tau_n$ , from which we derived the Kuramoto order parameter for a set of phases  $\theta_1(t + \tau_1), \dots, \theta_n(t + \tau_n)$ , wrapped on the interval  $[0, T]$ , that is, the times  $t + \tau_i$  are taken modulo  $T$ , and computed the associated order parameter. We repeated this randomization 1,000 times and obtained a stable distribution of the Kuramoto order parameter for phases with no specific phase relationship. This provided a level of Kuramoto order parameter consistent with asynchrony. We then tested whether the order parameter found for the original data was consistent with synchrony by comparing this value to the distribution of surrogate order parameters.

## Spatiotemporal wave

To assess whether the data were organized into a spatiotemporal wave pattern, we used our extensive dataset containing both the instantaneous positions and instantaneous phases for the cells that were detected by our automatic segmentation and tracking algorithm. For each pair of cells, we computed their instantaneous (physical) distance as well as their phase shift. This provided us with a very large dataset, which we organized according to ranges of distances, chosen so that each set contained approximately the same number of cell pairs. We used distances of less than 160  $\mu\text{m}$ , between 160 and 265  $\mu\text{m}$ , between 265  $\mu\text{m}$  and 530  $\mu\text{m}$  and larger than 530  $\mu\text{m}$ ; the number of cells at a distance larger than 530  $\mu\text{m}$  was not kept equal to the other numbers to keep sufficient resolution. We then plotted the distribution of phase shifts for each distance class, and used the two-sample Kolmogorov–Smirnov test (MATLAB function `kstest2`) to compare these distributions two-by-two, accounting for the classical sample-size bias of the test by selecting large subsets of equal size for each distance class<sup>36</sup>, and obtained a  $P$  value for whether the two samples were drawn from the same distribution. We consistently found that the distribution of phase shifts was not dependent on the distance between cells.

## Diffusion coefficient

To characterize cellular movement from automated cell tracks and test the hypothesis that the movement of the cells was consistent with freely diffusing particles (Brownian motion), we computed the mean square displacement of each cell in an automatically identified track in a given time lag. In detail, the mean square displacement is defined by:

$$\Delta_t^k = \langle x_{t+\tau}^k - x_t^k \rangle^2$$

in which  $k$  is a tracked cell label,  $t$  is time and the angular brackets indicate that an average on all possible values of  $t$  are taken (that is, if track  $k$  lasts up to time  $T_k$ , the average is taken for  $\{1, \dots, T_k - \tau\}$ ). Freely

moving cells with diffusivity  $D$  should have a linear mean squared displacement  $\Delta r^2 = 4D\tau$ . By fitting a linear curve to the mean square displacement for all cells, we obtained an estimate for  $D$  as well as a  $P$  value for assessing the validity of the linear fit (ANOVA).

### Period of oscillations

The period of oscillations in automatically tracked cells was computed using fast Fourier transform (MATLAB function `fft`) of the centred *HES7-Achilles* expression for each cell tracked (the centring consisted only of removing the mean value of the signal in time). Peaks of the Fourier transforms were identified using the `findpeaks` MATLAB function, and the most prominent peak was used to compute the period of the signal. To confirm this estimate of the period, we used an alternative method based on identifying the peaks in *HES7-Achilles* expression for each cell and computing the difference between the times of the peaks. We found a very good agreement between the two methods.

### Phase shifts

To assess the relative phase shift between two samples at the single-cell level (for example, control versus PD03), we first obtained the phases as a function of time for each automatically tracked cell as described in 'Phase analysis'. We then calculated the phase difference between all possible pairs of cells between the two samples at all time points, and displayed these data in histograms. We additionally computed the mean phase shift across all time points for all pairs of cells and the corresponding s.d. To compare the phase shift between different pairs of samples, we used non-parametric one-way ANOVA with the Kruskal–Wallis test.

### Cell division analysis

Our automated cell tracking algorithm (described in 'Automatic image segmentation and cell tracking') did not detect cell division, but rather selected one daughter cell at random and continued tracking without interruption. Thus, we resorted to manual tracking for the detection of cell division. We used the Fiji<sup>33</sup> plugin `ManualTracks` and recorded the time points at which cells underwent mitosis. Manual tracking was performed on the *pCAG-H2B-mCherry* channel, such that chromatin compaction during cell division was clearly identifiable and tracks were completely independent from *HES7-Achilles* intensity. Cell division time was defined as the time that elapsed between the time a cell first divides and the time that one of its daughter cells divides again. Once cell division events were manually identified, we used an automatic tracking to recover the tracks before and after cell division. In detail, given a cell division event at time  $t$  and at a given location of the field, we identified in our automatically identified cell the closest match. When the distance between the automatically and manually identified cells was small enough (here, below a distance of 21  $\mu\text{m}$ ), we recovered the *HES7-Achilles* expression from the associated already identified track. If there was no cell identified near the manually identified location (in rare cases, manually identified dividing cells had not been detected by the algorithm), we used locally a version of the automatic tracking algorithm (in a sub-image of  $5.3 \times 5.3 \mu\text{m}$ ) to derive a cell location and an associated *HES7-Achilles* expression. These data were then processed exactly as the automatically identified tracks, and we obtained the phases of the oscillations of the dividing cells. We then built the histogram of the phases at cell division, and used the one-sample Kolmogorov–Smirnov test to assess whether the distribution of phases was consistent with a uniform distribution, indicating no correlation between phase in the *HES7-Achilles* expression and cell division. To this end, we used the `makedist` MATLAB function to create a uniform distribution and used the `kstest` MATLAB function to compare our sample of phases at cell division with a uniform distribution. This provided a test of hypothesis together with the  $P$  value indicated in the legend of Extended data Fig. Sj.

### Statistical analyses

In box-and-whiskers plots, the middle hinge corresponds to median, lower and upper hinges correspond to the first and third quartiles, respectively, and the lower and upper whiskers correspond to the minimum and maximum, respectively. Ordinary one-way ANOVA was performed in cases in which data were Gaussian, and Tukey or Bonferroni correction was used for multiple comparisons. In cases in which data were not Gaussian (for example, phase shifts), we used a non-parametric one-way ANOVA with the Kruskal–Wallis test. For time series, such as the Kuramoto order parameter over time, we used paired ANOVA with matched time points. Details of statistical analyses are indicated in the figure legends. All differentiation experiments were performed a minimum of three independent times (rounds of differentiation), each containing at least three technical replicates (wells) per condition.

### Preparation of single-cell suspensions for scRNA-seq

Single-cell dissociation protocols for the various tissues and cells analysed were optimized to achieve >90% viability and minimize doublets before sample collection. For human iPS differentiation,  $3 \times 10^4$  *MSGN1-Venus* cells were seeded on Matrigel-coated 24-well plates 48 h before differentiation. Cells were differentiated as described in 'Human iPS cell culture and 2D differentiation'. All samples (days 1–4 and human iPS cell control samples) were dissociated, collected and captured on an inDrops setup on the same day, two biological replicates per sample. For dissociation, cells were briefly rinsed in PBS, and incubated in TrypLE Express (Gibco) for 5 min at 37 °C. Dissociated cells were run through a 30- $\mu\text{m}$  cell strainer, spun down at 200g for 4 min at 4 °C and resuspended in 100  $\mu\text{l}$  0.5% BSA in PBS.

For mouse ES cell differentiation,  $1 \times 10^4$  *pMsn1-Venus* cells were seeded on fibronectin-coated 6-well plates and differentiated as described in 'Mouse ES cell culture and 2D differentiation'. Samples for day 0 and days 2–5 were dissociated in TrypLE Express (Gibco) for 3–10 min, washed several times in PBS, passed through a 40- $\mu\text{m}$  cell strainer and resuspended in 0.1% BSA in PBS with Opti-Prep at a final density of 200,000 cells per millilitre. All samples were dissociated, collected and captured on the same day in biological duplicates.

For generating cell suspensions from mouse embryo tail buds, E9.5 embryos (25–28 somite stage) from CD-1 IGS mice (Charles River) were collected and the posterior part of the embryo, including the three most recently formed pairs of somites, was carefully dissected from 2 littermate embryos and subsequently processed as separate samples. Tissues were collected in PBS and dissociated in TrypLE Express for 10 min at 37 °C. Cells were rinsed in PBS and EDTA, transferred to 0.5% BSA in PBS, mechanically separated by trituration and run through a 30- $\mu\text{m}$  cell strainer. Cells were spun down at 200g for 4 min at 4 °C and resuspended in 100  $\mu\text{l}$  0.5% BSA in PBS.

The following numbers of cells were sequenced per sample: (1) human iPS cell differentiation samples (two biological replicates processed independently). For each replicate human iPS cell control, 1,000 cells; day 1, 1,500 cells; day 2, 1,500 cells; day 3, 1,500 cells; and day 4, 1,500 cells. (2) Mouse ES cell differentiation samples. ES cell day 0, 2,341 cells; day 2, 2,417 cells; day 3, rep. 1,310,6 cells; rep. 2,318,9 cells; day 4: rep. 1,2,939 cells; rep. 2,2,532 cells; day 5: rep. 1,1,894 cells; rep. 2,3,060 cells. (3) Mouse embryo samples: tail-bud cells from two E9.5 embryos ( $2 \times 3,000$  cells processed independently).

Every sample was collected as biological replicate and sequencing data from both samples were combined for data analysis. The actual number of cells captured on inDrops was twice as many as sequenced, for backup purposes.

### Barcoding, sequencing and mapping of single-cell transcriptomes

Single-cell transcriptomes were barcoded using inDrops<sup>12</sup> as previously reported<sup>37</sup>, using V3 sequencing adapters. Following within-droplet



# Article

reverse transcription, emulsions consisting of about 1,000–3,500 cells were broken, frozen at  $-80^{\circ}\text{C}$ , and prepared as individual RNA-seq libraries. inDrops libraries were sequenced on an Illumina NextSeq 500 using the NextSeq 75 High Output Kits using standard Illumina sequencing primers and 61 cycles for read 1 and 14 cycles for read 2, 8 cycles each for index read 1 and index read 2. Raw sequencing data (FASTQ files) were processed using the inDrops.py bioinformatics pipeline available at <https://github.com/indrops/indrops>. Transcriptome libraries were mapped to human or mouse reference transcriptomes built from the GRCh37/hg19 (GCF\_000001405.13) or GRCm38/mm10 (GCF\_000001635.20) genome assemblies, respectively. Bowtie version 1.1.1 was used with parameter  $-e\ 200$ .

## Processing of scRNA-seq data

Single-cell counts matrices were processed and analysed using ScanPy<sup>38</sup> (1.4.3) and custom Python scripts (Code Availability). Low-complexity cell barcodes, which can arise from droplets that lack a cell but contain background RNA, were filtered in two ways. First, inDrops data were initially filtered to only include transcript counts originating from abundantly sampled cell barcodes. This determination was performed by inspecting a weighted histogram of unique molecular identifier–gene pair counts for each cell barcode, and manually thresholding to include the largest mode of the distribution (in all cases  $>80\%$  of total sequencing reads). Second, low-complexity transcriptomes were filtered out by excluding cell barcodes associated with  $<250$  expressed genes. Transcript unique molecular identifier counts for each biological sample were then reported as a transcript  $\times$  cell table, adjusted by a total-count normalization, log-normalized, and scaled to unit variance and zero mean. Unless otherwise noted, each dataset was subset to the 2,000 most highly variable genes, as determined by a bin-normalized overdispersion metric. Mouse E9.5 data were filtered for doublet-like cells with Scrublet<sup>39</sup>, which simulates synthetic doublets from pairs of scRNA-seq profiles and assigns scores based on a  $k$ -NN classifier on the data transformed by principal component analysis (PCA).

## Low-dimensional embedding and clustering

Unless otherwise stated, processed single-cell data were projected into a 50-dimensional PCA subspace. The mouse E9.5 PSM ( $k=20$ ) nearest-neighbour graph used Euclidean distance and 20 PCA dimensions. The mouse ES cell and human iPS cell neighbour graphs were constructed using the batch-balanced bbknn method<sup>40</sup>. Clustering was performed using Louvain<sup>41</sup> and Leiden<sup>42</sup> community detection algorithms.

## Identification of differentially expressed genes

Transcripts with significant cluster-specific enrichment were identified by a two-sided Wilcoxon rank-sum test comparing cells of each cluster to cells from all other clusters in the same dataset. Genes were considered differentially expressed if they met the following criteria: log-transformed fold change  $>0$ , adjusted  $P$  value  $<0.05$ . False discovery rate (FDR) correction for multiple hypothesis testing was performed as described, by Benjamini–Hochberg<sup>43</sup>. The top 100 differentially expressed genes, ranked by FDR-adjusted  $P$  values, associated fold changes, and sample sizes (number of cells per cluster) are reported in Supplementary Table 1. Gene names for the top 20 differentially expressed transcripts are reported in Extended Data Figs. 2d (mouse E9.5), 3c (mouse E9.5 PSM), h (mouse ES cell) and m (human iPS cell).

## Pseudo-spatiotemporal ordering and identification of dynamically varying genes

Pseudo-spatiotemporal orderings were constructed by randomly selecting a root cell from the following clusters: neuromesodermal progenitor (mouse E9.5 PSM, Fig. 2a); day 0 ES cell (mouse ES cell, Fig. 2c); day 0 iPS cell (human iPS cell, Fig. 2e) and calculating the diffusion pseudotime distance of all remaining cells relative to the root. Trajectories were assembled for paths through specified clusters, with

cells ordered by diffusion pseudotime values, as previously reported<sup>44</sup>. Dynamically variable genes along the mouse E9.5 PSM trajectory were identified as follows. In brief, sliding windows of 100 cells were first scanned to identify the 2 windows with maximum and minimum average expression levels for all genes individually. For each gene, a  $t$ -test was then performed between these 2 sets of 100 expression measurements (FDR  $<0.01$ ). Scaled expression values for significant genes were then smoothened over a sliding window of 100 cells, ranked by peak expression and plotted as a heat map, shown in Fig. 2c. The full list of dynamically expressed genes appears in Supplementary Table 2.

## Machine-learning classification of cell states

Cell state prediction used the KNeighboursClassifier, RandomForestClassifier, LinearDiscriminantAnalysis (LDA), and MLPClassifier (NeuralNetwork) classifier methods from scikit-learn (0.20.3). Classifiers were trained on the full Louvain cluster-annotated PCA subspace-projected mouse E9.5 dataset ( $n=4,367$  cells) with default settings and  $k=20$  for KNeighboursClassifier. Mouse ES and human iPS cell states were predicted after subsetting matching gene symbols for the E9.5 variable gene list, and projecting into the E9.5-defined PCA subspace.

## Reporting summary

Further information on research design is available in the Nature Research Reporting Summary linked to this paper.

## Data availability

High-throughput sequencing data, raw sequencing data, raw and normalized count data, and single-cell clustering assignments generated in this study have been deposited and are available from NCBI Gene Expression Omnibus (GEO) accession number GSE114186, and can be visualized at <https://tinyurl.com/DiazPourquie2019>. Source Data corresponding to the following figure panels are available with the paper: Fig. 1b–f, 2a–h, 3a–d, f, h, 4b–i and Extended Data Figs. 1c, d, f–k, m–s, 2a–c, 3a, b, d–g, i–l, n, o, 4a–d, 5b, c, g–w, 6b, c, f–q, s–u, 7b–d. Online interactive versions and downloadable versions of the analysed scRNA-seq datasets, as well as scRNA-seq transcript  $\times$  cell count tables can be accessed at <https://tinyurl.com/DiazPourquie2019>, as follows. Mouse E9.5  $t$ -distributed stochastic neighbour-embedding ( $t$ -SNE) clustering analysis (Extended Data Fig. 2c) data are available from <https://tinyurl.com/DiazPourquie2019-mE95>. The mouse E9.5  $k$ -NN graph of paraxial mesoderm and neural clusters (Fig. 2a, b, Extended Data Fig. 3a–e) is available from: <https://tinyurl.com/DiazPourquie2019-mE95-PSM>. Data related to mouse ES cell cultures from day 0 to day 5 (Fig. 2c, d, Extended Data Figs. 3f–j) are available from: <https://tinyurl.com/DiazPourquie2019-mESC>. Data related to human iPS cell cultures from day 0 to day 4 (Fig. 2e, f, Extended Data Figs. 3k–o) are available from: <https://tinyurl.com/DiazPourquie2019-hiPSC>. Additional data, such as raw image files, are available from the corresponding author upon request; all materials used in this study—including stem cell lines carrying knock-in reporters—are available by request from the corresponding author.

## Code availability

Single-cell sequencing data were processed and analysed using publicly available software packages: <https://github.com/indrops/indrops> and <https://github.com/AllonKleinLab/SPRING>. Downstream analysis was performed in ScanPy<sup>38</sup> (1.4.3), using Python 3.6.8. Python code and Jupyter notebooks for reproducing single-cell analyses appearing in Fig. 2 and Extended Data Figs 2–4 are available at <https://github.com/wagnerde/Diaz2019>. This Github link also includes detailed instructions for installing the necessary Python software environment, including the following packages and their dependencies: anndata(0.6.22.post1), bbknn(1.3.6), fa2(0.3.5), ipython(7.8.0), jupyterlab(1.1.4),

leidenalg(0.7.0), louvain(0.6.1), matplotlib(3.0.3), multicoretsne(0.1), numba(0.45.1), numpy(1.17.2), pandas(0.25.1), pytables(3.5.2), python(3.6.7), python-igraph(0.7.1.post7), scanpy(1.4.4.post1), scikit-learn(0.21.3), scipy(1.3.1), scrublet(0.2.1), seaborn(0.9.0), statsmodels(0.10.1) and umap-learn(0.3.10). Force-directed layouts of single-cell graphs were generated using the ForceAtlas2 algorithm in Gephi (0.9.1). MATLAB code used for single-cell tracking and synchronization analysis is available at: <https://github.com/jonathan-touboul-brandeis/HumanSegmentationClock>.

28. Ran, F. A. et al. Genome engineering using the CRISPR–Cas9 system. *Nat. Protocols* **8**, 2281–2308 (2013).
29. Ocegueda-Yanez, F. et al. Engineering the AAVS1 locus for consistent and scalable transgene expression in human iPSCs and their differentiated derivatives. *Methods* **101**, 43–55 (2016).
30. Wang, H. et al. NOTCH1-RBPJ complexes drive target gene expression through dynamic interactions with superenhancers. *Proc. Natl Acad. Sci. USA* **111**, 705–710 (2014).
31. Morales, A. V., Yasuda, Y. & Ish-Horowitz, D. Periodic Lunatic fringe expression is controlled during segmentation by a cyclic transcriptional enhancer responsive to notch signaling. *Dev. Cell* **3**, 63–74 (2002).
32. Hayashi, S., Nakahata, Y., Kohno, K., Matsui, T. & Bessho, Y. Presomitic mesoderm-specific expression of the transcriptional repressor *Hes7* is controlled by E-box, T-box, and Notch signaling pathways. *J. Biol. Chem.* **293**, 12167–12176 (2018).
33. Schindelin, J. et al. Fiji: an open-source platform for biological-image analysis. *Nat. Methods* **9**, 676–682 (2012).
34. Delaune, E. A., François, P., Shih, N. P. & Amacher, S. L. Single-cell-resolution imaging of the impact of Notch signaling and mitosis on segmentation clock dynamics. *Dev. Cell* **23**, 995–1005 (2012).
35. Goldberg, J. M. & Brown, P. B. Response of binaural neurons of dog superior olivary complex to dichotic tonal stimuli: some physiological mechanisms of sound localization. *J. Neurophysiol.* **32**, 613–636 (1969).
36. Gordon, A. Y. & Lev B. K. in *Nonparametrics and Robustness in Modern Statistical Inference and Time Series Analysis: A Festschrift in Honor of Professor Jana Jurečková* (eds Antoch, J. et al.) 70–74 (Institute of Mathematical Statistics, 2010).
37. Zilionis, R. et al. Single-cell barcoding and sequencing using droplet microfluidics. *Nat. Protocols* **12**, 44–73 (2017).
38. Wolf, F. A., Angerer, P. & Theis, F. J. SCANPY: large-scale single-cell gene expression data analysis. *Genome Biol.* **19**, 15 (2018).
39. Wolock, S. L., Lopez, R. & Klein, A. M. Scrublet: computational identification of cell doublets in single-cell transcriptomic data. *Cell Syst.* **8**, 281–291.e9 (2019).
40. Polański, K. et al. BBKNN: fast batch alignment of single cell transcriptomes. *Bioinformatics* <https://doi.org/10.1093/bioinformatics/btz625> (2019).
41. Blondel, V. D. et al. Fast unfolding of communities in large networks. *J. Stat. Mech.* **2008**, P10008 (2008).
42. Traag, V. A., Waltman, L. & van Eck, N. J. From Louvain to Leiden: guaranteeing well-connected communities. *Sci. Rep.* **9**, 5233 (2019).
43. Macosko, E. Z. et al. Highly parallel genome-wide expression profiling of individual cells using nanoliter droplets. *Cell* **161**, 1202–1214 (2015).
44. Wolf, F. A. et al. PAGA: graph abstraction reconciles clustering with trajectory inference through a topology preserving map of single cells. *Genome Biol.* **20**, 59 (2019).
45. Loh, K. M. et al. Mapping the pairwise choices leading from pluripotency to human bone, heart, and other mesoderm cell types. *Cell* **166**, 451–467 (2006).
46. Zhou, H. et al. Conversion of mouse epiblast stem cells to an earlier pluripotency state by small molecules. *J. Biol. Chem.* **285**, 29676–29680 (2010).
47. Du, W., Prochazka, J., Prochazkova, M. & Klein, O. D. Expression of FGFs during early mouse tongue development. *Gene Exp. Patterns* **20**, 81–87 (2016).

**Acknowledgements** We thank members of the Pourquié laboratory, D. Ish-Horowitz, A. Klein and M. Heiman for critical reading of the manuscript and discussions. Research in the Pourquié laboratory was funded by a grant from the National Institute of Health (5R01HD085121). D.E.W. is supported by 1K99GM121852. M.D.-C. is supported by the NSF GRFP.

**Author contributions** M.D.-C. designed, performed and analysed biological experiments with O.P.; D.E.W. analysed scRNA-seq data. C.B. optimized the dissociation protocol for scRNA-seq and contributed to experiments with M.D.-C. A.H. performed mouse explant experiments. O.A.T. performed ChIP-qPCR experiments and helped M.D.-C. and S.D. to generate the mouse *Hes7-Achilles* line. S.D. helped M.D.-C. to generate the mouse *Hes7-Achilles* line and the human *HES7-Achilles*; *pCAG-H2B-mCherry* and *HES7-Achilles*; *MESP2-mCherry* lines. A. Michaut. helped with the quantifications. Z.A.T. generated the *MSGN1-YFP* line and helped M.D.-C. with generation of the *HES7-Achilles* line. K.Y.-K. and R.K. generated the destabilized Achilles construct. Y.N. and A. Miyawaki. generated the Achilles protein. J.T. performed the automated cell tracking and mathematical analysis of synchronization. M.D.-C., D.E.W., A.H., C.B., J.T. and O.P. wrote the manuscript; and O.P. supervised the project. All authors discussed and agreed on the results and commented on the manuscript.

**Competing interests** The authors declare the following competing interests: O.P. is scientific founder of Anagenesis Biotechnologies.

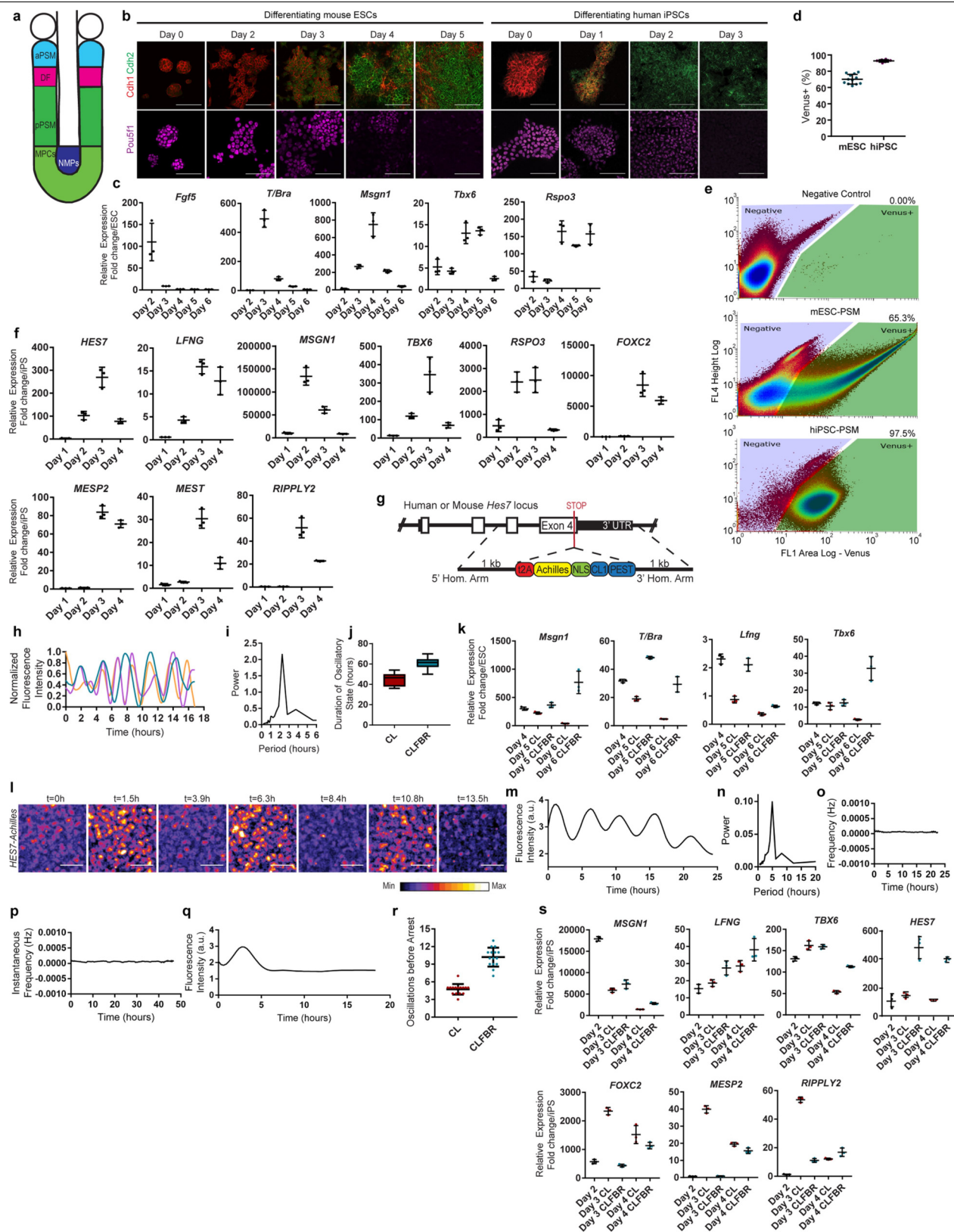
#### Additional information

**Supplementary information** is available for this paper at <https://doi.org/10.1038/s41586-019-1885-9>.

**Correspondence and requests for materials** should be addressed to O.P.

**Peer review information** *Nature* thanks Helen M. Blau and the other, anonymous, reviewer(s) for their contribution to the peer review of this work.

**Reprints and permissions information** is available at <http://www.nature.com/reprints>.

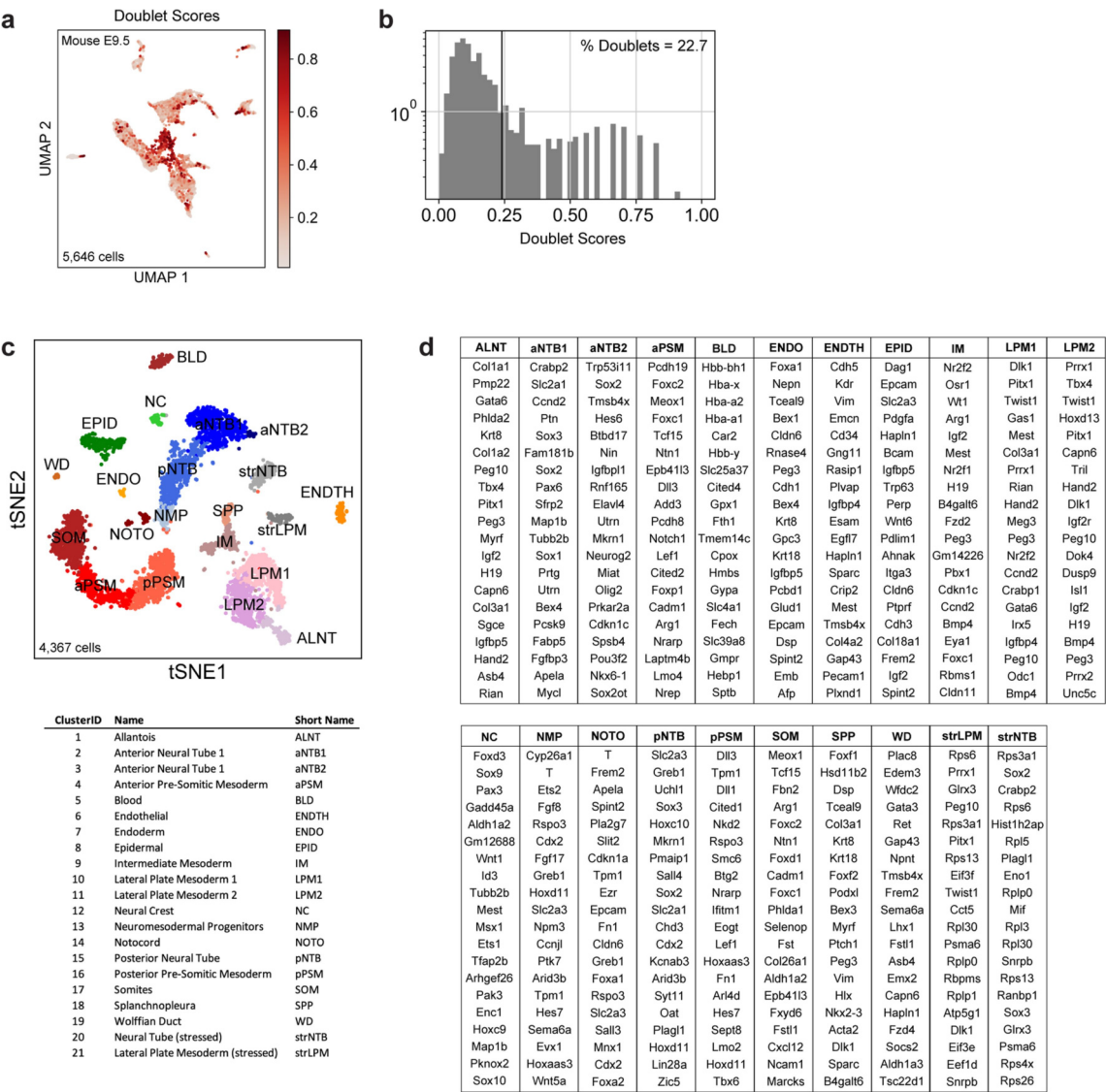


Extended Data Fig. 1 | See next page for caption.

**Extended Data Fig. 1 | Differentiation of mouse and human pluripotent stem cells towards PSM fate for the characterization of the segmentation clock in vitro.**

**a**, Scheme illustrating the maturation stages of paraxial mesoderm. DF, determination front; pPSM. **b**, Top, immunofluorescence staining for the cadherins CDH1 and CDH2 (top), and the pluripotency factor POU5F1 (bottom) in differentiating mouse ES cells (ESCs) (left) and human iPS cells (iPSCs) (right).  $n = 4$  independent experiments. Scale bar, 100  $\mu\text{m}$ . **c**, qRT-PCR for the epiblast marker *Fgf5*, the neuromesodermal progenitor or mesodermal marker *T*, and the mesodermal precursor cell and PSM markers *Tbx6*, *Msgn1* and *Rspo3* on days 2–6 of mouse ES cell differentiation. Relative expression is shown as the fold change relative to ES cells at day 0. Mean  $\pm$  s.d.  $n = 3$  biological replicates. **d**, Percentage induction of the mouse (m)ES cell *pMsgn1-Venus* reporter and the human (h)iPS cell *MSGN1-Venus* reporter, as determined by fluorescence-activated cell sorting (FACS). Mean  $\pm$  s.d.  $n = 12$  independent experiments (mouse ES cell),  $n = 8$  independent experiments (human iPS cell). **e**, Gating strategy and representative FACS plots for quantification of *pMsgn1-Venus* or *MSGN1-Venus* induction. **f**, qRT-PCR for cyclic genes (*HES7* and *LFNG*), posterior-PSM markers (*MSGN1*, *TBX6* and *RSPO3*), determination-front markers (*MESP2* and *RIPPLY2*) and anterior-PSM markers (*MEST* and *FOXC2*) on days 1–4 of human iPS cell (iPSC) differentiation. Relative expression is shown as the fold change relative to iPS cells at day 0. Mean  $\pm$  s.d.  $n = 3$  biological replicates. **g**, Diagram outlining the targeting strategy used to generate *Hes7-Achilles* and *HES7-Achilles* knock-in reporter lines in mouse ES cells and human iPS cells, respectively. **h**, Normalized HES7-Achilles fluorescence intensity for three PSM cells derived from mouse ES cells, imaged in CL medium on day 4 of differentiation.  $n = 4$  independent experiments. **i**, Representative Fourier transform of HES7-Achilles oscillations in PSM cells derived from mouse ES cells, indicating the predominant period.  $n = 19$  cells. **j**, Total time spent in the oscillatory state for *Hes7-Achilles* PSM cells derived from mouse ES cells, cultured in CL or CLFBR medium from day 4 onwards. The middle hinge corresponds to median, the lower and upper hinges correspond to the first and

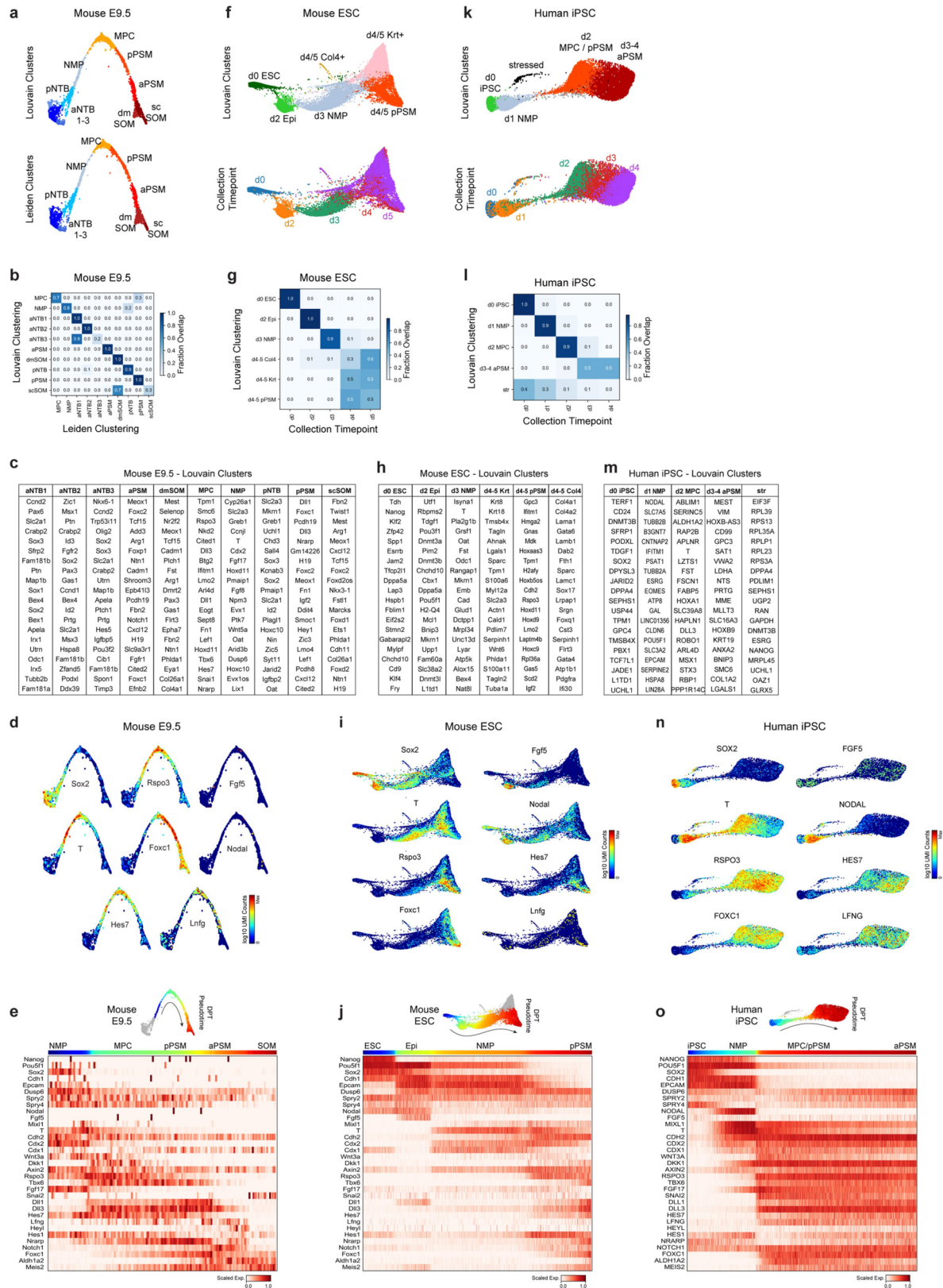
third quartiles, respectively, and the lower and upper whiskers correspond to the minimum and maximum, respectively.  $n = 8$  (CL),  $n = 12$  (CLFBR) independent experiments. **k**, qRT-PCR comparing relative expression levels of *Msgn1*, *Lfng*, *T* and *Tbx6* in PSM cells derived from mouse ES cells, cultured in CL or CLFBR medium from day 4 onwards. Relative expression is shown as the fold change relative to ES cells at day 0. Mean  $\pm$  s.d.  $n = 3$  biological replicates. **l**, Snapshots of HES7-Achilles fluorescence in PSM cells derived from human iPS cells, showing peaks and troughs over the course of 13.5 h in CL medium on day 2 of differentiation.  $n = 25$  independent experiments. Scale bar, 100  $\mu\text{m}$ . **m**, Representative quantification of HES7-Achilles fluorescence intensity in a small ROI from day 2 to day 3 of human iPS cell differentiation.  $n = 25$  independent experiments. **n**, Representative Fourier transform of *HES7-Achilles* oscillations, indicating the predominant period in PSM cells derived from human iPS cells, in CL medium on day 2.  $n = 25$  independent experiments. **o**, Representative instantaneous frequency in Hertz (calculated by Hilbert transformation) of *HES7-Achilles* oscillations in PSM cells derived from human iPS cells, from day 2 to day 3 of differentiation in CL medium.  $n = 25$  independent experiments. **p**, Representative instantaneous frequency in Hertz (calculated by Hilbert transformation) of *HES7-Achilles* oscillations in PSM cells derived from human iPS cells, from day 2 to day 3 of differentiation in CLFBR medium.  $n = 33$  independent experiments. **q**, Quantification of HES7-Achilles fluorescence in human iPS cells differentiated for 48 h without the BMP inhibitor LDN93189 (CHIR99021-only medium).  $n = 3$  independent experiments. **r**, Total number of *HES7-Achilles* oscillations for PSM cells derived from human iPS cells, cultured in CL or CLFBR medium from day 2 onwards. Mean  $\pm$  s.d.  $n = 15$  independent experiments. **s**, qRT-PCR comparing relative expression levels of *HES7*, *LFNG*, *TBX6* and *MSGN1* in PSM cells derived from human iPS cells, cultured in CL or CLFBR medium from day 2 onwards. Relative expression is shown as the fold change relative to iPS cells on day 0. Mean  $\pm$  s.d.  $n = 3$  biological replicates.



**Extended Data Fig. 2 | scRNA-seq analysis of the mouse E9.5 embryonic tail bud. a**, Prefiltering of doublet-like cells. UMAP embedding shows all original E9.5 cells ( $n = 5,646$ ), coloured by doublet score. Doublet scores indicate the extent to which a given single-cell transcriptome resembles a linear combination of two randomly selected cells (Methods and ref. <sup>39</sup>). **b**, Histogram of doublet scores. Scores  $> 0.24$  were filtered from subsequent analyses.

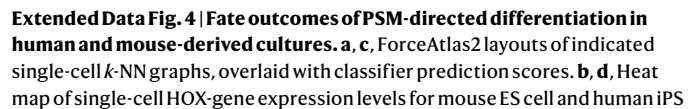
**c**,  $t$ -SNE embedding of E9.5 cells ( $n = 4,367$ ) post-doublet filtering. Individual cells are coloured according to annotated Louvain cluster identities. **d**, Top 20 positively enriched transcripts for each Louvain cluster relative to all other clusters, as detected by a two-sided Wilcoxon rank-sum test. Reported transcripts are ranked by FDR-corrected  $P$  values (Benjamini-Hochberg). Exact sample sizes are given in Supplementary Table 1.



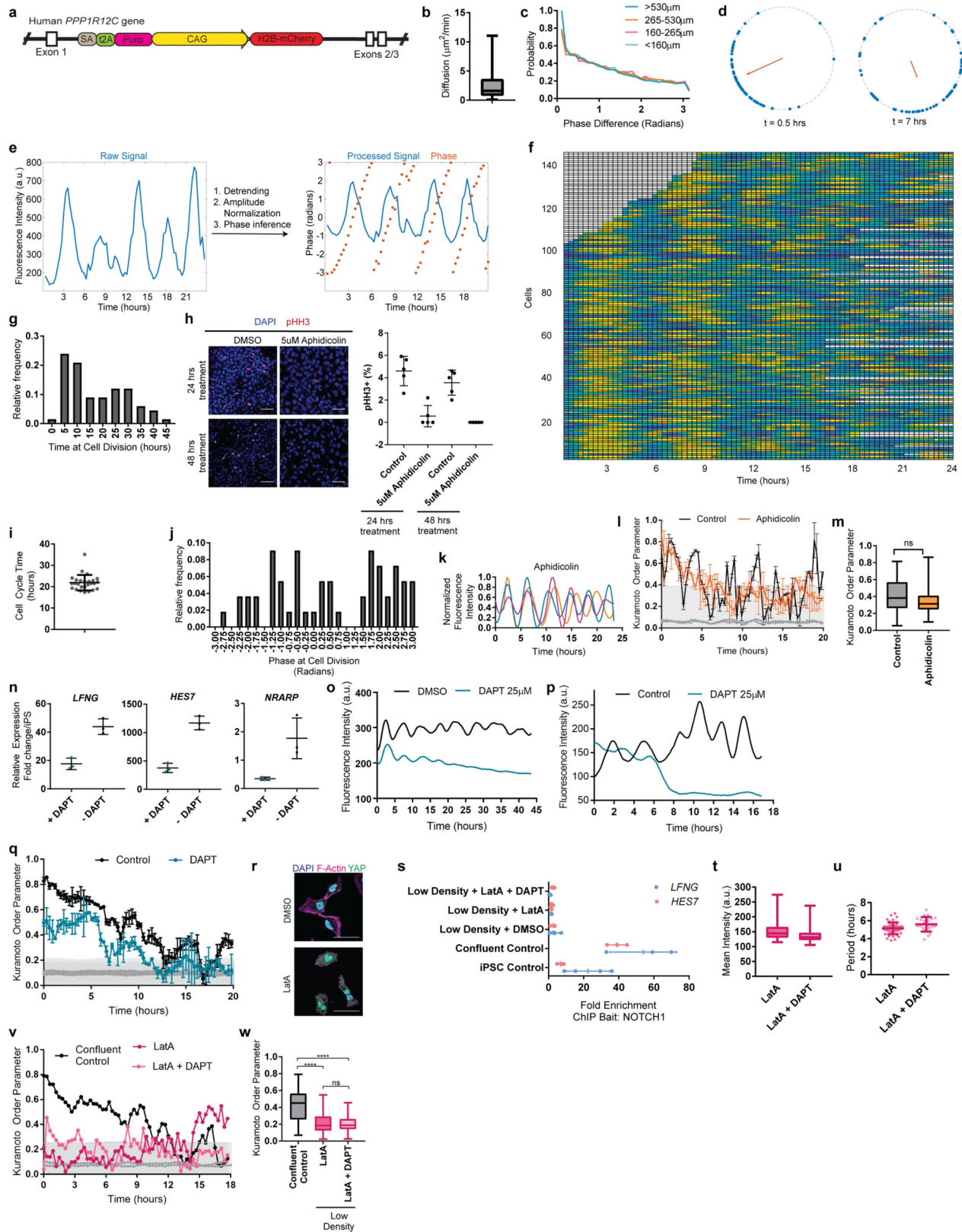


**Extended Data Fig. 3 | Comparative analysis of PSM differentiation trajectories in vitro and in vivo.** **a, f, k**, ForceAtlas2 layouts of mouse E9.5 embryos, mouse ES cell and human iPSC cell single-cell  $k$ -NN graphs, coloured by cluster identity and collection time points, as indicated. **b, g, l**, Confusion matrices plot the overlap of cluster and time-point assignments, row-normalized. **c, h, m**, Top 20 positively enriched transcripts for Louvain clusters relative to all other clusters in each dataset, as detected by a two-sided

Wilcoxon rank-sum test. Reported transcripts are ranked by FDR-corrected  $P$  values (Benjamini-Hochberg). Exact sample sizes are given in Supplementary Table 1. **d, i, n**, ForceAtlas2 layouts of single-cell  $k$ -NN graphs, overlaid with log-normalized transcript counts for indicated genes. **e, j, o**, Top, colours indicate pseudotemporal orderings. Bottom, heat map of selected markers of paraxial mesoderm differentiation. Approximate locations of cluster centres are indicated.



cell datasets. Columns (individual cells) are grouped by collection time point. Rows are individual HOX genes ordered by position. Approximate anatomical positions of HOX paralogues are indicated on the right.

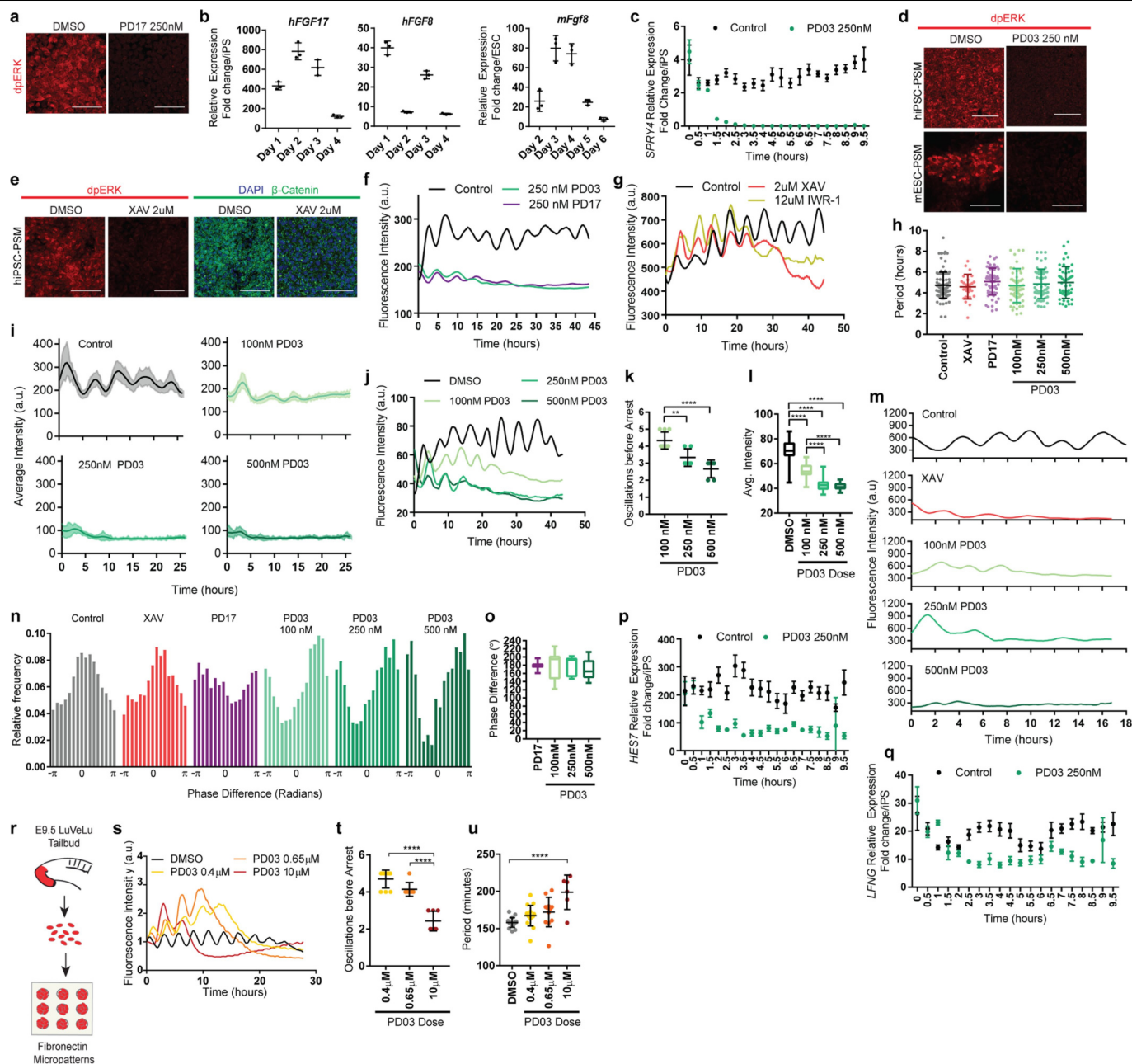


**Extended Data Fig. 5** | See next page for caption.

**Extended Data Fig. 5 | Analysis of the human segmentation clock at the single-cell level.** **a**, Scheme showing the insertion of a constitutively expressed *pCAG-H2B-mCherry* nuclear label in the safe harbour *AAVS1* locus in a *HES7-Achilles* human iPSC-cell background. **b**, Diffusion (square micrometres per minute) for individual human *HES7-Achilles* cells automatically tracked over a period of 24 h. The middle hinge corresponds to median, lower and upper hinges correspond to first and third quartiles, respectively, and the lower and upper whiskers correspond to the minimum and maximum, respectively.  $n = 76$  cells. **c**, Distribution of pairwise instantaneous phase shifts between individual oscillating human *HES7-Achilles* cells, binned by instantaneous distance between pairs of cells. *P* values for the pairwise Kolmogorov–Smirnov test are as follows:  $<160 \mu\text{m}$  versus  $160\text{--}265 \mu\text{m}$ : 0.6407,  $<160 \mu\text{m}$  versus  $265\text{--}530 \mu\text{m}$ : 0.1811,  $<160 \mu\text{m}$  versus  $>530 \mu\text{m}$ : 0.1340,  $160\text{--}265 \mu\text{m}$  versus  $265\text{--}530 \mu\text{m}$ : 0.1428,  $160\text{--}265 \mu\text{m}$  versus  $>530 \mu\text{m}$ : 0.6784, and  $265\text{--}530 \mu\text{m}$  versus  $>530 \mu\text{m}$ : 0.8171.  $n = 1,000$  observations. **d**, Distribution of phases along the unit circle at early, middle and late time points. Each dot represents one cell.  $n = 144$  cells. **e**, Illustration of phase determination. Representative raw *HES7-Achilles* fluorescence profile for an automatically tracked cell (left) and corresponding processed signal along with the inferred phase from Hilbert transform (right). **f**, Heat map of *HES7-Achilles* fluorescence intensity over time in automatically tracked cells. Each line represents one cell.  $n = 144$  cells. **g**, Histogram of the time (hours since onset of imaging) at cell division for manually tracked human *HES7-Achilles* cells.  $n = 67$  cells. **h**, Left, immunofluorescence staining for histone H3 phosphorylated at Ser10, in PSM cells derived from human iPSC cells, treated with vehicle control (DMSO) or  $5 \mu\text{M}$  aphidicolin for 24 or 48 h, starting on day 2 of differentiation.  $n = 5$  independent experiments. Scale bar,  $100 \mu\text{m}$ . Right, quantification of phosphorylated histone H3 (at Ser10) nuclei as a percentage of total nuclei. The middle hinge corresponds to median, the lower and upper hinges correspond to the first and third quartiles, respectively, and the lower and upper whiskers correspond to the minimum and maximum, respectively. **i**, Scatter plot showing the cell-cycle time in PSM cells derived from human iPSC cells, cultured in CLFBR medium. Mean  $\pm$  s.d.  $n = 26$  cells. **j**, Histogram of the *HES7-Achilles* oscillatory phase at the time of cell division in human iPSC-derived PSM cells cultures in CLFBR medium. Distribution is not significantly different from the uniform distribution: Kolmogorov–Smirnov test  $p = 0.225$ .  $n = 55$  cell divisions. **k**, Normalized *HES7-Achilles* fluorescence intensity profiles for 3 individual PSM cells derived from human iPSC cells, pre-treated with  $5 \mu\text{M}$  Aphidicolin for 24 h.  $n = 6$  independent experiments. **l**, Kuramoto order parameter over 20 h on day 3 of differentiation for human *HES7-Achilles* cells treated with vehicle control (DMSO) or  $5 \mu\text{M}$  aphidicolin for 24 h. The synchronization threshold is shown as the mean  $\pm$  s.d. of the Kuramoto order parameter for same dataset, but with randomized phases.  $n = 45$  cells (control) or 48 cells (aphidicolin). **m**, Comparison of the Kuramoto order parameter for oscillating *HES7-Achilles* cells treated with vehicle control (DMSO) or  $5 \mu\text{M}$  aphidicolin. The middle hinge corresponds to the median, the lower and upper hinges correspond to the first

and third quartiles, respectively, and the lower and upper whiskers correspond to the minimum and maximum, respectively. Paired two-sided *t*-test,  $P = 0.348$ .  $n = 45$  cells (control) or 48 cells (aphidicolin). **n**, qRT-PCR for Notch target genes *HES7*, *NRARP* and *LFNG* in PSM cells derived from human iPSC cells, treated with vehicle control (DMSO) or  $25 \mu\text{M}$  DAPT on day 2 of differentiation. Mean  $\pm$  s.d.  $n = 3$  biological replicates. **o**, Example of *HES7-Achilles* fluorescence intensity in a small ROI over a period of 45 h in cells treated with DMSO (vehicle control) or the  $\gamma$ -secretase inhibitor DAPT ( $25 \mu\text{M}$ ) in CLFBR medium.  $n = 16$  independent experiments. **p**, Representative example of *HES7-Achilles* fluorescence intensity profiles for PSM cells derived from mouse ES cells, treated with vehicle control (DMSO) or  $25 \mu\text{M}$  DAPT.  $n = 13$  independent experiments. **q**, Kuramoto order parameter over 20 h on day 2 of differentiation for human *HES7-Achilles* cells treated with vehicle control (DMSO) or  $25 \mu\text{M}$  DAPT. The synchronization threshold is shown as the mean  $\pm$  s.d. of the Kuramoto order parameter for same dataset, but with randomized phases.  $n = 131$  cells (control) or 110 cells (DAPT). **r**, Representative immunofluorescence staining for YAP, F-actin (phalloidin) and DAPI nuclear stain in isolated human PSM-like cells treated with DMSO or latrunculin A ( $350 \text{ nM}$ ). Scale bar,  $50 \mu\text{m}$ .  $n = 4$  independent experiments. **s**, ChIP-qPCR fold enrichment of the *LFNG* and *HES7* promoters in chromatin pulled down with an antibody against NOTCH1, relative to isotype IgG controls. Mean  $\pm$  s.d. iPSC-cell control,  $n = 4$ ; all other conditions,  $n = 3$  biological replicates. **t**, Mean *HES7-Achilles* fluorescence intensity for isolated human cells cultured with  $350 \text{ nM}$  latrunculin A alone, or in combination with  $25 \mu\text{M}$  DAPT. The middle hinge corresponds to the median, the lower and upper hinges correspond to the first and third quartiles, respectively, and the lower and upper whiskers correspond to the minimum and maximum, respectively.  $n = 18$  cells. **u**, Scatter plot showing the *HES7-Achilles* oscillatory period for isolated human cells cultured with  $350 \text{ nM}$  latrunculin A alone, or in combination with  $25 \mu\text{M}$  DAPT. Mean  $\pm$  s.d.  $n = 47$  (latrunculin A) or 22 (latrunculin A + DAPT) cells. **v**, Kuramoto order parameter over 18 h on day 2 of differentiation for human *HES7-Achilles* cells treated with DMSO, latrunculin A alone or latrunculin A in combination with DAPT. The synchronization threshold is shown as the mean  $\pm$  s.d. of the Kuramoto order parameter for the same dataset, but with randomized phases.  $n = 53$  cells (control), 18 cells (latrunculin A) or 18 cells (latrunculin A + DAPT). **w**, Comparison of the Kuramoto order parameter in confluent *HES7-Achilles* cells versus isolated cells treated with  $350 \text{ nM}$  latrunculin A alone, or in combination with  $25 \mu\text{M}$  DAPT. The middle hinge corresponds to the median, the lower and upper hinges correspond to the first and third quartiles, respectively, and the lower and upper whiskers correspond to the minimum and maximum, respectively. Paired one-way ANOVA with Bonferroni correction: confluent control versus LatA,  $P = 1.16 \times 10^{-6}$ ; confluent control versus latrunculin A + DAPT,  $P = 6.8 \times 10^{-13}$ ; latrunculin A versus latrunculin A + DAPT,  $P = 0.304$ .  $n = 53$  cells (control), 18 cells (latrunculin A) or 18 cells (latrunculin A + DAPT).



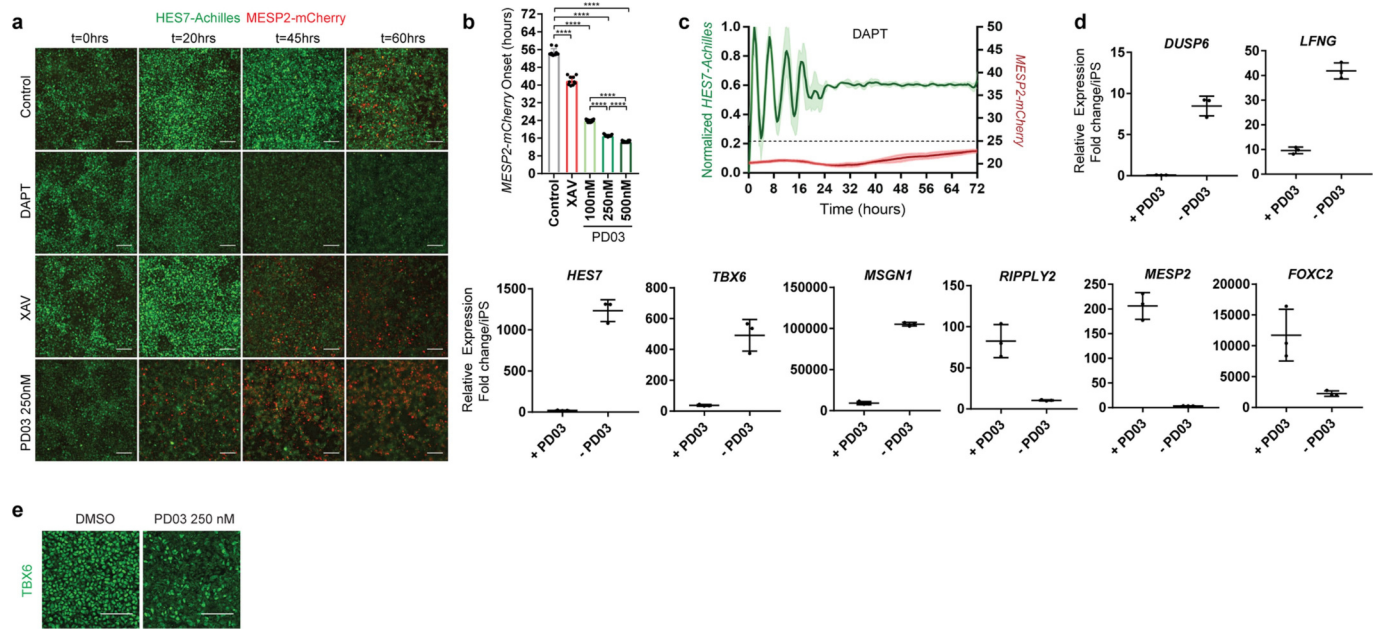


**Extended Data Fig. 6** | See next page for caption.



**Extended Data Fig. 6 | The role of FGF and WNT signaling in the regulation of segmentation clock properties.** **a**, Immunofluorescence staining for dpERK on day 2 of differentiation, following 3 h of treatment with DMSO (vehicle control) or the FGFR inhibitor PD173074 (250 nM) in CL medium.  $n = 4$  independent experiments. **b**, Left, qRT-PCR for the FGF ligands *FGF17* and *FGF8* on days 1–4 of human iPS cell differentiation. Relative expression is shown as the fold change relative to iPS cells at day 0. Mean  $\pm$  s.d.  $n = 3$  biological replicates. Right, qRT-PCR for the FGF ligand *Fgf8* on days 2–6 of mouse ES cell differentiation. Relative expression is shown as the fold change relative to ES cells at day 0. Mean  $\pm$  s.d.  $n = 3$  biological replicates. **c**, Time-course qRT-PCR for the FGF target gene *SPRY4* in PSM cells derived from human iPS cells, during the 10 h immediately after treatment with vehicle control (DMSO) or 250 nM PD03. Relative expression is shown as the fold change relative to ES cells at day 0. Mean  $\pm$  s.d.  $n = 3$  biological replicates. **d**, Immunofluorescence staining for dpERK in PSM cells derived from human iPS cells (top) or from mouse ES cells (bottom), treated with DMSO or PD03 (250 nM).  $n = 4$  independent experiments. **e**, Immunofluorescence staining for dpERK (left),  $\beta$ -catenin and nuclear stain (right) in PSM cells derived from human iPS cells, treated with vehicle control (DMSO) or 2  $\mu$ M XAV.  $n = 4$  independent experiments. Scale bar, 100  $\mu$ m. **f**, Representative examples of HES7–Achilles fluorescence intensity over the course of 45 h in a small area of interest within human cultures treated with DMSO (vehicle control), the MAPK inhibitor PD0325901 (250 nM), or the FGFR inhibitor PD173074 (250 nM) in CLFBR medium.  $n = 16$  independent experiments. **g**, HES7–Achilles fluorescence intensity over the course of 45 h in a small ROI within human cultures treated with DMSO (vehicle control), 2  $\mu$ M XAV or 12  $\mu$ M IWR-1 in CLFBR medium.  $n = 3$  independent experiments. **h**, *HES7*–*Achilles* oscillatory period of individual cells treated with vehicle control (DMSO), 2  $\mu$ M XAV, 250 nM PD17, or 100 nM, 250 nM or 500 nM PD03 on day 2 of differentiation. Mean  $\pm$  s.d. One-way ANOVA  $P$  values (NS, not significant): 0.9929, 0.4097, 0.9998, 0.9845 and 0.7425, from left to right on the graph.  $n = 27$  (XAV),  $n = 48$  (100 nM PD03),  $n = 57$  (all others) cells. **i**, Average fluorescence intensity profiles for automatically tracked individual *HES7*–*Achilles* human cells treated with vehicle control (DMSO) or increasing doses of PD03 (100 nM, 250 nM and 500 nM) on day 2 of differentiation. Mean  $\pm$  95% confidence interval.  $n = 68$  cells (control), 45 cells (100 nM), 35 cells (250 nM) or 36 cells (500 nM). **j**, Representative examples of HES7–Achilles fluorescence intensity profiles in a small ROI within human cultures treated with increasing doses of PD03 (100 nM, 250 nM and 500 nM) or vehicle control (DMSO).  $n = 8$  independent experiments. **k**, Number of HES7–Achilles oscillations before arrest in small ROIs within cultures treated with increasing doses of PD03 (100 nM, 250 nM and 500 nM). One-way ANOVA: 100 nM versus 250 nM,  $P = 0.0042$ ; 100 nM versus 500 nM,  $P = 2.0 \times 10^{-5}$ .  $n = 6$  independent experiments. **l**, Average HES7–Achilles fluorescence intensity in small ROIs over the course of the oscillatory regime (before the arrest of oscillations) in cells treated with vehicle control (DMSO) or increasing doses of PD03 (100 nM, 250 nM and 500 nM). The middle hinge corresponds to the median,

the lower and upper hinges correspond to the first and third quartiles, and the lower and upper whiskers correspond to the minimum and maximum. One-way ANOVA: control versus 100 nM,  $P = 6.7 \times 10^{-17}$ ; control versus 250 nM,  $P = 6.5 \times 10^{-21}$ ; control versus 500 nM,  $P = 1.9 \times 10^{-22}$ ; 100 nM versus 250 nM,  $P = 1.1 \times 10^{-17}$ ; 100 nM versus 500 nM,  $P = 2.5 \times 10^{-18}$ .  $n = 6$  independent experiments. **m**, Representative HES7–Achilles fluorescence intensity profiles for PSM cells derived from mouse ES cells, treated with vehicle control (DMSO), 2  $\mu$ M XAV, or 100 nM, 250 nM or 500 nM PD03.  $n = 12$  (control, XAV and 100 nM PD03) or  $n = 10$  (250 nM and 500 nM PD03) independent experiments. **n**, Histograms showing the instantaneous phase difference relative to control for individual cells treated with vehicle control (DMSO), 2  $\mu$ M XAV, 250 nM PD17, or 100 nM, 250 nM or 500 nM PD03. Details are given in ‘Phase shifts’ in Methods.  $n$  was fixed at 11,000 observations. **o**, Quantification of the average phase difference (in degrees) for HES7–Achilles oscillations in small ROIs in cells treated with 250 nM PD17, or 100 nM, 250 nM or 500 nM PD03 relative to control (DMSO) cells. The middle hinge corresponds to the median, the lower and upper hinges correspond to the first and third quartiles, respectively, and the lower and upper whiskers correspond to the minimum and maximum, respectively.  $n = 13$  (PD17),  $n = 17$  (100 nM),  $n = 7$  (250 nM) or  $n = 11$  (500 nM) independent experiments. **p, q**, Time-lapse qRT-PCR for the cyclic genes *HES7* (**p**) and *LFNG* (**q**) in PSM cells derived from human iPS cells, under control (DMSO) and 250-nM PD03 conditions. Samples were taken every 30 min immediately after treatment. Relative expression is shown as the fold change relative to ES cells at day 0. Mean  $\pm$  s.d.  $n = 3$  technical replicates. **r**, Outline of the experimental strategy used to assess the effect of FGF inhibition in primary mouse PSM cells carrying the LuVeLu reporter. The tail bud is dissected from E9.5 transgenic embryos, and cells are dissociated for seeding on fibronectin micropatterns. Oscillations of the LuVeLu reporter are examined in each micropattern. **s**, LuVeLu fluorescence intensity profiles in mouse tail-bud explant cells cultured on CYTOO micropatterns in CLFBR medium containing DMSO (vehicle control) or increasing doses of PD03 (0.4  $\mu$ M, 0.65  $\mu$ M and 10  $\mu$ M).  $n = 2$  independent experiments. **t**, Number of LuVeLu oscillations before arrest in mouse tail-bud explant cells cultured on CYTOO micropatterns treated with DMSO (vehicle control) or increasing doses of PD03 (0.4  $\mu$ M, 0.65  $\mu$ M and 10  $\mu$ M). Mean  $\pm$  s.d. One-way ANOVA: 0.4  $\mu$ M versus 0.65  $\mu$ M,  $P = 0.0642$ ; 0.4  $\mu$ M versus 10  $\mu$ M,  $P = 8.4 \times 10^{-9}$ ; 0.65  $\mu$ M versus 10  $\mu$ M,  $P = 2.9 \times 10^{-6}$ .  $n = 10$  micropatterns (0.4  $\mu$ M),  $n = 7$  micropatterns (0.65  $\mu$ M and 10  $\mu$ M). **u**, Average period of LuVeLu oscillations in mouse tail-bud explant cells cultured on CYTOO micropatterns treated with DMSO (vehicle control) or increasing doses of PD03 (0.4  $\mu$ M, 0.65  $\mu$ M and 10  $\mu$ M). Mean  $\pm$  s.d. One-way ANOVA: control versus 0.4  $\mu$ M,  $P = 0.2785$ ; control versus 0.65  $\mu$ M,  $P = 0.0658$ ; control versus 10  $\mu$ M,  $P = 2.7 \times 10^{-6}$ ; 0.4  $\mu$ M versus 0.65  $\mu$ M,  $P = 0.831$ ; 0.4  $\mu$ M versus 10  $\mu$ M,  $P = 3.05 \times 10^{-4}$ ; 0.65  $\mu$ M versus 10  $\mu$ M,  $P = 4 \times 10^{-3}$ .  $n = 18$  micropatterns (DMSO),  $n = 16$  micropatterns (0.4  $\mu$ M),  $n = 12$  micropatterns (0.65  $\mu$ M) and  $n = 6$  micropatterns (10  $\mu$ M).



**Extended Data Fig. 7 | Control of PSM maturation by FGF and WNT signalling in vitro.** **a**, Snapshots of *HES7-Achilles;MESP2-mCherry* double-reporter cells on days 2–5 of differentiation in CLFBR medium at 0, 20, 45 and 60 h. Cultures treated with DMSO (control), 25  $\mu$ M DAPT, 2  $\mu$ M XAV and 250 nM PD03 are shown.  $n = 10$  independent experiments. Scale bar, 100  $\mu$ m. **b**, Time of onset of *MESP2-mCherry* expression in PSM cells derived from human iPS cells treated with vehicle control (DMSO), 2  $\mu$ M XAV, 250 nM PD17 or 100 nM, 250 nM or 500 nM PD03. Onset of expression is defined by a threshold of 25 AU. Mean  $\pm$  s.d. One-way ANOVA: control versus XAV,  $P = 4.6 \times 10^{-15}$ ; control versus 100 nM PD03,  $P = 5.1 \times 10^{-17}$ ; control versus 250 nM PD03,  $P = 1.3 \times 10^{-17}$ ; control versus 500 nM PD03,  $P = 1.4 \times 10^{-18}$ ; 100 nM versus 250 nM PD03,  $P = 2.6 \times 10^{-15}$ ; 100 nM versus 500 nM PD03,  $P = 7.7 \times 10^{-16}$ ; 250 nM versus 500 nM PD03,

$P = 6.9 \times 10^{-5}$ ,  $n = 10$  independent experiments. **c**, *HES7-Achilles* and *MESP2-mCherry* fluorescence intensity profiles in small ROIs within PSM cultures derived from human iPS cells, treated with 25  $\mu$ M DAPT on days 2–5 of differentiation in CLFBR medium. Mean  $\pm$  s.d. Dotted line denotes the threshold for *MESP2* activation (25 AU).  $n = 15$  independent experiments. **d**, qRT-PCR for the genes *HES7*, *LFNG*, *MSGN1*, *TBX6*, *DUSP6*, *FOXC2*, *MESP2* and *RIPPLY2* in PSM cultures derived from human iPS cells, treated for 24 h with vehicle control (DMSO) or 250 nM PD03 in CLFBR medium. Relative expression is shown as the fold change relative to iPS cells at day 0. Mean  $\pm$  s.d.  $n = 3$  biological replicates. **e**, Immunofluorescence staining for TBX6 on day 3 of differentiation (CLFBR medium) in cells treated with DMSO or PD03 (250 nM).  $n = 4$  independent experiments. Scale bar, 100  $\mu$ m.

Extended Data Table 1 | Single-guide RNAs used in CRISPR–Cas9 targeting

Target Gene	Direction	sgRNA	PAM site	PAM site mutation in targeting vector
<i>hHES7</i>	Antisense	ACCTGCTCGCCCGGACGCCC	GGG	GGT
<i>mHes7</i>	Antisense	TAAGGAGGCACCCAAGCTAC	AGG	AAG
<i>hMESP2</i>	Antisense	GTCTCCAAAACGCGGGCGGT	GGG	GGT

**Extended Data Table 2 | Primary antibodies for immunofluorescence**

<b>Antibody</b>	<b>Species</b>	<b>Type</b>	<b>Source</b>	<b>Catalog Number</b>	<b>Dilution</b>
OCT3/4	Mouse	Monoclonal	Santa Cruz	Sc-5279	1:800
SOX2	Rabbit	Polyclonal	Millipore	AB5603	1:300
T/BRACHYURY	Goat	Polyclonal	R&D	AF2085	1:300
TBX6	Rabbit	Polyclonal	Abcam	ab38883	1:300
CDH1	Mouse	Monoclonal	Abcam	ab76055	1:300
CDH2	Rabbit	Polyclonal	Abcam	ab12221	1:300
dpERK	Rabbit	Monoclonal	Cell Signaling	4370P	1:400
β-CATENIN	Mouse	Monoclonal	BD	610153	1:400
YAP	Mouse	Monoclonal	Santa Cruz	sc-101199	1:200
pHistone H3 (Ser10)	Rabbit	Polyclonal	Santa Cruz	sc-8656	1:350

Extended Data Table 3 | Primer sequences for qPCR

Gene	Forward	Reverse	Reference
<i>hTBX6</i>	AAGTACCAACCCCGCATACA	TAGGCTGTCACGGAGATGAA	Loh <i>et al.</i>
<i>hMSGN1</i>	CTGGGACTGGAAGGACAGG	ACAGCTGGACAGGGAGAAGA	This study
<i>hHES7</i>	CTCCCTTGCCTCTAGGATTG	CTGAGGGTGGGAGACAGAAG	This study
<i>hLFNG</i>	CTGCTTGGAGGAAGGATTTG	TTGTGGTCAGCAGGAAGAGA	This study
<i>hAXIN2</i>	GGAGTGCCTTCATGGTTTCT	TGCATGTGTCAATGGTAGGG	This study
<i>hFGF8</i>	TCATCCGGACCTACCAACTC	CTCGGACTCGAACTCTGCTT	This study
<i>hFGF17</i>	GAAAGGTCAGCGACTGAAGG	TCTAGCCAGGAGGAGTTTGG	This study
<i>hMESP2</i>	AGCTTGGGTGCCTCCTTATT	TGCTTCCCTGAAAGACATCA	Loh <i>et al.</i>
<i>hRIPPLY2</i>	AAGAAGAGGAGACGCCGAAC	AGTCTGACTGGGTGCCTGAA	This study
<i>hFOXC2</i>	CCTCCTGGTATCTCAACCACA1	GAGGGTCGAGTTCTCAATCCC	Loh <i>et al.</i>
<i>hDUSP6</i>	CCAAATCATGGGCTCACTTT	CCATGCTCACACACACACAC	This study
<i>hSPRY2</i>	CTGTTTGCGGTGAAATGCT	TTGCCTAGGAGTGTCTGTGTTG	This study
<i>hNRARP</i>	CCTGCGTCACTTTCTGTCCT	AAGGGTCAGCAGCACTTCC	This study
<i>hHES7</i> <i>promoter</i>	AGATTGTAAGAGGTTGAGGCGGAC	GGAAGGATGACTTGGCGCTC	This study
<i>hLFNG</i> <i>promoter</i>	AGGCTCTGGCTGATCGGAAG	AGGTAATTAGCAGTCACCACCTCC	This study
<i>mFgf5</i>	CTGTACTGCAGAGTGGGCATCGG	GACTTCTGCGAGGCTGCGACAGG	Zhou <i>et al.</i>
<i>mT/Bra</i>	GCTTCAAGGAGCTAACTAACGAG	CCAGCAAGAAAGAGTACATGGC	This study
<i>mTbx6</i>	ATGTACCATCCACGAGAGTTGT	GGTAGCGGTAACCCTCTGTC	Chal <i>et al.</i>
<i>mMsgn1</i>	CGGCTTAGTCGAGCTGGATTA	CTCCGCTGGACAGACATCTTG	Chal <i>et al.</i>
<i>mRspo3</i>	ATGCACTTGCGACTGATTTCT	CAGCCTTGACTGACATTAGGATG	This study
<i>mFgf8</i>	CATGGCAGAAGACGGAGAC	CATGCAGATGTAGAGACCTGTC	Du <i>et al.</i>

Loh et al.<sup>45</sup>, Zhou et al.<sup>46</sup> and Du et al.<sup>47</sup> are cited in the table.



## Reporting Summary

Nature Research wishes to improve the reproducibility of the work that we publish. This form provides structure for consistency and transparency in reporting. For further information on Nature Research policies, see [Authors & Referees](#) and the [Editorial Policy Checklist](#).

### Statistics

For all statistical analyses, confirm that the following items are present in the figure legend, table legend, main text, or Methods section.

- |                                     |  |
|-------------------------------------|--|
| n/a                                 | Confirmed  |
| <input type="checkbox"/>            | <input checked="" type="checkbox"/> The exact sample size ( $n$ ) for each experimental group/condition, given as a discrete number and unit of measurement  |
| <input type="checkbox"/>            | <input checked="" type="checkbox"/> A statement on whether measurements were taken from distinct samples or whether the same sample was measured repeatedly  |
| <input type="checkbox"/>            | <input checked="" type="checkbox"/> The statistical test(s) used AND whether they are one- or two-sided<br><i>Only common tests should be described solely by name; describe more complex techniques in the Methods section.</i>   |
| <input checked="" type="checkbox"/> | <input type="checkbox"/> A description of all covariates tested  |
| <input type="checkbox"/>            | <input checked="" type="checkbox"/> A description of any assumptions or corrections, such as tests of normality and adjustment for multiple comparisons  |
| <input type="checkbox"/>            | <input checked="" type="checkbox"/> A full description of the statistical parameters including central tendency (e.g. means) or other basic estimates (e.g. regression coefficient) AND variation (e.g. standard deviation) or associated estimates of uncertainty (e.g. confidence intervals) |
| <input checked="" type="checkbox"/> | <input type="checkbox"/> For null hypothesis testing, the test statistic (e.g. $F$ , $t$ , $r$ ) with confidence intervals, effect sizes, degrees of freedom and $P$ value noted<br><i>Give <math>P</math> values as exact values whenever suitable.</i>                                       |
| <input checked="" type="checkbox"/> | <input type="checkbox"/> For Bayesian analysis, information on the choice of priors and Markov chain Monte Carlo settings  |
| <input checked="" type="checkbox"/> | <input type="checkbox"/> For hierarchical and complex designs, identification of the appropriate level for tests and full reporting of outcomes  |
| <input checked="" type="checkbox"/> | <input type="checkbox"/> Estimates of effect sizes (e.g. Cohen's $d$ , Pearson's $r$ ), indicating how they were calculated  |

Our web collection on [statistics for biologists](#) contains articles on many of the points above.

### Software and code

Policy information about [availability of computer code](#)

Data collection	Zen black (Zeiss), MIT Crispr Design Tool ( <a href="http://www.crispr.mit.edu">www.crispr.mit.edu</a> ; no longer available), In-Fusion cloning tools ( <a href="https://www.takarabio.com/learning-centers/cloning/in-fusion-cloning-tools">https://www.takarabio.com/learning-centers/cloning/in-fusion-cloning-tools</a> ), NEBuilder Assembly Tool ( <a href="https://nebuilderv1.neb.com/">https://nebuilderv1.neb.com/</a> ), Geneious 9.1.5, ApE v2.0.49.10.
Data analysis	Graphpad Prism 7, MATLAB R2018b, CFX Manager 3.1, ImageJ (Fiji), <a href="https://github.com/indrops/indrops">https://github.com/indrops/indrops</a> , <a href="https://github.com/AllonKleinLab/SPRING">https://github.com/AllonKleinLab/SPRING</a> , ScanPy41 (1.4.3), Python 3.6.8, anndata(0.6.22.post1), bbknn(1.3.6), fa2(0.3.5), ipython(7.8.0), jupyterlab(1.1.4), leidenalg(0.7.0), louvain(0.6.1), matplotlib(3.0.3), multicoretsne(0.1), numba(0.45.1), numpy(1.17.2), pandas(0.25.1), pytables(3.5.2), python-igraph(0.7.1.post7), scikit-learn(0.21.3), scipy(1.3.1), scrublet(0.2.1), seaborn(0.9.0), statsmodels(0.10.1), umap-learn(0.3.10), ForceAtlas2 algorithm in Gephi (0.9.1).

For manuscripts utilizing custom algorithms or software that are central to the research but not yet described in published literature, software must be made available to editors/reviewers. We strongly encourage code deposition in a community repository (e.g. GitHub). See the Nature Research [guidelines for submitting code & software](#) for further information.

### Data

Policy information about [availability of data](#)

All manuscripts must include a [data availability statement](#). This statement should provide the following information, where applicable:

- Accession codes, unique identifiers, or web links for publicly available datasets
- A list of figures that have associated raw data
- A description of any restrictions on data availability

*Provide your data availability statement here.*

## Field-specific reporting

Please select the one below that is the best fit for your research. If you are not sure, read the appropriate sections before making your selection.

☒ Life sciences ☐ Behavioural & social sciences ☐ Ecological, evolutionary & environmental sciences

For a reference copy of the document with all sections, see [nature.com/documents/nr-reporting-summary-flat.pdf](https://www.nature.com/documents/nr-reporting-summary-flat.pdf)

## Life sciences study design

All studies must disclose on these points even when the disclosure is negative.

Sample size	Sample sizes were not pre-determined. Rather, we ensured our sample sizes were sufficient by checking that inclusion of additional data points did not significantly change the variance (SD) of the data.
Data exclusions	During single cell RNA sequencing quality control steps, low complexity cell barcodes were excluded to avoid droplets that lack a cell but contain background RNA. Data was filtered to only include transcript counts originating from abundantly sampled cell barcodes. This determination was performed by inspecting a weighted histogram of Unique Molecular Identifier (UMI) – gene pair counts for each cell barcode, and manually thresholding to include the largest mode of the distribution (in all cases >80% of total sequencing reads). Additionally, low complexity transcriptomes were filtered out by excluding cell barcodes associated with <250 expressed genes. For analysis of oscillator synchronization, we excluded non-oscillating tracks to avoid potentially skewing the Kuramoto order parameter. This was done by filtering out cells with Fourier transform modulus below a specified threshold (i.e. 500).
Replication	To ensure the reproducibility of our findings, we carried out all experiments several independent times (exact n for each experiment reported in the figure legends). Each independent experiment contained technical triplicates. We ensured that these independent datasets of similar size did not change the reported results.
Randomization	Randomization is not relevant as the same cell lines were used in all cases.
Blinding	Blinding is not applicable to data collection (see above). In the case of time-lapse imaging analysis, all labels were removed and individual microscopy files were analyzed blindly in ImageJ/MATLAB for all conditions tested.

## Reporting for specific materials, systems and methods

We require information from authors about some types of materials, experimental systems and methods used in many studies. Here, indicate whether each material, system or method listed is relevant to your study. If you are not sure if a list item applies to your research, read the appropriate section before selecting a response.

### Materials & experimental systems

n/a	Involved in the study
<input type="checkbox"/>	<input checked="" type="checkbox"/> Antibodies
<input type="checkbox"/>	<input checked="" type="checkbox"/> Eukaryotic cell lines
<input checked="" type="checkbox"/>	<input type="checkbox"/> Palaeontology
<input type="checkbox"/>	<input checked="" type="checkbox"/> Animals and other organisms
<input checked="" type="checkbox"/>	<input type="checkbox"/> Human research participants
<input checked="" type="checkbox"/>	<input type="checkbox"/> Clinical data

### Methods

n/a	Involved in the study
<input type="checkbox"/>	<input checked="" type="checkbox"/> ChIP-seq
<input type="checkbox"/>	<input checked="" type="checkbox"/> Flow cytometry
<input checked="" type="checkbox"/>	<input type="checkbox"/> MRI-based neuroimaging

## Antibodies

Antibodies used	OCT3/4 (Santa Cruz sc-5279 Lot E2215 1:800), SOX2 (Millipore AB5603 Lot 3207627 1:300), T (R&D AF2085 Lot KQP0619021 1:300), TBX6 (Abcam ab38883 Lot GR3226767-3 1:300), CDH1 (Abcam ab76055 Lot GR260008-4 1:300), CDH2 (Abcam ab12221 Lot GR139340-27 1:300), dpERK (Cell Signaling 4370P Lot 17 1:400), beta-CATENIN (BD 610153 Lot 2146908 1:400), YAP (Santa Cruz sc-101199 Lot I0915 1:200), pHistoneH3 (Santa Cruz sc-8656 Lot D1615 1:350), Notch1 (Cell Signaling 3608S Lot 8 3.3 µg per IP), Acetylated (Lys9) Histone H3 (Cell Signaling 9649S Lot 13 0.5 µg per IP), Normal Rabbit IgG (Cell Signaling 2729S Lot 8 3.3 µg per IP)
Validation	All antibodies were validated by the suppliers and accurately represent expected expression patterns when tested on mouse embryos. - OCT3/4: Oct-3/4 Antibody (C-10) is recommended for detection of Oct-3/4 of mouse, rat and human origin by WB, IP, IF, IHC(P), FCM and ELISA; non cross-reactive with Oct-3/4 isoform B ( <a href="https://www.scbt.com/p/oct-3-4-antibody-c-10">https://www.scbt.com/p/oct-3-4-antibody-c-10</a> ) - SOX2: Anti-SOX2 Antibody, Cat. No. AB5603, is a highly specific rabbit polyclonal antibody SOX2 and has been tested for use in Immunocytochemistry, and Immunohistochemistry (Paraffin), and Western Blotting. ( <a href="http://www.emdmillipore.com/US/en/product/Anti-Sox2-Antibody,MM_NF-AB5603">http://www.emdmillipore.com/US/en/product/Anti-Sox2-Antibody,MM_NF-AB5603</a> ) -T: Detects human Brachyury in direct ELISAs and Western blots. In direct ELISAs, less than 10% cross-reactivity with recombinant

human (rh) TBX-6, rhTBX-2, rhTBX-5, and rhTBX-18 is observed. Reactivity to mouse and human. Applications: Western blot, ChIP, Immunocytochemistry, Immunohistochemistry. ([https://www.rndsystems.com/products/human-mouse-brachyury-antibody\\_af2085](https://www.rndsystems.com/products/human-mouse-brachyury-antibody_af2085))

- TBX6: Tested applications, Suitable for: IHC-Fr, ICC/IF, WB (<https://www.abcam.com/tbx6-antibody-ab38883.html>)
- CDH1: ab76055 does not cross react with VE Cadherin or N Cadherin. This product may give a weak signal in Western Blot when using unstimulated cell lines. Tested applications, Suitable for: Flow Cyt, ICC/IF, IHC-P, IHC-Fr, WB, IP, ELISA, ICC. Species reactivity, Reacts with: Mouse, Rat, Horse, Human. (<https://www.abcam.com/e-cadherin-antibody-m168-c-terminal-ab76055.html>)
- CDH2: Tested applications, Suitable for: Flow Cyt, IHC-Fr, WB, IHC-P, ICC/IF, ELISA. Species reactivity, Reacts with: Mouse, Rat, Human
- dpERK: Phospho-p44/42 MAPK (Erk1/2) (Thr202/Tyr204) (D13.14.4E) XP® Rabbit mAb detects endogenous levels of p44 and p42 MAP Kinase (Erk1 and Erk2) when dually phosphorylated at Thr202 and Tyr204 of Erk1 (Thr185 and Tyr187 of Erk2), and singly phosphorylated at Thr202. This antibody does not cross-react with the corresponding phosphorylated residues of either JNK/SAPK or p38 MAP kinases. Species Reactivity: Human, Mouse, Rat, Hamster, Monkey, Mink, D. melanogaster, Zebrafish, Bovine, Dog, Pig, S. cerevisiae. Applications Western Blotting, Immunoprecipitation, Immunohistochemistry (Paraffin), Immunofluorescence (Immunocytochemistry), Flow Cytometry. (<https://www.cellsignal.com/products/primary-antibodies/phospho-p44-42-mapk-erk1-2-thr202-tyr204-d13-14-4e-xp-rabbit-mab/4370>)
- beta-Catenin: Reactivity, Human (QC Testing) Mouse, Rat, Dog, Chicken (Tested in Development). Applications, Western blot (Routinely Tested), Immunohistochemistry, Immunoprecipitation, Immunofluorescence (Tested During Development). (<https://www.bdbiosciences.com/us/applications/research/stem-cell-research/cancer-research/human/purified-mouse-anti--catenin-14beta-catenin/p/610153>)
- YAP: raised against recombinant YAP of human origin, recommended for detection of YAP of mouse, rat and human origin by WB, IP, IF, IHC(P) and ELISA. (<https://www.scbt.com/p/yap-antibody-63-7>).
- pHistoneH3: recommended for detection of Ser 10 phosphorylated Histone H3 of mouse, rat, human, Drosophila melanogaster, Xenopus laevis and avian origin by WB, IP, IF, IHC(P) and ELISA; also reactive with additional species, including and equine, canine, bovine, porcine and avian. (<https://www.scbt.com/p/p-histone-h3-antibody-ser-10>)
- Notch1: Notch1 (D1E11) XP® Rabbit mAb detects intracellular epitopes between 2400 and 2500 amino acids of human Notch1. It recognizes both the full-length (~300 KDa) and the NTM region (~120 KDa), which consists of a short extracellular juxtamembrane peptide, a transmembrane sequence and the intracellular domain (NICD). The antibody cannot detect the extracellular (ligand-binding) domain of Notch1 following cleavage at the S2 site by ADAM-type metalloproteases. Species Reactivity: Human, Mouse, Rat. Applications: Western Blotting, Immunoprecipitation, Immunohistochemistry (Paraffin), Chromatin IP. (<https://www.cellsignal.com/products/primary-antibodies/notch1-d1e11-xp-rabbit-mab/3608>)
- Acetylated (Lys9) Histone H3: Acetyl-Histone H3 (Lys9) (C5B11) Rabbit mAb detects endogenous levels of histone H3 only when acetylated on Lys9. This antibody does not cross-react with other acetylated histones. Species Reactivity: Human, Mouse, Rat, Monkey, Zebrafish. Applications: Western Blotting, Immunoprecipitation, Immunohistochemistry (Paraffin), Immunofluorescence (Immunocytochemistry), Flow Cytometry, Chromatin IP, Chromatin IP-seq. (<https://www.cellsignal.com/products/primary-antibodies/acetyl-histone-h3-lys9-c5b11-rabbit-mab/9649>)

## Eukaryotic cell lines

Policy information about [cell lines](#)

Cell line source(s)	human iPS NCRM1 line was obtained from RUCDR Infinite Biologicals at Rutgers University <a href="https://commonfund.nih.gov/stemcells/lines#RMP-generated%20iPSC%20lines">https://commonfund.nih.gov/stemcells/lines#RMP-generated%20iPSC%20lines</a> Mouse E14 mESCs (129P2 genetic background) were obtained from BayGenomics.
Authentication	Authentication was unnecessary due to the unique morphology of human iPS and mouse ESC colonies, as well as their unique differentiation potential. We nevertheless stained for pluripotency markers (Oct4, Nanog, Sox2).
Mycoplasma contamination	All cell lines tested negative for mycoplasma contamination
Commonly misidentified lines (See <a href="#">ICLAC</a> register)	No commonly misidentified cell lines were used.

## Animals and other organisms

Policy information about [studies involving animals](#); [ARRIVE guidelines](#) recommended for reporting animal research

Laboratory animals	Mus musculus LuVeLu reporter line (Aulehla et al. 2008) E9.5 pups both male and female
Wild animals	The study did not involve wild animals
Field-collected samples	The study did not involve samples collected from the field.
Ethics oversight	The study protocol was approved by Brigham and Women's Hospital IACUC/CCM.

Note that full information on the approval of the study protocol must also be provided in the manuscript.

## ChIP-seq

### Data deposition

- ☐ Confirm that both raw and final processed data have been deposited in a public database such as [GEO](#).
- ☐ Confirm that you have deposited or provided access to graph files (e.g. BED files) for the called peaks.

Data access links <i>May remain private before publication.</i>	We performed ChIP-qPCR (not ChIP-seq), so all sections referring to high throughput sequencing data are not applicable. N/A
Files in database submission	N/A
Genome browser session (e.g. <a href="#">UCSC</a> )	N/A

### Methodology

Replicates	For ChIP-qPCR, we used n=3 or n=4 independent experiments as replicates (see figure legend for exact sample sizes).
Sequencing depth	N/A
Antibodies	Notch1 (Cell Signaling 3608S Lot 8 3.3 µg per IP), Acetylated (Lys9) Histone H3 (Cell Signaling 9649S Lot 13 0.5 µg per IP), Normal Rabbit IgG (Cell Signaling 2729S Lot 8 3.3 µg per IP)
Peak calling parameters	N/A
Data quality	N/A
Software	For qPCR data collection and analysis, CFX manager 3.1.

## Flow Cytometry

### Plots

Confirm that:

- ☒ The axis labels state the marker and fluorochrome used (e.g. CD4-FITC).
- ☒ The axis scales are clearly visible. Include numbers along axes only for bottom left plot of group (a 'group' is an analysis of identical markers).
- ☒ All plots are contour plots with outliers or pseudocolor plots.
- ☒ A numerical value for number of cells or percentage (with statistics) is provided.

### Methodology

Sample preparation	mESC-derived or human iPSC-derived PSM cells were differentiated in CL medium as indicated in Methods section. On the day of sorting, they were dissociated with TrypLE (mESC) or Accutase (hiPSC). The cells were resuspended in sorting buffer composed of PBS with 1% Penicillin/Streptomycin and 2% fetal bovine serum.
Instrument	BioRad S3 cell sorter with 488 and 561 lasers
Software	BioRad ProSort version 1.5
Cell population abundance	Sorting was not performed, we only used FACS for analysis.
Gating strategy	We first selected for singlets by using an FSC height vs. FCS area gate. We then selected viable cells and excluded cell debris by applying an FSC vs. SSC gate. For cell lines carrying Venus reporters (mESC pMsn1-Venus and hiPSC MSGN1-Venus), we used parental cell lines that do not carry the reporters as negative controls to determine the boundary between negative and positive cell populations. Parental lines were differentiated to a PSM state in parallel to experimental samples.

- ☒ Tick this box to confirm that a figure exemplifying the gating strategy is provided in the Supplementary Information.

# Coupling delay controls synchronized oscillation in the segmentation clock

<https://doi.org/10.1038/s41586-019-1882-z>

Received: 16 July 2018

Accepted: 5 November 2019

Published online: 8 January 2020

Kumiko Yoshioka-Kobayashi<sup>1,2</sup>, Marina Matsumiya<sup>1,3</sup>, Yusuke Niino<sup>4</sup>, Akihiro Isomura<sup>1,5,6</sup>, Hiroshi Kori<sup>7</sup>, Atsushi Miyawaki<sup>4,8</sup> & Ryoichiro Kageyama<sup>1,2,3,6\*</sup>

Individual cellular activities fluctuate but are constantly coordinated at the population level via cell–cell coupling. A notable example is the somite segmentation clock, in which the expression of clock genes (such as *Hes7*) oscillates in synchrony between the cells that comprise the presomitic mesoderm (PSM)<sup>1,2</sup>. This synchronization depends on the Notch signalling pathway; inhibiting this pathway desynchronizes oscillations, leading to somite fusion<sup>3–7</sup>. However, how Notch signalling regulates the synchronicity of HES7 oscillations is unknown. Here we establish a live-imaging system using a new fluorescent reporter (Achilles), which we fuse with HES7 to monitor synchronous oscillations in HES7 expression in the mouse PSM at a single-cell resolution. Wild-type cells can rapidly correct for phase fluctuations in HES7 oscillations, whereas the absence of the Notch modulator gene *lunatic fringe* (*Lfng*) leads to a loss of synchrony between PSM cells. Furthermore, HES7 oscillations are severely dampened in individual cells of *Lfng*-null PSM. However, when *Lfng*-null PSM cells were completely dissociated, the amplitude and periodicity of HES7 oscillations were almost normal, which suggests that LFNG is involved mostly in cell–cell coupling. Mixed cultures of control and *Lfng*-null PSM cells, and an optogenetic Notch signalling reporter assay, revealed that LFNG delays the signal-sending process of intercellular Notch signalling transmission. These results—together with mathematical modelling—raised the possibility that *Lfng*-null PSM cells shorten the coupling delay, thereby approaching a condition known as the oscillation or amplitude death of coupled oscillators<sup>8</sup>. Indeed, a small compound that lengthens the coupling delay partially rescues the amplitude and synchrony of HES7 oscillations in *Lfng*-null PSM cells. Our study reveals a delay control mechanism of the oscillatory networks involved in somite segmentation, and indicates that intercellular coupling with the correct delay is essential for synchronized oscillation.

The segmentation clock controls the periodic formation of somites, which are repetitive structures that lie along the body axis and give rise to vertebrae and ribs. The core of this clock system is controlled by cyclic expression of *Hes* or *Her* genes (such as *Hes7*<sup>9,10</sup>), and by the periodic activation of Notch, FGF and WNT signalling pathways in the PSM<sup>1,2</sup>. In mice, the expression of *Hes7* oscillates with an approximately 2-h periodicity, which defines the pace of segmentation<sup>9</sup>. Individual PSM cells carry their own clock, but are coupled to each other to generate coherent oscillation waves that lead to the formation of segmentation boundaries. This coupling is essential for segmentation, because uncoupling between cells results in severe somite fusion and morphological irregularities<sup>3–7</sup>. The Notch pathway is a critical mediator of this coupling mechanism in a range of species<sup>1–7</sup>. *Hes7* oscillations drive oscillatory expression of the Notch ligand gene *Delta-like1* (*Dll1*), which affects *Hes7* oscillations in neighbouring cells<sup>11,12</sup>. However, *Dll1*

alone is not sufficient for synchronous oscillations. In mice, LFNG—a glycosyltransferase for DLL1 and Notch proteins<sup>13</sup>—also exhibits oscillatory expression under the control of *Hes7* and has previously been suggested to be a key coupling factor: *Lfng*-knockout mice exhibit somite segmentation irregularities, as *Hes7* expression becomes asynchronous between PSM cells<sup>14–17</sup>. However, most previous analyses have been based on fixed samples and—as such—direct observations of single-cell clock oscillator dynamics are lacking.

Clock-gene reporters are powerful tools for studying oscillator dynamics but need improvement. Previous imaging analyses using a *Hes7*-promoter-driven destabilized luciferase reporter (pHes7-UbLuc) enabled ensemble detection of *Hes7* oscillations with a shorter period, and a substantially lower amplitude, in *Lfng*-knockout PSM than in the wild type<sup>16</sup> (Extended Data Fig. 1). The overall attenuation seen in the *Lfng*-knockout waveform could possibly result from the lower

<sup>1</sup>Institute for Frontier Life and Medical Sciences, Kyoto University, Kyoto, Japan. <sup>2</sup>Graduate School of Medicine, Kyoto University, Kyoto, Japan. <sup>3</sup>Graduate School of Biostudies, Kyoto University, Kyoto, Japan. <sup>4</sup>Laboratory for Cell Function and Dynamics, RIKEN Center for Brain Science, Wako, Japan. <sup>5</sup>Japan Science and Technology Agency, PRESTO, Saitama, Japan. <sup>6</sup>Institute for Integrated Cell-Material Sciences, Kyoto University, Kyoto, Japan. <sup>7</sup>Graduate School of Frontier Sciences, The University of Tokyo, Kashiwa, Japan. <sup>8</sup>Biotechnological Optics Research Team, RIKEN Center for Advanced Photonics, Wako, Japan. \*e-mail: rkageyam@infriant.kyoto-u.ac.jp



amplitude of oscillations of individual PSM cells, desynchronization between PSM cells or both. To discriminate between these possibilities, it is imperative to quantitatively follow the oscillations in individual PSM cells. A luciferase-based reporter system is not able to quantify *Hes7* oscillations in individual cells of the intact PSM because of its limited spatiotemporal resolution. Therefore, we established novel HES7 fluorescent reporter mice. We first produced a reporter for HES7 using the fast-maturing yellow fluorescent protein (YFP) 'Venus'<sup>18</sup> to make a Venus–HES7 fusion protein, but we were not able to obtain sufficient signal for single-cell quantification ( $n = 0$  out of 7 established mouse lines). Considering the short half-life of HES7 (22.3 min)<sup>19</sup>, fusion to this rapidly degraded protein was thought to prevent Venus from synthesizing its chromophore before degradation of the fused protein. We therefore performed directed evolution of the *Venus* gene through successive rounds of mutagenesis, screening and validation to improve the maturation rate (Methods). In total, 15 residues were subjected to site-directed random mutagenesis, and the subsequently constructed gene libraries were screened by selecting for bacterial colonies with fast maturation. We developed a faster-maturing YFP variant with eight amino acid substitutions, which we designate Achilles (Extended Data Fig. 2). In vitro experiments revealed that Achilles has the same spectral properties and maturation yield as Venus, but that Achilles outperforms Venus in terms of maturation speed (Fig. 1b, c, Extended Data Fig. 2).

We next generated transgenic mice carrying the *Hes7*-promoter-driven Achilles reporter, pHes7-Achilles-Hes7 (hereafter, Hes7-Achilles) (Extended Data Fig. 3); this reporter showed higher intensity and oscillation amplitude in signal detection than did the Venus reporter. Live imaging of PSM tissues from mice carrying the Hes7-Achilles reporter (Extended Data Fig. 3b)—which showed a pattern that was the most similar to endogenous HES7 protein expression among the tested constructs—successfully captured oscillatory expression at single-cell resolution (in  $n = 2$  out of 3 established mouse lines) (Fig. 1a, d). Furthermore, this line rescued the phenotype of *Hes7*-null mice (Extended Data Fig. 4), which suggests that the Achilles–HES7 fusion protein is biologically functional. Cell tracking and signal quantification enabled us to quantify the phase of HES7 oscillation in individual PSM cells over time (Fig. 1e, Extended Data Fig. 5). Using the Hes7-Achilles reporter, we compared HES7 oscillation dynamics between wild-type or *Lfng*<sup>+/−</sup> control and *Lfng*-knockout mice by culturing whole PSM tissues<sup>16</sup> and tail-bud regions<sup>20</sup>. In both control and *Lfng*-knockout PSM, each cell exhibited stable oscillation (Fig. 1d, e, Supplementary Videos 1, 2). Notably, in the control PSM, HES7 expression oscillated synchronously between neighbouring cells (Fig. 1d e, 2a). Phase fluctuation sometimes occurred—probably owing to cell division and migration—but this was immediately corrected in the control, such that synchrony was restored by the next cycle (Fig. 2a). By contrast, individual *Lfng*-knockout cells showed a smaller amplitude, a shorter period and more phase fluctuation than control cells in the PSM (Fig. 1d, e, 2a–c, Supplementary Videos 1, 2). The averaged HES7 expression levels decreased in the anterior *Lfng*-knockout PSM compared to the control (Fig. 2d). We assessed the degree of synchronization between oscillators by measuring the mean phase coherence (using the Kuramoto order parameter)<sup>21</sup>, which showed that *Lfng*-knockout PSM cells have a lower synchronization rate than control cells (Fig. 2e, f). We also performed tail-bud cultures and found milder, but similar, defects in *Lfng*-knockout tissue (Extended Data Fig. 6). Similar defects were observed in another, independent line of mice carrying the Hes7-Achilles reporter (Extended Data Fig. 6d–g). Furthermore, both acute inhibition of Notch signalling (by treatment with the Notch inhibitor DAPT (*N*-[*N*-(3,5-difluorophenylacetyl)-*L*-alanine]-*S*-phenylglycine *t*-butyl ester)) and acute knockdown of *Lfng* gradually led to similar defects in the control tail-bud cultures (Extended Data Fig. 7a–f), as previously observed in Notch-signalling mutants<sup>3</sup>. These data indicate that the lower amplitude at the population level in *Lfng*-knockout PSM originates from both lower amplitudes in individual cells and reduced synchronization across cells.

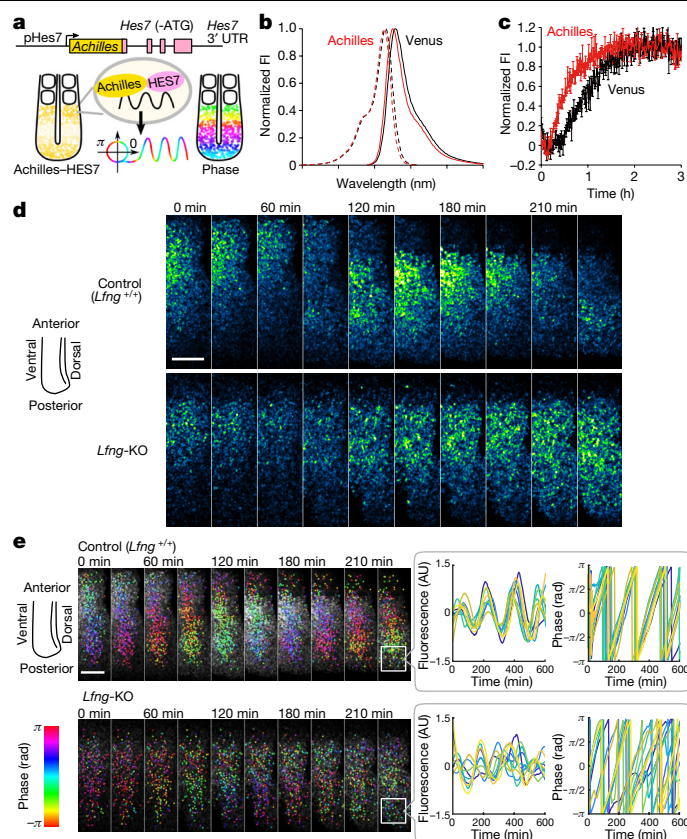


**Fig. 1 | Characterization of Achilles and analysis of oscillations of the Hes7-Achilles reporter in control and *Lfng*-knockout mice.** **a**, Structure of the *Achilles-Hes7* transgene. Expression of the Achilles–HES7 fusion protein was quantified and calculated for oscillation phase mapping in each PSM cell. UTR, untranslated region. **b**, Excitation (broken) and emission (solid) spectra of Achilles (red) and Venus (black). FI, fluorescence intensity. **c**, Time course of fluorescence intensities of Achilles (red) and Venus (black), synthesized from their mRNAs using the PURE system<sup>31</sup> (mean values  $\pm$  s.e.m. from three experiments). **d**, Live imaging of the Hes7-Achilles reporter in wild-type and *Lfng*-knockout (*Lfng*-KO) PSM by confocal microscopy. Z-projection images of the maximum intensity are shown. Signals were obtained at a single-cell resolution. The schema indicates the orientation of the PSM. **e**, Single-cell analysis of wild-type and *Lfng*-knockout PSM. Left, HES7 phase distribution in wild-type and *Lfng*-knockout PSM. Right, Fluorescence and phase time series from ten randomly selected cells in the posterior part of wild-type and *Lfng*-knockout PSM. AU, arbitrary unit. Scale bars, 100  $\mu$ m.

To address whether the lower amplitude in *Lfng*-knockout PSM arises from the lower amplitude of intrinsic oscillation or a coupling process, we examined expression of the Hes7-Achilles reporter in single isolated cells that had no interactions with their neighbouring cells. In these single-cell dissociation cultures<sup>22</sup> (Fig. 2g), HES7 oscillations were independent of Notch signalling (Extended Data Fig. 7g, h). Under this condition, both control and *Lfng*-knockout PSM cells maintained stable oscillations with similar periodicity and amplitudes that were only slightly different in each background (about 10% smaller in the *Lfng*-knockout cells) (Fig. 2h–k). Because the oscillation amplitude did not markedly differ between control and *Lfng*-knockout dissociated cells, the substantially smaller amplitudes detected in the intact *Lfng*-null PSM (Fig. 2c) probably result from abnormal cell–cell coupling through Notch signalling.

To understand the role of LFNG in cell–cell coupling mediated by Notch signalling, we directly assessed how oscillations are affected in mixed cultures of wild-type and *Lfng*-knockout cells using the Hes7-Achilles reporter. When a small ratio (1:20) of wild-type cells were mixed

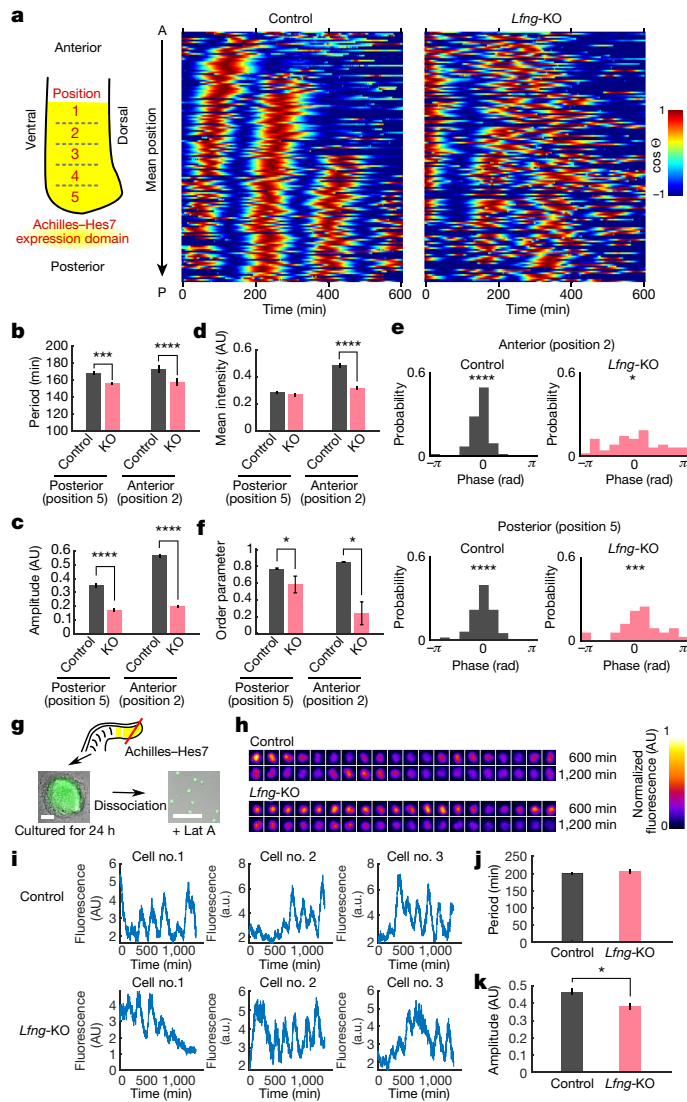


**Fig. 2 | Loss of *Lfng* affects oscillation period, amplitude and synchronization.** **a–k**, HES7 oscillations were examined in intact PSM tissues (**a–f**) and dissociated PSM cells (**g–k**). Wild-type (**a–f**) or *Lfng*<sup>+/−</sup> (**h–k**) PSM cells were used as controls. **a**,  $\cos \theta$  plots of single-cell time series in control and *Lfng*-knockout PSM. Each row corresponds to one cell. Tracks are aligned on the basis of the average position along the anterior (A)–posterior (P) axis. The HES7 expression domain was divided into 5 positions, and positions 2 and 5 in the schema were used for quantification of the anterior and posterior PSM, respectively (**b–f**). **b**, Oscillation period from time series of fluorescence of the Hes7-Achilles reporter in single PSM cells. **c**, Oscillation amplitude from time series of fluorescence of the Hes7-Achilles reporter in single PSM cells. **d**, Average expression levels of fluorescence of the Hes7-Achilles reporter in single PSM cells. At least 190 cells were examined for each genotype. Error bars indicate s.e.m. \*\*\* $P < 0.001$ , \*\*\*\* $P < 0.0001$ , unpaired  $t$ -test. **e**, Phase distribution at the first peak timing of average signals in the posterior and anterior PSM. At least 100 cells were examined for each genotype. \* $P < 0.05$ , \*\*\* $P < 0.001$ , \*\*\*\* $P < 0.0001$ , Rayleigh test. **f**, Kuramoto order parameter calculated using the phase shown in **e**. Error bars indicate s.e.m. \* $P < 0.05$ , unpaired  $t$ -test. **g**, Tail bud tissue was cultured for 24 h before dissociation. After dissociation, cells were cultured on fibronectin-coated plates in the presence of 0.5  $\mu$ M latrunculin A (lat A). Scale bars, 100  $\mu$ m. **h**, Examples of signals from the Hes7-Achilles reporter from regions of interest in dissociation cultures of PSM cells. **i**, Examples of signal of the Hes7-Achilles reporter in dissociation culture of PSM cells. **j**, Oscillation period of fluorescence of the Hes7-Achilles reporter in dissociated PSM cells. **k**, Oscillation amplitude from fluorescence of the Hes7-Achilles reporter in dissociated PSM cells. At least 100 cells were examined for each genotype. Error bars indicate s.e.m. \* $P < 0.05$ , unpaired  $t$ -test.

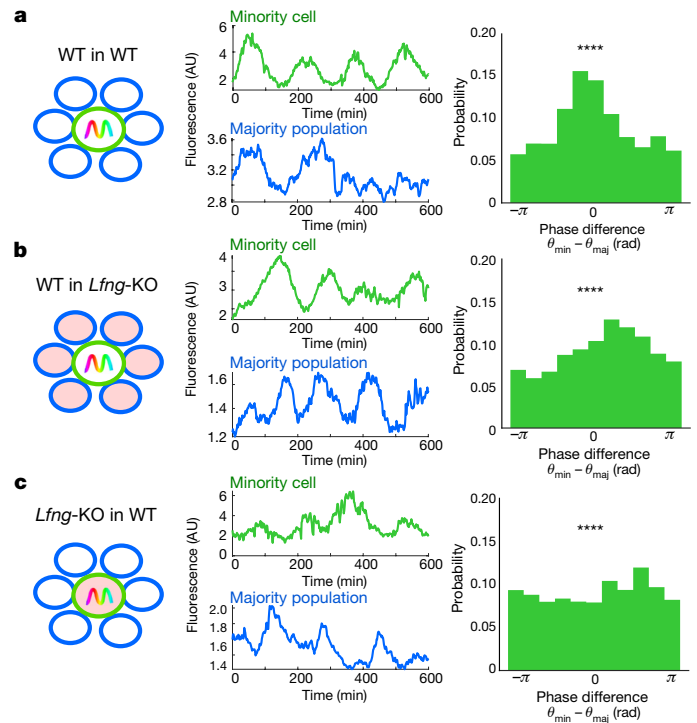


**Fig. 3 | Loss of *Lfng* affects timing information in cell–cell signal transmission.** **a**, Wild-type PSM cells expressing Achilles–HES7 or expressing both Achilles–HES7 and H2B–mCherry were mixed at a 20:1 ratio. **b**, Wild-type PSM cells (white) were mixed as a minority in *Lfng*-knockout cells (pink) in a 1:20 ratio. **c**, *Lfng*-knockout PSM cells (pink) were mixed as a minority in wild-type cells (white) in a 1:20 ratio. Fluorescence was quantified over time in the minority and majority cells. Only representative cells, as well as the population average, are shown (middle panels). The distribution of phase difference between the minority cells and their neighbouring cells was calculated at each time point (right panels). At least 150 minority cells were examined in 4 independent experiments for each mixture. \*\*\*\* $P < 0.0001$ , Rayleigh test.

into the *Lfng*-knockout cell population ('wild type in *Lfng*-knockout'), the wild-type cells expressed a normal level of HES7 and maintained roughly the same pace as *Lfng*-knockout cells (Fig. 3b, middle). The accuracy was decreased in this condition (Fig. 3b, right) compared with coupling between wild-type–wild-type cells (Fig. 3a), but this is most probably due to the fluctuation of inputs from neighbouring *Lfng*-knockout cells. Thus, DLL1 signals from *Lfng*-knockout cells were transmitted to wild-type cells. However, wild-type cells exhibited an advance in peak phase of about  $0.25\pi$  (corresponding to about 15 min), as compared to *Lfng*-knockout cells (Fig. 3b, right). This phase advance in wild-type cells compared to *Lfng*-knockout cells indicated that DLL1–Notch signal transmission from *Lfng*-knockout cells is faster than that from wild-type cells, suggesting that the absence of LFNG shortens the sending process in Notch signalling. By contrast, when mixing a small ratio (1:20) of *Lfng*-knockout cells into a wild-type population ('*Lfng*-knockout in wild type'), HES7 oscillations in *Lfng*-knockout cells showed lower amplitudes and did not keep phase well with wild-type cells, which indicates that the *Lfng*-knockout cells did not respond properly to DLL1 signals from wild-type cells (Fig. 3c) and suggests that LFNG regulates the amplitude of HES7 oscillations in the receiving process of Notch signalling. These data indicate that LFNG has dual functions: delaying the signal-sending process and increasing the amplitude in the signal-receiving process.

The coupling observed in the wild type in *Lfng*-knockout condition—but not in *Lfng*-knockout in wild type condition—could be due to asymmetric coupling of PSM cells, in which faster oscillators (such as *Lfng*-knockout cells) can accelerate slower oscillators (such as wild-type



cells), whereas slower oscillators cannot decelerate faster oscillators. To exclude this possibility, we co-cultured wild-type PSM cells with mutant PSM cells that exhibited faster HES7 oscillation by deletion of two introns from the *Hes7* gene<sup>23</sup> (In(3); Extended Data Fig. 8). This analysis showed that slower wild-type oscillators can decelerate a small ratio (1:20) of faster mutant oscillators (Extended Data Fig. 8b), indicating that the phase advance in the wild type in *Lfng*-knockout condition is not due to asymmetric coupling.

We further examined the role of *Lfng* in cell–cell coupling mediated by Notch signalling, using the recently developed optogenetic sender–receiver system<sup>12</sup>. In this system, expression of the Notch ligand DLL1 is optogenetically induced in sender cells, and the response in receiver cells is monitored using a *Hes1* reporter<sup>12</sup> (Fig. 4a). In these cells, endogenous *Hes1* expression oscillates with an approximately 2-h periodicity—similar to *Hes7* oscillations in the PSM<sup>12</sup>. Sender and receiver cells were co-cultured and, after optogenetic induction of *Dll1* expression, expression of the *Hes1* reporter in receiver cells was monitored using photomultiplier tubes. The presence of LFNG in DLL1 signal-sending cells increased the time required for the *Hes1* response (compare lanes 1 and 2 or lanes 4 and 5 in Fig. 4b, top; Fig. 4c) and decreased the amplitude in receiver cells (Fig. 4b, bottom). The delayed *Hes1* response was almost the same, irrespective of whether *Lfng* expression was sustained or oscillatory (compare lanes 2 and 3 or lanes 5 and 6 in Fig. 4b, top). We also found that the transport of DLL1 protein to the cell surface was delayed by about 15 min in the presence of *Lfng* compared to the absence of *Lfng* (Fig. 4d–h). However, the half-life of DLL1 protein was not affected by LFNG (Fig. 4i). By contrast, LFNG in receiver cells did not affect the delay (compare lanes 1 and 4 in Fig. 4b, top), but increased the amplitude of the *Hes1* response (compare lanes 1 and 4 in Fig. 4b, bottom). Thus, LFNG increases both the delay in the signal-sending process and the amplitude in the signal-receiving process, which agrees well with the results of the wild-type and *Lfng*-knockout mixed-cell-culture experiments.

Mathematical modelling (Extended Data Fig. 9a–c) suggests that the coupling delay ( $\tau_2$ ), the time required for *Hes7* from one cell to repress *Hes7* in its neighbouring cell, is very important for the dynamics of in-phase oscillations<sup>11,24,25</sup>. The in-phase oscillations are severely dampened when this delay is decreased or increased, which disrupts cell–cell synchrony (compare  $\tau_2 = 1.0$  with other  $\tau_2$  values in Extended Data Fig. 9d) and approaches a condition known as amplitude or oscillation death<sup>8</sup> (Extended Data Fig. 9e), in which the expression becomes steady (non-oscillatory). We speculate that by increasing the time required for intercellular DLL1–Notch signal transmission, LFNG may adjust the coupling delay to make it suitable for robust in-phase oscillations. It has previously been shown that expression level of the Notch intracellular domain—which is formed upon activation of Notch signalling—oscillates in the PSM dependently on *Lfng*<sup>16,17,26,27</sup> and that sustained expression of *Lfng* downregulates endogenous *Lfng* expression<sup>28</sup>, which suggests that LFNG is involved in the downregulation of Notch signalling. However, the average levels of HES7 expression decreased in the anterior *Lfng*-null PSM (Fig. 2d). Furthermore, it has previously been shown that sustained *Lfng* expression does not abolish the cyclic expression of endogenous *Hes7* in the PSM<sup>29</sup>. Thus, the repressor role of *Lfng* in the PSM remains obscure, and our data suggest that LFNG does not inhibit Notch signalling but rather increases the amplitude and the coupling delay (Fig. 4b).

To address the importance of the coupling delay in synchronized oscillations, we performed chemical library screening with PSM-like tissues derived from embryonic stem cells (ES cells)<sup>30</sup> to search for small molecules that could ameliorate the *Lfng*-knockout phenotype. Because the coupling delay decreased in the absence of *Lfng*, chemicals that increase the coupling delay may, at least partially, rescue the *Lfng*-knockout phenotype. Such chemicals would slightly increase the period of HES7 oscillations in wild-type cells (Extended Data Fig. 9e), although mechanisms other than the coupling delay could also affect the oscillatory period. We screened 431 compounds that target mainly signalling

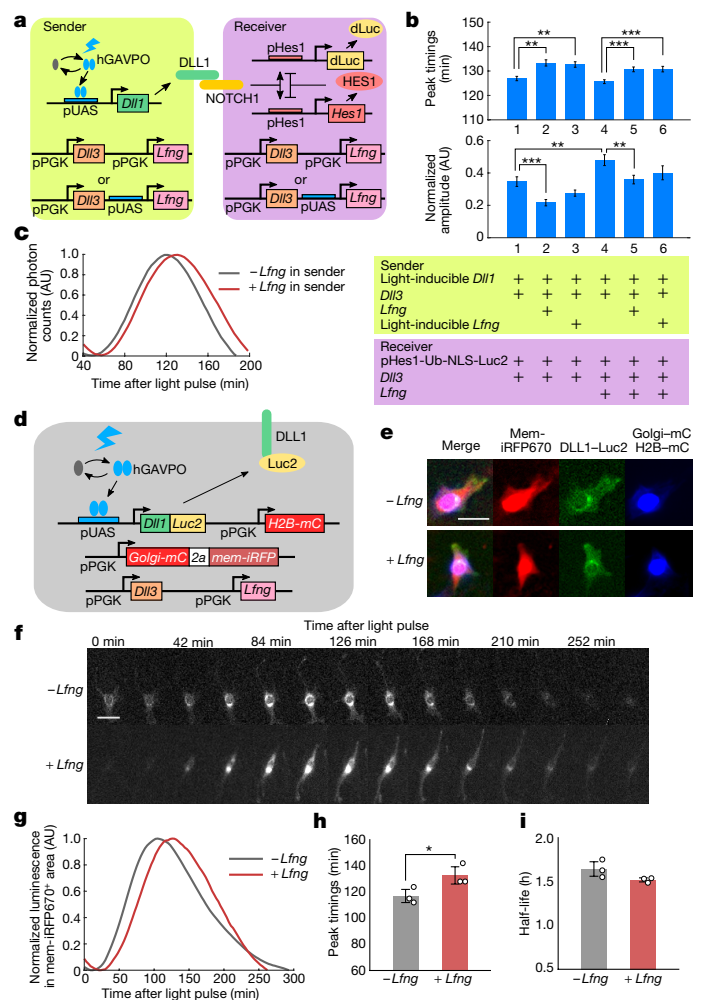


**Fig. 4 | LFNG in sending cells lengthened the time required for *Hes1* response to DLL1.** **a**, C2C12 myoblast sender cells carried the hGAVPO-based optogenetic *Dll1*-inducible system, whereas C2C12 myoblast receiver cells carried the *Hes1*-UbLuc2 reporter<sup>12</sup>. These cells were co-cultured, and *Hes1* reporter expression was monitored after light-induction of DLL1. **b**, Top, averages of peak timings in *Hes1* reporter signals were compared between receiver cells with and without *Lfng*. Bottom, averages of amplitude in *Hes1* reporter signals divided by mean signal intensity were compared between sender and receiver cells with and without *Lfng*. Oscillatory *Lfng* (light-inducible *Lfng*) expression was also induced in sender cells.  $n \geq 20$  for each combination. **c**, Representative time series of *Hes1* reporter signal in receiver cells co-cultured with sender cells that express *Dll1* with or without *Lfng*. **d**, DLL1-Luc2 fusion protein was expressed in C2C12 cells with or without *Lfng* using the hGAVPO-based optogenetic inducible system. Golgi-mCherry (mC)-2a-mem-iRFP670 was also expressed as a marker for image segmentation. **e**, DLL1-Luc2-expressing cells were co-cultured with wild-type C2C12 cells at 1:4 ratios. Luminescence, iRFP670 and mCherry signals were imaged with a charge-coupled device (CCD) camera after blue-light illumination. Snapshots of cells from multicolour imaging are shown. Scale bar, 50  $\mu$ m. **f**, Representative time series of DLL1-Luc2 images after light pulse. Scale bar, 50  $\mu$ m. **g**, Normalized DLL1-Luc2 signals at plasma membrane (iRFP<sup>+</sup> mCherry<sup>+</sup>) after light pulse. **h**, Peak timings of DLL1-Luc2 signals after light pulse. Average peak timing from three independent experiments are shown. **i**, Half-life of DLL1-Luc2 in the presence or absence of *Lfng*. Average half-life from three independent experiments is shown. Error bars indicate s.e.m. \* $P < 0.05$ , \*\* $P < 0.01$ , \*\*\* $P < 0.001$ , unpaired *t*-test.

and gene regulation, and found that 26 of them increased the period of *Hes7* oscillations by more than 10 min in PSM-like tissues derived from ES cells (Supplementary Table 1). Two of them (norcantharidin and kenpaullone) regulate WNT signalling, which is known to have crosstalk

with Notch signalling<sup>1,2</sup>. Thus, we analysed additional WNT signalling regulators and found that KY02111 (*N*-(6-chloro-2-benzothiazolyl)-3,4-dimethoxybenzene-propanamide), kenpauillone, IWR-I and C59 increased the coupling delay in the optogenetic sender–receiver system (Extended Data Fig. 10a, b). Kenpauillone significantly decreased the amplitude, but the others did not (Extended Data Fig. 10c). Among these compounds, KY02111 did recover the amplitude and synchrony of HES7 oscillations of *Lfng*-knockout PSM cells to some extent (Extended Data Fig. 10d–g), which suggests that this compound can partially rescue the amplitude and synchrony of HES7 oscillations in *Lfng*-knockout PSM cells by lengthening the coupling delay.

In summary, we have established a powerful live-cell imaging method that enables the quantification of oscillatory dynamics with single-cell resolution. Using this method, we have demonstrated how a phase delay can affect the collective dynamic oscillatory expression of genes. Although the pulsatile expression of the Notch ligand DLL1 can incompletely entrain oscillations in neighbouring cells<sup>12</sup>, the synchrony critically depends on the coupling delay<sup>11</sup> (Extended Data Fig. 9e). Our findings showed that LFNG is a key coupling factor that may make the delay of intercellular DLL1–Notch signal transmission suitable for robust synchronous oscillation. Furthermore, because *Lfng* mutations cause spondylocostal dysostosis, our study also raises the possibility that small compounds that correct the coupling delay have the potential to be used for treatment of this congenital disease.

## Online content

Any methods, additional references, Nature Research reporting summaries, source data, extended data, supplementary information, acknowledgements, peer review information; details of author contributions and competing interests; and statements of data and code availability are available at <https://doi.org/10.1038/s41586-019-1882-z>.

- Hubaud, A. & Pourqu  , O. Signalling dynamics in vertebrate segmentation. *Nat. Rev. Mol. Cell Biol.* **15**, 709–721 (2014).
- Oates, A. C., Morelli, L. G. & Ares, S. Patterning embryos with oscillations: structure, function and dynamics of the vertebrate segmentation clock. *Development* **139**, 625–639 (2012).
- Jiang, Y.-J. et al. Notch signalling and the synchronization of the somite segmentation clock. *Nature* **408**, 475–479 (2000).
- Riedel-Kruse, I. H., M  ller, C. & Oates, A. C. Synchrony dynamics during initiation, failure, and rescue of the segmentation clock. *Science* **317**, 1911–1915 (2007).
- Mara, A., Schroeder, J., Chalouni, C. & Holley, S. A. Priming, initiation and synchronization of the segmentation clock by *deltaD* and *deltaC*. *Nat. Cell Biol.* **9**, 523–530 (2007).
-   zbudak, E. M. & Lewis, J. Notch signalling synchronizes the zebrafish segmentation clock but is not needed to create somite boundaries. *PLoS Genet.* **4**, e15 (2008).
- Delaune, E. A., Fran  ois, P., Shih, N. P. & Amacher, S. L. Single-cell-resolution imaging of the impact of Notch signaling and mitosis on segmentation clock dynamics. *Dev. Cell* **23**, 995–1005 (2012).
- Ramana Reddy, D. V., Sen, A. & Johnston, G. L. Time delay induced death in coupled limit cycle oscillators. *Phys. Rev. Lett.* **80**, 5109–5112 (1998).
- Bessho, Y. et al. Dynamic expression and essential functions of *Hes7* in somite segmentation. *Genes Dev.* **15**, 2642–2647 (2001).
- Sparrow, D. B., Guill  n-Navarro, E., Fatkin, D. & Dunwoodie, S. L. Mutation of *Hairy-and-Enhancer-of-Split-7* in humans causes spondylocostal dysostosis. *Hum. Mol. Genet.* **17**, 3761–3766 (2008).
- Shimojo, H. et al. Oscillatory control of Delta-like1 in cell interactions regulates dynamic gene expression and tissue morphogenesis. *Genes Dev.* **30**, 102–116 (2016).
- Isomura, A., Ogushi, F., Kori, H. & Kageyama, R. Optogenetic perturbation and bioluminescence imaging to analyze cell-to-cell transfer of oscillatory information. *Genes Dev.* **31**, 524–535 (2017).
- Moloney, D. J. et al. Fringe is a glycosyltransferase that modifies Notch. *Nature* **406**, 369–375 (2000).
- Evrard, Y. A., Lun, Y., Aulehla, A., Gan, L. & Johnson, R. L. *lunatic fringe* is an essential mediator of somite segmentation and patterning. *Nature* **394**, 377–381 (1998).
- Zhang, N. & Gridley, T. Defects in somite formation in *lunatic fringe*-deficient mice. *Nature* **394**, 374–377 (1998).
- Niwa, Y. et al. Different types of oscillations in Notch and Fgf signaling regulate the spatiotemporal periodicity of somitogenesis. *Genes Dev.* **25**, 1115–1120 (2011).
- Okubo, Y. et al. *Lfng* regulates the synchronized oscillation of the mouse segmentation clock via *trans*-repression of Notch signalling. *Nat. Commun.* **3**, 1141 (2012).
- Nagai, T. et al. A variant of yellow fluorescent protein with fast and efficient maturation for cell-biological applications. *Nat. Biotechnol.* **20**, 87–90 (2002).
- Hirata, H. et al. Instability of *Hes7* protein is crucial for the somite segmentation clock. *Nat. Genet.* **36**, 750–754 (2004).
- Lauschke, V. M., Tsiairis, C. D., Fran  ois, P. & Aulehla, A. Scaling of embryonic patterning based on phase-gradient encoding. *Nature* **493**, 101–105 (2013).
- Pikovsky, A., Rosenblum, A. & Kurths, J. *Synchronization* (Cambridge Univ. Press, 2001).
- Hubaud, A., Regev, I., Mahadevan, L. & Pourqu  , O. Excitable dynamics and Yap-dependent mechanical cues drive the segmentation clock. *Cell* **171**, 668–682.e11 (2017).
- Harima, Y., Takashima, Y., Ueda, Y., Ohtsuka, T. & Kageyama, R. Accelerating the tempo of the segmentation clock by reducing the number of introns in the *Hes7* gene. *Cell Reports* **3**, 1–7 (2013).
- Lewis, J. Autoinhibition with transcriptional delay: a simple mechanism for the zebrafish somitogenesis oscillator. *Curr. Biol.* **13**, 1398–1408 (2003).
- Morelli, L. G. et al. Delayed coupling theory of vertebrate segmentation. *HFSP J.* **3**, 55–66 (2009).
- Morimoto, M., Takahashi, Y., Endo, M. & Saga, Y. The *Mesp2* transcription factor establishes segmental borders by suppressing Notch activity. *Nature* **435**, 354–359 (2005).
- Huppert, S. S., Ilagan, M. X., De Strooper, B. & Kopan, R. Analysis of Notch function in presomitic mesoderm suggests a  $\gamma$ -secretase-independent role for presenilins in somite differentiation. *Dev. Cell* **8**, 677–688 (2005).
- Williams, D. R., Shifley, E. T., Braunreiter, K. M. & Cole, S. E. Disruption of somitogenesis by a novel dominant allele of *Lfng* suggests important roles for protein processing and secretion. *Development* **143**, 822–830 (2016).
- Serth, K., Schuster-Gossler, K., Cordes, R. & Gossler, A. Transcriptional oscillation of *lunatic fringe* is essential for somitogenesis. *Genes Dev.* **17**, 912–925 (2003).
- Matsumiya, M., Tomita, T., Yoshioka-Kobayashi, K., Isomura, A. & Kageyama, R. ES cell-derived presomitic mesoderm-like tissues for analysis of synchronized oscillations in the segmentation clock. *Development* **145**, dev156836 (2018).
- Shimizu, Y. et al. Cell-free translation reconstituted with purified components. *Nat. Biotechnol.* **19**, 751–755 (2001).

**Publisher's note** Springer Nature remains neutral with regard to jurisdictional claims in published maps and institutional affiliations.

   The Author(s), under exclusive licence to Springer Nature Limited 2020

# Article

## Methods

No statistical methods were used to predetermine sample size. The experiments were not randomized and investigators were not blinded to allocation during experiments and outcome assessment.

### Generation of Achilles

Venus<sup>18</sup> was used as a starting template for PCR-based site-directed and semi-random mutagenesis with degenerate primers. Amplified cDNAs were subcloned in-frame into the BamHI and EcoRI sites of pRSET<sub>B</sub> and constructed vectors were transformed into *Escherichia coli* JM109(DE3). Colonies were screened for fluorescence using a trans-illuminator. Fifteen positions (Ser30, Tyr39, Gln69, Cys70, Ile128, Asp129, Tyr145, Asn146, Ser147, His148, Lys166, Ile167, Arg168, His169 and Ala206) were investigated and a variant with Ser30Arg, Tyr39Ile, Gln69Ala, Cys70Val, Ile128Ser, Asp129Gly, Tyr145Phe and Ala206Phe was chosen as Achilles. The nucleotide sequence reported in this paper has been deposited in the DDBJ/EMBL/GenBank under the accession number, LC381432 (Achilles).

### In vitro characterization of fluorescent proteins

JM109(DE3) cells expressing His-tagged fluorescent proteins were grown at 37 °C on a rotary shaker at 180 rpm for 17 h in LB medium. The bacteria were collected and resuspended in PBS with 10 mg/ml lysozyme and protease inhibitors (10 µM E-64, 10 µM leupeptin and 1 µM pepstatin A) and lysed by freeze–thaw cycling and sonication. Protein purification from the supernatant was carried out using Ni-NTA agarose, followed by buffer exchange into 50 mM HEPES-KOH (pH = 7.4) using a PD-10 column (GE Healthcare). Absorption and fluorescence spectra were measured using a spectrophotometer (U-3310, Hitachi) and a multimode microplate reader (Synergy Mx, BioTek), respectively. The molar extinction coefficient was calculated with protein concentrations measured using a Bradford protein assay kit (Bio-Rad), with BSA as the standard. Absolute fluorescence quantum yields were measured using an integrating sphere (C9920, Hamamatsu) with a multichannel analyser (C10027, Hamamatsu). A pH titration experiment was performed using buffers containing 25 mM of acetate (pH 4.0, 4.5 or 5.0), MES (pH 5.5, 6.0 or 6.5), HEPES (pH 7.0, 7.5 or 8.0) or borate (8.5, 9.0, 9.5 or 10.0).

### Imaging of bacterial colonies

Time-lapse imaging of transformed *E. coli* colonies was carried out using our homemade fluorescence analysing system, which consists of a Xenon light source (MAX-301, Asahi Spectra) and a cooled CCD camera (CoolSNAP HQ, Photometrics) controlled by MetaMorph (Universal Imaging). The 480AF30 (Omega Optical) and PB0540/020 (Asahi Spectra) filters were used for excitation and emission, respectively. The same amount of competent JM109(DE3) cells was used for transformation with the pRSET<sub>B</sub>-Achilles and pRSET<sub>B</sub>-Venus genes. After 3 h incubation at 37 °C, the plate was placed in a stage-top incubation chamber (IBC, Tokai Hit) kept at 37 °C and time-lapse imaging was immediately started. Images were analysed using ImageJ (National Institutes of Health) and the five-parameter sigmoidal curve (SigmaPlot (Systat Software)) gave the best-fit curve for the time-course data.

### Fluorescence measurement of synthesized proteins

Achilles and Venus cDNAs were inserted into the BamHI and EcoRI sites of pCS2 with a partial Kozak sequence CCACCATGG. The plasmids were linearized with *NotI* and mRNAs were synthesized using an mMESSAGE mMACHINE SP6 kit (Ambion). Protein synthesis was started by adding the synthesized mRNA to a cell-free protein-synthesizing system (PUREfrex 2.0, Gene Frontier)<sup>31</sup>. The reaction mixture was placed in a microplate reader (Synergy Mx, BioTek) at 37 °C and the fluorescence was monitored with excitation and emission wavelengths at 480 nm and 530 nm, respectively. The five-parameter sigmoidal curve (SigmaPlot (Systat Software)) gave the best-fit curve for the time-course data.

### Generation of Hes7-Achilles reporter transgenic mice

The reporter construct design is shown in Extended Data Fig. 3. *Venus-Hes7* and *Achilles-Hes7* transgenes were generated as follows. The XhoI-Kozak-Venus-Hes7 fragment was amplified by PCR, and then inserted between the genomic fragment of the *Hes7* promoter and the 3' UTR, which were used in the *pHes7-UbLuc* transgene<sup>32</sup>. Transgenic mice were generated by injecting the linearized constructs without backbone sequences into the pronuclei of fertilized eggs of ICR mice. All mice were handled in accordance with the Kyoto University Guide for the Care and Use of Laboratory Animals. Genotyping was performed using the following primers: forward, 5'-CGACC ACTAC CAGCA GAACA-3'; reverse, 5'-ATCCT CACTC CTAGT CCACA GAG-3'.

### Explant culture

Male mice carrying the *Hes7-Achilles* transgene were mated with wild-type ICR female mice, and then female mice at day 10 of pregnancy were killed. For live imaging that aimed at cell tracking and subsequent single-cell quantification, mice carrying the *Hes7-Achilles* transgene were crossed with mice of the ROSA26-H2B-mCherry line<sup>33</sup>. Embryos were dissected out in DMEM/F12 with 15 mM HEPES (Gibco) supplemented with 100 units per millilitre penicillin, 100 µg/ml streptomycin (Nacalai Tesque) and 0.2% BSA (Sigma). Culture medium for whole PSM tissues consisted of DMEM/F12 (Cell Culture Technologies) plus 1% BSA, 2 mM L-glutamine (Gibco), 1 g/l glucose (Wako) and 15 mM HEPES (Nacalai Tesque). For whole PSM cultures, tail regions including PSM and 2 or 3 formed somite pairs were embedded in 0.15% (for wide-field) or 0.3% (for confocal) low-melting-point agarose (SeaPlaque GTG, FMC) diluted in culture medium. The gel was set in a silicon ring attached onto a 35-mm glass-bottomed dish (14-mm diameter, Matsunami). Culture medium for tail buds was CO<sub>2</sub> 5%-equilibrated DMEM/F12 (Cell Culture Technologies) plus 1% BSA, 2 mM L-glutamine, 0.1 g/l glucose without HEPES, which was basically the same as has previously been established<sup>20</sup>. For tail-bud culture, a glass-bottomed dish was coated with fibronectin 50 µg/ml (Sigma) diluted in PBS for 2 h on a 35-°C hot plate. Tail-bud regions were excised and put onto a fibronectin-coated glass-bottomed dish with the anterior side down. Whole PSM tissues and tail-bud explants were maintained in a humidified chamber at 37 °C in 5% CO<sub>2</sub> and 80% O<sub>2</sub>, or in 5% CO<sub>2</sub>, respectively. To perturb Notch signaling, a 5 µM DAPT treatment or acute knockdown of *Lfng* was performed.

For acute knockdown of *Lfng*, two short hairpin RNAs (shRNAs) targeting mouse *Lfng* mRNA (*Lfng* shRNA no. 1: GCATAGCCTCTC-CGAGTACTTTCAAGAGAAGTACTCGGAGAGGCT ATGCTTTT; *Lfng* shRNA no. 2: CCCCTGAGCTATGGCATGTTTGAGAATCAAGAGTTCTCAACATGCCATAGCTCAGGGTTTT) and scrambled shRNA (GCCCGT-TATCGCAC TGATTTCATCAAGAGTGAATCATGCGATAACGGGCTTTT) were designed and inserted downstream of human U6 promoter. pPGK-iRFP670-NLS expression cassette was also attached to monitor transfected cells. For electroporation and subsequent imaging, tail-bud tissues from embryos carrying *Hes7-Achilles* transgene and *Rosa26-H2B-mCherry* allele, at embryonic day (E)10, were used and cultured following a previously established explant culture method<sup>22</sup>. Tail-bud mesenchyme cells were isolated, placed into an electrode chamber (CUI505P5, NEPAGENE) filled with 1 µg/ml shRNA-expression plasmid diluted with Opti-MEM (Thermo Fisher Scientific) and then incubated for 10 min at room temperature. Two successive poring pulses of 100 V for 5 ms, and 5 successive transfer pulses of 20 V for 50 ms, were applied using NEPA21 Super Electroporator (NEPAGENE). Tissues were then transferred onto a fibronectin-coated glass-bottomed dish. Time-lapse imaging was started after 6 h of incubation at 37 °C in 5% CO<sub>2</sub>.

### Live imaging

Confocal imaging was performed on a Zeiss LSM780 upright (for whole PSM culture), or inverted (for tail-bud culture) laser-scanning microscope. A 20× water immersion lens and a 40× oil immersion lens were



used for whole PSM culture and tail-bud culture, respectively. Achilles was excited with a 514-nm Argon laser. Additionally, for multicolour imaging aimed at cell tracking, mCherry was excited with a 561-nm diode-pumped solid-state laser. A Z-stack of 20–30 images was taken with 2–3- $\mu$ m depth intervals every 180 s (for whole PSM) or 90 s (for tail bud). Multicolour imaging was performed by simultaneous excitation using a 514/561-nm laser with 458/514/561/633-nm main beam splitter. Wide-field live imaging was performed either on an Olympus IX81 equipped with a cooled CCD camera (Princeton Instruments, VersArray 1 kb) or an Olympus IX83 equipped with an iKon-M (Andor) CCD camera. Signals from samples were collected by an Olympus (Tokyo)  $\times$ 10 UPlanApo objective. For bioluminescence imaging, 1 mM D-luciferin (Nacalai Tesque) was added to culture medium. Signal-to-noise ratios were increased by  $4 \times 4$  binning and 3-min exposure.

### Image processing, cell-tracking and signal quantification

For confocal images, the mCherry channel was used for cell tracking and signal normalization. Raw images were smoothed by Savitzky–Golay temporal filter with 5-frame window size and subjected to tracking by TrackMate<sup>34</sup> in Fiji/ImageJ. Parameters such as mean intensity and position in  $x$ – $y$ – $z$  directions for each cell at each time frame were taken from a 6- $\mu$ m-diameter circle at the centre of each cell. Further signal analysis was performed with custom-made programs in Matlab. Mean intensity in the Achilles channel was divided by mCherry intensity for normalization. To detrend time-series data, a trend line was drawn by taking the moving average of the signal with a window size of 240 min and then subtracted from the normalized signal. Savitzky–Golay filtering with third order and window size 60–80 min was applied to smooth the signal. Hilbert transform was performed to obtain instantaneous oscillation phase. Period and amplitude were quantified by peak detection on detrended and smoothed intensity. The definition of amplitude was the same as previously described<sup>35</sup>. For bioluminescence imaging, spike noise induced by cosmic rays was removed. The spatiotemporal pattern was obtained by averaging the signal along the left-to-right axis for each time point, and was then aligned in temporal sequence.

### Quantification of synchronization and statistical analysis

To evaluate whether a population of oscillators were synchronized, we applied the Rayleigh test to the phase distributions constructed from the single-cell traces of the phase information, as previously described<sup>12</sup>. Oscillation dynamics of population averages were quantified by taking the average signal in the whole area, and processing this signal in the same way as for the single-cell data to obtain the instantaneous phase. Relative phase shift from the collective oscillation for each cell was quantified by calculating the phase difference between the phases of neighbouring cells and the single-cell phase. To compare the synchronization efficiency, the Kuramoto order parameter was determined as previously described<sup>21</sup>. The order parameter was calculated using the relative phase shift. The anisotropy of phase data was assessed by Rayleigh test.

### Mixture experiments

A posterior half of the PSM was dissociated mechanically by pipetting up to 30 times, filtered through 10- $\mu$ m-pore cell strainer, and seeded into a silicon ring with 1.5-mm diameter and 2-mm height set in a glass-bottomed dish coated with fibronectin. Majority cells expressing Achilles–HES7 and minority cells expressing both Achilles–HES7 and H2B–mCherry were mixed at a 20:1 ratio. Cells were maintained in the culture medium used in tail-bud culture, plus 10  $\mu$ M Y-27632 (Wako). The oscillation phases in minority and majority cells were quantified by Hes7–Achilles reporter signal in the mCherry<sup>+</sup> or mCherry<sup>−</sup> area, respectively.

### Single-cell isolation culture

We followed previously described methods<sup>22</sup>, with some minor modifications. Tail-bud regions were treated in Accutase (Nacalai Tesque) for

5 min on a 35- $^{\circ}$ C hot plate, and ectodermal tissues were removed using a tungsten needle. Explant tissue was cultured on fibronectin-coated chamber cover glass (Laboratory-Tek) for 24 h in explant medium consisting of DMEM 4.5 g/l Glucose (Thermo Fisher no. 31053) plus 15% FCS (ES-cell-screened, Hyclone), 2 mM L-glutamine (Gibco), 100 U penicillin, 100 mg/ml streptomycin (Nacalai Tesque), 1 $\times$  non-essential amino acids (Gibco), 10 mM HEPES (Nacalai Tesque), 0.1 mM of  $\beta$ -mercaptoethanol (Gibco), 3  $\mu$ M Chir-99021 (Sigma no. SML1046), 200 nM LDN-193189 (StemRD no. LDN-02), 2.5  $\mu$ M BMS-493, 50 ng/ml mFGF4 (R&D), 1 mg/ml heparin (Sigma) and 10  $\mu$ M Y-27632 (Wako). Explant tissue was then detached using a P20 tip, collected in a 1.5-ml tube and dissociated by pipetting, filtered through a 10- $\mu$ m cell strainer, seeded onto 1% BSA-coated chamber cover glass and maintained in explant medium plus 0.5  $\mu$ M latrunculin A (Wako no. 125-04363).

### C2C12 sender–receiver assay

C2C12 cells with a light-inducible *Dll1* (sender) and pHes1-NLS-UbLuc reporter (receiver) have previously been established<sup>12</sup>. Various sender–receiver lines were newly established by introducing constructs with *Lfng* expression cassettes into the original sender or receiver line. All plasmids were based on the Tol2 transposon vector system (a gift from the Kawakami Laboratory). To establish stable cell lines, 0.5  $\mu$ g pCAGGS-mT2P, 0.125  $\mu$ g pKYK34-pEFs-Puro and 0.375  $\mu$ g pKYK28-pPGK-Dll3-HA-pPGK-iRFP670-NLS or pKYK29-pPGK-Dll3-HA-pPGK-iRFP670-NLS-pPGK-Lfng-Flag was transfected into original sender or receiver line, cultured in a 12-well plate at  $5 \times 10^4$  cell density using ViaFect transfection reagent (Promega). Cells were expanded and selected by 2  $\mu$ g/ml puromycin for one week. iRFP670<sup>+</sup> cells were then sorted using FACSaria III (BD Biosciences). Then,  $1.25 \times 10^5$  of sender cells and  $0.25 \times 10^5$  of receiver cells were mixed and plated onto black 24-well plates, and photon-counting measurements were performed every 3 min with 5-s blue-light exposure. Light stimuli were applied every 2.5 h with 30-s duration. Recorded traces were detrended and then smoothed using a Savitzky–Golay filter.

### Time-lapse imaging of DLL1–Luc2 fusion protein in C2C12 cells

C2C12 cells that carry the light-inducible DLL1–Luc2 fusion protein system and the *Dll3* and Golgi–mCherry–2a–mem-iRFP670 expression system, with or without the *Lfng* expression vector, were established, and the luciferase activity in iRFP<sup>+</sup> mCherry<sup>−</sup> regions was quantified.

### Culture of PSM-like tissue derived from ES cells, and chemical library screening

PSM-like tissues (iPSM colonies) were induced from mouse ES cells that carry the Hes7–UbLuc reporter, as previously described<sup>30</sup>. A single iPSM colony per well was cultured in gelatin-coated, black 24-well plates, and each small compound was added from day 4 onward. Hes7-promoter-driven luciferase activity was measured by a highly sensitive photomultiplier tube<sup>36</sup>. Small compounds that lengthened the period of Hes7 oscillations (Supplementary Table 1) were chosen for further analyses.

### Mathematical modelling

The HES7 level of cell  $i$  is described by  $X_i(t)$  (in which  $i = 1, 2, \dots, 36$  and  $t$  is time in hours). Here,  $\tau_1$  is the time required for Hes7 to affect its own formation in the same cell through negative feedback. The interaction between cells is simplified in the following manner. *Dll1* is inhibited by Hes7 in the same cell, and activates Hes7 in other cells. We regard this interaction as the mutual inhibition between two cells with delay  $\tau_2$  in Hes7 dynamics (Extended Data Fig. 9b). Thus,  $\tau_2$  represents the time required for Hes7 from one cell to repress Hes7 in its neighbouring cell. In dynamical equations of the model (Extended Data Fig. 9c), the interpretations of parameters are as follows:  $v$  is the maximum synthesis rate;  $r$  is the degradation rate;  $K_1$  and  $K_2$  correspond to the typical amounts of HES7 that account for the repression; and  $m$  and  $n$  are the Hill coefficients.  $N(i)$  represents the set of cells that neighbour cell  $i$ . In numerical simulations, we set  $v = 10$ ,  $r = 2$ ,  $K_1 = 1$ ,  $K_2 = 2$ ,  $m = 2$ ,  $n = 2$  and

# Article

$\tau = 0.75$ , and observed the dependence of dynamical behaviour on  $\tau_2$ . The same random initial condition was used for all cases. In parameter space for in-phase oscillation,  $\tau_2$  values longer or shorter than 1.0 result in smaller amplitudes and larger phase differences. The  $\tau_2$  dependence of oscillation amplitude ( $X_{\text{amp}}$ ) and dispersion among cells ( $X_{\text{dis}}$ ) are defined as follows. The oscillation amplitude  $X_{\text{amp}}(i)$  of cell  $i$  is defined as the difference between the maximum and minimum  $X_i(t)$  values for  $t_1 < t < t_2$ , in which  $t_1 = 100$  and  $t_2 = 200$ .  $X_{\text{amp}}$  is their average:

$$X_{\text{amp}} = \frac{1}{36} \sum_{i=1}^{36} X_{\text{amp}}(i)$$

$X_{\text{dis}}$  is the standard deviation of  $X_i(t) - \hat{X}(t)$  for  $t_1 < t < t_2$ :

$$X_{\text{dis}} = \sqrt{\frac{1}{36} \sum_{i=1}^{36} \frac{1}{t_2 - t_1} \int_{t_1}^{t_2} \{X_i(t) - \hat{X}(t)\}^2 dt}$$

$X_{\text{dis}}$  should be compared with  $X_{\text{amp}}$ : a smaller  $X_{\text{dis}}/X_{\text{amp}}$  value indicates a better synchronization. The oscillation amplitude  $X_{\text{amp}}(i)$  of cell  $i$  is defined as the difference between the maximum and minimum  $X_i(t)$  values for  $t_1 < t < t_2$ , in which  $t_1 = 100$  and  $t_2 = 200$ .  $X_{\text{amp}}$  is their average:

$$X_{\text{amp}} = \frac{1}{36} \sum_{i=1}^{36} X_{\text{amp}}(i)$$

For a time series of  $X_i(t)$  at different  $\tau_2$  values, the average HES7 level (Extended Data Fig. 9d) is calculated as:

$$\hat{X}(t) = \frac{1}{36} \sum_{i=1}^{36} X_i(t)$$

## Reporting summary

Further information on research design is available in the Nature Research Reporting Summary linked to this paper.

## Data availability

The nucleotide sequence for *Achilles* cDNA has been deposited in the DDBJ/EMBL/GenBank under the accession number LC381432. Raw data

for *Achilles* and all the other experiments are available on request from A.M. and the corresponding author, respectively. Correspondence and requests for materials should be addressed to A.M. (matsushi@brain.riken.jp) for *Achilles* cDNA and R.K. (rkageyam@infront.kyoto-u.ac.jp) for other materials.

## Code availability

Image processing and analysis were performed using Fiji (v.1.0) and Matlab (R2018a). Subsequent analysis was performed using custom Matlab scripts. The codes are available upon request from the corresponding author.

32. Takashima, Y., Ohtsuka, T., González, A., Miyachi, H. & Kageyama, R. Intronic delay is essential for oscillatory expression in the segmentation clock. *Proc. Natl. Acad. Sci. USA* **108**, 3300–3305 (2011).
33. Abe, T. et al. Establishment of conditional reporter mouse lines at ROSA26 locus for live cell imaging. *Genesis* **49**, 579–590 (2011).
34. Tinevez, J. Y. et al. TrackMate: an open and extensible platform for single-particle tracking. *Methods* **115**, 80–90 (2017).
35. Webb, A. B. et al. Persistence, period and precision of autonomous cellular oscillators from the zebrafish segmentation clock. *eLife* **5**, e08438 (2016).
36. Isomura, A. & Kageyama, R. An optogenetic method to control and analyze gene expression patterns in cell-to-cell interactions. *J. Vis. Exp.* **133**, e57149 (2018).

**Acknowledgements** We thank C. Vissers for critical reading, R. Sueda for technical help, F. Ishidate for live imaging, H. Miyachi for the generation of transgenic mice and M. Uesugi for providing KY02111. This work was supported by Core Research for Evolutional Science and Technology (JPMJCR12W2 to R.K.), Precursory Research for Embryonic Science and Technology (to A.I.), Grant-in-Aid for Scientific Research on Innovative Areas (Ministry of Education, Culture, Sports, Science, and Technology (MEXT), Japan (16H06480 to R.K.; 18H04734 to A.I.; 15H05876 to H.K.)) and the Brain Mapping by Integrated Neurotechnologies for Disease Studies (Brain/MINDS) (JP19dm0207001 to A.M.).

**Author contributions** K.Y.-K. developed Hes7 reporter mice, performed the experiments, analysed the data and wrote the manuscript; M.M. performed chemical library screening; A.I. analysed the data; Y.N. and A.M. developed *Achilles*, analysed the data and wrote the manuscript; H.K. performed mathematical modelling analysis; R.K. designed and supervised the project and wrote the manuscript.

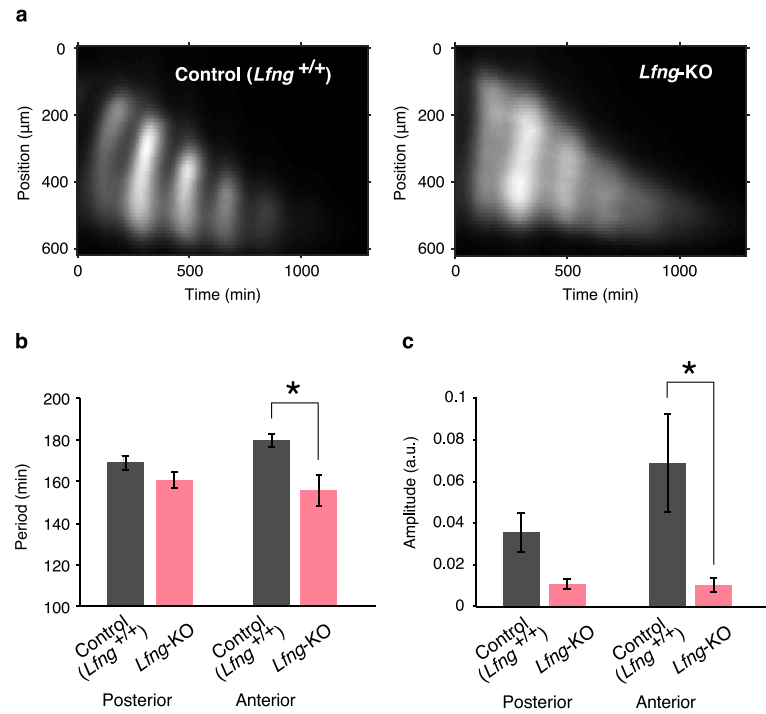
**Competing interests** The authors declare no competing interests.

## Additional information

**Supplementary information** is available for this paper at <https://doi.org/10.1038/s41586-019-1882-z>.

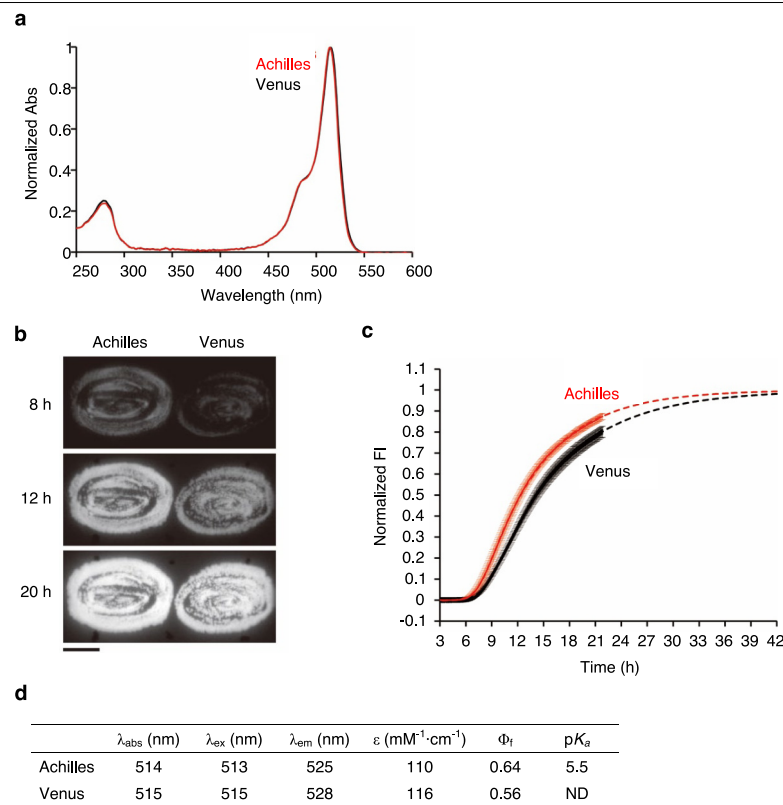
**Correspondence and requests for materials** should be addressed to R.K.

**Reprints and permissions information** is available at <http://www.nature.com/reprints>.

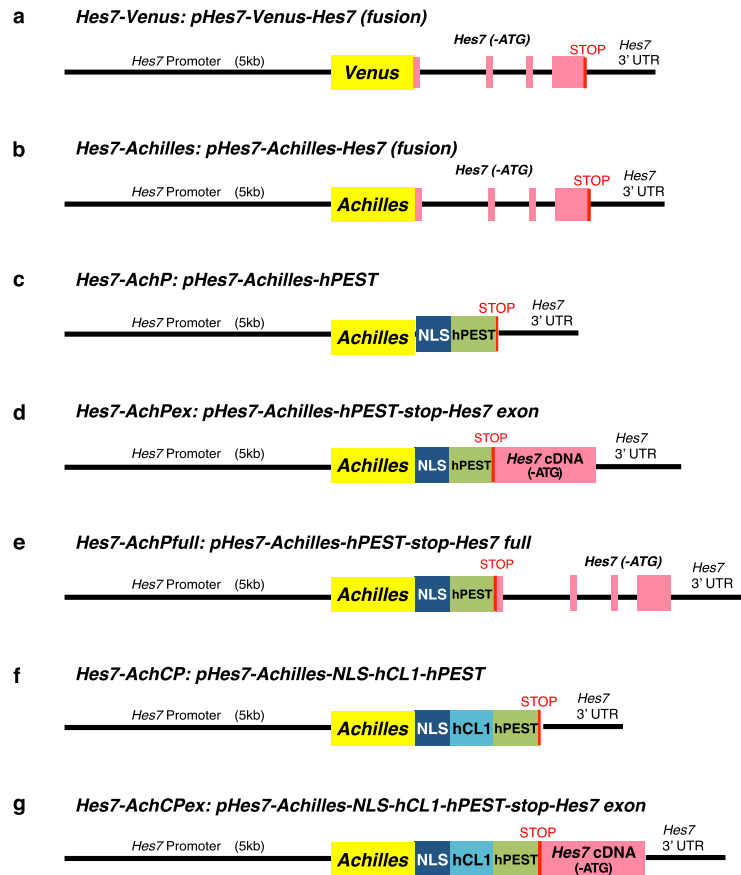


**Extended Data Fig. 1 | Loss of *Lfng* affects *Hes7* oscillation dynamics at a tissue level. a**, p*Hes7*-UbLuc imaging in wild-type and *Lfng*-knockout PSM. Spatiotemporal patterns along the anterior–posterior axis are shown. Top is

anterior. **b**, Period of *Hes7* oscillations in the anterior and posterior PSM ( $n = 4$  PSM samples). **c**, Amplitude of *Hes7* oscillations ( $n = 4$  PSM samples). Error bars indicate s.e.m. \* $P < 0.05$ , unpaired  $t$ -test.



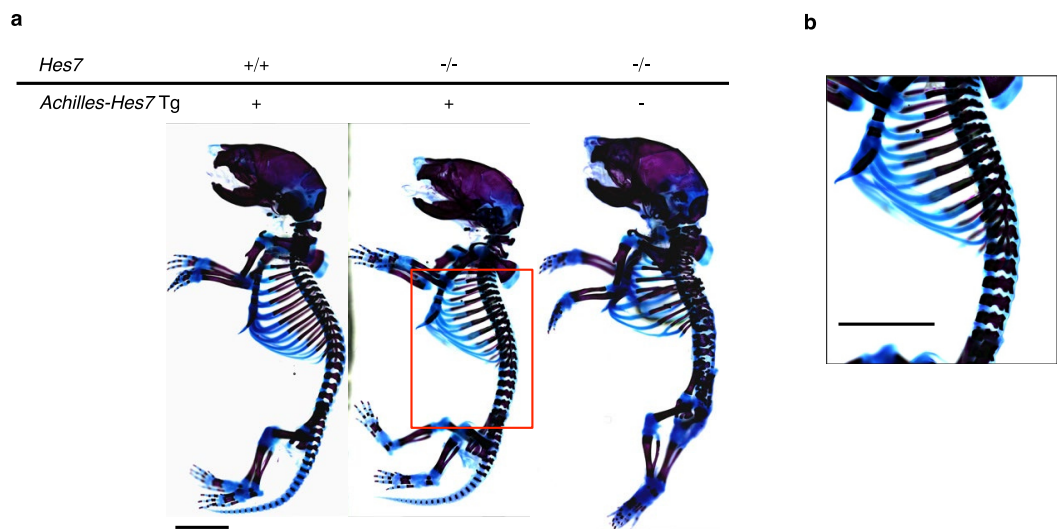
**Extended Data Fig. 2 | Comparative characterization of Achilles versus Venus.** **a**, Absorption (abs) spectra of Achilles (red) and Venus (black). **b**, Fluorescence images of bacteria that express Achilles and Venus. Bacterial colonies were grown at 37 °C and photographed at 8, 12, and 20 h after transformation. Exactly the same number of competent bacterial cells was used for transformation. Scale bar, 5 mm. **c**, Time course of fluorescence intensities of transformed *E. coli* colonies (mean values  $\pm$  s.e.m. from three experiments). The data were normalized to the final yields extrapolated by curve fitting (broken line). **d**, Comparison of properties of Achilles and Venus.



**Extended Data Fig. 3 | Schematic structures of fluorescent reporters for HES7.** **a**, Venus was inserted between the 5-kb *Hes7* promoter and the *Hes7* gene to drive expression of the Venus–HES7 fusion protein. **b**, Achilles was inserted between the 5-kb *Hes7* promoter and the *Hes7* gene to drive expression of the Achilles–HES7 fusion protein. **c**, Achilles fused to NLS–hPEST is expressed under the control of the *Hes7* promoter. **d**, *Hes7* cDNA without an initiation codon was inserted between the PEST sequence and the *Hes7* 3' UTR of the

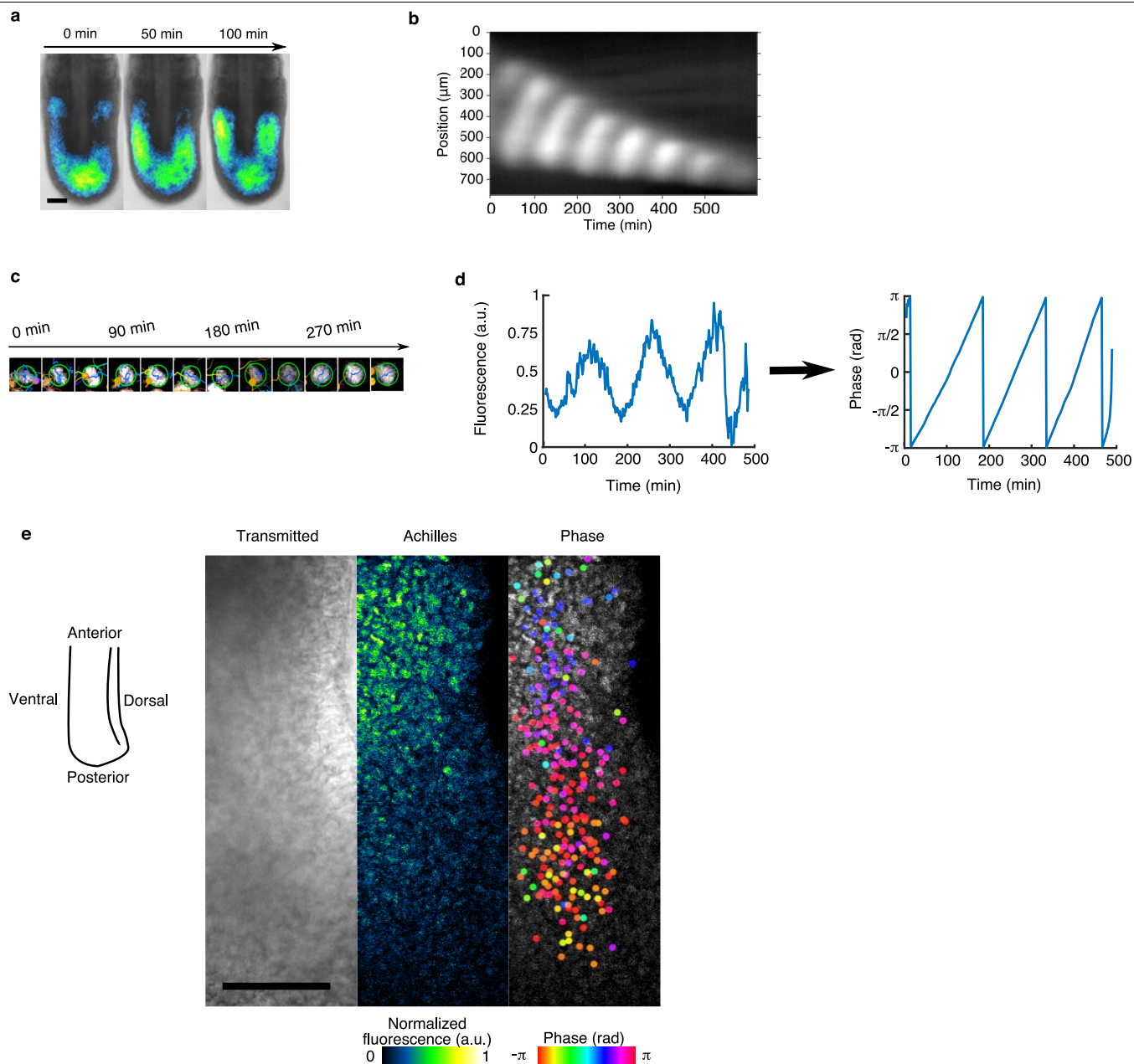
construct shown in **c** to enable the transcripts to mimic endogenous mRNA stability. **e**, The *Hes7* gene (exons + introns) without an initiation codon was inserted between the PEST sequence and the *Hes7* 3' UTR of the construct shown in **c**. **f**, Achilles fused to NLS–hCL1–hPEST is expressed under the control of the *Hes7* promoter. **g**, *Hes7* cDNA without an initiation codon was inserted between the PEST sequence and the *Hes7* 3' UTR of the construct shown in **f**.





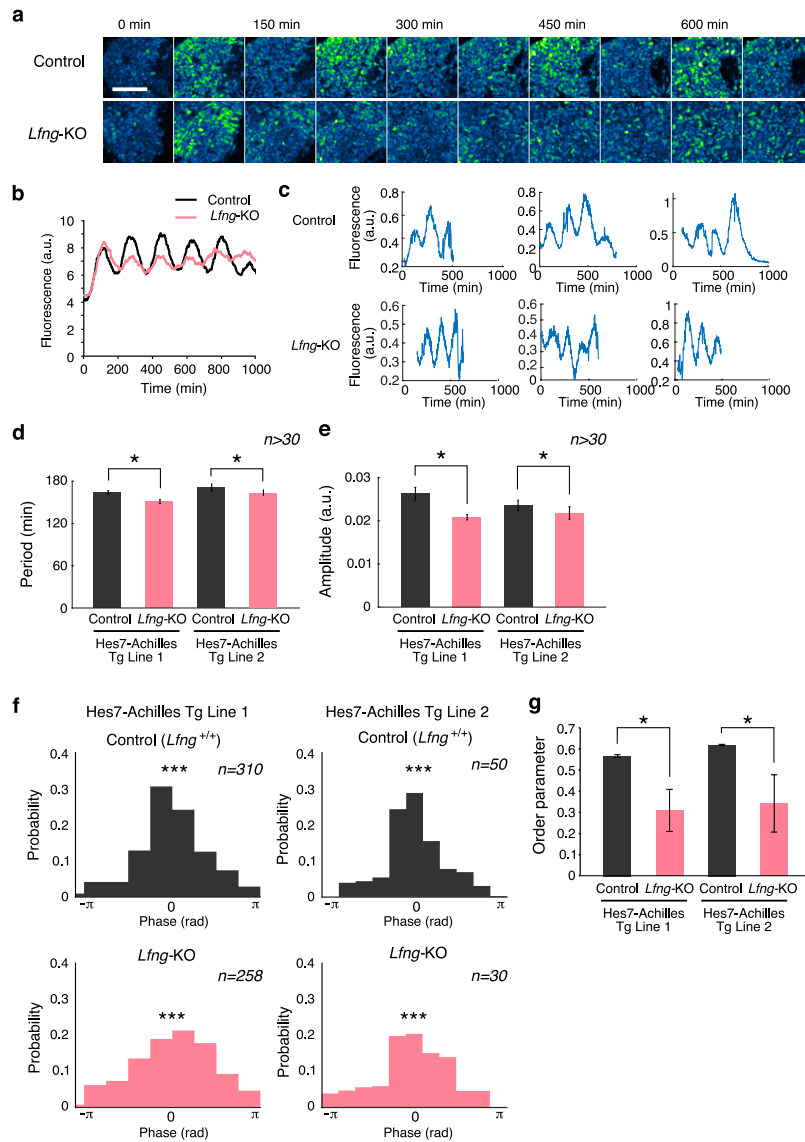
**Extended Data Fig. 4 | The Achilles–HES7 fusion protein is functional in segment formation. a,** Bone and cartilage were stained with Alizarin red and Alcian blue, respectively, at post-natal day (P)0. Achilles–HES7 rescued the

abnormal vertebra and rib formation seen in the *Hes7*-null background. **b,** Higher magnification of the thoracic-to-lumbar area in *Hes7*-*Achilles* transgene<sup>+</sup>, *Hes7*-null mouse in **a**. Scale bars, 5 mm.



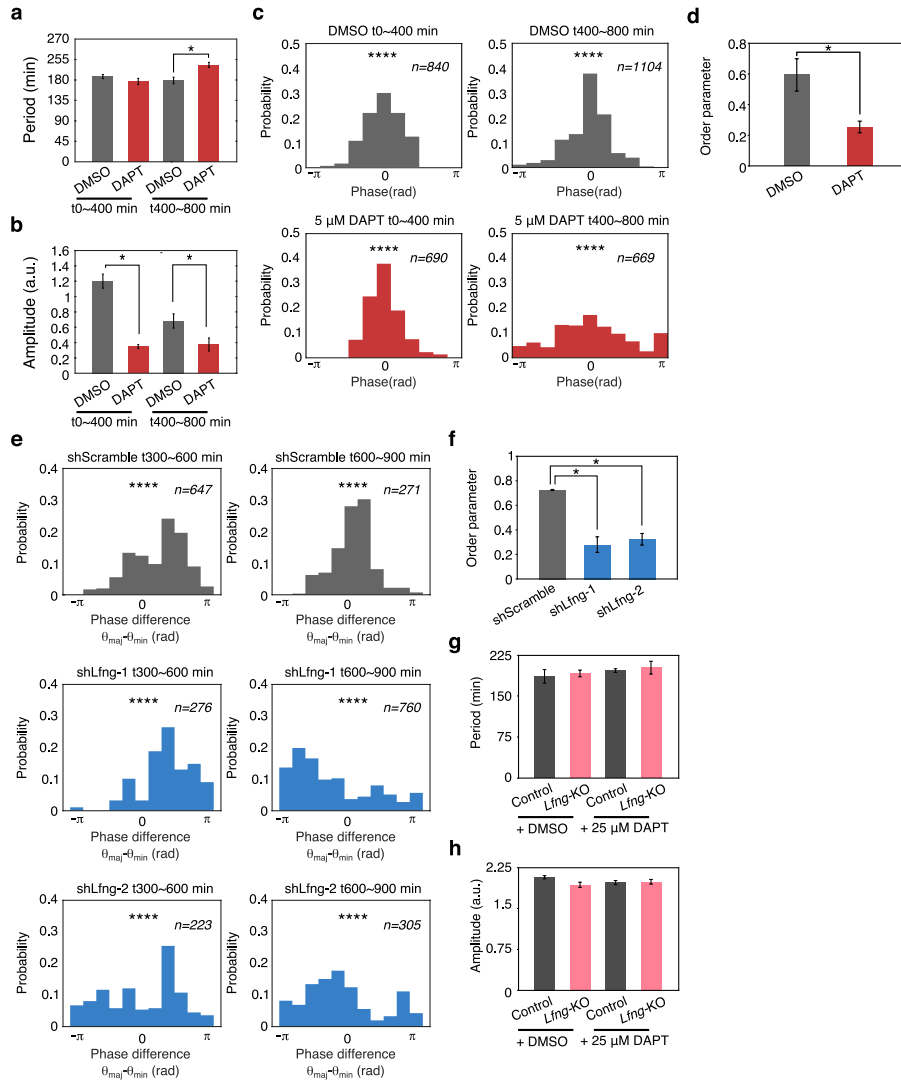
**Extended Data Fig. 5 | Observation of oscillation dynamics at the single-cell level to analyse the phase-coupling mechanism.** **a**, Live imaging (wide-field) of PSM carrying the Hes7-Achilles reporter at E10.5. **b**, Spatiotemporal expression pattern of signals from the Hes7-Achilles reporter in the PSM (wide-field). **c**, A representative cell tracked by Fiji and TrackMate. **d**, A representative

phase quantification. Fluorescence time series from a cell extracted by tracking was converted into phase information using Hilbert transform. **e**, HES7 oscillation phase, colour-mapped onto the original image. Scale bars, 100  $\mu\text{m}$ .



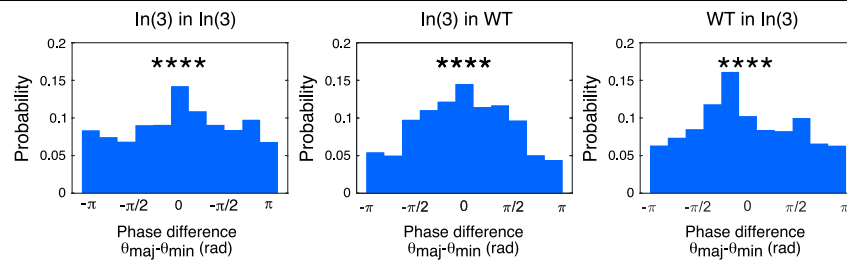
**Extended Data Fig. 6 | Synchronization of HES7 oscillation in tail-bud tissue cultures.** **a**, Expression of Hes7-Achilles reporter in wild-type and *Lfng*-knockout tail-bud tissue cultures. Scale bar, 100  $\mu$ m. **b**, Mean intensity of Hes7-Achilles reporter fluorescence in the whole area. **c**, Examples of time series of Hes7-Achilles reporter intensity from single-cell tracking data. **d**, **e**, Average period (**d**) and amplitude (**e**) of HES7 oscillations at a single-cell level. More than 30 cells for each genotype (control and two independent reporter lines) were

examined.  $n$ , number of peak pairs used for quantification. Error bars indicate s.e.m. \* $P < 0.05$ , unpaired  $t$ -test. **f**, Distribution of phase in single cells at the timing of peaks, in mean intensity time series in tail-bud cultures. Control and two independent reporter lines were examined. The number of cells examined ( $n$ ) is indicated. \*\*\* $P < 0.001$ , Rayleigh test. **g**, Kuramoto order parameter calculated using Achilles-HES7 oscillation phase quantified in **f**. Error bars indicate s.e.m. \* $P < 0.05$ , unpaired  $t$ -test.



**Extended Data Fig. 7 | Acute inhibitor or knockdown treatment of tail-bud and dissociated PSM-cell cultures.** **a–c**, Expression of the Hes7-Achilles reporter in wild-type tail-bud tissue cultures treated with DMSO control (grey bars) or the Notch inhibitor DAPT (red bars). Period (**a**), amplitude (**b**) and synchrony (**c**) of HES7 oscillations were quantified. Error bars indicate s.e.m. \* $P < 0.05$ , unpaired  $t$ -test. The number of cells examined ( $n$ ) is indicated. \*\*\*\* $P < 0.0001$ , Rayleigh test. **d**, Kuramoto order parameter calculated using Achilles–HES7 oscillation phase quantified in **c** (time ( $t$ ) = 400–800 min). Error bars indicate s.e.m. \* $P < 0.05$ , unpaired  $t$ -test. **e, f**, Expression of Hes7-Achilles

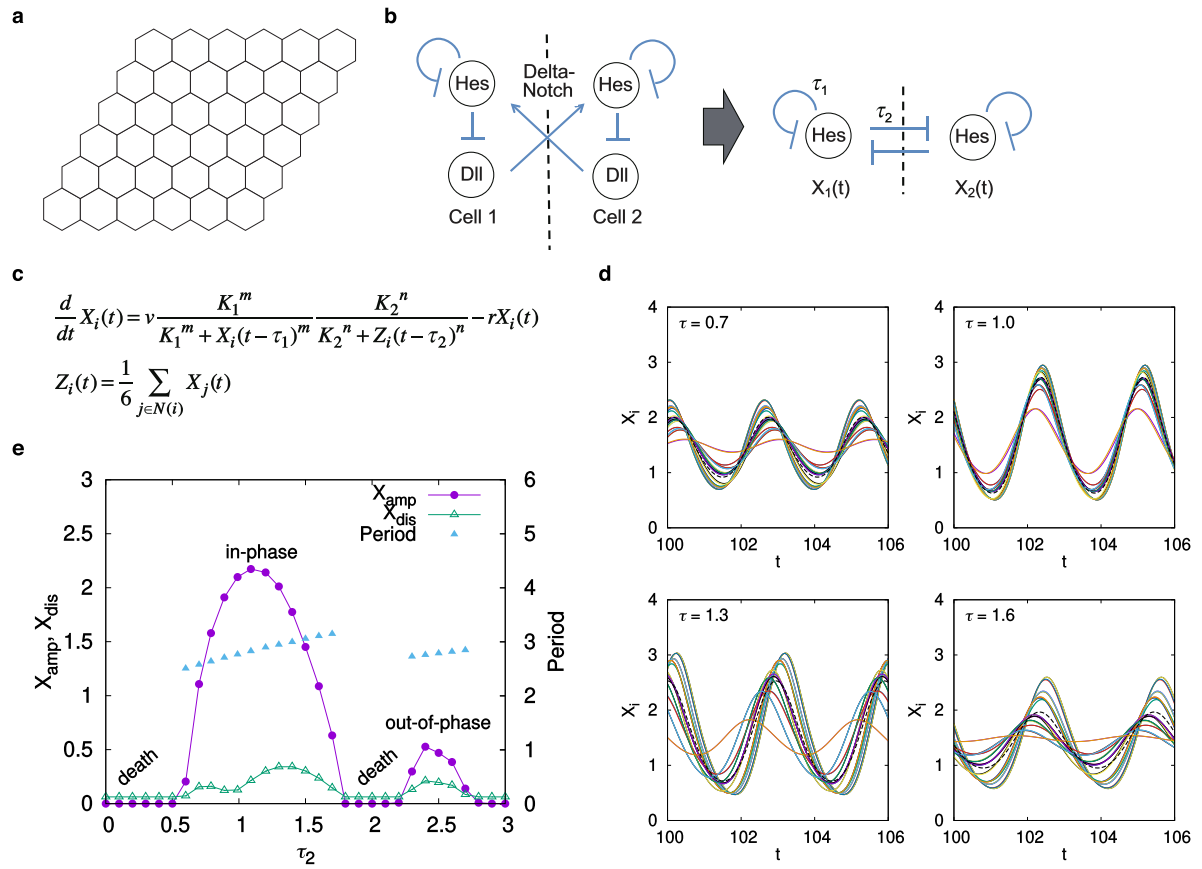
reporter wild-type tail-bud tissue cultures treated with scrambled shRNA (shScramble) (grey bars) or two different shRNAs against *Lfng* (shLfg-1 and shLfg-2) (blue bars). Synchrony (**e**) and Kuramoto order parameter (**f**,  $t = 600–900$  min) of HES7 oscillations were quantified. The number of cells examined ( $n$ ) is indicated. \*\*\*\* $P < 0.0001$ , Rayleigh test (**e**). Error bars indicate s.e.m. \* $P < 0.05$ , unpaired  $t$ -test (**f**). **g, h**, Expression of Hes7-Achilles reporter in dissociated PSM cell cultures treated with DAPT. Period (**g**) and amplitude (**h**) of HES7 oscillations were quantified. Error bars indicate s.e.m.



**Extended Data Fig. 8 | Mixed cultures of wild-type PSM cells and PSM cells carrying a faster *Hes7* oscillator.** Wild-type (period =  $126.6 \pm 2.0$  min) and mutant (In(3)) PSM cells that carry a faster *Hes7* oscillator (period =  $115.4 \pm 1.1$  min)<sup>23</sup> were mixed as a minority in mutant or wild-type cells at 1:20 ratio, and fluorescence in the minority and majority cells was quantified over time. **a**, A small ratio (1:20) of In(3) cells were mixed into an In(3)

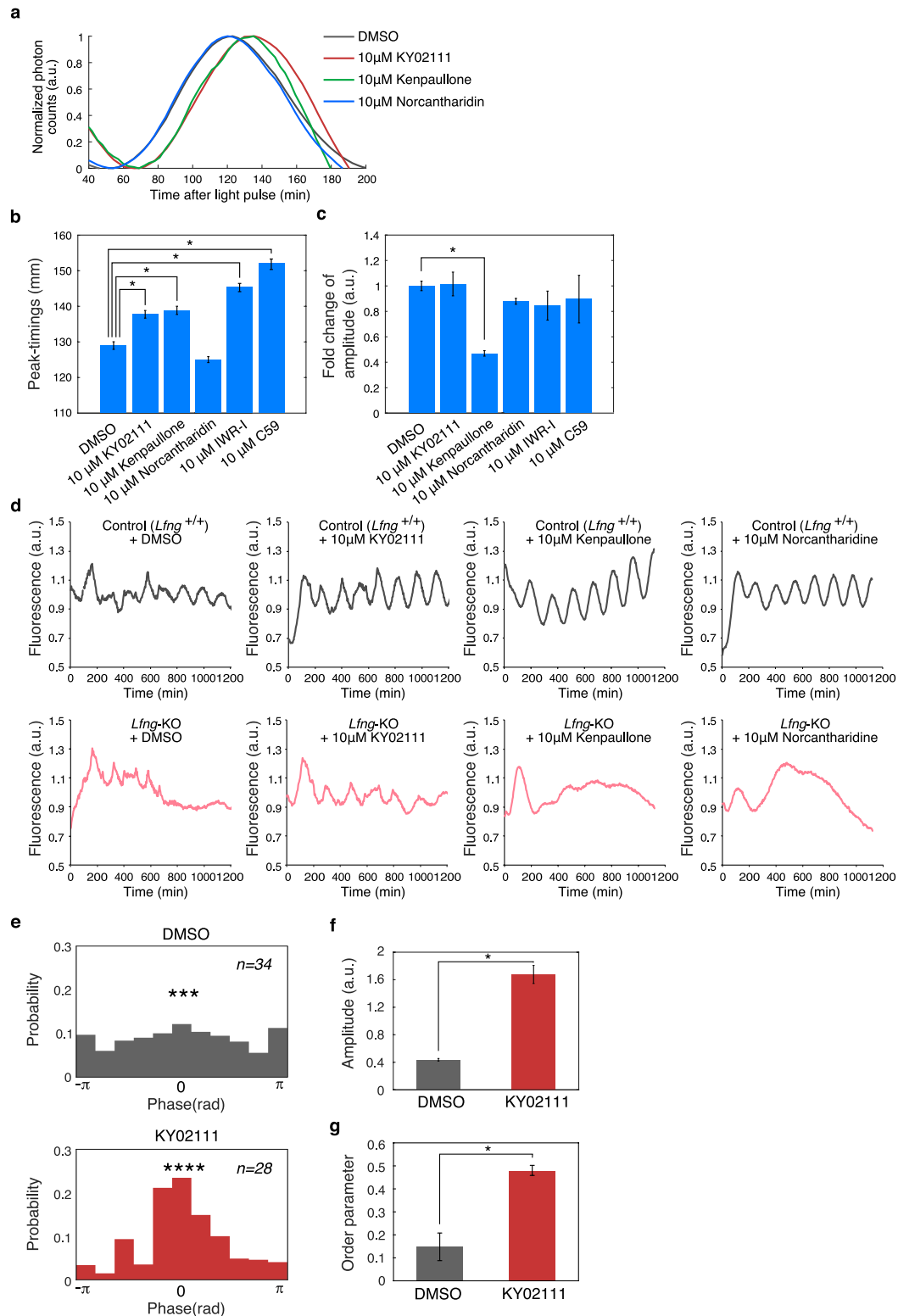
population. **b**, A small ratio (1:20) of In(3) cells were mixed into a wild-type population. **c**, A small ratio (1:20) of wild-type cells were mixed into an In(3) population. The distribution of phase difference between the minority cells and their neighbouring cells was calculated at each time point. At least 100 cells were examined for each genotype. \*\*\*\* $P < 0.0001$ , Rayleigh test.





**Extended Data Fig. 9 | Mathematical modelling and simulation.** **a**, System geometry. We consider  $6 \times 6$  cells, forming a hexagonal lattice with nearest-neighbour coupling. **b**, Schematic of the mathematical model. **c**, Dynamical equations of the model. **d**, Time series of  $X_i(t)$  for different  $\tau_2$  values. The dashed line is the average HES7 level (see ‘Mathematical modelling’ in Methods). In the

parameter space for in-phase oscillation,  $\tau_2$  values of longer or shorter than 1.0 result in smaller amplitudes and larger phase differences. **e**,  $\tau_2$ -dependence of oscillation amplitude ( $X_{\text{amp}}$ ) and dispersion among cells ( $X_{\text{dis}}$ ). The oscillation period is also shown.



**Extended Data Fig. 10 | KY02111 partially rescued the amplitude and synchrony of HES7 oscillations in *Lfng*-knockout PSM cells.** **a**, Effect of WNT-signalling-related chemical compounds on DLL1–Notch signalling delay was examined by a sender–receiver assay in C2C12 cells. Representative time series of the *Hes1* reporter signal in receiver cells after light induction of *Dll1* in the presence of DMSO, KY02111, kenpaulone or norcantharidin are shown. **b**, Peak timings of the *Hes1* reporter after blue-light stimulation.  $n > 10$  measurements for each condition. **c**, Fold change of amplitude of the *Hes1* reporter after blue-light stimulation.  $n > 10$  measurements for each condition. Error bars indicate s.e.m. \* $P < 0.05$ , unpaired *t*-test. **d**, Quantification of Hes7–Achilles reporter signals in central area (containing posterior PSM identity) of wild-type and

*Lfng*-knockout tail-bud cultures in the presence of 0.1% DMSO (control), KY02111, kenpaulone or norcantharidin. **e**, Distribution of phase in single cells at the timing of peaks in mean intensity time series, in *Lfng*-knockout tail-bud cultures in the presence of DMSO (control) or KY02111. The number of cells examined ( $n$ ) is indicated. \*\*\* $P < 0.001$ , \*\*\*\* $P < 0.0001$ , Rayleigh test. **f**, Average amplitude of HES7 oscillations in *Lfng*-knockout tail-bud cultures in the presence of DMSO (control) or KY02111. Error bars indicate s.e.m. \* $P < 0.05$ , unpaired *t*-test. **g**, Kuramoto order parameter calculated using Achilles–HES7 oscillation phase quantified in **e**. Error bars indicate s.e.m. \* $P < 0.05$ , unpaired *t*-test.

## Reporting Summary

Nature Research wishes to improve the reproducibility of the work that we publish. This form provides structure for consistency and transparency in reporting. For further information on Nature Research policies, see [Authors & Referees](#) and the [Editorial Policy Checklist](#).

### Statistics

For all statistical analyses, confirm that the following items are present in the figure legend, table legend, main text, or Methods section.

n/a Confirmed

- ☐ ☒ The exact sample size ( $n$ ) for each experimental group/condition, given as a discrete number and unit of measurement
- ☐ ☒ A statement on whether measurements were taken from distinct samples or whether the same sample was measured repeatedly
- ☐ ☒ The statistical test(s) used AND whether they are one- or two-sided  
*Only common tests should be described solely by name; describe more complex techniques in the Methods section.*
- ☒ ☐ A description of all covariates tested
- ☒ ☐ A description of any assumptions or corrections, such as tests of normality and adjustment for multiple comparisons
- ☐ ☒ A full description of the statistical parameters including central tendency (e.g. means) or other basic estimates (e.g. regression coefficient) AND variation (e.g. standard deviation) or associated estimates of uncertainty (e.g. confidence intervals)
- ☐ ☒ For null hypothesis testing, the test statistic (e.g.  $F$ ,  $t$ ,  $r$ ) with confidence intervals, effect sizes, degrees of freedom and  $P$  value noted  
*Give  $P$  values as exact values whenever suitable.*
- ☒ ☐ For Bayesian analysis, information on the choice of priors and Markov chain Monte Carlo settings
- ☒ ☐ For hierarchical and complex designs, identification of the appropriate level for tests and full reporting of outcomes
- ☒ ☐ Estimates of effect sizes (e.g. Cohen's  $d$ , Pearson's  $r$ ), indicating how they were calculated

*Our web collection on [statistics for biologists](#) contains articles on many of the points above.*

### Software and code

Policy information about [availability of computer code](#)

Data collection

We used the software ZEN for data collection by Zeiss LSM780.

Data analysis

Image processing and analysis were performed using Fiji(v1.0) and Matlab(R2018a). Subsequent analysis was performed on custom Matlab scripts. The codes are available upon requests.

For manuscripts utilizing custom algorithms or software that are central to the research but not yet described in published literature, software must be made available to editors/reviewers. We strongly encourage code deposition in a community repository (e.g. GitHub). See the Nature Research [guidelines for submitting code & software](#) for further information.

### Data

Policy information about [availability of data](#)

All manuscripts must include a [data availability statement](#). This statement should provide the following information, where applicable:

- Accession codes, unique identifiers, or web links for publicly available datasets
- A list of figures that have associated raw data
- A description of any restrictions on data availability

Accession code for Achilles sequence is provided. Raw data for all experiments are available upon requests.

### Field-specific reporting

Please select the one below that is the best fit for your research. If you are not sure, read the appropriate sections before making your selection.

- ☒ Life sciences ☐ Behavioural & social sciences ☐ Ecological, evolutionary & environmental sciences

# Life sciences study design

All studies must disclose on these points even when the disclosure is negative.

Sample size	Sample size was determined based on empirical data from initial experiments and published studies in order to obtain sufficient power for statistical comparison.
Data exclusions	For live imaging data, only tissues/cells that died, looked very unhealthy, drifted largely from focal area due to unsuccessful sampling procedures were excluded from data analysis.
Replication	For Hes7 reporter mice, we generated two independent lines and obtained similar results. All other experiments were repeated at least three times with similar results.
Randomization	Two researchers independently analyzed all the data, which were checked by the corresponding author.
Blinding	Investigators were blinded during data analysis.

# Reporting for specific materials, systems and methods

We require information from authors about some types of materials, experimental systems and methods used in many studies. Here, indicate whether each material, system or method listed is relevant to your study. If you are not sure if a list item applies to your research, read the appropriate section before selecting a response.

## Materials & experimental systems

## Methods

n/a	Involved in the study
<input checked="" type="checkbox"/>	<input type="checkbox"/> Antibodies
<input type="checkbox"/>	<input checked="" type="checkbox"/> Eukaryotic cell lines
<input checked="" type="checkbox"/>	<input type="checkbox"/> Palaeontology
<input type="checkbox"/>	<input checked="" type="checkbox"/> Animals and other organisms
<input checked="" type="checkbox"/>	<input type="checkbox"/> Human research participants
<input checked="" type="checkbox"/>	<input type="checkbox"/> Clinical data

n/a	Involved in the study
<input checked="" type="checkbox"/>	<input type="checkbox"/> ChIP-seq
<input checked="" type="checkbox"/>	<input type="checkbox"/> Flow cytometry
<input checked="" type="checkbox"/>	<input type="checkbox"/> MRI-based neuroimaging

## Eukaryotic cell lines

Policy information about [cell lines](#)

Cell line source(s)	C2C12 cell line was purchased from DS Pharma Biomedical (Osaka, Japan). ES cell line (E14TG2a) was purchased from RIKEN Bio Resource Center.
Authentication	Cell morphology and growth were checked regularly.
Mycoplasma contamination	All cell lines were negative for Mycoplasma contamination.
Commonly misidentified lines (See <a href="#">ICLAC</a> register)	NA

## Animals and other organisms

Policy information about [studies involving animals](#); [ARRIVE guidelines](#) recommended for reporting animal research

Laboratory animals	All mice used in this study were ICR, which were purchased from Japan SLC, Inc.
Wild animals	NA
Field-collected samples	NA
Ethics oversight	All animals were handled in accordance with the Kyoto University Guide for the Care and Use of Laboratory Animals.

Note that full information on the approval of the study protocol must also be provided in the manuscript.

# Recapitulating the human segmentation clock with pluripotent stem cells

<https://doi.org/10.1038/s41586-020-2144-9>

Received: 16 July 2018

Accepted: 20 February 2020

Published online: 1 April 2020

 Check for updates

Mitsuhiro Matsuda<sup>1,2,13</sup>, Yoshihiro Yamanaka<sup>3,4,13</sup>, Maya Uemura<sup>3,5</sup>, Mitsujiro Osawa<sup>6</sup>, Megumu K. Saito<sup>6</sup>, Ayako Nagahashi<sup>6</sup>, Megumi Nishio<sup>5</sup>, Long Guo<sup>7</sup>, Shiro Ikegawa<sup>7</sup>, Satoko Sakurai<sup>8</sup>, Shunsuke Kihara<sup>9</sup>, Thomas L. Maurissen<sup>8</sup>, Michiko Nakamura<sup>8</sup>, Tomoko Matsumoto<sup>8</sup>, Hiroyuki Yoshitomi<sup>3,5</sup>, Makoto Ikeya<sup>8</sup>, Noriaki Kawakami<sup>10</sup>, Takuya Yamamoto<sup>4,8,11,12</sup>, Knut Woltjen<sup>8</sup>, Miki Ebisuya<sup>1,2</sup>✉, Junya Toguchida<sup>3,5</sup> & Cantas Alev<sup>3,4</sup>✉

Pluripotent stem cells are increasingly used to model different aspects of embryogenesis and organ formation<sup>1</sup>. Despite recent advances in in vitro induction of major mesodermal lineages and cell types<sup>2,3</sup>, experimental model systems that can recapitulate more complex features of human mesoderm development and patterning are largely missing. Here we used induced pluripotent stem cells for the stepwise in vitro induction of presomitic mesoderm and its derivatives to model distinct aspects of human somitogenesis. We focused initially on modelling the human segmentation clock, a major biological concept believed to underlie the rhythmic and controlled emergence of somites, which give rise to the segmental pattern of the vertebrate axial skeleton. We observed oscillatory expression of core segmentation clock genes, including *HES7* and *DKK1*, determined the period of the human segmentation clock to be around five hours, and demonstrated the presence of dynamic travelling-wave-like gene expression in in vitro-induced human presomitic mesoderm. Furthermore, we identified and compared oscillatory genes in human and mouse presomitic mesoderm derived from pluripotent stem cells, which revealed species-specific and shared molecular components and pathways associated with the putative mouse and human segmentation clocks. Using CRISPR–Cas9-based genome editing technology, we then targeted genes for which mutations in patients with segmentation defects of the vertebrae, such as spondylocostal dysostosis, have been reported (*HES7*, *LFNG*, *DLL3* and *MESP2*). Subsequent analysis of patient-like and patient-derived induced pluripotent stem cells revealed gene-specific alterations in oscillation, synchronization or differentiation properties. Our findings provide insights into the human segmentation clock as well as diseases associated with human axial skeletogenesis.

We initially aimed to mimic and recreate in vitro the signalling events responsible for the stepwise emergence of presomitic mesoderm (PSM) and its derivatives during embryonic development, as also recently attempted by others<sup>2,4,5</sup>, via selective activation and inhibition of appropriate signalling pathways, using human induced pluripotent stem cells (iPS cells) as the starting material (Fig. 1a). We characterized the ability of our in vitro-induced human PSM cells to differentiate into somitic mesoderm and its two main derivatives: sclerotome, which gives rise to bone and cartilage of the axial skeleton, and dermomyotome, which gives rise to skeletal muscle and dermis of the emerging

embryo. RNA-sequencing (RNA-seq) analysis and subsequent characterization of in vitro-derived human PSM samples revealed that at each step of our induction and differentiation protocol, markers expected to be present—on the basis of either embryological studies in animal models or recent reports using stem cells<sup>2,4–6</sup>—were robustly and appropriately expressed at both transcript and protein levels (Fig. 1b–f, Extended Data Fig. 1, Supplementary Table 1), indicating that our stepwise approach follows the developmental trajectory and recapitulates ontogeny seen during embryonic somitic mesoderm development.

<sup>1</sup>Laboratory for Reconstitutive Developmental Biology, RIKEN Center for Biosystems Dynamics Research (RIKEN BDR), Kobe, Japan. <sup>2</sup>European Molecular Biology Laboratory (EMBL) Barcelona, Barcelona, Spain. <sup>3</sup>Department of Cell Growth and Differentiation, Center for iPS Cell Research and Application (CiRA), Kyoto University, Kyoto, Japan. <sup>4</sup>Institute for the Advanced Study of Human Biology (ASHBi), Kyoto University, Kyoto, Japan. <sup>5</sup>Department of Regeneration Science and Engineering, Institute for Frontier Life and Medical Sciences, Kyoto University, Kyoto, Japan. <sup>6</sup>Department of Clinical Application, Center for iPS Cell Research and Application (CiRA), Kyoto University, Kyoto, Japan. <sup>7</sup>Laboratory for Bone and Joint Diseases, RIKEN Center for Integrative Medical Sciences (RIKEN IMS), Tokyo, Japan. <sup>8</sup>Department of Life Science Frontiers, Center for iPS Cell Research and Application (CiRA), Kyoto University, Kyoto, Japan. <sup>9</sup>Department of Fundamental Cell Technology, Center for iPS Cell Research and Application (CiRA), Kyoto University, Kyoto, Japan. <sup>10</sup>Department of Orthopedics and Spine Surgery, Meijo Hospital, Nagoya, Japan. <sup>11</sup>AMED-CREST, AMED 1-7-1 Otemachi, Chiyodaku, Tokyo, Japan. <sup>12</sup>Medical-Risk Avoidance Based on iPS Cells Team, RIKEN Center for Advanced Intelligence Project (AIP), Kyoto, Japan.

<sup>13</sup>These authors contributed equally: Mitsuhiro Matsuda, Yoshihiro Yamanaka. ✉e-mail: miki.ebisuya@embl.es; alev.cantas.8m@kyoto-u.ac.jp



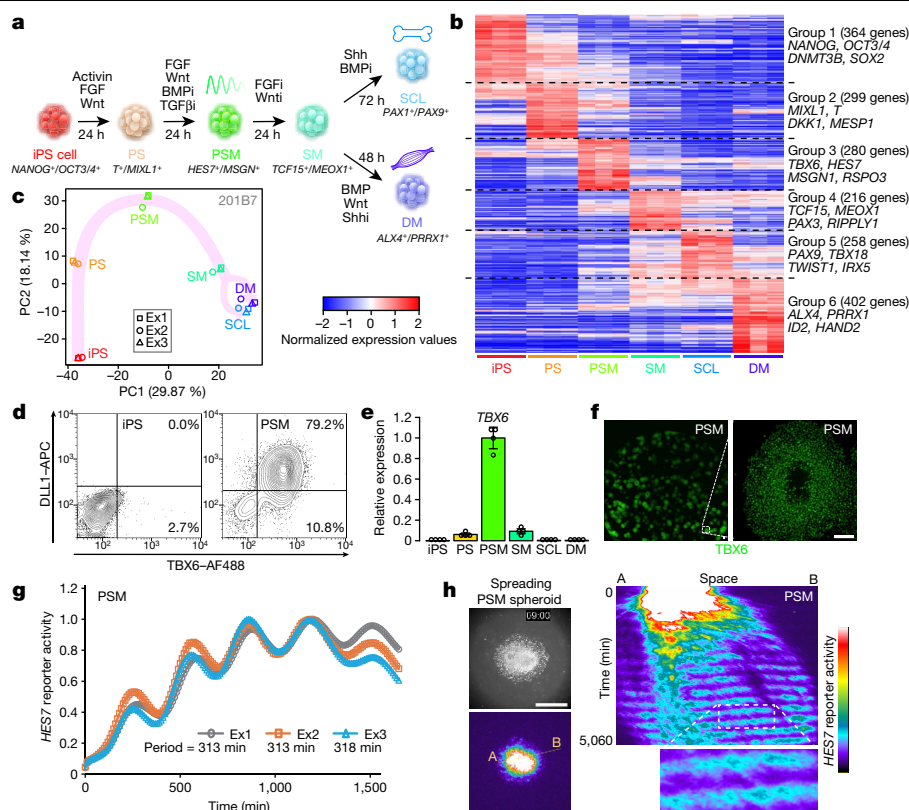


**Fig. 1 | Molecular and functional analysis of human PSC-derived PSM.**

**a**, Schematic overview of stepwise induction and differentiation of PSM from human PSCs. The 'i' suffix indicates inhibition of a pathway. DM, dermomyotome; PS, primitive streak; PSM, presomitic mesoderm; SCL, sclerotome; SM, somitic mesoderm. **b**, RNA-seq data of stepwise-induced PSM and derivatives. Fragments per kilobase of transcript per million mapped reads (FPKM) values for each gene were normalized to mean of all samples ( $n=3$ ). **c**, Principal component analysis (PCA) plot with suggested developmental trajectory highlighted in pink. ( $n=3$  experiments (Ex1–Ex3)). **d**, Representative flow cytometric evaluation of DLL1 and TBX6 protein expression in iPS cells and PSM ( $n=3$  experiments). **e**, Expression of *TBX6* transcript during different stages of human PSM induction and differentiation. Quantitative PCR with

reverse transcription (RT–qPCR) results of four independent experiments with the 201B7 cell line are shown; mean  $\pm$  s.d.,  $n=4$ . **f**, Representative expression of TBX6 protein in human PSM. Left, entire well. Right, enlarged view of bound area.  $n=3$  experiments. Scale bar, 100  $\mu$ m. **g**, Oscillation of *HES7* reporter activity in 2D culture of induced PSM. Signal was normalized to maximum oscillation peak. Period was calculated as average peak-to-peak interval using 1st to 5th peaks.  $n=3$ . **h**, Synchronization of *HES7* reporter activity in spreading PSM spheroid. Left, PSM spheroid attached to dish 9 h after the start of the experiment. Right, kymograph along the yellow line shown in left, bottom.  $n=3$  experiments. Scale bar, 500  $\mu$ m. Data, images and graphs shown in **b–d**, **f** and **h** are representative of three independent experiments.

## Oscillations in human in vitro PSM

We detected expression of *TBX6* and *DLL1*, two well-established markers of PSM<sup>7</sup>, at both transcript and protein level in our in vitro-derived human PSM samples (Fig. 1d–f, Extended Data Fig. 1d–f). We also detected specific and high-level expression of *HES7*—a known regulator of the segmentation clock in murine PSM<sup>8</sup>—in the human iPS cell-derived PSM (Fig. 1b, Extended Data Fig. 1c). On the basis of these observations, we generated a luciferase-reporter iPS cell line for human *HES7*-promoter activity (*HES7* reporter). We observed clear oscillation of the *HES7* reporter in induced human PSM in 2D culture (Fig. 1g) and determined the period of the in vitro human segmentation clock to be around five hours (Fig. 1g, Extended Data Fig. 2), which is similar to the four- to six-hour period reported for somite formation in primary human embryo samples<sup>9,10</sup> and oscillation in human mesenchymal cells<sup>11</sup>.

We then investigated whether it was possible to observe travelling-wave-like expression, which is caused by synchronization among oscillations in neighbouring cells. This has been reported in the context of explant studies using reporter mice and mouse embryonic stem cell-derived PSM<sup>12,13</sup>, but, to our knowledge, has never been observed in human PSM. We induced PSM fate in a 3D culture of human iPS cells and allowed spheroids to spread on a culture dish. In the spreading

PSM spheroid, we observed sustained oscillation and the clear presence of travelling waves (Supplementary Video 1), also indicated by the tilted slope in corresponding kymographs (Fig. 1h, Extended Data Fig. 2c). The periods of the in vitro human segmentation clock did not differ between the two different assay conditions (2D oscillation versus 3D synchronization assay) but remained stable at around five hours (Extended Data Fig. 2a, b).

## Derivatives of human in vitro PSM

To ensure that our in vitro-derived PSM is comparable to its in vivo counterpart, we assessed its capacity to differentiate to somitic mesoderm, sclerotome and dermomyotome. To induce somitic mesoderm, we mimicked the decrease in FGF and Wnt activity along the posterior–anterior axis of the PSM, as reported in the embryonic context<sup>14</sup>, by simultaneous inhibition of both pathways, leading to rapid and robust induction of somitic mesoderm expressing *TCF15*, a well-established marker of somite development<sup>15</sup>, at both transcript (Fig. 1b, Extended Data Fig. 1c) and protein level (Extended Data Fig. 3a, b). *MESP2*, a marker of segmentation, showed weak expression in induced human somitic mesoderm (Extended Data Fig. 3b). Even though our system exhibited robust differentiation towards somitic mesoderm, segmentation or formation of somite-like structures were not observed.

Dermomyotome and sclerotome cells derived from in vitro-induced human somitic mesoderm expressed appropriate developmental stage-specific markers such as *PAX7* and *PRRX1* (dermomyotome) or *FOXC2* (sclerotome) at the transcript and protein level (Fig. 1b, Extended Data Figs. 1c, 3c). Sclerotome derived from induced human somitic mesoderm also differentiated into bone and cartilage, and demonstrated endochondral bone formation upon transplantation in vivo, albeit lacking any apparent macroscopic segmental or vertebral patterns<sup>16</sup> (Extended Data Fig. 4). Further, in vitro-derived human dermomyotome cells displayed robust in vitro induction to skeletal muscle cells accompanied by expression of muscle markers at the protein level (Extended Data Fig. 5a, b). Functional analysis of induced human sclerotome and dermomyotome cells derived from a calcium-reporter iPS cell line (Gen1C) revealed the reproducible presence of contracting skeletal muscle cells and contractile bundles after three weeks of in vitro 2D differentiation culture of dermomyotome cells (Extended Data Fig. 5c, d, Supplementary Video 2). We thus showed that our in vitro-induced human PSM-like cells can be robustly differentiated further and give rise to functional somitic mesoderm derivatives including sclerotome and dermomyotome.

## Human and mouse in vitro segmentation clocks

Next, we investigated whether we could use this experimental system to increase our understanding of the human segmentation clock and of oscillation and synchronization in human PSM. We collected samples of human induced PSM during oscillation by monitoring the oscillatory activity of the *HES7* reporter and performed RNA-seq analysis (Extended Data Fig. 6a). Next-generation sequencing of the different PSM time points revealed a core set of about two hundred oscillating genes in human in vitro PSM (Fig. 2a, Supplementary Table 2). Pathway and Gene Ontology (GO) analysis of the identified gene clusters revealed that, in addition to enrichment of pathway members previously associated with the segmentation clock, such as Notch, Wnt or FGF signalling<sup>17</sup>, novel pathways were also represented in our dataset, including oscillating genes associated with TGF- $\beta$ , PI3K, ephrin, histone deacetylase and Hippo signalling (Fig. 2b, Supplementary Table 3). Consistent with previous reports in mouse PSM, treatment with inhibitors of Notch, FGF or Wnt pathways decreased the intensity of the *HES7* reporter in human in vitro-derived PSM (Extended Data Fig. 6b, c, Supplementary Video 3). Of note, we observed oscillatory activity of core components of the Hippo pathway and YAP signalling (*TEAD4* and *AMOTL2*) (Fig. 2a–c), which were recently reported to be important regulators of oscillatory activity in mouse PSM<sup>18</sup> (see also Supplementary Discussion 1).

To identify putative human-specific and evolutionary conserved components of the in vitro segmentation clock, we then analysed and compared our data with mouse epiblast stem cell (EpiSC)-derived in vitro mouse PSM, applying a similar strategy for induction and analysis as for the human cells. Mouse EpiSC-derived PSM showed a segmentation clock period of two to three hours, confirming earlier in vivo and in vitro mouse studies<sup>19</sup>, as well as indicating that the obtained human data are reflective of the in vivo condition. Next-generation sequencing analysis of mouse PSM time points revealed a set of about 170 oscillating genes in mouse in vitro-derived PSM, including both novel and previously reported oscillating components of the mouse segmentation clock<sup>20</sup> (Extended Data Fig. 7a, b, Supplementary Table 4).

GO-term and pathway analysis of the identified oscillating mouse genes revealed that major pathways identified in the human model were also present in the mouse model (Fig. 2b, Supplementary Table 5), with some species-specific differences in individual oscillating members of the same pathways (see also Supplementary Discussion 2). Comparison of the human and mouse oscillating gene sets further revealed the presence of genes oscillating in phase with *HES7*, including the circadian clock gene *PER1*, which to our knowledge, has not been linked to the

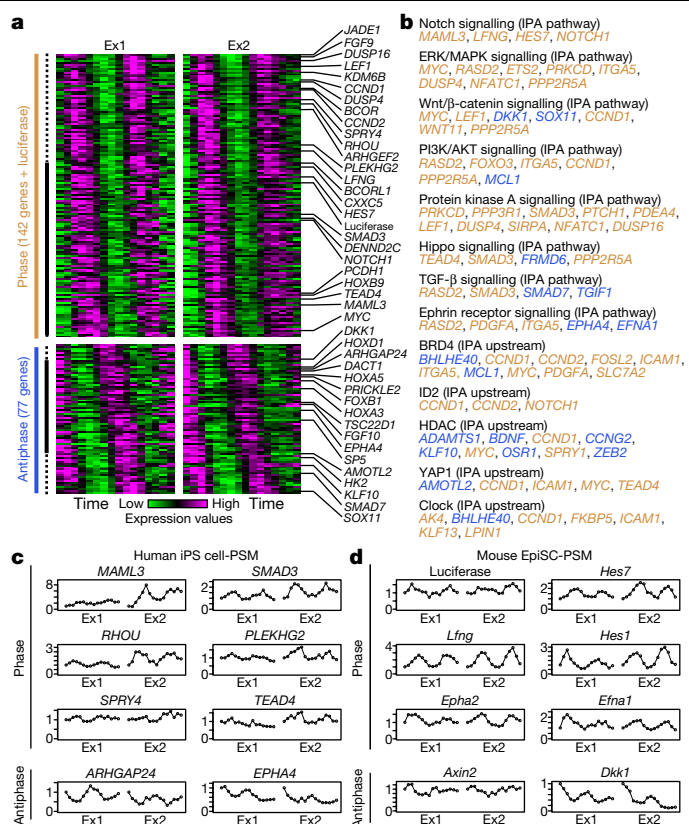


**Fig. 2 | Identification of phase and antiphase oscillating genes of in vitro human and mouse segmentation clocks.** **a**, Heat map of normalized gene expression levels for oscillating genes in human in vitro-derived PSM. Data shown for two independent biological datasets with 16 samples each. Identified phase- and antiphase-oscillating genes are highlighted on the right; unambiguously phase- or antiphase-oscillating genes highlighted on the left; solid and dotted black lines indicate unambiguous and ambiguous genes, respectively. **b**, Ingenuity pathway analysis (IPA) result of human phase (yellow) and antiphase (blue) oscillating genes. **c**, Validation of RNA-seq results by RT-qPCR for selected phase- and antiphase-oscillating genes with specific oscillatory expression in human iPS cell-derived PSM but not mouse EpiSC-derived PSM. Data shown for two independent biological datasets with 16 samples each. See also Extended Data Fig. 6d. **d**, RT-qPCR validation of phase- and antiphase-oscillating genes found to oscillate in mouse EpiSC-derived PSM. The same genes show oscillation in human PSC-derived PSM (see also Extended Data Fig. 6e, f). Data in **c** and **d** represent mean values of three technical replicates of two independent biological experiments.

segmentation clock (Extended Data Fig. 6e, f), as well as genes showing clear antiphase oscillatory expression (for example, *DKK1*). The phase cluster of human and mouse oscillating genes contained genes associated with the Notch pathway, such as *LFNG*<sup>21</sup>, whereas the antiphase cluster contained negative-feedback regulators associated with the Wnt pathway, such as *DKK1* and *SP5*<sup>22,23</sup> (Fig. 2a, b, Extended Data Figs. 6f, 7a), as previously reported for posterior PSM of mouse embryos<sup>24</sup>. Generating a dual luciferase-activity-based reporter cell line for *DKK1* and *HES7* promoter activities, we confirmed clear phase and antiphase reporter oscillations in human iPS cell-derived PSM (Extended Data Fig. 7d), suggesting that our induced PSM may represent posterior immature PSM rather than anterior mature PSM.

## Analysis of knockout human in vitro PSMs

As our assay systems were capable of assessing both oscillation and synchronization (Extended Data Fig. 7e) as well as identifying molecular features of the segmentation clock in induced PSM (Fig. 2, Extended

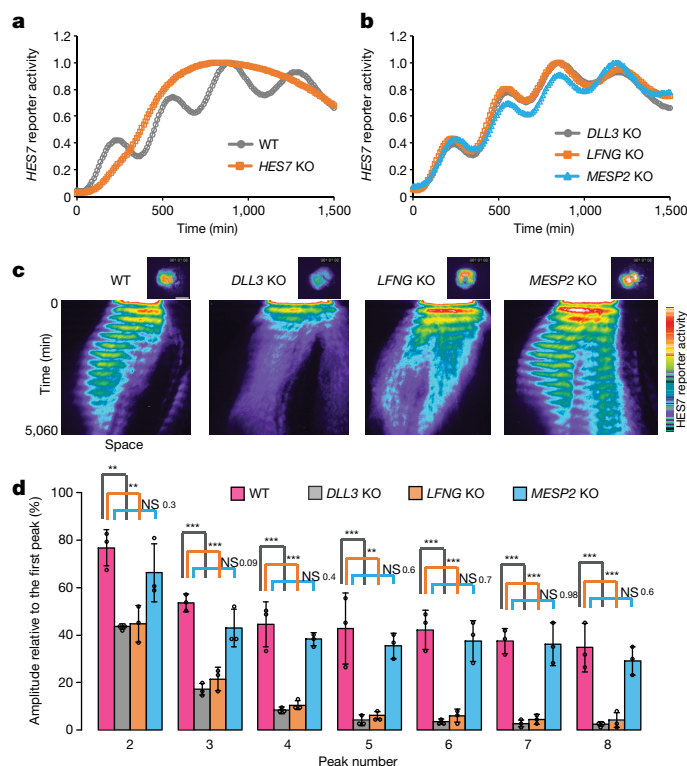


**Fig. 3 | Functional evaluation of targeted disruption of selected segmentation clock genes in human in vitro PSM.** **a**, Two-dimensional oscillation assay for wild-type (WT) and *HES7*-knockout (KO) PSMs. Signal was normalized to the maximum oscillation peak. **b**, Two-dimensional oscillation assay for *LFNG*-, *DLL3*- and *MESP2*-knockout PSMs. **c**, Three-dimensional synchronization (spheroid-spreading) assay for knockout PSMs. Kymograph along the yellow line in Supplementary Video 4 is shown. Scale bar, 500  $\mu$ m. **d**, Damping rate of oscillation amplitude in knockout PSMs. The detrended signal shown in Extended Data Fig. 8b was normalized to the first oscillation peak, and the value of each peak is shown. Data are mean  $\pm$  s.d.,  $n = 3$ .  $P$  values are from two-sided Dunnett's test. \* $P < 0.05$ , \*\* $P < 0.01$ , \*\*\* $P < 0.001$ ; NS, not significant. Data, graphs and images shown in **a–c** are representative of three independent experiments.

Data Figs. 6, 7), we next investigated whether they could be used to model anomalies of human axial skeletogenesis, such as segmentation defects of the vertebrae (SDV), which are known to be caused by mutations in genes associated with the segmentation clock (for example, *HES7*, *LFNG*, *DLL3* and *MESP2*)<sup>20,25–27</sup>. We used CRISPR–Cas9 technology to generate knockout reporter iPS cell lines with frameshifts or deletion mutations in these target genes (Extended Data Fig. 8a) and analysed their putative loss-of-function effect on oscillatory *HES7* reporter activity. Knockout of endogenous *HES7* itself led to clear loss of oscillatory activity of the *HES7* reporter in the 2D oscillation assay (Fig. 3a), similar to previous embryological studies using knockout mice<sup>8</sup>. Knockout reporter cell lines for *LFNG*, *DLL3* or *MESP2* continued to show strong oscillatory *HES7* activity (Fig. 3b), even though knockout mice for *LFNG* and *DLL3* have been reported to show defective oscillation patterns<sup>28,29</sup>. We reasoned that in our 2D oscillation assay, the phase (that is, timing) of oscillations is initially reset by medium change, resulting in collective oscillation even in the absence of a strong synchronization mechanism. We then examined the synchronization ability of knockout reporter cell lines for the above genes using the 3D synchronization (spheroid-spreading) assay of human induced PSM (Fig. 3c). The healthy control (wild type) and the knockout reporter cell line for *MESP2* produced sustained oscillations and occasional travelling waves (Supplementary Video 4), indicating intact synchronization among neighbouring cells.

By contrast, in lines with *LFNG* or *DLL3* knockout, oscillation damped quickly and clear travelling waves were not observed (Fig. 3c, d, Extended Data Fig. 8b, Supplementary Video 4). We interpreted this rapid loss of oscillatory activity as a sign of diminished synchronization. Unlike the 2D oscillation assay, spheroids in the 3D synchronization assay spread dynamically on the culture dish, and cell movements desynchronized oscillation phases. Without a proper synchronization mechanism, collective oscillation was quickly lost, even though oscillations in individual cells continued. Thus our 2D and 3D assay systems using induced human PSM were able to detect defects in oscillation and synchronization, respectively (Extended Data Fig. 8c).

Flow cytometric and transcriptome analysis showed no major differences between control cells and knockout reporter cell lines (*HES7*-, *DLL3*-, *LFNG*- and *MESP2*-knockout) at the iPS cell and PSM stages (Extended Data Fig. 8d, e). PSM-induction efficiency was high and comparable to healthy control cells in *HES7*-, *DLL3*- and *MESP2*-knockout reporter cell lines, and slightly reduced in *LFNG*-knockout iPS cell lines (Extended Data Fig. 8d). There were few differences in gene expression at the iPS cell and PSM stages when comparing knockout cell lines with the original healthy donor line, with *HES7*, *MESP2* and *LFNG* showing higher expression in *HES7*-knockout-derived PSM, as previously also shown in mice<sup>30</sup> (Extended Data Fig. 8e). Together, these results underline the overall value of a higher-order assay system that can assess gene or protein expression as well as more complex features such as oscillation or synchronization in human in vitro-derived PSM, thus making it possible to decipher functionally relevant and possibly disease-associated features specific to each loss- or gain-of-function mutation, which would otherwise remain inaccessible.

## Analysis of patient-derived in vitro PSM

To evaluate the utility of our model system to both assess key features of the human segmentation clock and address molecular mechanisms associated with human diseases affecting axial skeletogenesis, we generated a *HES7* reporter cell line with a point mutation (rs113994160: c.73C>T) causing a pathogenic missense mutation R25W in the helix–loop–helix domain of *HES7*, previously reported to cause spondylocostal dysostosis (SCD) and SDV in humans<sup>26</sup>. *HES7*<sup>R25W</sup>-homozygous mutants were created in the *HES7* reporter using single-stranded donor oligonucleotides (ssODN) templates (Fig. 4a, Extended Data Fig. 9a). In addition to this patient-like reporter cell line, we also derived iPS cells from patients showing clinical features of SCD, including segmentation defects along the entire spine and bilateral fusion of ribs (Extended Data Fig. 9, Supplementary Note 1). Following initial quality control and validation of the patient-derived iPS cell lines, named SCDP1 and SCDP2 (Extended Data Fig. 9b–f), we evaluated their in vitro-differentiation ability towards PSM together with the *HES7*<sup>R25W</sup> cell line. All three patient-like and patient-derived iPS cell lines showed high induction efficiency towards PSM, as assessed by flow cytometric analysis of *DLL1* expression (Fig. 4b, Extended Data Fig. 10a), indicating that their initial capacity to differentiate to PSM is not altered. We then performed 2D oscillation assays with all three cell lines and observed clear loss of oscillation for the *HES7*<sup>R25W</sup> point-mutation line, similar to that observed for the *HES7*-knockout cell lines. Conversely, SCDP1 and SCDP2 iPS cell-derived PSMs showed sustained oscillation, with SCDP1 also showing sustained oscillation in 3D assay (Fig. 4c, Extended Data Fig. 10b, c).

To expand our analysis of the patient-derived cell lines, we set out to determine putative underlying pathological mutations in both iPS cell lines. For the SCDP1 patient-derived cell line, we identified—via exome-sequencing—compound heterozygous variants in *MESP2*, c.258–261delCAGC (p.E88Gfs\*31, rs1452984345) and c.307G>T (p.E103\*, rs71647808). The first variant results in a frameshift that produces a truncated protein in the middle of the DNA-binding domain, and the second variant has previously been reported as a pathogenic founder



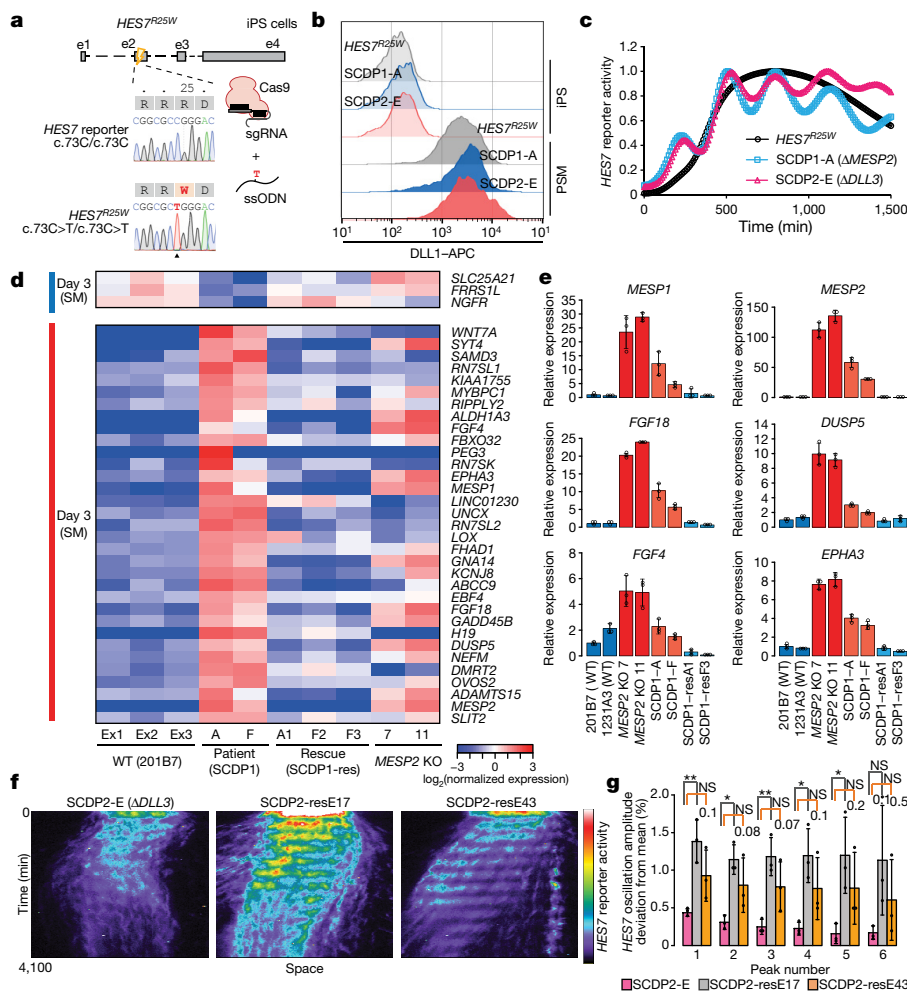


**Fig. 4 | In vitro recapitulation and molecular analysis of disease phenotypes using patient iPS cells and isogenic controls.** **a**, Overview of ssODN-based targeting strategy for generation of a point mutation (*HES7*<sup>R25W</sup>) reporter cell line. **b**, Evaluation of DLL1-positive PSM-induction efficiency of *HES7*<sup>R25W</sup> and iPS cell lines from patients with SCD (SCDP1 and SCDP2).  $n = 3$  experiments. **c**, Two-dimensional oscillation assay for *HES7*<sup>R25W</sup>, SCDP1-A and SCDP2-E PSM. Signal was normalized to the maximum oscillation peak.  $n = 3$  experiments. **d**, Heat map of putative genes related to SCD at the somitic mesoderm stage. Genes were upregulated or downregulated in the SCDP1-A and SCDP1-F patient cell lines and increases or decreases were inhibited in rescued cell lines (SCDP1-resA1, F2 and F3). RNA-seq data for two different *MESP2*-knockout cell lines (no. 7 and 11) are included. **e**, RT-qPCR-based validation of RNA-seq results. Data are mean  $\pm$  s.d.,  $n = 3$ . **f**, Three-dimensional synchronization assay of SCDP2 patient (SCDP2-E)- and isogenic rescue (SCDP2-resE17/43)-line-derived PSMs.  $n = 3$  experiments. Kymographs of Supplementary Video 5 are shown. **g**, Quantification of *HES7* reporter activity in patient and rescue PSMs. Value of each oscillation peak is shown, calculated from Extended Data Fig. 12f. Data are mean  $\pm$  s.d.,  $n = 3$  experiments. *P* values are from two-sided Dunnett's test. Data, images and graphs shown in **b**, **c**, **e** and **f** are representative of three independent experiments.

variant of SCD in a Puerto Rican population<sup>31</sup> (Extended Data Fig. 10d, Supplementary Note 2). The clear oscillatory activity of *HES7* in the oscillation assay of the SCDP1 cell line harbouring *MESP2* loss-of-function mutations (Fig. 4c) was similar to our observations for the human *MESP2*-knockout reporter cell lines (Fig. 3b). When assessed with the 3D synchronization assay, the SCDP1 patient cell line exhibited sustained collective oscillation and occasional travelling waves, indicating an intact synchronization mechanism (Extended Data Fig. 10b, c), similar to the results seen for the human *MESP2*-knockout iPS cell lines (Fig. 3c, d).

### Altered gene expression in patient-derived cells

To facilitate the molecular and functional analysis of the SCDP1 patient cell line, we generated isogenic controls by correcting the underlying predicted pathogenic mutations by gene targeting with CRISPR–Cas9. Allele-specific gene correction of *MESP2* was achieved using single guide RNAs (sgRNAs) targeting either the c.258\_261delCAGC or the c.307G>T mutation and homologous recombination with donor vectors bearing the wild-type *MESP2* sequence. Microhomology-assisted excision (MhAX) was used to remove the selection cassette<sup>32</sup> (Extended Data Fig. 10e–i), thereby effectively rescuing the disease-causing loss of *MESP2*, albeit heterozygously. Gene-edited iPS cells were confirmed to be karyotypically similar to the parental patient iPS cell line (Extended Data Fig. 10j–n). As no clear oscillation or synchronization phenotype could be observed for the analysed patient cell line, we searched for possible differences at the functional or molecular level by comparing patient (SCDP1-A and SCDP1-F) and corresponding rescued iPS cell lines (SCDP1-resA and SCDP1-resF). To this end, we induced and compared

the different stages of our in vitro induction and differentiation protocol using RNA-seq analysis of the patient and rescue cell lines (Fig. 4d, Extended Data Fig. 11a).

Comparison of clones from patients with those from healthy control and heterozygously corrected cell lines revealed the presence of an upregulated gene cluster at the somitic mesoderm stage in the analysed patient cell lines, which could be reversed by correction of either mutated allele (Fig. 4d). This observed pattern of upregulated genes was also shared with somitic mesoderm samples of two different *MESP2*-knockout cell lines subjected to the same type of induction and analysis. Genes apparently upregulated in patient somitic mesoderm and reduced upon rescue of either *MESP2* mutation included *FGF4*, *FGF18* and *DUSP5* (Fig. 4d, e), suggesting that abnormal FGF signalling could be a disease-associated molecular feature in SDV. Somitic mesoderm samples derived from *MESP2*-knockout iPS cells also showed higher levels of expression of *FGF4*, *FGF18* and *DUSP5* (Fig. 4d, e). It should be noted that mutations in FGF-pathway components have not been reported in SDV, despite extensive investigation of cases by whole-exome and genome sequencing. Knockout mouse lines for these genes also do not show defects in somite segmentation, but usually result in embryonic lethality before somite formation. Of note, *EPHA3*, which was previously reported to have a dominant-negative effect on somite patterning and axial organization in fish<sup>33</sup>, was also upregulated in SCDP1 patient- and *MESP2*-knockout-derived somitic mesoderm (Fig. 4d, e). Further, knockout and patient cell lines showed higher levels of expression of *MESP1* and *MESP2* compared with healthy or genetically corrected control samples, indicating possible disrupted negative-feedback regulation by *MESP2*. Several other genes associated with patterning during somitogenesis, for which genetic mutations in

patients with SCD were recently reported, including *LFNG*<sup>20</sup>, *RIPPLY2*<sup>34</sup> and *DMRT2*<sup>35</sup>, were also upregulated in somitic mesoderm derived from SCDP1 patient cell lines (SCDP1-A and SCDP1-F) harbouring *MESP2* loss-of-function mutations (Fig. 4d, e, Extended Data Fig. 11b), indicating reciprocal regulatory mechanisms that possibly connect these disease-associated genes at the molecular and functional level during the pathogenesis of SDV. Whether dysregulation of the previously mentioned patterning-associated genes in somitic mesoderm is indeed the causative factor leading to the development of SDV in patients with *MESP2* loss-of-function mutations remains to be elucidated and is the topic of ongoing research efforts. This will probably require the establishment of additional assay systems in which actual human somitogenesis—including the formation and patterning of 3D epithelial somites—can be achieved and assessed in vitro.

## Synchronization defect in patient PSM

In addition to SCDP1, we also searched for a disease-causing mutation in SCDP2 (Supplementary Note 1a, b), and identified a homozygous variant in *DLL3* (rs786200899: c.603\_604insGCGGT, p.P202Afs\*41) (Extended Data Fig. 12a, Supplementary Note 2). *DLL3* is the most clinically relevant and frequently mutated gene in SCD<sup>36</sup>. We performed gene correction and obtained several isogenic rescue lines in which the *DLL3* mutation was homozygously corrected (Extended Data Fig. 12b–e). Assessment of SCDP2-derived PSM with the 2D oscillation assay revealed sustained oscillation (Fig. 4c), whereas the 3D synchronization assay of SCDP2 lines showed rapid damping of oscillation (Fig. 4f, g, Extended Data Fig. 12f), as also previously shown for *DLL3*-knockout lines (Fig. 3c, d), indicating a defect in the synchronization ability of these patient-derived PSM cells. The synchronization phenotype was rescued upon isogenic correction of the *DLL3* mutation, with strong sustained oscillation and occasional travelling waves in the cases of PSM derived from the isogenic rescue cell lines (SCDP2-resE17 and SCDP2-resE43) (Fig. 4f, g, Extended Data Fig. 12f, Supplementary Video 5). Our approach is thus capable of recapitulating a human disease-causing phenotype associated with the loss of *DLL3* leading to defective synchronization at the PSM stage. How exactly the loss of synchronization is manifested in the abnormal patterning and formation of the developing human axial skeleton remains to be determined.

In summary, we have shown phase and antiphase oscillation and travelling-wave-like expression of key segmentation-clock genes in human in vitro-derived PSM, and have identified a putative molecular network of known and novel genes comprising the human and mouse segmentation clocks, with around five-hour and two- to three-hour periods in PSC-derived human and mouse PSM, respectively. We assessed the function of several disease-linked genes associated with the human segmentation clock, by applying our experimental model system in combination with patient-like and patient-derived iPSCs, thus effectively creating a human pluripotent stem cell-based model for SDV, which will further contribute to deciphering the molecular mechanisms underlying normal and pathological human axial skeletogenesis. Having access to a robust experimental model system that can be easily manipulated without the need for transgenic animals or primary tissues, while enabling assessment of genetic, environmental or epigenetic factors, will facilitate our molecular and functional understanding of the role the segmentation clock in development and disease.

## Online content

Any methods, additional references, Nature Research reporting summaries, source data, extended data, supplementary information, acknowledgements, peer review information; details of author contributions and competing interests; and statements of data and code availability are available at <https://doi.org/10.1038/s41586-020-2144-9>.

- McCauley, H. A. & Wells, J. M. Pluripotent stem cell-derived organoids: using principles of developmental biology to grow human tissues in a dish. *Development* **144**, 958–962 (2017).
- Chal, J. et al. Differentiation of pluripotent stem cells to muscle fiber to model Duchenne muscular dystrophy. *Nat. Biotechnol.* **33**, 962–969 (2015).
- Lee, J. H., Protze, S. I., Laksman, Z., Backx, P. H. & Keller, G. M. Human pluripotent stem cell-derived atrial and ventricular cardiomyocytes develop from distinct mesoderm populations. *Cell Stem Cell* **21**, 179–194 (2017).
- Loh, K. M. et al. Mapping the pairwise choices leading from pluripotency to human bone, heart, and other mesoderm cell types. *Cell* **166**, 451–467 (2016).
- Xi, H. et al. In vivo human somitogenesis guides somite development from hPSCs. *Cell Rep.* **18**, 1573–1585 (2017).
- Pourquie, O. Vertebrate somitogenesis. *Annu. Rev. Cell Dev. Biol.* **17**, 311–350 (2001).
- Hofmann, M. et al. WNT signaling, in synergy with T/EBX6, controls Notch signaling by regulating *Dll1* expression in the presomitic mesoderm of mouse embryos. *Genes Dev.* **18**, 2712–2717 (2004).
- Bessho, Y. et al. Dynamic expression and essential functions of *Hes7* in somite segmentation. *Genes Dev.* **15**, 2642–2647 (2001).
- Turnpenny, P. D. et al. Abnormal vertebral segmentation and the notch signaling pathway in man. *Dev. Dyn.* **236**, 1456–1474 (2007).
- Hubaud, A. & Pourquie, O. Signalling dynamics in vertebrate segmentation. *Nat. Rev. Mol. Cell Biol.* **15**, 709–721 (2014).
- William, D. A. et al. Identification of oscillatory genes in somitogenesis from functional genomic analysis of a human mesenchymal stem cell model. *Dev. Biol.* **305**, 172–186 (2007).
- Lauschke, V. M., Tsaiaris, C. D., François, P. & Aulehla, A. Scaling of embryonic patterning based on phase-gradient encoding. *Nature* **493**, 101–105 (2013).
- Matsumiya, M., Tomita, T., Yoshioka-Kobayashi, K., Isomura, A. & Kageyama, R. ES cell-derived presomitic mesoderm-like tissues for analysis of synchronized oscillations in the segmentation clock. *Development* **145**, dev156836 (2018).
- Wahl, M. B., Deng, C., Lewandoski, M. & Pourquie, O. FGF signaling acts upstream of the NOTCH and WNT signaling pathways to control segmentation clock oscillations in mouse somitogenesis. *Development* **134**, 4033–4041 (2007).
- Burgess, R., Rawls, A., Brown, D., Bradley, A. & Olson, E. N. Requirement of the paraxis gene for somite formation and musculoskeletal patterning. *Nature* **384**, 570–573 (1996).
- Fleming, A., Kishida, M. G., Kimmel, C. B. & Keynes, R. J. Building the backbone: the development and evolution of vertebral patterning. *Development* **142**, 1733–1744 (2015).
- Dequéant, M. L. et al. A complex oscillating network of signaling genes underlies the mouse segmentation clock. *Science* **314**, 1595–1598 (2006).
- Hubaud, A., Regev, I., Mahadevan, L. & Pourquie, O. Excitable dynamics and Yap-dependent mechanical cues drive the segmentation clock. *Cell* **171**, 668–682 (2017).
- Aulehla, A. et al. A  $\beta$ -catenin gradient links the clock and wavefront systems in mouse embryo segmentation. *Nat. Cell Biol.* **10**, 186–193 (2008).
- Sparrow, D. B. et al. Mutation of the *LUNATIC FRINGE* gene in humans causes spondylocostal dysostosis with a severe vertebral phenotype. *Am. J. Hum. Genet.* **78**, 28–37 (2006).
- Okubo, Y. et al. *Lfng* regulates the synchronized oscillation of the mouse segmentation clock via *trans*-repression of Notch signalling. *Nat. Commun.* **3**, 1141 (2012).
- Huggins, I. J. et al. The WNT target *SP5* negatively regulates WNT transcriptional programs in human pluripotent stem cells. *Nat. Commun.* **8**, 1034 (2017).
- Pedersen, L., Jensen, M. H. & Krishna, S. Dickkopf1—a new player in modelling the Wnt pathway. *PLoS ONE* **6**, e25550 (2011).
- Sonnen, K. F. et al. Modulation of phase shift between Wnt and Notch signaling oscillations controls mesoderm segmentation. *PLoS ONE* **17**, 1079–1090 (2018).
- Bulman, M. P. et al. Mutations in the human *Delta* homologue, *DLL3*, cause axial skeletal defects in spondylocostal dysostosis. *Nat. Genet.* **24**, 438–441 (2000).
- Sparrow, D. B., Guillén-Navarro, E., Fatkin, D. & Dunwoodie, S. L. Mutation of *HAIRY-AND-ENHANCER-OF-SPLIT-7* in humans causes spondylocostal dysostosis. *Hum. Mol. Genet.* **17**, 3761–3766 (2008).
- Whitlock, N. V. et al. Mutated *MESP2* causes spondylocostal dysostosis in humans. *Am. J. Hum. Genet.* **74**, 1249–1254 (2004).
- Niwa, Y. et al. The initiation and propagation of *Hes7* oscillation are cooperatively regulated by Fgf and Notch signaling in the somite segmentation clock. *Dev. Cell* **13**, 298–304 (2007).
- Kusumi, K. et al. *Dll3* pudgy mutation differentially disrupts dynamic expression of somite genes. *Genesis* **39**, 115–121 (2004).
- Chen, J., Kang, L. & Zhang, N. Negative feedback loop formed by *Lunatic fringe* and *Hes7* controls their oscillatory expression during somitogenesis. *Genesis* **43**, 196–204 (2005).
- Cornier, A. S. et al. Mutations in the *MESP2* gene cause spondylothoracic dysostosis/Jarcho-Levin syndrome. *Am. J. Hum. Genet.* **82**, 1334–1341 (2008).
- Kim, S. I. et al. Microhomology-assisted scarless genome editing in human iPSCs. *Nat. Commun.* **9**, 939 (2018).
- Lackmann, M. et al. Distinct subdomains of the EphA3 receptor mediate ligand binding and receptor dimerization. *J. Biol. Chem.* **273**, 20228–20237 (1998).
- McInerney-Leo, A. M. et al. Compound heterozygous mutations in *RIPPLY2* associated with vertebral segmentation defects. *Hum. Mol. Genet.* **24**, 1234–1242 (2015).
- Bouman, A. et al. Homozygous *DMRT2* variant associates with severe rib malformations in a newborn. *Am. J. Med. Genet. A* **176**, 1216–1221 (2018).
- Turnpenny, P. D. et al. Novel mutations in *DLL3*, a somitogenesis gene encoding a ligand for the Notch signalling pathway, cause a consistent pattern of abnormal vertebral segmentation in spondylocostal dysostosis. *J. Med. Genet.* **40**, 333–339 (2003).

**Publisher's note** Springer Nature remains neutral with regard to jurisdictional claims in published maps and institutional affiliations.

© The Author(s), under exclusive licence to Springer Nature Limited 2020



# Article

## Methods

No statistical methods were used to predetermine sample size. The investigators were not blinded to allocation during experiments and outcome assessment.

### Pluripotent stem cell generation and culture

Experiments were performed using mainly two human iPS cell lines derived from healthy donors, 1231A3<sup>37</sup> and 201B7<sup>38</sup>. Pluripotent stem cells of patients with SCD and presenting SDV were induced using patient-derived primary cell samples. Primary cell sample of the first patient with SDV was obtained from the NIGMS Human Genetic Cell Repository at the Coriell Institute for Medical Research (GM13539) and used for the derivation of iPS cell line SCDP1 (Extended Data Fig. 9, Supplementary Note 1). Primary tissue samples of a second patient with clinical features of SDV, including vertebral segmentation defects along the entire spine (C1 to sacrum) and bilateral fusion of ribs posteriorly, were obtained in Japan and used for derivation of iPS cell line SCDP2 (see also Extended Data Fig. 9g, Supplementary Note 1). All experiments followed relevant guidelines and regulations and were approved by ethics committees of the Kyoto University Graduate School and Faculty of Medicine, Kyoto, Japan and Meijo Hospital, Nagoya, Japan. Experimental use of patient-derived cells was also approved by ethics committees of the RIKEN BDR (Kobe) and RIKEN IMS (Yokohama). Informed consent was obtained from legal guardians of patients by relevant institutions. Reprogramming was performed with episomes (pCE-hOCT3/4, pCE-hSK, pCE-hUL, pCE-mp53DD, pCXB-EBNA1) under feeder-free conditions using StemFit medium and laminin-coated dishes (iMatrix511)<sup>37</sup>. Human iPS cells were maintained without feeder cells and cultured on iMatrix-511 silk (Nippi) coated dishes or plates with StemFit AK02N (Ajinomoto) medium supplemented with 50 U penicillin and 50 mg ml<sup>-1</sup> streptomycin (Gibco). Utilized iPS cell lines were regularly tested and reported negative for mycoplasma contamination.

### Stepwise induction of human somitic mesoderm

Human iPS cells were seeded on iMatrix-511 silk-coated plates or dishes at appropriate densities as single cells (for example,  $1.3 \times 10^4$  cells per well into 6-well plates;  $8.0 \times 10^4$  cells per dish into 10-cm dishes) 4–5 days before induction. All differentiation and induction steps were performed in chemically defined medium with insulin (CDMi)<sup>39</sup>, unless otherwise mentioned. Our stepwise protocol is similar to a recently published mesoderm induction protocol<sup>4</sup>, with some differences. Human primitive streak cells were induced by treatment of iPS cells with basic FGF (bFGF, 20 ng ml<sup>-1</sup>), CHIR99021 (10  $\mu$ M) and activin A (50 ng ml<sup>-1</sup>) for 24 h. PSM cells were induced from primitive streak cells by exposure to SB431542 (10  $\mu$ M), CHIR99021 (3  $\mu$ M), LDN193189 (250 nM) and bFGF (20 ng ml<sup>-1</sup>) for 24 h. Subsequently, somitic mesoderm cells were induced from PSM cells using PD173074 (100 nM) and XAV939 (1  $\mu$ M) for 24 h. For details of the used recombinant human proteins and small molecule agonists or inhibitors, see Supplementary Table 6. Further details of applied in vitro induction and differentiation protocols are shared in the open protocol repository Protocol Exchange<sup>40</sup>.

### Human sclerotome and dermomyotome induction

Following initial stepwise somitic mesoderm induction, human sclerotome cells were induced with combination of smoothened agonist (SAG, 100 nM) and LDN193189 (600 nM)<sup>41</sup> for 72 h. Dermomyotome cells were induced from human somitic mesoderm as previously described<sup>4</sup>, using a combination of CHIR99021 (3  $\mu$ M), GDC0449 (150 nM) and BMP4 (50 ng ml<sup>-1</sup>) for 48 h.

### In vitro 3D chondrogenic induction

Stepwise-induced human sclerotome cells were dissociated using Accutase (Life Tech), centrifuged and resuspended in CDMi before being seeded ( $2.0 \times 10^5$  cells per well) into 96-well low attachment plates

containing sclerotome induction medium with ROCK inhibitor Y27632 (Wako), forming 3D aggregates overnight. Initial 3D sclerotome spheres were transferred into low-attachment plates or dishes containing 3D chondrogenic induction medium<sup>42</sup> and cultured under standard conditions. Medium was changed every three days.

### In vitro skeletal muscle induction

Dermomyotome cells were dissociated using Accutase (Life Tech), centrifuged, resuspended in CDMi and seeded ( $2.5 \times 10^5$  cells per well) into Matrigel-coated 12-well plates in muscle induction medium containing ROCK inhibitor Y27632 (Wako). To induce human skeletal muscle cells, we applied the N2 medium established previously<sup>43</sup> with some modifications (DMEM/F12 (Gibco), 1% insulin–transferrin–selenium (Corning), 1% N2 Supplement (Gibco), 0.2% penicillin/streptomycin (Gibco), 1% L-glutamine (Gibco), 2% horse serum (Sigma-Aldrich)). Medium was changed every three days. Calcium imaging of dermomyotome-derived skeletal muscle activity in GCaMP-reporter line (Gen1C)<sup>44</sup> was performed using Nikon A1R MP (Multiphoton + N-STORM).

### In vivo xeno-transplantation of PSM derivatives

Male NOD/ShiJic-scidJcl mice were purchased from CLEA Japan and used at six weeks of age. Human sclerotome cells derived from healthy-donor (wild type) or homozygous and heterozygous luciferase reporter lines (625-A4 and 625-D4) were dissociated using Accutase (Life Tech) and resuspended in 100  $\mu$ l of CDMi before being mixed with the same volume of Matrigel as previously described<sup>4</sup>. Numbers of transplanted cells ranged from  $5.0 \times 10^5$  to  $1.2 \times 10^6$  cells per injection. Cells were injected into mice subcutaneously with a 26 G needle and 1-ml syringe (Terumo). Forming cartilage and bone tissues were taken out at 2 months after injection. Bioluminescence images were taken with IVIS Spectrum (PerkinElmer). Whole-mount images were taken with LEICA M205FA (Leica). Animal experiments were approved by the institutional animal committee of Kyoto University and performed in strict accordance with the Regulation on Animal Experimentation at Kyoto University.

### Quantitative PCR with reverse transcription

RNA was extracted with the RNeasy mini kit (Qiagen) following the manufacturer's instructions. cDNA was synthesized using Superscript III Reverse Transcriptase (Invitrogen) from 1  $\mu$ g total RNA. cDNA was diluted 1:10 in RNase-free water. RT-qPCR was performed using Thunderbird SYBR qPCR Mix (Toyobo) and QuantStudio 12K Flex Real-Time PCR System (Thermo Fisher). The expression values of target genes were normalized by b-actin expression from the same cDNA templates. For oscillation analyses, fold induction relative to time 0 was calculated as  $2^{-\Delta\Delta C_t}$  where  $\Delta\Delta C_t$  values were differences between  $\Delta C_t$  values at time 0 and each time point (technical triplicates). For other analyses, expression values of each biological replicate were calculated from technical triplicate or quadruplet qPCR reactions, and the mean and s.d. values were determined from the expression values of biological replicates. Details of used RT-qPCR primers are listed in Supplementary Tables 7.1 and 7.2.

### Immunocytochemistry

Cells were fixed with 2% paraformaldehyde (PFA) for 30 min and washed twice with PBS. Samples were permeabilized with 0.2% Triton X-100 (Sigma-Aldrich) in PBS for 10 min at room temperature and then washed with PBST (1% Tween 20 (Sigma-Aldrich) in PBS). Subsequently, samples were blocked in 5% skim milk for 1 h at room temperature and then stained with primary antibodies for overnight at 4 °C. Samples were then washed with PBST three times and stained with secondary antibodies for 1 h at room temperature. Antibodies were diluted in 10% blocking solution (5% skim milk) in PBST, washed with PBST twice and stained with DAPI for nuclear counterstaining for 5 min at room temperature. All images were taken using Nikon A1R MP (Multiphoton+N-STORM). For details of used primary and secondary antibodies see Supplementary Table 8.

## Histological analysis

Tissues were fixed with 4% PFA overnight at 4 °C. Fixed samples were washed with PBS twice and embedded in paraffin. Sections were sliced at 3 µm for immunostaining and 5 µm for other types of staining. Sections were stained with haematoxylin and eosin (H&E), safranin O, von Kossa, pentachrome, type I collagen (COL1) antibody, type II collagen (COL2) antibody and human nuclear antigen (HNA) antibody. Sections stained with antibodies were incubated for overnight at 4 °C. Secondary antibodies were applied with N-Histofine Simple Stain MAX PO (Nichirei Bioscience) for 30 min at room temperature. Signals were detected by N-Histofine DAB-3S kit (Nichirei Bioscience). For details of antibodies used see Supplementary Tables 8.1 and 8.2.

## Flow cytometric analysis

Cells were washed with PBS and dissociated using Accutase (Life Technologies) and centrifuged. Cells were resuspended ( $1.0 \times 10^7$  cells per ml) in fluorescence-activated cell sorting (FACS) buffer (0.1% BSA in PBS) and stained with allophycocyanin (APC)-conjugated DLL1 antibody for 30 min at 4 °C. Cells were then stained with DAPI to eliminate dead cells after washing with FACS buffer once and finally strained through a filter mesh. As for the co-staining of intracellular molecules TBX6 and brachyury (encoded by *T*) with DLL1, cells were fixed with 4% paraformaldehyde for 20 min at 4 °C after initial staining with DLL1 antibody and washed twice with staining medium, which contained PBS with 2% FBS. Samples were permeabilized with BD Perm/Wash buffer (BD Biosciences) for 15 min at room temperature and stained with TBX6 primary antibody or phycoerythrin (PE)-conjugated brachyury antibody for 60 min at room temperature and washed with BD Perm/Wash buffer twice. The cells stained with TBX6 antibody were stained with Alexa Fluor 488-conjugated secondary antibody for 60 min at room temperature. The samples were washed with BD Perm/Wash buffer twice and suspended into staining medium. Flow cytometric analysis was performed using LSR or BD FACS Aria II cell sorter (BD Biosciences). FACS data were analysed and graphs were generated using FlowJo software (FlowJo). For details of used antibodies see Supplementary Tables 8.3 and 8.4.

## Reporter constructs

For the human *HES7* reporter, human *HES7* promoter (5,937 bp) and 3' untranslated region (UTR) were fused to Luciferase2-NLS-d1PEST<sup>45</sup>. For the mouse *Hes7* reporter, mouse *Hes7* promoter and 3' UTR were fused to Ub-Luciferase2-NLS<sup>46</sup>. For the dual-reporter assay, the *HES7* promoter and 3' UTR were fused to NanoLuc-NLS-d1PEST, while human *DKK1* promoter (2,218 bp) and 3' UTR were fused to Luciferase2-NLS-d1PEST. These reporters were integrated into the genome using piggyBac transposition. See Extended Data Fig. 2a and Extended Data Fig. 7d for schematic overviews of used reporter constructs.

## Oscillation assay in 2D

Primitive streak and PSM were induced in a stepwise manner as described above. Luminescence was measured in the presence of D-luciferin (200 µM) with Kronos Dio Luminometer (Atto) from the timing of PSM induction. The obtained signal was detrended with Excel (Microsoft), and converted to the instantaneous phase with the Hilbert and Angel functions of Matlab (Mathworks). For the dual-reporter assay, *HES7* and *DKK1* reporter constructs were simultaneously introduced into the cells, and each luminescence was filtered and measured in the presence of Endurazine (Live Cell Ex-4377, Promega) (400 nM) and D-luciferin (1 mM). The dual-reporter cells were seeded on a 35-mm dish coated with iMatrix-511 at 3,000 cells per dish. After 4 days culture, medium was changed into CDMi containing SB431542 (10 µM), CHIR99021 (10 µM), DMH1 (2 µM) and bFGF (20 ng ml<sup>-1</sup>). After additional three days culture, the medium was changed into CDMi without inhibitors for measurement with Kronos Dio Luminometer (Atto). This

modified one-step protocol<sup>47</sup> was used only for Extended Data Fig. 7d. All other 2D oscillation measurements of human PSC-derived PSM were performed using our standard stepwise PSM induction protocol.

## Synchronization assay in 3D

To make 3D induced PSM spheroids, *HES7* reporter iPS cells were seeded into non-adhesive round bottom 96-well plates at 1,000–5,000 cells per well and cultured in CDMi containing BMP4 (50 ng ml<sup>-1</sup>), CHIR99021 (10 µM) and Y27632 (10 µM). After one day of culture, Y27632 was removed. After 18 h of culture, the medium was changed to CDMi containing DMH1 (2 µM) and CHIR99021 (10 µM). After 6 h culture, the spheroid was transferred to a fibronectin-coated glass bottom dish with CDMi containing DMH1 (2 µM) and D-luciferin (1 mM), and luminescence of the spreading spheroid was imaged with a customized incubator microscope LCV110 (Olympus). The signal was averaged over all area or region of interest (ROI). When needed, the signal was further detrended with Excel, and converted to the instantaneous phase with Matlab. When the signal was weak, the spike noise was removed initially with ImageJ as described previously<sup>48</sup>. Kymographs were made by averaging signals over ten pixels with Metamorph (Molecular Devices).

## Sampling for RNA-seq analysis of oscillating human genes

Our standard stepwise PSM-induction protocol was used with the following modifications. *HES7* reporter cells were seeded on a 35-mm dish coated with Matrigel. At 12 h during the second step (PSM induction), the cells were split into multiple 35-mm dishes at  $4.0 \times 10^5$  cells per dish and cultured in CDMi containing SB431542 (10 µM), LDN193189 (250 nM) and CHIR99021 (3 µM). After 12 h culture the medium was changed into CDMi containing SB431542 (10 µM), LDN193189 (250 nM), CHIR99021 (3 µM) and bFGF (20 ng ml<sup>-1</sup>). The luminescence was continuously monitored with Kronos Dio Luminometer using one sample, and the other 16 samples were frozen at each time point.

## Induction and sampling of murine EpiSC-derived PSM

Mouse EpiSCs were obtained from RIKEN BRC (AES0204)<sup>49</sup> and maintained on fibronectin-coated dishes with DMEM/Ham F-12 containing 15% knockout serum replacement, nonessential amino acids (0.1 mM), β-mercaptoethanol (0.1 mM), activin A (20 ng ml<sup>-1</sup>), bFGF (10 ng ml<sup>-1</sup>) and IWR-1-endo (2.5 µM). The mouse EpiSC line was tested and reported negative for mycoplasma contamination. For murine PSM induction, EpiSCs were seeded on 35-mm dishes coated with fibronectin and cultured overnight with the medium containing Y27632 (10 µM), activin A (20 ng ml<sup>-1</sup>) and bFGF (10 ng ml<sup>-1</sup>) but without IWR-1-endo. The medium was then changed to CDMi containing SB431542 (10 µM), LDN193189 (250 nM), CHIR99021 (10 µM) and bFGF (20 ng ml<sup>-1</sup>). After 30 h, the medium was changed again to CDMi containing SB431542 (10 µM), LDN193189 (250 nM), CHIR99021 (3 µM) and bFGF (20 ng ml<sup>-1</sup>). The luminescence was continuously monitored with Kronos Dio Luminometer using one sample, and the other 16 samples were frozen at each time point.

## Library preparation for RNA-seq analysis

Total RNA was extracted using RNeasy mini kit (Qiagen) following the manufacturer's instructions. RNA-seq libraries were generated from 200–300 ng total RNA with the TruSeq Stranded mRNA LT Sample Prep Kit (Illumina) according to the manufacturer's protocol, with the exception of the libraries used for RNA-seq analysis of human oscillating genes, which were generated from 120 ng total RNA using Neo-Prep system (Illumina) following the manufacturer's instructions. The obtained RNA-seq libraries were sequenced on NextSeq 500 (75–86 bp single-end reads, Illumina).

## RNA-seq data analyses

The sequenced reads were mapped to the hg38 human reference genome plus the luciferase reporter sequence using HISAT2 (v.2.1.0)<sup>50</sup>

with the GENCODE v.25 annotation gtf file after trimming adaptor sequences and low-quality bases by cutadapt-1.14<sup>51</sup>. The mapped reads with high mapping quality (MAPQ  $\geq 20$ ) were used for further analyses. For identification of the differentiation stage-related genes, the differentially expressed genes ( $\geq$  fivefold changes and  $q$  values  $\leq 0.05$  between any pair of samples) were extracted using Cuffdiff<sup>52</sup> within Cufflinks v.2.2.1 package and GENCODE v.25 annotation file, and the extracted genes were grouped into six stages based on the maximum expression levels (FPKM values determined by Cuffdiff) among the differentiation stages. The low expressed genes ( $\leq 10$  FPKM) across all stages were filtered out before grouping. For identification of the oscillation genes, the uniquely mapped reads were counted and normalized to calculate the gene expression levels using HTSeq (v.0.6.1)<sup>53</sup> with GENCODE v.25 annotation gtf file (protein-coding genes) and edgeR (v.3.18.1)<sup>54</sup> after filtering low-expressed genes (cpm  $\leq 1$ ) across all conditions in each experiment. Rhythmic genes were identified by ARSER (v.2.0)<sup>55</sup> with FDR<sub>BH</sub>  $\leq 0.03$  in both of two independent experiments for the human case and with FDR<sub>BH</sub>  $\leq 0.2$  in either of two independent experiments for the mouse case. The filtering genes for noise judged by ARSER in both experiments were excluded from human oscillation genes. For pathway and Gene Ontology analyses, DAVID web tools<sup>56</sup> and IPA (Qiagen, <https://www.qiagenbioinformatics.com/products/ingenuitypathway-analysis>) were used with a gene set including both phase and antiphase oscillating genes. For identification of the patient (SCDP1-A and SCDP1-F) related genes, fold changes with  $q$  values were calculated with HTSeq (v.0.6.1)<sup>53</sup> with GENCODE v.25 annotation gtf file and edgeR (v.3.18.1)<sup>54</sup>. The normalization counts (pseudocounts) determined by edgeR were used as expression values. The genes whose expression values were upregulated or downregulated ( $\geq$  threefold changes,  $q < 0.05$ , SCDP1 lines versus wild type), and increases or decreases were inhibited ( $\geq 50\%$ ,  $q < 0.05$ ) in the rescued lines, were defined as SCDP1-related upregulated or downregulated genes, respectively. The genes whose expression levels were low (average cpm  $\leq 5$ ) in both wild-type and SCDP1-lines were filtered out. For comparisons of expression profiles between knockout cell lines and their parental cell lines (wild type), FPKM values, fold changes and  $q$  values were calculated using Cuffdiff<sup>52</sup> within Cufflinks v.2.2.1 package and GENCODE v.25 annotation file (protein-coding genes). The PCA and representation of heat maps and scatter plots were performed using R software.

## CRISPR-Cas9 gene knockout

Gene knockout was performed using transient transfection of pSpCas9(BB)-2A-Puro (PX459) V2.0 (a gift from F. Zhang, Addgene plasmid #62988). Oligonucleotides encoding sgRNA protospacer sequences (Supplementary Table 7) were annealed and cloned as described previously<sup>57</sup>. sgRNAs were verified by sequencing. Plasmid DNA (1  $\mu$ g) was transfected into iPS cells by electroporation followed by selection with 0.5  $\mu$ g ml<sup>-1</sup> puromycin for 48 h. Surviving cells were allowed to recover and then replated at low density before picking isolated colonies. For overview of knockout reporter line establishment and details of sgRNAs used see Extended Data Fig. 8a and Supplementary Table 7.5.

## Generation of *HES7*<sup>Δ25W</sup> mutant lines

Target-specific gRNA sequences were cloned into pSpCas9(BB)-2A-Puro (PX459) V2.0. One-million human *HES7* reporter iPS cells were electroporated with 3  $\mu$ g each of targeting vector and ssODN, treated with 0.5  $\mu$ g ml<sup>-1</sup> puromycin 24 h after transfection for 48 h, and single clones were Sanger sequenced. Candidate clones were allele resolved using Zero Blunt TOPO PCR Cloning Kit (Invitrogen) and a clone identified with one correctly modified allele and one allele containing a 5-bp deletion was re-targeted with a gRNA specific to the 5-bp deletion, and single clones were obtained as outlined above. The detailed targeting process, used sgRNAs and ssODN templates are shown in Extended Data Fig. 9a, Supplementary Tables 7.5 and 7.8.

## Whole-exome sequencing and variant calling

Whole-exome sequencing was performed as previously described<sup>58,59</sup>. In brief, DNA (3  $\mu$ g) was sheared with S2 Focused-ultrasonicator (Covaris) and processed by SureSelectXT Human All Exon V5 (Agilent Technologies). Captured DNA was sequenced using HiSeq 2000 (Illumina) with 101-bp pair-end reads with seven indices. Image analysis and base calling were performed using HCS (v.2.0.10), RTA (v.1.17.21.3) and CASAVA (v.1.8.2) software (Illumina). Reads were mapped to the reference human genome (hg19) by Novoalign v.3.02.04. Aligned reads were processed with Picard (v.2.0.1) to remove PCR duplicates. Variants were called by GATK v.2.7-4 following GATK Best Practice Workflow v.3<sup>60</sup> and annotated by ANNOVAR (v.2016Mar30)<sup>61</sup>. All the variants of the candidate genes, which have been reported to cause SCD or congenital scoliosis, were evaluated using five databases: gnomAD, Human Gene Mutation Database (HGMD), SIFT, PolyPhen-2 and MutationTaster.

## Quality control of established iPS cells

Morphological images of iPS cell colonies were captured using an Olympus CKX41 microscope with a PlanApo 10 $\times$  0.75 NA objective lens (Olympus) and Nikon digital camera DS-Fil. Chromosomal G-banding analyses were performed by Chromocentre. Genomic DNA and total RNA were extracted with AllPrep DNA or RNA mini kit (Qiagen) following the manufacturer's instructions. Genomic DNA was diluted to 25 ng ml<sup>-1</sup> in distilled water. cDNA was synthesized using PrimeScript RT Master Mix (Takara) from 500 ng total RNA and diluted 1:10 in RNase-free water for expression analysis of *OCT3/4* (also known as *POU5F1*) and *NANOG* mRNA, and 1  $\mu$ g total RNA for TaqMan hPSC Scorecard analysis. *OCT3/4* and *NANOG* mRNA expression were confirmed by RT-qPCR with TaqMan assay using StepOnePlus Real-Time PCR Systems (Thermo Fisher). Primers and probe sequences are provided in Supplementary Table 7.3. The expression values of target genes were normalized by *GAPDH* expression from the same cDNA templates and calculated relative to 201B7 iPS cell line. Residual plasmids used for iPS cell establishment were analysed by TaqMan quantitative PCR using StepOnePlus Real-Time PCR Systems (Thermo Fisher). Primer and probe sequences (cmCAG: common-CAG) are designed on CAG-promoter region included in all of the episomal vectors for iPS cell generation and listed in Supplementary Table 7.3. The residual plasmid numbers were determined by a standard curve method with pCE-OCT3/4 episomal plasmid of known quantity using 50 ng genomic DNA of SCDP1 and SCDP2 iPS cells at passage 6.

## Initial validation of established iPS cells

Established (patient) iPS cells together with control human PSCs were differentiated into ectoderm, mesoderm and endoderm lineages using STEMdiff Trilineage Differentiation Kit (Stemcell Technologies). Human PSCs reaching 70–80% confluence were collected with TrypLE Select Enzyme (1 $\times$ ) (Thermo Fisher) and plated as a single cell suspension in mTeSR1 medium (Stemcell Technologies) containing 10  $\mu$ M Y27632 (Wako) on six-well plates coated with Matrigel (BD Biosciences). The cells were plated at 4.0  $\times 10^5$  cells, 2.0  $\times 10^5$  cells and 4.0  $\times 10^5$  cells per well for ectoderm, mesoderm and endoderm differentiation culture respectively and differentiated following the manufacturer's instructions. For FACS-based evaluation of undifferentiated PSCs and each of the three germ layers (1.0  $\times 10^6$  cells each) were fixed with 4% paraformaldehyde phosphate buffer solution (4% PFA/PBS) for 20 min at 4  $^{\circ}$ C and washed twice with staining medium, which contained PBS with 2% fetal bovine serum (FBS). Samples were permeabilized with BD Perm/Wash buffer (BD Biosciences) for 15 min at room temperature and stained with fluorescence-conjugated antigen-specific and isotype antibodies listed in Supplementary Tables 8.3 and 8.4. The samples were washed with BD Perm/Wash buffer twice and suspended into staining medium. Flow cytometric analysis was performed using LSR (BD Biosciences). FACS data was analysed and graphs were generated

using FlowJo software (FlowJo). For transcript level assessment of differentiation capacity, qPCR was performed with a 384-well TaqMan hPSC Scorecard panel (Thermo Fisher) by QuantStudio 12K Flex Real-Time PCR System (Thermo Fisher) using undifferentiated PSC and each of the three germ layers cDNA samples. Pluripotency and differentiation property into ectoderm, mesoderm and endoderm lineages were scored by hPSC Scorecard Analysis software, which is available on the Thermo Fisher website (<https://www.thermofisher.com/jp/en/home/life-science/stem-cell-research/taqman-hpsc-scorecard-panel.html>)<sup>62</sup>.

### Gene correction of patient-derived iPS cells

Correction of mutations in patient-derived iPS cells was performed using the MhAX method as previously described<sup>32</sup>. In brief, donor plasmids for correction of each mutant allele were created by PCR amplification of the homology arms from cloned haplotype-specific genomic DNA using the primers listed in Supplementary Table 7. For correction of *MESP2* mutations, the right homology arm was amplified from SCDP1 patient DNA corresponding to the matching mutant allele, and the left arm was amplified from normal 201B7 iPS cell DNA, which bears a similar haplotype. InFusion cloning (Clontech) was used to assemble the arms with a restriction-digested CAG::mCherry-*IRES*-puromycin selection cassette (Addgene plasmid 113876) and CAG::GFP plasmid backbone (Addgene plasmid 107281). PCR-amplified regions and InFusion junctions were verified by sequencing. Oligonucleotides encoding sgRNA protospacer sequences targeting *MESP2* or *DLL3* (Supplementary Table 7) were annealed and cloned into pX330-U6-Chimeric\_BB-CBh-hSpCas9 (a gift from F. Zhang, Addgene plasmid 42230) as described previously<sup>57</sup>. sgRNAs were verified by sequencing. For gene targeting, allele-matched donor plasmids (3 µg) and Cas9 and sgRNA expression plasmids (1 µg) were co-transfected by electroporation into  $1 \times 10^6$  SCDP1 or SCDP2 patient iPS cells, which were then divided and plated under feeder-free conditions for 48 h in AK02N medium (Ajinomoto) containing 10 µM ROCK inhibitor Y-27632 (Wako) before initiating antibiotic selection (0.5 µg ml<sup>-1</sup> puromycin, Sigma-Aldrich). Nine days after plating, puromycin-resistant cells were pooled and passaged. For SCDP1, GFP<sup>+</sup>mCherry<sup>+</sup> colonies were isolated, cultured, stored and processed for genomic DNA isolation under feeder-free conditions in 96-well format. iPS cell clones positive for PCR genotyping and sequencing were defrosted and expanded for genomic DNA extraction and Southern blot verification. For *DLL3*, GFP<sup>+</sup>mCherry<sup>+</sup> cells were sorted and cultured as populations for subsequent cassette excision. For cassette excision from clones or populations, 3 µg of the pX-eGFP-g1 expression plasmid (Addgene plasmid 107273) was transfected into  $1 \times 10^6$  gene-targeted patient iPS cells, which were then divided and plated under feeder-free conditions for 48 h in AK02N medium containing 10 µM Y-27632, followed by growth without selection for a total of 6 days. mCherry<sup>-</sup> cells were isolated by FACS on a BD FACS Aria II cell sorter, and plated at low density for clonal isolation after 8 days. Isolated clones were cultured, stored in 96-well format, then genotyped for cassette excision by PCR and sequencing before final verification by Southern blot.

### Genomic DNA extraction

Genomic DNA for PCR amplification and sequencing was isolated from  $0.5\text{--}1.0 \times 10^6$  iPS cells using a DNeasy Blood and Tissue Kit (Qiagen). Genomic DNA for Southern blotting was isolated from a single confluent well of a 6-well dish using lysis buffer (100 mM Tris-HCl, pH 8.5, 5 mM EDTA, 0.2% SDS, 200 mM NaCl, and 1 mg ml<sup>-1</sup> proteinase K) followed by phenol–chloroform extraction and ethanol precipitation from the aqueous phase. Genomic DNA was eluted from columns or resuspended from precipitate in TE pH 8.0.

### Southern blot analysis

For *MESP2* and *DLL3* gene correction, patient and rescued iPS cells were analysed by Southern blotting as described previously<sup>32</sup>. Probe regions were PCR amplified with Ex Taq (Takara) directly from genomic DNA or

cloned plasmid templates to incorporate DIG-labelled dUTP (Roche) using the primers described in Supplementary Table 7. Genomic DNA (5–10 µg) was digested with EcoRI (*MESP2*), HindIII (*DLL3*) or SacII (*DLL3*). SphI, a non-cutter at the *DLL3* locus, was included in SacII digestions to reduce DNA viscosity.

### iPS cell genotyping and SNP array

PCR primers flanking annotated coding exons of *DLL3* (Accession NG\_008256.1), *HES7* (Accession NG\_015816.1), *LFNG* (Accession NG\_008109.2) and *MESP2* (Accession NG\_008608.1) were designed using NCBI Primer-BLAST with optional settings filtering human repeats and SNPs, with primer pair specificity checking to *Homo sapiens* (taxid:9606). PCR primers for genotyping gene-edited cell lines were designed using similar principles. All genotyping primers are listed in Supplementary Table 7. Genomic PCR was carried out using KAPA HiFi HotStart (KAPA Biosystems) on a Veriti 96-well Thermal Cycler (Applied Biosystems) according to the manufacturer's instructions. Specific PCR conditions are available upon request. PCR products were treated with ExoSAP-IT Express (Affymetrix) and sequenced with the primers indicated in Supplementary Table 7 using BigDye Terminator v.3.1 Cycle Sequencing Kit (Applied Biosystems) on a 3130xl Genetic Analyzer (Applied Biosystems). Sequence analysis was performed using variant calling in Sequencher (Genecodes) or alignment in Snapgene (GSL Biotech). Genomic DNA from patient iPS cells and iPS cell clones rescued by gene editing were genotyped using an Infinium OmniExpress-24 v.1.2 (Illumina) SNP array according to the manufacturer's recommendations. Data collection was performed on an iScan Bead Array Scanner (Illumina). Data was compared to the reference human genome (hg19) using a combination of PennCNV, cnvPartition, GWAS tools, and MAD. Karyograms were prepared in R (v.3.2.5) using GWASTools (v.1.16.1)<sup>63</sup>.

### Reporting summary

Further information on research design is available in the Nature Research Reporting Summary linked to this paper.

### Data availability

All RNA sequencing data used for this study have been deposited in the NCBI Gene Expression Omnibus (GEO) under accession number GSE116935. SNP array data in the current publication have been deposited in and are available upon application from the dbGaP database under accession number phs001975.v1.p1 and their use is limited to health, medical and biomedical purposes. Source Data for Figs. 1–4 and Extended Data Figs. 1, 2, 5–12 are available in the online version of the paper.

### Code availability

Computational codes and scripts used in this study are available at GitHub (<https://github.com/mebisuya/SegmentationClock>) and upon request from the corresponding authors.

37. Nakagawa, M. et al. A novel efficient feeder-free culture system for the derivation of human induced pluripotent stem cells. *Sci. Rep.* **4**, 3594 (2015).
38. Takahashi, K. et al. Induction of pluripotent stem cells from adult human fibroblasts by defined factors. *Cell* **131**, 861–872 (2007).
39. Wataya, T. et al. Minimization of exogenous signals in ES cell culture induces rostral hypothalamic differentiation. *Proc. Natl Acad. Sci. USA* **105**, 11796–11801 (2008).
40. Yamanaka, Y., Uemura, M. & Alev, C. Stepwise in vitro induction of human somitic mesoderm and its derivatives. *Protoc. Exch.* <https://doi.org/10.21203/rs.2.22919/v1> (2020).
41. Zhao, J. et al. Small molecule-directed specification of sclerotome-like chondroprogenitors and induction of a somitic chondrogenesis program from embryonic stem cells. *Development* **141**, 3848–3858 (2014).
42. Yamashita, A. et al. Generation of scaffoldless hyaline cartilaginous tissue from human iPSCs. *Stem Cell Reports* **4**, 404–418 (2015).
43. Chal, J. et al. Generation of human muscle fibers and satellite-like cells from human pluripotent stem cells in vitro. *Nat. Protoc.* **11**, 1833–1850 (2016).

44. Mandegar, M. A. et al. CRISPR interference efficiently induces specific and reversible gene silencing in human iPSCs. *Cell Stem Cell* **18**, 541–553 (2016).
45. Li, X. et al. Generation of destabilized green fluorescent protein as a transcription reporter. *J. Biol. Chem.* **273**, 34970–34975 (1998).
46. Niwa, Y. et al. Different types of oscillations in Notch and Fgf signaling regulate the spatiotemporal periodicity of somitogenesis. *Genes Dev.* **25**, 1115–1120 (2011).
47. Nakajima, T. et al. Modeling human somite development and fibrodysplasia ossificans progressiva with induced pluripotent stem cells. *Development* **145**, dev165431 (2018).
48. Isomura, A., Ogushi, F., Kori, H. & Kageyama, R. Optogenetic perturbation and bioluminescence imaging to analyze cell-to-cell transfer of oscillatory information. *Genes Dev.* **31**, 524–535 (2017).
49. Sugimoto, M. et al. A simple and robust method for establishing homogeneous mouse epiblast stem cell lines by Wnt inhibition. *Stem Cell Reports* **4**, 744–757 (2015).
50. Kim, D., Langmead, B. & Salzberg, S. L. HISAT: a fast spliced aligner with low memory requirements. *Nat. Methods* **12**, 357–360 (2015).
51. Martin, M. Cutadapt removes adapter sequences from high-throughput sequencing reads. *EMBnet.journal* **17**, 10–12 (2011).
52. Trapnell, C. et al. Differential analysis of gene regulation at transcript resolution with RNA-seq. *Nat. Biotechnol.* **31**, 46–53 (2013).
53. Anders, S., Pyl, P. T. & Huber, W. HTSeq—a Python framework to work with high-throughput sequencing data. *Bioinformatics* **31**, 166–169 (2015).
54. McCarthy, D. J., Chen, Y. & Smyth, G. K. Differential expression analysis of multifactor RNA-Seq experiments with respect to biological variation. *Nucleic Acids Res.* **40**, 4288–4297 (2012).
55. Yang, R. & Su, Z. Analyzing circadian expression data by harmonic regression based on autoregressive spectral estimation. *Bioinformatics* **26**, i168–i174 (2010).
56. Huang, W., Sherman, B. T. & Lempicki, R. A. Systematic and integrative analysis of large gene lists using DAVID bioinformatics resources. *Nat. Protocols* **4**, 44–57 (2009).
57. Ran, F. A. et al. Genome engineering using the CRISPR–Cas9 system. *Nat. Protoc.* **8**, 2281–2308 (2013).
58. Guo, L. et al. Novel and recurrent XYLT1 mutations in two Turkish families with Desbuquois dysplasia, type 2. *J. Hum. Genet.* **62**, 447–451 (2017).
59. Guo, L. et al. Identification of a novel LRRK1 mutation in a family with osteosclerotic metaphyseal dysplasia. *J. Hum. Genet.* **62**, 437–441 (2017).
60. McKenna, A. et al. The genome analysis toolkit: a MapReduce framework for analyzing next-generation DNA sequencing data. *Genome Res.* **20**, 1297–1303 (2010).
61. Wang, K., Li, M. & Hakonarson, H. ANNOVAR: functional annotation of genetic variants from high-throughput sequencing data. *Nucleic Acids Res.* **38**, e164 (2010).
62. Bock, C. et al. Reference maps of human ES and iPSC cell variation enable high-throughput characterization of pluripotent cell lines. *Cell* **144**, 439–452 (2011).
63. Gogarten, S. M. et al. GWASTools: an R/Bioconductor package for quality control and analysis of genome-wide association studies. *Bioinformatics* **28**, 3329–3331 (2012).

**Acknowledgements** The authors thank B. McIntyre and P. O'Neill for critical reading of the manuscript; K. Mitsunaga for help with FACS analysis; Y. Ashida for help with development of human spheroid PSM-induction protocol; H. Hayashi for help with development of mouse PSM protocol; J. Asahira for help with RNA-seq experiments; A. Yamashita for help with 3D chondrogenic induction experiments; M. Shibata and T. Nakajima for help with development of

one-step PSM-induction protocol; M. Ohno and S. Nishimura for help with iPS cell quality control and validation; members of the Kageyama laboratory, K. Yoshioka-Kobayashi and A. Isomura for help with Hilbert transformation and M. Matsumiya for help with removing spike noise from images; the CiRA Genome Evaluation Group, in particular H. Dohi, F. Kitaoka, M. Nomura, T. Takahashi, M. Umekage and N. Takasu for performing SNP array analysis. This work was supported by the CiRA Fellowship Program of Challenge to C.A.; Naito Foundation Research Grant to C.A.; Grant-in-Aid for Challenging Exploratory Research (KAKENHI Number 16K15664) to C.A.; Grant-in-Aid for Scientific Research on Innovative Areas (KAKENHI Number 17H05777) to M.M.; Takeda Science Foundation Grant to M.E.; Japan Agency for Medical Research and Development (AMED) Grants Number 12103610 and 17935423 to M.K.S. for iPS cell generation and qualification, grant number JP19bm0804001 to K.W. for iPS cell gene editing and grant numbers JP18ek0109212 and 18ek0109280 to S.I. for genomic and exome studies of spondylocostal dysostosis, respectively; the Core Center for iPS Cell Research (AMED) to T.Y., K.W. and J.T. and the Acceleration Program for Intractable Disease Research Using Disease Specific iPS Cells (AMED) to K.W., J.T. and M.K.S.; the Kyoto University Hakubi Project to K.W.; the Cooperative Research Program (Joint Usage/Research Center Program) of the Institute for Frontier Life and Medical Sciences, Kyoto University to J.T., L.G. and S.I.. ASHBI is supported by the World Premier International Research Center Initiative (WPI), MEXT, Japan.

**Author contributions** C.A. conceived, designed and supervised the study; M.E. and M.M. conceived and developed mouse PSM-induction and human spheroid PSM-induction protocols and performed 2D-oscillation and 3D-synchronization assays with the help of C.A.; Y.Y., M.U. and C.A. developed stepwise PSM induction and other subsequent differentiation protocols and performed the majority of remaining in vitro and in vivo experiments; S.K. supported microscopy and calcium imaging; M. Nishio helped with xenotransplantation experiments; M.O., M.K.S. and A.N. established patient iPS cell lines used in this study and performed quality control of iPS cells; M.O. helped with FACS data analysis; L.G. and S.I. performed exome sequencing and database analysis; T.Y. analysed RNA-seq and RT-qPCR data with the help of S.S.; K.W. designed gene-knockout and gene-editing strategies; T.L.M. established *HES7* c.73C>T (R25W) mutant iPS cells; T.M. performed gene editing of patient iPS cells and Southern blotting; M. Nakamura performed sequence genotyping of patient and gene-edited iPS cells; Y.Y., M.U. and C.A. generated knockout lines with the help of M. Nakamura and K.W. and performed molecular and functional assays using knockout lines, patient-like and patient-derived iPS cells and gene-corrected isogenic controls; M.I. developed one-step PSM induction protocol; M.K.S. and H.Y. shared reagents and protocols; J.T. provided administrative support and, with N.K., helped with establishment of patient lines; C.A. analysed and interpreted the data and wrote the manuscript with the support of M.E. and K.W. All authors discussed and commented on the manuscript and agreed on the presented results.

**Competing interests** The authors declare no competing interests.

## Additional information

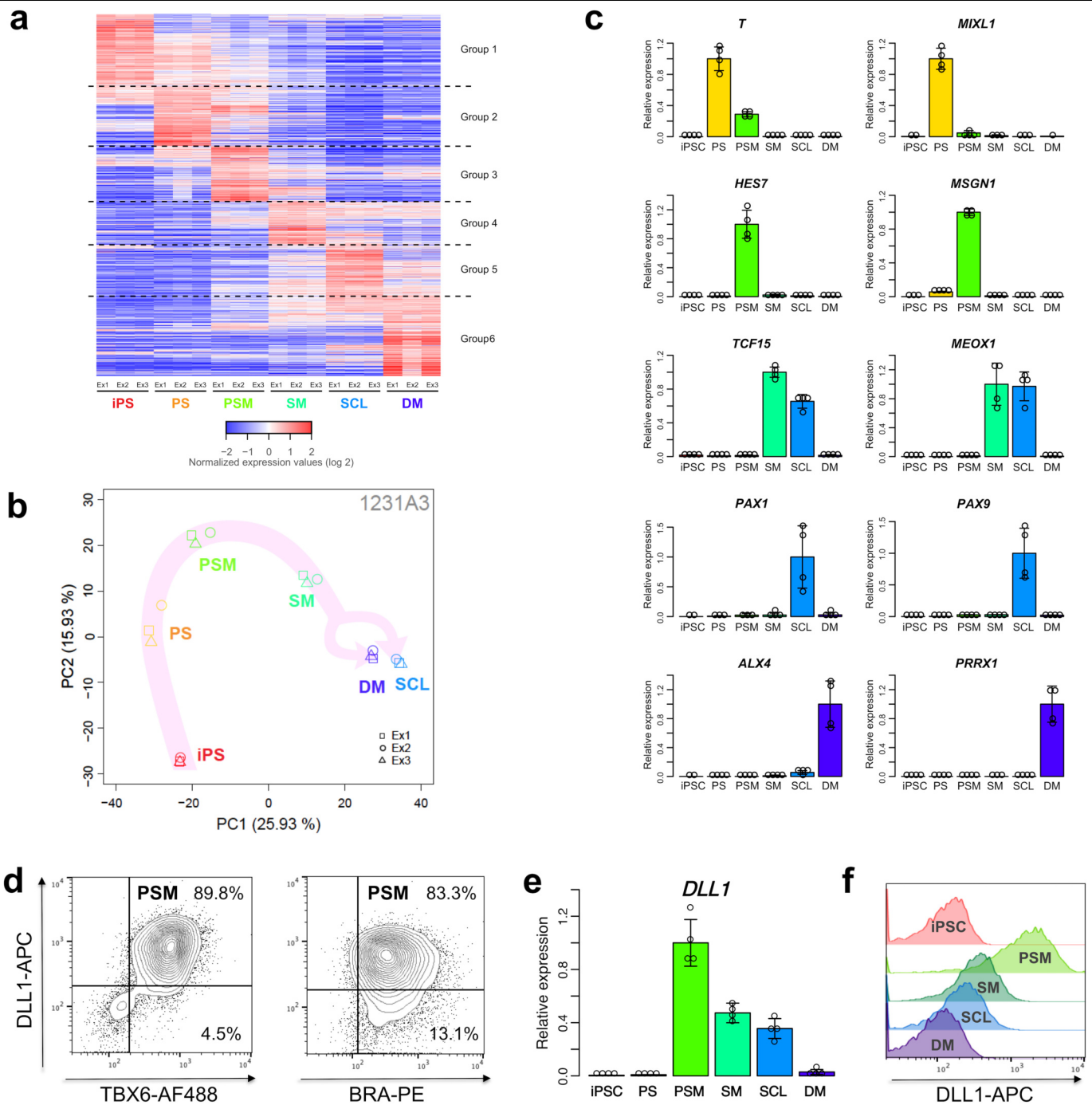
**Supplementary information** is available for this paper at <https://doi.org/10.1038/s41586-020-2144-9>.

**Correspondence and requests for materials** should be addressed to M.E. or C.A.

**Peer review information** *Nature* thanks Helen M. Blau, Duncan Sparrow and the other, anonymous, reviewer(s) for their contribution to the peer review of this work.

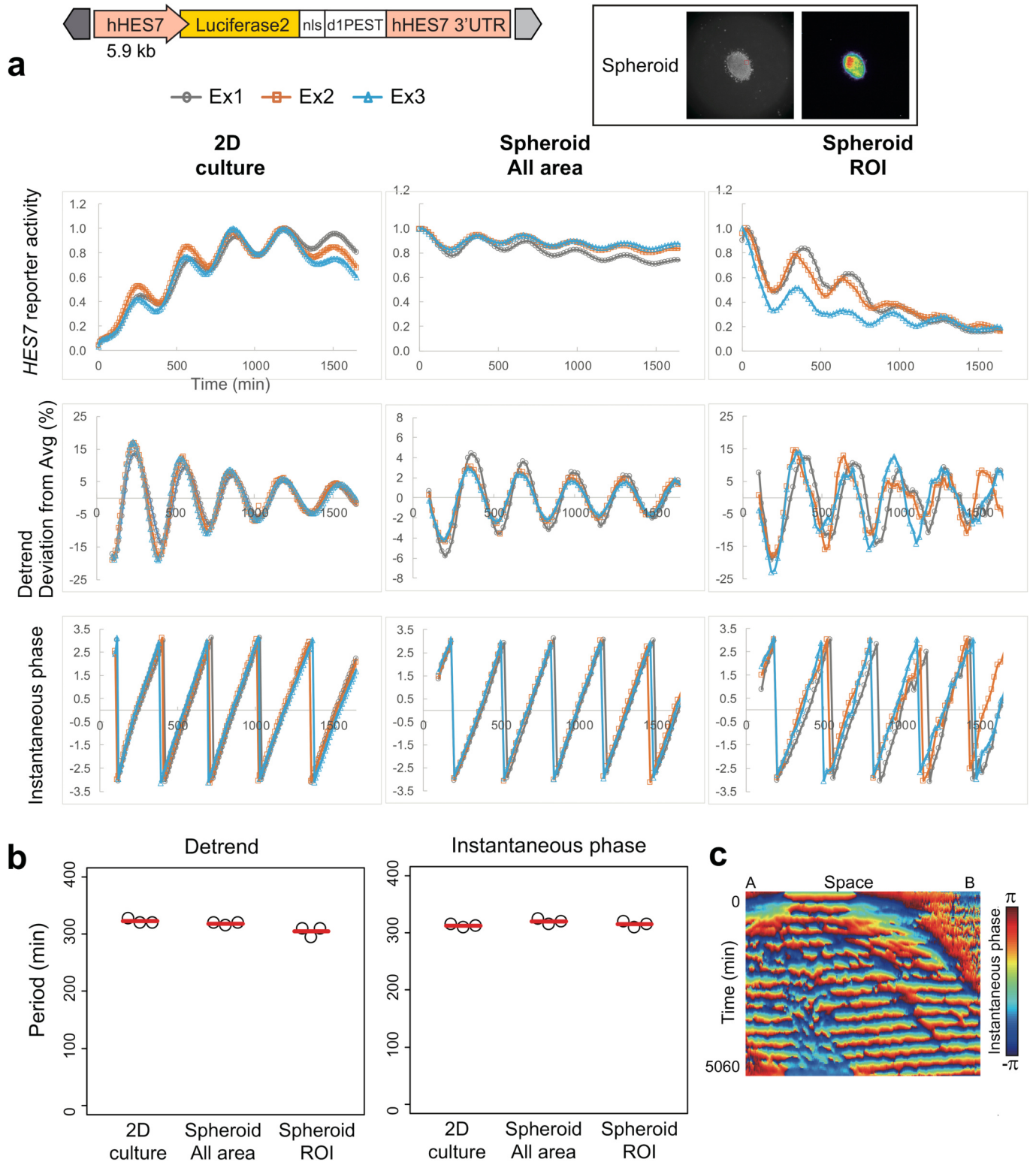
**Reprints and permissions information** is available at <http://www.nature.com/reprints>.





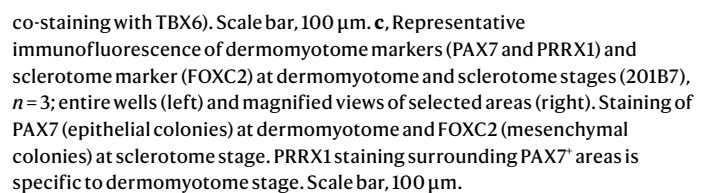
**Extended Data Fig. 1 | Characterization of stepwise-induced human PSM.**  
**a**, Heat map of gene expression levels in stepwise-induced human PSM and its derivatives (using iPSC cell line 1231A3). FPKM values of each gene were normalized to the mean of all samples. The gene order is the same as in Fig. 1b.  
**b**, PCA plot of transcript expression levels in human PSM and derivatives of three independent experiments (1231A3),  $n = 3$ . Proposed RNA-seq-based developmental trajectory is shown in pink.  
**c**, RT-qPCR-based validation of RNA-seq results; data of four independent experiments with three technical replicates each using 201B7 are shown. Data are mean  $\pm$  s.d.,  $n = 4$ . Similar

results were obtained for 1231A3 (data not shown). Open circles in some conditions indicate that there are less than four experiments because no  $C_t$  values for these samples were obtained after 45 cycles of PCR to calculate expression values.  
**d**, Representative flow cytometric evaluation of DLL1 and TBX6 (left) and DLL1 and brachyury (BRA) (right) expression at PSM stage (1231A3),  $n = 3$ .  
**e**, Representative expression of *DLL1* at transcript level during in vitro differentiation (201B7). Data are mean  $\pm$  s.d.,  $n = 4$ .  
**f**, Representative expression of DLL1 at protein level,  $n = 3$ . Correlation of FACS data with RT-qPCR results (201B7) shown in e.

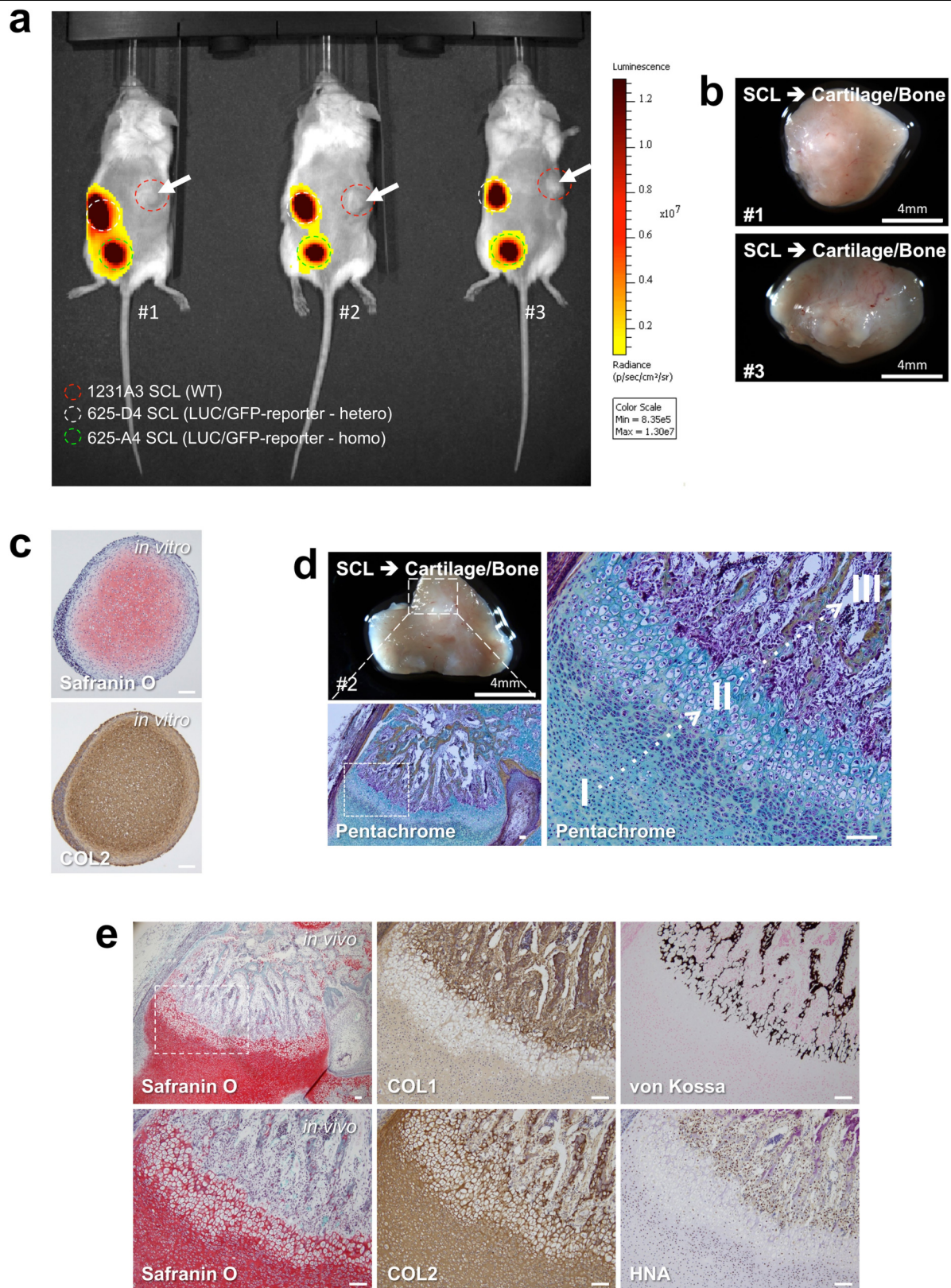


**Extended Data Fig. 2 | Characterization of human segmentation clock period in vitro PSM. a, *HES7* reporter activity in a 2D culture (the oscillation assay condition) and 3D spreading spheroid (the synchronization assay condition). Raw, detrended ( $\pm 100$  min window) and phase signals are shown. For spheroids, the signal was averaged over all area or ROIs indicated by the red line. 2D culture data are same as Fig. 1g and part of 3D-spheroid culture data are same as Fig. 1h. Data of three independent experiments are shown. Schematic**

depiction of reporter construct is shown on top. **b**, Human segmentation clock period quantification based on detrended and instantaneous phase signals. The period was calculated as the average peak-to-peak interval using the 1st to 5th peaks. The measure of centre is mean,  $n = 3$ . **c**, Instantaneous phase-based kymograph of travelling-wave-like *HES7* reporter activity in spheroid spreading assay shown in Fig. 1h. Representative data of three independent experiments are shown.





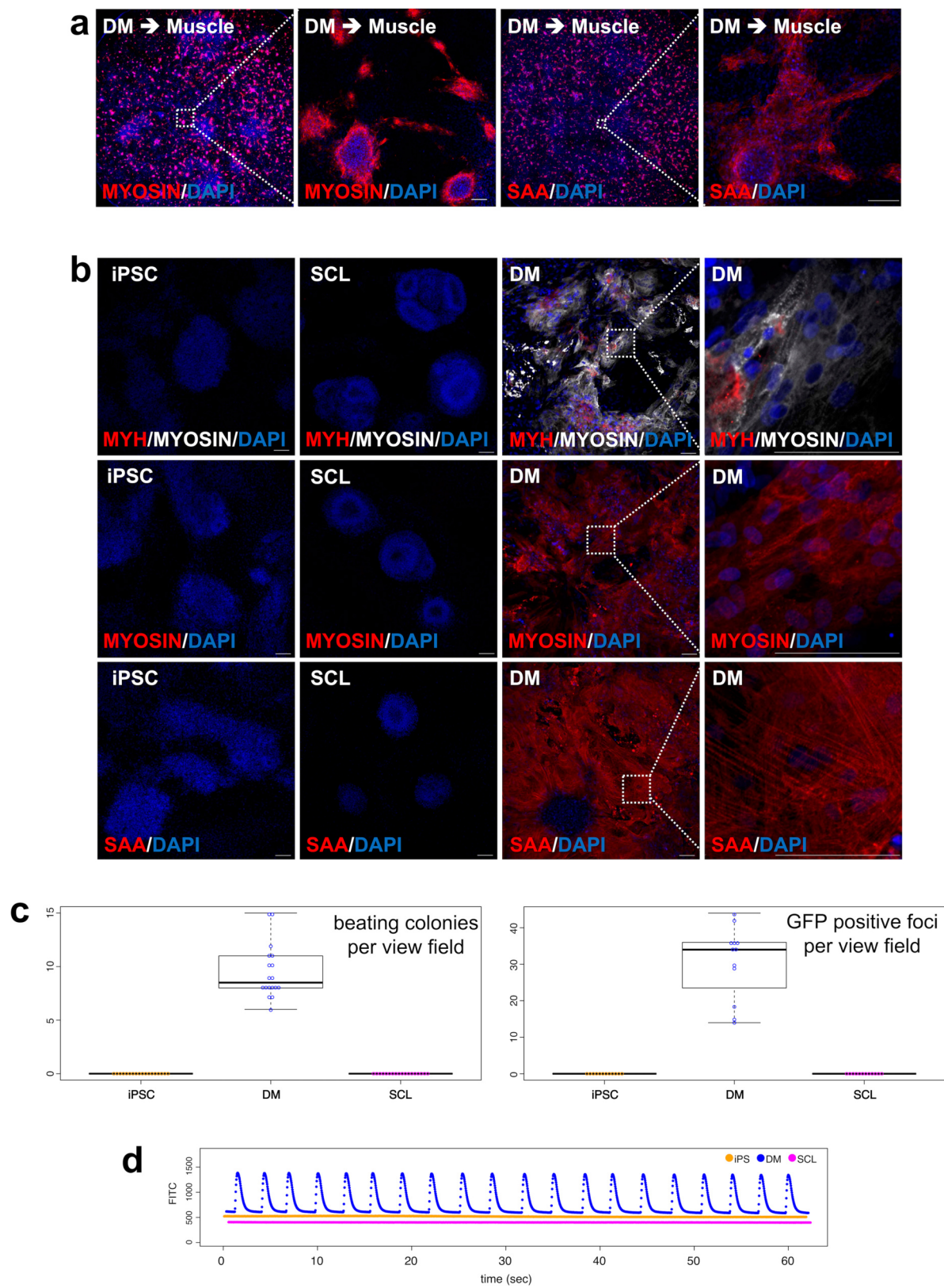


Extended Data Fig. 4 | See next page for caption.

**Extended Data Fig. 4 | Functional evaluation of human iPS cell-derived sclerotome.** **a**, Assessment of in vivo bone- and cartilage-forming ability of human induced sclerotome. Subcutaneous transplantation of PSC-derived sclerotome stepwise-induced from healthy control or wild-type (1231A3) and luciferase-reporter iPS cell lines (625-D4 and 625-A4). Evaluation of transplanted cells using IVIS at two months after transplantation; injection sides are marked with dashed or coloured circles. Cartilage and bone-forming areas of wild-type iPS cell line (1231A3) marked by white arrows. **b**, Whole-mount images of wild-type sclerotome-derived in vivo cartilage and bone tissues isolated from transplanted mice 1 and 3. Explant isolated from mouse 2 is shown in **d**. Scale bar, 4 mm. **c**, Representative staining of in vitro human sclerotome-derived cartilage (from 3D chondrogenic induction) sections.

Observed safranin O and type II collagen (COL2) signals are indicative of in vitro cartilage formation,  $n = 3$ . **d**, Representative whole-mount (top left) and histological staining of section (bottom left) of human induced sclerotome-derived in vivo cartilage and bone. Scale bar, 100  $\mu\text{m}$ . Representative pentachrome staining of marked area reminiscent of in vivo human endochondral bone formation;  $n = 3$ . I, proliferative human cartilage; II, hypertrophic cartilage; III, ossifying cartilage and forming human bone. Scale bar, 100  $\mu\text{m}$ . **e**, Representative sections and staining of area shown in **d**. Safranin O and COL2 staining in human in vivo sclerotome-derived cartilage areas; von Kossa and COL1 staining in ossifying cartilage and forming bone areas. Majority of cells contributing to cartilage or bone formation are HNA-positive and of human origin (right bottom);  $n = 3$ . Scale bar, 100  $\mu\text{m}$ .

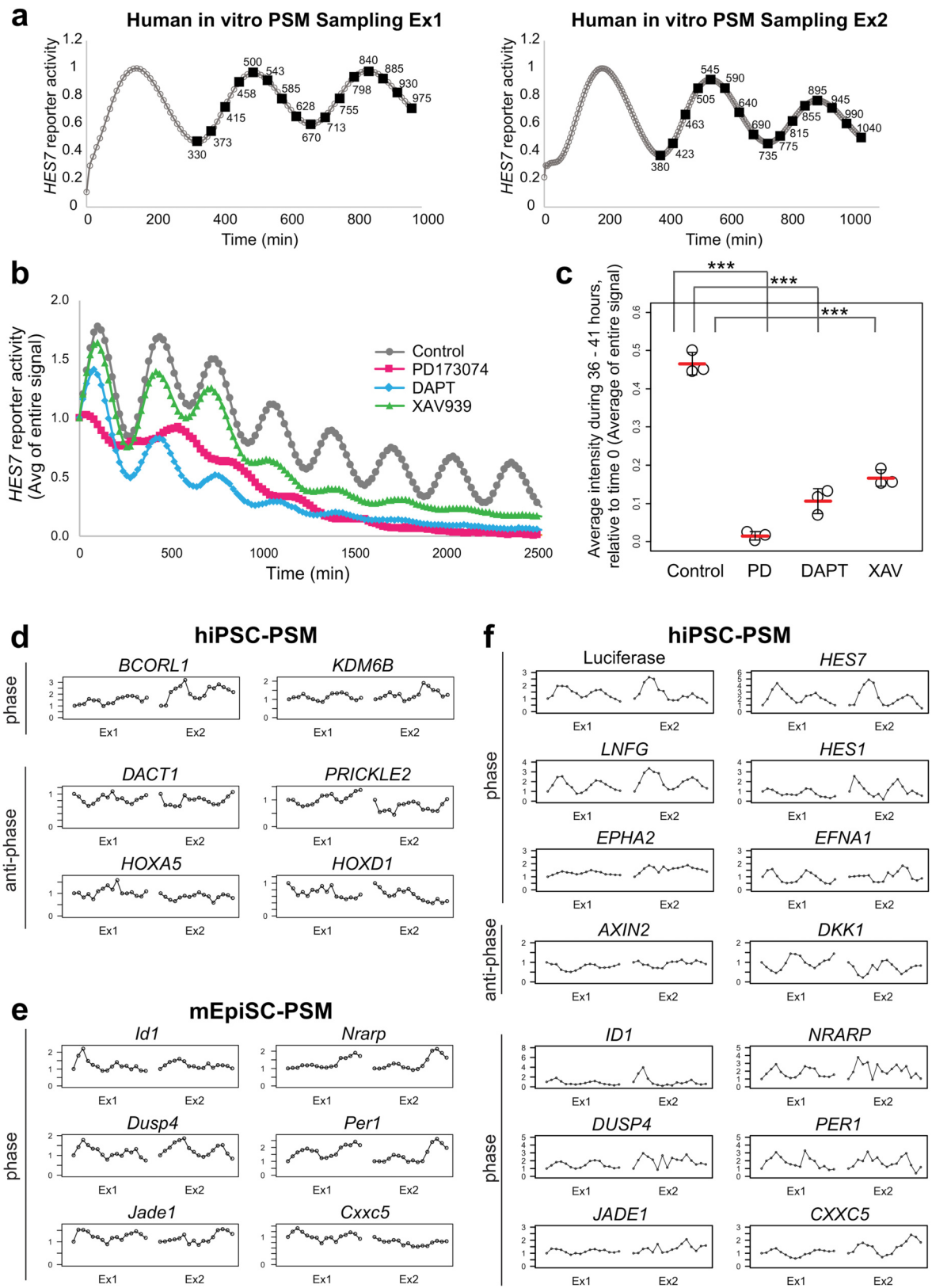




Extended Data Fig. 5 | See next page for caption.

**Extended Data Fig. 5 | Functional evaluation of human iPS cell-derived dermomyotome.** **a**, Evaluation of in vitro muscle induction from human induced dermomyotome. Myosin and sarcomeric  $\alpha$ -actinin (SAA) staining of in vitro dermomyotome-derived skeletal muscle; representative images of entire well (left) and magnified areas (right);  $n = 3$ . Scale bar, 100  $\mu\text{m}$ . **b**, Comparison of skeletal muscle induction of human iPS cell, and iPS cell-derived sclerotome and dermomyotome. Representative myosin heavy chain (MYH), myosin and sarcomeric  $\alpha$ -actinin staining only apparent in dermomyotome-based skeletal muscle differentiation. Right, magnified areas;

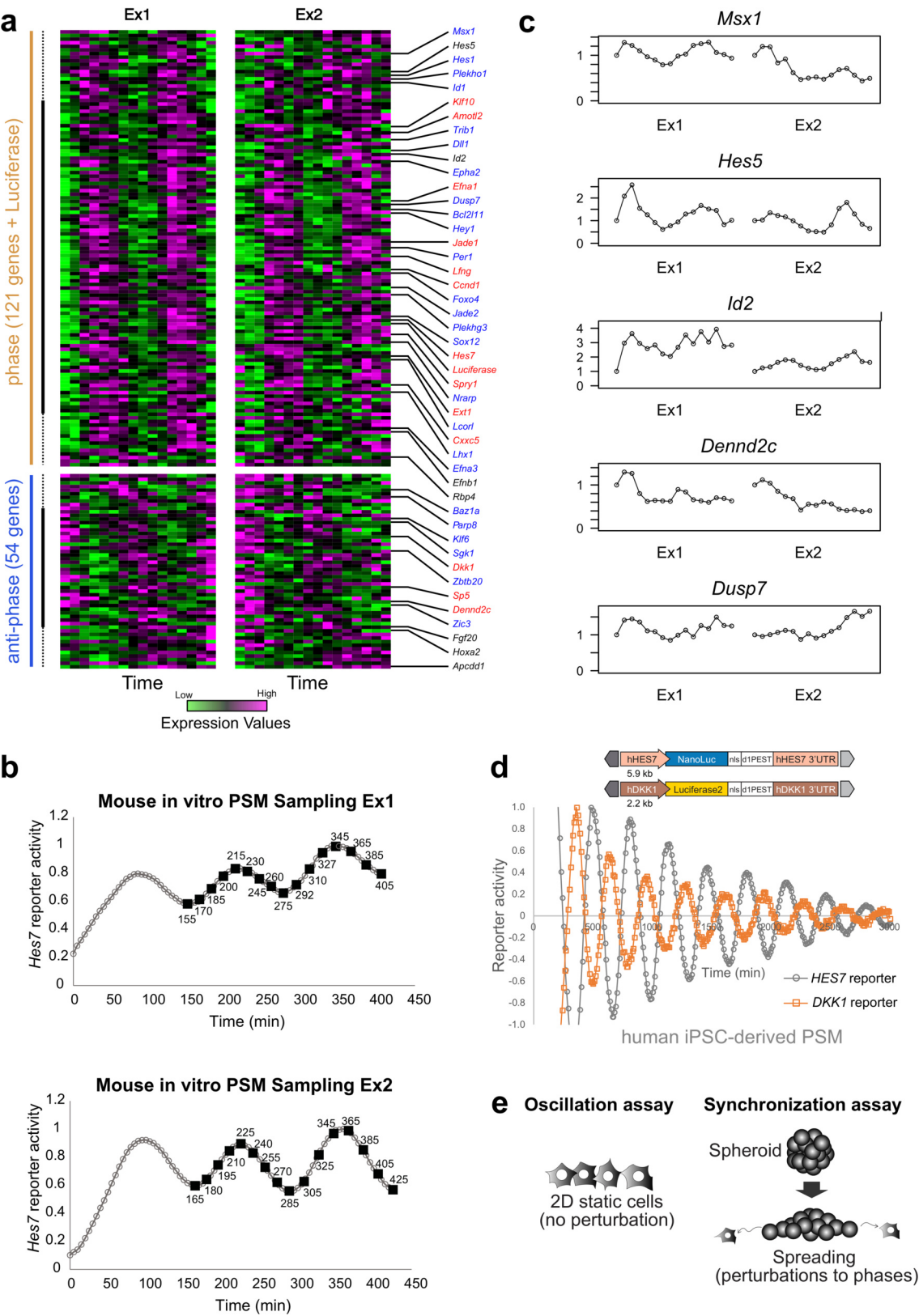
$n = 3$ . **c**, Quantification of contracting colonies and GFP-positive foci of iPS cell-, sclerotome- and dermomyotome-derived human skeletal muscle. Calcium-reporter iPS cell line (Gen1C) was used in all cases. Measurements of total 18 view fields in 6 independent experiments. In box-and-whisker plots, the middle line represents median value, box edges represent 25th and 75th quartiles and error bars show extreme values. **d**, Representative quantification of calcium GFP-reporter activity in iPS cell, sclerotome and dermomyotome as readout of spontaneous contraction-mediated GFP signal in induced human skeletal muscle cells;  $n = 3$ .



Extended Data Fig. 6 | See next page for caption.

**Extended Data Fig. 6 | RNA-seq analysis of human iPS cell-derived oscillating PSM.** **a**, Sampling of human oscillating PSM samples for RNA-seq. *HES7* reporter activity was continuously monitored with one sample, and the other samples were frozen at each time point indicated in the graph. **b**, Three-dimensional synchronization (spheroid-spreading) assay following inhibition of FGF (PD173074, 100 nM), Notch (DAPT, 10 mM), and Wnt (XAV939, 10 mM) signalling pathways. The *HES7* reporter signal was first averaged over all area, the background was subtracted and the signal was normalized to time 0. The background was defined as the average signal at time 0 over the 15 × 15-pixel area of the top left corner of the image. Representative graph of three independent experiments is shown. See also Supplementary Video 3. **c**, Average *HES7* reporter intensity during 36–41 h (2,160–2,440 min) of inhibitor treatment. Data are mean ± s.d.,  $n = 3$ ; two-sided Dunnett's test.

$*P < 0.05$ ,  $**P < 0.01$ ,  $***P < 0.001$ . **d**, Additional validation of RNA-seq results by RT-qPCR for phase and antiphase oscillating genes showing specific oscillatory expression in human iPS cell-derived PSM but not in mouse EpiSC-derived PSM. Data are shown for two independent biological datasets with 16 samples each. See also Fig. 2c. **e**, RT-qPCR validation of phase and antiphase oscillating murine genes found to oscillate in mouse EpiSC-derived PSM. Same genes show oscillation in human in vitro PSM. **f**, RT-qPCR validation of phase and antiphase oscillating genes identified by RNA-seq in human induced PSM. These genes were also validated to show clear oscillation in mouse EpiSC-derived PSM. See also Fig. 2d. In **e**, **f**, mean values of three technical replicas of two independent experiments (Ex1 and Ex2) for each time point and sample set are shown.

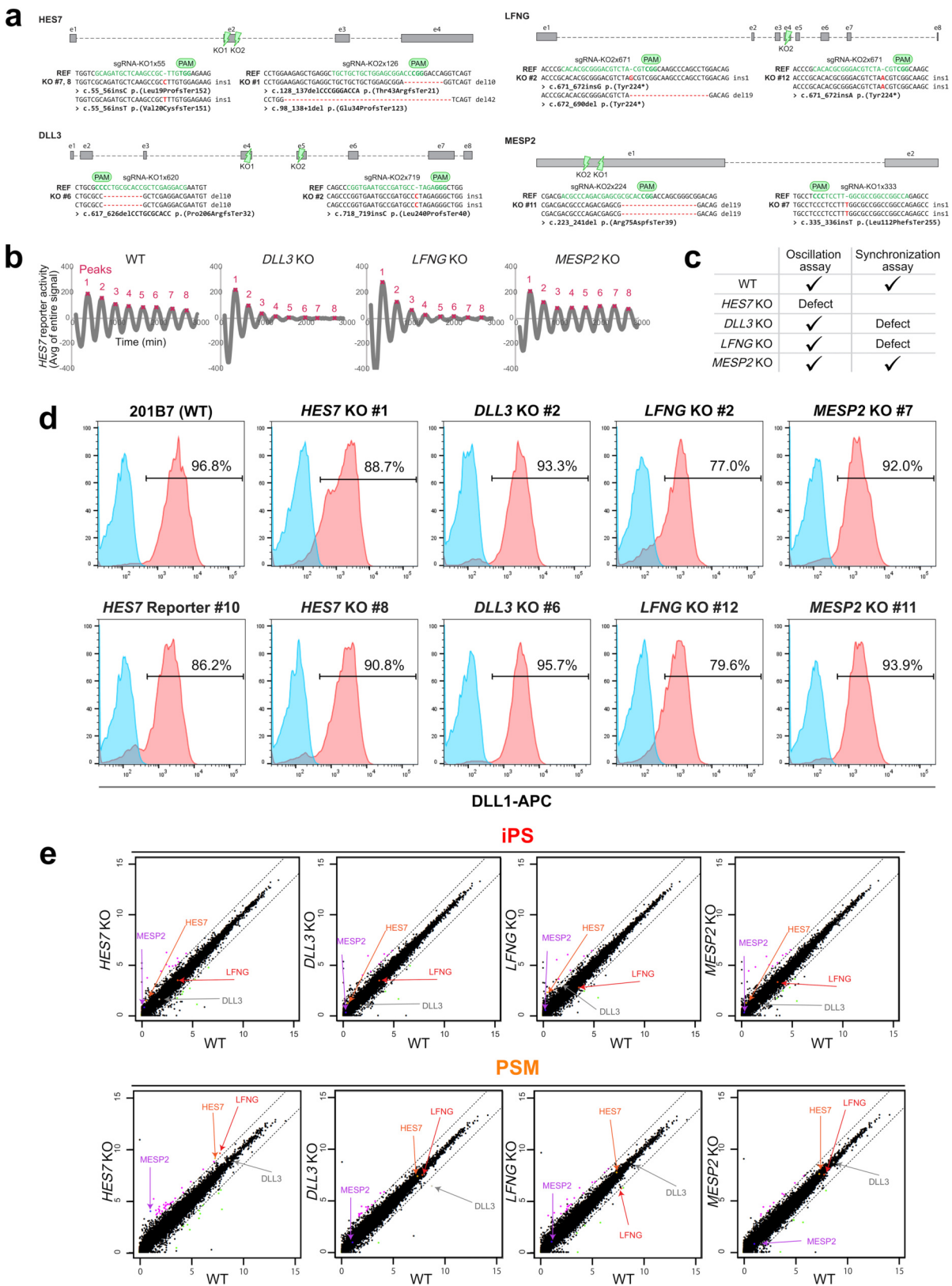


Extended Data Fig. 7 | See next page for caption.



**Extended Data Fig. 7 | RNA-seq analysis of mouse EpiSC-derived oscillating PSM.** **a**, Heat map of normalized gene expression levels for oscillating genes in mouse in vitro-derived PSM. RNA-seq results shown for two independent biological datasets with 16 samples each. Examples of identified phase and antiphase oscillating genes are highlighted on the right. Oscillating mouse genes marked in red and blue match with high- and low-stringency cut-off setting identified oscillating human induced-PSM genes, respectively. Unambiguously phase- or antiphase oscillating genes are highlighted on the left; solid and dotted black lines indicate unambiguous and ambiguous genes, respectively. See Supplementary Table 4 for complete list of identified high-stringency cut-off oscillating genes in mouse in vitro-derived PSM. See also Fig. 2 and Supplementary Table 2 for RNA-seq results of oscillating human segmentation clock genes identified in human iPS cell-derived PSM.

**b**, Sampling of mouse oscillating PSM samples for RNA-seq. *Hes7* reporter activity was continuously monitored with one sample, and the other samples were frozen at each time point indicated in the graph. **c**, RT-qPCR validation of identified mouse phase and antiphase oscillating genes. See also Fig. 2d and Extended Data Fig. 6e for validation of additional mouse oscillating genes. Mean values of three technical replicas of two independent experiments (Ex1 and Ex2) for each time point and sample set are shown. **d**, Results obtained for dual luciferase-reporter assay of *HES7* reporter (NanoLuc) and *DKK1* reporter (Luciferase2) in human PSC-derived PSM. The signal was detrended ( $\pm 2$ -h window) and normalized to the maximum oscillation peak. Representative graph of three independent experiments is shown. Top, schematic overview of reporter constructs. **e**, Schematic overview of 2D-oscillation and 3D-synchronization assays.

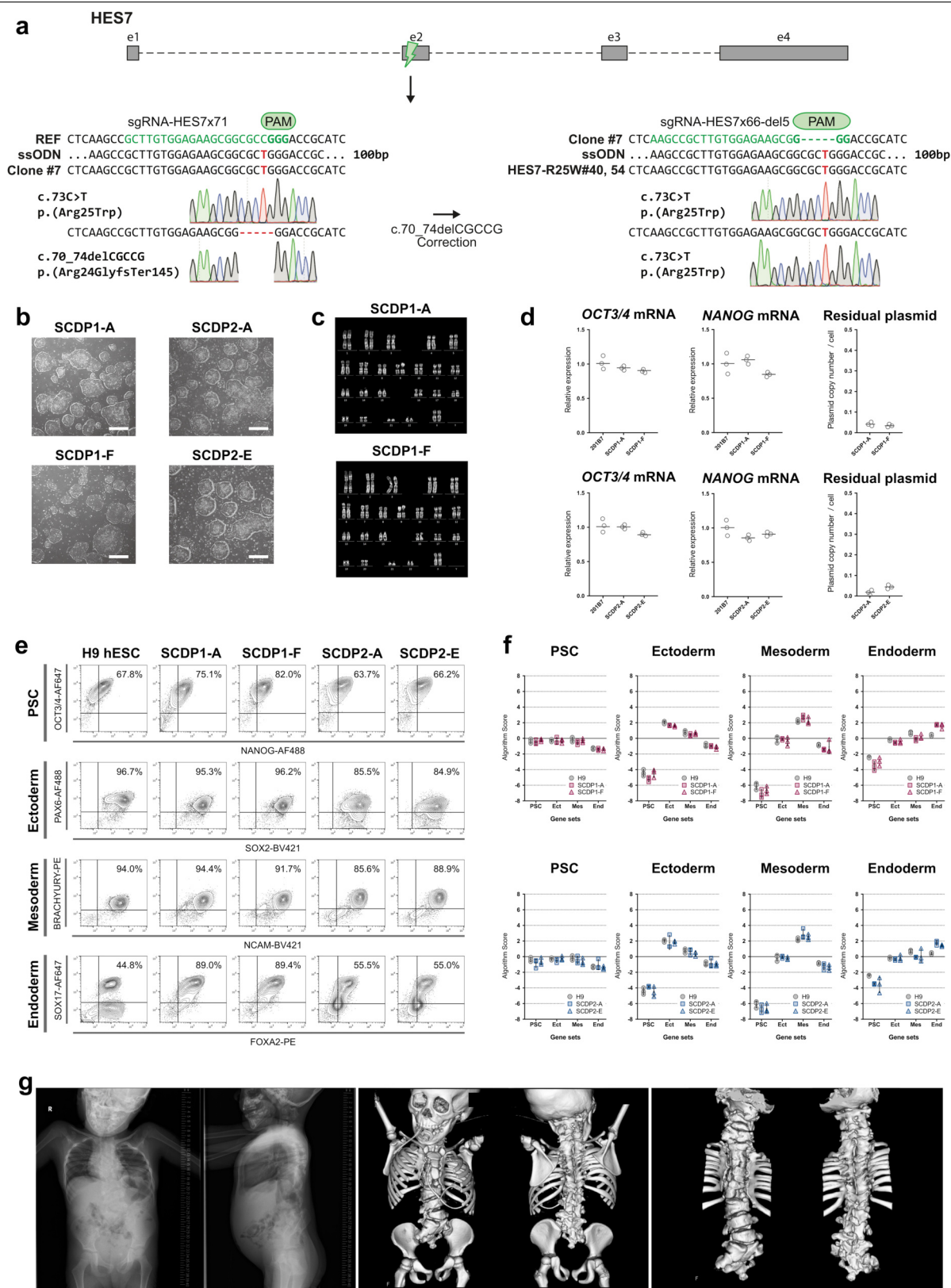


**Extended Data Fig. 8** | See next page for caption.

**Extended Data Fig. 8 | Characterization of knockout human reporter cell lines.**

**a.** Overview of knockout reporter cell line generation for *HES7*, *DLL3*, *LFNG* and *MESP2* genes. Positions of the sgRNAs used in this study are shown. sgRNAs were designed to target at or near regions of known pathogenic mutations, particularly those resulting in frameshifts and premature termination. Sequence analysis of iPS cell clones used in this study indicating insertion or deletion mutations generated by Cas9. Predicted effects on the protein sequence are listed below the sequence alignments. **b.** Damping rate of oscillation amplitude in knockout human PSMs. The signal of all area was averaged and detrended ( $\pm 100$ -min window). See also Fig. 3d for quantification of shown data,  $n = 3$ . **c.** Summary of results of oscillation and synchronization

assays. See Fig. 3a–d for details. **d.** Flow cytometric evaluation of DLL1 expression at PSM stage of healthy control and knockout human iPS cell lines. Blue, isotype control; red, DLL1-APC. PSM induction efficiency is high in all analysed samples; slight reduction of DLL1 induction efficiency in *LFNG*-knockout cell lines. Representative results of three independent experiments of two different knockout lines for each gene are shown (*HES7* KO #1 and #8, *DLL3* KO #2 and #6, *LFNG* KO #2 and #12, and *MESP2* KO #7 and #11);  $n = 3$ . **e.** Scatter plot of transcriptome analysis of wild-type and knockout cell lines at iPS cell and PSM stages. Positions of expression values for *MESP2*, *DLL3*, *LFNG* and *HES7* are highlighted with coloured arrows. Data are averages of two biological replicates,  $n = 2$ .



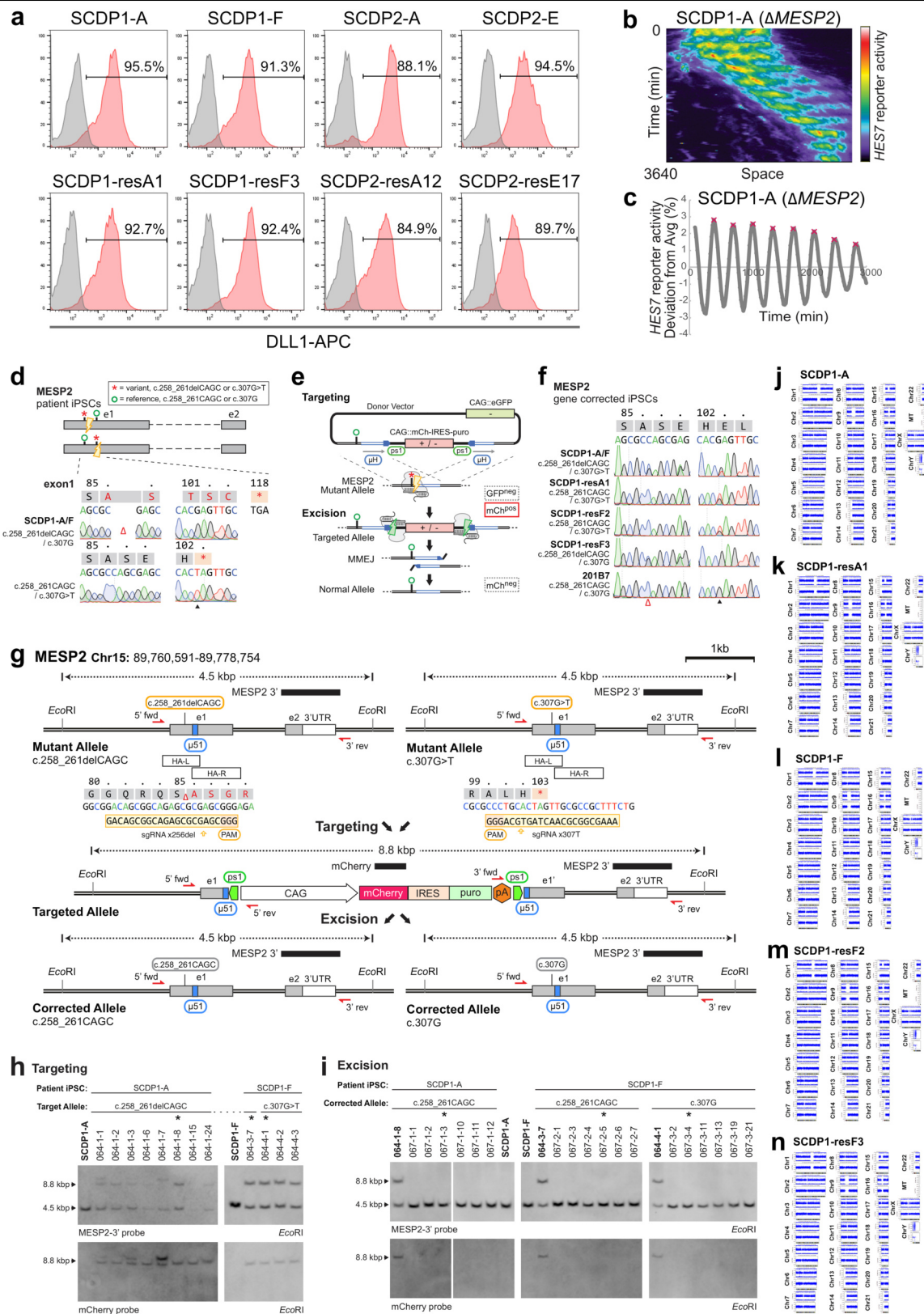
Extended Data Fig. 9 | See next page for caption.

**Extended Data Fig. 9 | Overview of *HES7*<sup>R25W</sup> mutant cell line generation and initial characterization of patient iPS cell lines SCDP1 and SCDP2.**

**a**, Schematic overview of the stepwise *HES7*-targeting approach for ssODN-mediated recreation of *HES7*<sup>R25W</sup> mutant cell lines. The first round of CRISPR–Cas9 targeting with ssODN resulted in a compound heterozygous line with the desired c.73C>T base modification and a 5-bp deletion (c.70\_74delCGCCG). The c.70\_74delCGCCG deletion creates a new PAM site. In the second targeting step, the c.70\_74delCGCCG allele was retargeted with a sgRNA specific to the deletion, and correction with the same ssODN resulted in a homozygous c.73C>T iPS cell line. **b**, Representative bright-field views of SCDP1 (SCDP1-A and SCDP1-F) and SCDP2 (SCDP2-A and SCDP2-E) iPS cell clones. Representative data of five independent experiments are shown. Scale bar, 500  $\mu$ m. **c**, Normal karyotype (46, XX) in both clones of SCDP1 patient iPS cell line by chromosomal G-banding analysis. The data of passage 10 is shown. **d**, Expression of pluripotency markers *OCT3/4* and *NANOG* in SCDP1 and SCDP2

clones compared with iPS cell line (201B7). Quantification of residual plasmid levels in SCDP1 and SCDP2 clones (right); mean value (horizontal bar) of three technical replicas for each of the four analysed clones are shown. **e**, FACS-based evaluation of differentiation capacity into three germ layers of healthy control (H9 hESC) and patient cell lines (SCDP1-A and SCDP1-F, SCDP2-A and SCDP2-E). Representative data of three independent experiments are shown;  $n = 3$ . **f**, Quantification of differentiation capacity of healthy control and patient cell lines into ectoderm, mesoderm and endoderm at the transcript level by TaqMan hPSC scorecard panel. Top, SCDP1-A and SCDP1-F; bottom, SCDP2-A and SCDP2-E. Same H9 hESC control data shown in both panels. Data of three independent experiments are shown;  $n = 3$ . **g**, X-ray and MRI images of a patient with SDV with a *DLL3* mutation (donor of SCDP2 iPS cell clones). Radiological images were obtained at Meijo Hospital, Nagoya, Japan with patient consent. Black bars were added to anonymize the image. See Supplementary Note 1 for details of clinical and radiological features of the patient.



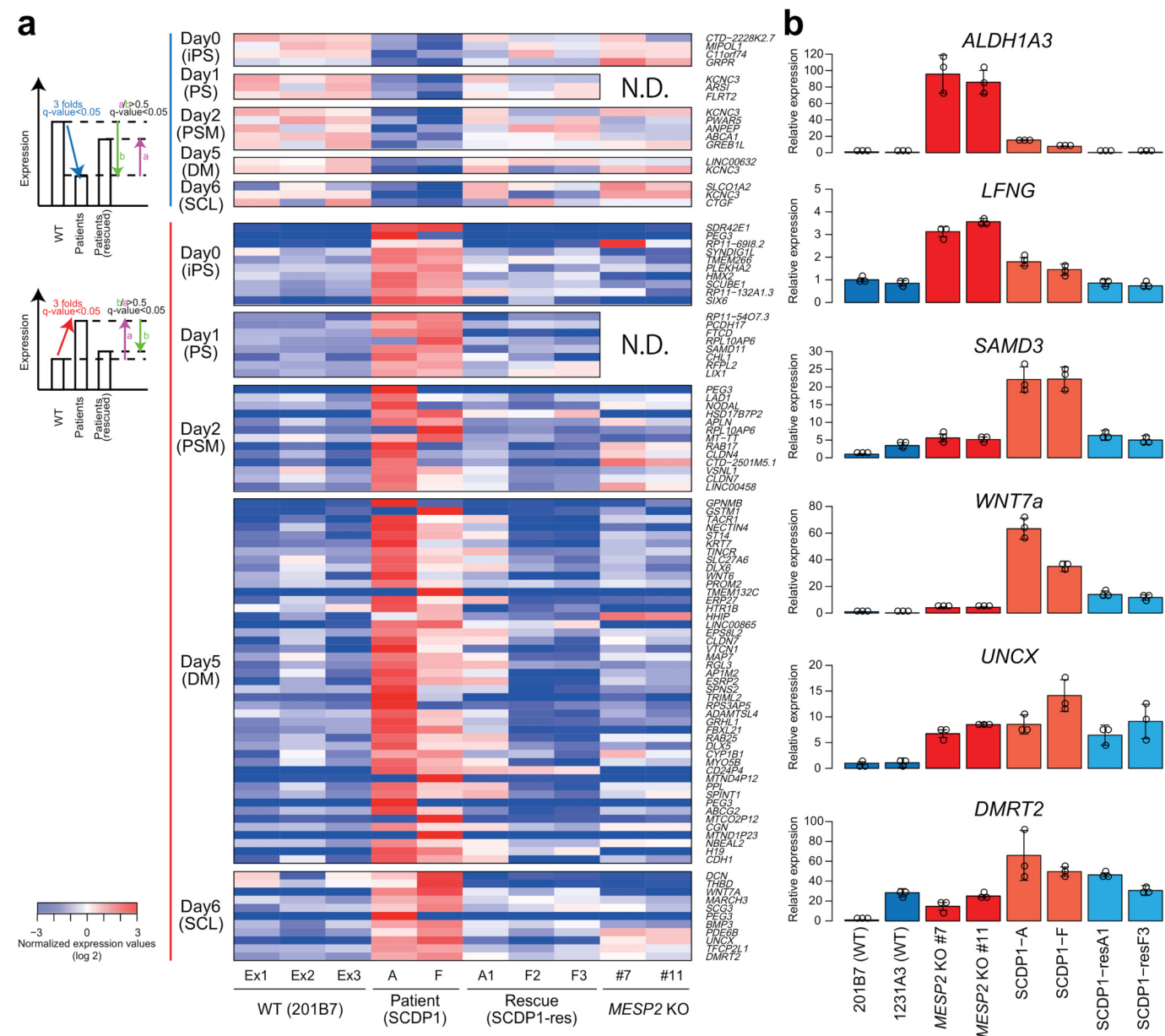


Extended Data Fig. 10 | See next page for caption.

**Extended Data Fig. 10 | Analysis of patient and rescue iPS cell line-derived PSM and allele-specific gene correction of SCDP1 patient iPS cell lines.**

**a**, Representative DLL1 expression in iPS cells (grey) and PSMs (red) derived from a patient with SCD with a compound mutation in *MESP2* (SCDP1-A and SCDP1-F), a patient with SCD with a mutation in *DLL3* (SCDP2-A and SCDP2-E) and corresponding isogenic rescue cell lines (SCDP1-resA1, SCDP1-resF3, SCDP2-resA12 and SCDP2-resE17).  $n = 3$ ; data for SCDP1-A and SCDP2-E are also used for Fig. 4b. **b**, Three-dimensional synchronization assay of SCDP1 patient PSM. Representative kymograph of three independent experiments is shown. **c**, Representative measurement of *HES7* reporter activity in PSM derived from SCDP1 patient cell line. After the spike noise was removed, the signal of the entire area was averaged. The signal was further detrended and normalized to the average ( $\pm 100$ -min window). **d**, Top, representative genotype of patients with SCD and iPS cells (SCDP1) with compound heterozygous mutations in *MESP2*. Bottom, sequence of each haplotype from patient genomic DNA. Red triangle indicates a deletion. Black triangle indicates a single nucleotide variation. **e**, Schematic of the gene-targeting procedure for allele-specific correction of *MESP2* mutations using MhAX. Details of the targeting and genotyping procedures are provided in **g**. **f**, Genotype of heterozygously corrected iPS cell subclones. 201B7 is included as a reference. Red triangle indicates a deletion. Black triangle indicates a single nucleotide variation. DNA sequencing was performed twice for each clone;  $n = 2$ . **g**, Detailed schematic of

gene-correction strategy of SCDP1 patient iPS cell clones. Depicted are two mutant or corrected *MESP2* alleles with coding and non-coding exons (grey and white), overlapping donor vector homology arms (HA-L and HA-R), engineered 51-bp microhomology ( $\mu$ 51, blue), inverted protospacers for cassette excision (ps1, green), genotyping primers (red arrows) and Southern blotting probes (black bars). Sequences of mutation-specific sgRNAs are shown below each mutant allele. The gene-targeted intermediate shows details of the CAG::mCherry-IRES-puro cassette used for enrichment. **h**, Southern blot analysis of targeted iPS cell clones. Samples marked with an asterisk were selected for cassette excision. **i**, Southern blot analysis of gene-corrected iPS cell clones following selection marker removal. Samples marked with an asterisk were selected for phenotyping (067-1-3, SCDP1-resA1; 067-2-5, SCDP1-resF2; 067-3-4 and SCDP1-resF3). Southern blots shown in **h** and **i** were performed once for two patient and rescue clones each. For gel source data of **h** and **i** see Supplementary Fig. 1. **j**, **k**, Resulting karyograms from SNP array analysis of SCDP1 patient iPS cell clone A (SCDP1-A) and corresponding rescued iPS cell line (SCDP1-resA1). **l-n**, Karyograms from SNP array analysis of iPS cell clone F (SCDP1-F) from a patient with SDV and corresponding rescued iPS cell lines (SCDP1-resF2/F3). No de novo CNVs were detected following gene editing and subcloning. These figures were created with Illumina Genome Viewer (v.1.9.0) on Illumina GenomeStudio v.2011.1 with Human:Build 37 genome.



**Extended Data Fig. 11 | RNA-seq analysis and RT-qPCR validation of SCDP1 patient and rescue samples. a**, Heat map of gene expression levels of transcripts differentially expressed in patient cell lines SCDP1-A and SCDP1-F, when compared to wild-type (201B7) and corrected rescue clones (SCDP1-resA (A1) and SCDP1-resF (F2 and F3)). Analysis covers all stages of stepwise PSM

induction and differentiation and for MESP2-knockout cell lines all stages except primitive streak. For somitic mesoderm-stage data see Fig. 4d. **b**, RT-qPCR-based validation of additional candidates found via RNA-seq to be upregulated in SCDP1 patient cell lines at the somitic mesoderm stage. Data are mean  $\pm$  s.d. from three independent experiments.



**Extended Data Fig. 12 | Gene correction and analysis of SCDP2 patient iPSC cell lines.** **a**, Representative genotype of cells from patients with SCD and iPSC cells (SCDP2) with mutation in *DLL3*—201B7 is included as a reference. Red triangle indicates insertion. **b**, Schematic of the gene-targeting procedure for allele-specific correction of *DLL3* mutation using MhAX. Details for the targeting and genotyping procedures are provided in **d**. The synonymous c.615C>G PAM blocking mutation is present only in the 3' microhomology. **c**, Genotype of homozygously corrected iPSC cell subclones (SCDP2-resA and SCDP2-resE). Black triangle indicates the synonymous blocking mutation. DNA sequencing performed twice for each clone;  $n = 2$ . **d**, Detailed schematic of gene-correction strategy of SCDP2 patient iPSC cell clones. Depicted are mutant or corrected *DLL3* alleles with coding and non-coding exons (grey and white), overlapping donor vector homology arms (HA-L and HA-R), engineered 30-bp microhomology (μ30, blue), inverted protospacers for cassette excision (ps1, green), genotyping primers (red arrows), and Southern blotting probes (black

bars). The same sgRNA used to generate *DLL3*-knockout iPSC cell lines was used for gene targeting. The gene-targeted intermediate shows details of the CAG::mCherry-IRES-puro cassette used for enrichment and FACS sorting of targeted cells as a population. Excision was performed without intermediate cloning. Owing to the c.615C/G mismatch between flanking microhomologies, two repair outcomes are possible. **e**, Southern blot analysis of gene-corrected iPSC cell clones following selection marker removal. Samples marked with an asterisk were selected for further characterization, with SCDP2-resE17 and SCDP2-resE43 used for analysis of oscillation phenotypes (Fig. 4f, g). For gel source data for **e**, see Supplementary Fig. 1. **f**, *HES7* reporter activity in 3D synchronization assay of PSM derived from SCDP2 patient and isogenic rescue cell lines (SCDP2-resE17 and SCDP2-resE43). After the spike noise was removed, the signal of the entire area was averaged. The signal was further detrended and normalized to the average ( $\pm 100$ -min window). Representative graphs of three independent experiments are shown. See also Fig. 4g.

## Reporting Summary

Nature Research wishes to improve the reproducibility of the work that we publish. This form provides structure for consistency and transparency in reporting. For further information on Nature Research policies, see [Authors & Referees](#) and the [Editorial Policy Checklist](#).

### Statistics

For all statistical analyses, confirm that the following items are present in the figure legend, table legend, main text, or Methods section.

- |                                     |   |
|-------------------------------------|---|
| n/a                                 | Confirmed   |
| <input checked="" type="checkbox"/> | <input checked="" type="checkbox"/> The exact sample size ( <i>n</i> ) for each experimental group/condition, given as a discrete number and unit of measurement  |
| <input checked="" type="checkbox"/> | <input checked="" type="checkbox"/> A statement on whether measurements were taken from distinct samples or whether the same sample was measured repeatedly   |
| <input checked="" type="checkbox"/> | <input checked="" type="checkbox"/> The statistical test(s) used AND whether they are one- or two-sided<br><i>Only common tests should be described solely by name; describe more complex techniques in the Methods section.</i>  |
| <input checked="" type="checkbox"/> | <input type="checkbox"/> A description of all covariates tested   |
| <input checked="" type="checkbox"/> | <input type="checkbox"/> A description of any assumptions or corrections, such as tests of normality and adjustment for multiple comparisons  |
| <input checked="" type="checkbox"/> | <input type="checkbox"/> A full description of the statistical parameters including central tendency (e.g. means) or other basic estimates (e.g. regression coefficient) AND variation (e.g. standard deviation) or associated estimates of uncertainty (e.g. confidence intervals) |
| <input checked="" type="checkbox"/> | <input type="checkbox"/> For null hypothesis testing, the test statistic (e.g. <i>F</i> , <i>t</i> , <i>r</i> ) with confidence intervals, effect sizes, degrees of freedom and <i>P</i> value noted<br><i>Give P values as exact values whenever suitable.</i>                     |
| <input checked="" type="checkbox"/> | <input type="checkbox"/> For Bayesian analysis, information on the choice of priors and Markov chain Monte Carlo settings   |
| <input checked="" type="checkbox"/> | <input type="checkbox"/> For hierarchical and complex designs, identification of the appropriate level for tests and full reporting of outcomes   |
| <input checked="" type="checkbox"/> | <input type="checkbox"/> Estimates of effect sizes (e.g. Cohen's <i>d</i> , Pearson's <i>r</i> ), indicating how they were calculated   |

Our web collection on [statistics for biologists](#) contains articles on many of the points above.

### Software and code

Policy information about [availability of computer code](#)

Data collection	QuantStudio 12K Flex Software (v1.2.4), BD FACSDiva software (LSR: v.8.0.1, Aria II: v.8.0.2), Living Image (v4.0), Kronos control software (v2.3, Atto), Metamorph (v7.6, Molecular Devices), NIS-Elements AR (v4.20.00)
Data analysis	cutadapt-1.14, HISAT2 (v2.1.0), Cufflinks package (v2.2.1), HTSeq (v0.6.1), edgeR (v3.18.1), ARSER (v2.0), DAVID web tools (DAVID 6.8) ( <a href="https://david.ncifcrf.gov/">https://david.ncifcrf.gov/</a> ), IPA (QIAGEN Inc., <a href="https://www.qiagenbioinformatics.com/products/ingenuitypathway-analysis">https://www.qiagenbioinformatics.com/products/ingenuitypathway-analysis</a> ), HCS (v2.0.10), RTA (v1.17.21.3), CASAVA (v1.8.2), Picard (v2.0.1), ANNOVAR (v2016Mar30), Sequencher (v5.1), Snapgene (v3.1.4 to v5.0.4), GWASTools (v1.16.1), PennCNV (v1.0.3), cnvPartition (v3.2.0), MAD (v1.0.1), Metamorph (v7.6, Molecular Devices), Matlab (v2018b, MathWorks), Fiji (v1.52p, ImageJ), Excel (Microsoft Office 2011/2016), R (v3.2.5, v3.3.1, v3.4.2, v3.5.1), FlowJo (v10.6.1)

For manuscripts utilizing custom algorithms or software that are central to the research but not yet described in published literature, software must be made available to editors/reviewers. We strongly encourage code deposition in a community repository (e.g. GitHub). See the Nature Research [guidelines for submitting code & software](#) for further information.

### Data

Policy information about [availability of data](#)

All manuscripts must include a [data availability statement](#). This statement should provide the following information, where applicable:

- Accession codes, unique identifiers, or web links for publicly available datasets
- A list of figures that have associated raw data
- A description of any restrictions on data availability

All RNA sequencing data utilized for this study have been deposited in Gene Expression Omnibus (<https://www.ncbi.nlm.nih.gov/geo/>) under the accession number GSE116935. SNP array data in the current publication have been deposited in and are available upon application from the dbGaP database under accession phs001975.v1.p1 ([http://www.ncbi.nlm.nih.gov/projects/gap/cgi-bin/study.cgi?study\\_id=phs001975.v1.p1](http://www.ncbi.nlm.nih.gov/projects/gap/cgi-bin/study.cgi?study_id=phs001975.v1.p1)) and their use is limited to health/medical/biomedical purposes. Utilized computational codes & scripts are available at GitHub (<https://github.com/mebisuya/SegmentationClock>) and from the corresponding authors upon request. Source Data for Figs. 1-4 and Extended Data Figs. 1, 2, 5-12 are available in the online version of the paper.



## Field-specific reporting

Please select the one below that is the best fit for your research. If you are not sure, read the appropriate sections before making your selection.

☒ Life sciences ☐ Behavioural & social sciences ☐ Ecological, evolutionary & environmental sciences

For a reference copy of the document with all sections, see [nature.com/documents/nr-reporting-summary-flat.pdf](https://www.nature.com/documents/nr-reporting-summary-flat.pdf)

## Life sciences study design

All studies must disclose on these points even when the disclosure is negative.

Sample size	No statistical method was used to predetermine the sample size. All experiments were performed (if not otherwise stated) with at least two (most of the time three) independent experiments, yielding similar and reproducible results.
Data exclusions	No samples/data were excluded.
Replication	Each experiment was reproduced and performed at least two times, with multiple biological and/or technical replicates if not otherwise stated. See figure legends and methods section for details.
Randomization	No particular randomization method was utilized. Animals used for experiments were randomly allocated.
Blinding	The investigators were not blinded during data collection and analysis.

## Reporting for specific materials, systems and methods

We require information from authors about some types of materials, experimental systems and methods used in many studies. Here, indicate whether each material, system or method listed is relevant to your study. If you are not sure if a list item applies to your research, read the appropriate section before selecting a response.

### Materials & experimental systems

n/a	Involved in the study
<input type="checkbox"/>	<input checked="" type="checkbox"/> Antibodies
<input type="checkbox"/>	<input checked="" type="checkbox"/> Eukaryotic cell lines
<input checked="" type="checkbox"/>	<input type="checkbox"/> Palaeontology
<input type="checkbox"/>	<input checked="" type="checkbox"/> Animals and other organisms
<input type="checkbox"/>	<input checked="" type="checkbox"/> Human research participants
<input checked="" type="checkbox"/>	<input type="checkbox"/> Clinical data

### Methods

n/a	Involved in the study
<input checked="" type="checkbox"/>	<input type="checkbox"/> ChIP-seq
<input type="checkbox"/>	<input checked="" type="checkbox"/> Flow cytometry
<input checked="" type="checkbox"/>	<input type="checkbox"/> MRI-based neuroimaging

## Antibodies

### Antibodies used

All antibodies used in this study are commercially available antibodies, which were validated by suppliers and other researchers in the field. Details on used antibodies are listed in Supplementary Table 8.

#### Primary antibodies used for immunocytochemistry

BRACHYURY, R&D Systems, #:AF2085, Lot: KQP0618021, Polyclonal Goat IgG, Dilution 1:100  
 COL1, Southern Biotech, #:1310-01, Lot: B2918-T858, Polyclonal Goat IgG, Dilution 1:200  
 COL2, Southern Biotech, #:1320-01, Lot: J0513-S328, Polyclonal Goat IgG, Dilution 1:200  
 FOXC2, DSHB, #:1B6, Lot: 8/17/17, Monoclonal Mouse IgG1, Dilution 1:10  
 HNA, Merck, #:MAB1281, Lot: 2366521, Clone: 235-1, Dilution 1:50  
 MESP2, DSHB, #:1D4, Lot: 6/1/17, Monoclonal Mouse IgG2b, Dilution 1:10  
 MYH, Abcam, #:ab91506, Lot: GR11678-3, Polyclonal Rabbit IgG, Dilution 1:2000  
 MYOSIN, DSHB, #:MF20-s, Lot: 12/7/17, Monoclonal Mouse IgG2b, Dilution 1:20  
 PAX7, DSHB, #:PAX7-s, Lot: 3/8/18, Monoclonal Mouse IgG1, Dilution 1:10  
 PRRX1, Sigma-Aldrich, #:HPA051084, Lot: G114643, Polyclonal Rabbit IgG, Dilution 1:100  
 SAA, Abcam, #:ab9465, Lot: GR266197-2, Clone: EA-53, Dilution 1:1000  
 TBX6, R&D Systems, #:AF4744, Lot: CAPT0217111, Polyclonal Goat IgG, Dilution 1:100  
 TCF15, Abcam, #:ab204045, Lot: GR268168-3, Polyclonal Rabbit IgG, Dilution 1:50

#### Secondary antibodies used for immunocytochemistry

Alexa Fluor® 488 Donkey Anti-Rabbit IgG (H+L), Invitrogen, #:A-21206, Lot: 2072687, Dilution 1:500  
 Alexa Fluor® 488 Goat Anti-Mouse IgG (H+L) Invitrogen, #:A-10680, Lot: 1917945, Dilution 1:500

Alexa Fluor® 555 Donkey Anti-Goat IgG H&L Abcam, #:ab150130, Lot: GR226396-1, Dilution 1:500  
 Alexa Fluor® 555 Goat Anti-Mouse IgG (H+L) Invitrogen, #:A-21422, Lot: 1180091, Dilution 1:500  
 Alexa Fluor® 647 Donkey Anti-Mouse IgG (H+L) Invitrogen, #:A-31571, Lot: 2045337, Dilution 1:500  
 Donkey Anti-Rabbit IgG Cy3 Merck, #:AP182C, Lot: 2984232, Dilution 1:500  
 Alexa Fluor® 647 Phalloidin Invitrogen, #:A-2228, Lot: 2101947, Dilution 1:100

#### Primary antibodies used for flowcytometry

BRACHYURY-PE, R&D Systems, #:IC2085P, Lot: LVB0213071, Polyclonal Goat IgG Dilution 1:50  
 DLL1-APC, R&D Systems, #:FAB1818A, Lot: AAYU0216061, Clone: 251127, Dilution 1:200  
 FOXA2-PE, BD Biosciences, #:561589, Lot: 7090765, Clone: N17-280, Dilution 1:50  
 NANOG-Alexa Fluor® 488, BD Biosciences, #:560791, Lot: 7110923, Clone: N31-355 Dilution 1:25  
 NCAM-BV421, BioLegend, #:318328, Lot: B241630, Clone: HCD56, Dilution 1:25  
 OCT3/4-Alexa Fluor® 647, BD Biosciences, #:560329, Lot: 7201923, Clone: 4O/Oct3, Dilution 1:25  
 PAX6-Alexa Fluor® 488, BD Biosciences, #:561664, Lot: 7174912, Clone: O18-1330, Dilution 1:25  
 SOX2-BV421, BioLegend, #:656114, Lot: B208882, Clone: 14A6A34, Dilution 1:50  
 SOX17-Alexa Fluor® 647, BD Biosciences, #:562594, Lot: 7104800, Clone: P7-969, Dilution 1:25  
 Anti-TBX6, R&D Systems, #:AF4744, Lot: CAPT0217111, Polyclonal Goat IgG, Dilution 1:25

#### Secondary antibodies & isotype controls used for flowcytometry

Alexa Fluor® 488 Anti-Goat IgG, Abcam, #:ab150129, Lot: GR246088-1, Polyclonal Goat IgG, Dilution 1:50  
 APC-conjugated Mouse IgG2b,k, BD Biosciences, #:555745, Lot: B163785, Clone: MG2b-57, Dilution 1:200  
 PE-conjugated Goat IgG, R&D Systems, #:IC108P, Lot: LVD0811021, Polyclonal Goat IgG, Dilution 1:50  
 Unconjugated Goat IgG, R&D Systems, #:AB108C, Lot: ES4119031, Polyclonal Goat IgG, Dilution 1:25  
 Alexa Fluor® 647-conjugated Mouse IgG1,k, BioLegend, #:400130, Lot: B205347, Clone: MOPC-21, Dilution 1:100  
 Alexa Fluor® 488-conjugated Mouse IgG1,k, BioLegend, #:400129, Lot: B277964, Clone: MOPC-21, Dilution 1:25  
 Alexa Fluor® 488-conjugated Mouse IgG2a,k, BioLegend, #:400233, Lot: B286502, Clone: MOPC-173, Dilution 1:25  
 PE-conjugated Mouse IgG1,k, BioLegend, #:400112, Lot: B244597, Clone: MOPC-21, Dilution 1:50  
 BV421-conjugated Mouse IgG1,k, BioLegend, #:400158, Lot: B243837, Clone: MOPC-21, Dilution 1:50

## Validation

Besides initial validation of utilized (commercial) primary antibodies by manufacturers/suppliers, antibodies were validated/ tested for possible signals at unrelated stages/controls; only antibodies with reproducible (differentiation stage) specific signals were used.

#### Primary antibodies used for immunocytochemistry

BRACHYURY, R&D Systems, AF2085 ([https://www.rndsystems.com/products/human-mouse-brachyury-antibody\\_af2085](https://www.rndsystems.com/products/human-mouse-brachyury-antibody_af2085))  
 Anti-BRACHYURY antibody was validated by the manufacturer by using human embryonic stem cells. There are 60 citations.

COL1, Southern Biotech, 1310-01 (<https://www.southernbiotech.com/?catno=1310-01&type=Polyclonal#&panel1-5&panel2-1>)  
 Anti-COL1 antibody was validated by the manufacturer by using rat kidney section postuninephrectomy. There are 35 citations.

COL2, Southern Biotech, 1320-01 (<https://www.southernbiotech.com/?catno=1320-01&type=Polyclonal#&panel1-1&panel2-1>)  
 Anti-COL2 antibody was validated by the manufacturer by using newborn mouse rib section, mouse tibial growth plate section, and mouse cartilage section. There are 34 citations.

FOXC2, DSHB, 1B6 (<https://dshb.biology.uiowa.edu/PCRP-FOXC2-1B6>)  
 Anti-FOXC2 antibody was validated by the manufacturer by using human samples. There is 1 citation.

HNA, Merck, MAB1281 ([http://www.merckmillipore.com/JP/en/product/Anti-Nuclei-Antibody-clone-235-1,MM\\_NF-MAB1281](http://www.merckmillipore.com/JP/en/product/Anti-Nuclei-Antibody-clone-235-1,MM_NF-MAB1281))  
 Anti-HNA antibody was validated by the manufacturer by using human neural stem cells. There are 126 citations.

MESP2, DSHB, 1D4 (<https://dshb.biology.uiowa.edu/PCRP-MESP2-1D4>)  
 Anti-MESP2 antibody was validated by the manufacturer by using human samples. There is 1 citation.

MYH, Abcam, ab91506 (<https://www.abcam.co.jp/fast-myosin-skeletal-heavy-chain-antibody-ab91506.html>)  
 Anti-MYH antibody was validated by the manufacturer by using sheep muscle tissue frozen section. There are 24 citations.

MYOSIN, DSHB, MF20-s (<https://dshb.biology.uiowa.edu/MF-20>)  
 Anti-MYOSIN antibody was validated by the manufacturer by using samples of amphibian, avian, chicken, fish, human, lizard, mammal, snake, xenopus, zebrafish. There are 121 citations.

PAX7, DSHB, PAX7-s (<https://dshb.biology.uiowa.edu/PAX7>)  
 Anti-PAX7 antibody was validated by the manufacturer by using samples of amphibian, avian, bovine, canine, fish, goat, human, mouse, ovine, porcine, rat, turtle, xenopus, zebrafish. There are 73 citations.

PRRX1, Sigma-Aldrich, HPA051084 (<https://www.sigmaaldrich.com/catalog/product/sigma/hpa051084?lang=en&region=US>)

Anti-PRRX1 antibody was validated by the manufacturer by using human malignant glioma. There are 4 citations.

SAA, Abcam, ab9465 (<https://www.abcam.co.jp/sarcomeric-alpha-actinin-antibody-ea-53-ab9465.html>)

Anti-SAA antibody was validated by the manufacturer by using mouse heart tissue, H9 hESC and CBiPSC6.2 cells. There are more than 100 citations.

TBX6, R&D Systems, AF4744 ([https://www.rndsystems.com/products/human-tbx6-antibody\\_af4744](https://www.rndsystems.com/products/human-tbx6-antibody_af4744))

Anti-TBX6 antibody was validated by the manufacturer by using embryonic mouse mesoderm (E9.5) and JOY6 human induced pluripotent stem cells undifferentiated and differentiated into mesoderm. There are 3 citations.

TCF15, Abcam, ab204045 (webpage is closed due to discontinuation of antibody.)

Anti-TCF15 antibody was validated by the manufacturer by using human lateral ventricle tissue.

Antibodies used for flowcytometric analysis

BRACHYURY-PE, R&D Systems, IC2085P ([https://www.rndsystems.com/products/human-mouse-brachyury-pe-conjugated-antibody\\_ic2085p](https://www.rndsystems.com/products/human-mouse-brachyury-pe-conjugated-antibody_ic2085p))

BRACHYURY-PE was validated by the manufacturer by using D3 mouse cell line by flowcytometry. There are 3 citations.

DLL1-APC, R&D Systems, FAB1818A ([https://www.rndsystems.com/products/human-dll1-apc-conjugated-antibody-251127\\_fab1818a](https://www.rndsystems.com/products/human-dll1-apc-conjugated-antibody-251127_fab1818a))

DLL1-APC was validated by the manufacturer by using T98G human glioblastoma cell line by flowcytometry. There are 13 citations.

FOXA2-PE, BD Biosciences, 561589 (<https://www.bdbiosciences.com/us/applications/research/intracellular-flow/intracellular-antibodies-and-isotype-controls/anti-human-antibodies/pe-mouse-anti-human-foxa2-n17-280/p/561589>)

FOXA2-PE was validated by the manufacturer by using definitive endoderm derived from H9 human embryonic stem (ES) cells. There are 6 citations.

NANOG-Alexa Fluor® 488, BD Biosciences, 560791 (<https://www.bdbiosciences.com/eu/applications/research/intracellular-flow/intracellular-antibodies-and-isotype-controls/anti-human-antibodies/alexa-fluor-488-mouse-anti-human-nanog-n31-355/p/560791>)

NANOG-Alexa Fluor® 488 was validated by the manufacturer by using H9 human embryonic stem cells. There are 7 citations.

NCAM-BV421, BioLegend, 318328 (<https://www.biolegend.com/en-us/products/brilliant-violet-421-anti-human-cd56-ncam-antibody-7143>)

NCAM-BV421 was validated by the manufacturer by using Human peripheral blood lymphocytes. There are 13 citations.

OCT3/4-Alexa Fluor® 647, BD Biosciences, 560329 (<https://www.bdbiosciences.com/us/applications/research/stem-cell-research/cancer-research/human/alexa-fluor-647-mouse-anti-oct34-40oct-3/p/560329>)

OCT3/4-Alexa Fluor® 647 was validated by the manufacturer by using H9 human embryonic stem (ES) cells. There are 6 citations.

PAX6-Alexa Fluor® 488 BD Biosciences, 561664 (<https://www.bdbiosciences.com/us/applications/research/intracellular-flow/intracellular-antibodies-and-isotype-controls/anti-human-antibodies/alexa-fluor-488-mouse-anti-human-pax-6-o18-1330/p/561664>)

PAX6-Alexa Fluor® 488 was validated by the manufacturer by using neural induction of H9 human embryonic stem (ES) cells. There are 4 citations.

SOX2-BV421, BioLegend, 656114 (<https://www.biolegend.com/en-us/search-results/brilliant-violet-421-anti-sox2-antibody-12705>)

SOX2-BV421 was validated by the manufacturer by using NCCIT cells. There are 6 citations.

SOX17-Alexa Fluor® 647, BD Biosciences, 562594 (<https://www.bdbiosciences.com/us/applications/research/intracellular-flow/intracellular-antibodies-and-isotype-controls/anti-human-antibodies/alexa-fluor-647-mouse-anti-human-sox17-p7-969/p/562594>)

SOX17-Alexa Fluor® 647 was validated by the manufacturer by using definitive endoderm derived from H9 human embryonic stem (ES) cells. There are 5 citations.

TBX6, R&D Systems, AF4744 ([https://www.rndsystems.com/products/human-tbx6-antibody\\_af4744](https://www.rndsystems.com/products/human-tbx6-antibody_af4744))

Anti-TBX6 was validated by the manufacturer by using embryonic mouse mesoderm (E9.5) and JOY6 human induced pluripotent stem cells undifferentiated and differentiated into mesoderm. There are 3 citations.

## Eukaryotic cell lines

Policy information about [cell lines](#)

Cell line source(s)

Human induced pluripotent stem (iPS) cell lines derived from healthy donors, i.e. 1231A3 (derived from commercially available peripheral blood) and 201B7 (derived from commercially available human fibroblasts) were used for majority of

experiments and obtained from/provided by the Center for iPS Cell Research and Application (CiRA). Additionally, human luciferase iPSC-reporter lines (625-A4 and 625-D4), which were utilized for xeno-transplantation experiments, were obtained from the Center for iPS Cell Research and Application (CiRA). Human iPSC (GCaMP) reporter line (Gen1C), which was used for calcium imaging experiments, was originally established by the Conklin Lab at the Gladstone Institute and shared with/provided by the Center for iPS Cell Research and Application (CiRA). SCDP1 patient sample was obtained from the NIGMS Human Genetic Cell Repository at the Coriell Institute for Medical Research (GM13539) and SCDP2 patient sample was obtained from a collaborating researcher at Meijo Hospital, Nagoya, Japan. Patient-derived iPSC lines were generated following strict guidelines of and approval by Kyoto University Graduate School and Medical Faculty, and Meijo Hospital, Japan. Mouse Epiblast Stem Cells (EpiSCs) were obtained from the RIKEN BioResource Research Center (RIKEN BRC) (#AES0204).

#### Authentication

Identity of cells generated/utilized in the lab/institute are commonly confirmed by multiple STR analyses using PowerPlex 16 HS System (Promega). For SCD patient and rescue iPSC clones SNP array analysis was also performed (see Methods section for details). Patient-like (knock-out) and patient-derived iPSC lines were also tested for presence of line-specific mutations via iPSC genotyping (see Methods section for details).

#### Mycoplasma contamination

All cell lines were tested negative for mycoplasma infection.

#### Commonly misidentified lines (See [ICLAC](#) register)

No commonly misidentified lines were used.

## Animals and other organisms

Policy information about [studies involving animals](#); [ARRIVE guidelines](#) recommended for reporting animal research

#### Laboratory animals

NOD/ShiJic-scid Jcl (NOD/SCID) male mice were purchased from CLEA Japan and utilized for experiments at six weeks of age.

#### Wild animals

No wild animals were used.

#### Field-collected samples

No field-collected samples were used.

#### Ethics oversight

Animal experiments were approved by the institutional animal research committee of the Center for iPS Cell Research and Application (CiRA), Kyoto University and performed following the guidance of Regulation on Animal Experimentation at Kyoto University

Note that full information on the approval of the study protocol must also be provided in the manuscript.

## Human research participants

Policy information about [studies involving human research participants](#)

#### Population characteristics

SCDP1 | Patient with mutations in MESP2; M-SDV-G (SCD2)

SCDP2 | Patient with mutation in DLL3; M-SDV-G (SCD1)

#### Recruitment

Patient samples utilized in this study were either obtained from the NIGMS Human Genetic Cell Repository at the Coriell Institute for Medical Research (SCDP1) or Meijo Hospital, Japan (SCDP2) based on provided clinical/radiological data indicating a patient with segmentation defects of the vertebrae (SDV).

SCDP1 | Patient with mutations in MESP2; M-SDV-G (SCD2):

Patient was diagnosed with spondyloathoracic dysostosis, malsegmentation of the spine, numerous hemivertebrae, "crab thorax" and lordosis. Primary tissue samples utilized for derivation of patient iPSCs (SCDP1) were provided by Coriell Institute for Medical Research (GM13539).

SCDP2 | Patient with mutation in DLL3; M-SDV-G (SCD1):

Patient was diagnosed with spondyloathoracic dysostosis, segmentation defects of the vertebrae with involvement of the entire spine (sacrum to C1), bilateral fusion of ribs posteriorly, with fanning out in a "crab-like" appearance, mild scoliosis and marked reduction of thoracic lordosis. Primary tissue samples utilized for derivation of patient iPSCs (SCDP2) were provided by Meijo Hospital, Nagoya, Japan.

#### Ethics oversight

All experiments followed relevant guidelines and regulations and were approved by Ethics committees of the Kyoto University Graduate School and Faculty of Medicine, Kyoto, Japan and Meijo Hospital, Nagoya, Japan. Informed consent was obtained from legal guardians of patients by relevant institutions.

Note that full information on the approval of the study protocol must also be provided in the manuscript.

## Flow Cytometry

### Plots

Confirm that:

- ☒ The axis labels state the marker and fluorochrome used (e.g. CD4-FITC).
- ☒ The axis scales are clearly visible. Include numbers along axes only for bottom left plot of group (a 'group' is an analysis of identical markers).
- ☐ All plots are contour plots with outliers or pseudocolor plots.
- ☒ A numerical value for number of cells or percentage (with statistics) is provided.

### Methodology

#### Sample preparation

Cells were washed with PBS and dissociated using Accutase (Life Technologies) and centrifuged. Cells were resuspended ( $1.0 \times 10^7$  cells/ml) in FACS buffer (0.1% BSA in PBS) and stained with allophycocyanin (APC)-conjugated DLL1 antibody for 30 minutes at 4°C. Then, cells were stained with DAPI to eliminate dead cells after washing with FACS buffer once and finally strained through a filter mesh. As for the co-staining of intracellular molecules TBX6 and BRACHYURY with DLL1, cells were fixed with 4% paraformaldehyde (PFA) for 20 minutes at 4°C after initial staining with DLL1 antibody and washed twice with staining medium, which contained PBS with 2% fetal bovine serum (FBS). Samples were permeabilized with BD Perm/Wash buffer (BD Biosciences) for 15 minutes at room temperature and stained with TBX6 primary antibody or phycoerythrin (PE)-conjugated BRACHYURY antibody for 60 minutes at room temperature and washed with BD Perm/Wash buffer twice. The cells stained with TBX6 antibody were stained with Alexa Fluor® 488-conjugated secondary antibody for 60 minutes at room temperature. The samples were washed with BD Perm/Wash buffer twice and suspended into staining medium. For FACS-based evaluation of undifferentiated PSCs and their differentiation capacity into three germ layers, cells ( $1.0 \times 10^6$  cells each) were fixed with 4% paraformaldehyde phosphate buffer solution (4% PFA/PBS) for 20 minutes at 4°C and washed twice with staining medium, which contained PBS with 2% fetal bovine serum (FBS). Samples were permeabilized with BD Perm/Wash buffer (BD Biosciences) for 15 minutes at room temperature and stained with fluorescence-conjugated primary antibodies listed in Supplementary Table 8.3. The samples were washed with BD Perm/Wash buffer twice and suspended into staining medium.

#### Instrument

Flow cytometric analysis was performed using LSR or BD FACSAria II cell sorter (BD Biosciences).

#### Software

FACS data was analyzed and graphs were generated using FlowJo software (FlowJo LLC, version 10.6.1).

#### Cell population abundance

Abundance of distinct cell populations of interest was determined using appropriate negative controls.

#### Gating strategy

Standard gating settings commonly utilized at FACS core facility of the institute were used. Besides using appropriate isotype controls, negative (control) cell samples were utilized to set appropriate gates and determine true positive cell populations.

- ☐ Tick this box to confirm that a figure exemplifying the gating strategy is provided in the Supplementary Information.



# Metabolites released from apoptotic cells act as tissue messengers

<https://doi.org/10.1038/s41586-020-2121-3>

Received: 29 January 2019

Accepted: 18 February 2020

Published online: 18 March 2020

 Check for updates

Christopher B. Medina<sup>1,2</sup>, Parul Mehrotra<sup>3,8</sup>, Sanja Arandjelovic<sup>1,2,8</sup>, Justin S. A. Perry<sup>1,2,8</sup>, Yizhan Guo<sup>4</sup>, Sho Morioka<sup>1,2</sup>, Brady Barron<sup>1,5</sup>, Scott F. Walk<sup>1,2</sup>, Bart Ghesquière<sup>6</sup>, Alexander S. Krupnick<sup>4,7</sup>, Ulrike Lorenz<sup>2,7</sup> & Kodi S. Ravichandran<sup>1,2,3,7</sup>✉

Caspase-dependent apoptosis accounts for approximately 90% of homeostatic cell turnover in the body<sup>1</sup>, and regulates inflammation, cell proliferation, and tissue regeneration<sup>2–4</sup>. How apoptotic cells mediate such diverse effects is not fully understood. Here we profiled the apoptotic metabolite secretome and determined its effects on the tissue neighbourhood. We show that apoptotic lymphocytes and macrophages release specific metabolites, while retaining their membrane integrity. A subset of these metabolites is also shared across different primary cells and cell lines after the induction of apoptosis by different stimuli. Mechanistically, the apoptotic metabolite secretome is not simply due to passive emptying of cellular contents and instead is a regulated process. Caspase-mediated opening of pannexin 1 channels at the plasma membrane facilitated the release of a select subset of metabolites. In addition, certain metabolic pathways continued to remain active during apoptosis, with the release of only select metabolites from a given pathway. Functionally, the apoptotic metabolite secretome induced specific gene programs in healthy neighbouring cells, including suppression of inflammation, cell proliferation, and wound healing. Furthermore, a cocktail of apoptotic metabolites reduced disease severity in mouse models of inflammatory arthritis and lung-graft rejection. These data advance the concept that apoptotic cells are not inert cells waiting for removal, but instead release metabolites as ‘good-bye’ signals to actively modulate outcomes in tissues.

Apoptosis occurs during development<sup>3</sup>, homeostatic tissue turnover, and in pathological settings<sup>1</sup>. Besides the known responses of phagocytes that engulf apoptotic cells<sup>4</sup>, the apoptotic process itself (independent of phagocytosis) can modulate physiological events, such as embryogenesis and tissue regeneration<sup>5</sup>, with pathologies arising when apoptosis is inhibited<sup>6</sup>. However, the mechanisms by which apoptotic cells themselves mediate these functions are not well understood. As apoptotic cells remain intact for a period of time, they could release soluble metabolites that diffuse within a tissue to influence neighbouring cells. Although a few soluble factors from apoptotic cells are reported as ‘find-me’ signals to attract phagocytes<sup>7</sup>, the full apoptotic secretome is not yet defined.

To profile the metabolite secretome of apoptotic cells, we used human Jurkat T cells, primary mouse thymocytes, or primary mouse bone-marrow-derived macrophages (BMDMs), all of which can undergo inducible, caspase-dependent apoptosis (caused by ultraviolet (UV)-light treatment, anti-Fas antibody crosslinking, or treatment with anthrax lethal toxin)<sup>8,9</sup> (Fig. 1a). As untargeted metabolomics require large numbers of cells, we optimized the parameters using Jurkat cells (for example, cell density, culture volume and duration after apoptosis), such that approximately 80% of the cells were apoptotic, while

maintaining cell membrane integrity (annexin V<sup>7</sup>AAD<sup>−</sup>) (Extended Data Fig. 1a, b). Supernatants and cell pellets from apoptotic cells and live cell controls were subjected to untargeted metabolomic profiling against a library of more than 3,000 biochemical features or compounds. Supernatants of apoptotic Jurkat cells (induced by UV irradiation) showed an enrichment of 123 metabolites (Fig. 1b, Extended Data Fig. 1c, d, Supplementary Table 1), and 85 of these 123 were reciprocally reduced in the apoptotic cell pellets (Extended Data Fig. 2a–f, Supplementary Table 2).

In untargeted metabolomics of supernatants from macrophages undergoing apoptosis (induced via anthrax lethal toxin<sup>9</sup>), we detected fewer metabolites (20 versus 123 in Jurkat cells), perhaps owing to differences in cell types, modality of death and/or quantities released (below detection limits). Notably, 16 of the 20 metabolites (80%) were shared with apoptotic Jurkat cells (Fig. 1b).

For further validation and quantification, we performed targeted metabolomics and analysed 116 specific metabolites (Methods) in the supernatants from Jurkat cells and primary mouse thymocytes after Fas-crosslinking (extrinsic cue for apoptosis) (Supplementary Table 3). This targeted panel included 43 of the metabolites released from apoptotic Jurkat cells (identified above), and included a 5-kDa filtering step

<sup>1</sup>Center for Cell Clearance, University of Virginia, Charlottesville, VA, USA. <sup>2</sup>Department of Microbiology, Immunology, and Cancer Biology, University of Virginia, Charlottesville, VA, USA. <sup>3</sup>VIB/UGent Inflammation Research Centre, Biomedical Molecular Biology, Ghent University, Ghent, Belgium. <sup>4</sup>Department of Surgery, University of Virginia, Charlottesville, VA, USA. <sup>5</sup>Department of Pharmacology, University of Virginia, Charlottesville, VA, USA. <sup>6</sup>Department of Oncology and VIB, KU Leuven, Leuven, Belgium. <sup>7</sup>Carter Immunology Center, University of Virginia, Charlottesville, VA, USA. <sup>8</sup>These authors contributed equally: Parul Mehrotra, Sanja Arandjelovic, Justin Perry. <sup>✉</sup>e-mail: Ravi@virginia.edu

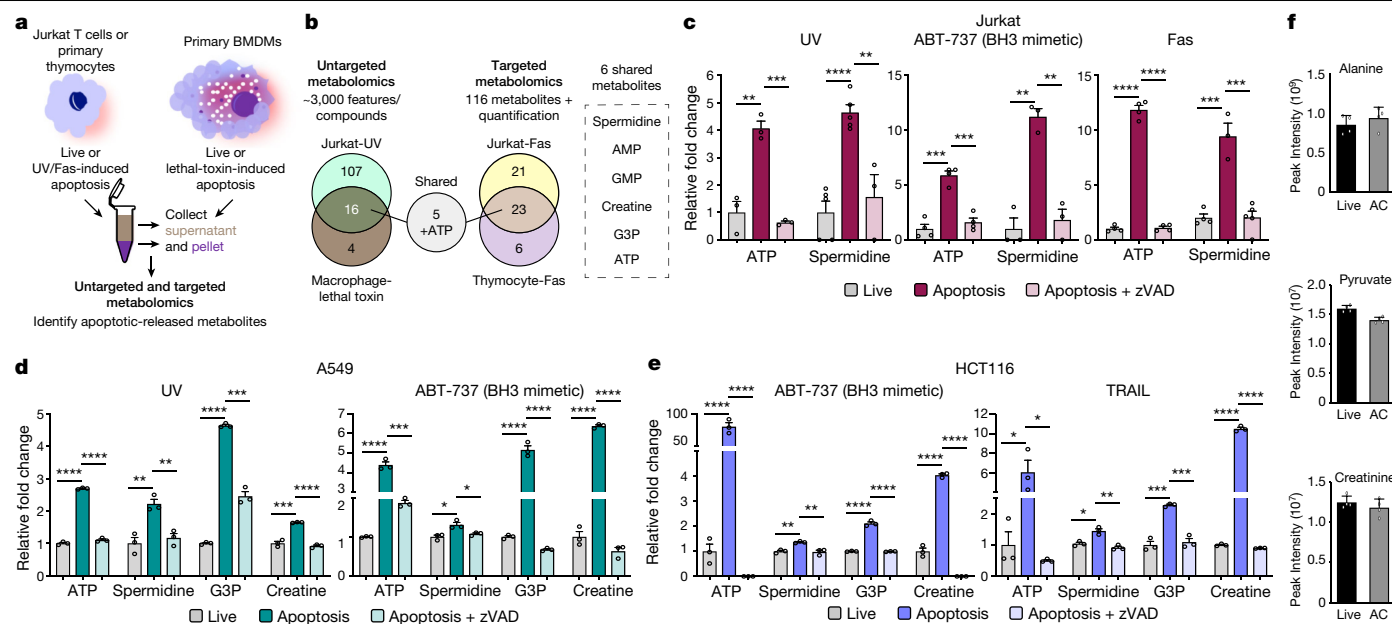


**Fig. 1 | Conserved metabolite secretome from apoptotic cells. a**, Schematic for assessing apoptotic metabolite secretomes. **b**, Venn diagrams illustrating the shared apoptotic metabolites identified across cell types, modalities of apoptosis induction, and the two metabolomic platforms tested, and the list of five shared metabolites plus ATP. G3P, glycerol-3-phosphate. **c–e**, Metabolite release from Jurkat T cells ( $n=3$  for ATP–UV, spermidine–UV + zVAD, spermidine–ABT, and spermidine–Fas;  $n=4$  for ATP–ABT, ATP–Fas and spermidine–Fas–live;  $n=5$  for spermidine–UV–live and spermidine–

Fas + zVAD) (**c**), A549 lung epithelial cells ( $n=3$ ) (**d**), and HCT-116 colonic epithelial cells ( $n=3$ ) (**e**) across different apoptotic stimuli, with or without inhibition of caspase using zVAD. **f**, Several abundant metabolites such as alanine (top), pyruvate (middle) and creatinine (bottom) were not released in the Jurkat T cell supernatants ( $n=4$ ). AC, apoptotic cell. \* $P<0.05$ , \*\* $P<0.01$ , \*\*\* $P<0.001$ , \*\*\*\* $P<0.0001$ , unpaired Student's  $t$ -test with Holm–Sidak method for multiple  $t$ -tests. Data are mean  $\pm$  s.e.m. (**c–e**) or mean  $\pm$  s.d. (**f**).

to exclude proteins and extracellular vesicles. This targeted analysis showed an enrichment of many metabolites seen with UV-induced apoptosis (Fig. 1b). Furthermore, metabolites released from apoptotic primary thymocytes overlapped with apoptotic Jurkat cells (Fig. 1b). Comparison of metabolites enriched or released in the apoptotic supernatant of Jurkat cells, thymocytes and macrophages (after Fas-, UV- or toxin-mediated apoptosis) identified five conserved metabolites: adenosine monophosphate (AMP), guanosine 5'-monophosphate (GMP), creatine, spermidine and glycerol-3-phosphate (Fig. 1b, Extended Data Fig. 3a). ATP represents the sixth shared metabolite (via luciferase assay) (Extended Data Fig. 3b), although ATP was not profiled in the metabolomic analyses for technical reasons.

To test other cell types and apoptotic modalities, we analysed the release of four conserved metabolites via analytical kits. Jurkat cells, A549 lung epithelial cells and HCT116 colonic epithelial cells were induced to undergo death via different apoptotic cues, such as UV radiation, treatment with the BH3-mimetic ABT-737 (which directly induces permeabilization of the mitochondrial outer membrane), and/or treatment with TRAIL (the cell extrinsic pathway) (Fig. 1c–e). We could readily detect apoptosis-dependent release of the tested metabolites, and attenuation by pan-caspase inhibitor zVAD (Fig. 1c–e, Extended Data Fig. 3c). The metabolites detected were not due to simple emptying of cellular contents during apoptosis, as many metabolites at high intracellular concentrations were not released (Fig. 1f). These data reveal apoptotic cells as a natural source of many metabolites with biological functions.

During the above analyses, we noted that despite the many cellular metabolites detected in the pellet only a subset is released; furthermore, even within a known metabolic pathway, only some were released. Such selectivity could arise from specific channels that open during apoptosis to permeate certain metabolites, and/or continued metabolic activity within the dying cell influencing the secretome. To test specific channels, we focused on pannexin 1 (PANX1) channels

that are activated during apoptosis by caspase-mediated cleavage<sup>10</sup> and can conduct ions and small molecules up to 1 kDa in size across the plasma membrane. In a PANX1-dependent manner<sup>10</sup>, apoptotic cells (but not live cells) take up the nucleic acid stain TO-PRO-3 dye (671 Da), whereas 7AAD (1.27 kDa) is excluded (Extended Data Fig. 4a, b). We tested the relevance of PANX1 by genetic and pharmacological approaches. Genetically, we used Jurkat cells expressing a dominant-negative PANX1 with a mutation in the caspase cleavage site<sup>10</sup> (PANX1-DN) or primary thymocytes from PANX1-deficient mice (*Panx1*<sup>-/-</sup>)<sup>11</sup>. We also used two pharmacological inhibitors, trovafloxacin (Trovan) and spironolactone, which had previously been identified in unbiased screens<sup>11,12</sup>. Disrupting PANX1 activity per se did not affect apoptosis (Extended Data Fig. 5a–e). Untargeted metabolomics of the supernatants from apoptotic Jurkat cells (UV-induced) with and without PANX1 inhibition revealed that PANX1 contributed to release approximately 20% of the apoptotic metabolites (25 out of 123) (Fig. 2a, Extended Data Fig. 6a). The PANX1-dependent metabolites included nucleotides, nucleotide-sugars, and metabolites linked to energy metabolism and amino acid metabolism; notably, most have not previously been reported to permeate through PANX1. A similar PANX1-dependent metabolite signature was shared between Jurkat cells and thymocytes; furthermore, as not all apoptotic metabolites released were PANX1-dependent, other mechanisms of metabolite release from apoptotic cells must also exist (Extended Data Fig. 6b–e). We noted eight shared PANX1-dependent apoptotic metabolites between Jurkat cells and primary thymocytes (Fig. 2b, Extended Data Fig. 7).

To test whether the apoptotic secretome might also be influenced by the metabolic activity within the dying cell, we chose the polyamine pathway for several reasons. First, the polyamine spermidine was released in considerable quantities from apoptotic Jurkat cells, macrophages, thymocytes and epithelial cells after different modes of apoptosis induction (Fig. 2c). Second, among the two metabolites immediately upstream of spermidine, putrescine was not released,

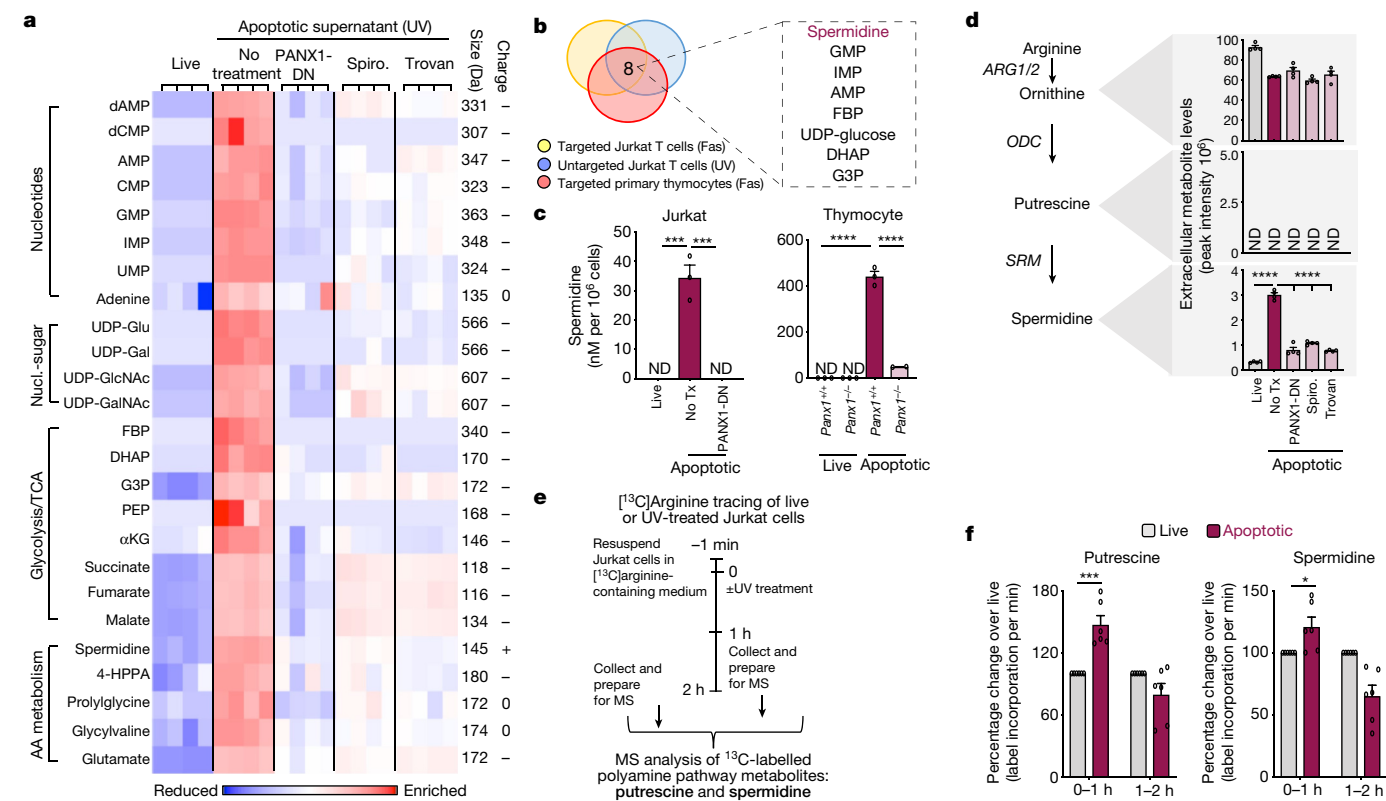


**Fig. 2 | Activation of PANX1 and continued metabolic activity of dying cells orchestrates metabolite release. a**, PANX1-dependent metabolite release. Heat map produced from untargeted metabolomics of supernatants from Jurkat T cells representing the metabolites that were statistically enriched or reduced ( $P < 0.05$ , two-sided Welch's two-sample  $t$ -test) in the apoptotic supernatants relative to live supernatants, and after inhibition of PANX1 by PANX1-DN or the PANX1 inhibitors spiroinolactone (Spiro.) or trovafloxacin (Trovan). Metabolites are grouped by pathway. Charge and relative sizes of the metabolites are also shown ( $n = 4$ ). 4-HPPA, 4-hydroxyphenylpyruvic acid;  $\alpha$ KG,  $\alpha$ -ketoglutarate; GalNAc,  $N$ -acetylgalactosamine; GlcNAc,  $N$ -acetylglucosamine; PEP, phosphoenolpyruvate. **b**, Three-way Venn diagram (left) illustrating the eight PANX1-dependent apoptotic metabolites observed (right) among the cell types and apoptotic modalities tested. ATP (not detected here) represents the ninth metabolite. **c**, Spermidine concentration per million cells in supernatants from targeted metabolomics in Jurkat cells (after 4 h Fas

crosslinking) (left) ( $n = 3$ ) or primary thymocytes with *Panx1* deletion (after 1.5 h Fas crosslinking) (right) ( $n = 3$ ). \*\*\* $P = 0.0002$ , \*\*\*\* $P = 0.0001$ , one-way analysis of variance (ANOVA) with Turkey's multiple comparison test. ND, not determined; No Tx, no treatment. **d**, Left, schematic of the polyamine metabolic pathway. Right, relative amounts of ornithine (top), putrescine (middle) and spermidine (bottom) in supernatants of Jurkat T cells in live and apoptotic conditions, with or without PANX1 inhibition ( $n = 4$ ). \*\*\*\* $P = 0.0001$ , one-way ANOVA with Turkey's multiple comparison test. **e, f**, Active polyamine metabolic activity during apoptosis. Experimental layout for [<sup>13</sup>C]arginine labelling (**e**), and incorporation of [<sup>13</sup>C]-labelled arginine into the polyamine pathway intermediates putrescine (**f**, left) or spermidine (**f**, right) after the induction of cell death ( $n = 6$ ). MS, mass spectrometry. \* $P = 0.025$ , \*\*\* $P = 0.0003$ , unpaired Student's  $t$ -test with Holm–Sidak method for multiple  $t$ -tests. Data are mean  $\pm$  s.e.m.

whereas ornithine was present comparably in live and apoptotic cell supernatants (Fig. 2d). Third, although exogenous supplementation of spermidine can reduce inflammation and improve longevity<sup>13</sup>, spermidine release from apoptotic cells provides the first natural or physiological extracellular source of this polyamine.

The upstream steps of spermidine generation involve arginine to ornithine to putrescine to spermidine, with each conversion regulated by specific enzymes. A recent report<sup>14</sup> has shown that although most mRNA gets degraded in apoptotic HCT-116 cells, a small fraction is retained. In our re-analysis of this mRNA dataset, the polyamine pathway enzyme transcripts were not degraded during apoptosis, including spermidine synthase (SRM) that converts putrescine to spermidine<sup>14</sup> (Extended Data Fig. 8a). We confirmed that in apoptotic Jurkat cells, the mRNA for spermidine synthase (SRM) was retained (Extended Data Fig. 8b). To address this more directly by metabolic flux labelling, we added medium containing [<sup>13</sup>C]arginine to Jurkat cells immediately before the induction of apoptosis, and traced incorporation of the label into putrescine and spermidine for the next few hours (Fig. 2e). Apoptotic cells displayed increased incorporation of the <sup>13</sup>C label into the polyamine pathway in the first hour, compared with live cells. After normalizing for total label incorporation and focusing on the carbons within the polyamine

pathway (Methods), apoptotic cells showed 40% and 25% greater incorporation of the <sup>13</sup>C label per minute into putrescine and spermidine, respectively, during the first hour (Fig. 2f). Although this dips during the second hour, it was still comparable to live cells. In addition, <sup>13</sup>C-labelled spermidine was detectable in the supernatants of apoptotic cells, and this was partially reduced by the inhibition of caspases (Extended Data Fig. 8c). Notably, despite its active generation (revealed by <sup>13</sup>C-labelling analysis), putrescine was not detected in apoptotic cell supernatants from Jurkat cells (or in the macrophage or thymocytes dataset) (Fig. 2d). Thus, apoptotic cells orchestrate the generation and release of select metabolites at least at two levels: caspase-dependent opening of specific channels (PANX1) and continued metabolic activity of certain pathways.

To test whether released metabolites derived from apoptotic cells signal to alter gene expression programs in healthy nearby cells such as phagocytes, we added supernatants from live or apoptotic Jurkat cells (same conditions as untargeted metabolomics) to phagocytic LR73 cells—a Chinese hamster ovary cell line that is useful for determining mechanisms or responses after efferocytosis<sup>15–17</sup> (Fig. 3a). RNA sequencing (RNA-seq) analysis of LR73 cells (after 4 h) indicated distinct transcriptional changes (Fig. 3b, Extended Data Fig. 9a). Pathway analysis, by curating each of the hits individually,

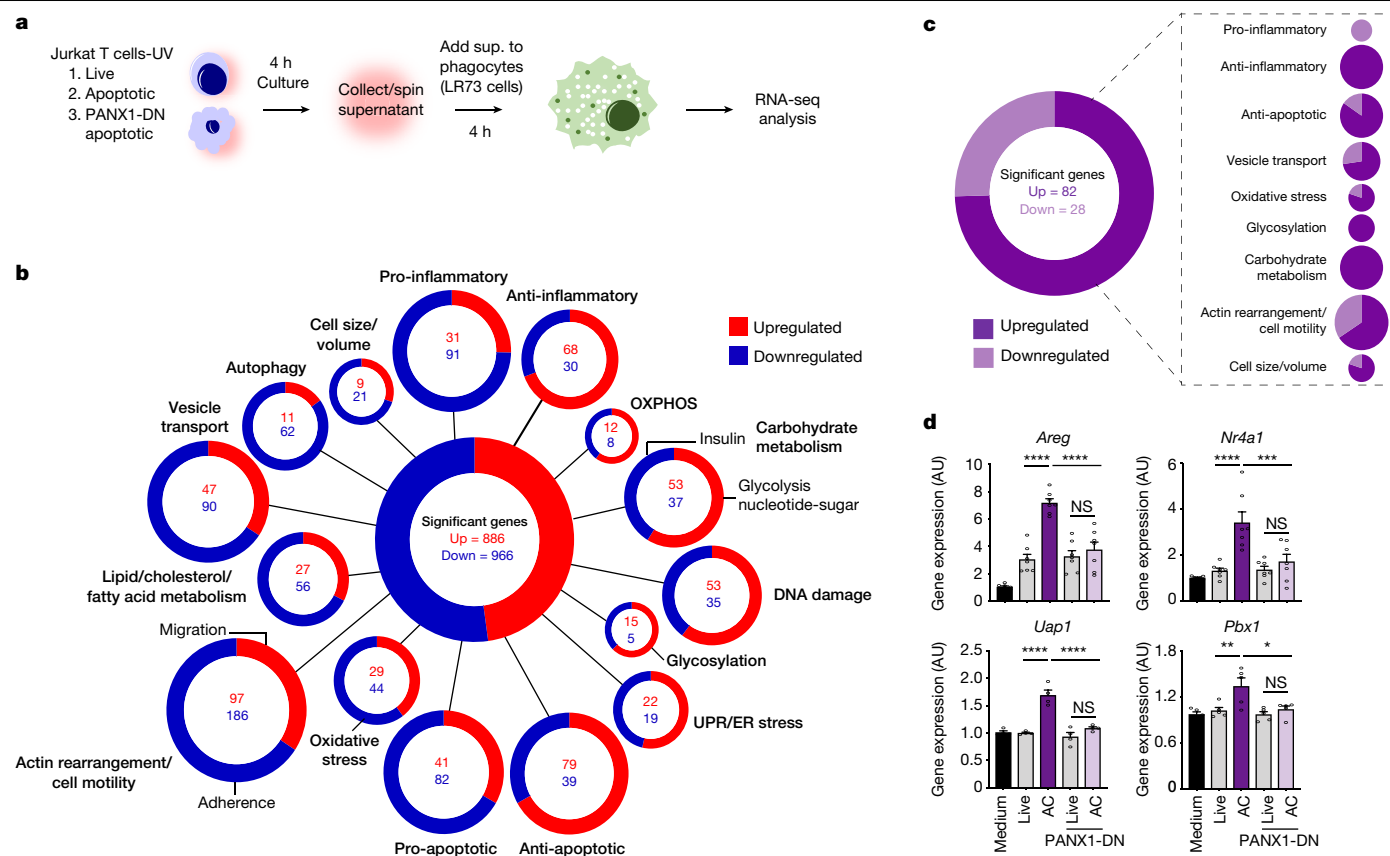


**Fig. 3 | Metabolites from apoptotic cells influence gene programs in live cells.** **a**, Schematic for assessing gene induction by apoptotic cell supernatants in LR73 cells. **b**, Gene expression programs induced in phagocytes by the apoptotic secretome. Display shows the differentially regulated genes (1,852 total, 886 upregulated, 966 downregulated), categorized per known or predicted function(s), literature and sequence similarity. Circle size is proportional to the number of differentially expressed genes ( $n = 4$ ) ( $P < 0.05$ ). OXPHOS, oxidative phosphorylation; UPR, unfolded protein response. **c**,

Differentially regulated genes in phagocytes in response to apoptotic cell supernatants with or without inhibition of the PANX1 channel (82 upregulated, 28 downregulated) ( $n = 4$ ). **d**, Validation of genes regulated by PANX1-dependent metabolites. LR73 cells were incubated with indicated supernatants for 4 h, and expression of *Areg* ( $n = 7$ ), *Nr4a1* ( $n = 7$ ), *Uap1* ( $n = 4$ ), and *Pbx1* ( $n = 5$ ) was determined in phagocytes by qPCR. AU, arbitrary units. \* $P = 0.014$ , \*\* $P = 0.009$ , \*\*\* $P = 0.0008$ , \*\*\*\* $P = 0.0001$ , one-way ANOVA with Turkey's multiple comparison test. Data are mean  $\pm$  s.e.m.

together with commonly used analysis software, revealed that the apoptotic secretome altered gene programs linked to cytoskeletal rearrangements, inflammation, wound healing or tissue repair, anti-apoptotic functions, metabolism and the regulation of cell size within the phagocyte (Fig. 3b), providing a molecular and metabolic basis for how apoptosis may influence essential tissue processes.

By comparing gene programs induced in live cells by supernatants from apoptotic cells versus conditions with genetic inhibition of PANX1, we identified 110 genes as differentially regulated on phagocytes by PANX1-dependent apoptotic metabolites (82 up and 28 down) (Fig. 3c); these include genes involved in anti-inflammatory processes, anti-apoptotic pathways, metabolism, and actin rearrangement (Fig. 3c). Secondary validation via quantitative PCR (qPCR) indicates that PANX1-dependent metabolites can alter genes linked to anti-inflammatory roles in phagocytes (*Nr4a1* and *Pbx1*)<sup>18,19</sup>, wound healing (*Areg* and *Ptgs2*)<sup>20,21</sup>, and metabolism (*Slc14a1*, *Sgk1* and *Uap1*)<sup>15,22</sup> (Fig. 3d, Extended Data Fig. 9b). Furthermore, filtration of supernatants through 3-kDa filters before the addition to phagocytes showed similar changes in gene transcription (Extended Data Fig. 9c), ruling out larger proteins or vesicles from dying cells. Thus, metabolites released from apoptotic cells, a subset of which is released in a PANX1-dependent manner, can alter selective gene programs in the surrounding cells that sense these metabolic signals.

To test whether apoptotic PANX1-dependent metabolites can induce gene expression changes in tissue phagocytes in vivo, we used *Panx1*<sup>fl/fl</sup>

*Cd4-cre* mice<sup>11</sup>, in which *Panx1* is targeted for deletion only within the thymocytes and not the thymic myeloid cells (Extended Data Fig. 10a, left). After confirming that *Panx1* was not deleted in the macrophages and dendritic cells (Extended Data Fig. 10a, right), and that comparable dexamethasone-induced thymocyte apoptosis occurs in control and *Panx1*<sup>fl/fl</sup>*Cd4-cre* mice (Extended Data Fig. 10b, c), we isolated CD11b<sup>+</sup> macrophages and CD11c<sup>+</sup> dendritic cells from the thymus and analysed changes in gene expression (Extended Data Fig. 10d, e). In wild-type mice, dexamethasone-induced apoptosis of thymocytes resulted in increased expression of *Uap1*, *Ugdh* and *Pbx1* in surrounding live myeloid cells (linked to anti-inflammatory macrophage skewing or glycosylation and transcription of *Il10*)<sup>19,23</sup> (Fig. 4a). This response was attenuated in mice lacking PANX1 channels in the dying thymocytes (Fig. 4a). Thus, apoptotic PANX1-dependent metabolites can induce gene expression changes in the surrounding tissue myeloid cells in vivo.

When tested individually, many of the metabolites did not strongly induce anti-inflammatory and tissue-repair genes from the RNA-seq (not shown). As these metabolites are concurrently released from apoptotic cells (Fig. 1), we then tested mixtures of six out of the eight PANX1-dependent metabolites (Fig. 2b) in two combinations: (i) spermidine, fructose-1,6-bisphosphate (FBP), dihydroxyacetone phosphate (DHAP), UDP-glucose, GMP and inosine-5'-monophosphate (IMP); and (ii) spermidine, GMP and IMP (Fig. 4b). All six have been previously administered in vivo in mice or rats without toxicity (Supplementary Table 4). We excluded AMP and glycerol-3-phosphate, as AMP can



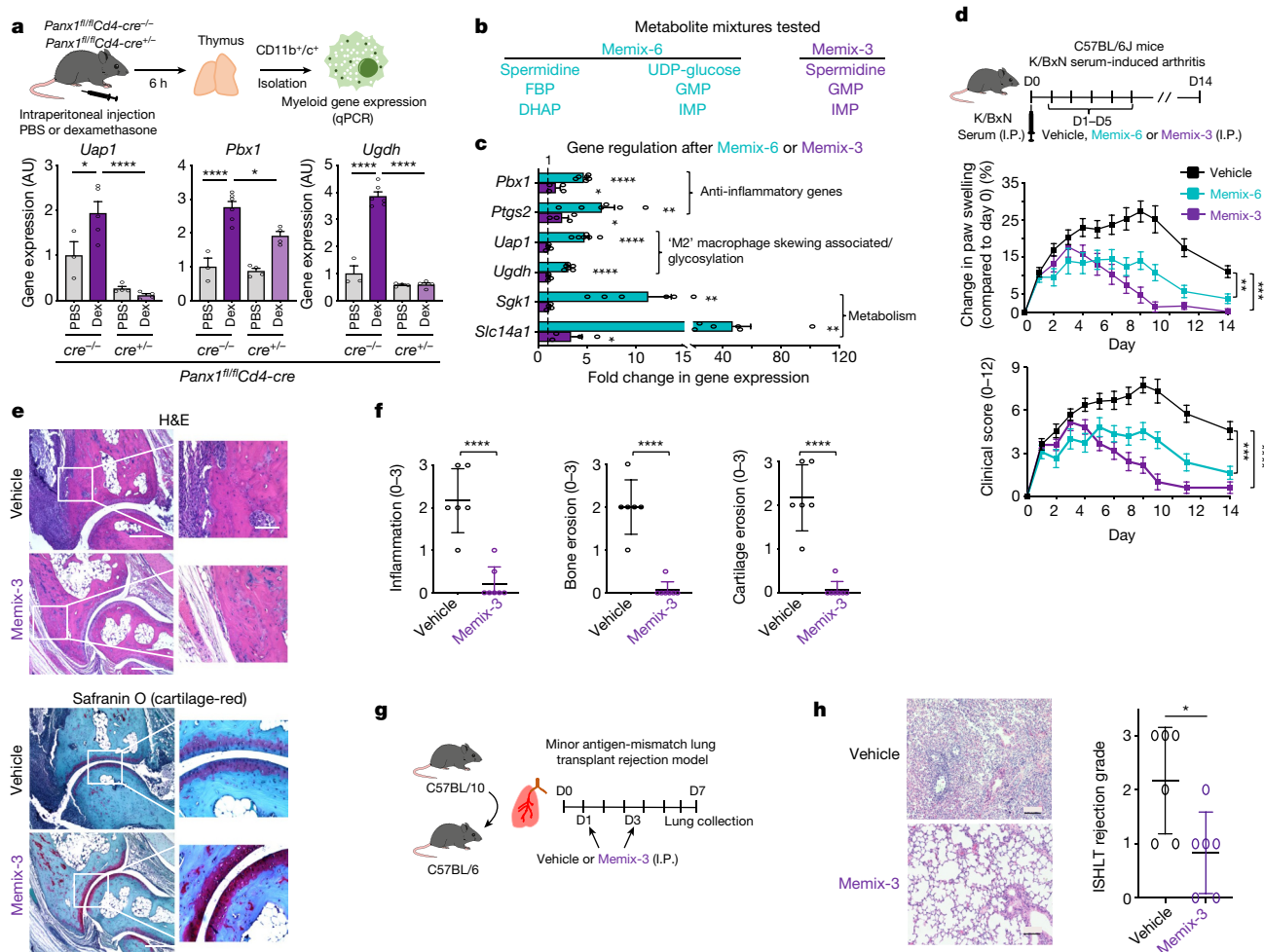


**Fig. 4 | PANX1-dependent metabolite release during apoptosis modulates phagocyte gene expression in vivo and can alleviate inflammation.** **a**, PANX1 expression in apoptotic thymocytes influences gene expression in myeloid cells in vivo. Control mice (*Panx1<sup>fl/fl</sup>Cd4-cre<sup>-/-</sup>*) or mice lacking PANX1 in thymocytes (*Panx1<sup>fl/fl</sup>Cd4-cre<sup>-/-</sup>*) were injected with dexamethasone (Dex) to induce apoptosis in thymocytes (*cre<sup>-/-</sup>* PBS *n* = 3, *cre<sup>-/-</sup>* Dex *n* = 6, *cre<sup>-/-</sup>* PBS, Dex *n* = 4). After 6 h, CD11b<sup>+</sup> CD11c<sup>+</sup> phagocytes were purified for qPCR analysis of *Uap1* (*P* = 0.032, \*\*\*\**P* < 0.0001), *Pbx1* (\*\*\*\**P* = 0.0001, \**P* = 0.0103), and *Ugdh* (\*\*\*\**P* < 0.0001). *P* values were determined by one-way ANOVA with Turkey's multiple comparison test. **b**, PANX1-dependent release of metabolites from apoptotic cells was compared across cell types and apoptotic conditions to design different metabolite mixtures, Memix-6 (blue) and Memix-3 (purple). **c**, Memix-6 (*n* = 6) and Memix-3 (*n* = 4) solutions mimic gene expression changes in phagocytes induced by apoptotic supernatants. \**P* < 0.05, \*\**P* < 0.01, \*\*\*\**P* < 0.0001, unpaired two-tailed Student's *t*-test. **d**, Top, schematic of arthritis induction and treatments (vehicle *n* = 16, Memix-6 *n* = 11, Memix-3 *n* = 12 mice). I.P., intraperitoneal. Middle, paw swelling was measured using a calliper and reported as the percentage change compared to day 0.

\*\**P* = 0.0028, \*\*\**P* = 0.0003. Bottom, scores were assessed on a scale of 1 to 4 per paw. \*\*\**P* = 0.0004, \*\*\*\**P* = 0.0001. *P* values determined by two-way ANOVA. **e**, Ankle inflammation and bone erosion were scored via haematoxylin and eosin (H&E) staining (left) and safranin O staining (right), respectively, from arthritic mouse paws on day 8 ('peak' disease). Increased magnifications of affected areas are shown. Scale bars, 0.4 mm (main panel), 0.1 mm (magnification). **f**, Clinical analysis of inflammation (left), bone erosion (middle) and cartilage erosion (right) was scored by an investigator blinded to treatments (vehicle *n* = 6, Memix-3 *n* = 7). \*\*\*\**P* < 0.0001, unpaired two-tailed Student's *t*-test. **g**, Memix-3 metabolite solution alleviates inflammation in a minor antigen-mismatch lung transplant model. Orthotopic left lung transplantation from C57BL/10 mice into C57BL/6 recipient mice, with Memix-3 administered on post-operation day 1 and 3. Lungs were obtained for histological scoring on day 7. **h**, H&E staining (left) and ISHLT rejection score<sup>28</sup> (right) in mice as in g (vehicle *n* = 6, Memix-3 *n* = 6). \**P* = 0.024, unpaired two-tailed Student's *t*-test. Data are mean ± s.e.m. (**a**, **c**, **d**) or mean ± s.d. (**f**, **h**). Scale bars, 100 μm.

be converted to adenosine, a known anti-inflammatory metabolite, and it was difficult to determine the optimal in vivo dose for glycerol-3-phosphate. The metabolite mixtures were quite potent in inducing gene expression in vitro, including genes linked to anti-inflammatory macrophage skewing or glycosylation (*Uap1* and *Ugdh*)<sup>23</sup>, transcription of *IL10* and inflammation resolution (*Pbx1*<sup>19</sup> and *Ptgs2*<sup>24</sup>), and metabolic processes (*Slc14a1* and *Sgk1*), some of which have also been shown to be involved in phagocytosis<sup>15</sup> (Fig. 4c). For simplicity, we have denoted the metabolite mixtures as 'Memix-6' and 'Memix-3' (Fig. 4b).

Given the anti-inflammatory gene signature induced by the metabolites, we next tested whether the Memix-6 and/or Memix-3 metabolites

attenuated inflammation in vivo in two contexts: a model of inflammatory arthritis and a model of lung-transplant rejection. In the arthritis model, a single injection of serum from arthritic transgenic K/BxN mice into C57BL/6J mice results in inflammation of the joints with progressive arthritic symptoms, followed by disease resolution<sup>25</sup>. Of relevance to our question, this arthritis model is dependent on myeloid cells<sup>25</sup>, with apoptosis known to occur during disease. We first asked whether the full apoptotic secretome could alleviate inflammation in this arthritis model, and found that this was the case (Extended Data Fig. 10f). Administration of Memix-6 or Memix-3 metabolites after the induction of arthritis when the disease symptoms are already noticeable



resulted in significant attenuation of paw swelling and other arthritic parameters, compared with treatment with vehicle controls (Fig. 4d). Because FBP alone can have ameliorative roles in arthritis<sup>26</sup>, we further tested Memix-3, which does not contain FBP. Memix-3 metabolites not only alleviated paw swelling and external clinical arthritis parameters, but also significantly protected the joints from inflammation, bone erosion and cartilage erosion (Fig. 4e, f).

We also tested Memix-3 in a model of lung-transplant rejection, in which local innate and adaptive immune responses orchestrated by graft-resident antigen-presenting myeloid cells dictate graft acceptance or rejection. We transplanted allografts from the left lung of C57BL/10 mice to a minor antigen-mismatched C57BL/6 recipient<sup>27</sup> (Fig. 4g), and treated the graft recipients with Memix-3 or saline vehicle control on post-operative days 1 and 3. On day 7 after engraftment, the control mice treated with saline showed severe acute rejection of allografts<sup>28</sup>. Notably, mice treated with Memix-3 had only minimal inflammation in the transplanted lungs (Fig. 4h), suggestive of amelioration of lung rejection. Complementary flow cytometric analysis of the lung showed reduced CD4 and CD8 cells in the transplanted lungs of mice treated with Memix-3 (data not shown). Thus, a subset of apoptotic metabolites can be harnessed for beneficial effects in two different inflammatory settings in vivo.

Collectively, the data presented here advance several concepts. First, we identify specific metabolites that are released from apoptotic cells (different cell types and modes of apoptosis induction); the specificity could arise from metabolic changes in the apoptotic cells (for example, sustained production of spermidine), and/or the opening of specific channels (such as PANX1). Second, apoptotic cells are not inert corpses awaiting removal; instead, via the release of metabolites as good-bye signals they actively modulate several gene programs in the neighbouring cells within a tissue. Third, the ability of a cocktail of apoptotic metabolites to attenuate arthritic symptoms and the rejection of lung transplantation provide a proof-of-concept that it is possible to harness the beneficial therapeutic properties of apoptosis in specific inflammatory conditions.

## Online content

Any methods, additional references, Nature Research reporting summaries, source data, extended data, supplementary information, acknowledgements, peer review information; details of author contributions and competing interests; and statements of data and code availability are available at <https://doi.org/10.1038/s41586-020-2121-3>.

1. Fuchs, Y. & Steller, H. Programmed cell death in animal development and disease. *Cell* **147**, 742–758 (2011).
2. Rothlin, C. V., Carrera-Silva, E. A., Bosurgi, L. & Ghosh, S. TAM receptor signaling in immune homeostasis. *Annu. Rev. Immunol.* **33**, 355–391 (2015).

3. Lindsten, T. et al. The combined functions of proapoptotic Bcl-2 family members bak and bax are essential for normal development of multiple tissues. *Mol. Cell* **6**, 1389–1399 (2000).
4. Gregory, C. D. & Pound, J. D. Cell death in the neighbourhood: direct microenvironmental effects of apoptosis in normal and neoplastic tissues. *J. Pathol.* **223**, 178–195 (2011).
5. Ryoo, H. D., Gorenc, T. & Steller, H. Apoptotic cells can induce compensatory cell proliferation through the JNK and the Wntless signaling pathways. *Dev. Cell* **7**, 491–501 (2004).
6. Ke, F. F. S. et al. Embryogenesis and adult life in the absence of intrinsic apoptosis effectors BAX, BAK, and BOK. *Cell* **173**, 1217–1230.e17 (2018).
7. Medina, C. B. & Ravichandran, K. S. Do not let death do us part: ‘find-me’ signals in communication between dying cells and the phagocytes. *Cell Death Differ.* **23**, 979–989 (2016).
8. Elliott, M. R. et al. Nucleotides released by apoptotic cells act as a find-me signal to promote phagocytic clearance. *Nature* **461**, 282–286 (2009).
9. Van Opendenbosch, N. et al. Caspase-1 engagement and TLR-induced c-FLIP expression suppress ASC/caspase-8-dependent apoptosis by inflammasome sensors NLRP1b and NLRC4. *Cell Rep.* **21**, 3427–3444 (2017).
10. Cheken, F. B. et al. Pannexin 1 channels mediate ‘find-me’ signal release and membrane permeability during apoptosis. *Nature* **467**, 863–867 (2010).
11. Poon, I. K. H. et al. Unexpected link between an antibiotic, pannexin channels and apoptosis. *Nature* **507**, 329–334 (2014).
12. Good, M. E. et al. Pannexin 1 channels as an unexpected new target of the anti-hypertensive drug spironolactone. *Circ. Res.* **122**, 606–615 (2018).
13. Madeo, F., Eisenberg, T., Pietrocola, F. & Kroemer, G. Spermidine in health and disease. *Science* **359**, eaan2788 (2018).
14. Liu, X. et al. PNP1 release from mitochondria during apoptosis triggers decay of poly(A) RNAs. *Cell* **174**, 187–201.e12 (2018).
15. Morioka, S. et al. Efferocytosis induces a novel SLC program to promote glucose uptake and lactate release. *Nature* **563**, 714–718 (2018).
16. Wang, Y. et al. Mitochondrial fission promotes the continued clearance of apoptotic cells by macrophages. *Cell* **171**, 331–345.e22 (2017).
17. Perry, J. S. A. et al. Interpreting an apoptotic corpse as anti-inflammatory involves a chloride sensing pathway. *Nat. Cell Biol.* **21**, 1532–1543 (2019).
18. Ipseiz, N. et al. The nuclear receptor Nr4a1 mediates anti-inflammatory effects of apoptotic cells. *J. Immunol.* **192**, 4852–4858 (2014).
19. Chung, E. Y. et al. Interleukin-10 expression in macrophages during phagocytosis of apoptotic cells is mediated by homeodomain proteins Pbx1 and Prep-1. *Immunity* **27**, 952–964 (2007).
20. Zaiss, D. M. W., Gause, W. C., Osborne, L. C. & Artis, D. Emerging functions of amphiregulin in orchestrating immunity, inflammation, and tissue repair. *Immunity* **42**, 216–226 (2015).
21. Goessling, W. et al. Genetic interaction of PGE2 and Wnt signaling regulates developmental specification of stem cells and regeneration. *Cell* **136**, 1136–1147 (2009).
22. Shayakul, C., Cléménçon, B. & Hediger, M. A. The urea transporter family (SLC14): physiological, pathological and structural aspects. *Mol. Aspects Med.* **34**, 313–322 (2013).
23. Jha, A. K. et al. Network integration of parallel metabolic and transcriptional data reveals metabolic modules that regulate macrophage polarization. *Immunity* **42**, 419–430 (2015).
24. Scher, J. U. & Pillinger, M. H. The anti-inflammatory effects of prostaglandins. *J. Invest. Med.* **57**, 703–708 (2009).
25. Korganow, A. S. et al. From systemic T cell self-reactivity to organ-specific autoimmune disease via immunoglobulins. *Immunity* **10**, 451–461 (1999).
26. Veras, F. P. et al. Fructose 1,6-bisphosphate, a high-energy intermediate of glycolysis, attenuates experimental arthritis by activating anti-inflammatory adenosinergic pathway. *Sci. Rep.* **5**, 15171 (2015).
27. Krupnick, A. S. et al. Orthotopic mouse lung transplantation as experimental methodology to study transplant and tumor biology. *Nat. Protocols* **4**, 86–93 (2009).
28. Stewart, S. et al. Revision of the 1996 working formulation for the standardization of nomenclature in the diagnosis of lung rejection. *J. Heart Lung Transplant* **26**, 1229–1242 (2007).

**Publisher's note** Springer Nature remains neutral with regard to jurisdictional claims in published maps and institutional affiliations.

© The Author(s), under exclusive licence to Springer Nature Limited 2020

# Article

## Methods

### Reagents

Trovafoxacin, spironolactone, dexamethasone, spermidine, FBP, DHAP, IMP and GMP were obtained from Sigma. UDP-glucose was obtained from Abcam, and annexin V-Pacific Blue was from BioLegend. 7AAD, TO-PRO-3 anti-CD11b-PE (clone M1/70), anti-CD11c-PE (clone N418), and anti-CD16/CD32 (clone 93) were obtained from Invitrogen. Antibodies specific for mouse CD95 were obtained from BD. Human anti-Fas (clone CH11) was obtained from Millipore. Other reagents were obtained as follows: ABT-737 (abcam), TRAIL (Sigma) and zVAD-FMK (Enzo).

### Mice

C57BL/10 and C57BL/6J wild-type mice were acquired from Jackson Laboratories. *Panx1*<sup>fl/fl</sup> and *Panx1*<sup>-/-</sup> mice have previously been described<sup>11</sup>. To generate mice with deletion of *Panx1* in thymocytes, *Panx1*<sup>fl/fl</sup> mice were crossed to *Cd4-cre* mice (Taconic). KRN T cell receptor (TCR) transgenic mice were a gift from D. Mathis and were bred to non-obese diabetic (NOD) mice (Jackson Laboratories) to obtain the K/BxN mice, which develop progressive spontaneous arthritis<sup>29</sup>. Serum was collected from 9-week-old K/BxN mice by cardiac puncture. Animal procedures were approved and performed according to the Institutional Animal Care and Use Committee (IACUC) at the University of Virginia.

### Apoptosis induction

Wild-type Jurkat E6.1 (ATCC) or dominant-negative PANX1-expressing (PANX1-DN)<sup>10</sup> cells were resuspended in RPMI-1640 containing 1% BSA, 1% penicillin-streptomycin-glutamine (PSQ), and 10 mM HEPES and treated with 250 ng ml<sup>-1</sup> anti-Fas (clone CH11), 10 μM ABT-737, or exposed to 150 mJ cm<sup>-2</sup> UV-C irradiation for 1–2 min (Stratalinker). Jurkat cells were incubated for 4 h after apoptosis induction. For apoptosis induction in the presence of PANX1 inhibitors, Jurkat cells were treated with spironolactone (50 μM) or trovafoxacin (25 μM) in RPMI containing 1% BSA and 1% PSQ.

Primary thymocytes isolated from 4–6-week-old wild-type or *Panx1*<sup>-/-</sup> mice were treated with 5 μg ml<sup>-1</sup> anti-Fas (clone Jo2), that was subsequently crosslinked with 2 μg ml<sup>-1</sup> protein G. Primary thymocytes were incubated for 1.5 h after apoptosis induction.

BMDMs from *B6*<sup>Nlrp1b<sup>+</sup> CI<sup>-/-</sup> CII<sup>-/-</sup></sup> mice (C57BL/6J mice that express a functional *Nlrp1b* transgene (*B6*<sup>Nlrp1b<sup>+</sup></sup>)) crossed with mice lacking caspase-1 (*CI*, also known as *Casp1*) and caspase-11 (*CII*, also known as *Casp4*) were a gift from M. Lamkanfi's laboratory. BMDMs were generated by culturing mouse bone marrow cells in RPMI medium conditioned with 10% dialysed serum and 1% penicillin-streptomycin. The medium was supplemented with 20 ng ml<sup>-1</sup> of purified mouse M-CSF. Cells were incubated in a humidified atmosphere containing 5% CO<sub>2</sub> for 6 days. BMDMs from wild-type B6 or *B6*<sup>Nlrp1b<sup>+</sup> CI<sup>-/-</sup> CII<sup>-/-</sup></sup> mice were seeded in 6-well plates and, the next day, either left untreated or stimulated with 500 ng ml<sup>-1</sup> anthrax protective antigen (500 ng ml<sup>-1</sup>, Quadratech) and anthrax lethal factor (250 ng ml<sup>-1</sup>, Quadratech). Supernatants from either untreated or treated BMDMs were collected. Cellular debris was removed via centrifugation, and the clarified supernatant was used for metabolic profiling.

A549 cells were treated with 10 μM ABT-737 or exposed to 600 mJ cm<sup>-2</sup> UV irradiation, and incubated for 24 h. HCT-116 cells were treated with 10 μM ABT-737 or 100 ng ml<sup>-1</sup> TRAIL and incubated for 24 h. All cells were pre-treated for 10 min with 50 μM zVAD before apoptosis induction in indicated experiments. All cells were incubated at 37 °C with 5% CO<sub>2</sub> for indicated times.

### Metabolite detection

Spermidine detection was measured using a colorimetric kit (Cloud-Clone) via manufacturer's protocol. In brief, supernatants taken from cells under specified conditions were centrifuged at 1,000g for 20 min.

All reagents were brought to room temperature before use. Then, 50 μl of sample was added to each well followed by equal volume of detection reagent A and the plate was mixed. Samples were incubated covered for 1 h at 37 °C. Wells were washed with wash solution three times before the addition of detection reagent B, after which samples were incubated for another 30 min at 37 °C. Samples were washed five more times. Substrate solution (90 μl) was then added to each well and incubated for 10 min at 37 °C, after which stop solution (50 μl) was added, and the plate was mixed and immediately measured at 450 nm on a plate reader (Flex Station 3). Analysis was performed by back calculation to the standard curve, background subtraction and normalization to live cell controls.

ATP was measured using a luciferase-based kit (Promega) via the manufacturer's protocol. All reagents were equilibrated to room temperature before use. In brief, supernatants taken from cells under specified conditions were immediately moved to ice, and centrifuged at 500g for 5 min. Samples were placed back on ice and 50 μl of samples and 50 μl of luciferase reagent were mixed in a 96-well opaque plate. Luminescence was immediately measured on the Flex Station 3. Analysis was performed by back calculation to the standard curve, background subtraction and normalization to live cell controls.

Glycerol-3-phosphate and creatine were measured on the basis of manufacturers' protocols (Abcam). In brief, supernatants were taken from specified culture conditions and spun at 500g. Then, 50 μl of supernatant was added to a 96-well plate. Detection reagents were prepared as indicated in the protocol and added to respective wells. Samples were incubated for 40 min or 1 h for glycerol-3-phosphate or creatine, respectively. Absorbance at 450 nm or fluorescence at excitation/emission 535/587 nm was measured for glycerol-3-phosphate or creatine, respectively.

### Flow cytometry of apoptosis and PANX1 activation

Apoptotic cells were stained with annexin V-Pacific Blue, 7AAD and TO-PRO-3 for 15 min at room temperature in annexin V binding buffer (140 mM NaCl, 2.5 μM CaCl<sub>2</sub>, 10 mM HEPES) and subjected to flow cytometry on Attune NxT (Invitrogen). Data were analysed using FlowJo v.10 software.

### Metabolomics analysis of apoptotic supernatant and cell pellet

Sample extraction, processing, compound identification, curation and metabolomic analyses were carried out at Metabolon and Human Metabolome Technologies (HMT)<sup>30</sup>. In brief, supernatants were separated from cell pellets via sequential centrifugation and frozen before shipment for metabolomic analysis. For HMT, supernatant samples were spiked with 10 μl of water with internal standards, then filtered through a 5-kDa cut-off filter to remove macromolecules and small vesicles. Cationic compounds were diluted and measured using positive ion mode electrospray ionization (ESI) via capillary electrophoresis–time-of-flight mass spectrometry (CE–TOF/MS). Anionic compounds were measured in the positive or negative ion mode ESI using capillary electrophoresis–tandem mass spectrometry (CE–MS/MS). Samples were diluted to improve the capillary electrophoresis–triple quadrupole mass spectrometry (CE–QqQMS) analysis. Peak identification and metabolite quantification were determined using migration time, mass-to-charge ratio, and the peak area normalized to the internal standard and standard curves. Concentrations reported are on a per million cell basis, which was derived by back calculations on the cell number that was used in the experimental set-up.

For untargeted metabolomics analysis by Metabolon, recovery standards were added to samples to monitor quality control of the analysis. Samples were precipitated in methanol with shaking for 2 min. Samples were then placed on the TurboVap to remove organic solvent and the samples were stored overnight under nitrogen gas. Samples were analysed under four different conditions; two for analysis by two separate reverse phase (RP)/ultra-performance liquid chromatography

(UPLC)–MS/MS methods with positive ion mode ESI, one for analysis by RP/UPLC–MS/MS with negative ion mode ESI, and one for analysis by HILIC/UPLC–MS/MS with negative ion mode ESI. Using a library based on authenticated standards that contains the retention time/index, mass-to-charge ratio ( $m/z$ ), and chromatographic data (including MS/MS spectral data) on all molecules in the library (Metabolon), the metabolite identification could be performed with reverse scores between the experimental data and authenticated standards. Although there may be similarities based on one of these factors, the use of all three data points can be used to identify biochemicals.

#### Metabolite flux experiments with [ $^{13}\text{C}$ ]arginine labelling

Cells were re-suspended in arginine-free RPMI medium containing 10% dialysed serum, supplemented with 1 mM  $^{13}\text{C}_6$ -labelled L-arginine HCl (Thermo Fischer Scientific). Cells were either exposed to UV or left untreated. This step was performed within 1 min of the addition of medium containing [ $^{13}\text{C}$ ]arginine to cells. Cells were then incubated at 37 °C. Samples were collected every hour to trace the incorporation of the label from arginine into the polyamine pathway for both UV-exposed and live cells. Where indicated, cells were pre-treated with zVAD-FMK to inhibit caspases.

Metabolite extraction from the pellet or supernatant was performed by adding 300  $\mu\text{l}$  of 6% trichloroacetic acid (TCA) to a pellet of 4 million cells on ice. The samples were then vortexed thoroughly at 4 °C, followed by centrifugation to remove cell debris. Supernatant (100  $\mu\text{l}$ ) was mixed with  $\text{Na}_2\text{CO}_3$  (900  $\mu\text{l}$  of 0.1 M, pH 9.3), followed by isobutyl chloroformate addition (25  $\mu\text{l}$ ). The mixture was incubated at 37 °C for 30 min and then centrifuged for 10 min at 20,000g. Supernatant (800  $\mu\text{l}$ ) was transferred to a fresh tube, followed by the addition of 1,000  $\mu\text{l}$  diethyl ether and vortexing. The mixture was allowed to sit at room temperature for 10 min for phase separation after which, 900  $\mu\text{l}$  of sample was collected in a fresh Eppendorf tube. The samples were dried via Speedvac. For liquid chromatography–mass spectrometry (LC–MS) analysis, 150  $\mu\text{l}$  of 1:1 mixture of 0.2% acetic acid in water and 0.2% of acetic acid in acetonitrile was added to the dried sample.

#### RNA-seq analysis

LR73 cells (ATCC) were plated at  $10^5$  per well in 24-well tissue culture plates and cultured for 16 h at 37 °C with 5%  $\text{CO}_2$ . The cells were then rinsed with PBS, and fresh supernatants taken from live Jurkat, apoptotic Jurkat (UV), or PANX1-DN apoptotic Jurkat (UV) cells were added for 4 h (as described in ‘Apoptosis induction’). Total RNA was collected using the Nucleospin RNA kit (Macherey-Nagel) and an mRNA library was constructed with Illumina TruSeq platform. Transcriptome sequencing using an Illumina NextSeq 500 cartridge was then performed on samples from four independent experiments. RNA-seq data were analysed using Rv1.0.136 and the R package DESeq2 for differential gene expression, graphical representation, and statistical analysis.

#### Quantitative reverse transcription PCR analysis

RNA was extracted from cells treated with different live or apoptotic supernatants. Where indicated, supernatants were filtered through a 3-kDa filter as suggested by manufacturer’s protocol. In brief, supernatants were separated from cells and large vesicles via sequential centrifugations. Supernatants were then added to 3-kDa filters (Millipore) and centrifuged for 1 h at 3,000g before the addition of supernatant to live LR73 cells. Nucleospin RNA kit (Macherey-Nagel) was used for RNA extraction and cDNA was synthesized using QuantiTect Reverse Transcription Kit (Qiagen). Gene expression of indicated genes was performed using Taqman probes (Applied Biosystems) and the StepOnePlus Real Time PCR System (Applied Biosystems).

#### Thymocyte death induction in vivo

Six- to eight-week-old *Panx1*<sup>fl/fl</sup> or *Panx1*<sup>fl/fl</sup> *Cd4-cre* mice were injected intraperitoneally with dexamethasone (250  $\mu\text{g}$ ). Thymus was obtained

6 h after injection and single cell suspensions were prepared using 70- $\mu\text{m}$  strainers (Fisher). An aliquot of digested tissue was taken to measure the extent of thymocyte cell death and PANX1 activation using annexin V-Pacific Blue, 7AAD, and TO-PRO-3, as described in ‘Flow cytometry of apoptosis and PANX1 activation’. Samples were acquired on Attune NxT (Invitrogen) and analysed using FlowJo v.10 Software.

#### Thymic myeloid cell isolation and gene expression

Six- to eight-week old *Panx1*<sup>fl/fl</sup> or *Panx1*<sup>fl/fl</sup> *Cd4-cre* mice were injected with dexamethasone and single cell suspensions of thymus were prepared as described above. After isolation, cells were incubated with anti-CD16/CD32 (Fc-Block, Invitrogen) for 20 min at 4 °C. Cells were then stained with anti-CD3-PE and run through a MACS kit using anti-PE microbeads to ‘de-bulk’ the cell suspension and remove most thymocytes. Cell flow-through (CD3-negative population) was collected and stained with anti-CD11b-PE and anti-CD11c-PE antibodies for 30 min at 4 °C. Stained cells were purified using the anti-PE MicroBeads MACS kit (Miltenyi Biotec), following the manufacturer’s protocol. Sample aliquots were run on the Attune NxT (Invitrogen) and analysed using FlowJo v.10 Software. Total RNA from purified cells was isolated Nucleospin RNA kit (Macherey-Nagel) for cDNA synthesis and quantitative reverse transcription PCR (qRT–PCR), as described in ‘Quantitative reverse transcription PCR analysis’.

#### Memix preparation and in vivo treatment

The metabolite mixture Memix-6 was composed of the six metabolites: spermidine, FBP, DHAP, GMP, IMP and UDP-glucose. Memix-3 was composed of spermidine, GMP and IMP. Concentrations of metabolites used for in vitro LR73 phagocyte treatment were as follows (based on targeted metabolomics): IMP (3.3  $\mu\text{M}$ ), DHAP (36  $\mu\text{M}$ ), FBP (0.5  $\mu\text{M}$ ), GMP (2.1  $\mu\text{M}$ ), UDP-glucose (2  $\mu\text{M}$ ) and spermidine (0.3  $\mu\text{M}$ ). Concentrations of metabolites used for in vivo mice treatment were as follows: IMP (100  $\text{mg kg}^{-1}$ ), DHAP (50  $\text{mg kg}^{-1}$ ), FBP (500  $\text{mg kg}^{-1}$ ), GMP (100  $\text{mg kg}^{-1}$ ), UDP-glucose (100  $\text{mg kg}^{-1}$ ) and spermidine (100  $\text{mg kg}^{-1}$ ).

#### K/BxN induced arthritis

C57BL/6J mice were given intraperitoneal injections of 150  $\mu\text{l}$  of serum from K/BxN mice on day 0 and paw swelling was measured at indicated time points using a calliper (Fisher). Measurements are presented as the percentage change from day 0. On day 1, mice were randomly assigned into three groups and given daily intraperitoneal injections of Memix-3, Memix-6 or vehicle up to day 5. In separate experiments, mice on day 1 were randomly assigned and given daily injections of either live or apoptotic supernatants up to day 5. Clinical scores were assigned for each paw as follows: 0, no paw swelling or redness observed; 1, redness of the paw or a single digit swollen, normal V shape of the hind foot (the foot at the base of the toes is wider than the heel and ankle); 2, two or more digits swollen or visible swelling of the paw, U shape of the hind foot (the ankle and the midfoot are equal in thickness); and 3, reversal of the V shape of the hind foot into an hourglass shape (the foot is wider at the heel than at the base of the toes). A combined clinical score of all paws is presented. Paw measurements and clinical score assignments were performed by an investigator blinded to the treatment groups.

#### Lung transplant rejection model

Orthotopic left lung transplantation was carried out according to previous reports<sup>27</sup>. To study the alteration of allo-immune response by a minor antigen-mismatched combination, C57BL/10 donor and C57BL/6 recipient mice were used. The recipient mice were administered with Memix-3 or vehicle intraperitoneally on post-operative days 1 and 3. On day 7, the recipient mice were euthanized and left lung allografts were obtained and processed for histology.

#### Histology

Lungs were fixed in formalin, sectioned and stained with H&E. The acute rejections were graded according to the International Society

# Article

for Heart and Lung Transplantation (ISHLT) A grade criteria by a lung pathologist who was blinded to the experimental settings<sup>28</sup>. For the model of arthritis, mice were euthanized at day 8 of K/BxN-serum-induced arthritis and the hind paws were fixed in 10% formalin (Fisher). Decalcification, sectioning, paraffin embedding, H&E staining and safranin O staining was performed by HistoTox Labs. Images of ankle sections were taken on an EVOS FL Auto (Fisher) and analysed using the accompanying software. Histology scoring was performed by an investigator blinded to the mouse treatment. For inflammation and cartilage erosion scoring, the following criteria were used: 0, none; 1, mild; 2, moderate; and 3, severe. For bone erosion scoring, the following criteria were used: 0, no bone erosions observed; 1, mild cortical bone erosion; 2, severe cortical bone erosion without the loss of bone integrity; and 3, severe cortical bone erosion with the loss of cortical bone integrity and trabecular bone erosion.

## Statistical analysis

Statistical significance was determined using GraphPad Prism 7, using unpaired Student's two-tailed *t*-test (paired and unpaired), one-way ANOVA, or two-way ANOVA according to test requirements. Grubbs' outlier test was used to determine outliers, which were excluded from final analysis. \**P* < 0.05, \*\**P* < 0.01, \*\*\**P* < 0.001. No statistical methods were used to predetermine sample size. Unless otherwise stated, experiments were not randomized and investigators were not blinded to allocation during experiments and outcome assessment.

## Reporting summary

Further information on research design is available in the Nature Research Reporting Summary linked to this paper.

## Data availability

RNA-seq data have been submitted to the Gene Expression Omnibus (GEO) under accession number GSE131906. Source Data for Figs. 1–4 and Extended Data Figs. 1–10 are provided with the paper. Other data

that support the findings of this study are available from the corresponding author upon request.

## Code availability

R code used for heat map generation, volcano plots and bioinformatic analysis is available from the corresponding author upon request.

29. Kouskoff, V. et al. Organ-specific disease provoked by systemic autoimmunity. *Cell* **87**, 811–822 (1996).
30. Evans, A. M., DeHaven, C. D., Barrett, T., Mitchell, M. & Milgram, E. Integrated, nontargeted ultrahigh performance liquid chromatography/electrospray ionization tandem mass spectrometry platform for the identification and relative quantification of the small-molecule complement of biological systems. *Anal. Chem.* **81**, 6656–6667 (2009).

**Acknowledgements** The authors thank members of the Ravichandran laboratory, and members of the Pannexin Interest Group at UVA for numerous discussions, and critical reading of the manuscript, and M. Lamkanfi for the *Nlrp1b* transgenic mice. This work is supported by grants to K.S.R. from NHLBI (P01HL120840), NIGMS R35GM122542, and the Center for Cell Clearance/University of Virginia School of Medicine, and the Odysseus Award from the FWO, Belgium, EOS Grant from the FWO (3083753-DECODE), and the NHLBI (P01HL120840) and NIAID (R21 AI139967 and R21 AI135455) to U.L. Additional support was received through the NIH T32 Pharmacology Training Grant (T32GM007055) (C.B.M. and B.B.), Mark Foundation Fellowship from the Cancer Research Institute and a K99 from the NCI (to J.S.A.P.), and the Kanye Foundation of Japan (to S.M.). Current address for Justin Perry: Immunology Program, Memorial Sloan-Kettering Cancer Center, New York, NY. P.M. is supported by a FWO-Senior postdoctoral fellowship.

**Author contributions** C.B.M. and K.S.R. designed the experiments. C.B.M. performed most experiments. P.M.M. performed the macrophage apoptosis and polyamine tracing experiments. S.A. and C.B.M. performed the arthritis experiments. J.S.A.P. assisted with the bioinformatic analyses. Y.G. and A.S.K. assisted with the lung transplant experiments. S.M., B.B. and S.W. provided experimental expertise on a few specific experiments. B.G. assisted with the polyamine mass spectrometry and U.L. provided mice and conceptual advice. C.B.M. and K.S.R. wrote the manuscript with input from co-authors.

**Competing interests** The authors declare no competing interests.

## Additional information

**Supplementary information** is available for this paper at <https://doi.org/10.1038/s41586-020-2121-3>.

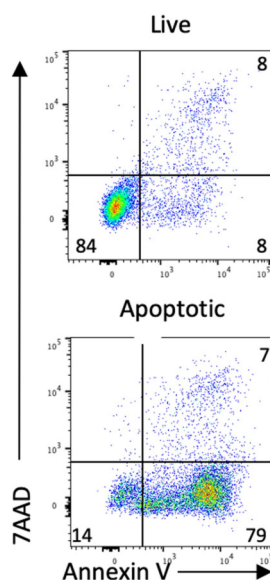
**Correspondence and requests for materials** should be addressed to K.S.R.

**Peer review information** Nature thanks Seamus Martin, Gary Siuzdak and the other, anonymous, reviewer(s) for their contribution to the peer review of this work.

**Reprints and permissions information** is available at <http://www.nature.com/reprints>.

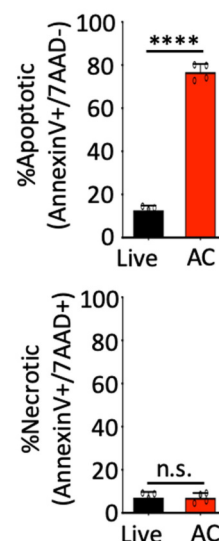
a

Jurkat cells – 4 hours UV treatment

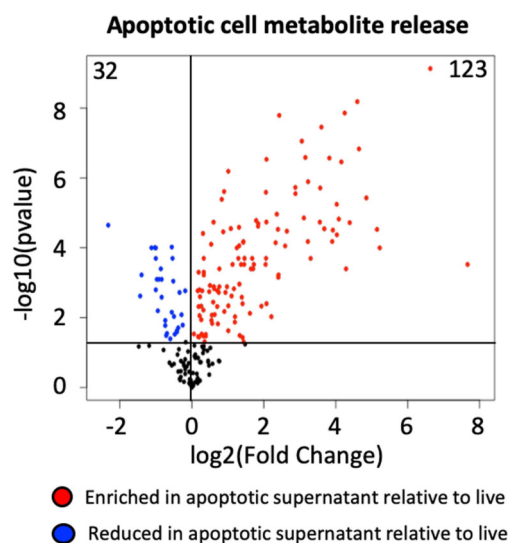


b

Jurkat cells – 4 hours UV treatment

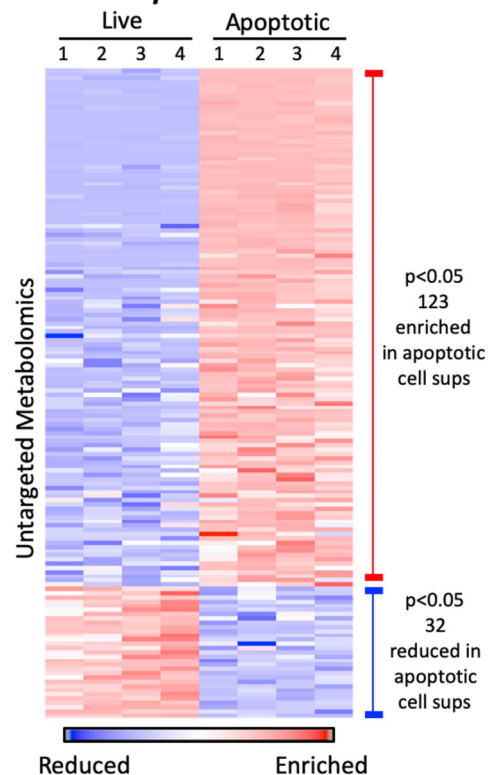


c



d

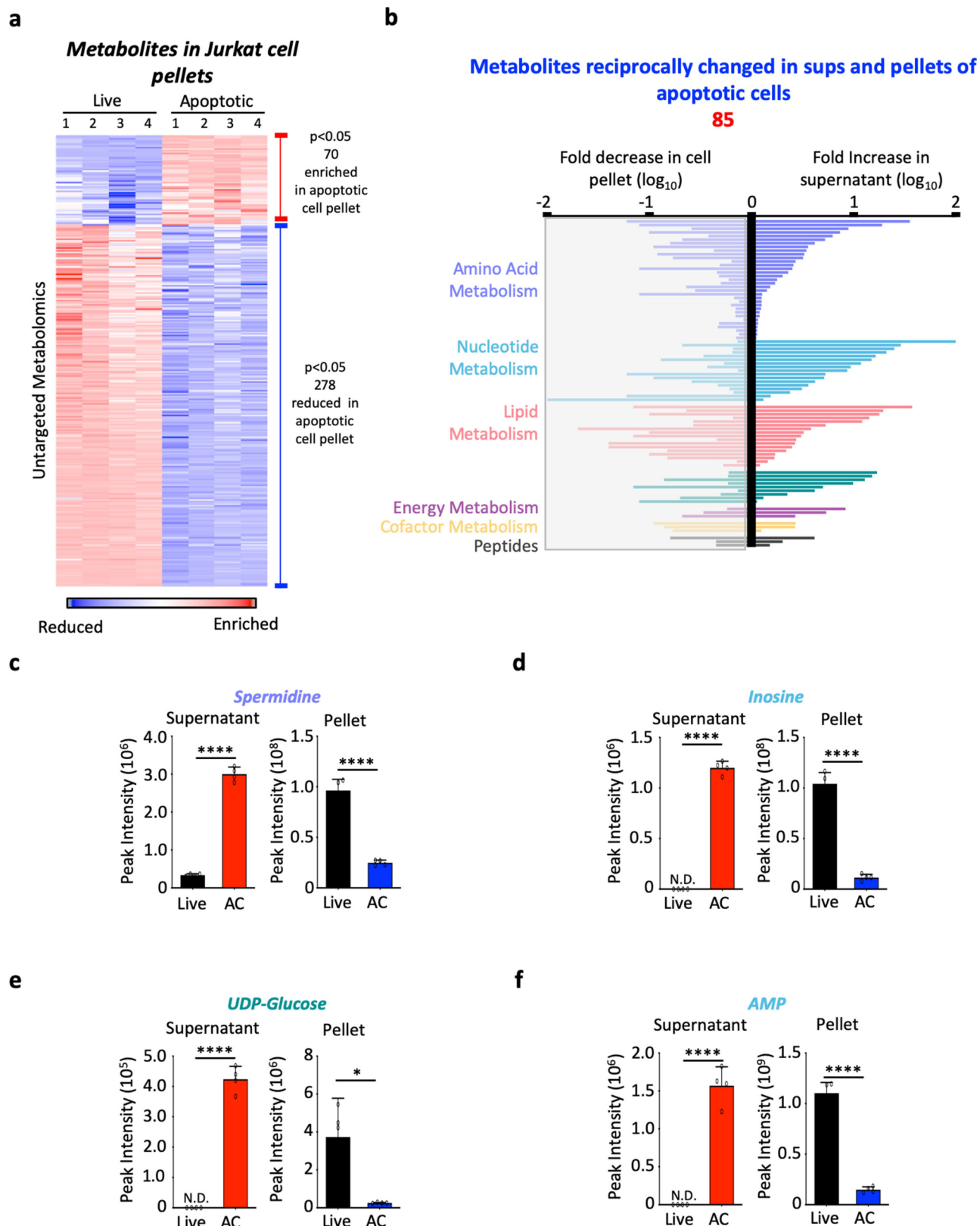
Metabolites in Jurkat cell supernatants



**Extended Data Fig. 1 | Metabolite release from apoptotic Jurkat cells.** a, Jurkat cells were induced to undergo apoptosis by UV irradiation. Staining with 7AAD and annexin V (AV) was used to determine the percentage of live (AV<sup>-</sup>7AAD<sup>-</sup>), apoptotic (AV<sup>+</sup>7AAD<sup>-</sup>) or necrotic (AV<sup>+</sup>7AAD<sup>+</sup>) cells after 4 h. b, Quantitative analysis of apoptosis (top) and secondary necrosis (bottom) ( $n=4$ ). Data are mean  $\pm$  s.d. \*\*\*\* $P<0.0001$ , unpaired two-tailed Student's  $t$ -test.

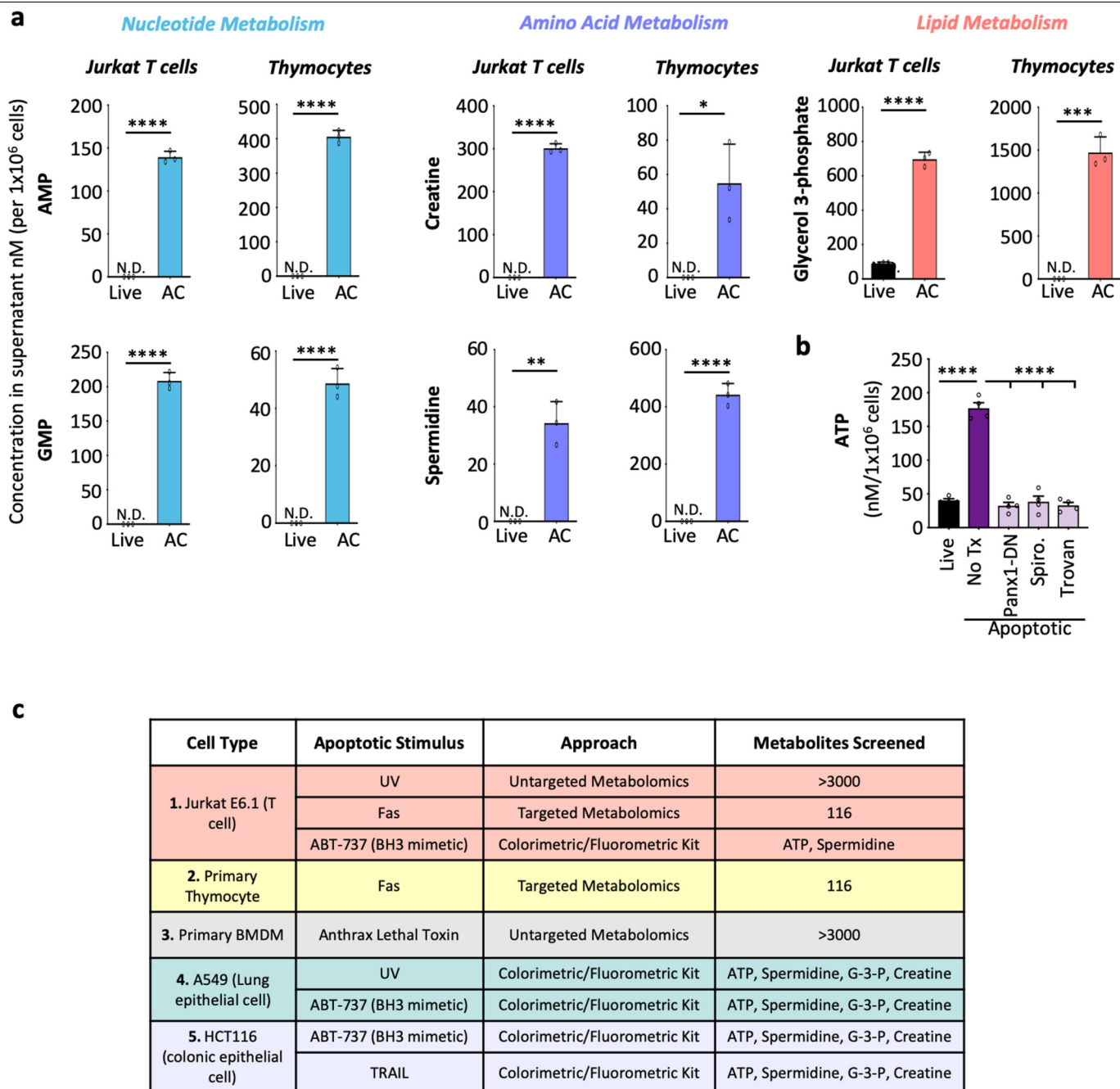
c, d, Volcano plot (c) and heat map (d) from untargeted metabolomics of supernatants from Jurkat T cells, representing statistically enriched or reduced ( $P<0.05$ , two-sided Welch's two-sample  $t$ -test) metabolites in the apoptotic supernatants relative to live supernatants. Data are representative of four biological replicates.





**Extended Data Fig. 2 | Reciprocal metabolite changes between apoptotic supernatant and pellet.** **a**, Heat map produced from untargeted metabolomics of Jurkat T cell pellets, representing statistically enriched or reduced ( $P < 0.05$ , two-sided Welch's two-sample  $t$ -test) metabolites in the apoptotic pellet relative to the live cell pellet ( $n = 4$  biologically independent samples). **b**, Bi-directional plot representing the 85 metabolites that were statistically enriched in the apoptotic supernatant and simultaneously

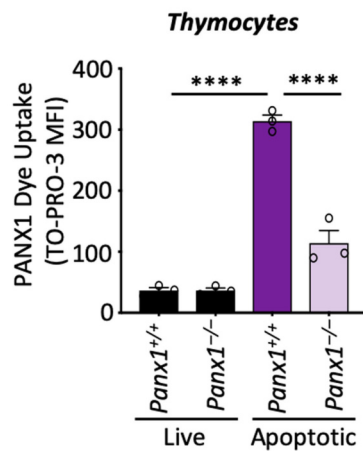
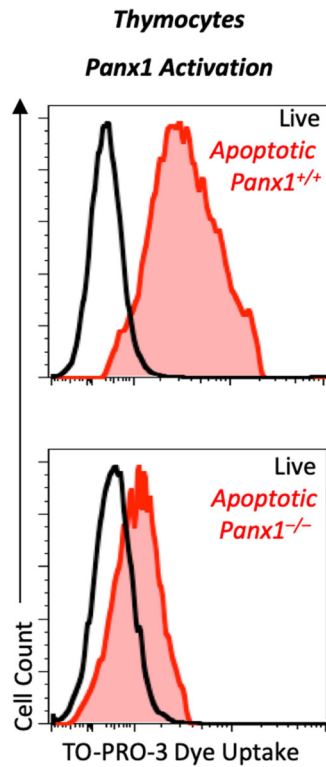
reduced in the apoptotic cell pellet relative to live cell conditions ( $P < 0.05$ , two-sided Welch's two-sample  $t$ -test). Metabolites were grouped by metabolic pathways ( $n = 4$  biologically independent samples). **c-f**, Mass spectrometry was used to determine the relative amount of spermidine (**c**), inosine (**d**), UDP-glucose (**e**) and AMP (**f**) in supernatants and cell pellets from Jurkat T cells in live and apoptotic conditions ( $n = 4$  biologically independent samples). \* $P = 0.014$ , \*\*\*\* $P < 0.0001$ , unpaired two-tailed Student's  $t$ -test. Data are mean  $\pm$  s.d.



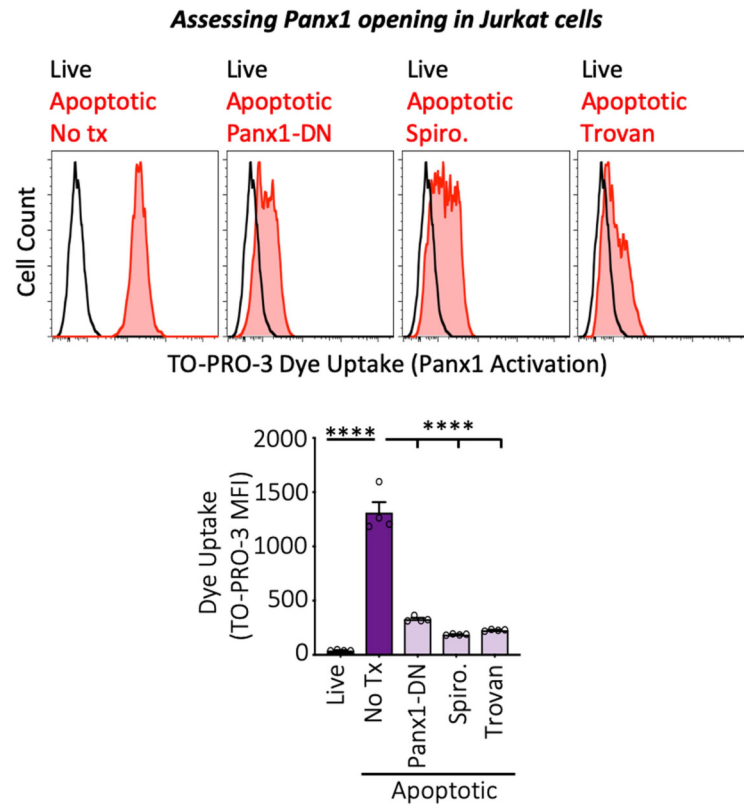
**Extended Data Fig. 3 | Conserved metabolite release during apoptosis. a,** Mass spectrometry was used to measure the concentration of the five metabolites that were released across all conditions and platforms tested, in live or apoptotic supernatants per million Jurkat T cells or isolated primary thymocytes (back-calculated from total cells used in experimental set-up) ( $n=3$ ). Metabolites are grouped by metabolic pathways. Data are mean  $\pm$  s.d.  $^*P=0.014$ ,  $^{**}P=0.0014$ ,  $^{***}P=0.0002$ ,  $^{****}P<0.0001$ , unpaired two-tailed

Student's  $t$ -test. **b,** The concentration of ATP released in the supernatant across the different apoptotic Jurkat cells was determined by luciferase assay ( $n=4$ ). Data are mean  $\pm$  s.e.m.  $^{****}P<0.0001$ , ordinary one-way ANOVA with Turkey's multiple comparison test. **c,** Table outlining the different cell types, apoptotic stimuli, techniques and metabolites screened for untargeted (more than 3,000 features or compounds) and targeted (116 metabolites) metabolomics, including ATP, spermidine, glycerol-3-phosphate and creatine.

a

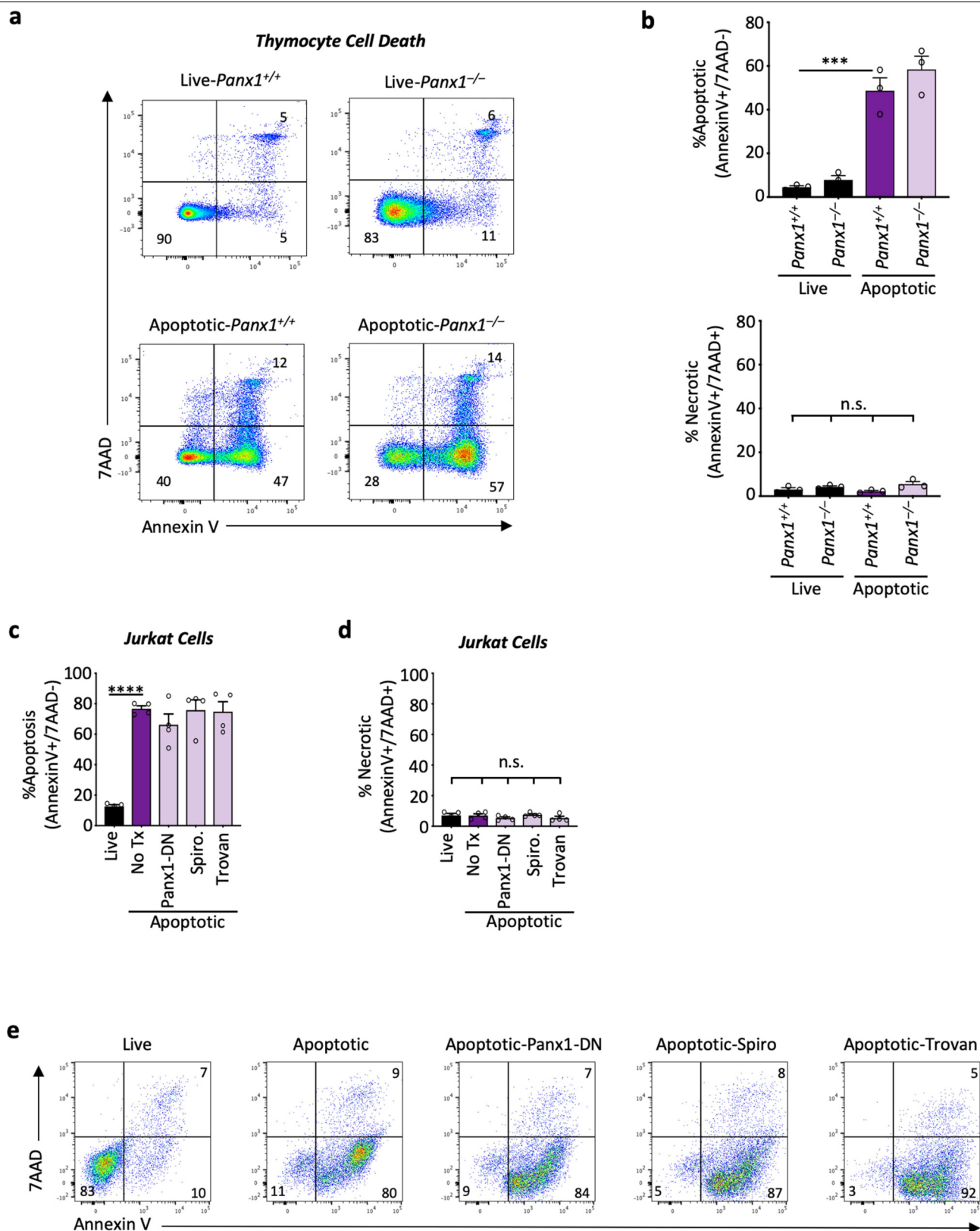


b



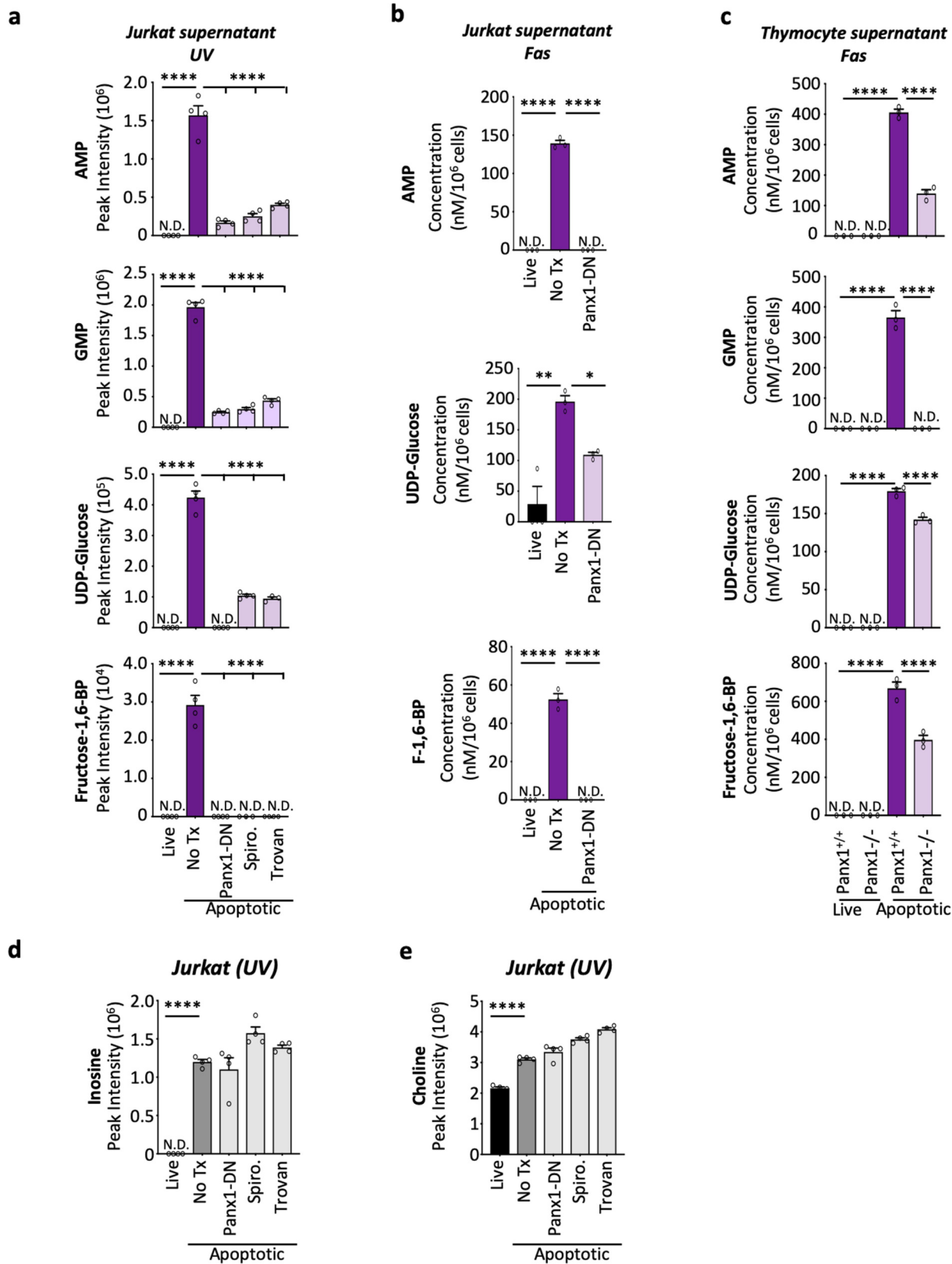
**Extended Data Fig. 4 | PANX1 activation and inhibition during cell death. a,** Top, representative histograms of TO-PRO-3 dye uptake in thymocytes across the different conditions. Bottom, PANX1 activation in live and apoptotic thymocytes from wild-type (*Panx1*<sup>+/+</sup>) and PANX1-knockout (*Panx1*<sup>-/-</sup>) mice as assessed via flow cytometry by measuring the mean fluorescent intensity of TO-PRO-3 dye uptake ( $n = 3$  biological replicates). Data are mean  $\pm$  s.e.m. \*\*\*\* $P < 0.0001$ , ordinary one-way ANOVA with Turkey's multiple comparison

test. **b,** Top, representative histograms of TO-PRO-3 dye uptake in Jurkat cells, across the different conditions described. Bottom, PANX1 activation as assessed by flow cytometry of the uptake of TO-PRO-3 dye in apoptotic wild-type Jurkat cells, Jurkat cells expressing mutant PANX1-DN, and Jurkat cells treated with PANX1 inhibitor spironolactone (50  $\mu$ M) or trovafloxacin (25  $\mu$ M) ( $n = 4$  biological replicates). Data are mean  $\pm$  s.e.m. \*\*\*\* $P < 0.0001$ , ordinary one-way ANOVA with Turkey's multiple comparison test.



**Extended Data Fig. 5 | PANX1 inhibition does not influence apoptotic cell death.** **a**, Control (*Panx1*<sup>+/+</sup>) or *Panx1*<sup>-/-</sup> thymocytes were treated with anti-Fas antibody (5  $\mu\text{g ml}^{-1}$ ) for 1.5 h. Cells were stained with 7AAD and annexin V to determine the percentage of live, apoptotic or necrotic cells, as in Extended Data Fig. 1a. **b**, Quantification of apoptosis (top) and secondary necrosis (bottom) of control and PANX1-knockout thymocytes ( $n=3$ ). Data are

mean  $\pm$  s.e.m. \*\*\* $P=0.0004$ , ordinary one-way ANOVA with Turkey's multiple comparison test. **c**, **d**, Quantification of apoptosis (**c**) and secondary necrosis (**d**) from Jurkat cells before metabolomics analysis ( $n=4$ ). Data are mean  $\pm$  s.e.m. \*\*\*\* $P<0.0001$ , ordinary one-way ANOVA with Turkey's multiple comparison test. **e**, Cells were stained with 7AAD and annexin V to determine the percentage of live, apoptotic or necrotic cells.



Extended Data Fig. 6 | See next page for caption.

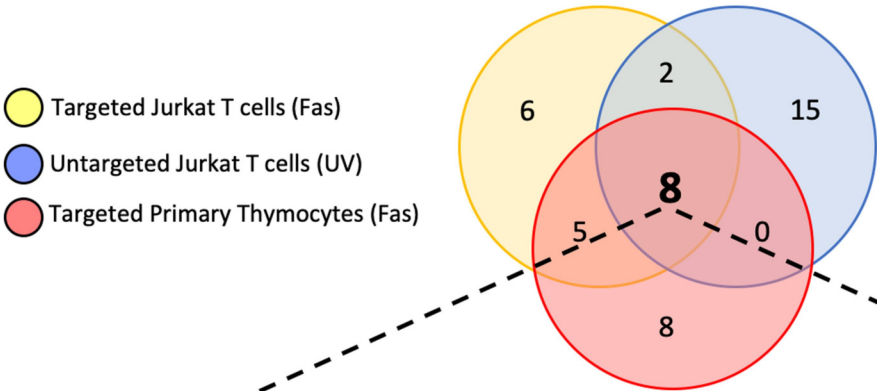


**Extended Data Fig. 6 | PANX1-dependent metabolite release during**

**apoptosis. a**, Mass spectrometry was used to determine the relative amounts of AMP, GMP, UDP-glucose and FBP in supernatants from Jurkat T cells across different conditions ( $n = 4$ ). Data are mean  $\pm$  s.e.m. \*\*\*\* $P < 0.0001$ , ordinary one-way ANOVA with Turkey's multiple comparison test. **b**, Jurkat cells were induced to undergo apoptosis by treatment with anti-Fas antibody ( $250 \text{ ng ml}^{-1}$ ). Mass spectrometry was used to measure the absolute concentration per million cells of AMP (top), UDP-glucose (middle) and FBP (F-1,6-BP) (bottom) in the supernatants of Jurkat T cells across different conditions (back-calculated from total cells used in experimental set-up) ( $n = 3$ ). Data are mean  $\pm$  s.e.m. \* $P = 0.031$ , \*\* $P = 0.0013$ , \*\*\*\* $P < 0.0001$ , ordinary

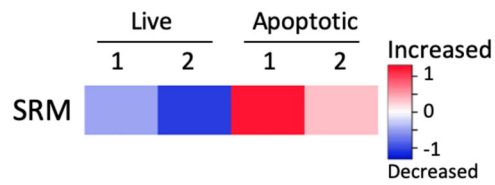
one-way ANOVA with Turkey's multiple comparison test. **c**, Mass spectrometry was used to determine the concentrations of AMP, GMP, UDP-glucose and FBP per million cells (back-calculated from total cells used in experimental set-up) in the supernatant from isolated primary thymocytes across different conditions ( $n = 3$ ). Data are mean  $\pm$  s.e.m. \*\*\*\* $P < 0.0001$ , ordinary one-way ANOVA with Turkey's multiple comparison test. **d, e**, Relative concentrations of inosine (**d**) and choline (**e**) in live, apoptotic or apoptotic supernatants in which PANX1 was inhibited were determined by mass spectrometry ( $n = 4$ ). Data are mean  $\pm$  s.e.m. \*\*\*\* $P < 0.0001$ , ordinary one-way ANOVA with Turkey's multiple comparison test.

Panx1 dependent metabolite release

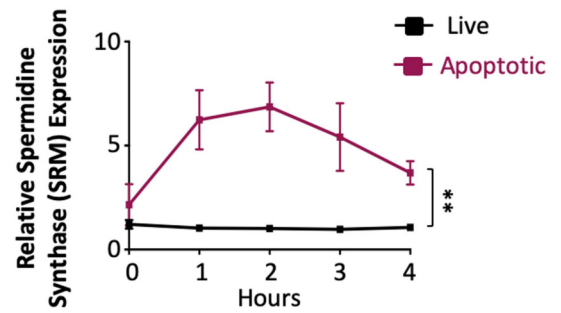
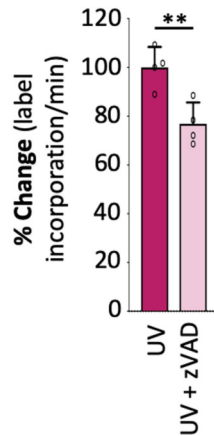


Panx1-depenedent metabolites (Consistent across all platforms/conditions)	Targeted (Jurkat) (nM/10 <sup>6</sup> cells)			Untargeted (Jurkat) (Peak Intensity)			Targeted (Thymocytes) (nM/10 <sup>6</sup> cells)		
	Live	Apoptotic	Apoptotic Px1DN	Live	Apoptotic	Apoptotic Px1DN	Live	Apoptotic Panx1 <sup>+/+</sup>	Apoptotic Panx1 <sup>-/-</sup>
spermidine	N.D.	34	N.D.	0.3x10 <sup>6</sup>	3.0x10 <sup>6</sup>	0.8x10 <sup>6</sup>	N.D.	441	49
dihydroxyacetone phosphate (DHAP)	N.D.	3559	650	N.D.	1.2x10 <sup>6</sup>	0.2x10 <sup>6</sup>	N.D.	1471	581
Glycerol 3 - phosphate	89	697	359	0.4x10 <sup>6</sup>	5.4x10 <sup>6</sup>	1.6x10 <sup>6</sup>	42	248	166
fructose- 1,6- biphosphate	N.D.	52	N.D.	N.D.	2.9x10 <sup>4</sup>	N.D.	N.D.	668	397
adenosine 5'-monophosphate (AMP)	N.D.	139	N.D.	N.D.	1.6x10 <sup>6</sup>	0.2x10 <sup>6</sup>	N.D.	406	140
inosine 5'-monophosphate (IMP)	28	330	55	N.D.	2.2x10 <sup>6</sup>	0.09x10 <sup>6</sup>	35	140	84
guanosine 5'-monophosphate (GMP)	N.D.	208	7	N.D.	2.0x10 <sup>6</sup>	0.2x10 <sup>6</sup>	N.D.	52	N.D.
UDP-glucose	87	196	109	N.D.	4.2x10 <sup>5</sup>	2.5x10 <sup>5</sup>	N.D.	182	142

Extended Data Fig. 7 | Conserved PANX1 secretome. a, Top, three-way Venn diagram comparing PANX1-dependent metabolites released from apoptotic cells across different conditions tested. Bottom, table showing the relative peak intensity (untargeted metabolomics) or absolute concentrations (targeted metabolomics) in the supernatant of the indicated cell treatments and knockout mice. N.D., not determined.

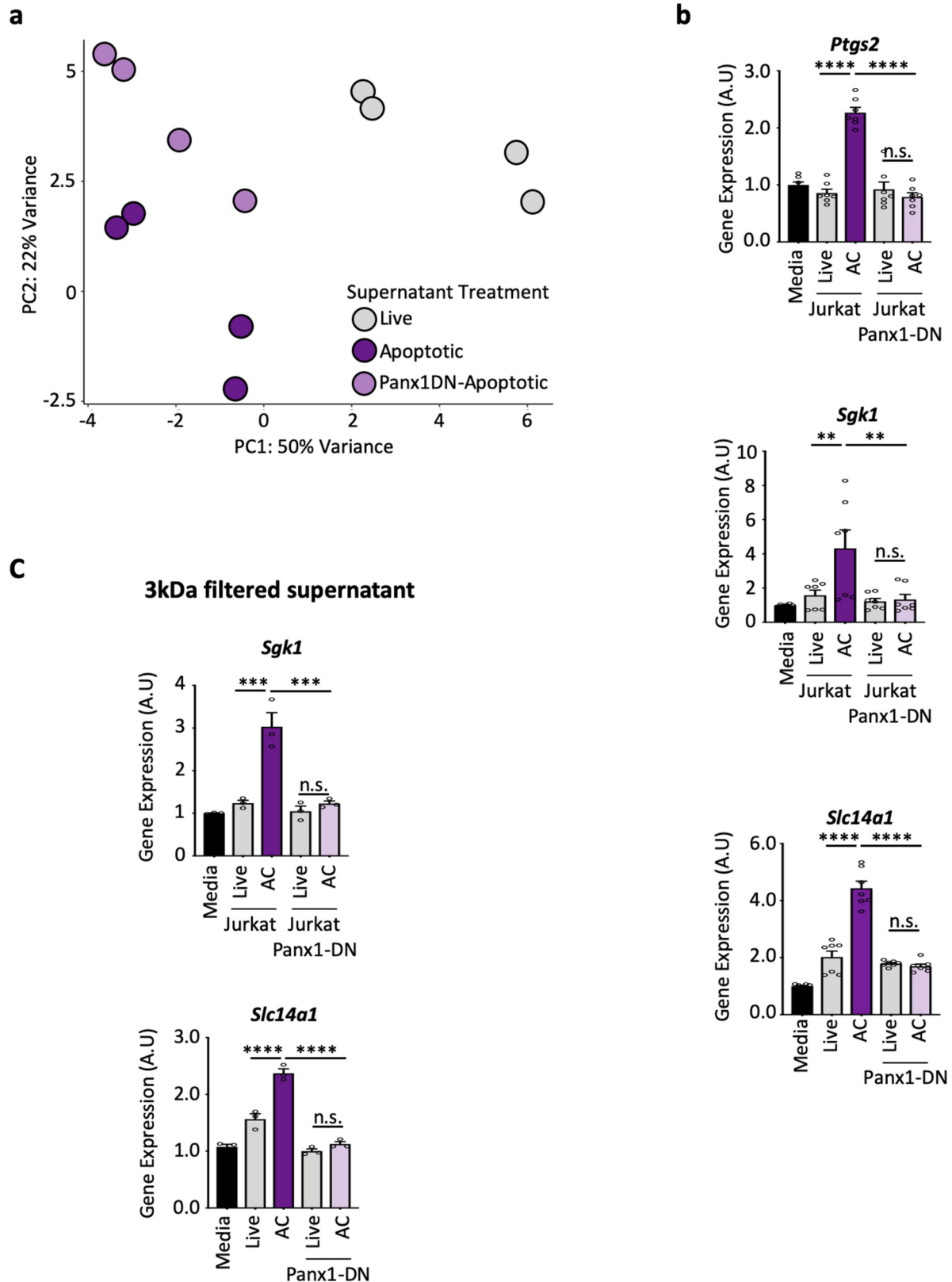
**a****HCT116 – Trail-induced apoptosis**

Analyzed by us using data from  
Liu, X et. al. Cell. 2018

**b****Jurkat – UV-induced apoptosis****c****<sup>13</sup>C-Labeled Spermidine release (Supernatant)**

**Extended Data Fig. 8 | Transcriptional and metabolic changes during apoptosis.** **a**, Re-analyses of RNA-seq data from apoptotic cells<sup>14</sup> demonstrating that the *SRM* mRNA levels are increased or retained during apoptosis. **b**, After induction of apoptosis ( $n=4$ ), *SRM* mRNA expression was assessed over time relative to live controls ( $n=5$ ). Data are mean  $\pm$  s.e.m.

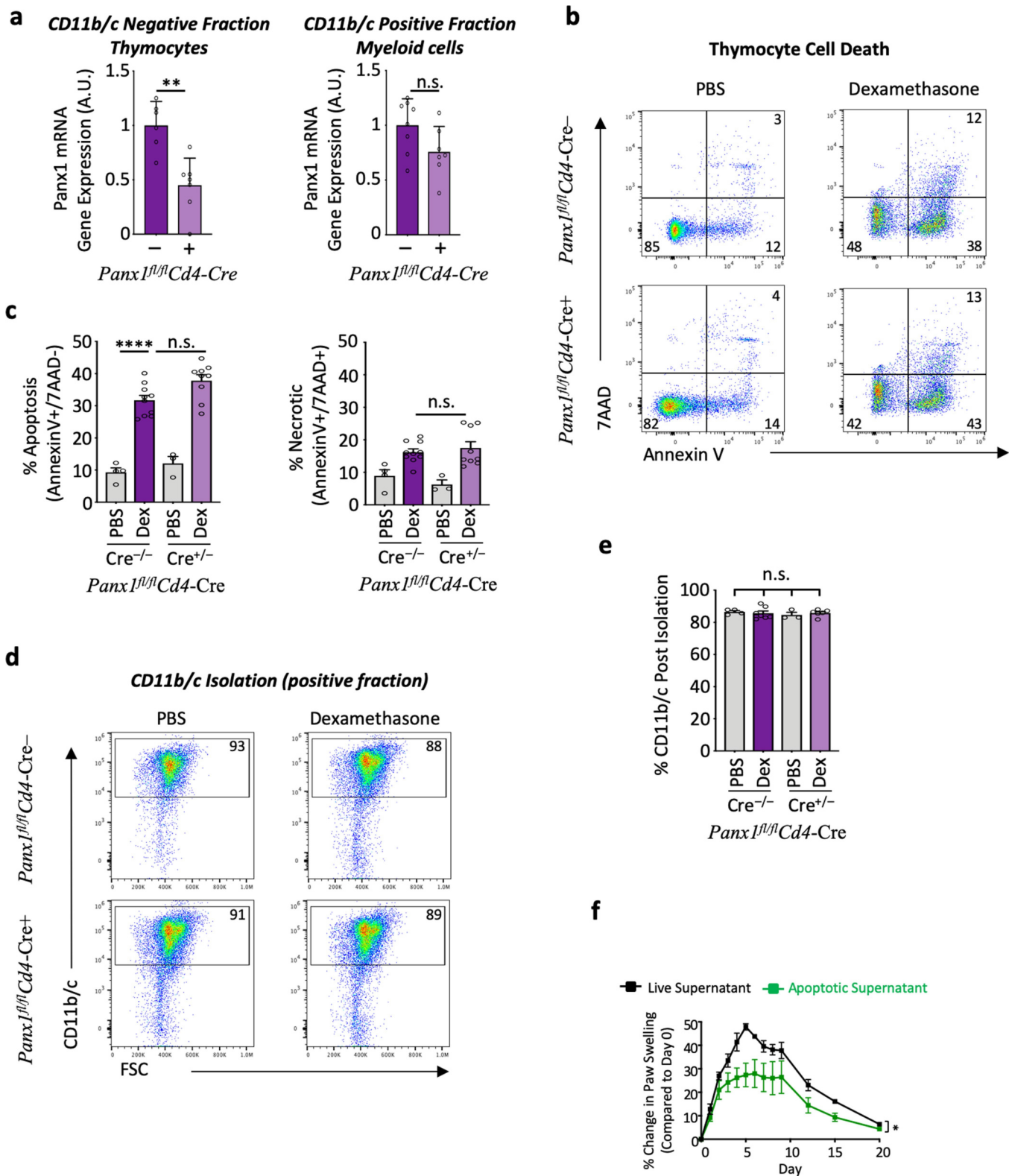
\*\* $P=0.007$ , two-way ANOVA. **c**, Incorporation of <sup>13</sup>C-labelled arginine into the polyamine pathway intermediate spermidine and release from Jurkat cells after apoptosis, and its partial reduction by the pan-caspase inhibitor zVAD ( $n=3$ ). Data are mean  $\pm$  s.d. \*\* $P=0.0088$ , unpaired two-tailed Student's *t*-test.



**Extended Data Fig. 9 | Transcriptional changes on surrounding phagocytes induced by PANX1-dependent metabolite release during apoptosis.**

**a**, Principal component (PC) analysis on the RNA-seq data as a quality control statistic ( $n = 4$  biological replicates). **b**, Experimental procedure is described in Fig. 3d. qPCR was used to assess gene expression changes in *Ptgs2* (top), *Sgk1* (middle) and *Slc14a1* (bottom) in phagocytes after treatment with supernatants from Jurkat cells or Jurkat cells expressing DN-PANX1 ( $n = 7$ ). Data are mean  $\pm$  s.e.m. Live-AC  $**P = 0.0074$  (live-AC *Sgk1*),  $**P = 0.0031$  (AC-AC

*Sgk1*),  $****P < 0.0001$ , ordinary one-way ANOVA with Turkey's multiple comparison test. **c**, Experimental procedure is as described in Fig. 3d, except before treatment of LR73 cells with supernatant, the supernatant was filtered through a 3-kDa filter to remove large molecules. qPCR was used to assess gene expression changes in *Sgk1* (top) and *Slc14a1* (bottom) in phagocytes after treatment with supernatants under specified conditions ( $n = 3$ ). Data are mean  $\pm$  s.e.m.  $***P = 0.0001$ ,  $****P < 0.0001$ , ordinary one-way ANOVA with Turkey's multiple comparison test.



Extended Data Fig. 10 | See next page for caption.



## Extended Data Fig. 10 | Analysis of thymic cell death in vivo and effects of supernatants during arthritis. **a**, Analysis of thymic populations used for experimental data in Fig. 4a. After thymus isolation, the CD11b<sup>+</sup>CD11c<sup>+</sup> population that contained thymocytes was used for mRNA isolation to test the efficiency of deletion of the *Panx1* allele. qPCR analysis of *Panx1* mRNA in control mice (*Panx1<sup>fl/fl</sup>Cd4-cre<sup>-/-</sup>*) (*n* = 6) or mice in which PANX1 has been knocked out in thymocytes (*Panx1<sup>fl/fl</sup>Cd4-cre<sup>+/-</sup>*) (*n* = 7). CD11b<sup>+</sup>CD11c<sup>+</sup> myeloid cells obtained from the thymus of *Panx1<sup>fl/fl</sup>Cd4-cre<sup>+/-</sup>* mice were analysed for *Panx1* expression to demonstrate that PANX1 was not deleted. PANX1 deletion was deleted only from thymocytes and not the myeloid cells that do not express CD4. Data are mean ± s.d. \*\**P* = 0.0015, unpaired two-tailed Student's *t*-test. **b**, Representative flow cytometric plots showing the extent of apoptosis induced by dexamethasone in control and *Panx1<sup>fl/fl</sup>CD4-Cre<sup>+</sup>* mice. After thymus isolation, cells were stained with 7AAD and annexin V to determine the percentage of live, apoptotic or necrotic cells, as in Extended Data Fig. 1a. **c**, Quantitative analysis of apoptosis (left) and secondary necrosis (right) of

CD11b<sup>+</sup>CD11c<sup>+</sup> thymic populations from *Panx1<sup>fl/fl</sup>CD4-Cre<sup>-</sup>* (PBS *n* = 4, Dex *n* = 10) or *Panx1<sup>fl/fl</sup>CD4-Cre<sup>+</sup>* (PBS *n* = 3, Dex *n* = 9) mice treated with PBS or dexamethasone. Data are mean ± s.e.m. \*\*\*\**P* < 0.0001, ordinary one-way ANOVA with Turkey's multiple comparison test. **d**, Representative flow cytometry plots demonstrating the purity of CD11b<sup>+</sup>CD11c<sup>+</sup> population after magnetic separation from the different mice and treatment conditions. **e**, Comparison of the CD11b<sup>+</sup>CD11c<sup>+</sup> cells isolated under different conditions (*cre<sup>-/-</sup>*: PBS *n* = 4, Dex *n* = 7; *cre<sup>+/-</sup>*: PBS *n* = 3, Dex *n* = 6). Data are mean ± s.e.m. *P* > 0.05 (n.s.), ordinary one-way ANOVA with Turkey's multiple comparison test. **f**, Apoptotic supernatants alleviate arthritic disease induced by serum from KBx/N mice. C57BL/6J mice were injected with serum from K/BxN mice to induce arthritis. Live (*n* = 4) or apoptotic (*n* = 5) supernatant was given for five days after arthritis induction. Paw swelling was measured using a calliper and reported as the percentage change compared with day 0. Data are mean ± s.e.m. \**P* = 0.0131, two-way ANOVA.

CD11b<sup>+</sup>CD11c<sup>+</sup> thymic populations from *Panx1<sup>fl/fl</sup>CD4-Cre<sup>-</sup>* (PBS *n* = 4, Dex *n* = 10) or *Panx1<sup>fl/fl</sup>CD4-Cre<sup>+</sup>* (PBS *n* = 3, Dex *n* = 9) mice treated with PBS or dexamethasone. Data are mean ± s.e.m. \*\*\*\**P* < 0.0001, ordinary one-way ANOVA with Turkey's multiple comparison test. **d**, Representative flow cytometry plots demonstrating the purity of CD11b<sup>+</sup>CD11c<sup>+</sup> population after magnetic separation from the different mice and treatment conditions. **e**, Comparison of the CD11b<sup>+</sup>CD11c<sup>+</sup> cells isolated under different conditions (*cre<sup>-/-</sup>*: PBS *n* = 4, Dex *n* = 7; *cre<sup>+/-</sup>*: PBS *n* = 3, Dex *n* = 6). Data are mean ± s.e.m. *P* > 0.05 (n.s.), ordinary one-way ANOVA with Turkey's multiple comparison test. **f**, Apoptotic supernatants alleviate arthritic disease induced by serum from KBx/N mice. C57BL/6J mice were injected with serum from K/BxN mice to induce arthritis. Live (*n* = 4) or apoptotic (*n* = 5) supernatant was given for five days after arthritis induction. Paw swelling was measured using a calliper and reported as the percentage change compared with day 0. Data are mean ± s.e.m. \**P* = 0.0131, two-way ANOVA.

## Reporting Summary

Nature Research wishes to improve the reproducibility of the work that we publish. This form provides structure for consistency and transparency in reporting. For further information on Nature Research policies, see [Authors & Referees](#) and the [Editorial Policy Checklist](#).

### Statistics

For all statistical analyses, confirm that the following items are present in the figure legend, table legend, main text, or Methods section.

n/a Confirmed

- ☐ ☒ The exact sample size ( $n$ ) for each experimental group/condition, given as a discrete number and unit of measurement
- ☐ ☒ A statement on whether measurements were taken from distinct samples or whether the same sample was measured repeatedly
- ☐ ☒ The statistical test(s) used AND whether they are one- or two-sided  
*Only common tests should be described solely by name; describe more complex techniques in the Methods section.*
- ☒ ☐ A description of all covariates tested
- ☐ ☒ A description of any assumptions or corrections, such as tests of normality and adjustment for multiple comparisons
- ☐ ☒ A full description of the statistical parameters including central tendency (e.g. means) or other basic estimates (e.g. regression coefficient) AND variation (e.g. standard deviation) or associated estimates of uncertainty (e.g. confidence intervals)
- ☒ ☐ For null hypothesis testing, the test statistic (e.g.  $F$ ,  $t$ ,  $r$ ) with confidence intervals, effect sizes, degrees of freedom and  $P$  value noted  
*Give  $P$  values as exact values whenever suitable.*
- ☒ ☐ For Bayesian analysis, information on the choice of priors and Markov chain Monte Carlo settings
- ☒ ☐ For hierarchical and complex designs, identification of the appropriate level for tests and full reporting of outcomes
- ☒ ☐ Estimates of effect sizes (e.g. Cohen's  $d$ , Pearson's  $r$ ), indicating how they were calculated

*Our web collection on [statistics for biologists](#) contains articles on many of the points above.*

### Software and code

Policy information about [availability of computer code](#)

#### Data collection

Gene functions were ascribed using Uniprot and article search engines to generate a composite lists. Pathway analyses were performed using the MSigDB resource by MIT-Broad Institute. StepOne Software v2.3, BD FACSDiva V8.0, Attune NxT, StepOnePlus v2.3 and NeqtSeq System Suite for the Illumina NextSeq v500, LC Q Exactive Focus (Thermo Scientific).

#### Data analysis

GraphPad Prism v.6 and v.7, SPSS v.22, R v3.3.2 (Bioconductor package DESeq2) , FlowJo v.8 and v.10 Mac, Xcalibur version 4.2.28.14 (Thermo Scientific). All code is available upon request

For manuscripts utilizing custom algorithms or software that are central to the research but not yet described in published literature, software must be made available to editors/reviewers. We strongly encourage code deposition in a community repository (e.g. GitHub). See the Nature Research [guidelines for submitting code & software](#) for further information.

### Data

Policy information about [availability of data](#)

All manuscripts must include a [data availability statement](#). This statement should provide the following information, where applicable:

- Accession codes, unique identifiers, or web links for publicly available datasets
- A list of figures that have associated raw data
- A description of any restrictions on data availability

#### Data Availability

RNA sequencing data presented in this study are in the NCBI GEO repository under the accession GSE131906.

# Field-specific reporting

Please select the one below that is the best fit for your research. If you are not sure, read the appropriate sections before making your selection.

☒ Life sciences ☐ Behavioural & social sciences ☐ Ecological, evolutionary & environmental sciences

For a reference copy of the document with all sections, see [nature.com/documents/nr-reporting-summary-flat.pdf](https://www.nature.com/documents/nr-reporting-summary-flat.pdf)

## Life sciences study design

All studies must disclose on these points even when the disclosure is negative.

Sample size	No statistical tests were used to determine sample size. For in vivo experiments, sample sizes were determined based on the numbers required to achieve statistical significance using indicated statistics.
Data exclusions	Statistical tests for outliers are routinely performed using Grubbs' test for outliers. No data was excluded in this manuscript.
Replication	Consistent results obtained from more than two technical replicates per experiment. A significant number of the experiments used at least 3-4 biological replicates.
Randomization	Allocation of mice was random in all in vivo experiments, including mice from different vivariums.
Blinding	In vivo experiments for disease models were all blinded. Researcher conducting experiments, data acquisition, data analysis, or histological scoring were blinded to treatment groups.

## Reporting for specific materials, systems and methods

We require information from authors about some types of materials, experimental systems and methods used in many studies. Here, indicate whether each material, system or method listed is relevant to your study. If you are not sure if a list item applies to your research, read the appropriate section before selecting a response.

### Materials & experimental systems

n/a	Involved in the study
<input type="checkbox"/>	<input checked="" type="checkbox"/> Antibodies
<input type="checkbox"/>	<input checked="" type="checkbox"/> Eukaryotic cell lines
<input checked="" type="checkbox"/>	<input type="checkbox"/> Palaeontology
<input type="checkbox"/>	<input checked="" type="checkbox"/> Animals and other organisms
<input checked="" type="checkbox"/>	<input type="checkbox"/> Human research participants
<input checked="" type="checkbox"/>	<input type="checkbox"/> Clinical data

### Methods

n/a	Involved in the study
<input checked="" type="checkbox"/>	<input type="checkbox"/> ChIP-seq
<input type="checkbox"/>	<input checked="" type="checkbox"/> Flow cytometry
<input checked="" type="checkbox"/>	<input type="checkbox"/> MRI-based neuroimaging

## Antibodies

Antibodies used	Annexin V-Pacific Blue was from BioLegend (Cat#640919, Lot#B262423). anti-CD11b-PE (clone M1/70)(Cat#12-0122-81 Lot#4278772), anti-CD11c-PE (clone N418)(Cat#12-0114-82), and anti-CD16/CD32(clone 93)(Cat#16-0161-85, Lot#4316711) were obtained from Invitrogen. Antibodies specific for Siglec-F-PE (clone E50-2440)(Cat#552126, Lot#7058859) and mouse CD95 (Cat#554254, Lot#35882) were obtained from BD. Human anti-Fas (clone CH11)(Cat#05-201, Lot#2782852) was obtained from Millipore.
Validation	All antibody lots are routinely tested by the manufacturers.

## Eukaryotic cell lines

Policy information about [cell lines](#)

Cell line source(s)	Human Jurkat Cell E6.1, HCT-116, and A549 were obtained from ATCC.
Authentication	Morphological shape of cell lines was monitored via microscopic examination.
Mycoplasma contamination	All cell lines used in the laboratory are regularly tested for mycoplasma contamination and tested negative. Additionally, all medias and serum lots used are regularly tested and tested negative.
Commonly misidentified lines (See <a href="#">ICLAC</a> register)	No commonly misidentified cell lines were used.

## Animals and other organisms

Policy information about [studies involving animals](#); [ARRIVE guidelines](#) recommended for reporting animal research

### Laboratory animals

C57BL/10 and C57BL/6J wild-type mice were acquired from Jackson Laboratories. To generate mice with deletion of Panx1 in thymocytes, Panx1<sup>fl/fl</sup> mice were crossed to Cd4-Cre mice (Taconic). KRN TCR transgenic mice were a gift from Dr. Diane Mathis at the Harvard Medical School, and were bred to NOD mice (Jackson Laboratories) to obtain the K/BxN mice. B6Nlrp1b+C1-/-C11-/- were a gift from Dr. Mohamed Lamkanfi's lab (VIB/UGent, Belgium). All mice used in this study were 6-12 week old. Males were used in arthritis studies and females were used for naphthalene lung model.

### Wild animals

No wild animals.

### Field-collected samples

No field collected samples.

### Ethics oversight

Animal procedures were approved and performed according to the Institutional Animal Care and Use Committee (IACUC) at the University of Virginia.

Note that full information on the approval of the study protocol must also be provided in the manuscript.

## Flow Cytometry

### Plots

Confirm that:

- ☒ The axis labels state the marker and fluorochrome used (e.g. CD4-FITC).
- ☒ The axis scales are clearly visible. Include numbers along axes only for bottom left plot of group (a 'group' is an analysis of identical markers).
- ☒ All plots are contour plots with outliers or pseudocolor plots.
- ☒ A numerical value for number of cells or percentage (with statistics) is provided.

### Methodology

#### Sample preparation

Thymocytes and myeloid cells in thymus were obtained by gentle mechanical disruption. Samples were filtered prior to staining and kept on ice during staining. All fluorescent antibodies were aliquotted in a sterile hood with minimal light exposure. Staining of samples were protected from light throughout.

#### Instrument

Data were collected on Attune NxT (Invitrogen).

#### Software

Data were analyzed using FlowJo V10 Software.

#### Cell population abundance

Purity of isolated samples was obtained by antibody stain and FACS. Sample purity was greater than 90%.

#### Gating strategy

Standard lymphocyte gates were applied, following by doublet exclusion using FSC-HxW and SSC-HxW. Myeloid cells in thymus were gated using CD11b and CD11c. Apoptosis of cells were gated using Annexin V and 7AAD. Pannexin-1 activation was measured using TO-PRO-3 dye. Representative Flow plots are shown in Figures and Extended Data.

- ☒ Tick this box to confirm that a figure exemplifying the gating strategy is provided in the Supplementary Information.

# CRISPR screens in cancer spheroids identify 3D growth-specific vulnerabilities

<https://doi.org/10.1038/s41586-020-2099-x>

Received: 25 April 2019

Accepted: 10 January 2020

Published online: 11 March 2020

 Check for updates

Kyuhoo Han<sup>1✉</sup>, Sarah E. Pierce<sup>2</sup>, Amy Li<sup>1</sup>, Kaitlyn Spees<sup>1</sup>, Grace R. Anderson<sup>1</sup>, Jose A. Seoane<sup>3,4</sup>, Yuan-Hung Lo<sup>3</sup>, Michael Dubreuil<sup>1,2</sup>, Micah Olivas<sup>1</sup>, Roarke A. Kamber<sup>1</sup>, Michael Wainberg<sup>5</sup>, Kaja Kostyrko<sup>6</sup>, Marcus R. Kelly<sup>2</sup>, Maryam Yousefi<sup>1</sup>, Scott W. Simpkins<sup>1</sup>, David Yao<sup>1</sup>, Keonil Lee<sup>1</sup>, Calvin J. Kuo<sup>2,3</sup>, Peter K. Jackson<sup>2,7</sup>, Alejandro Sweet-Cordero<sup>6</sup>, Anshul Kundaje<sup>1,5</sup>, Andrew J. Gentles<sup>8</sup>, Christina Curtis<sup>1,2,3,4</sup>, Monte M. Winslow<sup>1,2,9</sup> & Michael C. Bassik<sup>1,2,10✉</sup>

Cancer genomics studies have identified thousands of putative cancer driver genes<sup>1</sup>. Development of high-throughput and accurate models to define the functions of these genes is a major challenge. Here we devised a scalable cancer-spheroid model and performed genome-wide CRISPR screens in 2D monolayers and 3D lung-cancer spheroids. CRISPR phenotypes in 3D more accurately recapitulated those of in vivo tumours, and genes with differential sensitivities between 2D and 3D conditions were highly enriched for genes that are mutated in lung cancers. These analyses also revealed drivers that are essential for cancer growth in 3D and in vivo, but not in 2D. Notably, we found that carboxypeptidase D is responsible for removal of a C-terminal RKRR motif<sup>2</sup> from the  $\alpha$ -chain of the insulin-like growth factor 1 receptor that is critical for receptor activity. Carboxypeptidase D expression correlates with patient outcomes in patients with lung cancer, and loss of carboxypeptidase D reduced tumour growth. Our results reveal key differences between 2D and 3D cancer models, and establish a generalizable strategy for performing CRISPR screens in spheroids to reveal cancer vulnerabilities.

Despite the large increase in the catalogue of mutations observed across diverse cancer types (the ‘long tail’)<sup>1</sup>, it is frequently unclear which mutations are functional cancer drivers. Therefore, it is a central challenge to scalably investigate these genes in relevant cancer models to assign causality and identify cancer-specific vulnerabilities.

Existing in vitro and in vivo models are useful for defining the biological properties of cancer<sup>3–7</sup>, but each has limitations. Genetically engineered mouse models recapitulate tumour growth and microenvironment, but are limited by scalability, time and cost<sup>8</sup>. Xenograft-based models are limited in scale, and can be difficult to manipulate in vitro. Genome-scale investigation of cancer growth and drug sensitivity has largely relied on in vitro 2D cell culture<sup>9–12</sup>, which lacks many features of disease, such as hypoxia<sup>13</sup>, altered cell–cell contacts<sup>14</sup> and rewired metabolism<sup>15</sup>. In vitro organoid models alleviate some of these concerns<sup>3,16</sup>, but are much less scalable.

CRISPR has enabled substantially improved genetic screening in in vitro and in vivo cancer models<sup>9,11,12,17–19</sup>. Efforts such as DepMap have characterized cancer dependencies using genome-scale CRISPR screens in hundreds of cell lines, revealing previously undiscovered cancer drivers<sup>10,20–22</sup>. Nonetheless, it has been difficult to evaluate how differences in culture systems affect the ability to accurately uncover cancer drivers in vivo.

Here we devised a scalable method to propagate lung adenocarcinoma spheroids, and performed genome-wide CRISPR screens in both

2D monolayers and 3D spheroids. Growth phenotypes in 3D more accurately resembled those observed in tumours. Furthermore, genes with differentially stronger effects in 3D were enriched for those significantly mutated in human lung cancers. Among these genes, we identified carboxypeptidase D (CPD), a poorly characterized carboxypeptidase, as an important enzyme for maturation of insulin-like growth factor 1 receptor (IGF1R). Together, these results demonstrate a strategy for genome-scale CRISPR screens in 3D spheroids to identify actionable cancer vulnerabilities.

## Scalable 3D spheroid system for CRISPR screens

Although CRISPR screens performed in 2D monolayers have produced a wealth of information<sup>9–12,23</sup>, they often fail to replicate key aspects of tumour biology<sup>24</sup>. This is illustrated by phenotypes measured across more than 500 screens from the DepMap project. Although this resource has uncovered many valuable biological findings<sup>10,20–22</sup>, less than 1% of the top 1,000 hits show a positive growth effect (Fig. 1a). Indeed, inactivation of known tumour-suppressor genes often results in negative phenotypes in 2D culture (Fig. 1b).

We sought to develop a scalable 3D spheroid system to enable high-throughput screens that more closely approximate in vivo cancers. We optimized seeding density and methylcellulose concentrations

<sup>1</sup>Department of Genetics, Stanford University School of Medicine, Stanford, CA, USA. <sup>2</sup>Program in Cancer Biology, Stanford University School of Medicine, Stanford, CA, USA. <sup>3</sup>Department of Medicine, Stanford University School of Medicine, Stanford, CA, USA. <sup>4</sup>Stanford Cancer Institute, Stanford University School of Medicine, Stanford, CA, USA. <sup>5</sup>Department of Computer Science, Stanford University, Stanford, CA, USA. <sup>6</sup>Department of Pediatrics, University of California San Francisco, San Francisco, CA, USA. <sup>7</sup>Baxter Laboratory, Department of Microbiology and Immunology, Stanford University School of Medicine, Stanford, CA, USA. <sup>8</sup>Departments of Medicine and Biomedical Data Science, Stanford University School of Medicine, Stanford, CA, USA. <sup>9</sup>Department of Pathology, Stanford University School of Medicine, Stanford, CA, USA. <sup>10</sup>Program in Chemistry, Engineering and Medicine for Human Health (ChEM-H), Stanford University, Stanford, CA, USA. ✉e-mail: kyuhohan@stanford.edu; bassik@stanford.edu



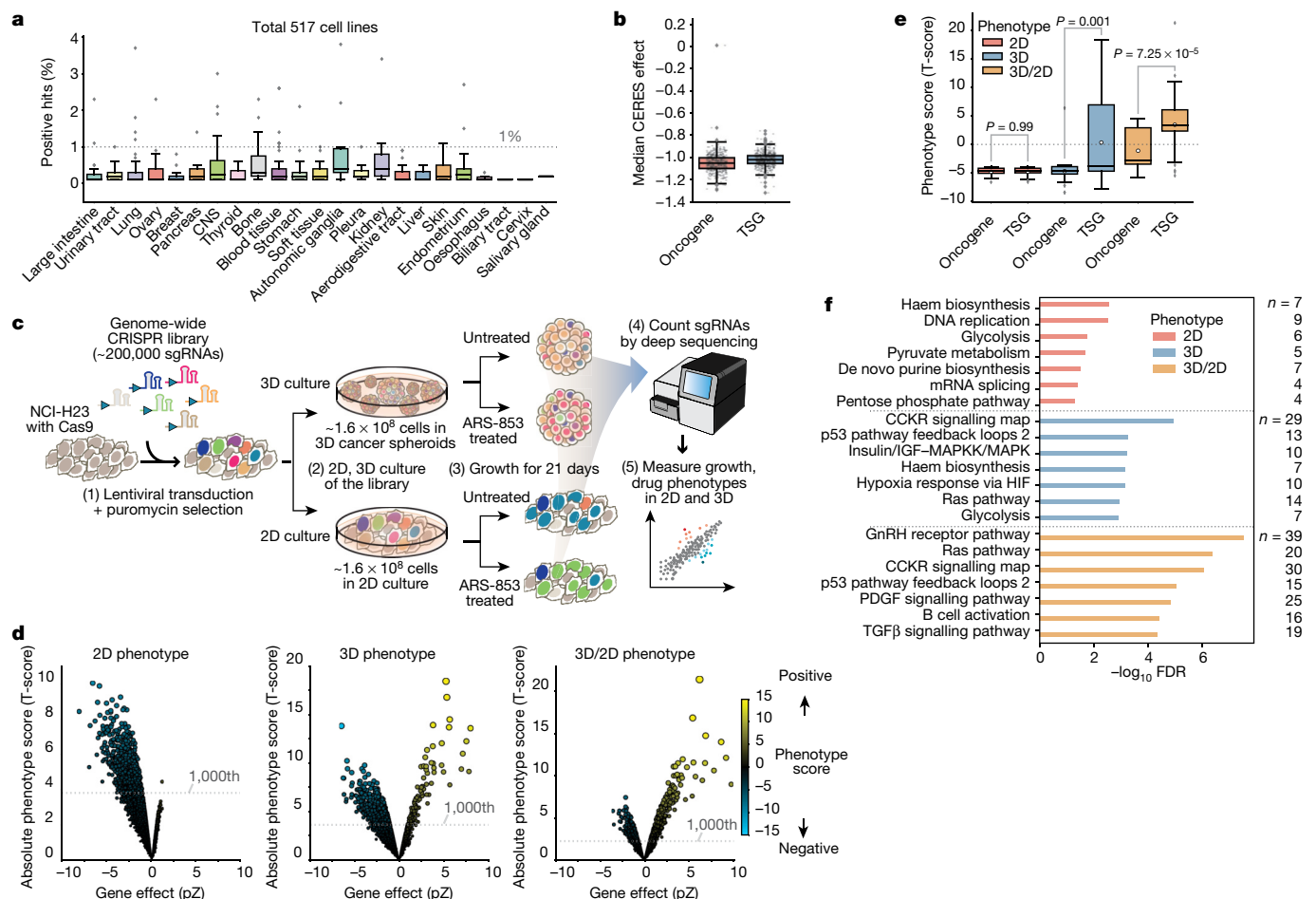


**Fig. 1 | Genome-wide screens performed on 3D cultures improve detection of cancer genes and pathways compared with those performed in 2D.**

**a**, Percentage of positive hits among the top 1,000 hits in the DepMap dataset<sup>10</sup>. Each point represents one cell line. **b**, Median CERES<sup>10</sup> effects of oncogenes and tumour-suppressor genes (TSGs) (annotated in COSMIC<sup>30</sup>) among top 1,000 hits of 517 DepMap cell lines; each data point represents one cell line. **c**, Schematic for CRISPR screens in H23 cells. **d**, Distributions of phenotypes. Values on the x axis show the effect size of each gene and the y axis shows absolute phenotype score (T-score) (see Methods). Dot size represents

absolute T-score. **e**, Phenotype scores for oncogenes and TSGs in top 1,000 hits in each condition. P values calculated using two-sided t-test. **f**, Enriched pathways among the top 1,000 hits from each condition analysed using PANTHER overrepresentation test (see Methods). Significance of enriched pathways were measured with Fisher's exact test and the Benjamini-Hochberg false-discovery rates (FDR) were subsequently computed (x axis). The number of genes in enriched pathways is shown on the right. In all box plots, box limits mark upper and lower quartiles, whiskers represent 1.5× the interquartile range and points show outliers.

(Extended Data Fig. 1a, Supplementary Video 1; see Methods) to enable propagation of approximately 200 million cells in 3D spheroids in low-attachment plates. This enabled us to perform genome-wide CRISPR screens in H23 lung adenocarcinoma cells grown in either 2D monolayers or 3D spheroids (Fig. 1c) using our custom single guide RNA (sgRNA) library<sup>25</sup>. Since H23 cells contain a *KRAS*<sup>G12C</sup> mutation, we also screened with ARS-853<sup>26–28</sup>, a cysteine-reactive *KRAS* inhibitor that frequently has stronger effects in 3D<sup>29</sup>.

### 3D phenotypes reflect cancer dependencies

Reproducibility and quality of 3D screening data were equivalent to those of the 2D data (Extended Data Fig. 1b–d, Supplementary Table 1), and it was immediately apparent that CRISPR screens in 3D uncovered many more positive growth phenotypes, whereas most hits from the 2D screens had negative phenotypes (Fig. 1d). This became more apparent when we examined genes with differential effects in 3D by normalizing 3D phenotypes against the corresponding 2D phenotypes (3D/2D) (see Methods). We next analysed phenotypes for oncogenes and tumour suppressor genes (TSGs) annotated in the COSMIC database<sup>30</sup> within the top 1,000 hits in 2D or 3D conditions. Both groups were similar in 2D, showing negative

median-growth phenotypes (Fig. 1e). In 3D spheroids, however, oncogenes and TSGs exhibited markedly different behaviours, with knockout of TSGs showing more positive-growth phenotypes; this was clearer when the 3D/2D phenotype was considered (Fig. 1e, Extended Data Fig. 1e).

Pathway-enrichment analysis revealed that a distinct set of cancer-specific pathways—including p53 and Ras pathways (known drivers in H23 cells)—was enriched among hits in 3D and 3D/2D phenotypes, whereas 2D hits were generally related to common essential cellular functions such as DNA replication (Fig. 1f). Together, these data suggest that screens in 3D more accurately capture features of cancer genes and pathways (Extended Data Fig. 1f).

### 3D hits are frequently mutated in cancer

We further investigated the phenotypes for genes frequently mutated in lung adenocarcinoma and squamous cell carcinoma<sup>31</sup> (hereafter, 'pan-lung'). When genes were sorted by the absolute value of their phenotypic strength, inactivation of the ten most-frequently mutated genes in the Pan-lung cancer cohort<sup>31</sup> showed weaker and more widely distributed effects in 2D (Extended Data Fig. 1g, Supplementary Table 2). By contrast, many of these frequently mutated genes showed stronger

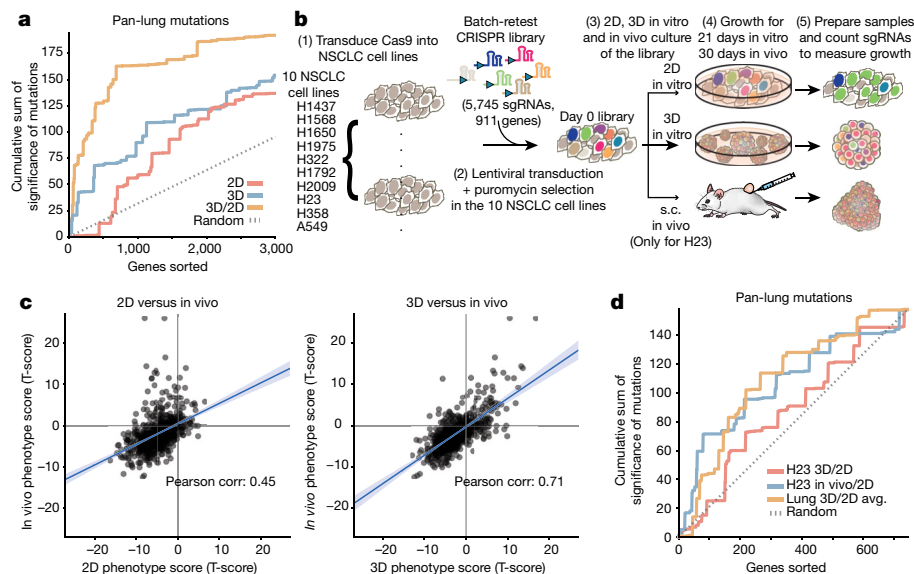


**Fig. 2 | Genes with differential 3D/2D phenotypes are enriched for significantly mutated lung cancer genes.** **a**, Cumulative sum of the significance of 11,249 pan-lung cancer genes from 1,144 patients with lung cancer<sup>31,51</sup> measured by MutSig2CV<sup>31</sup>. The x-axis shows phenotypes sorted by strength in 2D, 3D and 3D/2D. The top 3,000 genes are shown. **b**, Schematic for batch-retest CRISPR screens. s.c., subcutaneous injection. **c**, Comparisons between in vitro and in vivo phenotypes in the H23 batch-retest screens. Data

are fit by linear regression (blue line); shaded bands indicate 95% confidence intervals. Pearson corr., Pearson correlation coefficient. **d**, Significance of 744 pan-lung cancer genes measured by MutSig2CV<sup>31</sup>, displayed as cumulative sum plots against genes sorted by absolute values of 3D/2D phenotypes in H23 cells, average (avg.) 3D/2D phenotypes across 10 lung cancer lines, and H23 in vivo/2D phenotypes in batch-retest screens.

phenotypes in 3D spheroids. Notably, the 3D/2D phenotypes showed a further improved ability to detect strong phenotypes for genes that are frequently mutated in lung cancer. This is consistent with the pathway-enrichment analysis described above, and suggests that analysis of genes with differentially strong effects in 3D may increase the power to identify cancer drivers.

To systematically confirm this, we compared absolute CRISPR phenotypes (sorted by phenotypic strength) with the cumulative sum of significance of pan-lung cancer mutations<sup>31</sup> (Fig. 2a, Supplementary Table 3). Again, genes with stronger phenotypes in 3D and, to a greater extent, those with stronger phenotypes in 3D/2D, were enriched for significant lung-cancer mutations. We reasoned that two factors probably contribute to this enrichment. First, normalizing 3D with 2D phenotypes may unmask cancer-specific genes by minimizing the otherwise dominating effects of core essential genes (for example, ribosomal genes) that are critical for both 2D and 3D growth (Extended Data Fig. 1g). Second, as previously suggested<sup>32</sup>, 3D spheroids are more likely to mimic in vivo tumours.

Additional genome-wide screens in H1975 and H2009 lung cancer lines confirmed key advantages of 3D spheroids, including improved detection of cancer pathways and identification of the known drivers for each of these lines (EGFR–PI3K and p53–KRAS, respectively, Extended Data Figs. 2, 3, Supplementary Discussion).

### 3D spheroids better match tumour xenografts

To systematically compare CRISPR screens in 2D monolayers, 3D spheroids and tumour xenografts, we generated a small batch-retest sgRNA library targeting 911 top hits with differential 3D growth effects in our genome-wide screens (Fig. 2b, Supplementary Table 4). We transduced this library into H23 cells and compared growth in subcutaneous xenograft tumours with growth in 2D and 3D cultures. We optimized a protocol (see Methods) for in vivo CRISPR screening, and obtained highly reproducible data from tumour xenografts (Extended Data Fig. 4a, b, Supplementary Table 5). Notably, phenotypes of genes from 3D screens were much more closely correlated with those in mouse xenograft than those from 2D screens (Fig. 2c, Supplementary Discussion).

To search for common 3D-selective vulnerabilities in lung adenocarcinoma, we used the same batch-retest library to perform 2D and 3D screens across multiple cancer lines. We again observed marked differences between 2D and 3D screens in all lines (Supplementary Table 5). Averaging 3D/2D phenotypes across ten cell lines further increased detection of significant mutations observed in patients with lung cancer compared with phenotypes from the H23 cell line alone (Fig. 2d). Of note, comparison of in vivo phenotypes with 2D phenotypes (in vivo/2D) in H23 cells also increased detection of significant mutations compared with the in vitro 3D/2D phenotypes. Notably, top sensitizing hits from the averaged 3D/2D phenotypes include several known regulators of RAS–MAPK pathways<sup>33</sup> such as GRB2, SHOC2, PTPN11 (also known as SHP2), GAB1 and MAPK1.

### CPD module shows selective 3D growth effects

Given that genes with strong 3D/2D phenotypes are enriched for lung cancer mutations, we reasoned that these might include novel therapeutic targets. To identify such targets, we defined functional gene modules on the basis of their correlated phenotypes in DepMap<sup>22</sup> and examined their phenotypes. Simultaneous depletion of multiple genes from the same functional group should help define vulnerabilities within pathways/complexes; indeed, we identified a number of differentially enriched modules from expected genes, including KRAS, mTOR and Hippo pathways (Supplementary Discussion).

Notably, a module composed of genes correlated with CPD was the most strongly depleted in the 3D/2D phenotype (Fig. 3a, Extended Data Fig. 4c) and showed strong synthetic lethality with the KRAS(G12C) inhibitor specifically in 3D. This suggested that CPD and its functional interactors could be promising therapeutic targets. CPD is a poorly characterized member of the metallopeptidase family that cleaves C-terminal arginines and lysines from polypeptides<sup>34</sup>; it is localized in the *trans*-Golgi network<sup>35</sup>. CPD is correlated with *FURIN*, *ATP2C1*, *IGF1R*, *MET* and *GAB1* in a functional module (Fig. 3b, c, Extended Data Fig. 4d–f), but not with a control olfactory receptor gene. Given that *FURIN* and *ATP2C1* are critical for processing of *IGF1R* and *MET* in the *trans*-Golgi<sup>36–38</sup>, we hypothesized that CPD might have a related role.

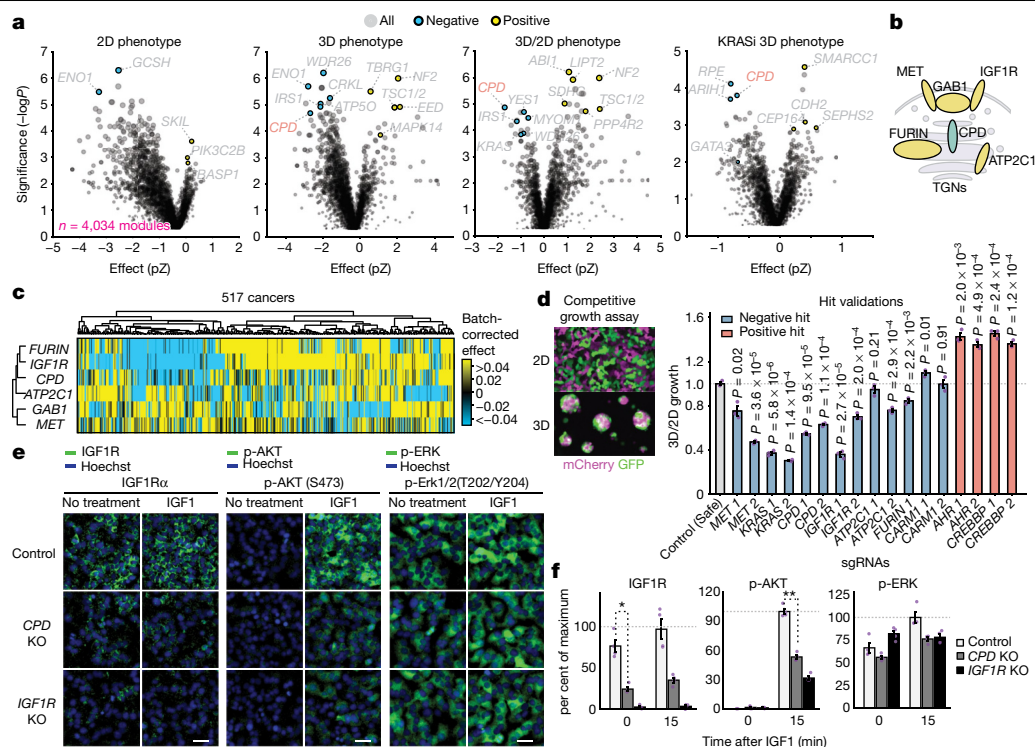


**Fig. 3 | The CPD module is critical for 3D spheroid growth and IGF1R function.** **a**, Top negative modules (blue). Top positive modules (yellow). The y axis shows significance of enrichment for co-essential modules ( $P$  values, two-sided Mann–Whitney  $U$ -test); the x axis shows average gene effects of co-essential modules (see Methods). KRASi, KRAS inhibitor. **b**, Proteins encoded by genes in the CPD co-essential module and their localization along the TGN–plasma membrane. **c**, Cluster map showing batch-corrected CERES gene effects for the CPD module. **d**, CPD module and selected top 3D/2D hits were validated with individual sgRNAs in competitive growth assays. Left

micrographs show example images of growth assays for control sgRNA in 2D and 3D. Data are mean  $\pm$  s.e.m.,  $n = 3$ ;  $P$  values calculated by two-sided  $t$ -test between the control and gene-targeting sgRNAs. Control (safe) sgRNAs are described in the Methods. **e**, Control, CPD-knockout (KO) and IGF1R-knockout H23 cells grown in 2D were stimulated with IGF1 (100 ng ml $^{-1}$ ) for 15 min and levels of IGF1R and activities of downstream effectors were measured by immunofluorescence. Scale bars, 20  $\mu$ m. **f**, Quantification of immunofluorescence in **e**. \* $P = 6.4 \times 10^{-4}$ , \*\* $P = 1.24 \times 10^{-5}$  (mean  $\pm$  s.e.m.,  $n = 4$ ; two-sided  $t$ -test).

To interrogate interactions within the CPD module in H23 cells, we measured all pairwise genetic interactions of 145 selected genes with strong 3D/2D phenotypes using CRISPR double-knockout screening<sup>39</sup> (Extended Data Fig. 5, Supplementary Tables 6, 7). Similar to their behaviour in DepMap, genetic interaction patterns of *FURIN* and *IGF1R* showed strong correlation with those of *CPD*.

Given the strong 3D/2D phenotypes of genes within the CPD module, we validated individual genes within the module and other strong hits using competitive growth assays and small-molecule inhibitors (Fig. 3d, Extended Data Fig. 6). We also observed that inducible knockdown of CPD in vitro in established H23 3D spheroids using tetracycline-inducible dCas9-KRAB<sup>17</sup> markedly reduced growth of spheroids (Extended Data Fig. 7), suggesting that targeting CPD can have an effect on further growth of established spheroids.

### IGF1R signalling is inhibited by CPD deletion

Since our data suggested CPD functionally interacts with *IGF1R*, we examined how CPD deletion affected IGF1R signalling pathways. We first measured protein levels of IGF1R and phosphorylation of its downstream effectors AKT and ERK1/2 following treatment with IGF1 (Fig. 3e, f) in H23 cells grown in 2D. We observed significant reduction of IGF1R protein levels and AKT phosphorylation in CPD-deficient H23 cells compared with control cells. By contrast, phospho-ERK1/2 levels were high and unchanged, probably owing to constitutively active KRAS in H23 cells. Levels of IGF1R were also significantly reduced in CPD-deficient H23 spheroids (Fig. 3g, h). In addition, CPD deletion reduced levels of IGF1R and phospho-AKT upon IGF1 addition in H322, A549 and H358 cells

(Extended Data Fig. 8). Lastly, we found that the effect of CPD deletion can be rescued by treating H23 cells with excess IGF1, but not by treatment with epidermal growth factor (EGF) or hepatocyte growth factor (HGF) (Extended Data Fig. 9a, b), suggesting that much of the 3D-selective CPD-knockout phenotype can be attributed to its regulation of *IGF1R*.

### CPD removes the IGF1Rα C-terminal RKRR motif

Since CPD is a carboxypeptidase, we considered whether IGF1R might be a substrate. IGF1R is translated as a single polypeptide (pro-IGF1R), which is cleaved by *FURIN* into  $\alpha$ - and  $\beta$ -chains<sup>2</sup> (Fig. 4a). pro-IGF1R does not end in lysine or arginine, and thus should not be a substrate for CPD; however, *FURIN* cleaves pro-IGF1R immediately after a central RKRR motif<sup>40</sup>, leaving these four positively charged amino acids at the C terminus of the  $\alpha$ -chain, creating a potential CPD substrate.

To test whether the RKRR motif is removed by CPD, we developed an assay to measure appearance of the 1D4 epitope<sup>41</sup>. Using the Rho1D4 antibody, which requires a free carboxylate group for binding, we could detect the presence of the 1D4 epitope specifically at the C terminus of a protein. We thus created an IGF1R reporter with a 1D4 epitope inserted immediately upstream of the RKRR motif (Fig. 4b). A Flag epitope on the  $\beta$ -chain was used to measure total protein levels.

When we transduced control H23 cells with the reporter, we observed strong 1D4 and Flag signals, suggesting that RKRR is removed and the 1D4 epitope is exposed at the C terminus of  $\alpha$ -chain (Fig. 4c, e). Deletion of CPD markedly reduced 1D4 staining, whereas total Flag–IGF1R remained unchanged, suggesting that CPD removes the RKRR motif. Consistent with these results, a *FURIN* inhibitor reduced the 1D4 signal



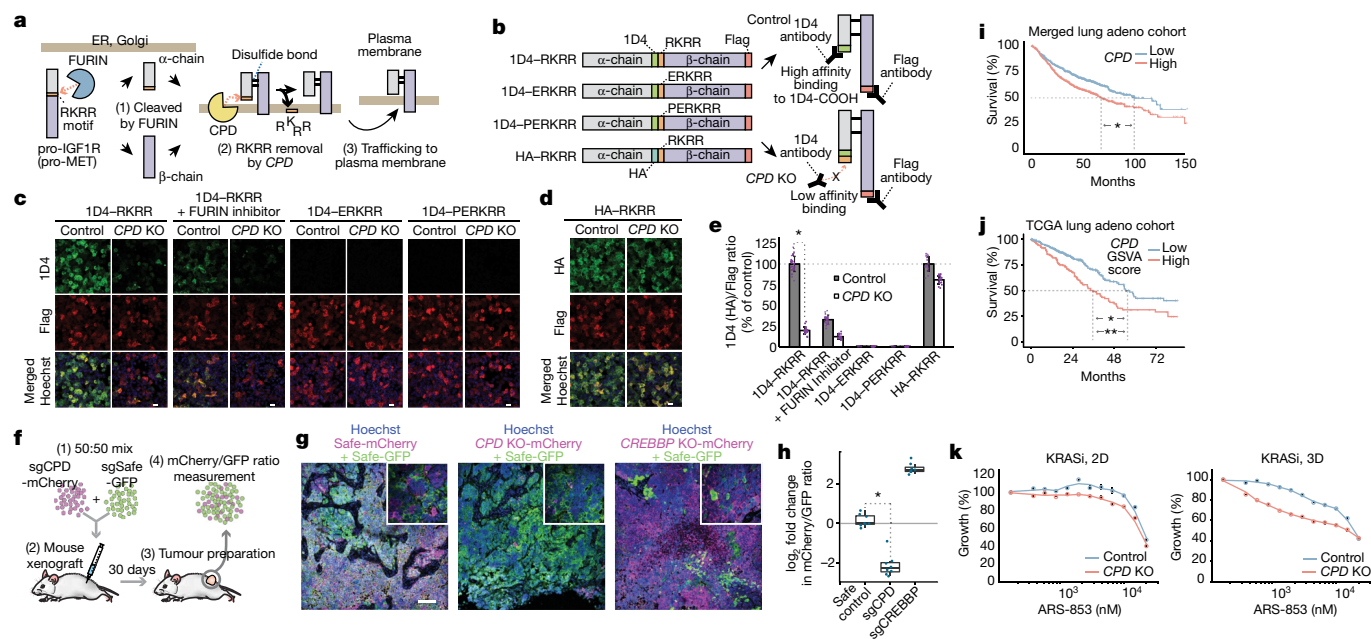


**Fig. 4 | CPD is a carboxypeptidase for the IGF1R  $\alpha$ -chain and loss of CPD inhibits in vivo tumour growth.** **a**, Proposed model of the CPD-IGF1R interaction. **b**, Schematic of 1D4 reporters used to test the model in **a**. **c**, Flag and 1D4 immunofluorescence from the 1D4 reporters, measured in control or CPD-knockout H23 cells grown in 2D culture, untreated or treated with FURIN inhibitor. Scale bars, 40  $\mu$ m. **d**, Immunofluorescence of HA-RKRR reporter in control or CPD-knockout H23 cells. Scale bar, 40  $\mu$ m. **e**, Ratios of 1D4 (or HA) to Flag immunofluorescence relative to the control 1D4-RKRR or to the control HA-RKRR for conditions in **c** and **d**.  $P = 1.38 \times 10^{-39}$ , two-sided *t*-test ( $n = 19, 30, 18, 12, 20, 21, 18, 18, 18$  and 18 from left to right, mean  $\pm$  s.d.). **f**, Schematic for the competitive tumour-growth assay. **g**, Immunofluorescence of mCherry and GFP signal in day 30 tumour sections. Scale bar, 100  $\mu$ m. Original magnifications: 10 $\times$  (main images), 20 $\times$  (insets). Immunofluorescence experiments were repeated on two tumours per condition. **h**, Changes in mCherry/GFP ratios between day 0 and day 30 following tumour

transplantation.  $P = 4.3 \times 10^{-39}$ , two-sided *t*-test;  $n = 8$  tumours per group. In the box plot, the centre line shows the median, box limits mark upper and lower quartiles, whiskers represent 1.5 $\times$  the interquartile range and points show outliers. **i**, Kaplan-Meier plot for patients with lung adenocarcinoma with high or low CPD expression. A median split was used and curve separation was assessed by two-sided log-rank test.  $n = 1,106$ ,  $P < 0.0001$ . **j**, Variation of the set of genes downregulated by CPD deletion in H23 spheroids were scored by gene-set variation analysis (CPD GSVA score; see Methods). Kaplan-Meier plot for survival of 479 patients with lung adenocarcinoma, divided into two groups with high or low CPD GSVA scores. Curve separation assessed by two-sided log-rank test ( $P = 9 \times 10^{-5}$ ) and Cox proportional-hazard test ( $P = 7.68 \times 10^{-4}$ ). **k**, CPD deletion sensitizes H23 cells to ARS-853, an inhibitor of KRAS(G12C). H23 cells in 2D or 3D culture treated with control or CPD sgRNA and indicated doses of ARS-853 for 72 h. Live cells were quantified using alamar blue ( $n = 4$ , mean  $\pm$  s.e.m.).

in both control cells and cells in which CPD was deleted. FURIN inhibition would be expected to prevent cleavage of pro-IGF1R and exposure of the RKRR motif. Insertion of even a single amino acid between the 1D4 and the RKRR motif diminished the 1D4 signal, demonstrating the precise requirement for the removal of RKRR. An IGF1R reporter with a control haemagglutinin (HA) epitope upstream of RKRR showed a strong HA signal in both control and CPD-depleted cells (Fig. 4d, e). Similarly, CPD-mediated removal of the RKRR motif was observed in H322 and A549 cells (Extended Data Fig. 9c, d). Together, these data demonstrate that CPD is a carboxypeptidase that is required for IGF1R maturation. Notably, pro-MET is also cleaved by FURIN after a KRKKR motif. Although we observed toxicity upon expression of a MET 1D4 reporter in H23 cells, we were able to express the reporter in H322 cells—deletion of CPD prevented removal of the KRKKR motif in these cells (Extended Data Fig. 9e). Therefore, MET is also a probable substrate of CPD.

### CPD as a therapeutic target for lung cancers

Given the known role of IGF1R signalling in cancers<sup>42</sup>, we further assessed whether CPD deletion affects in vivo tumour growth. We performed competitive growth assays by subcutaneous injection of a mixed pool of H23 cells that expressed either a sgRNA targeting CPD (labelled with mCherry) or a control sgRNA (labelled with GFP) into mice (Fig. 4f). Immunofluorescence images of tumour sections showed that the tumours were dominated by GFP-expressing cells, indicating

that cells deficient in CPD did not readily form tumours (Fig. 4g). By contrast, deletion of CREBBP, a strongly positive hit in the 3D spheroids, promoted tumour growth, as reflected by dominant mCherry signal in the tumours. Flow cytometry measurement of mCherry:GFP ratios confirmed these results (Fig. 4h).

We next investigated whether expression levels of CPD were prognostic for patient survival. In a meta-analysis of expression signatures from around 18,000 human tumours with survival outcomes using PRECOG<sup>43</sup>, high expression of CPD is a strong indicator for poor prognosis of patients with lung adenocarcinoma (Extended Data Fig. 10a, b). A Kaplan-Meier plot generated from the merged data confirmed this result (Fig. 4i). We also showed that high expression of genes downregulated in a CPD knockout (identified by RNA-seq) is an indicator of poor prognosis in patients (see Methods, Fig. 4j, Extended Data Fig. 10c, Supplementary Table 8).

KRAS mutations occur in about 17% of lung cancers<sup>44</sup>, and inhibitors have been developed<sup>26–29,45</sup> for the KRAS(G12C) mutant, the most common KRAS mutant in lung adenocarcinomas<sup>31,45</sup>. Since inhibition of IGF1R can inhibit growth of KRAS-mutant lung cancer<sup>46</sup> and CPD was a top synthetic lethal hit with ARS-853 in our screens (Fig. 3a), we examined how deletion of CPD affects the response of H23 cells to ARS-853. CPD deletion greatly sensitized H23 cells to the drug, particularly in 3D culture (Fig. 4k). Consistent with this, expression of genes downregulated in CPD-knockout spheroids more strongly predict the survival of patients with lung adenocarcinoma with KRAS mutations than with wild-type KRAS (Extended Data Fig. 10d, e).

We further investigated potential synergy between ARS-853 and loss of CPD in additional *KRAS*<sup>G12C</sup>-mutant lung cancer cell lines (Extended Data Fig. 10f, g). We observed even greater synergy in H358 cells, whereas no synergy was detected in H1792 cells. Of note, H1792 cells do not have a phenotype for loss of CPD (Supplementary Table 5), and show negligible IGF1R expression (Extended Data Fig. 10h). This suggests that IGF1R expression and/or dependency and *KRAS* mutation may serve as biomarkers for combinatorial therapies targeting CPD and *KRAS*(G12C) in lung cancers.

## Conclusions

Here we have demonstrated a robust strategy to conduct genome-scale CRISPR screens in 3D spheroids. Phenotypes in 3D more closely match expectations for oncogenes and TSGs, and are better aligned with those in tumour xenografts. Accurate in vitro modelling of loss-of-function phenotypes in tumours is likely to become important for personalization of therapeutic strategies (Supplementary Discussion). For example: CREBBP inhibitors have been used to treat various cancers<sup>47</sup>; however, in certain lung cancer lines tested here, *CREBBP* knockout had a negative effect on 2D growth, but a profoundly positive effect on growth in 3D spheroids and mouse xenografts (Fig. 3d, Fig. 4g, h, Supplementary Table 5), arguing against the use of CREBBP inhibitors in these cases.

Of note, genes with differentially strong effects in 3D culture versus 2D culture are enriched for frequently occurring lung cancer mutations. This could be because these genes govern the transition to more aggressive 3D growth, a hallmark of tumorigenesis<sup>24</sup>. This probably includes genes involved in cell adhesion or genes that enable responses to ‘tumour-like’ stresses in the spheroids, such as hypoxia or cell crowding.

Ongoing efforts to investigate the roles of matrix composition<sup>48</sup>, nutrient conditions<sup>49</sup>, cancer-associated fibroblasts<sup>50</sup> and tumour-infiltrating immune cells<sup>16</sup> have enabled substantial improvements in in vitro and patient-derived organoid models of cancer. The ability to systematically and scalably determine which genes are required for growth and survival in response to such distinct environmental cues should facilitate both improved models for drug-target identification and a better understanding of cancer growth.

## Online content

Any methods, additional references, Nature Research reporting summaries, source data, extended data, supplementary information, acknowledgements, peer review information; details of author contributions and competing interests; and statements of data and code availability are available at <https://doi.org/10.1038/s41586-020-2099-x>.

- Garraway, L. A. & Lander, E. S. Lessons from the cancer genome. *Cell* **153**, 17–37 (2013).
- Khatib, A.-M. et al. Inhibition of proprotein convertases is associated with loss of growth and tumorigenicity of HT-29 human colon carcinoma cells: importance of insulin-like growth factor-1 (IGF-1) receptor processing in IGF-1-mediated functions. *J. Biol. Chem.* **276**, 30686–30693 (2001).
- Unger, C. et al. Modeling human carcinomas: physiologically relevant 3D models to improve anti-cancer drug development. *Adv. Drug Deliv. Rev.* **79–80**, 50–67 (2014).
- Siolas, D. & Hannon, G. J. Patient-derived tumor xenografts: transforming clinical samples into mouse models. *Cancer Res.* **73**, 5315–5319 (2013).
- Sharpless, N. E. & Depinho, R. A. The mighty mouse: genetically engineered mouse models in cancer drug development. *Nat. Rev. Drug Discov.* **5**, 741–754 (2006).
- Boj, S. F. et al. Organoid models of human and mouse ductal pancreatic cancer. *Cell* **160**, 324–338 (2015).
- Debnath, J. & Brugge, J. S. Modelling glandular epithelial cancers in three-dimensional cultures. *Nat. Rev. Cancer* **5**, 675–688 (2005).
- Winters, I. P., Murray, C. W. & Winslow, M. M. Towards quantitative and multiplexed in vivo functional cancer genomics. *Nat. Rev. Genet.* **19**, 741–755 (2018).
- Shalem, O. et al. Genome-scale CRISPR-Cas9 knockout screening in human cells. *Science* **343**, 84–87 (2014).
- Meyers, R. M. et al. Computational correction of copy number effect improves specificity of CRISPR-Cas9 essentiality screens in cancer cells. *Nat. Genet.* **49**, 1779–1784 (2017).
- Wang, T., Wei, J. J., Sabatini, D. M. & Lander, E. S. Genetic screens in human cells using the CRISPR-Cas9 system. *Science* **343**, 80–84 (2014).
- Behan, F. M. et al. Prioritization of cancer therapeutic targets using CRISPR-Cas9 screens. *Nature* **568**, 511–516 (2019).
- Kim, J. W., Ho, W. J. & Wu, B. M. The role of the 3D environment in hypoxia-induced drug and apoptosis resistance. *Anticancer Res.* **31**, 3237–3245 (2011).

- Loessner, D. et al. Bioengineered 3D platform to explore cell–ECM interactions and drug resistance of epithelial ovarian cancer cells. *Biomaterials* **31**, 8494–8506 (2010).
- Dang, C. V. & Semenza, G. L. Oncogenic alterations of metabolism. *Trends Biochem. Sci.* **24**, 68–72 (1999).
- Neal, J. T. et al. Organoid modeling of the tumor immune microenvironment. *Cell* **175**, 1972–1988 (2018).
- Gilbert, L. A. et al. Genome-scale CRISPR-mediated control of gene repression and activation. *Cell* **159**, 647–661 (2014).
- Wang, T. et al. Gene essentiality profiling reveals gene networks and synthetic lethal interactions with oncogenic Ras. *Cell* **168**, 890–903 (2017).
- Chen, S. et al. Genome-wide CRISPR screen in a mouse model of tumor growth and metastasis. *Cell* **160**, 1246–1260 (2015).
- Pan, J. et al. Interrogation of mammalian protein complex structure, function, and membership using genome-scale fitness screens. *Cell Syst.* **6**, 555–568 (2018).
- Boyle, E. A., Pritchard, J. K. & Greenleaf, W. J. High-resolution mapping of cancer cell networks using co-functional interactions. *Mol. Syst. Biol.* **14**, e8594 (2018).
- Wainberg, M. et al. A genome-wide almanac of co-essential modules assigns function to uncharacterized genes. Preprint at *bioRxiv* <https://doi.org/10.1101/827071> (2019).
- Tsherniak, A. et al. Defining a cancer dependency map. *Cell* **170**, 564–576 (2017).
- Hanahan, D. & Weinberg, R. A. Hallmarks of cancer: the next generation. *Cell* **144**, 646–674 (2011).
- Morgens, D. W. et al. Genome-scale measurement of off-target activity using Cas9 toxicity in high-throughput screens. *Nat. Commun.* **8**, 15178 (2017).
- Ostrem, J. M., Peters, U., Sos, M. L., Wells, J. A. & Shokat, K. M. K-Ras(G12C) inhibitors allosterically control GTP affinity and effector interactions. *Nature* **503**, 548–551 (2013).
- Patricelli, M. P. et al. Selective inhibition of oncogenic KRAS output with small molecules targeting the inactive state. *Cancer Discov.* **6**, 316–329 (2016).
- Lito, P., Solomon, M., Li, L.-S., Hansen, R. & Rosen, N. Allele-specific inhibitors inactivate mutant KRAS G12C by a trapping mechanism. *Science* **351**, 604–608 (2016).
- Janes, M. R. et al. Targeting KRAS mutant cancers with a covalent G12C-specific inhibitor. *Cell* **172**, 578–589 (2018).
- Forbes, S. A. et al. COSMIC: somatic cancer genetics at high-resolution. *Nucleic Acids Res.* **45** (D1), D777–D783 (2017).
- Campbell, J. D. et al. Distinct patterns of somatic genome alterations in lung adenocarcinomas and squamous cell carcinomas. *Nat. Genet.* **48**, 607–616 (2016).
- Pampaloni, F., Reynaud, E. G. & Stelzer, E. H. K. The third dimension bridges the gap between cell culture and live tissue. *Nat. Rev. Mol. Cell Biol.* **8**, 839–845 (2007).
- Tidyman, W. E. & Rauen, K. A. The RASopathies: developmental syndromes of Ras/MAPK pathway dysregulation. *Curr. Opin. Genet. Dev.* **19**, 230–236 (2009).
- Song, L. & Fricker, L. D. Purification and characterization of carboxypeptidase D, a novel carboxypeptidase E-like enzyme, from bovine pituitary. *J. Biol. Chem.* **270**, 25007–25013 (1995).
- Varlamov, O. & Fricker, L. D. Intracellular trafficking of metalloproteinase D in AtT-20 cells: localization to the trans-Golgi network and recycling from the cell surface. *J. Cell Sci.* **111**, 877–885 (1998).
- Alarcón, C. et al. A Kex2-related endopeptidase activity present in rat liver specifically processes the insulin proreceptor. *Biochem. J.* **301**, 257–265 (1994).
- Komada, M. et al. Proteolytic processing of the hepatocyte growth factor/scatter factor receptor by furin. *FEBS Lett.* **328**, 25–29 (1993).
- Grice, D. M. et al. Golgi calcium pump secretory pathway calcium ATPase 1 (SPCA1) is a key regulator of insulin-like growth factor receptor (IGF1R) processing in the basal-like breast cancer cell line MDA-MB-231. *J. Biol. Chem.* **285**, 37458–37466 (2010).
- Han, K. et al. Synergistic drug combinations for cancer identified in a CRISPR screen for pairwise genetic interactions. *Nat. Biotechnol.* **35**, 463–474 (2017).
- Bassi, D. E., Fu, J., Lopez de Cicco, R. & Klein-Szanto, A. J. P. Proprotein convertases: “master switches” in the regulation of tumor growth and progression. *Mol. Carcinog.* **44**, 151–161 (2005).
- Hodges, R. S., Heaton, R. J., Parker, J. M., Molday, L. & Molday, R. S. Antigen–antibody interaction. Synthetic peptides define linear antigenic determinants recognized by monoclonal antibodies directed to the cytoplasmic carboxyl terminus of rhodopsin. *J. Biol. Chem.* **263**, 11768–11775 (1988).
- King, H., Aleksic, T., Haluska, P. & Macaulay, V. M. Can we unlock the potential of IGF-1R inhibition in cancer therapy? *Cancer Treat. Rev.* **40**, 1096–1105 (2014).
- Gentles, A. J. et al. The prognostic landscape of genes and infiltrating immune cells across human cancers. *Nat. Med.* **21**, 938–945 (2015).
- Pylayeva-Gupta, Y., Grabocka, E. & Bar-Sagi, D. RAS oncogenes: weaving a tumorigenic web. *Nat. Rev. Cancer* **11**, 761–774 (2011).
- Lindsay, C. R. & Blackhall, F. H. Direct Ras G12C inhibitors: crossing the rubicon. *Br. J. Cancer* **121**, 197–198 (2019).
- Molina-Arcas, M., Hancock, D. C., Sheridan, C., Kumar, M. S. & Downward, J. Coordinate direct input of both KRAS and IGF1 receptor to activation of PI3 kinase in KRAS-mutant lung cancer. *Cancer Discov.* **3**, 548–563 (2013).
- Lasko, L. M. et al. Discovery of a selective catalytic p300/CBP inhibitor that targets lineage-specific tumours. *Nature* **550**, 128–132 (2017).
- Gjorevski, N. et al. Designer matrices for intestinal stem cell and organoid culture. *Nature* **539**, 560–564 (2016).
- Huch, M. & Koo, B.-K. Modeling mouse and human development using organoid cultures. *Development* **142**, 3113–3125 (2015).
- Thoma, C. R., Zimmermann, M., Agarkova, I., Kelm, J. M. & Krek, W. 3D cell culture systems modeling tumor growth determinants in cancer target discovery. *Adv. Drug Deliv. Rev.* **69–70**, 29–41 (2014).
- Lawrence, M. S. et al. Discovery and saturation analysis of cancer genes across 21 tumour types. *Nature* **505**, 495–501 (2014).

**Publisher's note** Springer Nature remains neutral with regard to jurisdictional claims in published maps and institutional affiliations.

© The Author(s), under exclusive licence to Springer Nature Limited 2020



# Article

## Methods

### Cell lines

Ten non-small-cell lung carcinoma cell lines: NCI-H1437, NCI-H1568, NCI-1650, NCI-1975, NCI-H322, NCI-H1792, NCI-H2009, NCI-H23, NCI-H358 and A549, were purchased from the American Type Culture Collection. All cell lines were authenticated using the Human 9-Marker STR Profile test provided by IDEXX BioResearch and tested for mycoplasma contamination. Cells were cultured in RPMI 1640 (Gibco) supplemented with 10% FBS (HyClone), penicillin–streptomycin (Genesee), and GlutaMAX (Gibco). These 10 cell lines were transduced with a spCas9 lentiviral vector with a blasticidin selection marker (Addgene no. 52962), and selected with blasticidin ( $10 \mu\text{g ml}^{-1}$ ). Single-cell clones of these selected cell lines were individually tested for their Cas9-cutting efficiency by lentiviral infection with pMCB306<sup>39</sup>, a self-GFP-cutting reporter that has both GFP and an sgRNA against GFP on the same backbone. Single clones with high Cas9-cutting efficiency were established and used in the CRISPR screens and other biological assays.

### Large-scale 3D spheroid cultures

To culture lung cancer cells as 3D spheroids at genome scale, we used either pre-treated ultra-low attachment plates (Corning, no. 3261) or polyhema (Sigma, no. P3932) coated tissue culture plates. Methylcellulose (0.75%; Fisher, no. M-352) was added in RPMI 1640 growth medium to prevent excessive aggregation of cells in spheroid culture and to maintain even spheroid size. To determine an appropriate cell density for CRISPR screens, we tested multiple seeding densities of H23 cells ranging from 20,000 cells per  $\text{cm}^2$  to 150,000 cells per  $\text{cm}^2$ , with 500  $\mu\text{l}$  of growth medium per  $\text{cm}^2$ . H23 cells were seeded at multiple densities and their growth and death rates were monitored in an automated fluorescent microscope optimized for live-cell imaging (IncuCyte S3 or IncuCyte ZOOM, Essen Bioscience). Cell growth rates were monitored by mCherry expressed in the cell line and death rates were monitored by Sytox Green signal, which was added at 100 nM final concentration at the beginning of the experiment. Here, the number of live cells in spheroids was estimated by dividing total integrated mCherry intensities of spheroids by the average integrated mCherry intensity of single live cells measured at the initial cell-seeding phase. The number of dead cells was estimated similarly by dividing total integrated Sytox Green intensities of spheroids by the average integrated Sytox Green intensity of a single dead cell. We chose a cell density (50,000 cells per  $\text{cm}^2$ ) that showed about 30% peak cell death rate within 24 h after initial seeding. For all subsequent experiments, cells were initially seeded at 50,000 cells per  $\text{cm}^2$  density in 500  $\mu\text{l}$  of RPMI 1640 medium containing 0.75% methylcellulose. Spheroids were then split every 3–4 days. To passage cells, cancer spheroids were collected in methylcellulose media and diluted with PBS (~3 medium volumes) to reduce viscosity of the medium before centrifugation. Spheroids were then centrifuged at 800g for 15 min and medium and PBS was removed from the spheroid pellets. Accutase (Innovative Cell Technologies, no. AT104) was added to the pellets to dissociate the spheroids into single cells. We used 10 ml of accutase per 100 million cells in spheroids and incubated them for about 30 min until spheroids were fully dissociated into single cells. The single cells were then reseeded at the starting density (50,000 cells per  $\text{cm}^2$ , 500  $\mu\text{l}$  growth medium per  $\text{cm}^2$ ).

### Genome-wide and batch-retest CRISPR screens

The genome-wide CRISPR library and the batch-retest library were synthesized by Agilent and cloned as previously described<sup>25</sup>. The genome-wide CRISPR library was designed to have ~210,000 sgRNAs targeting 21,000 coding genes (10 sgRNAs per gene), with 13,500 negative control sgRNAs that are either scrambled, non-targeting sgRNAs or safe-sgRNAs targeting nonfunctional regions of human genomes. To design the batch-retest library, genes with 3D/2D phenotypes with

T-score cut-off (lower than  $-2.5$  or higher than  $3$ ) were first selected from the H23 genome-wide screens. We also included hits obtained in the 2D and 3D screens in the presence of the KRAS inhibitor, with phenotypes having a T-score cutoff (lower than  $-2.5$  or higher than  $2.5$ ). In addition, we included genes with known clinical drugs or druggable genes (such as kinase, phosphatase and other enzymes) and manually curated RAS-pathway genes that were hits in both 2D and 3D. The batch-retest library had 5,466 sgRNAs targeting these 911 hit genes (6 sgRNAs per gene) and 273 safe-sgRNAs. In brief, oligo pools for the libraries were synthesized (Agilent), PCR-amplified, digested with BstXI and BlnI restriction enzymes, and ligated into pMCB320 vector containing an mU6 promoter to drive sgRNA expression and a EF1a promoter to drive expression of mCherry fused to puromycin with a T2A linker. The plasmid libraries were then transfected into HEK239T cells to produce lentiviral pools, which were subsequently transduced into H23 cells and other indicated lung cancer cell lines. Cells were infected with the libraries at a multiplicity of infection of 0.3–0.5, and after 48 h were selected with puromycin ( $2 \mu\text{g ml}^{-1}$ ) for 3–5 days until the library-infected cell population was at least 90% mCherry positive (indicating presence of lentivirus). Cells were expanded for another 2–3 days and aliquots were saved as T0 stocks in liquid nitrogen. At the same time, the remaining cells were plated as 2D monolayer cultures or as 3D spheroids using the protocol described above. To maintain library complexity, the screens were performed at  $\sim 1,000\times$  cell number coverage per sgRNA for the genome-wide screens ( $\sim 200$  million cells) and at  $\sim 2,000\times$  cell number coverage for the batch-retest screens ( $\sim 10$  million cells). All screens were performed in biological replicates. In the genome-wide screens, we included an arm in which H23 cells were treated with ARS-853 at  $5 \mu\text{M}$  throughout the screens. Both 2D and 3D cultures were split every 3–4 days to keep cells in log growth phase throughout the screens. At day 21, cells were collected and stored in multiple cryovials (no. of cells in each cryovial for at least  $\sim 1,000\times$  library coverage) in liquid nitrogen for further processing. Genomic DNA was extracted from the samples with Qiagen Blood Maxi Kit (Qiagen, no. 51194). sgRNA cassettes were PCR-amplified from genomic DNA using Herculanase II Fusion polymerase (Agilent, no. 600679) and deep-sequencing adapters and sample barcodes were added during the PCR<sup>25</sup>. Finally, sgRNA compositions in the samples were measured with deep-sequencing on NextSeq 550 system (Illumina). Enrichments or disenrichments of sgRNAs either between T0 and end time point samples or between drug untreated and treated samples were then used to calculate growth or drug resistance phenotypes.

### Construction of CDKO library and CDKO screen

The  $145\times 145$  CRISPR double-knockout (CDKO) library was constructed as previously described<sup>39</sup>. In brief, 145 genes that have most negative 3D/2D phenotypes were chosen for the CDKO library. The three sgRNAs that showed the strongest effects in the genome-wide screens were chosen for each gene. A total of 463 sgRNAs (435 gene-targeting sgRNAs and 28 safe sgRNAs) were PCR-amplified from pooled oligo chips (Agilent) and cloned into pMCB320 and pKHH030, which are lentiviral vectors with mU6 or hU6 promoters, respectively. hU6-sgRNA-tracrRNA cassettes were then digested from the single-knockout CRISPR library based on pKHH030 and ligated into the single-knockout CRISPR library based on pMCB320 downstream of the mU6-sgRNA-tracrRNA cassettes. This generated the  $145\times 145$  CDKO library, which had 214,368 double-sgRNAs corresponding to 10,440 gene pairs. The CDKO screen was performed as other CRISPR screens at  $\sim 1000\times$  cell number coverage per sgRNA pair for 21 days in 2D monolayer H23 cells ( $\sim 200$  million cells). The screens were carried out in two experimental replicates starting from the same T0 population. Genomic DNA from both T0 and Day 21 samples were isolated and frequencies of double-sgRNAs were quantified by deep sequencing using a modified paired-end, single index protocol on NextSeq 550 as previously described<sup>39</sup>.

### Calculation of growth and drug resistance phenotypes

Effect sizes for sgRNAs were calculated as previously described<sup>17,39</sup>. In brief,  $\log_2$  fold enrichments of sgRNAs were first measured between two samples: T0 and day 21 samples for 2D and 3D phenotypes, T0 and day 30 samples for in vivo phenotypes, 2D day 21 and 3D day 21 samples for 3D/2D phenotypes, 2D day 21 and ARS-853 treated 2D day 21 samples for KRASi 2D phenotypes, and finally 3D day 21 and ARS-853 treated 3D day 21 samples for KRASi 3D phenotypes. The 3D/2D phenotypes were obtained by calculating enrichment of sgRNAs (read counts of sgRNAs) by comparing 2D day 21 samples with 3D day 21 samples directly. For any given phenotype, a median  $\log_2$  fold enrichment of all negative control sgRNAs (non-targeting and safe sgRNAs) was measured and this median value was subtracted from  $\log_2$  fold enrichments of all sgRNAs to account for systematic bias in screens. Lastly,  $\log_2$  fold enrichments of all sgRNAs were divided by the standard deviation of negative control sgRNAs to yield phenotype Z scores (pZ) of sgRNAs which we used as effect size of sgRNAs. Effect size of a gene is the median value of all sgRNAs that target the gene. We used modified *t*-value scores as our phenotype scores for genes, which account for both consistency and strength of all sgRNA effects for given genes.

Our phenotype scores based on *t*-value scores were computed as: phenotype score (T-score) =  $(U_{\text{gene}} - U_{\text{ctrl}}) / \sqrt{(S_{\text{var}}/N_{\text{exp}} + S_{\text{var}}/N_{\text{ctrl}})}$ , where  $U_{\text{gene}}$  is the median effect of all sgRNAs (pZ) for a given gene,  $U_{\text{ctrl}}$  is the median effect of all negative control sgRNAs (pZ), and  $S_{\text{var}}$  is  $\text{Var}_{\text{gene}} \times (N_{\text{exp}} - 1) + \text{Var}_{\text{ctrl}} \times (N_{\text{ctrl}} - 1)$ , where  $\text{Var}_{\text{gene}}$  is the variance of sgRNA effects (pZ) for a given gene,  $N_{\text{exp}}$  is the number of sgRNAs for a given gene and  $N_{\text{ctrl}}$  is the average number of sgRNAs per gene in a given screen.

To combine data from two experimental replicates, normalized pZ scores of sgRNAs from two replicates were pooled together and gene effects and phenotype scores were calculated from the pooled sgRNAs as described above.

### Calculation of genetic interaction scores

Genetic interactions of gene pairs in the CDKO library were computed as previously described<sup>39</sup>. In brief, the single-knockout phenotype of an sgRNA was calculated from phenotype Z scores of all double sgRNAs that have that sgRNA paired with control (safe) sgRNAs. Safe control sgRNAs target regions of the genome predicted to be non-functional<sup>25</sup>. The expected double-knockout phenotype of a double-sgRNA pair was computed by summing single-knockout phenotypes of two sgRNAs in the pair. The difference between the expected double-knockout phenotype and the observed double-knockout phenotype of a given double sgRNA was then defined as the raw genetic interaction (GI) score of the double sgRNA. The raw GI of the double sgRNA was then normalized by the standard deviation of 200 double sgRNAs that have the most similar expected double-knockout phenotypes to account for systematic bias of genetic interactions along increasing phenotype strength of double-sgRNAs. These normalized genetic interactions (norm GIs) of double sgRNAs were then used to calculate genetic interactions at the level of gene pairs. Three sgRNAs were assigned for each gene in the library, which gave a total of 9 combinations ( $3 \times 3$ ) for the gene pair in one orientation. Since there are two possible orientations for a gene pair (for example, A–B and B–A), there are at most 18 double sgRNAs that target a gene pair. The norm GI of a gene pair is simply the median value of all double-sgRNAs against the gene pair. We used  $GI_{\text{score}}$  and  $GI_{\text{Mscore}}$  as statistical scores to measure genetic interactions of gene pairs<sup>39</sup> in the CDKO library. In brief, the  $GI_{\text{score}}$  for a given gene pair was calculated on the basis of the modified *t*-value score and  $GI_{\text{Mscore}}$  is signed  $\log_{10}$  *P* value measured by Mann–Whitney *U*-test. Both scores take into account the strength and consistency of norm GIs of double sgRNAs, adjusted by observed noise levels reflected in non-interacting double-sgRNA controls that have at least one safe sgRNA in each pair. Mann–Whitney *U*-test *P* values were multiple-test corrected to compute

adjusted FDRs using Benjamini–Hochberg procedure. In the  $145 \times 145$  matrix of  $GI_{\text{score}}$ s, genes were hierarchically clustered with correlation distance calculated by Pearson correlation coefficients to generate the GI map. These correlation distances were also used to rank genes by their similarities to CPD in terms of their GI patterns. To combine data from two experimental replicates, norm GIs of double sgRNAs from two replicates were pooled together and norm GIs of genes and GI scores were then computed as described above.

### Annotation of cancer genes, TSGs and oncogenes

The Catalogue of Somatic Mutations in Cancer (COSMIC<sup>30</sup> v.86) was used to annotate genes as tumour suppressors or oncogenes. COSMIC is an expert-curated database of 719 somatic mutations for which roles in cancer are manually annotated by experts in the field. There are seven defined roles of the mutations in the database: oncogene, oncogene fusion, TSG, TSG fusion, fusion, oncogene–TSG and oncogene–TSG–fusion. For analysis of gene phenotypes and comparison to roles in cancer, we pooled genes in oncogene and oncogene–fusion categories and defined them as oncogenes. Genes in TSG and TSG–fusion categories were defined as TSGs.

### Analysis of lung cancer mutations

Comparisons between CRISPR phenotypes of genes and their significance as lung cancer mutations were performed using previously published data for lung cancers<sup>31</sup>. In the dataset, exome sequences and copy number profiles of 660 lung adenocarcinoma and 484 lung squamous cell carcinoma tumour–normal pairs were analysed. This generated a list of 11,249 genes that were reported to be mutated at least once in the lung cancer samples. Their mutational significances were computed with MutSig2CV<sup>31</sup> and also provided in the dataset. Sign-flipped  $\log_{10}$  MutSig2CV *q* values were then summed and displayed as cumulative sum plots along genes sorted by different screening phenotypes.

### Analysis of DepMap CRISPR datasets

The Avana dataset (v.18Q4) with CERES effects of ~18,000 genes across 517 cell lines was downloaded from the DepMap website (<https://dep-map.org/portal/download/>). To measure the percentage of positive hits in the CERES cell lines, absolute CERES effects were used to sort genes in descending order in each cell line. The first 1,000 genes were selected and the percentage of genes with positive CERES effects was measured in the 1,000 genes for each cell line. Cell lines were then grouped by their tissues of origin and the percentage of positive hits in each cancer were plotted as box plots (Fig. 1a). To define 50 core essential genes, we averaged CERES effects across the 517 cell lines. Genes were then sorted by average CERES effect in ascending order and the 50 genes with the most negative or toxic average CERES effects were defined as ‘core’ essential genes. To measure correlation of genes in terms of their cancer dependencies, CERES effects were first subject to a PCA-based correction method for genome-wide screening data<sup>21</sup>. This bias correction was shown to bolster the sensitivity and specificity of detecting true co-essentiality of gene pairs. Pearson correlation coefficients of genes were measured in the matrix of batch-corrected CERES effects.

### Identification of enriched co-essential functional modules

We used generalized least squares (GLS) to map co-essential interactions across all pairs of genes in the Avana dataset (v.18Q3) while automatically accounting for relatedness between cell lines<sup>22</sup>; unlike conventional approaches to co-essentiality mapping based on Pearson correlation, this approach yields non-inflated *P* values. We applied GLS to the matrix of CERES effects corrected with the PCA-based correction method described above<sup>21</sup>. We then applied the ClusterONE clustering algorithm<sup>52</sup>, originally developed to discover protein complexes de novo from protein–protein interaction data, to cluster genes into ‘co-essential modules’ in an unbiased fashion, based on their co-essentiality profiles across all other genes. Specifically, we ran ClusterONE on

the gene-by-gene matrix of GLS *P* values after row-wise FDR correction, with edge weights set to one minus the FDR *q* value<sup>53</sup>. To determine which co-essential modules were enriched in the different screening phenotypes, the probability that the distribution of members in a given module in terms of their phenotypes scores was significantly different from that of all genes was measured using Mann–Whitney *U*-test. Sign-flipped log<sub>10</sub> Mann–Whitney *U*-test *P* values and median effects of members in co-essential modules were plotted in volcano plots as *y* axis and *x* axis, respectively (Fig. 3a, Extended Data Fig. 4c). The most enriched co-essential modules from different screen phenotypes were then analysed. While we used GLS to define co-essential modules, we used batch-corrected CERES effects for visualizing co-essentiality of gene pairs in all scatter plots and cluster maps (Fig. 3c, Extended Data Fig. 4e, f).

## PANTHER pathway-enrichment analysis

To determine which pathways were enriched among the top hits from the different screen phenotypes, we uploaded the top 1,000 hits from each screen phenotype into the gene ontology knowledgebase website (<http://geneontology.org/>). We then performed the PANTHER overrepresentation test with PANTHER pathways<sup>54</sup> as the annotation dataset. Significance of enriched pathways was measured with Fisher's exact test and pathways that passed 5% FDR cutoff were displayed as significantly enriched pathways for each phenotype with the indicated Log10 FDR.

## Subcutaneous transplantation and analysis of subcutaneous tumours

Ten- to twelve-week-old female NSG mice<sup>55</sup> of similar weights were used for cell transplantation experiments. To determine the number of H23-derived cell lines to inject, several dilutions of cells ( $2 \times 10^5$ ,  $1 \times 10^6$ ,  $2 \times 10^6$  and  $4 \times 10^6$ ) were injected into both flanks and both shoulders of one NSG recipient mouse per dilution ( $n = 4$  mice; 16 tumours total). After ten days, 4 out of 4 palpable tumours formed from the  $4 \times 10^6$  cell injections, compared to 0 out of 4 for  $2 \times 10^5$  cell injections, 1 out of 4 for the  $1 \times 10^6$  cell injections and 1 out of 4 for the  $2 \times 10^6$  cell injections; therefore  $4 \times 10^6$  or more cells were used for all subsequent injections. For the batch re-test CRISPR screens, H23 cells were transduced with the library as described above. After selecting the cells with puromycin,  $8 \times 10^6$  library-transduced cells in 100  $\mu$ l PBS were injected into both flanks of NSG recipient mice. ( $n = 10$  mice; 20 tumours total). Ideally, this would represent  $\sim 13,000 \times$  cell number coverage for the library, although the actual cell number coverage per sgRNA was likely much lower since a large portion of injected cells would not contribute to tumour development after subcutaneous transplantation. Four weeks after transplantation, tumours were removed and homogenized using a tissue blender (Omni International, no. TH115-PCR), which was cleaned between each sample. Ten tumours from left flanks were pooled together as one experimental replicate and the other 10 tumours from right flanks were pooled together as the second experimental replicate. Genomic DNA was then extracted from these two pools using QIAamp DNA Blood Maxi Kit (Qiagen, no. 51194) with the manufacturer's protocol. To PCR-amplify sgRNA cassettes from genomic DNA for deep sequencing, we used  $\sim 15 \times$  more genomic DNA than what we would use for samples from in vitro CRISPR screens<sup>25,39</sup>. In brief, we scaled a reaction based on  $\sim 10 \mu$ g of genomic DNA in 100  $\mu$ l of PCR reaction for each  $\sim 300$  sgRNAs in the library. This was to account for genomic DNA that came from tumour infiltrating mouse cells. Amplified PCR samples were sequenced on a NextSeq 550 as described above. For the competitive growth assays in tumours, total  $4 \times 10^6$  H23-derived cells with roughly equal numbers of mCherry (gene-targeting sgRNAs) and GFP (safe sgRNAs) expressing cells in 100  $\mu$ l PBS were injected into both flanks of four NSG recipient mice per genotype ( $n = 12$  mice total across three groups; 24 tumours total). Thirty days after transplantation, subcutaneous tumours were individually dissected, roughly chopped using dissecting scissors and further dissociated into a single-cell suspension using collagenase IV,

dispase and trypsin at 37 °C for 30 min with rotation. After digestion, samples were passed through a 40- $\mu$ m filter and maintained in PBS with 2% FBS, 2mMEDTA, and 1 U ml<sup>-1</sup> DNase before analysis by fluorescence-activated cell sorting (FACS). For FACS analysis, mCherry/GFP ratio was determined at day 0 before subcutaneous injection and at day 30 from dissociated tumours. Log fold change of mCherry/GFP ratio between these two time points was calculated and normalized to the control mix (safe mCherry/safe GFP) (Fig. 3h). The Stanford Institute of Medicine Animal Care and Use Committee approved all animal studies and procedures.

## Histologic preparation and immunohistochemistry

Tumours from the in vivo competition assay were fixed with 4% formalin in PBS overnight and transferred to 70% ethanol before paraffin embedding. Paraffin-embedded tumours were sectioned into 4- $\mu$ m-thick slices, deparaffinized with xylene and ethanol and antigen-retrieved in citrate buffer. Immunohistochemical staining for GFP (Abcam, ab13970, 1:250) and mCherry (Abcam, ab167453, 1:250) was performed on these 4- $\mu$ m-thick sections. Alexa Fluor 488 secondary antibody (ThermoFisher Scientific, A-11039) and Alexa Fluor 594 secondary antibody (ThermoFisher Scientific, A-11012) were added with Hoechst to visualize GFP, mCherry and nuclei in the subsequent immunofluorescence imaging. Images were taken on an inverted epifluorescence microscope (Eclipse Ti, Nikon) using 10 $\times$  and 20 $\times$  objectives.

## The 1D4 reporter system

A 1D4 epitope<sup>41</sup> was placed just upstream of the RKRR motif in the IGF1R  $\alpha$ -chain and a Flag epitope was placed at the C terminus of the IGF1R  $\beta$ -chain (1D4–RKRR) (Fig. 4b). One or two additional amino acids were inserted between the 1D4 epitope and the RKRR motif in the control reporters (1D4–ERKRR, 1D4–PERKRR). An additional control reporter had an HA epitope instead of 1D4 (HA–RKRR reporter).

## Immunofluorescence imaging

For immunofluorescence imaging, cells were either fixed with 4% paraformaldehyde in PBS for 15 min at room temperature, or fixed with ice cold methanol at 4 °C for 15 min; for the CPD antibody (A305-514A-M, ThermoFisher), we used methanol fixation and used paraformaldehyde fixation for all other antibodies. Cells were washed twice with PBS and subsequently permeabilized with 0.2% Triton X-100 in PBS for 15 min at 4 °C for paraformaldehyde-fixed samples. Cells were blocked with 3% BSA in PBS for 1 h at room temperature. Primary and secondary antibodies were diluted in PBS containing 3% BSA. Cells were first incubated with the primary antibodies overnight at 4 °C. Cells were then washed three times with PBS and incubated with the secondary antibodies and Hoechst for 2 h before a triple wash in PBS. To quantify IGF1R-signalling activities in 2D monolayer cells, cells were processed in a 96-well multi-well plate and imaged either on inverted epifluorescence microscope (ImageXpress Micro, Molecular Devices) using a 10 $\times$  objective or on a spinning-disk confocal microscope (Eclipse Ti, Nikon, CSU-W1, Yokogawa) using a 20 $\times$  objective. More than four sites were acquired from each well and fluorescence signals were quantified across multiple image sites per condition. For the 1D4 assays, CPD staining and IGF1R staining in 3D spheroids, cells were processed in glass-bottom 24-well plates and imaged using the spinning-disk confocal microscope with a 10 $\times$  or 20 $\times$  objective. Primary antibodies were obtained from the following sources: IGF1R  $\alpha$ -chain and CPD antibodies from ThermoFisher (AHR0321, A305-514A-M); antibodies to MET, phospho-AKT (Ser437), phospho-ERK1/2 (Thr202/Tyr204) and Flag from Cell Signaling Technology (no. 8198, 4060, 4370 and 14793); Rho1D4 antibody from Millipore (MAB5356).

## Individual sgRNA validations using automated microscopy

H23 cell lines expressing the indicated sgRNAs were seeded either in tissue-culture treated (2D monolayers) or ultra-low-attachment (3D

spheroids) 24-well plates and loaded into an inverted epifluorescence microscope (IncuCyte S3 or IncuCyte ZOOM, Essenbioscience) compatible with live-cell imaging. For the competition assays, ~50,000 cells expressing gene-targeting sgRNA (mCherry) were mixed with ~50,000 cells expressing safe sgRNA (GFP) and seeded into a well in 24-well plates. Images were taken every 4 h for the next 72 h. mCherry/GFP ratios were then compared between 0 h and 72 h time points to track fold changes in the ratio. Fold changes in the ratios of samples were then normalized by the fold change in the ratio of safe mCherry and safe GFP mix to estimate relative 2D and 3D growth phenotypes of sgRNAs to the control. In addition, the normalized 3D fold changes were divided by the normalized 2D fold changes to estimate 3D/2D growth phenotypes of sgRNAs. For imaging colony size from H23 knockout cell lines, ~100,000 cells expressing gene-targeting sgRNAs (mCherry) were seeded into ultra-low attachment 24-well plates in the presence of 100 nM Sytox Green. Size and cell death of 3D spheroids from each knockout line was then monitored for the next 72 h. All experiments were performed in triplicate and sequences of sgRNAs used for the validation are listed in Supplementary Table 10.

### Rescue experiment with growth factors

The competitive growth assays between CPD null H23 cells and control H23 cells were performed in presence of 50 ng ml<sup>-1</sup> of IGF1 (PHG0071, ThermoFisher), EGF (E9644, Sigma-Aldrich) or HGF (294-HG-005, R&D Systems). The competitive growth assay was performed as described in the sgRNA validation experiments, but in this case, the indicated growth factor was added at the beginning of the experiment to measure its ability to rescue gene loss phenotypes.

### Drug-titration experiments

For the drug-titration experiments, ~16,000 cells were seeded into tissue-culture treated 96-well plates in RPMI 1640 growth medium (2D monolayers) or ultra-low attachment 96-well plates in RPMI 1640 growth medium with 0.75% methylcellulose. Cells were then grown for the next 72 h in presence of titrated inhibitors. At the 72 h point, 1/10th volume of alamarBlue reagent (ThermoFisher, DAL1100) was added to cells and incubated ~2 h for 2D monolayer cells and ~10 h for 3D spheroids at 37 °C. Fluorescence signals were then measured in a fluorescence plate reader (TECAN, no. 30016056; excitation at 560 nm, emission at 590 nm) to estimate relative number of live cells at different dosages of the inhibitors. Wild-type H23 cells were used in the experiments where efficacies of small molecule inhibitors were compared between 2D and 3D. To test whether CPD deletion sensitizes cells against ARS-853, H23 cells with safe sgRNA and with *CPD* sgRNA (no fluorescent marker) were used. Small inhibitors were obtained from the following sources: savolitinib from Selleckchem (no. S7674), linsitinib from VWR (no. 10189-468), FURIN inhibitor I from Sigma Aldrich (no. 344930) and ARS-853 from Cayman Chemical (no. 1629268-00-3).

### Immunoblotting

Cells were lysed in RIPA buffer containing phosphatase and protease inhibitor cocktails (Roche, no. 11697498001). Lysates were then incubated on ice for 15 min, then clarified at 16,000g, 4 °C, for 10 min. Protein was quantified using the Bradford method and lysates were made with NuPage Sample Buffer (4×). Membranes were then probed with KRAS and GAPDH antibodies (1:1,000 dilution) from ThermoFisher (no. 415700, AM4300). The following secondary antibodies were used at a 1:5,000 dilution: anti-rabbit or anti-mouse IRDye-conjugated secondary antibodies from Fisher Scientific (no. NC9401841, NC9401842, NC0110517 and NC9030091). Finally, membranes probed with the IRDye-conjugated antibodies were imaged on an infrared imaging system (Li-Cor, Odyssey CLx). Uncropped western blots are shown in Supplementary Fig. 1.

### Knocking down genes in established spheroids

To knockdown genes in established spheroids, we transduced rtTA and inducible KRAB-dCas9-T2A-mCherry<sup>17</sup> under control of a tet-on promoter into H23 cells. These cells were treated with doxycycline for two days and were sorted for mCherry signal by FACS to select cells that can reliably induce dCas9 expression upon doxycycline treatment. Doxycycline was withdrawn from the sorted cells and cells were sorted again for loss of mCherry signal to establish an inducible CRISPRi cell line that can turn off dCas9 upon doxycycline withdrawal. This cell line was transduced with CRISPRi sgRNAs against *CPD* and *KRAS*. These cells were then seeded to form spheroids for 48 h, after which doxycycline was added at 0.2 µg ml<sup>-1</sup> concentration to induce knockdown target genes in the established spheroids. Growth of spheroids was then monitored for the next 5 days in an automated microscope (IncuCyte S3, Essen Bioscience).

### PRECOG analysis

PRECOG analysis was performed as previously described<sup>43</sup>. In brief, lung adenocarcinoma datasets were merged by normalizing CPD expression within each cohort so that its mean and s.d. were 1 across stage 1 patients. The merged set of 1,321 patients was split into high versus low CPD on the basis of the median expression of CPD across the entire dataset. Kaplan–Meier analysis was used to assess association with overall survival, with *P* value calculated by log-rank test. PRECOG Meta-Z scores for genes in the CPD module across different cancer types were obtained from the PRECOG website (<https://precog.stanford.edu/>).

### RNA-seq experiment and analysis

H23 cells expressing control (safe) sgRNA or *CPD* sgRNA were cultured as 2D monolayers or 3D spheroids in 100-mm tissue culture plates. RNA was extracted with TRIzol (ThermoFisher, 15596026) and processed with a RNA-seq library preparation kit (Illumina, RS-122-2101) to produce libraries for deep sequencing on NextSeq 550. Library preparation and sequencing were performed according to the manufacturer's protocol. Sequencing reads were mapped to the combined indices of cDNAs and non-coding RNA transcripts from GRCh38 genome reference using Kallisto<sup>56</sup>. Differentially regulated genes between the two different conditions were analysed using Sleuth<sup>57</sup>. Here, Sleuth computed FDRs for differential regulation of transcripts. If a gene has multiple transcripts, the best FDR value from all the transcripts was chosen to represent the FDR for differential regulation of the gene. We then defined a set of differentially regulated genes using 5% FDR cut-off. Genes significantly downregulated in *CPD*-deleted 3D spheroids compared to control 3D spheroids were further analysed for their predictive power for survival rates of patients with lung cancer.

### TCGA outcome analysis in downregulated genes upon CPD deletion

TCGA lung adenocarcinoma gene expression data (FPKM-UQ) and outcome and clinical data were downloaded from [gdc.cancer.gov](https://gdc.cancer.gov). We used GSVA<sup>58</sup> to study the association with outcome of the genes associated with the *CPD*-deleted phenotype. RNA-seq counts were normalized using Limma voom<sup>59</sup>. Outcome data was censored to seven years. Kaplan–Meier plots were generated using the *survminer* package from Bioconductor. High versus low *CPD* GSVA score was defined using the 1/3 upper versus 1/3 lower quantiles. Log-rank test *P* values are reported. Additionally, we built a Cox proportional-hazard model to account for key clinical covariates including age, stage, gender and TP53 and KRAS status. We also studied the interaction between *CPD* GSVA score and *KRAS* mutation status using a Cox proportional-hazard model with the same covariates.

## Statistical analysis

The statistical significance used to compare the averages of two different experimental groups in all box plots and bar graphs in this study was computed using unpaired, two-tailed Student's *t*-test. No statistical methods were used to predetermine sample size. The experiments were not randomized, and investigators were not blinded to allocation during experiments and outcome assessment.

## Reporting summary

Further information on research design is available in the Nature Research Reporting Summary linked to this paper.

## Data availability

Sequencing data from all CRISPR screens and RNA-seq experiments are available under BioProject accession number PRJNA535417. All other data are available from the corresponding author upon reasonable request.

## Code availability

All screening data were analysed with custom Python scripts (v.2.7) that are available at [https://github.com/biohank/CRISPR\\_screen\\_analysis](https://github.com/biohank/CRISPR_screen_analysis). Custom Matlab scripts (v.2015b) were used to quantify signals from all immunofluorescence images and to analyse FACS data: these scripts can be requested from K.H.

52. Nepusz, T., Yu, H. & Paccanaro, A. Detecting overlapping protein complexes in protein-protein interaction networks. *Nat. Methods* **9**, 471–472 (2012).
53. Storey, J. D. & Tibshirani, R. Statistical significance for genomewide studies. *Proc. Natl Acad. Sci. USA* **100**, 9440–9445 (2003).
54. Mi, H., Muruganujan, A. & Thomas, P. D. PANTHER in 2013: modeling the evolution of gene function, and other gene attributes, in the context of phylogenetic trees. *Nucleic Acids Res.* **41**, D377–D386 (2013).
55. Shultz, L. D. et al. Human lymphoid and myeloid cell development in NOD/LtSz-scid *IL2Rγ*<sup>null</sup> mice engrafted with mobilized human hemopoietic stem cells. *J. Immunol.* **174**, 6477–6489 (2005).

56. Bray, N. L., Pimentel, H., Melsted, P. & Pachter, L. Near-optimal probabilistic RNA-seq quantification. *Nat. Biotechnol.* **34**, 525–527 (2016).
57. Pimentel, H. J., Bray, N., Puente, S., Melsted, P. & Pachter, L. Differential analysis of RNA-seq incorporating quantification uncertainty. *Nat. Methods* **14**, 687–690 (2016).
58. Hänzelmann, S., Castelo, R. & Guinney, J. GSEA: gene set variation analysis for microarray and RNA-seq data. *BMC Bioinformatics* **14**, 7 (2013).
59. Law, C. W., Chen, Y., Shi, W. & Smyth, G. K. voom: Precision weights unlock linear model analysis tools for RNA-seq read counts. *Genome Biol.* **15**, R29 (2014).

**Acknowledgements** We thank J. Sage and members of the Bassik laboratory for discussions and critical reading of the manuscript. This work was supported by the NIH Director's New Innovator Award Program (1DP2HD084069), NIH/NCI 1U01CA199261 to M.C.B., P.J. and A.S.-C., and NIH/NCI 1U01CA217851 to C.J.K, C.C. and M.C.B. This work was also partly supported by a Stanford SPARK Translational Research Grant. We also thank D. Mochly-Rosen and K. Grimes at Stanford University for their support of this work. K.H. is supported by the Walter V. and Idun Berry award. S.E.P. is supported by National Science Foundation.

**Author contributions** K.H. and M.C.B. conceived and designed the study. K.H. designed the scalable 3D culture system for genome-wide CRISPR screens. K.H., A.L. and K.S. performed the CRISPR screens. K.H. and S.E.P. performed *in vivo* mouse experiments including the *in vivo* CRISPR screens and the competition assay. K.H., S.E.P. and M.Y. performed immunohistochemistry on tumour sections from the competition assay. G.R.A., M.D., M.O. and R.A.K. performed the western blots for IGF1R in various cancer cell lines. K.H. designed the 1D4 reporter and performed the immunocytochemistry. A.L. performed the western blot for the 1D4 assay. K.H. performed and analysed the RNA-seq. J.A.S. analysed the TCGA data for patient survival outcomes associated with genes downstream of CPD. M.W. defined co-essential modules from the DepMap CRISPR dataset. K.H. and K.K. generated Cas9-expressing non-small-cell lung carcinoma lines. A.J.G. performed PRECOG analysis. K.H., K.S. and K.L. validated the hits from the CRISPR screens. K.H. performed the drug validations. K.H. wrote the Python and Matlab scripts to analyse the screening data and to quantify the immunofluorescence signals in microscope images. K.H. and M.C.B. wrote the manuscript. All authors discussed the results and the manuscript.

**Competing interests** The authors, through the Office of Technology Licensing at Stanford University, have filed patent applications on methods for inhibiting tumour growth by inhibiting CPD as well as systems and methods for identifying CPD inhibitors and other tumour suppressors and/or oncogenes.

## Additional information

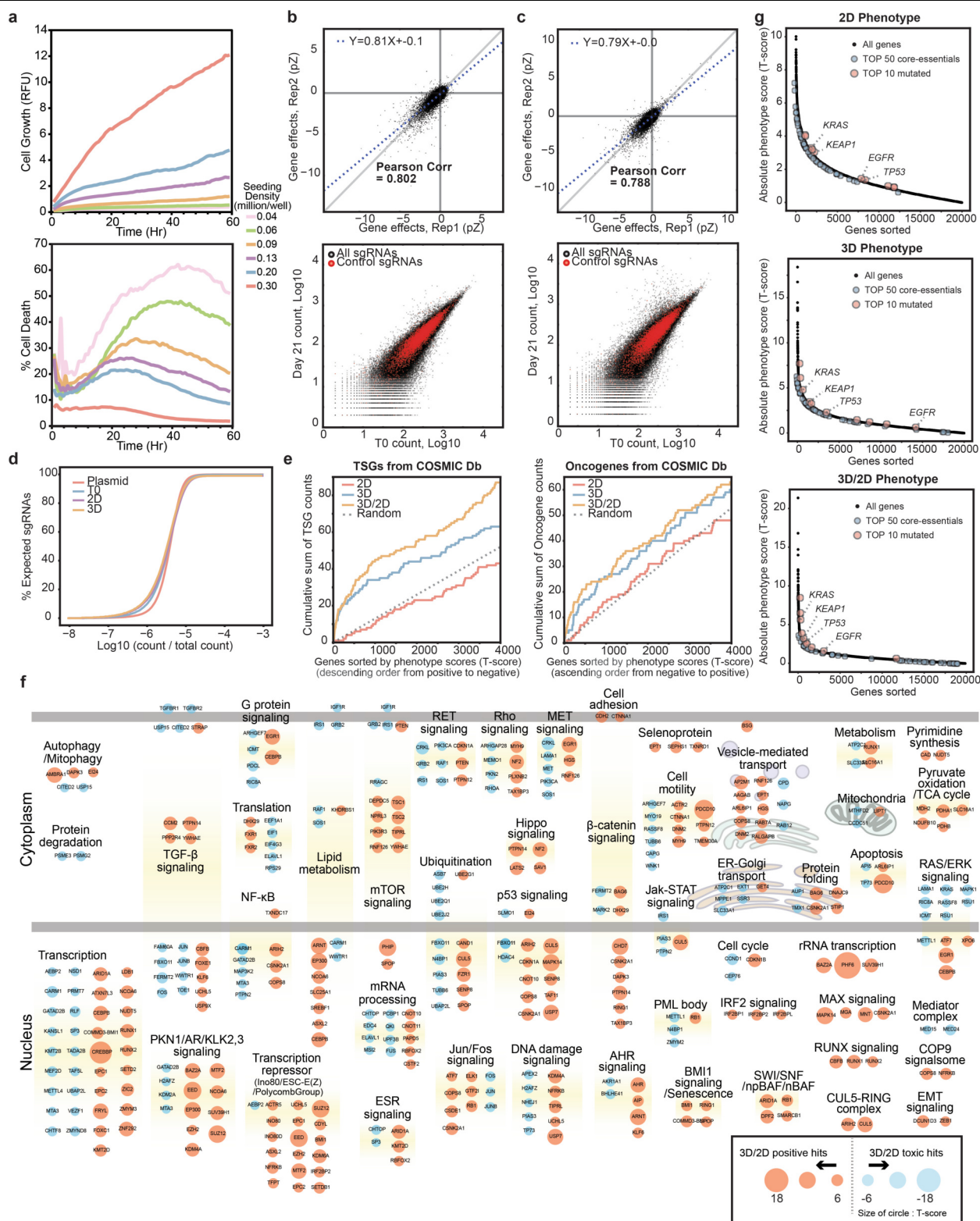
**Supplementary information** is available for this paper at <https://doi.org/10.1038/s41586-020-2099-x>.

**Correspondence and requests for materials** should be addressed to K.H. or M.C.B.

**Peer review information** *Nature* thanks Charles M. Rudin, Nicola Valeri and the other, anonymous, reviewer(s) for their contribution to the peer review of this work.

**Reprints and permissions information** is available at <http://www.nature.com/reprints>.





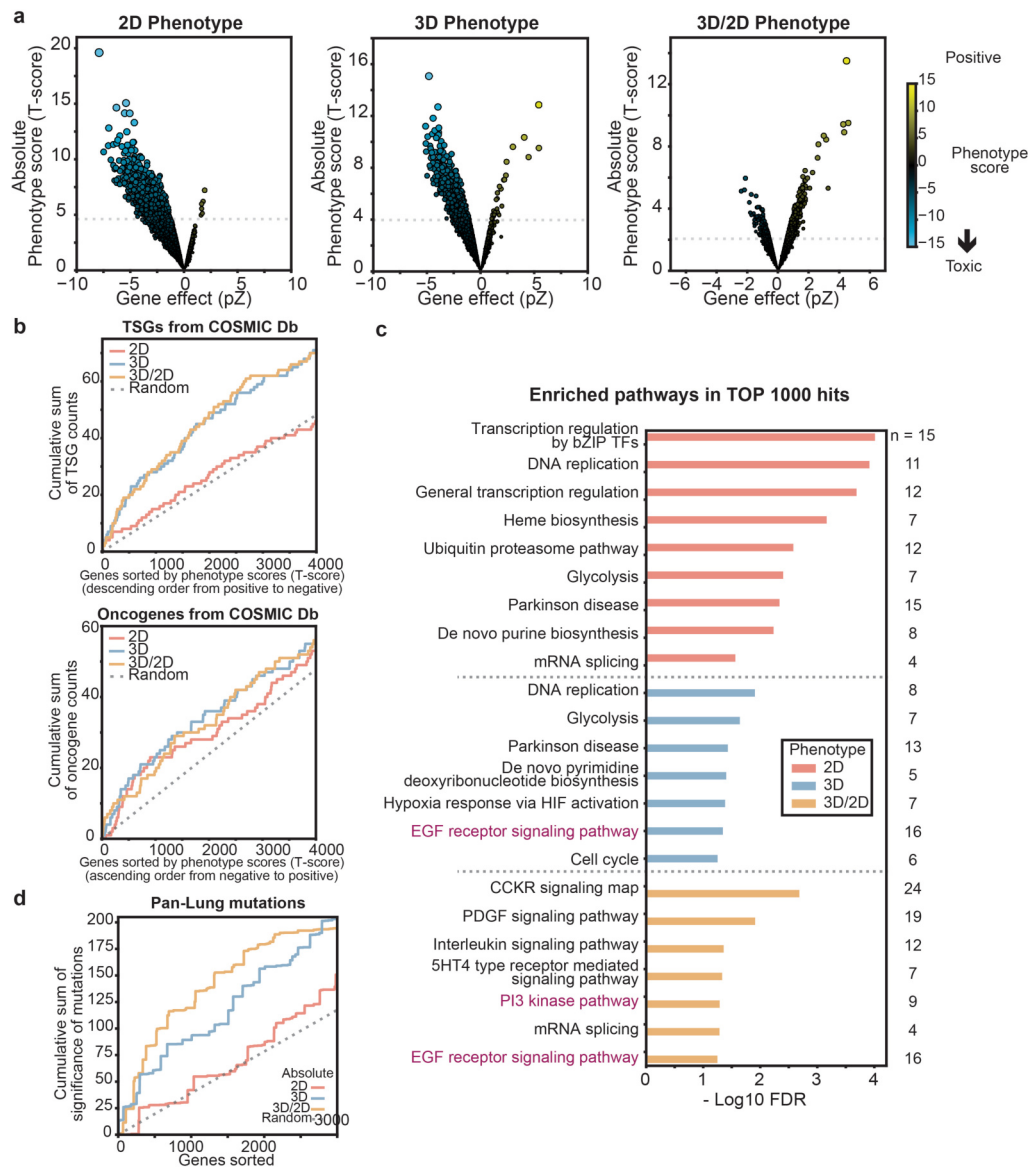
**Extended Data Fig. 1** | See next page for caption.

# Article

## Extended Data Fig. 1 | High quality and reproducibility of 2D and 3D genome-wide CRISPR screens and hits with differential effects in the two conditions.

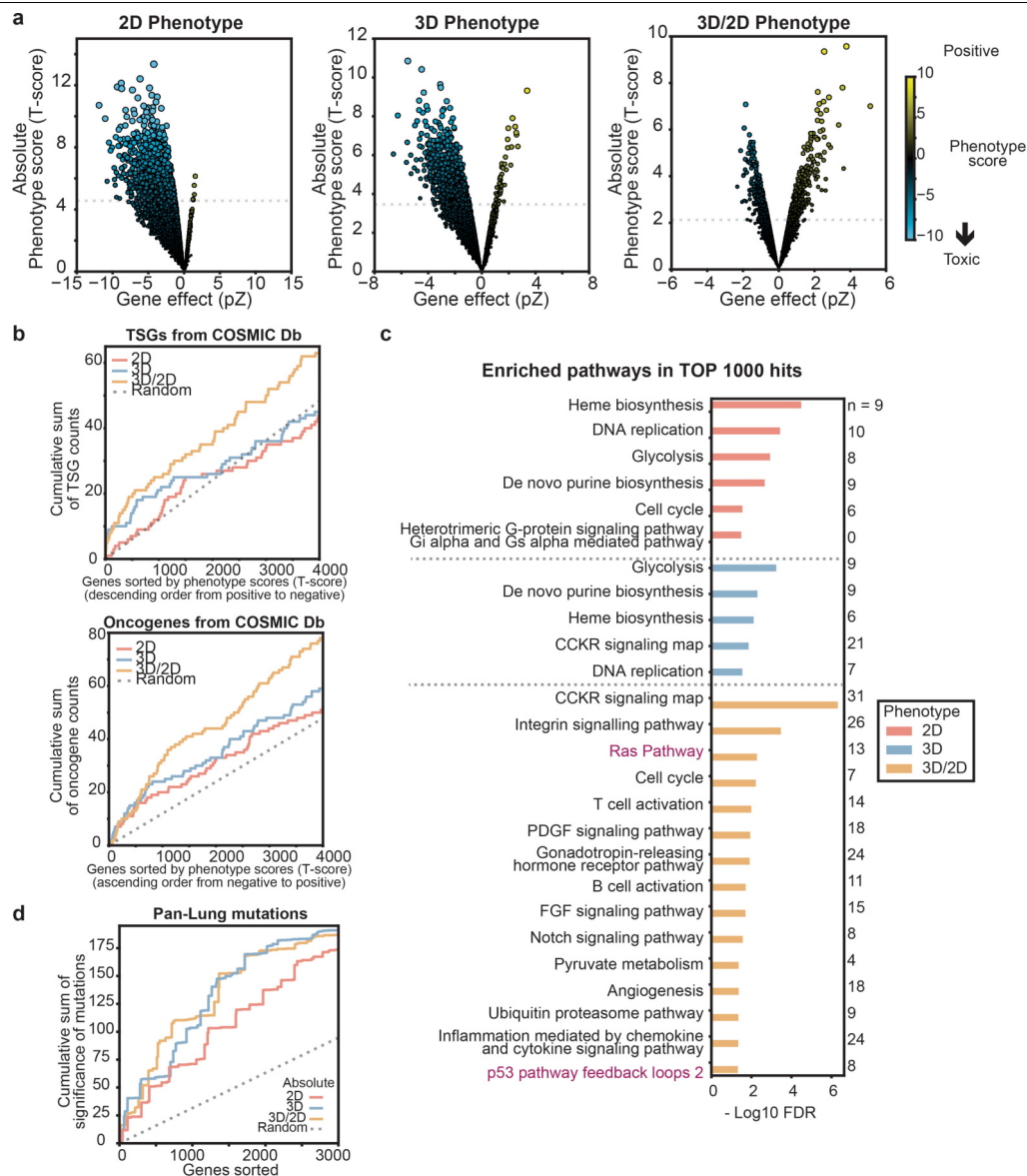
**a**, H23 cells expressing mCherry were seeded at different densities in ultra-low attachment plates in the presence of 0.75% methylcellulose. Sytox Green was added at 100 nM concentration. Average mCherry signal and Sytox Green signal measured across single cells were used to estimate the total numbers of live cells and dead cells at each seeding density. Cell growth and death rates were then monitored simultaneously on a live-cell microscope for 60 h. We aimed for a cell death rate of about 30% during the initial growth phase of spheroids, and  $10^5$  cells per well ( $1.9 \text{ cm}^2$ ) was the chosen cell seeding density for our genome-wide screens in 3D spheroids. **b**, Two-dimensional growth phenotypes of 20,463 genes were highly reproducible between experimental replicates (top). Sequencing counts of 208,687 sgRNAs in a T0 sample and a day 21 sample from the 2D genome-wide screens (bottom) show that most negative-control sgRNAs (red dots) are not enriched or disenriched between T0 and day 21 (black dots). This indicates the complexity of the genome-wide library was maintained throughout the 2D screen. In the top plot, the data are fit by a linear regression line (blue dotted line). The grey line marks a 1:1 diagonal. **c**, The quality and reproducibility of the 3D screens were comparable to those of the 2D screens, suggesting that the scalable 3D spheroid culture system is on a par with traditional 2D culture methods for its performance in genome-scale CRISPR screens.  $n = 20,463$  genes (top);  $n = 208,687$  sgRNAs

(bottom). In the top plot, the data are fit by a linear regression line (blue dotted line). The grey line marks a 1:1 diagonal. **d**, Cumulative distribution of sequencing reads for sgRNAs in the genome-wide CRISPR library. Read counts were normalized by total reads for each sample and the cumulative sums of sgRNAs were plotted as relative percentages of the number of expected sgRNAs. **e**, Cumulative sums of TSG counts (left) or oncogene counts (right) are plotted against genes sorted by their 2D, 3D or 3D/2D phenotypes (T-score) from the genome-wide screens in H23 cells. TSGs are expected to have positive growth phenotypes when deleted. Therefore, genes are sorted in descending order from the most positive to the most negative phenotypes in the left plot. Oncogenes are expected to have negative or toxic growth phenotypes and genes are sorted in ascending order in the right plot. Black dotted line, randomly sorted genes. The first 4,000 genes are displayed. **f**, Summary of hits with differential 3D/2D phenotypes. Top positive (red-filled circles) and negative (blue-filled circles) hits from the differential 3D/2D phenotypes reveal many cancer-relevant genes associated with transcriptional regulation, cell motility, cell adhesion and energy metabolism. Cancer-signalling pathways such as Ras–MAPK, TGF $\beta$ , MET, Rho,  $\beta$ -catenin and Hippo signalling are highly represented. Sizes of circles are proportional to 3D/2D phenotype scores. **g**, The 10 most significant pan-lung cancer genes<sup>31</sup> and 50 top core essential genes are marked. Genes sorted by absolute phenotype (T-score) in 2D, 3D and 3D/2D (see Methods).



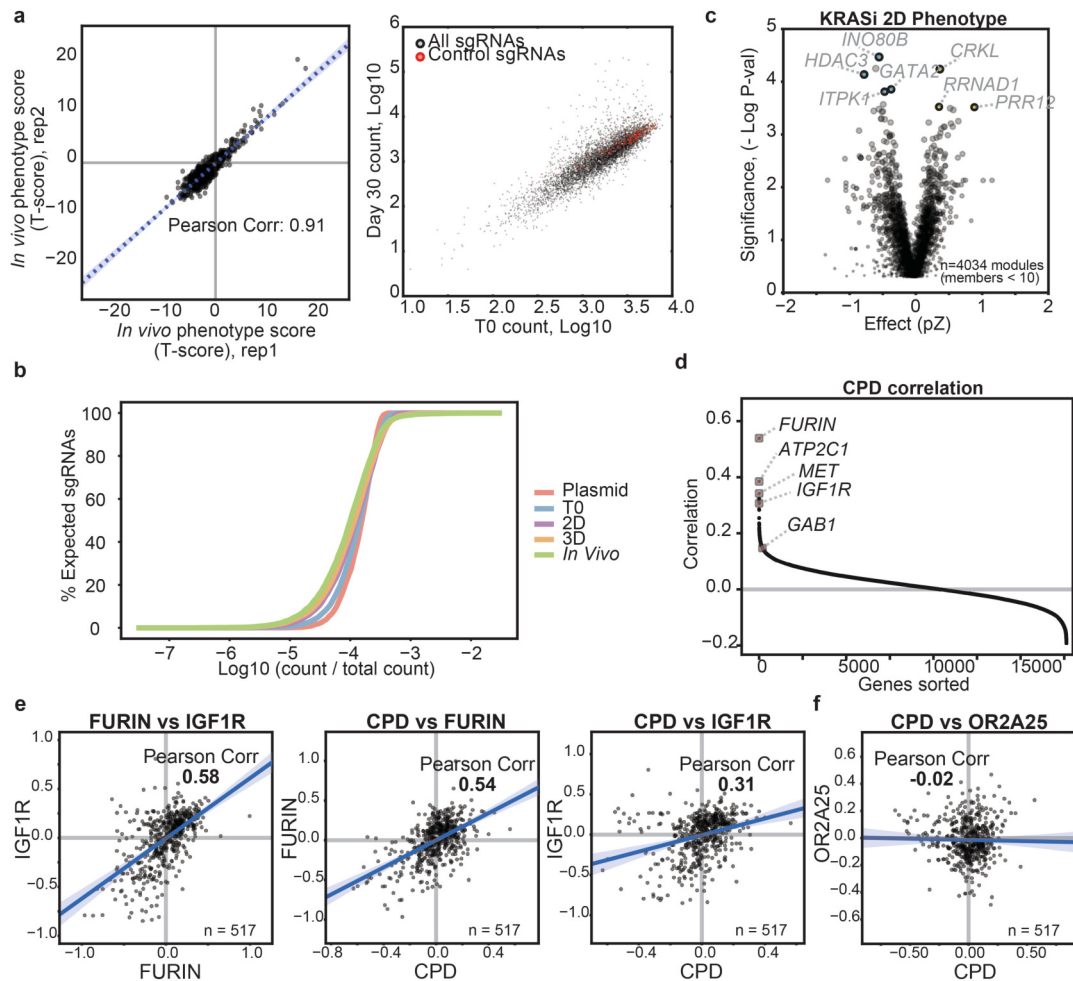
**Extended Data Fig. 2 | Genome-wide 2D and 3D CRISPR screens in H1975, a lung adenocarcinoma line with *EGFR*<sup>L858R</sup> mutation.** **a**, Distributions of 2D and 3D phenotypes are shown as volcano plots. The y axis represents absolute T-score for each gene, and the x axis represents effect size of each gene. Size of dots represents absolute T-score of genes. **b**, Prediction of TSGs or oncogenes with 2D, 3D, 3D/2D phenotypes in H1975 cells. Cumulative sums of TSGs counts (top panel) or oncogenes counts (bottom panel) are plotted against genes sorted by their 2D, 3D, or 3D/2D phenotypes (T-score) from the genome-wide screens in H1975 cells. These data indicate 3D or differential 3D/2D phenotypes show marked improvement for prediction of TSGs when compared to the 2D phenotypes, with marginal improvement for predicting oncogenes. In the box plots, centre lines mark median, box limits mark upper and lower quartiles,

whiskers show 1.5× interquartile range and points indicate outliers. **c**, Enriched pathways among the top 1,000 hits from each culture condition were analysed using PANTHER overrepresentation test. Significance of enriched pathways was measured with Fisher's exact test and the Benjamini–Hochberg FDR was subsequently computed (x axis). The EGFR signalling pathway, a known driver for H1975 cells, is enriched in only 3D or 3D/2D phenotypes. Number of genes for enriched pathways are marked to the right of bars. **d**, The cumulative sum of the significance of 11,249 pan-lung cancer mutations from 1,144 patients with lung cancer as measured by MutSig2CV is displayed on the y axis, whereas the x axis shows phenotypes for genes sorted by their strength in 2D (solid red line), 3D (solid blue line) or 3D/2D (solid yellow line). Black dotted line, randomly sorted genes. Top 3,000 genes are shown.



**Extended Data Fig. 3 | Genome-wide 2D and 3D CRISPR screens in H2009, a lung adenocarcinoma line with *KRAS*<sup>G12A</sup> mutation. a**, Distributions of 2D and 3D phenotypes are shown as volcano plots. The y-axis represents absolute T-score for each gene, and the x-axis represents effect size of each gene. Size of dots represents absolute T-score of genes. **b**, Prediction of TSGs or oncogenes with 2D, 3D and 3D/2D phenotypes in H2009 cells. Cumulative sums of TSG counts (top) or oncogene counts (bottom) are plotted against genes sorted by their 2D, 3D or 3D/2D phenotypes (T-score) from the genome-wide screens in H2009 cells. These data indicate that 3D phenotypes, and in particular the differential 3D/2D phenotypes show improved prediction of both TSGs and oncogenes when compared with 2D phenotypes. In the box plots, centre lines mark median, box limits mark upper and lower quartiles, whiskers show

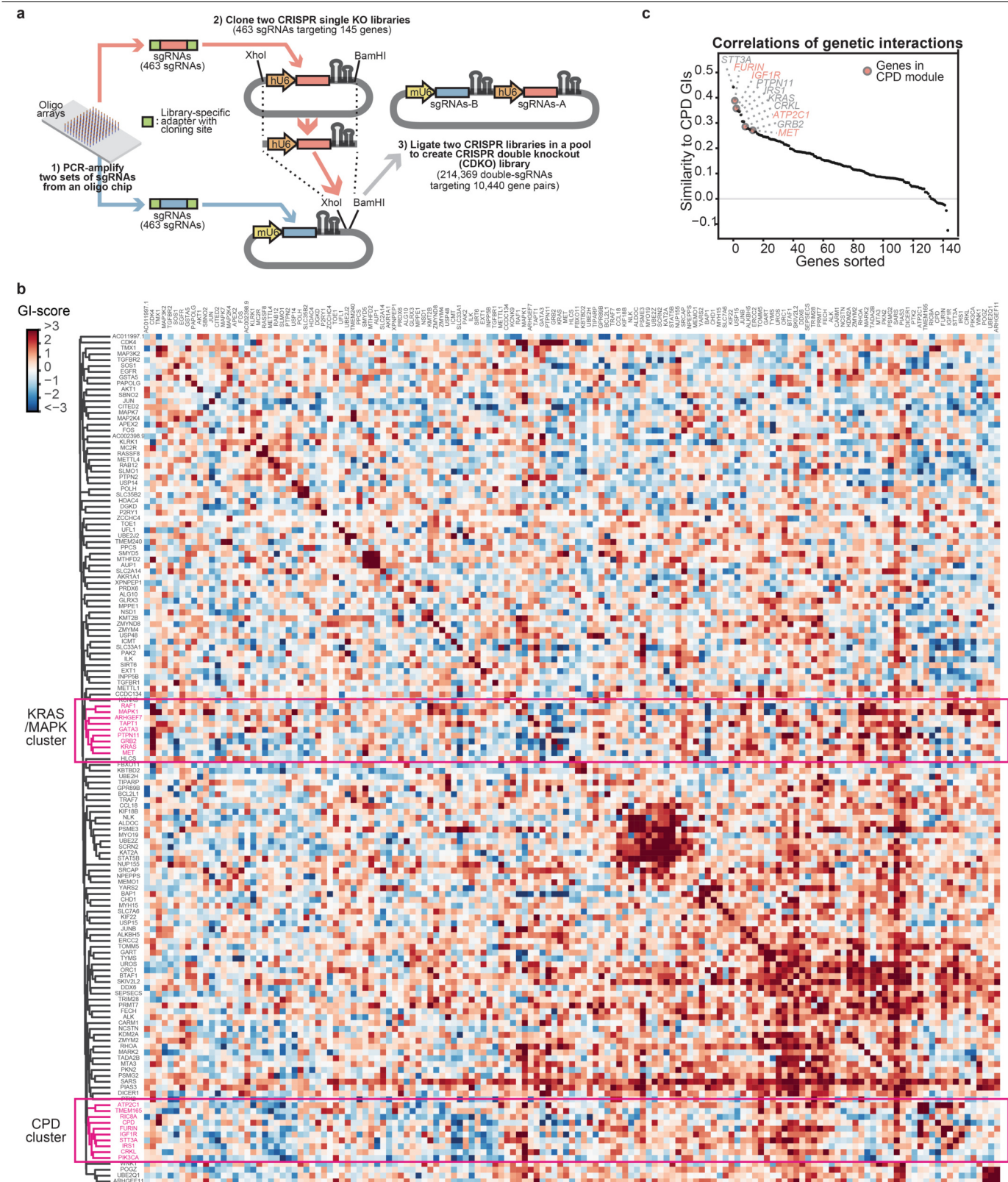
1.5× interquartile range and points indicate outliers. **c**, Enriched pathways among the top 1,000 hits from each culture condition were analysed using PANTHER overrepresentation test. Significance of enriched pathways was measured with Fisher's Exact test and the Benjamini–Hochberg FDR was subsequently computed (x axis). The Ras pathway, a known driver for H2009 cells, is enriched in 3D/2D phenotypes. Numbers of genes for enriched pathways are marked to the right of bars. **d**, The cumulative sum of the significance of 11,249 pan-lung cancer mutations from 1,144 patients with lung cancer as measured by MutSig2CV is displayed on the y axis, while the x axis shows phenotypes for genes sorted by their strength in 2D (solid red line), 3D (solid blue line) or 3D/2D (solid yellow line). Black dotted line, randomly sorted genes. Top 3,000 genes are shown.



**Extended Data Fig. 4 | High quality and reproducibility of optimized in vivo CRISPR screens and analysis of the *CPD* co-essential module.** **a**, A CRISPR sgRNA library targeting 911 hits with differential growth effects in 3D versus 2D (Supplementary Table 4) was introduced into H23 cells, and introduced by subcutaneous injection into NSG mice. After 30 days, tumours were collected and sgRNAs were amplified. In vivo growth phenotypes of 911 genes were highly reproducible between experimental replicates (left). Sequencing counts of T0 samples and day 30 samples from the in vivo batch-retest screens (right). In the left plot, the data are fit by a linear regression line (blue dotted line). **b**, Cumulative distribution of sequencing reads for sgRNAs in the batch-retest library in H23 cells. Read counts were normalized by total reads for each sample and the cumulative sums of sgRNAs were plotted as relative percentages of the number of expected sgRNAs. **c**, The 4,034 co-essential gene

modules based on the DepMap CRISPR dataset are plotted as volcano plots for KRAS 2D phenotype scores. The y axis shows significance of enrichments of co-essential modules as measured in log *P* values from the two-sided Mann-Whitney *U*-test (see Methods); the x axis shows average gene effects of members in CERES modules. **d**, Genes in the *CPD* module are indicated among 17,634 genes sorted by their correlations to *CPD*. Pearson correlation coefficients between *CPD* and other genes are measured in batch-corrected CERES effects in the DepMap CRISPR dataset. **e**, CERES effects of *CPD*, *FURIN* and *IGF1R* are shown as correlation plots. CERES effects are batch-corrected before plotting<sup>21</sup>. Blue lines, regression lines. Blue shaded translucent bands, 95% confidence intervals. **f**, Lack of correlation between *CPD* and *OR2A25*, an olfactory receptor, in their CERES effects across 517 cancer lines.

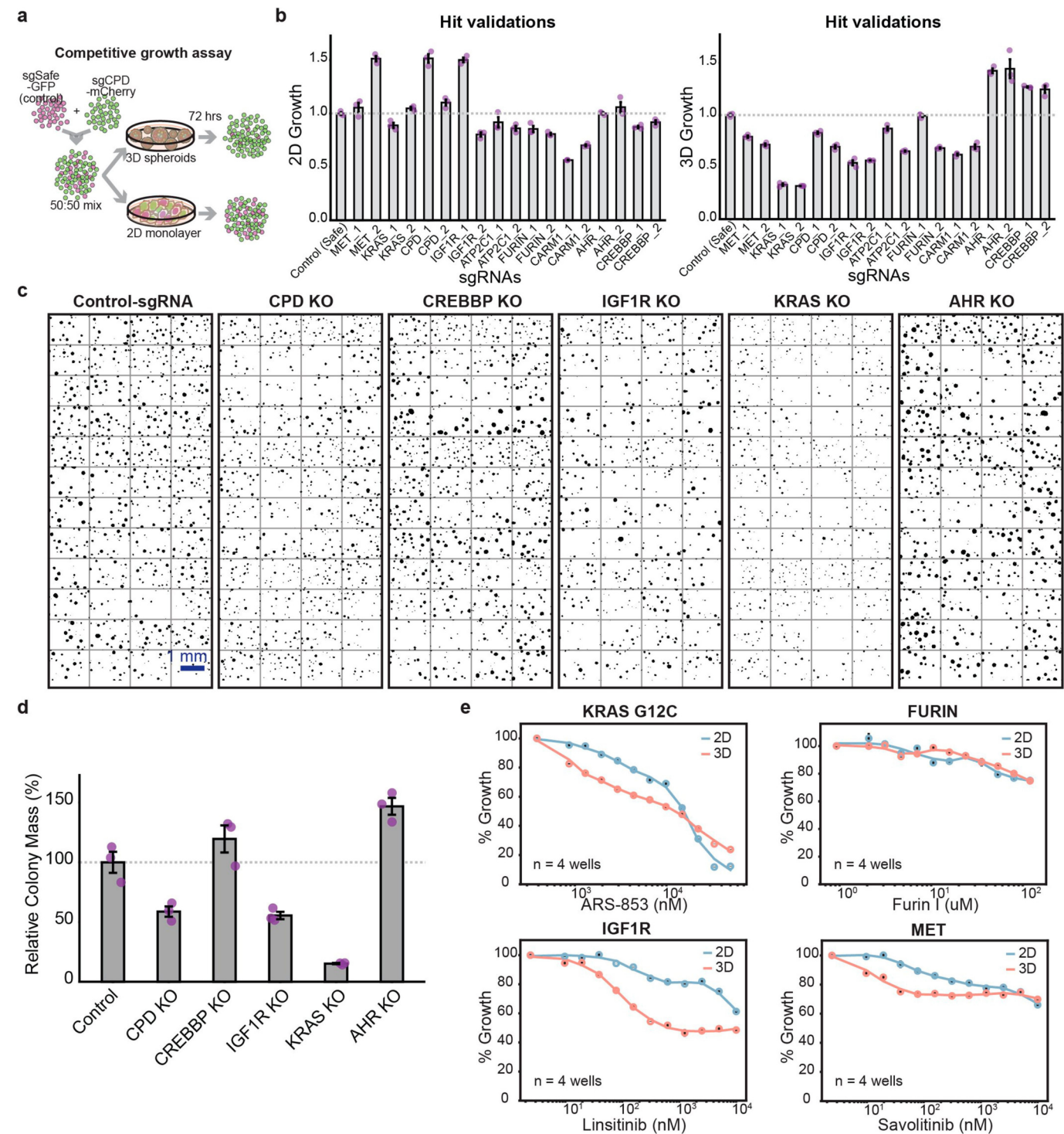




Extended Data Fig. 5 | See next page for caption.

**Extended Data Fig. 5 | Analysis of *CPD* co-essential module with a  $145 \times 145$  gene genetic-interaction map.** **a**, Cloning of CDKO library. A total of 463 sgRNAs targeting 145 hits from the 3D/2D phenotypes were PCR-amplified from an oligonucleotide array. These 145 hits include members of the *CPD* co-essential module. sgRNAs were separately cloned into two lentiviral vectors with either a mU6 or a hU6 promoter to generate two CRISPR single-knockout libraries. hU6-sgRNA cassettes were then cut out from one library and ligated into the other library containing the mU6 promoter. This generated a CDKO library with all possible pairwise combinations of the 463 sgRNAs (214,369 double sgRNAs). This CDKO library was used to measure genetic interactions

(GIs) of 10,440 gene pairs ( $145 \times 145$  combinations). **b**, The  $145 \times 145$  genetic-interaction map; the  $145 \times 145$  matrix of genetic-interaction scores are shown as a heat map. The 145 genes are clustered by the similarities of their genetic interactions (Pearson correlation coefficients of genetic interactions) in the map. Members of the *CPD* co-essential module form a cluster (marked with red box) in this genetic-interaction map, consistent with their correlations in the DepMap CRISPR dataset. **c**, A genetic-interaction map validates the *CPD* co-essential module in H23. Correlations of genetic interactions are used to sort 145 genes on the basis of their similarities to genetic interactions of *CPD*. Genes in the *CPD* module are marked with red dots along the sorted genes.

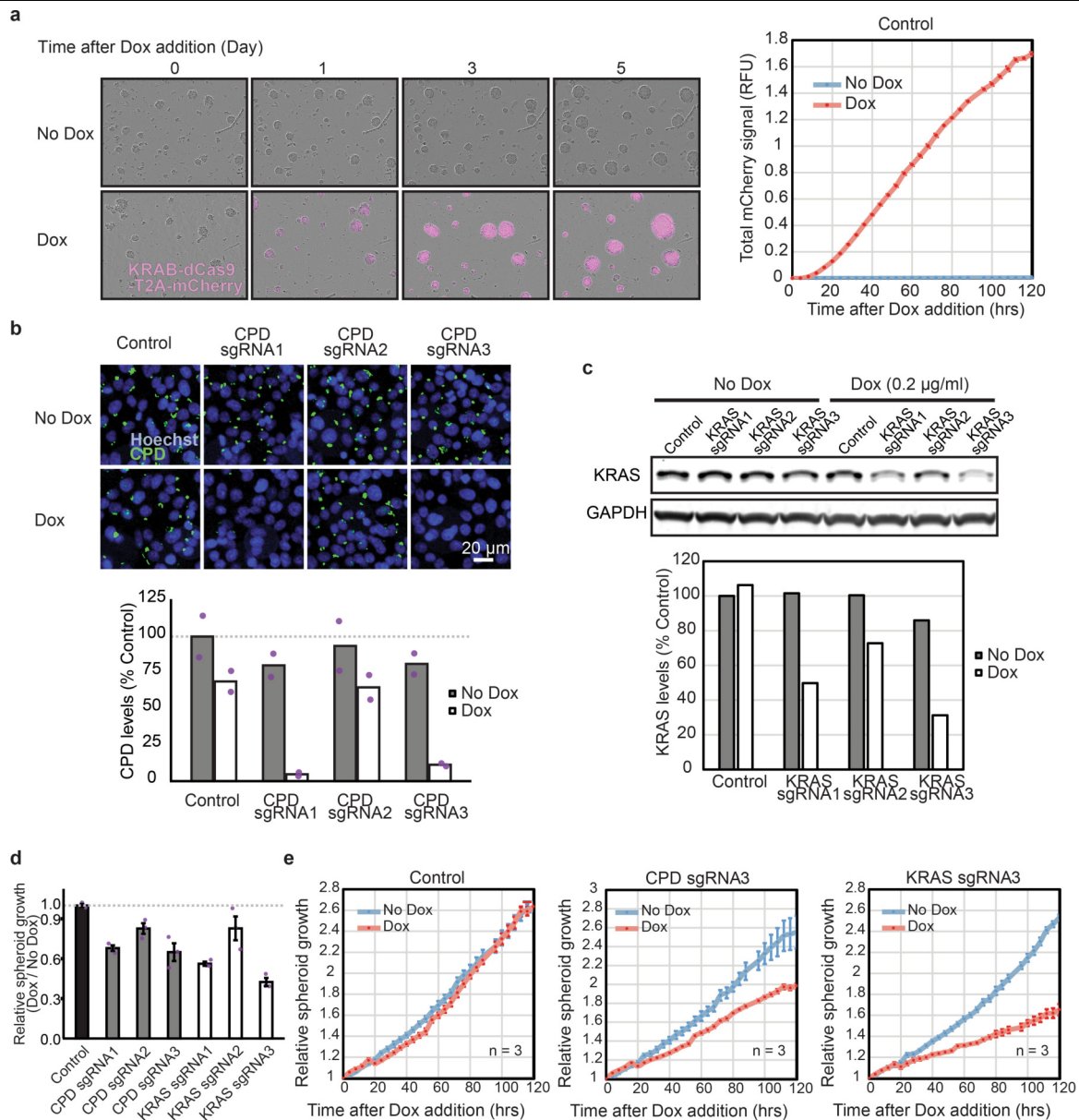


Extended Data Fig. 6 | See next page for caption.

**Extended Data Fig. 6 | Validation of individual sgRNAs targeting top hits with differential 3D/2D growth effects.** **a**, A schematic showing the competitive growth assay used to validate individual sgRNAs in 2D and 3D conditions. Cells expressing a gene-targeting sgRNA (mCherry) are mixed with cells expressing a control sgRNA (safe sgRNA, encoding GFP). Relative changes of mCherry to GFP ratios are monitored to compute growth phenotypes of gene-targeting sgRNAs. **b**, Genes within the *CPD* module and selected top hits with differential effects in 3D versus 2D growth were targeted with individual sgRNAs and subjected to competitive growth assays in both 2D and 3D culture. Relative 2D and 3D growth phenotypes of individual sgRNAs were measured by tracking changes in ratios of mCherry (gene-targeting sgRNAs) to GFP (control sgRNA) in the assays by automated fluorescence microscopy. ( $n = 3$  wells in a 24-well plate, mean  $\pm$  s.e.m.). **c**, Binary masks of H23 spheroids with the indicated gene knockouts. H23 knockout cell lines expressing sgRNAs against top hits from the 3D/2D phenotypes were seeded at equal density on ultra-low

attachment plates. 3D spheroids generated from the knockout lines were imaged in a fluorescent microscope 72 h after seeding. For each knockout line, 48 images were taken from three wells in a 24-well plate using a 10 $\times$  objective. Binary masks were then generated from mCherry signals of 3D spheroids. Forty-eight images were then stitched together to be shown as one large image for each knockout. **d**, Relative colony masses of H23 spheroids with gene knockouts are quantified and displayed in bar graphs ( $n = 3$  wells in a 24-well plate, mean  $\pm$  s.e.m.). **e**, Genes in the *CPD* module and *KRAS* were targeted with corresponding small-molecule inhibitors. Cells were seeded in 96-well plates in 2D (blue line) and 3D (red line) conditions, and grown in the presence of titrating doses of inhibitors for 72 h. Live cells were quantified with alamar blue assays. Relative growth of treated cells compared with the untreated samples are plotted in the drug titration curves.  $n = 3$  wells in a 96-well plate for linsitinib and  $n = 4$  for all other drugs; mean  $\pm$  s.e.m.



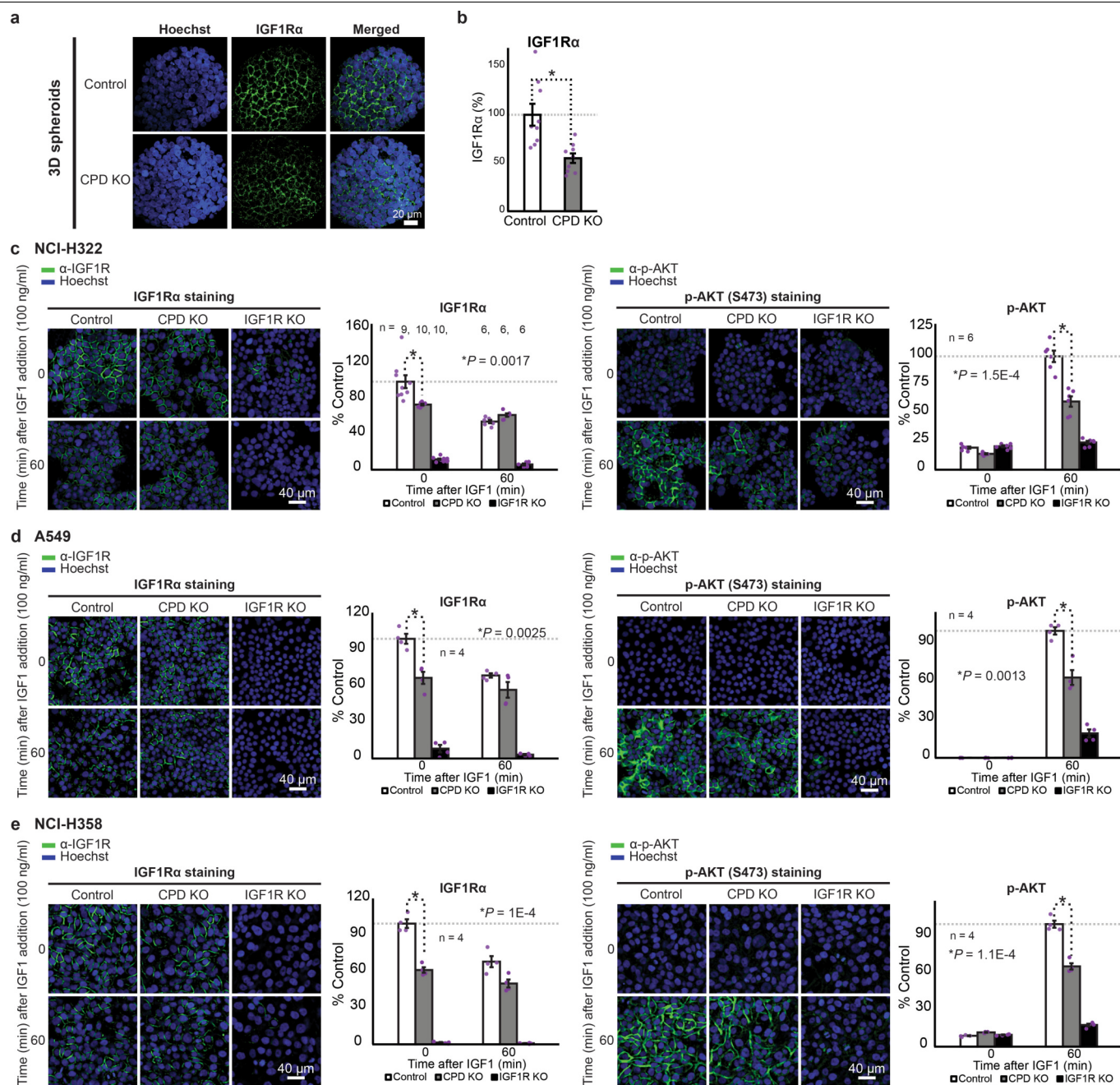


**Extended Data Fig. 7 | Induced CPD knockdown in established H23 spheroids slows growth.**

**a**, Doxycycline (Dox; 0.2  $\mu$ g ml<sup>-1</sup>) was added to established spheroids at 48 h after initial seeding. Spheroids were expressing both mCherry and KRAB-dCas9 separated by a T2A sequence under the same doxycycline-inducible promoter. Addition of doxycycline rapidly induced KRAB-dCas9-T2A-mCherry expression in spheroids. ( $n = 3$  wells in a 24-well plate, mean  $\pm$  s.e.m.). **b**, Immunofluorescence staining of CPD (green) showed that CPD sgRNAs 1 and 3 robustly reduced CPD levels in H23 cells expressing the inducible KRAB-dCas9 upon doxycycline addition. CPD sgRNA 2 was less effective. Mean intensities of CPD immunofluorescence of two biological replicates were measured in the bottom bar plot. **c**, Immunostaining of KRAS (green) by western blot showed that KRAS sgRNAs 1 and 3 robustly reduced KRAS levels in H23 cells expressing the inducible KRAB-dCas9 upon doxycycline addition. KRAS sgRNA 2 was less effective. These experiments were repeated twice to confirm the result. **d**, Relative spheroid growth, five days after doxycycline addition, comparing doxycycline-treated and untreated

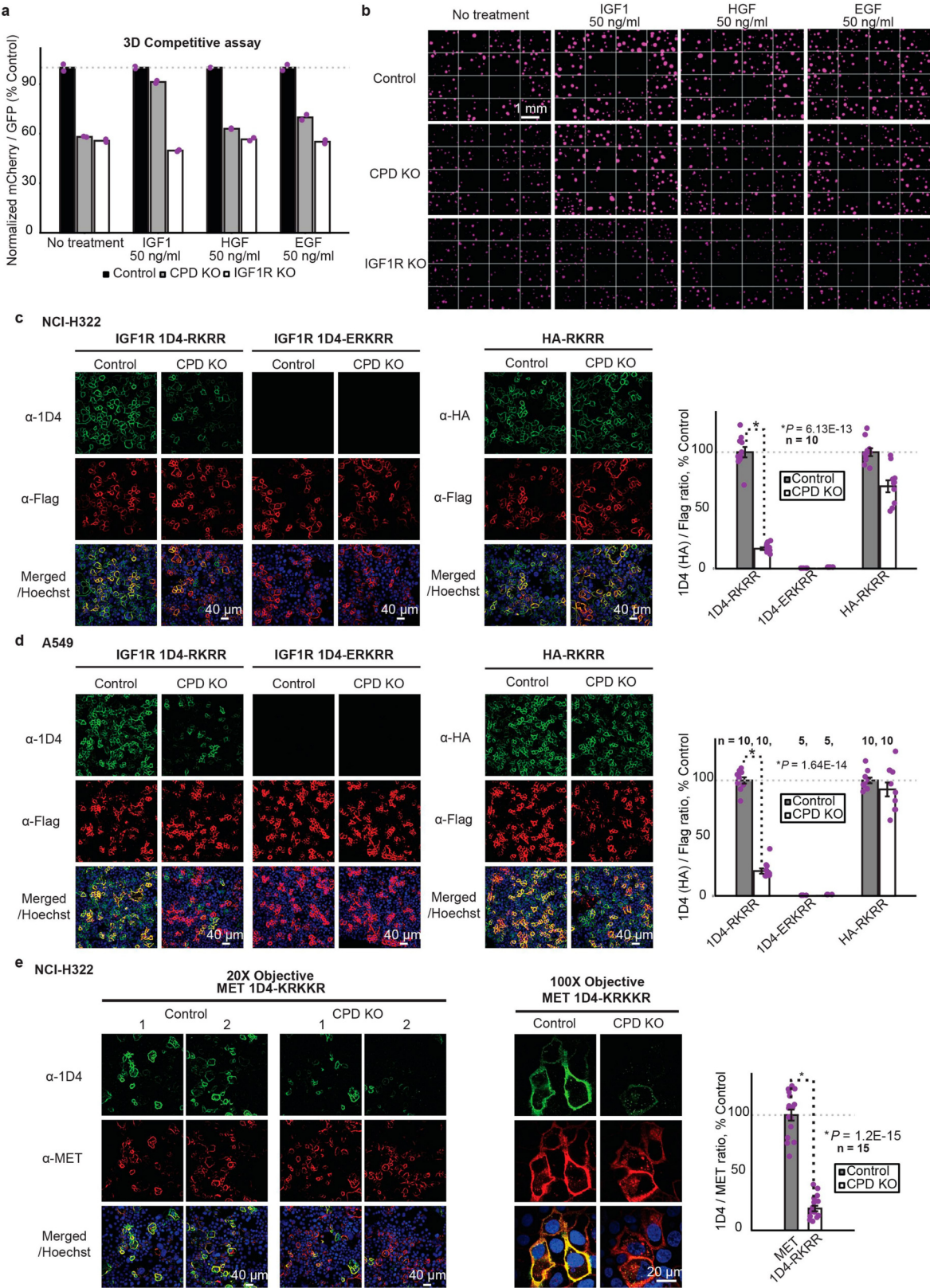
samples, measured in control cells and cells expressing CPD and KRAS sgRNA cells. H23 cells with inducible KRAB-dCas9-T2A-mCherry were first transduced with gene-targeting sgRNAs using a lentivirus that also expressed a GFP marker. Cells were seeded and allowed to form spheroids for 48 h. Doxycycline was then added and growth of spheroids in doxycycline-treated or untreated samples was monitored by GFP signal for another five days. Spheroids expressing CPD sgRNAs 1 or 3 and spheroids expressing KRAS sgRNAs 1 or 3 showed markedly reduced growth upon doxycycline addition, whereas spheroids expressing control sgRNA did not show any difference between doxycycline-treated and untreated samples ( $n = 3$  wells in a 24-well plate, mean  $\pm$  s.e.m.). **e**, Growth of spheroids expressing control sgRNA, CPD sgRNA 3 or KRAS sgRNA 3 were monitored after doxycycline addition. Cells were seeded to form spheroids in the first 48 h and growth of spheroids was monitored by GFP fluorescence for the next 5 days ( $n = 3$  wells in a 24-well plate, mean  $\pm$  s.e.m.).





**Extended Data Fig. 8 | CPD deletion inhibits the IGF1R pathway in H322, A549 and H358 cells. a**, Representative immunofluorescence images of IGF1R  $\alpha$ -chain (green) in control and CPD-knockout H23 spheroids. **b**, Quantification of immunofluorescence in **a**. IGF1R  $\alpha$ -chain intensities averaged across nine spheroids per condition.  $*P = 2.2 \times 10^{-3}$  ( $n = 9$ , two-sided  $t$ -test; mean  $\pm$  s.e.m.).

**c–e**, IGF1R and phosphorylated AKT levels were quantified from immunofluorescence images for H322 (**c**), A549 (**d**) and H358 (**e**) cells. The dotted grey line marks a 100% level ( $P$  values calculated using two-sided  $t$ -test; mean  $\pm$  s.e.m.).

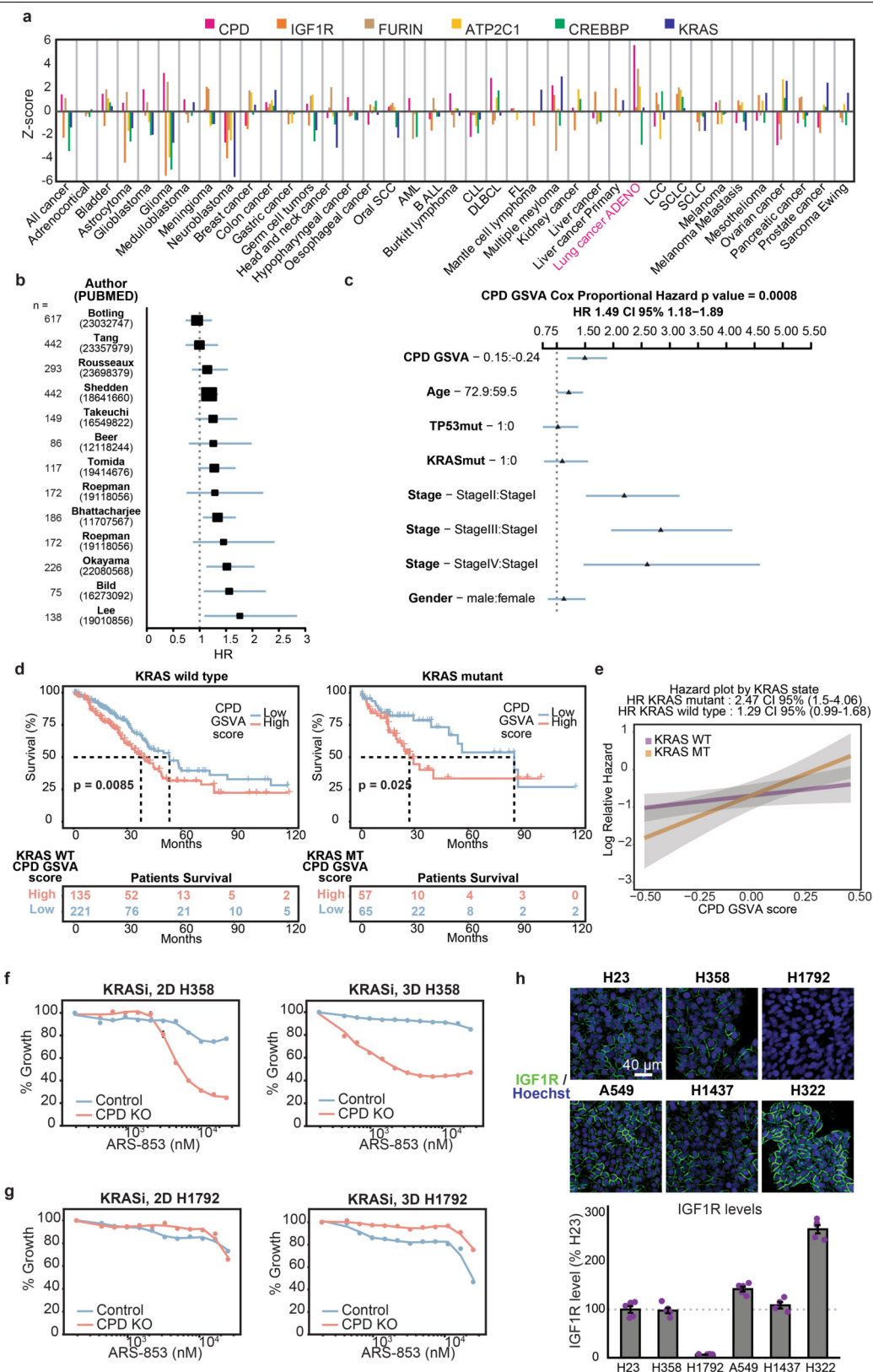


Extended Data Fig. 9 | See next page for caption.

**Extended Data Fig. 9 | *CPD* deletion acts through the IGF1R pathway to inhibit 3D growth in H23 cells and *CPD* removes the *FURIN*-recognition motif from the C terminus of IGF1R and MET  $\alpha$ -chain.** **a**, The growth phenotype observed upon *CPD* deletion in H23 cells is rescued by addition of excess IGF1 (50 ng ml<sup>-1</sup>) to the growth medium. A *CPD*- or *IGF1R*-targeting sgRNA with mCherry cDNA and a safe sgRNA with GFP cDNA were transduced into H23 cells separately, mixed in 50:50 ratio, and cultured in 3D spheroids for 72 h. Ratios of mCherry to GFP at 72 h, normalized to the ratio at T0, were plotted in the bar graphs. Deletion of either *CPD* or *IGF1R* reduced 3D growth of spheroids, as reflected in the reduced mCherry-to-GFP ratios compared with control. Treating cells with excess IGF1 ligand (50 ng ml<sup>-1</sup>) rescued *CPD*-deletion phenotypes, whereas addition of EGF or HGF did not. This suggests that partial inhibition of the IGF1R pathway by *CPD* deletion can be compensated by over-activation of the pathway with the excess IGF1 ligand. IGF1 could not rescue the *IGF1R* deletion phenotype ( $n = 2$  wells in a 24 well plate; mean  $\pm$  s.e.m.). **b**, Control, *CPD*-knockout and *IGF1R*-knockout spheroids

were treated with the indicated growth factors. Sixteen images of mCherry fluorescence in spheroids expressing a gene-targeting sgRNA vector with mCherry marker were stitched together to create the images shown. **c, d**, IGF1R-1D4 reporters (see Fig. 4b) showed that removal of the *FURIN*-recognition site RKRR from the C terminus of IGF1R  $\alpha$ -chain after *FURIN* cleavage is severely impaired by *CPD* deletion in H322 (**c**) and A549 (**d**) cells. *P* values calculated using two-sided *t*-test; mean  $\pm$  s.e.m. **e**, A MET-1D4-KRKKR reporter (with 1D4 epitope inserted upstream of the *FURIN*-recognition site KRKKR in MET, as with IGF1R in Fig. 4b) showed that removal of KRKKR from the C terminus of MET  $\alpha$ -chain is severely impaired by *CPD* deletion in H322 cells. Total *MET*-reporter levels were measured using an antibody against MET and ratios of 1D4 to MET signal were used to assess the degree of the KRKKR processing in control and *CPD*-null background. Error bars show s.e.m. of biological replicates in a 96-well plate. *P* values calculated using two-sided *t*-test; mean  $\pm$  s.e.m.





Extended Data Fig. 10 | See next page for caption.

**Extended Data Fig. 10 | Targeting *CPD* may have therapeutic effects in patients with lung cancer.** **a**, Meta-*Z* scores of genes in the *CPD* module across different cancer types, from PRECOG analysis<sup>43</sup>. Positive *Z* score predicts that high expression of a given gene is associated with poor prognosis of disease. Pink bars show that high *CPD* expression predicts poor prognosis of lung adenocarcinoma (ADENO) (*Z* score = 5.59, PRECOG meta-FDR =  $3.23 \times 10^{-6}$ ). **b**, Forest plot showing hazard ratios (HR) of *CPD* measured from different datasets (authors and PubMed IDs for the datasets are indicated on the y axis). The HR is the increase in risk of death for each unit increase in expression of *CPD* (see Methods). Blue error bars indicate 95% confidence intervals. Number of patient samples used for each study is listed to the left of the plot. **c**, Forest plot showing the hazard ratios from an adjusted two-sided Cox proportional-hazard model, using the *CPD* GSVA score as a continuous variable adjusted by age, *TP53*, *KRAS*, stage and gender. **d**, Kaplan–Meier plots for patients with lung cancer with wild-type (left) or mutant (right) *KRAS*. Variation of a gene set downregulated by *CPD* deletion in H23 spheroids was first scored by GSVA (*CPD* GSVA score) in patients with lung cancer. Differences in survival among patients with lung cancer with high versus low *CPD* GSVA score are illustrated in Kaplan–Meier plots. High *CPD* GSVA scores are significantly associated with

poor prognosis in both wild-type and mutant *KRAS* patient groups. However, the separation between high and low *CPD* GSVA groups is larger among *KRAS*-mutant patients than wild-type patients, suggesting an interaction between *CPD* and *KRAS* mutations in patients with lung cancer. *P* values calculated using a two-sided log-rank test. **e**, Hazard plots illustrating the two-sided Cox proportional log relative hazard by expression levels of *CPD* in *KRAS*-mutant versus *KRAS* wild-type samples. Grey shading corresponds to 95% confidence intervals. **f**, *CPD* deletion sensitizes H358 cells to ARS-853, a *KRAS* inhibitor. H358 cells with control safe sgRNA (blue line) or *CPD* sgRNA (red line) were treated with increasing doses of ARS-853 for 72 h in both 2D (top) and 3D (bottom). Live cells were then quantified using alamar blue assay. Relative growth of treated cells compared with the untreated cells is plotted against ARS-853 concentration. *n* = 4 wells in a 96-well plate, mean ± s.e.m. **g**, *CPD* deletion does not show synergy with ARS-853 in H1792 cells. Similar plots as in **f** were generated for H1792 cells (*n* = 4 wells in a 96-well plate, mean ± s.e.m.). **h**, IGF1R was quantified from immunofluorescence images of IGF1R staining across six lung cancer cell lines. H1792 cells show very low IGF1R expression compared with the other five cell lines. *n* = 4 for H1437, *n* = 5 for all other cell lines, mean ± s.e.m.



## Reporting Summary

Nature Research wishes to improve the reproducibility of the work that we publish. This form provides structure for consistency and transparency in reporting. For further information on Nature Research policies, see [Authors & Referees](#) and the [Editorial Policy Checklist](#).

### Statistics

For all statistical analyses, confirm that the following items are present in the figure legend, table legend, main text, or Methods section.

- |                                     |  |
|-------------------------------------|--|
| n/a                                 | Confirmed  |
| <input type="checkbox"/>            | <input checked="" type="checkbox"/> The exact sample size ( $n$ ) for each experimental group/condition, given as a discrete number and unit of measurement  |
| <input type="checkbox"/>            | <input checked="" type="checkbox"/> A statement on whether measurements were taken from distinct samples or whether the same sample was measured repeatedly  |
| <input type="checkbox"/>            | <input checked="" type="checkbox"/> The statistical test(s) used AND whether they are one- or two-sided<br><i>Only common tests should be described solely by name; describe more complex techniques in the Methods section.</i>   |
| <input type="checkbox"/>            | <input checked="" type="checkbox"/> A description of all covariates tested   |
| <input type="checkbox"/>            | <input checked="" type="checkbox"/> A description of any assumptions or corrections, such as tests of normality and adjustment for multiple comparisons  |
| <input type="checkbox"/>            | <input checked="" type="checkbox"/> A full description of the statistical parameters including central tendency (e.g. means) or other basic estimates (e.g. regression coefficient) AND variation (e.g. standard deviation) or associated estimates of uncertainty (e.g. confidence intervals) |
| <input type="checkbox"/>            | <input checked="" type="checkbox"/> For null hypothesis testing, the test statistic (e.g. $F$ , $t$ , $r$ ) with confidence intervals, effect sizes, degrees of freedom and $P$ value noted<br><i>Give <math>P</math> values as exact values whenever suitable.</i>                            |
| <input checked="" type="checkbox"/> | <input type="checkbox"/> For Bayesian analysis, information on the choice of priors and Markov chain Monte Carlo settings  |
| <input checked="" type="checkbox"/> | <input type="checkbox"/> For hierarchical and complex designs, identification of the appropriate level for tests and full reporting of outcomes  |
| <input type="checkbox"/>            | <input checked="" type="checkbox"/> Estimates of effect sizes (e.g. Cohen's $d$ , Pearson's $r$ ), indicating how they were calculated   |

Our web collection on [statistics for biologists](#) contains articles on many of the points above.

### Software and code

Policy information about [availability of computer code](#)

#### Data collection

NextSeq Control Software (v2.2.0, Illumina) was used for deep-sequencing of CRISPR screening (Fig. 1,2) and RNA-seq samples (Figure 4). Incucyte ZOOM/S3 control softwares (v2018a, ESSEN) were used to acquire microscopy images for the competition assay (Figure 3). MetaXpress (v1.7, Molecular Devices) was used to acquire microscopy images for the IF experiments on the IGF1R signaling pathways (Figure 3). NISElements (v4.4, Nikon) was used to acquire confocal IF microscopy images (Figure 4). BD CSampler controller (v227, BD Biosciences) was used to acquire FACS data for the in vivo competition assay (Figure 4).

#### Data analysis

All screening data were analyzed with custom Python scripts (v2.7). They are available at [https://github.com/biohank/CRISPR\\_screen\\_analysis](https://github.com/biohank/CRISPR_screen_analysis). Custom Matlab scripts (v2015b) were used to quantify signals from all IF images and to analyze FACS data and these scripts will be available upon request to K.H.. RNA-seq data was mapped using Kallisto (Bray et al., 2016) and differentially regulated genes were analyzed using Sleuth (Pimentel et al., 2017). PRECOG analysis was performed with custom python scripts previously described in Gentles et al., 2015; request for the scripts can be made to A.J.G.. Custom R scripts (v3.5.3) were used to study association between expression scores of CPD-downstream targets and clinical outcome of TCGA lung adenocarcinoma and they will be available upon request to J.A.S.. Incucyte ZOOM or S3 software (v2018a, ESSEN) was used for automated microscopy analysis. Significance of lung cancer mutations were analyzed using MutSig2CV (Lawrence et al., 2013) available at <https://software.broadinstitute.org/cancer/cga/mutsig>.

For manuscripts utilizing custom algorithms or software that are central to the research but not yet described in published literature, software must be made available to editors/reviewers. We strongly encourage code deposition in a community repository (e.g. GitHub). See the Nature Research [guidelines for submitting code & software](#) for further information.

## Data

Policy information about [availability of data](#)

All manuscripts must include a [data availability statement](#). This statement should provide the following information, where applicable:

- Accession codes, unique identifiers, or web links for publicly available datasets
- A list of figures that have associated raw data
- A description of any restrictions on data availability

Sequencing data from all CRISPR screens and RNA-seq experiments are available under BioProject accession number PRJNA535417.

## Field-specific reporting

Please select the one below that is the best fit for your research. If you are not sure, read the appropriate sections before making your selection.

☒ Life sciences ☐ Behavioural & social sciences ☐ Ecological, evolutionary & environmental sciences

For a reference copy of the document with all sections, see [nature.com/documents/nr-reporting-summary-flat.pdf](https://www.nature.com/documents/nr-reporting-summary-flat.pdf)

## Life sciences study design

All studies must disclose on these points even when the disclosure is negative.

### Sample size

10- to 12-week old, female NSG mice of similar weights were used for cell transplantation experiments. To determine the number of cells to inject for H23-derived cell lines, several dilutions of cells ( $2 \times 10^5$ ,  $1 \times 10^6$ ,  $2 \times 10^6$ , and  $4 \times 10^6$ ) were injected into both flanks and both shoulders of one NSG recipient mouse per dilution (n=4 mice; 16 tumors total). After ten days, 4/4 palpable tumors formed from the  $4 \times 10^6$  cell injections, compared to 0/4 for  $2 \times 10^5$  cell injections, 1/4 for the  $1 \times 10^6$  cell injections, and 1/4 for the  $2 \times 10^6$  cell injections, and so  $4 \times 10^6$  or more cells were used for all subsequent injections.

For the gene-expression/patient survival analysis in Fig 4i, see "PRECOG analysis" in the Method. For the gene-expression/patient survival analysis in Fig4j, see "RNA-seq experiment and analysis" and "TCGA outcome analysis in downregulated genes upon CPD deletion" in the Method.

For all CRISPR screens and RNA-seq experiments, experiments were performed in two replicates. We determined to perform these experiments in two replicates based on the current standard in the field, which has yielded enough power to detect meaningful/specific biological effects.

For in vitro validation assays, sample size is indicated in the figure legend for each experiment. The sample size was determined based on previous experience for each experiment to detect specific effects and it was not predetermined with any statistical methods.

### Data exclusions

No data was excluded

### Replication

Each in vivo presented in the paper was repeated in multiple mice (20 tumor flanks in 10 mice for in vivo CRISPR screening in Fig. 2c, d; 4 mice per genotype for the competitive growth assay in Fig. 4f-h)

All other in vitro validation assays were successfully replicated and noted in the figure legends. Detailed materials and methods for non-standard in vitro experiments are described in the Method section.

### Randomization

For all the mice experiments, mice were randomly allocated to each experimental groups

### Blinding

N/A

## Reporting for specific materials, systems and methods

We require information from authors about some types of materials, experimental systems and methods used in many studies. Here, indicate whether each material, system or method listed is relevant to your study. If you are not sure if a list item applies to your research, read the appropriate section before selecting a response.

### Materials & experimental systems

n/a	Involved in the study
<input type="checkbox"/>	<input checked="" type="checkbox"/> Antibodies
<input type="checkbox"/>	<input checked="" type="checkbox"/> Eukaryotic cell lines
<input checked="" type="checkbox"/>	<input type="checkbox"/> Palaeontology
<input type="checkbox"/>	<input checked="" type="checkbox"/> Animals and other organisms
<input checked="" type="checkbox"/>	<input type="checkbox"/> Human research participants
<input checked="" type="checkbox"/>	<input type="checkbox"/> Clinical data

### Methods

n/a	Involved in the study
<input checked="" type="checkbox"/>	<input type="checkbox"/> ChIP-seq
<input type="checkbox"/>	<input checked="" type="checkbox"/> Flow cytometry
<input checked="" type="checkbox"/>	<input type="checkbox"/> MRI-based neuroimaging

## Antibodies

### Antibodies used

KRAS (ThermoFisher 415700, Lot # SJ260203, Dilution 1:1000 for Western Blot), IGF1R- $\alpha$  (ThermoFisher AHR0321, Lot # UB2717301, 1:200 for IF), CPD (ThermoFisher A305-514A-M, Lot # 1, 1:200 for IF), MET (Cell Signaling Technology 8198, Lot # 4, Dilution 1:200 for IF), phospho-AKT (Ser437) (Cell Signaling Technology 4060, Lot # 24, 1:200 for IF), phospho-ERK1/2 (Thr202/Tyr204) (Cell Signaling Technology 4370, Lot # 17, Dilution 1:200 for IF), Flag (Cell Signaling Technology 14793, Lot # 5, Dilution 1:1000 for IF), GAPDH (ThermoFisher AM4300, Lot # 274128, Dilution 1:1000 for western blot), Rho1D4 (Millipore MAB5356, Lot # 3068439, Dilution 1:2000 for IF)

### Validation

CPD antibody was validated by IF (Ext. Data Fig. 7b) on CPD knockdown H23 cells.

IGF1R antibody was validated by IF (Fig. 3e,f) on IGF1R knockout H23 cells and by IF (Ext. Data Fig. 8) on IGF1R knockout NCI-H322, A549, and NCI-H358 cell lines.

Rho1D4 antibody was validated by IF on Rho1D4 reporter expressing H23 cells (Fig. 4c,e), NCI-H322 and A549 cells (Ext. Data Fig. 9c-e)

See the following "Manufacturers Statement" for the other antibodies :

K-Ras Antibody (415700) is specific for human K-Ras (K-Ras2, Ki-Ras, c-K-ras, GTPase KRas) protein (accession # NP\_004976.2, P01116), which is 100% homologous with mouse, 95% with rat, and 94% with bovine, respectively. Reactivity has been confirmed on western blots with human HeLa and WI-38 cell lysates as well as rat KNRK and mouse NIH 3T3 cell lysates, and identifies the target band at ~21 kDa. The reactivity has been also confirmed with rat KNRK cells using immunoprecipitation and with HeLa cells by immunofluorescence. Based on amino acid sequence homology, reactivity with bovine is also expected. Product Citations: Kopp, F., Wagner, E. & Roidl, A. The proto-oncogene KRAS is targeted by miR-200c. *Oncotarget* 5, 185–195 (2014).

Met (D1C2) Rabbit mAb recognizes endogenous levels of total human Met protein. Monoclonal antibody is produced by immunizing animals with a synthetic peptide corresponding to residues near the carboxy terminus of human Met protein. Product Citations: Matsumoto, S. et al. GREB1 induced by Wnt signaling promotes development of hepatoblastoma by suppressing TGF $\beta$  signaling. *Nat. Commun.* 10, 3882 (2019); Willbold, R. et al. Excess hepsin proteolytic activity limits oncogenic signaling and induces ER stress and autophagy in prostate cancer cells. *Cell Death Dis.* 10, 601 (2019); Jiang, S. et al. WNT5B governs the phenotype of basal-like breast cancer by activating WNT signaling. *Cell Commun. Signal.* 17, 109 (2019).

Phospho-Akt (Ser473) (D9E) Rabbit mAb detects endogenous levels of Akt only when phosphorylated at Ser473. Species Reactivity: Human, Mouse, Rat, Hamster, Monkey, D. melanogaster, Zebrafish, Bovine. Monoclonal antibody is produced by immunizing animals with a synthetic phosphopeptide corresponding to residues around Ser473 of human Akt. Product Citations: Du, M. et al. Osthole inhibits proliferation and induces apoptosis in BV-2 microglia cells in kainic acid-induced epilepsy via modulating PI3K/AKT/mTOR signalling way. *Pharm. Biol.* 57, 238–244 (2019); Wang, Y., Li, B. & Zhang, X. Scutellaria barbata D. Don (SBD) protects oxygen glucose deprivation/reperfusion-induced injuries of PC12 cells by up-regulating Nrf2. *Artif. Cells Nanomed. Biotechnol.* 47, 1797–1807 (2019); Li, X., Zhang, Q. & Yang, Z. Silence of MEG3 intensifies lipopolysaccharide-stimulated damage of human lung cells through modulating miR-4262. *Artif. Cells Nanomed. Biotechnol.* 47, 2369–2378 (2019).

Phospho-p44/42 MAPK (Erk1/2) (Thr202/Tyr204) (D13.14.4E) Rabbit mAb detects endogenous levels of p44 and p42 MAP Kinase (Erk1 and Erk2) when dually phosphorylated at Thr202 and Tyr204 of Erk1 (Thr185 and Tyr187 of Erk2), and singly phosphorylated at Thr202. This antibody does not cross-react with the corresponding phosphorylated residues of either JNK/SAPK or p38 MAP kinases. Species Reactivity: Human, Mouse, Rat, Hamster, Monkey, Mink, D. melanogaster, Zebrafish, Bovine, Dog, Pig, S. cerevisiae. Monoclonal antibody is produced by immunizing animals with a synthetic phosphopeptide corresponding to residues surrounding Thr202/Tyr204 of human p44 MAP kinase. Product Citations: Li, X., Ma, A. & Liu, K. Geniposide alleviates lipopolysaccharide-caused apoptosis of murine kidney podocytes by activating Ras/Raf/MEK/ERK-mediated cell autophagy. *Artif. Cells Nanomed. Biotechnol.* 47, 1524–1532 (2019); Gao, Y. et al. Mechanical strain promotes skin fibrosis through LRG-1 induction mediated by ELK1 and ERK signalling. *Commun Biol* 2, 359 (2019); Wang, S. et al. Enhancement of Macrophage Function by the Antimicrobial Peptide Sublancin Protects Mice from Methicillin-Resistant Staphylococcus aureus. *J Immunol Res* 2019.

Flag DYKDDDDK Tag (D6W5B) Rabbit mAb detects exogenously expressed DYKDDDDK proteins in cells. The antibody recognizes the DYKDDDDK peptide, which is the same epitope recognized by Sigma's Anti-FLAG® antibodies, fused to either the amino-terminus or carboxy-terminus of the target protein. Monoclonal antibody is produced by immunizing animals with a synthetic DYKDDDDK peptide. Product Citations: Wang, D. et al. Optimized CRISPR guide RNA design for two high-fidelity Cas9 variants by deep learning. *Nat. Commun.* 10, 4284 (2019); Ji, L. et al. USP7 inhibits Wnt/ $\beta$ -catenin signaling through promoting stabilization of Axin. *Nat. Commun.* 10, 4184 (2019); Chuang, S. K., Vrla, G. D., Fröhlich, K. S. & Gitai, Z. Surface association sensitizes *Pseudomonas aeruginosa* to quorum sensing. *Nat. Commun.* 10, 4118 (2019).

## Eukaryotic cell lines

### Policy information about cell lines

#### Cell line source(s)

NCI-H1437, NCI-H1568, NCI-H1650, NCI-H1975, NCI-H322, NCI-H1792, NCI-H2009, NCI-H23, NCI-H358, and A549 are from ATCC

#### Authentication

All cell lines were authenticated by the vendor (ATCC). Authentication includes an assay to detect species specific variants of the

cytochrome C oxidase I gene (COI analysis) to rule out inter-species contamination and short tandem repeat (STR) profiling to distinguish between individual human cell lines and rule out intra-species contamination. After transducing Cas9 into the 10 cell lines, we authenticated them again by Human 9-Marker STR Profile test provided by IDEXX BioResearch.

Mycoplasma contamination

We tested the 10 cell lines for mycoplasma contamination with IDEXX BioResearch and all cell lines were negative for Mycoplasma sp.

Commonly misidentified lines  
(See [ICLAC](#) register)

N/A

## Animals and other organisms

Policy information about [studies involving animals](#); [ARRIVE guidelines](#) recommended for reporting animal research

Laboratory animals

10- to 12-week old female NSG mice of similar weights

Wild animals

This study did not involve wild animals.

Field-collected samples

This study did not involve samples collected from the fields.

Ethics oversight

The Stanford Institute of Medicine Animal Care and Use Committee approved all animal studies and procedures

Note that full information on the approval of the study protocol must also be provided in the manuscript.

## Flow Cytometry

### Plots

Confirm that:

- ☒ The axis labels state the marker and fluorochrome used (e.g. CD4-FITC).
- ☒ The axis scales are clearly visible. Include numbers along axes only for bottom left plot of group (a 'group' is an analysis of identical markers).
- ☒ All plots are contour plots with outliers or pseudocolor plots.
- ☒ A numerical value for number of cells or percentage (with statistics) is provided.

### Methodology

Sample preparation

Subcutaneous tumors formed from injections of human cancer cell lines were individually dissected, roughly chopped using dissecting scissors, and further dissociated into a single-cell suspension using collagenase IV, dispase, and trypsin at 37 degrees for 30 minutes with rotation. After digestion, samples were passed through a 40uM filter and maintained in PBS with 2% FBS, 2mM EDTA, and 1 U/mL DNase before FACS analysis.

Instrument

BD Accuri

Software

BD CSampler controller was used to perform FACS on dissociated tumor cells and custom matlab scripts were used to analyze and display FCS data generated in BD CSampler software.

Cell population abundance

Purity of samples varied a lot among different tumor samples, but the purity of samples were determined by either GFP or mCherry fluorescence signals in cells.

Gating strategy

The same cell lines cultured in vitro were used to set the gates for the subcutaneously injected tumor cells.

- ☒ Tick this box to confirm that a figure exemplifying the gating strategy is provided in the Supplementary Information.

# Parental-to-embryo switch of chromosome organization in early embryogenesis

<https://doi.org/10.1038/s41586-020-2125-z>

Received: 3 April 2019

Accepted: 16 January 2020

Published online: 25 March 2020

 Check for updates

Samuel Collombet<sup>1,2,10</sup>, Noémie Ranisavljevic<sup>1,3,10</sup>, Takashi Nagano<sup>4,9,10</sup>, Csilla Varnai<sup>4,5</sup>, Tarak Shisode<sup>6</sup>, Wing Leung<sup>4,9</sup>, Tristan Piolot<sup>1</sup>, Rafael Galupa<sup>1,2</sup>, Maud Borensztein<sup>1</sup>, Nicolas Servant<sup>7</sup>, Peter Fraser<sup>4,8,11</sup>✉, Katia Ancelin<sup>1,11</sup>✉ & Edith Heard<sup>1,2,11</sup>✉

Paternal and maternal epigenomes undergo marked changes after fertilization<sup>1</sup>. Recent epigenomic studies have revealed the unusual chromatin landscapes that are present in oocytes, sperm and early preimplantation embryos, including atypical patterns of histone modifications<sup>2–4</sup> and differences in chromosome organization and accessibility, both in gametes<sup>5–8</sup> and after fertilization<sup>5,8–10</sup>. However, these studies have led to very different conclusions: the global absence of local topological-associated domains (TADs) in gametes and their appearance in the embryo<sup>8,9</sup> versus the pre-existence of TADs and loops in the zygote<sup>5,11</sup>. The questions of whether parental structures can be inherited in the newly formed embryo and how these structures might relate to allele-specific gene regulation remain open. Here we map genomic interactions for each parental genome (including the X chromosome), using an optimized single-cell high-throughput chromosome conformation capture (HiC) protocol<sup>12,13</sup>, during preimplantation in the mouse. We integrate chromosome organization with allelic expression states and chromatin marks, and reveal that higher-order chromatin structure after fertilization coincides with an allele-specific enrichment of methylation of histone H3 at lysine 27. These early parental-specific domains correlate with gene repression and participate in parentally biased gene expression—including in recently described, transiently imprinted loci<sup>14</sup>. We also find TADs that arise in a non-parental-specific manner during a second wave of genome assembly. These *de novo* domains are associated with active chromatin. Finally, we obtain insights into the relationship between TADs and gene expression by investigating structural changes to the paternal X chromosome before and during X chromosome inactivation in preimplantation female embryos<sup>15</sup>. We find that TADs are lost as genes become silenced on the paternal X chromosome but linger in regions that escape X chromosome inactivation. These findings demonstrate the complex dynamics of three-dimensional genome organization and gene expression during early development.

We performed allele-specific single-cell HiC, modified from previous studies<sup>12,13</sup>, on single blastomeres (at the 1-, 2-, 4-, 8- and 64-cell stages, as well as oocytes) from highly polymorphic F<sub>1</sub> hybrid embryos that were obtained by crossing female *Mus musculus domesticus* (C57Bl/6J) with male *Mus musculus castaneus* CAST/EiJ (Fig. 1a, b). After excluding cells with poor data quality (Methods, Extended Data Fig. 1a), we used the relative coverage of the two X chromosomes to investigate sex-specific differences beyond autosomes (Extended Data Fig. 1b). Finally, we used cell cycle phasing<sup>13</sup> to remove cells in the pre-M and M phases, in which chromosomes lose their organization into compartments and/or domains<sup>13,16</sup> (Extended Data Fig. 1c–e). Looking first at the total

contacts (that is, not split between alleles), we detected the formation of TAD-like domains, with clear boundaries that appeared at specific stages of development (Extended Data Fig. 1f). This was confirmed by DNA fluorescence in situ hybridization (FISH) on three-dimensional (3D) preserved embryos using intra- or interdomain-specific probes (Extended Data Fig. 2).

## Asymmetric chromosome architecture

Previous studies have investigated the dynamics of TADs in mouse embryos on the basis of TAD atlases defined in embryonic stem cells,

<sup>1</sup>Institut Curie, PSL Research University, CNRS UMR3215, INSERM U934, UPMC Paris-Sorbonne, Paris, France. <sup>2</sup>EMBL, Heidelberg, Germany. <sup>3</sup>Department of Reproductive Medicine - Gynecology, CHU and University of Montpellier, Montpellier, France. <sup>4</sup>Nuclear Dynamics Programme, The Babraham Institute, Cambridge, UK. <sup>5</sup>Centre for Computational Biology, University of Birmingham, Birmingham, UK. <sup>6</sup>Department of Applied Mathematics, Florida State University, Tallahassee, FL, USA. <sup>7</sup>Institut Curie, PSL Research University, INSERM U900, Mines ParisTech, Paris, France. <sup>8</sup>Department of Biological Science, Florida State University, Tallahassee, FL, USA. <sup>9</sup>Present address: Laboratory for Nuclear Dynamics, Institute for Protein Research, Osaka University, Suita, Japan. <sup>10</sup>These authors contributed equally: Samuel Collombet, Noémie Ranisavljevic, Takashi Nagano. <sup>11</sup>These authors jointly supervised this work: Peter Fraser, Katia Ancelin, Edith Heard. ✉e-mail: pfraser@bio.fsu.edu; Katia.Ancelin@curie.fr; Edith.Heard@embl.org



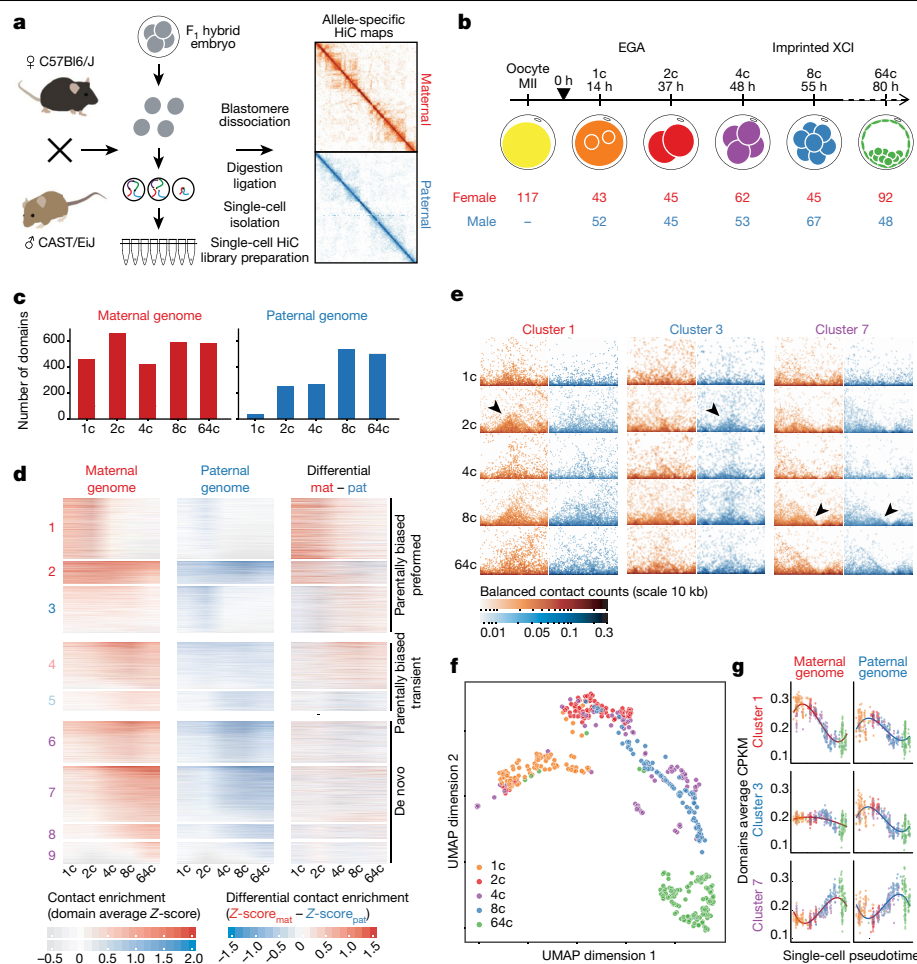


**Fig. 1 | Single-cell HiC approach to studying chromosome organization in preimplantation embryos in the mouse.** **a**, Scheme of the single-cell HiC method on mouse F<sub>1</sub> embryos. **b**, Timeline of embryo collection at selected stages. The numbers of blastomeres after quality-filtering and sex assignment are indicated (c refers to cell stage). EGA, embryonic genome activation; XCI, X chromosome inactivation. **c**, Number of domains at different stages, on the maternal (red) or paternal genome (blue). **d**, Clustering of domain dynamics (rows) through stages (columns). Colour scale indicates contact enrichment

and have not attempted to identify any alternative, embryo-specific domains<sup>5–9,11</sup>. Our allelic data revealed that parental genomes display a notably asymmetric structural organization before the eight-cell stage; the maternal genome displays most of the domains called at the one- and two-cell stages (Fig. 1c). We detected two independent gains in domain number—the first at the two-cell stage, and the second at the eight-cell stage. The second round of domain formation at the eight-cell stage correlated with a previously reported progressive acquisition of TADs<sup>8,9</sup> (Extended Data Fig. 3a). To better capture the dynamics of allelic domain organization, we quantified the contact enrichment inside domains (Methods) for both parental genomes at each stage and performed an unsupervised clustering (Fig. 1d, Extended Data Fig. 3a, b). We found that domains fall into three main categories. The first category (clusters 1–3) comprises parentally biased preformed domains, which are present as early as the one-cell stage and show a bias for the maternal (Fig. 1e, left) or paternal genome (Fig. 1e, middle). Most of these domains (those in clusters 1 and 3) disappear by the 4-cell stage, but a subset of maternally preformed domains (cluster 2) becomes balanced by the blastocyst stage (64-cell stage). A second category (clusters 4 and 5) of domain exhibits a more-transient bias for one allele, and generally has a weaker structure. In the third set (clusters 6–9), domains are acquired symmetrically on the two parental genomes at

inside domains (average Z-score (Methods)) and the difference in enrichment between the two alleles. Mat, maternal; pat, paternal. **e**, Snapshots of HiC maps from the maternal (red) and paternal (blue) alleles for 3 regions, in cluster 1, cluster 3 and cluster 7. Arrowheads indicate the domains of interest. **f**, Single-cell projection in reduced space (uniform manifold approximation and projection (UMAP)) based on the quantification of domain contacts ( $n = 470$  cells). **g**, Cluster average contacts per kilobase per million (CPKM) in single cells, ordered by pseudotime from the trajectory in f.

different stages after embryonic genome activation (Fig. 1e, right), as previously described<sup>8,9</sup> (Extended Data Fig. 3c).

We also assessed whether these dynamics were discernible in single cells, and were not an effect of the evaluation on pseudo-bulk data. Notably, the quantification of domain contacts in single cells was sufficient to capture the developmental trajectories of early embryos (Fig. 1f, Extended Data Fig. 3d–i), as well as capturing the dynamics of the clusters that we identified in the pseudo-bulk data (Fig. 1g, Extended Data Fig. 3d–i).

In conclusion, our results identify parent-of-origin-specific levels of chromosome organization as early as the 1-cell stage that are mostly resolved as the 2 genomes mature towards the 64-cell stage, except for cluster 2. These data reconcile those of previous studies<sup>5,8,9</sup>, and provide insights into the early differential organization of the two parental genomes.

## Parental domains and histone modification

To evaluate whether this unusual parental asymmetry in structure might be linked to specific chromatin states, we integrated our data with chromatin immunoprecipitation and sequencing (ChIP-seq) data for histone modifications from early embryos<sup>17,18</sup>. Notably,

parental-specific early domains (clusters 1–3) coincide with large accumulations of the Polycomb-associated mark, trimethylation of histone H3 at Lys27 (H3K27me3); the strongest enrichment of this mark is associated with the maternal genome, whereas the de novo-formed domains (clusters 6–9) are depleted for this mark (Fig. 2a, b, Extended Data Fig. 4a–e). Whereas H3K27me3 domains are maintained up to the eight-cell stage and diminish thereafter (Fig. 2c), the structural domains are lost or transformed by the four-cell stage—concomitantly with a transient gain in the H3K4me3 mark (Fig. 2c, Extended Data Fig. 4f). We note that the enrichment of H3K27me3 occurs during oogenesis (Extended Data Fig. 4g) and that the domains of cluster 2 appear as early as postnatal day 5, but not in sperm (Extended Data Fig. 4h).

Parentally preformed domains also exhibit interactions between domains similar to the patterns of A and B compartments (Fig. 2d). We found that the parentally preformed domains form allele-specific B-like compartments at the two-cell stage (Fig. 2e, Extended Data Fig. 4i, j). These domains also display stronger interactions between domains at the 2-cell stage than do the de novo domains at the 64-cell stage (Fig. 2f, Extended Data Fig. 4k). Parentally preformed domains are depleted for CTCF motifs flanking their borders (Extended Data Fig. 4i), which points towards an independency for this factor (as has previously been shown for compartments<sup>19</sup>). Altogether, these results suggest that parental-specific domains might form local compartments associated with the Polycomb-repressive mark after fertilization, which later dissolve into the classical A and B compartments (Fig. 2g).

## Parental domains and transient imprint

To evaluate how the allele-specific dynamics of chromosome organization relate to gene expression, we examined previously published RNA-sequencing data<sup>20</sup> obtained from equivalent F<sub>1</sub> hybrid preimplantation embryos. We found that parentally preformed domains are associated with generally lower gene expression (Fig. 3a, top, Extended Data Fig. 5a) and an average lower expression on the structured allele (Fig. 3a, bottom), as well as a higher frequency of strongly biased genes (Extended Data Fig. 5b). Gene ontology analysis revealed that silenced genes within early preformed clusters are significantly enriched for terms associated with tissue morphogenesis, such as neurogenesis or osteogenesis (Extended Data Fig. 5c), the expression of which is required only at late developmental stages. Conversely, symmetric de novo clusters were predominantly enriched in genes that drive the patterning of the embryo at preimplantation (such as cell cycle, lineage specification, metabolism and gene regulation).

Maternally preformed domains encompass most genes that have previously been described as transiently maternally imprinted<sup>14,21</sup> (19 out of 27 genes), such as the X inactivation centre locus (Fig. 3b, Extended Data Fig. 6a, b). Indeed, at the two-cell stage *Xist* is encompassed in a maternal-specific domain, the left border of which coincides with the *Xist* TAD that has previously been described in embryonic stem cells<sup>22</sup>; the right border of this maternal-specific domain is slightly shifted with respect to the previously described *Xist* TAD, and excludes the *Xist* transactivator *Rlim* (Extended Data Fig. 6c). Accordingly, *Xist* is maternally repressed, whereas the adjacent *Rlim* is kept expressed on the maternal allele and becomes silenced upon X chromosome inactivation<sup>23</sup> (Fig. 3c). We noticed a similar pattern of shifting from maternal imprinted domains at the two-cell stage to TADs at the blastocyst stages for other transiently imprinted genes, such as *Tle3*, *Enc1* and *Mbnl2* (Extended Data Fig. 6d–h).

To investigate the importance of such domains for imprinted gene regulation, we focused on the maternal 3D domain spanning the *Jpx* and *Ftx* loci, within a region that has previously been proposed to be sufficient for imprinted X chromosome inactivation<sup>23</sup> (Fig. 3d). *Jpx* is a putative regulator of *Xist*<sup>24</sup>. We found that mice with a deletion encompassing

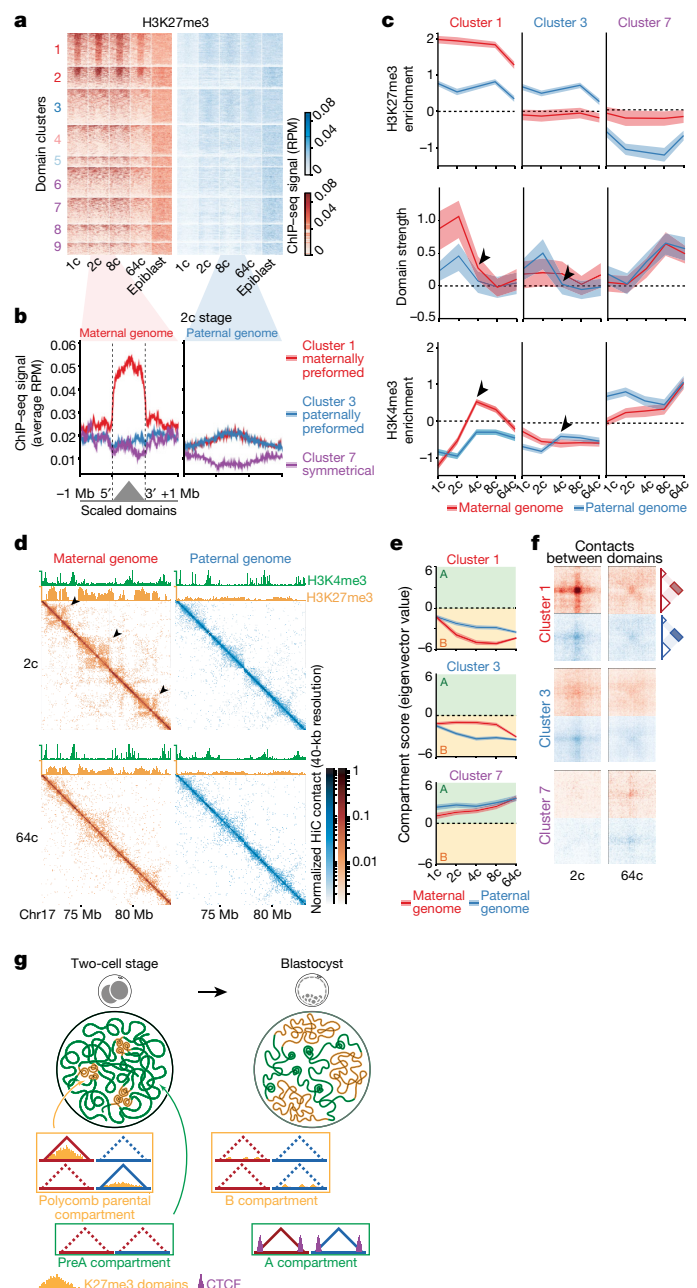


**Fig. 2 | Early domains are associated with Polycomb and form local compartments.** **a**, Heat maps of H3K27me3 ChIP-seq signal on domains (scaled to 1 Mb) from each cluster, on the maternal (red) (left) and paternal (blue) (right) alleles. Data are taken from Gene Expression Omnibus (GEO) accession GSE76687. RPM, reads per million reads sequenced. **b**, Average ChIP-seq signal at the 2-cell stage on the maternal (left) and paternal (right) alleles, for cluster 1 ( $n = 375$  domains), cluster 3 ( $n = 387$  domains) and cluster 7 ( $n = 287$  domains). **c**, Quantification of H3K27me3 (top) or H3K4me3 (bottom) enrichment (versus mean of the genome (Methods)) or domain strength (middle, average Z-score) for cluster 1, cluster 3 and cluster 7 ( $n$  values as in **b**). Lines represent the mean, and shading represents the 95% confidence interval of the mean. The maternal allele is in red and paternal allele is in blue. H3K4me3 data are taken from GSE71434. **d**, Snapshots of ChIP-seq and HiC maps (40-kb resolution) on the maternal (left) and paternal (right) alleles for a locus on chromosome 17. **e**, Dynamics of compartment scores (principal component analysis first eigenvectors) for cluster 1, cluster 3 and cluster 7 ( $n$  values as in **b**). The A and B compartments are assigned on the basis of gene density (Methods). Line represents the mean, and shading represents the 95% confidence interval of the mean. **f**, Average HiC map enrichment of long-distance interactions (>1 Mb) around the intersection between domain centres ( $n$  values as in **b**). **g**, Model of the parental preformed local compartment to de novo-acquired conventional A and B compartments.

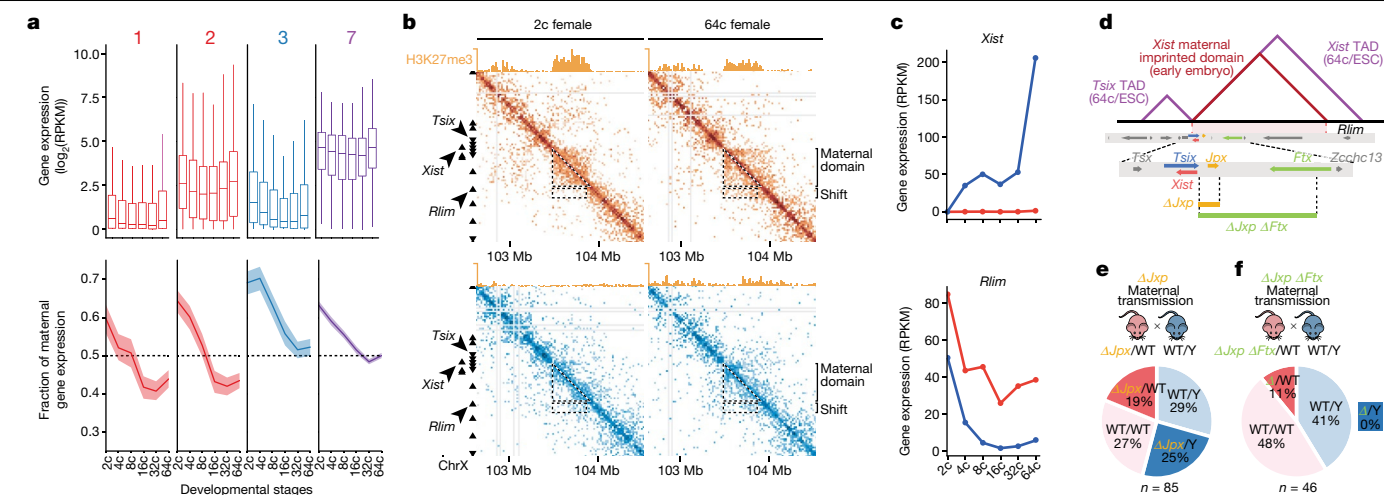


**Fig. 3 | Parental preformed domains are associated with a transient imprint.**

**a**, Distribution of gene expression (top) and fraction of maternal expression (maternal/(maternal + paternal)) for genes present within the domains of selected clusters. Box plots (top) represent  $\pm 1.5\times$  interquartile range, 25th and 75th percentiles and median values. Lines represent the mean, and shading represents the 95% confidence interval of the mean. RPKM, reads per kilobase of transcript per million mapped reads. **b**, Snapshots of HiC on the maternal (red) and paternal (blue) genome, and H3K27me3 ChIP-seq, at the

*Xist* locus (female cells only were pooled;  $n=43$  at the 2-cell stage,  $n=83$  at the 64-cell stage). **c**, Allele-specific expression of *Rlim* and *Xist* from the 2-cell stage to the 64-cell stage. **d**, Scheme of the X inactivation centre and of the CRISPR deletions that we engineered. ESC, embryonic stem cell. **e**, Genotype distribution after maternal transmission of *Jpx* deletion ( $n=85$  pups). WT, wild type. **f**, Genotype distribution after maternal transmission of *Jpx* and *Ftx* deletion ( $\Delta$ ) ( $n=46$  pups).

*Jpx* are viable, and that normal expression of *Xist* occurs in these mice (Fig. 3e, Extended Data Fig. 6i, j). Whereas *Ftx* deletion alone is dispensable for imprinted X chromosome inactivation in preimplantation embryos<sup>25</sup>, the maternal transmission of the deletion containing *Jpx* and *Ftx* strongly compromised female viability (5  $\Delta Jpx$ -*Ftx*/wild-type

female mice out of 46 pups received the deleted allele, corresponding to 11% transmission) and no viable male could be obtained (0% transmission) (Fig. 3f). Taken together, our analysis identifies a minimal control region for imprinting in proximity to *Xist*, and opens up new possibilities for testing other transient imprint regions.

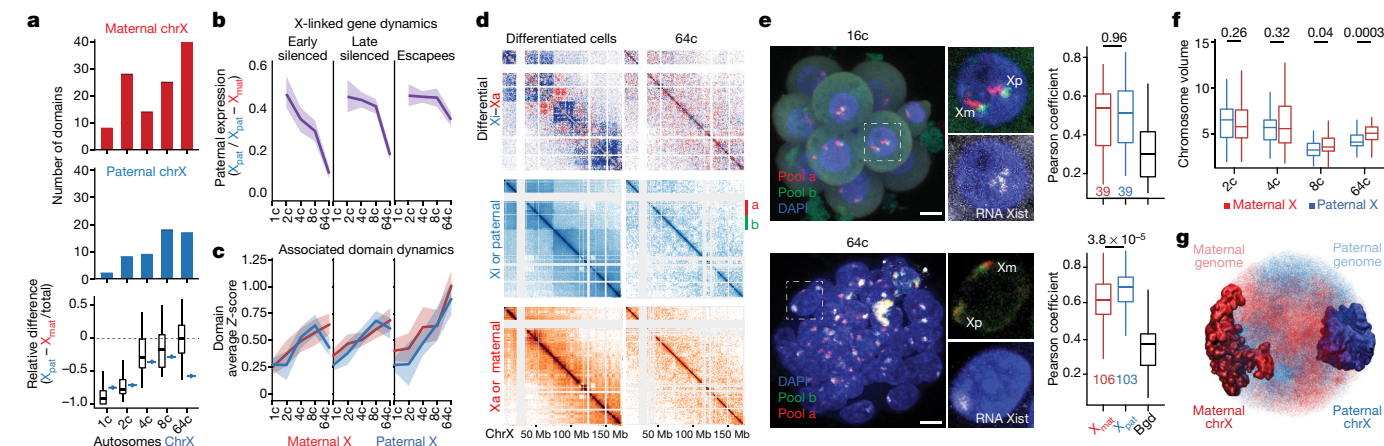


**Fig. 4 | Structural changes at the paternal X chromosome during imprinted X chromosome inactivation.**

**a**, Number of domains called on the maternal X chromosome (red) and on the paternal X chromosome (blue) over preimplantation development, and the relative difference of domains on the paternal versus maternal alleles (autosomes in black, X chromosome in blue). Box plot represents the  $\pm 1.5\times$  interquartile range, 25th and 75th percentiles and median value for all autosomes ( $n=19$ ). **b**, Expression dynamics for early-silenced, late-silenced and escapee genes ( $n=40$ , 76 and 52, respectively, as in a previous study<sup>20</sup>). **c**, Structural changes in the corresponding domains that contain genes in the categories shown in **b**. **d**, Parental differential (top) and allele-specific (bottom and middle) HiC contact maps (pooled female cells) over the entire X chromosome (resolution of 640 kb) in neural progenitor cells (left) and at 64-cell stage (right). DNA FISH probes (oligonucleotide pools a and b) are indicated in colours over the centromeric megadomain. Lines represent the mean and shading represents the 95% confidence interval of the mean. Xa, active X chromosome; Xi, inactive X chromosome. **e**, Representative

3D RNA-DNA FISH images of 16-cell stage (top) or 64-cell stage (bottom) embryo with corresponding box plot ( $\pm 1.5\times$  interquartile range, 25th and 75th percentiles and median value) quantifications for signal correlations. Statistical significance ( $P < 0.001$ ) was assessed using Wilcoxon's rank-sum test (two-sided).  $n=39$  nuclei from 8 female embryos for 16-cell stage;  $n=106$  and 103 signals from 106 nuclei from 4 female embryos for 64-cell stage. DNA is counterstained with DAPI. Scale bar, 10  $\mu$ m. Bgd, background; Xm, maternal X chromosome; Xp, paternal X chromosome. **f**, Dynamics of the volume of the paternal and maternal X chromosomes. Box plots represent  $\pm 1.5\times$  interquartile range, 25th and 75th percentiles and median value. *P* values are indicated above the box plot, and were calculated using Mann-Whitney *U* test (two-sided).  $n=43$ , 46, 35 and 83 single cells for the 2-cell, 4-cell, 8-cell and 64-cell stages, respectively. **g**, Three-dimensional model of whole-genome conformation for 64-cell-stage single cell number 118. Maternal chromosomes are in red; paternal chromosomes are in blue; autosomes in thin line and X chromosomes are highlighted. The model was computed at 500-kb resolution.



## Features of imprinted X inactivation

In differentiated female cells, the inactive X chromosome is organized into two megadomains rather than into A and B compartments, and displays a marked weakening of TADs<sup>26,27</sup>; however, little is known of the dynamics of this organization during development. Pooling only female cells, we found that the paternal X chromosome displays a strong deficit in domains compared to its maternal counterpart (Fig. 4a). Whereas preformed maternal domains are lost, domains that are formed *de novo* become weaker on the paternal genome by the blastocyst stage, with the exception of a small subset of domains (Extended Data Fig. 7a). Comparing the dynamics of structural domains with those of gene expression, we found that early silenced loci on the paternal X chromosome show a marked loss of domain strength only after the eight-cell stage (that is, after silencing initiation), and domains that contain late-silenced genes display little structural change (although imprinted X chromosome inactivation is largely complete) (Fig. 4b, c). Although we cannot formally exclude that this might be due to differences in sensitivity between RNA sequencing and single-cell HiC, these results suggest that the loss of TAD structure on the paternal X chromosome would follow or accompany, rather than precede, gene silencing.

Using 3D modelling of chromosomes, we also found that early silenced genes are localized more at the centre of the paternal X chromosome whereas escapees tend to be located at its periphery (Extended Data Fig. 7b), similar to differentiated cells<sup>28</sup>. However, megadomains do not appear on the paternal X chromosome (Fig. 4d) despite a higher colocalization of intradomain probes by DNA FISH (Fig. 4e), which suggests a global compaction of the inactive paternal X chromosome. Three-dimensional modelling confirmed that the paternal X chromosome was substantially smaller (by approximately a third) than its maternal homologue at the 64-cell stage (Fig. 4f) and adopted a more globular shape (whereas the maternal X chromosome is more elongated) (Fig. 4g), as has previously been reported in somatic cells<sup>26</sup>.

## Conclusions

Here we show that higher-order chromatin structure matures from parental-specific and early repressive compartments towards a progressive establishment of TADs in early development in the mouse (Fig. 2g). This developmental switch might illustrate the autonomous mechanisms at play—cohesin-dependent and -independent—that have previously been observed for the 3D organization of the genome<sup>29</sup> and that might also reflect the unusual chromatin landscape and nuclear organization of the early embryo, compared to later developmental stages<sup>1,30</sup>. Early compartments are Polycomb-marked and are accompanied by contrasting allelic gene-expression states. These parentally preformed repressive domains may be important in counterbalancing genome-wide embryonic genome activation for transiently imprinted genes such as *Tle3* (the dose of which affects the pluripotency programs<sup>31</sup>) or *Xist* (which is central to the process of gene dose compensation in females<sup>32</sup>). Our study also illustrates that, after embryonic genome activation, structures tend to be TAD-like and their appearance is generally linked to active chromatin states. In the case of the paternal X chromosome, the loss of TAD structure during X chromosome inactivation is a late event that seems to follow—rather than precede—gene silencing. Furthermore, we find that there is progressive compaction of the paternal X chromosome, but no megadomain formation, by the blastocyst stage. Local domains are maintained only across escapee loci, suggesting that local structure might require an active chromatin state and/or transcription.

Overall, our study provides broad insights into the intricate interplay between chromosome folding and parental gene activity with the developmental potential of the early embryo.

## Online content

Any methods, additional references, Nature Research reporting summaries, source data, extended data, supplementary information, acknowledgements, peer review information; details of author contributions and competing interests; and statements of data and code availability are available at <https://doi.org/10.1038/s41586-020-2125-z>.

- Burton, A. & Torres-Padilla, M.-E. Chromatin dynamics in the regulation of cell fate allocation during early embryogenesis. *Nat. Rev. Mol. Cell Biol.* **15**, 723–735 (2014).
- Wu, J. et al. The landscape of accessible chromatin in mammalian preimplantation embryos. *Nature* **534**, 652–657 (2016).
- Dahl, J. A. et al. Broad histone H3K4me3 domains in mouse oocytes modulate maternal-to-zygotic transition. *Nature* **537**, 548–552 (2016).
- Liu, X. et al. Distinct features of H3K4me3 and H3K27me3 chromatin domains in pre-implantation embryos. *Nature* **537**, 558–562 (2016).
- Flyamer, I. M. et al. Single-nucleus Hi-C reveals unique chromatin reorganization at oocyte-to-zygote transition. *Nature* **544**, 110–114 (2017).
- Battulin, N. et al. Comparison of the three-dimensional organization of sperm and fibroblast genomes using the Hi-C approach. *Genome Biol.* **16**, 77 (2015).
- Jung, Y. H. et al. Chromatin states in mouse sperm correlate with embryonic and adult regulatory landscapes. *Cell Rep.* **18**, 1366–1382 (2017).
- Ke, Y. et al. 3D chromatin structures of mature gametes and structural reprogramming during mammalian embryogenesis. *Cell* **170**, 367–381.e20 (2017).
- Du, Z. et al. Allelic reprogramming of 3D chromatin architecture during early mammalian development. *Nature* **547**, 232–235 (2017).
- Wu, J. et al. Chromatin analysis in human early development reveals epigenetic transition during ZGA. *Nature* **557**, 256–260 (2018).
- Gassler, J. et al. A mechanism of cohesin-dependent loop extrusion organizes zygotic genome architecture. *EMBO J.* **36**, 3600–3618 (2017).
- Nagano, T. et al. Single-cell Hi-C reveals cell-to-cell variability in chromosome structure. *Nature* **502**, 59–64 (2013).
- Nagano, T. et al. Cell-cycle dynamics of chromosomal organization at single-cell resolution. *Nature* **547**, 61–67 (2017).
- Inoue, A., Jiang, L., Lu, F., Suzuki, T. & Zhang, Y. Maternal H3K27me3 controls DNA methylation-independent imprinting. *Nature* **547**, 419–424 (2017).
- Okamoto, I., Otte, A. P., Allis, C. D., Reinberg, D. & Heard, E. Epigenetic dynamics of imprinted X inactivation during early mouse development. *Science* **303**, 644–649 (2004).
- Naumova, N. et al. Organization of the mitotic chromosome. *Science* **342**, 948–953 (2013).
- Zheng, H. et al. Resetting epigenetic memory by reprogramming of histone modifications in mammals. *Mol. Cell* **63**, 1066–1079 (2016).
- Zhang, B. et al. Allelic reprogramming of the histone modification H3K4me3 in early mammalian development. *Nature* **537**, 553–557 (2016).
- Nora, E. P. et al. Targeted degradation of CTCF decouples local insulation of chromosome domains from genomic compartmentalization. *Cell* **169**, 930–944.e22 (2017).
- Borenstein, M. et al. Xist-dependent imprinted X inactivation and the early developmental consequences of its failure. *Nat. Struct. Mol. Biol.* **24**, 226–233 (2017).
- Inoue, A., Jiang, L., Lu, F. & Zhang, Y. Genomic imprinting of *Xist* by maternal H3K27me3. *Genes Dev.* **31**, 1927–1932 (2017).
- Nora, E. P. et al. Spatial partitioning of the regulatory landscape of the X-inactivation centre. *Nature* **485**, 381–385 (2012).
- Okamoto, I. et al. Evidence for *de novo* imprinted X-chromosome inactivation independent of meiotic inactivation in mice. *Nature* **438**, 369–373 (2005).
- Tian, D., Sun, S. & Lee, J. T. The long noncoding RNA, *Jpx*, is a molecular switch for X chromosome inactivation. *Cell* **143**, 390–403 (2010).
- Soma, M., Fujihara, Y., Okabe, M., Ishino, F. & Kobayashi, S. *Ftx* is dispensable for imprinted X-chromosome inactivation in preimplantation mouse embryos. *Sci. Rep.* **4**, 5181 (2014).
- Giorgetti, L. et al. Structural organization of the inactive X chromosome in the mouse. *Nature* **535**, 575–579 (2016).
- Deng, X. et al. Bipartite structure of the inactive mouse X chromosome. *Genome Biol.* **16**, 152 (2015).
- Chaumeil, J., Le Baccon, P., Wutz, A. & Heard, E. A novel role for *Xist* RNA in the formation of a repressive nuclear compartment into which genes are recruited when silenced. *Genes Dev.* **20**, 2223–2237 (2006).
- Schwarzer, W. et al. Two independent modes of chromatin organization revealed by cohesin removal. *Nature* **551**, 51–56 (2017).
- Borsos, M. et al. Genome–lamina interactions are established *de novo* in the early mouse embryo. *Nature* **569**, 729–733 (2019).
- Laing, A. F., Lowell, S. & Brickman, J. M. Gro/TLE enables embryonic stem cell differentiation by repressing pluripotent gene expression. *Dev. Biol.* **397**, 56–66 (2015).
- Galupa, R. & Heard, E. X-chromosome inactivation: a crossroads between chromosome architecture and gene regulation. *Annu. Rev. Genet.* **52**, 535–566 (2018).

**Publisher's note** Springer Nature remains neutral with regard to jurisdictional claims in published maps and institutional affiliations.

© The Author(s), under exclusive licence to Springer Nature Limited 2020

## Methods

### Data reporting

No statistical methods were used to predetermine sample size. The experiments were not randomized and the investigators were not blinded to allocation during experiments and outcome assessment.

### Mouse embryo collection, single-cell dissociation and formaldehyde fixation

Five-week-old female C57BL/6J mice were purchased from Charles River. Animal care and use for this study were performed in accordance with the recommendations of the European community (2010/63/UE). All experimental protocols were approved by the ethics committee of the Institut Curie CEEA-IC118 under the number APAFIS#8812-2017020611033784v2, given by national authority in compliance with the international guidelines. When stated, intraperitoneal injection of 5 IU pregnant mare's serum gonadotropin, followed 46 h later by injection of 5 IU human gonadotropin, were applied to induce ovulation of female mice. DNA FISH was performed on embryos collected from superovulated C57BL/6J (B6) female mice (except for the blastocyst stage), mated with C57BL/6J (B6) male mice. The single-cell HiC protocol was applied to blastomeres of embryos collected from crosses between C57BL/6J (B6) female mice and CAST/Eij male mice. In the case of the one-cell, two-cell and four-cell stages, some embryos were collected after female superovulation. Embryos were collected from the reproductive tracts in M2 medium at defined time periods according to mating and/or hCG administration (given in this order): 14 h or 21 h for 1-cell stage (pronuclear stage 3 or 4), 37 h or 44 h for late 2-cell stage, 48 h or 55 h for 4-cell stage, 55 h or 62 h for 8-cell stage and 80 h for blastocyst stages (approximately 60 to 64 cells) (64-cell stage). B6 pure oocytes were collected 15 h after hCG injection. Embryos were included in the analyses when they showed a normal morphology and the correct number of blastomeres for their developmental stage. Zona pellucida and polar bodies were removed using acid Tyrode's solution and/or gentle pipetting (except in a few cases for the blastocyst stage). Embryos were incubated in  $\text{Ca}^{2+}$ - and  $\text{Mg}^{2+}$ -free M2 medium for 5 to 30 min to remove the polar body in zygotes or to isolate individual cells at subsequent stages. For the blastocyst stage, incubation with  $\text{Ca}^{2+}$ - and  $\text{Mg}^{2+}$ -free M2 medium was replaced with a 5-min incubation in TrypLE (Invitrogen). During the picking, the origin of the blastomere (inner cell mass or trophectoderm) was not recorded). Blastomeres were mechanically dissociated, rinsed three times in PBS/acylated BSA (Sigma) before being fixed for 10 min in a 2% formaldehyde solution at room temperature. Fixation was stopped by transferring cells to a 127-mM glycine solution (5 min on ice). Blastomeres from different embryos were pooled from this step onwards to perform the single-cell HiC procedure post-fixation.

### Single-cell HiC procedure

The procedure for embryo blastomeres was optimized from a previous study<sup>13</sup>. Care was taken at every step to reduce putative contamination between solutions. In brief, following fixation, and rapid rinses in 1× PBS solution 1% acetylated BSA (Sigma), blastomeres were permeabilized for 30 min on ice in 10 mM Tris-HCl (pH 8), 10 mM NaCl, 0.2% IGEPAL CA-630 containing complete EDTA-free protease inhibitor cocktail (Roche). Cells were transferred to a protein low binding tube (Sigma) containing 0.3% SDS diluted with 1.24× NEBuffer3 for 60 min at 37 °C with constant agitation. Triton X-100 was added to 2% final and incubation was extended for 60 min, before addition of 625 U of MboI (New England Biolabs) and overnight incubation. To label the digested DNA ends, a mix containing 28.4 μM final of dCTP, dGTP and dTTP and biotin-14 dATP were added with 25 U DNA polymerase I, large (Klenow) fragment (New England Biolabs) for 60 min with constant agitation. After spinning, blastomeres were treated with 10 U of T4 DNA ligase (Thermo Fisher) in presence of 1× reaction buffer with 1× BSA (both by

New England Biolabs) at 16 °C for at least 4 h. After spinning, blastomeres were resuspended with PBS 1× and BSA 1 mg/ml to dispatch them individually into PCR tubes (in strips; one per tube) before storage at −80 °C until further processing.

### Library preparation and sequencing

To prepare single-cell HiC libraries from single nuclei in PCR strips, 5 μl of PBS was added to each well and crosslinks reversed by incubating at 65 °C overnight. HiC concatemer DNA was fragmented and linked with sequencing adapters using the Nextera XT DNA library preparation kit (Illumina), by adding 10 μl of Tagment DNA buffer and 5 μl of Amplicon Tagment mix, incubating at 55 °C for 20 min, then cooling down to 10 °C, followed by addition 5 μl of Neutralize Tagment buffer and incubation for 5 min at room temperature. HiC ligation junctions were then captured by Dynabeads M-280 streptavidin beads (Thermo Fisher) (20 μl of original suspension per single-cell sample). Beads were prepared by washing with 1× BW buffer (5 mM Tris-Cl pH 7.5, 0.5 mM EDTA, 1 M NaCl), resuspended in 4× BW buffer (20 mM Tris-Cl pH 7.5, 2 mM EDTA, 4 M NaCl; 8 μl per sample), and then mixed with the 25-μl sample and incubated at room temperature overnight with gentle agitation. The beads were then washed 4 times with 200 μl of 1× BW buffer, twice with 200 μl of 10 mM Tris-Cl pH 7.5 at room temperature, and resuspended in 25 μl of 10 mM Tris-Cl pH 7.5. Single-cell HiC libraries were amplified from the beads by adding 15 μl of Nextera PCR master mix, 5 μl of i7 Index primer of choice and 5 μl of i5 Index primer of choice. Samples were then incubated at 72 °C for 3 min, 95 °C for 30 s followed by the thermal cycling at 95 °C for 10 s, 55 °C for 30 s and 72 °C for 30 s for 18 cycles, and then incubated at 72 °C for 5 min. The supernatant was separated from the beads and purified one by one with AMPure XP beads (Beckman Coulter; 0.6 times volume of the supernatant) according to manufacturer's instructions and eluted with 30 μl each of 10 mM Tris-Cl pH 8.5. The eluate was purified once more with AMPure XP beads (equal volume to the previous eluate) and eluted with 11 μl of 10 mM Tris-Cl pH 8.5.

Before sequencing, the libraries were quantified by quantitative PCR (Kapa Biosystems) and the size distribution was assessed with Agilent 2100 Bioanalyzer (Agilent Technologies). The libraries were sequenced by 2× 150-bp paired-end run using either a HiSeq 1500, HiSeq 2500 or NextSeq 500 (Illumina).

### Bioinformatics analysis

All data were mapped to the mouse genome mm10, using the C57BL/6J/CAST-Eij single nucleotide polymorphisms (SNPs) from the mouse genome project (v.5 SNP142), and the gene annotation from ensembl (v.92). Analyses were performed in R (v.3.4.2) and Bioconductor (v.3.6). Gene ontology was performed using the package ClusterProfiler (v.3.10.1).

### HiC data processing

Data were processed with HiC-Pro<sup>33</sup> (v.2.11.0) in allele-specific mode. The following parameters were used: - For mapping: -very-sensitive -L 30 -score-min L,-0.6,-0.2 -end-to-end -reorder. No minimal fragment size, insert size or contact distance were defined. - For processing: GET\_ALL\_INTERACTION\_CLASSES=0 GET\_PROCESS\_SAM=0 RM\_SINGLETON=1 RM\_MULTI=1 RM\_DUP=1. - for iced scaling: MAX\_ITER=100 FILTER\_LOW\_COUNT\_PERC=0.02 FILTER\_HIGH\_COUNT\_PERC=0 EPS=0.1. Only pairs with both reads having MAPQ > 30 were kept.

### Cell cycle phasing

Cell cycle phasing was done by plotting the proportion of short-range contacts (between 25 kb and 2 Mb) versus long-range contacts (between 2 Mb and 12 Mb) in single cells. An ellipsoid was fitted to the single-cell points, as in a previous publication<sup>34</sup>. The reference in polar coordinates was set to the segment going from the centre of the ellipsoid to the point of coordinates [0.15, 0.35], which corresponds to the beginning



# Article

of the left-ascending part of the single-cell trajectory. Cells in the G1, S and G2 phases were defined as those in the angle between 0 and  $-0.35\pi$  ( $65^\circ$  anticlockwise). For each stage, contacts from all cells phased in G and S were pooled (all contacts or genome-specific contacts independently) and matrices at 10- and 40-kb resolution were created using cooler (v.0.7.9, parameter: -balance). Data were visualized in HiGlass<sup>35</sup>.

## Domain calling

Domains were first identified on the 40-kb matrices, independently for each stage, on both the maternal and paternal genomes, using 3dNetMod<sup>36</sup> (v.1.0.10.06.17), with parameters favouring sensitivity over specificity: - PRE\_PROCESSING: region\_size 150, overlap 100, logged True, qnorm False. - GPS: badregionfilter True, scale genome wide, plateau 8, chaos filter True, chaos\_pct 0.85, diagonal\_density 0.65, consecutive\_diagonal\_zero 20. - MMCP: num\_part 20, plots False, pctile\_threshold 0, pct\_value 0. - HSV: size\_threshold 7, size\_s1 600000, size\_s2 1200000, size\_s3 3000000, size\_s4 6000000, size\_s5 12000000, var\_thresh1 0, var\_thresh2 50, var\_thresh3 100, var\_thresh4 100, var\_thresh5 100, boundary\_buffer 80000. For the analysis of the X chromosome in female cells, domains were called from the female pseudo-bulk HiC maps.

## Domain average enrichment

We converted the HiC matrices to Z-score matrices, in which the scores are normalized to the distribution of scores for the same contact distance, as in a previous publication<sup>37</sup>. In brief, for any two loci  $i$  and  $j$  on chromosome  $c$ , separated by a distance  $n$  and with a balanced count of contacts  $C_{i,j}$ , the corresponding Z-score is  $Z_{i,j} = (C_{i,j} - \mu_n) / \sigma_n$ , in which  $\mu_n$  and  $\sigma_n$  are the mean and standard deviation of the distribution of contact counts for any pair of loci distant by  $n$ . Z-score matrices were calculated on the 40-kb matrices with HiCExplorer<sup>37</sup> (v.2.1.1) using the HiCFindTads function (parameters: -correctForMultipleTesting None -minDepth 60000000 -maxDepth 200000000 -step 60000000 -thresholdComparisons 1 -delta 0). For analysis of the X chromosome, contacts from female cells only were pooled and matrices obtained in the same way.

The average contact enrichment of domains was computed by averaging the Z-score over the domain upper triangle, excluding the diagonal. For a domain  $D_{i,j}$  spanning bins  $i$  to  $j$ , the upper triangle  $T$  in matrix  $M$  is the submatrix  $T[a,b]$  with  $a \in \{i, \dots, j-1\}$  and  $b \in \{i+1, \dots, j\}$  and  $b > a$ . This was calculated using the custom function hicSummarizePerRegion for HiCExplorer, available from the E.H. laboratory GitHub version of HiCExplorer at <https://github.com/heard-lab/HiCExplorer>, branch SummarizePerRegion, or directly from <https://github.com/heard-lab/HiCExplorer/blob/SummarizePerRegion/hicexplorer/hicSummarizeScorePerRegion.py>. We kept only domains with an average Z-score  $> 0.5$ .

## Overlapping domain filtering

As largely overlapping domains with very similar boundaries can be called within or between different time points, we further filtered redundancy using a custom script (available on GitHub, from [https://github.com/heard-lab/HiCTools/blob/master/FilterRegions\\_MinMutualOverlap\\_maxScore.r](https://github.com/heard-lab/HiCTools/blob/master/FilterRegions_MinMutualOverlap_maxScore.r)). In brief, starting from a set of domains  $D_n = 0$  equal to the set of all domains  $D_{all}$ , and the empty sets  $D_{overlap}$  and  $D_{highest}$ , the following steps were used: (1) From  $D_n$ , all pairs of overlapping domains are compared two by two. (2) If their overlap represents more than 70% of each other's lengths, they are added to the set  $D_{overlap}$ . (3) For each pair of overlapping domains ( $>70\%$ ), only the domain with the highest score is kept and added to the set  $D_{highest}$ . (4)  $D_{n+1}$  is assigned the union of  $D_{highest}$  and all domains from  $D_{all}$  that were not in  $D_{overlap}$ . The procedure is repeated from step 1 to step 4 until  $D_{n+1} = D_n$ . The reinjection in step (4) of all domains from  $D_{all}$  that were not in  $D_{overlap}$  allows us to keep isolated domains, as well as avoiding chains between pairs of domains. For stage-specific analysis (Figs. 1c, 4a) this procedure was applied to the domains called at each stage and on each genome

individually. For the dynamic analysis across stages, sets of all domains called individually at each stage and on each genome (after this redundancy filtering) were pooled together as one set and filtered with the same procedure, resulting in one common set of domains.

## Clustering

Domain dynamics clustering was performed using the R package Mfuzz (2.26.0)<sup>38</sup>, using as input the average Z-score per domain (row) in each stage from the 1-cell stage to the 64-cell stage, on the maternal and paternal genomes (columns). Fuzzification parameter  $m$  was estimated using the mestimate() function. The number of clusters was defined as nine, on the basis of the minimal distance between cluster centroids.

## Single-cell analysis

The sum of contacts per domain for each genome per single cell was computed using the function hicSummarizePerRegion (as described in 'Domain average enrichment'), excluding the diagonal. The matrix of counts (domains on rows, single-cell maternal genome and single-cell paternal genome on columns) was used as input for monocle3<sup>39</sup>. Data were processed using the preprocess\_cds function using the first 75 components of the principal components analysis (parameters: num\_dim = 75, method = "PCA", norm\_method = "log"). Dimension reduction was performed using UMAP with the reduce\_dimension function (max\_components = 2) and graph for pseudotime inferred using learn\_graph (parameters: use\_partition = FALSE, learn\_graph\_control = list(minimal\_branch\_len = 3). For cluster average score, counts per domains were converted to CPKM by dividing the counts by the total number of contacts in domains per allele (divided by  $10^6$ ), and by the domain length in kb.

## Compartments and domain interactions

Compartments were called using HiTC (v.1.26.0)<sup>40</sup>. An aggregate plot of interaction between pairs of domains was performed using a custom function hicAggregateContact for HiCExplorer (available on GitHub, from <https://github.com/deeptools/HiCExplorer>, branch aggregateGenome; parameters: -range 1000000:999000000 -numberOfBins 200 -avgType mean -genome -regionReferencePosotion centre), which also output the list of pairs of domains with respect to the distance threshold (that is, distance of more than 1 Mb). Only domains that did not contain another domain were used to avoid redundancy between domains that contained one another. The normalized contact counts of the intersection between pairs of domains was calculated using a custom function hicSsummarizeScorePerRegion for HiCExplorer (available on GitHub, from <https://github.com/heard-lab/HiCExplorer>, branch SummarizePerRegion, or directly from <https://github.com/heard-lab/HiCExplorer/blob/SummarizePerRegion/hicexplorer/hicSummarizeScorePerRegion.py>; parameter: -summarizeType sum).

## Chromosome 3D modelling

Three-dimensional models of chromosomes (allele-specific) was performed using the programs Dip-C and Hickit<sup>41</sup>. We performed 3 rounds of 3D reconstruction at 100-kb resolution with 3D haplotype imputation (parameters: -temps 20 -s 8 4 2 0.4 0.2 0.1), and then 2 rounds of 3D reconstruction at 20-kb resolution with 3D haplotype imputation (parameter -temps 20 -s 8 4 2 0.4 0.2 0.1 0.04 0.02). Chromosome volumes were calculated using the alpha-convex hull algorithms from the R package alphashape3d ( $\alpha = 0.6$ ).

## ChIP-seq analysis

Reads were trimmed using Trimgalore (v.0.4.4), mapped using STAR<sup>42</sup> (2.5.3a, parameters: -outFilterMultimapNmax 1 -outFilterMismatchNmax 999 -outFilterMismatchNoverLmax 0.06 -alignIntronMax 1 -alignMatesGapMax 2000 -alignEndsType EndToEnd -outSAMattributes NH HI NM MD), and removed when they mapped to the mitochondrial genome. The remaining reads were split by allele using SNPsplit

(v.0.3.2). Allele-specific and unassigned .bam files were sorted, duplicates removed using Picard (v.2.18.2, parameters: REMOVE\_DUPLICATES = true ASSUME\_SORTED = true) and pooled as the total reads. BigWig of coverage files were done using DeepTools<sup>43</sup> bamCoverage (parameters: -extendReads -binSize 1, with -extendReads 200 for single-end data). A scaling factor was calculated as  $10^6/\text{total number of reads}$ , and the same factor was given as the parameter 'scaleFactor' for both allelic signals. The heat map and average plots of signal were performed using DeepTools computeMatrix scale-regions (with parameters: -regionBodyLength 1000000 -beforeRegionStartLength 1000000 -afterRegionStartLength 1000000 -binSize 50000) as well as plotHeatmap and plotProfile. For quantification of ChIP-seq in domains, reads were counted using the featureCounts function from Subread<sup>44</sup> (v.1.28.1, parameters: -p -s 0). Data scaling was performed in R using DESeq2 (v.1.18.1), calculating the sizeFactor on the count of total reads and applying it to the allele-specific counts. Enrichment relative to background was calculated as the ChIP-seq signal per domain in RPKM, divided by the average RPKM on the genome calculated in 10-kb bins.

### RNA-sequencing analysis

Single-cell RNA-sequencing data were processed similarly to those from ChIP-seq, except for the mapping, for which the following parameters were used: -outFilterMultimapNmax 1 -outFilterMismatchNmax 999 -outFilterMismatchNoverLmax 0.06 -alignIntronMax 500000 -alignMatesGapMax 500000 -alignEndsType EndToEnd -outSAMAttributes NH HI NM MD. The quantification of expression was performed using featureCounts (parameters: -p -s 0 -t exon -g gene\_id). Data were then analysed in R using DESeq2<sup>45</sup> (v.1.18.1), calculating the sizeFactor on the count of total reads and applying it to the allele-specific counts. Filtering was performed similarly that in a previous publication<sup>20</sup>. In single-cell data, a pseudo-RPKM score was calculated as the normalized count  $\times 1,000/\text{gene length in base pairs}$ ; as the previously used protocol<sup>20</sup> is 3'-biased and does not recover more than the last 3 kb of the transcripts (longer genes (>3 kb) were assigned a length of 3 kb). In single-cell data, genes with a pseudo-RPKM value < 5 (not allele-specific) and a count of reads lower than 10 reads on both alleles were assigned as lowly expressed. An allelic *D*-score ( $\text{expression}_{\text{maternal}}/(\text{expression}_{\text{maternal}} + \text{expression}_{\text{paternal}})$ ) was calculated only for genes that were not lowly expressed, to avoid artefactual strong bias due to noisy low-expressed genes. Single-cell data were then pooled in pseudo-bulk by stage, and for each gene an average *D*-score was calculated only when more than 20% of single cells had an allelic *D*-score calculated (that is, did not show too low expression on both alleles). Average pseudo-RPKM values were calculated by averaging the pseudo-RPKM values of all single cells without filtering.

### DNA FISH probes

Probes for DNA FISH on the X chromosome were obtained as previously described<sup>22</sup>, or using BAC DNA for chromosome 13 (purchased from CHORI RP24-278M23; RP23-325G4; RP23-2B17; RP23-222A16; RP24-389D15; RP23-302B3; RP23-359G6; RP23-326J5; RP23-307F19) or were purchased from MYcroarray (fluorescent oligonucleotides, average length 45 bp, 5'-modified with Atto 448 or Atto 550, average density: one oligonucleotide every 3 kb). Oligonucleotides were designed to tile the following consecutive 18-Mb regions: chromosome X: 35,000,000–53,000,000 (termed pool a) and chromosome X: 53,000,000–72,000,000 (termed pool b)<sup>26</sup>. To prepare the probe mix for DNA FISH, 100 ng of labelled BAC DNA was used, along with 5 µg of Cot-1 DNA and resuspended in formamide before adding equal volume of hybridization buffer (2×, 20% dextran sulfate; 4× SSC; 1 mM EDTA; 0.1% TritonX-100; 0.5 mg/ml BSA; 1 mg/ml PVP). Oligonucleotide probes were used in formamide at 10% final concentration.

### DNA FISH procedure on embryonic stem cells

FISH on cells from tissue culture was performed as previously described<sup>22,46</sup>. Feeder-free male mouse embryonic stem cells (E14;

GSM1366337) were cultured on gelatin-coated coverslips no. 1.5 (1 mm) and fixed in 3% paraformaldehyde for 10 min at room temperature. Permeabilization was then performed on ice for 5 min in 1× PBS containing 0.5% Triton X-100 and 2 mM vanadyl-ribonucleoside complex (New England Biolabs). Coverslips were preserved in 70% EtOH at -20 °C. Prior to FISH, samples were dehydrated through an ethanol series (80%, 95% and 100%, twice) and air-dried quickly. DNA FISH was preceded by sample denaturation in 50% formamide in 2× SSC at pH 7.2 at 80 °C for 40 min. After overnight hybridization at 42 °C, washes were carried out at 45 °C, 3 times 5 min in 50% formamide in 2× SSC at pH 7.2 and 3 times 5 min in 2× SSC. DAPI at 0.2 mg/ml was used for counterstaining and mounting medium consisting of 90% glycerol, 0.1× PBS, 0.1% *p*-phenylenediamine at pH 9 (Sigma).

### Three-dimensional DNA FISH procedure on embryos and *Xist* RNA FISH combined with DNA FISH using oligonucleotide probes

Collected embryos were prefixed for 1 min at room temperature in paraformaldehyde (PFA) 1% 1 mg/ml polyvinylpyrrolidone (PVP), pre-permeabilized for 1 min at room temperature in PFA 0.5% and TritonX-100 0.4% and fixed for 10 min at room temperature in PFA 4%. After a brief wash in PBS 1× with PVP 1 mg/ml and TritonX-100 0.05% (PBS-TP), embryos were permeabilized for 1 h at 37 °C in PBS 1× with TritonX-100 0.5% (with RNase A 5 µl/ml in case of DNA FISH). After a brief rinse in PBS-TP, embryos were transferred into hybridization buffer 1× and equilibrated overnight with 1 mg/ml Cot-1 DNA mix at 37 °C. Embryos and probes were denatured for 10 min at 83 °C and put back for at least 3 h at 37 °C. After competition in Cot-1 mix, embryos were moved into the probe mix overnight at 37 °C. Excess of probes was eliminated through 3 washes at 45 °C in SSC 2× solution and SSC 0.2× solution for 10 min each. Embryos were then briefly washed in PBS 1× and mounted in a Vectashield drop containing DAPI under oil on a glass-bottomed plate, coated with poly-lysine.

### Microscopy and image analysis

Combined RNA and DNA FISH imaging was performed on an inverted confocal microscope (Zeiss) LSM700 with a Plan apo DICII (numerical aperture 1.4) 63× oil objective. Z-sections were taken every 0.4 µm. Structured illumination for DNA FISH was performed using an OMX system (Applied Precision) as in a previous publication<sup>22</sup>. Signals from all channels were realigned using fluorescent beads before each session of image acquisition. For colocalization analysis, analysis was restricted to a region of interest of identical volume around the FISH signal. The respective intensities of red and green channels were retrieved semi-automatically using the JACoP ImageJ plugin, and box plot distribution of the Pearson correlation coefficient was compared using Wilcoxon's rank-sum statistics with R.

### Engineering mice

The mouse mutant lines were generated following a previously described strategy<sup>47</sup>, with minor modifications. Single-guide (sg)RNAs were designed using CRISPOR<sup>48</sup>. For deleting the locus containing *Jpx* and *Ftx*, we used sgRNAs no. 57 (GGTACAATTATGCAACCTG), no. 58 (ATACTCCGATTACATACTC), no. 61 (TGCCCAAGCAAAAAGCGTGA) and no. 62 (AAAGTATTGACACCTTACCC). For deleting the *Jpx* locus, we used sgRNAs no. 57, no. 58 and no. 59 (TGCCCAAGCAAAAAGCGTGA) and no. 60 (AGTTAGATACACACCAAGT). T7-sgRNA PCR products were used as the template for in vitro transcription with the MEGAshortscript T7 kit (Life Technologies) and the products were purified using the MEGAclear kit (Life Technologies). sgRNAs were eluted in DEPC-treated RNase-free water, and their quality was assessed by electrophoresis on an agarose gel after incubation at 95 °C for 3 min with denaturing agent provided with the in vitro transcription kits. *Cas9* mRNA (Tebu-bio, L-7206) and sgRNAs were injected at 100 ng/µl and 50 ng/µl, respectively, into the cytoplasm of mouse B6D2F1 zygotes from eight-week-old superovulated B6D2F1 (C57BL/6J × DBA2) female mice mated to stud male mice of the same background. Zygotes with well-recognized pronuclei were collected in M2 medium (Sigma) at E0.5. Injected embryos were cultured in M16

# Article

medium (Sigma) at 37 °C under 5% CO<sub>2</sub>, until transfer at the one-cell stage the same day or at the two-cell stage the following day to the infundibulum of the oviduct of a pseudogestant CD1 female at E0.5 (25–30 embryos were transferred per female). All weaned mice (N0) were genotyped for presence of deletion (locus covering *Jpx* and *Ftx*, primers RG140.1: TGC-TACCGGTCACAGATATAAGT and RG145: TCTGGGATGCTTGTTCACAA;*Jpx* locus, primers RG140.1 and RG143: ACAAGGTGAGCGATGAGACA). Mice carrying deletion alleles were crossed to B6D2F1 mice and their progeny screened again for the presence of the deletion allele; PCR products were sequenced to determine the exact location of the deletions (locus covering *Jpx* and *Ftx*, chromosome X: 100,683,288–100,801,657, mm9; *Jpx*: 100683306–100702361, mm9). The F<sub>1</sub> mice were considered the ‘founders’ and bred to B6D2F1 mice; their progeny was then backcrossed to B6D2F1 mice, to generate heterozygous mice and lines were kept in heterozygosity. To establish mouse embryonic fibroblasts, single embryos were recovered at day 13.5 of gestation after the confirmation of vaginal plugs on *ΔJpx*/wild-type females bred with wild-type/Y or *ΔJpx*/Y males. Head and internal organs were removed and the body cavity was incubated for 1 h at 37 °C in TripLE (Invitrogen). After repetitive pipetting up and down, the resulting chunks were put in culture for 24–48 h until collected to prepare RNA with Trizol extraction for further examination by quantitative PCR. The level of gene expression was normalized to the geometric mean of the expression level of *Ppia* and *Gapdh* housekeeping genes according to geNorm method<sup>49</sup> to assess the relative expression of *Xist* and *Jpx*. The following primers were used and are listed as forward reverse and in 5′ to 3′: *Gapdh*, ccccaacactgagcatctcc/attatgggggtctgggatgg; *Ppia*, ttaccatcaaacattctctg/aacccaagaacttcagtgagagc; *Jpx*, ataaaatggcggtccac/ggccagtttctccactctcc; and *Xist*, ggttctctctccagaa-gctaggaa/tggtagatggcattgtgtattatgg

## Reporting summary

Further information on research design is available in the Nature Research Reporting Summary linked to this paper.

## Data availability

The HiC data generated and analysed are available in the GEO repository under accession number GSE129029. Previously published data were downloaded from GEO: H3K27me3 in early embryos (GSE76687); H3K27me3 in day-5 post-natal oocytes (GSE93941); single-cell RNA sequencing in early embryos (GSE80810); and HiC in gametes and early embryos (GSE82185). Source Data for Figs. 3, 4 and Extended Data Fig. 2, 6 are provided with the paper. Any other relevant data are available from the corresponding authors upon reasonable request.

## Code availability

The code developed for this study is available on the GitHub repository of the laboratory of E.H. (<https://github.com/heard-lab>).

33. Servant, N. et al. HiC-Pro: an optimized and flexible pipeline for Hi-C data processing. *Genome Biol.* **16**, 259 (2015).
34. Pu, J., Zheng, B., Leader, J. K. & Gur, D. An ellipse-fitting based method for efficient registration of breast masses on two mammographic views. *Med. Phys.* **35**, 487–494 (2008).
35. Kerpedjiev, P. et al. HiGlass: web-based visual exploration and analysis of genome interaction maps. *Genome Biol.* **19**, 125 (2018).
36. Norton, H. K. et al. Detecting hierarchical genome folding with network modularity. *Nat. Methods* **15**, 119–122 (2018).
37. Ramirez, F. et al. High-resolution TADs reveal DNA sequences underlying genome organization in flies. *Nat. Commun.* **9**, 189 (2018).
38. Kumar, L. & E. Futschik, M. Mfuzz: a software package for soft clustering of microarray data. *Bioinformatics* **2**, 5–7 (2007).
39. Cao, J. et al. The single-cell transcriptional landscape of mammalian organogenesis. *Nature* **566**, 496–502 (2019).
40. Servant, N. et al. HiTC: exploration of high-throughput ‘C’ experiments. *Bioinformatics* **28**, 2843–2844 (2012).
41. Tan, L., Xing, D., Chang, C.-H., Li, H. & Xie, X. S. Three-dimensional genome structures of single diploid human cells. *Science* **361**, 924–928 (2018).
42. Dobin, A. et al. STAR: ultrafast universal RNA-seq aligner. *Bioinformatics* **29**, 15–21 (2013).
43. Ramirez, F., Dündar, F., Diehl, S., Grüning, B. A. & Manke, T. deepTools: a flexible platform for exploring deep-sequencing data. *Nucleic Acids Res.* **42**, W187–W191 (2014).
44. Liao, Y., Smyth, G. K. & Shi, W. The Subread aligner: fast, accurate and scalable read mapping by seed-and-vote. *Nucleic Acids Res.* **41**, e108 (2013).
45. Love, M. I., Huber, W. & Anders, S. Moderated estimation of fold change and dispersion for RNA-seq data with DESeq2. *Genome Biol.* **15**, 550 (2014).
46. Chaumeil, J., Augui, S., Chow, J. C. & Heard, E. in *The Nucleus* (ed. Hancock, R.) 297–308 (Springer, 2008).
47. Wang, H. et al. One-step generation of mice carrying mutations in multiple genes by CRISPR/Cas-mediated genome engineering. *Cell* **153**, 910–918 (2013).
48. Haeussler, M. et al. Evaluation of off-target and on-target scoring algorithms and integration into the guide RNA selection tool CRISPOR. *Genome Biol.* **17**, 148 (2016).
49. Vandesompele, J. et al. Accurate normalization of real-time quantitative RT-PCR data by geometric averaging of multiple internal control genes. *Genome Biol.* **3**, RESEARCH0034 (2002).

**Acknowledgements** We thank the Institut Curie Animal facility for animal welfare and husbandry; the imaging facility PICTiBiSA@BDD for technical assistance; members of the E.H. laboratory for critical input; Y. Komarnitskaya for graphic design; and F. Ramirez and G. Richard for their help with bioinformatic analysis. This work was supported by FRM (FDM20140630223 and FDM40917) to N.R., ERC Advanced Grant DEVOCHROMO to P.F., by ERC Advanced Investigator Awards ERC-ADG-2014 671027 and Labellisation la Ligue, Labex DEEP: ANR-11-LBX-0044, IDEX PSL: ANR-10-IDEX-0001-02 PSL to E.H.

**Author contributions** N.R., T.N., P.F., K.A. and E.H. designed the experiments. N.R., T.N. and W.L. performed the single-cell HiC experiments. S.C., K.A. and N.S. designed and performed the single-cell HiC data analysis and integration. C.V. and T.S. produced the chromosome modelling data. N.R. and K.A. performed DNA FISH on preimplantation embryos. N.R. and T.P. performed structured illumination microscopy and image analysis. R.G. and K.A. engineered CRISPR deletions. M.B. set up single-cell dissociation and collected embryos with N.R. The manuscript was written by S.C., K.A. and E.H. with contributions from N.R., C.V. and P.F., and input from all authors.

**Competing interests** The authors declare no competing interests.

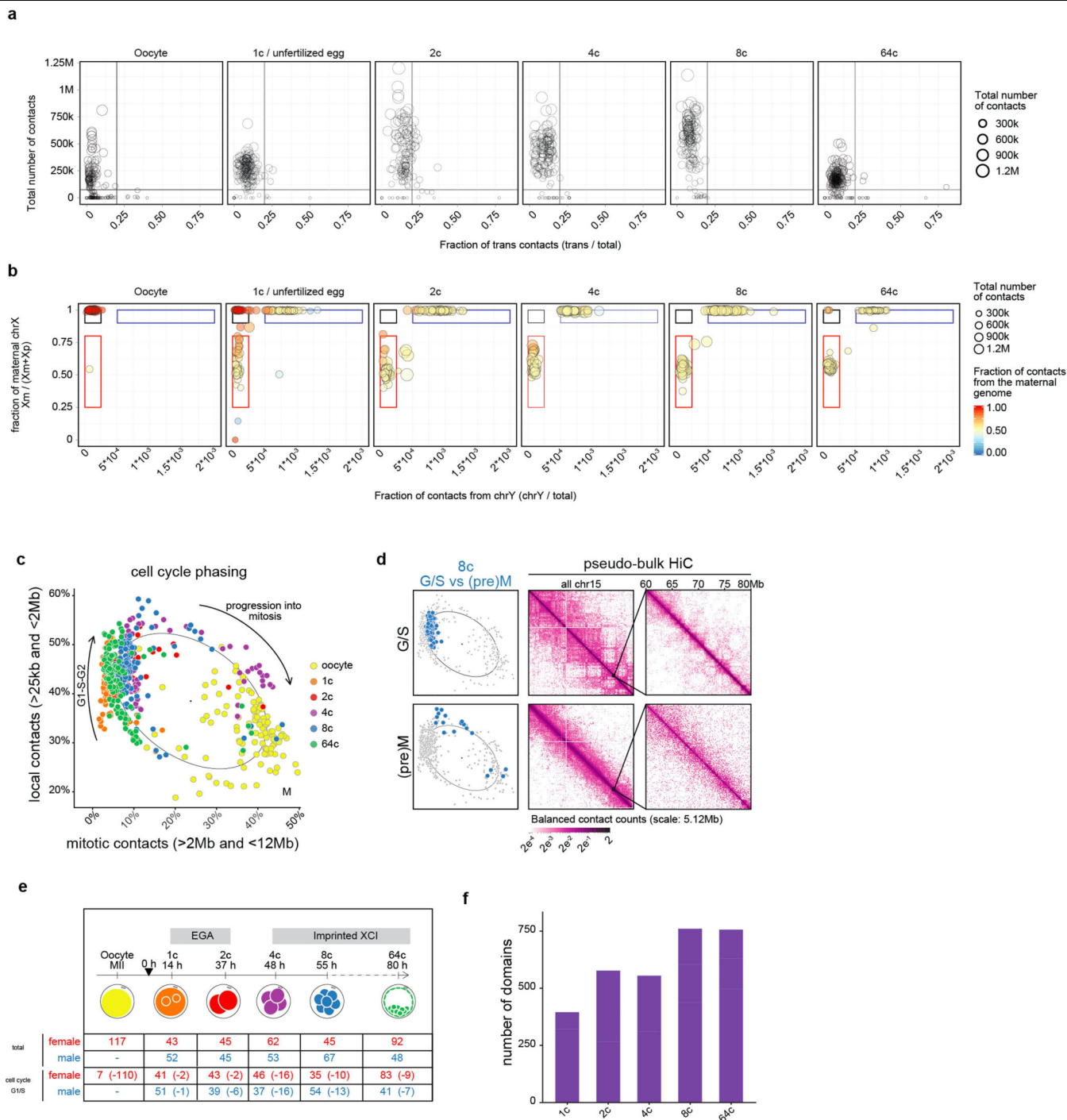
## Additional information

**Supplementary information** is available for this paper at <https://doi.org/10.1038/s41586-020-2125-z>.

**Correspondence and requests for materials** should be addressed to P.F., K.A. or E.H.

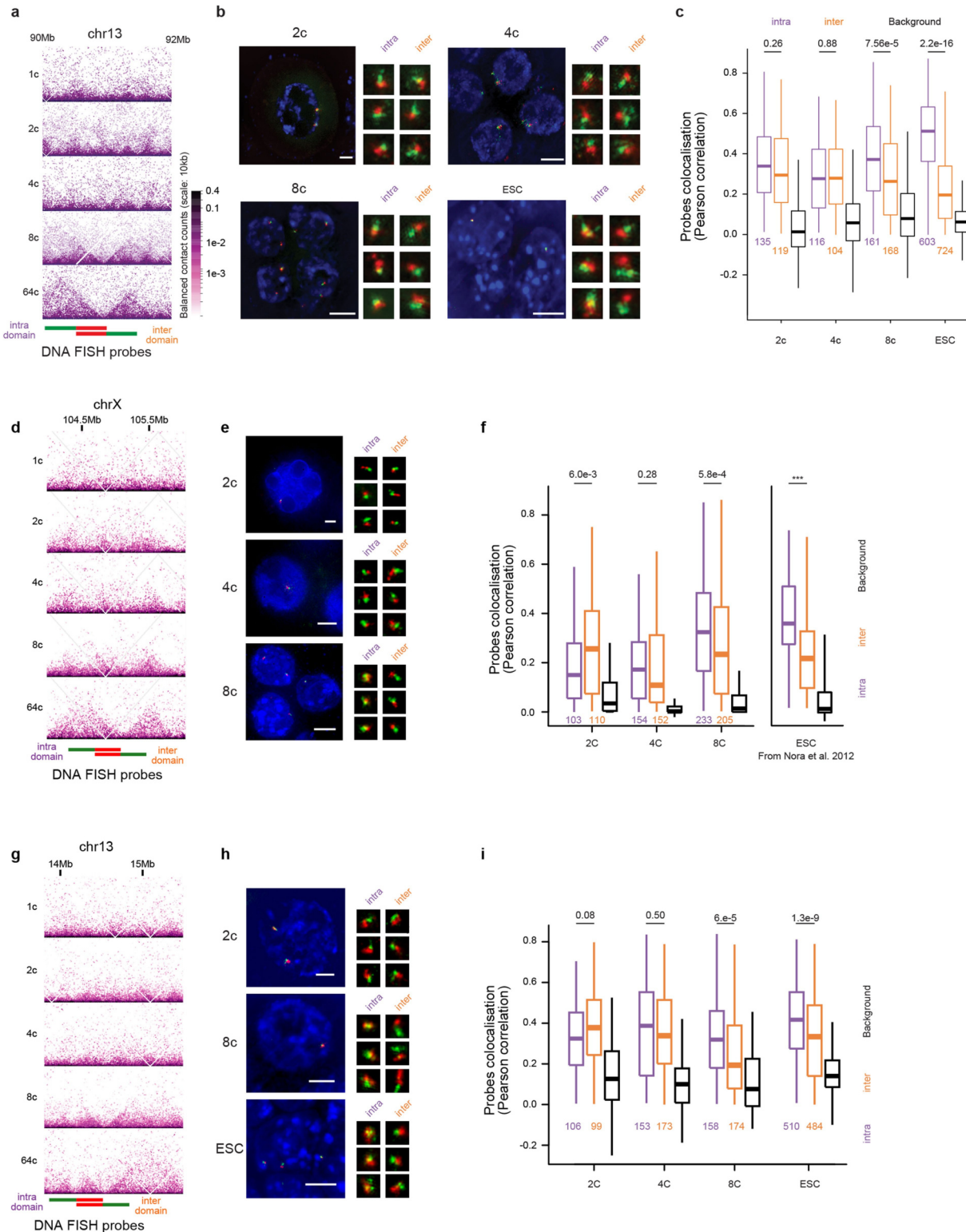
**Peer review information** Nature thanks Takashi Sato and the other, anonymous, reviewer(s) for their contribution to the peer review of this work.

**Reprints and permissions information** is available at <http://www.nature.com/reprints>.



**Extended Data Fig. 1 | Single-cell HiC approach to studying chromosome organization in mouse preimplantation embryos.** **a**, Distribution of total contact versus *trans* ratio per single blastomere, according to developmental stage with given thresholds for exclusion. **b**, Fraction of maternal contacts on the X chromosome versus contacts on the Y chromosome. The colour of each dot indicates the fraction of reads that cover the maternal genome. Red rectangles highlight female diploid cells, blue rectangles highlight male cells and black rectangles highlight haploid cells (that is, oocytes or polar bodies). Cells outside these frames were excluded. **c**, Percentage of short-range

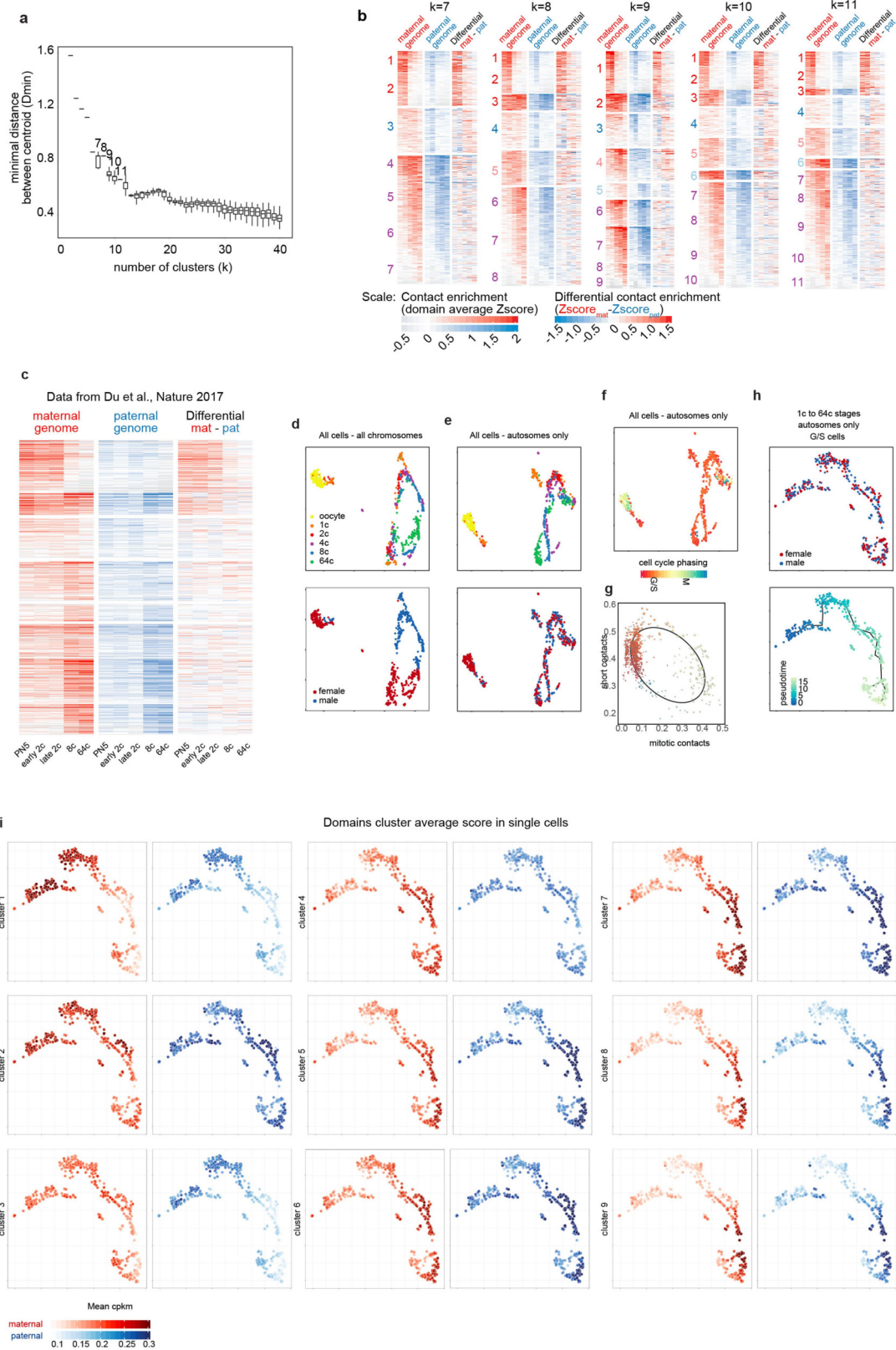
(25 kb–2 Mb) versus long-range or mitotic contacts (2–12 Mb) per single cell, coloured by developmental stages. **d**, Subset of the single cells at eight-cell stage, either in G1, S or G2 phase (top) or going towards mitosis (bottom), and their corresponding pseudo-bulk HiC heat maps. **e**, Table for the number of single blastomeres per stage of development that passed quality control, and the selected number after cell cycle phasing that were used to produce the subsequent analysis and heat maps. **f**, Bar plot of domain numbers for each developmental stage.



**Extended Data Fig. 2 | HiC view and DNA FISH for two independent genomic loci.** **a, d, g**, HiC contact maps for different genomic locations (as indicated), from the 1-cell to 64-cell stage. **b, c, e, f, h, i**, Analysis of the genomic locations for boundary formation (red and green probes in bottom of **a, d** and **g**) by 3D DNA FISH in two-cell-stage to eight-cell-stage embryos and embryonic stem cells (ESC), with insets of signal for the two independent pools (**b, e, h**). The total number of combined signals (red plus green) is reported in the box plot in the adjacent panels (**c, f, i**). DNA is stained by DAPI (blue). Scale bar, 10  $\mu$ m. **c,**

Box plot ( $\pm 1.5 \times$  interquartile range, 25th and 75th percentiles and median value) distribution of Pearson's correlation coefficient for red and green signals (in pools 1 and 2) of DNA FISH analysis. **a–c**, Chromosome 13 (region 90 Mb–92 Mb). **d–f**, X chromosome (region 104 Mb–105 Mb). **g–i**, Chromosome 13 (region 14 Mb–15 Mb). All experiments are performed in biological replicates,  $n$  is the combined signal number, centre lines denote the median coefficient. Statistical significance ( $P < 0.001$ ) was assessed using Wilcoxon's rank sum test (two-sided).

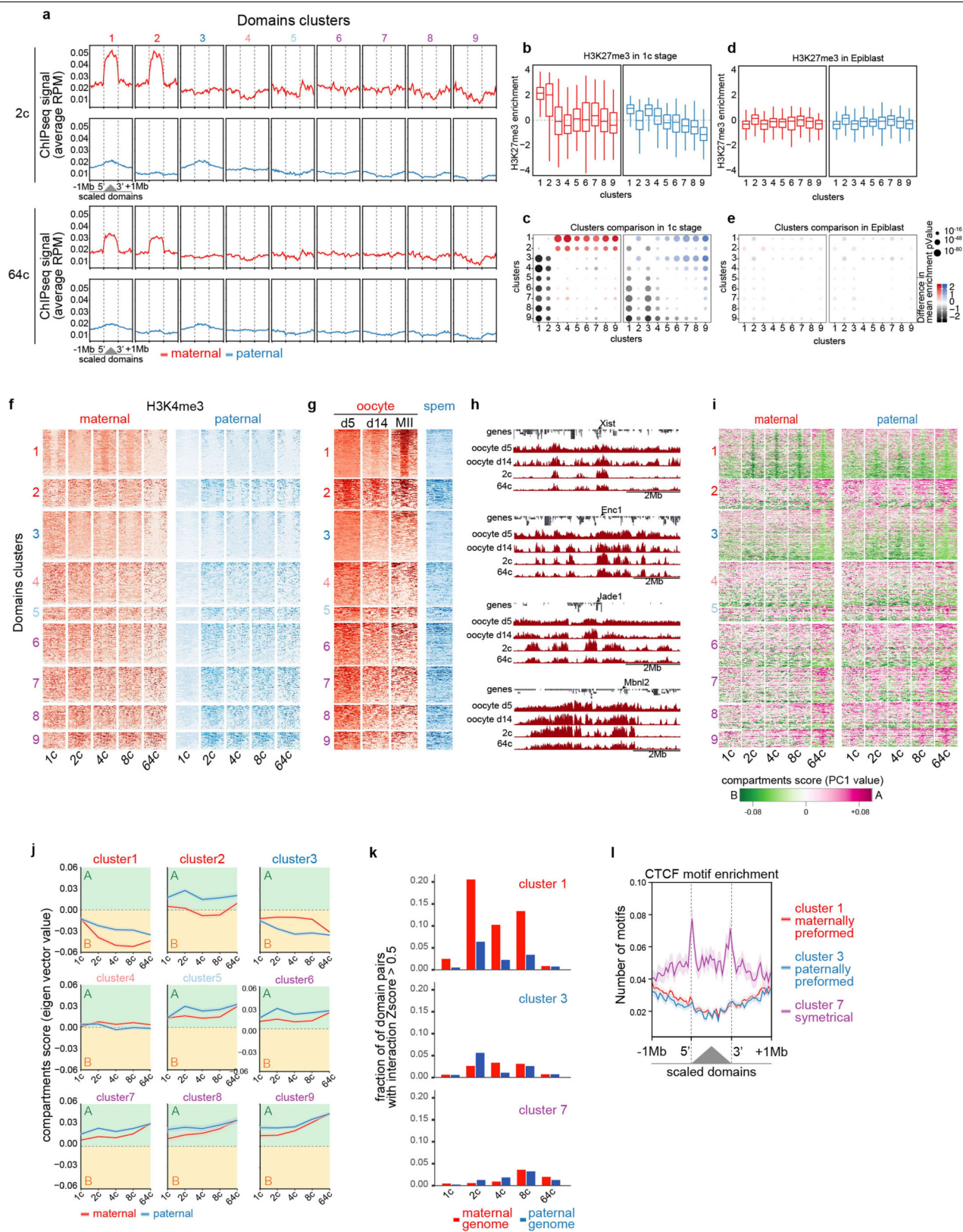




**Extended Data Fig. 3** | See next page for caption.

**Extended Data Fig. 3 | Dynamics of domains in single cells.** **a**, Distribution of the minimal distance between cluster centroids ( $D_{\min}$ ) for a predefined number of clusters ( $k$ ) ranging from 2 to 40. Clustering was performed 100 times for each value of  $k$ . The optimal number of clusters is the highest value of  $k$  before the value  $D_{\min}$  becomes stagnant. **b**, Heat maps representing the result of clustering for different values of  $k$ . The same main categories are found for  $k > 8$ . The contact enrichment colour scale corresponds to the maternal (red) and paternal (blue) heat maps; the differential contact enrichment scale corresponds to the differential (maternal – paternal) heat maps. **c**, Heat maps showing domain enrichment in the bulk HiC data from GSE82185, with the same order as our clustering in Fig. 1d and showing similar dynamics. **d**, Single-cell

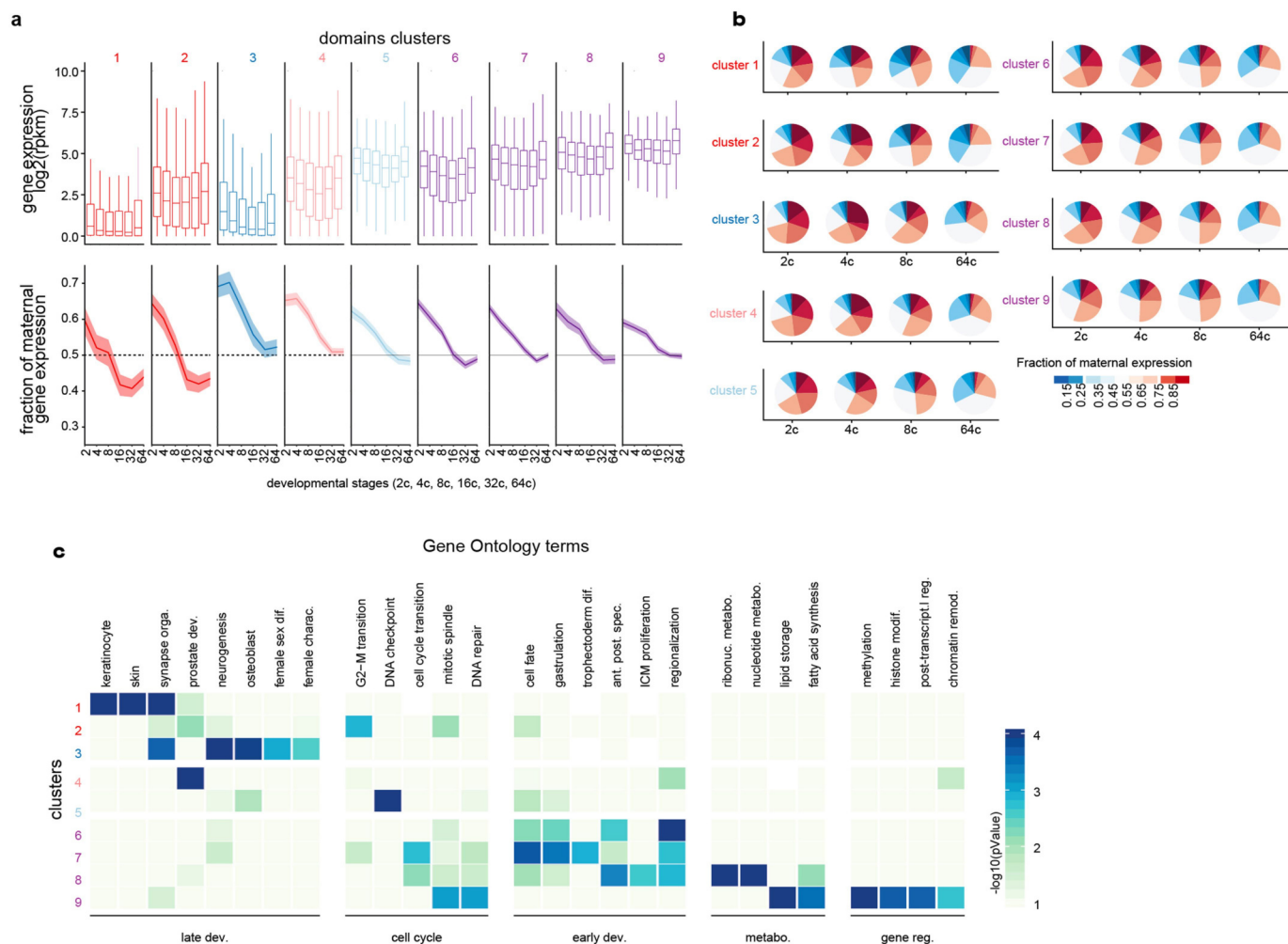
projection by UMAP from the quantification of domain contacts on each allele, using all cells and all chromosomes, coloured by stage (top) or by sex (bottom).  $n = 669$  single cells. **e**, As in **d** but excluding domains on the X chromosome. **f**, As in **e** but coloured by cell cycle phasing. **g**, Cell cycle phasing based on short-range versus mitotic contacts, with the same colour scale as in **f**. **h**, Single-cell projections after excluding oocytes, all cells in pre-M and M phase and domains on the X chromosome, as in Fig. 1f, coloured by sex (top) or by pseudotime overlaid with the inferred trajectory (bottom).  $n = 470$  single cells. **i**, As in **h**, coloured by mean count per kb per million (CPKM) on each allele, for the nine clusters identified in Fig. 1d.



**Extended Data Fig. 4** | See next page for caption.

**Extended Data Fig. 4 | Chromatin changes and compartment formation over preimplantation.** **a**, Average profile of H3K27me3 ChIP-seq signal at the domains for each parental allele at the 2-cell and 64-cell stages in clusters 1 to 9.  $n = 375, 238, 387, 338, 110, 327, 287, 194$  and  $141$  for each cluster from 1 to 9). **b**, Distributions of H3K27me3 domain enrichment per cluster, on the maternal (red) and paternal (blue) genomes at the one-cell stage. Box plots represent  $\pm 1.5 \times$  interquartile range, 25th and 75th percentile and median value.  $n$  values are the same as in **a**. **c**, Statistical comparison, two-by-two, between each distribution in **b**.  $P$  values are calculated using a Wilcoxon test (two-sided, not paired).  $n$  values are the same as in **a**. **d, e**, As in **b, c** for H3K27me3 ChIP-seq data from epiblasts. **f**, Heat maps of H3K4me3 ChIP-seq signal at domains of each

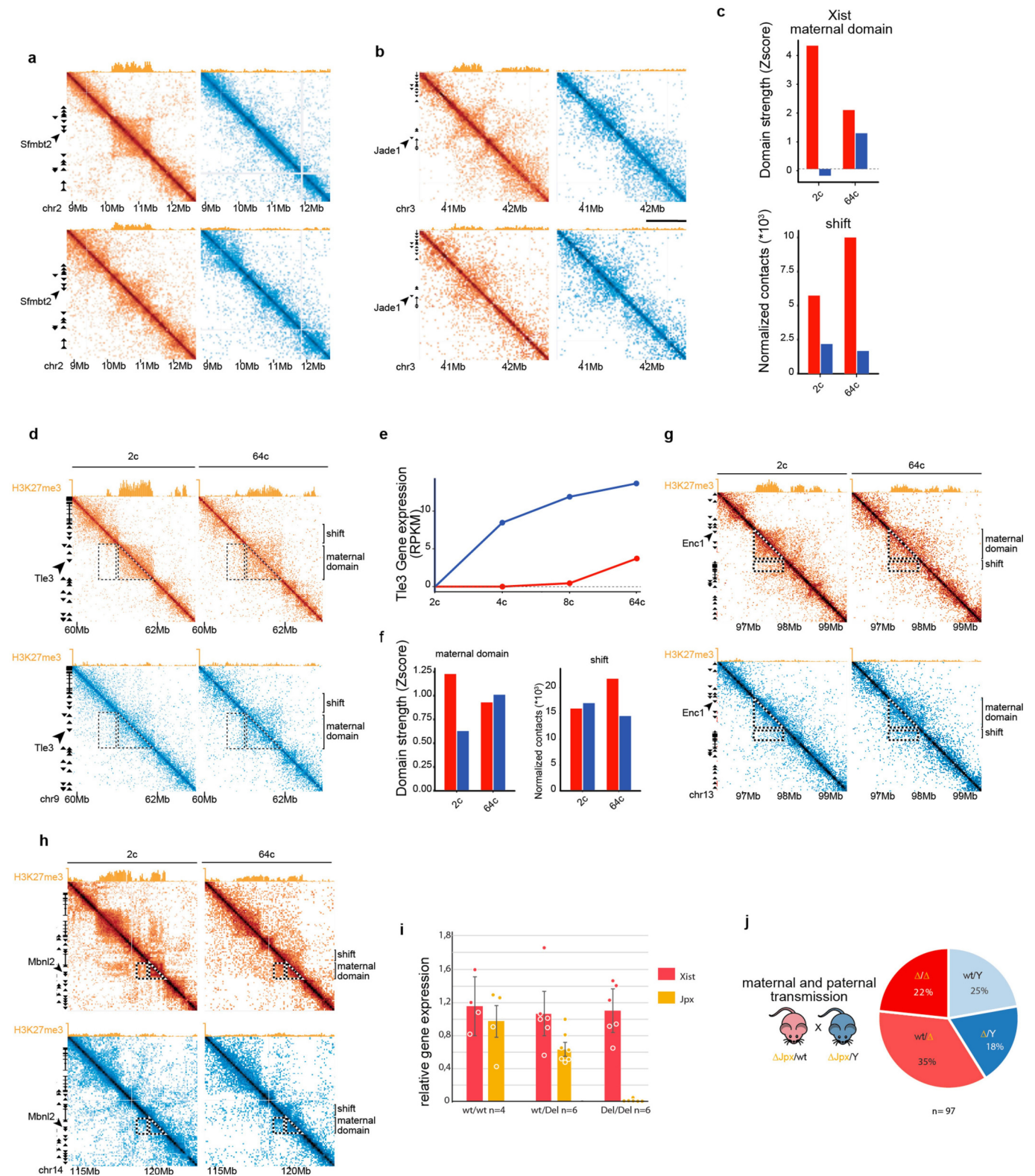
cluster  $\pm 1$  Mb, with parental origin. **g**, Heat maps of H3K27me3 ChIP-seq signal at domains of each cluster  $\pm 1$  Mb in oocytes (post-natal day 5 or day 14; or ovulatory oocytes (MII)). **h**, Snapshots of H3K27me3 ChIP-seq signal covering 6 Mb at transiently imprinted loci (*Xist*, *Enc1*, *Jade1* and *Mbnl2*) for different stages of oogenesis, or the maternal allele in the 2-cell and 64-cell stages. **i**, Compartment scores at domains of clusters 1–9, according to parental origin. **j**, Dynamics of the compartment scores for each cluster. Lines represent the mean, and shading represents the 95% confidence interval of the mean.  $n$  values are the same as in **a**. **k**, Bar plot of long-range interactions per stage, corresponding to the average heat map in Fig. 2f. **l**, CTCF-motif enrichment around domains.



**Extended Data Fig. 5 | Gene expression and functional annotation of domain clusters. a,** Distribution of gene expression (top;  $n = 797, 353, 612, 621, 268, 699, 562, 278$  and  $193$  genes for clusters 1 to 9) and fraction of maternal expression (maternal/(maternal + paternal), bottom;  $n = 232, 249, 256, 502, 258, 664, 497, 179$  and  $269$  genes for which an allelic ratio could be calculated for clusters 1 to

9, respectively) for genes present within domains of the different clusters. **b,** Pie charts for allelic expression bias from the 2-cell to the 64-cell stage for genes within clusters 1 to 9. **c,**  $P$  value (hypergeometric test) of Gene Ontology term enrichment in genes within each domain cluster.

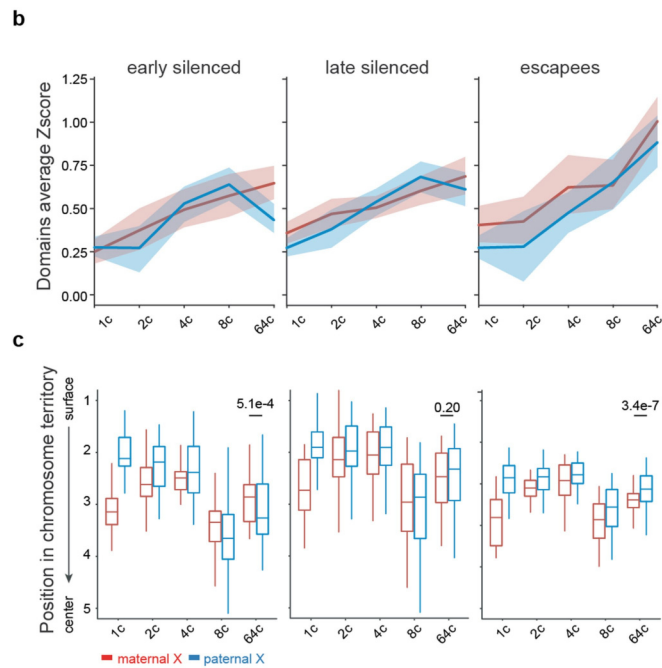
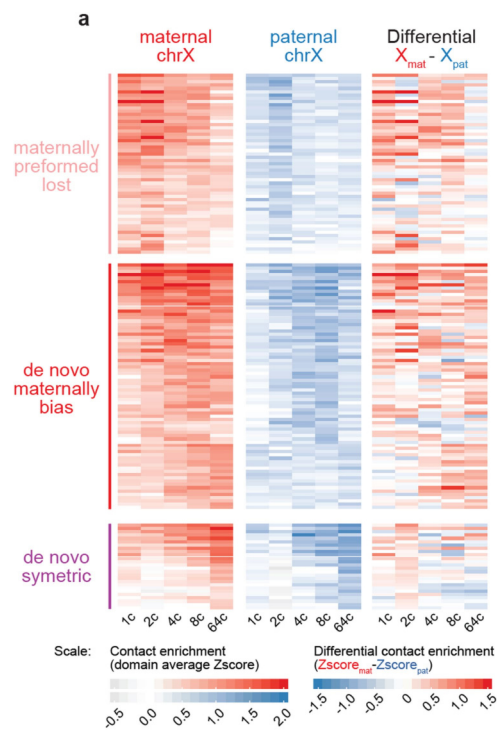




Extended Data Fig. 6 | See next page for caption.

**Extended Data Fig. 6 | Structural tuning at maternal early domains during preimplantation.** **a**, Snapshots of HiC matrices and H3K27me3 ChIP-seq signal, showing the parental differences between the 2-cell and 64-cell stages for maternal (red) and paternal (blue) genomes at chromosome 2 (9–13.5 Mb) containing *Sfmbt2*. **b**, As in **a**, for chromosome 3 (40–43 Mb) containing *Jade1*. **c**, Quantification of contacts within the region presented in Fig. 3b. **d**, Snapshot of HiC matrices and H3K27me3 ChIP-seq signal, showing the parental differences between the 2-cell and 64-cell stages for maternal (red) and paternal (blue) genomes at chromosome 9 (60–62.5 Mb) containing *Tle3*. **e**, Gene-expression dynamic for *Tle3* for maternal (red) and paternal (blue) alleles. **f**, Quantification of contacts within the region shown in **d**. **g**, Snapshots of HiC matrices and H3K27me3 ChIP-seq signal, showing the parental differences between the 2-cell and 64-cell stages for maternal (red) and

paternal (blue) genomes at chromosome 13 (96–100 Mb) containing *Enc1*. **h**, As in **g**, for chromosome 14 (115–122 Mb) containing *Mbnl2*. **i**, Relative gene expression for *Xist* (in red) or *Jpx* (in yellow) in mouse embryonic fibroblasts derived from embryos issued from crossing  $\Delta jpx$ /wild-type female mice with wild-type/Y or  $\Delta jpx$ /Y male mice. The three genotypes analysed are indicated, as well as the number of independently derived mouse embryonic fibroblast cultures from independent single embryos ( $n = 4, 6$  and  $6$  for wild-type/wild-type, wild-type/ $\Delta jpx$  and  $\Delta jpx/\Delta jpx$  genotypes, respectively). Bar plot represents the mean of each independent expression value (for each embryo), error bars represent the s.d. and each dot represents an individual embryo value. **j**, Pie chart distribution of the genotypes obtained after mating  $\Delta jpx$ /wild-type female mice with  $\Delta jpx$ /Y male mice.  $n = 104$  pups.



**Extended Data Fig. 7 | Analysis of X-linked gene position within the X chromosome as development progresses. a**, Clustering of X chromosome domain dynamics for contact enrichment (average Z-score). Domain number,  $n = 55, 75$  and  $26$  domains for each cluster. **b**, Structural changes. Lines represent the mean, and shading represents the 95% confidence interval of the

mean. **c**, Radial positions of X-linked genes, classified as early silenced, late-silenced and escapees as in a previous study<sup>20</sup>.  $n$  values are as in Fig. 4b. Box plot represents  $\pm 1.5 \times$  interquartile range, 25th and 75th percentiles and median value. Statistical difference was assessed using Wilcoxon's rank sum test (two-sided).

## Reporting Summary

Nature Research wishes to improve the reproducibility of the work that we publish. This form provides structure for consistency and transparency in reporting. For further information on Nature Research policies, see [Authors & Referees](#) and the [Editorial Policy Checklist](#).

### Statistics

For all statistical analyses, confirm that the following items are present in the figure legend, table legend, main text, or Methods section.

- | n/a                                 | Confirmed   |
|-------------------------------------|---|
| <input type="checkbox"/>            | <input checked="" type="checkbox"/> The exact sample size ( $n$ ) for each experimental group/condition, given as a discrete number and unit of measurement   |
| <input type="checkbox"/>            | <input checked="" type="checkbox"/> A statement on whether measurements were taken from distinct samples or whether the same sample was measured repeatedly   |
| <input type="checkbox"/>            | <input checked="" type="checkbox"/> The statistical test(s) used AND whether they are one- or two-sided<br><i>Only common tests should be described solely by name; describe more complex techniques in the Methods section.</i>  |
| <input checked="" type="checkbox"/> | <input type="checkbox"/> A description of all covariates tested   |
| <input checked="" type="checkbox"/> | <input type="checkbox"/> A description of any assumptions or corrections, such as tests of normality and adjustment for multiple comparisons  |
| <input checked="" type="checkbox"/> | <input type="checkbox"/> A full description of the statistical parameters including central tendency (e.g. means) or other basic estimates (e.g. regression coefficient) AND variation (e.g. standard deviation) or associated estimates of uncertainty (e.g. confidence intervals) |
| <input type="checkbox"/>            | <input checked="" type="checkbox"/> For null hypothesis testing, the test statistic (e.g. $F$ , $t$ , $r$ ) with confidence intervals, effect sizes, degrees of freedom and $P$ value noted<br><i>Give <math>P</math> values as exact values whenever suitable.</i>                 |
| <input checked="" type="checkbox"/> | <input type="checkbox"/> For Bayesian analysis, information on the choice of priors and Markov chain Monte Carlo settings   |
| <input checked="" type="checkbox"/> | <input type="checkbox"/> For hierarchical and complex designs, identification of the appropriate level for tests and full reporting of outcomes   |
| <input checked="" type="checkbox"/> | <input type="checkbox"/> Estimates of effect sizes (e.g. Cohen's $d$ , Pearson's $r$ ), indicating how they were calculated   |

Our web collection on [statistics for biologists](#) contains articles on many of the points above.

### Software and code

Policy information about [availability of computer code](#)

#### Data collection

Provide a description of all commercial, open source and custom code used to collect the data in this study, specifying the version used OR state that no software was used.

#### Data analysis

programs used:  
 R 3.4.2  
 Bioconductor 3.6  
 HiC-Pro 2.11.0  
 3dNetMod 1.0.10.06.17  
 HicExplorer 2.1.1  
 monocle 3  
 HiTC 1.26.0  
 Dip-C  
 Hickit  
 Trimalore 0.4.4  
 picard 2.18.2  
 DeepTools 3.0  
 Subread 1.28.1  
 DESeq2 1.18.1  
 Codes developed for this study are openly available on our github repository : <https://github.com/heard-lab>.

For manuscripts utilizing custom algorithms or software that are central to the research but not yet described in published literature, software must be made available to editors/reviewers. We strongly encourage code deposition in a community repository (e.g. GitHub). See the Nature Research [guidelines for submitting code & software](#) for further information.

## Data

Policy information about [availability of data](#)

All manuscripts must include a [data availability statement](#). This statement should provide the following information, where applicable:

- Accession codes, unique identifiers, or web links for publicly available datasets
- A list of figures that have associated raw data
- A description of any restrictions on data availability

All data generated in this study are available on GEO database under the number GSE129029

## Field-specific reporting

Please select the one below that is the best fit for your research. If you are not sure, read the appropriate sections before making your selection.

☒ Life sciences ☐ Behavioural & social sciences ☐ Ecological, evolutionary & environmental sciences

For a reference copy of the document with all sections, see [nature.com/documents/nr-reporting-summary-flat.pdf](https://www.nature.com/documents/nr-reporting-summary-flat.pdf)

## Life sciences study design

All studies must disclose on these points even when the disclosure is negative.

Sample size	Sample size was not predetermined. Embryos were collected at many different development stages from independent females. Number (of cell and / or embryos are indicated for each appropriate section. We used sample size commonly used and accepted for each type of experiments (DNA FISH and single cell HiC) to allow for basic statistical inference while using an justifiable number of mice.
Data exclusions	no data were excluded from the analysis except for some single cell HiC when genomic coverage was inappropriate (extra chromosomal content, only maternal content). We also removed single cell HiC data with insufficient coverage (see Materials and Methods as well as extended figure 1
Replication	experiments were repeated independantly n=3 or more
Randomization	No randomization was used as animals were utilized to produced embryos at specific developmental time. However samples were treated, to when possible in parallel, and were all analyzed in parallel
Blinding	No experimental blinding was used as embryos embryo was done at specific developmental time post mating of animals.

## Reporting for specific materials, systems and methods

We require information from authors about some types of materials, experimental systems and methods used in many studies. Here, indicate whether each material, system or method listed is relevant to your study. If you are not sure if a list item applies to your research, read the appropriate section before selecting a response.

### Materials & experimental systems

n/a	Involved in the study
<input checked="" type="checkbox"/>	<input type="checkbox"/> Antibodies
<input type="checkbox"/>	<input checked="" type="checkbox"/> Eukaryotic cell lines
<input checked="" type="checkbox"/>	<input type="checkbox"/> Palaeontology
<input type="checkbox"/>	<input checked="" type="checkbox"/> Animals and other organisms
<input checked="" type="checkbox"/>	<input type="checkbox"/> Human research participants
<input checked="" type="checkbox"/>	<input type="checkbox"/> Clinical data

### Methods

n/a	Involved in the study
<input checked="" type="checkbox"/>	<input type="checkbox"/> ChIP-seq
<input checked="" type="checkbox"/>	<input type="checkbox"/> Flow cytometry
<input checked="" type="checkbox"/>	<input type="checkbox"/> MRI-based neuroimaging



## Eukaryotic cell lines

Policy information about [cell lines](#)

Cell line source(s)	mouse embryonic stem cells mESCs E14 were used in this study as control (GSM1366337)
Authentication	as the cells used in this study have been recurrently used by the authors in previous studies they have not been authenticates
Mycoplasma contamination	ESCs were tested negative for mycoplasma
Commonly misidentified lines (See <a href="#">ICLAC</a> register)	cells used are not in the ICLAC database

## Animals and other organisms

Policy information about [studies involving animals](#); [ARRIVE guidelines](#) recommended for reporting animal research

Laboratory animals	We used adult animals (from 6 weeks to 3 months for females, and 8 weeks to 1 year for males) for producing preimplantation embryos (first 4 days post mating). C57Bl/6J females (purchased from Charles river) were mated onto CASTeJ/J males (purchase from Jackson Laboratory) for the HiC data and B6D2F1 females were mated onto B6D2F1 males for DNA FISH data. For CRISPRCas9 engineered animals we used B6D2F1 donor embryos transferred into pseudopregnat OF1 females. After founder identification the line was backcross on B6D2F1 animals
Wild animals	this study does not contain any wild animals
Field-collected samples	this study does not contain animals collected from the fields.
Ethics oversight	Animal care and use for this study were performed in accordance with the recommendations of the European community (2010/63/UE). All experimental protocols were approved by the ethics committee of Institut Curie CEEA-IC118 under the number APAFIS#8812-2017020611033784v2 given by national authority in compliance with the international guidelines.

Note that full information on the approval of the study protocol must also be provided in the manuscript.


# U1 snRNP regulates chromatin retention of noncoding RNAs

<https://doi.org/10.1038/s41586-020-2105-3>

Received: 26 November 2018

Accepted: 9 January 2020

Published online: 11 March 2020

 Check for updates

Yafei Yin<sup>1</sup>✉, J. Yuyang Lu<sup>1</sup>, Xuechun Zhang<sup>1</sup>, Wen Shao<sup>1</sup>, Yanhui Xu<sup>1</sup>, Pan Li<sup>1,2</sup>, Yantao Hong<sup>1</sup>, Li Cui<sup>1</sup>, Ge Shan<sup>3</sup>, Bin Tian<sup>4</sup>, Qiangfeng Cliff Zhang<sup>1,2</sup> & Xiaohua Shen<sup>1</sup>✉

Long noncoding RNAs (lncRNAs) and promoter- or enhancer-associated unstable transcripts locate preferentially to chromatin, where some regulate chromatin structure, transcription and RNA processing<sup>1–13</sup>. Although several RNA sequences responsible for nuclear localization have been identified—such as repeats in the lncRNA *Xist* and Alu-like elements in long RNAs<sup>14–16</sup>—how lncRNAs as a class are enriched at chromatin remains unknown. Here we describe a random, mutagenesis-coupled, high-throughput method that we name ‘RNA elements for subcellular localization by sequencing’ (mutREL-seq). Using this method, we discovered an RNA motif that recognizes the U1 small nuclear ribonucleoprotein (snRNP) and is essential for the localization of reporter RNAs to chromatin. Across the genome, chromatin-bound lncRNAs are enriched with 5′ splice sites and depleted of 3′ splice sites, and exhibit high levels of U1 snRNA binding compared with cytoplasm-localized messenger RNAs. Acute depletion of U1 snRNA or of the U1 snRNP protein component SNRNP70 markedly reduces the chromatin association of hundreds of lncRNAs and unstable transcripts, without altering the overall transcription rate in cells. In addition, rapid degradation of SNRNP70 reduces the localization of both nascent and polyadenylated lncRNA transcripts to chromatin, and disrupts the nuclear and genome-wide localization of the lncRNA *Malat1*. Moreover, U1 snRNP interacts with transcriptionally engaged RNA polymerase II. These results show that U1 snRNP acts widely to tether and mobilize lncRNAs to chromatin in a transcription-dependent manner. Our findings have uncovered a previously unknown role of U1 snRNP beyond the processing of precursor mRNA, and provide molecular insight into how lncRNAs are recruited to regulatory sites to carry out chromatin-associated functions.

To identify *cis* elements that contribute to the localization of RNA to chromatin, we developed and performed REL-seq screens with saturated fragment coverage of nine representative lncRNA and mRNA transcripts in mouse and human cells (Extended Data Fig. 1a–f and Supplementary Note 1). The strategy involves expressing a randomly fragmented RNA sequence alone or fusing it with a minigene encoding green fluorescent protein (GFP), and then analysing its subcellular location through sequencing. We detected a total of 26 chromatin-enriched RNA fragments (enChrs;  $P < 0.05$ ), mainly 50–500 nucleotides in length, in the sense orientation of the host chromatin-associated RNAs but not in cytoplasm-located mRNAs (Extended Data Fig. 2 and Supplementary Tables 1, 2). To uncover key residues that contribute to RNA localization, we chose a 162-nucleotide *NXFI*-enChr, identified from an isoform of *NXFI* in which the introns are retained in the final mRNA, for random mutagenesis followed by REL-seq (mutREL-seq; Extended Data Figs. 1b, 2g). Out of 23 mutations with impaired chromatin binding, 19 are located in a loop region (positions 39–45) containing 7 nucleotides, which, together with 2 upstream nucleotides, comprise a U1-recognition site that base pairs perfectly with the 9-nucleotide 5′ targeting sequence of U1 snRNA (Fig. 1a, b, Extended

Data Fig. 1g–j and Supplementary Note 2). The majority of enChrs overlap with predicted U1-recognition sites and/or exhibit strong binding signals of U1 snRNA, as shown by RNA affinity purification followed by RNA sequencing (RAP-RNA-seq)<sup>17</sup>, except for repeat-associated enChrs in *Xist* (Extended Data Figs. 1k, 2, Supplementary Table 2 and Supplementary Discussion 1).

U1 snRNP defines the 5′ splice sites of pre-mRNAs and initiates spliceosome assembly at introns—a process that involves sequential recruitments of U1, U2 and then U4/U6–U5 tri-snRNPs<sup>18</sup>. It has been reported that the 5′ splice site regulates the nuclear retention of a handful of mRNAs<sup>19,20</sup>. To test a role of U1 recognition in RNA–chromatin retention, we constructed GFP reporters that harbour U1 motifs but lack the 3′ splice site, in vectors containing either a polyadenylation signal (PAS) or a *Malat1* 3′-end sequence (Extended Data Fig. 3a, b). The *Malat1* 3′-end sequence stabilizes GFP RNA through a triple-helix RNA structure<sup>21,22</sup>, thus bypassing the inhibitory effect of U1 snRNP on polyadenylation and RNA stability<sup>23</sup>. The wild-type but not mutant U1-targeting sequences promoted the chromatin association of GFP in both the PAS and the 3′ *Malat1* reporters (Extended Data Fig. 3c–g and Supplementary Note 3). In addition, *NXFI*-enChr RNA captured core

<sup>1</sup>Tsinghua-Peking Joint Center for Life Sciences, School of Medicine and School of Life Sciences, Tsinghua University, Beijing, China. <sup>2</sup>Beijing Advanced Innovation Center for Structural Biology, Tsinghua University, Beijing, China. <sup>3</sup>School of Life Sciences, University of Science and Technology of China, Hefei, Anhui Province, China. <sup>4</sup>Department of Microbiology, Biochemistry and Molecular Genetics, Rutgers New Jersey Medical School and Rutgers Cancer Institute of New Jersey, Newark, NJ, USA. ✉e-mail: yafei@tsinghua.edu.cn; xshen@tsinghua.edu.cn

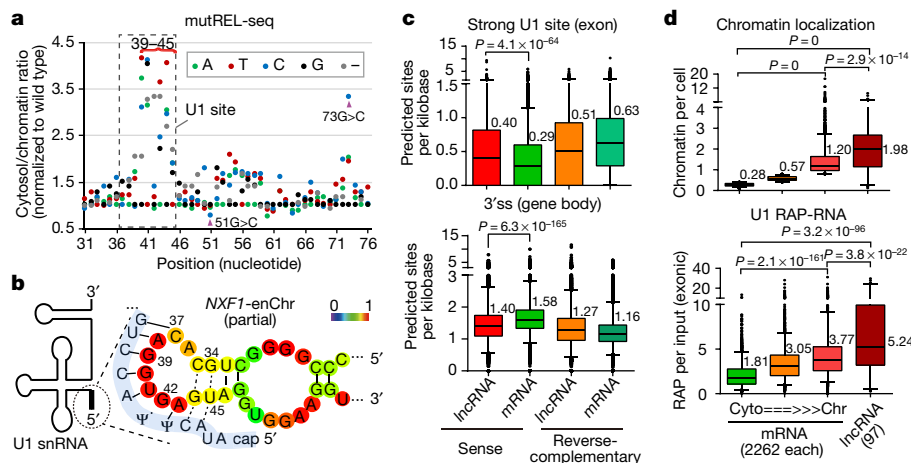


**Fig. 1 | MutREL-seq identifies a U1-recognition site that contributes to RNA-chromatin tethering.** **a**, MutREL-seq identifies a seven-nucleotide region (dashed box) that contributes to chromatin retention of *NXF1*-enChr. The y-axis shows the fold change of cytoplasmic versus chromatin signals, normalized to that in wild-type cells. Grey dots indicate deletions. **b**, Predicted secondary structure of *NXF1*-enChr and its interaction with U1 snRNA.  $\Psi$ : G wobble base-pairing is indicated by dots. The scale bar shows the probability of base-pairing (or lack of pairing). **c**, Densities of predicted strong U1-recognition sites in exons (top) and 3' splice sites (3'ss) in the gene body

(bottom) of lncRNAs (U1 site:  $n = 3,385$ ; 3'ss:  $n = 7,661$ ) and mRNAs (U1 site:  $n = 47,298$ ; 3'ss:  $n = 78,227$ ) in mice. Genes with transcript length (for U1 sites) or genomic length (for 3'ss) of more than 1 kilobase (kb) were analysed. **d**, Enrichment in chromatin localization (top) and U1 RAP-RNA signals (bottom) in mRNAs ( $n = 2,262$  genes in each group) and lncRNAs ( $n = 97$ ; fragments per kilobase per million mapped reads (FPKM) of more than 1; no overlap with mRNA) that are ranked from low to high levels of chromatin association (left to right). For **c** and **d**, box plots show 5th, 25th, 50th, 75th and 95th percentiles, with median values labelled.  $P$ -values, two-sided  $t$ -tests.

components of U1 snRNP, whose knockdown impaired the chromatin binding of reporter RNA (Extended Data Fig. 3h–m, Supplementary Table 3 and Supplementary Note 4). To test a role of the 3' splice site in RNA localization, we inserted an *ACTB* intron into a *GFP* reporter. Mutation of the 3' splice site dramatically increased chromatin-bound *GFP* RNA, in a manner dependent on an intact 5' U1 site (Extended Data Fig. 3n). These results demonstrate that U1 snRNP promotes the chromatin association of a reporter RNA that harbours a 5' U1-recognition site but lacks the 3' splice sequence.

Although U1 motifs tend to be depleted in gene exons, lncRNA transcripts exhibit substantially higher densities of the U1-recognition motif in exons, yet lower densities of 3' splice sites in the gene body, compared with mRNA (Fig. 1c and Extended Data Fig. 4a–d). In addition, the densities of predicted U1-recognition sites and levels of U1 snRNA binding increase gradually from the most cytoplasm-enriched mRNA to chromatin-enriched mRNA and then to lncRNAs, whereas their expression decreases with increased chromatin association (Fig. 1d and Extended Data Fig. 4e, f).

The global enrichment of U1 snRNA recognition sites and binding on lncRNAs led us to explore their role in the localization of lncRNAs to chromatin. We used antisense morpholino oligonucleotides (AMOs) to block the 5'-end-recognition sequence of U1 snRNA. Given the broad involvement of U1 snRNP in cellular functions, we performed a short-term, 2-h treatment with U1 AMOs in mouse embryonic stem cells (mESCs). This attenuated splicing—unlike prolonged treatment—did not elicit apoptosis (Extended Data Fig. 5a–d and Methods). We then performed strand-specific sequencing of total RNAs isolated from chromatin, nucleoplasm and cytoplasm fractions, and calculated relative enrichments in each compartment. Among 1,282 lncRNAs with detectable expression in mESCs, only 4 were upregulated on chromatin, whereas 337 (26.3%;  $P < 0.05$ ) showed decreased chromatin associations yet increased cytoplasm or nucleoplasm signals (Fig. 2a, b, Extended Data Figs. 5e, f, 6 and Supplementary Table 4).

To reveal immediate effects in an inducible way, we sought to deplete the U1 snRNP component SNRNP70 by using an auxin-inducible degron (AID) system (SNRNP70<sup>AID</sup>) in mESCs (Methods). Four-hour treatment with auxin led to a 90% depletion of SNRNP70 protein, which impaired the binding of U1 snRNA to its targeted lncRNAs, and attenuated splicing, but

had a minor effect on the expression of the lncRNAs analysed, and did not elicit apoptosis (Extended Data Fig. 5g–k). Consistently, total RNA-seq of auxin-treated SNRNP70<sup>AID</sup> mESCs revealed 346 chromatin-downregulated lncRNAs (27%;  $P < 0.05$ ), which substantially overlap with those affected by U1 AMOs and show increased signals in the cytoplasm and/or nucleoplasm fractions (Fig. 2, Extended Data Figs. 5f, l, m, 6 and Supplementary Table 5). The sets of chromatin-downregulated lncRNAs following U1 AMO and/or SNRNP70<sup>AID</sup> treatment exhibit stronger U1 snRNA binding activities and higher expression levels compared with lncRNAs that are not downregulated, providing evidence that U1 snRNP promotes chromatin association of its target lncRNAs (Extended Data Fig. 5n).

We then investigated whether the U1 mechanism regulates the localization of mature transcripts after a lncRNA is made. Sequencing of polyadenylated RNA (polyA-seq) revealed that degradation of SNRNP70<sup>AID</sup> led to roughly 23.6% of lncRNAs (295;  $P < 0.05$ ) being downregulated on chromatin, which correlated significantly ( $R = 0.49$ ,  $P = 5.0 \times 10^{-19}$ ) with the change in total RNA-seq (Fig. 2a, b, Extended Data Figs. 6, 7a–c and Supplementary Table 6). To investigate whether newly synthesized polyA RNA shows similar changes, we pulse-labelled SNRNP70<sup>AID</sup> mESCs with 4-thiol-uridine (4sU) and performed thiol-linked alkylation for metabolic sequencing (SLAM-seq<sup>24</sup>). Chemical conversion of the newly incorporated 4sU into cytidine discriminates new transcripts from pre-existing transcripts (Extended Data Fig. 7d, e). Among 492 polyA lncRNAs with new transcripts detectable by SLAM-seq, 115 (23.4%) were downregulated on chromatin in auxin-treated mESCs, while only 3 were upregulated (Fig. 2c and Supplementary Table 7). New transcripts and all transcripts (new plus pre-existing) show highly correlated changes ( $R = 0.81$ ,  $P = 4.1 \times 10^{-117}$ ) upon SNRNP70<sup>AID</sup> degradation (Extended Data Fig. 7f). Notably, both well spliced lncRNAs (for example, *Meg3* and *Rian*) and poorly spliced lncRNAs (such as *Lncenc1*, *Tsix* and *Pvt1*) show decreased chromatin binding after U1 inhibition (Extended Data Fig. 6). These findings rule out a kinetic effect due to delayed release of nascent or unspliced RNAs from their transcription sites that contributes mainly to chromatin retention.

Chromatin-downregulated lncRNAs with slightly longer transcript length exhibit similar distributions of total RNA signals across the gene body before and after U1 inhibition, and do not show higher decreases in expression compared with lncRNAs that are not downregulated (Extended Data Figs. 5n, 7g, h), arguing against globally premature

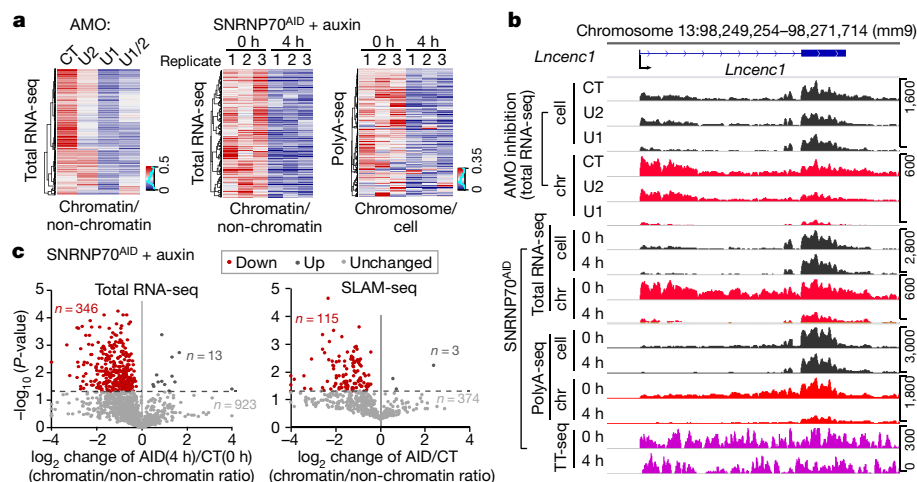


**Fig. 2 | U1 snRNP regulates lncRNA-chromatin retention.** **a**, Heat maps showing, left, the chromatin/non-chromatin ratio (where ‘non-chromatin’ refers to cytoplasm plus nucleoplasm) of 337 chromatin-downregulated lncRNAs in total RNA-seq upon AMO treatment; and right, the chromatin/non-chromatin ratio of 346 chromatin-downregulated lncRNAs in total RNA-seq and the chromatin/cell ratio (where ‘cell’ refers to the whole cell) in polyA-seq upon SNRNP70<sup>AID</sup> degradation. See also Extended Data Fig. 5f. CT, no auxin. **b**, A genome-browser view of the *Lncenc1* locus; see also Extended Data Fig. 6g. In this panel, mm9 is a mouse

genome assembly. The top two sets of tracks show the total RNA-seq of whole-cell and chromatin fractions after treatments with control (CT), U2 or U1 AMOs. The lower three sets of tracks show total and polyA RNA-seq of whole-cell and chromatin fractions and TT-seq in SNRNP70<sup>AID</sup> mESCs at 0 h or 4 h of auxin treatment. **c**, Volcano plots showing fold changes ( $\log_2$ ) of the chromatin/non-chromatin ratio of 1,282 lncRNAs identified by total RNA-seq or of 492 newly synthesized lncRNAs identified by SLAM-seq upon SNRNP70<sup>AID</sup> depletion. AID, plus auxin. *P*-values were obtained by two-sided *t*-test for three biological replicates.

termination<sup>25</sup>. To further assess potential transcriptional changes, we performed transient transcriptome sequencing of nascent transcripts (TT-seq) and RNA polymerase II (Pol II) chromatin immunoprecipitation followed by sequencing (ChIP-seq). Acute degradation of SNRNP70<sup>AID</sup> did not alter the overall transcription rate and the distribution of paused and elongating Pol II across the genome (Extended Data Fig. 7i–k). Moreover, depletion of *EXOSC3*—an essential subunit of the RNA exosome—failed to rescue the observed decreases of chromatin-bound lncRNAs in SNRNP70<sup>AID</sup> mESCs (Extended Data Fig. 7l). These combined analyses elucidate a direct effect of U1 snRNP in tethering both nascent and polyadenylated lncRNAs to chromatin, excluding the possibility that there are indirect consequences due to changes in transcription dynamics, RNA processing and decay on lncRNA–chromatin associations under our assay conditions of inhibiting U1 snRNP for short periods of time.

We detected substantial amounts of SNRNP70 and SNRPC on chromatin, and this association was sensitive to high-salt extraction (Extended Data Fig. 8a). Mass-spectrometry analysis of the SNRNP70 complexes identified proteins involved in transcription regulation, such as the Pol II large subunit POLR2A and elongation factors SPT5 and SPT6, besides splicing factors (Extended Data Fig. 8b, c and Supplementary Table 8). Using native chromatin extracts that were released by the nuclease benzonase—which degrades RNA and DNA—we confirmed that SNRNP70 captured phosphorylated Pol II (S2P, phosphorylated at serine 2) and SPT6 in wild-type but not auxin-treated SNRNP70<sup>AID</sup> mESCs (Extended Data Fig. 8d). Reciprocal co-immunoprecipitation of phosphorylated Pol II (SSP and S2P), but not hypophosphorylated Pol II (8WG16), captured SNRNP70 and SNRPC (Fig. 3a). Thus, U1 snRNP binds transcriptionally engaged Pol II on chromatin, in a manner that is likely to be independent of RNA and DNA. Treatment of mESCs with the transcription inhibitors flavopiridol or triptolide reduced levels of chromatin-bound SNRNP70 and SNRPC proteins and also U1 snRNA (Fig. 3b and Extended Data Fig. 8a, e–g), consistent with a previous report of disrupted enrichment of U1 snRNA in the gene body of active genes by flavopiridol<sup>17</sup> (Supplementary Discussion 2). Inhibition of transcription also led to reduced chromatin associations of analysed lncRNAs (Fig. 3b and Extended Data Fig. 8e). These results suggest a central role of the active Pol II machinery in promoting the chromatin association of U1 snRNP and its target lncRNAs.

We then investigated whether other spliceosome components might contribute to lncRNA–chromatin retention. Treatment of mESCs with the drug E7107, which specifically targets the U2 snRNP<sup>26</sup>, also attenuated chromatin associations of analysed lncRNAs (Fig. 3b and Extended Data Fig. 8e). By contrast, inhibiting the recruitment of the U4/U6–U5 tri-snRNPs to the catalytically active spliceosome by using the drug isoginkgetin<sup>27</sup> or by depletion of the tri-snRNP components PRPF8 or SNRNP200 failed to have an effect (Fig. 3b and Extended Data Fig. 8e, h). We further inactivated U2 or both U1 and U2 (U1/2) snRNAs with AMOs. Inhibition of U2 snRNA alone had a much subtler effect, altering the localization of a subset of chromatin-bound lncRNAs, and inhibition of both U1/2 snRNAs did not result in a stronger effect than did inhibition of U1 snRNA alone (Fig. 2a, b and Extended Data Figs. 5a–f, 6). We posit that precatalytic recognition by U1 snRNP, and to a lesser degree by U2 snRNP, but not splicing per se primarily controls lncRNA–chromatin retention. Notably, for promoter-associated upstream antisense (ua) RNAs and enhancer (e)RNAs<sup>2–5</sup>, inhibition of U2 snRNA as well as U1 snRNP also led to decreased chromatin but increased cytosolic signals (Extended Data Fig. 9).

Lastly, to reveal the biological significance of U1 mechanism, we focused on *Malat1*, which binds to thousands of genomic sites to regulate transcription, pre-mRNA splicing and nuclear architecture<sup>17,28</sup>. Mature transcripts of *Malat1* are neither spliced nor polyadenylated, providing an ideal example to reveal how U1 snRNP affects its chromatin localization, independently of splicing and PAS-mediated RNA decay<sup>21–23</sup>. U1 snRNA binds extensively to *Malat1* RNA, although it is not spliced, and inhibition of U1 snRNP led to decreased levels of *Malat1* on chromatin without severely altering its expression (Extended Data Figs. 2c, 5b and 6a). We performed *Malat1* chromatin isolation by RNA purification and sequencing (ChIRP-seq) and RNA fluorescence in situ hybridization (FISH). Rapid degradation of SNRNP70<sup>AID</sup> caused drastically reduced *Malat1* binding at active genes across the genome, and abolished the punctate, speckle-like staining pattern of *Malat1*, whereas the localization of SC35 protein—a marker of nuclear speckles—was not affected (Fig. 3c, d and Extended Data Fig. 10a–e). Moreover, treatment with triptolide also abolished *Malat1* binding to its own and other genomic sites (Extended Data Fig. 10d), implying a Pol II transcription-dependent retargeting of *Malat1* to chromatin.



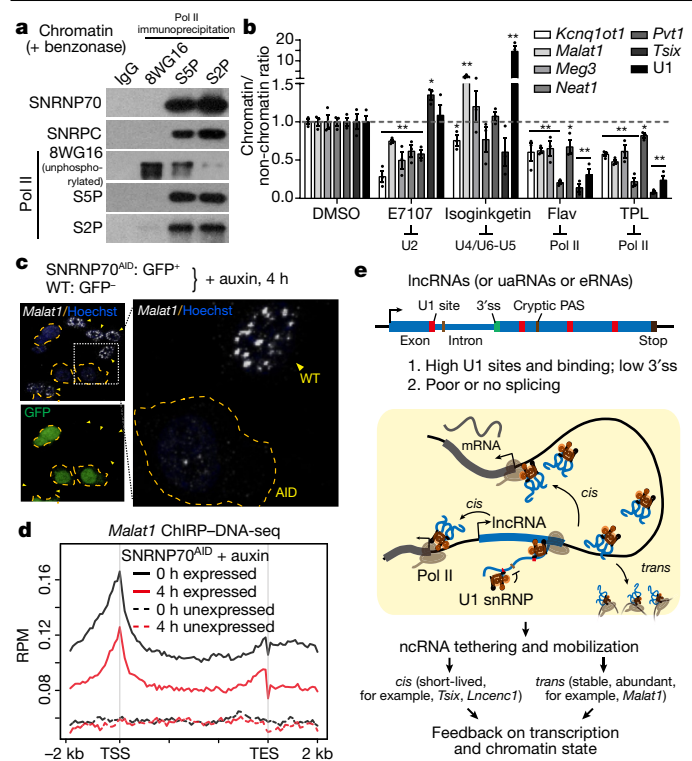


**Fig. 3 | U1 tethers and mobilizes lncRNAs to chromatin by interacting with transcriptionally engaged Pol II.** **a**, Co-immunoprecipitation and western blot analysis of chromatin fractions released by benzonase;  $n = 3$  independent experiments. **b**, Relative chromatin/non-chromatin ratios of representative lncRNAs and U1 snRNA in various treatments. DMSO, dimethylsulfoxide (vehicle); Flav, flavopiridol; TPL, triptolide. Data are mean  $\pm$  s.e.m.  $P$ -values were obtained by two-sided  $t$ -test for three biological replicates.  $^*P < 0.05$ ,  $^{**}P < 0.01$ . **c**, FISH of *Malat1* RNA. SNRNP70<sup>AID</sup> mESCs (GFP<sup>+</sup>, dashed circles) and wild-type mESCs (WT; GFP<sup>-</sup>, arrows) were mixed and treated with auxin for 4 h. A zoomed-in view of the boxed region is shown on the right. Hoechst staining indicates DNA.  $n = 3$  independent experiments; the statistical summary is shown in Extended Data Fig. 10c. **d**, Meta-analysis of *Malat1* ChIRP-DNA-seq signals across the gene body of 10,675 expressed and 7,933 unexpressed genes. TSS, transcriptional start site. **e**, U1 snRNP mobilizes lncRNAs to chromatin during their synthesis and function. Top, after an lncRNA (or uaRNA or eRNA) is synthesized, it binds persistently to U1 snRNP owing to an imbalanced distribution of 5' and 3' splice sites. Bottom, this provides a way to mobilize lncRNA transcripts to nearby gene or regulatory sites within their chromatin neighbourhoods (for many cis-regulatory lncRNAs) or to distal chromatin regions (as exemplified by the lncRNA *Malat1*). Retargeting of lncRNAs by U1 snRNP to cis and/or trans genomic sites may be achieved in part through their interactions with engaged Pol II. Consequently, chromatin-bound lncRNAs may function as an RNA glue to hold U1 snRNP and the Pol II machinery at regulatory sites, creating a reservoir of regulatory factors for feedback regulation of transcription and chromatin state. For gel source data, see Supplementary Fig. 1.

In summary, unlike mRNAs, lncRNAs are enriched with U1-recognition sites but depleted of 3' splice sites (Fig. 3e). Dynamic interaction of U1 snRNP with transcriptionally engaged Pol II may provide a means of mobilizing U1 snRNP and its interacting lncRNA transcripts to cis and trans genomic sites for feedback regulation of transcription and chromatin state<sup>11–13</sup>. This U1 model provides a parsimonious mechanism that is generally applicable to hundreds of noncoding transcripts, although other mechanisms—such as those involving repetitive sequences<sup>14–16,29</sup>—may also exist to achieve lncRNA association with chromatin. This newly identified function of U1 snRNP adds to other findings that suggest a role for U1 beyond splicing, such as facilitating promoter directionality through the U1–PAS axis<sup>23,30</sup>, and promoting transcriptomic integrity through U1 telescripting<sup>25</sup>. It is possible that these mechanisms work

in concert to ensure the proper expression and function of lncRNAs on chromatin (Extended Data Fig. 10f).

## Online content

Any methods, additional references, Nature Research reporting summaries, source data, extended data, supplementary information, acknowledgements, peer review information; details of author contributions and competing interests; and statements of data and code availability are available at <https://doi.org/10.1038/s41586-020-2105-3>.

- Hon, C. C. et al. An atlas of human long non-coding RNAs with accurate 5' ends. *Nature* **543**, 199–204 (2017).
- Kim, T. K. et al. Widespread transcription at neuronal activity-regulated enhancers. *Nature* **465**, 182–187 (2010).
- Core, L. J., Waterfall, J. J. & Lis, J. T. Nascent RNA sequencing reveals widespread pausing and divergent initiation at human promoters. *Science* **322**, 1845–1848 (2008).
- Preker, R. et al. RNA exosome depletion reveals transcription upstream of active human promoters. *Science* **322**, 1851–1854 (2008).
- Seila, A. C. et al. Divergent transcription from active promoters. *Science* **322**, 1849–1851 (2008).
- Schlackow, M. et al. Distinctive patterns of transcription and RNA processing for human lncRNAs. *Mol. Cell* **65**, 25–38 (2017).
- Li, W., Notani, D. & Rosenfeld, M. G. Enhancers as non-coding RNA transcription units: recent insights and future perspectives. *Nat. Rev. Genet.* **17**, 207–223 (2016).
- Derrien, T. et al. The GENCODE v7 catalog of human long noncoding RNAs: analysis of their gene structure, evolution, and expression. *Genome Res.* **22**, 1775–1789 (2012).
- Luo, S. et al. Divergent lncRNAs regulate gene expression and lineage differentiation in pluripotent cells. *Cell Stem Cell* **18**, 637–652 (2016).
- Yin, Y. et al. Opposing roles for the lncRNA *haunt* and its genomic locus in regulating HOXA gene activation during embryonic stem cell differentiation. *Cell Stem Cell* **16**, 504–516 (2015).
- Yan, P., Luo, S., Lu, J. Y. & Shen, X. Cis- and trans-acting lncRNAs in pluripotency and reprogramming. *Curr. Opin. Genet. Dev.* **46**, 170–178 (2017).
- Engreitz, J. M. et al. Local regulation of gene expression by lncRNA promoters, transcription and splicing. *Nature* **539**, 452–455 (2016).
- Kopp, F. & Mendell, J. T. Functional classification and experimental dissection of long noncoding RNAs. *Cell* **172**, 393–407 (2018).
- Ridings-Figueroa, R. et al. The nuclear matrix protein CIZ1 facilitates localization of Xist RNA to the inactive X-chromosome territory. *Genes Dev.* **31**, 876–888 (2017).
- Sunwoo, H., Colognori, D., Froberg, J. E., Jeon, Y. & Lee, J. T. Repeat E anchors Xist RNA to the inactive X-chromosome compartment through CDKN1A-interacting protein (CIZ1). *Proc. Natl Acad. Sci. USA* **114**, 10654–10659 (2017).
- Lubelsky, Y. & Ulitsky, I. Sequences enriched in Alu repeats drive nuclear localization of long RNAs in human cells. *Nature* **555**, 107–111 (2018).
- Engreitz, J. M. et al. RNA-RNA interactions enable specific targeting of noncoding RNAs to nascent pre-mRNAs and chromatin sites. *Cell* **159**, 188–199 (2014).
- Will, C. L. & Lührmann, R. Spliceosome structure and function. *Cold Spring Harb. Perspect. Biol.* **3**, a003707 (2011).
- Huang, Y. & Carmichael, G. G. A suboptimal 5' splice site is a cis-acting determinant of nuclear export of polyomavirus late mRNAs. *Mol. Cell. Biol.* **16**, 6046–6054 (1996).
- Lee, E. S., Akef, A., Mahadevan, K. & Palazzo, A. F. The consensus 5' splice site motif inhibits mRNA nuclear export. *PLoS ONE* **10**, e0122743 (2015).
- Brown, J. A., Valenstein, M. L., Yario, T. A., Tycowski, K. T. & Steitz, J. A. Formation of triple-helical structures by the 3'-end sequences of MALAT1 and MENB noncoding RNAs. *Proc. Natl Acad. Sci. USA* **109**, 19202–19207 (2012).
- Wilusz, J. E. et al. A triple helix stabilizes the 3' ends of long noncoding RNAs that lack poly(A) tails. *Genes Dev.* **26**, 2392–2407 (2012).
- Boelens, W. C. et al. The human U1 snRNP-specific U1A protein inhibits polyadenylation of its own pre-mRNA. *Cell* **72**, 881–892 (1993).
- Herzog, V. A. et al. Thiol-linked alkylation of RNA to assess expression dynamics. *Methods* **14**, 1198–1204 (2017).
- Kaida, D. et al. U1 snRNP protects pre-mRNAs from premature cleavage and polyadenylation. *Nature* **468**, 664–668 (2010).
- Folco, E. G., Coil, K. E. & Reed, R. The anti-tumor drug E7107 reveals an essential role for SF3b in remodeling U2 snRNP to expose the branch point-binding region. *Genes Dev.* **25**, 440–444 (2011).
- O'Brien, K., Matlin, A. J., Lowell, A. M. & Moore, M. J. The biflavonoid isoginkgetin is a general inhibitor of pre-mRNA splicing. *J. Biol. Chem.* **283**, 33147–33154 (2008).
- Tripathi, V. et al. The nuclear-retained noncoding RNA MALAT1 regulates alternative splicing by modulating SR splicing factor phosphorylation. *Mol. Cell* **39**, 925–938 (2010).
- Chillón, I. & Pyle, A. M. Inverted repeat Alu elements in the human lncRNA-p21 aptamer a conserved secondary structure that regulates RNA function. *Nucleic Acids Res.* **44**, 9462–9471 (2016).
- Almada, A. E., Wu, X., Kriz, A. J., Burge, C. B. & Sharp, P. A. Promoter directionality is controlled by U1 snRNP and polyadenylation signals. *Nature* **499**, 360–363 (2013).

**Publisher's note** Springer Nature remains neutral with regard to jurisdictional claims in published maps and institutional affiliations.

© The Author(s), under exclusive licence to Springer Nature Limited 2020



## Methods

### Cell culture, transfection, and treatment

Mouse mESCs (46C) were maintained in complete ESC culture medium under standard ESC culture conditions as described<sup>31</sup>. HEK 293T and HeLa cells were maintained in standard eukaryote cell culture medium. Cell lines were not authenticated, and were routinely tested for mycoplasma contamination by polymerase chain reaction (PCR). Lipofectamine 3000 was used for transfection. The plasmids from the REL-seq pools or reporters were co-transfected with plasmids expressing the pBASE transposase. At 12–16 h after transfection, the medium was replaced with the appropriate medium containing 250 µg ml<sup>-1</sup> hygromycin B (Thermo Fisher) for 2 days; the cells were then transferred into a 10-cm plate for subsequent subcellular fractionation assays. For drug treatments, under culture conditions, cells were treated with 1 µM E7107 (an inhibitor of U2 snRNP<sup>26</sup>, from Y. Shi's laboratory), with 1 µM flavopiridol (a transcription inhibitor<sup>32</sup>; Selleck, catalogue number S1230), or with 1 µM triptolide (another transcription inhibitor<sup>33</sup>; Abcam, ab120720) for 1 h, or with 100 µM isoginkgetin (an inhibitor of U4/6-U5 snRNP<sup>27</sup>; MedChemExpress, HY-N2117) for 2 h.

### Construction of the SNRNP70<sup>AID</sup> cell line

To construct the auxin-inducible degron (AID)<sup>34</sup> cell line for SNRNP70, we co-transfected into mESCs an exogenous SNRNP70 expression construct with its amino terminus fused to 3× FLAG–biotin–AID tags in the *PiggyBac* vector (PB–3FB–AID–SNRNP70; hygromycin-resistant), together with E3 ligase expression plasmids for the AID system (PB–Tir1; neomycin-resistant) and plasmids expressing the transposase pBASE. After selection with drugs for five days, endogenous SNRNP70 was deleted through the CRISPR/Cas9 system and single clones were picked as described<sup>10</sup>. Clones with homozygous deletion of endogenous SNRNP70 and rapid removal of exogenous AID-tagged SNRNP70 were used for downstream experiments. The auxin analogue indole-3-acetic acid (IAA) was used to induce the degradation of AID-tagged SNRNP70 protein.

### Subcellular fractionation assay

Subcellular fractionation was performed as described with the following modifications<sup>35</sup>. Cytoplasmic buffer containing 0.05% or 0.15% NP-40 was used to isolate the cytoplasmic fraction of mESC or 293T cells respectively. The whole of each subcellular fraction was spiked and mixed thoroughly with 5 µl of 0.1 ng µl<sup>-1</sup> spike-in RNA (containing two in vitro transcribed RNAs, *lacZ* and *mCherry*; for polyA RNA-seq or SLAM-seq, ERCC spike-in (Thermo Fisher) was used). For total RNA-seq, ribosomal RNAs were removed using Ribo-Zero rRNA removal kits (Epicentre); for polyA RNA-seq, polyA RNAs were isolated using Dynabeads mRNA purification kits (Thermo Fisher). RNA-seq libraries were constructed using NEBNext Ultra II directional RNA library prep kits (NEB). For reverse transcription with quantitative PCR (RT–qPCR) or RNA-seq data analysis, the ratio of each fraction versus total input was calculated by normalizing to the spiked transcript. For protein analysis, the same ratio of lysate from the different fractions versus input was used for western blotting.

We also performed a subcellular fractionation with sequentially increasing salt concentrations as described<sup>36</sup>. Briefly, isolated nuclei were washed for 10 min with soluble nuclear buffer (1 mM EDTA, 0.2 mM EGTA), then washed sequentially with soluble nuclear buffer supplemented with 75 mM, 150 mM, 300 mM or 600 mM NaCl. The pellet was then digested with benzonase nuclease, and the supernatant was harvested after spinning at 14,000 r.p.m. for 15 min. The supernatant of each step was collected, and the same portion of each collected sample was used for further western blotting.

### REL-seq and mutREL-seq

DNA fragments of candidate genes were obtained from PCR of genomic DNA (*Malat1*, *Neat1*, *NXFI-IR* (where IR is the retained intron 10 of *NXFI*),

*NR\_028425* and the 3' untranslated repeat (UTR) region of *NCL*) or complementary DNA (*ACTB*, *NANOG*, 5'-UTR and the coding-sequence region of *NCL*). For *Xist*, the pCMV-*Xist* plasmid (which also contains a roughly 2-kilobase region of the last exon of *Tsix*) was ordered from Addgene and used for REL-seq<sup>37</sup>. DNA samples were sonicated to obtain a mixture of short DNA fragments of the expected size (Extended Data Fig. 1c and Supplementary Table 1). For mutREL-seq, random mutagenesis was achieved through error-prone PCR as described<sup>38</sup>.

The short DNA fragments were end-repaired and adenylated using a DNA library construction kit according to the manufacturer's instruction (NEB). In-house-designed 'Y-shaped' adaptors (Supplementary Table 9) were then ligated to the prepared fragments, and the ligation products were further size-selected by agarose-gel purification. Note that the adaptor can be ligated in both sense and antisense directions. The reverse-complement inserts, which were generated as an insertion by-product, serve as an internal control for the sense strand. The purified products were amplified, digested by *AscI* and *NotI*, and ligated with *AscI*- and *NotI*-digested 5AI, 3AI (which refer to 3' or 5' of the *ACTB* intron) or GFP reporter vectors. The products were further purified by ethanol precipitation and the pellet was dissolved in 1 µl of water. See Supplementary Note 1 for a description of the three reporter vectors. The purified ligation products were transformed into electrocompetent cells (Takara) through electroporation and plated evenly on two 15-cm agar plates. After overnight growth, the cells were harvested by scraping, and the plasmids were then extracted and co-transfected with pBASE into mESCs or 293T cells as described above. These two cell lines were chosen as they can be efficiently transfected, and they represent pluripotent and fully differentiated cells in mice and humans, respectively. After 2 days of drug selection, cells were plated onto a 10-cm plate, and subcellular fractionation was performed and RNA was extracted from the different fractions using TRIzol reagent. RNAs were further treated with DNase I for 20 min to remove residual DNA, and reverse-transcribed with SuperScript III reverse transcriptase (Thermo Fisher). A specific reverse-transcription primer that binds downstream of the insertion site was used for reverse transcription (Supplementary Table 9). Reverse transcription was performed at 50 °C for 40 min and at 55 °C for another 20 min. Ten units of exonuclease I were added and incubated at 37 °C for 20 min to remove the free reverse-transcription primers. The reaction was stopped by heating the sample at 95 °C for 10 min to inactivate all of the enzymes. Then, 0.5 µl of 10 mg ml<sup>-1</sup> RNase A was added and incubation was carried out at 37 °C for 20 min to degrade the RNA. Complementary DNAs were purified through ethanol precipitation and used as templates for PCR and library construction.

PCR was performed using primers that bind on either side of the inserted fragments. For the 5AI or 3AI reporter, one primer specifically targeted the exon junction site of the spliced *ACTB* intron 3, while the other primer targeted the adaptor sequence. For the GFP reporter, both of the primers were designed to target the adaptor sequences (Supplementary Table 9). The PCR products were then purified using 1× Ampure XP beads, and libraries for the different samples were constructed using NEBNext Ultra II DNA library prep kits (NEB, E7645).

### RNA pull-down assay

RNA pull-down assays were performed as reported with some modifications<sup>39</sup>. Briefly, biotinylated *NXFI*-enChr sense or antisense (*NXFI*-enChr-as) RNA was obtained by in vitro transcription with biotin-UTP incorporation. We denatured 2 µg of purified biotinylated RNA at 90 °C for 2 min, and then transferred it onto ice for 2 min. We added a one-quarter volume of 5× RNA structure buffer (final concentration 10 mM Tris pH 7, 0.1 M KCl, 10 mM MgCl<sub>2</sub>) and incubated the mixture at room temperature for 20 min. The folded RNA was mixed with the precleared mESC nuclear extract, and incubated at room temperature for 1 h. Prewashed streptavidin beads were added and incubated at room temperature for another 2 h. The beads were washed five times with RIP wash buffer (200 mM KCl, 25 mM Tris pH 7.4), then eluted with

# Article

nuclear lysis buffer (50 mM Tris-Cl, pH 7.5, 10 mM EDTA, 1% SDS) at room temperature for 2 min. A one-fifth volume of 6× SDS sample buffer was added and boiled for 5 min at 95 °C, and the protein sample was used for western blotting or prepared for mass-spectrometry analysis.

## AMO inhibition

Treatment with AMOs for U1, U2 or U1/2 snRNA inhibition was performed as described with modifications<sup>25,30,40,41</sup>. Briefly, roughly  $2.5 \times 10^6$  mESCs were nucleofected with various AMOs by electroporation using a Nucleofector (Amaxa) and then immediately plated in a six-well plate. For each treatment with scrambled control (CT), U1 or U2 AMOs, the AMO concentration was 7.5 nmol per 100 µl (75 µM) per nucleofection. For inhibition of both U1/2, 5 nmol per 100 µl of U1 and U2 AMOs (50 µM each) were co-transfected. AMO sequences are listed in Supplementary Table 9. After 2 h of AMO nucleofection, cells were harvested for RNA-seq (whole cells) or subcellular fractionation for downstream experiments and analyses. Note that the AMO-treated mESCs were nicely attached to the culture plate and no obvious morphological changes were observed at the end of the 2-h treatment time. However, mESCs appear to be more sensitive to U1 and/or U2 AMOs than were cell lines used in previous studies, where AMO treatment was performed for 8 h (refs. <sup>25,30,40,41</sup>). After 4-h treatment with U1, U2 or U1/2 AMOs, mESCs started to become detached from the culture plate, indicating cell death. Extensive cell death was observed at 8 h of AMO nucleofection. Therefore, we chose to analyse the immediate effects of U1 and/or U1 inhibition on RNA subcellular localization after 2 h of treatment instead of 8 h. Short-term treatments appear to be suitable for studying lncRNA and ncRNA transcripts with relatively short half-lives<sup>42</sup>.

## Co-immunoprecipitation

Co-immunoprecipitation was performed as described with some modifications<sup>43</sup>. mESC nuclei were isolated using hypotonic buffer and washed with benzonase digestion buffer (50 mM HEPES, pH 7.5, 200 mM NaCl, 5 mM MgCl<sub>2</sub>, 0.1 mM Na<sub>3</sub>VO<sub>4</sub>, 0.1% NP-40, 10% glycerol) at 4 °C for 30 min. The pellet was resuspended with benzonase digestion buffer containing 1 µl benzonase nuclease (Sigma, E1014) and rotated at 4 °C for 30 min to isolate the chromatin extract. For antibody immunoprecipitation, we added 2 µg of antibody to each sample and used protein G magnetic beads (Thermo Fisher) for the pull-down. FLAG M2 magnetic beads (Sigma) were used for FLAG immunoprecipitation.

For co-immunoprecipitation coupled with stable-isotope labelling by amino acids in cell culture followed by mass spectrometry (colP-SILAC), wild-type mESCs were cultured with heavy SILAC media and mixed with equal amounts of SNRNP70<sup>AID</sup> mESCs (FLAG-tagged) cultured in light SILAC media. The co-immunoprecipitation procedure was as described above, except that pull-down was performed with FLAG beads and the proteins were eluted with FLAG peptide. The eluate was concentrated through acetone precipitation. Protein identity and relative enrichment were determined by mass spectrometry. Proteins with scores larger than 20 and light/heavy ratios larger than 2 were defined as SNRNP70-interacting proteins (Supplementary Table 8).

## SLAM-seq of subcellular fractionation samples

The SLAM-seq protocol was modified from a previous report<sup>24</sup>. Briefly, SNRNP70<sup>AID</sup> mESCs were treated with auxin for 2 h, then allowed to incorporate 4sU (300 mM final) for 3 h in the presence of auxin. The purpose of this 3-h 4sU labelling is to make sure that most of the new transcripts are fully transcribed, processed and localized. SNRNP70<sup>AID</sup> mESCs treated with 4sU but without auxin were used as controls. Subcellular fractionation was performed as described above and RNAs from each fraction were extracted. The RNAs were further treated with chemical reactions as described<sup>44</sup> and 3'-end mRNA-seq libraries were constructed using a commercially available kit (QuantSeq 3'mRNA-Seq library prep kit, Lexogen). Deep sequencing was performed and data

were analysed using SLAM-DUNK<sup>45</sup>, with the last exon of lncRNAs as the reference. The remaining parameters were left as defaults.

## TT-seq

The TT-seq protocol was modified from a previous report<sup>46</sup>. Auxin-treated or untreated SNRNP70<sup>AID</sup> mESCs were allowed to incorporate 4sU (500 mM final) for 10 min; cells were then harvested and RNAs were extracted by TRIzol. Labelled RNAs were further biotinylated as described<sup>47</sup> and fragmented with 0.1× NaOH on ice for 10 min. The fragmented RNAs were subjected to purification as described<sup>47</sup>. RNA-seq library construction, deep sequencing and data analysis were further performed as described above and below.

## RNA FISH

*Malat1* single-molecule inexpensive FISH (smRNA FISH) was performed as described<sup>48</sup>. Immunofluorescence was carried out according to the protocol provided by Cell Signaling Technology. To reduce variations arising from experimental or imaging procedures, we constructed a SNRNP70<sup>AID</sup> mESC line with stable integration of a *GFP* gene (*GFP*<sup>+</sup>). SNRNP70<sup>AID</sup>-*GFP*<sup>+</sup> mESCs were mixed with wild-type *GFP*-negative mESCs (*GFP*<sup>-</sup>) before plating for RNA FISH or immunofluorescence. The probes used for *Malat1* FISH are listed in Supplementary Table 9.

## ChIRP-seq

Auxin-treated or untreated SNRNP70<sup>AID</sup> cells were crosslinked using 2 mM dithiobis succinimidyl propionate (DSP) for 30 min, followed by 15 min of crosslinking with 3.7% formaldehyde. The crosslinked cells were first partially digested with 12 U ml<sup>-1</sup> DNase I at 37 °C for 10 min, then sonicated at 25% amplitude for 30 s. Subsequent procedures were performed as described<sup>10,49</sup>. The probes used for *Malat1* ChIRP are listed in Supplementary Table 9. For ChIRP RNA, auxin-treated or untreated SNRNP70<sup>AID</sup> mESCs were crosslinked with 2% formaldehyde for 10 min. Subsequent procedures were performed as described<sup>10</sup>.

## REL-seq data analysis

Sequences corresponding to vectors and adaptors were removed from the REL-seq sequencing data using BEDTools<sup>50</sup>. The remaining 'clean' reads were mapped to the mouse genome (mm9) through TopHat<sup>51</sup>. To compare read densities, we divided the genomic regions of candidate genes into multiple bins, each ten base pairs in length. For each sample, the number of reads located in each bin was counted and further normalized by the total reads mapped to those bins. The fold changes were calculated by dividing the read density of the chromatin fraction by the read density of the cytoplasm fraction. To identify the chromatin-enriched regions, we calculated the fold changes of the different samples, and carried out a *t*-test to compare the fold change of each sample with the median fold change of the corresponding sample. Only a bin with a *t*-test *P*-value of less than 0.05 and a fold change greater than 1.5 was recognized as a bin with significant chromatin enrichment. Neighbouring bins, within a distance of 50 nucleotides, were merged as a region with significant chromatin enrichment. As most of the inserts were much larger than 50 nucleotides, merged inserts with a length of less than 50 nucleotides were discarded. Because we used very stringent selection criteria across all REL-seq data sets generated with different libraries in three AI (*ACTB* intron) and *GFP* reporter vectors in both human and mouse cell lines, the enChrs we identified may underrepresent the total number of regulatory RNA signals for chromatin association in the cell.

To identify inserts that were enriched in different fractions, we reconstructed inserts by identifying their ends through the mapping of paired-end reads. The abundance of different inserts in the different fractions was counted, and fold changes of different clones were calculated by dividing the insert abundance in the chromatin fraction by the insert abundance in the cytoplasm fraction. Only inserts with a maximum read number larger than ten and a minimum no less than one

were used for the analysis. The cutoff of fold changes for chromatin-enriched inserts is annotated in the relevant figure legends.

For *NXFI*-enChr mutREL-seq, 'clean' reads were mapped through Novoalign onto a reference sequence, built in-house, which contained only the sequence of the *NXFI*-enChr region. The different mutations at each position were counted. The cytoplasmic/chromatin ratio of each mutation was calculated by dividing the normalized reads (normalized by wild-type reads) in the cytoplasmic fraction by that in the chromatin fraction.

### RNA-seq data analysis

RNA-seq data from fractionation of human K562 cells were downloaded from the ENCODE project (<https://www.encodeproject.org>)<sup>52,53</sup>. Alignments of RNA-seq data to human genome assembly hg19 were performed using Tophat v2.0.10 (ref.<sup>54</sup>). Fragments per kilobase of exon model per million mapped reads (FPKM) were calculated using Cufflink 2.1.1 to represent expression levels of transcripts. Gencode v19 was used as the human gene annotation. Similarly, RNA-seq data from subcellular fractionation of mouse cells were mapped to mouse genome assembly mm10 (for comparisons and correlation analyses) or mm9 (for tracks showing sequencing signals), and the corresponding FPKM were calculated with the Gencode vM9 annotation. For data analysis of strand-specific RNA-seq data, the strand information of each mapped read was first converted into absolute strand information relative to the genome; then the FPKM was calculated through Cufflinks 2.1.1 using stranded RNA-seq parameters.

For RNA-seq analysis of whole-cell and subcellular fractionated samples, raw reads of mouse subcellular fractionation RNA-seq data were mapped to mouse genome assembly mm9 for sequencing signal analysis tracks or mm10 for FPKM calculations. For the analysis of relative gene abundance in different subcellular fractions, we constructed an in-house reference file by combining the genome assembly mm10 with our in-house spike-in sequence (*lacZ* and *mCherry*). The RNA-seq data of each fraction were mapped to the in-house reference. The FPKM value of each gene was calculated (with Gencode vM9 annotation), and the ratio of reads that mapped to spike-in was also calculated ((reads mapped to spike-in)/(total mappable reads)). The FPKM value of each gene was further normalized by the corresponding ratio of spike-in, and the ratio of each fraction was calculated by dividing the normalized FPKM value of each fraction by the sum of all three fractions (cytosol plus nucleus plus chromatin). The sequencing signal track of subcellular fractionation samples was also normalized by the ratio of spike-in. lncRNAs with a minimum FPKM of more than 0 and a maximum FPKM in all samples of more than 1 were chosen as mESC-expressed lncRNAs. To identify U1 snRNP-regulated lncRNAs, we first normalized the RNA signals in each compartment to spike-in RNA controls and then calculated relative enrichments on chromatin (chromatin/non-chromatin ratio) by comparing normalized RNA signals in the chromatin to the non-chromatin (cytoplasm plus nucleoplasm) fractions. Only those lncRNAs that showed greater decreases in the chromatin fraction than in the nucleoplasm and cytoplasm fractions (a chromatin/non-chromatin ratio of less than one;  $P < 0.05$ ) upon U1 snRNP depletion were selected as U1 snRNP-regulated lncRNAs. In addition, we also compared lncRNA abundance in each of the chromatin, cytoplasm and nucleoplasm fractions to the total amount of lncRNA in all fractions, depicted as 'chromatin/total', 'cytoplasm/total' and 'nucleus/total'.

We used the following published data sets in our analysis: total RNA-seq of whole cells and the chromatin fraction of K562 cells, GSE30567; U1 and *Malat1* RAP in mESCs<sup>17</sup>, GSE55914; Pol II NTD ChIP-exo-seq in mESCs<sup>55</sup>, GSE64825; Pol II 8WG16 ChIP-seq in mESCs<sup>56</sup>, GSE49847; Ser 2 and Ser 5 phosphorylated Pol II ChIP-seq in mESCs<sup>57</sup>, GSE112114.

### Correlation analysis

We used two methods—bioinformatics prediction and U1 RAP-RNA—to analyse the U1-recognition site. Prediction of U1 snRNP recognition

sites was performed as described<sup>30</sup>. On the basis of their maximum entropy scores, we categorized the predicted U1 snRNP recognition sites into predicted strong (top 50% of sites) and medium (bottom 25% to 50% of sites). We calculated the number of U1-recognition sites in the intron and exon regions for each transcript. The average density of predicted U1-recognition sites was calculated by dividing the total number of predicted U1-recognition sites in all exons (or all introns, and so on) by the total length of all exons (or all introns and so on). Only transcripts with a total exon length (or intron length) greater than 1 kilobase were chosen for further comparison of the density of predicted U1-recognition sites in lncRNAs and mRNAs.

Only genes with FPKM values of more than 1 were used to compare mRNAs with different chromatin-association tendencies and lncRNAs. As RNA-seq data of mouse subcellular fractions are unstranded, lncRNA transcripts that overlapped with coding genes were discarded. Transcripts that are entirely located in repeat elements were also discarded. The fold enrichment of each transcript was calculated by dividing the FPKM in chromatin RNA-seq data by the FPKM of the respective total RNA-seq data. For Extended Data Fig. 4e, we used FPKM values of transcripts (isoforms) rather than genes for analysis, as different isoforms of the same gene may show a different chromatin-association tendency.

For U1 RAP-RNA analysis, we obtained U1 RAP-RNA data from ref.<sup>17</sup>, which used formaldehyde crosslinking to obtain the U1 snRNA interacting RNAs. We first calculated the number of reads in the intron and exon region for each transcript. Only those transcripts containing at least ten reads in each sample were kept for further analysis. To calculate the U1 enrichment for the intron and exon region of a target RNA, we divided the reads mapping to the target exon or intron of each transcript in RAP-RNA by the respective input with normalization of sequencing depth. The fold enrichment of the U1 RAP-RNA signal in lncRNAs and coding genes was calculated and compared. The *t*-test (two-sided) was used to calculate the significance of the difference between two groups.

### Genome-wide prediction of 3' splice sites

To identify the genome-wide distribution of predicted 3'ss, we generated a fasta file containing all 4,096 possible arrangements of eight-nucleotide motifs ending with 'AG'. Those motifs were mapped to the mouse or human genome through bowtie-1.0.0 to obtain the genomic distribution of each eight-nucleotide motif. Each mapped coordinate plus 12-nucleotide upstream and 3-nucleotide downstream (23 nucleotides in total) was used to calculate the 3'ss score (by MaxEntScan<sup>58</sup>). Each coordinate with a score larger than 8.0 was recognized as a predicted 3' splice site (the median scores of Gencode vM9 annotated 3' splice sites were 8.7 in coding genes and 8.0 in lncRNAs).

### Other bioinformatics analyses

The secondary structures of the wild-type and mutated *NXFI*-enChr regions were predicted from the Vienna RNA website with default parameters<sup>59,60</sup>. The analysed REL-seq tracks and other tracks are shown in Integrative Genomics Viewer (IGV)<sup>61</sup>. Metaplots were drawn using *ngs.plot*<sup>62</sup>.

### Reporting summary

Further information on research design is available in the Nature Research Reporting Summary linked to this paper.

### Data availability

All sequencing data are available in the Sequence Read Archive database under accession numbers SRP214639 and SRP125289. For gel source data, see Supplementary Fig. 1. Source data for Fig. 2a–c are provided with the paper (Supplementary Tables 4–7). All other data are available from the corresponding author upon reasonable request. Sequencing data have been deposited in the Gene Expression Omnibus under accession numbers GSE107131 and GSE134287.

31. Shen, X. et al. EZH1 mediates methylation on histone H3 lysine 27 and complements EZH2 in maintaining stem cell identity and executing pluripotency. *Mol. Cell* **32**, 491–502 (2008).
32. Chao, S. H. & Price, D. H. Flavopiridol inactivates P-TEFb and blocks most RNA polymerase II transcription in vivo. *J. Biol. Chem.* **276**, 31793–31799 (2001).
33. Titov, D. V. et al. XPB, a subunit of TFIIH, is a target of the natural product triptolide. *Nat. Chem. Biol.* **7**, 182–188 (2011).
34. Nishimura, K., Fukagawa, T., Takisawa, H., Kakimoto, T. & Kanemaki, M. An auxin-based degron system for the rapid depletion of proteins in nonplant cells. *Nat. Methods* **6**, 917–922 (2009).
35. Bhatt, D. M. et al. Transcript dynamics of proinflammatory genes revealed by sequence analysis of subcellular RNA fractions. *Cell* **150**, 279–290 (2012).
36. O'Hagan, H. M. et al. Oxidative damage targets complexes containing DNA methyltransferases, SIRT1, and polycomb members to promoter CpG Islands. *Cancer Cell* **20**, 606–619 (2011).
37. Wutz, A. & Jaenisch, R. A shift from reversible to irreversible X inactivation is triggered during ES cell differentiation. *Mol. Cell* **5**, 695–705 (2000).
38. McCullum, E. O., Williams, B. A., Zhang, J. & Chaput, J. C. Random mutagenesis by error-prone PCR. *Methods Mol. Biol.* **634**, 103–109 (2010).
39. Tsai, M. C. et al. Long noncoding RNA as modular scaffold of histone modification complexes. *Science* **329**, 689–693 (2010).
40. Li, Z. et al. Exon-intron circular RNAs regulate transcription in the nucleus. *Nat. Struct. Mol. Biol.* **22**, 256–264 (2015); corrigendum 24, 194 (2017).
41. Berg, M. G. et al. U1 snRNP determines mRNA length and regulates isoform expression. *Cell* **150**, 53–64 (2012).
42. Clark, M. B. et al. Genome-wide analysis of long noncoding RNA stability. *Genome Res.* **22**, 885–898 (2012).
43. Shen, X. et al. Jmjd3 modulates polycomb activity and self-renewal versus differentiation of stem cells. *Cell* **139**, 1303–1314 (2009).
44. Schofield, J. A., Duffy, E. E., Kiefer, L., Sullivan, M. C. & Simon, M. D. TimeLapse-seq: adding a temporal dimension to RNA sequencing through nucleoside recoding. *Nat. Methods* **15**, 221–225 (2018).
45. Neumann, T. et al. Quantification of experimentally induced nucleotide conversions in high-throughput sequencing datasets. *BMC Bioinformatics* **20**, 258 (2019).
46. Schwalb, B. et al. TT-seq maps the human transient transcriptome. *Science* **352**, 1225–1228 (2016).
47. Dölken, L. et al. High-resolution gene expression profiling for simultaneous kinetic parameter analysis of RNA synthesis and decay. *RNA* **14**, 1959–1972 (2008).
48. Tsanov, N. et al. smFISH and FISH-quant—a flexible single RNA detection approach with super-resolution capability. *Nucleic Acids Res.* **44**, e165 (2016).
49. Chu, C., Qu, K., Zhong, F. L., Artandi, S. E. & Chang, H. Y. Genomic maps of long noncoding RNA occupancy reveal principles of RNA-chromatin interactions. *Mol. Cell* **44**, 667–678 (2011).
50. Quinlan, A. R. & Hall, I. M. BEDTools: a flexible suite of utilities for comparing genomic features. *Bioinformatics* **26**, 841–842 (2010).
51. Kim, D. et al. TopHat2: accurate alignment of transcriptomes in the presence of insertions, deletions and gene fusions. *Genome Biol.* **14**, R36 (2013).
52. Harrow, J. et al. GENCODE: the reference human genome annotation for The ENCODE Project. *Genome Res.* **22**, 1760–1774 (2012).
53. Tilgner, H. et al. Deep sequencing of subcellular RNA fractions shows splicing to be predominantly co-transcriptional in the human genome but inefficient for lncRNAs. *Genome Res.* **22**, 1616–1625 (2012).
54. Trapnell, C. et al. Differential gene and transcript expression analysis of RNA-seq experiments with TopHat and Cufflinks. *Nat. Protoc.* **7**, 562–578 (2012); erratum 9, 2513 (2014).
55. de Dieuleveult, M. et al. Genome-wide nucleosome specificity and function of chromatin remodellers in ES cells. *Nature* **530**, 113–116 (2016).
56. Yue, F. et al. A comparative encyclopedia of DNA elements in the mouse genome. *Nature* **515**, 355–364 (2014).
57. Zhang, T. et al. A variant NuRD complex containing PWWP2A/B excludes MBD2/3 to regulate transcription at active genes. *Nat. Commun.* **9**, 3798 (2018).
58. Yeo, G. & Burge, C. B. Maximum entropy modeling of short sequence motifs with applications to RNA splicing signals. *J. Comput. Biol.* **11**, 377–394 (2004).
59. Gruber, A. R., Lorenz, R., Bernhart, S. H., Neuböck, R. & Hofacker, I. L. The Vienna RNA websuite. *Nucleic Acids Res.* **36**, W70–W74 (2008).
60. Lorenz, R. et al. ViennaRNA Package 2.0. *Algorithms Mol. Biol.* **6**, 26 (2011).
61. Robinson, J. T. et al. Integrative genomics viewer. *Nat. Biotechnol.* **29**, 24–26 (2011).
62. Shen, L., Shao, N., Liu, X. & Nestler, E. ngs.plot: quick mining and visualization of next-generation sequencing data by integrating genomic databases. *BMC Genomics* **15**, 284 (2014).
63. Wang, R., Zheng, D., Yehia, G. & Tian, B. A compendium of conserved cleavage and polyadenylation events in mammalian genes. *Genome Res.* **28**, 1427–1441 (2018).
64. Gruber, A. R., Lorenz, R., Bernhart, S. H., Neuböck, R. & Hofacker, I. L. The Vienna RNA websuite. *Nucleic Acids Res.* **36**, W70–W74 (2008).
65. Ntini, E. et al. Polyadenylation site-induced decay of upstream transcripts enforces promoter directionality. *Nat. Struct. Mol. Biol.* **20**, 923–928 (2013).

**Acknowledgements** We thank G. Dreyfuss, P. Sharp, J. Steitz, N. Proudfoot, Y. Shi, J. Zhu, Z. Wang and members of the Shen Laboratory for suggestions. Grant support is from the National Natural Science Foundation of China (31630095 and 31925015 to X.S.; 31900439 to Y.Y. and 91740204 to Q.C.Z.), the National Basic Research Program of China (2018YFA0107604 and 2017YFA0504204 to X.S.; and 2018YFA0107603 and 2019YFA0110002 to Q.C.Z.), the US National Institutes of Health (R01GM084089 to B.T.), and the Center for Life Sciences and Beijing Advanced Innovation Center for Structural Biology at Tsinghua University (to X.S. and Q.C.Z.). Y.Y. is a recipient of the Outstanding Postdoctoral Program of the Tsinghua Center for Life Sciences.

**Author contributions** X.S. and Y.Y. conceived the project and wrote the manuscript. Y.Y. performed most experiments and bioinformatics analyses. X.Z. and W.S. helped with subcellular fractionation; Y.H. and L.C. helped to construct SNRNP70<sup>ΔD</sup> mESCs; J.Y.L. and Y.X. helped with correlation analysis of U1-RNA localization; P.L. carried out prediction of U1-recognition sites under the guidance of Q.C.Z.; G.S. provided initial batches of AMOs; B.T. helped with 3' ss analysis.

**Competing interests** The authors declare no competing interests.

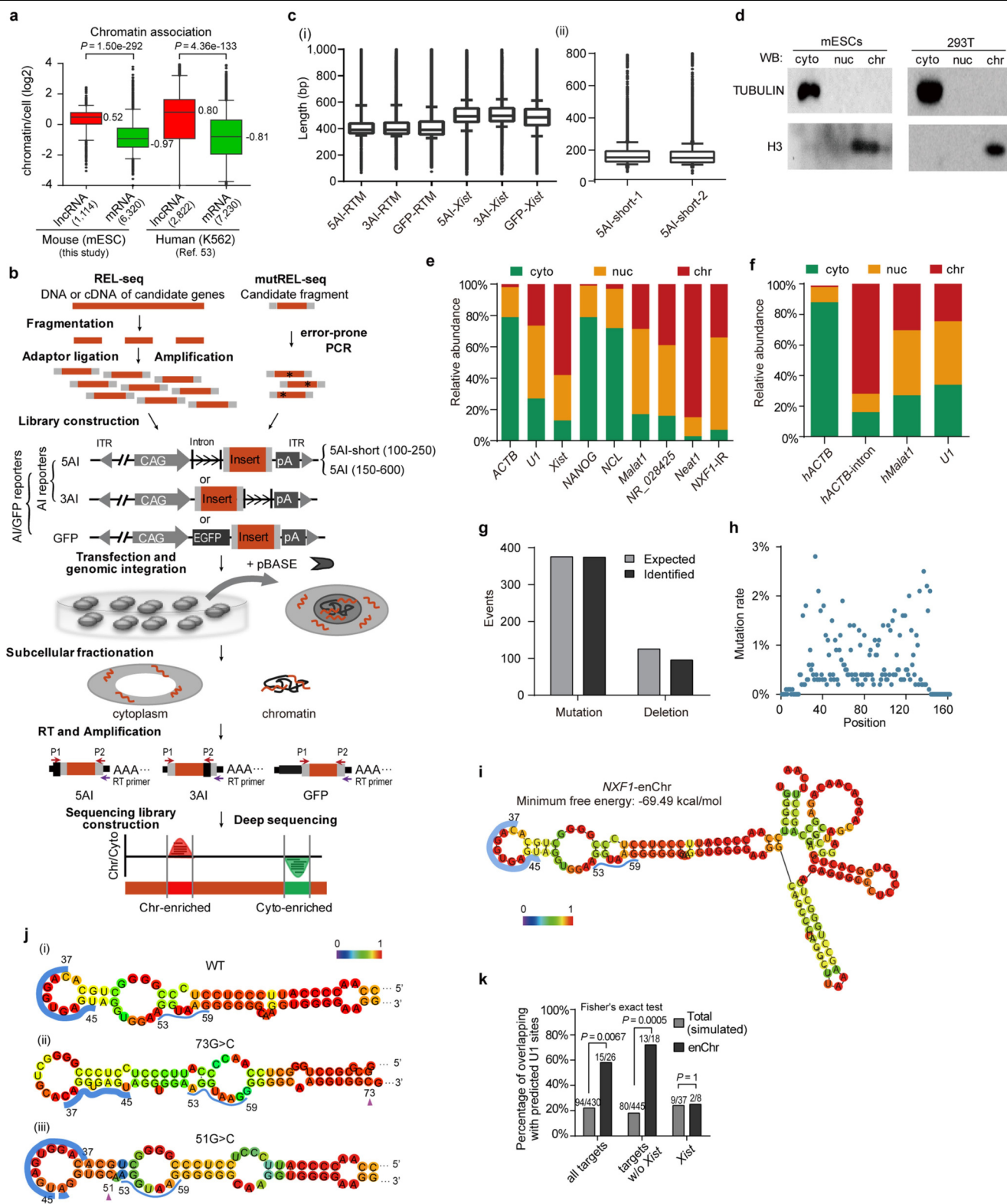
## Additional information

**Supplementary information** is available for this paper at <https://doi.org/10.1038/s41586-020-2105-3>.

**Correspondence and requests for materials** should be addressed to Y.Y. or X.S.

**Peer review information** Nature thanks Zhaohui Qin, Claes Wahlestedt and the other, anonymous, reviewer(s) for their contribution to the peer review of this work.

**Reprints and permissions information** is available at <http://www.nature.com/reprints>.



Extended Data Fig. 1 | See next page for caption.

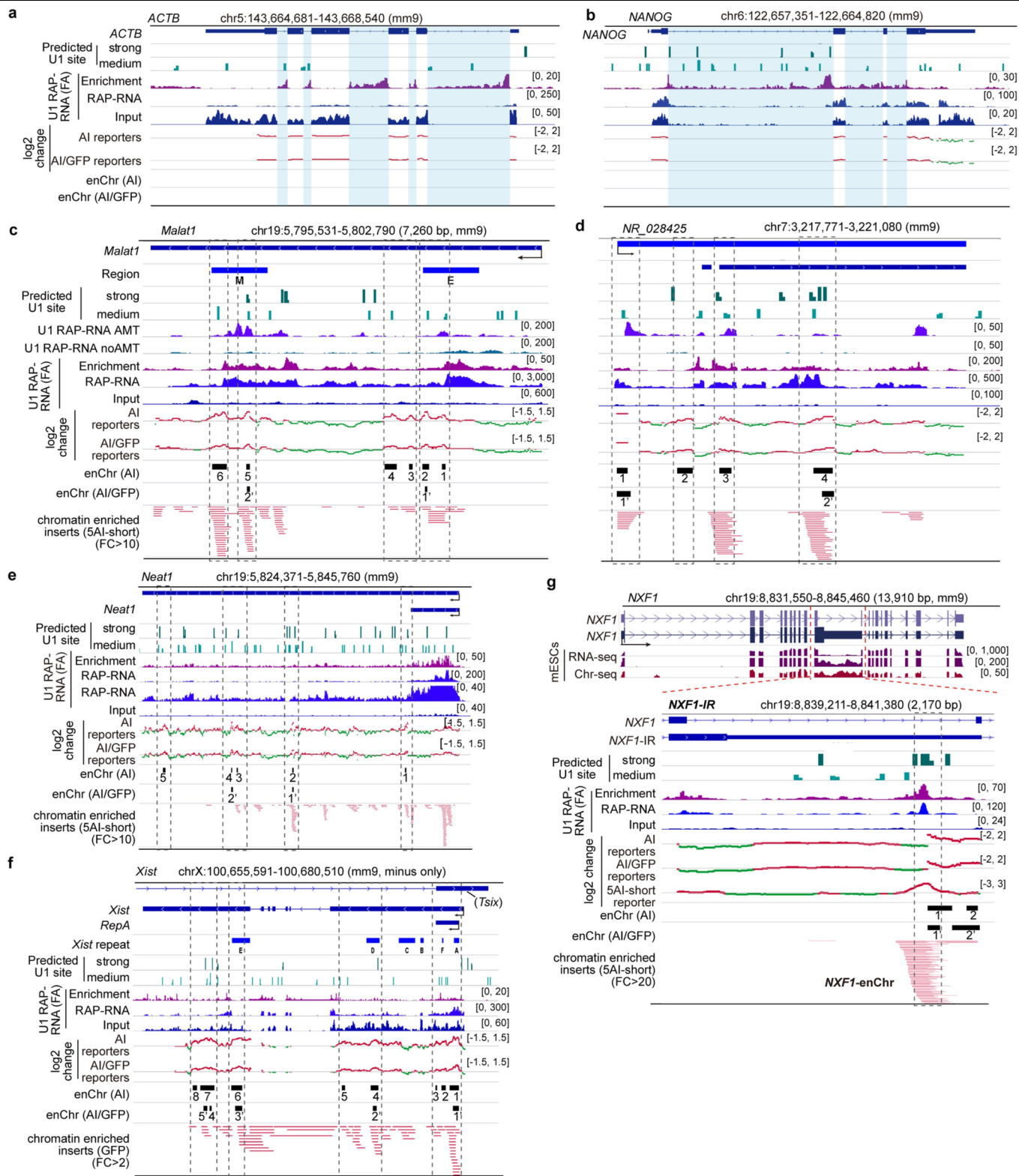


# Article

## Extended Data Fig. 1 | REL-seq and mutREL-seq for identification of *cis* elements that contribute to the subcellular localization of RNA.

**a**, Comparisons of chromatin enrichment between lncRNAs and protein-coding mRNA genes in human and mouse. We fractionated chromatin-bound RNA in mESCs and compared the RNA-seq profiles of chromatin RNA to total RNA from whole cells. We also analysed a previously published RNA-seq data set (chromatin and cell) from human K562 cells<sup>53</sup>. lncRNAs with FPKM values of greater than 1 and protein-coding genes with FPKM values of greater than 5 were used for the analysis. Data for samples connected by brackets were compared with two-sided *t*-tests. Consistent with previous reports<sup>6,8</sup>, lncRNAs as a class are significantly enriched in the chromatin fraction in both mouse and human cells. Box plots show 5th, 25th, 50th, 75th and 95th percentiles, with median values labelled beside the box plots and sample sizes ( $n \geq 1,114$ ) labelled on the *x* axis. **b**, Detailed pipelines for REL-seq and mutREL-seq. For REL-seq, DNA fragments from candidate genes are randomly fragmented, ligated with adaptors, amplified, and inserted into three types of reporters in the *PiggyBac* transposon vector (including 5AI, 3AI and GFP reporters). The reporters are co-transfected with *PiggyBac* transposases (pBASE) and stably integrated into the genome. RNA from the cytoplasm (cyto) and chromatin (chr) fractions is reverse-transcribed (RT) with primers indicated by purple arrows, and amplified with primers P1 and P2 for subsequent high-throughput sequencing. Sequences that are enriched in different subcellular fractions are identified by comparing the read intensities or insert abundance in the chromatin fraction with that of the cytoplasmic fraction. For mutREL-seq, a candidate fragment (*NXFI-enChr*) is randomly mutagenized through error-prone PCR, and the products are further inserted into the 5AI reporter vector and subjected to downstream procedures similar to those described for REL-seq. Asterisks represent mutation sites. ITR, inverted terminal repeat sequences of the *PiggyBac* transposon system. See also Supplementary Note 1. **c**, Box plots showing the length of inserts of RTM (RNA transcript mixture, without *Xist*) and *Xist* REL-seq libraries in 5AI, 3AI and GFP reporters (i) and 5AI-short reporters (ii). Box plots show 5th, 25th, 50th, 75th and 95th percentiles.

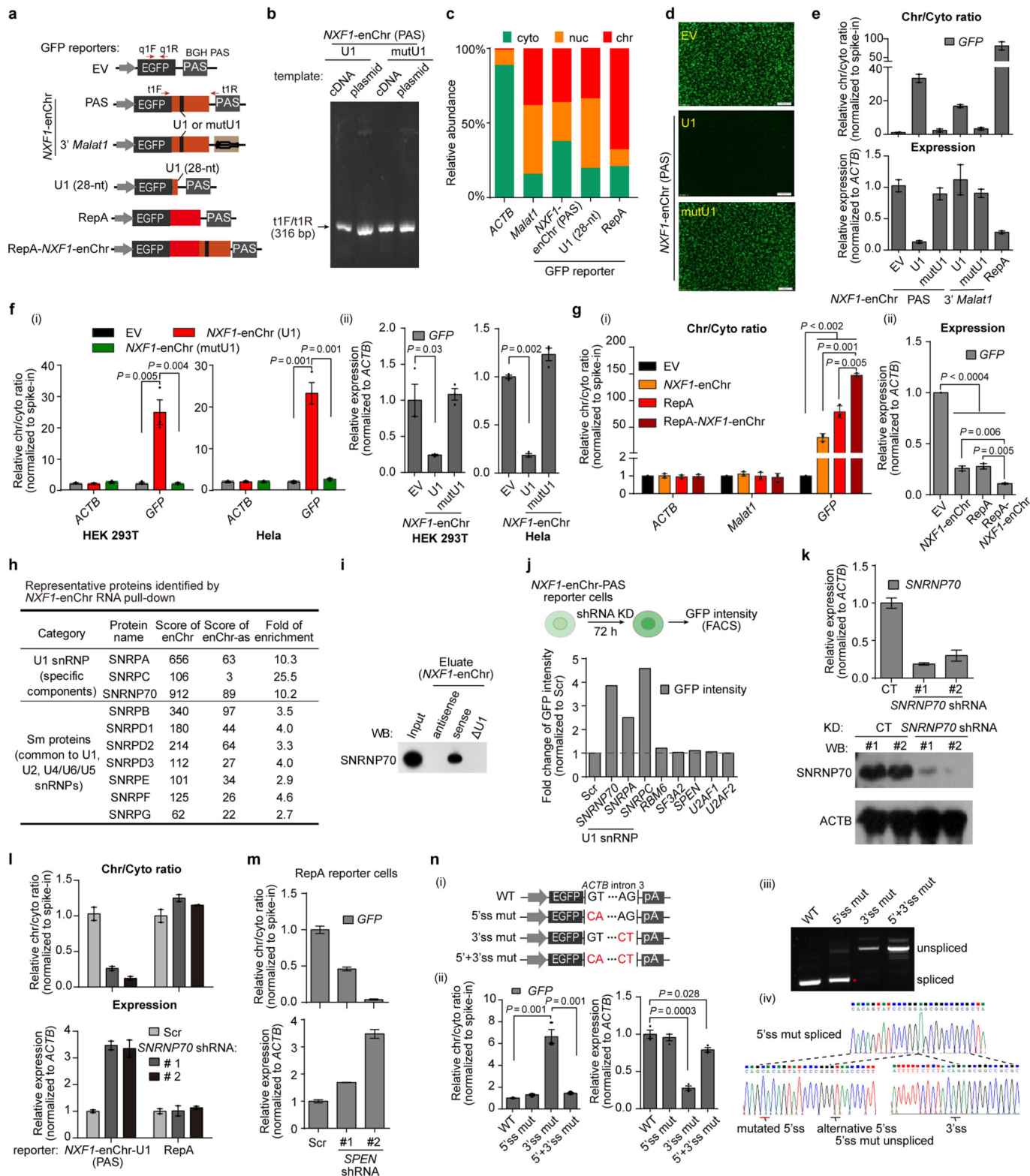
In i,  $n = 20,000$  randomly selected inserts for each group. In ii,  $n = 19,748$  for 5AI-short-1;  $n = 15,091$  for 5AI-short-2. **d**, Western blot analysis of marker proteins in subcellular fractions of mESCs or HEK 293T cells. Tubulin and histone H3 are used as marker proteins for the cytoplasmic and chromatin fractions, respectively.  $n = 3$  independent experiments. **e, f**, RT-qPCR analysis of the relative abundance of marker genes and candidate genes for REL-seq in subcellular fractions of mESCs (**e**) or human HEK 293T cells (**f**). *ACTB* and *Xist* are used as markers of mouse cytoplasmic and chromatin fractions, respectively; *hACTB* and *hACTB*-intron (intronic region of *hACTB*) are used as markers of human cytoplasmic and chromatin fractions, respectively. **g**, Numbers of mutation or deletion events expected and identified by mutREL-seq. A total of 469 mutation events, including 374 mutations (coverage 99.7%) and 85 deletions (coverage 68%), were identified over the 125-base-pair (bp) length of the *NXFI-enChr* DNA, indicating saturated mutagenesis. **h**, Analysis of the mutation rate. PCR mutations are spread across the *NXFI-enChr* sequence, ruling out a PCR bias towards the core 7-nucleotide mutations at positions 37–45. Notably, the two binding sites for PCR primers at the 5' (1–18-bp) and 3' (144–162-bp) ends of *NXFI-enChr* were less likely to be mutated, compared to the middle region with an average of 0.2%–3% mutation rate at each nucleotide position. This excludes the possibility that the sequences were misread. **i**, Predicted secondary structure of *NXFI-enChr* RNA. The U1-recognition site at positions 37–45 is highlighted with a thick blue line. A weak U1-recognition site at positions 53–59 is highlighted with a thin blue line. The coloured bar represents the probability of base-pairing or being unpaired (red, high probability of pairing (or lack of pairing); blue, low probability). **j**, Comparison of predicted secondary structures of the wild-type (i) and mutant (ii, iii) *NXFI-enChr* (partial sequences are shown). Purple triangles (ii, iii) highlight mutation sites. See also Supplementary Note 2. **k**, The percentage of enChrs or all target sequences ('total' = (sum of length)/(median length of enChr)) used for REL-seq analysis that overlap with predicted U1-recognition sites. *P*-values (one-sided Fisher's exact test) and sample sizes are shown at the top.



**Extended Data Fig. 2** | See next page for caption.

**Extended Data Fig. 2 | Genome-browser views of representative genes showing REL-seq results.** The enChrs (shown as thick black bars, also highlighted by dashed boxes) indicate regions with significant chromatin enrichment that were identified by AI/GFP or AI reporter screens ( $P < 0.05$ , fold change greater than 1.5). Representative chromatin-enriched inserts from respective reporters (SAI-short or GFP) are shown at the bottom of each panel. **a, b**, No enChrs were identified by REL-seq in the cytoplasm-localized protein-coding *ACTB* (**a**) and *NANOG* (**b**) transcripts. In these transcripts, U1 signals are mainly confined to the intronic regions and appear to be depleted in exons. Scales are shown in square brackets at the right of each track. **c–g**, REL-seq identified multiple enChrs in mouse *Malat1* (**c**), *NR\_028425* (**d**), *Neat1* (**e**), *Xist* (**f**), and *NXF1-IR* (**g**) transcripts. In **c**, two mouse regions homologous to regions E and M in human *Malat1* are shown with thick blue lines. In **f**, only minus-strand tracks are shown. The plus-strand tracks for *Tsix*, which is transcribed in the antisense direction to *Xist* RNA, are shown in Extended Data Fig. 6c. The locations of different repeats in *Xist* are shown as thick blue lines. In **g**, multiple

strong U1-recognition sites are clustered in the 162-nucleotide *NXF1*-enChr (highlighted by dashed boxes) and nearby sequences. U1 snRNP also binds strongly (roughly 70-fold maximal enrichment versus the input) to this region, with peak signals that are centred at the 7-nucleotide U1 motif revealed by mutREL-seq (Fig. 1a), providing evidence for direct interactions of *NXF1*-enChr RNA and U1 snRNP in vivo. The predicted strong or medium U1-recognition sites are shown underneath the *NXF1* gene annotation. RNA-seq signals of U1 RAP–RNA with formaldehyde (FA) or 4'-aminomethyltrioxalen (AMT) crosslinking and respective input controls are also shown. AMT generates interstrand crosslinks between uridine bases to detect the direct RNA–RNA interactions of highly expressed transcripts<sup>17</sup>. FA stabilizes both direct and indirect interactions of proteins and nucleotides. Also shown is the average fold change ( $\log_2$ ) of the read intensity of the chromatin fraction compared with that of the cytoplasmic fraction in inserts from AI/GFP reporters or AI reporters. Red lines represent chromatin enrichment, while green lines represent chromatin depletion, of signals.



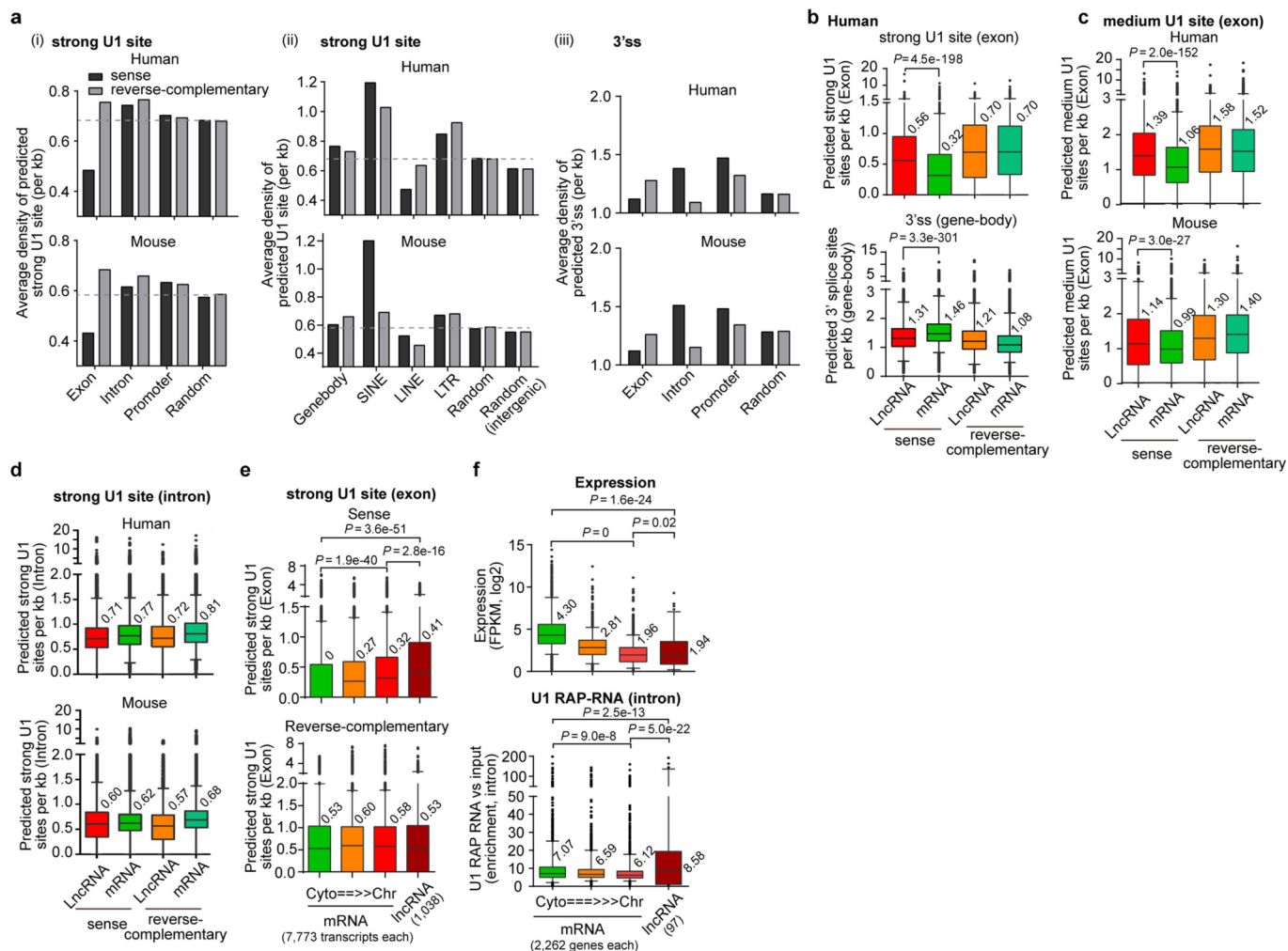
Extended Data Fig. 3 | See next page for caption.

# Article

**Extended Data Fig. 3 | Reporter assays reveal a key role of the U1 motif and U1 snRNP in RNA–chromatin association.** **a**, Diagrams showing the *GFP* reporters that we constructed and analysed here. EGFP, enhanced GFP; EV, empty vector; PAS, bovine growth hormone (BGH) polyadenylation signal; 3' *Malat1*, 3' termination sequence of *Malat1*; U1 (28-nt), a short 28-nucleotide *NXF1*-enChr sequence that encompasses two U1-recognition motifs (one strong and one weak site from position 32 to 59 in *NXF1*-enChr). The *NXF1*-enChr *GFP* reporters (PAS and 3' *Malat1*) contain the 162-nucleotide *NXF1*-enChr sequences with either a wild-type U1-recognition site or a mutated site (mutU1, vertical black line). To rule out an indirect effect of RNA degradation on its chromatin localization, we replaced the PAS with the 3' termination sequence of *Malat1*. The 3' end of *Malat1* possesses a triple-helix structure, which resembles the viral expression and nuclear retention element (ENE) and stabilizes the *Malat1* transcripts<sup>21,22</sup>. To assess the specificity of U1-mediated chromatin association, we also constructed *GFP* reporters carrying RepA alone and RepA with *NXF1*-enChr. We used two primer pairs (q1F/q1R and t1F/t1R; red arrows) to analyse the expression and potential splicing of the insert. **b**, The insertion of *NXF1*-enChr (U1) did not elicit splicing. The agarose gel picture shows PCR products amplified by primers t1F and t1R in mESCs expressing the *NXF1*-enChr (PAS) or *NXF1*-enChr-mutU1 (PAS) constructs. cDNAs were used as templates and the corresponding plasmids were used as control templates.  $n = 2$  independent experiments. **c**, Subcellular fractionation and RT–qPCR analysis of *GFP* RNA in various reporters. Endogenous expression of *ACTB* and *Malat1* serves as internal controls. **d**, GFP fluorescence imaging of mESCs expressing the EV, *NXF1*-enChr (PAS) or *NXF1*-enChr-mutU1 (PAS) constructs shown in **a**. GFP fluorescence is much weaker in cells expressing the *NXF1*-enChr-PAS construct.  $n = 4$  independent experiments. **e**, RT–qPCR analysis of chromatin/cytosol ratios (top) and relative expression (bottom) of *GFP* RNA in mESCs. The relative chromatin/cytosol ratio was normalized to a spike-in RNA that was prepared by in vitro transcription. Data shown as mean  $\pm$  s.e.m.;  $n = 2$  biological replicates. **f**, RT–qPCR analysis of the chromatin/non-chromatin ratio (i) and relative expression (ii) of *GFP* RNA in human HEK 293T and Hela cells. Similar results to those shown in **e** were observed in human cells, suggesting a conserved U1-based mechanism in humans and mice. **g**, Additive effect of

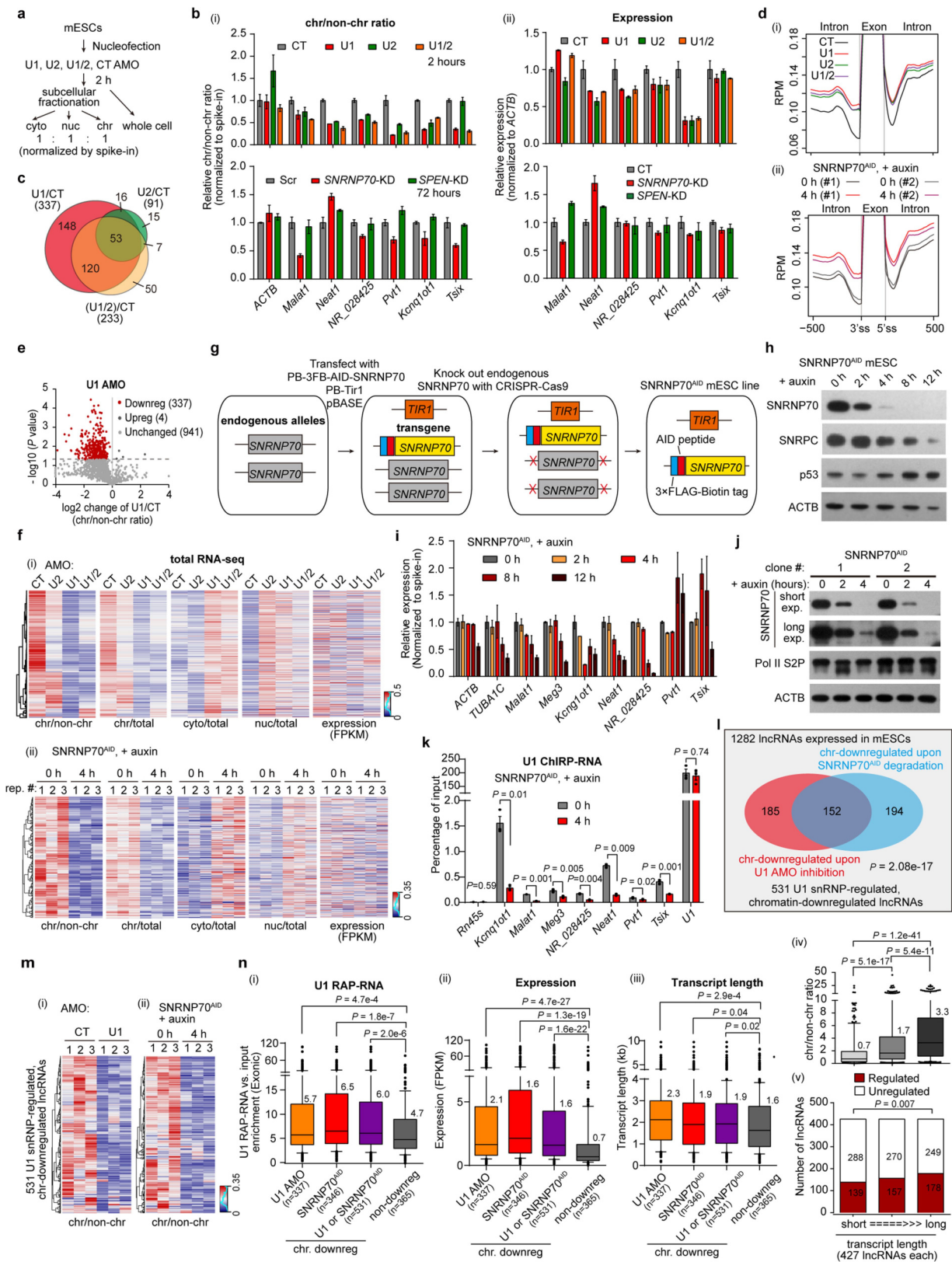
multiple enChrs in promoting RNA–chromatin association. The RepA-*NXF1*-enChr reporter exhibited significantly higher chromatin enrichment than RepA or *NXF1*-enChr alone. In **f**, **g**, data are shown as mean  $\pm$  s.e.m.;  $P$ -values obtained by two-sided  $t$ -test with three biological replicates. **h**, Representative proteins identified by *NXF1*-enChr RNA pull-down assay. The mass-spectrometry scores of proteins identified by *NXF1*-enChr and *NXF1*-enChr-as RNA pull-down are shown, together with their fold enrichment in the *NXF1*-enChr sample relative to the antisense control (enChr-as). Sm proteins are general components of snRNPs that bind snRNAs. **i**, Western blot confirming the specific interaction between SNRNP70 and *NXF1*-enChr. Controls were the antisense sequence and the sequence with a deletion of the strong U1-recognition site ( $\Delta$ U1).  $n = 3$  independent experiments. **j**, RNAi in mESCs harbouring the *NXF1*-enChr (PAS) GFP reporter. Depletion, using short hairpin RNA (shRNA) knockdown (KD) of the three core components of U1 snRNP (*SNRNP70*, *SNRPA* and *SNRPC*), but not of *SPEN* or splicing regulators (*RBM6*, *U2AF1/2* and *SF3A2*), led to 2.5–4.5-fold increases in GFP signals analysed by FACS. **k**, Knockdown efficiency of *SNRNP70* using two shRNAs in mESCs. Top, RT–qPCR, mean  $\pm$  s.e.m.; bottom, western blot.  $n = 2$  independent experiments. **l**, **m**, RT–qPCR analysis of the chromatin/cytosol ratio (top) and relative expression (bottom panel) of *GFP* RNA in mESCs after knocking down *SNRNP70* (**l**) or *SPEN* (**m**) in mESCs expressing the *NXF1*-enChr-U1 reporter or RepA-*GFP* reporter. Means  $\pm$  s.e.m. are shown.  $n = 2$  biological replicates. Scr, scrambled control shRNA. **n**, Mutation analysis of the 5' and 3' splice sites using a *GFP* reporter carrying the intron-3 sequence of *ACTB*. **i**, The mutation scheme. **ii**, RT–qPCR analysis of relative chromatin/non-chromatin ratios (left) and expression (right) of *GFP* RNA in mESCs expressing different constructs. **iii**, PCR bands of spliced and unspliced transcripts. Splicing was abolished in the 3'ss and 5'+3'ss mutants. Splicing was detected in the 5'ss mutant reporter (red asterisk) owing to the presence of an alternative 5'ss downstream of the mutated site. **iv**, Results of sequencing PCR fragments of the 5'ss mutant reporter. Data are shown as mean  $\pm$  s.e.m., and include three biological replicates.  $P$ -values obtained from two-sided  $t$ -test. See also Supplementary Notes 3 and 4. For gel source data, see Supplementary Fig. 1.





**Extended Data Fig. 4 | Differential distributions of U1-recognition sites and 3' splice sites in mRNA and lncRNA genes.** **a**, Average density of predicted strong U1-recognition sites in genic regions (i) and repeat elements (ii), and average density of predicted 3'ss in genic regions (iii), in humans (top panels) and mice (bottom panels). Random sequences, random intergenic sequences, and reverse-complementary sequences serve as controls for the background. LINE and SINE, long and short interspersed nuclear elements; LTR, long terminal repeat. **b**, Comparison of the density of predicted strong U1-recognition sites in the reverse-complementary strand of exons (top) and of 3'ss in the gene-body region (bottom) of lncRNAs (U1 site,  $n = 4,731$ ; 3'ss,  $n = 21,512$ ) and mRNA genes (U1 site,  $n = 68,881$ ; 3'ss,  $n = 139,458$ ) in humans. Only genes with transcript lengths (for U1 site) or genomic lengths (for 3'ss) larger than 1 kilobase were analysed. **c**, Densities of predicted medium-strength U1-recognition sites in exons of lncRNAs and mRNA genes in humans (top; lncRNA,  $n = 4,731$ ; mRNA,  $n = 68,881$ ) and mice (bottom; lncRNA,  $n = 3,385$ ;

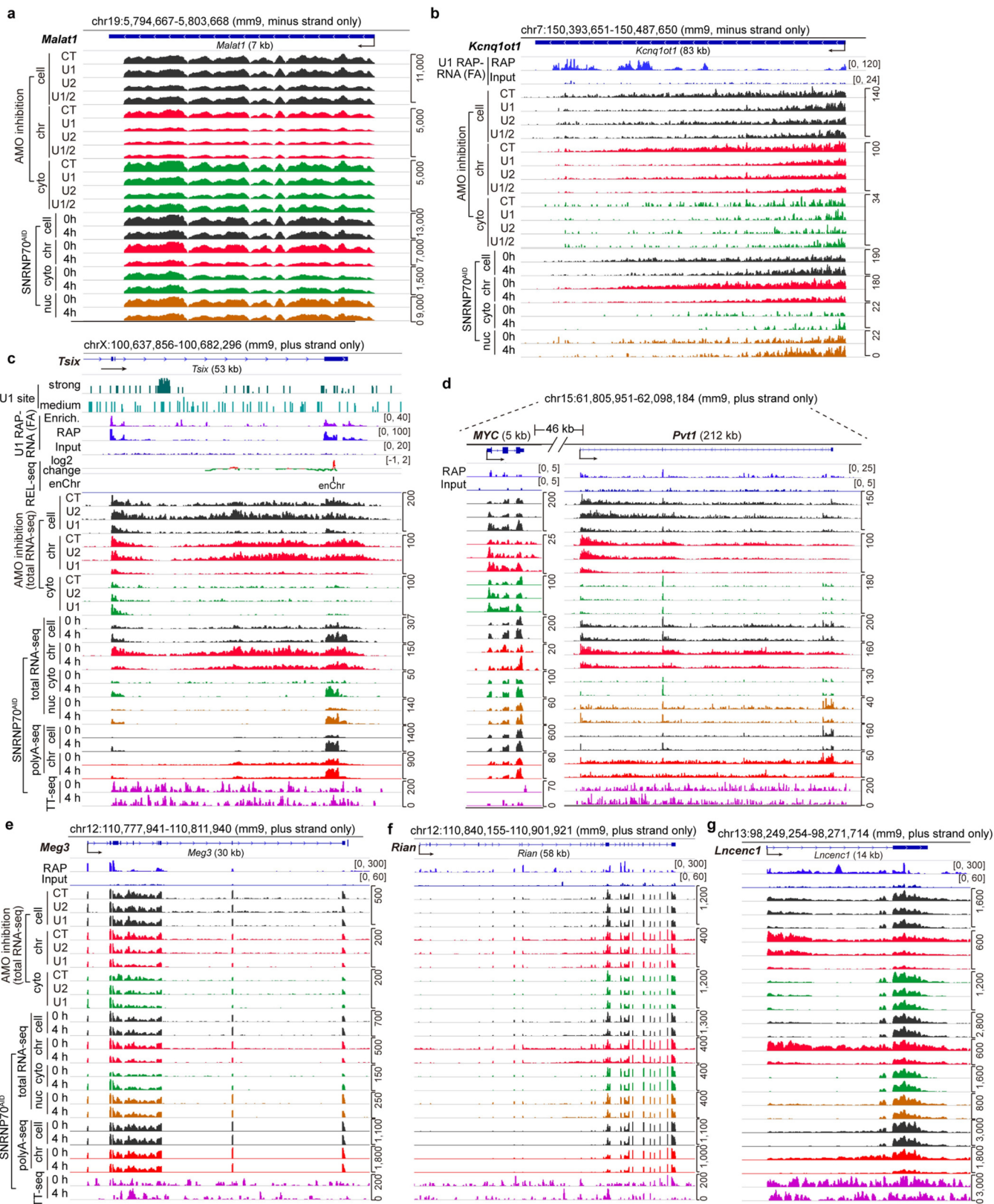
mRNA,  $n = 47,298$ ). Transcripts with total exon lengths of more than 1,000 nucleotides were analysed. **d**, Densities of predicted strong U1-recognition sites in introns of lncRNA and mRNA genes in humans (top; lncRNA,  $n = 15,885$ ; mRNA,  $n = 130,431$ ) and mice (bottom; lncRNA,  $n = 6,467$ ; mRNA,  $n = 72,688$ ). **e**, Densities of predicted strong U1-recognition sites in the sense strand (top) and reverse-complementary strand (bottom) of mRNA with different levels of chromatin-binding activity ( $n = 7,773$  each) and lncRNA ( $n = 1,038$ ) transcripts (from low to high: green, low; orange, moderate; red, high; dark red, lncRNA). **f**, Comparison of expression (top) and fold enrichment of U1 RAP-RNA signals in introns (bottom) in mRNA genes ( $n = 2,262$  each group) and lncRNAs ( $n = 97$ ) with different levels of chromatin binding. LncRNAs that show detectable expression (FPKM values greater than 1) and no overlap with protein-coding genes were used. In **b-f**,  $P$ -values are based on two-sided  $t$ -tests. Box plots show 5th, 25th, 50th, 75th and 95th percentiles, with median values labelled by the box plots.



Extended Data Fig. 5 | See next page for caption.

**Extended Data Fig. 5 | U1 snRNP regulates the chromatin retention of lncRNAs.** **a**, Scheme illustrating inhibition of U1 and/or U2 snRNA by AMO nucleofection followed by strand-specific RNA-seq analysis of total RNAs isolated from whole cells and from three subcellular fractions: cytoplasm (cyto), nucleoplasm (nuc) and chromatin (chr). CT, scramble control AMO. **b**, RT-qPCR of the chromatin/non-chromatin ratios (i) and relative expression (ii) of representative lncRNAs in mESCs after 2-h treatments with the control (CT), U1, U2 or U1/2 AMOs (upper panels), or after 72 h of knockdown with scramble (Scr), *SNRNP70* or *SPEN* shRNAs (bottom panels). (Non-chromatin refers to cytoplasm plus nucleoplasm.) Means  $\pm$  s.e.m. are shown.  $n = 2$  biological replicates. Consistent with inhibition of U1 snRNA, knockdown of *SNRNP70*—a core component of U1 snRNP—also led to decreased chromatin signals of individual lncRNAs. **c**, Venn diagram showing lncRNAs with decreased chromatin associations upon U1, U2 or U1/2 inhibition. Compared with U1 AMO (337), inhibition of U2 snRNA affected a smaller number (91) of lncRNAs, most of which (69) belong to U1-regulated lncRNAs. Inhibition of both U1/2 snRNA did not elicit a stronger effect than inhibition of U1 alone. Note that inhibition of both U1 and U2 used a lower concentration of U1 and U2 AMOs (50  $\mu$ M each) than the 75  $\mu$ M used to inhibit U1 alone. **d**, Metaplots of whole-cell RNA-seq reads in intron-exon junctions upon inhibition of U1 and/or U2 snRNA (i) or upon *SNRNP70*<sup>AID</sup> degradation (ii). RPM, read count per million mapped reads. **e**, Volcano plot showing the fold change ( $\log_2$ ) of the chromatin/non-chromatin ratio of lncRNAs ( $n = 1,282$ ) upon inhibition of U1 snRNA (using AMOs, 2 h).  $P$ -values obtained by two-sided  $t$ -test with three biological replicates. **f**, Heat maps showing the ratio of chromatin/non-chromatin, the ratio of each fraction versus the normalized total RNA contents, and the expression level of 337 lncRNAs with decreased chromatin association upon U1 AMO inhibition (i); or 346 chromatin-downregulated lncRNAs in total RNA-seq upon *SNRNP70*<sup>AID</sup> degradation (ii). Upon U1 AMO inhibition or *SNRNP70*<sup>AID</sup> degradation, these lncRNAs show decreased chromatin association, while their relative abundance in cytoplasmic and nucleoplasm fractions even increased. **g**, Diagram showing the construction of the *SNRNP70*<sup>AID</sup> mESC line, which expresses an AID- and FLAG-tagged *SNRNP70* (*SNRNP70*<sup>AID</sup>) in a

transgene with the two endogenous *SNRNP70* alleles inactivated. *TIRI*, DNA expressing E3 ligase for the AID system. **h**, **i**, Time-course expression analysis by western blot (**h**) and by RT-qPCR (**i**) in *SNRNP70*<sup>AID</sup> mESCs upon addition of auxin for 0–12 h.  $n = 2$  independent experiments. For panel **i**, means  $\pm$  s.e.m. are shown. RNA expression was normalized by a *lacZ* spike-in that was added into the same numbers of cells. At 4 h of auxin treatment, the expression of p53 protein and the RNA transcripts analysed exhibited modest changes compared to the changes after 8–12 h. **j**, Auxin-induced rapid degradation of *SNRNP70*<sup>AID</sup> did not affect the phosphorylation of Pol II at Ser 2 (S2P). ACTB serves as a loading control.  $n = 3$  independent experiments. **k**, RT-qPCR analysis showing enrichments of candidate lncRNAs captured by U1 ChIRP before (0 h) and after (4 h) *SNRNP70*<sup>AID</sup> depletion. U1 binding to its target candidate lncRNAs was severely impaired in auxin-treated mESCs (4 h), indicating that the function of U1 snRNA requires an intact snRNP complex. Data shown as mean  $\pm$  s.e.m., from three biological replicates.  $P$ -values obtained by two-sided  $t$ -test. **l**, The overlap of a total of 531 U1-snRNP-regulated, chromatin-downregulated lncRNAs from U1 AMO inhibition (red) or *SNRNP70*<sup>AID</sup> degradation (blue).  $P$ -values obtained by exact hypergeometric probability. **m**, Heat map showing changes of the chromatin/non-chromatin ratio upon U1 AMO inhibition (i) or degradation of *SNRNP70*<sup>AID</sup> (ii) for the set of 531 U1-snRNP-regulated, chromatin-downregulated lncRNAs shown in **l**. The patterns of chromatin/non-chromatin ratio changes are highly similar for both treatments. **n**, Analysis of U1 RAP-RNA signals (i), expression levels (FPKM) (ii) and transcript lengths (iii–v) in the various sets of lncRNAs shown in **l**. Box plots show 5th, 25th, 50th, 75th and 95th percentiles, with median values labelled by the box plots and sample sizes ( $n \geq 337$ ) labelled on the  $x$  axis. We further divided mESC-expressed lncRNAs into three groups on the basis of their transcript length (from shortest to longest). iv, v, The chromatin/non-chromatin ratio of total RNA-seq (iv) and the numbers of U1-snRNP-regulated and unregulated lncRNAs (v) in each group ( $n = 427$ ). Longer lncRNAs appear to exhibit stronger chromatin retention and to be preferentially affected upon *SNRNP70*<sup>AID</sup> degradation.  $P$ -values obtained by two-sided Mann-Whitney test for i–iv, one-sided Fisher's exact test for v. For gel source data, see Supplementary Fig. 1.

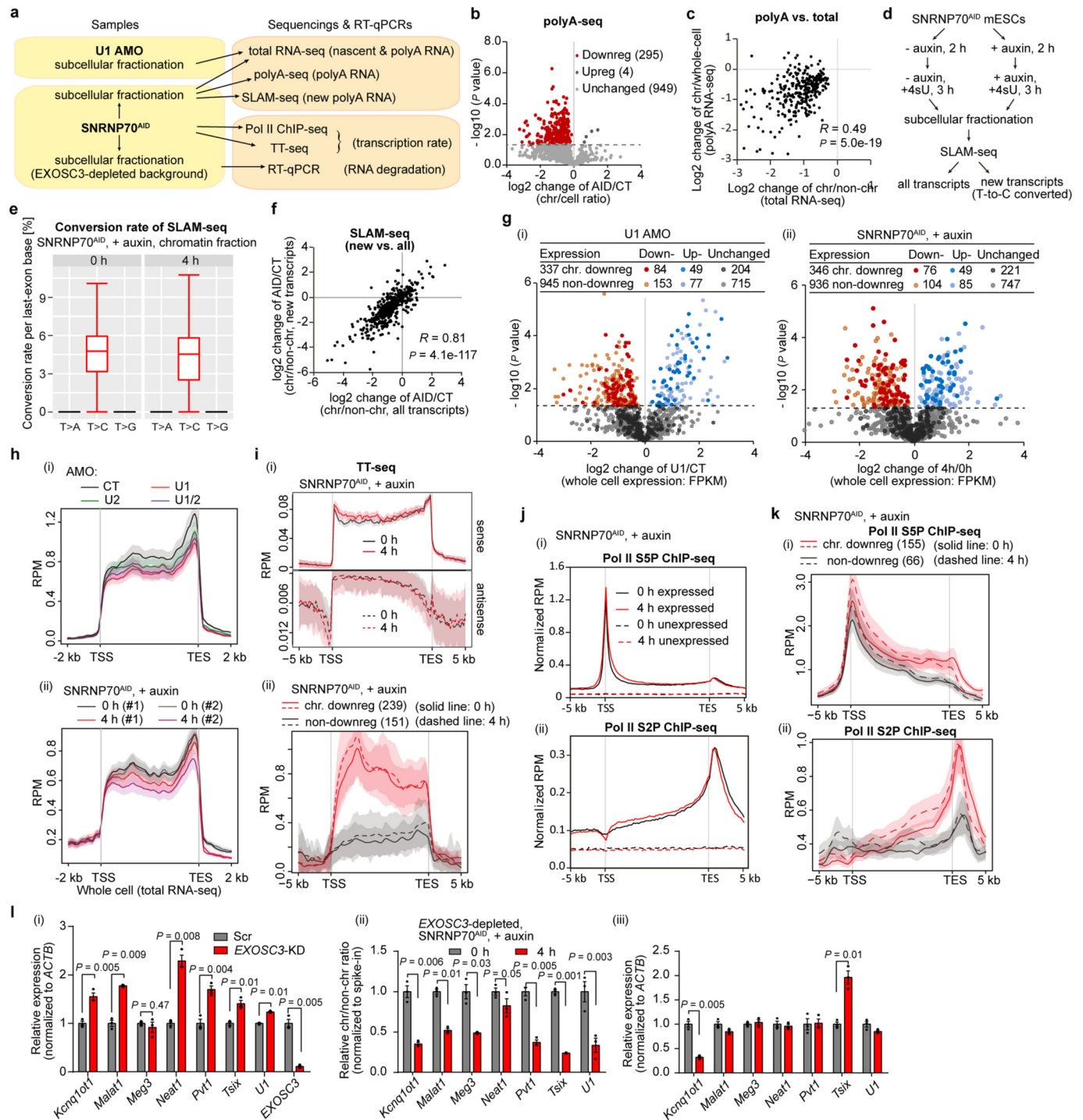


**Extended Data Fig. 6 |** See next page for caption.

**Extended Data Fig. 6 | Sequencing tracks of representative lncRNA and mRNA genes.** **a**, *Malat1*. **b**, *Kcnq1ot1*. **c**, *Tsix*. **d**, *Pvt1* and its upstream protein-coding gene, *MYC*. **e**, *Meg3*. **f**, *Rian*. **g**, *Lncenc1*. In the *Tsix* locus (**c**), the top three sets of tracks show the predicted U1-recognition sites (strong or medium, indicated by blue vertical lines), U1 RAP–RNA-seq with formaldehyde (FA) crosslinking (including enrichment ratio, reads signals of U1 RAP and the input control), and the REL-seq result. The lower two sets of tracks show total RNA-seq after AMO treatments, and total and polyA RNA-seq and TT-seq of SNRNP70<sup>ΔID</sup> mESCs at 0 h or 4 h of auxin treatment. Total RNA-seq analysis revealed decreased chromatin levels of *Tsix* transcripts after inhibition of U1 snRNA or degradation of SNRNP70<sup>ΔID</sup>. Intriguingly, polyA-seq showed a more dramatic increase of polyadenylated *Tsix* transcripts in the whole-cell sample compared with that in the chromatin fraction upon SNRNP70<sup>ΔID</sup> degradation. Coincidentally, an U1-associated enChr (black vertical line) was identified by REL-seq at roughly 2.2 kb upstream of the annotated transcription end site

(TES) of *Tsix*. In addition, strong binding of U1 snRNA was detected extensively across the whole exon at the 3' end of *Tsix*. Thus, U1 snRNP may inhibit the PAS of *Tsix* to promote its degradation and chromatin retention. Inhibition of U1 snRNP by degradation of SNRNP70<sup>ΔID</sup> thus appears to enhance polyadenylation, stability and nuclear export of *Tsix*, leading to the observed increases of polyA RNA in both whole-cell and chromatin fractions. Nevertheless, the chromatin/whole-cell ratio of polyA *Tsix* still decreases after SNRNP70<sup>ΔID</sup> degradation. Two well spliced lncRNAs *Meg3* (**e**) and *Rian* (**f**) show few intronic signals in both total and polyA RNA-seq. In **d–g**, U1 RAP–RNA-seq (FA), total RNA-seq after AMO treatments, and total and polyA RNA-seq and TT-seq tracks of SNRNP70<sup>ΔID</sup> mESCs at 0 h or 4 h auxin treatment are shown. Some very large lncRNAs—such as *Kcnq1ot1* (**b**, 83.4 kb in the genome sequence), *Tsix* (**c**, 53.4 kb) and *Pvt1* (**d**, 213 kb)—show decreased RNA signals in the downstream gene body upon U1 AMO treatment; however, this effect was less obvious in SNRNP70<sup>ΔID</sup> mESCs.

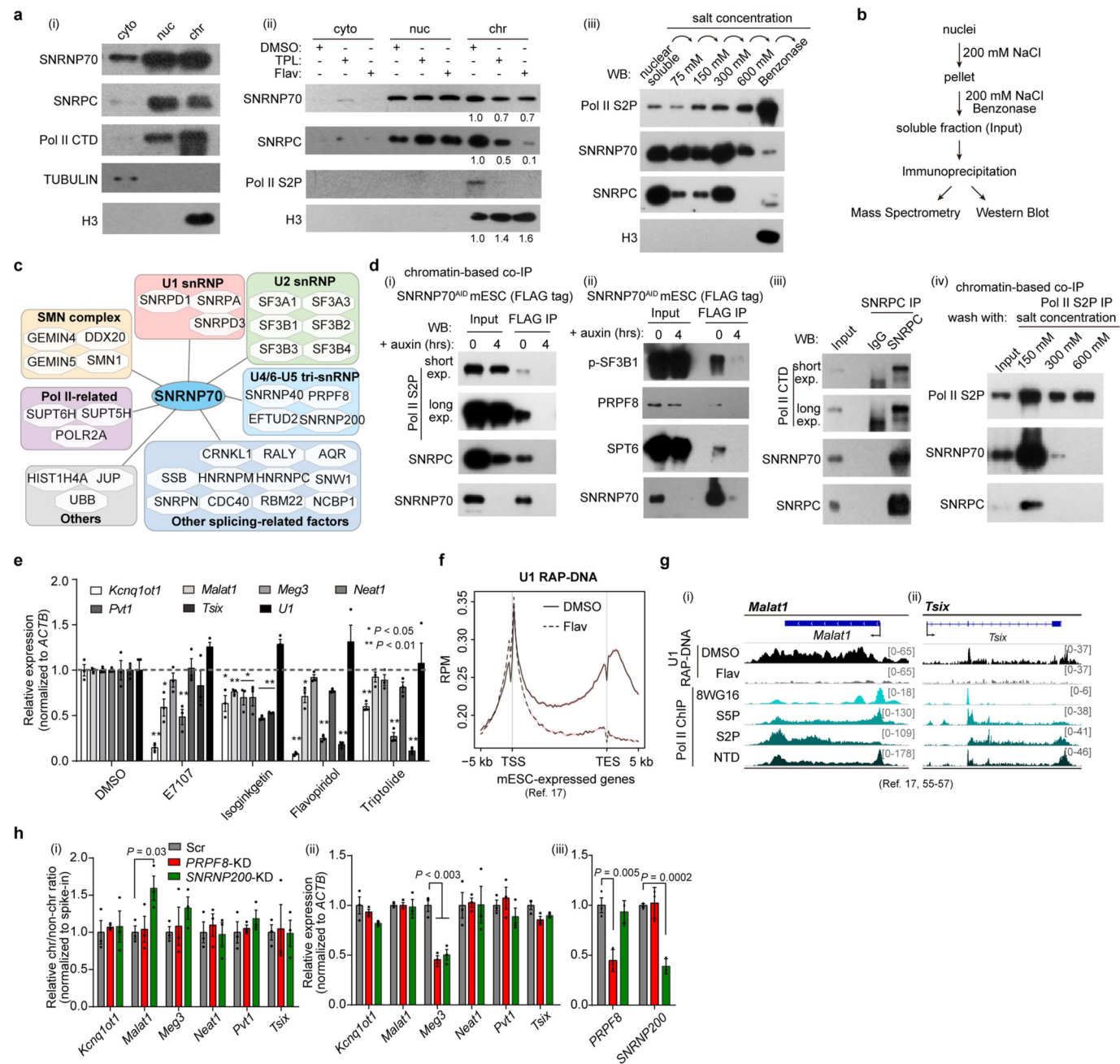




Extended Data Fig. 7 | See next page for caption.

**Extended Data Fig. 7 | Analysis of the direct causality of U1 snRNP in regulating lncRNA–chromatin retention.** **a**, Summary of experiments that we carried out to systematically investigate the effects of acute inhibition of U1 snRNP on lncRNA–chromatin associations, transcription dynamics, and RNA processing and decay. **b**, Volcano plot of polyA RNA-seq showing the fold change ( $\log_2$ ) in the chromatin/whole-cell ratio of lncRNAs upon SNRNP70<sup>AID</sup> degradation. Red dots and deep grey dots indicate lncRNAs that show a significant decrease or increase, respectively, in their chromatin/cell ratio by comparing SNRNP70<sup>AID</sup> (4-h auxin treatment) versus control (0 h) ( $P < 0.05$ ; two-sided  $t$ -test with three biological replicates). **c**, Correlation plot of polyA and total RNA-seq analysis of SNRNP70<sup>AID</sup> mESCs. The set of chromatin-downregulated lncRNAs shows significantly correlated changes in chromatin localization upon degradation of SNRNP70<sup>AID</sup> ( $n = 346$ ). **d**, SLAM-seq analysis of chromatin and non-chromatin (cytoplasm and nucleoplasm) fractions in SNRNP70<sup>AID</sup> mESCs. SNRNP70<sup>AID</sup> mESCs were treated with or without auxin for 2 h and then labelled with 4sU for 3 h. After chemical conversion of the incorporated 4sU nucleotides to cytidine, RNA from various subcellular fractions was isolated for 3'-end polyA-seq library construction. **e**, Box plots showing the conversion rate detected by SLAM-seq of chromatin fractions in the last exon of genes with detectable new transcript ( $n = 24,097$ ) before (0 h) and after (4 h) SNRNP70<sup>AID</sup> degradation. Box plots show 5th, 25th, 50th, 75th and 95th percentiles. **f**, Pearson correlation analysis of the change in chromatin/non-chromatin ratio for new versus all transcripts of lncRNAs with detectable new transcripts ( $n = 492$ ) identified by SLAM-seq. **g**, Volcano plots showing expression changes of mESC-expressed lncRNAs ( $n = 1,282$ ) after treatment with U1AMO (i) or degradation of SNRNP70<sup>AID</sup> (ii). Chromatin-downregulated or non-downregulated lncRNAs were further classified into 'downregulated (down-)', 'upregulated (up-)' or 'unchanged' according to their expression changes in whole-cell samples. lncRNAs with reduced chromatin association upon inhibition of U1 snRNA or SNRNP70<sup>AID</sup> do not show greater downregulated expression by comparison with all lncRNAs. Only a small proportion of them (84 of 337 U1-regulated and 76 of 346 SNRNP70-regulated) show decreased transcript levels.  $P$ -values obtained by two-sided  $t$ -test;  $n = 3$  biological replicates. **h**, Metagene analysis of whole-cell RNA-seq reads for the

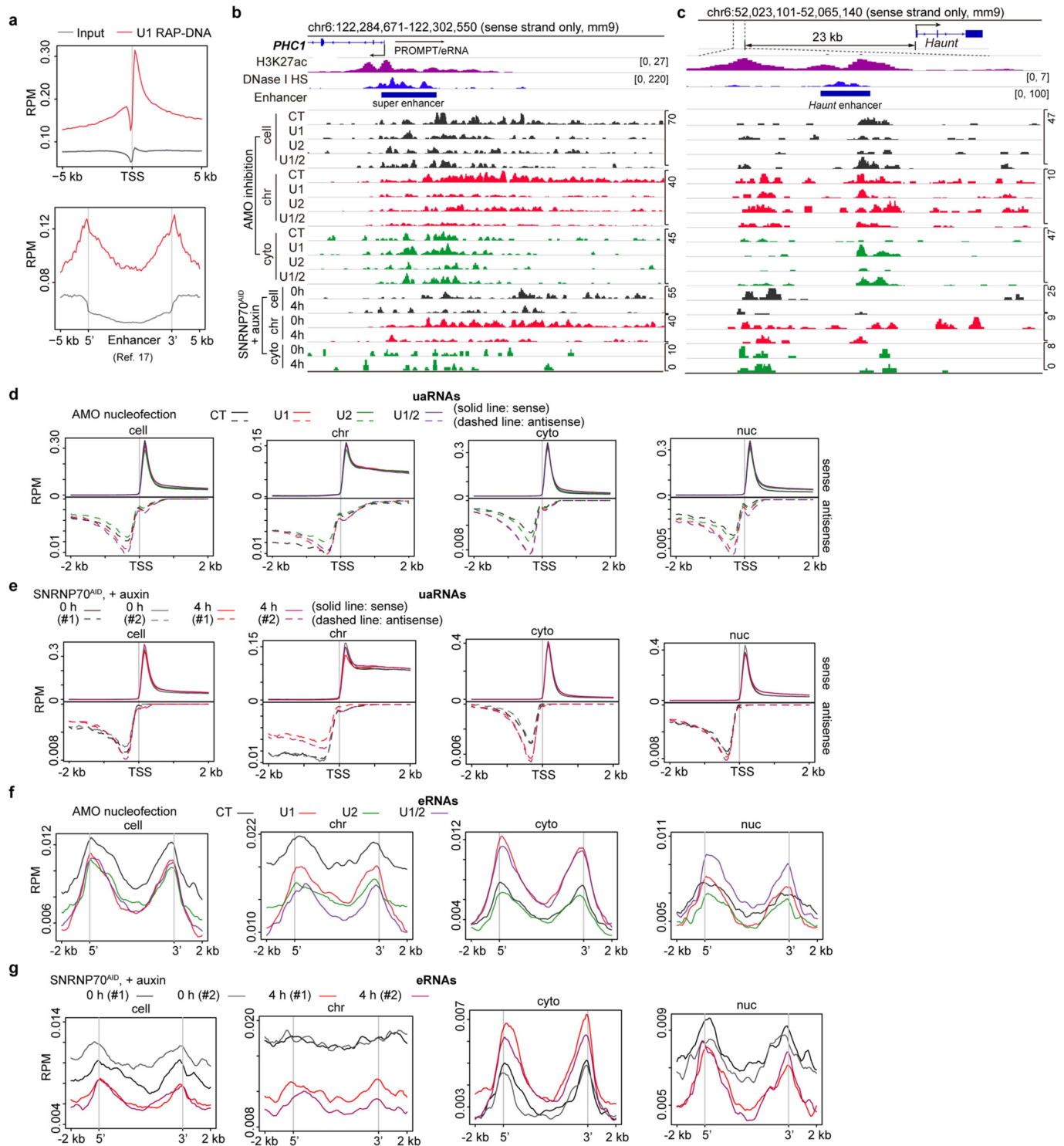
set of U1-snRNP-regulated, chromatin-downregulated lncRNAs in mESCs. Only lncRNAs that do not overlap with any protein-coding gene on the same strand were analysed ( $n = 239$ ). Similar read-distribution patterns were observed in control cells and in cells treated with U1, U2 or U1/U2 AMOs (i) or in cells subjected to auxin-induced degradation of SNRNP70<sup>AID</sup> for 0 h or 4 h (ii). Thus, rapid inhibition of U1 snRNP did not cause global transcription termination, although we did observe decreased downstream RNA signals in a few very long lncRNAs, such as *Kcnq1ot1* (83 kb), in agreement with the proposed role of U1 telescripting in protecting the transcription integrity of very large transcripts<sup>25</sup>. In addition, we conjecture that the slight decreases in total transcript levels are likely to be post-transcriptionally mediated by RNA degradation instead of an effect of U1 inhibition on nascent transcription (see panels **i–k** below). **i**, Metagene analysis of TT-seq signals in all mESC-expressed genes ( $n = 10,675$ ) (i) and chromatin-downregulated ( $n = 239$ ) and non-downregulated lncRNAs ( $n = 151$ ) (ii) upon SNRNP70<sup>AID</sup> degradation. Only lncRNAs that do not overlap with any protein-coding gene on the same strand were analysed. **j, k**, Metagene analysis of ChIP-seq signals of Pol II S5P ('paused' Pol II; i) and S2P ('elongating' Pol II; ii) across the gene body and upstream/downstream 5-kb region of all mESC-expressed genes ( $n = 10,675$ ) and unexpressed genes ( $n = 7,933$ ) (**j**) or chromatin-downregulated ( $n = 155$ ) and non-downregulated ( $n = 66$ ) lncRNAs upon SNRNP70<sup>AID</sup> degradation (**k**). Only lncRNAs that do not overlap with any protein-coding gene on either strand were analysed. For **h–k**, shadings represent 95% confidence intervals for the average enrichment. **l**, RT-qPCR analysis of the knockdown efficiency and lncRNA expression level change (i), chromatin/non-chromatin ratio (ii) and relative expression (iii) in SNRNP70<sup>AID</sup> mESCs depleted of *EXOSC3* by RNA inhibition. Knockdown was analysed at 72 h after shRNA viral infection. The observation of increased expression for most lncRNAs analysed is consistent with a role of *EXOSC3* in mediating RNA degradation (i). Knockdown of *EXOSC3* blocked RNA degradation for most lncRNAs analysed (iii), but failed to rescue their decreased chromatin associations induced by auxin (ii). Thus, the effect of U1 snRNP in promoting lncRNA-chromatin binding is not caused by increased RNA degradation. Means  $\pm$  s.e.m. are shown;  $P$ -values obtained by two-sided  $t$ -test for three biological replicates.



Extended Data Fig. 8 | See next page for caption.

**Extended Data Fig. 8 | U1 snRNP regulates lncRNA–chromatin association through its interaction with transcriptionally engaged Pol II.** **a**, Western blots of SNRNP70, SNRPC, Pol II and marker proteins with no treatment (i), or treated with DMSO, triptolide (TPL), or flavopiridol (Flav) for 1 h (ii), or in nuclear fractions sequentially extracted with increasing concentrations of salt (NaCl) (iii). For i, iii,  $n = 3$  independent experiments, for ii,  $n = 2$  independent experiments. **b**, Scheme for co-immunoprecipitation of the chromatin fraction. Benzonase was used to digest all DNA and RNA and to elute proteins from chromatin. **c**, Proteins captured by SNRNP70 coIP-SILAC. Native chromatin extracts that were released by benzonase were subjected to anti-FLAG co-immunoprecipitation of SNRNP70<sup>AID</sup> protein (FLAG-tagged) coupled with stable-isotope labelling by amino acids in cell culture, followed by mass spectrometry. SNRNP70 purification captured the U1 and U2 snRNPs, as well as several components of the U4/6-U5 snRNPs and other splicing factors. Notably, the SNRNP70 interactome also identified proteins involved in transcription regulation, such as POLR2A, SPT5 and SPT6. **d**, Chromatin-based co-immunoprecipitation (in the presence of benzonase) and western blot analysis confirming the interactions between U1 snRNP and the proteins identified in **c**. Panels i, ii show co-immunoprecipitation of FLAG-tagged SNRNP70<sup>AID</sup> protein. SNRNP70<sup>AID</sup> mESCs treated with auxin for 4 h serve as the negative control. Panel iii shows that co-immunoprecipitation of endogenous SNRPC captured

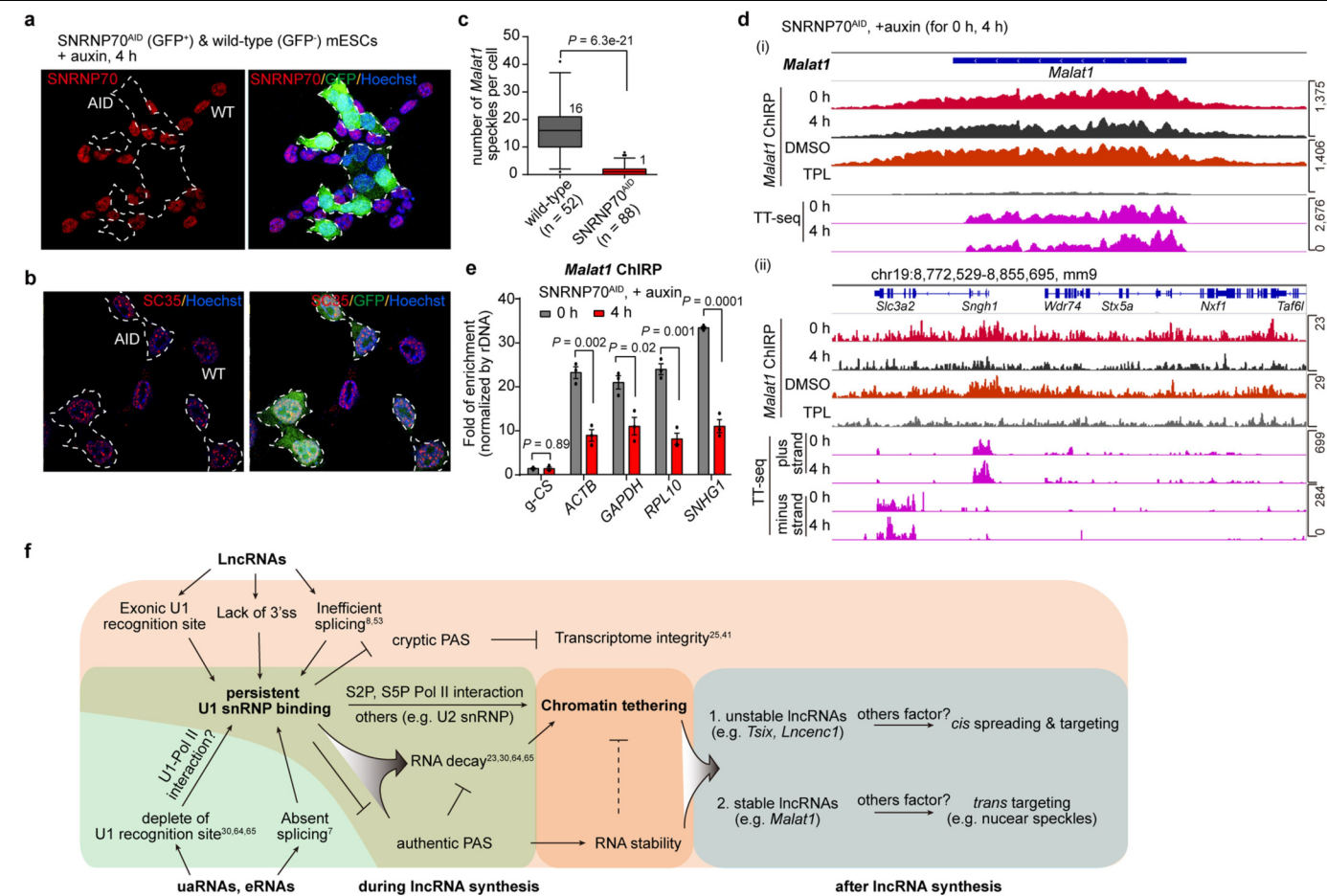
the total Pol II. Panel iv shows that co-immunoprecipitation of Pol II S2P captured SNRNP70 under a physiological salt condition (150 mM) but not in high-salt conditions, suggesting dynamic associations between U1 snRNP and engaged Pol II.  $n = 3$  independent experiments. **e**, RT-qPCR analysis of the expression of representative lncRNAs and U1 snRNA upon treatment with DMSO (control), 1  $\mu$ M with E7107 (inhibitor of U2 snRNP), 1  $\mu$ M of flavopiridol (transcription inhibitor) or 1  $\mu$ M of triptolide (transcription inhibitor) for 1 h, or with 100  $\mu$ M of isoginkgetin (inhibitor of U4/6-U5 snRNP) for 2 h. Means  $\pm$  s.e.m. are shown;  $P$ -values obtained by two-sided  $t$ -test with three biological replicates. **f**, Metagene analysis of U1 RAP–DNA-seq signals for all *Ensembl* genes in mESCs treated with DMSO or with flavopiridol (Flav) for 1 h. Flavopiridol treatment led to reduced U1 RAP–DNA signals downstream of the TSS across the gene body. Red shading represents 95% confidence intervals for the average enrichment. **g**, Genome-browser views of U1 RAP–DNA-seq and Pol II ChIP-seq at the *Malat1* and *Tsix* loci. 8WG16, hypophosphorylated Pol II; NTD, N-terminal domain of Pol II, representing the total Pol II. **h**, Relative chromatin/non-chromatin ratio (i), expression-level change of representative lncRNAs (ii) and knockdown efficiency of targeted genes (iii) after mESCs were treated with *PRPF8* or *SNRNP200* shRNAs for 72 h. Means  $\pm$  s.e.m. are shown;  $P$ -values obtained by two-sided  $t$ -test with three biological replicates. For gel source data, see Supplementary Fig. 1.



**Extended Data Fig. 9 | Inhibition of U1 and U2 snRNPs downregulates the chromatin association of uaRNAs and eRNAs.** **a**, Metaplots of U1 RAP-DNA-seq, showing enrichment of U1 snRNA in the chromatin proximity of regulatory DNA sequences. The top panel shows a  $\pm 5$ -kb window flanking TSSs of *Ensembl* genes that do not overlap with any other gene within 2 kb ( $n=18,972$ ), and the bottom panel shows a  $\pm 5$ -kb window flanking enhancers that do not overlap with a gene within 2 kb ( $n=3,767$ ). **b**, **c**, Sequencing tracks showing chromatin and cytoplasmic RNA-seq signals of uaRNAs/eRNAs in the *PHC1* promoter (**b**) and *Haunt* enhancer (**c**). **d**, **e**, Metaplots of RNA-seq reads of uaRNAs from whole cells and subcellular fractions in AMO-treated samples (**d**) and

SNRNP70<sup>AID</sup>-degraded samples (**e**) in a  $\pm 2$ -kb window flanking the TSSs of *Ensembl* genes that do not overlap with any other gene within 2 kb ( $n=18,972$ ). The uaRNAs show upregulated overall expression and more dramatic increases in the cytoplasmic and nucleoplasmic fractions after U1 or U1/2 inhibition, while there are comparable (U1 AMO) or slightly decreased (U1/2 AMO) uaRNA signals in the chromatin fraction at the TSS-to-1-kb upstream region. **f**, **g**, Metaplots of RNA-seq reads of eRNAs from whole cells and subcellular fractions in AMO-treated samples (**f**) and SNRNP70<sup>AID</sup>-degraded samples (**g**) in a  $\pm 2$ -kb window flanking enhancers that do not overlap with any gene within 2 kb ( $n=3,767$ ).





# **Extended Data Fig. 10 | U1 snRNP tethers and mobilizes lncRNAs to**

**chromatin.** **a, b**, Immunofluorescence analysis of SNRNP70 (**a**) and SC35 (**b**) in auxin-treated SNRNP70<sup>AID</sup> and wild-type mESCs. SNRNP70<sup>AID</sup> ESCs marked by stably integrated *GFP* transgenes (GFP<sup>+</sup>, highlighted with dashed white lines) and GFP-negative wild-type mESCs (GFP<sup>-</sup>) were mixed and treated with auxin for 4 h.  $n = 3$  independent experiments. **c**, Quantification of the numbers of *Malat1* speckles (equivalent diameter greater than 0.5  $\mu\text{m}$ ) identified by RNA FISH (Fig. 3c). Box plots show 5th, 25th, 50th, 75th and 95th percentiles, with median values labelled by the plots and sample sizes (wild type,  $n = 52$ ; SNRNP70<sup>AID</sup>,  $n = 88$ ) labelled on the x axis.  $P$ -values obtained by two-sided Mann-Whitney test. **d**, Sequencing tracks of *Malat1* ChIP-DNA-seq and TT-seq in *Malat1* (i) and representative loci that are targeted by *Malat1* (ii). In both panels, the top set of tracks show *Malat1* ChIP-seq upon SNRNP70<sup>AID</sup> degradation (at 0 h and 4 h) or upon treatment with DMSO control or triptolide (TPL). The bottom set of tracks show TT-seq upon SNRNP70<sup>AID</sup> degradation (at 0 h and 4 h). In panel ii, TT-seq signals on both plus and minus strands are shown. We used the mm9 mouse genome assembly. **e**, qPCR analysis of *Malat1* ChIP-DNA of SNRNP70<sup>AID</sup> mESCs before (0 h) and after (4 h) treatment with auxin. Data are shown as mean  $\pm$  s.e.m., for three biological replicates.  $P$ -values obtained by two-sided  $t$ -test. **f**, Mechanistic representation of U1 snRNP and its interplay with Pol II and PASs in regulating the tethering and mobilization of noncoding RNA on chromatin. Notably, lncRNAs, uaRNAs and eRNAs share many features, including chromatin association, inefficient or absent splicing and polyadenylation, low-level expression and short half-lives<sup>7,8,42,53,63</sup>. lncRNAs in general are enriched with 5' U1-recognition sites but depleted of 3' splice sites. For uaRNAs and eRNAs, U1 binding on chromatin is enriched at enhancer DNA sequences and TSSs (the 5' end of uaRNAs), even though U1-recognition

sites are depleted in uaRNA DNA sequences<sup>17,30,64,65</sup>. U1 snRNP may bind uaRNAs and eRNAs through co-transcriptional U1–Pol II interactions. Splicing releases the U1 snRNP from pre-mRNAs<sup>18</sup>. However, lncRNAs, uaRNA and eRNAs remain associated with U1 snRNPs because of inefficient or absent splicing (the lack of 3' ss could be one reason)<sup>8,53</sup>. Through its interaction with transcriptionally engaged Pol II, U1 snRNP is tethered to chromatin and subsequently retains its associated lncRNAs and ncRNAs on chromatin. Meanwhile, the inhibitory function of U1 snRNP on polyadenylation promotes transcription elongation at cryptic PASs and RNA decay at authentic PASs<sup>23,25,30,41,65</sup>. Rapid RNA turnover renders these transcripts less likely to leave the chromatin, contributing in part to their enrichment on chromatin and lack of nuclear export. Although the properties of chromatin binding and instability appear to be intrinsically coupled for lncRNAs and chromatin-bound unstable ncRNAs, U1 snRNP and the RNA-degradation machinery appear to play independent yet synergistic roles in facilitating RNA–chromatin association. Coupled chromatin association and instability of many lncRNA transcripts may contribute to the observed *cis*-targeting and regulatory functions in their chromatin neighbourhoods. Most short-lived lncRNA transcripts spread locally within their neighbourhoods, while a few stable and abundant lncRNAs, such as *Malat1*, exist long enough to be trans-targeted to other genomic sites. For stable lncRNAs, persistent binding with U1 snRNP, and perhaps engaged Pol II, may drive lncRNA mobilization to distinct nuclear compartments (such as nuclear speckles) or to thousands of *trans* genomic sites (in the case of *Malat1*). Possibly, these highly expressed lncRNAs have developed evolutionarily to take advantage of the U1-tethering mechanism to achieve *trans* functions. In addition to U1 snRNP, U2 snRNP (but not the splicing reaction), and perhaps other factors, contributes to this process.

## Reporting Summary

Nature Research wishes to improve the reproducibility of the work that we publish. This form provides structure for consistency and transparency in reporting. For further information on Nature Research policies, see [Authors & Referees](#) and the [Editorial Policy Checklist](#).

### Statistical parameters

When statistical analyses are reported, confirm that the following items are present in the relevant location (e.g. figure legend, table legend, main text, or Methods section).

n/a Confirmed

- ☐ ☒ The exact sample size ( $n$ ) for each experimental group/condition, given as a discrete number and unit of measurement
- ☐ ☒ An indication of whether measurements were taken from distinct samples or whether the same sample was measured repeatedly
- ☐ ☒ The statistical test(s) used AND whether they are one- or two-sided  
*Only common tests should be described solely by name; describe more complex techniques in the Methods section.*
- ☒ ☐ A description of all covariates tested
- ☒ ☐ A description of any assumptions or corrections, such as tests of normality and adjustment for multiple comparisons
- ☐ ☒ A full description of the statistics including central tendency (e.g. means) or other basic estimates (e.g. regression coefficient) AND variation (e.g. standard deviation) or associated estimates of uncertainty (e.g. confidence intervals)
- ☐ ☒ For null hypothesis testing, the test statistic (e.g.  $F$ ,  $t$ ,  $r$ ) with confidence intervals, effect sizes, degrees of freedom and  $P$  value noted  
*Give  $P$  values as exact values whenever suitable.*
- ☒ ☐ For Bayesian analysis, information on the choice of priors and Markov chain Monte Carlo settings
- ☒ ☐ For hierarchical and complex designs, identification of the appropriate level for tests and full reporting of outcomes
- ☐ ☒ Estimates of effect sizes (e.g. Cohen's  $d$ , Pearson's  $r$ ), indicating how they were calculated
- ☐ ☒ Clearly defined error bars  
*State explicitly what error bars represent (e.g. SD, SE, CI)*

Our web collection on [statistics for biologists](#) may be useful.

### Software and code

Policy information about [availability of computer code](#)

#### Data collection

Bio-Rad CFX384 Real Time System was used for RT-qPCR data collection. Illumina HiSeq 2500 and HiSeq X TEN were used for sequencing data collection. nikon A1RMP microscopy and related softwares were used for collecting and analyzing FISH and IF data.

#### Data analysis

For RNA-seq, REL-seq, TT-seq, and ChIP-seq data analysis, Bowtie v2.2.3, Bowtie v1.0.0, Tophat v2.0.10, Cufflink v2.1.1, BEDTools v2.17.0, macs v1.4.2 and Novoalign v3.02.05 were used. Integrative Genomics Viewer v2.3.97 were used for signal visualization of sequencing data. R studio v3.4.3, Excel 2016, and GraphPad Prism v6.0 were used for statistical analysis. FlowJo v7.6.1 was used for FACS analysis. Image J v1.8.0 was used for quantification of Western blot. "RNAfold v2.4.13 web server" (<http://rna.tbi.univie.ac.at/cgi-bin/RNAWebSuite/RNAfold.cgi>) was used for RNA secondary structure predication.

For manuscripts utilizing custom algorithms or software that are central to the research but not yet described in published literature, software must be made available to editors/reviewers upon request. We strongly encourage code deposition in a community repository (e.g. GitHub). See the Nature Research [guidelines for submitting code & software](#) for further information.

## Data

Policy information about [availability of data](#)

All manuscripts must include a [data availability statement](#). This statement should provide the following information, where applicable:

- Accession codes, unique identifiers, or web links for publicly available datasets
- A list of figures that have associated raw data
- A description of any restrictions on data availability

The main data supporting the findings of this study are available within the article and Supplementary Information files. Sequencing data have been deposited in the GEO database under the accession number GEO: GSE107131 and GSE134287, and will be available after the manuscript is formally accepted. All other data supporting the findings of this study are available from the corresponding author upon reasonable request.

## Field-specific reporting

Please select the best fit for your research. If you are not sure, read the appropriate sections before making your selection.

☒ Life sciences ☐ Behavioural & social sciences ☐ Ecological, evolutionary & environmental sciences

For a reference copy of the document with all sections, see [nature.com/authors/policies/ReportingSummary-flat.pdf](https://nature.com/authors/policies/ReportingSummary-flat.pdf)

## Life sciences study design

All studies must disclose on these points even when the disclosure is negative.

Sample size	No statistical calculations were performed to estimate sample size. For REL-seq analysis, we included eight libraries and two representative cell lines (mouse embryonic stem cells and human HEK 293T), which are sufficient for screening technologies. See methods and supplementary note 1. For RNA-seq, we included three independent biological replicates, which are sufficient for sequencing analysis. Sample size determination in RT-qPCR and other graphs were described as previous published study and experimental knowledge.
Data exclusions	No data were excluded.
Replication	All experiments were repeated (biological repeats) at least twice. All attempts of replications were successful.
Randomization	There is not any bias when harvesting samples or collecting data.
Blinding	Experiments in this study were not done blinded. The samples harvest process made it impossible to be blinded. Data were collected in parallel to minimize bias.

## Reporting for specific materials, systems and methods

### Materials & experimental systems

n/a	Involved in the study
<input type="checkbox"/>	<input checked="" type="checkbox"/> Unique biological materials
<input type="checkbox"/>	<input checked="" type="checkbox"/> Antibodies
<input type="checkbox"/>	<input checked="" type="checkbox"/> Eukaryotic cell lines
<input checked="" type="checkbox"/>	<input type="checkbox"/> Palaeontology
<input checked="" type="checkbox"/>	<input type="checkbox"/> Animals and other organisms
<input checked="" type="checkbox"/>	<input type="checkbox"/> Human research participants

### Methods

n/a	Involved in the study
<input type="checkbox"/>	<input checked="" type="checkbox"/> ChIP-seq
<input type="checkbox"/>	<input checked="" type="checkbox"/> Flow cytometry
<input checked="" type="checkbox"/>	<input type="checkbox"/> MRI-based neuroimaging

## Unique biological materials

Policy information about [availability of materials](#)

Obtaining unique materials All unique materials generated and described in this study will be provided upon reasonable request to the corresponding authors.

## Antibodies

Antibodies used	Antibodies used for IP and western blot: SNRNP70 (Santa Cruz, sc-390988, E-4, lot: D0915, 1:500); SNRPC (Abcam, ab192028, EPR16034, lot: GR180605-1, 1:5000); Histone H3 (Easybio, BE2013-100 lot:80920815, 1:10000); TUBULIN (CWBIO, CW0098M, 1:2000); ACTB (Abclonal, AC004, lot: 01270/30337, 1:5000); RNAPII CTD (Abcam, ab52202, 1:2000); Hypophosphorylated RNAPII (Covance, MMS-126R, 8WG16, 1:2000 for western blot 1:200 for IP); RNAPII Ser5P (CST, 13523, D9N5I, lot: 1, 1:5000 for western blot; 1:300 for IP and ChIP); RNAPII Ser2P for IP and western blot (CST, 13499, E1Z3G lot: 1, 1:5000 for western blot; 1:300 for IP and ChIP), RNAPII Ser2P for western blot (Covance, MMS-129R, H5, lot: 14943202, 1:1000); p53 (Abclonal, A5761, 1:1000); SNRNP200 (Abclonal, A6063, lot: 0102340101, 1:1000); PRPF8 (Sangon, D163565, lot: D163565-0025, 1:1000); p-SF3B1 (Abclonal, AP0844, lot: 2158550301, 1:2000); Spt6 (CST, 15616S, D6J9H, lot: 1, 1:2000); SC35 (abcam, ab11826, 1:500 for IF).
Validation	<p>Anti-SNRNP70 (Santa Cruz, sc-390988, E-4, lot: D0915), this antibody has been claimed to react with mouse SNRNP70 by the manufacturer. Validation data for the antibodies used can be found as follows: <a href="https://www.scbt.com/p/u1-snrnp-70-antibody-e-4">https://www.scbt.com/p/u1-snrnp-70-antibody-e-4</a>.</p> <p>Anti-SNRPC (Abcam, ab192028, EPR16034), this antibody has been claimed to react with mouse .. by the manufacturer. Validation data for the antibodies used can be found as follows: <a href="https://www.abcam.com/u1-c-antibody-epr16034-ab192028.html">https://www.abcam.com/u1-c-antibody-epr16034-ab192028.html</a>.</p> <p>Anti-Histone H3 (Easybio, BE3021-100), this antibody has been claimed to react with mouse Histone H3 by the manufacturer (<a href="http://www.bioeasytech.com/home/product/article/id/11.html">http://www.bioeasytech.com/home/product/article/id/11.html</a> ) and also confirmed by our data.</p> <p>Anti-TUBULIN (CWBIO, CW0098M), this antibody has been claimed to react with mouse TUBULIN by the manufacturer. Validation data for the antibodies used can be found as follows: <a href="https://www.cwbio.com/uploads/websitespdf/98be23fc-9451-4a27-93f6-02375421a1e5.pdf">https://www.cwbio.com/uploads/websitespdf/98be23fc-9451-4a27-93f6-02375421a1e5.pdf</a></p> <p>Anti-ACTB (Abclonal, AC004), this antibody has been claimed to react with mouse ACTB by the manufacturer. Validation data for the antibodies used can be found as follows: <a href="https://abclonal.com.cn/catalog/AC004">https://abclonal.com.cn/catalog/AC004</a>.</p> <p>Anti-RNAPII CTD (Abcam, ab52202), this antibody has been claimed to react with the CTD of mouse Polymerase II by the manufacturer. Validation data for the antibodies used can be found as follows: <a href="https://www.abcam.com/rna-polymerase-ii-ctd-repeat-ysptps-antibody-ab52202.html">https://www.abcam.com/rna-polymerase-ii-ctd-repeat-ysptps-antibody-ab52202.html</a>. This antibody has been used by Li et al, 2015 to detect Pol II by western blot, and also confirmed by our data.</p> <p>Anti-Hypophosphorylated RNAPII (Covance, MMS-126R, 8WG16), this antibody has been claimed to react with mouse Polymerase II by the manufacturer. This antibody has been used for ChIA-PET by Bertolini et al, 2019, and also confirmed by our data.</p> <p>Anti-RNAPII Ser5P (CST, 13523, D9N5I), this antibody has been claimed to react with mouse Ser5 phosphorylated Pol II by the manufacturer. Validation data for the antibodies used can be found as follows: <a href="https://www.cellsignal.com/products/primary-antibodies/phospho-rpb1-ctd-ser5-d9n5i-rabbit-mab/13523">https://www.cellsignal.com/products/primary-antibodies/phospho-rpb1-ctd-ser5-d9n5i-rabbit-mab/13523</a>. This antibody has been used by Jiang et al, 2018 for ChIP assay, and also confirmed by our data.</p> <p>Anti-RNAPII Ser2P (CST, 13499, E1Z3G), this antibody has been claimed to react with mouse Ser2 phosphorylated Pol II by the manufacturer. Validation data for the antibodies used can be found as follows: <a href="https://www.cellsignal.com/products/primary-antibodies/phospho-rpb1-ctd-ser2-e1z3g-rabbit-mab/13499">https://www.cellsignal.com/products/primary-antibodies/phospho-rpb1-ctd-ser2-e1z3g-rabbit-mab/13499</a>.</p> <p>Anti-RNAPII Ser2P (Covance, MMS-129R, H5), this antibody has been claimed to react with mouse Ser2 phosphorylated Pol II by the manufacturer. This antibody has been used for ChIP by Espinosa et al, 2003, and also confirmed by our data.</p> <p>Anti-p53 (Abclonal, A5761), this antibody has been claimed to react with mouse p53 by the manufacturer. Validation data for the antibodies used can be found as follows: <a href="https://abclonal.com.cn/catalog/A5761">https://abclonal.com.cn/catalog/A5761</a>.</p> <p>Anti-SNRNP200 (Abclonal, A6063), this antibody has been claimed to react with mouse SNRNP200 by the manufacturer. Validation data for the antibodies used can be found as follows: <a href="https://abclonal.com.cn/catalog/A6063">https://abclonal.com.cn/catalog/A6063</a>.</p> <p>Anti-PRPF8 (Sangon, D163565), this antibody has been claimed to react with mouse PRPF8 by the manufacturer. Validation data for the antibodies used can be found as follows: <a href="https://www.sangon.com/productDetail?productId=D163565">https://www.sangon.com/productDetail?productId=D163565</a>.</p> <p>Anti-p-SF3B1 (Abclonal, AP0844), this antibody has been claimed to react with mouse phosphorylated SF3B1 by the manufacturer. Validation data for the antibodies used can be found as follows: <a href="https://abclonal.com.cn/catalog/AP0844">https://abclonal.com.cn/catalog/AP0844</a>.</p> <p>Anti-SPT6 (CST, 15616S, D6J9H), this antibody has been claimed to react with mouse SPT6 by the manufacturer. Validation data for the antibodies used can be found as follows: <a href="https://www.cellsignal.com/products/primary-antibodies/spt6-d6j9h-rabbit-mab/15616">https://www.cellsignal.com/products/primary-antibodies/spt6-d6j9h-rabbit-mab/15616</a>.</p> <p>Anti-SC35 (abcam, ab11826), this antibody has been claimed to react with mouse SC-35 by the manufacturer. Validation data for the antibodies used can be found as follows: <a href="https://www.abcam.com/sc35-antibody-sc-35-nuclear-speckle-marker-ab11826.html">https://www.abcam.com/sc35-antibody-sc-35-nuclear-speckle-marker-ab11826.html</a>. This antibody has been used for IF by Gavrilov et al, 2013, and also confirmed by our data.</p>

## Eukaryotic cell lines

### Policy information about cell lines

Cell line source(s)	HEK293T cells were obtained from ATCC (CRL-3216), Hela cells were obtained from ATCC (CCL-2), and mouse ESCs (E14T, 46C) was a gift from Austin Smith's lab.
Authentication	The cell lines have been used in the lab for over 3 years, so authentications were not performed. The SNRNP70-AID cell line constructed in this study were confirmed by PCR and Western blot.
Mycoplasma contamination	All cell lines have been tested for mycoplasma contamination free by PCR.
Commonly misidentified lines (See ICLAC register)	No cell lines used in this study were found in the database of commonly misidentified cell lines that is maintained by ICLAC and NCB BioSample.

## ChIP-seq

### Data deposition

- ☒ Confirm that both raw and final processed data have been deposited in a public database such as [GEO](#).
- ☒ Confirm that you have deposited or provided access to graph files (e.g. BED files) for the called peaks.

#### Data access links

May remain private before publication.

<https://www.ncbi.nlm.nih.gov/geo/query/acc.cgi?acc=GSE134287> (token: qvmvsqgoxjglxwj)

#### Files in database submission

70AID-0h\_Pol2S2P.bed; 70AID-4h\_Pol2S2P.bed; 70AID-0h\_Pol2S5P.bed; 70AID-4h\_Pol2S5P.bed

#### Genome browser session

(e.g. [UCSC](#))

Provide a link to an anonymized genome browser session for "Initial submission" and "Revised version" documents only, to enable peer review. Write "no longer applicable" for "Final submission" documents.

### Methodology

#### Replicates

ChIP-seq for each condition replicated once.

#### Sequencing depth

70AID-0h\_Pol2S2P: total reads--8762112, uniq mapping ratio--75.41%, reads length--143nt, paired-end;  
70AID-4h\_Pol2S2P: total reads--8373124, uniq mapping ratio--73.72%, reads length--143nt, paired-end;  
70AID-0h\_Pol2S5P: total reads--7259811, uniq mapping ratio--90.16%, reads length--150nt, paired-end;  
70AID-4h\_Pol2S5P: total reads--7373872, uniq mapping ratio--90.49%, reads length--150nt, paired-end.

#### Antibodies

Ser2P Pol II: Cell Signaling Technology, 13499; Ser5P Pol II: Cell Signaling Technology, 13523

#### Peak calling parameters

bowtie2 -x ./mm10 -1 sample\_R1.fastq -2 sample\_R2.fastq -k 1 -S sample.sam  
macs14 -t sample.sam -c input.sam -g mm -n sample\_input -p 1e-5 -B -S

#### Data quality

70AID-0h\_Pol2S2P: FC > 5, FDR < 5%, 5890 peaks;  
70AID-4h\_Pol2S2P: FC > 5, FDR < 5%, 7055 peaks;  
70AID-0h\_Pol2S5P: FC > 5, FDR < 5%, 14780 peaks;  
70AID-4h\_Pol2S5P: FC > 5, FDR < 5%, 16170 peaks.

#### Software

Bowtie2, Bedtools, macs, ngs.plot

## Flow Cytometry

### Plots

Confirm that:

- ☐ The axis labels state the marker and fluorochrome used (e.g. CD4-FITC).
- ☐ The axis scales are clearly visible. Include numbers along axes only for bottom left plot of group (a 'group' is an analysis of identical markers).
- ☐ All plots are contour plots with outliers or pseudocolor plots.
- ☐ A numerical value for number of cells or percentage (with statistics) is provided.

### Methodology

#### Sample preparation

Cells expressing a GFP reporter fused with different insert were harvested, and perform FACS analysis directly to measure the GFP intensity change. The flow cytometry was used for a mini-screen, no plot shown. The summary of GFP intensity changes was shown in Extended Data Figure 3j.

#### Instrument

BDCalibur

#### Software

Data collection: BD FACSDiva 8.0; Data analysis: FlowJo 7.6.1

#### Cell population abundance

No sorting was conducted.

#### Gating strategy

FSC/SSC were used to discern single cells from doublets/multiple cells. Samples without GFP reporter transfection were used to establish boundaries between negative and positive cells.

- ☐ Tick this box to confirm that a figure exemplifying the gating strategy is provided in the Supplementary Information.



# Author Correction: Tertiary lymphoid structures improve immunotherapy and survival in melanoma

---

<https://doi.org/10.1038/s41586-020-2155-6>

---

Correction to: *Nature* <https://doi.org/10.1038/s41586-019-1914-8>

---

Published online 15 January 2020



Check for updates

---

Rita Cabrita, Martin Lauss, Adriana Sanna, Marco Donia, Mathilde Skaarup Larsen, Shamik Mitra, Iva Johansson, Bengt Phung, Katja Harbst, Johan Vallon-Christersson, Alison van Schoiack, Kristina Lövgren, Sarah Warren, Karin Jirström, Håkan Olsson, Kristian Pietras, Christian Ingvar, Karolin Isaksson, Dirk Schadendorf, Henrik Schmidt, Lars Bastholt, Ana Carneiro, Jennifer A. Wargo, Inge Marie Svane & Göran Jönsson

---

In the Acknowledgements section of this Article, the sentence: “The research leading to these results has received funding from the European Community’s Horizon 2020 Framework Programme for Research and Innovation (H2020-MSCA-ITN-2014) under Grant Agreement no. 247634” should be: “This project has received funding from the European Union’s Horizon 2020 research and innovation programme under the Marie Skłodowska-Curie grant agreement no. 641458”. This has been corrected online.



KRISTIN LEE/GETTY

## HACKS TO HELP RESEARCHERS PUT WORDS ON THE PAGE

Productivity coaches, boot camps and online meet-ups can assist scientists with getting their writing done. **By Roberta Kwok**

**H**annah James started to fret about her unfinished thesis in March 2017. The then-fourth-year PhD student in archaeological geochemistry had to write about 60,000 words on her analyses of human teeth. Every couple of weeks since 2015, she had attended sessions organized by her university's research skills and training group that helped students to focus on writing while holed up in a room on campus for several hours or an entire day.

But James was having trouble clarifying the

main points of her thesis, and needed a longer block of time to concentrate and put her ideas on paper. And it was hard for her to work outside the group sessions – she found herself

**“We find ourselves running around and being busy, getting a lot done, but the paper is not getting written.”**

distracted by e-mail or minor details in her graphs. James was hoping to submit her thesis to the Australian National University (ANU) in Canberra in a year's time, but had produced only 10,000 words that seemed usable. “I just hit a point of panic,” she says.

So she signed up for a three-day programme that October called Thesis Boot Camp. For many ANU students who are nearing deadlines, joining the programme signals desperation, says Inger Mewburn, the university's director of researcher development and founder of The

## Work/Careers

Thesis Whisperer, a blog about finishing a PhD. “There’s a lot of crying.”

With 27 other participants, James attended classroom sessions that lasted from Friday afternoon to Sunday evening. Mewburn gave the students exercises, such as writing without using the delete key, to discourage perfectionism. A psychologist offered one-on-one consultations and tips for dealing with challenges such as negative thoughts. And students received a large Lego-like block for every 5,000 words that they produced. James, inspired to dump her thoughts out of her head, wrote more than 20,000.

Having achieved that, she continued to attend writing meet-ups. She still had to put back her thesis deadline, partly because she switched to a part-time PhD programme in December 2017, but she submitted her 78,000-word dissertation in February this year. “I found motivation again,” she says.

James’s story will sound familiar to any researcher who has struggled to complete a paper, dissertation, grant proposal or book chapter. When schedules are crammed with laboratory work, teaching or administration, scientists often delay writing. “We basically find ourselves running around and being busy, getting a lot done, but the paper is not getting written,” says Olga Degtyareva, founder of Productivity for Scientists, a company in Dunfermline, UK, that helps researchers to overcome procrastination and be more productive. Even when scientists do have time, they might endlessly delete and revise, let their attention wander, or be so sensitive to potential criticism of their ideas that they are unable to string sentences together on paper.

And yet writing is crucial to propelling careers. PhD students often need papers on their CV to land postdoctoral posts, and publication records and grant funding can tilt tenure decisions. “You need to be able to show you’ve been productive,” says Anna Clemens, a Prague-based editor and writing coach for scientists.

Some researchers, like James, rely on writing at meet-ups. Others use professional services such as classes or coaching. Productive scientists often make an effort to improve their writing process, whether by scheduling weekly times or using mental hacks to focus. Disentangling a paper’s core ideas, breaking a project down into bite-sized tasks and finding the right software (see ‘Kick-start writing’) can ease the pain.

But the first step is to prioritize writing. “It’s very easy to put it last on the list,” Mewburn says.

### A personal system

Early-career researchers often struggle with barriers to their writing, according to a 2019 study co-designed by Prolifiko, a company in Leeds, UK, that offers coaching and a digital platform to improve writers’ productivity. In 2018, the firm surveyed 593 academics

## KICK-START WRITING

**These software tools and resources might boost productivity.**

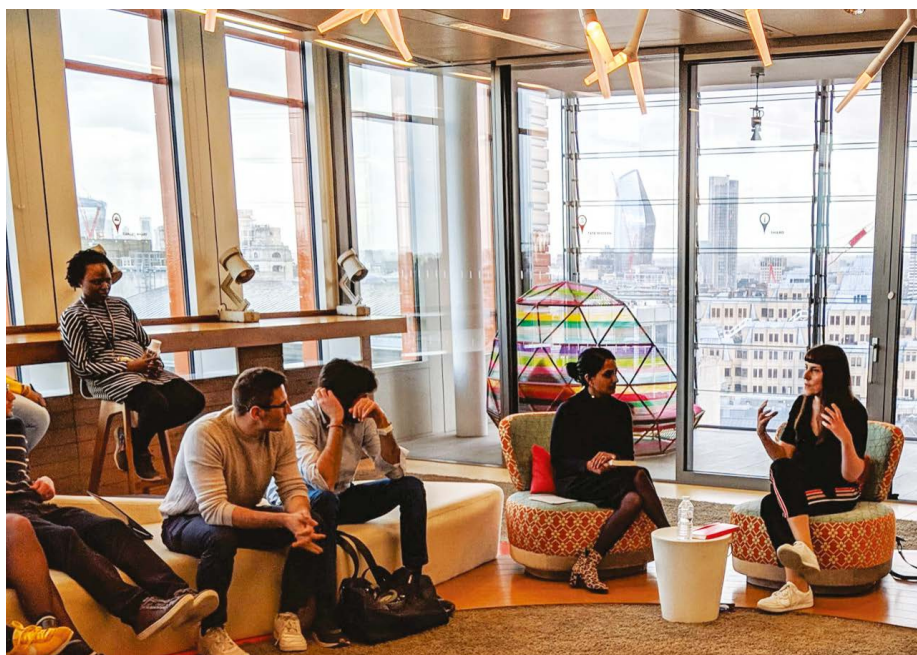
- **Academic Phrasebank.** A website maintained by the University of Manchester, UK, that offers common phrases for academic writing ([www.phrasebank.manchester.ac.uk](http://www.phrasebank.manchester.ac.uk)).
- **Scapple.** Software that helps writers to chart connections between ideas.
- **Scrivener.** Writing software that includes features for outlining, dividing a project into sections and tracking word-count targets.
- **Shut Up & Write!** A community of writers operated by the non-profit organization Writing Partners in San Francisco, California, with writing meet-ups in 47 countries.
- **Freedom** and **LeechBlock.** Productivity apps that block distracting websites.
- **TextExpander** and **Typelt4Me.** Software that expands user-specified keywords into longer phrases.

from various disciplines around the world and categorized participants by career stage: early (up to 5 years’ experience), mid (6–15 years), and late (at least 16 years’ experience). When asked to choose from a list of factors that hindered writing and publishing, 46% of early-career researchers picked “feeling overwhelmed with a lack of control”, compared with 33% and 19% of mid- and late-career participants, respectively. Procrastination

was common; one early-career participant responded, “I play chicken with deadlines,” and another reported, “I get sucked into Facebook ... Hours go by and [I’ve] done nothing.” Others struggled with negative thoughts. “Some days I feel physically sick at writing or reading anything that has to do with my PhD,” one researcher said. Meanwhile, mid-career participants were more likely to cite heavy workloads, everyday interruptions and family commitments as barriers.

But career stage wasn’t rigidly linked to writing success. The team found examples of experienced scholars who were ‘miserable and blocked’ and younger researchers who were ‘super productive’, says Chris Smith, co-founder of Prolifiko. What mattered was having a system, such as setting a writing schedule or asking a co-author to hold the researcher to deadlines. People who consistently used certain tactics to push writing forward tended to experience fewer blocks. Sixty-one per cent of them reported feeling very satisfied with their writing, compared with 20% of those who had never thought about a system, Smith says.

Writing systems span many approaches, Smith notes. Although the conventional advice is to write every day, “it’s not the only way”, he says. What’s important is “having a personal system that suits you”. Mid-career researchers were more likely to set aside weekly or monthly slots (a method called time-blocking), perhaps because they were too busy to write each day. Those who wrote daily reported higher levels of satisfaction, but time-blocking writers tended to publish more, Smith says. People who wrote



**Bec Evans (far right), co-founder of the writing-productivity company Prolifiko, gives a presentation at Google in London.**

CHRIS SMITH



during holidays or sabbaticals were the least satisfied. Smith speculates that they might have felt stressed about completing other work first, or have unrealistic expectations about the amount they could accomplish during their time off.

Daniel Vreeman decided in 2010 that he needed a better system. Vreeman, a biomedical-informatics researcher then at Indiana University School of Medicine in Indianapolis, had been writing during gaps in his packed schedule. But squeezing in half an hour or an hour between meetings was inefficient, he says. So, on his calendar he blocked off half a day per week for writing; if people asked about that slot, he or his assistant told them that he had another commitment. Later, Vreeman increased the block to a full day on Fridays. Although he makes exceptions for travel or unavoidable administrative work, meeting his goal more frequently “is better than not meeting it at all”, says Vreeman, who now works at a satellite office in Fishers, Indiana, for the non-profit research institute RTI International in Research Triangle Park, North Carolina. Each year, he writes on average 4 papers, 6 grant proposals, 8 conference abstracts, 10 blog posts, 10 technical documents, 20 grant progress reports and a book chapter.

Researchers with more harried schedules might find Vreeman’s method unfeasible, but they can still be productive. In early 2014, structural engineer Eva Lantsoght was teaching three new classes at the University of San Francisco de Quito in Ecuador. Scheduling more than a 2-hour block for writing papers was often “impossible”, she says. So Lantsoght broke each paper into small tasks and tackled them during 1- or 2-hour slots. For motivation, she sometimes used the ‘pomodoro’ time-management technique, which involves doing 25 minutes of focused work at a time. In this way, Lantsoght published eight papers based on her dissertation over the following two years.

After learning to deal with overwhelming demands during her physics research career, Degtyareva set up Productivity for Scientists in 2011. In her online courses, she provides her students with productivity strategies, such as telling them to choose a target journal and download the guidelines and manuscript template. “You can literally start filling in the blanks,” she says. Students must complete one task per day, and other participants hold them accountable.

In 2013, Marina Cortês, then a postdoc in cosmology at the University of Edinburgh, UK, was feeling uninspired. She would make herself try to write a paper by “brute force” even when she was tired. After seeing a presentation by Degtyareva, Cortês signed up for the writing class, which, she says, helped her to prioritize rest and well-being. She started

sleeping more and working with greater focus for shorter periods. Cortês, now a cosmologist at the Perimeter Institute for Theoretical Physics in Waterloo, Canada, wrote three papers over the course of those classes. One was highlighted in a viewpoint article that year in the online magazine *Physics*, and another won the 2014 Buchalter Cosmology Prize.

Some researchers feel motivated to write by participating in meet-ups. Shut Up & Write!, a community operated by the non-profit organization Writing Partners in San Francisco, California, runs free writing meet-ups year-round in 47 countries. And academic researchers can join an online event called AcWriMo every November to set themselves ambitious writing goals and tweet about their

**“I don’t think the best strategy is to just sit down and start writing.”**

progress. PhD students can look for thesis boot camps offered by their institution or local facilitators; for example, freelance writer and facilitator Peta Freestone, based in Edinburgh, designed an early version of the ANU boot camp and has since run many such programmes in Europe and Asia.

### Find the story

Sometimes, the problem is not time or motivation, but a lack of focus. Degtyareva advises clients to choose one paper – say, the easiest of the ones they wish to write. And Clemens says that scientists should work out the problem that the paper addresses and the key message before tackling a draft. “I don’t think the best strategy is to just sit down and start writing,” she says. When Clemens edits papers by researchers who haven’t done this preparation, she sometimes deletes entire paragraphs that aren’t relevant.

Diagramming ideas can help, Mewburn says. She recommends using software called Scapple to create ‘mind maps’ – concepts connected by lines. Mewburn also suggests constructing a literature-review matrix, a table in which each column is a relevant paper and each row a theme; scientists should fill each cell with what that paper says about that theme. Seeing whether each study leaves one or more themes unaddressed helps researchers to identify gaps on which their study could shed light, Mewburn says.

Communicating research is fundamental to scientists’ jobs, notes Clemens. “If you’re a scientist, you’re a writer,” she says.

**Roberta Kwok** is a freelance writer in Kirkland, Washington.

## nature masterclasses

### Online Course in Scientific Writing and Publishing

Delivered by Nature Research journal editors, researchers gain an unparalleled insight into how to publish.

→ Try a free sample of the course at [masterclasses.nature.com](https://masterclasses.nature.com)



Bite-size design for busy researchers  
Subscribe as a lab or institution

W [masterclasses.nature.com](https://masterclasses.nature.com)

in Follow us on LinkedIn

f Skills and Careers Forum for Researchers

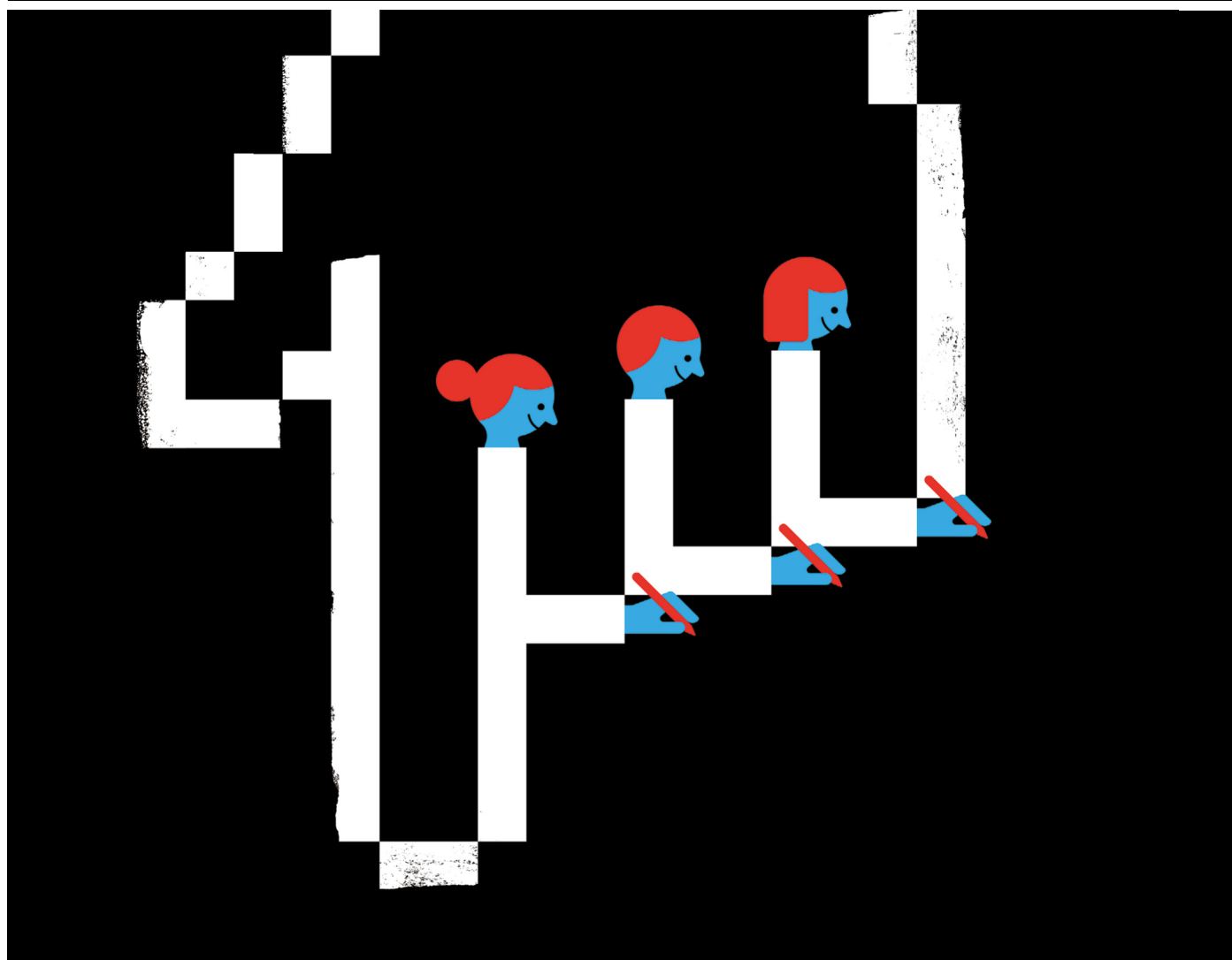


ILLUSTRATION BY THE PROJECT TWINS

# COLLABORATIVE WRITING: BEYOND GOOGLE DOCS

A small but growing suite of tools allows researchers to author and edit scientific documents as a team, no e-mail required. **By Jeffrey M. Perkel**

**D**raft scientific manuscripts are typically confidential. So, when Elana Fertig was asked to take a look at an in-development paper on a functional gene-annotation strategy, she expected to receive the file in a private e-mail. What she got was a public announcement, shared on Twitter.

The paper had been written by Olga Botvinnik, a computational biologist at the Chan Zuckerberg Biohub in San Francisco, California, who is an advocate of the global movement to make research more accessible. In November 2019, as Botvinnik started preparing her paper, she decided to try this open-science

ethos out for herself. “I wanted to walk the walk of open science,” Botvinnik says.

Botvinnik managed her paper as if it were open-source software. She wrote it in a plain-text editor and placed text files alongside data sets and code for generating figures on the code-sharing site GitHub. She invited her four co-authors to submit edits using Git, software that tracks precisely how and when a file has been changed. And she used a dedicated tool called Manubot to render the document as a user-friendly manuscript, which she then published online and tweeted to the world.

Fertig, a computational biologist at the Johns Hopkins School of Medicine in

Baltimore, Maryland, says it was a “funny experience” to be tweeted an unpublished paper. “It’s a very different way of writing than the traditional academic science of not putting it out before it’s a finished product.”

Botvinnik’s manuscript was just a shell at this point: two of the figures were placeholders, and the methods section read, “We did things.” But, she says, the fact that the draft was publicly accessible made it easy to solicit feedback from co-authors and the broader community. “It’s definitely been very, very helpful to be able to show someone, ‘Here’s what I’m thinking so far. Here are some figures; here’s some text. What do you think?’”



Say ‘collaborative writing’ and most researchers probably think of Google Docs, the ubiquitous word processor that allows multiple authors to co-edit a document online in real time. But Google Docs lacks features that some scientists require, such as reference management, support for code and data and the ability to directly submit articles to journals and preprint servers.

Manubot is one of a small but growing number of tools specifically designed for collaborative writing; others include Overleaf, Authorea, Fidus Writer and Manuscripts.io. These tools not only close some of the key feature gaps, but also provide a glimpse of where scientific communication might move next.

## Partners in editing

Most collaborative writing tools offer researchers a range of useful functions. Team members can keep documents private or share them with select collaborators; track changes and comment on the text; and edit documents simultaneously or asynchronously with their collaborators.

Science-focused programs supplement those with features aimed at the research community, such as built-in citation management. (Some citation managers can integrate with Google Docs using plug-ins, such as Zotero and Paperpile.) Users can generally import libraries from reference managers such as Zotero or Mendeley, or query external databases directly. The ‘cite’ button in Authorea, for example, allows users to search PubMed or CrossRef, or pull in articles by DOI or URL. In Fidus Writer, references can be added from Zotero with a simple drag-and-drop.

Manubot features cite-by-identifier, which builds bibliographies using a DOI, a PubMed or arXiv identifier or a URL, without the need for a reference manager. Inserting “@doi:10.1371/journal.pcbi.1007128” into a Manubot article, for instance, instructs the tool to find and insert a reference to the paper itself.

Botvinnik calls this approach “pretty magical”, because it circumvents the problem of researchers using (and trying to synchronize) different reference managers and libraries. “I like that I can just use the DOI and it works, and everyone else knows that there is one source of truth for the citation: the DOI,” she says.

Authorea and Overleaf support LaTeX, the typesetting language preferred by physicists, mathematicians and computer scientists. In 2017, CERN, Europe’s particle-physics laboratory near Geneva, Switzerland, adopted Overleaf as its preferred collaborative authoring platform; some 4,800 users have signed up, says CERN computing engineer Nikos Kasious. LaTeX is quite an advanced system, however, so Authorea and Manubot might be better options if a simpler file format is needed. Both use the plain-text language Markdown.

Using Authorea and Manuscripts.io, authors can embed and execute software code in their

articles, and bundle figures together with the data used to create them – such features support computational reproducibility. “The intention is that you can create dynamic representations of your work, which include code, data and figures, and the narrative, all versioned together,” says Matias Piipari, founder of Manuscripts.io, which (like Authorea) is now owned by the publisher Wiley.

## “As such tools gain traction, scientific articles become ever more dynamic.”

For those who prefer Google Docs, New Zealand-based Stencila is developing a plug-in that allows authors to enhance documents with executable code blocks, data tables and equations. Based on steganography, a cryptographic trick in which data are encoded in images, Stencila’s plug-in was written to “bridge that gap between the coders and the clickers”, says founder Nokome Bentley. “It’s taking the code to the environment that clickers are used to.”

## Coder workflows

Manubot, by contrast, tends to appeal to coders. Developed in the laboratory of bio-informatician Casey Greene at the University of Pennsylvania in Philadelphia, the tool was designed to manage the writing of a review article on deep-learning – and coordinate its three dozen authors. The challenge: keeping track of which collaborators contributed which bit of text, line by line. “We expected to have a large number of contributors and we wanted to be able to look at the ‘atomic’ changes of one person and one group of changes,” Greene says. That is, instead of navigating a tangled mess of tracked changes, Greene wanted to be able to review each change individually, and to keep the online draft automatically up to date.

Manubot solves those problems by cobbling together various open-source tools, says Daniel Himmelstein, a Greene lab postdoc who helped to lead Manubot’s development. These include Pandoc, which provides file-conversion functionality, and GitHub Actions, which automates functions such as document creation. To set up a Manubot project, users clone a dedicated GitHub repository to their computer and modify it using a standard programming text editor, such as Emacs or SublimeText. Changes are then pushed back to GitHub, which logs them and rebuilds the document in HTML, Word or PDF format. Collaborators can modify the manuscript by submitting changes in the form of a GitHub ‘pull request’ (explore our example Manubot project at [go.nature.com/39eqosg](https://go.nature.com/39eqosg)). The result is elegant, but complex.

And all of this extra functionality can require advanced programming skills. Fertig has

written grant applications using Manubot, and is comfortable with GitHub. But she won’t be using Manubot to write collaborative papers, because the level of programming it involves tends to be beyond the reach of her clinician co-authors. “There’s no way they have the bandwidth to pick up Manubot,” she says.

## Easing submission

Increasingly, developers are fitting these tools with features to better encapsulate the scientific process. Some, for instance, support JATS XML, a file format commonly used in scientific publishing.

JATS XML is a structured, semantic file format that provides a rich set of metadata tags for article elements such as author names, article sections, funding sources and database accession numbers. Giuliano Maciocci, head of product and user experience at the open-access journal *eLife*, explains that the format “decouples the structure of the article from its presentation”, which makes the data easier to search, access and manipulate.

Editors typically build documents by converting author-submitted files into a format they can publish in, Maciocci says – a labour-intensive, error-prone process. To help automate this process, *eLife* is developing a tool called Libero Editor, which it hopes to release this year. Based on the Texture editor, the tool will allow *eLife* staff and authors to create and work with JATS XML documents from beginning to end. Manuscripts.io can already import JATS-formatted content, Piipari says, and it, together with Fidus Writer and the Stencila plug-in can export to that format as well.

Authorea allows authors to directly submit articles to around 41 journals and preprint archives, according to founder Alberto Pepe – and to embed interactive figures, executable code and data. Roberto Peverati, a computational chemist at the Florida Institute of Technology in Melbourne, was asked to contribute to one such journal, Wiley’s *International Journal of Quantum Chemistry*, in part to test drive Authorea. “I found it really very pleasant,” Peverati says.

As such tools gain traction, scientific articles become ever more dynamic – and responsive. On 20 March, Greene’s postdoc researcher Halie Rando created a Manubot project to try to make sense of the exploding COVID-19 literature. Within days, dozens of researchers had expressed interest in contributing. “With something as fast-moving as COVID-19, we have an urgent need for consilience, but many members of the scientific community are more isolated than usual,” Rando explains. Manubot provides a forum for these far-flung researchers to work together. “We hope to update it rapidly as new information emerges.”

**Jeffrey M. Perkel** is technology editor at *Nature*.



## Where I work Maria Josefa Verdugo

Photographed by  
Esther Horvath.

**E**verything's cold when you're handling an Arctic Ocean ice core about 500 kilometres from the North Pole: your feet, your fingers, your face.

The air temperature here can be as low as  $-35^{\circ}\text{C}$ . At that point, every part of me wants to go back inside the RV *Polarstern* – a German icebreaker and my research home – to take off my wet latex gloves and warm up.

I convince myself that I'll be OK. Another researcher watches me closely for signs of frostbite, and I'm watching her too. A crew member keeps an eye out for polar bears. I summon my self-control and finish my work – measuring the ice's temperature, salinity and methane concentrations. It's all part of my PhD research on marine geochemistry at the Alfred Wegener Institute for Polar and Marine Research in Bremerhaven, Germany.

I spent from September to December 2019 on the *Polarstern* as part of an expedition called MOSAiC (Multidisciplinary drifting Observatory for the Study of Arctic Climate). This multinational project, running till September, is the first year-round expedition to explore climate in the far north – one

of the largest uncharted areas in climate research. About 60 researchers and 40 crew members live on board at a time – a small community drifting along with the ice pack. This picture was taken in mid-afternoon on 10 November, well after the Sun had dropped below the horizon for the long polar night.

I'm from Chile, and I didn't grow up around a lot of cold, snow and ice. But I've learnt to embrace it. During my free time, I would sometimes wrap up in heavy winter wear for short walks on the ice with some friends and a polar-bear guard. We were too far north to see the northern lights, but the ice glowed in starlight and moonlight. Sometimes we didn't even need headlamps.

I feel lucky to be a part of this tremendous expedition. It's an adventure. And I also have a lot of time to think. Time moves at a different speed on the ice.

**Maria Josefa Verdugo** is a PhD student in marine biogeochemistry at the Alfred Wegener Institute for Polar and Marine Research in Bremerhaven, Germany.

**Interview by Chris Woolston.**